MC 2017 Lausanne

Microscopy Conference

21–25 AUGUST 2017
LAUSANNE | SWITZERLAND

PROCEEDINGS

www.mc2017.ch

conventus
CONGRESSMANAGEMENT

DREILÄNDERTAGUNG
The MC 2017 is an EMS extension, and jointly organized by
SSOM – Swiss Society for Optics and Microscopy
ASEM – Austrian Society for Electron Microscopy
DGE – German Society for Electron Microscopy e.V.

Content

PL.01
The future of electron microscopy

G. Van Tendeloo[1,2], S. Bals[1], S. Van Aert[1], J. Verbeeck[1,] J. Hadermann[1], D. Schryvers[1]

[1]EMAT, University of Antwerp, Belgium
[2]NRC, Key State Laboratory, Wuhan University of Technology, Hubei, China

staf.vantendeloo@uantwerpen.be

In order to look into the future of electron microscopy it is important to first look into the past: where do we come from? From the initial start with Ruska till about the eighties electron microscopy was mainly descriptive. Imaging was only in TEM, the resolution was limited to a few Angstrom and neither EDX nor EELS were really well developed. Only at the end of the 20th century and particularly after the introduction of aberration corrected imaging, scientists focused on quantitative interpretation of the results.
This is the way modern electron microscopy should further evolve in the future. Too many researchers still consider an electron microscope as a big (and expensive) magnifying glass. One should see EM as a very valuable analytical instrument, able to provide quantitative data on structure, composition and electronic structure. In that way the results can not only be used as input for theoretical predictions, but also contribute to explain and understand physical/chemical/mechanical properties of (nano)materials. In this lecture we will provide illustrative examples for this.
Another dangling problem in EM is the study of soft matter. Beam damage often hampers correct or detailed interpretation of the results. Not only polymers, but also e.g. organic solar cell materials or metal organic frameworks (MOFs) suffer from this effect. A new generation of very sensitive cameras helps to overcome part of this problem, but a correct interpretation of these highly underexposed and noisy images is not a straightforward problem and correct statistical methods/algorithms should be used in order not to induce artifacts.

Acknowledgements:
We are very grateful for collaborations with Artem Abakumov, Rolf Erni, Marta Rossell, Tom Wilhammar, Jean-Marie Tarascon, Luis Liz-Marzan, Daniel Vanmaekelbergh. Collaborators Annick De Backer, Karel Van den Bos, Thomas Altantzis, Maria Meledina and Stuart Turner are highly acknowledged. Financial support mainly was provided by FWO, IAP, ERC and European Projects ESTEEM2, ESMI and Eurotapes.

PL.03
Field mapping for semiconductor research by off-axis electron holography and diffraction based techniques

D. Cooper[1,2], V. Boureau[1,2], B. Haas[1,2], N. Bernier[1,2], J.-L. Rouviere[1,2]

[1]Univ. Grenoble Alpes, Grenoble, France
[2]CEA, LETI, MINATEC Campus, Grenoble, France

david.cooper@cea.fr

In this presentation we will provide a brief introduction discussing the motivations behind the miniaturization of semiconductor devices which leads to the requirement of transmission electron microscopy to provide characterisation. We will focus on techniques that can be used to measure fields with nanometer resolution. Off-axis electron holography which uses an electron biprism to interfere an electron wave that has passed through a specimen with one that has passed through only vacuum to form an interference pattern known as the hologram. From the hologram the modulations in electron phase can be measured from which the electrostatic potential calculated. Other techniques such as differential phase contrast and diffraction based techniques (4D STEM) can be used to recover information about the potentials from the deflection of a transmitted beam. In this presentation we will show how they can be used in a semiconductor research environment to provide useful information about dopant potentials and strain fields with nm-scale resolution.

We will compare results acquired by the different techniques on both dopant and deformation mapping. Figure 1(a) shows a potential map of a pMOS device that has been acquired by off-axis electron holography. Although the measurement of the carrier concentration is complicated due to artifacts with specimen preparation and charging under the electron beam, the position of the electrical junction can be measured. Figure 1(b) shows a field map acquired by DPC. Here a segmented detector has been used to determine the deflection of a convergent beam as it passes through the doped specimen. In this presentation we will discuss the advantages and disadvantages of using these different techniques on different types of semiconductor specimens such as silicon CMOS devices and also IIIV materials for light emission.

Deformation is a key parameter used to improve device performance. Figure 1(c) shows a STEM image of a SiGe recessed source and drain device. Dark field electron holography has been performed on the device and deformation maps for the (d) in-plane, εx and (e) growth, εy directions can be seen. These experimental results can be compared to those obtained using precession electron diffraction shown in Figure 1(f) and 1(g) which shows deformation maps for the εx and εy directions respectively.

We will also present results obtained by switching a resistive memory device in-situ in the TEM. Different types of $SrTiO_3$ devices have been electrically connected using a movable probe to apply a voltage to the electrode. The device is examined by combinations of STEM, electron energy loss spectroscopy (EELS) and holography to demonstrate that the movement of oxygen vacancies leads to changes in the electrical conductivity from a high resistive (HRS) state to a low resisitive state (LRS). Figure 2 shows where a resistive device has been switched and the movement of oxygen vacancies mapped with 1 nm spatial resolution by comparing the changes in the Ti L3 eg and 2tg edges which correspond to changes in the Ti – O bonds. We will discuss the experimental procedure and prospects for routine in-situ biasing experiments in the TEM.

These experiments have been performed on the platforme nanocharacterisation (PFNC) at Minatec.

We thank the European Research Council for funding Stg:305535 “Holoview”.

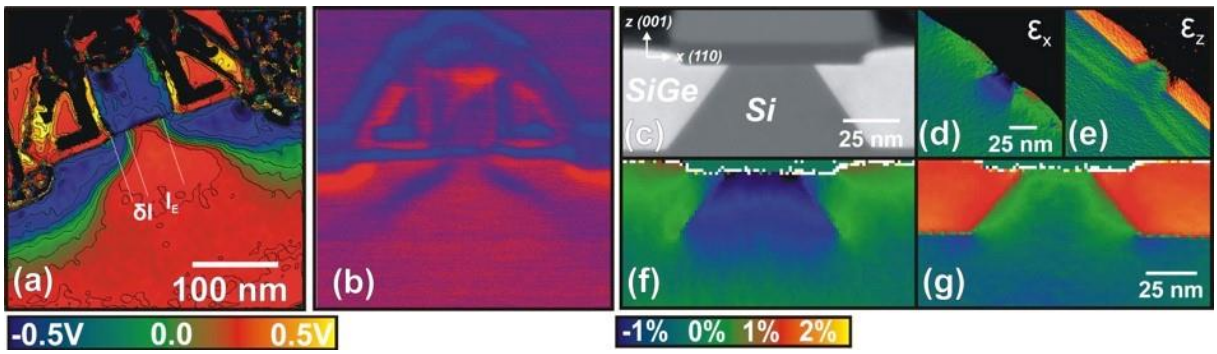

Figure 1. (a) Potential map of a pMOS device acquired by off-axis electron holography. (b) Field map of the same device acquired by DPC. (c) STEM image of a SiGe/Si device. (d) and (e) show εx and εy maps acquired by dark field electron holography. (f) and (g) show maps of the same device acquired using precession diffraction.

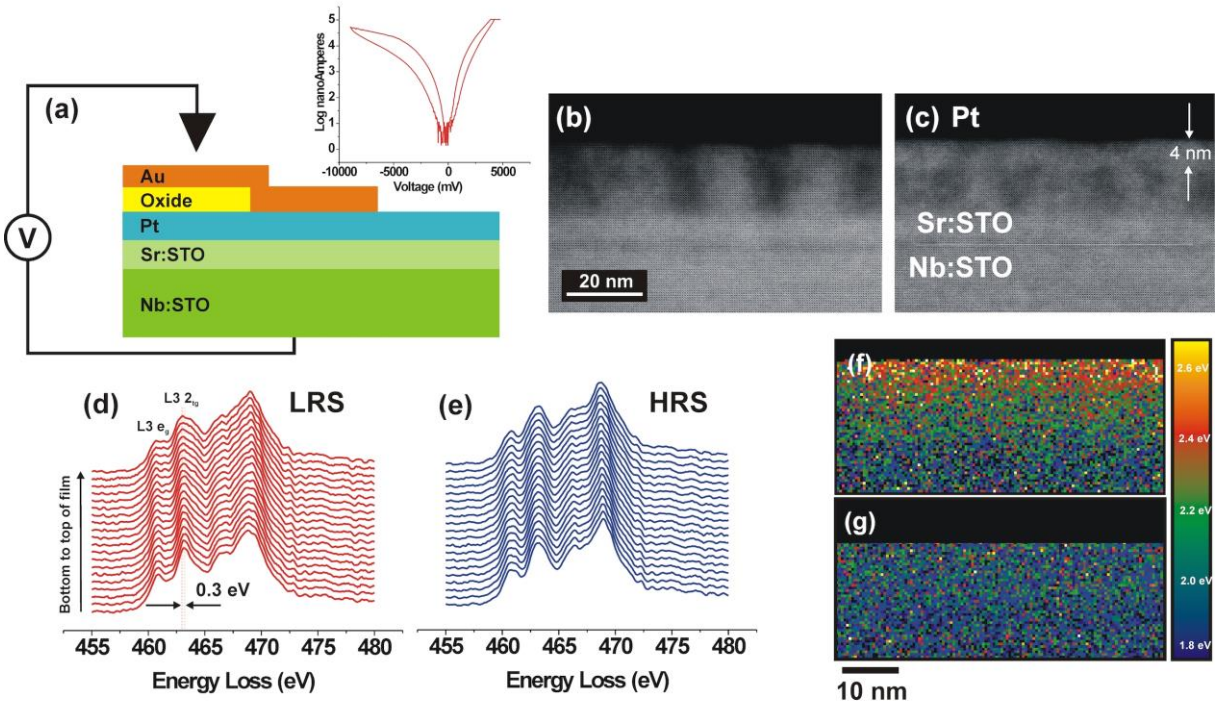

Figure 2. (a) Shows schematic of specimen examine and VI characteristics during forming. (b) and (c) HAADF STEM images of the Sr:STO active layer before and after forming. (d) and (e) Ti EELS spectra acquire across region of interest for the device in a LRS and HRS showing changes in the L3 eg and t2g peaks across the active layer. (f) and (g) maps showing the shift of the L3 2tg peak for devices in a LRS and HRS state respectively.

PL.04
Cryo-electron microscopy of biological particles in vitrified water

J. Dubochet[1]

[1]University of Lausanne

jacques.dubochet@unil.ch

Biological material is predominantly made out of water but water evaporates in the vacuum of an electron microscope.
Cryo-electron microscopy wants to keep water in the specimen by cooling it at a temperature where evaporation is negligible, but water freezes upon cooling and ice is as bad as no water.
Brüggeller and Mayer (1980) discovered that liquid water can be vitrified namely, it can be made solid without changing significantly its structure (so we believe). We succeeded in turning vitrification into a simple and reproducible method for preparing biological samples in a thin film of immobilised water (Adrian et al., 1984). With this method we could obtain a 3-d model of a virus at 35 Å resolution (Vogel et al., 1986).
Since then, many scientists contributed to the staggering advance of image processing; cryo-electron microscopes have been further improved for the task; lately a breakthrough was achieved with new electron detectors. Thanks to these efforts, it is now possible to achieve close to atomic resolution for single particles in vitreous water on a nearly routine basis. Improving the resolution by a factor of 10 is truly a remarkable achievement since it means that the density of information has been multiplied by one thousand in 30 years.
Cryo-electron microscopy is entering a new age as a research tool in biochemistry and in molecular medicine.

[1] Mayer, E. & Brüggeller, P. (1980). Complete vitrification in pure liquid water and dilute aqueous solutions. *Nature, 288*, 569-571.
[2] Adrian, M., Dubochet, J., Lepault, J. & McDowall, A. W. (1984). Cryo-electron microscopy of viruses. *Nature, 308*, 32-36.
[3] Vogel, R. H., Provencher, S. W., Von Bonsdorff, C.-H., Adrian, M., & Dubochet, J. (1986). Envelope structure of semliki forest virus reconstructed from cryo-electron micrographs. *Nature, 320*, 533-535.

ERL.01
The history of phase plates and their applications in cryo-EM

R. Danev[1]

[1]Max Planck Institute of Biochemistry, Martinsried, Germany

danev@biochem.mpg.de

Phase plates are devices that produce phase contrast and thus greatly improve the visibility of low-contrast samples in the transmission electron microscope (TEM). They were proposed seventy years ago by Boersch [1], in the early days of development of the electron microscope. TEM phase plates are based on the same optical principles as phase plates used in light microscopy, originally developed by Zernike in the 1930s. However, the practical implementation for TEM is much more challenging because of the electrostatic charge of electrons, their strong interactions with matter and much smaller device dimensions.

In the 1950s–70s several groups experimented with phase plates for TEM but due to practical problems, mainly related to beam-induced charging and contamination, they were not able to produce long-lasting usable phase plates (for a detailed historical overview see ref. [2]). In addition to the practical difficulties, the need for a working phase plate at that time was not very strong. Biological samples were prepared using resin embedding and heavy metal staining and phase plates were mainly foreseen as a way to reduce defocus artefacts by enabling in-focus phase contrast. The research and experimental work on phase plates had a hiatus during the 1980s–90s when other performance enhancing devices, such as field emission guns, energy filters, Cs-correctors, CCD cameras, computer controlled optics etc., became main development targets.

In 1998, motivated in part by the advent of cryo-electron microscopy (cryo-EM) and its inherent contrast problems, Prof. Kuniaki Nagayama at the National Institute for Physiological Sciences, Okazaki, Japan, started a project on the development of a usable phase plate. I joined his lab as a Ph.D. student as we managed to produce a relatively well-performing thin film Zernike phase plate (ZPP) [3]. In the following decade we continued research and applications of the ZPP and developed other types of phase plates, such as the half-plane Hilbert phase plate [2]. Despite the encouraging results, including cryo-EM single particles and cryo-tomography applications, the thin film phase plates continued to present practical challenges in terms of short lifespan, difficulty of use and fringing artefacts.

In 2011 I joined the department of Prof. Wolfgang Baumeister at the Max Planck Institute of Biochemistry, Martinsried, Germany. In that year, we started a joint project with the FEI Company (now Thermo Fischer Scientific) with the aim of developing an easy-to-use reliable phase plate suitable for ubiquitous use in cryo-EM. During the project we discovered a peculiar behavior of heated amorphous carbon films which developed negative potential on their surface when irradiated with an intense electron beam. This led to the development of the Volta phase plate (VPP) [4], named after the Volta potential above the surface of a material. The VPP resolved most of the practical issues of the ZPP – it was much easier to use, had a long lifespan and did not generate fringing artefacts. In the last three years our efforts shifted from development to workflow improvement and applications. The VPP has already demonstrated significant performance benefits in cryo-EM single particle analysis and cryo-tomography (Fig. 1) [5].

[1] H Boersch H, Z. Naturforschg. **2a** (1947) p. 615.
[2] K Nagayama, J. Electron Microsc. **60(s1)** (2011) p. S43.
[3] R Danev and K Nagayama, Ultramicroscopy **88** (2001) p. 243.
[4] R Danev *et al*, PNAS **111** (2014) p. 15635.
[5] R Danev and W Baumeister, Curr. Opin. Struct. Biol. **46** (2017) p. 87.
[6] J Mahamid *et al*, Science **351** (2016) p. 969.

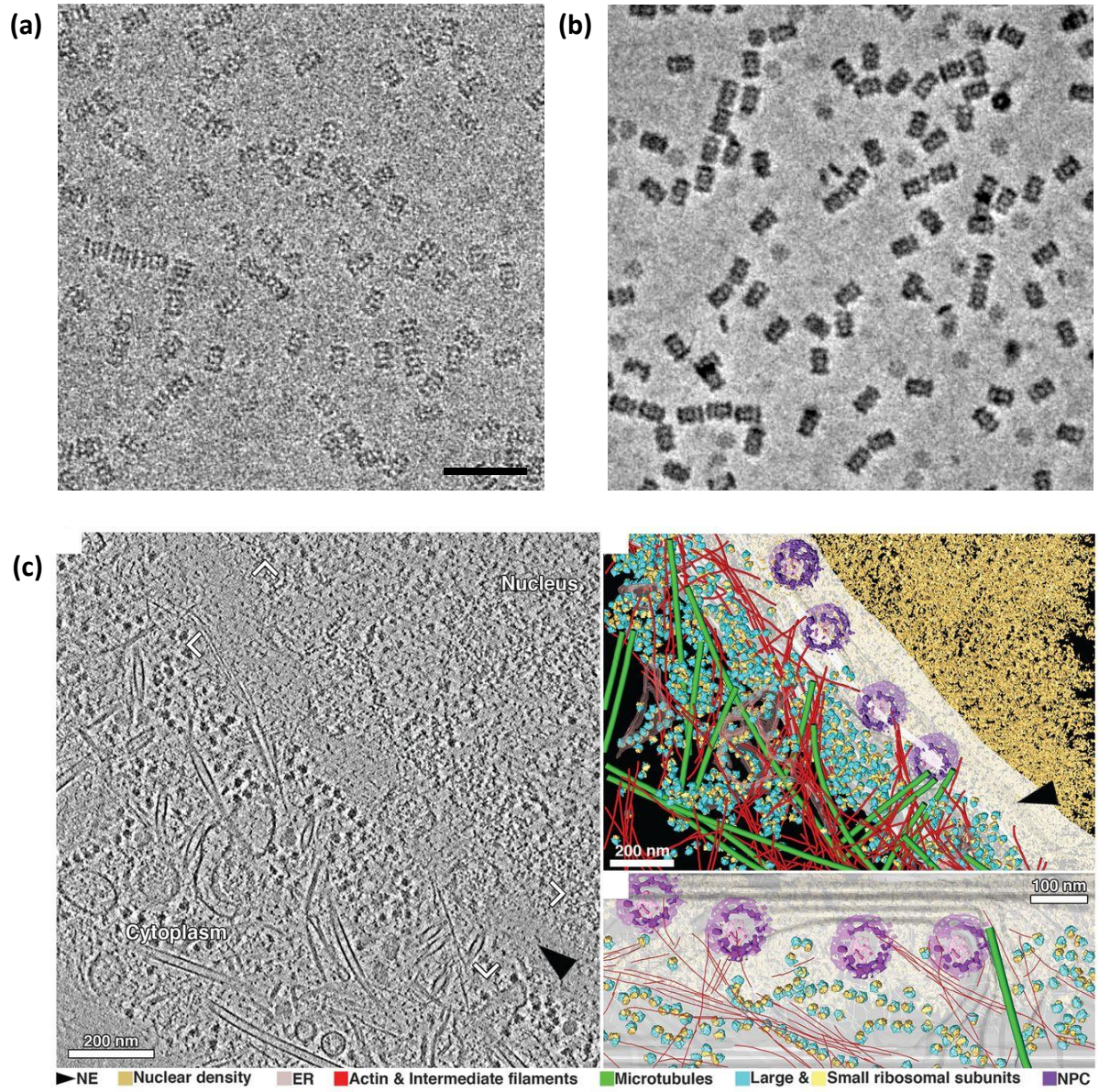

Figure 1. Cryo-EM with the Volta phase plate (VPP). (a) Conventional 1.5 mm defocus phase contrast image images of 20S proteasome molecules embedded in vitreous ice. (b) VPP in-focus image of the same sample. (c) VPP cryo-tomography of the HeLa cell nuclear periphery [6]. Scale bar: 50 nm.

ERL.02
New techniques for optimum quantitative analysis of electron microscopy data

S. Van Aert[1]

[1]EMAT, University of Antwerp, Antwerp, Belgium

sandra.vanaert@uantwerpen.be

In recent years, visual interpretability of transmission electron microscopy images was significantly improved by aberration corrected electron optics. Still, in order to properly interpret all information contained in an atomic resolution image, quantitative methods are required. For this purpose, statistical parameter estimation theory has been shown to provide reliable results. The aim of parameter estimation theory is to measure unknown structure parameters as accurately and precisely as possible from experimental images [1, 2]. Use is made of a physics-based model describing the interaction of electrons with the material under study, the transfer in the microscope, and the detection. The unknown structure parameters are estimated by fitting this model to the experimental images.
Progress in applying statistical parameter estimation theory enables us to measure unknown structure parameters with high accuracy and precision from experimental images. An overview is shown in Figure 1. This theory allowed us to measure 2D atomic column positions with a precision down to picometer scale [3, 4] or to measure the octahedral tilt in manganite heterostructures [5]. In terms of chemistry, HAADF STEM is often used. While such images are sensitive for the chemical composition, direct visual interpretation becomes inadequate whenever the difference in atomic number of distinct atomic column types is small or if the signal-to-noise ratio (SNR) is poor. To overcome this problem, statistical parameter estimation theory is used to quantify the total intensity of scattered electrons in each atomic column [6]. These intensities or so-called scattering cross sections are used to differentiate between atomic columns with different composition. Experiments on images of perovskite thin films show that columns with a difference in atomic number of only 3 can be discerned. The high chemical sensitivity of this model-based method could be further exploited to count the number of atoms with single atom sensitivity [7, 8]. By combining counting results obtained from images under different viewing directions, we have been able to reach atomic resolution in 3D which was an important milestone in the development of new electron microscopy techniques in general [7]. For heterogeneous materials, atom-counting is becoming even more challenging since small changes in atom ordering in the column have an effect on the scattering cross sections. To circumvent the need for time-consuming image simulations to compute scattering cross sections of mixed columns, an atomic lensing model is proposed based on the principles of the channelling theory. In this manner, the number of both Ag and Au atoms could be counted from an experimental HAADF STEM image of a Ag-coated Au nanorod [9]. Recently, we have shown that new possibilities emerge when combining atom-counting from a single projection image with energy minimisation to obtain a relaxed 3D reconstruction [10-12]. In Figure 2, this method is validated against state-of-the-art compressive sensing electron tomography [12]. For this purpose, three projected ADF STEM images of a Au nanorod have been acquired along different major zone axes. The close match confirms the accuracy of this new atom-counting/energy minimization approach.

[1] S. Van Aert et al., IUCrJ 3 (2016) 71.
[2] A. De Backer et al., Ultramicroscopy 171 (2016) 104.
[3] S. Bals et al., Physical Review Letters 96 (2006) 096106.
[4] S. Van Aert et al., Advanced Materials 24 (2012) 523.
[5] Z. Liao et al., Nature Materials 15 (2016), 425.
[6] S. Van Aert et al., Ultramicroscopy 109 (2009) 1236.
[7] S. Van Aert et al., Nature 470 (2011) 374.
[8] S. Van Aert et al., Physical Review B 87 (2013) 064107.
[9] K. van den Bos et al., Physical Review Letters 116 (2016) 246101.
[10] S. Bals et al., Nature Communications 3 (2012) 897.
[11] L. Jones et al., Nano Letters 14 (2014) 6336.
[12] A. De Backer et al., Nanoscale 9 (2017) 8791.

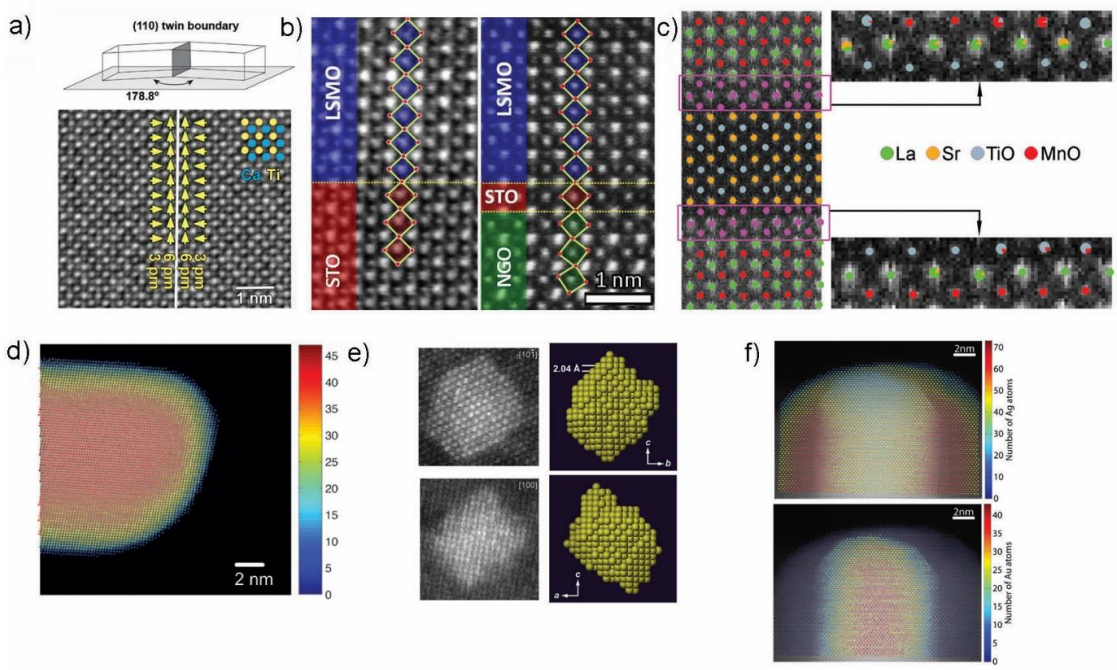

Figure 1. (a) Locating 2D atomic columns down to picometer scale precision [4]. (b) Measurement of oxygen octahedral tilt in manganite heterostructures [5]. (c) Quantitative characterisation of an interface where the difference in atomic number between the TiO and MnO columns is only 3 [6]. (d) Counting the number of atoms in a Au nanorod with single atom sensitivity [8]. (e) 3D reconstruction of a Ag particle by combining atom counts obtained from two viewing directions [7]. (f) Number of Ag and Au atoms counted from an experimental HAADF STEM image of a Ag-coated Au nanorod [9].

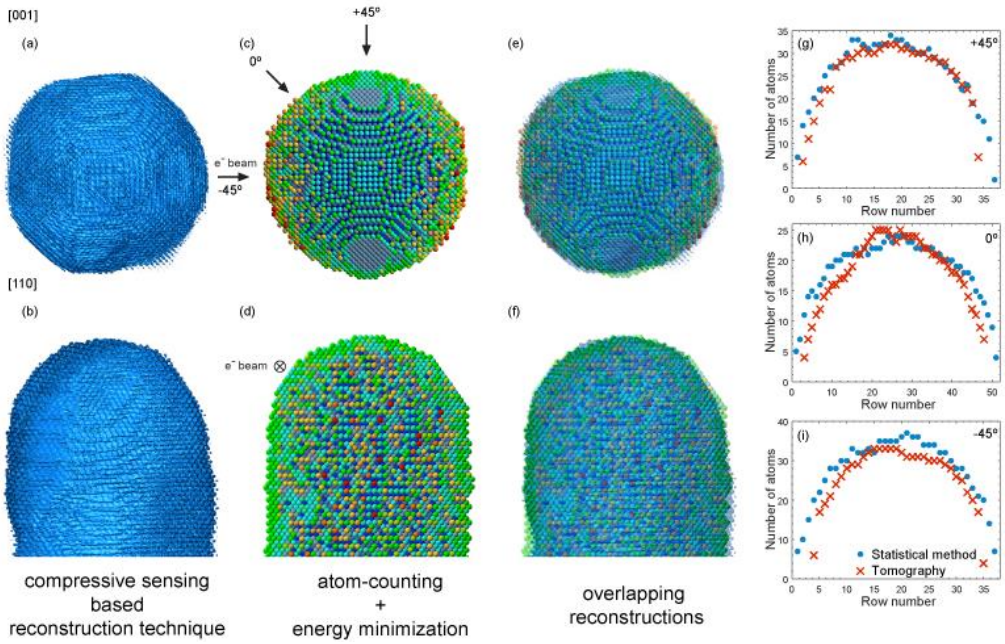

Figure 2. Comparison of the atom-counting/energy minimization and atomic resolution tomography reconstruction. (a,b) Compressive sensing based reconstruction of a Au nanorod. (c,d) Reconstruction based on the atom-counting/energy minimization approach (the coloring of the Au atoms indicates the nearest neighbor coordination). (e,f) Overlap of reconstructions shown in (a,c) and (b,d). (g,h,i) Comparison of atom-counts along different orientations from an orthogonal slice from the compressive sensing based reconstruction (red crosses) and atom-counting results obtained from the three ADF STEM projection images (blue dots) [12].

HRL
Electron waves for comprehensive analysis of materials properties

Hannes Lichte[1], Felix Börrnert[1], Bernd Einenkel[1], Andreas Lenk[1], Axel Lubk[1], Falk Röder[1], Jan Sickmann[1], Sebastian Sturm[1], Karin Vogel[1], Daniel Wolf[1]

[1]formerly Triebenberg Laboratory*, Technische Universität Dresden, Dresden, Germany
*closed by TU Dresden by September 2016

Hannes.Lichte@Triebenberg.de

Transmission Electron Microscopy is wave optics. The object information is found both in amplitude and phase of the object exit wave. Alas, the intensity image recorded on a detector only represents the amplitude distribution whereas the phase distribution is lost. This means a substantial loss of object information, e.g. about the intrinsic electromagnetic fields in an object, which largely determine the properties.
Phases can only be measured by interference. Therefore, holography offers a powerful means for analyzing the complete electron wave including all object properties encoded in the electron phase, such as electric and magnetic fields. Due to the restrictions of electron coherence, the most powerful method up to now is off-axis image plane electron holography. It allows measuring the object phase shift on the scale reaching from several micrometers down to atomic resolution. Recent developments in Holographic Tomography give access to the 3D-distribution of electromagnetic fields.
At medium resolution with details larger than about 2 nm, the aberrations of the electron lenses can be neglected, and hence the reconstructed wave agrees with the object wave. Thus, the reconstructed phase distribution can directly be interpreted in terms of the object. This is the basis for achieving perfect phase contrast without defocusing or staining hence for determining

- Mean Inner Potentials in solids
- Functional potentials such as drift-diffusion potentials across pn-junctions
- Electric potentials across interfaces
- Trapping of charges at surfaces and interfaces
- Electric potential distributions in charge-modulated structures
- Magnetic fields in and around magnetic structures down to a nanoscale
- Magnetic leakage fields at structural inhomogeneities
- Ordering of magnetic nanoparticles
- Mechanical strain

and others. All these details are significant parts of the object structure, since they determine the functionality, e.g. in semiconductors and magnetics, and hence are indispensable for a comprehensive understanding of their properties.
At atomic resolution, because of the aberrations, amplitude and phase of the reconstructed wave differ considerably from the object wave and hence cannot be interpreted directly. First, the aberrations have to be corrected by appropriate processing. Then, both in amplitude and phase, lateral resolution can be achieved as high as determined by the information limit offered by the TEM used for recording the hologram. The resulting phase images allow details of the atomic structure to be revealed, such as

- Atomic potentials
- Difference of atomic numbers of different constituents
- Number of atoms in an atomic column

Recent developments

- Holographic Tomography. To obtain full 3D-information, the methods of holography and tomography are combined: A tilt series of holograms is recorded, from which the corresponding 2D-phase image series is reconstructed. Following tomographic procedures, from these 2D-images, the 3D-representation is reconstructed, which allows uniquely determining 3D electric potential distributions and magnetic fields as well as elastic and inelastic attenuation coefficients.
- In situ Holography. The better the performance, the more object details contributing to the phase shift have to be considered. Therefore, we have to strengthen in-situ experiments where only the parameter of interest is varied, and hence a better defined insight in solid state science is gained and used for a more detailed and accurate modeling of the substance under investigation.
- Inelastic Holography. By inelastic processes, coherence with respect to the elastic electrons is destroyed. However, the electron wave “newborn” by an inelastic event, such as excitation of a plasmon, has an appreciable area of coherence of about 30nm diameter in the object. This was measured by inelastic holography in an EFTEM path of rays. Strictly speaking, due to

entanglement of the electrons with the object, these phenomena can only be described correctly by density matrices, which incorporate the propagation of coherence through the TEM.

In summary, one can say that, after 60 years of development, electron holography is an established method for comprehensive wave optical characterization of solids including their intrinsic electromagnetic fields. The performance, essentially restricted by quantum noise, allows atomic resolution both laterally and in signal. Any improvement of electron microscopes, such as of lateral resolution and of brightness of the electron gun, will enhance the capabilities of this unrivalled method for nanocharacterization.

MS 1: Functional materials and semiconductors

MS1.001 invited
Interfaces in semiconductor heterostructures – requirements for quantitative, atomically-resolved STEM imaging and their intrinsic structure

A. Beyer[1], K. Volz[1]

[1]Philipps-Universität Marburg, Faculty of Physics and Materials Science Center, Marburg, Germany

kerstin.volz@physik.uni-marburg.de

Introduction: Modern semiconductor devices consist of several different materials, forming a heterostructure. The internal interfaces between the semiconductors often have a decisive influence on the functionality of the devices. Hence, the structure and composition of the interface are important and should be correlated to the growth conditions as well as to the optical and electrical properties of the devices. Modern STEM (Scanning Transmission Electron Microscopy) methods of course provide – especially when aberration correctors are used – the necessary atomic resolution.
Objectives: The interfaces between different semiconductors are quantified at an atomic scale with a special emphasis, which intrinsic interface structure forms depending on the properties of the semiconductor materials. To this end, polar/non-polar interface configurations are examined as well as strained and lattice-matched ones.
Moreover, the factors, which need to be taken into account when aiming for quantitative information across internal interfaces using STEM will also be discussed in this presentation.
Materials and Methods: All semiconductor heterostructures for this study are grown by metal organic vapour phase epitaxy. As an example for a lattice-matched, polar/non-polar interface GaP/Si (001) is investigated. The characteristic interface structure resulting from the charge redistribution at this interface is compared to the also lattice-matched, but non-polar interface in (Ga,In)P/GaAs (001) heterostructures. As examples for strained interfaces Ga(P,As)/GaP as well as (Ga,In)As/GaAs interfaces are investigated.
Aberration-corrected STEM is used to characterize the interfaces at atomic resolution using a double-aberration corrected JEOL 2200 FS. Complementary frozen-phonon simulations using a highly parallelized, home-written code (STEMSalabim) are applied to derive the quantitative element depth profiles. Contrast simulations of strained in comparison to strain relaxed thin TEM specimens are also used to address the thin foil relaxation of TEM specimens, which has a significant impact on the scattered electron intensity, especially at or close to interfaces.
Kinetic as well as thermodynamic driving forces for the formation of certain interface structures are addressed by simulations using a kinetic Monte Carlo (KMC) code as well as by density functional theory (DFT).
Results: Quantitative atomic resolution in STEM imaging can be achieved when the experimental images are compared to frozen phonon simulations, which take the geometric aberrations as well as the source size and distribution of the microscope used into account. The agreement between simulation and experiment can be optimized when also the amorphous layers, generated at the top and bottom of the specimen as a result of sample preparation are considered. These simulations are used to quantify the atomically-resolved composition across different semiconductor interfaces, as enumerated above.
Using KMC and DFT simulations, it will be shown that – due to kinetic as well as thermodynamic driving forces - an intrinsic pyramidal, highly non abrupt, interface is formed between GaP and Si, which can also be correlated to the properties of optical excitations at this interface. The reason for the formation of this structure is the charge redistribution between the Si-P and Si-Ga wrong-bonds formed at this interface. In contrast to GaP/Si (001) the material system (Ga,In)P/GaAs (001), for example, allows for the formation of abrupt interfaces.
For strained interfaces, one observes – depending on the properties of the materials, which form the interface – either abrupt interfaces or segregated ones.

Conclusion: With several important examples it is shown that the atomically resolved structure of internal interfaces can be tackled using aberration-corrected STEM imaging and complementary contrast simulation. The factors, which need to be taken into account when contrast simulations are performed will be discussed as well as several examples of intrinsic interface structures in semiconductor heteroepitaxy will be given and correlated to the optoelectronic excitations across those interfaces.

We gratefully acknowledge support of the German Science Foundation (DFG) in the framework of the SFB 1083 Structure and Dynamics of Internal Interfaces.

MS1.002 invited
EELS and nanoCL for probing electronic and optical defect-induced phenomena in functional

L. H. G. Tizei[1], A. Gloter[1], M. Kociak[1], A. Zobelli[1], G. Tieri[1], O. Stéphan[1]

[1]Université Paris-Sud, Laboratoire de Physique des Solides, Orsay, France

odile.stephan@u-psud.fr

The field of electron scanning transmission electron microscopy (STEM) has recently achieved a succession of impressive successes linked with the development of aberration correctors, enabling atomically-resolved spectroscopy and new imaging modes, which are spreading worldwide. The development of Electron Energy-Loss Spectroscopy (EELS) detectors with single electron sensitivity offers new opportunities for collecting EELS spectra with enough signal to noise ratio to evaluate doping and chemical changes at the order of a few percents while keeping an atomic resolution. Similarly, recent progress in the collection of visible-range photons emitted by a sample illuminated by a focused beam has enabled novel cathodo-luminescence (CL) experiments in a STEM for exploring the optical (emission) properties of materials down to the nanometer scale and ultimately for entering the field of quantum nano-optics [1]. Combining these multiple investigation channels is of particular relevance for investigating and tuning the role of defects such as atomic dopants, stacking faults or interfaces on the properties of functional materials. Some examples such as interface driven effects in oxide heterostructures or the intimate link between structural defects and optical properties of 2D semiconducting materials will be reviewed. This includes a discussion on:

- the relation between the electronic charge distribution and interface reconstruction in manganite-nickelate [2] or manganite-ferroelectric [3] heterostructures,
- the interplay between Cr dopants and vacancy clustering in the structural and optical properties of WSe2 [4],
- stacking order effects on near band edge excitons in h-BN [5],
- the identification of point defects in h-BN as bright UV single photon emitters [6].

[1] L. H. G. Tizei and M. Kociak, *Spectrally and spatially resolved cathodoluminescence of nanodiamonds: local variations of the NV^0 emission properties,* Nanotechnology **23**, 175702 (2012)
[2] Gibert et al., *Interfacial Control of Magnetic Properties at LMO/LNO Interfaces,* Nano letters **15**, 7355 (2015)
[3] Marinova et al., *Depth profiling charge accumulation from a ferroelectric into a doped Mott insulator*, Nano letters **15**, 2533 (2015)
[4] L. H. G. Tizei, unpublished results
[5] R. Bourrelier et al., Nanometric Resolved Luminescence in h-BN Flakes: Excitons and Stacking Order, ACS Photonics **1***, 857 (2014)*
[6] Romain Bourrellier et al., *Bright UV Single Photon Emission at Point Defects in h-BN,* Nano Lett., **16**, 4317 (2016)

MS1.003
Energy-filtered TEM studies on silicon nanoparticles acting as quantum dots in single electron transistors

D. Wolf[1,2], X. Xu[1], T. Prüfer[1], G. Hlawacek[1], L. Bischoff[1], W. Möller[1], H. J. Engelmann[1], S. Facsko[1]
J. von Borany[1], K. H. Heinig[1], R. Hübner[1]

[1]Helmholtz-Zentrum Dresden-Rossendorf, Institute of Ion Beam Physics and Materials Research, Dresden, Germany
[2]Leibniz Institute for Solid State and Materials Research, Dresden, Germany

d.wolf@hzdr.de

The miniaturization of computing devices and the introduction of the internet of things generate an increasing demand for the development of low-power devices. Single electron transistors (SETs) are ideally suited for this demand, because they are promising very low power dissipation devices. For room-temperature operation of an SET it is necessary to create a single quantum dot (QD) with a diameter below 5 nm exactly positioned between source and drain at a tunnel distance of only a few nanometers. Within the IONS4SET project [1], we aim to achieve this goal by ion irradiation induced Si-SiO_2 mixing and subsequent thermally activated self-assembly of single Si nanocrystals surrounded by a thin SiO_2 layer. This process is illustrated in Fig. 1 by means of simulations results.
Here, we present energy-filtered (EF)TEM studies in order to monitor the influence of process parameters, such as stack geometry, ion fluence for irradiation, annealing temperature and annealing time, on the self-assembly of Si QDs. Fig. 2 shows representative EFTEM micrographs of a Si-SiO_2-Si layer stack imaged using different electron energy-loss (EEL) windows. The Si plasmon-loss filtered images yield thereby the best signal-to-noise for detection of Si nanodots, because the Si plasmon peak is the most intense peak with a relatively small FWHM of 4 eV in the EEL spectrum.
Moreover, since the obtained (raw) EFTEM images provide only qualitative information about the Si concentration in the oxide layer, they cannot give a clear answer if for example the observed contrast corresponds to one or more Si nanodots (NDs) in projection. Therefore, EFTEM images are quantified further by converting them into so-called thickness over mean free path length (MFPL) t/λ_{Si} maps, in which λ_{Si} is the MFPL corresponding to the chosen energy range. The experimental t/λ_{Si} maps are then compared with simulated t/λ_{Si} maps of a single Si ND. Fig. 3 depicts that our approach enables us not only to detect single Si nanodots (Fig. 3c,e) but also to count them if they are arranged in projection direction of the electron beam (Fig. 3d,f). For these experiments, the layer stacks were irradiated with Ne+ ions within an Orion NanoFab (Zeiss). This allows controlled line or point irradiation and ensures Si QD formation within a confined region. In a next step, confined regions will be established by fabricated nanopillars that enhances reproducibility as the volume relevant for the self-assembly of the nanocluster will be better defined.

[1] We thank for financial support within the European Union"s Horizon 2020 research and innovation program under Grant Agreement No 688072 (Project IONS4SET).

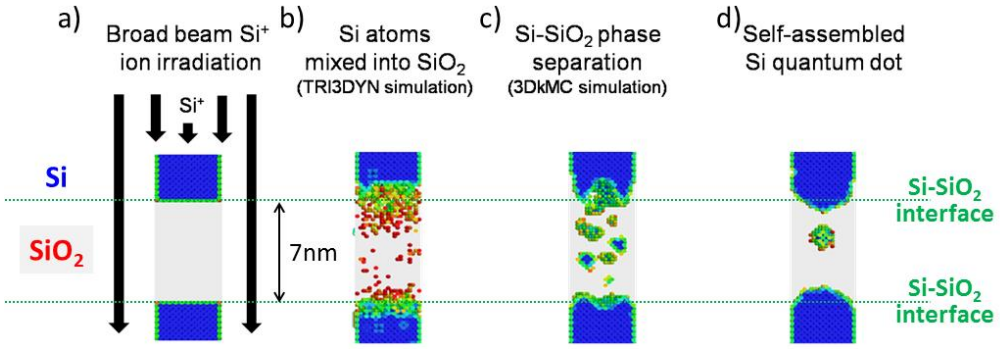

Figure 1. Simulation of Si quantum dot self-assembly inside a Si-SiO2(7nm)-Si layer stack. Si^+ ion irradiation at kinetic energies of 30 to 50 keV (a) leads to ion beam mixing across the interfaces (b). Subsequent annealing of the metastable system induces firstly Si-SiO_2 phase separation (c) and finally the formation of a single Si quantum dot (d).

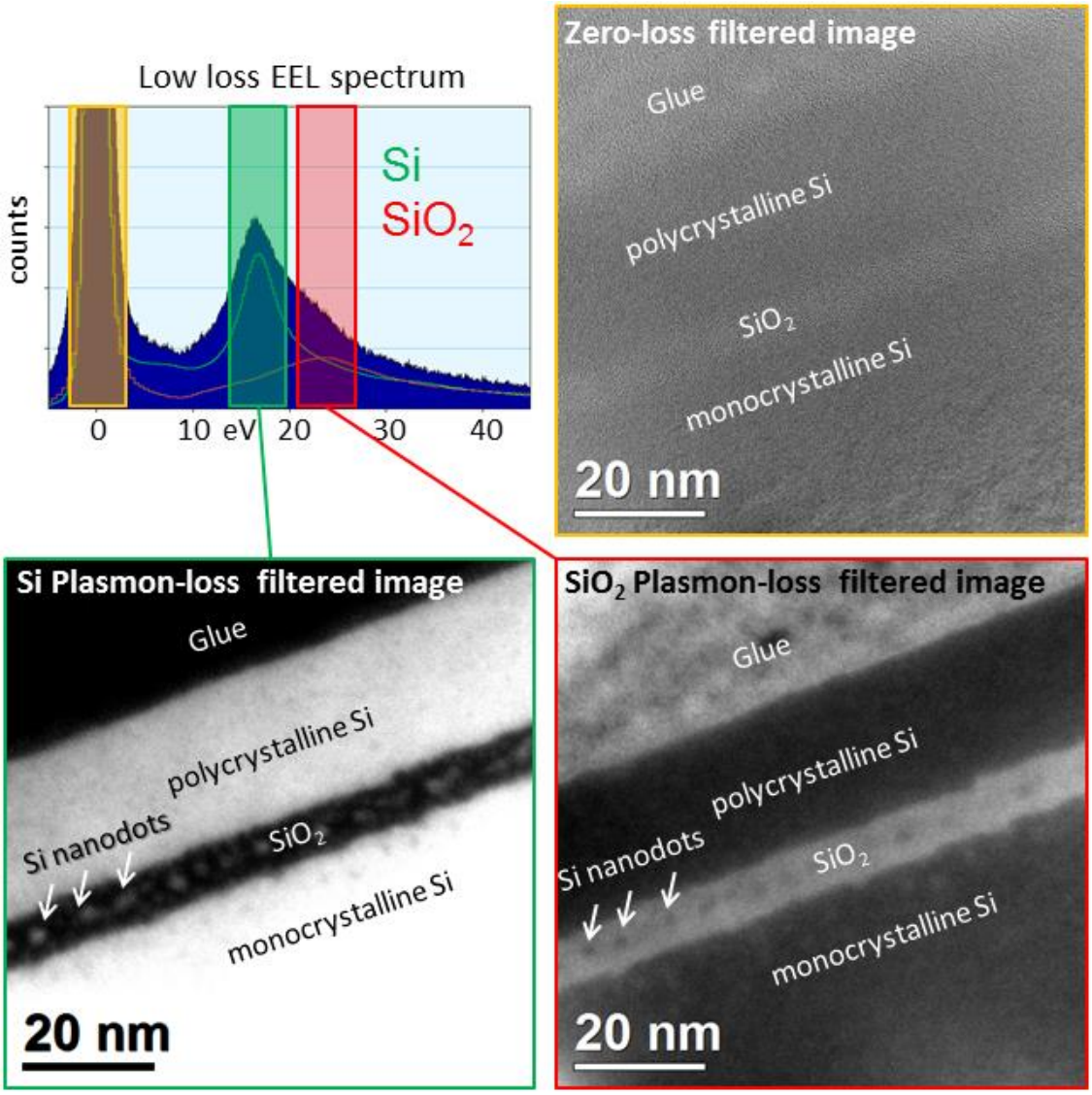

Figure 2. EFTEM imaging of a Si-SiO_2-Si layer stack broad-beam irradiated with 30 keV Si+ ions. The images are taken at 0 eV, 17 eV, and 25 eV using 5 eV, 7 eV, and 5 eV slit widths for the zero-loss, Si plasmon-loss, and SiO_2 plasmon-loss images, respectively. The 2-3nm small Si nanodots can only by observed as bright (dark) contrast in the Si (SiO_2) plasmon-loss, whereas in the zero-loss image they are not visible.

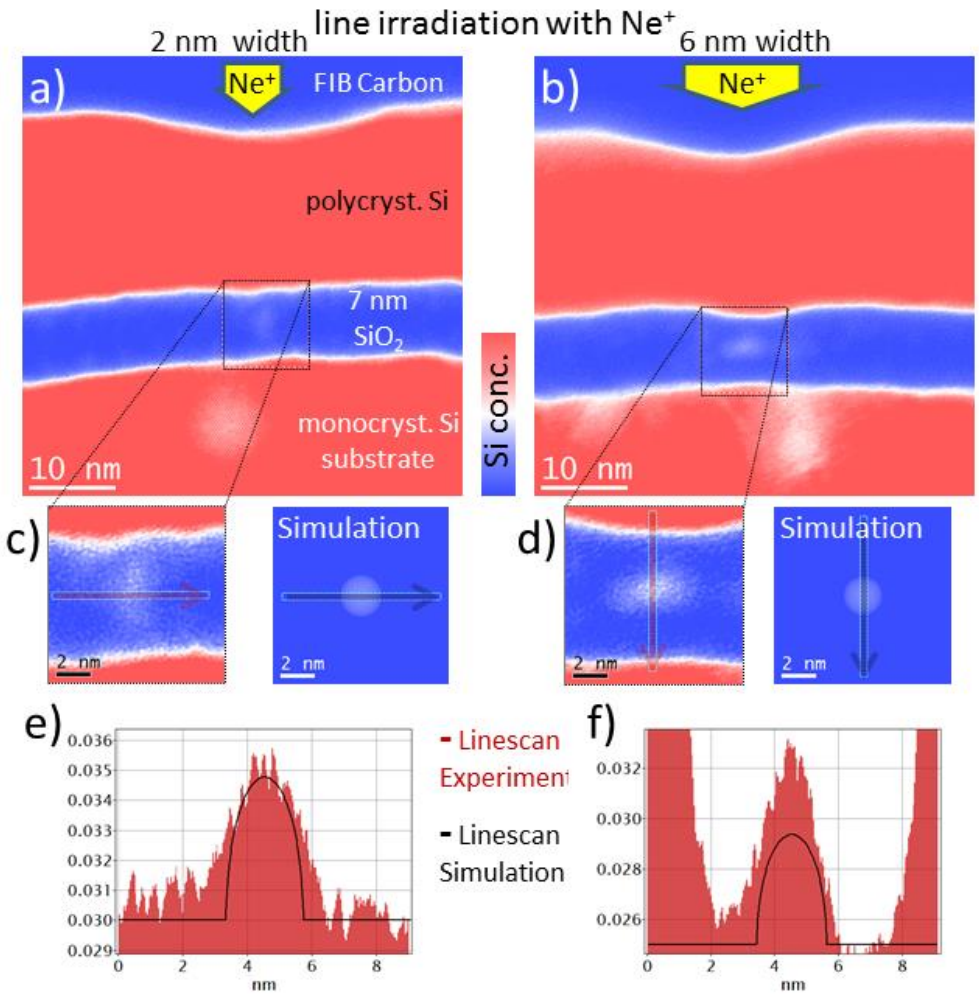

Figure 3. EFTEM imaging of a Si-SiO_2-Si layer stack line-irradiated with 30 keV Ne^+ ions. a,b) Experimental thickness over MFPL (t/λ_{Si}) map gained from a Si plasmon-loss TEM image. c,d) Inset of the Si QD and its simulated t/λ_{Si} map. e,f) Line profiles along the line scans in (c) and (d) suggest that there is a single ND in (e) and there are two NDs in projection in (f).

MS1.004
Morphology of InAs/InAlGaAs quantum dots emitting in the low-loss telecom wavelength ran

M. Schowalter[1,2], C. Carmesin[3], M. Lorke[3], D. Mourad[3], T. Grieb[1,2], K. Müller-Caspary[4], M. Yacob[5]
J. P. Reithmaier[5], M. Benyoucef[5], A. Rosenauer[1,2], F. Jahnke[3]

[1]Universität Bremen, Institut für Festkörperphysik, Bremen, Germany
[2]Universität Bremen, Mapex center for materials and processes, Bremen, Germany
[3]Universität Bremen, Institut für Theoretische Physik, Bremen, Germany
[4]University Antwerp, EMAT, Antwerp, Belgium
[5]Universität Kassel, Institut für Nanostrukturtechnologie und Analytik (INA), Kassel, Germany

schowalter@ifp.uni-bremen.de

Among the main challenges for quantum information technology is the realization of deterministic single photon sources with emission energies in the low-loss telecom band [1]. InAs/InAlGaAs/InP is a promising material system, since it allows growth of quantum dots that emit within this energy range [2, 3]. To achieve a deeper understanding of the emission properties, a detailed characterization of the morphology of the quantum dots including composition determination within the dots is necessary. In this contribution we developed a technique for the composition quantification in this quaternary alloy based on quantitative STEM. Measured composition and morphology were then used in atomistic tight-binding simulations to model the inhomogeneous broadening of the photoluminescence of the dot ensemble.
Fig. 1a shows an overview of the structure exhibiting the top of the InP/InAlGaAs DBR structure on which the InAs/InAlGaAs active region was grown. An overview of the active region (Fig. 1b) shows that the quantum dots exhibit a pyramidal shape with (1-13) side facets. A higher intensity (Figs. 1c, d) on top of their side facets is observed that hint on a diffusion of In out of the dot towards the cap layer.
To quantify the composition within the dots quantitative STEM as outlined in [4] was employed. However, since the barrier consists of a quaternary material, an intermixing of the metals is possible and the method of [4] needs to be extended. For that purpose, Reference: data of HAADF intensity and strain (Fig. 2 a, b) were simulated as a function of thickness, In and Al concentration. Isolines of strain and intensity in these data exhibit an angle of 45° and therefore the two quantities are sufficiently independent to be used for quaternary composition quantification. Strain and intensity were measured from HRSTEM images and then compared with the Reference: data set to determine both compositions.
Fig. 3 a-d show In and Al concentration distributions within a quantum dot as well as composition profiles through the center of the dot. Both composition distributions exhibit the pyramidal shape of the quantum dot. Regions on top of the side facets (with increased intensity in fig. 1 c and d) exhibit a slightly larger In concentration as well as a slightly reduced Al concentration. The In concentration profile increases to a constant value of about 86 %, whereas the Al concentration drops towards about 7 % suggesting equal Al and Ga concentration. Since the pyramidal quantum dot is embedded in the InAlGaAs matrix, the true concentration within the dot must be increasing linearly from bottom to top.
For further atomistic-tight binding simulations, the pyramidal shape as well as the linearly increasing In concentration within the dot were adopted. Simulations were carried out as a function of the size of the pyramid base from 40 – 60 nm with constant diameter to height ratio and as a function of In concentration at the base of the pyramid from 70 to 100 % (assuming an equal distribution of the remaining lattice sites by Al and Ga atoms). Only a shift of about 20 meV due to the size, but a shift of about 200 meV by varying the In concentration was found. In this way, the inhomogenous broadening of the photoluminescence of the dot ensemble of 150 meV can be explained by the variation of the In concentration.

[1] L. Brusberg, C. Herbst, M. Neitz, H. Schröder, and K. D. Lang, 2014 The European Conference on Optical Communication (ECOC) , pp. 1-3, ISSN 1550-381X.
[2] M. Benyoucef, M. Yacob, J. P. Reithmaier, J. Kettler,and P. Michler, Applied Physics Letters 103, 162101(2013)
[3] M. Yacob, J. P. Reithmaier, and M. Benyoucef, Applied Physics Letters 104, 022113 (2014)
[4] A. Rosenauer et al., Ultramicroscopy **109** (2009) 1171

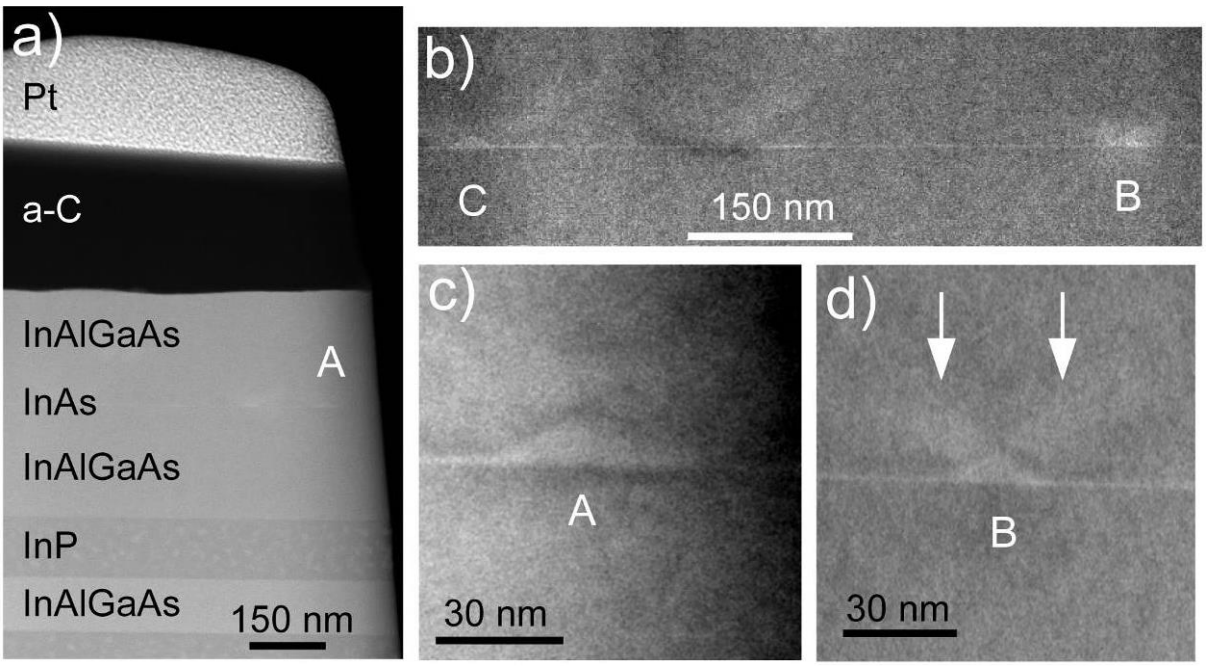

Figure 1. a) STEM overview image of the sample. b) STEM image of the active region. c) and d) HAADF STEM images of two quantum dots.

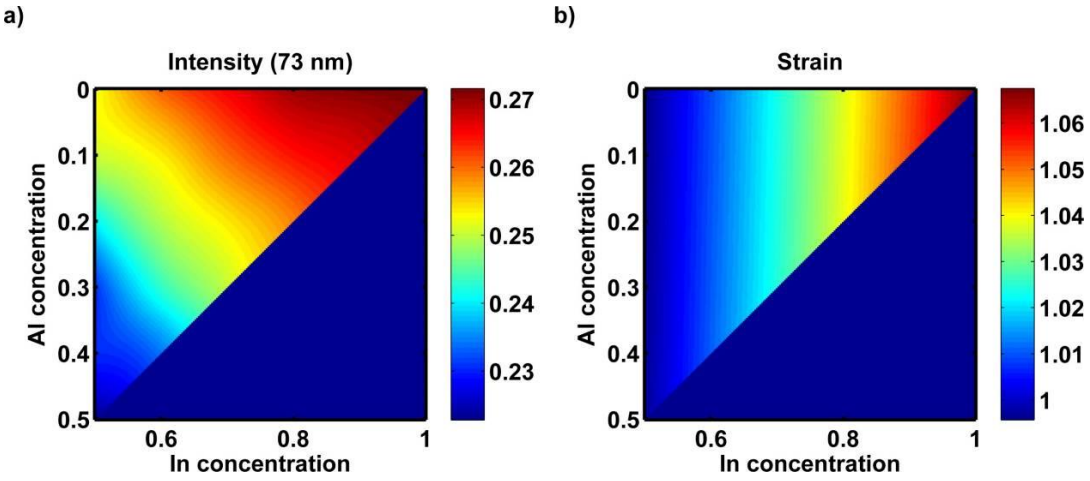

Figure 2. a) Simulated HAADF STEM intensity and b) strain as a function of In and Al concentration.

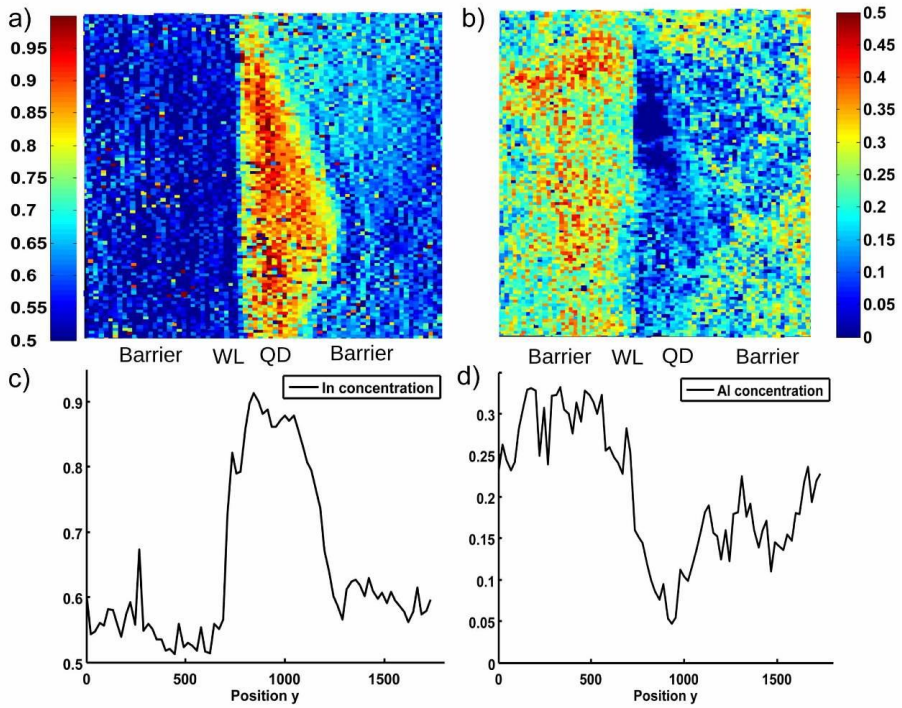

Figure 3. a) and b) In and Al concentration maps of a quantum dot. c) and d) Respective concentration profiles through the middle of the dot.

MS1.005
Anisotropic polarization in a Bi0.8Ca0.2FeO3 thin film investigated by combined HAADF/ABF imaging

M. Campanini[1], R. Erni[1], M. D. Rossell[1]

[1]EMPA, Dübendorf, Switzerland

marco.campanini@empa.ch

In the last decade BiFeO3 (BFO) has been widely investigated for being one of the few multiferroic materials that exhibits ferroelectricity and ferromagnetism at room temperature. Despite the G-type antiferromagnetic ordering, the arrangement of spins in a cycloidal structure along the [110] direction of the R3c structure of BFO suppresses its macroscopic magnetization; nevertheless, it has been proven that this spiral spin structure can be destroyed by Ca doping, obtaining a canted antiferromagnetic structure which is weakly ferromagnetic.1
In order to preserve an overall charge neutrality in Bi1-xCaxFeO3, alongside with the Ca substitution on perovskite A sites, oxygen vacancies are spontaneously produced and structures with oxygen-vacancies ordering have been commonly reported in a range of doping of 0.2<x<0.5.2
Although the macroscopic effects of doping on the magnetoelectric properties of bulk BFO have been extensively investigated, the detailed atomic configuration in these doped materials and a direct correlation between the structure and their properties at a very local scale is still missing. More recently high-quality epitaxial single crystal BFO thin films have been fabricated and they represent the best candidates to address unresolved questions about this intriguing material.
In this work, high angle annular dark-field (HAADF) and annular bright-field (ABF) imaging performed in aberration-corrected scanning transmission electron microscopy (STEM) were employed to elucidate the mechanism of doping/O-vacancy ordering in a Bi0.8Ca0.2FeO3 thin film and to correlate its polarization to the atomic scale structure.
A single-crystalline 85 nm thick Bi0.8Ca0.2FeO3 film was grown on (001) SrTiO3 substrate, using pulsed laser deposition.
We have employed HAADF to map the Ca doping while ABF was successfully used to visualize O distribution and O vacancies ordering. The fitting of the peaks in the HAADF/ABF images, carried out using a modified version of the algorithm proposed by Yankovich3, permits to directly access the projected crystallographic structure and to make quantitative analysis.
The polarization maps and other structural distortions were calculated from the precise position of the atomic columns in the structure.
The investigated Bi0.8Ca0.2FeO3 thin film displays a regular arrangement of O vacancies in a periodic superstructure, superimposed to a doping gradient in between the layers (Fig.1).
The atomic configuration of the layers containing ordered O vacancies was obtained analyzing HAADF and ABF intensities, while the coupling between different polar and non-polar distortion is explained by direct structural imaging along different crystallographic orientations.
By mapping the polarization at the atomic scale, we observed the establishing of a periodic ferroelectric distortion with an anisotropic nature, displaying two different periodicities along the [001] and [100] perovskite directions (Fig.2).
Remarkably, we show that this anisotropic polarization is strictly related to the Ca doping gradient, which is able to actively alter the ordering of the lone pair of Bi atoms.
A direct correlation between the structure of the doped material and the polarization has been pointed out at atomic scale thanks to quantitative HAADF/ABF analysis.
The presented findings highlight the relevance of anisotropic doping for advanced multiferroic materials engineering, representing an additional degree of freedom that can be exploited –together with the epitaxial strain–4 to tailor the properties and control the coupling between different ferroic orderings in magnetoelectric thin films5.

[1] H. Chou et al., *Acta Mat.* 2016, 111, 297-304
[2] J. A. Schiemer et al., *Chem Mat.* 2013, 25, 4436-4446
[3] A. B. Yankovich et al., *Nat. Comm.* 2013, 5, 4155
[4] R. Guzman et al., *Nano Lett.* 2016, 2221-2227
[5] We acknowledge funding through NCCR MARVEL, supported by SNSF.

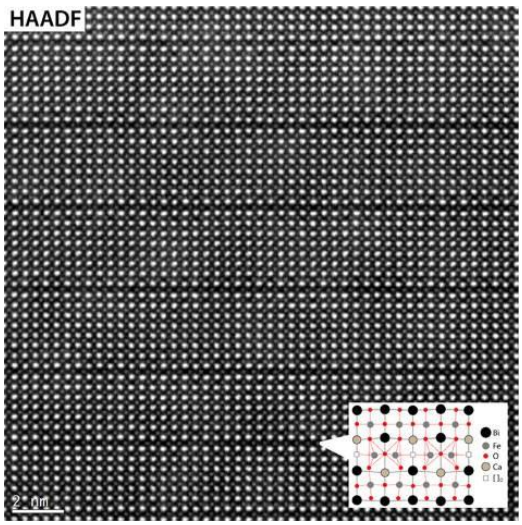

Figure 1. Ordering of O vacancies and structure of the defective layers in Bi0.8Ca0.2FeO3.

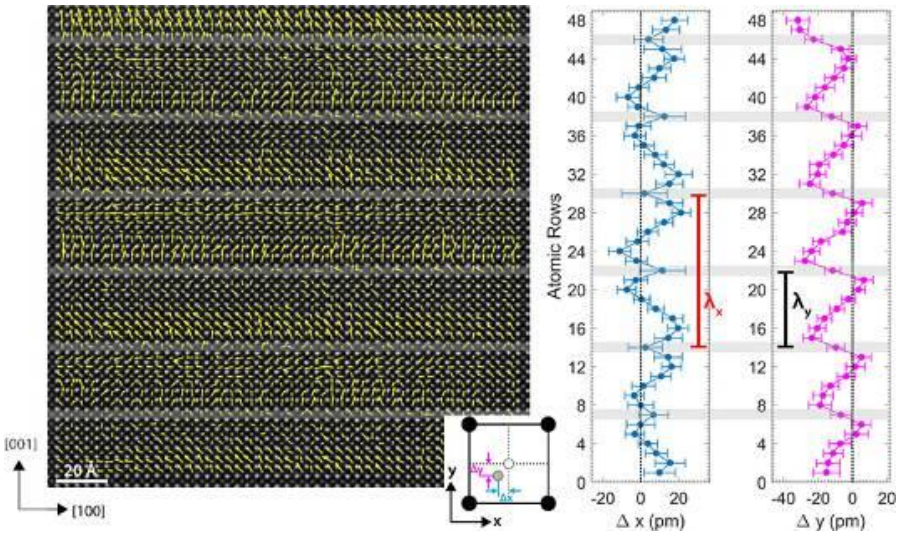

Figure 2. Polarization map and Fe atomic displacements due to the lone pair ordering on Bi sites.

MS1.006
Quantitative characterization of nanosized conducting filaments formed by atomic-scale defects in redox-based resistive switching memories

H. Du[1,2], C.-L. Jia[1,3,4], A. Koehl[3], J. Barthel[1,2], R.Dittmann[3], R. Waser[3,5,6], J. Mayer[1,2,6]

[1]Forschungszentrum Jülich GmbH, Ernst Ruska-Centrum für Mikroskopie und Spektroskopie mit Elektronen, Juelich, Germany
[2]RWTH Aachen University, Gemeinschaftslabor für Elektronenmikroskopie, Aachen, Germany
3Forschungszentrum Jülich GmbH, Peter Grünberg Institute, Jülich, Germany
4Xi'an Jiaotong University, School of Electronic and Information Engineering, Xi'an, China
5RWTH Aachen University, Institut für Werkstoffe der Elektrotechnik II (IWE II), Aachen, Germany
6Jülich-Aachen Research Alliance, Future Information Technology (JARA-FIT), Jülich-Aachen , Germany

jen@pdi-berlin.de

Introduction: Redox-based resistive switching phenomena are found in many metal oxides and hold great promise for applications in next-generation memories and neuromorphic computing systems. Resistive switching involves the formation and disruption of electrically conducting filaments through ion migration accompanied by local electrochemical redox reactions. These structural changes are often explained by point defects, but so far clear experimental evidence of such defects is missing.
Objectives: In this work [1], we apply STEM, EELS and EDX imaging techniques to quantitatively characterize nanosized conducting filaments in electroformed Au/FeSrTiO3/Nb:SrTiO3 thin film devices, providing direct experimental evidence for the point defect nature of the conducting filaments.
Materials and Methods: SrTi0.98Fe0.02O3 thin films about 17 nm in thickness were expitaxially grown on a 0.5-wt% Nb doped SrTiO3 substrate by PLD. Electric forming was performed on individual devices by a sweep to 5 V setting the devices into the ON state. Cross-sectional TEM specimens were cut by FIB and further thinned by Ar-ion beam milling. STEM and EDX spectrum imaging was conducted with an FEI ChemiSTEM microscope at 200kV. Monochromated EELS spectrum imaging was performed with the FEI PICO microscope at 200 kV with spectrum energy resolution of 0.2–0.3 eV. Image simulations were performed with the Dr. Probe software package.
Results: In both ABF and HAADF images, we observed V-shaped areas showing darker contrast in the compared with their surroundings (Fig. 1). This provides a first indication that these areas are conducting filaments viewed in cross-section.
A Ti3 distribution map was obtained by monochromated EELS spectrum imaging (Fig. 2), which clearly reveals four different V-shaped defect areas in the film developed to different stages of completion from the top anode towards the cathode i.e. he conducting substrate. The shape of the filaments can be explained by the electric field and chemical gradients around the filaments driving ion drift and chemical diffusion, respectively.
Quantitative EDX analysis indicates also considerable Sr- and O-vacancies in the filaments. By taking both Sr-deficiency and static lattice distortion into account, multislice STEM image simulations can qualitatively reproduce the decrease of mean intensity in both ABF and HAADF images of the filaments. Intriguingly, atomic resolution STEM imaging reveals that the perovskite lattice is maintained intact at such high defect concentrations and considerable lattice distortions (Fig. 3).
Conclusion: The present work [1], for the first time, provides clear experimental evidence for the existence of multiple nanosized conducting filaments formed solely by atomic-scale point defects in a SrTiO3 based thin film device. First insights into the switching mechanism are deduced from a snapshot simultaneously showing multiple nanosized filaments in different evolutionary stages. The coexistence of a high Ti3 concentration along with Sr- and O-vacancies in the conducting filaments, provides atomic scale explanations for the resistive switching mechanisms. The results shed unique light on the complexity of the conducting filaments formation that cation and anion defects need to be considered jointly.

References:
[1] H.Du, et al, Chem. Mater. 2017, DOI: 10.1021/acs.chemmater.7b00220
[2] This work is supported by DFG under SFB 917 and MA 1280/40-1.

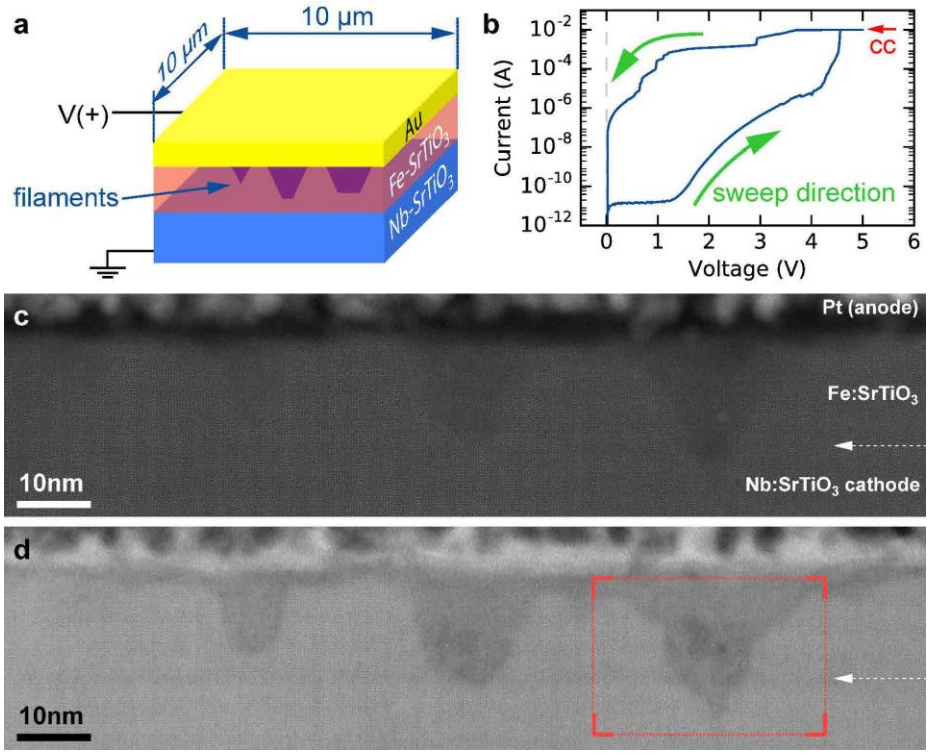

Figure 1. a) Schematic of an electroformed ON-state Au/Fe:SrTiO3/Nb:SrTiO3 device. b) I-V curve of the electroforming process. Overview HAADF c) and ABF d) STEM images of the device cross-section, arrows indicate the film/substrate interface.

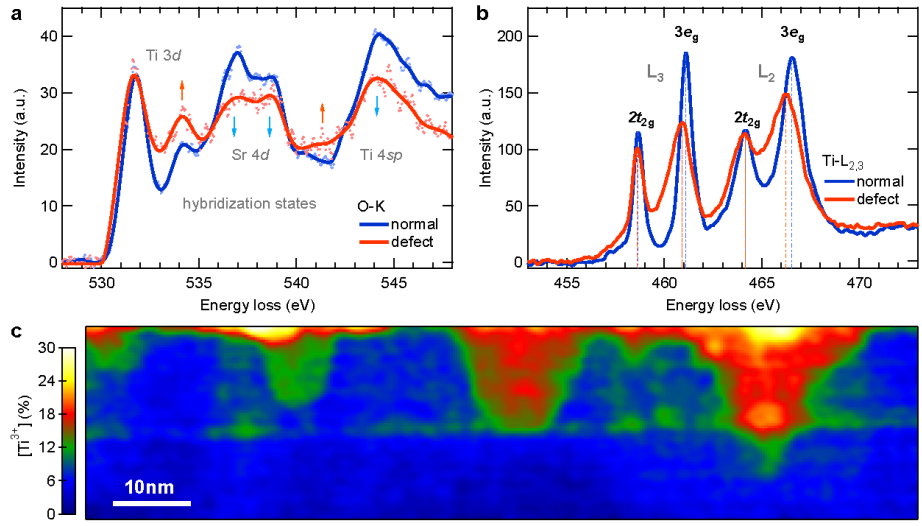

Figure 2. a) and b) EELS fine structures for O-K and Ti L2,3 edges, respectively. Blue line: normal SrTiO3 dominated by Ti4 , red line: defect SrTiO3 with the highest amount of Ti3 for the filaments. (c) Ti3 distribution map.

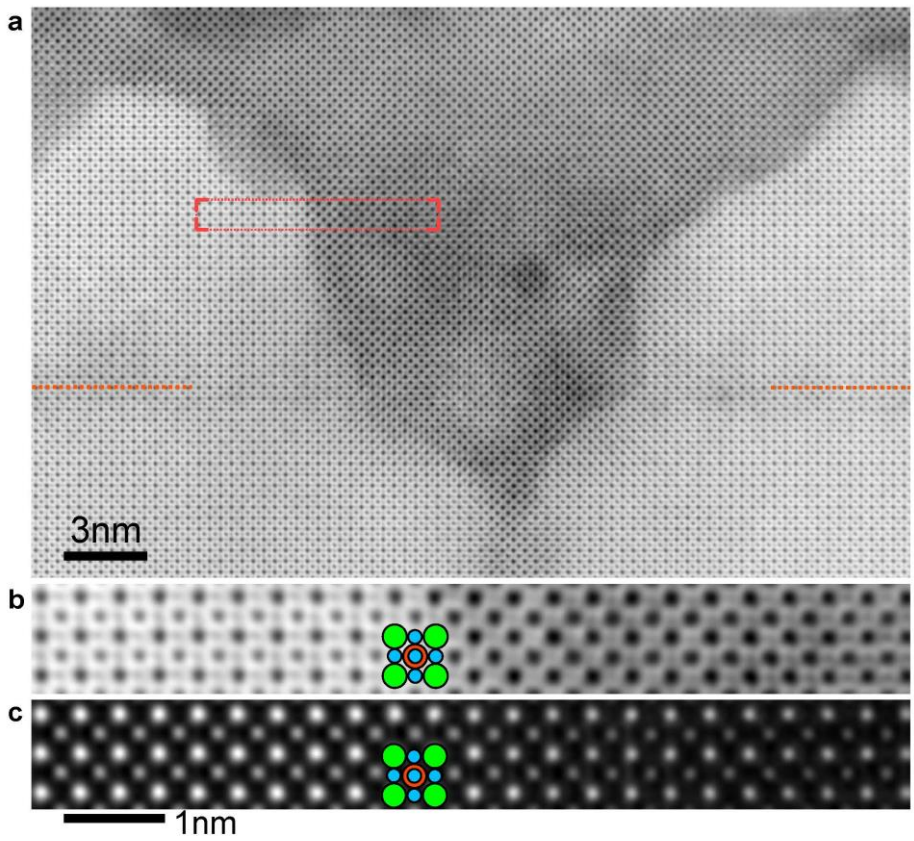

Figure 3. a) ABF image of the region marked in Fig 1d. Lines denote the film/substrate interface. b) Magnified part marked in a). c) Corresponding HAADF image to b). Atomic symbol Sr: green, Ti: red, O: blue.

MS1.P001
Structural properties of Fe_3Si/Ge/Fe_3Si thin film stacks on GaAs

B. Jenichen[1], S. Gaucher[1], J. Herfort[1], U. Jahn[1], H. Kirmse[2], M. Hanke[1], A. Trampert[1]

[1]PDI, Berlin, Germany
[2]HUB, Berlin, Germany

jen@pdi-berlin.de

Introduction: A high structural quality of ferromagnet/semiconductor/ferromagnet (FM/SC/FM) thin film systems can be achieved by reducing the mismatch of the lattice parameters of the films. Following this rule Fe_3Si/Ge/Fe_3Si thin-film stacks were fabricated on GaAs(001) using molecular beam epitaxy (MBE).[1] Lattice matched Co_2FeSi/Ge/Co_2FeSi tri-layer stacks were grown on Ge(111) as well.[2] Objectives: On the GaAs(001) substrates the quality of the Ge layer between the two Fe_3Si films had to be improved, because the direct growth of a semiconductor film on a metal still remains difficult. Therefore, in the present work we realize highly perfect epitaxial films using solid phase epitaxy (SPE).[3] Materials and Methods: The Fe_3Si/Ge/Fe_3Si films prepared by MBE and SPE were characterized by high-resolution transmission electron microscopy (TEM), reflection high-energy electron diffraction (in-situ during annealing), energy dispersive x-ray spectroscopy (EDX) in the TEM, electron backscattered diffraction (EBSD) and x-ray diffraction (XRD).
Results: All the films show a high structural quality over large areas as evidenced by TEM, EBSD and XRD. EBSD reveals only one single orientation of the top Fe_3Si film and at the same time the image quality is very high. We find evidence for a spontaneously formed vertical superstructure in the Ge film (Fig.1,2). The XRD curves exhibit superstructure maxima caused by the ordered regions as well as clear thickness fringes resulting in interference patterns. We find evidence for the diffusion of silicon and iron into the Ge film, i.e. the semiconductor layer is not pure Ge but a mixed crystal consisting of Ge with Fe and Si. This film is no longer fully lattice matched with the GaAs substrate but tetragonally strained without plastic relaxation. XRD curves were simulated assuming a FeSi/Ge superlattice for the Ge(Fe,Si) film in correspondence with the EDX results.
Conclusion: The SPE approach is therefore a suitable tool to explore the combination of ferromagnetic Heusler alloys with semicondoctors in FM/SC/FM systems, a step towards the implementation of new vertical spintronics devices.

References:
[1] B. Jenichen et al., *Thin Solid Fims*, **556**, 120 (2014)
[2] M. Kawano et al., *J. Appl. Phys.* , **119**, 045302 (2016),
[3] S. Gaucher et al. Appl. Phys. Lett., accepted for publication.

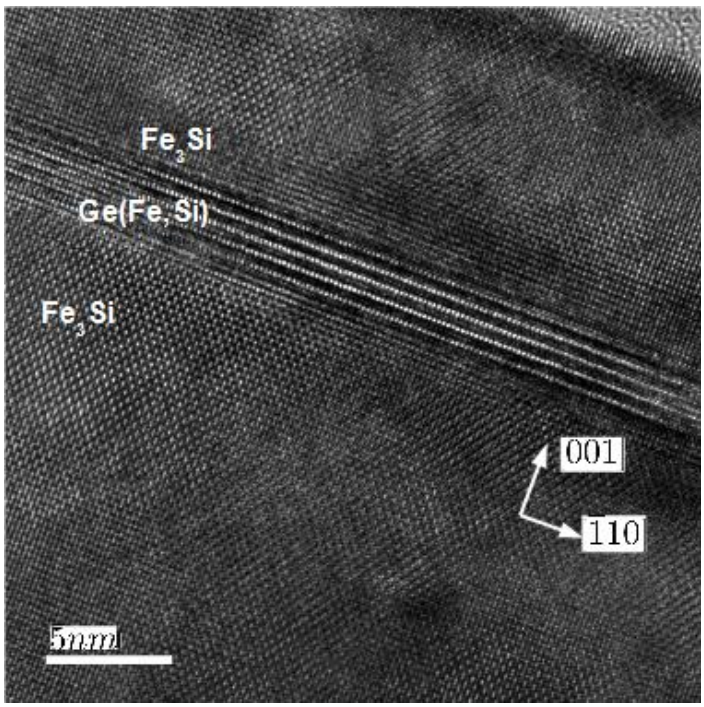

Figure 1. TEM micrograph of a $Fe_3Si/Ge/Fe_3Si$ thin-film stack, the superstructure region in the Ge layer is clearly visible.

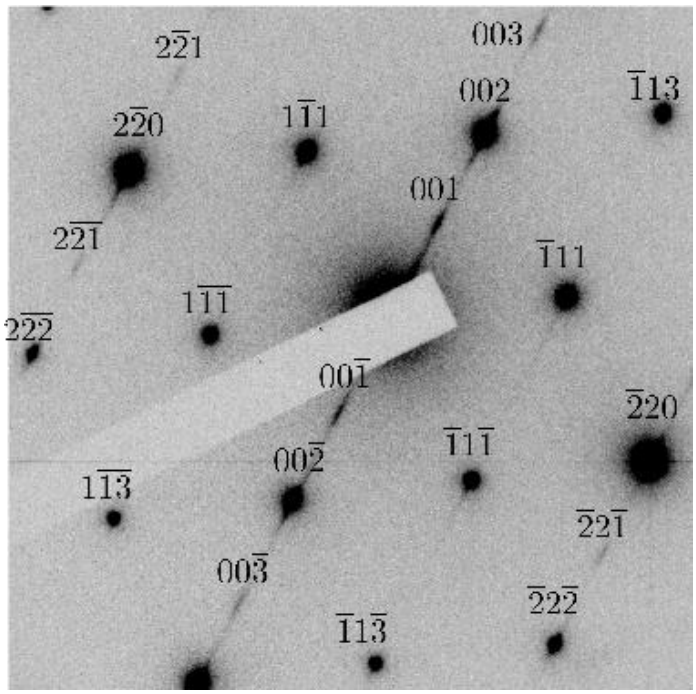

Figure 2. SAD pattern of the sample imaged in Fig. 1 (contrast inverted).

MS1.P002
In situ TEM of the transformation fatigue of TiNi based shape memory alloys

T. Wuttke[1], C. A. Volkert[1]

[1]University of Göttingen, Institute of Materials Physics, Göttingen, Germany

twuttke@gwdg.de

Introduction**:** Shape Memory Alloys (SMAs) are named after their ability to recover plastic deformation upon heating. The key mechanism responsible for this behavior is a reversible diffusionless solid-state phase transition between a highly twinned martensitic state and an untwinned austenitic phase [1]. This allows to use SMAs as actuators in various industrial, scientific and medical fields [2, 3].
A big drawback for many SMAs is the so called transformation fatigue. This term describes the cumulative increase of irreversible plastic deformationduring thermal or mechanical cycling which results in a limited lifetime of the SMA [4].
Objectives: Our goal was to study the change in microstructure of TiNi based SMAs during thermal cycling using in-situ TEM techniques.
Materials and Methods**:** Both $Ti_{51}Ni_{49}$ and $Ti_{50}Ni_{30}Cu_{20}$ alloys were prepared with vacuum arc melting. Binary TiNi alloys are known to be strongly affected by transformation fatigue while the addition of copper increases the lifetime [5]. TEM specimens were prepared with a combination of ion polishing and FIB.
Experiments have been carried out using a Gatan heating holder and a Nanofactory STM-holder. The later features a moveable tungsten tip on a piezo actuator, mounted opposite to the specimen. Voltage application between tip and specimen allows to rapidly cycle the temperature several hundred times in a few minutes using Joule heating.
Results**:** Figure 2 shows the microstructural development of a $Ti_{51}Ni_{49}$ alloy over the course of 200 thermal cycles. Since each image shows the sample at room temperature, there should be no changes in case of a perfectly reversible phase transformation.
Three observations can be made. First, the amount of well ordered twinned martensite decreases with increasing cycle count. The term ordered martensite refers to the nicely twinned microstructure of a single martensite variant in contrast to the chaotic microstructure of several competing variants. Second, the total amount of martensite also decreases. This is partly due to thermal drift but mostly due to a movement of the interface in favor of the austenite. Third, defects appear at the austenite-martensite interface. Interestingly, these changes are not strictly irreversible but are occasionally undone during later cycles, as one can see when comparing cycle 48 and 73 in figure 2. In average, the amount of ordered martensite decreases nevertheless, as is shown in figure 3.
Similar experiments were carried out with $Ti_{50}Ni_{30}Cu_{20}$ samples for which no microstructural changes have been observed.
Conclusion**:** In case of $Ti_{51}Ni_{49}$ the formation of martensite becomes more and more difficult with increasing cycle count. This hints at the formation of defects which hinder the movement of the interface. Martensite nucleation has a stochastic element which might explain why the formed martensite occasionally appears in a less chaotic microstructure compared to earlier cycles.
$Ti_{50}Ni_{30}Cu_{20}$ is known for its increased lifetime and therefore serves as a control experiment where microstructural changes were neither expected nor observed.

[1] K. Otsuka and X. Ren, Physical metallurgy of Ti-Ni-based shape memory alloys, Progress in Materials Science (2005)
[2] Jan Van Humbeeck, Non-medical applications of shape memory alloys, Materials Science and Engineering: A (1999)
[3] N.B Morgan, Medical shape memory alloy applications—the market and its products, Materials Science and Engineering: A (2004)
[4] P. Pappas et al., Transformation fatigue and stress relaxation of shape memory alloy wires, Smart Mater. Struct. 16 (2007)
[5] Jun Cui et al., Combinatorial search of thermoelastic shape-memory alloys with extremely small hysteresis width, Nature Materials 5, 286 - 290 (2006)

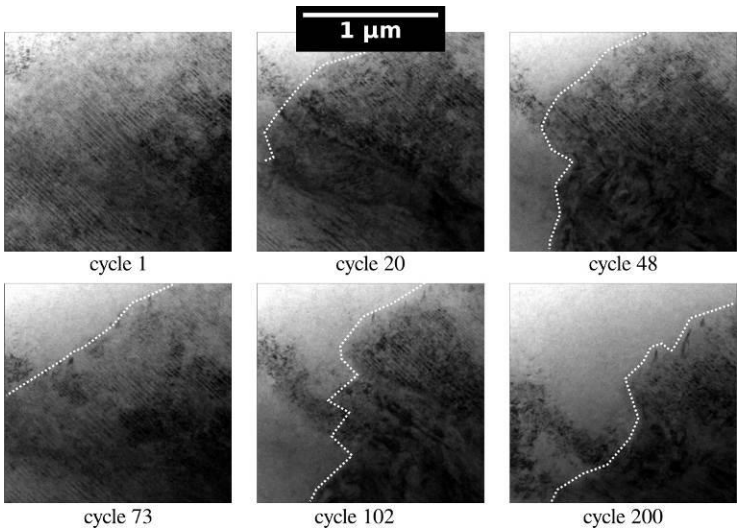

Figure 1. Microstructural changes of a TiNi alloy during thermal cycling. Shown is the sample in the cold state after a certain amount of transformation cycles have been carried out.

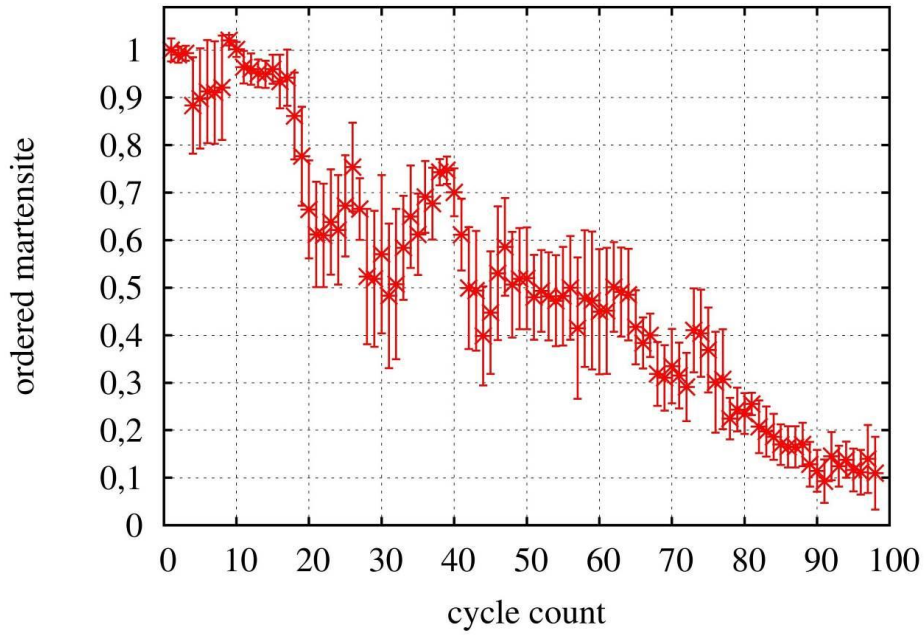

Figure 2. Thermal cycling of a TiNi alloy. Shown is the running average of the area fraction of ordered martensite in relation to the initial state.

MS1.P003
Atomic structure and domain-wall pinning in samarium-cobalt-based permanent magnets with increased iron content

M. Duerrschnabel[1], M. Yi[2], K. Uestuener[3], M. Liesegang[4,3], M. Katter[3], H. J. Kleebe[1], B. X. Xu[2]
O. Gutfleisch[4], L. Molina-Luna[1]

[1]TU Darmstadt, Material- and Geosciences, Darmstadt, Germany
[2]TU Darmstadt, Mechanics of Functional Materials Division, Darmstadt, Germany
[3]Vacuumschmelze GmbH & Co. KG, Hanau, Germany
[4]TU Darmstadt, Functional Materials, Darmstadt, Germany

duerrschnabel@geo.tu-darmstadt.de

Introduction: A higher saturation magnetization obtained by an increased iron content is essential for yielding higher energy products in rare-earth Sm_2Co_{17}-type pinning controlled permanent magnets (PM).[1-9] These PM are used for high-temperature industrial applications due to their high intrinsic corrosion resistance and temperature stability.[10-14] The Fe content controls the phase formation of a $Sm(Cu,Co,Fe)_5$ diamond-shaped cellular structure that dominates the density and strength of the pinning sites and thus the coercivity.[15] However, the exact structure of the Zr-rich platelet phase (Z-phase) and its influence on the magnetic properties is still under debate.
Objectives: By a combination of ultra-high resolution experimental and theoretical methods, we were able to reveal the atomic structure of the single phases. With this knowledge we established a direct structure-property correlation by relating the microscopic data (Fig. 1) to the macroscopic magnetic properties (Tab. 1). Furthermore, we directly imaged the Z-phase and unraveled the exact position of the Zr atoms via atomic resolution high-angle annular dark-field (HAADF) imaging (Fig. 2). Additionally, we established micromagnetic simulations (Fig. 3) by using the structural information retrieved by electron microscopy as basis.
Materials and Methods: A 200 kV Jeol JEM 2100F and a Jeol ARM 200F (scanning) transmission electron microscope (STEM) was used to determine the microstructure and atomic resolution images.
Results: See Figures 1-3 and Table 1.
Conclusion: This contribution presents a detailed microstructural and chemical investigation of Sm_2Co_{17}-type sintered PM with different iron content. Low iron content leads to superstructure type ordering of the Zr-rich platelets, which contributes to the formation of a well-developed 1:5 phase and thus a diamond-shaped cellular structure. The coercivity is dominated by the density and strength of the pinning sites in the 1:5 phase while modified by the Z-phase. Via direct atomic scale observation we demonstrate for the first time that Zr preferably replaces the Sm atoms located at the Sm1 site in the $SmCo_3$ structure yielding a modified structure with the following sum formula: Zr_2SmCo_9. This would enable a comprehensive way of tailoring the magnetic properties. An enhanced understanding of the pinning mechanisms in Sm_2Co_{17} yields a new viable route to apply these thermal and chemical protocols for improved magnetic performances also to other systems than Sm_2Co_{17}.

References:
[1] Liu et al., J. Appl. Phys. 85 (1999), 2800–2804.
[2] Xiong, et al., Acta Mater. 52 (2004), 737–748.
[3] Feng et al. Intermetallics 18 (2010), 1067–1071.
[4] Hadjipanayis et al., IEEE Trans. Magn. 36 (2000), 3382–3387.
[5] Guangliang et al., Rare Met. Mater. Eng. 37 (2008), 396–399.
[6] Li et al. Trans Nonferrous Met Soc China 14 (2004), 790–793.
[7] Liu et al. IEEE Trans. Magn. 25 (1989), 3785–3787.
[8] Huang et al., J. Appl. Phys. 75 (1994), 6280–6282.
[9] Mishra et al., J. Appl. Phys. 52 (1981), 2517–2519.
[10] Zhou et al., Appl. Phys. Lett. 77 (2000), 1514–1516.
[11] Gutfleisch, J. Phys. D Appl. Phys. 33 (2000), R157–R172.
[12] Gutfleisch et al., Adv. Mater. 23 (2011), 821–842.
[13] Handstein et al. IEEE Trans. Magn. 39 (2003), 2923–2925.
[14] Gutfleisch in Nanoscale Magnetic Materials and Applications, (Springer US, 2009), 337–372.
[15] Rabenberg et al., J. Appl. Phys. **53** (1982), 2389–2391.
[16] The authors thank the LOEWE project RESPONSE funded by the Ministry of Higher Education, Research and the Arts of the Hessen state.

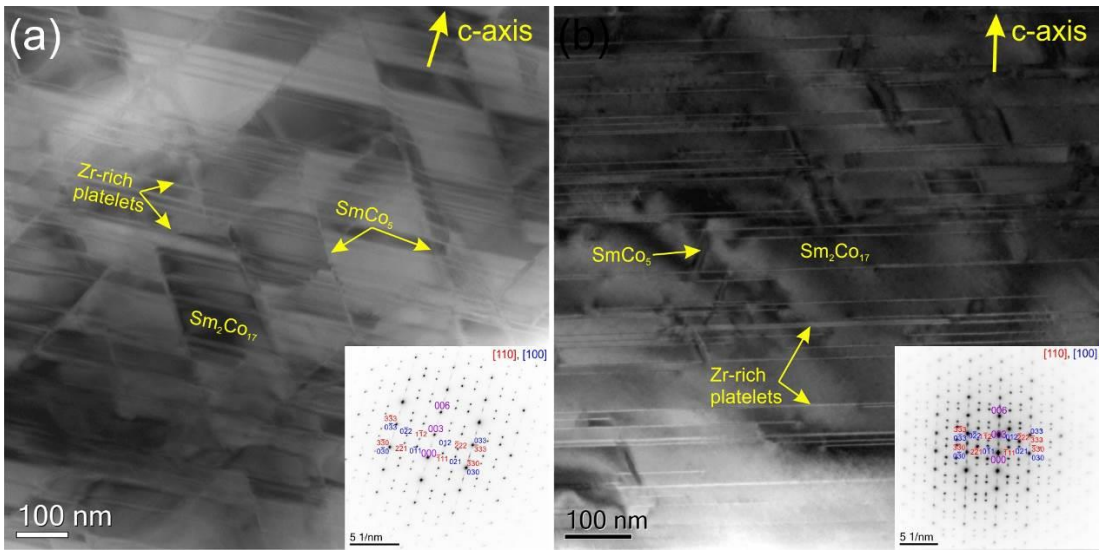

Figure 1. Nanoscale phase distribution. Bright-field TEM image with inset diffraction pattern of a sample containing (a) sample 1 and (b) sample 2.

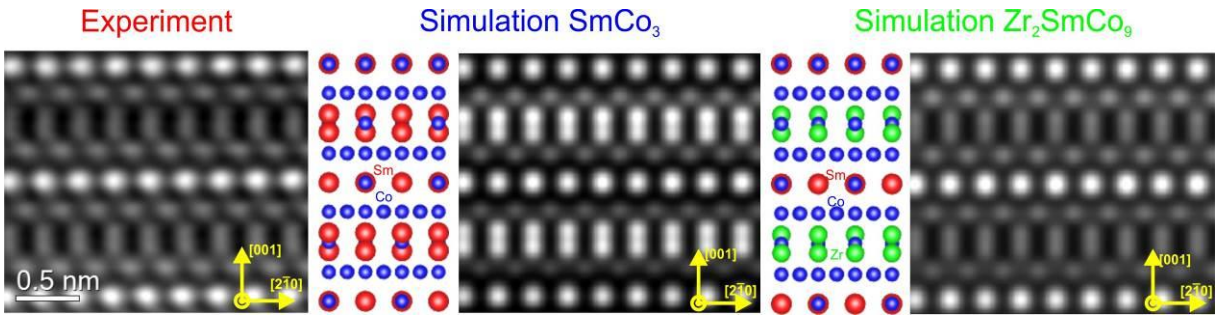

Figure 2. Atomic-resolution HAADF-STEM images of the Z-phase. Experimental (left) and simulated atomic resolution STEM-HAADF Z-contrast images for $SmCo_3$ (center) and Zr_2SmCo_9 (right) viewed along the [120] zone axis.

Sample	Nominal Fe content [wt%]	B_r [T]	H_{cB} [kA/m]	H_{cJ} [kA/m]	$(B{\cdot}H)_{max}$ [kJ/m³]
1	19	1.2	870	2380	262
2	23	0.9	250	280	100

Table 1. Iron content and magnetic properties of the samples extracted from demagnetization curves obtained at T = 20°C.

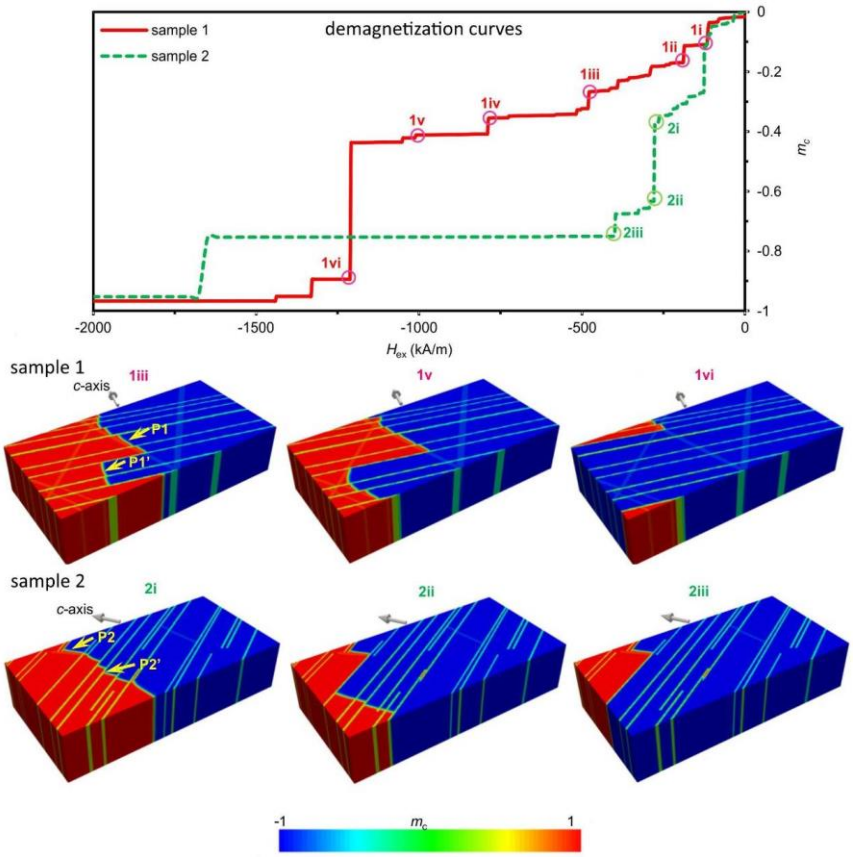

Figure 3. Micromagnetic based simulations describing the domain wall pinning effects.

MS1.P004
Structural analysis of Nd-Fe-B magnets using aberration-corrected STEM

M. Shirai[1], K. Watanabe[1], H. Matsumoto[1], H. Inada[2], T. Yotsuji[2]

[1]Hitachi High-Technologies Corporation, Application Development Dept., Hitachinaka, Japan
[2]Hitachi High-Technologies Corporation, Electron Microscope System Design 1st Dept., Hitachinaka, Japan

manabu.shirai.yd@hitachi-hightech.com

Characteristic properties of functional materials depend heavily on the interface nanostructures. Therefore, it is important to characterize and control their grain boundaries when developing new materials. For example, Nd-Fe-B permanent magnets currently attract great attention because of their magnetic performance. They are widely used for large scale applications such as magnetic recording media, wind turbines and automobiles. It is well known that their magnetic properties are sensitive to the microstructure of grain boundaries. The increasing miniaturization of a grain and the grain boundaries makes imaging with sub angstrom resolution essential when evaluating such materials. Recent developments of the aberration corrector allow for a smaller electron probe with higher intensity. This allows us to obtain higher resolution images and perform higher sensitivity elemental analysis. In the present study, Nd-Fe-B permanent magnets were studied by aberration-corrected STEM.

We observed a commercial Nd-Fe-B permanent magnet using aberration-corrected STEM (Hitachi High-Technologies HF5000 and HD-2700) operated at 200 kV. These instruments are equipped with two EDX detectors (X-MAX 100TLE Silicon Drift Detector (SDD)), in which each SDD has a 100 mm2 sensor and windowless configuration[1]. The Dual SDD system enables us to perform high sensitivity elemental analysis. These Dual SDD detectors are placed in opposition at 90 degree and 270 degree relative to the specimen holder. Figure 1 shows signal intensity of the dual SDD at a tilt angle of 0 and ±5 degree. The individual detector signals are represented by blue and red spectra. The yellow spectrum represents the sum of the individual spectra. We observe that the signal intensity from each detector changes when the specimen holder is tilted. At the same time, the total intensity (of both detectors) changes only a little for different tilt angle. This enables us to obtain EDX spectra independently of the specimen tilting angle. Thus, this system is very useful for EDX tomography. Specimens suitable for STEM observation were prepared by NB5000 FIB-SEM with Hitachi in-situ micro-sampling technique[2]. The thinned specimen was used for STEM observations and EDX analysis.

Figure 2 shows an atomic-resolution dark field STEM image at the grain boundary. Nd atomic columns corresponding to [110] crystal orientation were clearly observed as bright dots in the left crystal. It was confirmed that an amorphous layer of a few nm and microcrystals exist in the grain boundary. Figure 3 presents a dark field STEM image and corresponding EDX elemental mapping images of Fe, Nd and Pr. Each grain was mainly composed of Fe. Fe appeared to be absent in the grain boundary and the triple junction of the boundary. On the other hand, concentration of Nd and Pr were low in the grain area. They were distributed in the triple junction of the boundary. We performed EDX linescan to examine detailed elemental distribution at the grain boundary. Figure 4 shows a dark field STEM image and corresponding line profiles of EDX scanning. The intensities of Fe and other elements (Nd and Pr) showed a complementary distribution in the profiles. The grain boundary phase was enriched with Nd and Pr. It is suggested that the magnetic properties of Nd-Fe-B magnets are attributed to this segregation at the grain boundary.

Our study was conducted to investigate the structure of Nd-Fe-B magnets using aberration corrected STEM. It provided important findings, which will serve to guide the analyses of nano and atomic structures of Nd-Fe-B magnets.

References:

[1] T. Hashimoto et al., Microsc. Microanal. 20, 2014, 604-605
[2] T. Ohnishi et al., Proc. 25th International Symposium for Testing and Failure Analysis, 1999, 449-453

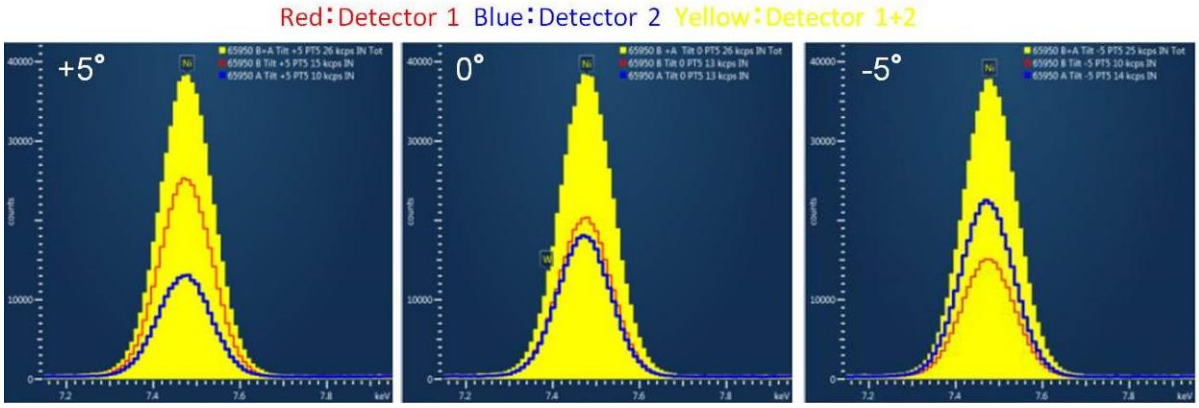

Figure 1. The intensities of dual SDD at specimen angle of 0 and ±5 degree.

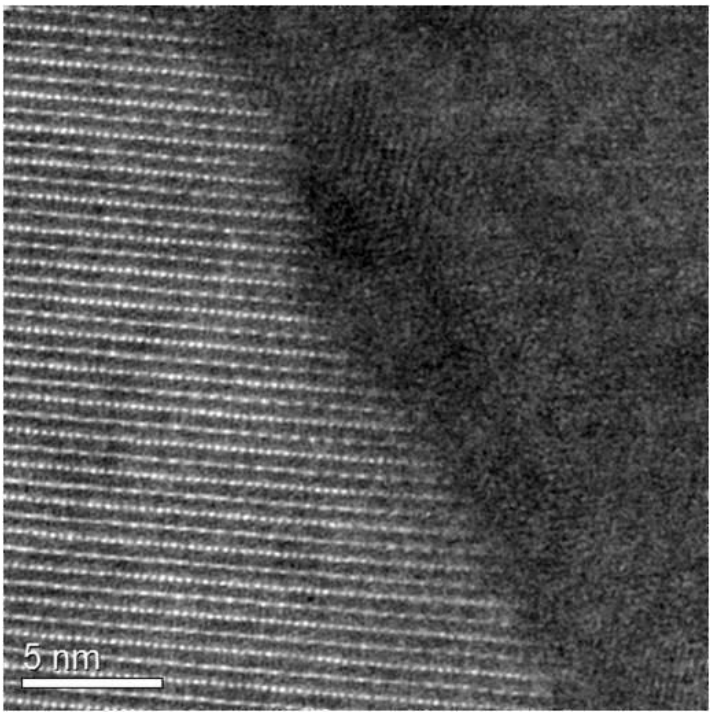

Figure 2. High resolution dark field STEM image of Nd-Fe-B.

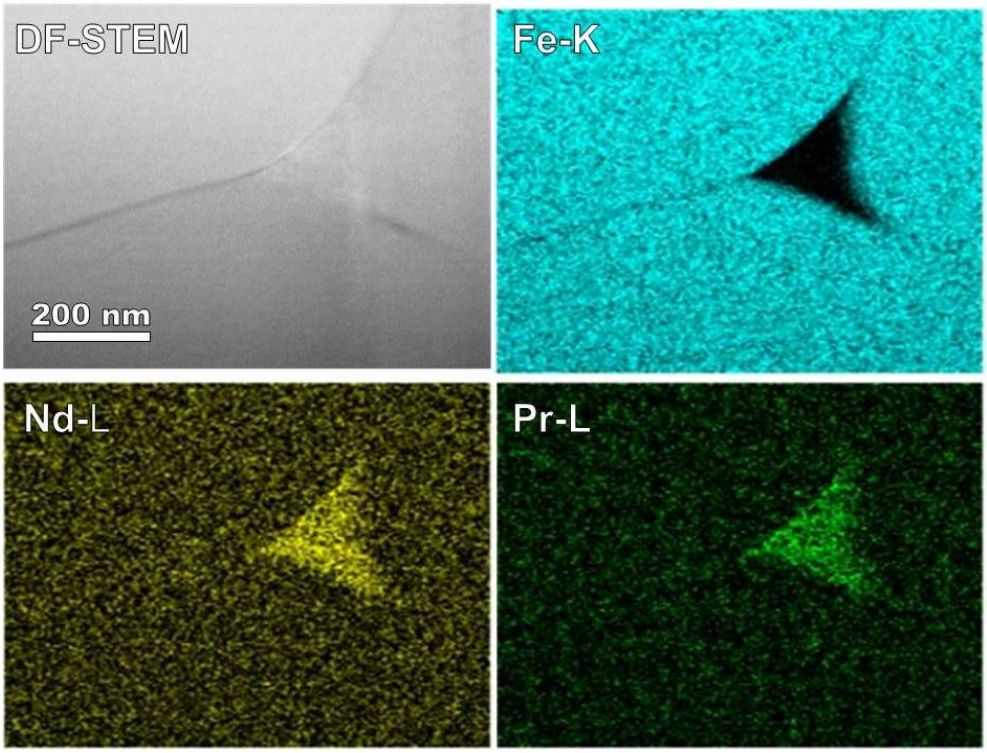

Figure 3. Dark field STEM image and EDX elemental mapping images of Nd-Fe-B.

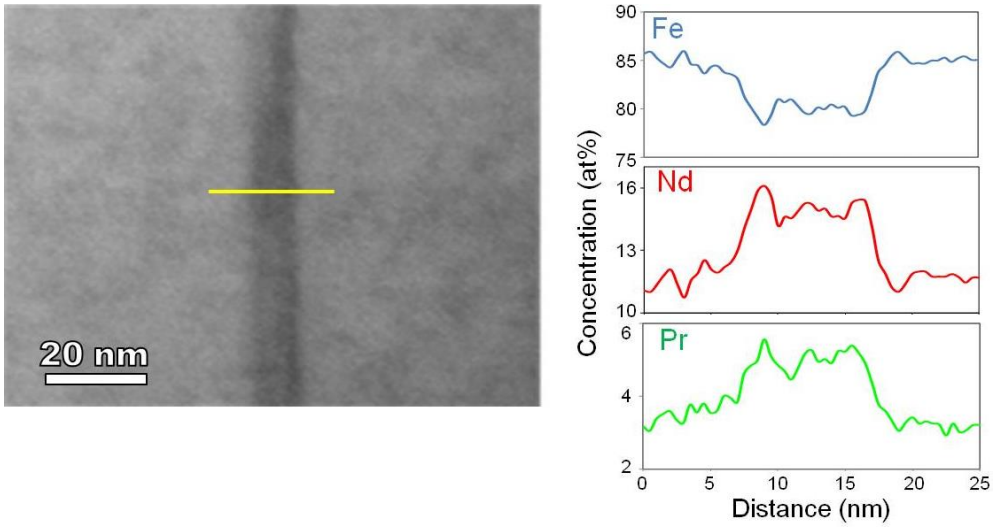

Figure 4. Dark field STEM image and EDX linescan profiles of Nd-Fe-B.

MS1.P005
Atomic structure of "W"-quantum well heterostructures investigated by aberration-corrected STEM and complementary contrast simulation

P. Kükelhan[1], A. Beyer[1], C. Fuchs[1], W. Stolz[1], K. Volz[1]

[1]Philipps-Universität Marburg, Materials Science Center and Faculty of Physics, Marburg, Germany

pirmin.kuekelhan@physik.uni-marburg.de

Introduction: III/V semiconductor heterostructures have a large variety of applications. By substituting atoms on both group III- and group V-sub lattices of the crystal structure it is possible to form quantum well (QW) heterostructrures. A so called "W"-QW heterostructure consists out of three QWs enabling laser emission based on the type-II transition [1]. (GaIn)As/Ga(AsSb)/(GaIn)As "W"-QW heterostructures are suited for laser application at 1300 nm [2], a wavelength which is extremely interesting for telecommunication applications. A variation of the atomic structure and composition leads to a change of the optoelectronic characteristics, particularly the bandgap is tunable.
Objectives: The knowledge of the atomic structure, especially at the interfaces of the QWs, is important for a future improvement of the optoelectronic quality. Therefore, a quantitative analysis of the atomic structure of different "W"-QW heterostructures is performed by Scanning Transmission Electron Microscopy (STEM). For this quantitative analysis, especially the influence of the strain in the material has to be considered. To take this into account and for general comparison, simulations of STEM images, particularly across large regions, are carried out.
Materials and Methods: Atomic resolution high angle annular dark field STEM (HAADF-STEM) enables to investigate the atomic structure of the QW heterostructures and to evaluate both sub lattices independently. For this purpose, samples have been prepared by grinding and polishing with a Multiprep™ System (Allied High Tech Systems) and a precision ion polishing system (Gatan model 691). A double aberration corrected JEOL JEM2200FS was used to characterize the samples.
Additionally, complementary simulations of HAADF-STEM images have been conducted [3]. Thereby, the multislice method was used, including thermal diffuse scattering in the frozen phonon approximation. Chromatic aberration was considered through a defocus series. Simulated supercells can be relaxed by a finite element method using elastic theory [4] and a valence force field approach [5] to incorporate the strain of the crystal.
Results: The intensities of the atomic columns in the resulting HAADF-STEM images are influenced by the composition as well as the strain of the material. Therefore, by taking into account the strain of the heterostructure, the intensity profiles of the III-/V-sub lattices in HAADF-STEM images are investigated. The different QWs are clearly identified and analyzed quantitatively. This quantitative analysis includes the thickness of the QWs and the character of the interfaces for different growth conditions. By comparison of experimental and simulated HAADF-STEM images the atomic structure of the QW heterostructure can be assessed more precisely. Additionally, the intensities of the atomic columns can be used to determine the distribution of In and Sb.
The derived structural information from different samples is correlated to the applied growth conditions and the resulting optoelectronic properties.
Conclusion: The combination of STEM and complementary contrast simulation is an appropriate approach to evaluate the atomic structure of "W"-QW heterostructure samples. By this, one can take into account influences on the intensity of the atomic columns as for example the strain of the material. With an enhanced knowledge of the atomic structure, a further improvement of the optoelectronic properties is made possible.

[1] Möller, C., Appl. Phys. Lett. 108 (7) (2016) 071102.
[2] Fuchs, C., Journal of Crystal Growth (2016).
[3] Oelerich, J. O., Submitt. to Ultramicroscopy. (2016).
[4] Keating, P. N., Phys. Rev. 145 (1966) 637–645.
[5] De Caro, L., Acta Crystallogr. Sect. A Found. Crystallogr. 53 (1997) 168–174.

MS1.P006
GaAs nanocrystals epitaxially grown on nano-patterned (001) Si substrates – strain and defect distribution

R. Kozak[1], I. Prieto[1,2], O. Skibitzki[3], Y. Arroyo Rojas Dasilva[1], R. Erni[1], T. Schroeder[3,4], H. von Känel[1,2] M. D. Rossell[1]

[1]EMPA, Electron Microscopy Center, Dübendorf, Switzerland
[2]ETH Zurich, Laboratory for Solid State Physics, Zurich, Switzerland
[3]IHP, Frankfurt (Oder), Germany
[4]Brandenburgische Technische Universitaet, Institute of Physics, Cottbus, Germany

roksolana.kozak@empa.ch

GaAs nanocrystals (NCs) monolithically integrated on Si nano-pillars and tips (Fig. 1a,b) are promising novel materials for application in optoelectronic devices such as high-speed field-effect transistors, solar cells, photodiodes and lasers [1]. However, the growth of GaAs on Si is very challenging due to their very large lattice and thermal expansion mismatch. Thus, the design and development of such devices with enhanced performances and functionalities requires control and optimization of the structural quality (strain, defect densities, etc.) of the constituent parts.
Here, we present a detailed study on the growth, defects and strain analysis of GaAs/Si nanostructures by means of different scanning transmission electron microscopy (STEM) techniques.
Details about the production of the nano-patterned (001) Si wafers and the GaAs NCs growth are described elsewhere (see [2]-[4]).
For the electron microscopy studies of the GaAs/Si nanostructures, several lamellas were prepared using a FEI Helios Nanolab 450S focused ion beam. Atomic resolution images were acquired in STEM mode using a double spherical aberration-corrected JEOL JEM-ARM200F microscope operated at 200 kV. Additionally, the strain distribution in the GaAs NCs and the compressively strained Si nano-tips were investigated by geometrical phase analysis (GPA) [5] and low-loss EELS.
A detailed examination of the high-angle annular dark field (HAADF-) STEM images of the GaAs/Si interfaces (Fig. 1c) has led to the identification of line defects, in particular, 60º misfit dislocations (with Burgers vectors **b** = 1/2*a*[0-1-1] and **b** = 1/2*a*[101]), 90º and 30º Shockley partial misfit dislocations (**b** = 1/6*a*[-2-1-1] and **b** = 1/6*a*[-11-2], respectively), stair-rod dislocations (**b** = 1/6*a*[1-10]) and planar defects, such as intrinsic and extrinsic stacking faults, and coherent twin boundaries. Both, the GPA analysis (Fig. 1d) and the number of found misfit dislocations indicate that the GaAs NCs are in a completely relaxed state. In general, the number of defects (including stacking faults, twins, dislocation cores of stair-rod dislocation) per square area of the GaAs particle (in nm^2) is lower in the GaAs NCs grown on nano-tips than on pillars (Fig. 1e). It also decreases with increasing GaAs size suggesting that the defects mainly form at the interface and then propagate through the entire crystal.
In order to obtain additional information on the strain distribution along the Si nano-tip, low-loss EEL spectra of the heterostructures were also acquired. An unambiguous blue shift of the Si plasmon peak towards the top of the nano-tip is found and correlated to the compressive strain state of the Si nano-tip embedded in the SiO_2 mask.
In summary, the abovementioned dislocation analysis and low-loss EELS data point towards a fully plastically relaxed GaAs particle grown on compressed (001) Si nano-tips and -pillars. Additionally, we show that the GaAs NCs grown on Si tips contain fewer defects than the ones on pillars.

References:
[1] A.D. Bartolomeo, F. Giubileo, G. Luongo, et al., accepted in 2D Materials, (2017).
[2] O. Skibitzki, I. Prieto, R. Kozak, et al., Nanotechnology, 28 (2017) 135301-135310.
[3] G. Niu, G. Capellini, M.A. Schubert, et al., Sci. Rep., 6 (2016) 1-11.
[4] I. Prieto, R. Kozak, O. Skibitzki, et al., Nanotechnology, 28 (2017) 135701-135708.
[5] M.J. Hytch, E. Snoeck, R. Kilaas, Ultramicroscopy, 74 (1998) 131-146.

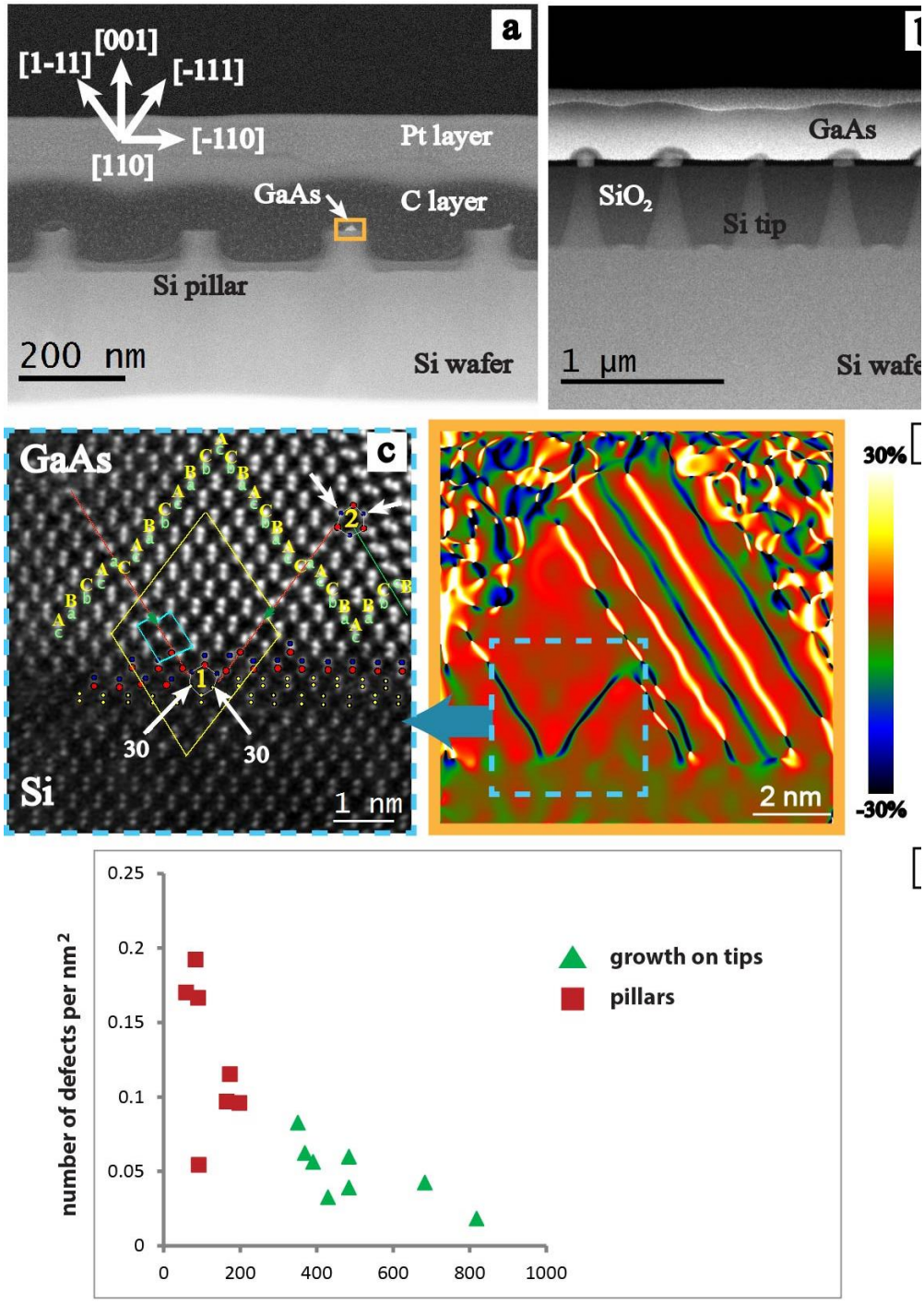

Figure 1. a, b) HAADF-STEM images of the prepared FIB lamellas showing the GaAs nanocrystals grown on top of Si nano-pillars and -tips, respectively. c) Magnified image of the area indicated by a square in panel (a). d) Corresponding $\varepsilon_{\text{in-plane}}$ lattice mismatch strain image obtained by GPA. e) Defect density analysis of GaAs crystals grown on Si nano-pillars and -tips.

MS1.P007
(S)TEM study of the ferromagnetic barrier in $YBa_2Cu_3O_{7-\delta}$ grown on STO(100) and STO(110)

I. Ivanov[1], S. Soltan[2,3], Z. Zhang[1]

[1]Erich Schmid Institute of Materials Science, Austrian Academy of Sciences, Electron Microscopy Group, Leoben, Austria
[2]Max-Planck-Institute for Solid State Research, Stuttgart, Germany
[3]Max-Planck-Institute for Intelligent Systems, Stuttgart, Germany

ivanov.yup@gmail.com

The growing interest to the interfaces between half-metal ferromagnet manganite LCMO and high-temperature superconductor YBCO is motivated not only by fundamental questions aimed at understanding the relation between the electronic and crystallographic structures, and thus, the interface properties, but also by potential applications of hybrid oxide superconductor/ferromagnet/superconductor (SFS) structures in superconducting electronics and quantum computing [1]. In general, it is well established that competitive interactions between ferromagnetic and superconducting layers in superlattices lead to a suppression of superconductivity and magnetism [2]. Ultra-thin LCMO ferromagnetic layer with a thickness of a few unit cells grown in between two thick YBCO superconducting layers could help to overcome this limitation. The main difficulty is a technological one and arises from the length scale required to obtain a supercurrent. As a starting point, the thickness of the ferromagnetic LCMO barrier must be comparable to the superconducting coherence length that is 1.6 nm. Therefore, the realization of planar SFS-Josephson junctions requires a barrier thickness in the range of 2–3 unit cells, which is experimentally achievable by variation of the orientation of YBCO layers.
Here we present the systematic study of the SFS - $YBa_2Cu_3O_{7-\delta}/La_{2/3}Ca_{1/3}MnO_3/ YBa_2Cu_3O_{7-\delta}$ grown at (100) and (110) orientations of $SrTiO_3$(STO) substrate by high resolution Transmission Electron Microscopy (S)TEM and Electron Energy Loss Spectroscopy (EELS).
A (100) or (110) oriented layers of YBCO with the thickness of 20 nm and 2 nm barrier layer of LCMO were subsequently deposited by pulsed laser deposition (PLD) technique on SrTiO3 (STO) single crystals with (100) or (110) orientation. The cross-sections for (S)TEM studies were prepared by using standard Focused Ion Beam (FIB) protocol. The experiments were carried out by a TEM/STEM JEOL2100F operated at 200 kV, equipped with an image-side CS -corrector (CEOS) and a Gatan image filter (Tridiem).
Figure 1a shows (100) oriented SFS. As deduced from STEM and EELS data, smooth 20 nm YBCO layers separated by 2 nm ferromagnetic barrier layer of LCMO are clearly visible. The interfaces are atomically sharp with the atomic plane sequences at the top and bottom interfaces: YBCO-BaO-MnO-La(Ca)O-LCMO and LCMO-MnO-BaO-YBCO. Note, depending on the barrier layer thickness (4 or 5 unit cells), copper oxide layer close to the interface is CuO2 or CuO. YBCO(100) layers show also a high concentration of $Y_1Ba_2Cu_4O_7$ intergrowths, complex defects which can be as a pinning sites for superconducting vortices.
Figure 1c shows the SFS grown on (110) oriented STO substrate. As shown in the inset of the figure the orientation of the c-axis of YBCO layers is at 45 deg with respect to the (110) plane of the substrate. The EELS spectrum image on the fig. 1d identifies the 2 nm LCMO barrier layer. The growth direction of LCMO layer is similar to the case of YBCO (100), along [001] direction. The roughness of the (110) oriented YBCO layers is much higher than ones grown on (100) STO. As a result, the location of the LCMO barrier layer is varied along [110] direction within 8 nm range (roughness for (110) YBCO layers). The interfaces are atomically sharp along (001) direction with the same atomic plane sequence as for (100) oriented SFS.
The observed structural difference of the SFS grown with different orientations allows us to correlate its interfacial structure with measured magnetic and superconducting properties, in particular the supercurrent tunnelling for (110) oriented YBCO [3].

References:
[1] Nat. Mater. 11, 675 (2012).
[2] Nat. Phys. 8, 539 (2012).
[3] Jour. Appl. Phys. 118 (22), 223902 (2015).

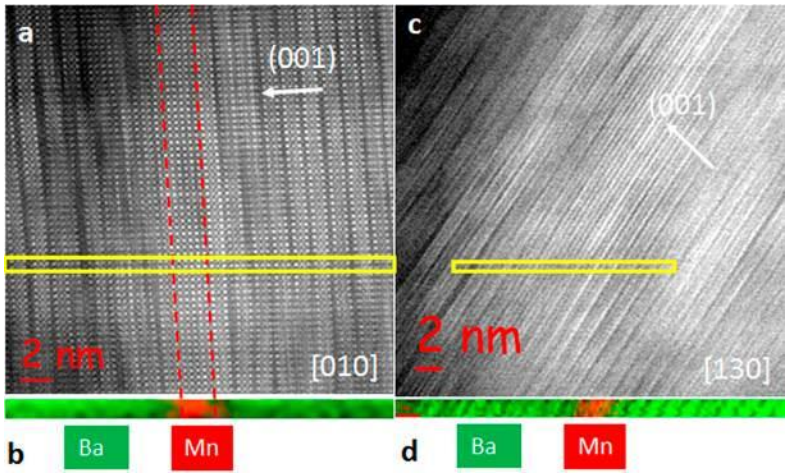

Figure 1. STEM (a, c) and EELS(b, d) data for SFS grown in (100) orientation (a, b) and (110) orientation (c, d).

MS1.P008
Elucidating the formation of Bi-rich nano-clusters in annealed Ga(As,Bi) epilayers – revisiting the significance of crystal polarity, dislocation loops and native point defects

M. Wu[1,2,3], J. Puustinen[3], E. Luna[2], J. Hilska[3], P. Schweizer[1], M. Guina[3], A. Trampert[2], E. Spiecker[1]

[1]Institute of Micro- and Nanostructure Research, Materials Science, FAU Erlagnen-Nuremberg, Erlangen, Germany
[2]Paul-Drude-Institut für Festkörperelektronik, Microstructure, Berlin, Germany
[3]Tampere University of Technology, Optoelectronics Research Centre, Tampere, Finland

mingjian.wu@fau.de

III-V-Bi (with Ga(As, Bi) as the prototype) is a unstable material system where many types of atomic ordering and nano-scale microstructures develop due to the inherent instability of the alloy constituents [2-5], which are of great interest and potential for semiconductor nanotechnology [1]. Our recent findings that size-homogeneous Bi-rich nano-clusters (NCs) can form spontaneously after rapid thermal annealing (RTA) of Ga(As,Bi) epilayers, open the possibility to create Bi-rich quantum dot-like structures with potential for optoelectronic applications [2]. However, a clear insight into the formation mechanism and the dominating effects is still missing, which hinders the predictable optimization of the fabrication processes. The current work aims to gain such insight by *in-situ* and *ex-situ* advanced TEM studies.
We observed the formation and growth of Bi-rich NCs during *in-situ* annealing of Ga(As,Bi) epilayers at 780ºC (Fig. 1) in the TEM. *In-situ* observation clearly reveals a significantly longer time for the formation and growth of Bi-rich NCs compared to RTA. The formation of DLs, which was identified in *ex-situ* observations, did not occur during the *in-situ* annealing in the TEM. This demonstrates that the DLs formed subsequent to the formation of NCs, and possibly as agglomeration of point defects. The results also suggest that the native point defects are crucial in assisting the diffusion of Bi atoms upon annealing.
Static *ex-situ* observations revealed preferential faceting of the Bi-rich NCs in some high-temperature annealed samples (Fig. 2). Once the crystal polarity was determined, we find that the interface area of Ga{111} is ~6 times of As{111} planes in these samples. We may deduce the possible type of point defects (interstitial- or vacancy-type) that dominate in assisting the diffusion of Bi atoms and formation of Bi-rich NCs and attached DLs, if the absolute sign and magnitude of the Burgers vector of the dislocations would be known, which also requires the knowledge of the crystal polarity. High-resolution STEM imaging and convergent beam electron diffraction (CBED) are applied to determine the crystal polarity [6], and large angle CBED (LACBED) is used to determine the full Burgers vector of the DLs (Fig. 3). The results turned that Bi atoms have indeed a preferential precipitation to the Ga{111} planes. The Burgers vector of the DLs is $\mathbf{b} = \frac{1}{2}[-101]$. The formation of this type of Burgers vector is deduced to be a Frank partial loop of collapsed vacancy disk by agglomeration of out-diffused As anti-sites, whereas the stacking fault is later removed by Shockley partial loops. This hypothesis is supported by HRSTEM observations on the dislocation core structures from edge-on segments of the DLs and occasionally identified very short sections of intrinsic type stacking faults.

MW and ES gratefully acknowledge financial support by the German Research Foundation via the Research Training Group GRK1896 and the Cluster of Excellence EXC315. JP, JH and MG acknowledge financial support from Academy of Finland (No. 259111)

[1] Dietl, T. (2006). Nat. Mater., 5, 673.
[2] Wu, M., et. al. (2014). Nanotechnology, 25(20), 205605.
[3] Luna, E., et. Al. (2015). J. Appl. Phys., 117, 185302.
[4] Wu, M., et. al (2015). Nanotechnology, 26(42), 425701.
[5] Wu, M., et. al.. (2014). Appl. Phys. Lett., 105(4), 041602.
[6] Spiecker, E. (2002). Ultramicroscopy, 92, 111

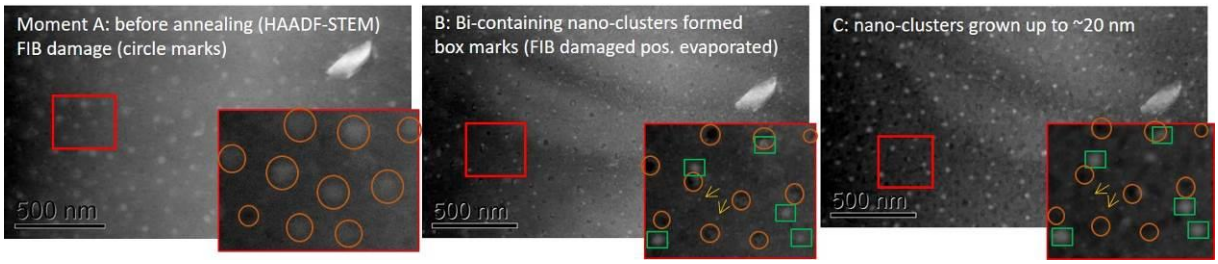

Figure 1. Snapshots before (A), during (B) and after 550 s (C) *in-situ* annealing at 780C of a plan-view Ga(As, Bi) epilayer.

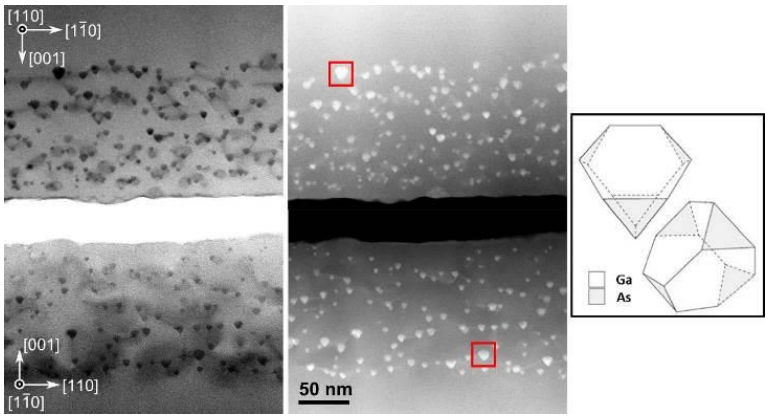

Figure 2. Simultaneous ABF- (left) and HAADF- (middle) STEM images of a cross-section Ga(As, Bi) epilayer after RTA at 800C for 60s, acquired along [1-10] (bottom) and [110] (top) zone axis. NCs and DLs are clearly visible. Preferential faceting of the NCs is evidenced. Once the crystal polarity determined, we find the interface area of Ga{111} are ~6 times of As{111} (right).

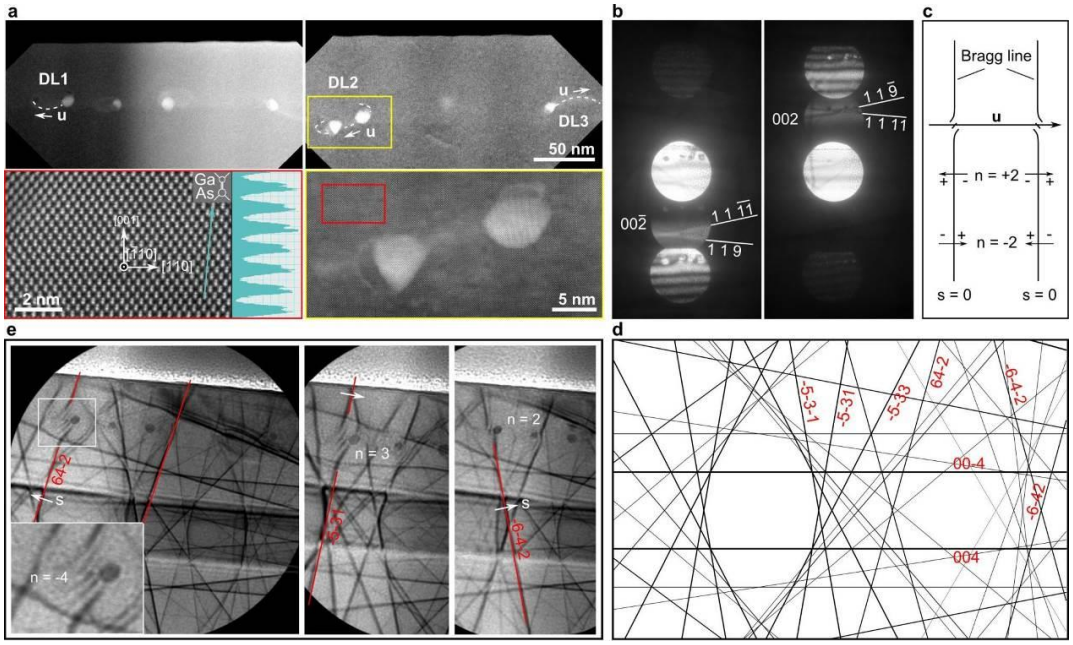

Figure 3. Determination of the crystal polarity by HRSTEM (a) and CBED (b), to be in [-110] projection. Cherns-Preston rule (c) is applied to determine the absolute Burgers vector of DLs with 3 independent HOLZ line twist and splitting (e) in LACBED pattern, to be **b** = ½[-101] (all three DLs result in the same b, only patterns at DL1 shown). (d) calculated kinematic LACBED pattern at [2-30] pole.

MS1.P009
Influence of the interface on electric properties and growth of non-thermodynamic equilibrium phases – hexagonal GdScO3 and LaLuO3 on GaN (0001)

T. C. U. Tromm[1], J. Schubert[1], W. Zander[1], D. Meertens[2], M. Kruth[2], H. Hardtdegen[1], S. Mantl[1]
M. Luysberg[2]

[1]Forschungszentrum Jülich GmbH, Peter-Grünberg-Institut (PGI9-IT), Jülich, Germany
[2]Forschungszentrum Jülich GmbH, Ernst Ruska Centrum 1, Jülich, Germany

t.tromm@fz-juelich.de

Introduction: III-V-nitrides are of growing interest due to their application as high electron mobility transistors, high power and high frequency devices and light emitting diodes (LEDs). For device fabrication suitable high-k oxides are needed, which exhibit a high permittivity and a wide band gap. Further, a low interface trap density is critical for the device structure to achieve a good sub-threshold slope and a high drive current, since the GaN misses a native oxide.
Objectives: Ternary oxides like LaLuO3 (LLO) and GdScO3 (GSO) are promising candidates, because of the possible epitaxial growth by pulsed laser deposition (PLD) which reduces the density of interfacial traps. These materials are known to grow either amorphous, cubic (Ia-3) or in the orthorhombic (*Pbnm)* phase. Surprisingly, we recently discovered a hexagonal phase for GSO and LLO deposited on GaN (0001) by pulsed laser deposition[1, 2]. This hexagonal phase is not the thermodynamic equilibrium phase and evolves despite a huge mismatch between the GaN and the LLO and GSO of 18 % and 13 %, respectively. To date the driving force for the stabilization of this phase is unknown. Here, we investigate the structure and composition of the interface on the atomic scale by advanced transmission electron microscopy and spectroscopy.
Materials and Methods: The GSO and LLO layers were deposited on 3 µm hexagonal n-doped GaN (0001) grown on α-Al2O3 (0001) by metalorganic vapor epitaxy [3]. The oxides were deposited by PLD using a KrF excimer laser (pulse width 20 ns, wavelength 248 nm and fluence 2.5 Jcm-1) at a substrate temperature of up to 900 °C. Stoichiometric GSO and LLO targets were used. Cross sectional specimen were prepared by focused ion beam followed by Ar ion milling. A Titan 80-200 equipped with a Cs probe corrector and a Super-X detector was used to acquire high resolution HAADF images and EDX spectra. For electrical characterization Pt was deposited on the oxides. Capacitance-voltage (CV) and current-voltage (IV) curves were measured using an Agilent E4980A.
Results: IV measurements reveal a high resistance of the layers exhibiting no leakage up to 5 MV/cm and 8 MV/cm for GSO and LLO, respectively. To determine the permittivity (k) of the layers, a CET plot is extracted from measured CV curves for different oxide thicknesses (s. Figure 1). The capacity of the oxides is inversely proportional to the oxide thickness. The determined permittivities are 25±5 and 31±2 for GSO and LLO, respectively. A first investigation of hexagonal GSO on GaN with STEM exhibits an atomically sharp interface (see Figure 2). Due to changes in the crystal tilt local variations in contrast arise within the GSO layer. A detailed investigation of the atom row distance exhibit an enhanced spacing of 0.31nm compared to 0.26 nm within GaN and 0.29 nm within the GSO layer. Furthermore, an interfacial layer in the GSO is obvious, which can be deduced from the darker contrast of the first atom row at the interface. EDX measurements of this interfacial layer (not shown here) reveal an enrichment with Sc, , while the next three atom rows show a higher Gd-content compared to the stoichiometric composition measured in the center of the oxide.
Conclusion: Whether this compositional segregation of GSO could be the reason for the stabilization and growth of the hexagonal phase and its impact on electrical properties will be discussed in this presentation.

References:
[1] Tromm, T.C.U., et al., *Ternary rare earth based oxides for Nitride based devices.* ECS Transactions, 2016. **72**(2): p. 307-317.
[2] Schäfer, A., et al., *Polymorphous GdScO3 as high permittivity dielectric.* Journal of Alloys and Compounds, 2015. **651**: p. 514-520.
[3] Hardtdegen, H., et al., *Uniform III-nitride growth in single wafer horizontal MOVPE reactors.* physica status solidi (a), 2005. **202**(5): p. 744-748.

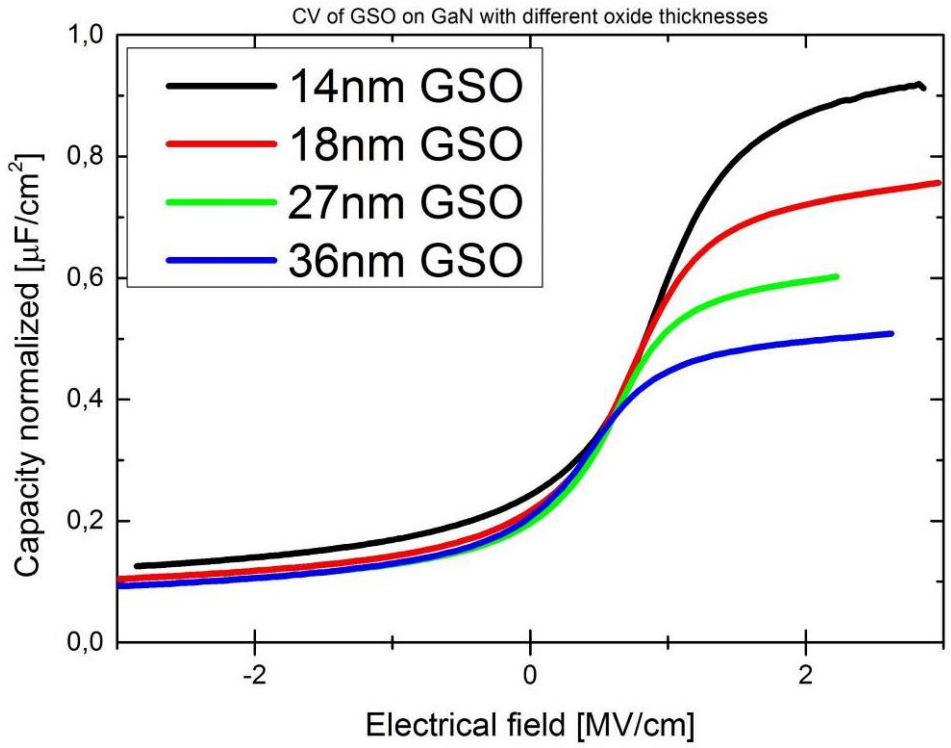

Figure 1. CV of GSO on GaN with different oxide thickness.

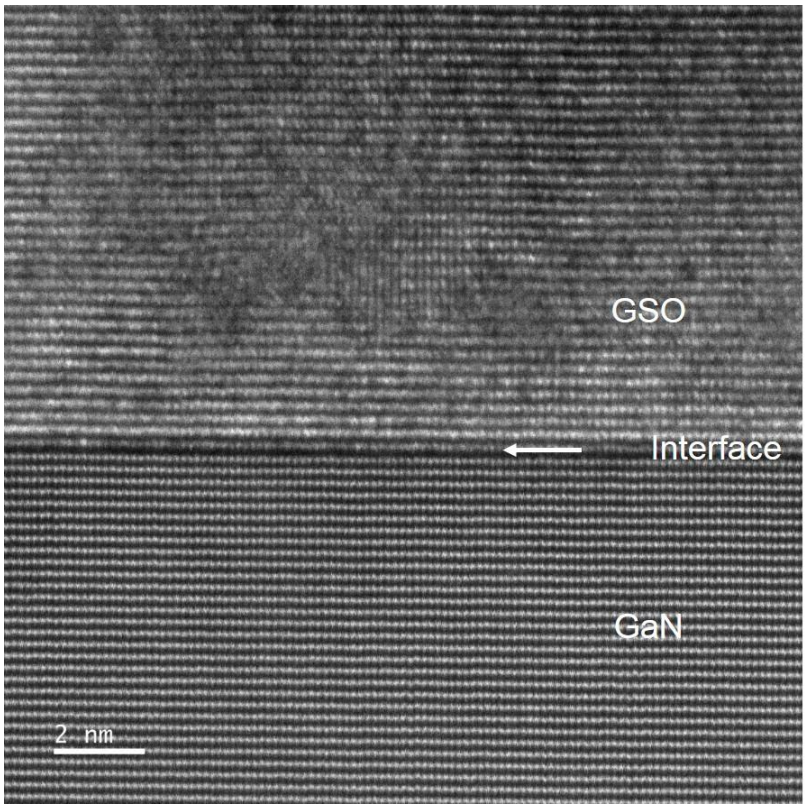

Figure 2

MS1.P010
Quantitative structural characterization of Ga(NAs) quantum well heterostructures on (001) Si substrates

S. Gupta[1], A. Beyer[1], L. Duschek[1], P. Ludewig[1], W. Stolz[1], K. Volz[1]

[1]Philipps-Universität Marburg, Materials Science Center and Faculty of Physics, Marburg, Germany

guptash@staff.uni-marburg.de

Introduction**:** The realization of monolithically integrated optoelectronic (OEIC) and photonic circuits (PIC) on Si substrate would remarkably increase the functionality of Si microelectronics. One of the main challenges to realize Si based OEIC and PIC is to integrate an efficient and stable laser material on exact (001) Si [1].
Hence, heteroepitaxial integration of direct band gap III-V semiconductors on Si substrates are an important research topic. A particularly promising approach is to use Ga(NAsP) as the active laser material as it can be grown lattice matched to Si substrates [2].
Objectives: The optical and electronic properties of OEIC and PIC devices are strongly associated to the quality of their active layers [3]. The quality of the layers can be determined by the roughness of the optically active quantum wells at both interfaces and by the composition fluctuation within the layers. Using STEM in annular dark field mode, we have performed a systematic quantitative structural analysis of ternary Ga(NAs) quantum well (QW) structures on Si substrates.
Materials and Methods**:** The investigated $Ga(N_xAs_{1-x})$/GaP/(BGa)(AsP)-multiple quantum well heterostructures (MQWH) were grown pseudomorphically strained on exactly oriented (001) Si-substrates using thin GaP buffer layers by metal organic vapor phase epitaxy (MOVPE). For electron microscopy investigation, cross-sectional (S)TEM samples were prepared by grinding and polishing with a MultiprepTM System (Allied High Tech Systems) and argon ion milling with a Gatan precision polishing system. The samples were investigated in a double-Cs corrected JEOL JEM 2200 FS field emission (S)TEM operating at 200 kV. Images were acquired at two different inner angles of the annular dark field detector (30 and 86 mrad) and evaluated using home written Matlab program.
Results**:** Three samples with different nitrogen concentration, as derived by high resolution X-ray diffraction, x=0.092, 0.152 and 0.168 have been investigated. The nominal structural details of the investigated samples is shown in fig.1(a) and the corresponding overview images are shown in fig.1(b) to fig.1(d).
There is no sign of phase separation in all the three samples. However, the samples with N fractions of 9.2% and 16.8%, shown in fig.1(b) and fig.1(d) respectively, show defects in contrast to the sample with a N fraction of 15.2%, shown in fig.1c. It has been observed that the lower interfaces of each Ga(NAs) QW in all the samples are abrupt while the upper interfaces are rough. The defect density as well as the upper interface roughness is found to be larger for the sample with 16.8% N in comparison to the samples with 9.2% N and 15.2% N. On the contrary, the composition fluctuation in Ga(NAs) QW for the sample with 15.2% N is observed to be larger than in the other two samples. The nominal composition as well as the composition fluctuation derived from low resolution STEM have also been compared to an evaluation of the N content using atomic resolution STEM high angle annular dark field (HAADF) experimental images and complementary multislice simulations.
Conclusion: Quantitative evaluation of STEM images is a useful technique to optimize the growth of MQWH and hence device structures. The structure with 15.2% N in Ga(NAs) QW exhibits the highest crystalline quality.

References:
[1] Read, G. W., et al., *IEEE Journal of Selected Topics in Quantum Electronics*, *21*(6), 377-384, 10.1109/JSTQE.2015.2424923
[2] Liebich, S., et al.," *Applied Physics Letters* 99.7 (2011): 071109, http://dx.doi.org/10.1063/1.3624927
[3] Wegele, T., et al., *Journal of Physics D: Applied Physics* 49.7 (2016): 075108, doi:10.1088/0022-3727/49/7/075108

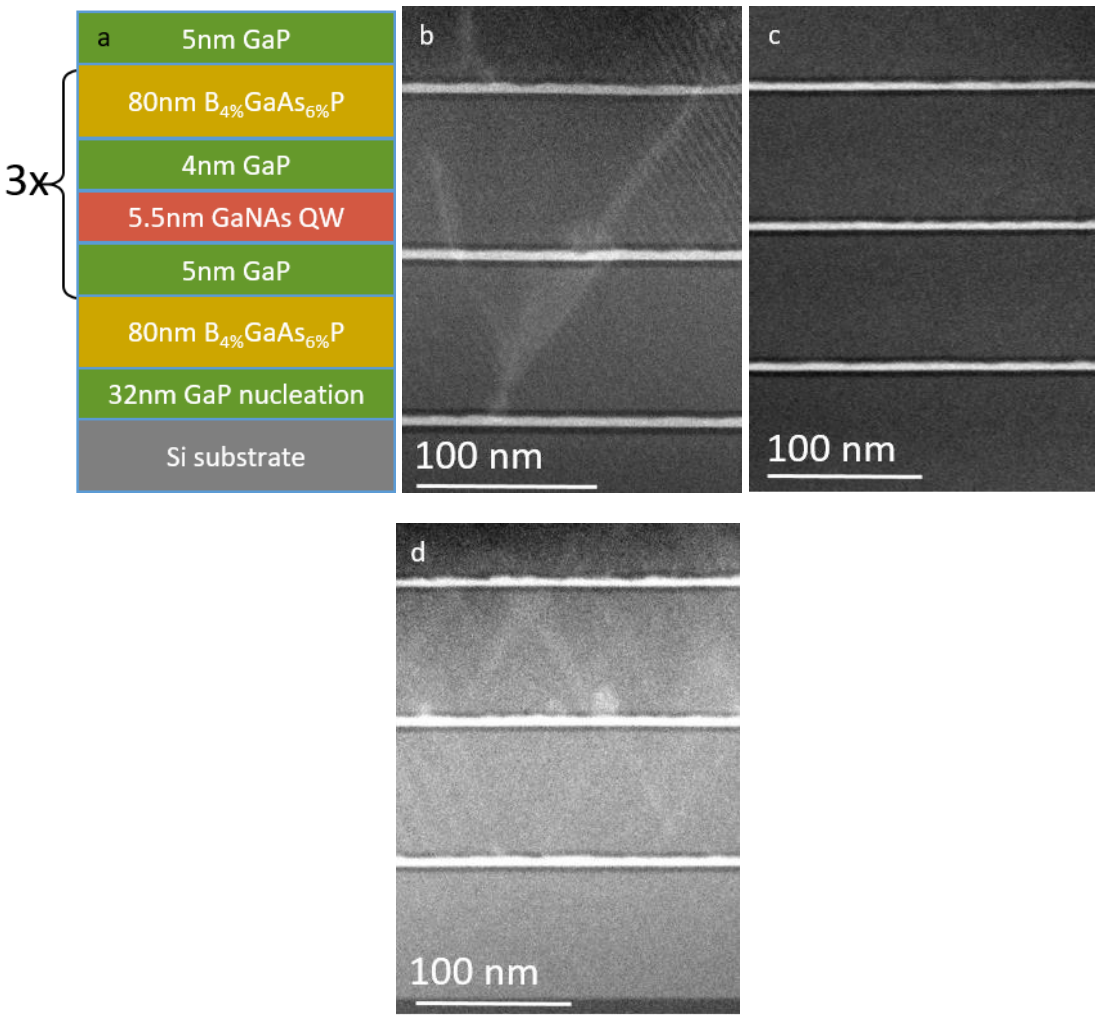

Figure 1. (a) shows the schematic structure of Ga(NAs)/GaP/(BGa)(AsP) MQWH on (001) Si-substrate. (b), (c) and (d) show overview images of samples with N-fractions of 9.2%, 15.2% and 16.8% respectively.

MS1.P011
Structure-property relationships in process-optimized (Nd,Dy)-Fe-B magnets

S. Selle[1], T. Höche[1], A. Dirks[2], C. Recknagel[3], C. Weck[4]

[1]Fraunhofer Institute for Microstructure of Materials and Systems IMWS, Center for Applied Microstructure Diagnostics CAM, Halle, Germany
[2]Fraunhofer Institute for Silicate Research ISC, Project Group Materials Recycling and Resource Strategies IWKS, Hanau, Germany
[3]Fraunhofer Institute for Manufacturing Technology and Advanced Materials IFAM, Dresden, Germany
[4]Fraunhofer Institute for Manufacturing Technology and Advanced Materials IFAM, Bremen, Germany

susanne.selle@imws.fraunhofer.de

Compared to other permanent magnets, (Nd,Dy)-Fe-B magnets have by far the highest energy density. One reason is the high coercivity triggered by an extremely high magnetocrystalline anisotropy. Regarding the rare earth elements Nd and Dy, the partial substitution of Nd with Dy improves the coercivity even more, especially if Dysprosium is located at the grain boundaries. In this way, the thermal stability is increased and this makes the material suitable for high-temperature applications like electric engines in vehicles or generators in wind turbines. Due to the predicted growth of green technologies, the recommended economic use of the raw material led to various efforts to minimize or even substitute Dysprosium. One direction considers process-optimized synthesis of the (Nd,Dy)-Fe-B system in order to minimize material waste and post-processing steps. Thereby the technology of metal injection molding (MIM) is one kind of near-netshape processing. Another approach deals with microstructure optimization of the Dy-free Nd-Fe-B system via new sintering techniques like spark plasma sintering (SPS).
To relate microstructure with magnetic properties, SEM and TEM were employed to reveal the microstructure of the MIM and SPS samples. In the case of MIM processing, SEM measurements were imaging the phase content on the µm scale whereas TEM resolved the characteristics of the grain boundaries on the nm scale. The SPS material was analyzed with regard to compaction (SEM) and condition of grain boundaries (TEM).
During the MIM process, Dy is added to an organic binder which is mixed with the Nd-Fe-B base powder to increase the possibility that Dy can be found mainly at the grain boundaries. Nanocrystalline Nd-Fe-B powder from melt-spun flakes served as the starting material for the SPS process, where temperature and filling ratio variation were adjusted for an optimization of the microstructure with regard to level of compactness and related magnetic measurements. Analysis with the SEM was done on mechanically or ion polished surfaces of the bulk material depending on the necessary lateral dimensions of the investigated sample area. Phase composition analysis was done by energy-dispersive X-ray spectrometry (EDXS). EDXS was also employed during TEM analysis together with selected-area electron diffraction (SAED) and Lorentz microscopy.
Regarding the MIM Process, various samples with different Dy content and Dy sources in the binder have been analyzed by SEM and TEM. TEM samples were prepared with focused ion beam (FIB) machining to ensure the existence of grain boundaries in the lamella. One of the results shows that, if the target value of Dy was chosen to high, no complete debindering took place and formation of the α-Fe phase occurred (Fig. 1). Results concerning the SPS-processed samples show different degrees of compaction on the µm scale depending on the sintering temperature T_S. TEM analysis dealt with the structure of flake boundaries as well as the grain boundary phase between the nanocrystalline particles.

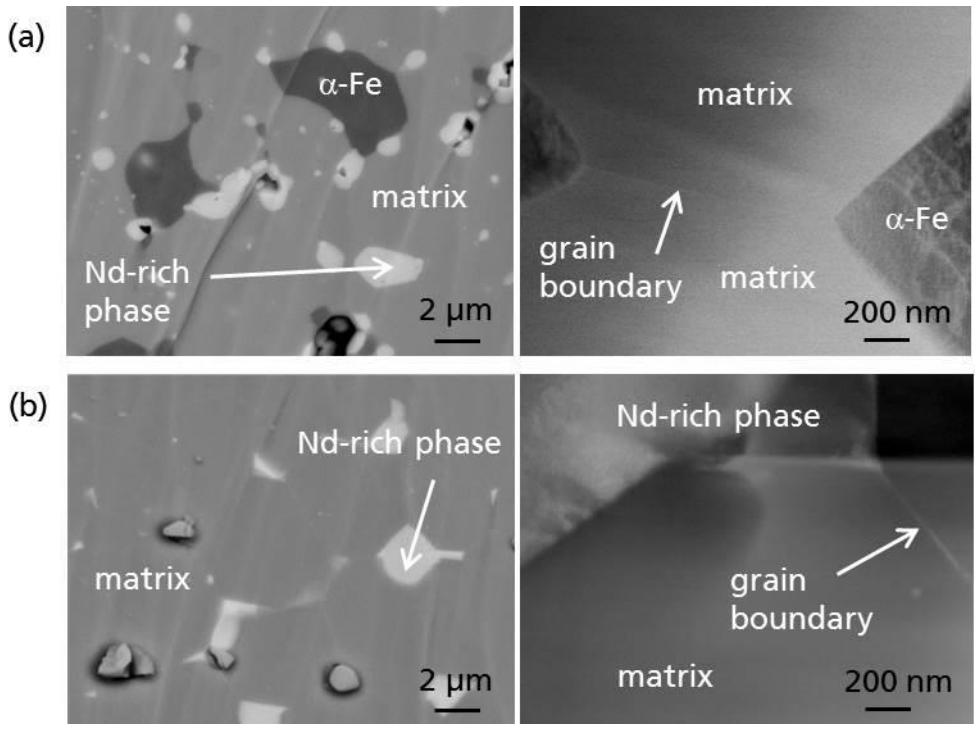

Figure 1. SEM micrographs (left) and STEM micrographs (right) showing phase composition of MIM-processed (Nd,Dy)-Fe-B material with different Dy sources and nominal values for Dy. (a) Dy-acetate as Dy source in the binder and theoretically expected value of 1 mass% Dy after debindering. (b) Dy-carbonate as Dy source in the binder and theoretically expected value of 0.6 mass% Dy after debindering.

MS1.P012
HRTEM studies of tailored nanostructures in epitaxially grown FeRh thin films

M. S. Gorji[1,2], D. Wang[1,3], R. Witte[1], S. Schlabach[3,4], R. Kruk[1], C. Kübel[1,3], H. Hahn[1,2]

[1]Karlsruhe Institute of Technology , Institute of Nanotechnology, Eggenstein-Leopoldshafen, Germany
[2]Technical University Darmstadt, KIT-TUD-Joint Research Laboratory Nanomaterials, Darmstadt, Germany
[3]Karlsruhe Institute of Technology, Karlsruhe Nano Micro Facility, Eggenstein-Leopoldshafen, Germany
[4]Karlsruhe Institute of Technology, Institute for Applied Materials, Eggenstein-Leopoldshafen, Germany

saleh.gorji@partner.kit.edu

Magnetic properties of FeRh thin films can be modified by epitaxially growing it on a crystalline substrate with different lattice parameters, where the strain (compressive or tensile) between the FeRh and the substrate lattices alters the nanostructure of the thin film [1,2]. Understanding these nanostructures is the key to reproduce and tune the functional magnetic properties of FeRh thin films. The thin films investigated here were epitaxially grown on MgO substrate, with and without W and, W-V buffer layers. The cross sectional TEM lamella of epitaxial FeRh thin films were prepared by focused ion beam and studied by aberration corrected transmission electron microscopy (TEM). In the case of FeRh grown on MgO 001 with a lattice mismatch of ~0.3%, a slight distortion is observed at the interface while the crystal structure (B2-phase CsCl) of the thin film is mainly intact. The FeRh films grown on a W surface (lattice mismatch of ~6%) undergo a structural change to a new lower symmetric orthorhombic Cmcm phase, which was identified by high-resolution TEM (HRTEM). This orthorhombic structure forms nano grains with a finely twinned arrangement to adapt to the W 110 lattice constant (Figure 1a). The results are in agreement with XRD measurement and were also confirmed by DFT calculation [1]. Along with the transition from the body centered tetragonal (bct) phase to this Cmcm phase, a suppression of the magnetic order was observed. Furthermore finely controlled structural modification were studied, where the FeRh thin film were epitaxially grown on W-V with various W:V ratios, thus changing the lattice constant of W-V buffer layer. In the case of W0.25V0.75, the co-existence of both bct and Cmcm phases was confirmed by HRTEM (Figure 1b). In this small to medium strain regime, instead of forming single phase equilibrium structure, the strain is accommodated by adaptive nanostructures containing two phases. This shows that it is possible to fine tune the magnitude of the antiferromagnetic component, which is attributed to bct FeRh, in the thin films.

References:

[1] Ralf Witte, Robert Kruk, Markus E. Gruner, Richard A. Brand, Di Wang, Sabine Schlabach, Andre Beck, Virgil Provenzano, Rossitza Pentcheva, Heiko Wende, Horst Hahn, *Physical Review B* (2016) 93, 104416.

[2] Ralf Witte, Robert Kruk, Alan Molinari, Di Wang, Sabine Schlabach, Richard A Brand, Virgil Provenzano and Horst Hahn, *Journal of Physics D* (2017) 50, 025007.

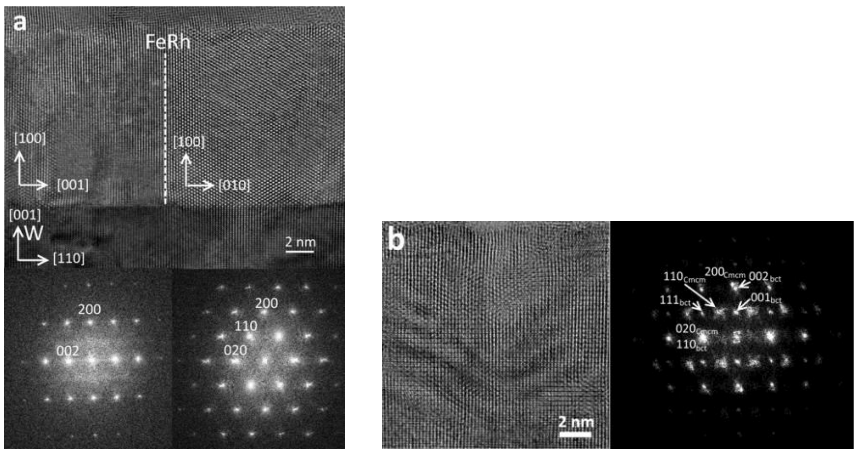

Figure 1. a HRTEM image and the corresponding FFTs of FeRh/W in Cmcm phase with two grains with 90° rotated in-plane orientation; b) a HRTEM image and the corresponding FFT of FeRh/W0.25V0.75, showing overlapped Cmcm and bct phases.

MS1.P013
STEM and EDX analyses of III-V layers for lateral current injection lasers integrated on silicon

M. SOUSA[1], Y. Baumgartner[1], L. Laurenius[1,2], H. Hahn[1], D. Caimi[1], L. Czornomaz[1]

[1]IBM Research GmbH, Rueschlikon, Switzerland
[2]Infinera, Stockholm, Sweden

sou@zurich.ibm.com

Many Datacom/Telecom applications could benefit from platforms developed for the silicon (Si) industry as they operate around 1.3 or 1.55 µm where Si is transparent. Si is inefficient as a light-source, whence the need for III-Vs for integrated lasers.
To develop Si photonics operating at 1.3 µm, a stack of thin In*x*Al*y*Ga1-*x*-*y*As layers with alternating In and Al contents (x = 0.49 or 0.62; y = 0.14 or 0. 29) has been grown on an InP substrate by metalorganic chemical vapor phase epitaxy at 550°C and transferred with wafer bonding onto a SiO2/Si wafer [1] to serve as a fully CMOS integrated light source.
A multi quantum wells (MQW) structure is used to achieve high modal gain [2; 3]. The MQW stack can be contacted vertically or, better, laterally, to reduce its total thickness and make it CMOS-compatible.
Yet, lateral current injection (LCI) is only possible if side walls between the InAlGaAs MQW region and lateral InP contacts is free of defects and impurities. Any contamination or native oxides could indeed lead to carrier recombination or force carriers to tunnel through the barrier created at such interfaces, which in turn lowers the laser efficiency. It is thus crucial to optimize the etch process for InAlGaAs to achieve smooth, defect-free sidewalls before epitaxial regrowth of the contacts.
STEM and EDX analyses using a double aberration-corrected JEOL ARM 200F microscope have been performed to investigate various cleaning recipes of the MQW interfaces. High-Angle Annular Dark Field (HAADF) images have been acquired at 200 kV and EDX scans performed using a liquid nitrogen free Si drift detector.
Photoluminescence and high resolution X-ray diffraction measurements were carried out to optimize the growth of a succession of defect-free strained layers, alternating tensile and compressive films (Fig.2a, b).
Two different surface preparations of the MQWs lateral interfaces before the contacts epitaxial regrowth were investigated: (a) H3PO4:H2O2:H2O wet etch followed by H2SO4 surface passivation and (b) low power dry etch process based on Cl2 [4].
Process (a) led to an overetch of the MQW structure (Fig 1a) [3]. EDX analyses revealed the presence of oxygen (formation of Al2O3) on the side walls (Fig 1b).
As this reduces the injection efficiency, process (b) was developed. HAADF images do not show any overetch (Fig. 1c) and elemental contamination could not be detected by EDX (fig. 2c).
STEM and EDX analyses have been performed to characterize the III-V MQWs and monitor the interface quality. An optimized etch recipe allowed defect-free interfaces to be obtained between the MQW stack and lateral InP contacts. This is a promising step towards the realization of an efficient LCI laser device on Si.

[1] L. Czornomaz et al, IEDM 2012, pp.23.4.1-23.4.4
[2] Okamura *et al*, Optics Express, **17**,15 pp12564-12570
[3] L. Laurenius, Master thesis, 2016
[4] H. Hahn *et al*, submitted to DRC 2017

The authors acknowledge support from the BRNC OpTeam.
This project received funding from the H2020 ICT project (grant No 688003).

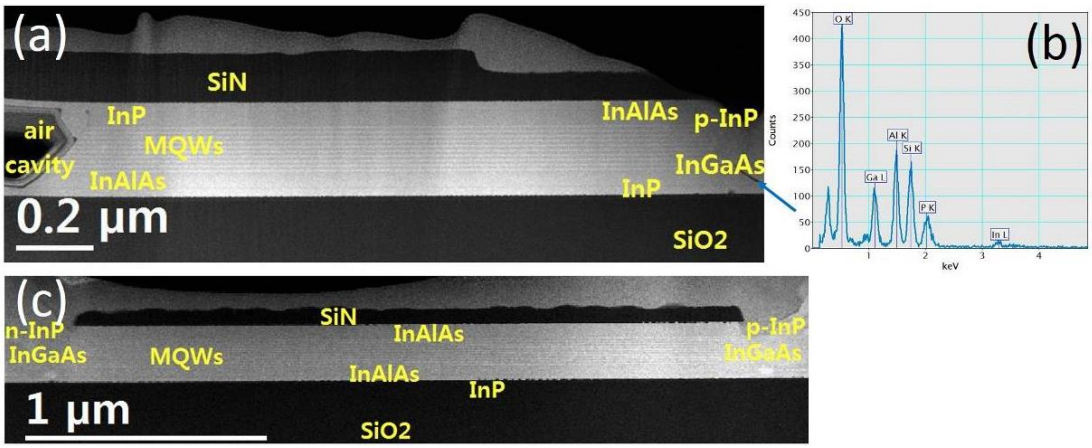

Figure 1. (a): HAADF image overview of LCI laser obtained with wet etch process. The MQW stack is overetched and EDX reveals O contamination at the interface with the contacts (b). (c): HAADF image overview of LCI laser obtained with dry etch. The MQW expands over 2.9 µm and is 200 nm thick. *Both:* On top and bottom InAlAs acts as a buffer while in between lays an alternation of thin In0.62Al0.29Ga0.22As quantum wells under tensile strain and thicker In0.49Al0.14Ga0.24As barrier under compressive strain. The overall structure is relaxed. On the sides, one can see *p*- and *n*-InP contacts and InGaAs markers. SiN hard mask and InP seed layer bonded on SiO2 are also present.

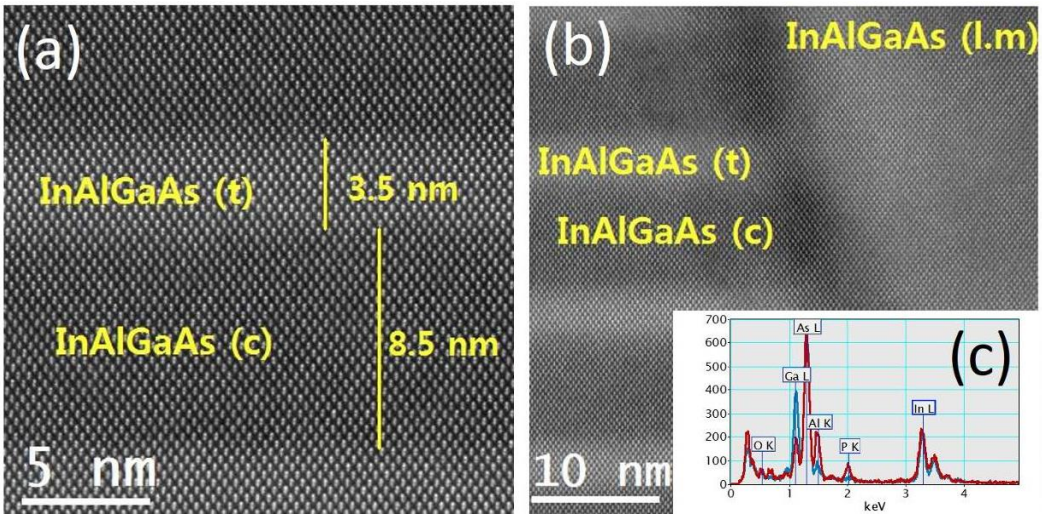

Figure 2. (a) HAADF image of the MQW (similar quality obtained for both etch processes): the alternate deposition of 3.5 nm thick In0.62Al0.29Ga0.22As (InAlGaAs (t)) and 8.5 nm thick In0.49Al0.14Ga0.24As (InAlGaAs (c)) is defect-free. (b): Zoom of Fig.1c over RHS crystalline interface between the MQW and contact region. (c): EDX analysis revealed a P rich interface for the dry etch process (red), as opposed to the wet etch (blue).

MS1.P014
Imaging charge ordering and octahedral rotations in strain-engineered $LaVO_3$ thin films

D. T. L. Alexander[1], H. Meley[2], L. T. Obserson[1], M. C. Spadaro[3,4], V. Grillo[4], S. D'Addato[3,4]
J. M. Triscone[2], S. Gariglio[2]

[1]Ecole Polytechnique Fédérale de Lausanne (EPFL), Interdisciplinary Centre for Electron Microscopy (CIME), Lausanne, Switzerland
[2]University of Geneva, DQMP, Geneva, Switzerland
[3]University of Modena and Reggio Emilia, FIM Department, Modena, Italy
[4]S3 Research Center, CNR NANO, Modena, Italy

duncan.alexander@epfl.ch

The ABO_3 perovskite has great flexibility for accommodating A and B cations of different ionic radii by structure and symmetry changes, giving rise to a variety of physical properties. There is interest in using this flexibility to create an artificial ferroelectric, by stacking layers of alternate orthorhombic lattices to break their dipole compensation [1]. Towards this goal, here we study the effect of epitaxial strain on the atomic structure of candidate $LaVO_3$ thin films. The main aim is to identify cation (A, B) and O anion positions with picometre precision in $LaVO_3$ films epitaxially strained in biaxial tension or compression. Taken with structural predictions by density functional theory (DFT), this information is vital for monitoring strain effects on atomic structure.

$LaVO_3$ films were grown by pulsed laser deposition on $SrTiO_3$ and $DyScO_3$ substrates to induce compressive and tensile strain respectively. Cross section TEM lamellae, prepared by mechanical polishing and ion beam milling, were imaged by scanning transmission electron microscopy (STEM) with a double aberration corrected FEI Titan Themis 60-300 at 200 or 300 kV. Fast frame series were taken and then aligned and averaged using SmartAlign [2]. Atomic column positions were identified using Ranger [3], and used as input to calculate atomic strain maps with a custom MATLAB script. Multislice image simulations were performed using STEM_CELL on supercells with characteristics representative of the samples [4], calculating atomic strain maps for comparison with experimental results.

Figure 1 shows example data from $LaVO_3$ on $SrTiO_3$. Part (a) is a high angle annular dark field (HAADF) image of (A, B) cation columns at the film/substrate interface. In part (b) the (A) cation positions are identified, showing alternate La displacements of antiferroelectric charge ordering in the $LaVO_3$ film that confirm predictions from DFT [5]. The overlaid shear strain map shows that this ordering begins directly at an atomically sharp film/substrate interface. While this $LaVO_3$ film consists of in-plane domains at 90°, similar analysis of a mono-domain film on $DyScO_3$ unexpectedly finds a 90° flip around its out-of-plane orthorhombic long axis after exactly 9 cube-type unit cells growth.

For measuring O positions in their tilted/rotated octahedra we test annular bright field (ABF) and integrated differential phase contrast (IDPC) imaging. Figure 2 shows example data from the $DyScO_3$ substrate on its [110] orthorhombic axis, used as a known Reference: with similarly tilted/rotated octahedra. Using frame averaging followed by sub-unit frame integration, displaced pairs of O columns are visible, corresponding well to the atomic structure projection. With optimisation of light atom imaging, we aim to identify minute displacements of O sites to discriminate between DFT predictions of $LaVO_3$ on $SrTiO_3$, as suggested is possible from the multislice image simulations.

[1] J. M. Rondinelli and C. J. Fennie, Adv. Mater. **24**, 1961 (2012).
[2] L. Jones et al., Adv. Struct. Chem. Imag. **1**, 8 (2015).
[3] L. Jones, http://lewysjones.com/software/ranger/
[4] http://tem-s3.nano.cnr.it/?page_id=2.
[5] DFT calculations were done by the group of Philippe Ghosez at the University of Liège.

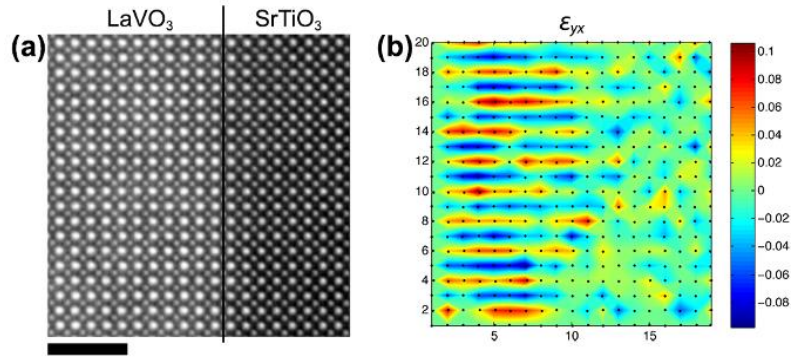

Figure 1. a) Frame-averaged HAADF image of $LaVO_3/SrTiO_3$ interface on the substrate's [100] axis. b) Loci of the A site La and Sr cations identified with few pm precision and shear strain map showing the charge ordering of the La cations. Scale bar: 2 nm.

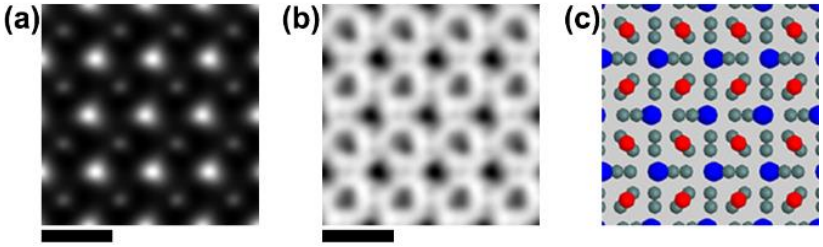

Figure 2. Frame-averaged and sub-frame integrated a) HAADF and b) ABF images of [110] oriented $DyScO_3$. Displaced pairs of O sites visible in the ABF image correspond well to the structural projection shown in c) (Dy: blue; Sc: red; O: grey). Scale bar: 0.5 nm.

MS1.P015
Combined TEM/spectral luminescence study of defects in oxygen implanted silicon

D. Danilov[1], O. Vyvenko[1], A. Loshachenko[1], N. Sobolev[2]

[1]Saint Petersburg State University, Saint Petersburg, Russian Federation
[2]Ioffe Institute, Saint Petersburg, Russian Federation

d.danilov@spbu.ru

Ion implantation is a common industrial technique to produce well-controlled doping and defects profile in wafers [1, 2]. Due to the particular character of the ion-matter interaction the depth distribution of the defects in the implantation region every time is non-uniform so that different kinds of defects are created at different depths. Recently, we found that oxygen implanted silicon subjected to subsequent multistep anneal possessed rather intense electroluminescence band near 0.8 eV with a complex spectral content [3]. In this work, we succeeded to retrieve spectral response of the defects situated at different depth in the implantation region. That allowed us to separate the spectral contributions of nanoscale oxygen precipitates (OP) and oxygen-free threading dislocations (TD).
The n-type Cz-Si wafer was subjected to the oxygen implantation with the fluence of 3x1015 cm-2 and multistep precipitation treatment [4]. The p+n junction and Ohmic contact were created by vapour –phase epitaxy. The luminescence properties of the defects were investigated by cathodoluminescence (CL) and electroluminescence (EL). The characterization of defects structure in the implantation region was provided by transmitting electron microscopy (TEM). The cross section TEM foil preparation was carried out by sequential mechanical grinding and final polishing by Ar ions.
Cross-sectional TEM images revealed that the implantation region could be divided into three layers with well distinguishable defect content: TD, SD+OP, and OP as they are marked in Fig. 1(a). The first one, near the surface, consists solely of threading dislocations of the density of about 1011cm-2, the second one has composed from diverse structure defects and small OPs and the third one contains only nanoscale OPs with the layer density of 1010cm-2.
In order to find correspondence between the luminescent properties and the type of the defects in the structure under investigation we utilized the fact that the minority carriers injected by the forward current and by electron beam with 30kV flow in opposite directions and their density of exhibit maximum at the surface or in the depth of about 5 μm, respectively. In this way, EL and CL have to be mostly sensitive to the defects at the surface or at the deepest part of the implanted region. Indeed, EL showed the narrow D1 line of well-known dislocation-related luminescence [5] while CL revealed the appearance of the 0.82 eV line with the prolonged high-energy tail which can be ascribed to nanoscale OPs [3].

All experimental results were obtained in IRC for Nanotechnology, Research Park of SPbU.

References:
[1] N.A. Sobolev, O.B. Gusev, E.I. Shek, V.I. Vdovin, T.G. Yugova, A.M. Emel'yanov, J Lumin, 80 (1998) 357-361.
[2] S. Libertino, S. Coffa, J.L. Benton, Phys Rev B, 63 (2001).
[3] D.V. Danilov, O.F. Vyvenko, N.A. Sobolev, V.I. Vdovin, A.S. Loshachenko, E.I. Shek, P.N. Aruev, V.V. Zabrodskiy, Solid State Phenom, 242 (2015) 368-373.
[4] K. Bothe, R.J. Falster, J.D. Murphy, Appl Phys Lett, 101 (2012).
[5] N.A. Drozdov, A.A. Patrin, V.D. Tkachev, Jetp Lett, 23 (1976) 597-599.

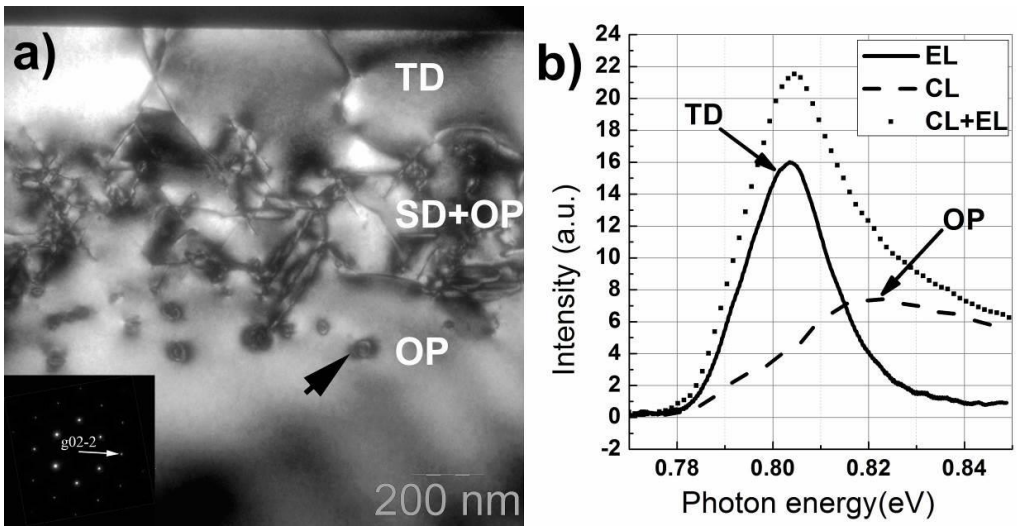

Figure 1. a) Dark-field cross-sectional TEM image of the sample. TD - threading dislocations region, SD+OP – the region of structure defects and oxygen precipitates, OP – the region of big oxygen precipitates. Insert black figure shows diffraction pattern from the film. b) Luminescent measurements results. Solid line – electroluminescent spectrum (Current density was 0.05 A*cm-2). Dashed line – cathodoluminescent spectrum (Accelerating voltage was 30kV). Dotted line – the spectrum, obtained both with electron irradiation and with the injection current.

MS1.P016
Towards the fabrication of microlense structures in GaAs using focused ion beam milling

G. Neusser[1], M. Sartison[2], S. L. Portalupi[2], M. Jetter[2], P. Michler[2], C. Kranz[1], B. Mizaikoff[1]

[1]University of Ulm, Institute of Analytical and Bioanalytical Chemistry, Ulm, Germany
[2]University of Stuttgart, Institut für Halbleiteroptik und Funktionelle Grenzflächen, Stuttgart, Germany

gregor.neusser@uni-ulm.de

Introduction: Challenges in using quantum dots (QDs) as light sources are related to the collection efficiency of photons emitted by the QD. One possibility to enhance the light extraction was demonstrated recently by Sartison et al.[1] by using low-temperature, in-situ photolithography and femtosecond 3D direct laser writing for fabrication of solid immersion lenses directly above QDs. The efficiency may be further improved by lenses fabricated from the solid-state matrix surrounding of the QDs[2]. In the here presented approach, InAs Qds are embedded in a GaAs matrix. The fabrication of smooth GaAs surfaces using focused ion beam (FIB) milling is challenging due to a preferential etching of arsenic, which leads to the formation of gallium rich droplets during the milling process[3].
Objectives: In this study, we present an approach for the fabrication of lense structures with diameters ranging from 10 to 1 µm within GaAs using FIB milling. These lenses will be fabricated directly above a QD in order to enhance the light extraction efficiency.
Methods: The fabrication steps were performed using a Helios NanoLab 600 (FEI). The FIB was opperated at 30 kV and 28 pA . A set of overlapping concentric circle patterns was used to achieve the geometry of the lense structures. All circles had the same outer diameter, the inner diameter of the patterns, (i.e. the inner area of the circle pattern not altered by FIB milling), became successively smaller with each circle, as did the depth of the pattern. Gallium droplets formed during the milling process were removed by exposure of the strutures to concentrated sulfuric acid (H_2SO_4) for five minutes. Remnant droplets were afterwards removed by exposing the sample to the Ga-ion beam FIB for about 10 seconds. Alternatively, the sample was structured under cryogenic conditions attenuating the droplet formation. Cryo Fib milling was performed at – 140°C with a PP2000 Quorum Cryo system connected to the Helios NanoLab 600.
Results: FIB milling at room temperature produces, as expected, gallium droplets at the surface of the lenses (Fig. 1a). The droplets were removed by H_2SO_4 followed by short term exposure to the Ga-ion beam (Fig. 1b). The so produced surface of the lense shows a lot of small dents and curvatures. These inhomogenities seem to be the result of an inhomogeneous abrasion of material due to the appearance of the gallium droplets during the milling procedure. Milling under cryogenic temperatures does not avoid the formation of gallium droplets completely, but reduces the size of the droplets significantly, improving the overall appearance and roughness of the surface.
Conclusion: In the present study, we investigate the FIB milling approaches for the fabrication of µm-sized lenses in GaAs. The size of gallium droplets formed during the milling process can be reduced by milling under cryogenic conditions. Remaining droplets can be removed via exposure to concentrated H_2SO_4. Overall, this may be a valuable approachfor the fabrication of solid immersion lenses above QDs improving the collection efficiency of photons emitted by the QD.

References:
[1] M. Sartison, S. L. Portalupi, T. Gissibl, M. Jetter, H. Giessen and P. Michler, *Sci. Rep.*, 2017, **7**, 39916.
[2] W. L. Barnes, G. Björk, J. M. Gérard, P. Jonsson, J. A. E. Wasey, P. T. Worthing and V. Zwiller, *Eur. Phys. J. D*, 2002, **18**, 197–210.
[3] A. Lugstein, B. Basnar and E. Bertagnolli, *J. Vac. Sci. Technol. B Microelectron. Nanom. Struct.*, 2002, **20**, 2238.

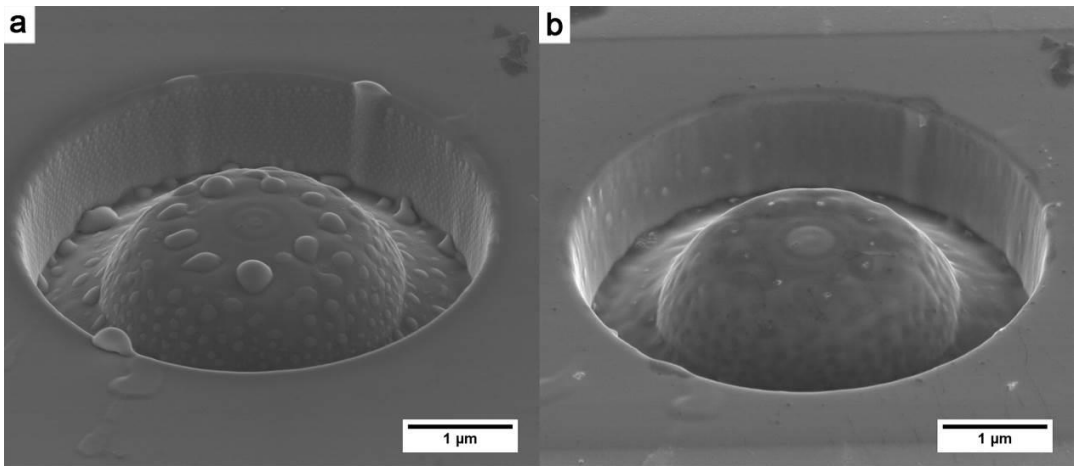

Figure 1. Secondary electron (SE) images of lense structures milled in GaAs at room temperature, a) after FIB milling, b) after exposure to H_2SO_4 followed by 10 seconds of exposure to FIB.

MS1P.017
Nanoscale characterization of crystalline phase-change materials for novel applications

A. M. Mio[1], M. Luysberg[2], M. Küpers[3], P. M. Konze[3], O. Cojocaru-Mirédin[1], M. Zhu[1], J. Mayer[4]
R. Dronskowski[3], M. Wuttig[1]

[1]RWTH Aachen University, I.Physikalisches Institut IA, Aachen, Germany
[2]Forschungszentrum Jülich GmbH, Ernst-Ruska-Center, Jülich, Germany
[3]RWTH Aachen University, Institute of Inorganic Chemistry, Chair of Solid-State and Quantum Chemistry, Aachen, Germany
[4]RWTH Aachen University, Central Facility for Electron Microscopy, Aachen, Germany

mio@physik.rwth-aachen.de

Introduction: Although Phase-Change Materials (PCMs) have been in use since the 1980s for high-density data storage in optical media [1], the discovery of the phase-change prototype GeTe stems from the early 20th century already [2]. Lately, the use of these alloys has been extended to solid-state non-volatile memories. Very recently it has been shown that multi-layered crystalline phase-change memories, arranged in chalcogenide superlattices (CSLs), can exhibit improved functional properties [3]. Moreover, it has been argued that many PCMs, which intrinsically possess low thermal conductivity, also exhibit promising thermoelectric figure of merit, providing possible applications for heat energy harvesting.
The use of PCMs as optical data storage relies on very fast (<100 ns) phase transitions and on the pronounced optical contrast between the amorphous and crystalline state. The origin of this large optical contrast has been alluded to a phenomenon dubbed resonant bonding [4].
Objectives: The development of CSLs in PCMs, multi-level memories and thermoelectrics requires a precise control of nanoscale inhomogeneities, structural arrangement and chemical bonding. With this aim, we present a nanoscale study, which correlates different microscopy and nano-analysis techniques, comparing promising chalcogenide alloys with conventional PCMs.
Materials and Methods: Promising (GeTe)x-(GeSe)y chalcogenides have been fabricated in single crystals by Chemical Vapor Transport [5]. The alloy GeSe0.75Te0.25, in particular, exhibits a metastable rhombohedral phase and a stable hexagonal phase. This material has been compared with conventional PCMs, mainly represented by (GeTe)*x*-(Sb2Te3)*y* (GST) alloys, fabricated by sputtering, Molecular Beam Epitaxy and solvothermally synthesis.
Materials have been investigated by means of High Angular Annular Dark Field (HAADF) Cs-corrected Scanning Transmission Electron Microscopy (S/TEM), Energy Dispersive X-ray Spectroscopy (EDS) and Electron Diffraction.
Results: In GeSe0.75Te0.25, the hexagonal stable phase presents unique structural and chemical properties. With respect to the trigonal phase of (GeTe)*x*-(Sb2Te3)*y*, in which odd 2*n*+5 layers of Te–Sb–Te– (Ge–Te)*n*–Sb-Te are divided by vacancy layers, the hexagonal phase in crystalline GeSe0.75Te0.25 exhibits van der Waals gaps dividing blocks of 4 layers (Se/Te–Ge–Ge–Se/Te) along the c-axis (fig. 1).
Furthermore, while GeTe-like phases typically resemble the rock-salt motif and are characterized by polar covalent anion-cation bonds, the unit cell in GeSe0.75Te0.25 comprises two A–Ge–Ge–A layers (with A being Se and Te in a 3:1 ratio), thereby giving rise to an unexpected Ge–Ge bond. This atomic arrangement has been determined from single-crystal X-ray diffraction and was corroborated from the HAADF Z-contrast STEM micrographs and also confirmed by local EDS.
A quantum-chemical bonding analysis of DFT total-energy calculations reveals the existence of Ge–Ge bonds in GeSe0.75Te0.25 which allow to reshuffle electrons from antibonding Ge–Te into bonding Ge–Ge contacts, thereby lowering the energy [6].
Conclusion: In the present work, we have studied the hexagonal phase of GeSe0.75Te0.25. With respect to trigonal (GeTe)*x*-(Sb2Te3)*y*, hexagonal GeSe0.75Te0.25 is divided by van der Waals gaps, along the *c*-axis, in blocks of four layers characterized by the Se/Te–Ge–Ge–Se/Te motif. For the first time we have observed in chalcogenide alloys this particular Ge–Ge bond correlating HAADF STEM and local EDS.

[1] M. Wuttig, N. Yamada, Nat. Mater. **6**, 824 (2007).
[2] W. Klemm, G. Frischmuth, Z. Anorg. Allg. Chem. **218**, 249 (1934).
[3] R. E. Simpson R E, et al. Nat. Nano. **6**, 501 (2011).
[4] K. Shportko et al., Nat. Mater. **7**, 653 (2008).
[5] H. Schäfer, *Chemische Transportreaktionen*, Verlag Chemie, Weinheim 1962.
[6] Küpers et al., Angew. Chem. Int. Ed. 2017, *in press*, DOI: 10.1002/anie.201612121

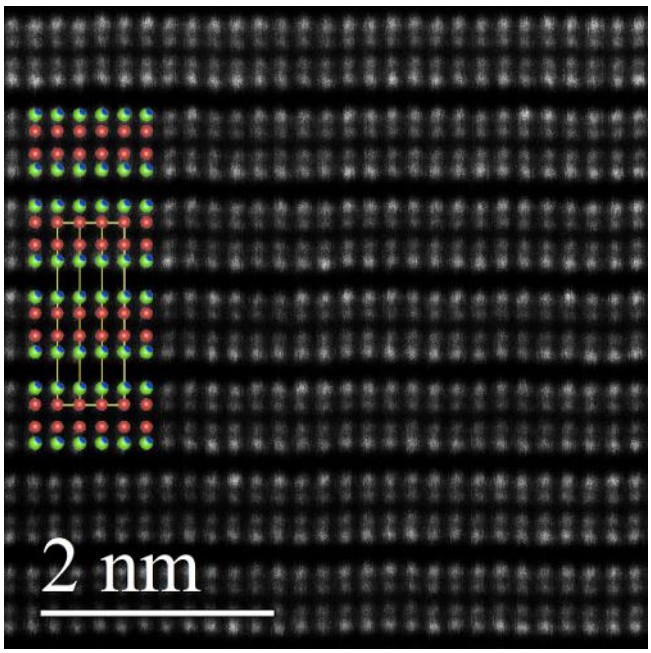

Figure 1. HAADF-STEM micrograph of GeSe0.75Te0.25 along the [1-10] zone axis. The atomic positions in this zone axis are also shown (Ge red, Se green, Te blue).

MS1.LBP01
In situ heating studies of diffusion barrier layers for semiconductor devices

D. Knez[1,2], E. Fisslthaler[2], M. Dienstleder[2], W. Grogger[1,2], F. Hofer[1,2]

[1]Graz University of Technology, Institute for Electron Microscopy and Nanoanalysis, Graz, Austria
[2]Graz Centre for Electron Microscopy, Graz, Austria

daniel.knez@felmi-zfe.at

Knowledge about thermodynamic properties of diffusion barrier layers is highly valuable for further development of semiconductor devices. Such barrier layers are introduced between the metal contact and the semiconducting material to prevent metal atoms from diffusing into the latter. The layer needs to meet several requirements. It has to be as thin as possible to minimise the influence on the electrical behaviour, but should be sufficiently robust to withstand even elevated temperatures over the full lifespan of the device. To obtain deeper understanding of aging processes of such devices and the underlying mechanisms we perform *in situ* heating experiments via STEM on metal/barrier/semiconductor layer stacks.
For STEM experiments, we use a probe corrected FEI Titan3 60-300 microscope. This microscope is equipped with a Super-X detector (EDXS) and a Gatan Quantum energy filter for EELS. *In situ* heating experiments are performed with a DENSsolutions Wildfire D6 holder, equipped with a heatable MEMS device. Figure 1a shows an overview image of such a heating chip.
Exemplary, we present an *in situ* study of a Cu/Ru/SiO2/Si layer stack. In this case, the Ru layer acts as a barrier to prevent Cu atoms to diffuse into the Si crystal. In previous studies, the formation of copper silicide has been reported above temperatures of 250 °C [1]. With this sample we aimed to study the failure of the barrier layer and the subsequent formation of the silicide.
Samples were prepared via focussed ion beam milling with Ga+ within a FEI FIB Nova 200, and mounted on the heatable chip. Figure 1b gives an image of the lamella, which is positioned above a hole in the chip (marked with a red circle in Figure 1a). A carbon layer is vapour-deposited on each side of the lamella to prevent unwanted surface migration of metal atoms[2]. In Figure 1c the configuration of the layer stack confined between two carbon layers is illustrated.
Figure 2 shows results of the heating experiment. At room temperature all layers can clearly be distinguished via HAADF contrast and EDX elemental analysis. The sample was then heated with a constant heating rate of 10 °C/min. At a temperature of approximately 480 °C we observe that the Ru barrier layer locally breaks and Cu diffuses through the resulting holes into the Si, until the Cu layer is completely dissolved. Cu particles with a size of approximately 5-10 nm are formed and start to diffuse through the crystalline Si, forming copper silicide on their paths.
We were able to directly observe the silicide formation process in the TEM in real time and to study the formation mechanisms.

Acknowledgments
We acknowledge financial support by the Austrian Research Promotion Agency (FFG) in the project "Quantitative Analyse innerer Grenzflächen" (850220/859238).

References:
[1] M. Setton, J. van der Spiegel, B. Rothman, *Appl. Phys. Lett.* **1990**, *57*, 357.
[2] N. Dalili, P. Li, M. Kupsta, Q. Liu, D. G. Ivey, *Micron (Oxford, England 1993)* **2014**, *58*, 25.

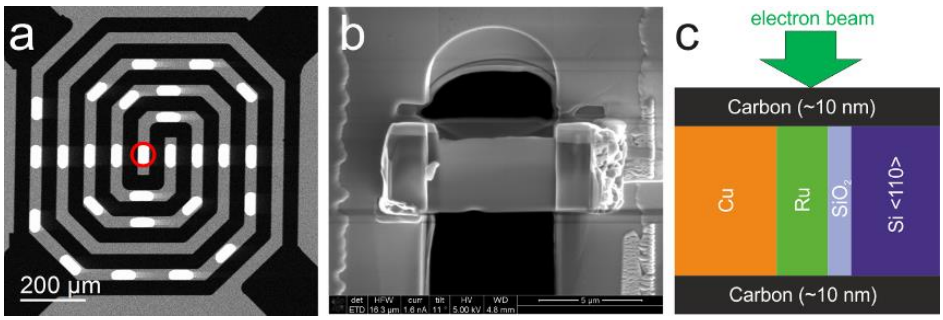

Figure 1

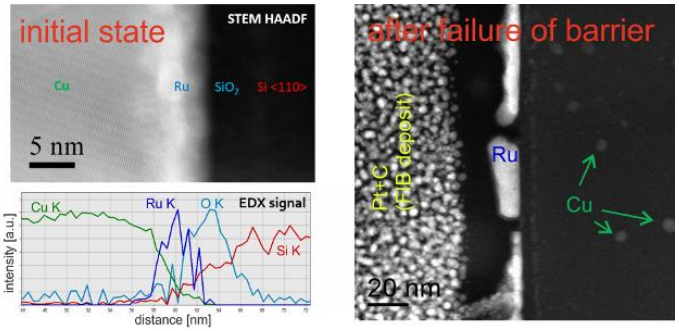

Figure 2

MS 2: Interfaces and surfaces, coatings and thin films

MS2.001 invited
Dislocation-pipe diffusion in nitride superlattice thin films as observed by STEM in direct atomic resolution

M. Garbrecht[1], L. Hultman[1], T. D. Sands[2], B. Saha[3]

[1]Linköping University, Linköping, Sweden
[2]Virginia Tech, Blacksburg, VA, United States of America
[3]University of California, Berkeley, CA, United States of America

magnus.garbrecht@liu.se

Device failure from diffusion short circuits in microelectronic components occurs via thermally induced migration of atoms along high-diffusivity paths: dislocations, grain boundaries, and free surfaces [1-3]. Knowledge about the structural features along which diffusion paths in solids are formed is hence of great importance. For instance, kinetic processes limited by grain-boundary and/or dislocation diffusion in materials are known to be diffusion creep, precipitation, coarsening, solute segregation, strain aging, grain boundary migration, and sintering. Even well-annealed single-grain metallic films contain dislocation densities of about 10^{14} m^{-2}; hence dislocation-pipe diffusion (DPD) becomes a major contribution at working temperatures. While its theoretical concept was established already in the 1950s [4] and its contribution is commonly measured using indirect tracer, spectroscopy, or electrical methods [5], no direct observation of DPD at the atomic level has been reported.
Aberration-corrected STEM with an image- and probe-corrected and monochromated FEI Titan^3 60-300 kV instrument equipped with a high-brightness XFEG source and Super-X EDS detector for ultra-high count rates, operated at 300 kV, was employed [6].
We present atomically-resolved STEM images of the onset and progression of diffusion along threading dislocations in sequentially annealed nitride metal/semiconductor superlattices [7-10]. The STEM micrographs are accompanied by EDS maps and GPA analysis (Fig 1). From the images showing the same region at different time-steps during annealing, diffusivity coefficients are calculated directly. Most importantly, we show that this type of diffusion is independent of concentration gradients in the system but governed by the reduction of strain fields in the lattice [11].
Our images of the formation of pipes around the dislocation core and at different time steps in an annealing series are the first direct experimental observations of this phenomenon at atomic resolution employing TEM techniques.

[1] R. S. Barnes, Nature 166, 1032-1033 (1950).
[2] A. D. Le Claire, Philos. Mag. 42, 468-474 (1951).
[3] N. A. Gjostein, In: Diffusion, H.I. Aaronson (Ed.), Am. Soc. for Metals, Ohio (1973).
[4] R. Smoluchowski, Phys. Rev. 87, 482-487 (1952).
[5] H. Mehrer, *Diffusion in Solids*, Springer Series in Solid State Sciences, vol. 155, Berlin, 2007.
[6] The Knut and Alice Wallenberg (KAW) Foundation is acknowledged for the Electron Microscope Laboratory in Linköping
[7] T. D. Sands et.al Mater. Sci. Rep. 5:98–170, (1990).
[8] J. L. Schroeder et al., J. Mater. Sci. 50: 3200-3206, (2015).
[9] B. Saha et al., Phys. Rev. B. 93, 045311:1-11, (2016).
[10] M. Garbrecht et al., J. Mater. Sci., 51(17), 8250 (2016).
[11] M. Garbrecht, et al., submitted (2017)

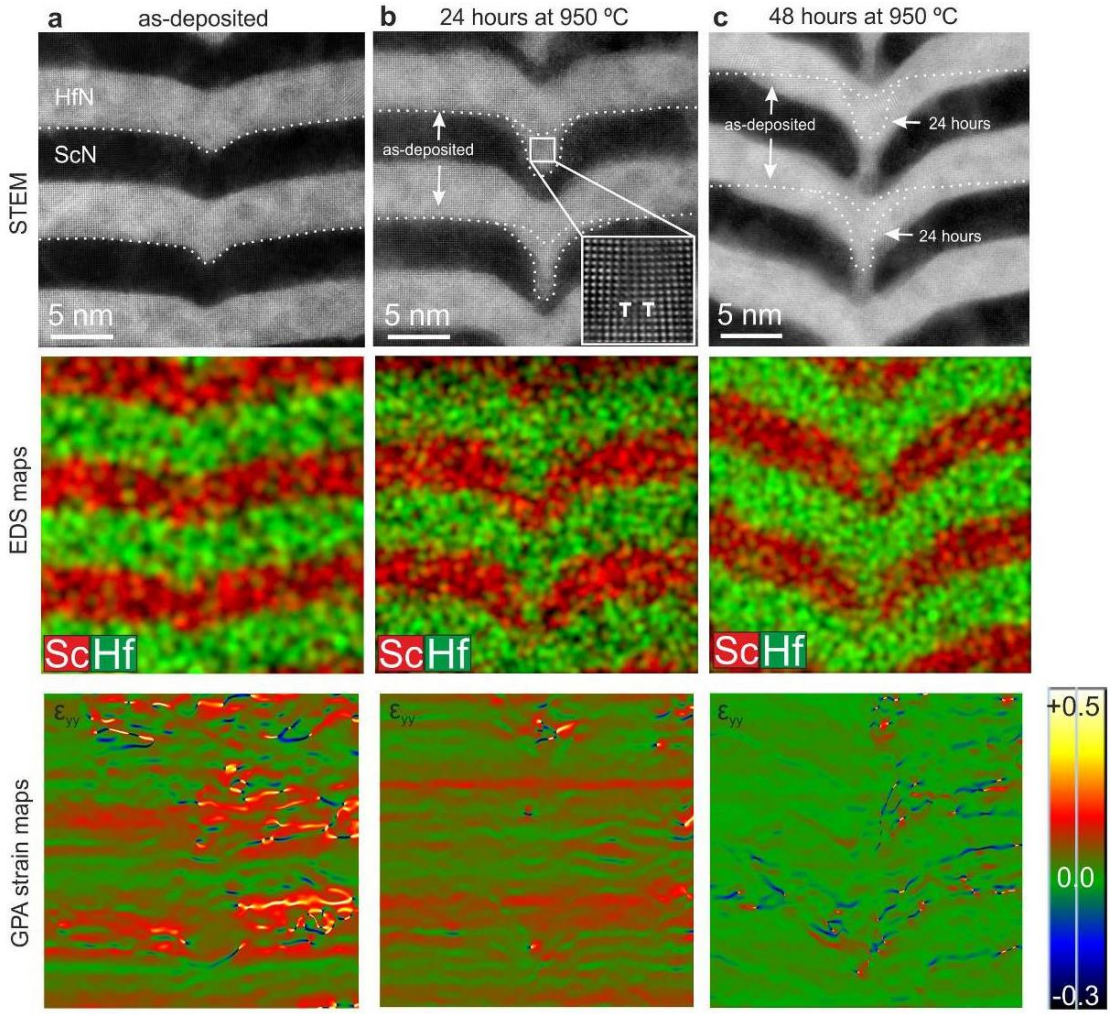

Figure 1. The operation of dislocation-pipe diffusion by strain fields around a threading dislocation line. High-resolution STEM micrographs, corresponding EDS- and strain mapping of the same area of a HfN/ScN superlattice sample as-deposited (a), and after annealing for 24 h and 48 h, respectively, at 950 °C (b) and (c). The onset of Hf diffusion along the dislocation line after deposition is already visible in a. From the change in the shape of the Hf diffusion front after annealing in b, the diffusion length can be directly measured and an average value calculated. The enlarged region in the inset in (b) shows pairs of edge dislocations at the cores of the vertical dislocation line, in the center along which the diffusion occurs. Strain mapping reveals high strain fields around the dislocation line of the as-deposited sample a, that become significantly reduced by the diffusion of Hf after 24 h of annealing (b), and relaxes the lattice almost entirely once the pipe formation is completed (c). Shown is the y-component of the strain tensor ε_{yy}, i.e. parallel to the direction of diffusion.

MS2.002
Al_2O_3 oxide bandgap dependence on the ALD deposition temperature in diamond-MOS structures studied by VEELS

J. Piñero[1], D. Araujo[2], M. Gutierrez[2], J. Pernot[3,4,5]

[1]Universidad de Cádiz, Didáctica de la Matemática, Puerto Real, Spain
[2]Universidad de Cádiz, Ciencias de los Materiales, IM y QI, Puerto Real, Spain
[3]Université Grenoble Alpes, Institut Néel, Grenoble, France
[4]Institut Universitaire de France, Paris, France
[5]CNRS, Institut Néel, Grenoble, France

josecarlos.pinero@gm.uca.es

Introduction: Power devices fabricated using wide-bandgap semiconductors such as SiC and GaN demonstrate better performance than those fabricated using the conventional semiconductor Si. In this respect, the extreme properties of diamond that semiconducting diamond has a strong potential to be used in power electronics. In particular, the developments of diamond-based MOSFET, δ-FETs and SBDs have attracted special interest. Recently, inversion channel in diamond MOSFET with normally off characteristic has been achieved in O-terminated (111) diamond with an Al2O3 layer grown by atomic layer deposition (ALD) at 300ºC. However, a comprehensive picture of ALD-deposited MOS structures, grown over O-terminated diamond did not emerge clearly.
Objectives: The impact of the deposition temperature of the ALD-deposited layer in the oxide bandgap motivates the present study, in which two different diamond-MOSCAP oxides deposited by ALD are analyzed by a combination of CTEM and STEM techniques. In particular, HREM and EELS allows studying the crystallinity and the bandgap of such oxide layers; stablishing a correlation between the nanocrystalline structure and the electric properties versus the ALD temperature.
Materials and Methods: Material: Two different ALD-deposited Al2O3 layers grown at 100 and 380ºC (samples #A and #B) over CVD boron-doped diamond (boron concentration ≈1017cm-3). Deposition performed over oxygen-terminated diamond surfaces (oxygenated by deep UV ozone treatment).
Method: Samples nano-machined with a Quanta 200 3D FIB system. Electron-transparent specimens are characterized by HREM and STEM-EELS using a JEOL-2010F FEG electron microscope.
Results: Figure 1 shows TEM BF micrographies of #A and #B. Right side of Fig.1 reveals a 30nm tick polycrystalline oxide layer of sample #A, as can be deduced by the presence of grains in the oxide layer (black arrows are used to highlight the grains). On the other hand, a 40nm thick monocrystalline oxide layer is observed in sample #B, as can be appreciated in left side of Fig.1.
Grain formation in low-temperature ALD deposited Al2O3 layers could be related with bad behavior in diamond-MOS structures, even affecting its morphology and modifying oxide layer thickness point by point. This feature may have a strong impact in the related device (insofar that the fundamental bandgap of Al2O3 depends on its crystalline form) and can modify the energy-band diagram configuration of the oxide/diamond interface point by point.
To evaluate this, VEELS measurements has been carried out to calculate the oxide. However, different methodologies for bandgap calculations have been reported in literature, and one has to choose the appropriate procedure in order to overcome the main difficulties that involves working in the low loss EELS range, as presented Figure 2 (where ZLP, Cerenkov-related peak, surface and volume plasmons are evidenced). The previously listed signals are undesirable and may mask the real value of the fundamental bandgap derived by linear fitting of the EELS spectra.
By mean of an appropriate deconvolution method, the previously described signals were removed, thus allowing a linear fit of the fundamental bandgap, as presented in Figure 3. This procedure eases local bandgap information, and can be used to track bandgap variations along the ALD-deposited oxide layer. As can be appreciated in Fig.3b and d, Al2O3 bandgap in #A is significantly smaller than that of #B.
Conclusions: TEM-EELS experiments in Al2O3 oxide films allow measuring the oxide bandgap by applying the linear-fit method with a previous signal processing. Signal processing is mandatory to avoid the combined effect of the Cerenkov radiation and the aluminum surface plasmon. CTEM imaging confirms the presence of polycrystalline oxide layer in sample #A while a monocrystalline oxide layer is observed in sample #B. The resulting grain structure is then related with the Eg values obtained by VEELS, confirming that 380ºC ALD deposition temperature creates Al2O3 stable layers suitable to be used in diamond-based electronics.

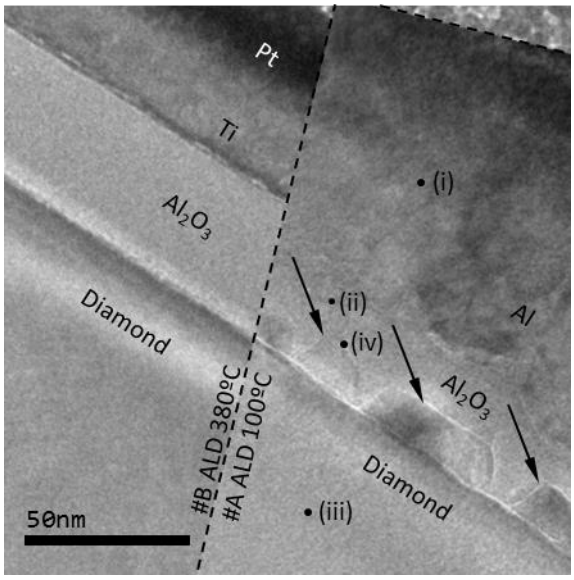

Figure 1

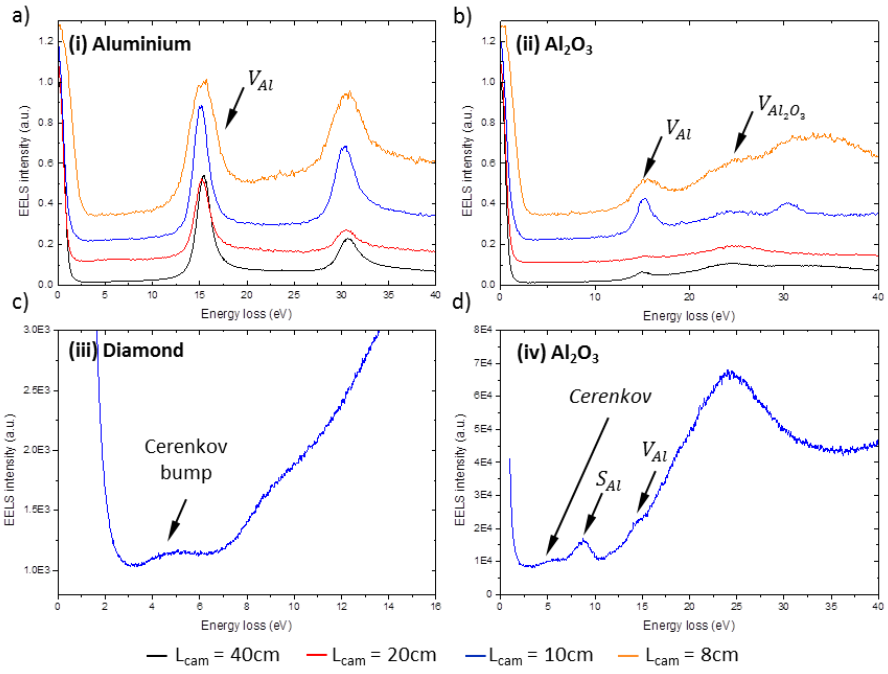

Figure 2

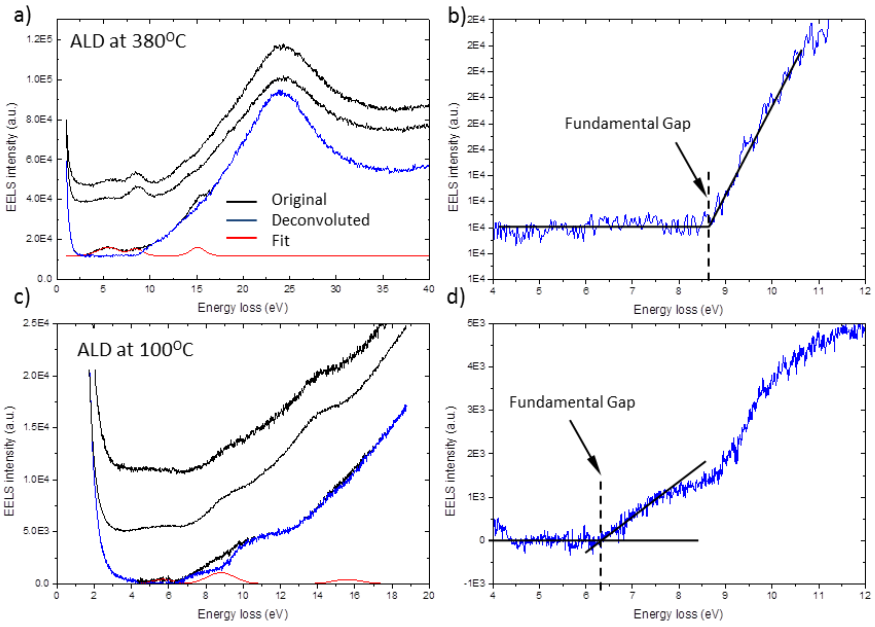
a)
ALD at 380°C
Original
Deconvoluted
Fit
EELS intensity (a.u.)
Energy loss (eV)
b)
Fundamental Gap
EELS intensity (a.u.)
Energy loss (eV)
c)
ALD at 100°C
EELS intensity (a.u.)
Energy loss (eV)
d)
Fundamental Gap
EELS intensity (a.u.)
Energy loss (eV)

Figure 3

MS2.003
Atomic structure of a novel hard coating – transmission electron microscopy study of Mo_2BC

S. Gleich[1], R. Soler[2], H. Bolvardi[3], K. G. Pradeep[3], H. Fager[3], J. M. Schneider[3], G. Dehm[2], C. Scheu[1]

[1]Max-Planck-Institut für Eisenforschung GmbH, Nanoanalytics and Interfaces, Düsseldorf, Germany
[2]Max-Planck-Institut für Eisenforschung GmbH, Structure and Nano-/ Micromechanics of Materials, Düsseldorf, Germany
[3]RWTH Aachen University, Materials Chemistry, Aachen, Germany

s.gleich@mpie.de

Hard coatings earn their name as they exhibit excellent mechanical properties including high mechanical stiffness and hardness. They are commonly used for cutting tools to protect them from wear resulting in a longer lifetime. However, this application of hard coatings requires also a moderate ductility to reduce the probability of crack formation and propagation. *Ab initio* calculations predicted Mo_2BC as a promising candidate in this field combining these unique properties of high hardness and stiffness on the one hand as well as moderate ductile behavior on the other hand.[1]
The mechanical properties of Mo_2BC in particular and hard coatings in general are dependent on the nanostructure. As the growth of these coatings is usually far away from thermodynamic equilibrium and small changes of the synthesis conditions can have a significant influence on the structure, a prediction of the resulting nanostructure is difficult. Thus, a detailed understanding of the nanostructure of hard coatings is crucial to continuously optimize them and finally taking benefit from the outstanding properties in the future.
In our work, various transmission electron microscopy (TEM) techniques, including conventional TEM, high-resolution TEM, scanning TEM (STEM) and selected area electron diffraction were used to study the nano and atomic structure of Mo_2BC hard coatings deposited at different substrate temperatures (T_s) ranging from 380 °C to 630 °C.[2] The measurements were performed at 200 kV using a CM 20 TEM and a JEOL JEM-2200FS and at 300 kV using a probe corrected FEI Titan Themis 60-300. The crystalline quality of the Mo_2BC coatings strongly depends on T_s. It is fully crystalline in case of T_s = 630 °C, evolving a textured structure which consists of densely packed columnar grains with a diameter of around 10 nm (see Figure 1a). The grain boundaries exhibit a less ordered atomic arrangement and lattice defects can be detected (see Figure 1a and b) in STEM high-angle annular dark field (HAADF). Furthermore, electron energy loss spectroscopy (EELS) revealed Ar-rich regions in the structure (see Figure 2a). Atom probe tomography (APT) measurements confirmed that these regions are homogeneously distributed in the structure (see Figure 2b). The argon is incorporated in the coating during the high power pulsed magnetron sputtering deposition process. The structure of the Mo_2BC coatings synthesized at lower T_s (380 °C to 580 °C) is also crystalline, but grain size decreases with decreasing T_s. Again, Ar-rich regions are detected in these coatings. However, the amount of argon in the coatings increases with decreasing T_s. Finally, the mechanical properties of the Mo_2BC coatings were investigated by nanoindentation and micro beam bending experiments. The obtained hardness, elastic modulus and fracture toughness values correlate with the nanostructure of the Mo_2BC coatings detected by TEM investigations.
In conclusion, we reveal the detailed nano and atomic structure of Mo_2BC hard coatings by combining various TEM techniques. Thereby, we prove the influence of deposition parameters on the nanostructure evolution of Mo_2BC coatings and show that this determines the mechanical properties.

References:
[1] J. Emmerlich, D. Music, M. Braun, P. Fayek, F. Munnik and J. M. Schneider, *Journal of Physics D-Applied Physics* **2009**, *42*.
[2] H. Bolvardi, J. Emmerlich, S. Mraz, M. Arndt, H. Rudigier and J. M. Schneider, *Thin Solid Films* **2013**, *542*, 5-7.

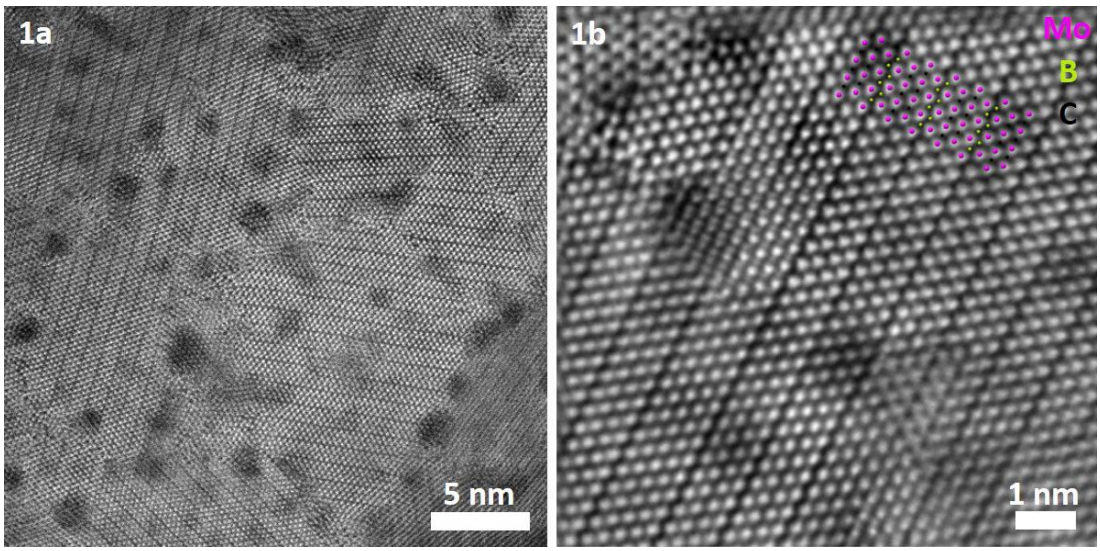

Figure 1. a) STEM HAADF micrograph in plan-view showing the nanostructure of the Mo_2BC coating synthesized at the highest substrate temperature (T_s = 630 °C). Ar-rich regions, visible as dark appearing, spherical features, are located in the grain boundary network as well as within the grains; b) Zoom in one of the grains revealing the atomic structure of Mo_2BC with lattice defects.

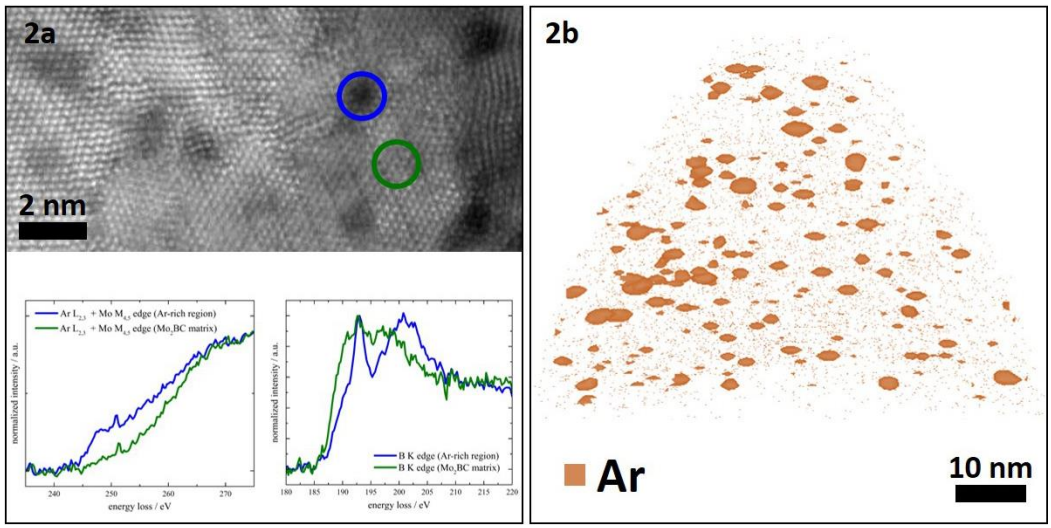

Figure 2. a) EELS point measurements in an argon-rich region (blue) and in the Mo_2BC matrix (green); b) APT reconstruction of the Mo_2BC coating (T_s of 630 °C) showing an isoconcentration surface of 1 at.% Ar in orange.

MS2.004
Quantification of the internal magnetization in skyrmions in FeGe

S. Schneider[1,2], D. Pohl[1], U. K. Rößler[1], M. Schmidt[3], A. Lubk[1], T. Gemming[1], K. Nielsch[1,2]
S. T. B. Goennenwein[2], B. Rellinghaus[1]

[1]IFW Dresden, Dresden, Germany
[2]TU Dresden, Dresden, Germany
[3]Max-Planck Institute for Chemical Physics of Solids, Dresden, Germany

sebastian.schneider@ifw-dresden.de

Introduction: Novel nanoscale magnetic phenomena such as skyrmions, which are a prospect for future data storage [1], cause a steadily increasing demand for ultra-high resolution quantitative magnetic characterization. Here, transmission electron microscopy (TEM) provides the possibility to locally correlate the magnetic properties of the sample with its structure and chemical composition thereby providing for a more complete picture of the underlying physics.
Objectives: Although skyrmions have been observed in a variety of materials both in reciprocal [2] and real-space [3], so far there is only a limited number of experiments, which aim at resolving the internal magnetic structure of this complex nanoscopic spin textures [4, 5, 6]. Especially their three-dimensional arrangement throughout the volume of the sample and the influence of the surface on the emergence of the skyrmion phase are still under discussion and are thus the main objectives of this work.
Materials and Methods: The occurrence of skyrmions is investigated on a FeGe single crystal with B20 structure. A thin lamella is cut from the crystal in [001] orientation using a FIB. In a liquid nitrogen TEM holder the lamella is cooled to a temperature of 90 K, and the TEM investigations are conducted in Lorentz mode with an objective lens that was excited to provide for an out-of-plane magnetic field of 85 mT. Skyrmions are observed upon slightly defocussing the image (cf. Fig. 1). The in-plane magnetization is reconstructed from a focal series of images applying a Gerchberg-Saxton type algorithm.
Results: Stable arrangements of skyrmions are observed over extended areas of the sample where the thickness of the lamella is larger than 40 nm (cf. Fig. 1). Below this thickness no skyrmions can be observed. Reconstruction of the phase distribution of the transmitted electron wave from a focal series of a sample area with coexisting skyrmion and helical phases yields an internal in-plane magnetization of the skyrmions of up to 100 mT (cf. Fig. 2), which is four to five times smaller than the expected theoretical value.
Conclusion: To correlate the magnetic moment distribution of the skyrmions to the structure of the sample volume-sensitive complementary techniques to Lorentz TEM, which can directly measure the out-of plane magnetization with nanometer precession, have to be applied. Electron energy-loss magnetic chiral dichroism (EMCD) provides for this prerequisite. However, EMCD mostly works for samples with thicknesses smaller than 20 nm. It is thus important to understand, whether the disappearance of the skyrmion phase is due to physical reasons or rather an artefact due to the sample preparation (e.g., by generating near-surface defects through the ion irradiation during the FIB cut).

[1] Hsu et al., Nature Nanotechnology **12** (2017), p. 123–126
[2] Mühlbauer et al., Science **323** (2009), p. 915
[3] Yu et al., Nature **465** (2010), p. 901–904
[4] Romming et al., Phys. Rev. Lett. **114** (2015), 177203
[5] McGrouther et al., New J. Phys. **18** (2016), 095004
[6] Shibata et al., Phys. Rev. Lett. **118** (2017), 087202

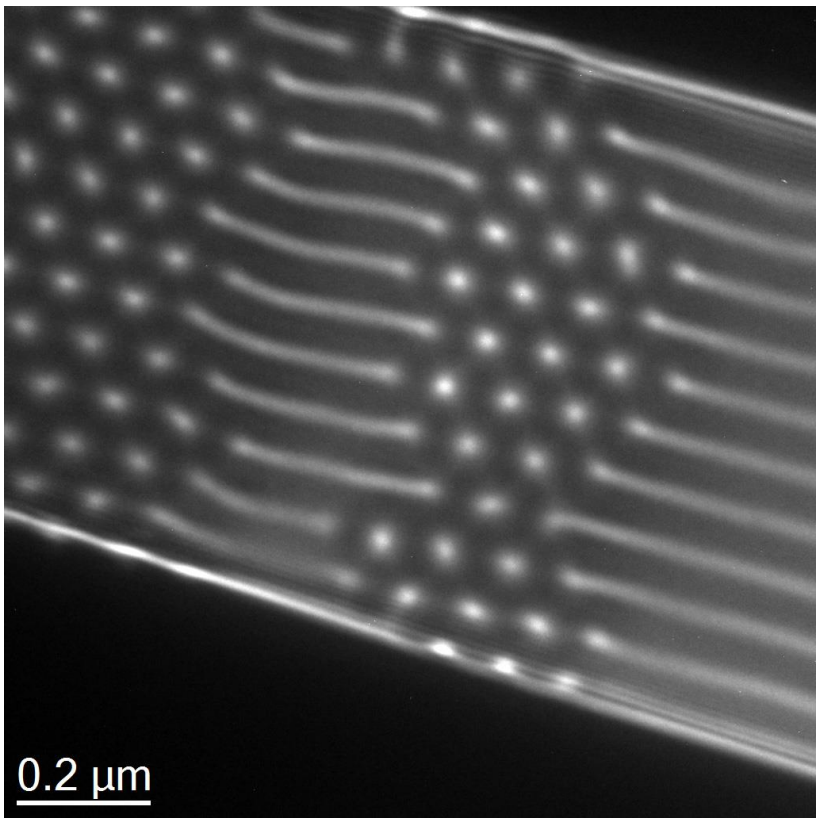

Figure 1. Defocused Lorentz TEM image of a sample area of the FeGe lamella with coexisting helical and skyrmion phases.

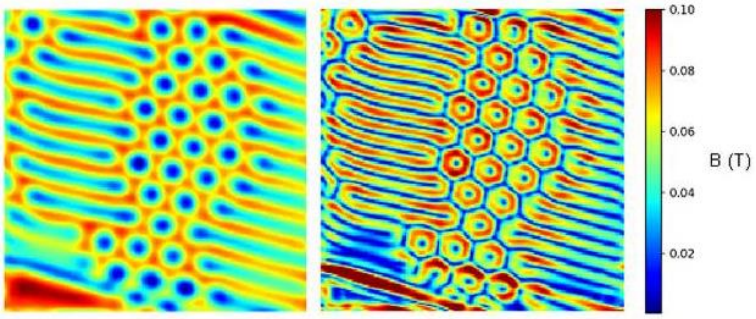

Figure 2. Left: Reconstruction of the phase distribution of the transmitted electron wave of the same sample area as in Fig. 1 using Focal Series Reconstruction. Right: Distribution of the in-plane magnetic field |B| calculated from the phase distribution.

MS2.005
Direct observation of the atomic structure of complex grain boundaries in Ge crystals grown on Si pillars by HAADF-STEM

Y. Arroyo Rojas Dasilva[1], F. Isa[2,1], R. Erni[1], G. Isella[3], H. von Känel[2,1], P. Gröning[4], M. D. Rossell[1]

[1]EMPA, Microscopy Center, Dübendorf, Switzerland
[2]ETH , Laboratory for Solid State Physics, Zurich, Switzerland
[3]Politecnico di Milano and IFN-CNR, L-NESS and Department of Physics, Como, Italy
[4]EMPA, Department of Advanced Materials and Surfaces, Dübendorf, Switzerland

yadira.arroyo@empa.ch

Ge crystals grown on micrometer-sized Si(001) pillars exhibit a high density of misfit and threading dislocations at and near the heterointerface due to the large lattice mismatches (4.2 %). Beside dislocations other defects have been observed[1]: coherent twin boundaries (CTBs), incoherent twin boundaries (ITBs) and stacking faults. Grain Boundaries (GBs) have been studied by using transmission electron microscopy (TEM)[2] and several theoretical models have proposed[3]. The models described by Papon et al[3] for grain boundaries introduce single atomic columns, which according to our experimental results are critical for the proper description of the grain boundary structures. In this work we present an analysis by high-angle annular dark-field scanning transmission electron microscopy (HAADF-STEM) of grain boundaries in Ge crystals grown on patterned Si substrates and relate our experimental findings to the theoretical models proposed by Papon et al.[3].

The samples consist of 8 µm tall Ge crystals grown on 5 µm wide, square Si(001) pillars by Low Energy Plasma Enhanced Chemical Vapor Deposition (LEPECVD)[4]. The {110} Si pillar sidewalls are passivated by a ~ 100 nm thick SiO_2 layer. The Ge crystals were characterized by TEM using a JEOL JEM-ARM 200F operated at 200 kV on specimens prepared by mechanical polishing, dimple grinding and Ar ion milling at 3 kV.

The atomic structure of the grain boundaries is characterized by using the structural units and grain boundary patterns described by Papon[3] (Figure 1a). Figure 1b shows and overview image indicating the position of the grain boundaries which were studied. The red dashed line shows the limit between the polycrystalline Ge/SiO^2 and single crystal Ge/Si(001) regions. The labels A, B, and C refer to the three specific grain boundaries. The boundary B is perpendicular to A, and C is enclosed inside of A and B. Figure 1c shows an image of the A and B boundaries, which at lower magnification is indicated by the red ellipse in Figure 1b. This area consists of alternated A (yellow) and B (green) boundaries forming three steps and correspond to 3∑{111} CTB and 3∑{112} ITB. Label C indicates two triple joints: one consists of two 3∑{111} CTB forming a ∑9{122} GB and the other corresponds to one 3∑{111} and one 3∑{112} forming a ∑9{122} GB.

Some examples of the atomic structure of GBs are shown in Figure 2. The atomic structures of the CTB and ITB are shown in Figures 2a and 2b, respectively. The CTB corresponds to a series of 6_b ring, while the ITB contains 4 original patterns; a symmetric 5_{f2}, 6_{bl}, 6_{bl}, and 7_b ring. The single atomic columns are in the 5_{f2} ring and are located along the ITB opposite to each other (blue circles). Figure 2c reveals a different atomic structure of the ITB taken near to the edge of the crystal. This structure has different original patterns compared to the ones observed in Figure 2b. It has an asymmetric pattern with sequence 6_{f2}, 6_{bl}, 7_1, 6_b and 5 rings. The single atomic columns are located in the 6_{f2} ring and they are not in front of each other, they are shifted with respect to the grain boundary (blue circles). Therefore, the ITB changes its structure along the boundary.

Figure 2d shows a triple joint formed by two CTB forming a zigzag ∑9{122} GB. The original pattern of the ∑9{122} GB consists of 7 and 5 rings. The angle between the CTB is obtuse forming the zigzag GB due to a small step in the junction[5].

We conclude that that the models proposed for Papon et al. are adequate to explain the experimental data of grain boundaries in the micron-sized Ge poly-crystals.

References:
[1] Y. Arroyo Rojas Dasilva et al. Scripta Mater., 127:169, 2016.
[2] H. Sawada et al J. Electron. Microsc., 51:353, 2002.
[3] A. M. Papon et al. Scripta Metall 19:391, 1985.
[4] C.V. Falub et al. Science 335:1330, 2012.
[5] M. Kohyama et al. Mater.Trans., 45:1461, 2004.

a)

Angle θ	Σ	GB plane	Pattenrs	Structural Unit Models
70.5°	3	{111}	6_b 6_b	
109.5°	3	{112}	6_{f2} 6_{bl} 6_b 7_1 5 or 5_{f2} 6_{bl} 7_b 6_{bl} or 7_2 6_{bl} 5_{f2} 5_{f2} 7_2 6_{bl} or 5 7_b 5 7_b	O- C recostruction along the <110> direction
38.94°	9	{122}	7 5 7 5	

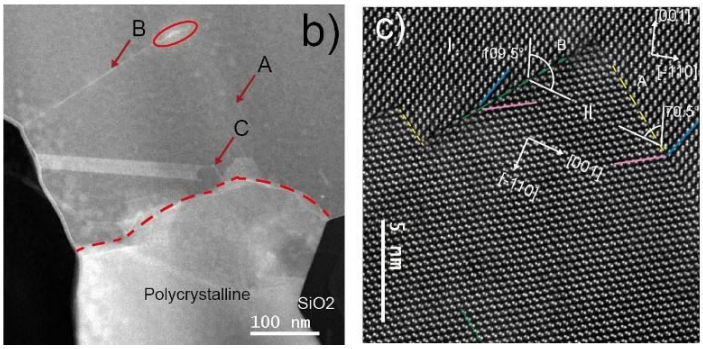

Figure 1. a) Patterns of grain boundaries (after Papon[3]), b) position of the grain boundaries and c) CTB and ITB.

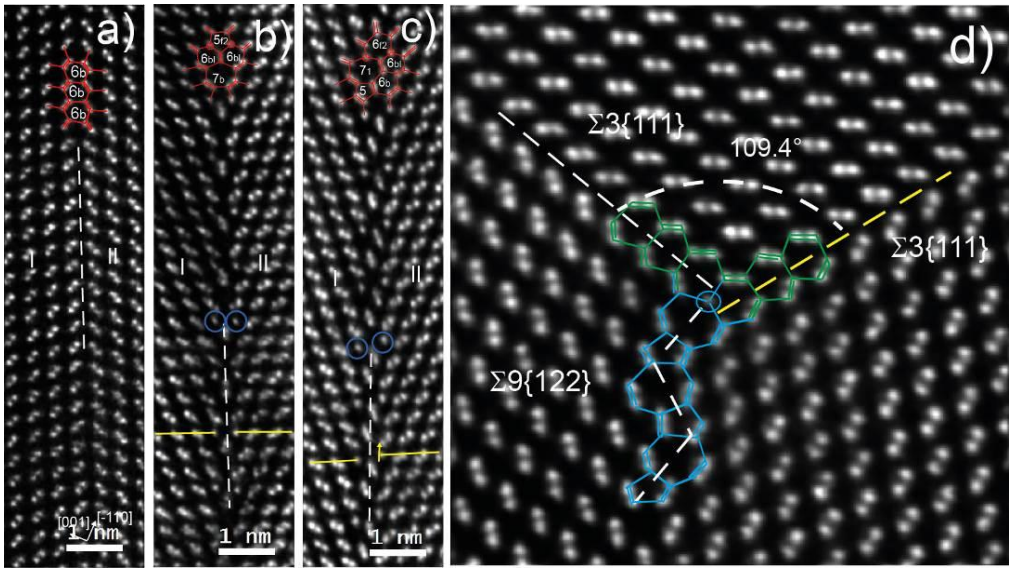

Figure 2. Examples of GBs: a) CTB, b) ITB with symmetric pattern, c) ITB with asymmetric pattern, and d) triple joint.

MS2.006
Structure of hybrid interfaces – arrangement of organic molecules on a crystalline inorganic surface

H. Kirmse[1], M. Sparenberg[2], S. Blumstengel[2], C. T. Koch[1]

[1]Humboldt-Universität zu Berlin, Institut für Physik, AG SEM, Berlin, Germany
[2]Humboldt-Universität zu Berlin, Institut für Physik, AG Photonik, Berlin, Germany

holm.kirmse@physik.hu-berlin.de

Introduction: Hybrid inorganic/organic interfaces are subject of vivid fundamental research in both, life science and materials sciences. Such hybrid interfaces occur in many systems, including heavy-atom markers in cell biology, bone implants in medicine, and metal nanoparticles on carbon nanotubes in materials science. Structural and chemical investigations are usually performed at the micro- and mesoscale but rarely on the nano- or atomic scale. Here we concentrate on the nanoscale.
Objectives: Our studies focus on uncovering the arrangement of conjugated organic molecules on a crystalline inorganic substrate. Moreover, we want to know whether the conjugated molecules form a crystalline structure. In extension to this approach we like to test how the functionalization of just one end of the conjugated molecules influences this arrangement.
Materials and Methods: As a model system for optoelectronics applications the materials combination of para-sexiphenyl (6P) deposited on a planar ZnO substrate is chosen. In particular, 6P molecules are deposited onto differently oriented ZnO crystal facets, viz. polar (0001) and non-polar (10$\underline{1}$0). TEM samples were prepared by mechanical pre-thinning and final Ar+ ion milling applying liquid nitrogen cooling. Alternatively, ultramicrotomy was applied. High-resolution TEM imaging was performed at a defocus of -1000 nm being the optimum for the (100) lattice plane distance of monoclinic 6P of 2.6 nm.
Results: Fig. 1 shows a cross sectional view of the 6P layer on polar (0001)ZnO covered by ZnO again. The (100) lattice fringes (cf. arrows) are aligned parallel to the ZnO surface indicating upright standing 6P molecules. The ZnO top layer is identified to be textured [1].
In contrast, 6P forms needle-like structures when deposited on non-polar (10$\underline{1}$0)ZnO (cf. Fig. 2). The needles are completely enclosed by the overgrowing ZnO. The orientation of the (100) lattice fringes of 6P indicate that the molecules are lying flat on the substrate surface. This is also confirmed by image contrast simulations [2] and explained by electrostatic coupling between the molecules and the dipolar electrostatic field generated by the Zn-O dimers at the (10$\underline{1}$0) substrate surface [3].
In order to study the arrangement of functionalized molecules on ZnO [4], optimum imaging conditions were identified. Fig. 3 represents an HRTEM image contrast simulation for difluorinated 6P (6P-F2). For the end-to-end and tip-to-tip alignment a defocus of - 500 nm is optimal (specimen thickness 100 nm).
Finally, a hypothetical structure model of a 6P-F2/(10$\underline{1}$0)ZnO interface was created (see Fig. 4) and HRTEM simulations were performed utilizing the QSTEM software package [5]. While the position of the fluorinated tip can hardly be identified from the HRTEM image, it is clearly seen in the projected potential which can be extracted from defocus series. Further alignments of 6P-F2 on ZnO will be discussed as well.
Conclusion: The arrangement of conjugated 6P and 6P-F2 molecules on ZnO is characterized by HRTEM. This is successfully done despite of the striking different properties of organic and inorganic materials. It was evidenced that the molecules form crystalline structures. This structure is even preserved when overgrown by ZnO. Different alignment of the 6P molecules were evidenced depending on the polarity of the ZnO substrate. The alignment of difluorinated molecules on ZnO can be concluded from defocus series.

References:
[1] S. Blumstengel et al., J. Cryst. Gr. **402** (2014) 187.
[2] H. Kirmse et al., Cryst. Growth & Design **16** (2016) 2789.
[3] F. Della Sala et al., Phys. Rev. Lett. **107** (2011) 146.
[4] M. Sparenberg et al., Phys. Chem. Chem. Phys. **16** (2014) 26084.
[5] QSTEM software package: http://qstem.org.

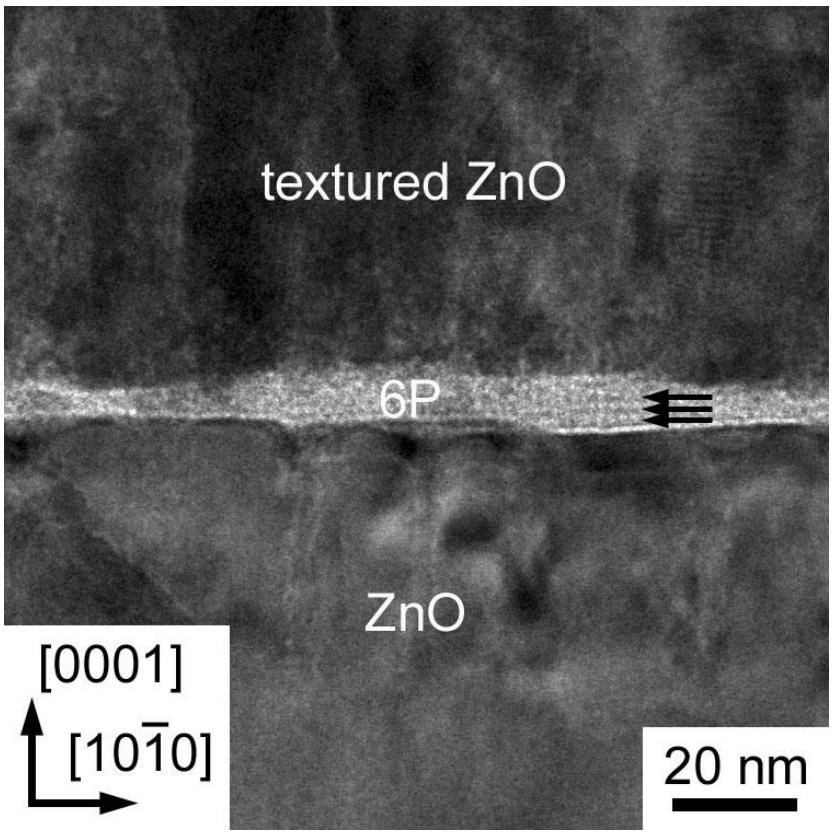

Figure 1. HRTEM image of upright-standing 6P molecules on (0001)ZnO.

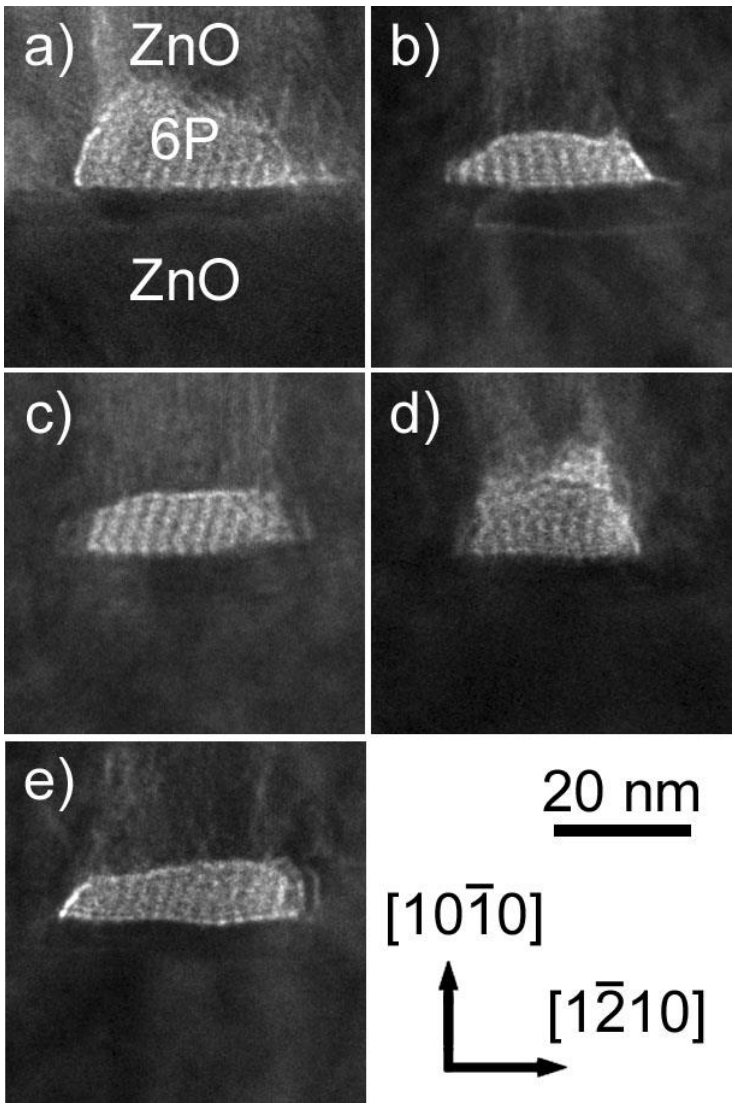

Figure 2. HRTEM image of flat-lying 6P molecules on (10$\underline{1}$0)ZnO.

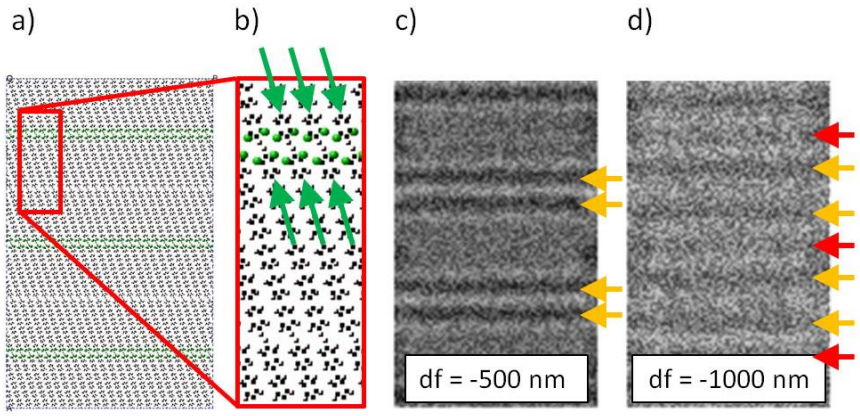

Figure 3. HRTEM image contrast simulation for 6P-F2 molecules oriented tip-to-tip and end-to-end: a) structure model, b) magnified view, c) and d) HRTEM image contrast simulation for 100 nm sample thickness and defocus of -500 nm and df = -1000 nm, respectively.

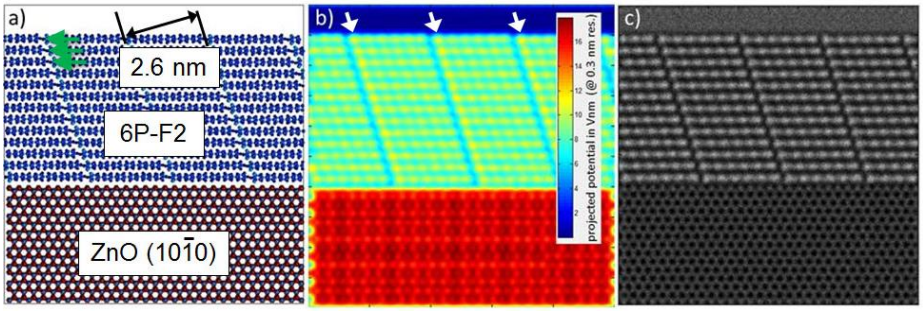

Figure 4. Simulation for 6P-F2 / (10$\underline{1}$0)ZnO interface; a) structure model with fluorinated tip pointing to the left (cf. arrows), b) projected potential with indication of fluorinated tip, c) simulated HRTEM image [5] for Cs = 1 mm, df = -67 nm, and t = 5 nm, neglecting atomic vibrations.

MS2.007
Contamination mitigation strategy for low energy scanning electron microscopy of multilayered graphene

E. Mikmekova[1], J. Polčák[2,3], S. Sluyterman[4], M. Lejeune[5], L. Frank[1]

[1]Institute of Scientific Instruments of CAS, v.v.i., Electron Microscopy and Spectroscopy of Surfaces, Brno, Czech Republic
[2]Brno University of Technology, CEITEC—Central European Institute of Technology, Brno, Czech Republic
[3]Brno University of Technology, Institute of Physical Engineering , Brno, Czech Republic
[4]Thermo Fisher Scientific, Materials & Structural Analysis (formerly FEI), Eindhoven, Netherlands
[5]Universite Picardie Jules Verne, Laboratoire de physique de la matière condensée, Amiens, France

eliska.mikmekova@gmail.com

In order to count the layers number of two-dimensional crystals such as graphene with an electron microscope we need to obtain a contrast contribution from a single layer of carbon atoms. This task requires increasing the scattering rate of incident electrons by means of a drastic lowering of their energy below 10 eV. A well-known problem can detrimentally affect the quality of the ultra-low voltage imaging, namely a specimen contamination. Even a small amount of hydrocarbon contamination can have a severe impact on the obtained results. During the scanning of the surfaces by electrons, the image usually gradually darkens because the hydrocarbon layer is deposited on the top. This effect can be described as an electron stimulated deposition. The surface diffusion of hydrocarbon molecules around the irradiated area is use as a source of building atoms, i.e. precursor. On the other hand, the effect of electron stimulated desorption occurs at the same time, especially at low electron energies, and then depends which process, deposition or desorption, is dominated.
Our experiments have showed the fact that prolonged bombardment with electrons (also with adding of oxygen) in a range of hundreds or even tens of eV gradually increases the transmissivity of graphene. It is caused by the removal of adsorbed gas molecules. Common cleaning methods, such as solvent rinsing, heating, ions bombarding and plasma etching have their limitations. In particular, electron-induced cleaning involves numerous operating parameters (including landing electron energy, electron dose, sample biasing, etc.) and it can lead to irradiation damage of the beam sensitive samples. On the other hand, this in-situ cleaning method and the utilizing of slow electrons can eliminate this electron irradiation damage. The quality of graphene was checked by Raman spectroscopy, XPS and TEM techniques after the electron beam irradiation.
Regarding ultra-low energy reflectivity, oscillations have been observed by UHV low energy electron microscopy experiments and explained by simulations, where n-1 periods of oscillations appear below 8 eV on n-layer graphene [1,2]. We have observed the same phenomenon also in the high vacuum (10^{-4} Pa) SEM micrographs after cleaning by slow electrons.
Experiments have been performed in a FEI SEM microscope equipped with the beam deceleration mode and the effects of landing electron energy, samples biasing, electron dose, heating, oxygen flow, etc. on the cleaning efficiency of electrons were studied in details. Our results are demonstrated in the Figures 1, 2, 3.

References:
[1] R.M. Feenstra, N. Srivastava, Q. Gao, M. Widom, B. Diaconescu, T. Ohta, G.L. Kellogg, J.T. Robinson, I.V. Vlassiouk, Physical Review B 87, 041406 (2013).
[2] E. Mikmeková, L. Frank, I. Müllerová, B.W. Li, R.S. Ruoff, M. Lejeune, Diamond and Related Materials, in press, DOI: 10.1016/j.diamond.2015.12.012.

Acknowledgment
The work was financially supported from the European Commission for the Marie Curie Initial Training Network (ITN) SIMDALEE2: Grant No. 606988 under FP7- PEOPLE-2013-ITN and from the Technology Agency of the Czech Republic (Competence center Electron microscopy, no: TE01020118).

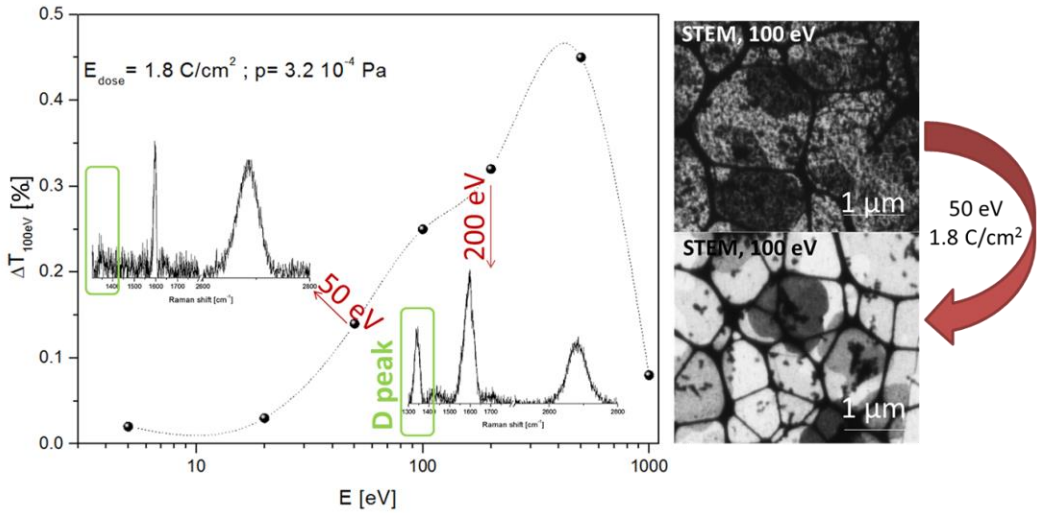

Figure 1. Dependence of the electron landing energies on the transmissivity changes of graphene, including the Raman spectra and representative STEM images obtained at 100 eV before and after beam irradiation by 50 eV electrons.

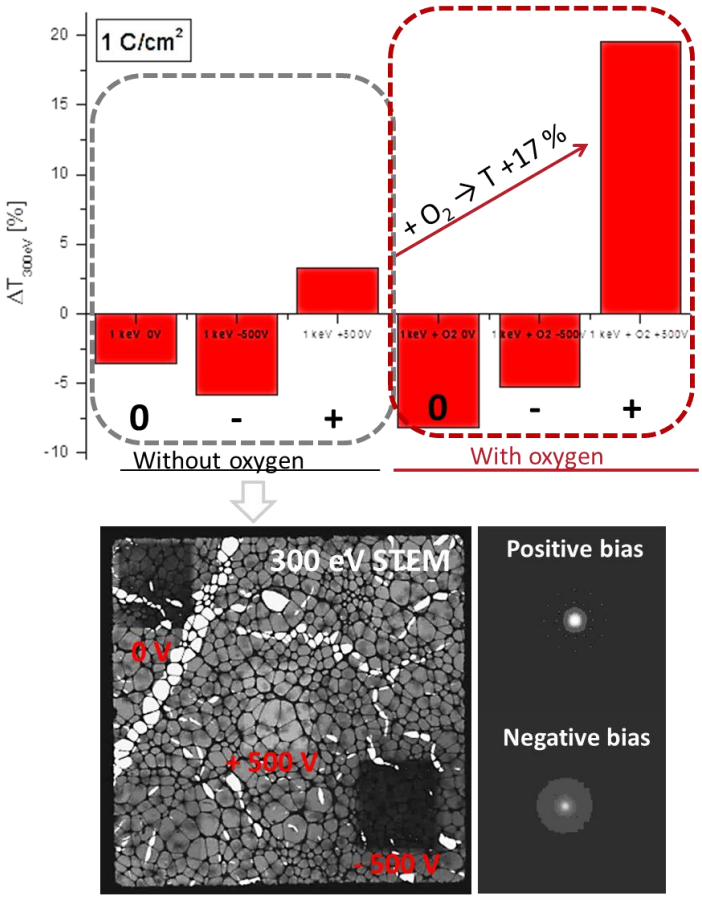

Figure 2. Influence of oxygen presence and the specimen bias on the cleaning process efficiency of the graphene flakes observed in STEM and TEM tools.

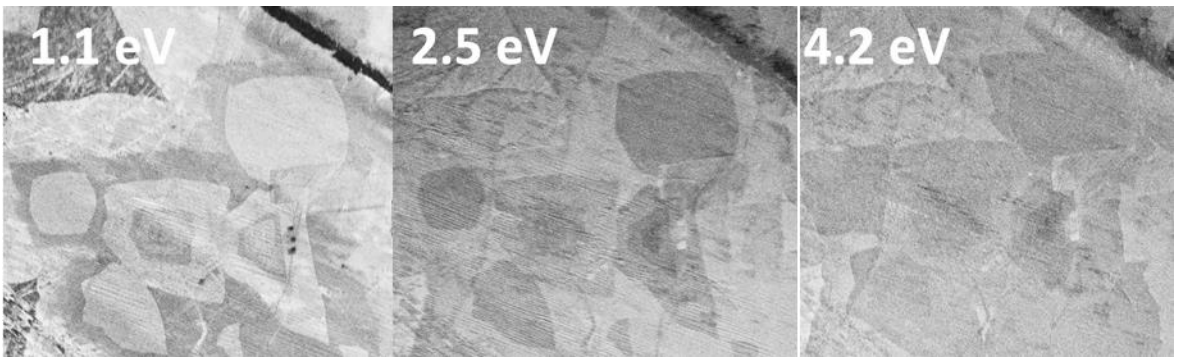

Figure 3. Ultra-low energy observation of graphene multilayers on Cu substrate after soft cleaning by slow electrons (50 eV) in commercial SEM equipped with the beam deceleration mode (FEI, HR SEM Magellan).

MS2.008 invited
Atomic and electronic structures of a $SrMoO_3$-based all-oxide epitaxial ferroelectric varactor

L. Molina-Luna[1], R. Egoavil[2], P. Komissinskiy[1], A. Mani[1], A. Radetinac[1], M. Nikfalazar[3], P. Salg[3]
A. Wiens[3], Y. Zheng[3], R. Jakoby[3], H. Maune[3], G. van Tendeloo[2], J. Verbeeck[2], L. Alff[1]

[1]TU Darmstadt, Department of Material- and Geosciences, Darmstadt, Germany
[2]University of Antwerp, EMAT, Antwerp, Belgium
[3]TU Darmstadt, Institute for Microwave Engineering and Photonics, Darmstadt, Germany

molina@geo.tu-darmstadt.de

Introduction**:** The functionality of perovskite oxides depends mostly on the electronic configuration of the *B*-site cations. Here we investigate interface engineered highly conducting $SrMoO_3$ (SMO) thin-film electrodes as enabling material for all-oxide ferroelectric varactors. The high electric conductivity of SMO with the Mo 4*d* t_{2g}^2 electronic state is related to the absence of magnetic interactions and reduced correlation effects. The reported conductivity of 2×10^5 S/cm of the SMO single crystal at room temperature remarkable and is higher than the conductivity of Pt.[1]
Objectives**:** By using scanning transmission electron microscopy (STEM) in combination with electron energy-loss spectroscopy (EELS) we were able to reveal the atomic and electronic structure in an all-oxide ferroelectric epitaxial varactor heterostructure with the SMO thin-film bottom electrode.
Materials and Methods**:** Transmission electron microscopy studies of the samples were performed at room temperature using the aberration-corrected scanning transmission electron microscope (STEM) FEI Titan3 80–300, operated at an acceleration voltage of 300 kV, equipped with a high-brightness field-emission electron source (X-FEG) and a high-resolution electron energy-loss spectrometer. The electronic structure changes across the oxide layers were investigated by monochromatic STEM-EELS (Figure 1 and 2).
Results**:** See Figure 1 and 2.
Conclusion**:** The remarkable result is that in spite of the contradicting thermodynamic oxidation conditions, the dielectric $Ba_xSr_{1-x}TiO_3$ and the highly conducting $SrMoO_3$ can be effectively coupled under preservation of their physical properties in an epitaxial heterostructure with negligible cation intermixing and valence change. The resulting interface is atomically sharp down to the unit cell scale. Surprisingly, a few unit cells of $SrTiO_3$ are sufficient to engineer the interface, allowing the utilization of the Pt like conducting $SrMoO_3$ in oxide electronic applications.

References:
[1] Nagai et al., *Appl. Phys. Lett.* **87**, 024105 (2005).
[2] Aso et al., *Sci. Rep.* **3**, 2214 (2013).
[3] Kourkoutis et. al., *Philos. Mag.* **90**, 4731-4749 (2010).
[4] Chen, Y. Z., et. al., *Nat. Mater.* **14**, 801-806 (2015).
[5] Noh et. al., *J. Phys.: Condens. Matter* **20**, 485208 (2008).
[6] The authors acknowledge the DFG within KO 4093/1-1 and JA 921/31-1, as well as the BMBF VIP+ project 03VP01150 and the EU Framework Program under Grant Agreement 312483 –ESTEEM2 (integrated Infrastructure Initiative –I3).

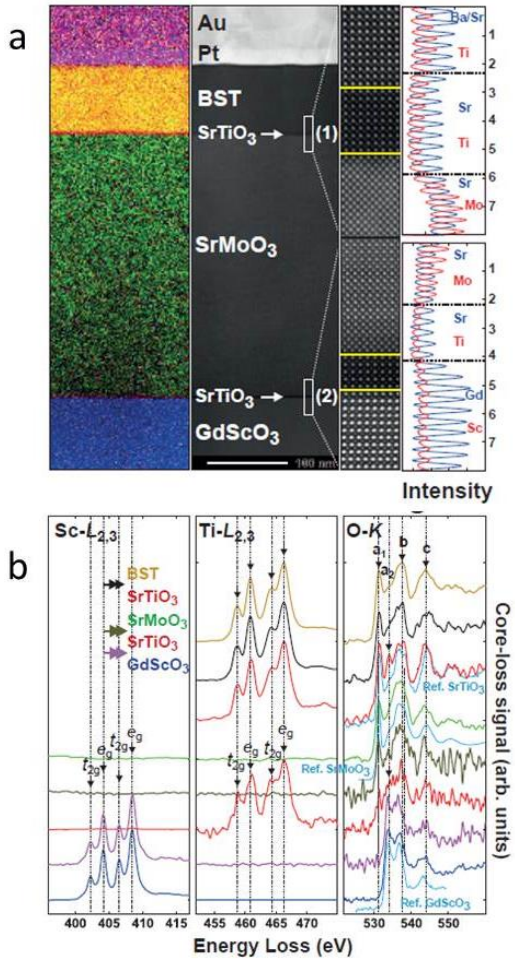

Figure 1. STEM-EELS and ELNES analyses of the varactor heterostructure.

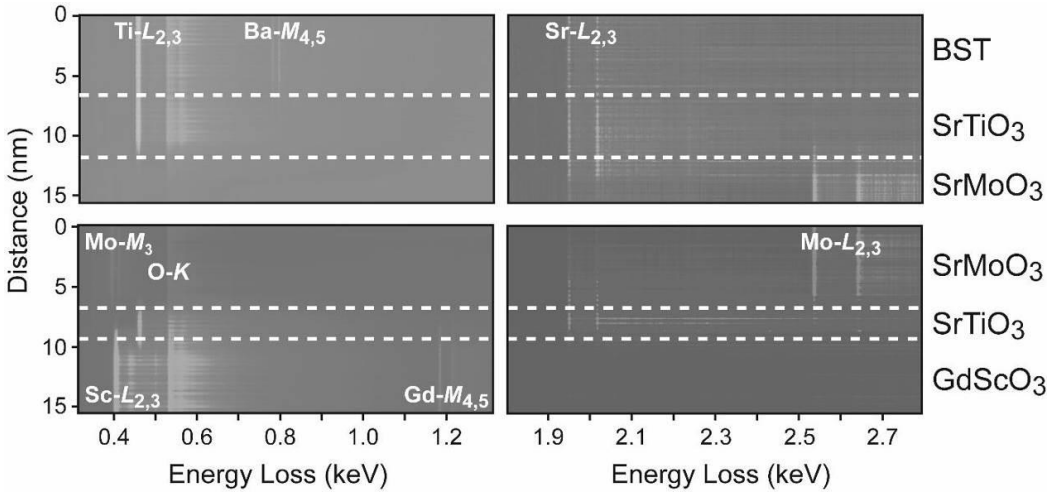

Figure 2. EELS line scans across the interfaces of the varactor heterostructure.

MS2.009
Functional domain walls in ferroelectric Pb(Zr1-xTix)O3 single crystals and thin films

X. Wei[1,2], T. Sluka[2], B. Fraygola[2], L. Feigl[2], B. Wang[3], Z. Ye[3], M. Heggen[1], R. Dunin-Borkowski[1], C. Jia[1] N. Setter[2,4]

[1]Forschungszentrum Jülich GmbH, Jülich, Germany
[2]EPFL-Swiss Federal Institute of Technology, Lausanne, Switzerland
[3]Simon Fraser University, Burnaby, Canada
[4]Tel-Aviv University, Ramat Aviv, Israel

x.wei@fz-juelich.de

In recent years, ferroelectric domain walls (DWs) have been found to possess exceptional physical properties that are distinct from those of domains and enable them to play a role as functional entities in nanoelectronic devices[1]. This technological potential motivates the intense exploration of the internal structure of the DWs (on a unit-cell scale) and the DW response to external fields [2,3]. Investigated by (scanning) transmission electron microscopy ((S)TEM), the structure and behavior of DWs in two material systems of Ti-rich Pb(Zr1-xTix)O3 (PZT) single crystals and thin films are presented in this talk.
(1) By using negative spherical-aberration imaging (NCSI) technique, our atom-resolved TEM study reveals Néel-like DWs in Ti-rich (x = 0.54, 0.60) PZT single crystals (see Fig. 1(a,b)), in which nanometer-scale monoclinic order coexists with tetragonal order. Our quantitative TEM study, combined with phase-field simulation, concludes that charging and clamping effects at phase boundaries promote formation of the Néel-like DWs[4]. Discovery of the continuous polarization rotation not only provides a foundation for exploring chiral DWs in ferroelectrics, but also facilitates the development of miniature piezoelectric devices based on such DWs.
(2) In x = 0.9 PZT thin films, our annular-bright-field (ABF) STEM study reveals that charging of the ferroelastic 90° DWs can be controlled by mutually coupled DW bending, type of doping, polarization orientation and work-function of the adjacent electrodes (see Fig. 1(c,d)). In particular, the doping dominates over other parameters in controlling the DW conductivity[5]. Understanding the interplay between these parameters in the PZT films allows us to control and optimize conductivity of such ferroelastic DWs in the oxide ferroelectrics. Furthermore, it also paves the way for utilization of DWs in future nanoelectronic devices.

[1] Catalan, G., Seidel, J., Ramesh, R. & Scott, J. F. Domain wall nanoelectronics. ***Rev. Mod. Phys.*** 84, 119-156 (2012).
[2] Jia, C.-L. *et al.* Atomic-scale study of electric dipoles near charged and uncharged domain walls in ferroelectric films. ***Nat. Mater.*** 7, 57-61 (2007).
[3] Li, L. *et al.* Giant Resistive Switching via Control of Ferroelectric Charged Domain Walls. ***Adv. Mater.*** 28, 6574-6580 (2016).
[4] Xian-Kui Wei, C.-L. J., Tomas Sluka, Bi-Xia Wang, Zuo-Guang Ye & Nava Setter. Néel-like domain walls in ferroelectric Pb(Zr,Ti)O3 single crystals. ***Nat. Commun.*** 7, 12385 (2016).
[5] Wei, X. *et al.* Controlled Charging of Ferroelastic Domain Walls in Oxide Ferroelectrics. ***ACS Appl. Mater. Interfaces***, doi:10.1021/acsami.6b13821 (2017).

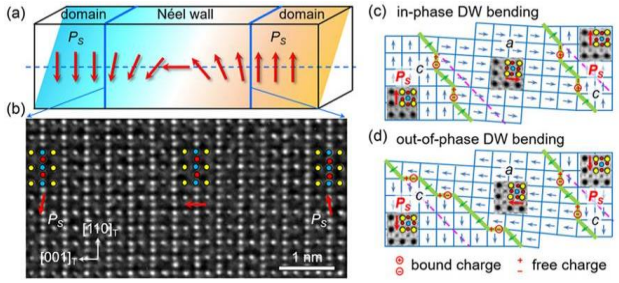

Figure 1. (a) Schematic representation of a Néel-type DW. (b) The Néel-like DW imaged in x = 0.60 PZT crystal. (c) The in-phase and (d) out-of-phase bent ferroelastic DWs in the x = 0.9 PZT thin films.

MS2.010
Atomic resolved STEM-EELS studies of $LaAlO_3/SrTiO_3$ bi-interfaces

G. Tieri[1,2], A. Gloter[2], D. Li[1], S. Gariglio[1], J. M. Triscone[1], O. Stéphan[2]

[1]Université de Genève, Geneva, Switzerland
[2]Laboratoire de Physique des Solides (U-PSUD), Orsay, France

giulio.tieri@u-psud.fr

Introduction: The study of epitaxial heterostructure of transition metal perovskite oxides is of tremendous interest for the ability to stabilize original electronic and/or magnetic phases at the interface. Among many, one of the most spectacular case is the high-mobility 2 dimensional electron liquid (2DEL) formed when a thin film of insulating $LaAlO_3$ (LAO) is grown on an insulating $SrTi^{4+}O_3$ (STO) substrate [1]. The mechanisms commonly proposed to explain such observation are categorizable in i) electronic reconstructions due to charge transfer to the interface (e.g. the polar catastrophe scenario) ii) chemical effects such as cations intermixing or cation transfer, or off-stoichiometry composition (e.g. O vacancies).
Objectives**:** We intend to compare in the same multilayer system two conductive LAO/STO interfaces, the first interface grown on the STO substrate (hereafter called "conventional" LAO/STO interface) and the second interface grown on a STO film (hereafter called "novel" LAO/STO interface) [2,3]. The interest in these heterostructures is linked to the possibility of realizing coupling effects between two 2DELs. Additionally it is important to investigate such novel interface for the possibility already reported to transfer it on different substrates [3].
Materials and Methods**:** A Nion UltraSTEM™ aberration-corrected Scanning Transmission Electron Microscope (STEM) equipped with Electron Energy-loss Spectroscopy (EELS) facilities has been operated at 100 kV for the spectroscopy and 200 kV for the imaging experiments. The multilayers investigated are built by the following sequence of layers: TiO2-terminated [001]-oriented STO substrate – LAO film – STO film – LAO film – vacuum. The films are typically deposited at 800-1100° and at an O_2 pressure of 10^{-6} mbar using Pulsed Laser Deposition.
Results**:** We found that the conventional interface displays a clear and systematic Al enrichment whereas the novel one does not, even if both are grown in the same conditions [4]. Importantly we observe that the diffusion of the LAO cations into the STO is strongly asymmetric: La diffuses on a long range (more than 20 u.c. in the substrate) while Al diffuses not more than 1 u.c. . It is meaningful here to recall that La can dope bulk STO substituting Sr and making it conducting [5]. In term of electronic structure the two interfaces are different, with electronic doping (Ti^{3+}) only measurable by EELS at the novel interface, this despite that both interfaces are conducting according to transport measurements. In term of structure as seen by dark-field imaging, the LAO layer at the conventional interface, i.e. at the bottom of the heterostructure, grows coherent with the substrate instead for the novel interface, we observe the systematic formation of edge dislocations.
Conclusions**:** The missing spectroscopic fingerprint of Ti^{3+} for the conventional conducting interface may suggest the possibility that the 2DEL is indeed strongly delocalized resulting in a spatial density below the experimental sensibility. By contrast in the case of the novel interface where the STO film represents a limit on the delocalization of the 2DEL, Ti^{3+} is clearly detected. Moreover the fact that the artificial interface isn't Al enriched insinuates possibility of cation transfer e.g. to the surface. These results compose an articulated scenario in which electron reconstruction, cation transfer and cation intermixing are at play in the formation of 2DELs.

[1] A. Ohtomo and H.Y. Hwang, *Nature* **427**, 423 (2004).
[2] D. Li *et al*., APL *Materials* **2**, 012102 (2014).
[3] C.W. Bark *et al*., PNAS **108.12**, 4720 (2011).
[4] M.P. Warusawithana *et al*, *Nature Communication,* 4:235 (2015)
[5] Sunstrom *et al*, Chem. Mat., **4** 346-353 (1992)

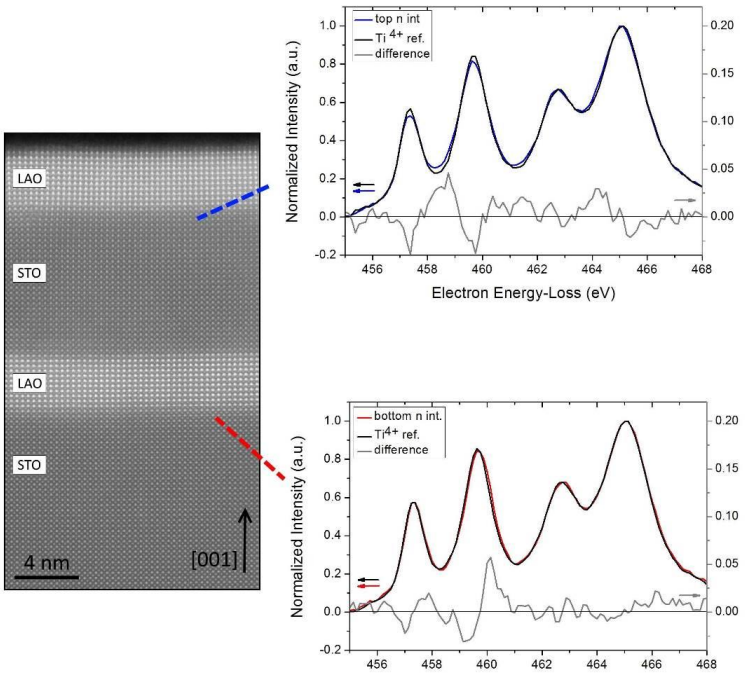

Figure 1. EELS measure of the Ti-$L_{2,3}$ with information on the Ti valence at the novel (top) and conventional (bottom) conducting interfaces. The novel interface displays spectroscopic evidences of electron doping on 3d bands.

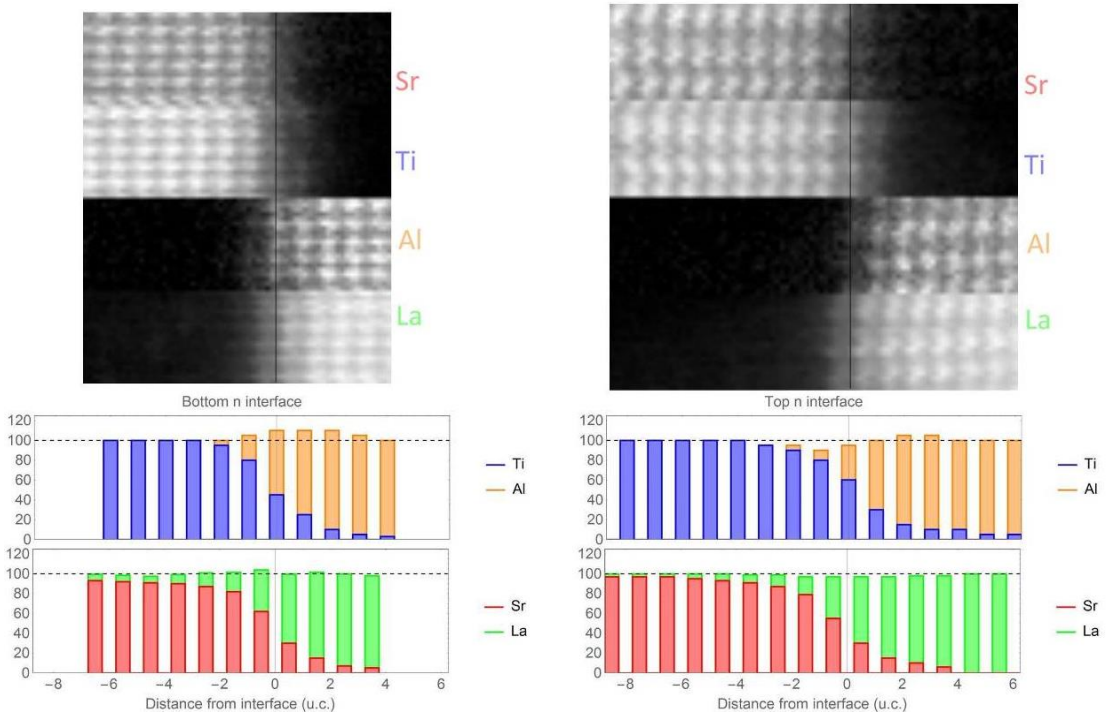

Figure 2. Cation concentration as obtained by STEM-EELS measurements at the conventional (left) interface and novel (right) interface showing different intermixing and notably Al enrichment of the conventional one.

MS2.011
Dopant distribution and octahedral distortions at superconducting complex oxide bilayer interfaces

Y. E. Suyolcu[1], Y. Wang[1], W. Sigle[1], F. Baiutti[2], G. Cristiani[3], J. Maier[2], G. Logvenov[3], P. A. van Aken[1]

[1]MPI for Solid State Research, StEM, Stuttgart, Germany
[2]MPI for Solid State Research, Physical Chemistry of Solids, Stuttgart, Germany
[3]MPI for Solid State Research, Technology, Stuttgart, Germany

y.e.suyolcu@fkf.mpg.de

Introduction and Objectives: Interfaces can drastically change material properties. Complex oxide material systems show a particularly rich variety of such new properties [1], as for example, magnetism, changes in electronic and ionic conductivities, or even superconductivity. It is now well accepted that these effects appear even after small variations in composition and structure of oxide interfaces [2].
Materials and Methods: Here we present results of doped lanthanum cuprate ($La_{1.6}M_{0.4}CuO_4$ (LMCO), M = Ca, Sr, Ba) systems where we systematically varied the dopant ionic radius while the dopant valence state was fixed. Metallic LMCO layers were deposited on (001) $LaSrAlO_4$ followed by a second insulating La_2CuO_4 layer, using atomic-layer-by-layer molecular beam epitaxy. The layer system was structurally characterized using high-angle annular dark-field (HAADF) and annular bright-field (ABF) imaging in a probe-corrected (DCOR, CEOS GmbH) JEOL JEM-ARM200F microscope. Chemical analysis was performed by electron energy-loss spectroscopy (EELS) and energy-dispersive X-ray spectroscopy.
Results and Conclusions: For all dopants perfect epitaxial growth is observed without the presence of misfit dislocations (Fig. 1). This is due to the small misfit of 1.5 % and the small total thickness of 8 nm. Thus, the layers are under compressive strain. Dopants were found to be inhomogeneously distributed in the metallic layer and EELS spectrum imaging shows distinct differences among the three dopant species. Whereas Sr distribution is closest to homogeneity, Ca tends to accumulate at the substrate interface and Ba atoms tend to migrate towards the surface and insulating layer. This can be understood from minimization of strain energy.
All three systems exhibit superconducting behaviour and the critical temperature is found to depend on the dopant species. Precise measurement of *c*-lattice parameters shows that the critical temperature is not, as expected, linearly related with the *c*-lattice parameter, i.e. with the distortion of oxygen octahedra [3]. This will be discussed in conjunction with the dopant redistribution.

[1] Hwang, H. Y. et al., Nat. Mater. **11,** 103–113 (2012).
[2] Kan, D. et al., Nat. Mater. **15,** 432–437 (2016).
[3] Suyolcu, Y.E. et al., Microscopy and Microanalysis, **22(S3)** 308 (2016).

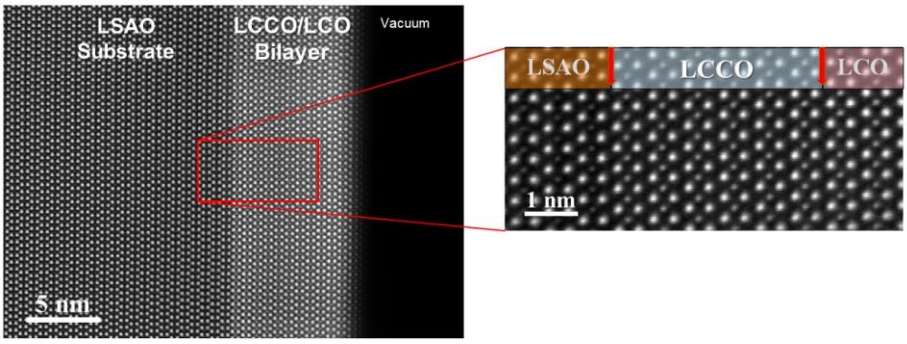

Figure 1. STEM-HAADF image of Ca-doped bi-layer showing a coherent interface and high structural quality.

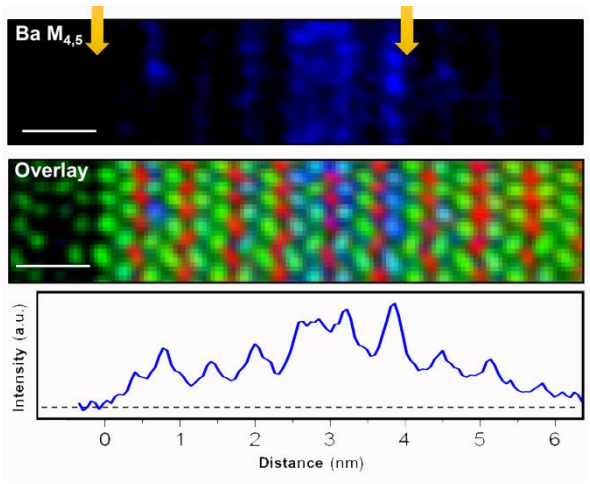

Figure 2. (top) Atomically resolved Ba-M4,5 edge elemental map. Arrows indicate the nominal interface positions. Substrate is left, metallic layer between arrows, and insulating layer right. (center) RGB map of Cu (red), La (green), and Ba (blue). (bottom) Averaged Ba profile.

MS2.012
Quantitative spectroscopic analysis of memristive oxide triple layers

J. Strobel[1], G. Haberfehlner[2], R. Popescu[3], G. Kothleitner[2], L. Kienle[1]

[1]Technical Faculty, CAU Kiel, Kiel, Germany
[2]Technical University Graz, Institute for Electron Microscopy and Nanoanalytics, Graz, Austria
[3]Karlsruhe Institute of Technology, Laboratory of Electron Microscopy, Karlsruhe, Germany

just@tf.uni-kiel.de

Introduction*:* Memristive devices are in the focus of intensive research because they lead the path towards non-Boolean computation, enabling imitation of neuromorphic networks such as the human brain. The devices rely on atomistic effects such as anion or cation movement in order to change their macroscopic electrical resistance. Understanding these atomistic effects is a great challenge for current electron microscopy investigations.
Objectives: The aim of the investigations was to find the mechanism behind memristive behaviour in a combined Schottky and tunnel barrier device consisting of three distinct oxide layers. Oxygen vacancies are expected to change the height of the Schottky barrier and also influence the tunnel barrier. Accordingly, advanced analytical methods – electron energy-loss spectroscopy (EELS) on a monochromated scanning transmission electron microscope (STEM) as well as energy dispersive X-ray spectroscopy (EDX) – have been applied in order to accurately and quantitatively map all chemical features of the device.
Materials and Methods: The triple oxide layer has the layer sequence Au/NbOy/AlOx/NbOz/Nb, where the NbOy layer forms the Schottky barrier and AlOx is the tunnel barrier. Investigations by a combined STEM-EELS and EDX approach were chosen to reliably map and quantify light as well as heavy elements. Special care was given to sample preparation without inducing any artifacts, as the critical layers are all below 3 nm thick. Quantitative EDX measurements are compared to high quality EELS data in correlated experiments allowing quantification by EDX, EELS ionization cross-section and energy-loss near edge structure (ELNES).
Results: The two different Nb oxide layers exhibit distinct but different oxidation states, forming one insulating and one conductive Nb oxide. The ELNES of the oxygen K-edge in the AlOx layer exhibits a pronounced pre-peak feature associated with the presence of oxygen vacancies, that leave localized Al(3s) states in the middle of the band gap. EDX, EELS and ELNES produced reasonably congruent results. The oxidation state of the NbOz layer hints towards oxidation during reactive sputter deposition of the above lying oxide layers.
Conclusion: The results demonstrate the investigational complexity of seemingly trivial oxide layer systems and the consequential necessity for highest quality spectroscopic analysis by both EDX and EELS. The trade-off between signal-to-noise-ratio, illumination time, spectral range, energy and spatial resolution must be carefully considered in order to receive the required information, without obscuring features or creating beam-induced artifacts. The benefit of acquiring this spectroscopic information will be discussed, especially with respect to electrical simulations on these memristive devices.

Acknowledgements
The authors gratefully acknowledge funding by the DFG through the research unit FOR2093 (project B2) and by the European Union within the 7th Framework Program (FP7/2007-2013) under Grant Agreement no. 312483 (ESTEEM2). JS and LK would like to thank Mrs. Christin Szillus and Mrs. Martina Dienstleder for sample preparation by FIB and NanoMill and Prof. Ferdinand Hofer as well as Prof. Dagmar Gerthsen for supporting the investigations as well as Mr. Mirko Hansen for device fabrication and Mr. Hermann Kohlstedt and Mr. Martin Ziegler for valuable discussions. The authors acknowledge the support of the Karlsruhe Nano Micro Facility (KNMF) for Electron Microscopy and Spectroscopy facilities.

MS2.013
Understanding the growth mechanism of solid-state reaction in oxides from the atomic interface structures

C. Li[1], G. Habler[1], T. Griffiths[2], P. Jerabek[3], L. C. Götze[4], T. J. Pennycook[5], C. Mangler[5], J. Meyer [5] R. Abart [1]

[1]University of Vienna, Department of Lithospheric Research, Vienna, Austria
[2]Max Planck Institute for Iron Research GmbH, Department of Microstructure Physics and Alloy Design, Düsseldorf, Germany
[3]Charles University, Institute of Petrology and Structural Geology, Prague, Czech Republic
[4]Freie Universität Berlin, Institute of Geological Sciences, Berlin, Germany
[5]University of Vienna, Faculty of Physics, Vienna, Austria

lichen0320@gmail.com

Solid-state reactions can produce intermediate phases between reactants in functional thin films [1], ceramic oxides [2] and natural minerals [3]. This interlayer growth involves two processes: *interface reactions* and *elemental diffusion*, the coupling of which changes during different growth stages. In order to understand the growth mechanisms, it is crucial to understand the atomic structure at the reaction fronts - the interfaces.

The reaction of MgO and Al_2O_3 to form $MgAl_2O_4$ provides an ideal model system for studying the kinetics of solid-state reactions [4]. Electron Backscatter Diffraction (EBSD) mapping (Figure 1) shows that the $MgAl_2O_4$ spinel layer splits into two different orientations: MgO-orientated $MgAl_2O_4$ and Al_2O_3-orientated $MgAl_2O_4$ both with topotaxial relations. Interface areas with prominent orientation characteristics are then extracted using focused ion beam (FIB) for atomic imaging via scanning transmission electron microscopy (STEM).

The $MgAl_2O_4$/MgO reaction-front has a periodic scalloped shaped interface with misfit dislocations at cusps spaced ~23 planes (~ 4.5 nm) apart, consistent with the ~4.3% lattice mismatch (Figure 2). In 3D the interface has a periodic hilly-shape, where the misfit dislocations together with the periodic curved interface segments form supercells. At the $MgAl_2O_4$/Al_2O_3 interface, step-associated partial dislocations are observed (Figure 3). An oxygen plane is shared between Al_2O_3 and $MgAl_2O_4$ when the stacking sequence of oxygen changes from hexagonal close-packed (hcp) to face-centered cubic (fcc).

With the atomic configuration of the interfaces determined, the interlayer growth mechanism can be explained: the growth occurs by inter-diffusion of cations in a stationary oxygen sublattice. At the MgO/$MgAl_2O_4$ interface, both sides have fcc oxygen sublattices that can be considered to be continuous at the dislocation-free portions, and the structure transformation only requires an exchange of Al^{3+} for Mg^{2+}. However the movement of the misfit dislocations can only occur by climbing, which requires a supply of extra oxygen and higher activation energies. Therefore propagation of the misfit dislocations lags behind during interface migration and causes the 3D interface geometry with cusps pointing back. The $MgAl_2O_4$ /Al_2O_3 interface is more complicated as α-Al_2O_3 has a pseudo-hcp oxygen lattice therefore a stacking sequence change is needed in the oxygen sublattices. Growth of $MgAl_2O_4$ can occur by partial dislocation glide along the interface steps, which is more dominant at late growth stages. The fundamental understanding of the interface reaction on the atomic scale in this system should also helps to understand solid-state reactions in other materials. [5]

References:

[1] C. Li, J. Poplawsky, N. Paudel, T. J. Pennycook, S. J. Haigh, M. M. Al-Jassim, Y. Yan, and S. J. Pennycook, IEEE J. Photovoltaics **4**, 1636 (2014).
[2] C. B. Carter and M. G. Norton, Ceramic Materials (Springer Science & Business Media, 2013).
[3] R. H. Vernon, A Practical Guide to Rock Microstructure (Cambridge University Press, 2004).
[4] C. Li, T. Griffiths, T. J. Pennycook, C. Mangler, P. Jeřábek, J. Meyer, G. Habler, and R. Abart, Philos. Mag. **96**, 2488 (2016).
[5] This research was funded by the EU Marie Skłodowska-Curie grants No. 656378 – Interfacial Reactions (CL) and the Austrian Science Fund (FWF) I1704-N19 (GH).

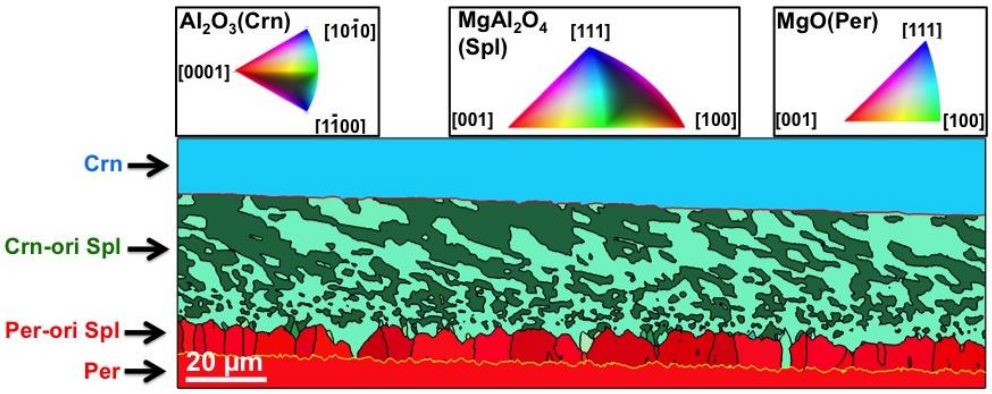

Figure 1. EBSD map showing Al_2O_3-ori $MgAl_2O_4$ including twin structure (dark and light green), and MgO-ori $MgAl_2O_4$ (red). [4].

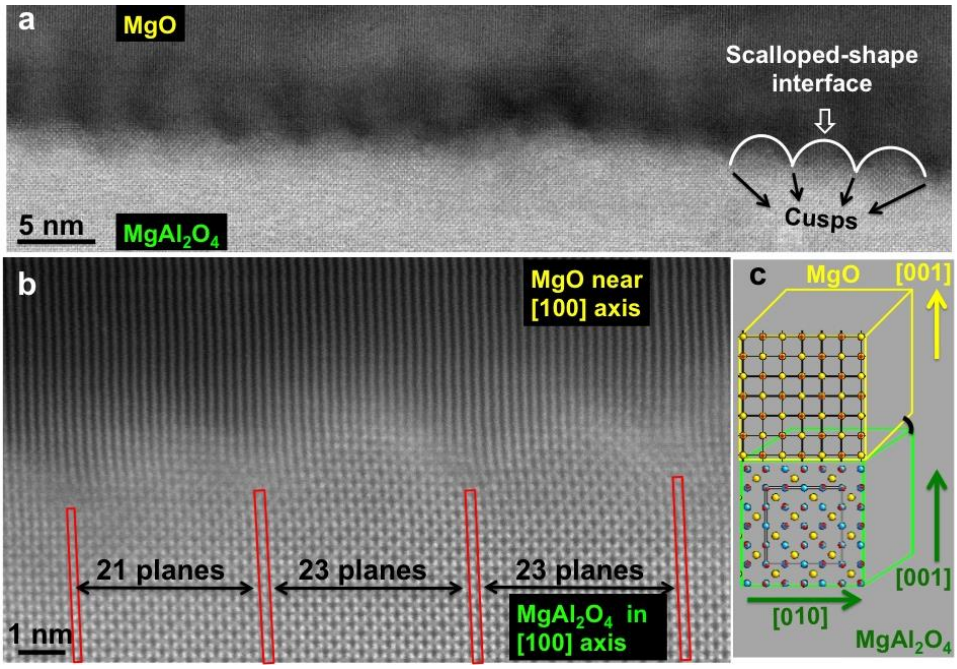

Figure 2. (a) STEM image shows a scalloped-shape $MgAl_2O_4$/MgO interface. (b) Periodic misfit dislocations at the cusps position with ~4.5 nm spacing. Red boxes indicated extra planes. (c) Sketch shows the orientation relationship. [4].

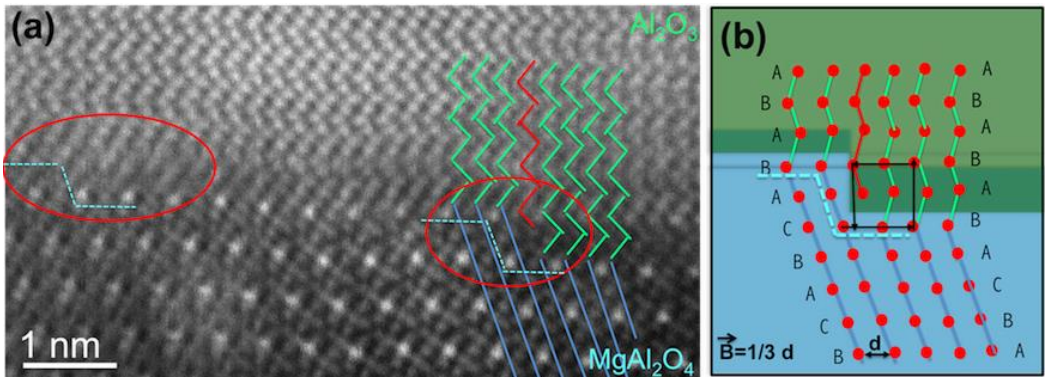

Figure 3. (a) STEM image shows step-associated partial dislocations (red circles) at $MgAl_2O_4$/Al_2O_3 interface. Red lines indicated extra planes. (b) Sketch shows oxygen lattice arrangement.

MS2.014
A nano beam electron diffraction study of strain distributions in deformed thin epitaxial metal layers

A. Graff[1], F. Meyer[2], F. Burmeister[2], F. Altmann[1]

[1]Fraunhofer IMWS, CAM, Halle, Germany
[2]Fraunhofer IWM, Freiburg, Germany

andreas.graff@imws.fraunhofer.de

Due to its excellent thermal and electrical properties, pure or doped single crystal diamond wafer material is a candidate for future high performance electronic devices. Hereby, heteroepitaxial deposition of diamond on (100) oriented Iridium by plasma assisted CVD is regarded as promising route to an electronic grade (100) diamond wafer [1]. (100) Iridium films can be deposited on various single crystal substrates or multilayer stacks.
Depending on the substrate material and the temperature during deposition Iridium thin films will be exposed to additional thermomechanical mismatch when cooling down to room temperature after processing resulting in an elastic and plastic deformation of the film and a related biaxial stress field. Since diamond has a very low thermal expansion coefficient, knowledge about the amount of residual elastic deformation is crucial for the process design. To measure the biaxial strain in the Iridium films Nano Beam Electron Diffraction (NBED) was used to determine the distribution of different strain components.
Iridium was deposited by rf-magnetron sputtering onto YSZ and sapphire (a-plane) single crystals at different temperatures for (100) oriented growth. The morphology and orientation of the thin films were determined by XRD, SEM and EBSD (Zeiss Supra, EDAX). TEM cross section samples were prepared either by Focused Ion Beam (FIB)[2] or by classical face to face method. The TEM, STEM and NBED investigations were performed at 300kV (FEI, Titan 60-300). For NBED analysis a commercial software [3] (FEI, Epsilon) was used with optimized parameters for the precise detection of electron diffraction spots and their positions.
The example presented in the abstract relates to an Iridium film grown on YSZ (100) at a substrate temperature of 350°C. XRD and EBSD reveal a mainly (100) orientated Iridium film (Figure 1). The hetero epitaxial growth of the Iridium thin film is validated by HRTEM and NBED measurements (Figure 2). Moreover, the local probing technique allows us to determine the crystal lattice constants and strain distributions inside single oriented grains (Figure 2). The distribution of the in plane and out of plane strain components prove the expected compressive strain parallel to the interface as a result of the thermomechanical stress due to the difference in the thermal expansion coefficients between Iridium and YSZ.
To characterize the properties of thin epitaxial metal films the NBED technique can be helpful to analyze the structure and the local strain distributions inside the film with higher lateral resolution than XRD.

References:
[1] M. Schreck, H. Roll, and B. Stritzker, App. Phys. Let. Vol. 74, no. 5 (1999) 650-652
[2] M. Simon-Najasek, S. Huebner, F. Altmann, A. Graff, Microelectron Reliab, 54 (2014) 1785-1789
[3] Williamson, M. J., van Dooren, P., & Flanagan, J, IEEE 22nd IPFA (2015) 197-200

Acknowledgement
The work is supported by Fraunhofer-Zukunftsstiftung under project "DiaLe"

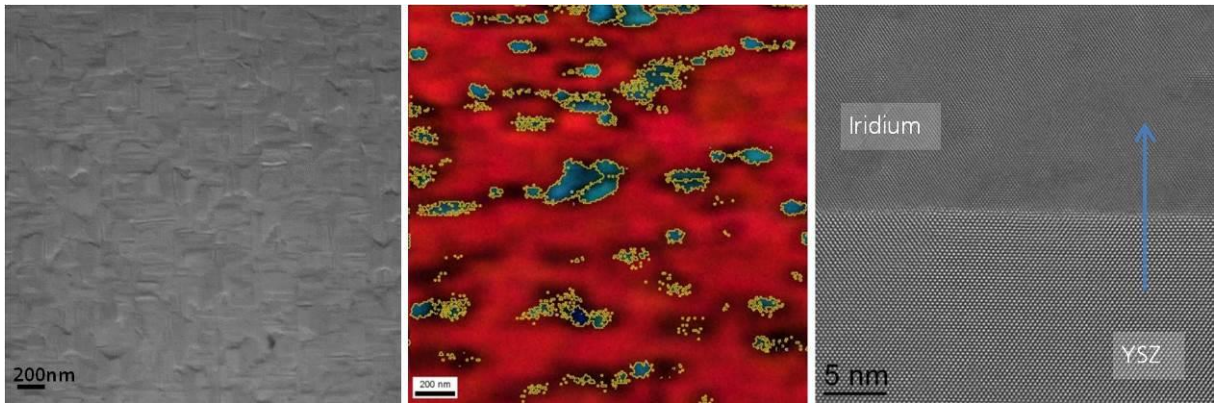

Figure 1. Left: SEM image of the Iridium film surface. Middle: EBSD measurements of the Iridium film with inverse pol figure plot. Right: HRTEM image of the Iridium YSZ interface.

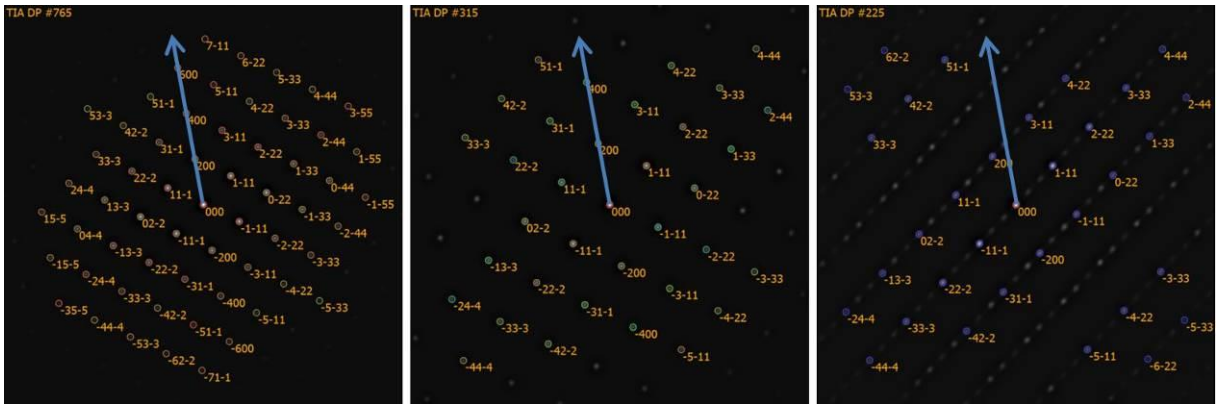

Figure 2. Processed NBED patterns: Left: YSZ (100) substrate. Middle: Epitaxial Iridium film. Right: Twin boundary in the Iridium film (wrong automated indexing).

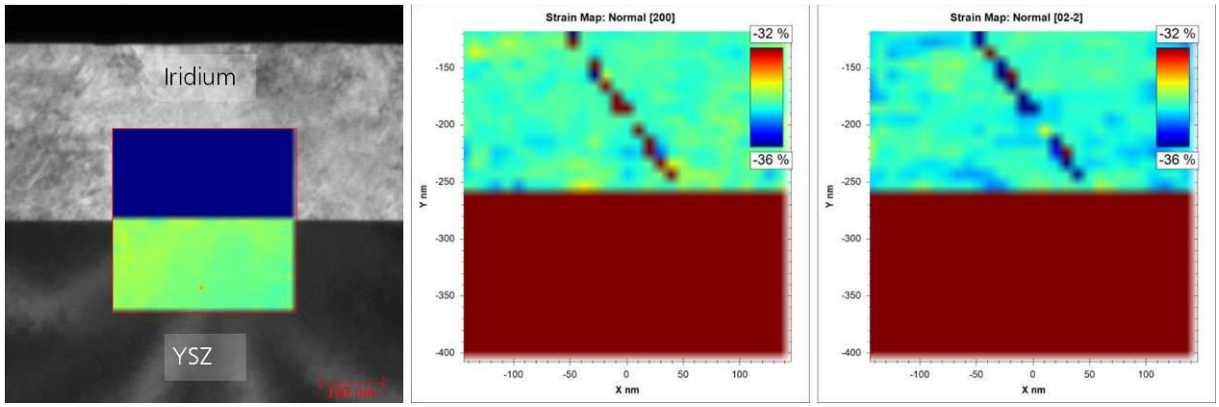

Figure 3. Left: NBED dark field image of the oriented Iridium film on YSZ with in plane strain variation (Reference: data). Middle: Color coded strain distribution in the (200) direction perpendicular to the substrate surface Right: Color coded strain distribution in the (02-2) direction parallel to the sample surface. Twin boundary in the center of the Iridium film not indexed properly.

MS2.P001
Microstructure of alumina coating on steel P92 after thermal cycling

I. Dörfel[1], M. Nofz[1], R. Sojref[1], W. Schulz[1], R. Saliwan Neumann[1], R. Hesse[1], C. Meyer[1], A. Kranzmann[1]

[1]Bundesanstalt für Materialforschung und -prüfung, Werkstofftechnik, Berlin, Germany

ilona.doerfel@bam.de

Keywords: coating, thermal cycling, TEM

Introduction: Alumina coatings are one possibility to increase the corrosion resistance, lifetime and application range of thermally loaded steel components, e.g. in modern power plants where the use of the Oxy-fuel technology corrosive fuel gas (H2O-CO2-O2-SO2 at 650 °C) affects the steel parts. In previous investigations the efficacy of protective alumina coatings on steel P 92 under those conditions was demonstrated [1]. A shutdown and re-start of power plants or parts of them causes thermal stresses of the components which can cause detrimental effects like microstructural changes in the steel itself [2], changes in its oxidation behavior, delamination or microstructural changes in the coating. All those effects can lead to failure of the components, resulting in lifetime reduction.
Objectives: As a first step, we concentrate on the influence of thermal cycling tests and observe the impact on the microstructure of the coating and the interface in laboratory air. These investigations will help understanding the processes which occur, show directions of potentially necessary changes of the coating due to improved thermal stress behaviour.
Materials and Methods: P 92 is a ferritic-martensitic steel, containing 9% Cr which forms protective Cr-oxide-rich scales in dry environments and non-protective ones in water-containing environments [3, 4]. Coupons of P 92, having ground surfaces [5], were dip-coated via a sol-gel process [5] and subjected to thermal cycling for 500 h (1000 cycles) in laboratory air in a temperature range between room temperature and 660° C (Fig.1). The resulting mass loss was determined by weighing.
Samples for TEM investigations were produced as cross sections normal to the sample surface by FIB preparation (Quanta 3D, (FEI)). The TEM/STEM investigations were performed using a JEM2200FS (JEOL) operated at 200 kV. The microstructure of the coating and the interface after cycling tests was characterized via TEM, HREM, and STEM images, electron diffraction as well as EDX and EFTEM methods.
Results: At steep edges in the surface profile the coating was imperfect and cracks have formed during the thermal cycling (Fig.2). Flat surface regions are well-covered. The whole interface region between the steel and the coating shows a dense Cr-oxide-rich zone, which can form protective regions in case of local failure. The Cr-oxide zone is followed by a region of mixed oxides, containing Cr, Mn, Fe, and Al in variable composition, to which a porous δ-Al2O3 zone is joined (Fig.3).
Conclusions:

- Alumina coatings promote the formation of dense, Cr-rich zones at the interface, which makes the system self-healing.
- These zones are stable during thermal stresses, even in regions with cracked coatings.
- They cause reduction of outward diffusion and mass loss during thermal cycling.

References:

[1] M. Nofz, I. Dörfel, R. Sojref, N. Wollschläger, M. Mosquera-Feijoo, A. Kranzmann, submitted to Corr.Sci.
[2] A. Czyrska-Filemonowicz, A. Zielinska-Lipiec, P.J. Ennis, JAMME, 19 (2006) 43.
[3] M. Schütze, M. Schorr, D.P. Renusch, A. Donchev, J.P.T. Vossen, Materials Research, 7 (2004) 111.
[4] J. Ehlers, D.J. Young, E.J. Smaardijk, A.K. Tyagi, H.J. Penkalla, L. Singheiser, W.J. Quaddakkers, Corr. Sci. 48 (2006) 3428.
[5] M. Nofz, I. Dörfel, R. Sojref, N. Wollschläger, M. Mosquera-Feijoo, A. Kranzmann, J Sol-Gel Sci.Technol. 81 (2017) 185.

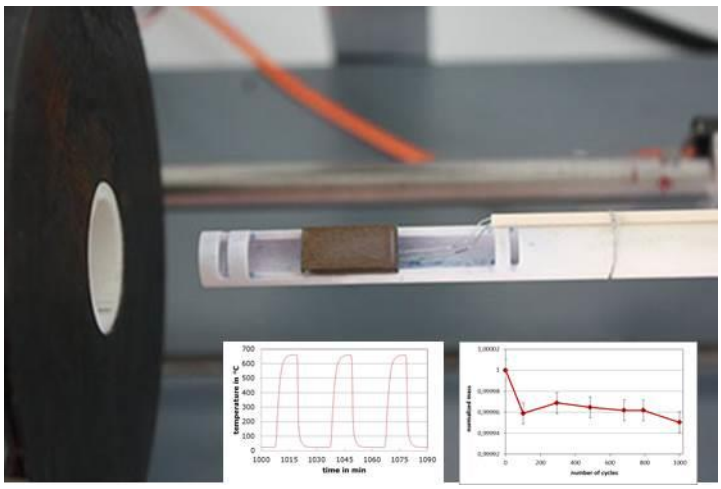

Figure 1. Sample on the way into the oven. The insets show a section of the temperature profile and the mass loss graph.

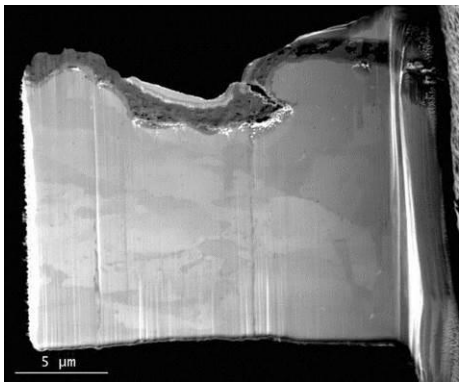

Figure 2. FIB image of a TEM lamella showing a crack in the coating.

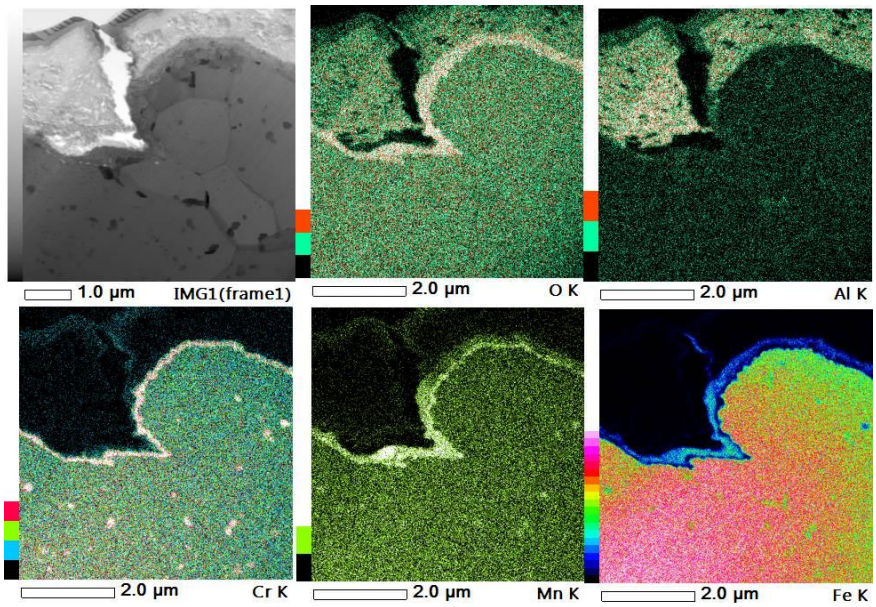

Figure 3. STEM bright field image of the crack region with elemental maps of O, Al, Cr, Mn, and Fe.

MS2.P002
Analysis of polarization-mediated thermal stability of CoFeB/BiFeO3 heterointerface by aberration-corrected scanning transmission electron microscopy

X. Shen[1], Q. Zhang[2], L. You[3], C. Wan[2], Z. Yuan[2], X. Zhang[2], L. Huang[2], W. Kong[2], H. Wu[2], R. Yu[1]
J. Wang[3], X. Han[2]

[1]Institute of Physics, Laboratory of Advanced Materials & Electron Microscopy, Beijing, China
[2]Institute of Physics, State Key Laboratory of Magnetism, Beijing, China
[3]Nanyang Technological University, School of Materials Science and Engineering, Singapore, Singapore

xshen@aphy.iphy.ac.cn

Introduction: Hybrid interfaces comprising ferromagnetic metals and ferroelectric/multiferroic oxides have attracted many scientists due to their unique properties and widespread applications for the nextgeneration magnetoelectric memories, in which magnetism can be tuned electrically via strain-/spin-mediated couplings across the interfaces.
Objectives: However, oxidation of the metal or ferromagnetic layers is detrimental to the device performance. Besides, the annealing process is usually indispensible to obtain higher tunneling magnetoresistance ratio before magnetic tunneling junctions can be applied, which could lead to the chemical reaction between oxygen and metal atoms, further deteriorating the interfacial coupling in a ferromagnetic/ferroelectric (multiferroic) heterostructure. Therefore, analysis of thermal stability of the metal/oxide interface is at the core of the reliability of the interface-mediated magnetoelectric effect.
Materials and Methods: We chose CoFeB/BiFeO3 (BFO) as the metal/oxide system in this study and used the pulsed laser deposition for growing films. Annealing process was carried out in a vacuum system with a base pressure of 10−4 Pa and a static magnetic field of 5 kOe. Further investigation on the interface structure was carried out by cross-sectional scanning transmission electron microscopy (STEM), energy dispersive X-ray spectroscopy (EDS), and electron energy-loss spectroscopy (EELS) experiments using JEM-ARM200F (JEOL) with double CS correctors for the condenser lens and objective lens.
Results: The annular bright field (ABF), EDS and EELS experiments were performed using a Cs-corrected transmission electron microscope. As shown in Figure 1a for STO/BFO/CoFeB(4)/Cu(2)/Co(4)/Ir22Mn78(12)/Ta(5 nm), interdiffusion can be observed and the interfaces become rough after 300 °C annealing process. In Figure 1b, oxygen element is observed throughout the BFO and STO substrate and begins to decrease in GMR multilayers in oxidized sample. By analysis of EELS spectroscopy (Figures 1d1 and 1d2), it is indicated that partial Co element in Co layer is also oxidized by oxygen ion from BFO. During the annealing process, Co element in CoFeB layer is oxidized by oxygen ions (Figure 1c). Figure 1e indicates that CoO and Co3O4 might form during the annealing process.
Conclusion: The oxidation at the interface between BFO and GMR multilayers is confirmed by combining STEM and EELS with macroscopic magnetic characterizations. This work could be helpful to introduce annealing process to BFO/ ferromagnetic interface while maintain the magnetic properties of ferromagnetic layer.

Reference:
[1] Qintong Zhang, Lu You, Xi Shen, Caihua Wan, Zhonghui Yuan, Xuan Zhang, Li Huang, Wenjie Kong, Hao Wu, Richeng Yu, Junling Wang*, and Xiufeng Han*, *Adv. Mater.*, 27(43), 6934, 2015.

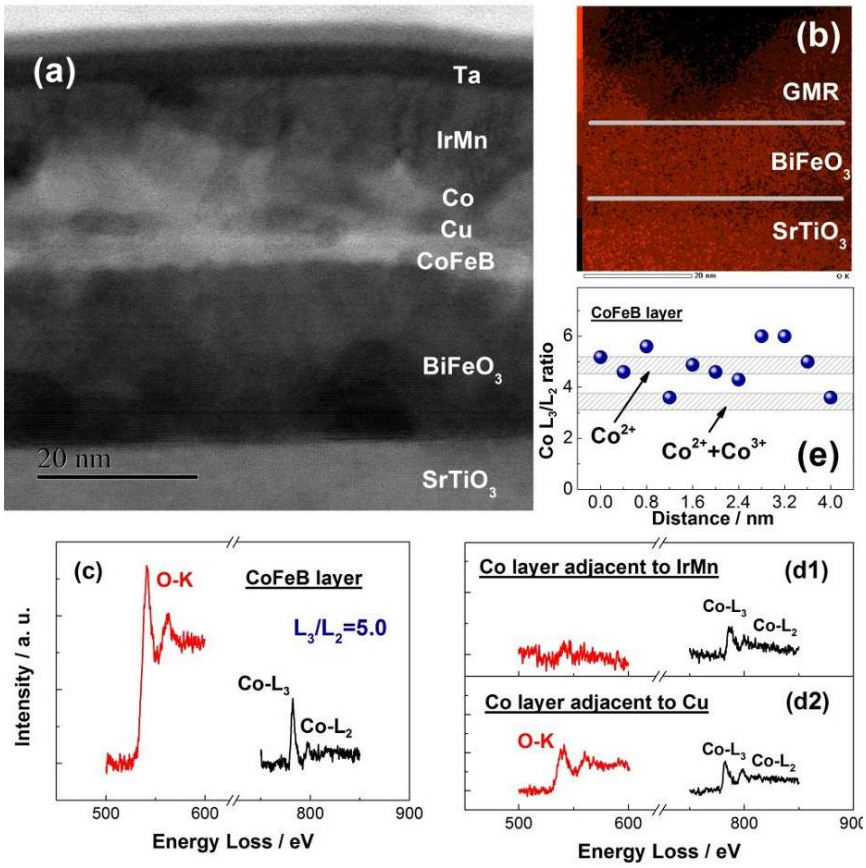

Figure 1. a) The cross-section ABF image of STO/BFO/CoFeB(4)/Cu(2)/Co(4)/Ir22Mn78 (12)/Ta(5 nm) after 300 °C annealing. b) EDS mapping of oxygen element in STO/BFO/GMR (not the same area as (a) but the same sample). c) EELS spectra of O-K edge and Co-L2,3 edge in CoFeB layer with subtraction of the background. d1) EELS spectra of O-K and Co-L2,3 in Co layer adjacent to IrMn without oxidation. d2) EELS spectra of O-K and Co-L2,3 in Co layer adjacent to Cu with partial oxidation. e) Profiles of EELS L3/L2 intensity ratios of Co in the CoFeB layer (scan step is 0.4 nm).

MS2.P003
Characterization of biocompatible Ti-Nb-Zr thin layers prepared by magnetron sputtering

M. Karlik[1,2], E. Frutos[3], J. Veselý[2]

[1]CTU in Prague, Department of Materials, Prague 2, Czech Republic
[2]Charles University, Department of Physics of Materials, Prague 2, Czech Republic
[3]CTU in Prague, Deparment of Control Engineering, Prague 6, Czech Republic

Miroslav.Karlik@fjfi.cvut.cz

The ideal surface modification, in form of a coating, on biomaterial for orthopedic implant applications, is one that exhibits excellent biocompatibility with no adverse cytotoxicity, excellent corrosion resistance, and a good combination of mechanical properties such as high strength and good fatigue resistance, low elastic modulus and good wear resistance. Sputtering techniques are extremely versatile to produce nanostructured, homogeneous, dense, compacts and crack-free coatings. This technique offers multiple possibilities in the in-situ design of complex (near) pure β-Ti textured coatings, with body centered cubic phase (bcc), free of toxic elements. β-rich Ti-Nb-Zr coatings allow the combination of three different phases (α, α" and β), depending on the concentrations of Nb and Zr, which offer the best mechanical properties a priori. The focus of this work is to design ternary coatings, capable of providing a direct bond between the metallic surface and surrounding bone, and their nano-mechanical characterization.
Thin layers ~1 μm thick with nominal composition (wt.%) Ti-22Nb-10Zr were prepared on Si substrate by magnetron sputtering, using different bias voltage included in the range of 0 to -150 Volts. Mechanical characterization (Berkovich hardness, Young´s modulus and residual stresses) has been carried out by advanced instrumented nano-indentation techniques. Phase analysis of these surfaces and their dependence with bias voltage value has been performed by X-ray diffraction in combination with TEM characterization (diffraction contrast imaging, EDS, SAD, NanoMEGAS DigiSTAR phase and orientation mapping - Fig.1). Finally, surface biocompatibility has been tested by MG-63 cell culture proliferation.
Results include grain size, texture and residual stress magnitude of Ti-22Nb-10Zr as a function of sputtering conditions. Furthermore, the magnitude of the residual stress is correlated with the concentration of β and α" phases formed due to different bias voltage used during the deposition process. The increasing bias voltage facilitates the transformation from β to α", changing compressive residual stresses magnitude from -700 MPa, at -63 volts, to -100 MPa, at -148 volts. The cell culture proliferation tests show that the biocompatibility of Ti-22Nb-10Zr thin layers is similar to pure Ti, which is a guarantee for the use of these coatings for medical applications.

The authors wish to express their thanks for the financial support of project No. CZ.02.1.01/0.0/0.0/15_003/0000485, financed by ERDF, and the Czech Science Foundation through the project 14-32801P.

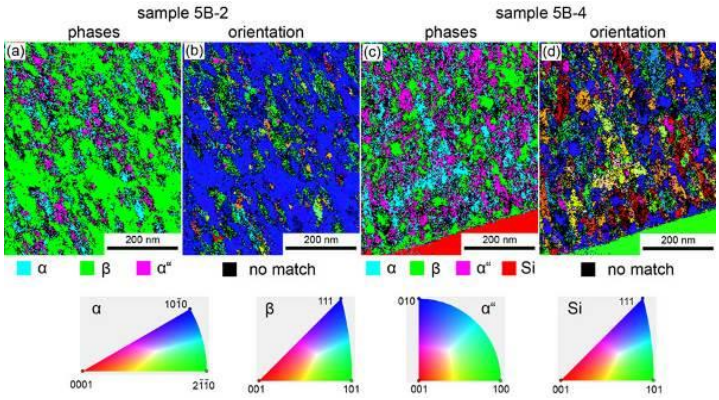

Figure 1. TEM nanodiffraction phase imaging and orientation maps of Ti-Nb-Zr thin layers on Si substrate recorded with NanoMEGAS ASTAR system.

MS2.P004
Efficient phase separation of $Ge_{1-x}Sn_x$ epilayers with free running Sn precipitates

H. Groiß[1,2,3], M. Glaser[4], M. Schatzl[4], M. Brehm[4], D. Gerthsen[3], D. Roth[5], P. Bauer[5], F. Schäffler[4]

[1]CEST Competence Center for Electrochemical Surface Technology, Wiener Neustadt, Austria
[2]Johannes Kepler University Linz, Center of Surface and Nanoanalytics (ZONA), Linz, Austria
[3]Karlsruhe Institute of Technology, Laboratory for Electron Microscopy, Karlsruhe, Germany
[4]Johannes Kepler University Linz, Institute of Semiconductor and Solid State Physics, Linz, Austria
[5]Johannes Kepler University Linz, Institute of Experimental Physics, Division Atomic Physics and Surface Science, Linz, Austria

heiko.groiss@jku.at

Recently, a breakthrough was achieved with the demonstration of lasing in strain-relaxed GeSn epilayers [1], [2]. Despite this major achievement, the thermal stability of $Ge_{1-x}Sn_x$ films with Sn contents far above the solid solubility limit of ≈0.5% remains a concern regarding the high processing temperatures of up to 1000°C routinely employed during the fabrication of Si integrated circuits.
We investigated $Ge_{1-x}Sn_x$ epilayers grown by MBE at low temperatures of 120 °C and at high growth rates of 1 Å/s^{-1} to implement Sn contents of more than 14 percent in fully coherent, single crystalline epilayers. The properties of the samples were characterized by high resolution transmission electron microscopy (HRTEM), X-ray diffraction (XRD) and Rutherford back-scattering experiments (RBS), which show a linear lattice constant increase with x for all films, Vegard's law is applicable up to x = 14%.
To assess the thermal stability and the precipitation kinetics of the epilayers under well-controlled experimental conditions we use series of un-capped $Ge_{1-x}Sn_x$ films. These films were either grown with varying temperatures up to 400 °C, or post-growth annealed *in-situ* in the environment of the MBE chamber at temperatures up to 400 °C. Additionally, a similar series was grown, but annealing was performed in the vacuum environment of a scanning electron microscope (SEM) with a heatable sample holder. In all three cases we found strong decomposition effects above the β-Sn melting point of T_m = 231.1 °C.
We compiled video sequences of the phase separation process from time-resolved SEM annealing experiments to gain information on the underlying decomposition kinetics. The most spectacular effect is the formation of liquid tin droplets, which are moving over the surface. In doing so, they collect Sn by dissolving the metastable GeSn epilayer in the area in contact with the droplet. While the dissolved Sn content increases the volume of the melt, dissolved Ge becomes re-deposited as an essentially strain-relaxed Ge layer by a kind of liquid-phase epitaxy at the trailing edge of the droplet. The deposited Ge trails are of high crystal quality and exhibit a complex surface pattern that results from interface-energy minimization. The droplets move on the surface along preferential crystallographic directions of the strained GeSn layer, avoiding already existing Ge trails. The GeSn film in front of the moving droplet was found to remain fully strained with its original Sn concentration.
The minimization of the Gibbs free energy, including the concentration-, strain- and interface-energy terms, provides the driving force for the phase separation process and the droplet movement. The enhanced diffusion through the liquid Sn droplets makes the phase separation of metastable GeSn layers particularly efficient.

[1] K. P. Homewood, M. A. Lourenço, Optoelectronics: The rise of the GeSn laser, Nature Photonics 9, 78–79, (2015), doi:10.1038/nphoton.2015.1
[2] S. Wirths, R. Geiger, N. von den Driesch, G. Mussler, T. Stoica, S. Mantl, Z. Ikonic, M. Luysberg, S. Chiussi, J. M. Hartmann, H. Sigg, J. Faist, D. Buca, D. Grützmacher, Lasing in direct-bandgap GeSn alloy grown on Si, Nature Photonics 9, 88–92, (2015) doi:10.1038/nphoton.2014.321

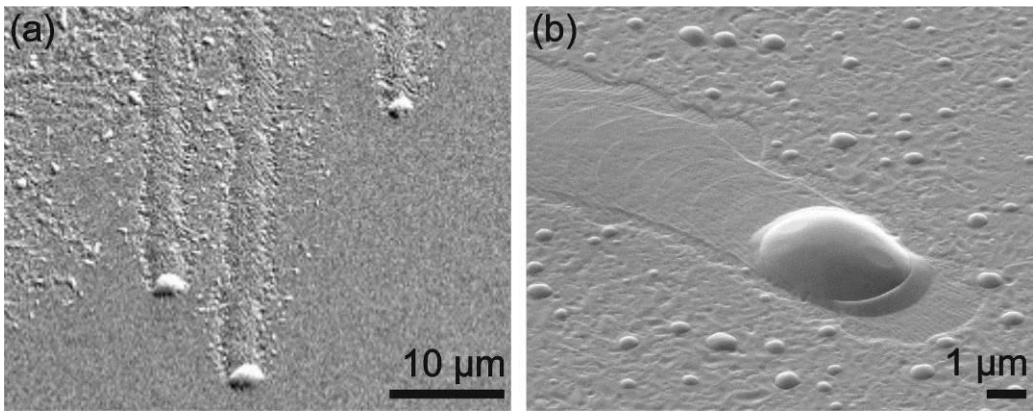

Figure 1. (a) SEM image from a video sequence recorded during the annealing SEM experiments. Three large Sn droplets form the phase separation front. (b) Large Sn droplet and smaller secondary droplets after the *in-situ* annealing in the SEM.

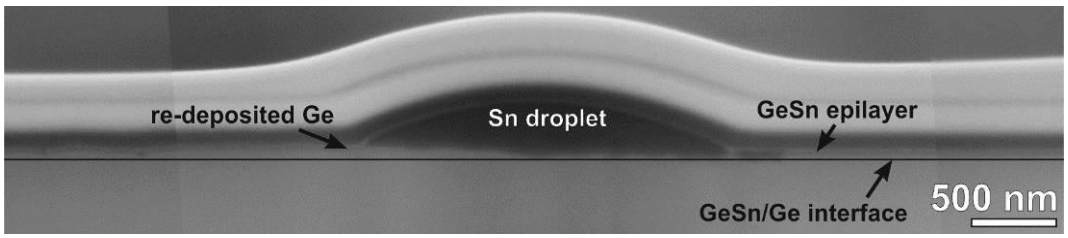

Figure 2. Cross sectional SEM image of a Sn droplet after annealing. On the right hand side the intact, strained GeSn film is visible, on the left hand side the re-deposited Ge-layer.

MS2.P005
Investigations of the quantitative lateral analytical resolution at metal layers with a field emission electronprobe microanalyser

J. Nissen[1], D. Berger[1]

[1]Technische Universität Berlin, Zentraleinrichtung Elektronenmikroskopie, Berlin, Germany

joerg.nissen@tu-berlin.de

Keywords: FE-EPMA, WDX, lateral analytical resolution, quantitative element analysis

X-ray element analysis with high lateral resolution becomes more important for the investigation of features on the nanoscale. Hereby, not only the qualitative resolution, but especially the quantitative resolution, which delivers the exact element composition, is in the focus of interest. Whereas for the qualitative resolution the rise of the X-ray signal intensity of an element, measured as egde profile at the interface of two different materials, from 16 to 84% is regarded, for the quantitative resolution a X-ray intensity from 1 to 99% has to be taken into account. Measurements at an Au-Si interface resulted in a qualitative lateral resolution of 26 nm, quantitatively 90 nm [1]. Since resolution measurements by edge profils depends on the adjacent elements it makes more sense to determine the quantitative resolution from the smallest feature for which a precise quantitative element analysis is feasible.
For this work we generated these features by deposition of thin metallic layers. To study the Z-dependence of the lateral analytical resolution we choose as layer materials the low Z (13) element aluminium, silver with mean Z (47) and gold as high Z (79) element [2]. To determine the lateral resolution, we analyse the layers of 18 specimens in cross-section, which has to prepared very carefully by use of a focused Ga ion beam (FIB). Fig. 1 shows the typically layer structure with the layer to be measured, in this case a 265 nm thick Ag-layer, and two adjacent palladium layers to prevent fluorescence effects from the Si-substrate and the FIB-Pt-protection layer.
For X-ray analysis we use a field emission electron microprobe analyzer (FE-EPMA) with wavelength dispersive X-ray spectrometers (WDX). A quantification result of 100.0 ± 0.5 wt% of the particular element indicates that the source volume of the emitted X-rays is completely inside the layer. For comparison we estimated the X-ray generating volume by Monte Carlo (MC) simulations (casino v2.48) of the electron scattering in the material for electron energies between the primary energy and the critical ionization energy of the according element X-ray line (Fig. 2). Furthermore, the quantitative lateral resolution Rs is calculated using the equation of Merlet and Llovet: $Rs= (4(Rx-Zm)^2+do^2)^{1/2}$ [3] (Fig. 4), where Rx is the ionization range and Zm the depth of the maximum of the X-ray distribution. Figure 3 shows an overview of the measured, simulated and calculated lateral resolutions as a function of the atomic number at 15, 8 and 5 keV primary electron energy.
On one hand the resolution improves with lower energy, due to the reduction of the electron interaction volume inside the material. On the other hand the resolution becomes worse with lower atomic number owing to the lower density of the material and hence the increasing spread of electrons. However, at 5 keV there is no significant difference between Au (79) and Ag (47). For the Ag measurement the overvoltage is low in relation to the critical ionization energy of the Ag Lα X-ray line at 3.352 keV. Hence, the range of excited Ag Lα X-rays is small.
The best quantitative lateral analytical resolution we can achieve is 155 nm, measured at Au with 5 keV. Obviously, there is a good correspondence of measurements, simulations and calculations.

[1] Berger D and Nissen J 2014 *IOP Conf. Ser.: Mater. Sci. Eng.* **55** 012002
[2] Berger D and Nissen J 2016 *IOP Conf. Ser.: Mater. Sci. Engng.* ***109*** *012001.*
[3] Merlet C and Llovet X 2012 *IOP Conf. Ser.: Mater. Sci. Eng.* ***32***

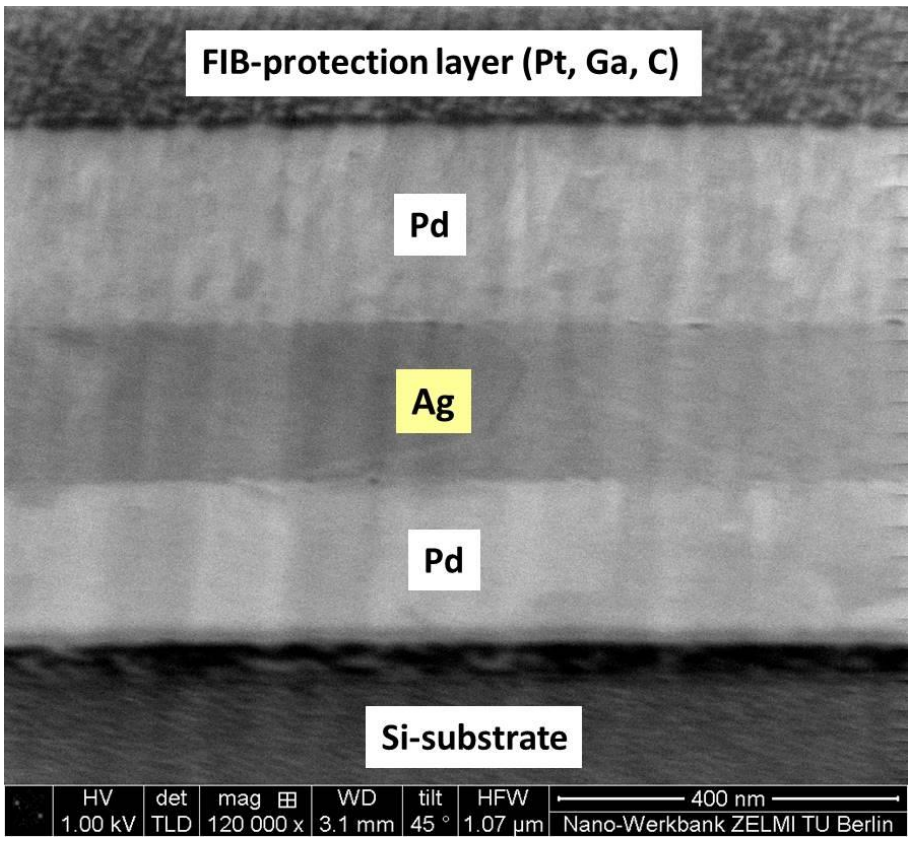

Figure 1. SE-image of the layer structure.

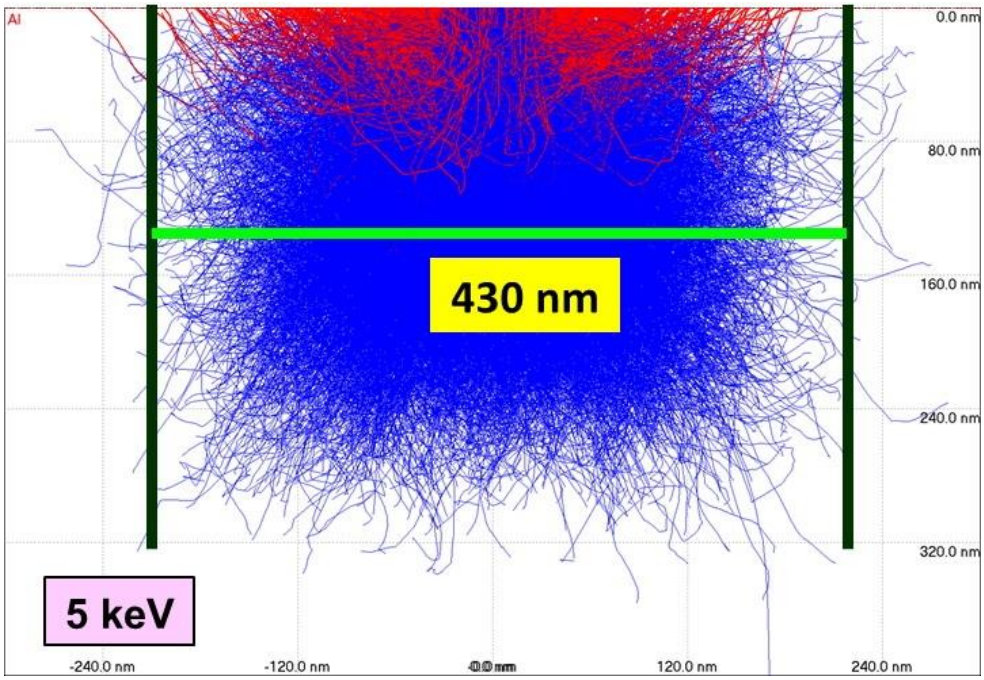

Figure 2. Lateral analytical resolution in Al determined by MC simulation at 5 keV.

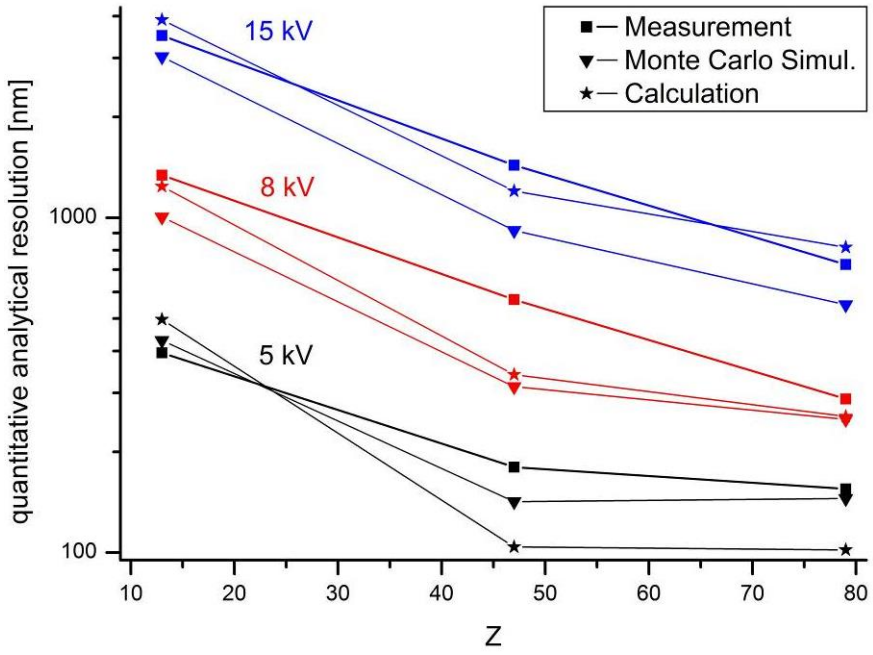

Figure 3. Quantitative lateral analytical resolution as a function of atomic number at 15, 8 and 5 keV primary electron energy.

$$R_S = \sqrt{4 \cdot \left(R_x - Z_m\right)^2 + {d_0}^2}$$

Figure 4

MS2.P006
Oxygen octahedral picker – a dedicated software tool for lattice and oxygen octahedral distortions quantification at perovskite oxide interfaces

Y. Wang[1], U. Salzberger[1], W. Sigle[1], Y. E. Suyolcu[1], P. A. van Aken[1]

[1]Max Planck Institute for Solid State Research, Stuttgart Center for Electron Microscopy, Stuttgart, Germany

y.wang@fkf.mpg.de

The multifaceted magnetic, electrical, and structural functionalities of perovskite oxides critically depend on distortions of their crystal lattice [1]. These distortions include the displacement of cations, deformation of oxygen octahedra (BO_6, where B is a transition metal atom), and collective tilts of the octahedral network. Controlling and engineering these distortions in the constituent oxides are crucial in designing and fabricating hetero-structures with novel functional properties that are absent in the bulk form. Atomistic understanding of these distortions and elucidation of their influence on the final properties requires imaging and measuring of atomic positions of both cations and oxygen. With the application of spherical aberration (*C*s) correctors, sub-Angstrom atomic resolution is nowadays regularly achievable in both TEM and STEM. The recent application of the annular bright-field (ABF) imaging technique in perovskite oxides has become increasingly popular, as it enables simultaneous imaging of heavy and light elements and allows for simultaneous acquisition of other signals [2, 3]. Quantitative analysis of atom-column positions in high-resolution STEM images helps us gain new insight into materials behavior and address material problems. However, there are rare resources about methods for indexing atomic column positions in atomic resolution images, especially for the case of ABF images, as well as for the measurement accuracy.

In this contribution, we report the development of a software tool [4], written in Digital Micrograph scripting language [5], to extract quantitative information of the crystal lattice and of oxygen octahedron distortions of perovskite oxides from annular dark-field (ADF) and ABF STEM images. The program is composed of two scripts: "B atom navigator" and "oxygen octahedral picker" ("O-O picker"), enabling analysis of the simultaneously acquired ADF and ABF images. The second script uses the B atomic column positions obtained from the first script to detect surrounding oxygen atomic columns and to map all the octahedra on the ABF image. Center-of-mass and two-dimensional (2D) Gaussian fitting methods are implemented to locate positions of individual atom columns. The final results provided by this software are the coordinates of detected atomic columns, the atomic column intensities, the distances between the atomic columns, and the angles between selected atomic columns, based on the selection of the user, as shown in Fig. 1.

The precision of atomic column distance measurements are evaluated on both simulated and experimental images. We demonstrate that sub picometer precision can be achieved on simulated STEM images. Experimentally, under a daily reproducible working condition (sample drift and slight sample contamination present), we can achieve 3 picometer and 4 picometer precisions for ADF and ABF images, respectively. Figure 2 shows the details of the measurement precision test.

Finally, using practical examples, we demonstrate that the program works well for different orientations of the perovskite structure and interfaces. The application of this picometer precision measurement at hetero-structure interfaces will be discussed [6].

References:

[1] R H Mitchell "Perovskites: Modern and Ancient", (Almaz, Thunder Bay)
[2] S D Findlay *et al.*, Appl.Phys.Lett. **95** (2009), p.191913.
[3] E Okunishi *et al.*, Microsc.Microanal.**164** (2009), p.15.
[4] Y Wang *et al.*, Ultramicroscopy **168** (2016), p.46.
[5] D R G Mitchell, B Schaffer, Ultramicroscopy **103** (2005), p.319.
[6] Y Wang *et al.*, ACS Appl.Mater.Interfaces **8** (2016), p.6763.

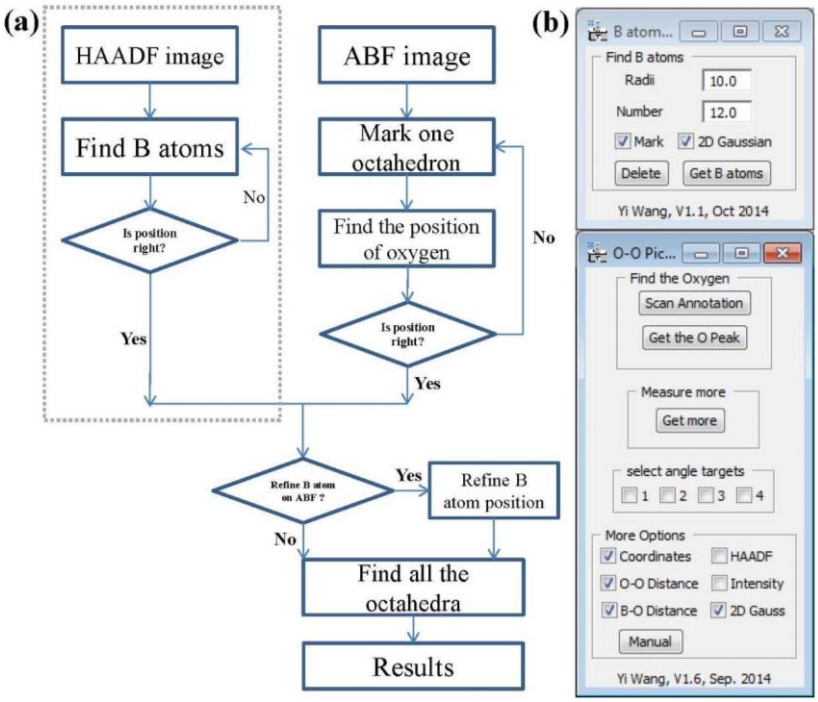

Figure 1. (a) Flow chart of the script, starting with image and ending in the results. (b)The user interface of the scripts, B atom navigator (top) and oxygen octahedral picker (bottom).

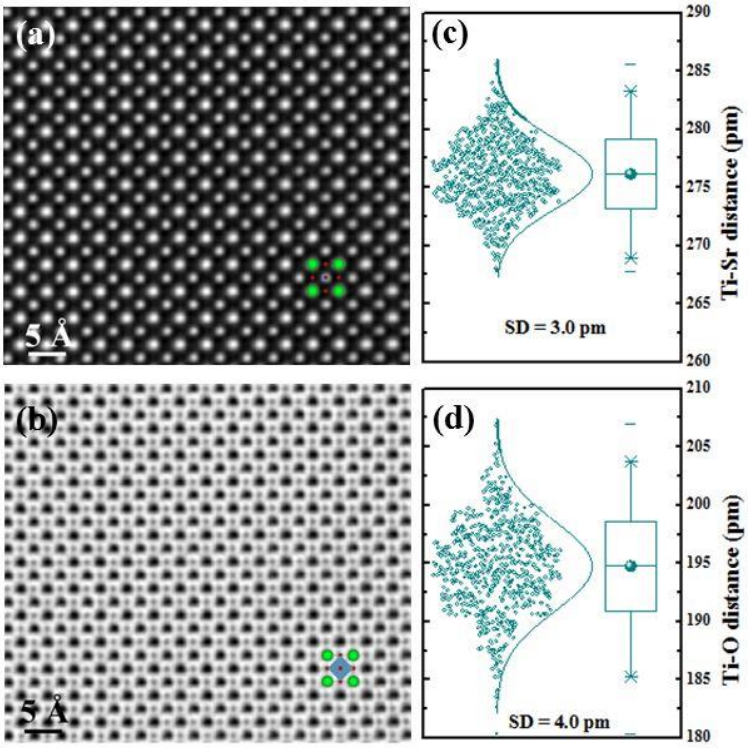

Figure 2. Simultaneously acquired ADF (a) and ABF (b) images of $SrTiO_3$ along the [001] zone axis. 7 frames were acquired with a short dwell time (2 µs per pixel), the frame series were then aligned and averaged. Box-and-whisker plot of the measured Ti—Sr and Ti—O atomic column distance from ADF (c) and ABF (d) images, respectively. The statistics are based on 168 TiO_6 octahedra (12 u.c. x 14 u.c.) measurements.

MS2.P007
Etching response of Zn contained Al-Mg-Si alloys

Y. Tomuro[1], T. Saito[2], î Bauger[2], S. Wenner[3], C. D. Marioara[4], R. Holmestad[3], L. Seungwon[1], S. Ikeno[1] K. Matsuda[1]

[1]university of Toyama, Toyama, Japan
[2]Hydro, Sunndalsøra, Norway
[3]NTNU, Trondheim, Norway
[4]SINTEF, Trondheim, Norway

ikenolab@eng.u-toyama.ac.jp

Introduction: Zn in aluminum alloys can influence to surface condition of extruded products. Several reports are available about the effect of Zn to the etching in Al alloys. The uneven surface is caused by preferential grain etching (PGE). Zn containing alloys (≥ 0.1 wt.%) showed strong preferential attack of grains[1].
Objective: The aim of this research is to understand the effect of Zn, especially, the amount of Zn in Al alloy for preferential grain etching and observe the surface condition by SEM, TEM and AFM.
Materials and Methods: 6060 alloys with different amount of Zn (0.00%, 0.03%, 0.05%Zn, wt.%) were fabricated by casting and homogenized at 848K for 486ks. Then, samples were extruded, and samples had the dimension of 25mm×4mm. Solution treatments (ST) were conducted at 813K for 3.6ks (T4 condition). After ST, samples were undergone the two-step aging to the peak aging (T6 condition). Vickers microhardness measurement was conducted to estimate the mechanical property. Preferential etching was conducted using sodium hydroxide solution at 353K for 1,2 and 3 min. Microstructure observation was carried out using SEM (HITACHI S-3500H), OM (OLYMPUS BX51M), AFM (HITACHI 5100N) and TEM (JEOL ARM 200F).
Results: After ST, hardness value showed almost the same regardless Zn contents. Hardness of T4 condition was two times higher than T4 condition, regardless chemical compositions. After PGE test, only 0.05%Zn alloy showed PGE, in T4 condition, PGE started after 2 min, however, in T6 condition started after 3 min. EDS mapping result of 0.05%Zn_WQ_T4 sample revealed no Zn segregation on the grain boundary. Some precipitates included Mg and Si were observed on grain boundary was confirmed by EDS. In the case of 0.05%Zn_WQ_T6 samples, Zn was observed in precipitates both in matrix and on the grain boundary by EDS mapping.
Conclusion:

- Zn addition does not influence to precipitation hardening because of its small amount.
- 6060 alloys containing 0.05%Zn showed PGE because of Zn in matrix at T4 condition.
- T6 condition samples showed less PGE than T4 condition samples.

References:

[1] Muhammad Umar Farooq Chandia, Øystein Bauger, Trond Furu, Proceedings of the 12th International Conference on Aluminum Alloys (2010) p.781.

MS2.P008
Tuning the magnetism of epitaxial cobalt oxide thin films by electron beam irradiation

Q. Q. Lan[1,2], X. J. Zhang[1], X. Shen[1], H. W. Yang[1], H. R. Zhang[1], X. X. Guan[1], W. Wang[1], Y. Yao[1]
Y. G. Wang[1], Y. Peng[2], B. G. Liu[1], J. R. Sun[1], R. Yu[1]

[1]Institute of Physics, Chinese Academy of Sciences, Laboratory of Advanced Materials & Electron Microscopy, Beijing, China
[2]Lanzhou University, Key Laboratory for Magnetism and Magnetic Materials of the Ministry of Education, Lanzhou, China

rcyu@aphy.iphy.ac.cn

Tuning magnetic properties of perovskite thin films is a central topic of recent studies because of its fundamental significance. In this work, we demonstrated the modification of the magnetism of $La_{0.9}Ca_{0.1}CoO_3$ (LCCO) thin films by introducing stripe-like superstructure in a controllable manner using the electron beam irradiation (EBI) in a transmission electron microscope. The microstructure, electronic structure, strain change and origin of magnetism of the LCCO thin films were studied in details using aberration-corrected scanning transmission electron microscopy, electron energy loss spectroscopy and *ab initio* calculations based on density functional theory.[1] The results indicate that the EBI induced unit cell volume expansion accompanies the formation of oxygen vacancies and leads to the spin state transition of Co ions. The low spin state of Co^{4+} ions depress the stripe-like superstructure, while higher spin states of Co ions with lower valences are conductive to the formation of "dark stripes". Our work clarifies the origin of magnetism of epitaxial LCCO thin films, benefiting a comprehensive understanding of correlated physics in cobalt oxide thin films.

Reference:

[1] Q. Q. Lan, X. Shen, H. W. Yang, H. R. Zhang, J. Zhang, X. X. Guan, Y. Yao, Y. G. Wang, R. C. Yu, Y. Peng, J. R. Sun, *Appl. Phys. Lett*., **107**, 242404 (2015).

MS2.P009
Interactive sub surface characterization in a hybrid SEM/AFM

F. Hitzel[1], F. Zhou[2]

[1]Semilab Germany GmbH, Braunschweig, Germany
[2]Carl Zeiss Microscopy GmbH, Materials Sciences, Oberkochen, Germany

fhitzel@hitzel.com

Combined Scanning Electron Microscope / Focused Ion Beam (SEM/FIB) systems are nowadays a well-established technology for precise imaging and analysis of 3D structures in nanometer scale. It is widely used in e.g. failure analysis where the region of interest (ROI) is beneath the sample surface. A fully integrated Atomic Force Microscopy (AFM) in such system [1] can deliver additionally local quantitative electrical parameters layer for layer, such as conductivity, capacitance, work function or electrical potential, dopant level [2, 3]. The GEMINI lens design in [1] ensures an electrical and magnetic field free environment on the sample for undistorted AFM measurements of electrical or magnetic properties. However, the ion beam damage and milling inaccuracy may make a reliable AFM measurement difficult or even impossible. In this paper, we present another solution for accessing sub-surface layers: Exact interactive manipulation in SEM.

In Fig. 1, a hard diamond tip has been used (adama ad-150-nm, doped diamond) to apply a circular cut to the surface. The sample is a piece of processed silicon wafer with an electronic circuit. Images 1-4 for show the sequence of cutting, which has been performed by manually moving the tip on the surface while observing the status with the SEM and while the AFM feedback loop controls the force applied to the surface. One can see that not only the circular center of the cut part can be completely removed, but also several layers of the sample become exposed, the top layer having a thickness of 30 nm, the layer below having a thickness of about 100 nm. After cutting, the area has been scanned using the same tip simultaneously measuring the current. As current source the electron beam was used, which during the scanning was placed in constant distance to the tip. The sample was grounded. The results are shown in the AFM micrographs on the right side in Fig. 1. The top image shows the pure topography, the lower image shows the topography with overlayed current (blue color). It can clearly be seen that the highest current could be measured on the layer 30 nm below the top layer, clearly indicating that this is the layer with highest conductivity.

In Fig. 2, a diamond cantilever with larger tip was used. Here, scanning with higher force leads to a polishing of the surface removing a few nm of material with every scan, i.e. a total different behavior than in Fig. 1. By this, a 3D current measurement could be performed, as indicated on the right side of Fig. 2. In the first image, the surface was still covered with a nonconductive layer, which is nearly removed on the second scan and totally gone on the third scan. In the fourth image, the conductive layer starts already disappearing.

In summary, the AFM in the SEM enables possibilities to access information of buried layers which no other system can provide. Depending on the type of AFM tip, either cutting or polishing behavior can be achieved. This in many cases can make the cross section preparation or FIB cutting unnecessary and results in uncontaminated exposition of surfaces.

Thanks to Helmholz Zentrum Berlin for providing the equipment for these experiments.

References:

[1] N. Anspach, F. Hitzel, F. Zhou, Soeren Eyhusen, Microsc. Microanal. 20 (3), 2014
[2] R. Saive, M. Scherer, C. Mueller, J. Schinke, M. Kroeger, W. Kowalsky, Adv. Func Mat. **23** (47) 2013, pp. 5854
[3] R. Saive, C. Mueller, J. Schinke, R. Lovrincic, W. Kowalsky, Appl. Phys. Lett. **103,** 243303 (2013)

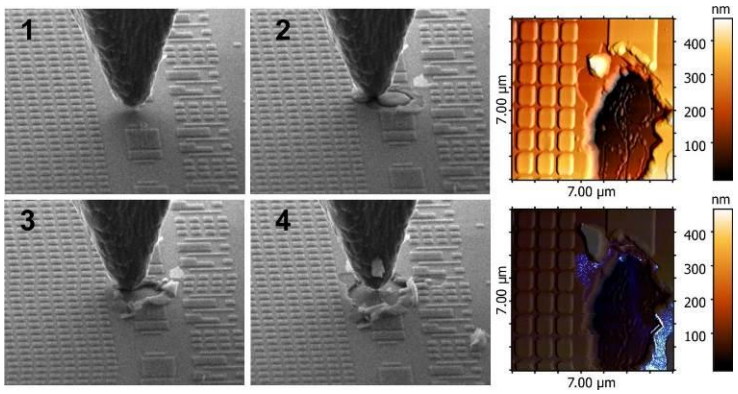

Figure 1. Interactive cutting by hard diamond tip.

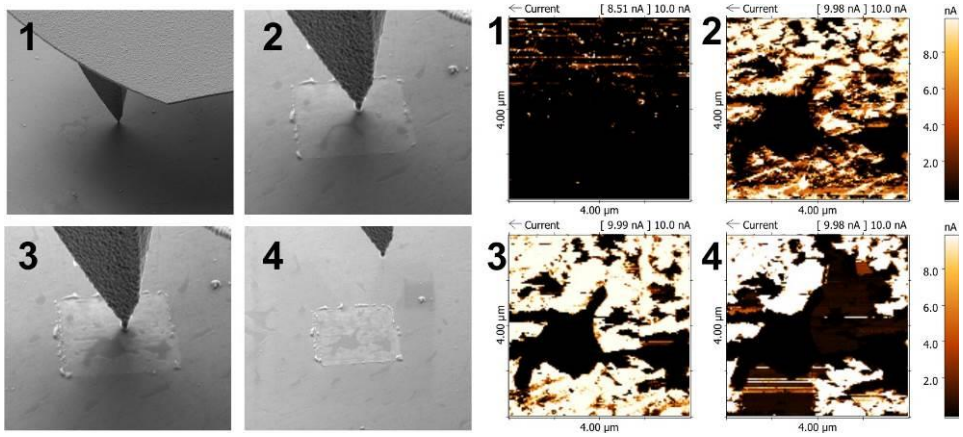

Figure 2. Large area polishing with wider tip. In parallel, a current measurement was performed.

MS2.P010
Advanced building nanoarchitectures identified in strongly iron-enriched incisors

V. Srot[1], J. Deuschle[1], B. Bussmann[1], B. Pokorny[2,3], P. A. van Aken[1]

[1]Max-Planck-Institute for Solid State Research, Stuttgart Center For Electron Microscopy, Stuttgart, Germany
[2]Environmental Protection College + Institute ERICo, Velenje, Slovenia
[3]Slovenian Forestry Institute, Ljubljana, Slovenia

V.Srot@fkf.mpg.de

Introduction: Teeth are a superb demonstration of ideally designed nanoarchitectures consisting of simple compounds. Continuously growing incisors of rodents combine precisely constructed components in a very unique and optimally designed functional device [1]. They are adjusted to heavy gnawing loads by a smart construction, where hard and resistant enamel covers only the front part of the teeth, while softer bulk dentin is being gradually removed [1] forming a self-sharpening device.
Objectives: Advanced transmission electron microscopy (TEM) techniques combined with measurements of mechanical properties exposed striking microstructural and compositional adjustments in incisors of coypu (*Myocastor coypus* Molina).
Materials and Methods: In the present study [2], incisors of coypu were investigated. The microstructure and nanochemistry were investigated by analytical scanning (S)TEM including energy-dispersive X-ray spectroscopy (EDX) and electron energy-loss spectroscopy (EELS) and by measurements of their mechanical properties.
Results: Chemical analysis [2] revealed a chemically diverse Fe-rich surface layer (Fe-SL) covering pigmented enamel (Fe-EN) (Fig. 1a) consisting of three loosely separated amorphous phases, namely ferrihydrite, (**Fe**,Ca)-phosphate and (**Ca**,Fe)-phosphate. The underlying Fe-EN consists of needle-shaped hydroxyapatite (HA) crystals that are arranged with their long axis towards the surface of the tooth and are surrounded by chemically different Fe-rich material, ferrihydrite, present within the pockets. The upper surface of the Fe-EN, which is tightly interwoven with the Fe-SL, is identified as an additional transition zone (TZ) (Fig. 1b). Much smaller randomly oriented HA crystal fragments are surrounded with chemically different material that appears to be Ca phosphate enriched with Fe.
Although the components possessing different microstructure, chemistry and unique mechanical properties are coexisting, the rodent´s incisors need to be considered as one functional device. Such teeth are subjected to specially challenging mechanical conditions, and therefore extraordinary functional design that can withstand repeated mechanical load and ensure structural stability is required. Mapping of the mechanical properties (modulus (E) and hardness (H)) demonstrate the presence of four regions, namely the Fe-SL, Fe-EN, enamel (EN) and dentin (D) (Fig. 2). The relatively soft Fe-SL seems to have an important protection function to cushion the pressure applied to teeth while gnawing. The TZ could act as a crack stopping or deflection zone to prevent the underlying enamel from failure. The presence of HA crystals and soft ferrihydrite within the pockets gives a mechanically improved Fe-EN, while the transition to EN shows a gradual decrease of the mechanical properties. The comparison between Fe-EN and EN revealed a close connection between the microstructure and mechanical properties (Fig. 3). The sudden drop at the dentin-enamel junction is followed by lower values of the modulus and hardness of dentin. Hence during gnawing, softer dentin is removed at much higher rate than the hard enamel, creating a sharp cutting edge and maintaining the functionality of the incisors.
Conclusions: Natural composite materials combine ideally designed architectures consisting of simple compounds. We have shown strong mutual correlation among the microstructure, chemical composition and mechanical properties and fascinating adaptations in rodent´s incisors.

References:
[1] PY Chen, J McKittrick and MA Meyers, Prog Mater Sci **57** (2012), 1492.
[2] V Srot et al., ACS Nano **11** (2017), 239.

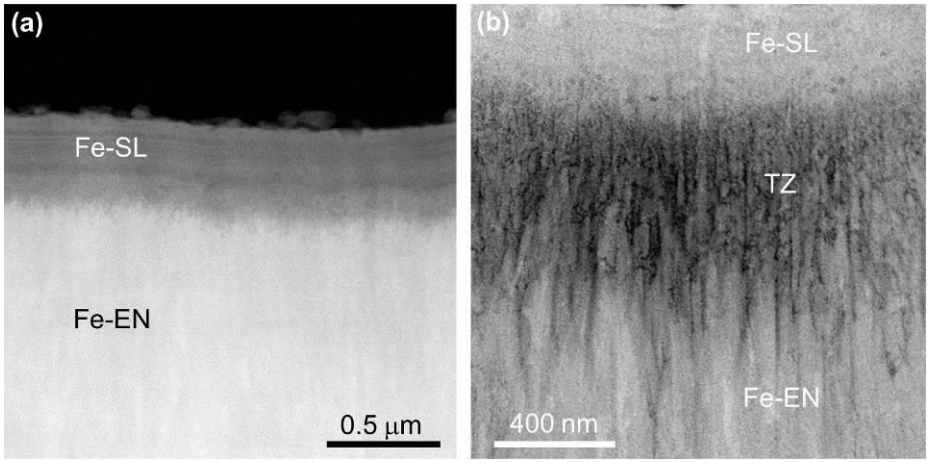

Figure1. (a) ADF-STEM image of the interface between the Fe-SL and Fe-EN. (b) HAADF-STEM image shows the presence of a TZ between the Fe-SL and Fe-EN.

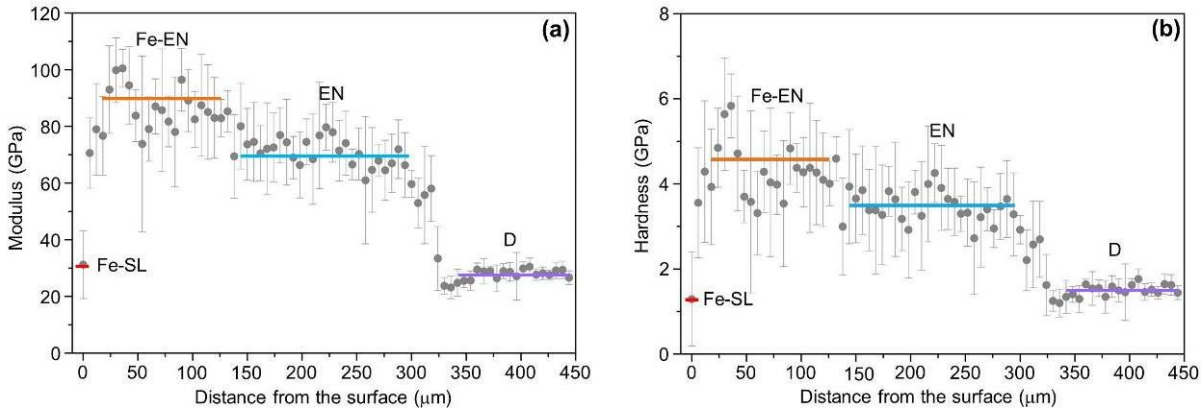

Figure 2. Nanoindentation measurements showing (a) modulus (E) and (b) hardness (H) obtained on the cross-section of a rodent´s incisor.

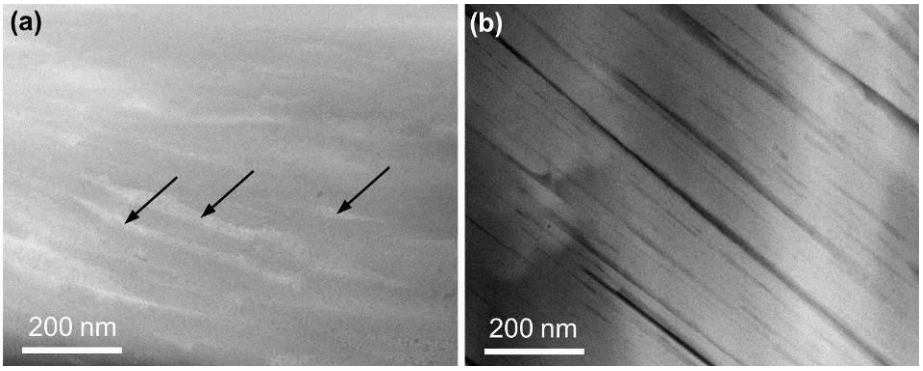

Figure 3. HAADF-STEM images from (a) Fe-EN and (b) EN. The arrows in (a) indicate a few positons of ferrihydrite filled pockets.

MS2.P011
Estimation of thickness and composition of thin films from EDX

S. Schulze[1], S. Hahn[2], D. Lehmann[1], D. Dentel[1], D. R. T. Zahn[1]

[1]TU Chemnitz, Physik, Chemnitz, Germany
[2]TU Chemnitz, Maschinenbau, Chemnitz, Germany

schulze@physik.tu-chemnitz.de

Introduction: Estimating thickness and composition of thin films in the nanometer range deposited on substrates can be time consuming and quite inaccurate using optical methods or microbalances for instance. As compared with such methods it is fast and simple to take one or more X-ray spectra with EDX in a scanning electron microscope. The intensities of characteristic X-rays of thin film and of substrate materials contain all the necessary information about film thickness and composition together in each single EDX-spectrum. The development of information, however, requires ZAF-like corrections adapted to the thin film situation.
Objectives: Our goal was the development of a reliable algorithm for quantification and thickness determination of thin films on top of a plane substrate. The measured intensity ratio of X-rays from the coating to that of the substrate depends sensitively on film thickness. For taking into account the alterations of X-ray generation by substrate backscattering and of the absorption in the coating the depth distribution function of X-ray production as given by Packwood and Brown /1/ has been modified to adapt to the thin film situation.
Materials and Methods: The depth distribution function of Packwood and Brown /1/ Figure 1: Formulas can be considered to resolve into two individual parts, one due to transmitted electrons and another one due to back scattered electrons. This forms the basis for modifications to the formula above using an effective back scattering coefficient of the substrate to construct practical depth distribution functions of quantum production in the coating as well as in the substrate, respectively.
Using these equations for predefined sets of thickness, composition, and electron energy allows the calculation of k-ratios to be expected for the characteristic X-ray line intensities with respect to standards. With a one-time measurement of intensity ratios between the bulk standards for thin film and substrate lines at a given electron energy we are able to compare calculated with measured film over substrate intensity ratios. The best fitting parameters thickness and composition can be derived by optimizing the calculated k-ratios.
Results: Thickness gradated Platinum films on top of Silicium substrates have been sputtered with the deposition time varied. Mass thicknesses from our EDX-measurements at varying electron energies go close together with thickness measurements from optical ellipsometry with a mass density of our sputtered films found to be 15 g/cm³.
NiTi exhibits its excellent mechanical properties of a shape memory alloy due to the reversible trans-formation from austenite to martensite for Ni contents of (51 ± 2) at-% only. Small variations in composition result in completely different microstructures and in phase separation. For thin NiTi films deposited on MgO substrates and subsequent heat treated in order to obtain an austenitic state at room temperature the results of EDX could be very much improved by the use of the thin film correction as proposed here.
Conclusion: The thin film correction procedure proposed here determines the mass thickness as well as the composition of thin compound films on flat substrates quite proper.

[1] Packwood, Brown: X-ray spectroscopy, Vol. 10, 3 (1981)

$$\phi(\rho z) = \gamma_0 exp(-\alpha^2(\rho z)^2) \cdot \left[1 - \frac{\gamma_0 - \phi_0}{\gamma_0} \cdot exp\left(-\beta(\rho z)\right)\right]$$

$$\phi_C(\rho z) = \phi_{Packwood} \cdot \frac{\eta_{eff}}{\eta_{0C}} + \left(1 - \frac{\eta_{eff}}{\eta_{0C}}\right) \cdot \gamma_0 exp(-\alpha^2(\rho z)^2)$$

$$\phi_S(\rho z) = \left(1 - 2\left(\eta_{eff} - \eta_{0S}\right)\right) \cdot \phi_{Packwood} \cdot \left(\rho z \cdot \frac{\overline{\rho z_S}}{\overline{\rho z_C}}\right)$$

Figure 1

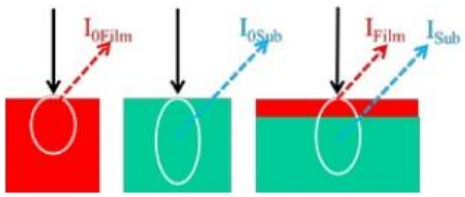

$$k_{Film} = \frac{I_{Film}(D)}{I_{0Film}}; \quad k_{Sub} = \frac{I_{Sub}(D)}{I_{0Sub}}$$

$$\underbrace{\frac{I_{Film}}{I_{Sub}}}_{\text{from sample spectrum}} = \underbrace{\frac{k_{Film}}{k_{Sub}}(D)}_{\text{calculated}} \cdot \underbrace{\frac{I_{0Film}}{I_{0Sub}}}_{\text{measured only once for } E_0}$$

Figure 2. Description of quantities linking the algorithm with the experiment.

Eo	Pt MA	Pt LA
	[µg/cm²]	[µg/cm²]
5 keV	16	
10 keV	19	
15 keV	19	
20 keV	18	20
25 keV	16	19
30 keV	15	18

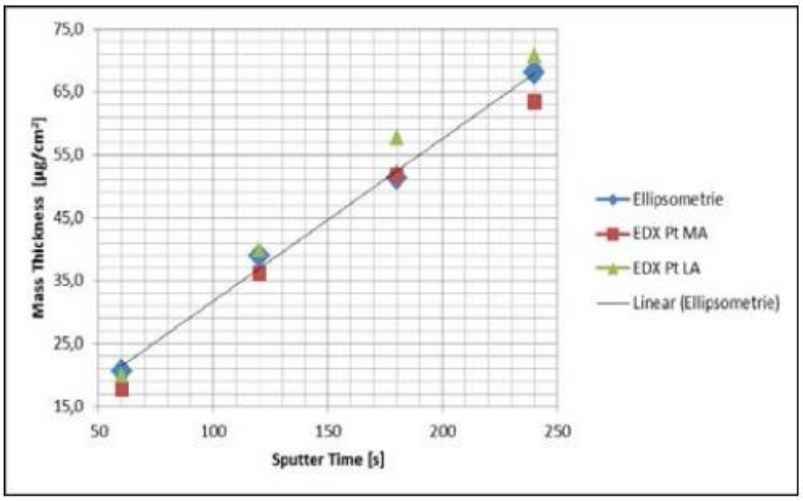

Figure 3. Thickness of Pt on Si.

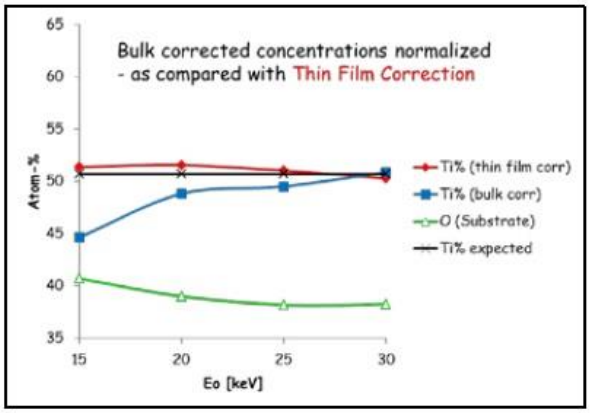

Figure 4. Our correction as compared with standard ZAF (bulk corr).

MS2.P012
Surface morphology of zinc oxide thin film deposited by sol-gel method

K. Lukaszkowicz[1], P. Boryło[1], M. M. Szindler[1], M. Szindler[1]

[1]Silesian University of Technology, Faculty of Mechanical Engineering, Institute of Engineering Materials and Biomaterials, Gliwice, Poland

paulina.borylo@polsl.pl

Introduction: Currently, in the world, transparent conductive layers (TCL) made from metal oxides are more widely used in many industries, for example as a component of: LCD displays, solar cells, gas microwave and heating layer. They are characterized by high conductivity of the layer and transparency similar to glass. Commonly used TCL is indium tin oxide (ITO). These layers are characterized by very high transmittance of visible light (> 85%) and low resistance (10-4 Ω cm). Another commonly used material for the transparent conductive layer is phosphorus-doped tin oxide (FTO). This material has properties similar to the popular ITO. Transparency FTO layer is about 82%, and the resistance between 4.0 10-4 Ω cm and 6.0 × 10-4 Ω cm. The conductivity of ZnO is more than 3.0 eV, while the transparency its over 70%. There are various methods for producing transparent conductive layers. The traditional ZnO thin films are produced by high temperature methods like physical vapour deposition (PVD) or chemical vapour deposition (CVD). Interesting also seems the use of sol gel method. In comparison to the CVD, PVD, sol-gel technology requires far less complicated equipment, is less expensive, and the depositing does not require high temperatures.
Objectives: The aim of this paper was to investigate changes in surface morphology and optical parameters of thin films of zinc oxide. Thin films were prepared using sol gel spin coating method.
Materials and Methods: $Zn(C2H3O2)2{\cdot}2H2O$ (Chempur) was dissolved in the mixture of isopropanol IPA (Sigma–Aldrich) as a solvent, and 2-amino-ethanol (MEA) (Sigma–Aldrich), as both a complexing agent and a base, while stirring at 50 °C for 2 h. The molar ratio of Zn to MEA was kept constant at 1. Then the solution was spin coated with the various spin speed (2000, 3000 and 4000 rpm) on the glass substrates and in some cases annealed at 400ºC for 2h. The microanalysis have been investigated by the Energy-dispersive X-ray spectroscopy EDS. The changes in surface topography was observed by the atomic force microscope AFM and scanning electron microscope SEM. The results of roughness have been prepared in the software XEI Park Systems and optical parameters by the spectrometer UV/VIS.
Results: The study of the surface topography was performed using scanning electron microscope SEM. At too high concentrations of the zinc acetate in a solution on the surface of a thin film there are a number of delaminations and precipitations. The reduction of the concentration of zinc acetate in the solution and increase the spin speed allows a deposition of the uniform ZnO thin films without any delaminations. The study of the surface topography was performed by atomic force microscope AFM working in a non-contact mode. Deposited thin films are characterized by a uniform surface topography without any precipitations. The roughness results was made in the XEI software. The deposited zinc oxide thin films had a high transparency in the visible region, more than 90%
Conclusion: Results and their analysis allow to conclude that the zinc acetate concentration in solution and spin speed, which is an important factor in spin coating technology has a significant influence on surface morphology and optical reflection of thin films zinc oxide. Known sol gel zinc oxide morphology and optical parameters and the possibility of obtaining a uniform thin films show that it can be good material for optoelectronic and photovoltaic application.

MS2.P013
TEM investigation of interface layers in doped ZnO / (n-type) GaN heterostructures

K. Vaideeswaran[1], I. Marozau[1], G. Christmann[1], S. Nicolay[1], J. Dutson[2], S. Thornley[2], M. Hopkins[3]
O. Sereda[1], M. M. Dadras[1]

[1]CSEM SA, Neuchatel, Switzerland
[2]Plasma Quest Ltd., Hampshire, United Kingdom
[3]University of Bath, Department of Electronic and Electrical Engineering, Bath, United Kingdom

kvn@csem.ch

The electronics industry currently uses Indium Tin Oxide (ITO) as a transparent electrode, and is currently faced with the need for an alternative transparent conducting oxide (TCO) due to increasing cost and a shortage of availability of Indium. Given the wide variety of applications that employ the use of such conducting layers, including Light Emitting Diodes (LEDs), touch-screen displays, flexible electronics, the demand for such functional layers is increasingly growing. While fulfilling its functional requirements (low resistance and high transparancy for visible light), the alternative material will also have to be easily available, inexpensive, and have a lower environmental impact.
Currently, among the high potential alternatives are ZnO doped with B (ZnO:B) or with Al (ZnO:Al), which have been shown to fulfil the required functional criteria[1]. Nevertheless, the integration of such a material with existing electronic devices remains a challenge owing to the high influence of the interface of the performance characteristics of the layer [2]. Specifically, in the case of GaN based LEDs, the interfacial microstructure and properties can intervene heavily in the functional properties of the layer such as interfacial resistance and I-V characteristics. These properties may be modified by varying the deposition process parameters, as well as the pre-deposition treatment steps.
The current study involves the detailed understanding of the microstructural evolution of the interface between the doped ZnO layers and the GaN substrate through Transmission Electron Microscopy (TEM). Microstructal investigation when combined with the processing history, and the electrical properties of the layer, would yield a detailed understanding on the interplay between the processing parameters, the microstructure and its effect on the electrical behaviour of the conducting layer.
Doped ZnO layers are deposited on n-type GaN substrates through Low Pressure- Chemical Vapor Deposition (LP-CVD) or sputtering. Additionally, a H2/N2 pre-plasma treatment is carried out in certain cases to modify the interface. TEM samples are prepared by Focussed Ion Beam (FIB) thinning. Electrical properties of each sample are also evaluated.
Electrical characterisation indicates in general an improved ohmic contact at the interface in samples prepared with a pre-plasma treament step. Preliminary observations from TEM analyses of the interface show a variation in the the microstructure depending on the processing history of the sample. The presence of amorphous layers and defect concentrated layers have been observed in both deposition techniques, and are seen to differ based on the fabrication parameters. Expansive and detailed observations of the interface are currently ongoing.

This research has received funding from the European Unions Horizon 2020 research and innovation programme under grant agreement No 641864 (INREP).

References:
[1] Choi YS et al, IEEE Transactions on Electron Devices. 2010;57(1):26-41.
[2] Hwang D K et al, Applied Physics Letters, 2005; 86: 222101

MS2.P015
Observation of the distribution of alloying elements at the metal-oxide interface of Zr alloys after irradiation by means of high resolution analytical TEM

A. Baris[1], R. Schäublin[2], S. Abolhassani[1]

[1]Paul Scherrer Institut, NES, Villigen, Switzerland
[2]ETH, Zürich, Switzerland

sousan.abolhassani@psi.ch

Introduction: This paper reports on the recent studies performed on zirconium alloys used as fuel cladding for the nuclear power plants. The irradiation degradation induces, after a certain residence time in the reactor, an intensive modification of the microstructure and the redistribution of alloying elements. This in turn modifies the properties of the cladding. One of the important modifications is the dissolution of the alloying elements under irradiation. In order to determine these changes and correlate the modifications to the change of properties, one of the techniques used is analytical electron microscopy (AEM). In this study, such characterization by AEM is reported.
Objectives: As mentioned above, in this study, the aim is to perform analytical electron microscopy to search for the dissolution of alloying elements and to trace the elements in the material. Once the adapted techniques are used, the comparison of different alloys, will lead to a better understanding of the differences of behavior.
Materials and Methods: The materials used in this study, have been provided and reported in previous projects and have been published in previous papers [1-3]. Small segments of samples with different residence time, in the reactor have been selected and TEM lamellas have been prepared from their metal-oxide interface by means of Focused Ion Beam (FIB) using an NVision40 FIB-SEM. Furthermore, samples prepared by electro-polishing have also been prepared. The TEM specimens have been examined by a JEOL2010 using Oxford-Instrument and an INCA software. Subsequently it has been examined by an FEI Talos F200X equipped with a (Chem S/TEM). The distribution of different alloying elements will be reported from each material.
Results: Examinations have shown that in the case of certain alloys, alloying elements such as Fe and Ni, segregate at the metal grain boundary. In some cases such segregations are already observed prior to irradiation (Figure 1). However, these phenomena have been observed to intensify under irradiation. Furthermore, the observation of such paths for the diffusion of certain alloying elements could explain the causes of enrichment of some alloying elements such as Fe at the outer surface of the cladding.
Conclusion: The analysis of microstructure of Zr based alloys used as fuel cladding after different residence times in the reactor, have shown that some alloying elements could migrate through the metal grain boundaries. The comparison of the current study, with those performed before, confirms the fact that such grain boundaries could provide fast paths for the diffusion of alloying elements to the outer surface of the claddings.

References:
[1] Abolhassani, S., et al. Corrosion and Hydrogen Uptake in Zirconium Claddings Irradiated in Light Water Reactors, Zirconium in the Nuclear Industry, STP1543, pp. 1–29, doi:10.1520/STP154320130007, ASTM International, West Conshohocken, PA 2013.
[2] Valizadeh, et al.,Effects of Secondary Phase Particle Dissolution on the In-Reactod Performance of BWR Cladding. Zirconium in the Nuclear Industry: 16th Symposium, ASTM International, West Conshohocken, PA, 2011, p. 729.
[3] Ledergerber, et al. Fuel Performance Beyond Design - Exploring the limits. Proceedings of 2010 LWR Fuel Performance/Top Fuel/WRFRM, American Nuclear Society, Orlando, FL, Sept 26–29, 2010, Paper 0044.

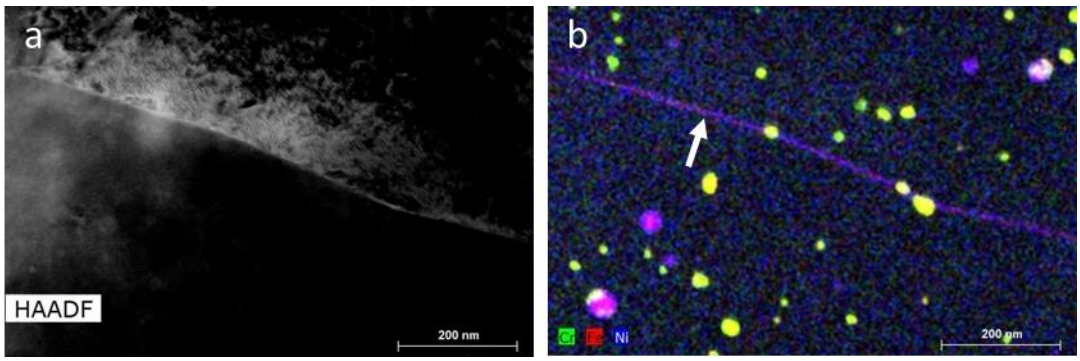

Figure 1. HAADF and EDS map using ChemiSTEM on the FEI TALOS F200X (Chem S/TEM) of the alloying elements in a non-standard Zr cladding before irradiation. The grain boundary segregation is very well observable. Cr has not shown segregation in the grain boundaries of this cladding material.

MS2.P016
Study on the CrN/AlN multilayers by atomic resolution TEM

Z. Zhang[1], X. Gu[1], D. Holec[2], M. Bartosik [3], P. H. Mayrhofer[3]

[1]Erich Schmid Institute of Materials Science, Austrian Academy of Sciences, Leoben, Austria
[2] Montanuniversität Leoben, Department of Physical Metallurgy and Materials Testing,, Leoben, Austria
[3]TU Wien, , Institute of Materials Science and Technology, , Vienna, Austria

zaoli.zhang@oeaw.ac.at

Introduction: Nitride multilayered structures have received substantial attention in practical applications and fundamental research owing to the exceptional mechanical properties and some new physical phenomena possibly being introduced by interfaces present in multilayers.

CrN/AlN multilayers have been shown to exhibit peak hardness of∼40 GPa and simultaneously a low friction coefficient for a certain bilayer period (Λ). These improvements in mechanical properties have a close relationship with the existence of a metastable face-centered cubic (*fcc*) AlN phase which can be epitaxially stabilized in thin films. The physical mechanism and consequences of the epitaxial stabilization are not yet well understood due to the complexity of the multilayered films, such as dislocations, diffusion, strains etc.. and rather limited atomic-resolution studies of the interface structure and composition performed up to date. To reveal the intrinsic physics pertained to the multilayers is a key to understand their unique properties and to design novel multilayered materials.

Objectives

In this study, the objectives are: 1) characterize the microstructure and atomic structure of CrN/AlN multilayer; 2) explore the origin of the hardness enhancement in the CrN/AlN multilayered structures using atomic resolution TEM and associated techniques.

Materials and Methods: Here, the CrN/AlN multilayers with a nominal bilayer period (Λ) of 6.0, 5.5, and 2.0 nm were used. CrN/AlN multilayer films were prepared in an AJA Orion 5 lab-scale magnetron sputtering system equipped with one 3-inch Cr (99.5% purity) and two 2-inch Al (99.5% purity) targets. Prior to the depositions, the Si (100) substrates were ultrasonically pre-cleaned in acetone and ethanol and mounted in the deposition chamber. After reaching a vacuum below 0.1 mPa, the substrates were thermally cleaned at 500 °C for 20 min. as well as plasma cleaned in a pure Ar atmosphere of a total pressure of 4 Pa for 10 min. at the same temperature. During the deposition, the substrate temperature was kept constant at 470 °C, the substrates were rotated with about 1 Hz, and a bias voltage of −70 V was applied to the substrates (to ensure dense coating morphologies).

A JEOL 2100F field emission microscope (200kV) equipped with an image-side Cs-corrector which possesses a 1.2 Å resolutions at 200 kV was used. The aberration coefficients were set to be sufficient small, i.e. CS ~ - 15.0 µm. The HRTEM images were taken under a condition of slightly over-focus.

Theoretical calculations using density function theory (DFT) were performed to corroborate the experimentally observed phenomena.

Results:

1) High-resolution TEM (HRTEM), together with quantitative atomic displacement measurements and DFT calculations, has been applied to CrN/AlN multilayers with different bi-layer periods. It is revealed that the dislocation densities are higher in CrN than in AlN layers, and a relatively lower value along the growth direction than in in-plane direction when the bilayer period is small (Λ = 2.0 nm). The dislocation density decreases with decreasing the bilayer period due to the enhanced inter-diffusion across the interfaces.
2) Relative strain fields revealed by geometrical phase analysis oscillate, corresponding to the bilayer period, and their magnitude increases with decreasing bilayer period.
3) Interplanar spacing oscillations in the CrN/AlN multilayers were experimentally observed by quantitative HRTEM measurements, which were corroborated by first principles calculations. These oscillations are closely related to changes in the electronic structure introduced by the presence of the interfaces.
4) Electron spectroscopy and microscopy were further employed to analyse the strain distributions in the multilayers and obtain generalized relationships between the electronic structure on the one hand, and (non-)stoichiometry or strains in the strained multilayers on the other hand. These observations were successfully interpreted by means of theoretical calculations.

Conclusions: The interplay among dislocations, strains within the layers, inter-diffusions as well as the bilayer period length most likely dictates the final mechanical property. The present study provides atomic-scale insights in the mechanisms of extraordinary strength pertaining to the CrN/AlN multilayers.

MS2.LBP01
Microscopic investigation of material transport and crystallization during the Al-induced layer exchange process

J. Wirth[1], S. M. Kraschewski[1], E. Spiecker[1]

[1]IMN Erlangen, Material Science, Erlangen, Germany

janis.wirth@fau.de

The Al-induced layer exchange (AlILE) process uses metal-induced crystallization to fabricate polycrystalline Si or Ge layers at low temperatures. While the process is most commonly applied to Si (Si-AlILE) the small difference in atomic numbers of Al and Si makes it difficult to directly reveal the transport of the two materials by material contrast in (transmission) electron microscopy. Using Ge instead of Si, material sensitive imaging benefits from the much larger difference in the atomic number. Similar to Si-AlILE, Ge-AlILE is characterized by a layer exchange using a stack of Ge/oxide/Al on glass substrate at temperatures of 220-417 °C. Upon heating Ge diffuses into the Al layer and forms crystalline precipitates. Subsequently, the precipitates grow laterally forming an almost continuous polycrystalline Ge film [1-3]. The Al originally contained in the bottom layer is pushed up into the top layer. For Si-AlILE it was shown that the push-up of Al even occur in unreacted regions far away from the crystallization front [2].
In situ light microscopy (LM) experiments of the process at 400 °C show a dendritic growth of the Ge precipitates with resulting precipitate sizes of 50-150 µm (Figure 1). The process time for the complete Ge-ALILE process was in range of 2-7 h (Figure 1b). While LM characterizes the overall process the microscopic mechanisms of material transport and crystallization can only be studied by scanning electron microscopy (SEM) and transmission electron microscopy (TEM).
Figure 2 exemplarily shows a post-mortem SEM analysis of a partly crystallized Ge-AlILE sample. Using cross-section imaging with back scattered electrons (BSE) the push-up of Al in an unreacted sample region is clearly revealed confirming that the same mechanism is operative as in the case of Si-AlILE [2]. The phenomenon can be interpreted as follows: Upon nucleation and lateral growth of Ge crystallites in the Al layer pressure builds up which is eventually released by transport of Al into the top layer. Due to the presence of a thin oxide layer initiation of this push-up process requires perforation of the interfacial oxide layer and therefore occurs only in certain locations [2]. The thin oxide layer also plays a major role as barrier layer for the in-diffusion of Ge in the early stages of Ge-AlLILE where it controls the density of Ge nuclei and thus the grain size of the resulting polycrystalline Ge layer.
Combining LM, SEM, TEM (*ex situ* and *in situ*) experiments, an in-depth characterization of the whole Ge-AlILE process is attempted.

[1] J. Schneider et al., J. Non-Cryst. Solids **352**, (2006)
[2] B. Birajdar et al., Scripta Materialia **66** (2012)
[3] K. Nakazawa et al., J. Solid State Science **2** (2013)

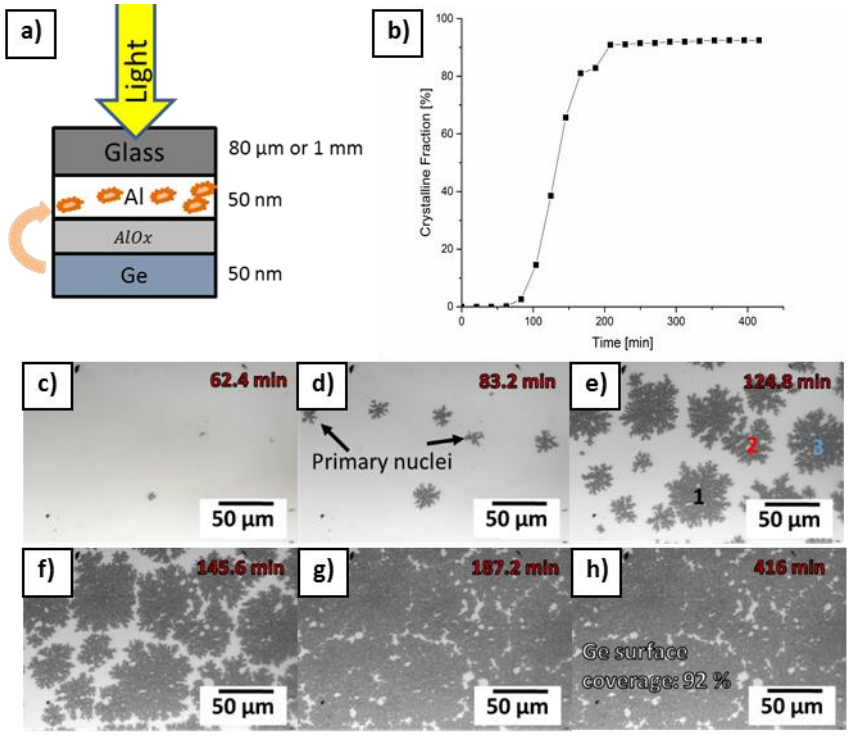

Figure 1. a) *In situ* LM experimental setup: The layer stack is turned upside down in order to reveal Ge crystallization in reflection geometry. b) Temporal evolution of Ge crystallization (covered area fraction) upon annealing at 400 °C, c) – h): *in situ* LM images at different stages of the Ge-AlLILE process: dendritic c-Ge crystallites appear as dark areas.

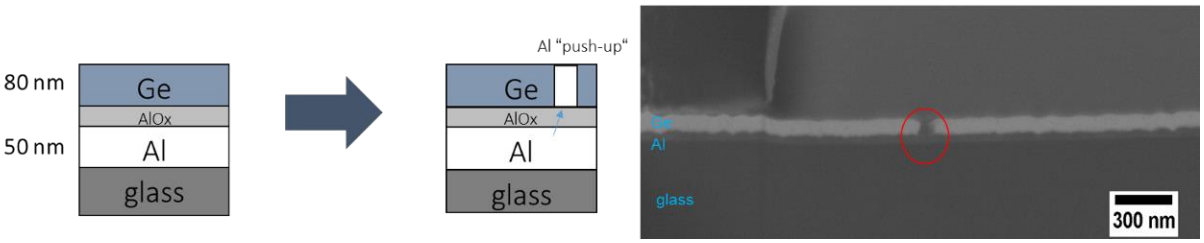

Figure 2. SEM image (BSE) of FIB cross-section clearly revealing Al push-up in unreacted sample areas (compare Ref. [2]).

MS 3: Energy-related materials

MS3.001 invited
Designing nanomaterials synthesis and degradation experiments in the liquid cell through radiation chemistry control

P. Abellan[1], T. Woehl[2]

[1]SuperSTEM Laboratory, Daresbury, United Kingdom
[2]University of Maryland, Department of Chemical and Biomolecular Engineering, College Park, PA, United States of America

pabellan@superstem.org

Radiolytic synthesis routes and remediation methodologies exploit the chemical effects of the absorption of high-energy ionizing radiation on solutions to grow nanomaterials and to break-down pollutant molecules [1,2]. In the (S)TEM, the growth and degradation of materials can be investigated in-situ using the 60-300kV electron beam in combination with liquid cells. Another type of experiment is one aimed at monitoring dynamic processes which are not triggered by the electron beam. In this regard, a myriad of new holder and chip designs have already enabled capabilities such as electrochemical measurements, localized heating or chemical mixing. For all experiments, a main challenge which affects the reproducibility and reliability of the measurements is the understanding (and hopefully control) of the effect of the electron beam on the liquid sample. Indeed, small changes in the chemistry of a solution can have drastic consequences, such as that the pH of the solution can decrease with electron dose during irradiation (of e.g. DI water [3]) while it can increase if the irradiated solution includes certain solutes (such as Ce species [4]).
Many theoretical and experimental efforts have been devoted to understanding how irradiation in the (S)TEM affects DI water and different aqueous solutions, since water is a commonly used solvent. Fewer works can be found exploiting the radiation chemistry of organic solvents, even though they can present interesting properties, such as the generation of much lower number of reactive species for the case of hydrocarbons and other nonpolar systems using the same incident electron dose as compare to water [5]. More generally, when irradiating a solution both: reducing and oxidizing species are typically formed, control of radiation damage can be achieved by either reproducing a selective reducing or oxidizing environment (by canceling out competing reactions) or by minimizing the overall effect of the beam. This is achieved with the addition of substances that selectively convert some of the reactive primary radicals into a different type of reactant or into inert species. Here I will discuss general methods for finding more suitable synthesis or corrosive environments for controlled nanoparticles formation or dissolution in the liquid cell [6]. Much of the presentation will focus on the solvent radiolysis which is what predominantly dictates the species and yields involved in the chemical processes leading to nanostructure synthesis and degradation.[7]

References:
[1] J. Belloni, *Catal. Today*, 2006, **113**, 141-156; S.-H. Choi et al., *Colloids Surf., A*, 2005, **256**, 165-170; J. Belloni et al., *New J. Chem.*, 1998, **22**, 1239-1255.
[2] M. A. J. Rodgers and Farhataziz, *Radiation Chemistry: Principles and Applications*, VCH Publishers, New York, N.Y. , 1987.
[3] N. M. Schneider et al., *The Journal of Phys. Chem. C*, 2014, **118**, 22373-22382
[4] P. Abellan et al., *RSC Advances*, 2017, **7**, 3831-3837
[5] P. Abellan et al., *Langmuir*, 2016, **32**, 1468-1477.
[6] Woehl & Abellan, *Journal of Microsc.* 2016, DOI: 10.1111/jmi.12508
[7] SuperSTEM is the UK EPSRC National Facility for Aberration-Corrected STEM, supported by the Engineering and Physical Science Research Council.

MS3.002
Identifying key structural features of OER active IrO_x catalysts

E. Willinger[1], C. Massué[1], R. Schlögl[2,1], M. G. Willinger[2,1,3]

[1]MPI für Chemische Energiekonversion, Heterogene Reaktionen, Mülheim an der Ruhr, Germany
[2]Fritz-Haber-Institut der Max-Planck-Gesellschaft, Anorganische Chemie, Berlin, Germany
[3]MPI für Kolloid- und Grenzflächenforschung, Kolloidchemie, Potsdam, Germany

kudrenko@fhi-berlin.mpg.de

Efficient conversion of renewable energy to chemical fuels plays an important role in the realization of a sustainable, carbon neutral energy supply [1]. Hydrogen, which will be required in large quantities as a key ingredient of chemical fuels, can be produced by electrochemical water splitting using electricity from renewable sources. So far, X-ray amorphous iridium (hydr)oxides have been identified as most promising catalysts for the oxygen evolution reaction (OER). Although comprehensive spectroscopic and theoretical studies have provided some insight on its electronic structure [2], information about the arrangement of relevant structural units within the amorphous phase is missing. Considering the importance of the reaction, a genuine understanding of the catalyst structure−function relationship is urgently required.

We thus performed a detailed comparative structural investigation of amorphous iridium (hydr)oxides that show distinct differences in their catalytic properties. One of the samples was synthesized at the Fritz-Haber-Institute (IrO_x-FHI), the other one was a commercial benchmark iridium (hydr)oxide from Alfa Aesar (IrO_x-commercial). Samples were investigated using a combination of complementary imaging and diffraction methods that are provided by state-of-the-art analytical transmission electron microscopes.

Using real-space atomic scale imaging in combination with analysis of the atomic pair distribution function abstracted from electron diffraction (ePDF), we were able to identify key structural motifs that are linked to high water splitting activity. The electronic structure resulting from the structural arrangement was investigated by electron energy loss spectroscopy (EELS) and compared to Reference: phases. Our results show that high activity is related to the presence of interconnected, single unit cell sized Hollandite-like structural domains. These domains are cross-linked through under-coordinated oxygen/iridium atoms. The less active and unstable IrO_x Reference: sample contains, besides the Hollandite-like structural domains, a substantial amount of rutile-like structural motifs (Figure 1). The latter are thermodynamically more stable and known to be catalytically less active [3]. Compared to the flexible hollandite-like framework, the rutile phase results in a faster structural collapse and deactivation.

The work nicely demonstrates the analytic potential of electron microscopy. It shows how the combination of complementary tools that are uniquely provided in a single instrument allows to abstract detailed structure-activity correlations in an amorphous material that were so far not accessible.

References:
[1] Schlögl, R. Topics in Catalysis **59** (2016), p. 772.
[2] V. Pfeifer et al., Phys.Chem.Chem.Phys., **2016**, 18, 2292.
[3] Wei Sum et al., ACS Appl. Mater. Interfaces, **2016**, 8, 820.

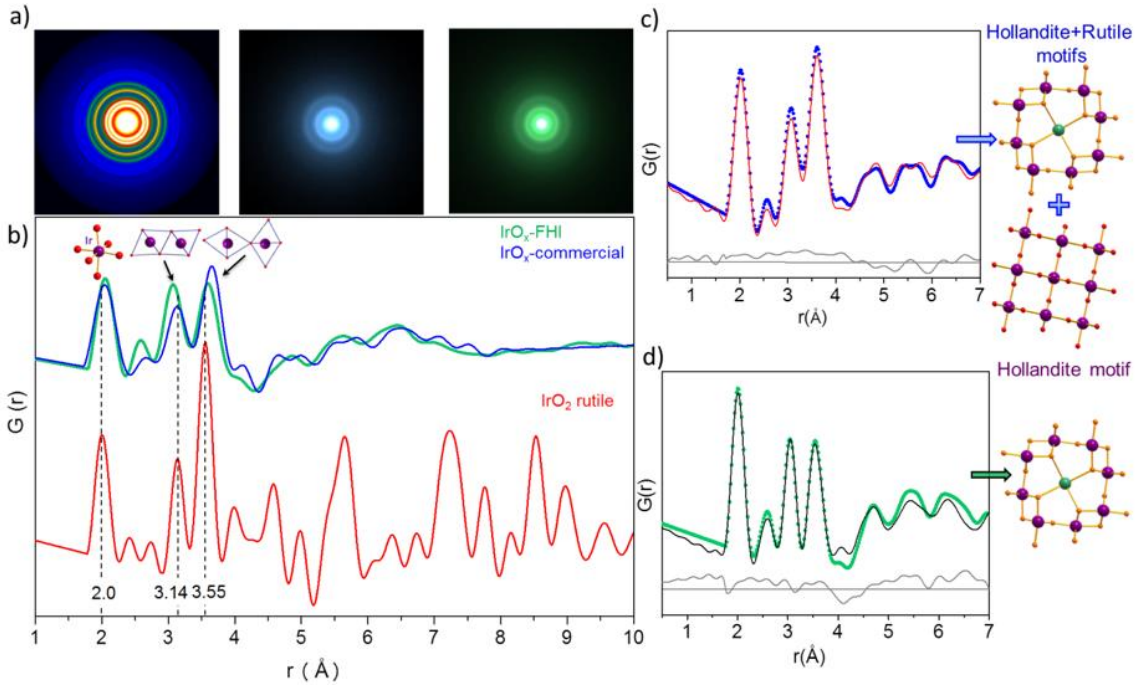

Figure 1. ePDF analysis of IrOx hydroxides. (a) SAED pattern and corresponding ePDFs (b) of nanocrystalline IrO2-Rutile (red), IrOx-commercial (blue) and IrOx-FHI (green) samples; (c) the refined ePDF of the IrOx-commercial and (d) the refined ePDF of the IrOx-FHI samples, respectively. Different portions of edge- and corner shared units are found in the two compared hydroxides.

MS3.004
In situ TEM observation of microstructural changes during lithiation of lithium manganese oxide

T. Erichsen[1], B. Pfeiffer[1], C. Nowak[1], V. Roddatis[1], C. A. Volkert[1]

[1]Georg-August-University, Institute of Materials Physics, Göttingen, Germany

terichsen@ump.gwdg.de

Lithium ion batteries are currently the most widely used portable and rechargeable electrochemical storage systems due to their high energy density. The performance and reliability of lithium batteries is determined by atomic scale phenomena, such as diffusion and interface reactions. While there are many different Li-based cathode materials in use or being considered, spinel-type $LiMn_2O_4$ provides a good model system to study electrochemical processes at a local scale. It has a strong coupling between structural and electronic/valence properties and is phase separating for higher contents of Li. This creates a solid/solid interface which allows both sides of an electrochemical reaction to be studied inside a transition electron microscope (TEM). Previous studies on $LiMn_2O_4$ have been using XRD or XAS measurements or were limited to ex-situ TEM except for in-situ diffraction studies on LMO nanowires. Therefore, there is only limited information on the mechanisms of the phase transformation.
Using a Nanofactory STM-TEM-holder to bring Li into contact with a FIB-prepared, polycrystalline $LiMn_2O_4$ lamella, we are able to drive an electrochemical reaction front into the TEM specimen. A sharp interface is observed to move through the lamella, converting the original single crystal cubic spinel $LiMn_2O_4$ into a twinned tetragonal Li_2Mn_2O4 lamellar structure. The expected decrease in Mn valence and increase in Li content as a result of lithiation are confirmed using STEM-EELS, however the exact chemical structure of the interface between the cubic and tetragonal phases and between the twin variants has not yet been resolved. Furthermore, the reason for the formation of the twin structure is not known, but there are indications in STEM that the interfaces are defective. Correlative microscopy studies of the lamellar structure with laser-assisted APT show that the Li distribution is homogeneous within the twinned structure. High resolution TEM studies are underway to reveal the interface structures of the lithiation front and of the twin boundaries.
Financial support through the DFG (German Science Foundation) under SFB 1073 Atomic scale control of energy conversion (project C05) is gratefully acknowledged.

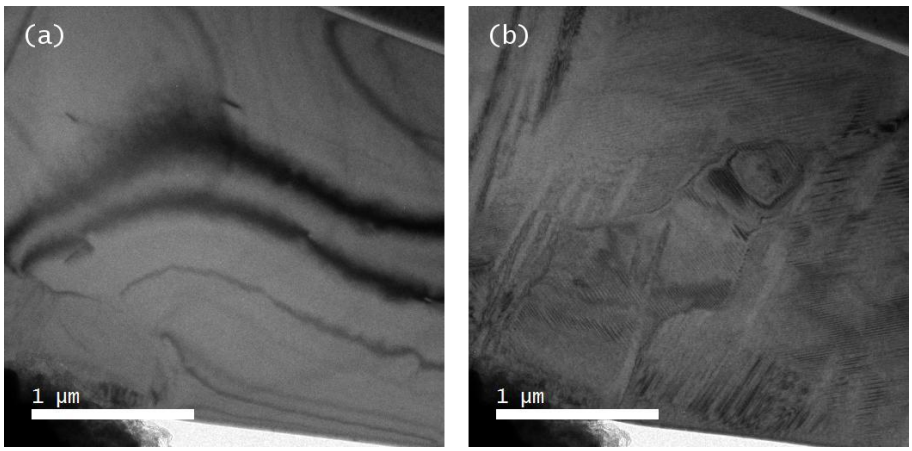

Figure 1. Li_xMn_2O4 during in-situ lithiation in the TEM. The Li electrode with the native oxide/nitride is seen in the lower left corner of both images. (a) Bright field image taken immediately after contacting the lamella and applying a -5V bias. The dark stripes result from bending. The region near the Li electrode has already been transformed and shows a sharp interface to the original material. (b) Bright field image taken after 180s of lithiation. The whole lamella now consists of three domains of striped contrast with different orientations.

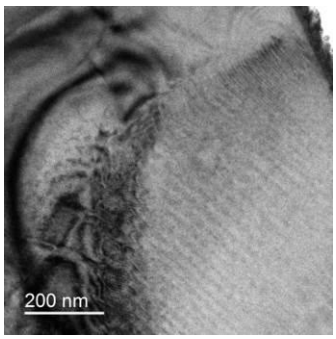

Figure 2. BF image of the lithiation front. The top left region is as-prepared $LiMn_2O_4$ spinel while the bottom right region is transformed into a twinned tetragonal $Li_2Mn_2O_4$.

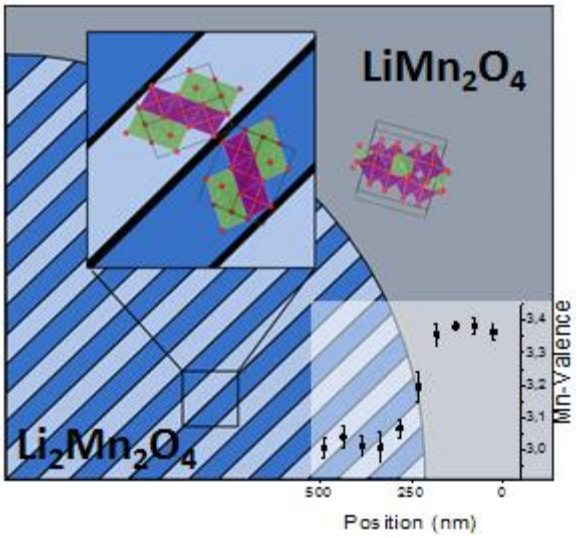

Figure 3. Schematic of our current results showing the orientation relationship between the initial $LiMn_2O_4$ spinel and the twinned tetragonal $Li_2Mn_2O_4$. STEM EELS measurements (inset) show a strong change in valence across the interface.

MS3.005
Electron energy loss spectroscopy of black TiO2 nanowires

A. Folger[1], J. Kalb[2], L. Schmidt-Mende[2], C. Scheu[1,3]

[1]Max-Planck-Institut für Eisenforschung GmbH, Nanoanalytics and Interfaces, Düsseldorf, Germany
[2]University of Konstanz, Department of Physics, Konstanz, Germany
[3]RWTH Aachen University, Materials Analytics, Aachen, Germany

a.folger@mpie.de

TiO_2 plays a key role in electrochemical and photo-physical applications like photo-catalysis and as electrode material in solar cells and Li-ion batteries. Especially hydrothermally grown rutile TiO_2 nanowire (NW) arrays are promising as the 1 D structure results in a large surface area and a directed electron path towards the substrate. The main drawback of pristine TiO_2 is its comparable large band gap of around 3 eV, which allows only absorption and photoconductivity in the UV-range only. Along with the efforts to improve these properties, e.g. by doping, surface defect engineered black TiO_2 attracted a lot of interest.[1] Within the last years many different approaches to fabricate black TiO_2 have been developed, however the origin of the colour and its related properties are still not understood completely.
In our present work, transmission electron microscopy (TEM) in combination with spatially resolved electron energy loss spectroscopy (EELS) was used to solve the origin of our black TiO2 NWs. These NWs were hydrothermally grown on fluorine doped tin oxide substrate and heat treated in N_2 atmosphere at 500°C. The TEM analysis were performed at 200 kV using a JEOL JEM-2200FS and at 300 kV using a probe corrected FEI Titan Themis 60-300. Latter, equipped with a high-resolution electron energy loss spectrometer (Gatan high-resolution Quantum ERS energy filter), was used for the EELS analysis in scanning TEM (STEM) mode. Our investigation shows that these black TiO_2 NWs exhibit a three phase core-shell like structure. Elemental analysis prove that all phases consist only of Ti and O and we detect no nitrogen. Thus, we can exclude that nitrogen doping is the origin of the black color. High resolution TEM analysis reveal a crystalline core and shell, whereas the thin top layer is amorphous (Figure 1). The core consists of single-crystalline rutile TiO_2, which is riddled by oxygen vacancy condensation induced voids. The shell is an oxygen deficient TiO_{2-x} material with a pseudo-rutile crystal structure and the amorphous TiOx top layer is not completely disordered but imitates the (hh0) lattice periodicity of rutile TiO_2.
EELS analysis across the three phases show that the electronic structure of the black TiO2 NWs is more complicated and that especially the interface between the two crystalline materials plays a key role. The position and intensity of the Ti-$L_{3,2}$ edge is used, to determine the $Ti^{4+}/(Ti^{3+}+Ti^{4+})$ ratio with high lateral resolution.[2] This analysis reveals an electron rich area at the interface between the two crystalline materials (Figure 2). In this area, an electron rich, conductive layer is formed, which might be the reason for both, the black color and the superior properties of black TiO2 material.
The results of our TEM investigation are correlated to the properties of black TiO2 NWs. We performed current-voltage measurements parallel to the [001] growth direction and found that the black TiO2 nanowires, compared to their white counterpart (as-grown or heat treated in air), have changed electron transport properties.

[1] K. Zhang, J. Phys. Chem. Lett., 2017, 8 (1), 199–207.
[2] E. Stoyanov et al., Am. Mineral., 2007, 92, 577–586.

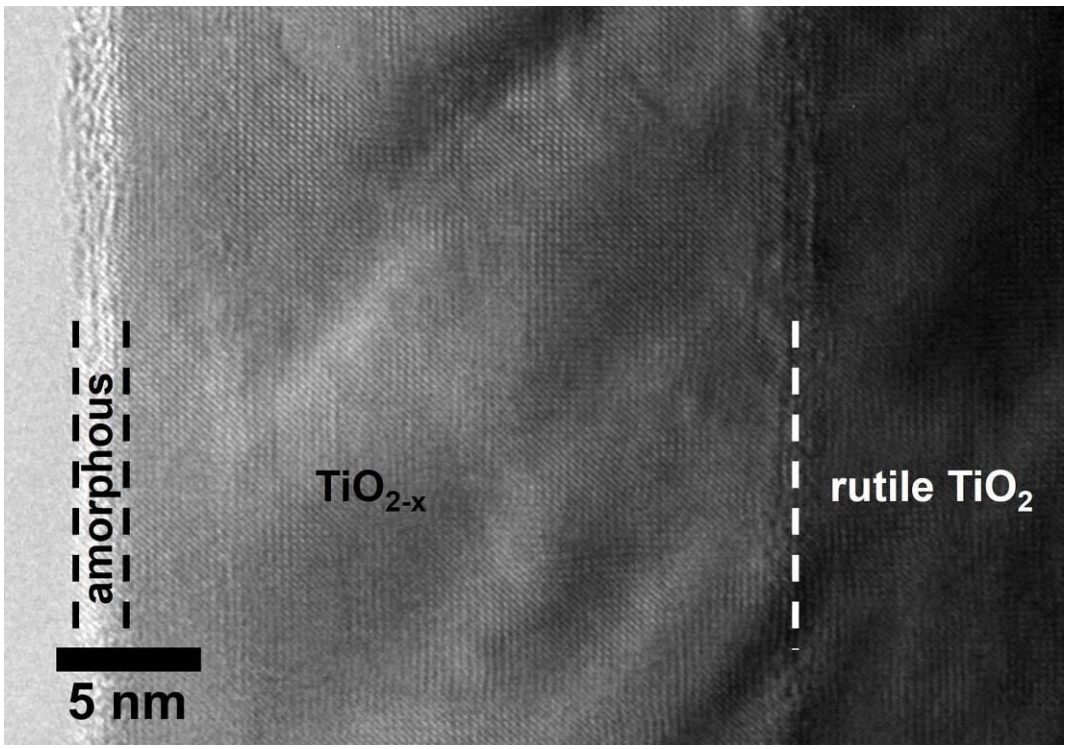

Figure 1. HR-TEM image of the surface of the black TiO_2 NW showing three layers: amorphous TiO_x, crystalline TiO_{2-x} shell and single-crystalline rutile TiO_2 core.

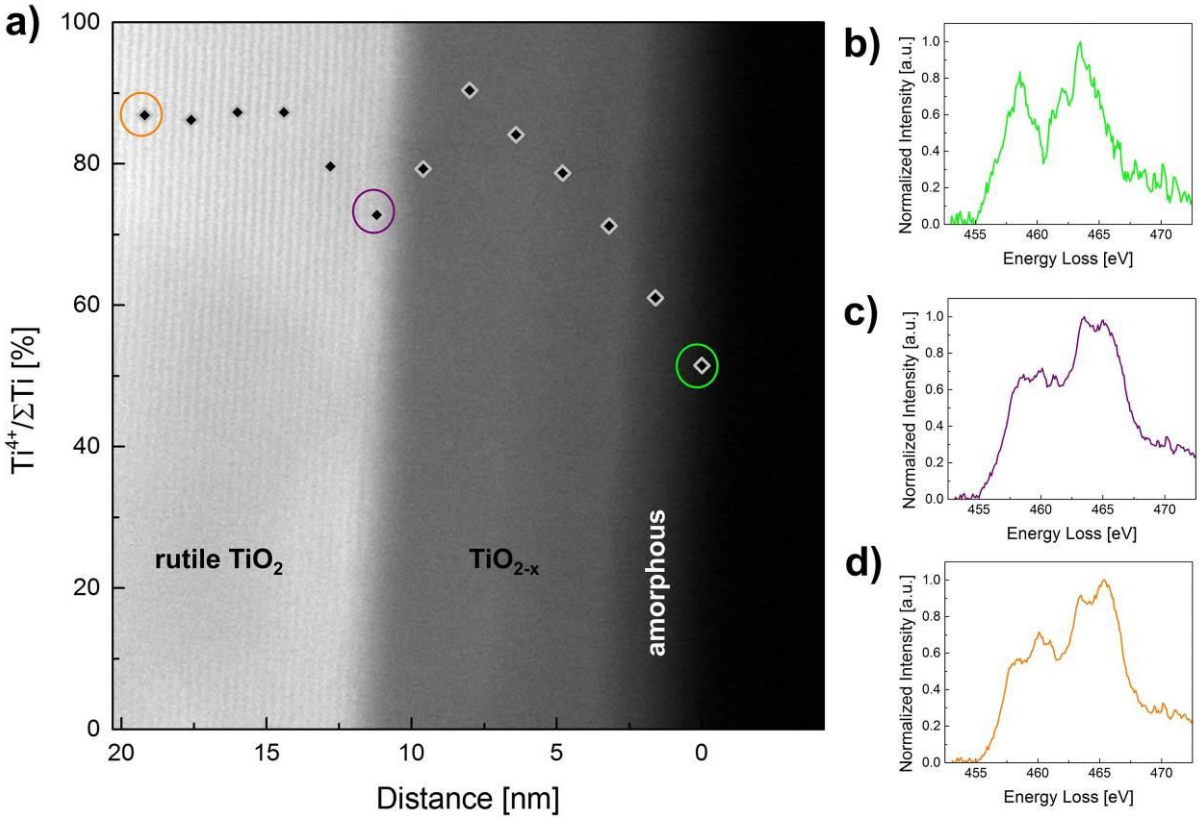

Figure 2. a) Concentration gradient of Ti^{4+} overlaid with a high-angle annular dark field STEM image. Selected EEL spectra used for the calculation are shown in b)-d). They correspond to b) the amorphous layer, c) the interface between the two crystalline materials with metal-like properties and d) the single-crystalline rutile TiO_2.

MS3.006
TEM Investigations of new electrode materials for batteries

D. Geiger[1], P. Balasubramanian[2], F. Müller[3,4], H. Zhang[3,4], M. Mancini[2], D. Bresser[3,4], D. Buchholz[3,4]
A. Gutsche[3], I. Hasa[3,4], S. Jeong[3,4], B. Qin[3,4], P. Axmann[2], M. Wohlfahrt-Mehrens[2], H. Nirschl[3]
S. Passerini[3,4], U. Kaiser[1]

[1]Ulm University, Ulm, Germany
[2]Zentrum für Sonnenenergie und Wasserstoff-Forschung Baden-Württemberg (ZSW), Ulm, Germany
[3]Helmholtz Institute Ulm (HIU), Ulm, Germany
[4]Karlsruhe Institute of Technology (KIT), Karlsruhe, Germany

dorin.geiger@uni-ulm.de

Recent intensive investigations of new electrode materials for batteries attest the dynamics of the research on more efficient energy storage. Higher performance in terms of energy density, lifetime safety and costs has to be achieved. Therefore it is important to unravel their structure to understand the reaction behavior. In this respect, one of the most powerful methods is the aberration-corrected HRTEM, which can deliver the structure in atomic resolution if a certain electron dose can be accepted. However, this method meets two big challenges, i.e., most often the materials cannot be prepared with the desired orientation and they are often fast destroyed by the imaging electrons.
For TEM investigations we used the image Cs-corrected FEI Titan 80-300 kV operated at 300 and 80 kV, the new Cs/Cc-corrected SALVE FEI Microscope 20-80 kV [1,2] at 40 kV and Philips CM20 at 200 kV. Three newest battery materials studies are presented here. The first one, exploits the electrochemical activity of the Ni2+/3+ redox couple in the mixed-polyanionic structure Na4Ni3(PO4)2(P2O7). This new material exhibits a remarkably high operating voltage when cycled in sodium cells both in carbonate- and ionic liquid-based electrolytes. Ionic liquid-based electrolyte and carbon coating enable reversible redox activity of Ni2+/3+ at the operating voltage of 4.8 V vs. Na+/Na. The second investigated material is the polyanionic lithium vanadium mono-diphosphate, Li9V3(PO4)2(P2O7)3 [LVPP], showing higher energy density and thermal stability, due to the strong binding of the phosphate anions. A facile synthesis method of LVPP has been designed and the corresponding yield was analysed including TEM methods. The third group of investigations relates to the impact of the cobalt/iron dopant content ratio and of the carbon coating on the doped ZnO for lithium-ion anodes. Samples of different dopant ratios Zn0.9Co0.1O, Zn0.9Fe0.1O, Zn0.94Fe0.06O, Zn0.98Fe0.02O have been investigated to find out their influence on the reversible formation of Li2O, with the interesting result that even relatively low dopant concentrations can be sufficient to enable it.
Not only crystal structure and particle size distribution but also carbon coating as an essential aspect of optimal battery functionality have been investigated (fig. 1). It turns out that the carbon amount starts to be efficient at ~15 wt% becoming optimal at ~20 wt%. During TEM specimen preparation no additional grinding was used to preserve the original state of the synthesized powder material. The beam sensitivity of the samples was difficult to characterize quantitatively, because of the large inhomogeneity of the powder particles but we could confirm the expected crystallographic structure of the synthesized particles also by using TEM image simulations with JEMS and QSTEM (fig.2).
Especially the TEM investigations of LVPP emphasize as technical challenge, due to its high beam sensitivity. Working fast, at low dose and not using crystal orientation, structure damage can be minimized, but to find a suitable particle only patience can help.

[1] U. Kaiser et al., Ultramicroscopy 111, (2011), p.1239.
[2] Linck et al. PRL 117, 076101 (2016)
[3] F. Müller et al., Journal of The Electrochemical Society, **164** (1) A6123-A6130 (2017)

Acknowledgement
This work was supported by the German Ministry for Education and Research (BMBF) in the frame of the joint research project "Li-EcoSafe - Development of economical and safe lithium ion batteries".

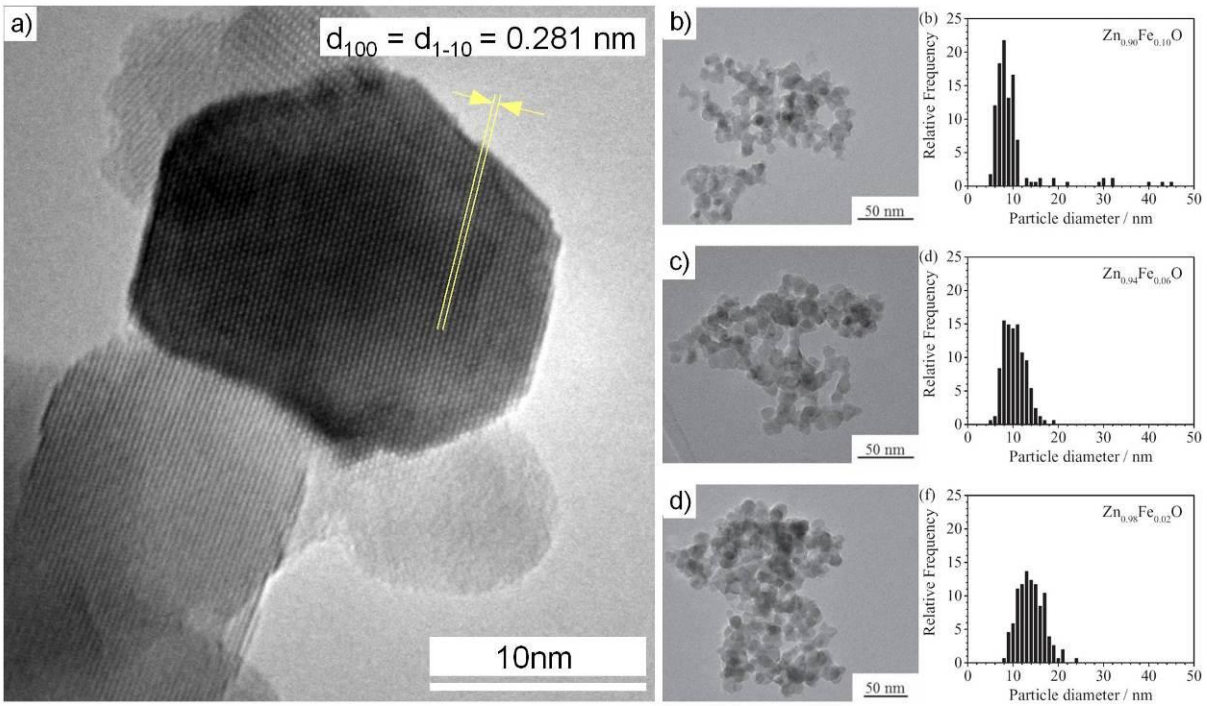

Figure 1. a) [0001]-oriented Co-doped ZnO nanoparticle imaged with CM20 at 200 kV. TEM images with particle size histograms of b) Zn0.90Fe0.10O, c) Zn0.94Fe0.06O, and d) Zn0.98Fe0.02O show a decrease of the mean particle size with increasing dopant concentration, confirming XRD, BET, and SAXS measurements.

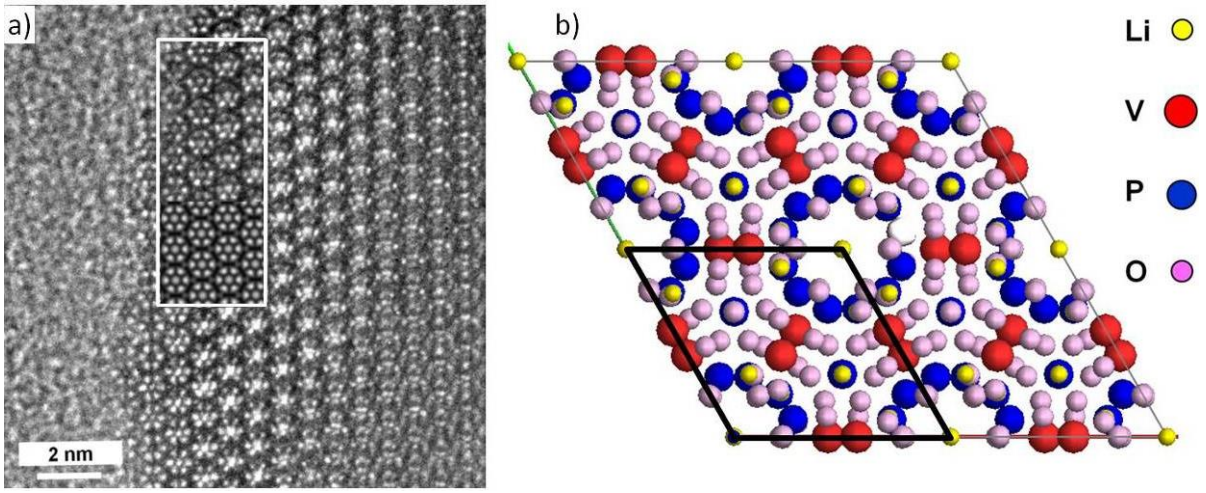

Figure 2. a) Cs-corrected HRTEM image at 300 kV of [0001]-oriented Li9V3(P2O7)4(PO4)2 with corresponding simulation (lower part of the white rectangle), b) [0001]-projected LVPP structure (JEMS), one unit cell marked in black.

MS3.007 invited
Advanced transmission electron microscopy for catalysts characterization

J. Zecevic[1]

[1]Utrecht University, Utrecht, Netherlands

j.zecevic@uu.nl

Introduction: Advanced transmission electron microscopy techniques are becoming increasingly important, as they allow imaging materials not only at nano- and atomic-scale, but also in three dimensions (electron tomography) or under gas and liquid environment (in-situ TEM). Recently developed liquid-phase TEM (LP-TEM) has a great potential for nanoscale imaging of processes relevant for catalysts synthesis and application. LP-TEM studies performed in the past years mainly focused on the growth of metallic nanoparticles from solutions, and pointed to important effects the electron beam can have [1-2]. Radiolysis of water and aqueous solutions proved to be the most challenging as it leads to the formation of highly reactive species such as e_{aq}-, $H^{\bullet}$, $OH^{\bullet}$, H_2, H_2O_2, H^+, OH^-. These species can locally change the chemistry in the LP-TEM cell, triggering reactions such as reduction of metal ions or dissolution of oxides. Our recent study showed that this change in chemistry can destabilize amorphous silica [3], leading to its reshaping and dissolution. Establishing imaging conditions in LP-TEM under which adverse effects will be minimized and suppressed is of great importance for further development and application of this technique.
Objectives: The aim of this study was to gain the understanding of the degradation mechanisms of amorphous silica in LP-TEM and to develop a method that would prevent or at least mitigate this degradation. Besides silica, we aimed to investigate the stability of other oxide materials in LP-TEM that are relevant for catalysis.
Materials and Methods: Oxide samples (Stöber silica and P25 titania) were fixed on the SixNy window of an Si chip (Protochips Inc.) by adding a 0.5 µL droplet of their sonicated isopropanol dispersion. The LP-TEM experiment was operated in flow mode with a flow of 2 µL/min of either pure H_2O, or solution of acetic or ascorbic acid. Experiments were performed on a Talos F200X (FEI), in STEM mode with a 9.5 µs/pixel dwell time operated at 200 kV acceleration voltage.
Results: As seen from LP-TEM experiments, the stability of oxide materials under the electron beam differs greatly and depends on the type of liquid (e.g. pure water, acetic or ascorbic acid). While titania appeared to be stable under the electron beam irradiation in water (Figure 1a), Stöber silica seemed to have undergone dissolution (Figure 1b) as was observed in earlier study [3]. By submerging Stöber silica in aqueous solutions containing various concentrations of up to 1.0 M acetic acid during in situ imaging in LP-TEM, we observed that silica can be significantly stabilized (Figure 1c-d). Besides acetic acid, ascorbic acid also showed moderate effect on stabilization of silica (Figure 1d). The rationale behind this stabilization effect is that acetic acid acts as a scavenger for $e^-_{(aq)}$, $OH^{\cdot}$ and $H^{\cdot}$ radicals formed in radiolysis of water, preventing thus the cleavage of silica"s siloxane bonds and their reaction with reducing radicals which might lead to silica dissolution.
Conclusions: As demonstrated in this study, by carefully considering liquid and support radiation chemistry, adverse effects of electron beam in LP-TEM can be overcome. This is a promising start in further development of the LP-TEM technique and its utilization for studies of many relevant catalyst syntheses and catalytic processes.

[1] N. de Jonge, F. M. Ross, Nat. Nanotech. 6 (2011) 695.
[2] J. E. Evans et al. Nano Lett. 11 (2011) 2809.
[3] Zečević, J., et al., Small 13 (2017) 1602466.

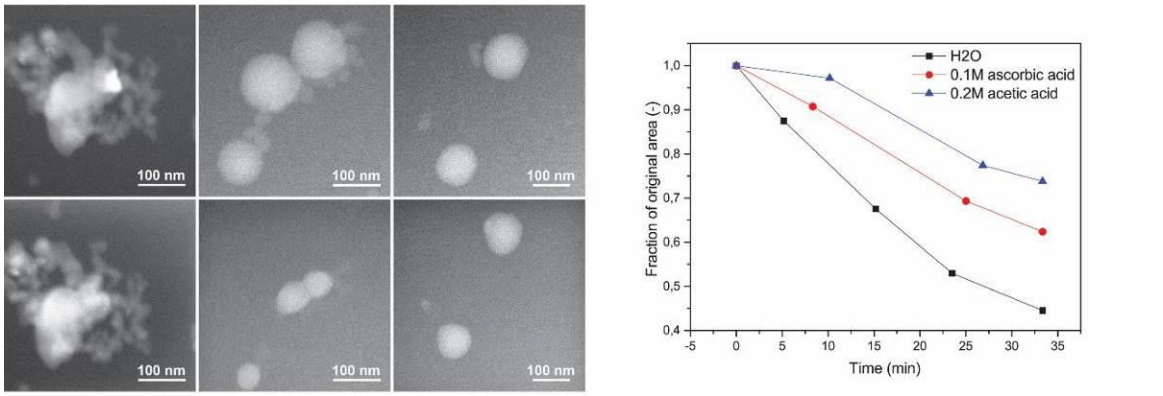

Figure 1. LP-TEM comparison of beam damage. (a-c) The top images show before and the bottom images after 34 minutes of continuous STEM irradiation of TiO_2 (a), SiO_2 in H_2O (b) and SiO_2 in 0.2M acetic acid in H_2O (c). (d) Decrease in SiO_2 TEM surface area as a function of time/total electron dose in water with different concentrations of solutes.

MS3.008
Correlative approach to reveal the morphology of organic bulk heterojunction solar cells

S. Rechberger[1], C. J. Brabec[1], H. Ade[2], E. Spiecker[1]

[1]Friedrich-Alexander Universität Erlangen-Nürnberg, Werkstoffwissenschaften, Erlangen, Germany
[2]North Carolina State University, Physics, Raleigh, NC, United States of America

stefanie.rechberger@fau.de

In the last years, significant improvement of the power conversion efficiency could be achieved in the field of organic photovoltaics (OPV) using novel materials and adapted device engineering. For further improvement the morphology is an indispensable parameter, especially the nanoscale morphology of organic bulk heterojunction (BHJ) solar cells. This nanoscale morphology depends not only on the involved materials but also on their molecular weight and their annealing treatment.
Analytical Transmission Electron Microscopy (TEM) is a versatile tool to characterize the morphology of organic solar cells concerning on the one hand the interfaces of the various layers and on the other hand the material distribution in BHJ active layers. This is achieved by combining high-resolution imaging with analytical techniques like electron energy-loss spectroscopy (EELS) and energy filtered TEM (EFTEM) as well as energy-dispersive X-ray spectroscopy (EDXS). For EFTEM of BHJ layers we present three concepts using different information: i) the elemental information, ii) the plasmonic information, and iii) pre-carbon imaging. Advanced X-ray techniques like grazing-incidence wide angle X-ray scattering (GIWAXS) and resonant soft X-ray scattering (RSoXS) are complementary reciprocal space techniques to probe the detailed molecular microstructure. GIWAXS determines the crystallinity whereas RSoXS probes nano- to mesoscale domains, including domain spacing, relative domain purity and chemical sensitivity.
Here, we present results on a high-efficiency small molecule photovoltaic system composed of a quinquethiophene based molecule (DRCN5T) as electron donor and [6, 6]-phenyl-C71-butyric acid methyl ester ($PC_{70}BM$) as electron acceptor.[1] The morphologies of different post-processing strategies, including thermal annealing (TA), solvent vapor annealing (SVA), and two-step annealing (TA-SVA) treatments are revealed and correlated to the device performance. Figure 1 shows the J-V characteristics of the organic BHJ solar cells with different processing conditions, WO (without), TA, SVA and TA-SVA as well as the morphology study of the active layers using EFTEM (elemental maps of sulfur), 2D GIWAXS patterns and RSoXS profiles. The results of the various techniques are in good agreement and provide a consistent picture of the morphology / device performance interplay [1]. The best device performance of 8.9 % is achieved by a TA-SVA treatment leading to an interpenetrating network with well-expressed fibrillary structures and the highest domain purity with well ordered molecules. The comparison of TA and SVA treated systems is especially interesting as both systems have equally high device performances of 6.2 % but different morphologies. SVA treated systems exhibit domains with similar fibrillary structures as the best performing device (TA-SVA), but the order of the molecules is worse. TA annealing leads to better ordered systems, but the domain shape is less favorable. Based on these results different thermodynamic driving forces are suggested for the two post-treatment technologies.
The correlative approach using analytical TEM, GIWAXS and RSoXS is a powerful toolset to reveal the morphology of organic BHJ solar cells and elucidate the morphology / device performance relation, which will additionally be demonstrated by further OPV systems.

[1] J. Min, X. Jiao, V. Sgobba, B. Kan, T. Heumüller, S. Rechberger, E. Spiecker, D.M. Guldi, X. Wan, Y. Chen, H. Ade, C.J. Brabec, Nano Energy 28 (2016) 241-249

Financial support by the German Science Foundation (DFG) within the frameworks of the SFB 953 Synthetic Carbon Allotropes and the Cluster of Excellence EXC 315 Engineering of Advanced Materials is gratefully acknowledged.

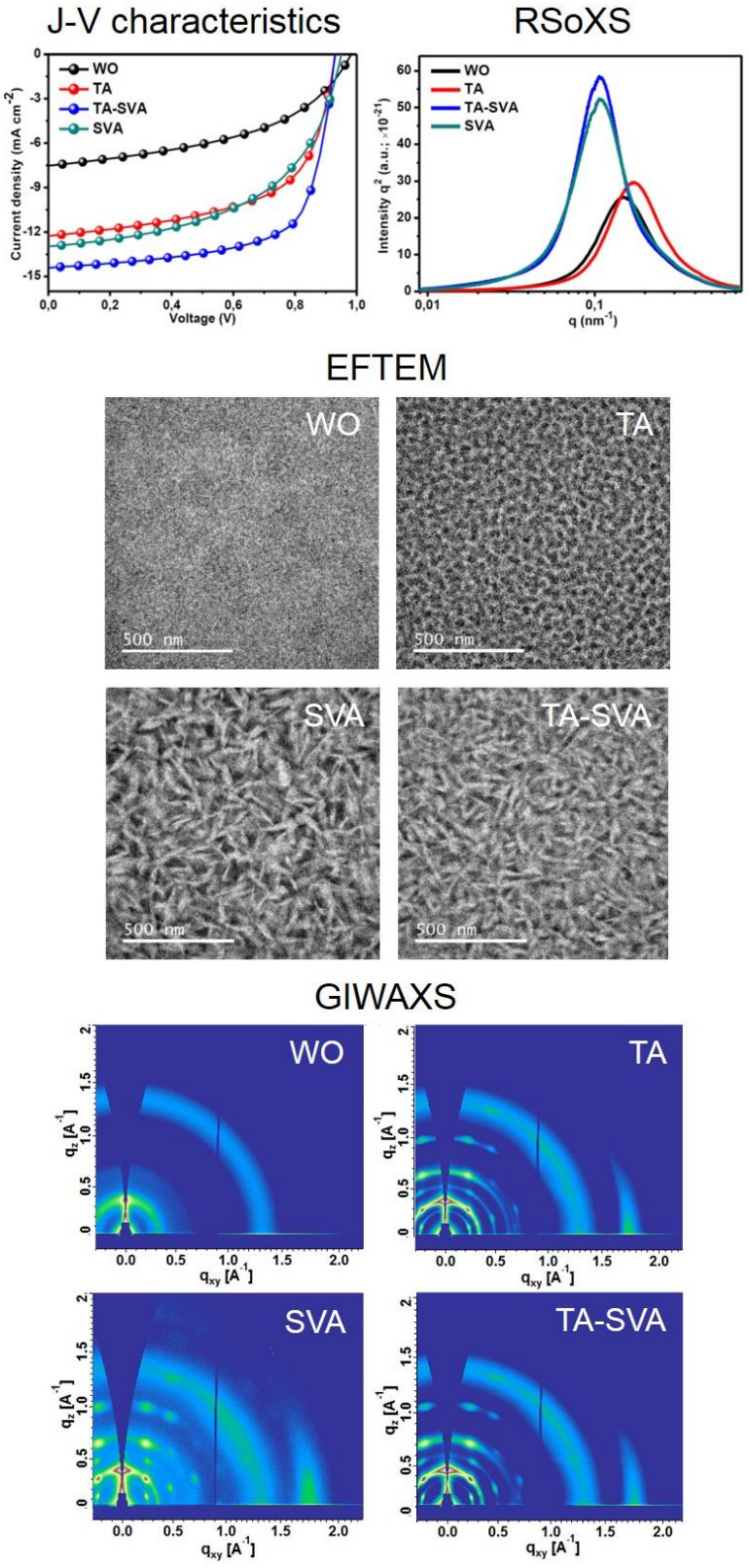

Figure 1. J-V characteristics of the organic BHJ solar cells (DRCN5T: PC70BM) with different processing conditions, WO, TA, SVA, TA-SVA. Morphology study of the active layers: RSoXS profiles, elemental maps of sulfur based on EFTEM imaging and 2D GIWAXS patterns.

MS3.009
Tracking ionic migration in organic-inorganic metal-halide perovskite solar cells using in situ and ex situ transmission electron microscopy

Q. Jeangros[1], M. Duchamp[2], J. Werner[1], F. Sahli[1], R. Dunin-Borkowski[3], B. Niesen[1], C. Ballif[1]
A. Hessler-Wyser[1]

[1]Ecole Polytechnique Fédérale de Lausanne, Photovoltaics and Thin Film Electronics Laboratory, Neuchâtel, Switzerland
[2]Nanyang Technological University, School of Material Science and Engineering, Singapore, Singapore
[3]Forschungszentrum Jülich, Ernst Ruska-Centre for Micorscopy and Spectroscopy with Electrons, Jülich, Germany

quentin.jeangros@epfl.ch

Organic-inorganic metal-halide perovskite solar cells are a promising low cost technology for photovoltaic applications, with record efficiencies that have increased from 3% in 2009 to >22% in 2016.1,2 Although the absorber and contact materials can be tuned to combine the technology with high-efficiency Si solar cells in tandem devices,3 commercial applications are hindered by stability issues that are still under debate.4 In particular, the migration of ions from the absorber material to the hole and electron selective contacts is thought to result in hysteresis in the current-voltage (*J-V*) characteristics of the cell. However, this behavior has not been visualized experimentally.5,6

Here, *ex situ* and *in situ* electrical biasing in the transmission electron microscope (TEM) were performed to assess the migration of species during the fabrication of a cell and its operation. Thin lamellae were extracted from both as-fabricated and tested single junction and tandem cells using a conventional focused ion beam (FIB) lift-out method. The original materials contained either a methylammonium lead iodide (MAPbI3) or a cesium formamidinium lead halide (CsFAPbI3-xBrx) absorber. *In situ* experiments involved contacting the as-deposited FIB-prepared samples to a microelectromechanical systems (MEMS) chip in an electrical biasing TEM specimen holder6 (Fig. 1a). TEM characterisation of the electrically contacted samples involved using (scanning) TEM (STEM) imaging, selected-area electron diffraction, energy-dispersive X-ray spectroscopy and electron energy-loss spectroscopy at 200 kV.

The manufacturing parameters were found to result in iodide diffusion into the Spiro-OMeTAD hole collector, with the amount of iodide in the contact increasing when the hole transport layer was positively biased in both *ex situ* and *in situ* experiments. Reversing the polarity had the effect of driving some of the iodide back towards the absorber and eventually into the fullerene-based electron contact. The migration of iodide towards the positive contact, which may explain the hysteresis phenomena, was found to be associated with the formation of PbI2 nanoparticles and nanometric voids at the interface between the perovskite and the positively biased contact (Fig. 1b). Hole transport material dopants appeared to segregate at some of the interfaces in the cell, likely affecting carrier transport.

Different mechanisms that can contribute to a change in the optoelectronic properties of the cell, including dopant and ion migration, PbI2 particles and void formation, were identified both *ex situ* and *in situ*. This work highlight the need for detailed analysis of perovskite/hole transport layer interactions during cell operation to improve the stability of such devices.

Acknowledgments
The authors acknowledge the Swiss National Science Foundation Sinergia project DisCO, the European Union Seventh Framework Program (Grant Agreement 312483 - ESTEEM2) and M. Kruth, D. Merteens and V. Migunov for valuable discussions and support.

[1] A. Kojima *et al.*, *Journal of the American Chemical. Society*, 2009, **131**, 6050–6051.
[2] NREL research cell efficiency records, 2016, http://www.nrel.gov/ncpv/.
[3] J. Werner *et al.*, *Journal of Physical Chemistry Letters*, 2016, **7**, 161–166.
[4] S. D. Stranks *et al.*, *Nature Nanotechnology*, 2015, **10**, 391–402.
[5] I. Levine *et al.*, *Journal of Physical Chemistry C*, 2016, **120**, 16399-16411
[6] S. Meloni *et al.*, *Nature Communications*, 2016, **7**, 10334:1-9
[7] Q. Jeangros *et al.*, *Nano Letters*, 2016, **20**, 1638–1645.

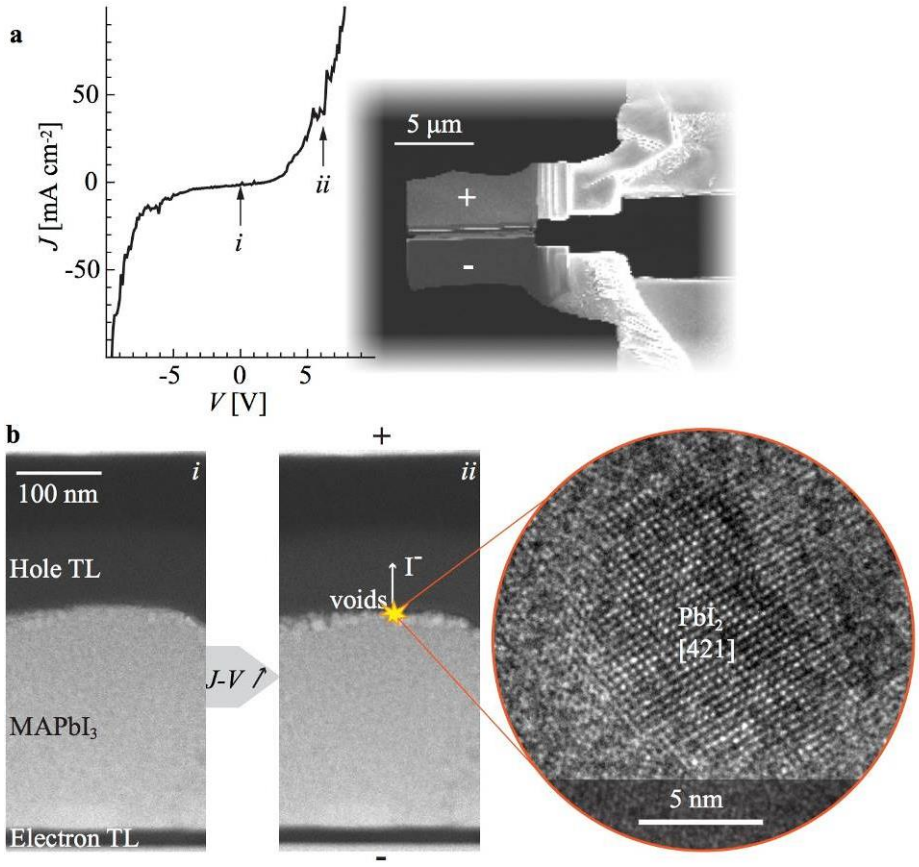

Figure 1. (a) *J-V* curve recorded *in situ* in the TEM alongside the MEMS-contacted TEM lamella. (b) STEM high-angle annular dark-field images recorded (i) before and (ii) after applying a bias of 6 V to the sample, resulting in ~50 mA cm-2 passing through it, the migration of iodide towards the positively biased electrode and the formation of voids and PbI2 at the interface with the hole transport layer (TL).

MS3.010
Revealing mechanisms of extraordinary thermal stability of high-efficiency organic photovoltaics

M. Pfannmöller[1], S. Ben Dkhil[2], O. Margeat[2], R. Schröder[1,3], S. Bals[4], J. Ackermann[2]

[1]Heidelberg University, Centre for Advanced Materials, Heidelberg, Germany
[2]Aix Marseille University, CINaM, Marseille, France
[3]Heidelberg University Hospital, Cryo Electron Microscopy, Heidelberg, Germany
[4]University of Antwerp, EMAT, Antwerp, Belgium

m.pfannmoeller@uni-heidelberg.de

Introduction: Organic solar cells (OSCs) made of semiconducting organic donor and acceptor molecules are convenient photovoltaic systems to produce energy in various novel architectural settings. Efficiencies in the lab exceed 10% and modules can be printed as semi-transparent, colourful, and flexible devices that attract interest as attested in the German Pavillon at the Expo 2015[1].
Objectives: Nevertheless, for the most versatile combination of polymeric donor and fullerene acceptor blends, long-term stability needs to be improved[2]. We introduce a system and workflow to obtain PTB7:PC70BM OSCs with efficiencies of >7% that are thermally stable up to temperatures of 140°C. After annealing for 24 h, a loss in performance of only 10% is observed. Most importantly, by applying spectroscopic imaging using scanning transmission electron microscopy (STEM) in combination with electron energy-loss spectroscopy (EELS) we show the underlying reason of the stability: Demixing is entirely suppressed. Spectroscopic imaging offers reliable visualization at the nanoscale for OSC model systems[3]. With thorough parameters setting and quantitative post processing of EEL signals, compositions of material domains can now be quantified at a resolution of several nanometers. Extending this method to non-fullerene acceptor systems enables us to study relations between structure and function for OSC systems that promise extension of performance beyond 12%.
Materials and Methods: For the spectroscopic imaging we used optimized PTB7:PC70BM layers floated onto holey carbon film grids before STEM-EELS imaging using an FEI Titan 60-300 microscope equipped with a Gatan Enfinium spectrometer. Step sizes for scanning were set to 3 nm with identical parameters throughout all investigations.
Results: Figure 1a presents EEL spectra for pure PTB7 and PC70BM systems and for a blend of a ratio of 1:1.5 wt%. The dotted lines represent Lorentzian fits to (σ+π) plasmons for accurate determination of the plasmon peak energy. Figure 1b shows that spectra for PTB7 and hence the electronic structure does not change after 24 h heating. In Figure 1c,d a dark-field image and the map of plasmon peak energies of a blend layer prepared with the additive diiodooctane (DIO) are depicted. Here, fullerenes only mix with the polymer up to 23% whilst the excess is found in large agglomerates. This number can be estimated when assuming approximate linearity of the plasmon signal after initial damage and fitting of pure to mixed signals. After heating at 140°C for 24 h, there is no change as shown in Figure 1e,f. This structure does not produce a high efficiency which is why for depositing the blend, DIO is added. DIO induces thermal instability. However, the fine-structured morphology is stable as well when DIO is removed due to heating at 140°C (Figure 2a,b).
Conclusion: We provide evidence that even small fullerene-enriched domains do not alter and that PTB7-enriched domains have the same maximum concentration of PC70BM as in the case of no DIO addition. Hence, this concentration represents a thermodynamic minimum of mixing enthalpy and stabilizes the structure at the nanometer scale. Devices can be exposed to elevated ambient temperatures after annealing at 140°C without loss in performance so that any warming up during outdoor operation will not affect efficiency.

References:
[1] German pavilion at EXPO 2015 incorporates organic photovoltaics. *OPE Journ*., 24 Apr 2015, Web, 5 Mar 2017.
[2] P. Cheng & X. Zhan, *Chem. Soc. Rev.* 2016, 45, 2544.
[3] M. Pfannmöller et al., *Nano Lett.* 2011, 11, 3099.

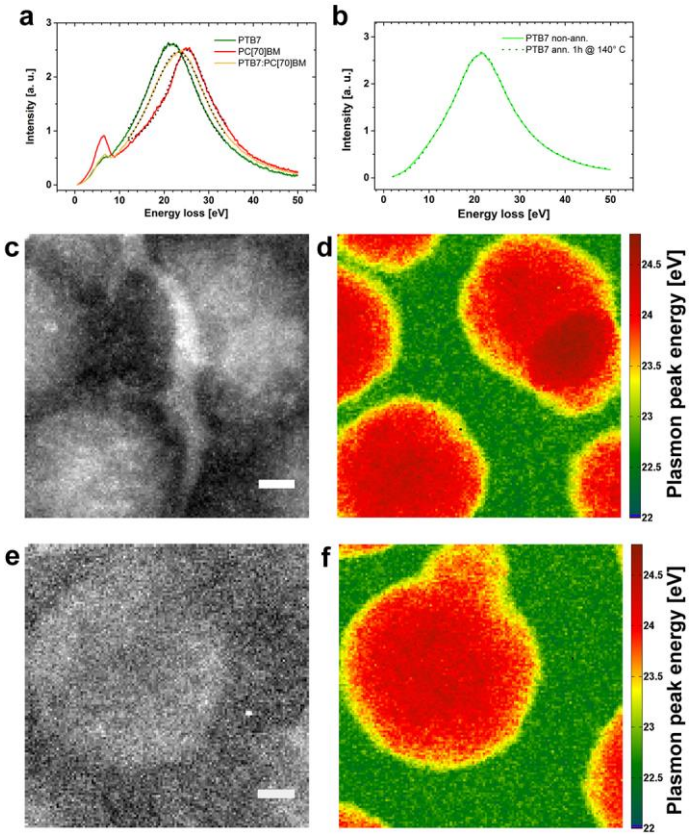

Figure 1. (a) EEL spectra from pure and mixed PTB7 and PC70BM with Lorentzian fits of the bulk plasmons. (b) Spectra of non-annealed and annealed PTB7. (c,d) Dark-field STEM and plasmon peak maps of a blend prepared without DIO. (e,f) Same preparations but after annealing for 24 h at 140°C. Scale bars: 50 nm.

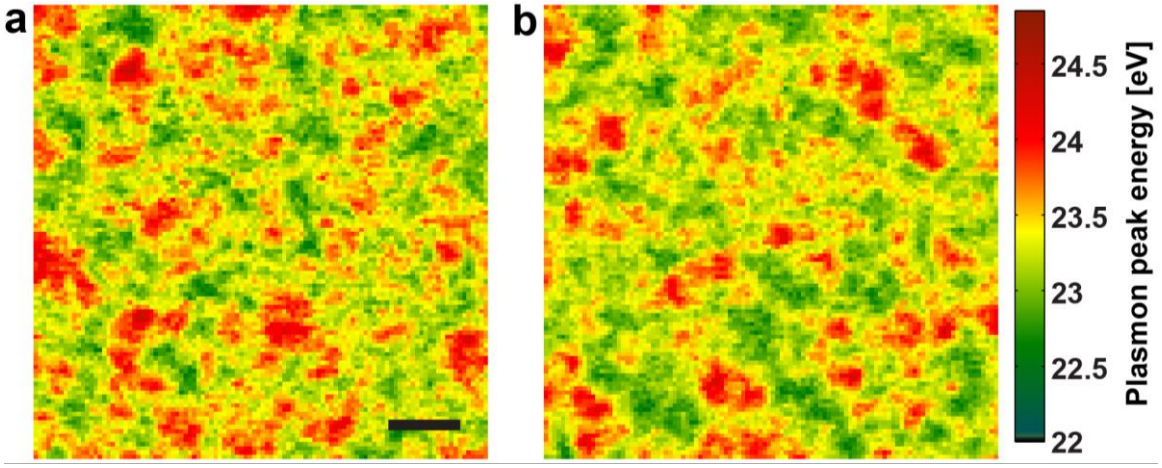

Figure 2. Plasmon peak maps of PTB7:PC70BM blends prepared with DIO inducing a fine morphology. Structural features are stable when comparing the non-annealed (a) with the sample annealed for 24 h at 140°C (b). Scale bar: 50 nm.

MS3.011
Tailoring of plasmon resonances in TiN/(Al,Sc)N superlattices for applications in energy-harvesting devices

M. Garbrecht[1], L. Hultman[1], M. H. Fawey[2,3], T. D. Sands[4], B. Saha[5]

[1]Linköping University, Linköping, Sweden
[2]Karlsruhe Institute of Technology (KIT), Institute of Nanotechnology (INT), Karlsruhe, Germany
[3]Technische Universität Darmstadt, Joint Research Laboratory Nanomaterials, Darmstadt, Germany
[4]Virginia Tech, Blacksburg, VA, United States of America
[5]University of California, Berkeley, CA, United States of America

magnus.garbrecht@liu.se

Alternative designs of plasmonic metamaterials for applications in solar energy-harvesting devices are necessary due to the high losses that pure noble metal-based nanostructures suffer from in the visible spectrum. In the present study we demonstrate the design of a material based on a superlattice architecture with systematically varying dielectric interlayer thicknesses that result in a continuous shift of surface plasmon energies. Plasmon resonance characteristics of metal/semiconductor TiN/(Al,Sc)N superlattice thin films were analyzed using aberration-corrected and monochromated STEM-EELS [1].

Surface plasmons of metallic nanostructures localize light below the diffraction limit and can generate intense electric near-fields with well-defined resonances within the optical window [2]. Applications include single-molecule spectroscopy, molecular sensors, photothermal cancer therapy, photocatalytics, and photovoltaics [3]. Plasmonic nanostructures comprise hitherto mostly noble metals like gold and silver, which are not compatible with standard CMOS technology for continuous film growth due to their limited chemical and thermal stability. As an alternative, the extraordinarily temperature stable and chemically inert transition metal nitrides have been found to exhibit plasmonic properties similar to gold [4-6].

Transition metal nitrides such as TiN can be grown as a constituent of single-crystal thin-film epitaxial metal/semiconductor superlattices with low defect densities, exhibiting high melting points and mechanical hardness [5-10]. In addition to its high chemical and thermal stability, a TiN/(Al,Sc)N superlattice architecture with metal/dielectric interfaces has been proven a promising hyperbolic metamaterial in the visible spectral range and demonstrated large enhancement of its densities of photon states which could be useful in various quantum electronic and optoelectronic applications [11]

We have investigated the influence of semiconductor interlayer thicknesses on the bulk and surface plasmons of TiN in thin film superlattices with systematically increasing (Al,Sc)N interlayer thicknesses [12]. While the TiN bulk plasmon keeps a constant value of about 2.50 eV, the surface resonance continuously decreases with increasing interlayer thickness until converging at about 2.16 eV once the interlayer reaches a thickness comparable to the one of TiN (Fig. 1).

This effect can be understood to be the result of resonant coupling between the TiN bulk- and surface plasmons across the dielectric interlayers at very low (Al,Sc)N thicknesses. The detected plasmon resonance energies correspond to wavelengths between 500-600 nm, i.e. in the visible light range of the electromagnetic spectrum. Our results show that by carefully controlling the (Al,Sc)N interlayer thickness in the superlattice stack, TiN surface plasmon energies can be tailored, potentially enhancing the efficiency of solar energy-harvesting devices.

[1] The KAW Foundation is acknowledged for Linköpings EM Laboratory.
[2] M. I. Stockman, Opt. Express 19, 22029 (2011).
[3] S. A. Maier, Plasmonics: Fundamentals and Applications (Springer Science & Business Media, 2007).
[4] G. V. Naik et al., Opt. Mater. Express 2, 478 (2012).
[5] A. A. Herzing et al., Appl. Phys. Lett. 108, 171107 (2016).
[6] B. Saha et al., Sands, Phys. Rev. B 90, 125420 (2014).
[7] B. Saha et al., Appl. Phys. Lett., 105:151904, (2014).
[8] J. L. Schroeder et.al, J. of Mater. Sci. 50: 3200-3206, (2015).
[9] B. Saha et al., Phys. Rev. B., 93, 045311, (2016).
[10] M. Garbrecht et al., J. Mater. Sci. 51(17), 8250 (2016).
[11] B. Saha et al., Phys. Rev. B 90, 125420 (2014).
[12] M. Garbrecht et al., submitted, (2017).

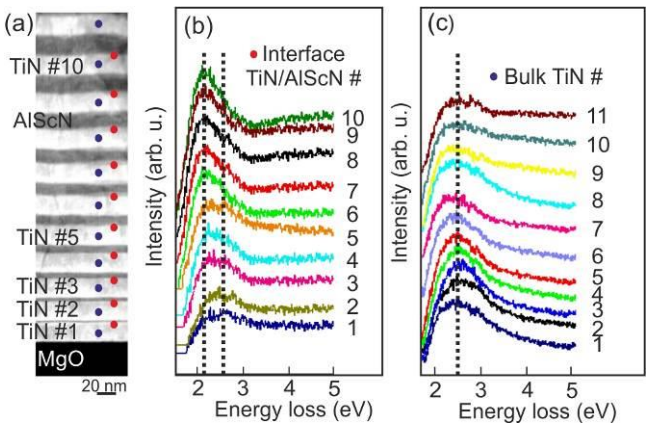

Figure 1. EELS spectra taken from the positions marked in the STEM overview (a): Surface (b), and bulk (c) TiN inelastic scattering profiles after background subtraction showing a systematic reduction in surface plasmon resonance energy with increasing (Al,Sc)N interlayer thickness (b), while the TiN bulk plasmon resonances show no systematic changes (c).

MS3.012
Understanding and controlling atomic layer deposited TiO_2 on carbon-based nanomaterials – growth, structure and interface

Y. Zhang[1], C. Guerra-Nuñez[1], I. Utke[1], J. Michler[1], P. Agrawal[1], M. D. Rossell[1], R. Erni[1]

[1]EMPA, Zürich, Switzerland

yucheng.zhang@empa.ch

Introduction: Combining unique properties of the oxide TiO_2 and carbon-based nanomaterials *i.e.* carbon nanotubes (CNTs) and single layer graphenes (SLGs) leads to enhanced performance for many important applications *e.g.* photocatalysis, solar cells, and nanoelectronics. However, controlled deposition of thin conformal oxide films on CNTs and SLGs using atomic layer deposition (ALD) is still challenging as the early stages of nucleation and subsequent growth are not yet well understood. Here we adopted ALD to grow TiO_2 on multiwalled CNTs (MW-CNTs)[1-3] and SLGs[4], using advanced (scanning) transmission electron microscopy ((S)TEM) to characterise the structure and chemistry.
Objectives: This work aims to understand nucleation and growth of ALD TiO_2 on CNTs and SLGs using (S)TEM, in order to gain control over the morphology and crystallinity of the nanocomposite.
Methods: TiO2 was deposited on MW-CNTs and SLGs using $Ti(OCH(CH_3)_2)_4$ and H_2O as precursors in an ALD reactor. Effect of deposition conditions such as temperature (60-220°C), number of cycles (20-750 cycles) and surface pre-treatment was studied using (S)TEM. Atomic-scale imaging performed on an aberration-corrected JEOL ARM200CF microscope operated at 80 kV, combined with image simulation and advanced image-processing technique *i.e.* exit-wave reconstruction (EWR), was adopted to study the atomic structure of nuclei at the early stages of ALD. The sample cross-section was analysed with STEM electron energy loss spectroscopy (EELS), to learn about bonding at the interface.
Results: The ALD temperature plays an important role in nucleation at an early stage *e.g.* after 20 cycles. As shown in Fig. 1, the nucleation density decreases with an increasing temperature. HR-TEM imaging reveals the nuclei crystallinity also depends on the temperature, with crystalline nanoparticles formed at 220°C and an amorphous thin film at 60°C. This results in different morphologies of TiO_2 on MW-CNTs or SLGs after many ALD cycles, either a conformal and amorphous layer or a coalesced polycrystalline layer comprising of faceted nanoparticles, controllable simply by tuning the ALD temperature and number of cycles[1-2]. With the knowledge of the temperature effect, an anatase TiO_2 on CNT core−shell nanostructure possessing high conformity and large domain monocrystalline was achieved by an initial deposition at a low temperature of 60°C followed by an annealing at 450°C in vacuum, the nanostructure shown in Fig. 2. In addition, atomic-scale imaging identifies the presence of rocksalt TiO at the early stage both on CNTs and SLGs[1,4,5].
Conclusion: Through (S)TEM characterization of TiO_2 deposited on CNTs and SLGs, an understanding of ALD nucleation and growth was obtained. By tuning the ALD parameters *e.g.* temperature and number of cycles, various morphologies of TiO_2 films can be achieved on inert surfaces of CNTs and SLGs. Using atomic-scale imaging, the atomic structure of the nuclei was revealed and the information regarding the interface obtained. This study paves the way towards atomic-scale engineering of nanocomposites based on metal oxides and carbon-based nanomaterials using ALD.

[1] Zhang, Y.; *et al*, *J. Phys. Chem. C* 2015**, 119**, 3379
[2] Guerra-Nunez, C.; *et al*, *Nanoscale* 2015**, 7**, 10622
[3] Zhang, Y.; *et al*, *Chem. Mater.* 2016**, 28**, 3488
[4] Zhang, Y.; *et al*, *Chem. Mater.* 2017**,** *10.1021/acs.chemmater.6b05143*
[5] This project has received funding from the European Research Council (ERC) under EUs Horizon 2020 programme (grant agreement No 681312)

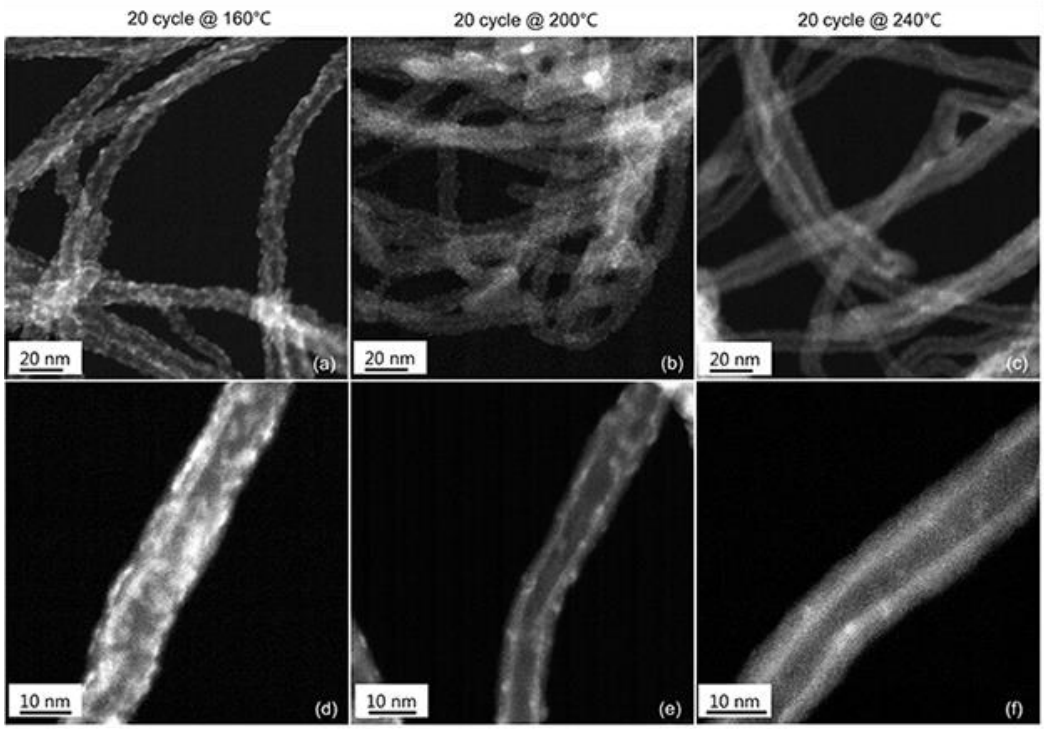

Figure 1. High angle annular dark field (HAADF) images show nucleation of TiO2 on MW-CNTs after 20 ALD cycles at different temperatures. The top row shows an overview of the sample and the bottom row zooms in on individual CNTs (Zhang Y., Reprinted by permission of American Chemical Society[1]).

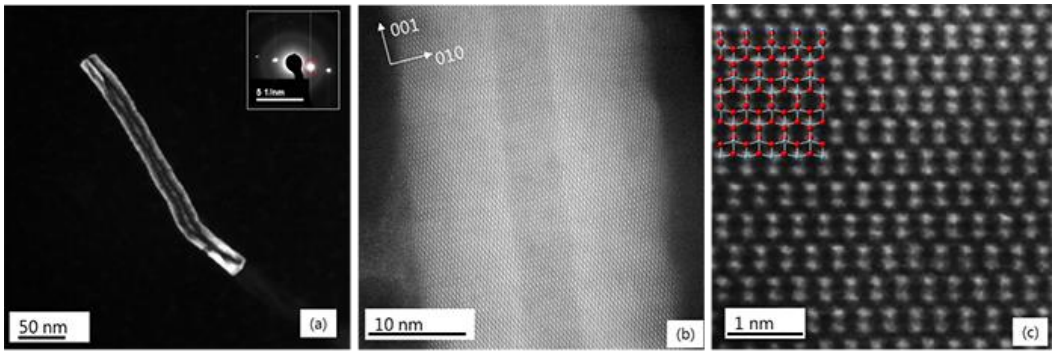

Figure 2. High conformity and large domain monocrystalline TiO_2-CNT core-shell nanostructure: (a) A dark-field image shows the size of the monocrystalline domain in the anatase layer. (b) and (c) are atomic-scale HAADF images of the anatase layer, with the superimposed atomic model of anatase (Zhang Y., Reprinted by permission of American Chemical Society[3]).

MS3.013
Precipitates in Al, Gl, Mo-doped higher manganese silicide crystals

E. Suvorova[1], Y. Solomkin[2], M. Cantoni[3], P. Buffat[3]

[1]A.V. Shubnikov Institute of Crystallography , Moscow, Russian Federation
[2]Ioffe Physical Technical Institute, St. Petersburg, Russian Federation
[3]Ecole Polytechnique Fédérale de Lausanne, CIME, Lausanne, Switzerland

suvorova@ns.crys.ras.ru

Introduction and Objectives: Doping of crystals allows modifications of their structure and therefore their physical and chemical properties. For thermoelectric materials, introducing foreign impurities aims to increase the electrical and to decrease thermal conductivity for a higher thermoelectric figure of merit. Higher Manganese Silicide (HMS), p-type thermoelectric material, has received a renewed interest owing to the abundance and low cost of the constituents.
It was expected that complex Mo, Ge, Al-doping could improve the performance of the HMS materials. However, if an improvement is observed, the expectation to get a figure of merit larger than unity is still not reached. We focus our interest to detecting the presence of secondary phases, identifying their nature, size and crystallographic relationships with the HMS matrix. The relative contribution to internal strains due to lattice misfits and thermal expansion mismatch between the matrix and precipitates was considered. All this should shed light on the reasons interfering achievement of higher parameters
Materials and Methods: HMS samples doped either with Ge only at different concentrations - Mn(Si0.99Ge0.01)1.75 and Mn(Si0.995Ge0.005)1.75 - as well as with Al, Ge, and Mo together with the general formula (Mn0.98Mo0.02)[(Si0.98Ge0.02)1.75]0.99Al0.01 were studied by SEM (Zeiss MERLIN) and X-rays EDS (Oxford Instruments, SDD detector) at 1 - 30 kV accelerating voltages.
The TEM investigation was performed with a FEI Tecnai Osiris microscope fitted with a ChemiSTEM EDS microanalyser (200 kV X-FEG). The crystal structure of secondary phases was studied by conventional BF/TEM, HRTEM, and SAED. The map elements distribution and phase compositions at the nanoscale were obtained by X-ray EDS spectrometry in BF-HAADF STEM using quantitative analysis ESPRIT (Bruker) software.
The crystallographic texture of the HMS matrix and secondary phase precipitates and orientation relationships were derived from electron backscattered diffraction (EBSD) patterns obtained on an ingot longitudinal section along the growth direction X-axis (Fig. 1) in a SEM Philips XL-30 FEG fitted with an HKL Channel 5 system (Oxford Instruments) and by SAED on transverse TEM thin foils.
Results and Conclusion: The central region about 3 cm long is the only one suitable for applications in the investigated (Fig. 1a) ingots about 8 cm long and 1.1 cm nominal diameter.
HMS ingot is a mosaic crystal with the [2 17 3] direction pointing to the growth direction (X-axis). The structure of the HMS is Mn4Si7. The secondary phases Ge-Si (Fig.2), MoSi2, MnSi, Mn5Si3 form in Mn4Si7 doped by Ge, Mo, and Al. Segregation of Al was observed at the interfaces Ge-Si/ Mn4Si7.
Matrix/precipitates orientation relationships allowed us to find lattice misfits and to compare their contribution with the contribution of the thermal expansion mismatch to crystal deformation. Relaxation can occur by formation of interfacial dislocations and cracking if the difference between lattices is large. The role of thermal expansion mismatch is rather negligible in comparison with the lattice misfits.
The spread of values of thermoelectrical parameters and still low figure of merit for HMS materials can be explained by formation of cracks in crystals. Doping slightly improved HMS performance due to smaller deformations with lower level of cracking and suppression of MnSi precipitates formation having metallic properties.

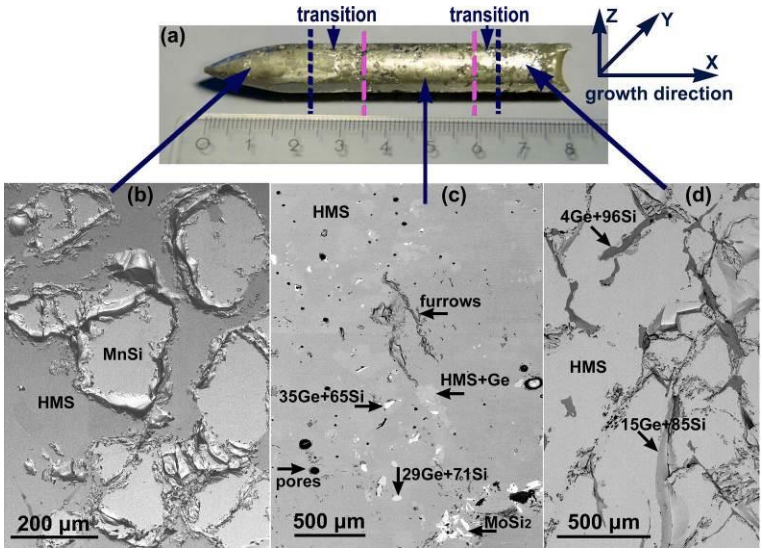

Figure 1. HMS crystal (a), SEM from the heterogeneous parts (b, d); central part (c).

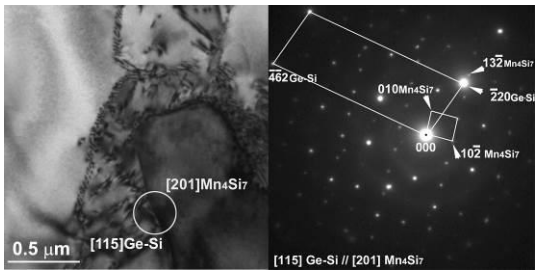

Figure 2. Interface between Mn4Si7 and Ge-Si precipitate. TEM image and SAED.

MS3.P002
Mechanical properties and failure of Ag nanowire transparent electrodes studied by means of in situ tensile testing in the TEM

N. Schrenker[1], M. Mačković[1], G. D. Spyropoulos[2], M. Göbelt[3], S. Christiansen[4], C. J. Brabec[2]
E. Spiecker[1]

[1]Friedrich-Alexander University Erlangen-Nuremberg, Institute of Micro- and Nanostructure Research & Center for Nanoanalysis and Electron Microscopy (CENEM), Erlangen, Germany
[2]ZAE Bayern: Bavarian Center for Applied Energy Research, Erlangen, Germany
[3]Max Planck Institute for the Science of Light, Erlangen, Germany
[4]Freie Universität Berlin, Physics Department, Berlin, Germany

nadine.schrenker@fau.de

Organic (opto)electronics have undergone a rapid development in recent years. Applications are for instance organic solar cells (OSCs), flexible displays or "smart clothing", which means clothing with integrated electronics. For such applications it is decisive that the active layers as well as the electrodes withstand mechanical loading. Indium tin oxide (ITO), which is still a common material as electrode, behaves brittle under deformation and is relatively expensive. Metallic nanowire networks, especially silver nanowires (AgNWs), are highly promising alternatives [1,2]. They fulfill the requirement of a low sheet resistance combined with high transmittance. On a macroscopic scale bending tests as well as tensile tests revealed the excellent performance of Ag NW films, since the increase of resistance is small compared to ITO films [3,4].
In order to understand failure mechanisms and prospectively optimize the deformation behavior of AgNW electrodes *in situ* mechanical testing in the TEM is conducted. *In situ* tensile tests of single Ag NWs were performed with a Hysitron PI95 TEM Picoindenter™. Moreover, tensile tests of AgNW networks on different flexible substrates such as PEDOT:PSS and PET, which are both used for flexible OSCs, were performed with a Gatan TEM straining holder 654. For these straining tests a dogbone-shaped sample of the AgNW polymer composite is cut in a Focused Ion Beam. The Ag NW network is prepared by doctor blading. On a nanometer scale tensile tests of single 5-fold twinned Ag NWs show a ductile behavior and a size effect of the strength. The pristine NWs are almost defect free except for the twin boundaries. *In situ* testing reveals nucleation and propagation of partial dislocations during straining. Tensile tests of Ag NW networks in the TEM provide direct insights in the behavior of the network as well as the response of the whole AgNW polymer composite (Fig. 1(a)). A map of the local strain was determined via digital image correlation and depicts a homogeneous strain distribution (Fig. 1 (b)). The fracture behavior of the Ag NWs is ductile (Fig. 1 (c,d)), whereas the PEDOT:PSS film fracture appears to be rather brittle. Since the interaction of mechanical and electrical properties is crucial for applications in (opto)electronics, we are currently working on combining *in situ* mechanical and electrical measurements in the TEM.

[1] Guo, F. *et al., Energy Environ. Sci.* **8,** (2015).
[2] Yao, S. & Zhu, Y, *Adv. Mater.* **27,** 1480–1511 (2015).
[3] Ok, K.-H. *et al.,Sci. Rep.* **5,** 9464 (2015).
[4] Nickel, F. *et al., Sol. Energy Mater. Sol. Cells* **130,** 317–321 (2014).

Acknowledgement
The authors gratefully acknowledge the financial support of the German Research Foundation (DFG) within the research training group GRK 1896.

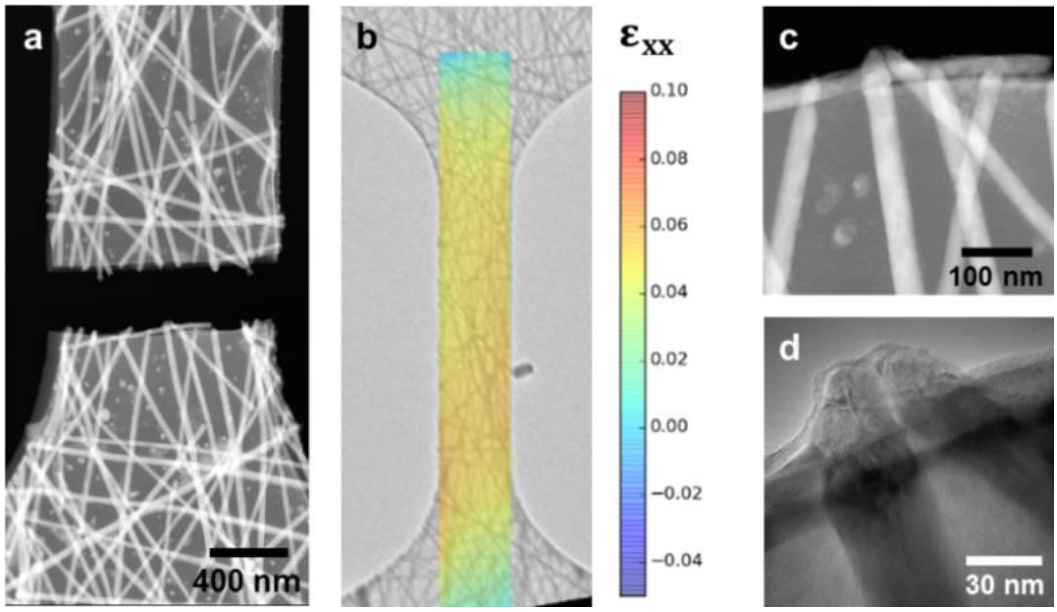

Figure 1. (a) STEM image of an Ag NW network on a PEDOT:PSS film after fracture of an *in situ* tensile test in the TEM. (b) Determination of the local strain of the sample shown in (a) via digital image correlation). (c) and (d) depict the ductile fracture of the Ag NWs.

MS3.P003
Growth and degradation of octahedral Pt-alloy nanoparticle catalysts for fuel cells

M. Heggen[1], M. Shviro[1], L. Gan[2], C. Cui[2], P. Strasser[2], R. Dunin-Borkowski[1]

[1]Forschungszentrum Jülich GmbH, Ernst Ruska Centre, Jülich, Germany
[2]TU Berlin, Department of Chemistry, Berlin, Germany

m.heggen@fz-juelich.de

Octahedral Pt-Ni nanoparticles are highly attractive as fuel cell catalysts due to their extraordinarily high activity for the oxygen reduction reaction (ORR). A deep understanding of their atomic-scale structure, degradation and formation is a prerequisite for their use as rationally designed nanoparticle catalysts with high activity and long-term stability.
Here, we present results from a comprehensive microstructural study of the growth and degradation behavior of various octahedral Pt-alloy nanoparticles using transmission electron microscopy (TEM) and Cs-corrected high-angle annular dark-field scanning transmission electron microscopy (HAADF-STEM) combined with electron energy-loss spectroscopy (EELS) and energy-dispersive X-ray spectroscopy (EDX). We show that octahedral nanoparticles often show compositional anisotropy in the form of Ni-rich (111) facets, which lead to complex structural degradation during ORR electrocatalysis. The Ni-rich (111) facets are etched preferentially, resulting in the formation of first concave octahedra and then Pt-rich skeletons that have less active facets [1]. Furthermore, we reveal element-specific anisotropic growth as the reason for the compositional anisotropy and limited stability. During solvothermal synthesis, a Pt-rich nucleus evolves into precursor nanohexapods, followed by the slower step-induced deposition of Ni on the concave hexapod surface to form octahedral facets (Figure) [2]. Whereas the growth of Pt-rich hexapods is a ligand-controlled kinetic process, the step-induced deposition of the Ni-rich phase on the concave surface resembles a thermodynamically-controlled process and is accomplished over a much longer time. Furthermore, we demonstrate how Pt atom surface diffusion may produce a protective Pt surface layer on top of the Ni-rich facets, resulting in advanced and more stable octahedral catalysts. During *in situ* heating up to 800 °C using a microelectromechanical systems (MEMS) chip heating holder (DENSsolutions, Delft, NL), we observed that Pt-rich corner atoms diffuse and fill the concave Ni-rich {111} facets, thereby forming octahedral nanoparticles with flat Pt-rich {111} surfaces [3].

References:
[1] Gan L, Cui CH, Heggen M, Dionigi F, Rudi S, Strasser P, Science 2014; 346: 1502.
[2] Cui CH, Gan L, Heggen M, Rudi S, Strasser P, Nature Materials 2013; 12: 765.
[3] Gan L, Heggen M, Cui CH, Strasser P, ACS Catalysis 2016; 6: 692.

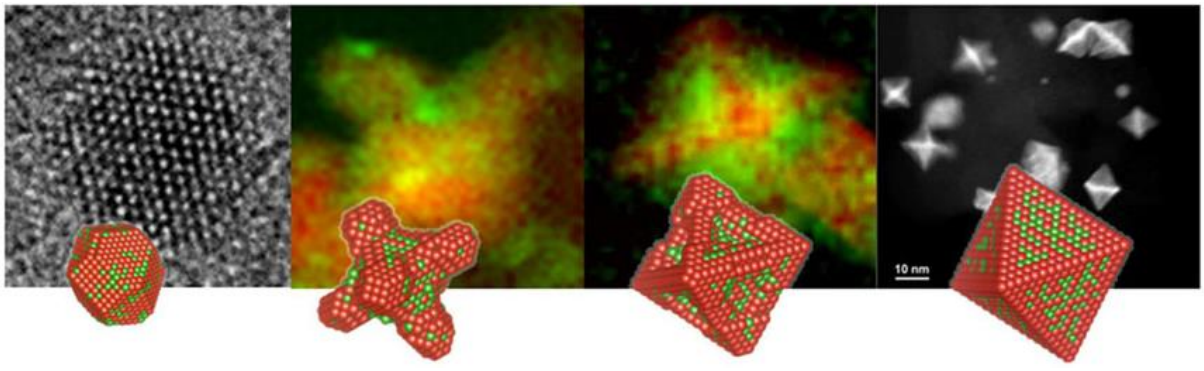

Figure 1. Microstructural study comprising high-resolution TEM, HAADF-STEM and EELS mapping, uncovering an element-specific compositionally-anisotropic growth mechanism of octahedral PtNi nanoparticles. The electron microscopy images and the corresponding models show the elemental distributions of Pt (red) and Ni (green) in particles that are at different states of growth after 4, 8, 16, and 42 hours of solvothermal synthesis.

MS3.P004
Advanced characterization of electrodes using electron- and X-ray microscopy techniques

J. Jankovic[1], D. Susac[1], A. Ash[1], A. Putz[1], J. Stumper[1]

[1]Automotive Fuel Cell Cooperation, R&D, Burnaby, Canada

jasna.jankovic@afcc-auto.com

Introduction: Proton Exchange Membrane Fuel Cells (PEMFC) are being considered as one of the most promising solutions to replace internal combustion engines for zero emission transportation. Fuel cells in general convert chemical energy of a fuel (typically hydrogen) and oxidant (air or oxygen) into useful electricity via electro-chemical reactions, producing only water as a byproduct. The reactions happen in the heart of the fuel cell – the membrane electrode assembly (MEA), consisted of two porous electrodes and a proton exchange polymer membrane between them. Efficiency and durability of a fuel cell very much depends on the microstructure and spatial distribution of all the components in the electrodes, especially in the catalyst layer. Understanding the electrode microstructure and its effects on performance is crucial for further development of fuel cells. At AFCC, we have been developing novel methods for PEMFC electrode material characterization and imaging, enabled by the advancement of the microscopy techniques and computer calculation power. This talk will summarize some of our material characterization methods and approaches.
Objectives: Objective of our work is to provide structural parameters for the components of fuel cells, most commonly catalyst layers, utilizing advanced microscopy and spectroscopy techniques. Furthermore, the obtained structural parameters are correlated to the catalyst layer properties, such as electrical conductivity and gas diffusivity, and in-situ fuel cell performance. The structure-property-performance correlations help fundamental understanding of the processes during fuel cell operation and enable improvement in efficiency and durability of fuel cells.
Materials and Methods: Various catalyst layers (cathode and anode decals), as well as beginning of life (BOL) and end of life (EOL) MEAs have been analyzed. Porous catalyst layers typically consist of carbon-supported Pt, as catalyst for hydrogen oxidation reaction (HOR) or oxygen reduction reaction (OER), mixed with proton-conductive perfluorosulfonic acid (PFSA) ionomer. The analyzed anodes may also contain oxygen evolution reaction catalysts (OER). Microscopy and spectroscopy techniques, such as Scanning Electron Microscopy with Focused Ion Beam and Energy Dispersive Spectroscopy (SEM-FIB, SEM-EDX), Transmission Electron Microscopy with Energy Dispersive Spectroscopy (TEM-EDX), 3D Electron Tomography, and Micro-Computed Tomography (m-CT), were utilized to obtain a number of structural parameters.
Results: Examples of the advanced characterization of catalyst layers and correlations to layer properties and performance will be provided. For instance, methods for obtaining OER catalyst agglomerate size and apparent surface area using SEM-EDX and TEM-EDX, and correlation to layer conductivity and performance are explained. Further, cathode porosity and pore size distribution determination using SEM-FIB and TEM-EDX will be shown. A range of catalyst layer structural parameters possible to determine from TEM-EDX and some correlations with performance will also be reviewed. Finally, an advanced approach of 3D multi-scale imaging and property simulation will be shown.
Conclusion: Understanding of the correlations between electrode microstructure, properties and performance of the Proton Exchange Membrane Fuel Cells is crucial to further improve their efficiency and durability. Advanced microscopy and spectroscopy techniques have been utilized to extract a number of structural parameters that have been successfully correlated to electrode properties and fuel cell performance. These novel approaches are key for further understanding and performance improvement of fuel cells, bringing them closer to mass commercialization.

MS3.P005
Critcat – towards replacement of critical catalyst materials by improved nanoparticle control and rational design

X. Wei[1], M. Heggen[1], L. Liu[2], J. Akola[3], R. Dunin-Borkowski[1]

[1]Forschungszentrum Jülich GmbH, Jülich, Germany
[2]International Iberian Nanotechnology Laboratory (INL), Braga, Portugal
[3]Tampere University of Technology, Tampere, Finland

x.wei@fz-juelich.de

CritCat, a project funded by the Horizon 2020 Framework Programme for Research and Innovation of the European Commission, is aimed towards the replacement of critical catalyst materials by improved nanoparticle control and rational design. Catalytic technology for sustainable energy conversion and storage depends strongly on the use of rare platinum group metals (PGMs), and will therefore be greatly affected by their imminent shortage. The CritCat project is intended to provide solutions for the substitution of PGMs by exploring the properties of ultra-small transition metal (TM) alloy, carbide, phosphide, sulphide and oxide nanoparticles, in order to achieve optimal catalytic performance with earth-abundant materials. The focus of the project is on industrially-relevant chemical reactions and emerging energy conversion technologies, in which PGMs currently play an instrumental role, particularly in the context of hydrogen and synthesis gas fuels. Improvements in the sizes, shapes and surface structures of nanoparticle catalysts will be achieved by using novel cluster/nanoparticle synthesis techniques to produce samples of improved quality, combined with experimental characterization, high-level computer simulations of catalytic reactions and algorithms for large-scale materials screening and machine learning based on theoretical and experimental input.
In this contribution, we will introduce the background and objectives of the CritCat project and present preliminary microstructural investigations on novel ultra-small TM alloy clusters and carbide, phosphide, sulphide and oxide nanoparticle catalysts. Nickel phosphides, for example, are efficient electrocatalysts for the hydrogen evolution reaction (HER). We present the results of a microstructural investigation on the structure and composition of mixed Ni5P4, Ni2P, and NiP2 nanosheets grown on Ni foam. A statistical analysis on the electron diffraction patterns reveals that the Ni5P4 nanosheets are mostly oriented along the [001] zone axis. The electrocatalytic reaction mechanism of the nickel phosphide nanosheets subjected to a catalytic test in 0.5 M H2SO4 is further investigated by using energy dispersive X-ray spectroscopy.

MS3.P006
Correlative scanning/transmission electron microscopy and spectroscopy on perovskite solar cells

C. Harreiß[1], T. Yokosawa[1], P. Schweizer[1], S. Rechberger[1], Y. Hou[2], I. Levchuk[2], C. J. Brabec[2]
E. Spiecker[1]

[1]Institute of Micro- and Nanostructure Research & Center for Nanoanalysis and Electron Microscopy (CENEM), Erlangen, Germany
[2]Institute of Materials for Electronics and Energy Technology, Erlangen, Germany

christina.harreiss@fau.de

Inorganic-organic hybrid solar cells have attracted great attention in the field of photovoltaic technology within the last few years, since their power conversion efficiencies rose from 3.8% to about 22% in the last seven years.[1] This tremendous progress can be traced back to the numerous advantages of perovskite solar cells like low-cost and simple fabrication processes as well as high absorption over the visible range, high flexibility in perovskite design and excellent charge transport properties.[1,2]
Since the morphology of the perovskite solar cells highly influences the device performance and efficiency, it needs to be investigated in order to get a better understanding about the whole device. Especially the morphology of the perovskite absorber layer that highly depends on the chemical composition of the precursors and can be further influenced by thermal annealing or the use of additives, should be investigated since it determines the charge transportation properties and thus also the efficiency of the solar cell.
Transmission electron microscopy (TEM) and focused ion beam scanning electron microscopy (FIB/SEM) are approved techniques to study the morphology of perovskite solar cells. In this work the possibility of correlative scanning and transmission electron microscopy as analysis tool for perovskite solar cells in combination with spectroscopic techniques like energy dispersive X-ray spectroscopy (EDXS) will be demonstrated. First of all the morphology of the perovskite film that plays a crucial role in determining the solar cells efficiency can be investigated by performing top-view SEM images. The top-view SEM image of the perovskite film gives information about the film quality and the grain size. In Figure 1A a top-view SEM image of a perovskite film on a PEDOT:PSS substrate is pictured with a uniform film quality without any pinholes and grain sizes around 140 to 280 nm. Figure 1B shows a cross-sectional FIB/SEM image of the same perovskite device. Thereby the thickness and also the quality of every layer in the perovskite solar cell can be analyzed. In this case, uniform and well-separated layers can be identified. Additionally, cross-sections of the same perovskite solar cell can be investigated in the TEM and high resolution TEM (HRTEM) images can be recorded in order to get information about the orientation of the grains in the perovskite films, which is up to now very unique in the field of perovskite solar cells (Fig. 1C/D). Furthermore, we can determine the elemental distribution within the perovskite film by simultaneous EDXS measurements (Fig. 1E).
Recently there are some developments in the field of perovskite research towards the design of new forms of perovskites like perovskite nanoparticles[3] or perovskite hollow spheres (Fig. 2). Currently investigations regarding the inner morphology of perovskite hollow spheres via correlative FIB/SEM, TEM and EDXS measurements are under way in our laboratories.

References:
[1] N. K. Elumalai, M. A. Mahmud, D. Wang, A. Uddin, *Energies* **2016**, *9*, 861.
[2] F. H. Isikgor, B. Li, H. Zhu, Q. Xu, J. Ouyang, *J. Mater. Chem. A* **2016**, *4*, 12543.
[3] I. Levchuk, P. Herre, M. Brandl, A. Osvet, R. Hock, W. Peukert, P. Schweizer, E. Spiecker, M. Batentschuk, C. J. Brabec, *Chem. Commun.* **2017**, *53*, 244.

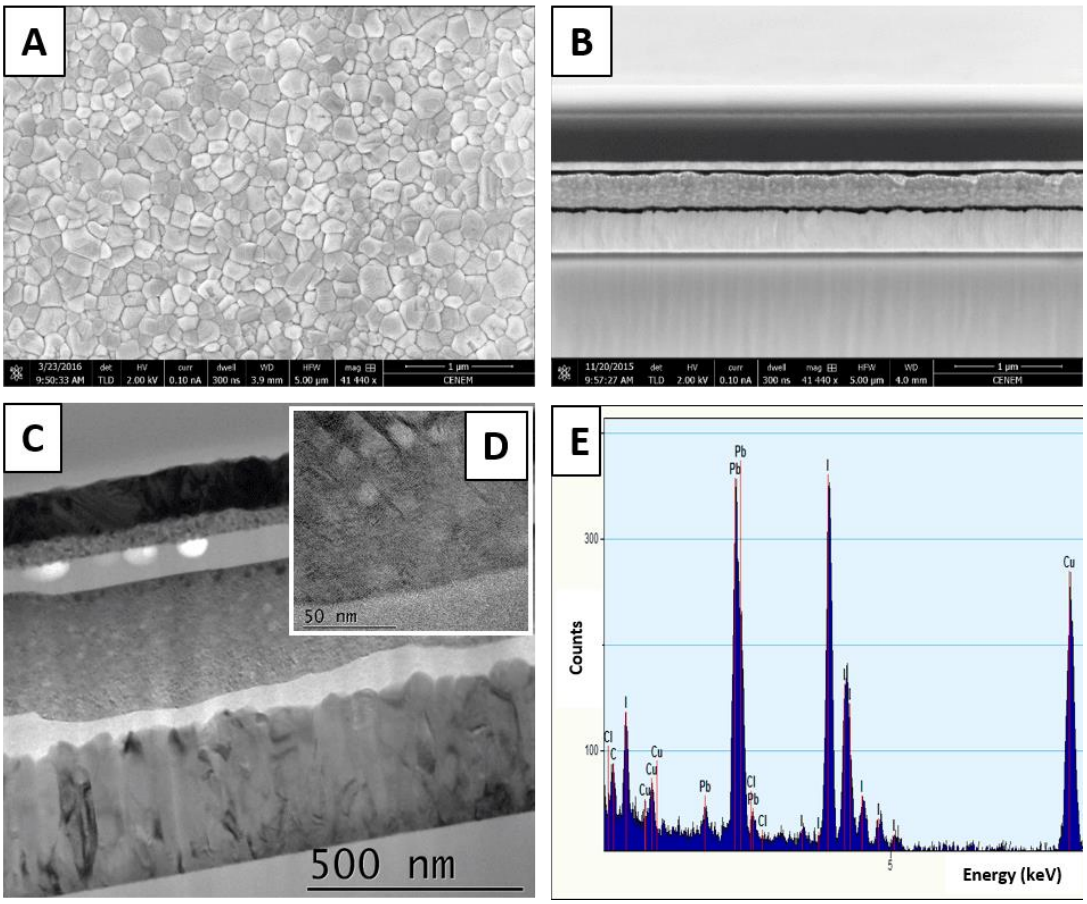

Figure 1. Top-view SEM image of the perovskite film prepared on a PEDOT:PSS substrate (A), cross-sectional FIB/SEM image of a complete perovskite device (B), bright-field (BF) cross-sectional TEM image of the same perovskite device (C), HRTEM image of the perovskite absorber layer (D) and EDXS analysis of the perovskite absorber layer (E).

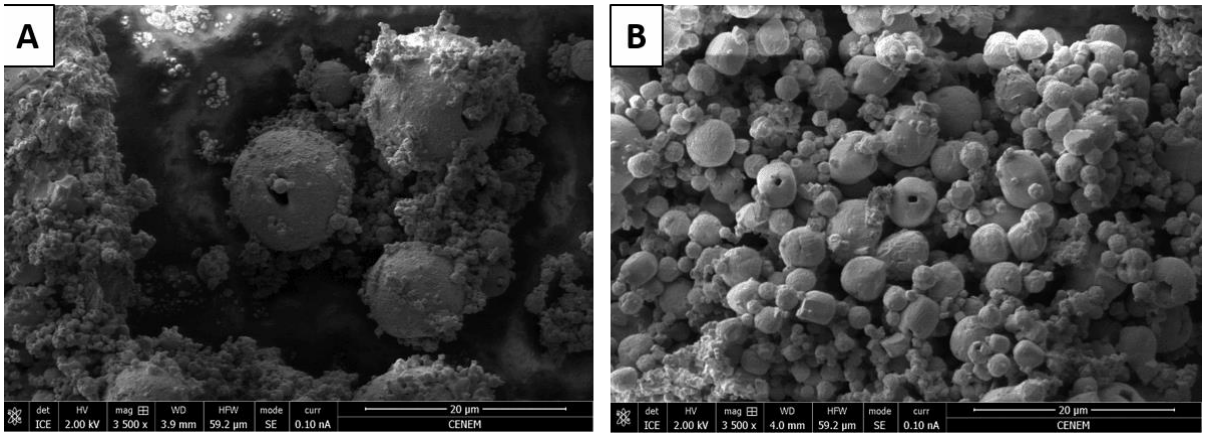

Figure 2. SEM images of $MAPbI_3$ (A) and $MAPbBr_3$ perovskite hollow spheres (B).

MS3.P007
Transmission electron microscopy of two-dimensional MXene sheets

D. Anjum[1], B. Ahmed[2], H. Alshareef[2]

[1]King Abdullah University of Science & Technology (KAUST), Imaging and Characterization Lab, Thuwal, Saudi Arabia
[2]King Abdullah University of Science and Technology (KAUST), MAterials Science & Engineering, Thuwal, Saudi Arabia

dalaver.anjum@kaust.edu.sa

Two-dimensional (2d) materials possess a number of interetsing bulk properties due to quantum confinement effects [1]. As a result, these perform better than their bulk counterparts for various applications including electronics and energy-storage. MXene is a generic name for a family of 2d transition metal carbides and nitrides. MXenes are prepared by etching the Group A metal from its parent MAX (Ti3AlC2) phase [2]. It can be applied as anode material for lithium ion baterry (LIB) due to its 2d nature which provides gallery spacing for Li+ ion shuttling during charge/discharge process [3]. As-prepared MXene shows reasonable charge storage performance and excellent cyclic stablity. However, hydrogen peroxide (H2O2) treatment of these sheets forms titanium oxide (TiO2) on their surface and consequently doubles their charge storage capacity [4]. Atomic structure of MXenes, in fact, determines their bulk properties and thus it is essential to charcterize them with a technique capable of providing atomic scale resolution e.g. transmission electron microscopy (TEM). Hence we present herein a study on the TEM-characterization of both as-prepared and partially-oxidized MXene sheets.
MXene sheets were prepared by treating Ti2AlC powder with hydroflouric acid (HF) and while partially-oxidized MXene sheets were prepared by oxidizing those with H2O2 at room temperature [4]. A TEM of model Titan 80-300 ST from FEI Company was utilized to carry out the analysis. Microscope was also equipped with a GIF to perform energy-filtered TEM (EFTEM) and electron energy-loss spectroscopy (EELS) anlayses for generating the elemental maps of Ti, C, and O and applying the white lines analysis on the Ti-L23 edge of Ti, respectively. In thi way, the ratios of Ti-L3 to Ti-L2 peaks were measured and then linked to the valence states of Ti in these samples [5].
TEM anlaysis revealed a large and unifrom sizes for as prepared MXene sheets (Figure 1A). Their corresponding selected area electron diffratcion (SAED) pattern and HRTEM images were found to be free of noise (Figure 1B-C). It can be attributed to superier structural packing of MXene sheets. Side-view image of sheets also revealed a high quality (Figure 1D). The darker regions in the EFTEM image of partially-oxidized MXene sheets can be attributed to the presence of partially oxidized regions on their surfaces (Figure 2A). It was confirmed by a composite elemental map of Ti, C, and O in Figure 2C. An EELS spectrum, in Figure 2B, of partially oxidized MXene sheet showed the presence of all elements including Fluorine (F). The incorporation of F, basically, took place during the treatment of MAX with HF and it generally functionalizes the surface. Finally the ratio of Ti-L3 to Ti-L2 of Ti-L23 energy-loss edge was determined and it was found to be decreasing with increasing O concentraion which can be attributed to the decrease in Ti+3 fraction in MXene sheets.
In summary, these results demonstrate that a TEM analysis provides the atomic scale information on the structure of MXene sheets and also it enables to establish their structure-property relationship. Hence its application to 2d materials is essential for energy-related applciations.

References:
[1] Wonbong Choi *et al*, Critical Reviews in Sol. Stat. & Mat. Sci., **35** (**2010**) p.52-71.
[2] M. Naguib *et al*, Advanced Materials 23 (**2011**) p. 4248-4253.
[3] Raghavan B. Rakhi *et al*, Chemistry of Materials, 27, (**2015**) p. 5314−5323.
[4] Bilal Ahmed *et al*, Nanoscale, **8**, (**2016**) p. 7580-7587.
[5] Peter. A. van Aken *et al.*, Phys. Chem. Minerals 29 (**2002**) p. 188-200.

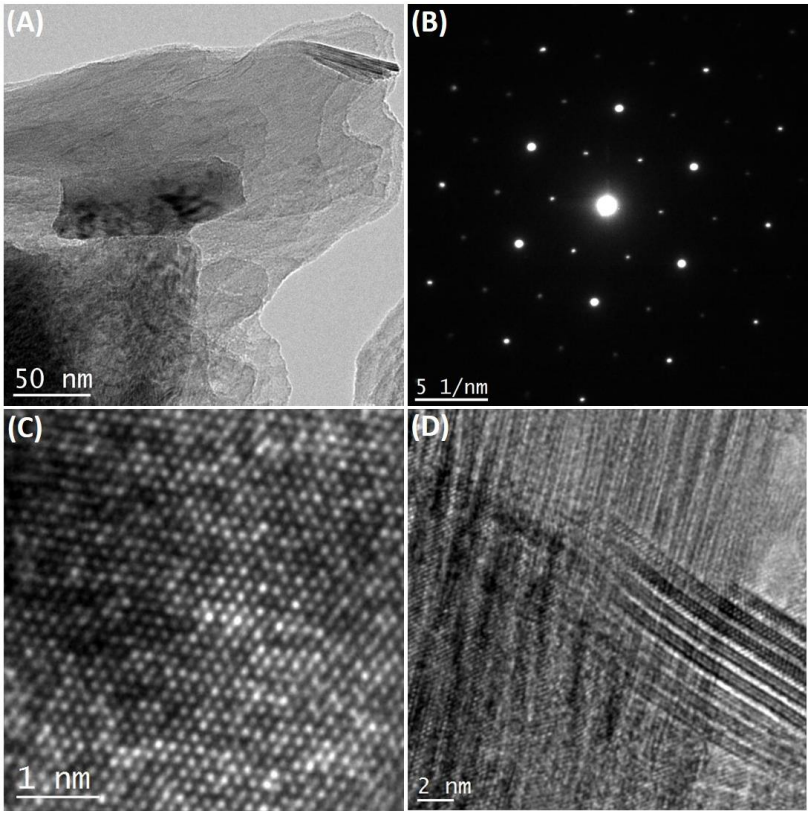

Figure 1. TEM analysis of MXene sheets. (A): Plan-view TEM image. (B): Corresponding SAED pattern showing the hexagonal symmetry for the structure of MXene. (C): HRTEM image from the flake shown in (A). (D): Side-view HRTEM image from a flake.

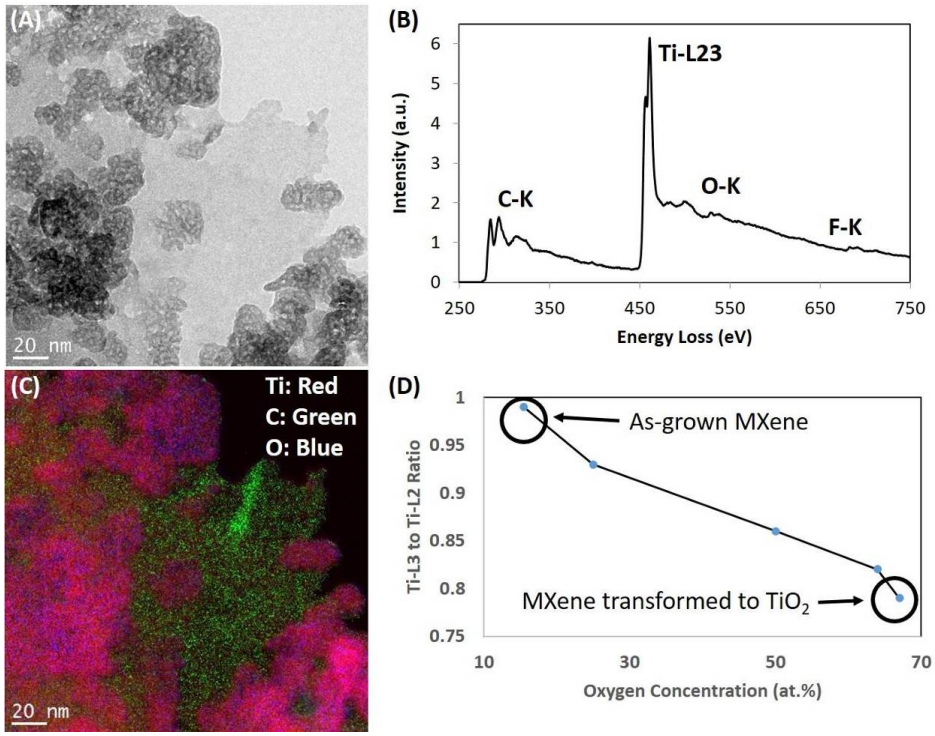

Figure 2. EFTEM analysis of partially oxidized MXene sheet. (A): Plan-view TEM image. (B): Corresponding background removed EELS spectrum. (C): RGB Composite map of Ti, C, and O elements. (D): Ti-L3 to Ti-L2 ratios as a function of oxygen concentration.

MS3.P009
Advanced nanoanalytics of energy materials using SIMS-based correlative microscopy

S. Eswara[1], L. Yedra[1], J. N. Audinot[1], T. Wirtz[1]

[1]Luxembourg Institute of Science and Technology (LIST), Advanced Instrumentation for Ion Nano-Analytics (AINA), MRT Department, Belvaux, Luxembourg

santhana.eswara@list.lu

Innovations in the development of next-generation energy materials rely crucially on the availability of advanced techniques that can overcome a multitude of characterization challenges. To develop new design concepts and to understand the physical and chemical characteristics of the materials, it is often necessary to complement high-resolution structural imaging with: (i) high-sensitivity mapping of dopants, (ii) analysis of isotopes and (iii) analysis of low Z elements (H, Li, B). Transmission Electron Microscopy (TEM) is well-known for high-resolution structural imaging down to atomic resolution, but, the conventional analytical methods associated with TEM such as Energy Dispersive X-ray Spectroscopy (EDX) or Electron Energy-Loss Spectroscopy (EELS) are often inadequate to meet the challenges listed above. On the other hand, Secondary Ion Mass Spectrometry (SIMS) is an excellent technique for the analysis of dopants and isotopes of all elements of the periodic table. However, the lateral resolution of SIMS imaging is fundamentally limited by the ion-solid interaction volume. Thus, the individual techniques have their own specific strengths and limitations.
To overcome the individual limitations of the techniques, we developed correlative multi-technique paradigms combining TEM-SIMS [1] and Helium Ion Microscopy (HIM)-SIMS [2]. The application of these new correlative techniques will be discussed in the context of energy materials with examples which correspond to the three characterization challenges listed above. The examples also represent three broad categories of energy materials: (i) Solar Energy: Direct imaging of dopant distributions across Si-metallization interface [3], (ii) Hydrogen Energy: Use of isotopes to study embrittlement mechanisms [4] and (iii) Lithium Batteries: correlative structural-chemical analysis of lithiated electrodes.

References:
[1] L. Yedra, S. Eswara, D. Dowsett, T. Wirtz, In-situ Isotopic Analysis at Nanoscale using Parallel Ion Electron Spectrometry: A Powerful New Paradigm for Correlative Microscopy, Sci. Rep. 6, 28705, 2016
[2] P. Gratia et al, Intrinsic Halide Segregation at Nanometer Scale Determines the High Efficiency of Mixed Cation/Mixed Halide Perovskite Solar Cells, J. Am. Chem. Soc. 138 (49) 15821–15824, 2016
[3] P. Kumar et al, Direct imaging of dopant distributions across the Si-metallization interfaces in solar cells: Correlative nano-analytics by electron microscopy and NanoSIMS, Solar Energy Materials and Solar Cells, 160, 398-409, 2017
[4] R. Hu et al, Spatially-resolved observation of trapped hydrogen/deuterium in TWIP steel, Int. J. Hyd. Energy (Submitted), 2017

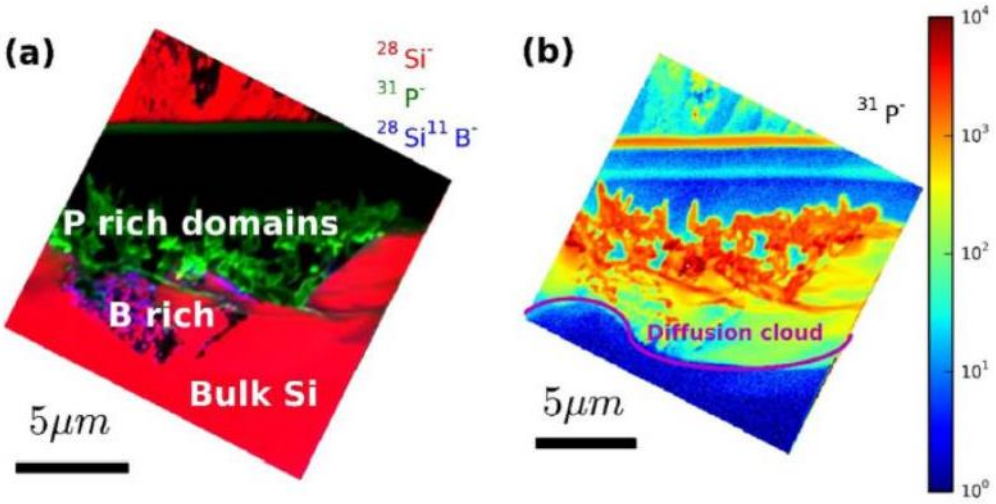

Figure 1. An example application in solar energy materials in which dopant distributions are imaged directly across a Si-metallization interface. (a) Correlative overlay image of Si, P and B, (b) distribution of P in the emitter area. Note, the P distribution in log scale covers 4 orders-of-magnitude. Adapted from our work in [3].

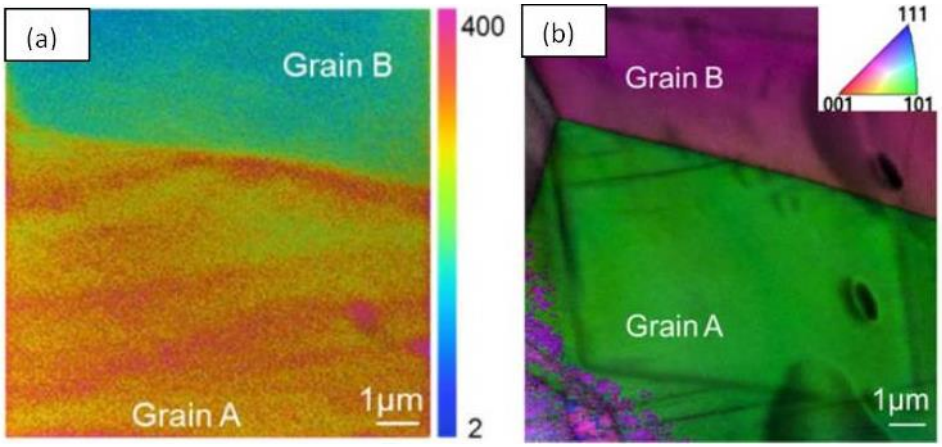

Figure 2. An example application in hydrogen energy materials in which deuterium is used as an isotopic label to study correlation between microstructure and chemistry. (a) SIMS ratio image of D/h. (b) EBSD map of the same area. The correlative imaging suggests that there is a local enrichment of deuterium along the nanotwins. This has implications in understanding hydrogen embrittlement mechanisms. Adapted from our work in [4].

MS3.P010
TEM investigation of electrolyte dependent altering of a highly efficient silicon microwire anode type

G. Neubüser[1], S. Hansen[1], R. Adelung[1], L. Kienle[1]

[1]Kiel University, Kiel, Germany

gn@tf.uni-kiel.de

Introduction: Recently developed silicon microwire array anodes supplied enormous capacities up to 4200 mAh/g[1] that surpass currently available carbon based types by a factor of ten. An enormous surface to volume ratio enables such a high capacity. Initially crystalline silicon wires take up lithium ions (lithiation) from the electrolyte solution and a surface amorphization accompanied by a volume increase about a factor of four takes place[2]. Unfortunately these processes normally cause a capacity drop especially in the first three to five cycles as the charging reaction´s reversibility is insufficient. In our work this problem was overcome by tailoring the electrolyte with suitable polymeric additives that stabilized the solid electrolyte interface (SEI) and improved the anode´s long term stability.
Objectives: The main objective is the TEM assisted characterization of a new kind of anode that provides both, very high capacities and high charging rates in order to use it for high performance batteries. Charging effects on initially crystalline silicon in dependence of the respective electrolytes and charging speeds are being investigated by transmission electron microscopy (TEM). Further the focus lies on chemical and structural characterization of the SEI.
Materials and Methods**:** Investigated anodes consist of arrays of crystalline silicon microwires with thicknesses of about 1.2 µm and lengths of 70 µm[3]. Different electrolyte additives e.g. diethylene glycol or lithium nitrate have been used in order to obtain better cycling stability. For a proper sample handling highly specialized preparation processes were adapted including Focused Ion Beam (FIB) milling and Ultramicrotomy. Air sensitive samples were prepared in a glove box under argon atmosphere and transferred in a sealed bag to the TEM. Experiments were conducted by methods of scanning electron microscopy (SEM) and TEM. For microstructural characterization high resolution TEM and selected area electron diffraction (SAED) have been performed. Chemical analyses comprised scanning TEM-EDX and electron energy loss spectroscopy (EELS).
Results**:** Different TEM investigations observed degradation effects namely amorphization and delamination which are responsible for occurring decrease of the anodes performance. Their impact was shown to depend on cycling speed and the properties of the surrounding SEI. In order to improve the anodes performance different cycling speeds and also different electrolyte compositions have been tested and microstructural as well as chemical properties of the respective samples have been compared and evaluated by methods of TEM. The careful and complete performance of the initial three charging/discharging cycles provides a properly developed SEI. Occurring stresses arising from shrinking during delithiation get compensated by an intact SEI. Present as a shell surrounding the wires it prevents a delamination of tentatively cracked surface layers. Further polymeric additives increase the SEI´s elasticity so it can expand during the volume increase instead of get fractured and flake off.
Conclusion**:** High capacity silicon based anodes have been developed by successful tailoring of their SEI. Thus degrading effects have been minimized by a more functional SEI. TEM results have shown the impact of polymeric additives on the performance of the SEI and subsequently the whole anode.

References:
[1] Nazri GA, Pistoia G (2009) Lithium Batteries: Science and Technology. Springer, New York
[2] Leblanc D, Wang C, He Y, Bélanger D, Zaghib K (2015) In situ transmission electron microscopy observations of lithiation of spherical silicon nanopowder produced by induced plasma atomization. J. Power Sources 279:522-527
[3] Quiroga-González E, Ossei-Wusu E, Carstensen J, Föll H (2011) How to Make Optimized Arrays of Si Wires Suitable as Superior Anode for Li-ion Batteries. ECS Trans. 35(34):3-15

MS3.P011
Thermal stability of Zn-Sn-O – correlation between optoelectronic properties and microstructure

F. Landucci[1,2], Q. Jeangros[2,3], I. Marozau[4], O. Sereda[4], E. Rucavado[2], C. Spori[2], M. Morales Masis[2] C. Ballif[2], C. Hébert[1], A. Hessler-Wyser[2]

[1]EPFL, CIME, Lausanne, Switzerland
[2]EPFL, PV LAB, Neuchâtel, Switzerland
[3]University of Basel, Physics, Basel, Switzerland
[4]CSEM, Neuchâtel, Switzerland

federica.landucci@epfl.ch

Transparent Conductive Oxides (TCOs) have several and diverse applications in various optoelectronic devices. TCOs applied in solar cells that need high temperature steps during their fabrication and/or operation1 require their optoelectronic properties to remain thermally stable for the correct functionalization of the device. Indium-based TCOs have been the Reference: materials in this field, but indium is a scarce and expensive element2, therefore, more sustainable commercialization requires inexpensive and abundant materials.
The present work aims to study the thermal stability of an indium-free TCO, by investigating the structural changes induced by the heating as well as the correlation with its electrical properties.
Sputtered amorphous zinc tin oxide (ZTO), with the stoichiometry of Zn0.05Sn0.3O0.65 was used as a starting material. In situ heating experiments were performed in an X-rays PANalytical X"Pert PRO diffractometer (XRD), from room temperature, up to a maximum of 1050°C, in two different environments: air and vacuum (~10-3 mbar). A heating rate of 5°C/min was used, before a rapid quench (50°C/min) to room temperature. Electrical measurements were performed using a Hall effect setup in the Van der Pauw configuration. Optical properties were measured in a Perkin-Elmer Lambda 950 Spectrometer. To complete the structural analysis and confirm the XRD results, High Resolution and Scanning Transmission Electron Microscopy (HRTEM and STEM) together with Energy Dispersive Spectroscopy (EDX) were performed in an FEI Osiris microscope operated at 200 kV.
The XRD patterns (Fig. 1) show that a transition from the amorphous phase to a crystalline phase occurs at 570 °C in air and at 930 °C in vacuum, where the new peaks related to crystalline (101), (200) and (211)-reflections of SnO2 appear. Crystalline ZTO, on the other hand, was not detected in our experiments. Based on the obtained results, it is believed that oxygen in the atmosphere plays an important role in the difference of crystallization temperatures. The oxygen contained within the material is likely to be embedded in a molecular form (probably water), so that it would not be available for the formation of tin dioxide, as also suggested by additional Thermal Desorption Spectroscopy and Rutherford Backscattering experiment (not shown here). This could be the reason of the retarded crystallization during vacuum annealing. High Angle Annular Dark Field (HAADF) TEM reveals small grains within the structure after crystallization and EDX maps highlight that zinc evaporates from the film, leaving voids in the crystallized structure (Fig 2). Electrical properties show different trends at different annealing temperatures and a complete decrease of mobility and free carrier concentration after crystallization. Zinc is confirmed as a key player in the material thermal stability. The influence of atmosphere leads to the conclusion that oxygen accelerates the crystallization process, after which the films becomes completely resistive. The poor electrical properties after crystallization can be ascribed to three main factors: i) mobility is limited by scattering at grain boundaries, ii) after crystallization a non degenerate SnO2 crystalline phase is formed, iii) porous structure is formed after zinc evaporation.

[1] Feldmann et al. Appl. Phys. Let. 104 (18), 2014. [2] Service Science 327 (1597), 2010

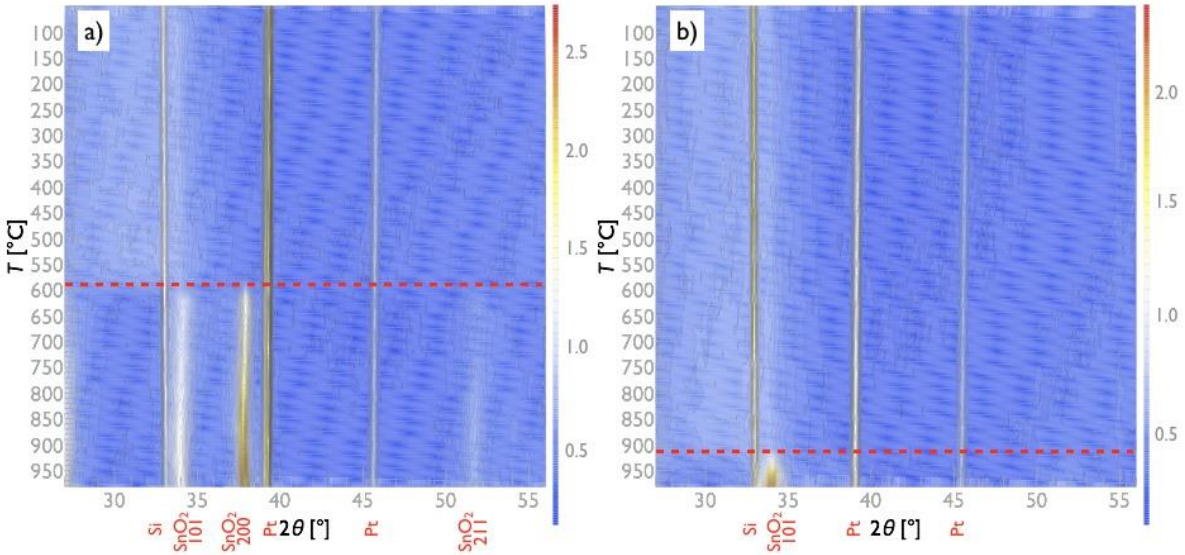

Figure 1. XRD patterns of in situ air a) and vacuum b) annealing, the dashed lines indicate the crystallization threshold.

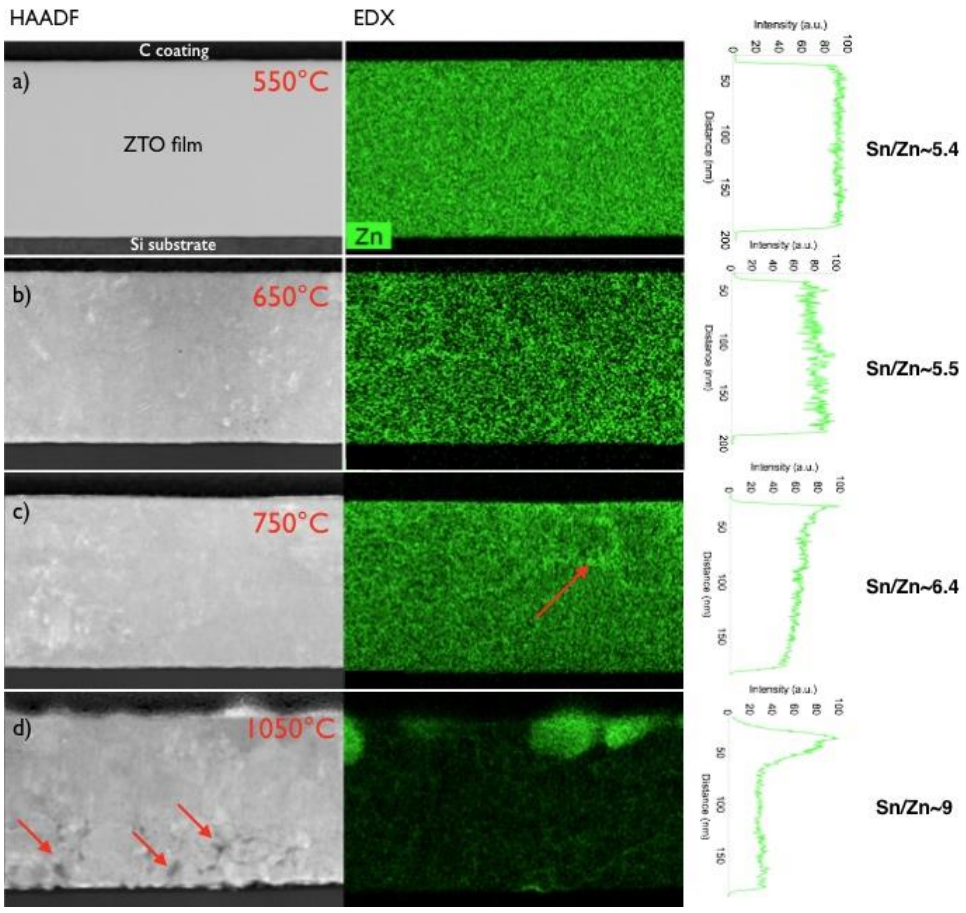

Figure 2. STEM images and EDX maps of samples annealed to four different temperatures in air. After the crystallization threshold (570°C in air) grains appear in the structure b); the accumulation of zinc towards grain boundaries is highlighted in c) and voids are visible towards the substrate in d). The four plots indicate the local content of zinc along the cross section. The calculated ratio between tin and zinc is also highlighted.

MS3.P012
Imaging zeolite NaA

G. Algara-Siller[1], T. Lunkenbein[1], R. Schlögl[1], M. G. Willinger[1]

[1]Fritz-Haber-Institut der MPG, Inorganic chemistry, Berlin, Germany

algarasiller@fhi-berlin.mpg.de

Introduction: Zeolites have been studied thoroughly using different TEM techniques [1], but until now the mechanisms for radiation damage in zeolites are not fully understood due to the complexity of their structure. Some works have given a general indication on the origin of the radiation damage [1-4]. From these works, it can be derived that the main factors for the stability of a zeolite under the electron beam are: Si/Al ratio i.e. the lower the ratio the more sensitive to electron irradiation; the type of the cations; and the water content

Materials and Methods: In this work we present the synthesis and TEM characterisation of zeolite NaA (LTA framework). This type of zeolite has a Si/Al ratio of 1 and exhibits sodium cations in the channels. Zeolite NaA was synthesized based on the synthetic protocol of Wenqing et al.[5] In order to know the sample purity we characterised the sample, previous to TEM, by XRD and XRF. The results show that the sample is NaA zeolite with a 1.10(5) Si/Al ratio. HRTEM characterisation was performed in an aberration-corrected TITAN 80-300.

Results and Conclusion: We found that using electron dose rates up to 10^3 e/nm^2 s the atomic structure of such material can be obtained over a timespan that is necessary for imaging. In addition, we did not observe any significant influence of the electron energy (80 KeV, 200 KeV and 300 KeV) used for characterization. The latter result suggests that by using an electron energy above 80 KeV, the damage due to electronic excitations (e.g. radiolysis) and knock-on are simultaneously taking place. These results are in agreement with previous findings reported by Urgulu et al. [4]. Although the structure of zeolite could be obtained, invariable damage occurred during recording, however, at a slow rate. In conclusion, these results are one step forward for the understanding of radiation damage mechanisms in molecular sieves, and a step towards imaging the cation positions.

[1] Bursill L.A., Lodge E.A., Thomas J.M. et al. Nature 286 (1980)
[2] Csencsits R., Gronsky R. Ultramicrosocpy 23 (1987)
[3] Bursill L.A., Thomas J.M., Rao K.J. Nature 289 (1981)
[4] Ugurlu et al. Physical Review B 83 (2011)
[5] Wenqing et al., Proceedings of the 7th International Zeolite Conference, Elsevier (1986)

MS3.P013
FIB based fabrication of an operative Pt/HfO_2/TiN device for resistive switching inside a transmission electron microscope

A. Zintler[1], U. Kunz[1], Y. Pivak[2], S. Ulhas[1], S. Vogel[1], H. J. Kleebe[1], L. Alff[1], L. Molina-Luna[1]

[1]TU Darmstadt, Department of Material- and Geosciences, Darmstadt, Germany
[2]DENSsolutions, Delft, Netherlands

alexander.zintler@gmail.com

Introduction: Recent advances in microelectromechanical systems (MEMS) based chips for *in situ* transmission electron microscopy are opening exciting new avenues in nanoscale research. The capability to perform current-voltage measurements while simultaneously analyzing the corresponding structural, chemical or even electronic structure changes during device operation would be a major breakthrough in the field of nanoelectronics. In this work, we demonstrate for the first time how to electrically contact and operate a lamella cut in a focused ion beam (FIB) system[1] from a resistive random access memory (RRAM)[2] device based on a Pt/HfO_2/TiN metal-insulator-metal (MIM) structure. The electrical switching characteristics[3] of the electron-transparent lamella were comparable to a conventional Reference: device. The lamella structure was initially found to be in a low resistanve state and could be reset progressively to higher resistance states by increasing the positive bias applied to the Pt anode.
Objectives: Fabrication of a working Pt/HfO_2/TiN MIM device for resistive switching. A FIB routine was developed that preserves device integrity and incorporates the necessary electrical contacts that prove the bulk-like cyclability.
Materials and Methods: The starting specimen is a MIM structure (Pt/HfO_2/TiN) grown by MBE and PVD (for the Pt working electrode). It consists of a single crystalline aluminum oxide substrate upon which a bottom 100 nm in size titanium nitride (TiN) electrode, a 20 nm HfO_2 active layer and a 400 nm top electrode consisting of platinum were subsequently deposited.
Results: Figure 1(a) shows the thinned, free standing lamella with deposited Pt contacts and geometry limiting the active area to the electron transparent region. In Fig. 1(b) an ADF-STEM view of the MIM structure proving layer integrity (inset: BF-STEM) is shown. Initial low resistance state (1) followed by a series of progressive reset curves with increasing positive bias on Pt anode are plotted in figure 2(a). An identical set of reset voltages applied to the Reference: bulk device is given in fig. 2(b). Differing switching voltages are due to added Ohmic resistances in the path. Additional cycling not shown. Device integrity was conserved throughout the preparation process. Figure 2(a) shows the successful resistive switching characteristics performed directly on the FIB fabricated Pt/HfO_2/TiN lamella. The initially low resistive device progressively reset to a high resistance state by increasing the positive bias applied to the Pt anode leading to gradual dissolution of the defective pathway. Full unipolar cyclability was proved with consecutive set and reset processes.
Conclusion: The close resemblance in the electrical behavior of the bulk and the lamella device shown in this contribution demonstrates that the described fabrication process is viable. For the first time, we have been able to operate a FIB prepared Pt/HfO_2/TiN lamella device in a state that is suitable for TEM observation. It was possible to electrically cycle the device. The proposed fabrication methodology is a platform towards developing a characterization tool for imaging resistive switching devices *in operando*. Investigating the corresponding structural changes such as possible nanofilament formation[4,5] during the resistive switching process would be essential for improving the performance of next-generation nonvolatile memory devices.

References:
[1] Fawey et al. *Micr. Res. Tech.* 79 (2016) 615-624.
[2] Sawa et al., *Mater. Today.* 11 (2008) 28–36.
[3] Goux et al., *Electrochem. Solid-State Lett.* 13 (2010) G54–G56.
[4] K.H. Xue et al., *IEEE Trans. Electron Devices.* 61 (2014) 1394–1402.
[5] Privitera et al., *Solid-State Electron.* 111 (2015) 161–165.

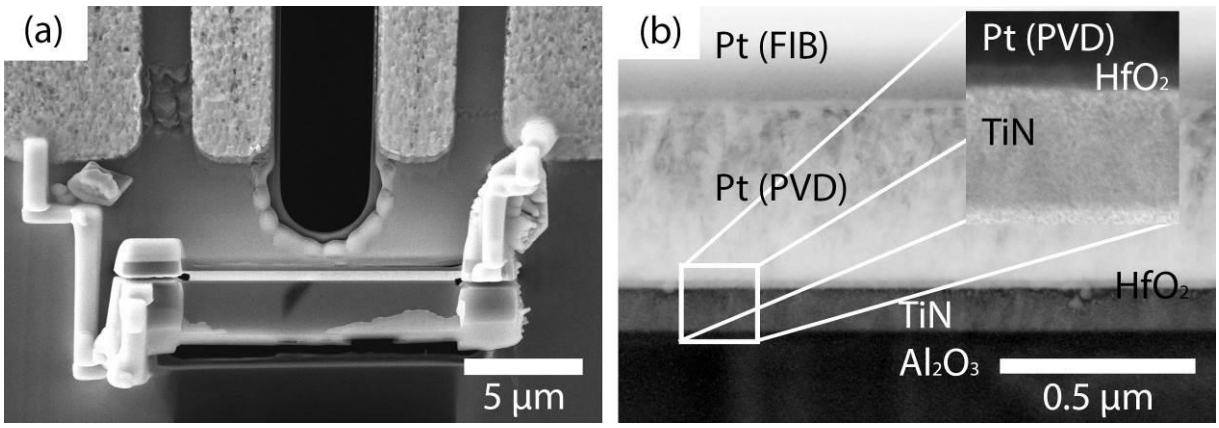

Figure 1

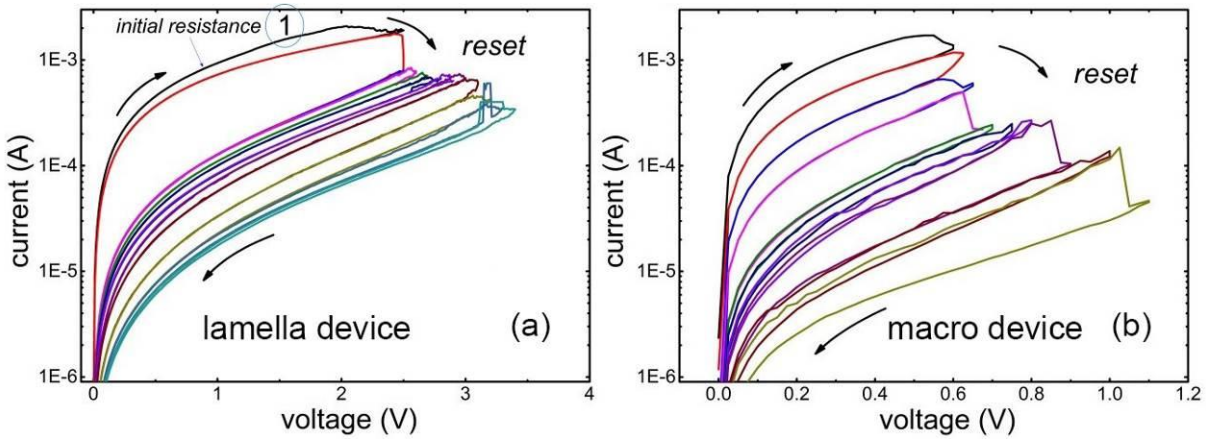

Figure 2

MS3.P014
High resolution EBIC investigations on CdTe thin film solar cells

O. Zywitzki[1], T. Modes[1], D. Hirsch[1], C. Metzner[1], T. Kopte[1], B. Siepchen[2], B. Späth[2], C. Kraft[2], C. Drost[2]
V. Krishnakumar[2]

[1]Fraunhofer Institute for Organic Electronics, Electron Beam and Plasma Technology (FEP), Dresden, Germany
[2]CTF Solar GmbH, Dresden, Germany

olaf.zywitzki@fep.fraunhofer.de

Introduction: One of the most important steps in manufacturing of polycrystalline CdTe thin film solar cells with high efficiencies is the chlorine activation treatment. The resulting complex changes to the structure and properties are still not fully understood and are therefore a topic of scientific discussion. A promising method for better understanding of the effect of polycrystalline microstructure on electronic properties of CdTe solar cells is the measurement of the electron beam induced current (EBIC) simultaneously to FE-SEM imaging in channelling contrast [1, 2].
Objectives: The aim of the present work was the investigation of the effect of polycrystalline CdTe microstructure and of activation temperature on the measured EBIC signal distributions.
Materials and Methods: CdS and CdTe layers were deposited by closed space sublimation [3] at nearly constant substrate temperature of 520 °C on a fluorine doped tin oxide (FTO) coated float glass substrate. The temperature during activation treatment was varied between 400 and 440 °C with a constant time of 25 min. A magnetron sputtered molybdenum layer was used as metallic back contact.
For high resolution investigations of microstructure and interfaces, cross sections of the complete solar cells were prepared using a broad ion beam preparation technique (Cross Section Polisher, SM-0910, Jeol). The cross sections of the solar cells were investigated by field emission scanning electron microscopy (SU8000, Hitachi) using crystal orientation and the atomic number contrast of backscattered electrons. Simultaneously to the FE-SEM imaging the electron beam induced current signal distribution was measured. By the selection of a small electron beam accelerating voltage of 2 keV the electron range in the sample can be limited to about 25 nm, which enables a high lateral resolution.
Results: The polycrystalline CdTe layers exhibit a block-like microstructure with a relative large lateral grain size between 1 and 2 µm.
After activation treatment at 400 °C the grain boundary near regions show a higher EBIC signal than the centre of the grains. Some small grains near to the pn-junction show a very high EBIC signal (Fig. 1 a, b). With increasing activation temperature the EBIC signal distribution becomes more homogenous between grain boundary near regions and the centre of the grains (Fig. 1 c, d). Simultaneously a drastic change in interface roughness between CdS and CdTe layer can be recognized. This can be explained by grain growth and agglomeration of the CdS layer and sulphur tellurium interdiffusion at the interface. At higher activation temperatures the CdTe layer is partially in direct contact to the FTO layer.
Conclusions: The EBIC results can be discussed as a direct evidence for a passivation of grain boundary near regions by CdCl2 activation treatment. The estimated diffusion length of minority carriers is in the range between 1 and 2 µm. The more homogenous EBIC signal distribution at higher activation temperatures can be explained by the occurring chlorine diffusion process. It can be assumed that the chlorine is incorporated into the CdTe layer at first by fast grain boundary diffusion. The further diffusion must occur by the slower volume diffusion into the individual CdTe grains.
The detected sulphur tellurium interdiffusion at the CdS/CdTe interface increase the EQE values of the solar cells in short wavelength range by the dissolution of the CdS layer and in long wavelength range by the reduction of CdTe band gap.

References:
[1] O. Zywitzki et al., Journal of Applied Physics, 1114, 163518 (2013)
[2] C. Li et al., Physical Review Letters 112, 156103 (2014)
[3] B. Siepchen et al., Thin Solid Films 535, 224 (2013).

Acknowledgement
We would like to thank for the funding of this research by European Union and the Free State of Saxony.
Funding Reference: 100 206 775/3005

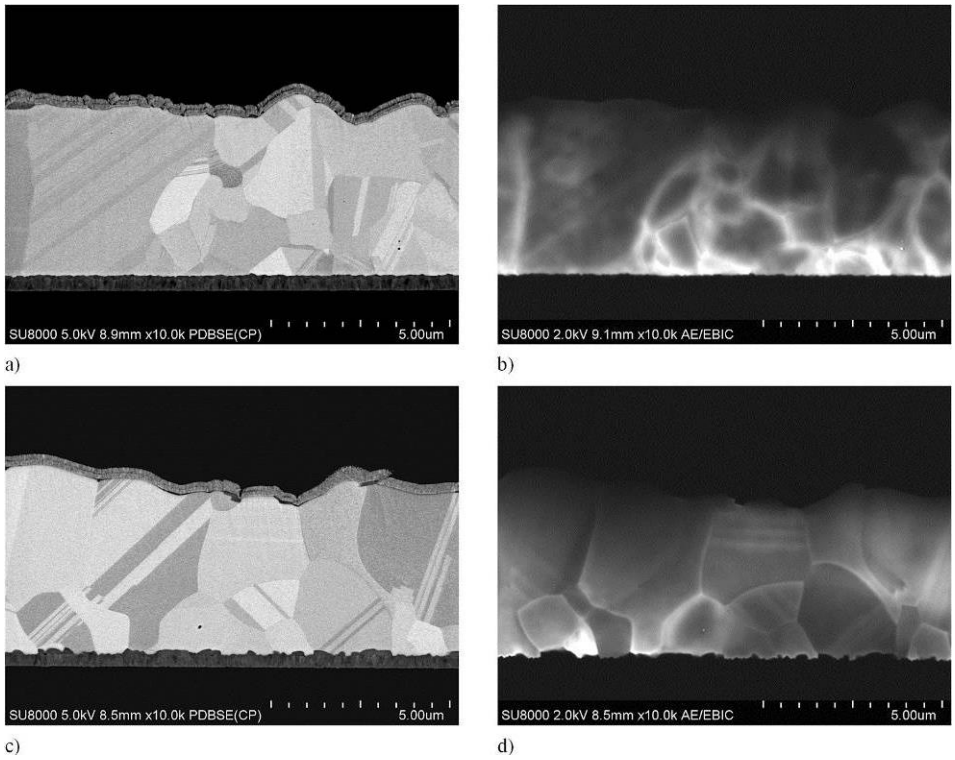

Figure 1. FE-SEM micrographs of ion polished cross sections of CdTe thin film solar cells in crystal orientation contrast and the corresponding EBIC signal distributions for chlorine activation treatments at 400 °C (a, b) and 440 °C (c, d).

MS3.P015
Designing strontium titanate-based thermoelectrics – insight into defect chemistry mechanism

M. H. Aguirre[1], A. V. Kavalevsky[2], S. Populoh[3], S. G. Patricio[2], N. Ferreira[2,4], S. M. Mikhalev[5]
D. P. Fagg[5], J. Frade[2]

[1]Institute of Nanoscience of Aragón, University of Zaragoza, Laboratory of Advanced Microscopy, Physics Condensed Matter, Zaragoza, Spain
[2]CICECO – Aveiro Institute of Material, Department of Materials and Ceramic Engineering, University of Aveiro, Aveiro, Portugal
[3]ABB Switzerland Ltd., Semiconductors, Lenzburg, Switzerland
[4]i3N, Physics Department, University of Aveiro, Aveiro, Portugal
[5]TEMA-NRD, Aveiro Institute of Nanotechnology, Mechanical Engineering Department, University of Aveiro, Aveiro, Portugal

maguirre@unizar.es

Introduction**:** A major challenge in developing highly efficient thermoelectric materials consists in targeting the delicate balance of its functional properties: electrical (σ) and thermal (κ) conductivities and the Seebeck coefficient (α). The heat-to-electrical energy conversión is limited by the Carnot Efficiency and charaterized by the figure of merit ZT = α2*σ*T/κ. Among oxides, donor-substituted strontium titanate bears the prospect as *n*-type thermoelectric material due to its specific electronic structure. Tunability can be achieved via introduction of defects, which leads to the prevalence of lattice contribution to the thermal conductivity, while enhancing phonon scattering by substitution or micro/nanoengineering approaches [1]. Recent work finds convincing thermoelectric performance in SrTiO3 –based materials by introducing an A-site deficiency [2,3], resulting in noticeably improved power factor and appearance of unusual "glass-like" behavior of the thermal conductivity.
Objectives**:** To improve the SrTiO3 thermoelectric performance a partial A- and/or B-site (co-) substitutions with rare-earth and/or transition metal cations are done providing a reasonable electrical conductivity and suppressing the thermal conductivity by impurity scattering. However, the results are often inconsistent and contradictory regarding the substitution mechanisms since are very sensitive to the processing conditions. The work presented here uncovers the particular role of various structural defects in electrical and thermal transport in Sr1-yTi0.9Nb0.1O3-δ, by combined different techniques such as Electron Microscopy and measurements of thermoelectric properties among others.
Materials and Methods: SrTiO3-based materials was prepared by conventional solid state route (SryTi0.90Nb0.10O3±d y= 1.05; 1,00; 0.97; 0,95; 0,93) in reducing and oxidizing atmospheres. XRD at room temperature was used to identify the phase composition and calculate the evolution of the unit cell parameters by profile matching methods using Fullprof software. SEM couple with EDS detectors and TEM-STEM-HAADF with EDX and EELS techniques were used to study the crystal structure, morphology and composition at the micro and nano level. The electrical properties (total conductivity (σ) and Seebeck coefficient (α)) were measured simultaneously in a 10% H2–90% N2 mixture atmosphere from 1273 K to 373 K. Thermal diffusivity (D) and specific heat capacity (cp) studies were performed under similar conditions using Netzsch LFA 457 Microflash and Netzsch DSC404 C equipment, respectively.
Results: The prevailing defect types were controlled by introducing nominal A-site deficiency, from Ruddlesden-Popper-type (RP) and other oxygen-rich defects, confirmed by TEM (Fig. 1c), to oxygen nonstoichiometry, estimated by thermogravimetry (TG). Combined electrical conductivity/TG/XPS studies suggest that presence of cation- and oxygen vacancies is favorable for high mobility of the charge carriers (Fig. 1a), while oxygen-rich planar defects have a negative impact on the electrical performance. Noticeable deviations from stoichiometric oxygen content were found to decrease the lattice thermal conductivity (Fig. 1b), suggesting good phonon scattering ability for oxygen vacancies, vacant A-sites and oxygen-excessive defects.
Conclusions**:** Introduction of A-site cation vacancies provides a synergistic effect of combining fast charge transport in the perovskite lattice and suppressing the thermal conductivity mostly due to simultaneous generation of oxygen vacancies. The presence of oxygen vacancies promotes more efficient phonon scattering compared to Ruddlesden–Popper-type layers.

References:
[1] H.Ohta, et al, *Inorg. Chem.* **47**, 8429 (2008**)**.
[2] A.V. Kovalevsky, et al *J. Phys. Chem. C.* **118**, 4596 (2014).
[3] S.R. Popuri et al *RSC Adv.* **4**, 33720 (2014).

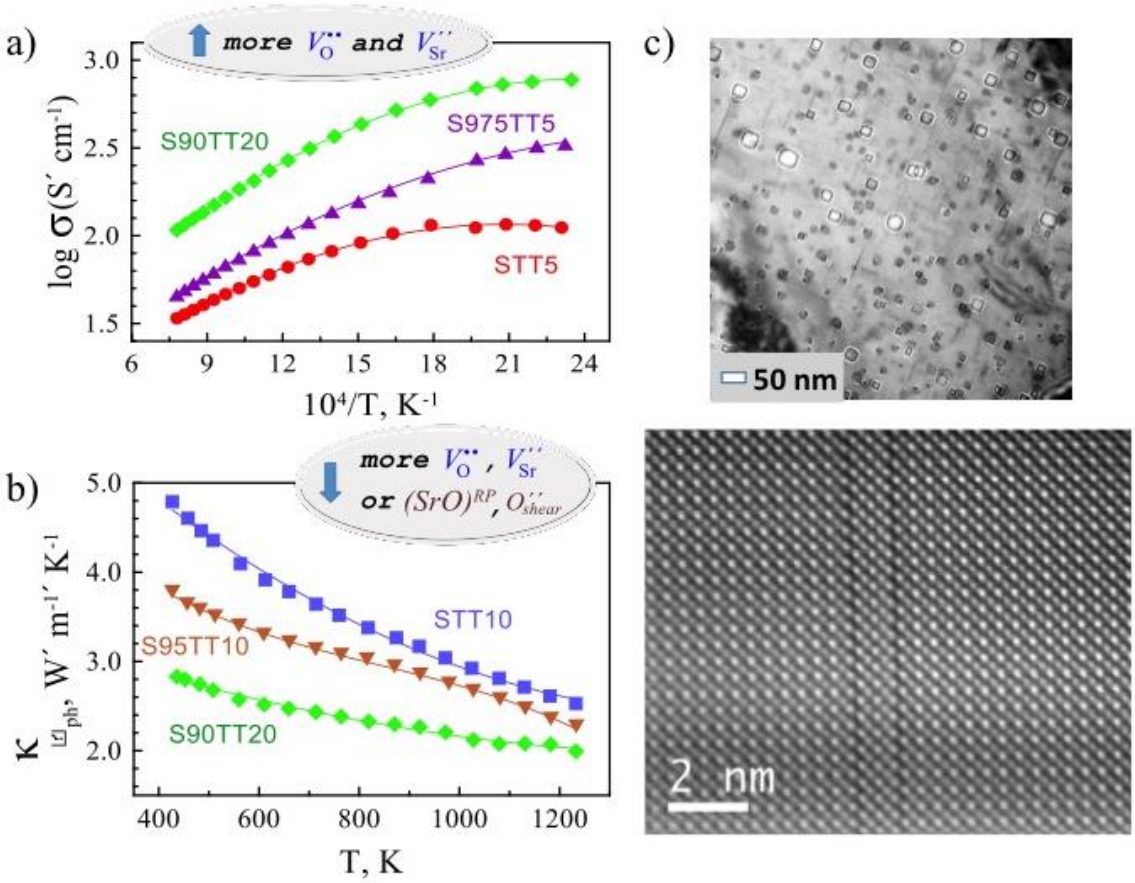

Figure 1. a) Temperature dependencies of the electrical conductivity; b) Lattice thermal conductivity and c) High-resolution STEM-HAADF images of Sr1.05Ti0.9Nb0.1O3± d) lamellar sample.

MS3.P016
Analytical TEM studies of novel CIGSSe absorber layers in thin-film solar cells

A. Pasha[1], R. Schneider[1], N. Firman[1], P. Eraerds[2], R. Lechner[2], T. Dalibor[2], D. Gerthsen[1]

[1]Karlsruhe Institute of Technology, Laboratory for Electron Microscopy, Karlsruhe, Germany
[2]AVANCIS GmbH, R&D, München, Germany

altaf.pasha@kit.edu

Thin-film solar cells with absorber layers of $Cu(In,Ga)(Se,S)_2$ (CIGSSe) are promising low-cost photovoltaic materials with tunable temperature coefficient and better shading tolerance. The band-gap energy is one essential parameter of solar cells, which influences their efficiency. For CIGSSe absorbers the band-gap energy can be tailored by the specific chemical composition of the layer and/or by introducing of chemical gradients. For CIGSSe, the band gap can be widened by increasing the S and Ga content. Therefore, the aim of this study was to prepare thin-film CIGSSe layers of different composition and verify the intended processing results by analytical transmission electron microscopy (TEM).

Thin-film solar cells with CIGSSe absorbers were fabricated by a sequential process, where in the first step CuGa and In layers were deposited by DC magnetron sputtering and subsequently Se was thermally evaporated. Secondly, the CIGSSe semiconductor was formed by selenization and sulfurization of the elemental precursor stack applying rapid thermal processing (RTP) (cf. [1]). Two different CIGSSe batches A and B were synthesized by varying the elemental ratio of Cu, Ga, and In during sputtering and by controlling the S partial pressure of the RTP process. In detail, the S content of CIGSSe batch A should basically be low, only near to the layer surface a S gradient was intended. For batch B, an increased Ga content was expected throughout the absorber. Cross-section TEM samples were prepared from the CIGSSe layers in the conventional way, including grinding, polishing, and finally Ar+ ion thinning. TEM investigations of the absorber layers were performed at 200 kV in an FEI Technai Osiris with a Bruker ChemiSTEM system for energy-dispersive X-ray spectroscopy (EDXS).

From the CIGSSe batches A and B, EDXS maps were recorded in the scanning TEM (STEM) mode. In each case, the qualitative map data was quantified by applying the thin-film Cliff-Lorimer approximation. Element line profiles in growth direction were obtained at different positions from the quantified EDXS maps. Fig. 1 shows as an example the local distribution of the elements Cu (in red color), In (green), Ga (blue), Se (turquois), and S (pink) for batch A. Ga is enriched in the lower absorber region. There is a gradual decrease of Ga towards the absorber surface and nearly no Ga in the upper half of the absorber. The local In concentration behaves opposite. In batch A the overall S content (3 - 4 at.%) is low. There is a slight increase to about 8 at.% near to the surface.

As intended, the Ga content in batch B is clearly different. With approximately 24 at.% it is distinctly higher than in batch A. It is nearly constant up to center of the CIGSSe absorber layer. From about 600 nm up to the surface the Ga/In ratio continuously decreases. In topmost regions the Ga concentration is still 3 at.%, whereas the In content amounts to approximately 24 at.%. Moreover, in batch B the average S concentration is also higher than in batch A and shows a pronounced increase in near-surface regions. The STEM/EDXS results obtained from CIGSSe batches A and B clearly show different microchemistries of the two absorber layers. It is demonstrated that the local element composition within the absorber can be tailored by varying process parameters during the sequential layer fabrication.

[1] J. Palm, V. Probst, F.H. Karg, Solar Energy 77 (2004), 757

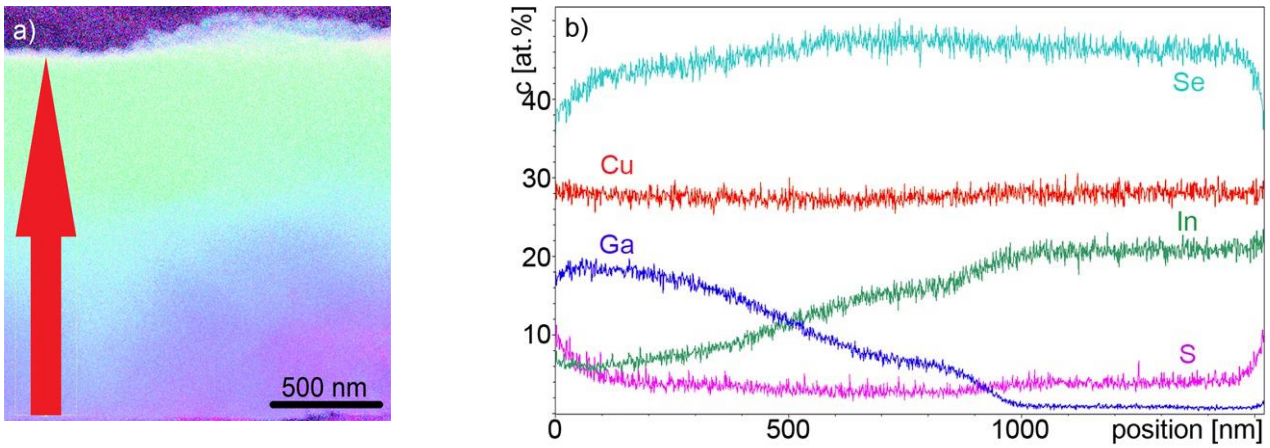

Figure 1. a) Quantified EDXS map of the CIGSSe absorber A, the arrow marks the position of line-profile analysis, b) corresponding local element concentrations in the absorber layer.

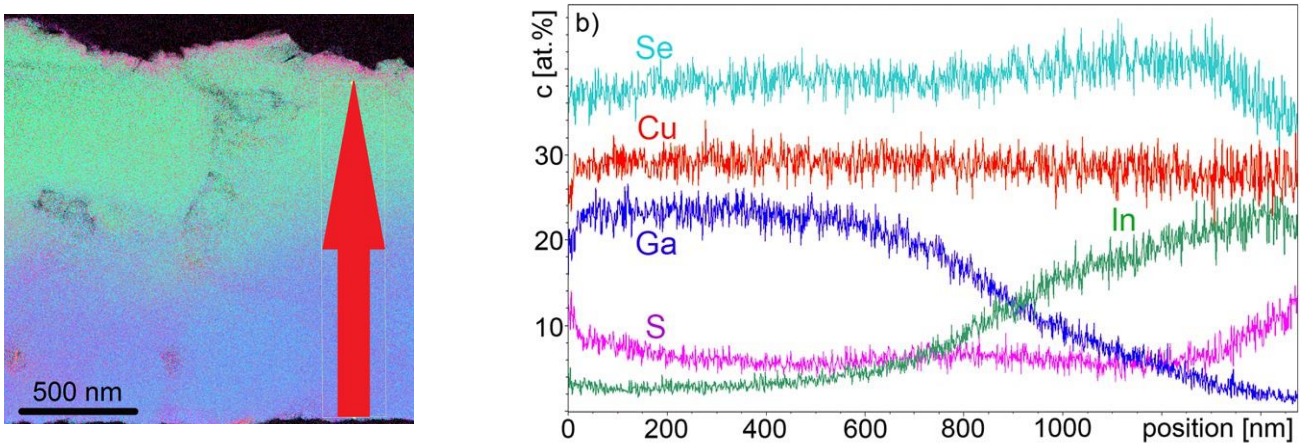

Figure 2. a) Quantified EDXS map of the CIGSSe absorber B, b) corresponding element concentrations in the layer.

MS3.P017
Microstructural appearance of various processed HV spinel cathodes using SEM/FIB investigations

A. Kopp[1], M. H. P. Maurício[2], S. Paciornik[2], H. Blank[3], T. Bernthaler[1], G. Schneider[1]

[1]Universtity Aalen, Materials Research Institute, Aalen, Germany
[2]DEQM PUC-Rio, Rio de Janeiro, Brazil
[3]Carl Zeiss Microscopy GmbH, Oberkochen, Germany

andreas.kopp@hs-aalen.de

Introduction: Quality and function of a Li-ion battery are mainly determined by the microstructure of the electrode coatings. The coatings are compressed to improve the adhesion between electrode and current collector and to increase the volumetric energy density. The calendering process is one of the major processing steps having an influence on the conductivity of the electrode. However, too high compression rates have negative effects on the performance of the battery and lead to a decrease in the ionic conductivity, which is the governing factor of the performance of Li-ion batteries. The morphology of the pore network mainly determines the ionic conductivity. To achieve a good performance, an optimal balance of active material, pores, binder and carbon black has to be adjusted. Therefore it is important to analyze the three dimensional appearance of the microstructure and phase distribution of constituents in the electrodes. HV (high voltage) spinels (LiNi0,5Mn1,5O4) are promising materials due to low material costs, a high operation voltage and thermal stability.
Objectives: We focus on a multilevel approach using X-ray microscopy, SEM and FIB investigations for a three dimensional characterization of battery cathodes with different porosities to show and analyze the influence of different process parameters on the microstructure of the cathodes.
Materials and Methods: Three different compression states of HV spinel cathodes are investigated. One foil represents the pristine condition. The cathodes have an area weight of 194 g/m² and are compressed to a loading of 2.5 g/cm³, 2.8 g/cm³ and 3,12 g/cm³. The foils were scanned with an X-ray microscope (XRadia Versa 520) to get a 3D overview of the volumetric particle distribution. Later the foils were investigated with SEM (ZEISS Crossbeam 540) to measure the layer thickness and phase fraction of active material and pores. Machine learning algorithms are used for segmentation of the particles. These algorithms can be trained on different microstructure features for segmentation. To get a better understanding of the three dimensional microstructure, FIB tomography volumes are acquired on different locations like the top / bottom of the coating. Therefore further information about the microstructural homogeneity along the electrodes is achieved.
Results: A linear dependency between the layer thickness, phase fraction and density can be found in the cathode foils. SEM images of the surface of the foils show the influence of the compression on the microstructure very clearly. Figure 1 shows the SEM images of the different foils. With increasing compression less pores can be seen on the surface. Figure 2 shows the FIB cross sections for the pristine and strongest compressed foil (3,12 g/cm³). It can clearly be seen that free pore space between the particles and pores within the binder decreases with increasing compression. The compression leads to particle breakage near the surface. Figure 2 a) shows bigger particles consisting of different sub particles. In the compressed foil in Figure 2 b) the bigger particles near the surface are broken. This leads to an increase of the surface area of the HV spinel.
Conclusion: First investigations show the strong influence of the compression on the cathode microstructure. Further investigations will focus on the particle damage due to compression and the influence on particle size, adhesion to the current collector and particle size distribution. Three-dimensional FIB tomography will be applied.

References:
[1] J. Fehrenbach, P. Weiss, and C. Lorenzo, Variational Algorithms to Remove Stationary Noise: Applications to Microscopy Imaging, *IEEE Transactions on Image Processing*, vol. 21, no. 10, pp. 4420–4430, Oct. 2012.

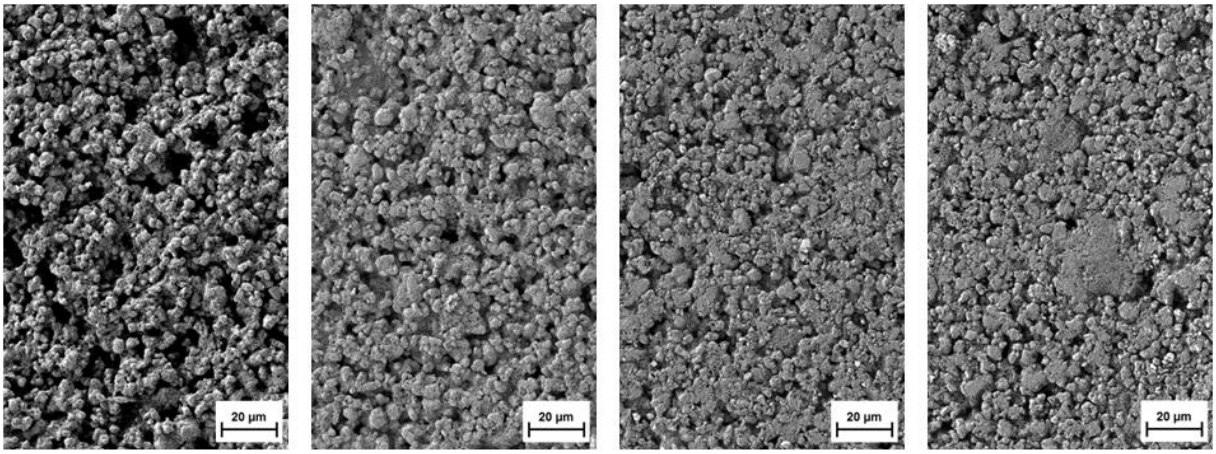

Figure 1. Surface of electrodes – pore volume is decreased with increasing compression, SEM image magnification 500x.

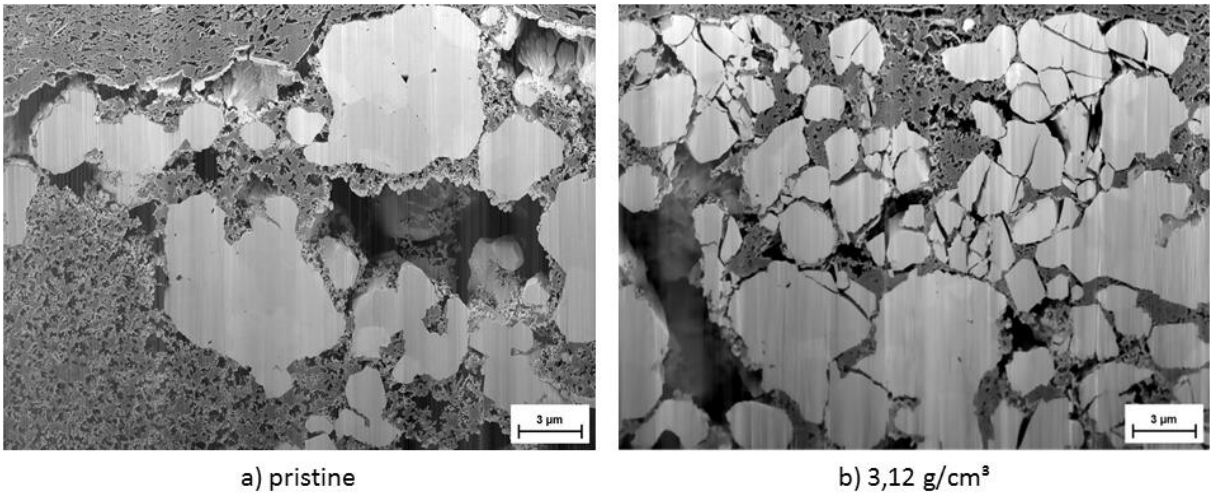

Figure 2. FIB cross sections show severe particle damage in compressed electrodes, SEM image magnification 4,000x, restored image using VSNR [1].

MS3.P018
Challenges in TEM sample preparation of solvothermally synthesized $CuInS_2$ thin films

A. Frank[1], A. S. Wochnik[2], C. Scheu[1]

[1]Max-Planck-Institut für Eisenforschung GmbH, Nanoanalytics and Interfaces, Düsseldorf, Germany
[2]Ludwig-Maximilians University, Munich, Germany

a.frank@mpie.de

The energy need of our society is growing from year to year. Being sustained with enough power to run our devices all the time requires new ways in energy generation. Because of the sun offering more than enough power it is a highly active research field to find possibilities to use and convert this energy. Copper indium disulfide, $CuInS_2$, is a Chalcopyrite material which shows very promising properties for a lot of photophysical and -electrochemical applications.[1, 2, 3] It offers a direct band gap of 1.5 eV and a high absorption coefficient of 10^5 cm^{-1}.[4]
In this work, around 500 nm thick $CuInS_2$ films have been grown solvothermaly onto Fluorine-doped tin oxide (FTO) substrates following a strategy first published by Peng et al.[5] and modified in our earlier work,[6] but using the amino acid L-cysteine as sulfur source. Characterization of the samples was mainly done with electron microscopic techniques. The semiconducting properties of $CuInS_2$ are tunable between p- and n-type depending on its chemical composition,[7] therefore the focus is laid on analyzing the elemental composition.
Due to the large interaction volume in scanning electron microscopy (SEM) not only Cu, In and S can be detected with energy-dispersive X-ray (EDX) spectroscopy of the films but also tin from the substrate gives a signal. However, the In and Sn L edges overlap which leads to difficulties in the quantification. (Scanning) transmission electron microscopy ((S)TEM) can overcome the problem as the contribution of the substrate can be avoided. (S)TEM investigations have been performed with a C_s corrected FEI Titan Themis 60 - 300. To prevent artefacts or alteration of the samples different TEM sample preparation techniques have been tested: FIB sectioning, scratch sample preparation and conventional cross section preparation. The investigated $CuInS_2$ films have a nanostructured morphology as visible in the SEM micrographs and possess a tetragonal Chalcopyrit crystal structure as determined with X-ray diffraction (XRD) (see Fig.1).
From this materials FIB lamellae have been prepared using a FEI Helios Nanolab 600 (Fig.2). FIB preparation offers the advantage for side-specific sample preparation, but STEM EDX measurements revealed a drastic loss in sulfur (Fig.2). Additionally, it can be seen that the $CuInS_2$ is removed partly as the film thickness decreased and the material is transformed into an amorphous phase. For scratch samples, an influence of the preparation on the sample can be mainly avoided. Accordingly, the STEM EDX quantifications lead to stoichiometric $CuInS_2$ (Fig.3). Also the crystallinity of the sample can be proven by HR-TEM and electron diffraction, and $CuInS_2$ in its tetragonal Chalcopyrit modification can be confirmed. However, a determination of the film thickness is not possible. Conventional cross section preparation is a time intensive possibility of preparing TEM samples. Nevertheless, this method leads to samples in which the film thickness can be determined and also a change in crystallinity and chemical composition can be minimized (Fig.4). However, a Cu signal stemming from the brass tube where slices of the films were embedded can occur.
To summarize, FIB sectioning is not well suited to prepare TEM samples from solvothermally grown $CuInS_2$ films as the chemical composition is drastically altered. One should use scratch or conventional prepared samples.

[1] Zhao, et al., *Appl Phys A* **2016**, *122*.
[2] Luo, et al., *Nano Lett* **2015**, *15*, 1395.
[3] Adam, et al., *Electrocatalysis* **2015**, *6*, 405.
[4] Tell, et al., *Phys Rev B* **1971**, *4*, 2463.
[5] Peng, et al., *J Alloy Compd* **2009**, *481*.
[6] Wochnik, et al., *J Mater Sci* **2012**, *47*.
[7] Look, et al., *J Phys Chem Solids* **1976**, *37*.

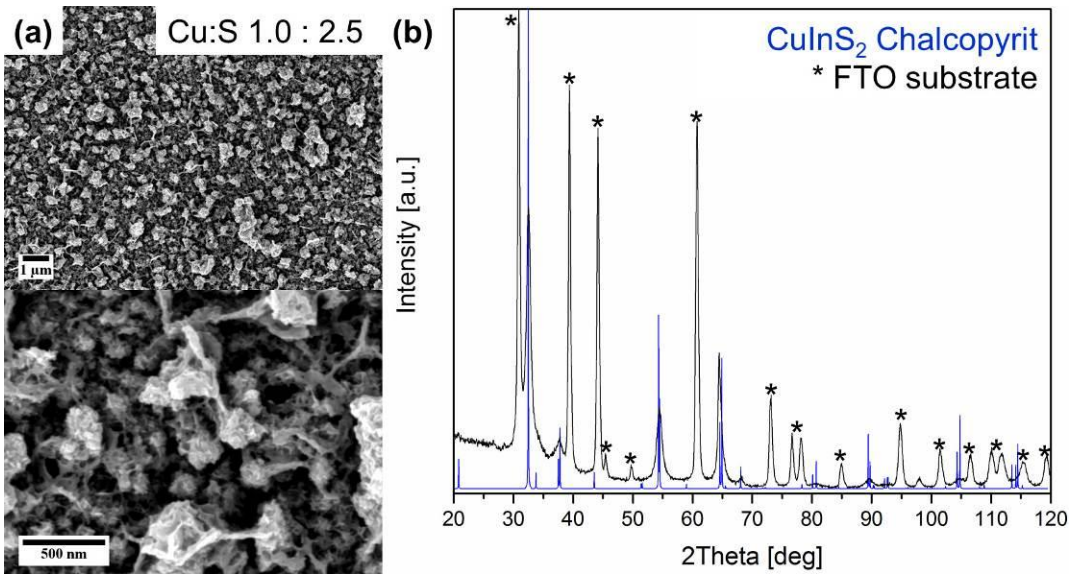

Figure 1. (a) SEM images and (b) XRD spectrum of a $CuInS_2$ film on FTO substrate.

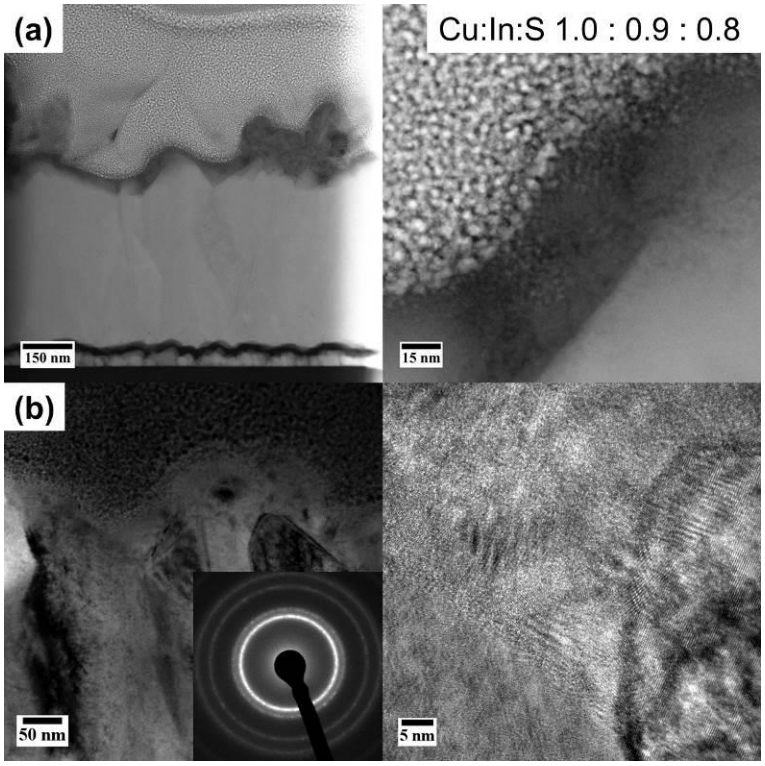

Figure 2. (a) STEM and (b) TEM images of a $CuInS_2$ thin film sample prepared with FIB sectioning.

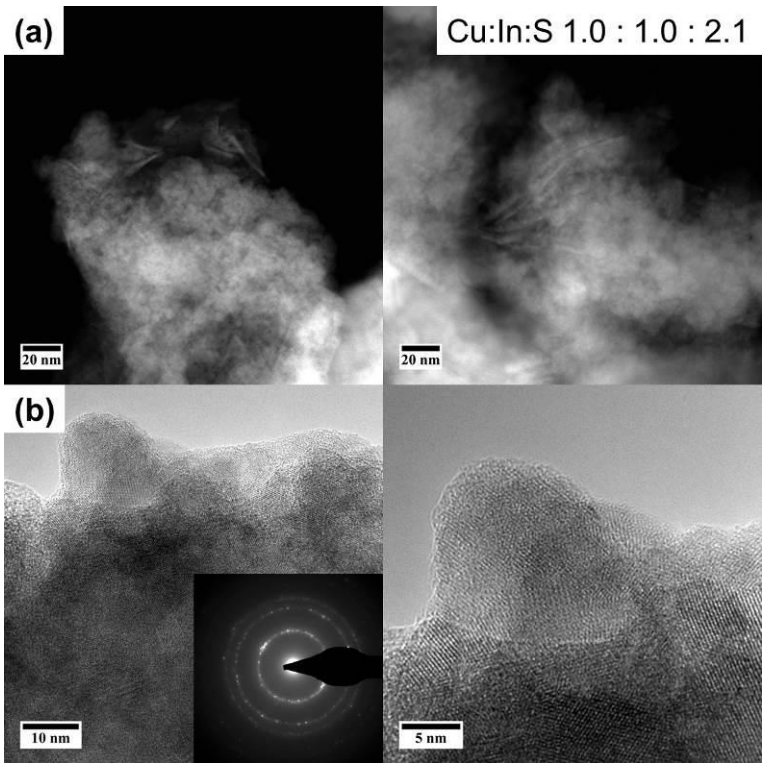

Figure 3. (a) STEM and (b) TEM images of a $CuInS_2$ thin film scratch sample.

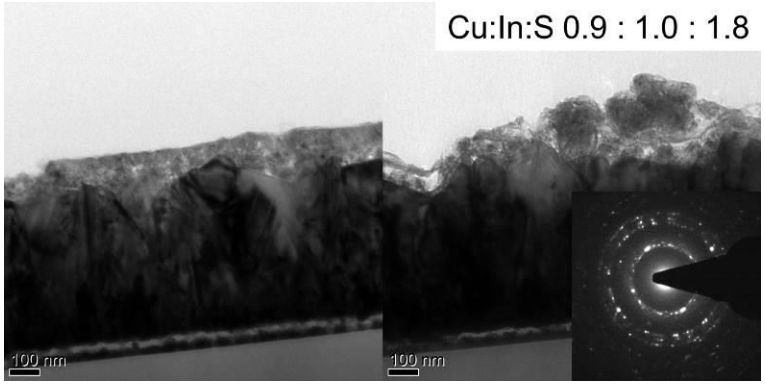

Figure 4. TEM images of a $CuInS_2$ thin film sample prepared by a conventional preparation route. Please note that the film thickness is lower due to a different amount of precursor used to fabricate the film.

MS3.P019
C_s corrected STEM analysis – operation related nanoscale degradation processes in high-temperature polymer-electrolyte-membrane fuel cells

K. Hengge[1], M. Perchthaler[2], C. Heinzl[2], D. Varley[1], C. Scheu[1]

[1]Max-Planck-Institut für Eisenforschung GmbH, Nanoanalytik und Grenzflächen, Düsseldorf, Germany
[2]elcore GmbH, München, Germany

k.hengge@mpie.de

High-temperature polymer-electrolyte-membrane fuel cells (HT-PEMFCs) are devices to produce energy and heat by use of one of the most simple redox reactions known: the oxidation of hydrogen (H_2) and the reduction of oxygen (O_2), while the only side product is water. To realize FC operation, among other requirements, a good stability and performance continuity of the catalyst are crucial. Catalyst degradation comprises nanometer-scale processes like particle diffusion, agglomeration, dissolution, detachment or Ostwald ripening, but also sub-nanometer-scale events like CO poisoning. In our research work we investigated HT-PEMFCs before and after operation in a real FC system which we stopped prematurely to get insight into intermediate states during long-term operation. To meet all requirements for an efficient FC performance, carbon supported platinum nanoparticles (Pt NPs) were used as cathode catalyst layer (CL) and a carbon supported Pt/Ru alloy was the anode CL. The latter is known to effectively prevent CO poisoning of the anode. Scanning electron microscopy (SEM) was used to obtain an overview of the quality of the single layers of the investigated membrane-electrode-assemblies (MEAs). By use of a backscattered electron detector, anode- and cathode side could easily be identified. Detailed analysis of the catalyst NPs was performed with the help of a C_s corrected scanning transmission electron microscope (STEM) from FEI (60 - 300 Titan Themis). Site specific sectioning to obtain electron transparent samples was performed with a focused ion beam (FIB) microscope from FEI (Helios NanoLab600). Fig. 1 displays overview SEM micrographs of the cross-sections of an as-prepared MEA (Fig. 1a) and an operated MEA (Fig. 1b). After FC operation a bright band is present in the membrane area adjacent to the cathode CL (see inset in Fig. 1b). STEM analysis of this band and its origin were performed with FIB lamellae from the interface region between membrane and cathode CL as displayed in Fig. 2a. The cathode CL is located on the right side and a bright band of catalyst NPs is present in the membrane, around 2.3 ± 0.2 µm away from the interface region. A magnified area of the band and the surrounding membrane section is displayed in Fig. 2b. Clearly, two types of nanoparticles are present: star-like shaped particles and spherical NPs. In-depth STEM analysis of these particles is challenging since the polymer-membrane is heavily prone to electron beam induced damage, so it gets destroyed easily. Nevertheless we found that the band is formed by the star-like shaped particles exhibiting a mean diameter of 14.7 ± 4.7 nm. Additionally particles are also present in the membrane in direction of the anode CL. An EDX map exhibiting the elemental distribution of Pt and Ru within three of these particles is displayed in Fig. 2c. Both catalyst elements are distributed uniformly. Quantification revealed an average composition of 71 atom% Ru and 29 atom% Pt. Electron diffraction experiments revealed that these particles adopt the hcp lattice of Ru while Pt/Ru particles located in the anode CL possess the Pt fcc structure. In between the band and the cathode CL we found spherical NPs, composed of pure Pt, with a diameter of 2 – 3 nm on average. A high resolution (HR) STEM micrograph of one of these particles is presented in Fig. 2d. Our results show that catalyst dissolution, migration and precipitation take place at both anode and cathode CLs; the effect is more pronounced at the anode side. The Pt/Ru particles formed in the membrane adopt a different crystal structure and composition as the ones originally located at the anode CL.

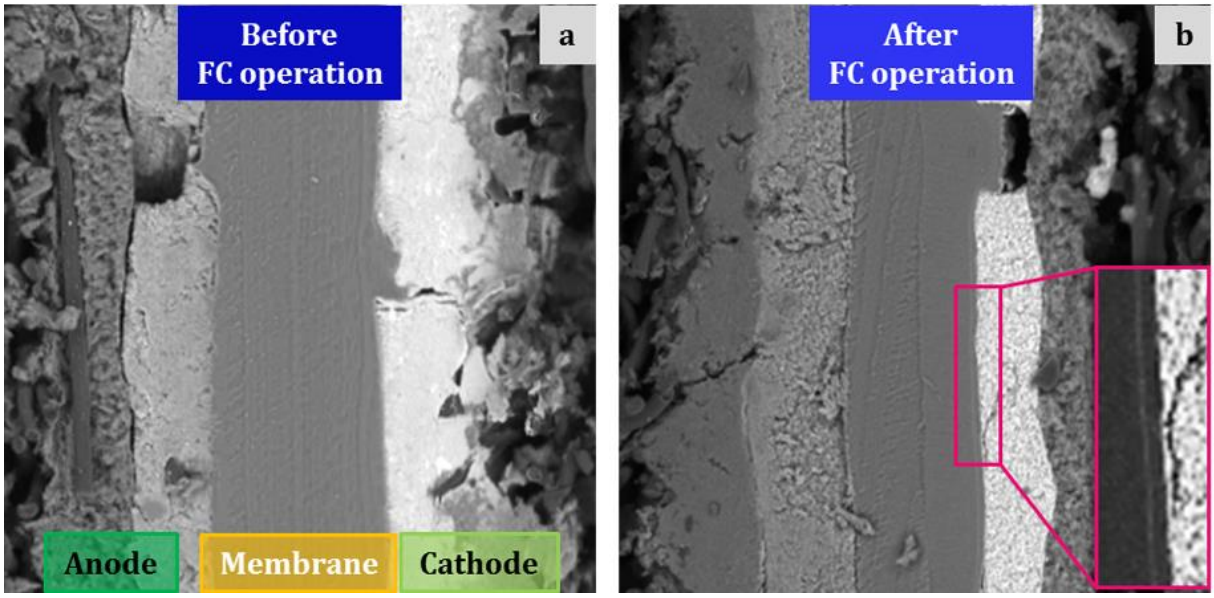

Figure 1

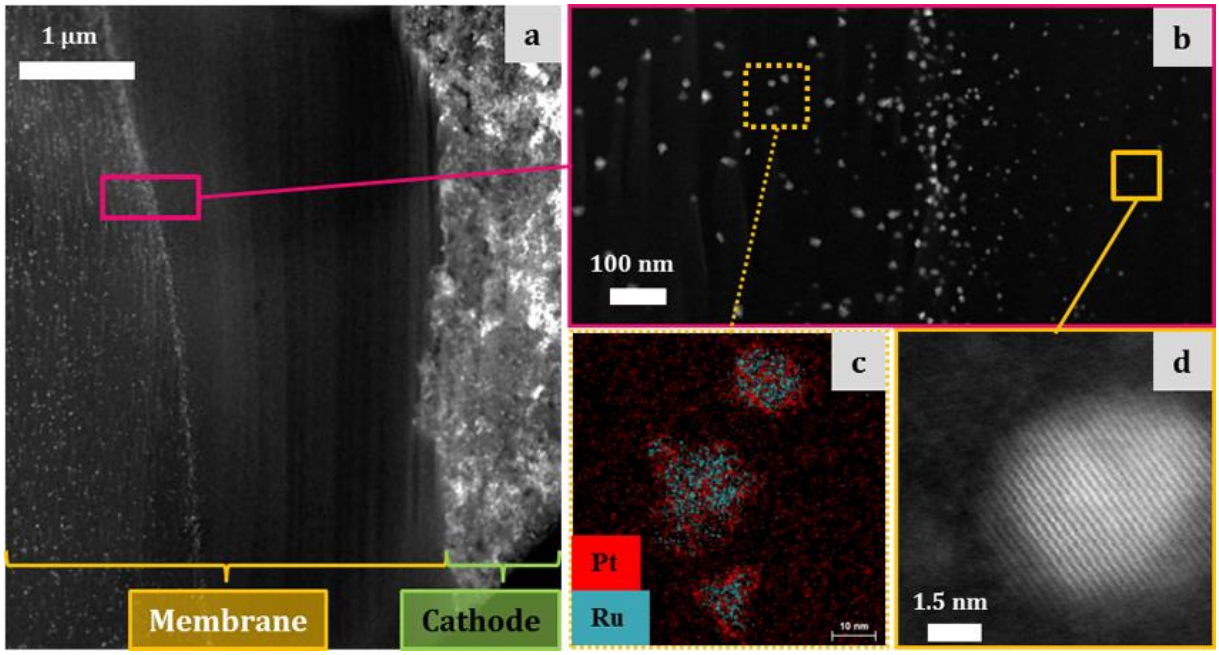

Figure 2

MS3.P020
In situ STEM measurement of grain growth in $CuInSe_2$ during $Cu_{2-x}Se$ in-diffusion

E. Simsek Sanli[1], H. Stange[2], D. Greiner[3], D. Abou-Ras[3], N. Schäfer[3], R. Mainz[3], W. Sigle[1]
P. A. van Aken[1]

[1]Max Planck Institute for Solid State Research, Stuttgart Center for Electron Microscopy, Stuttgart, Germany
[2]Technische Universität Berlin, Berlin, Germany
[3]Helmholtz-Zentrum Berlin für Materialien und Energie GmbH, Berlin, Germany

e.simsek@fkf.mpg.de

Introduction: Polycrystalline $Cu(In,Ga)Se_2$ (CIGS) thin-film solar cells exhibit high power-conversion efficiencies of >22 % [1]. CIGS absorber layers for the highest efficiency solar cells are deposited by a three-stage co-evaporation process [2]. In the second stage of this process, Cu-Se is deposited on top of an In-Ga-Se precursor layer. The growing Cu-In-Ga-Se layer is initially Cu-poor ([Cu]/([In]+[Ga])<1), then Cu-rich ([Cu]/([In]+[Ga])>1) towards the end of the second stage. Grain growth and defect annihilation are known to occur during the Cu-poor/Cu-rich transition. Excess $Cu_{2-x}Se$ is assumed to play a crucial role in these microstructure changes, once the stoichiometric $Cu(In,Ga)Se_2$ composition is exceeded.
Objectives: Our aim in the present study was to elucidate the relation of $Cu_{2-x}Se$ in-diffusion and microstructure changes by studying the grain growth in $CuInSe_2$ during the Cu-poor/Cu-rich transition by in-situ heating scanning transmission electron microscopy (STEM).
Materials and Methods: We prepared a Cu-poor $CuInSe_2$ (CIS) thin film with a Cu_2Se capping layer on top. We first confirmed the composition of the ternary CIS and the Cu_2Se capping layer by energy-dispersive X-ray spectroscopy (EDXS). Subsequently, we heated the sample from 30 °C to 450 °C within the microscope and probed the changes in the microstructure by low-angle annular dark-field (LAADF) imaging. After the sample had cooled down, we repeated the STEM-EDXS measurement in order to detect compositional changes in the absorber layer. In addition to the STEM investigations, we performed transmission Kikuchi diffraction (TKD) to obtain the local orientation of each grain and to estimate the grain boundary planes.
Results: We could detect the movement of grain boundaries resulting in grain growth as shown in Fig. 1a-b by the yellow-dotted ovals. It can be seen that the defect-free grains grow towards the high defect density grains. STEM-EDXS line-scans along the lines indicated by the red arrows (Fig. 1c-d) confirm that during annealing the excess Cu in the Cu_2Se grains diffuses into the Cu-poor CIS lattice and results in a homogeneous composition over the whole layer. The homogeneous elemental distribution along the film is a result of cation redistribution, because the Se sublattice is preserved for both phases [3]. Fig. 1e shows the orientations of the grains.
Conclusion: This contribution provides the first direct in-situ view of grain boundary movement in CIS during Cu in-diffusion. The results provide valuable insights about structural and chemical changes during the crucial second stage of the CI(G)S thin-film absorber fabrication process.

References:
[1] Jackson, P., et al., *Effects of heavy alkali elements in Cu(In,Ga)Se2 solar cells with efficiencies up to 22.6%.* Physica Status Solidi (RRL) – Rapid Research Letters, 2016. **10**(8): p. 583-586.
[2] Gabor, A.M., et al., *High-efficiency CuInxGa1−xSe2 solar cells made from (Inx,Ga1−x)2Se3 precursor films.* Applied Physics Letters, 1994. **65**(2): p. 198.
[3] Wada, T., et al., *Growth of CuInSe2 crystals in Cu-rich Cu-In-Se thin films.* Journal of Materials Research, 1997. **12**(6): p. 1456-1462.

Acknowledgements
The work was supported by Helmholtz Virtual Institute HVI-520 "Microstructure Control for Thin-Film Solar Cells".

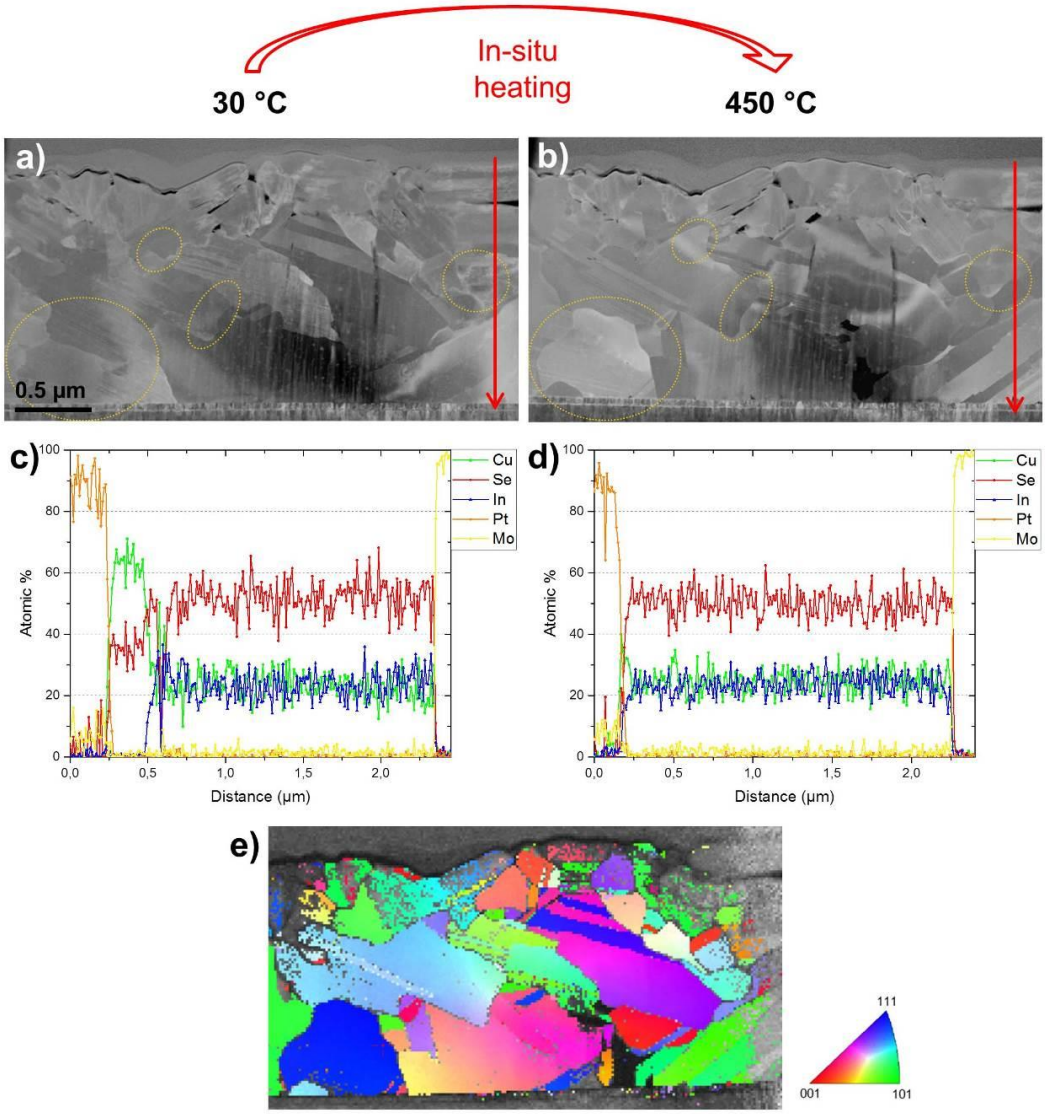

Figure 1. STEM-LAADF image of the sample a) before and b) after in-situ heating. STEM-EDXS line-scans c) before and d) after the heating experiment from the same positions as indicated by the red arrows. e) The TKD orientation map acquired from the same region.

MS3.P021
ELNES simulations of IrO_x catalysts for water splitting

W. Hetaba[1,2], E. Willinger[1,2], M. G. Willinger[2,3], R. Schlögl[1,2]

[1]Max-Planck-Institute for Chemical Energy Conversion, Department of Heterogeneous Reactions, Mülheim an der Ruhr, Germany
[2]Fritz Haber Institute of the Max Planck Society, Department of Inorganic Chemistry, Berlin, Germany
[3]Max-Planck-Institute of Colloids and Interfaces, Department of Colloid Chemistry, Potsdam, Germany

hetaba@fhi-berlin.mpg.de

Question: Iridium oxides and hydroxides are promising catalysts for water splitting due to their high stability and activity. [1] In order to gain greater insight into their functionality and (electronic) structure, a number of microscopical and analytical techniques were applied to iridium oxide and potassium iridium oxide as well as IrO_x-hydroxides. [2] Previous work suggests that the amorphous IrO_x-hydroxides can consist of IrO_2-rutile and $K_{0.25}IrO_2$-hollandite structural motifs. With the purpose to improve understanding of the electronic structure, EELS analysis was performed.
Methods: In this work, DFT based simulations of the O-K edge ELNES for different iridium oxides were performed, analysed and compared to experimental spectra. We used the FP-LAPW code WIEN2k and the TELNES subroutine [3] to carry out the calculations for three materials: IrO_2 [4] and two hollandite structures, $K_{0.25}IrO_2$ [5] and KIr_4O_8 [6], which have different octahedral distortions. In Table 1, the positions of the oxygen atoms in the hollandite structures are given. The results were analysed with respect to the contribution of the different oxygen atoms to the total spectrum.
Results: Figure 1 shows the total O-K edge ELNES of the three calculated structures. The relative intensities of the first and second peak differ for the investigated materials. Furthermore, the ELNES of the two hollandite structures exhibits a shoulder in the onset of the third peak at ~7 eV after the edge onset and the second peak is shifted towards lower energy losses compared to that of the spectrum of IrO_2.
In Figures 2 and 3, the total O-K ELNES of KIr_4O_8 and $K_{0.25}IrO_2$ are shown together with the corresponding contributions of the different oxygen atoms. From these plots it is clear that for KIr_4O_8 the atoms O2 and for $K_{0.25}IrO_2$ the atoms O1 have the highest contribution to the features in the fine-structure that make the difference to the spectrum of IrO_2. In both materials, these are the atoms having the smallest distances to the K atom.
Conclusions: Comparison of the calculated and experimental spectra of IrO_2 and $K_{0.25}IrO_2$ (not shown) leads to a good agreement. Furthermore, the simulations confirm the results of experimental EELS measurements and pair distribution function analysis of previous work [2]. This suggests that the amorphous IrO_x-hydroxide synthesized at FHI is best described by hollandite structural motifs. Additionally, the calculated spectra allow to distinguish the contributions of each atom at different crystallographic positions to the total spectrum. This improves the understanding of the structure-property relationship of these highly promising catalyst materials.

[1] Massue et al., ChemSusChem, DOI: 10.1002/cssc.201601817
[2] Willinger et al., in preparation
[3] Blaha et al., WIEN2k, TU Wien (2001), ISBN 3-9501031-1-2
[4] Talanov et al., Inorganic Chemistry (2014) **53**, 4500-4507
[5] Bestaoui et al., Journal of Solid State Chemistry (1995) **118**, 372-377
[6] Bolzan et al., Acta Crystallographica (1997), **B53**, 373-380

KIr_4O_8	*I4/m*			
Atom	Wyckoff-pos.	x	y	z
O1	8h	0.8402	0.5451	0.0
O2	8h	0.8484	0.7968	0.0

$K_{0.25}IrO_2$	*I12/m1*			
Atom	Wyckoff-pos.	x	y	z
O1	4i	0.141	0	0.193
O2	4i	0.782	0	0.151
O3	4i	0.549	0	0.188
O4	4i	0.857	0	0.857

Table 1. Space groups and oxygen positions of the two investigated hollandite structured iridium oxides.

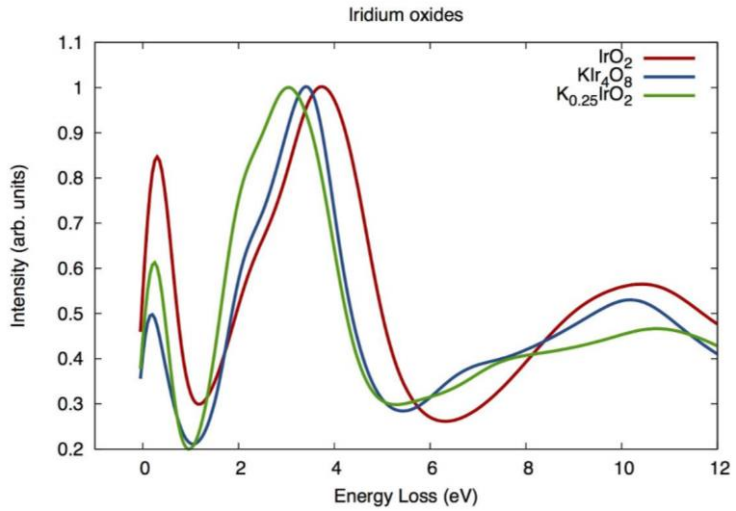

Figure 1. Oxygen K-edge ELNES calculation for iridium oxide and two potassium iridium oxides.

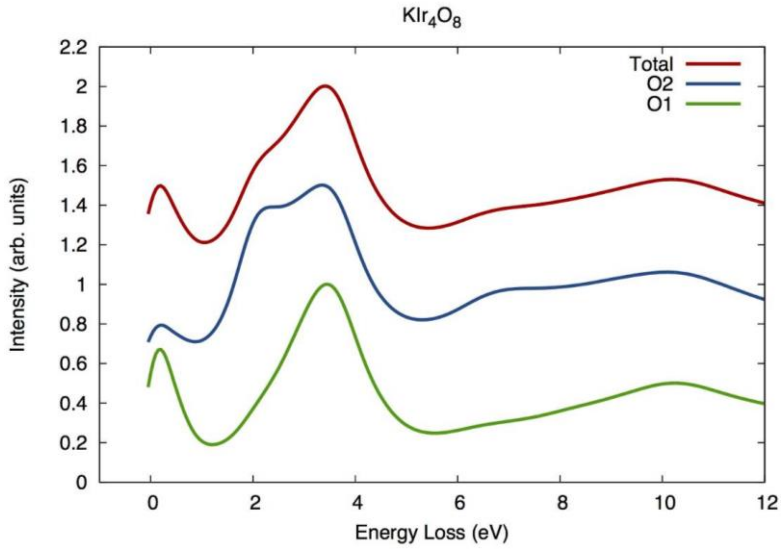

Figure 2. Total oxygen K-edge ELNES of KIr_4O_8 and the contributions of the two oxygen atoms at different crystallographic positions.

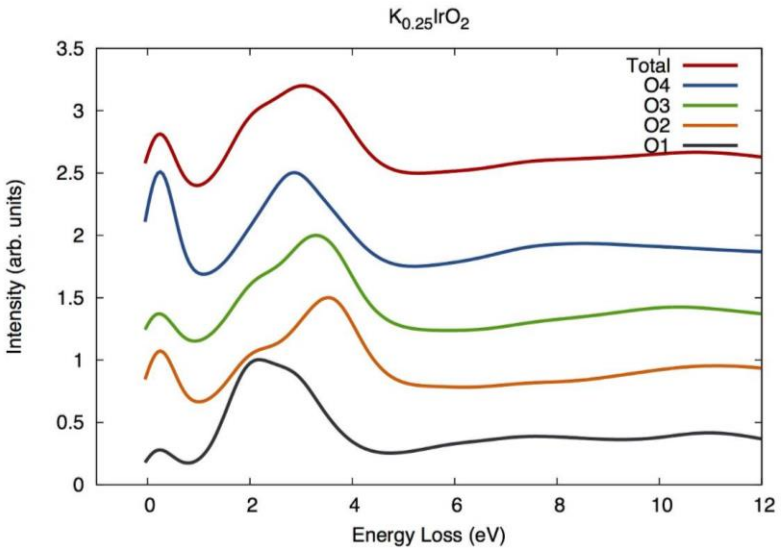

Figure 3. Total oxygen K-edge ELNES of $K_{0.25}IrO_2$ and the contributions of the four oxygen atoms at different crystallographic positions.

MS3.P022
Effect of thermal cycles on microstructure of Er_2O_3 thin film with Y_2O_3 layer for advanced breeding blanket system

M. Tanaka[1], S. Lee[2], K. Matsuda[2], Y. Hishinuma[3], T. Tanaka[3], T. Muroga[3], S. Ikeno[4]

[1]University of Toyama, Graduate School of Science and Engineering for Education, Toyama-shi, Japan
[2]University of Toyama, Graduate School of Science and Engineering for Research, Toyama-shi, Japan
[3]National Institute of Fusion Science, Toki-shi, Japan
[4]University of Toyama, Professsor of Emeritus, Toyama-shi, Japan

mt.nnn1119@gmail.com

Introduction: In breeding blanket system of nuclear fusion reactor, it is needed an advanced type of coating for leak controlling of tritium and reducing Magneto-Hydro-Dynamic (MHD) pressure drop. The materials for MHD insulating coating must fulfill some severe conditions. It has been reported that Er_2O_3 is the processing as the features which excellent electrical resistance and a permeation control effect. Hishinuma *et al.*[1)] succeeded in fabrication of Er_2O_3 film by metal organic chemical vapor deposition (MO-CVD) method as a new technology for large area coating on broad and complicated shaped components[2)]. MO-CVD method is a proper procedure to form homogeneous and large area coating layer synthesized from a metal organic complex.
Objectives: The aim of this research is to estimate the thermal stability of the Er_2O_3 coating layer deposited on buffer- Y_2O_3 thin film on stainless steel 316 (SUS316) plate before and after thermal cycles by means of microstructure observation.
Materials and Methods: The buffer-layers of Y_2O_3 was formed by RF-sputtering method on a SUS316 substrate plates and, then Er_2O_3 thin film coated by MO-CVD method. The one sample had been added thirty thermal cycles at around 973 K in argon atmosphere. Scanning, transmission, scanning-transmission electron microscopes and atomic force microscope SEM (Hitachi S3500), TEM (JEOL 4010T), STEM (JEOL JEM-2800) and AFM (Hitachi 5100N) were used for analyzing surface and cross-sectional of samples. Small cross sectional TEM samples were prepared by FIB method.
Result: SEM images before and after thermal cycling show that small particles have confirmed on the surface of Er_2O_3 thin film and, it was refined after thirty times of thermal cycling. The surface morphology of AFM-3D image also shows refinement of particles, too. All XRD peaks indexed with Er_2O_3 and Y_2O_3, then it revealed that Er_2O_3 layer with Y_2O_3 thin film has good thermal stability with 222 preferential peak. Cross-sectional TEM images of Er_2O_3 layer with Y_2O_3 thin film before thermal cycling show that the thickness of Er_2O_3 and Y_2O_3 layer are 620 nm and 690 nm, respectively. In the same area, the high-magnification images of the two layers indicated 111 growth direction. Cross sectional image after thermal cycling shows that the thickness for Er_2O_3 and Y_2O_3 layer are 620 nm and 690 nm, only the thickness of Er_2O_3 layer decreased from 620 nm to 390 nm. In our recent report for the single layer of Er_2O_3 thin film on the SUS316 substrate, the thickness of Er_2O_3 layer decreased after thermal cycling in Ref. 3. STEM-EDS map images of Er, Y, O, Cr, Fe and Ni before thermal cycling show that white contrast layer existed between Y_2O_3 layer and SUS316 substrate included Fe, Cr and O elements, while it was noted that downward convex layer was generated between Y2O3 layer and the substrate by thermal cycles, and the result of STEM-EDS map suggested that the iron-oxide layer was formed during thermal cycles. As the results, thermal cycles effected the structure of layers and decreased the thickness of Er_2O_3 thin film.
Conclusion:

(1) SEM and AFM images show that the shape of $Er_{2O}3$ thin film extremely changed before and after thermal cycling, and particle size decreased dramatically.
(2) The result of XRD analysis revealed that Er_2O_3 layer with Y_2O_3 thin film has good thermal stability and 222 preferential peak, and high power-field TEM image shows the growth direction has been 111 direction.
(3) TEM cross sectional images revealed that the thickness of $_{Er2O3}$ thin film decreased from 620 nm to 390 nm after thermal cycling, and the thickness of Y_2O_3 layer kept during thermal cycling.
(4) Before thermal cycling the white contrast layer has been existed between Y_2O_3 thin film and SUS316 substrate, STEM-EDS map detected Fe, Cr and O, while after the un-known layer has been included Fe and O after thermal cycling.

Reference:

[1] B. A. Pint, P. F. Tortorelli, A. Jankowski, J. Hayes, T. Muroga, A. Suzuki, O. I. Yeliseyeva and V. M. Chernov, J. Nucl. Mater. 329-333, 119 (2004).

[2] Y. Hishinuma, T. Tanaka, T. Tanaka, T. Nagasaka, Y. Tasaki, A. Sagara and T. Muroga, Fusion Eng. Des. 86, 2530-2 (2011).
[3] M. Tanaka, M. Takezawa, Y. Hishinuma, T. Tanaka, T. Muroga, S. Ikeno, S. Lee and K. Matsuda, Fusion Eng. Des. 11, 2405120 (2016).

MS3.P024
High-resolution electron microscopy analyses of Pt nanoparticles deposited on stainless steel in simulated boiling water reactor environment

S. Rowthu[1], L. Veleva[1], P. Grundler[1], S. Ritter[1]

[1]Paul Scherrer Institut (PSI), Nuclear Energy and Safety Research Division, Villigen, Switzerland

sriharitha.rowthu@psi.ch

Introduction**:** For the safe and reliable operation of nuclear power plants a tight control of corrosion issues of reactor components is essential. Stress corrosion cracking (SCC) in boiling water reactors (BWRs) has caused enormous capacity losses and has been a major concern for three decades [1]. The radiolysis products of water (O2/H2O2) result in a highly oxidising environment, which leads to high electrochemical corrosion potentials (ECPs) and therefore also to high SCC susceptibility. The ECP can be decreased by adding a reductant such as H2. To improve the efficiency of the added H2, the online noble metal chemical addition (OLNC) technology was developed by General Electric. It consists of injecting noble metal compounds (Na2Pt(OH)6) into reactor feedwater of a BWR [2], which decomposes to form metallic Pt nanoparticles. These nanoparticles deposit on all the water wetted surfaces and catalyse the reduction of O2/H2O2 in the presence of H2, thus decreasing the ECP and mitigating SCC of reactor components.
Objective**:** To verify and increase the efficiency of the OLNC technology the deposition behaviour of Pt particles on stainless steel surfaces is investigated in detail at PSI.
Materials and Methods: For this purpose specimens are exposed to simulated BWR conditions using a custom built high-temperature water loop. In depth microscopy analyses are being carried out to evaluate the spatial distribution of Pt particles, their average particle size, and size distribution which are important parameters that need to be studied. It is highly recommended and beneficial to limit the amount of Pt injection into the reactor to restrict excessive amounts of Pt getting deposited on fuel rods. To this effect, smaller particle sizes need to be obtained, as they additionally provide high surface area for the catalysis activity.
Results**:** Figure 1a shows an example of a Pt-treated specimen with particles deposited rather evenly on the oxide layer surface. The corresponding Pt particle size distribution can be seen in Figure 1b. The average particle size on this test is 11.5 nm. It could be found that the average particle size is decreasing with decreasing Pt injection rate.
It could be demonstrated in lab tests, as well as in an actual BWR plant, that the Pt surface loading slowly decreases with time [3]. Therefore it is of great interest to find out more about how the Pt particles are bonded on the surface of the oxide crystals.
To identify the shape of single Pt particles and possible preferential sites were Pt particles deposit on, TEM and STEM studies (combined with EDS) have been performed. Some examples are shown in Figure 2. Pt particles are found on Cr rich as well as on Ni rich oxide crystals.
Conclusion**:** The spatial as well as the size distribution of Pt particles on the stainless steel oxide were successfully assessed. Smaller Pt injection rates produce smaller Pt particles which are more efficient at SCC mitigation and they are evenly spread over the oxide film.

References:
[1] R. Kilian, and A. Roth, "Corrosion Behaviour of Reactor Coolant System Materials in Nuclear Power Plants," *Materials and Corrosion,* 2002, **53**, 727-739.
[2] P. V. Grundler, and S. Ritter, "Noble Metal Chemical Addition for Mitigation of Stress Corrosion Cracking: Theoretical Insights and Applications," *PowerPlant Chemistry,* 2014, **16**(2), 76-93.
[3] P. V. Grundler, S. Ritter, L. Veleva, G. Ledergerber, and R. S. Pathania, "Investigation of the platinum deposition behavior on stainless steel surfaces in a boiling water reactor plant," *Int. LWR Materials Reliability Conference and Exhibition 2016* (2016).

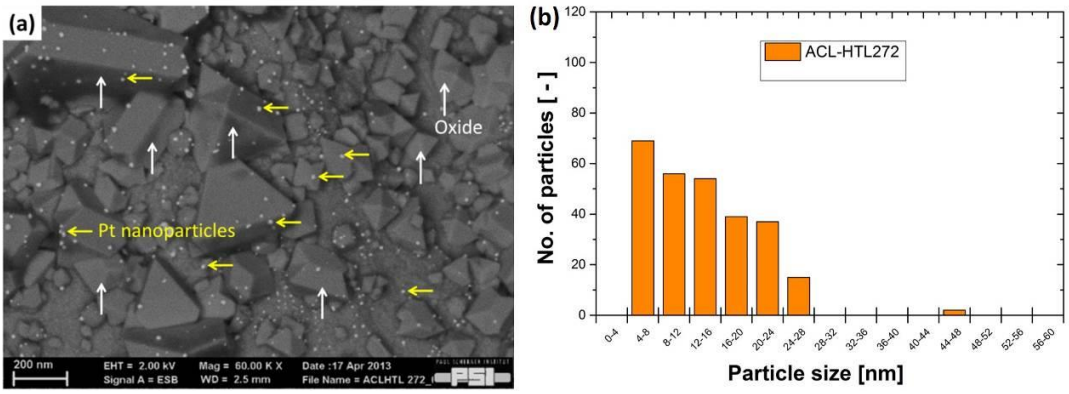

Figure 1. (a) High resolution back scattered electron SEM image showing the distribution of Pt nanoparticles deposited atop oxidised stainless steel. (b) Corresponding Pt particle size distribution.

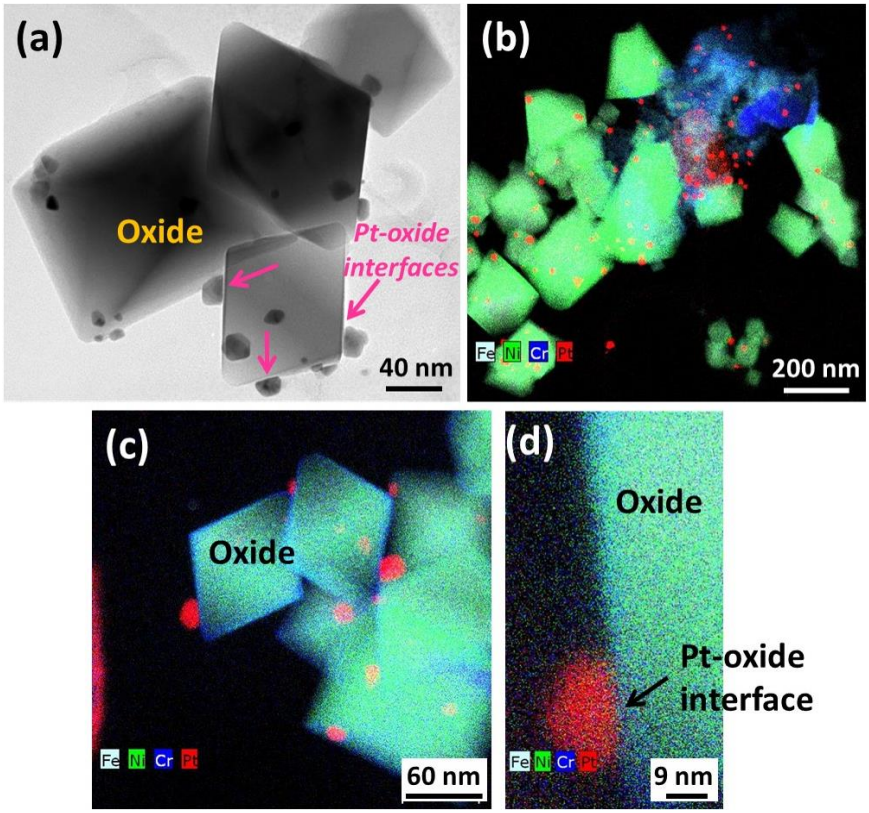

Figure 2. (a) TEM image (brightfield) of few Pt particles atop oxide crystals, also showing Pt-oxide interfaces. (b) EDS mapping of Pt distribution atop (Fe, Ni, Cr)-based oxide indicating that there are no preferential sites for Pt deposition. (c-d) EDS mappings of Pt particle-oxide interface at low and high magnifications. The latter image demonstrates an oval shaped Pt particle at an oxide interface.

MS3.P025
FIB-tomography of spheroidized graphite particles for lithium ion batteries

M. Mundszinger[1], M. Rapp[2], U. Golla-Schindler[1,3], U. Kaiser[1]

[1]Electron Microscopy Group of Material Science, Ulm, Germany
[2]ZSW – Zentrum für Sonnenenergie- und Wasserstoff- Forschung Baden-Württemberg, Ulm, Germany
[3]Material Research Institute (IMFAA), Aalen, Germany

manuel.mundszinger@uni-ulm.de

In modern lithium ion batteries (LIB), natural graphite is used as anode material. In this work, this natural graphite anode material is investigated. For spheroidisation, particle design mills are utilised. The milling process is fully mechanical and uses impact and shear forces. The raw material are graphite flakes with diameters up to 300 µm.
Spheroidisation of the graphite for the usage in LIBs has several advantages compared to the flat graphite flakes. While charging the battery, lithium ions intercalate into the graphite layers through crystal defects. In the case of graphite flakes, these defects occur on the break lines of the flakes and constitute the paths for intercalation. Intercalation from the top part is not possible. Spheroidisation breaks the crystal lattice and offers additional paths for lithium intercalation. Furthermore, graphite flakes tend to arrange in the flattest possible configuration in the battery and thus hinder the lithium ions to intercalate [1]. While a LIB is charged and discharged, the solid electrolyte interface (SEI) builds up. The SEI is a result of chemical reactions of the electrolyte on the surface of the graphite. This reaction binds lithium ions and the capacity of the battery decreases. Spheres have the best surface/volume ratio and help to decrease the impacts of the SEI on the battery capacity.
The milling process in the particle design mills does not produce homogeneous outcome, the graphite particles have considerably different sizes with different electrochemical characteristics. Figure 1 shows particles from one and the same batch, sorted regarding the diameter; (a1) coarse (25 µm to 35 µm), (b1) mid (15 µm to 25 µm) and (c1) fine (10 µm to 15 µm). The corresponding FIB cross-sections are presented underneath in (a2) -(c2). The images show that the smaller the particles are, the rougher the appearance is. The FIB cross sections show the folded structure which stems from the graphite flake raw material and shows elongated pores. The cross sections indicate that the porosity decreases with decreasing particles size. For quantitative comparison of the particles, FIB-tomography is utilised. Hereby two different kinds of pores can be found, open pores with connection to the particle surface and closed ones. From FIB-tomograms the porosity was calculated. Porosity is the volume fraction of the pores (open or closed or the combined volume) and the whole particle volume (consisting of the graphite and the complete pore volumes) following . The porosity directly affects the qualities of a LIB; a huge porosity lowers the energy density of the battery. Open pores increase the surface of the particles and therefore more SEI builds up.
In summary, we investigated natural graphite anode after spheroidisation from the same sample batch. We classified the particle into three groups and quantified significant different pore sizes and pore characteristics in dependence of the particle size group. [2]

[1] M. Mundszinger, S. Farsi, M. Rapp, U. Golla-Schindler, U. Kaiser, M. Wachtler, "Morphology and texture of spheroidized natural and synthetic graphites", *Carbon* 111, 764-773, (2017).
[2] We thank the German Federal Ministry of Education and Research (BMBF) for financial support in the frame of the Li-EcoSafe-project, contract no. 03X4636.

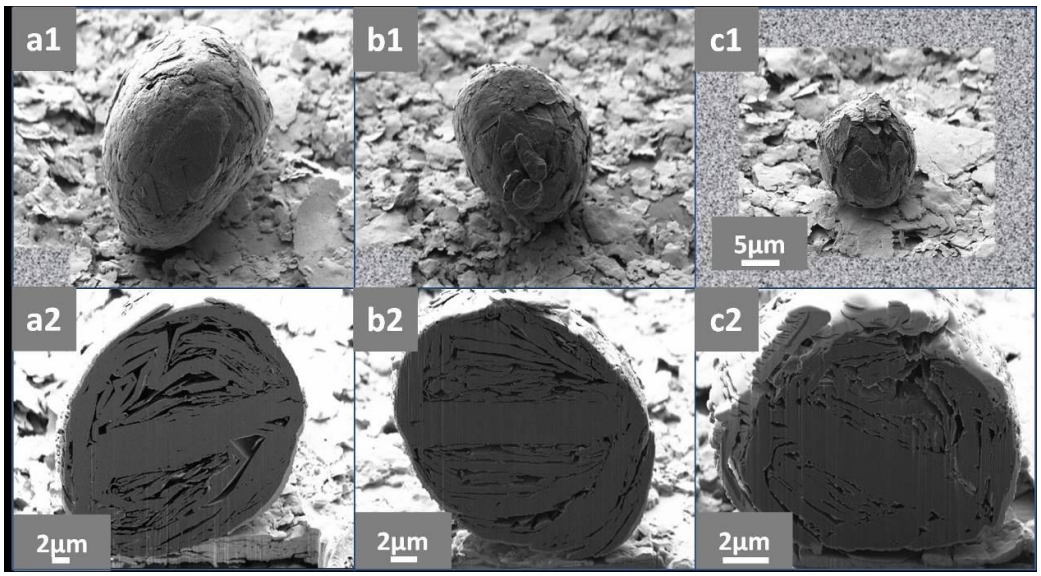

Figure 1. 1 kV SEM images (a1-c1) together with the corresponding FIB cross-sections (a2-c2) of spheroidised graphite particles in dependence of their sizes. (a) coarse, (b) mid and (c) fine particles. (a1-c1) show the particles and (a2-c2) FIB cross sections. All particles stem from the same sample batch.

MS3.P026
In situ formation and electric-field induced dynamics of core-shell $Bi_{1/2}Na_{1/2}TiO_3$–$xSrTiO_3$ piezoelectric particles

L. Molina-Luna[1], S. Wang[2], Y. Pivak[3], A. Zintler[1], M. Yi[2], Q. Xu[3,4], N. Liu[5], C. Dietz[5], R. W. Stark[5]
H. J. Kleebe[1], B. Xu[2], M. Acosta[1]

[1]Technische Universität Darmstadt, Department of Materials and Geosciences, Darmstadt, Germany
[2]Technische Universität Darmstadt, Department of Materials and Geosciences, Mechanics of Functional Materials Division, Darmstadt, Germany
[3]DENSsolutions, Delft, Netherlands
[4]TU Delft, Kavli Centre of NanoScience, National Centre for HREM, Delft, Netherlands
[5]Technische Universität Darmstadt, Department of Materials and Geosciences, Physics of Surfaces, Darmstadt, Germany

molina@geo.tu-darmstadt.de

Introduction**:** Ferroic materials play a key role in a wide range of technologically relevant devices. They all share the common feature that the microstructure and domains determine to a great extent their functionality. Among the promising piezoelectric materials for actuation applications is the solid solution $Bi_{0.5}Na_{0.5}TiO_3$ (BNT)-$SrTiO_3$ (ST).[6–9] Recently it was found that this material is characterized by a core-shell microstructure that largely determines its electromechanical and dielectric properties.[1,10] In this contribution, we reveal the core-shell and domain formation in nanoparticles during a calcination process by means of in-situ TEM experiments. The solid state chemical reactions occurring upon heating could be followed in real time and the temperature-dependent core-shell formation and structural evolution was investigated. Furthermore, combined in situ TEM electric-field (at elevated temperatures) and Finite Element Analysis (FEAP) based modelling revealed a strain dependant response in the BNT-ST nanoparticle that includes an interplay between the core and the shell regions and induces nanometer sized polar regions. When an electric-field of up to 20 kV/mm is applied a monodomain state forms in the core region and tends to align in the direction of the applied electric field.
Objectives**:** Controlled heating and biasing TEM experiments on lead-free solid solution $Bi_{1/2}Na_{1/2}TiO_3$ (BNT)-$xSrTiO_3$ (ST) system.
Materials and Methods: In situ TEM experiments were performed using a dedicated in-situ TEM DENSsolutions double-tilt holder and a MEMS biasing/heating chip.
Results**:** See Figure 1 and Figure 2.
Conclusion We demonstrate the formation of functional core-shell nanoparticles synthesized *in situ* in a TEM via the solid-state-route. Piezoelectric force microscopy was used to confirm the piezoelectric activity at room temperature of fully synthesized nanoparticles. The resulting core-shell type nanostructure is a direct consequence of the slow diffusion of Sr^{2+} cations.

References:
[1] M. Acosta, *et. al.,* J. Am. Ceram. Soc. 97 (2014) 1937–1943.
[2] Y. Hiruma, *et. al.,* Appl. Phys. Lett. 92 (2008) 262904.
[3] W. Krauss, e*t. al.,* J. Eur. Ceram. Soc. 30 (2010) 1827–1832.
[4] H.-L. Li, *et. al.,* J. Eur. Ceram. Soc. 36 (2016) 2849–2853.
[5] M. Acosta *et. al.,* J. Am. Ceram. Soc. 98 (2015) 3405–3422.
[6] J. Koruza e*t. al.,* J. Eur. Ceram. Soc. 36 (2016) 1009–1016.

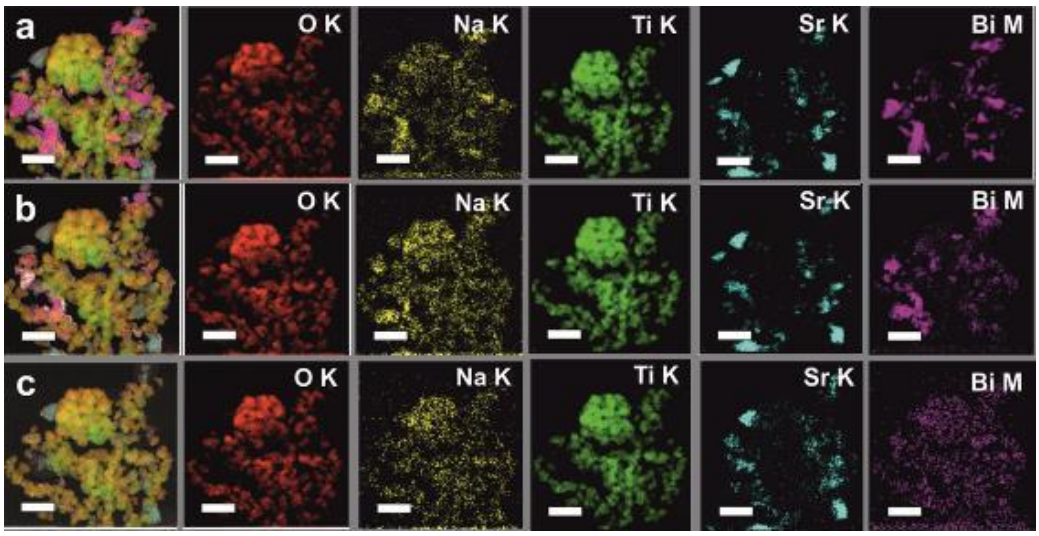

Figure 1. Energy-dispersive x-ray mapping at elevated temperatures. STEM-EDS mapping of the core-shell formation in $Bi_{1/2}Na_{1/2}TiO_3$ (BNT)-x$SrTiO_3$ at high-temperature color coded image and corresponding elemental maps at a) 300 °C, b) 600 °C and c) 600 °C after in situ heating treatment at 800 °C for two hours. Scale bar: 250 nm.

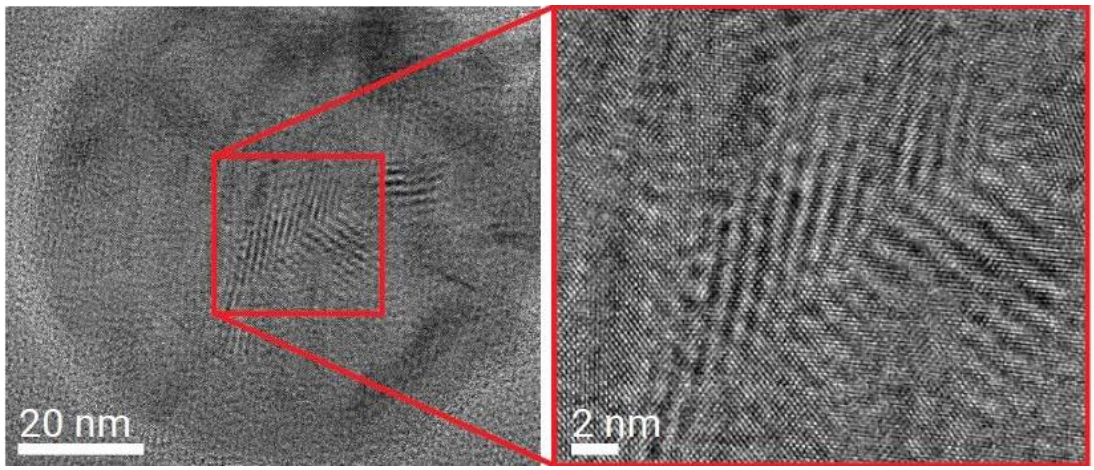

Figure 2. $Bi_{1/2}Na_{1/2}TiO_3$ (BNT)-x$SrTiO_3$ Core-shell nanoparticle. RTEM image of a $Bi_{1/2}Na_{1/2}TiO_3$ (BNT)-x$SrTiO_3$ core-shell nanoparticle formed after the complete calcination process in the TEM. A strained area within the core that contains nanodomains is observed.

MS3.LBP01
Antisite disorder and bond valence compensation in Li_2FePO_4F cathode for Li-ion batteries

O. Karakulina[1], N. Khasanova[2], O. Drozhzhin[2], A. Tsirlin[3], J. Hadermann[1], E. Antipov[2], A. Abakumov[1,4]

[1]University of Antwerp, Electron Microscopy for Materials Science (EMAT), Antwerp, Belgium
[2]Lomonosov Moscow State University, Chemistry, Moscow, Russian Federation
[3]University of Augsburg, Center for Electronic Correlations and Magnetism, Augsburg, Germany
[4]Skolkovo Institute of Science and Technology, Skoltech Center for Electrochemical Energy Storage, Moscow, Russian Federation

olesia.karakulina@uantwerpen.be

The way the crystal structure of a cathode material changes during operation of Li-ion battery has a crucial impact on its electrochemical performance [1]. The main feature of such compounds is their framework or layered structure, which is formed by transition metals along with oxygen atoms or polyanion groups. They contain voids, which are filled with Li in discharged state and become partially empty at charged state of the battery. In the latter case, transition metal atoms can migrate into the empty Li position and block the Li-ion pathways. If such migration is not reversible, it can result in a voltage fade. Such disorder is not well studied for polyanion cathode materials, except for olivines $LiMPO_4$ (M=Fe, Co). Therefore, we studied the promising Li_2FePO_4F cathode material, which is a A_2MPO_4F polymorph with three-dimensional structure. To determine the crystal structure of the resulting phase, electron diffraction tomography (EDT) was used. This method allows to obtain crystallographic information from single crystals of 200 nm size and it provides qualitative and quantitative information about the Li atoms. Moreover, EDT is not hindered by the presence of secondary phases added for making a functioning battery.

Li_2FePO_4F was prepared by electrochemical exchange of Li for Na in $LiNaFePO_4F$ [2].To speed up cation diffusion, elevated temperature (75^{o}C) was used. Indeed, Na was completely removed as determined by EDX. For the preliminary structure refinement we used a structure model based on $LiNaFePO_4F$, in which Na was replaced to Li. It results in an excess of scattering density in the Li positions and deficiency of it in the Fe ones, which shows the presence of Fe-Li antisite disorder. Therefore, the Li and Fe atoms were then refined as mixed, which led to a decrease in reliability factor RF from 0.295 to 0.219. It appears that nearly 30% of Li occupies Fe positions and vise versa [3].

To find the origin of such dramatic anti-site disorder, we also studied the crystal structure of Li_2FePO_4F prepared at room temperature and of $LiFePO_4$ cycled at 100^{o}C. in the first case the disorder was present, whereas in the last case it was absent. Therefore, elevated temperature cannot be considered as the primary reason for anti-site defects in these polyanion compounds. We suppose that the difference in the crystal structure of Li_2FePO_4F and $LiFePO_4$ is the main factor for their dissimilar behavior. In contrast to $LiFePO_4$, where all oxygen atoms are connected with Li, Fe and P, the Li_2FePO_4F structure has two oxygens that are connected with one P and three Li atoms, two out of which are electrochemically active atoms. As a result, Li removal leads to underbonding of these oxygen atoms. This cannot be compensated by shrinking of bonds with P. Therefore, Fe^{3+} atoms partially migrate into the Li position to eliminate this misbalance. It does not occur in $LiFePO_4$, since all oxygen atoms are connected with electrochemically active Li and Fe, which compensate each other.

[1] Sathiya, M., Abakumov, A. M., Foix, D., Rousse, G., Ramesha, K., Saubanère, M., Doublet, M. L., Vezin, H., Laisa, C. P., Prakash, A. S., Gonbeau, D., VanTendeloo, G. & Tarascon, J.-M. (**2015**). Nat. Mater. 14, 230–238.
[2] Khasanova, N. R., Drozhzhin, O. A., Storozhilova, D. A., Delmas, C. & Antipov, E. V. (**2012**). Chem. Mater. 24, 4271–4273.
[3] Karakulina, O. M., Khasanova, N. R., Drozhzhin, O. A., Tsirlin, A. A., Hadermann, J., Antipov, E. V. & Abakumov, A. M. (**2016**). Chem. Mater. 28, 7578–7581.

MS3.LBP02
Revealing the pseudosymmetry by dictionary-based indexing approaches for new insights of microstructural properties of CuInSe2

N. Schäfer[1], M. De Graef[2], T. Rissom[1], D. Abou-Ras[1]

[1]Helmholtz-Zentrum Berlin, Berlin, Germany
[2]Carnegie Mellon University, Department of Materials Science and Engineering, Pittsburgh, PA, United States of America

norbert.schaefer@helmholtz-berlin.de

Electron backscatter diffraction (EBSD) represents a powerful technique to reveal the microstructure of polycrystalline materials. Based on characteristic electron backscatter diffraction patterns (EBSP), crystallographic orientations of individual grains with respect to a Reference: coordinate system can be determined [1]. EBSD has been used to investigate grain boundaries, orientation and microstrain distributions within CuInSe2 absorber layers in the recent years [2-4]. Due to very small deviations from lattice constant c/a = 2 ratio in the crystal lattice, which is referred as pseudosymmetry, the chalcopyrite-type structure is treated like a cubic sphalerite structure.
New approaches using energy weighted dynamically simulated EBSP might reveal new insights of absorber layer structures and possible a better understanding of structure-property relationships.

[1] Abou-Ras et al., Cryst. Res. Technol. 43, No. 3, 234 – 239 (2008).
[2] Abou-Ras et al., Acta Materialia 118 (2016) 244-252.
[3] Schäfer et al., J. Appl. Cryst. 49 (2), 632-635, 2016.
[4] Schäfer et al., Ultramicroscopy (2016) 169, 89-97.

MS3.LBP03
Influence of various buffers in Cu(In,Ga)Se2 solar cells by electron beam-induced current measurements

N. Schäfer[1], M. Krause[1], A. Nikolaeva[1], J. Márquez[1], C. Hages[1], S. Levcenko[1], W. Witte[2], D. Hariskos[2]
L. Lepetit[3], N. Barreau[3], G. Moldovan[4], T. Unold[1], D. Abou-Ras[1]

[1]Helmholtz-Zentrum Berlin , Stuttgart, Germany
[2]Zentrum für Sonnenenergie- und Wasserstoff-Forschung Baden-Württemberg (ZSW), Stuttgart, Germany
[3]Institut des Matériaux Jean Rouxel, Université de Nantes, Nantes, France
[4]point electronic GmbH, Halle, Germany

norbert.schaefer@helmholtz-berlin.de

Electron-beam-induced current (EBIC) in a scanning electron microscope [1-3] (SEM) is established as a standard tool for analysis of local short-circuit current densities at electrical junctions [4,5]. The present work gives insight into how EBIC measurements are applied to investigate the influence of different buffer layers. Cu(In,Ga)Se2 layers were coevaporated by in-line multi-stage or 3-stage processes and various buffers were grown by either chemical bath deposition (CBD) or physical vapor deposition (PVD). Cross-sectional specimens of completed solar cells were polished only mechanically. A 4-5 nm thick carbon layer was deposited on the cross-section to reduce surface recombination and to preserve the surface. EBIC measurements were performed using a Zeiss UltraPlus SEM with a point electronic amplifier system at 7 kV and beam currents of approx. 20 pA to avoid high-injection conditions.

[1] Leamy, J. Appl. Phys. 53, R51 (1982)
[2] SEM Microcharacterization of Semiconductors, edited by D.B. Holt and D.C. Joy (Academic Press, London, 1989)
[3] Han et al., Ultramicroscopy, Volume 176, May 2017, Pages 80-85
[4] Abou-Ras et al., AIP Advances 5, 077191 (2015)
[5] Kedem et al., J. Phys. Chem. Lett. 6, 2469−2476 (2015).
[6] Nichterwitz et al., Thin Solid Films 517, pp. 2554-2557 (2009)

MS3.LBP04
Microstructural characterization of $Ce_{0.8}Gd_{0.2}O_{1.9}$ impregnated $La_{0.6}Sr_{0.4}Co_{0.8}Fe_{0.2}O_{3-\delta}$ electrodes

M. A. Floridia[1], J. Ascolani-Yael[2,3], A. Montenegro Hernández[2,3], L. Mogni[2,3], A. Caneiro[1,2,3]

[1]YPF Tecnología, Berisso, Argentina
[2]Comisión Nacional de Energía Atómica, San Carlos de Bariloche, Argentina
[3]CONICET, San Carlos de Bariloche, Argentina

maria.a.floridia@ypftecnologia.com

Introduction: Solid oxide fuel cells (SOFC) are ceramic devices that transform chemical energy into electrical energy with high efficiency. The cells efficiency is mainly limited by the polarization losses associated to ohmic and electrochemical processes, such as oxygen reduction reaction -ORR- at the cathode. The cathode polarization resistance is especially important as operation temperature decreases. This is a big issue since much effort is being made towards lowering the operation temperatures to below 700ºC (IT-SOFC) to reduce, among other things, the different cell components degradation.
One adopted strategy to decrease the cathode polarization resistances, which has generated considerable expectation, is the cathode's surface modification through the so called "wet impregnation technique". This approach consists of synthesizing a catalyst material (which can be a metal, another electrode material, an ion-conducting material or a mixed ionic electronic conductor (MIEC) on top of an already electrochemically-active electrode's surface.
La0.6Sr0.4Co0.8Fe0.2O3-δ (LSCF) is a perovskite structured oxide which is a candidate to be used as a cathode for intermediate temperature solid oxide cells (IT-SOFC) due to its properties as a mixed conductor.
This work presents a microstructural characterization by SEM and TEM of surface modification of LSCF electrodes impregnated by Ce0.8Gd0.2O1.9 (GDC) nanoparticles.
Objectives**:** Considering that the IT-SOFC operates at high temperature during prolonged periods of time, the evaluation of the stability of GDC nanoparticles is an essential issue. By using TEM we have studied the morphology of the GDC nanoparticles on the surface of LSCF before and after annealing at 700 ºC during 500 h in air.
Materials and Methods: LSCF powder was obtained by a chemical method. This material was impregnated with a Ce and Gd nitrates solution. A heat treatment at 800°C for 1 h was performed in order to grow the GDC nanoparticles on the surface of LSCF powder.
The morphology of the Ce0.8Gd0.2O1.9 impregnated La0.6Sr0.4Co0.8Fe0.2O3-δ particles was observed with a FEG-SEM (FEI Nova NanoSEM 230) microscope operated at 5 kV. The impregnated particles and the LSCF/GDC interfaces were analyzed by TEM using a TALOS F200X microscope operating at 200 kV.
Results: Figure 1 shows a SEM image of 10% GDC impregnated LSCF particles. The LSCF grain size is roughly around 100-300 nm. A spatially homogeneous distribution of CGO particles of about 15 nm in size can be observed on the LSCF surface. The SEM images of the GDC impregnated LSCF particles after annealing at 700°C for 500 h did not reveal the presence of the GDC nanoparticles.
Figure 2 shows a TEM image of a LSCF particle impregnated with GDC before the annealing at 700°C for 500 h. The size of GDC particles, which can be observed on the LSCF surface, agrees with those informed by SEM. GDC nanoparticles show crystallographic orientation relationships with LSCF. The presence of semi-coherent interfaces can also be observed. The FFT corresponding to LSCF and a GDC particle are shown.
The TEM image in fig. 3 corresponds to a GDC impregnated LSCF after annealing. The GDC nanoparticles seem to be melted on the LSCF surface which explains why they could not be detected by SEM.
Conclusions**:** High resolution TEM allows to analyze the morphological stability of GDC nanoparticles on LSFC electrode surfaces. Despite the high melting point of bulk GDC, an annealing at 700°C is enough to cause morphological changes in small GDC nanoparticles.

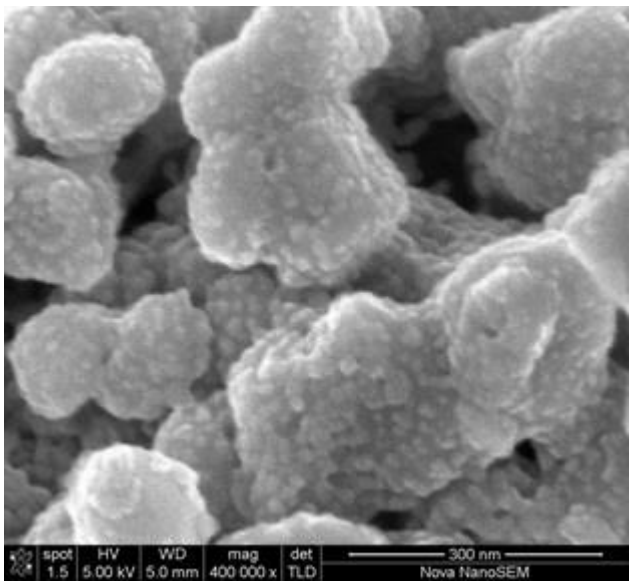

Figure 1. SEM micrograph of GDC impregnated LSCF particles.

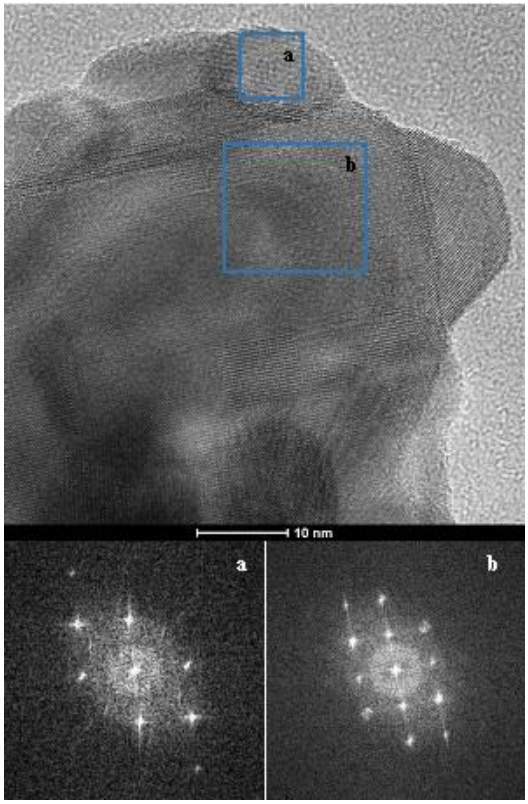

Figure 2. HRTEM image of GDC impregnated LSCF. The FFT corresponding to GDC and LSCF regions are shown.

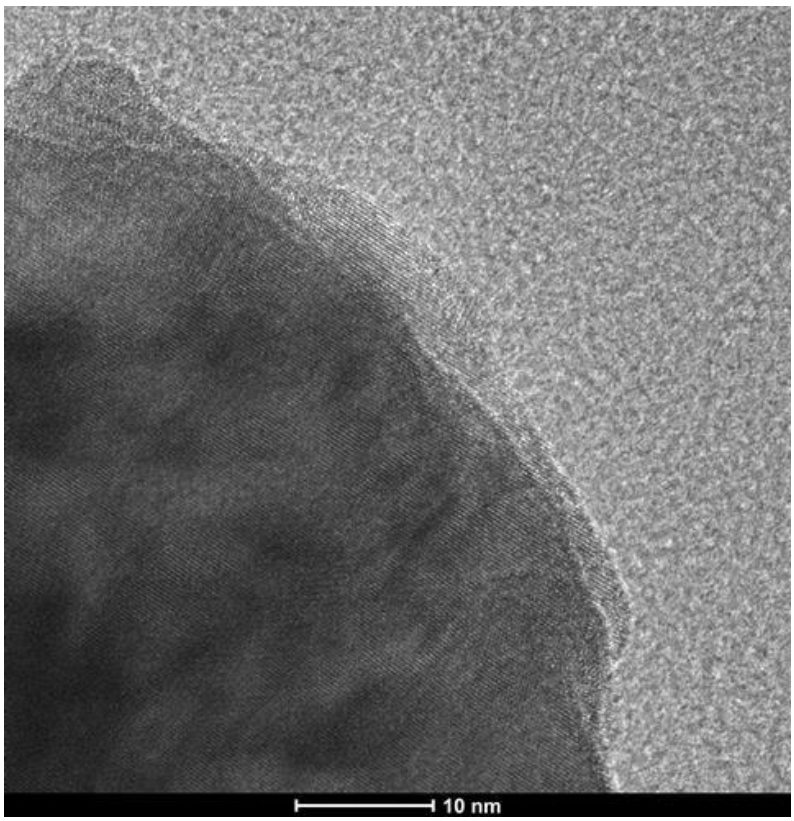

Figure 3. HRTEM image of GDC impregnated LSCF after annealing at 700 oC during 500 h.

MS 4: Metals, alloys and intermetallics

MS4.001 invited
Exploiting the potential of MEMS-based heating chips applied to realistic complex multicomponent high temperature Ni-base superalloys.

Y. Eggeler[1], E. Spiecker[1]

[1]University of Erlangen-Nuremberg, Erlangen, Germany

yolita.eggeler@fau.de

Single crystal Ni-base superalloys exhibit outstanding high temperature properties and are used as turbine blade material in advanced gas turbines, where they withstand high temperatures and mechanical loads in harsh environments. Superalloys are multicomponent in nature with many alloying elements added. Their high temperature properties are associated with their complex two phase γ/γ' microstructure consisting of cuboidal γ' precipitates, with average edge length of 400 nm. The precipitates exhibit an ordered L12 crystal structure (vol. frac. ca. 80%), and are coherently embedded in a solid solution γ fcc matrix [1]. To ensure precipitation hardening at temperatures relevant to gas turbine applications, 700-1100 °C, the stability of the γ/γ' phases is of fundamental importance. At high temperatures the γ' - precipitates start to dissolve until a stable γ' - volume fraction is reached [2][3]. This transition requests kinetic processes of the alloying elements involved, the local γ and γ' composition changes, while the nominal alloy composition remains constant.
In this study we make an attempt to resolve such transient phenomena in Ni-base superalloys and thereby gain information on elemental diffusion of alloying elements in these complex alloys. We take advantage of the microstructure itself, as a complex micro-diffusion couple, where the γ and γ'- phases are seperated by its distinct sharp interfaces, see Figure 1 (a). The modern MEMS-based heating chips allow precisely controlled heating experiments with quenching rates of 1500°C per second [3]. In combination with a FEI Titan Themis³ 300 equipped with a SuperX detector, assuring high EDXS counting rates, ChemiSTEM EDXS measurements are conducted, and the chemical and microstructural evolution is assessed [5].
Figure 1, shows the initial γ/γ' microstructure state of the ERBO1 superalloy [6]. The initial state is defined by a previous heat treatment for 100 hours at 850°C, water quenched, in a vertical furnace. The white rectangle in Figure 1(a) indicates the region where the ChemiSTEM EDXS measurement was conducted. The chemical distribution, extracted from the EDXS maps, are shown as Line profiles in Figure 1(b) for all elements involved.
Two types of experiments are conducted and shown on the example of the Cr-concentration in Figure 2. The long-term heating experiment, Figure 2 (a), was conducted for 200 min. The Cr concentration for both phases shows a steep slope in the beginning which than saturates, indicating that the Cr concentration state for 950°C is reached.
The short-term heating experiment, shown in Figure 2 (b) addresses the kinetics of the Cr diffusion in the γ and γ' phase. As expected a concentration gradient from the center of the γ phase towards the interface is clearly resolved after 30 seconds at 900°C. These results give insight into interdiffusion coefficients of Cr in a complex multi element environment. More general, such data contain valuable information on the kinetics of interdiffusion of alloying elements in a real superalloy microstructure. Quantitative evaluation of diffusion profiles will enable to simultaneously determine interdiffusion coefficients of various alloying elements.
In order to evaluate thin foil and surface effects cross sections prepared from TEM lamellae after heating experiments are investigated. Moreover, the experimental results will be validated by complementary ex situ experiments on bulk samples employing quenching in a vertical oven. Finally, the results will be compared with thermodynamic and kinetic data from theoretical calculations.

[1] R.C.Reed, Superalloys Cambridge University Press, (2006)
[2] A.Royer et al., Acta Materialia, (1998) Vol46
[3] Y.M.Eggeler et al., Proc. International Microcopy Congress IMC18 2016, Prag, Czech 2014
[4] DENSsolutions, Wildfire Brochure 2016, http://info.denssolutions.com/wildfire
[5] Y.M.Eggeler et al., Proc. European Microcopy Congress 2016, Lyon, France 2016
[6] A.B.Parsa et al., Adv. Eng. Mater.(2014), DOI: 10.1002/adem.201400136

Acknowledgement
This work has been carried out within the framework of the SFB-TR 103 "Single Crystal Superalloys".

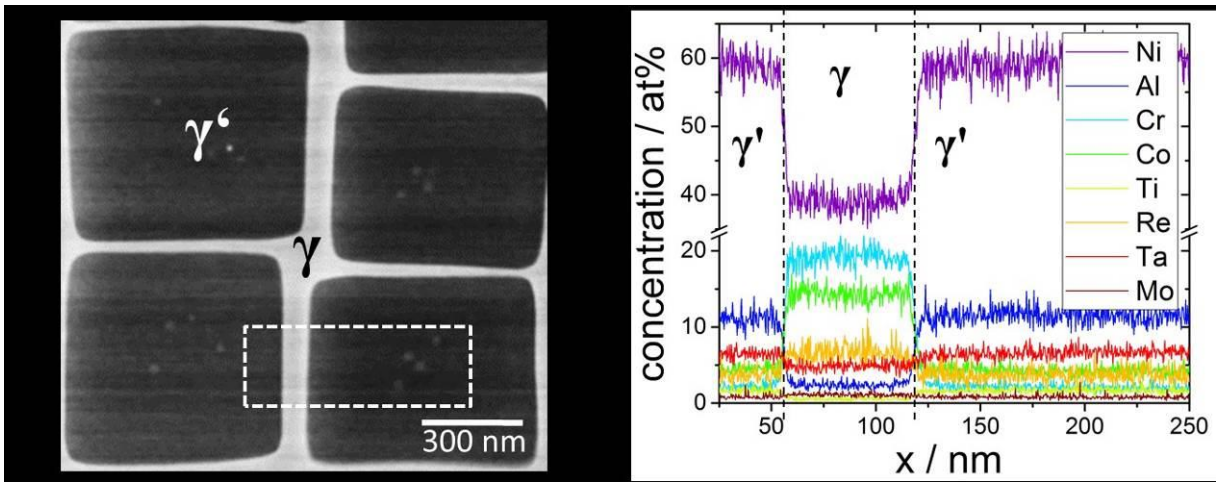

Figure 1

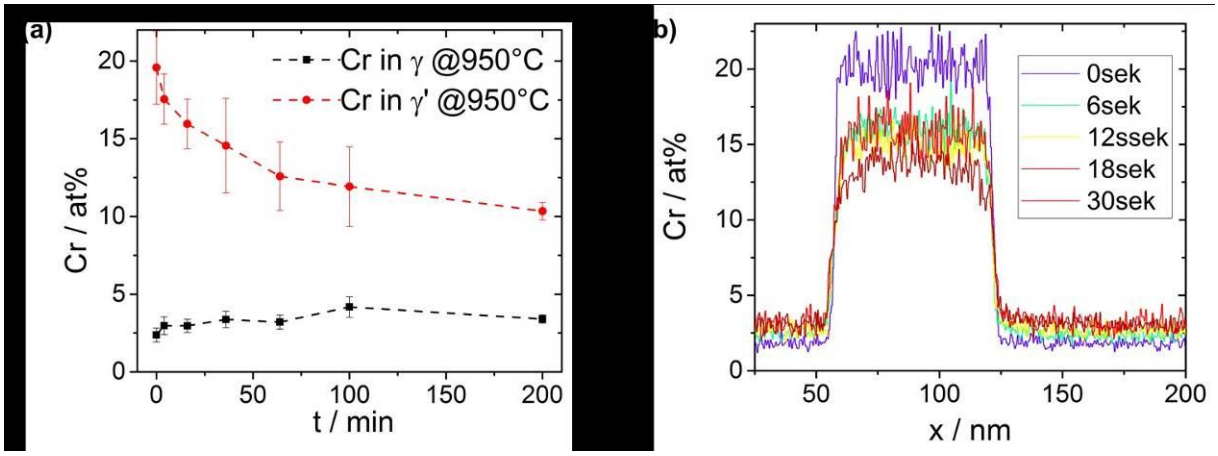

Figure 2

MS4.002
Characterization of Intermetallic NiBe nanoprecipitates in CoCr superalloys

T. LaGrange[1], R. Cosimati[2], D. Mari[2]

[1]École Polytechnique Fédérale de Lausanne, Interdisciplinary Centre for Electron Microscopy, Lausanne, Switzerland
[2]École Polytechnique Fédérale de Lausanne, Laboratory of Physics of Complex Matter, Lausanne, Switzerland

thomas.lagrange@epfl.ch

Cobalt based superalloys were developed in the 1930s as castable biomedical materials and for applications that require superior mechanical performance in corrosive, high-temperature environments. Most commercial CoCr superalloys contain a cocktail of additives composing of Ni, Ti, W, Mo, and C, which provide substitutional solid-solution strengthening by increasing the Peierls-Nabarro barrier for dislocation motion. Under specific thermal treatments, the Ti and Ni additives form coherent intermetallic precipitate phases that provide increased strength at high temperatures, but their concentrations are kept low to avoid excessive carbide formation that degrade mechanical properties. Here, we study microstructural changes due to Be additives, which are unknown in such complex, multicomponent alloys. In copper-based alloys, Be additives are well-known to precipitate into GP zones and improve mechanical properties via precipitate hardening mechanisms. Beryllium has a low solubility in most alloys and an affinity to form intermetallic compound, especially with Ni and Ti, and thus secondary precipitation of the Be intermetallics is likely. We aim to characterize the chemical composition and atomic structure of the Be containing phases in both thermal treated and wrought alloys to make correlations with mechanical properties of the bulk alloys.

Using aberration corrected HR-STEM and EDS analysis in a double aberration corrected FEI Titan Themis operating at 300 kV, we have characterized CoCr materials alloyed with and without Be additives. Beryllium is difficult to defect in alloys containing Ni, as the K edge of the Be overlaps with the M edges of Ni. Semi-quantitative analysis of the HAADF signal suggests that the Ni-rich, nanoprecipitates and GP zones contain a significant amount of beryllium. The EDS maps in Figure 1 confirm that the precipitates primarily contain Ni and thus should have similar Z contrast and intensity as the matrix, though it does not. The precipitates, therefore, must have a high concentration of lighter Z element, the only one having an affinity to form compounds with Ni and Co is beryllium. In addition, electron diffraction analysis indirectly confirms that the nanoprecipates contain Be; the nanoprecipitates have a structure closely matching an order, B2, NiBe intermetallic phase. This crystallographic analysis of the B2 NiBe intermetallic compounds nanoprecipitates also shows that they have a Bain relationship with the FCC matrix phase ({010}BCC/{010}FCC and BCC/ FCC). The most convincing evidence is the direct observation Be atomic columns using a special imaging technique, integrated differential phase contrast imaging (IDPC), as shown in Figure 2 B).

In the wrought alloys, we observe Guinier-Preston (GP) zones, having similar orientation relationships as the nanoprecipitates and being 1-2 monolayer thick and elliptically shaped with the major axis of 20-30 nm. The GP zones generate large coherency strains as seen by intense strain contrast around the GP zones in the ADF-STEM images, and they grow along three matrix directions, two orientations that are on-edge and one that lies in the plane of the [110] Z.A. shown in Figure 3 A). The atomic column intensities of the GP zone is much lower than the matrix (Figure 3 B) and C)), and though Be cannot be directly detected, we speculated that the GP having similar HAADF contrast has a structure and composition analogous to the nanoprecipitates. We speculate that the nanoprecipates form via the ripening of GP zones. Beryllium being observed in secondary phases is the first direct link that the improved mechanical properties may result from precipitation hardening rather than the perceived solid-solution mechanism.

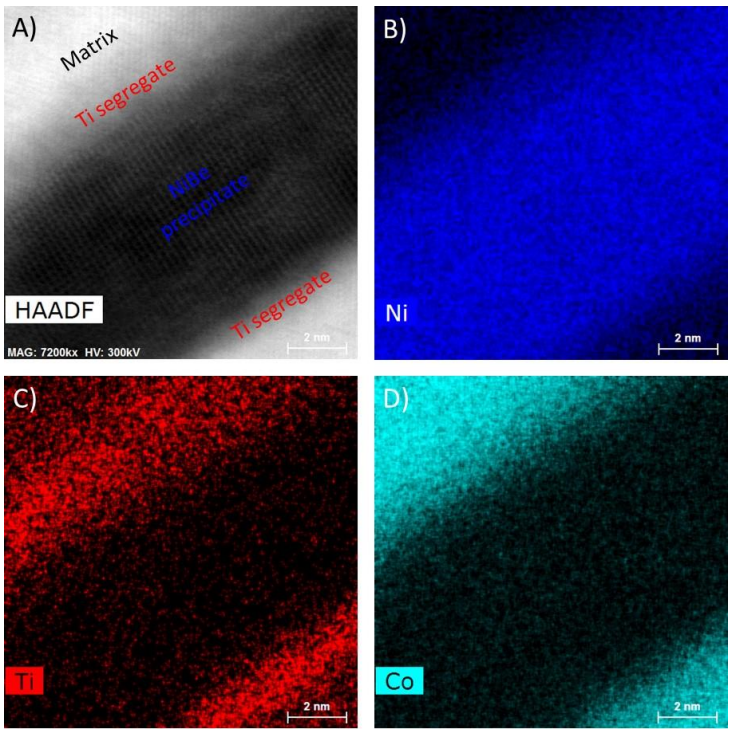

Figure 1. A) HAADF AC-STEM image of the nanoprecipitate, B) corresponding Ni at. % EDS Map showing that the nanoprecipitate contains primarily Ni, C) Ti at. % EDS map showing that Ti segregates to the precipitate interface, D) Co at. % EDS map, nanoprecipitate.

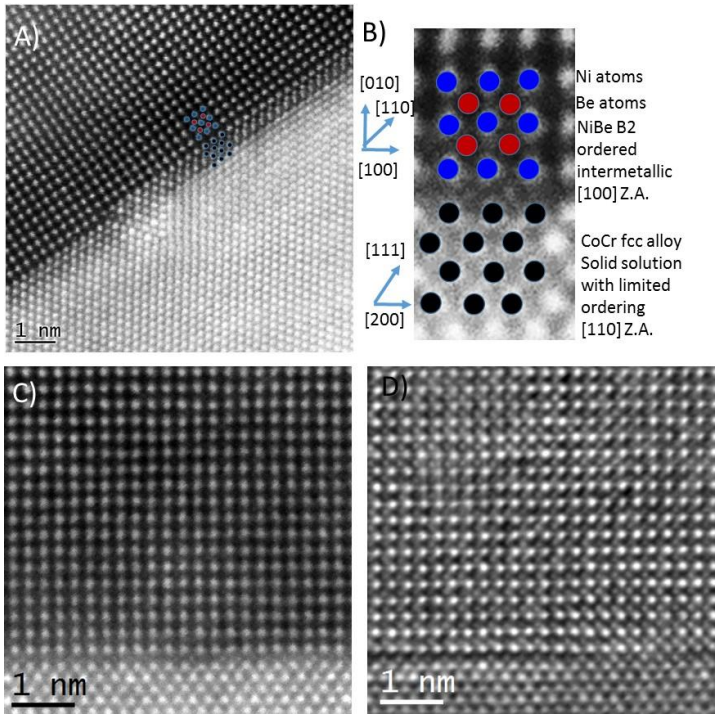

Figure 2. A) HAADF AC-STEM image of NiBe nanoprecipitate with overlaid model of atom, B) description of orientation relationship, C) higher magnification HAADF image and D) corresponding IDPC image of the same precipitate in which Be atomic columns are visible.

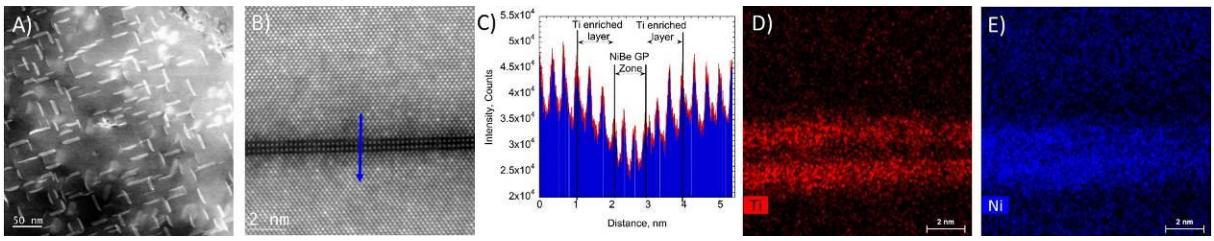

Figure 3. A)ADF STEM image showing the strain contrast around NiBe GP zones, B) HAADF AC-STEM image of a NiBe GP zone on-edge, C) HAADF intensity trace across the GP zone in B) marked by the blue arrow, D) corresponding EDS Ti map of B), E) corresponding EDS Ni map of B).

MS4.003
Characterization of FeO octapods by advanced 2D and 3D electron microscopy

N. Winckelmans[1], B. Goris[1], A. Feld[2], A. Weimer[2], H. Weller[2], S. Bals[1]

[1]University of Antwerp/EMAT, Physics, Antwerp, Belgium
[2]Institute of Physical Chemistry, Hamburg, Germany

naomi.winckelmans@uantwerpen.be

Introduction: Supermagnetic ironoxide nanoparticles (NPs) are promising contrast agents in magnetic resonance imaging. For such applications, it is important to determine the morphology of the NPs as well as the oxidation state of iron, since both have a large influence on the magnetic properties.[1-2] Electron tomography is a powerful technique for the 3D characterization of the morphology of NPs. Nevertheless, resolving the oxidation state of complex NPs in 3D remains challenging, but recently, first results have been published.[3-4]
Objectives: Here, we determine the ironoxide phases as well as their 3D distribution inside octapod shaped NPs by high resolution (HR) HAADF-STEM and EELS tomography. Furthermore, we investigated the growth mechanisms and surface facets by HR imaging.
Materials and Methods: HR HAADF-STEM imaging and EELS experiments were performed using an aberration-corrected cubed FEI-Titan electron microscope operated at 300 kV and 120 kV, respectively. The tilt series were acquired over a ±65° range with a tilt increment of 10°. EELS tomography series were reconstructed according to the procedure recently proposed by Goris et al.[3]
Results: A Fourier analysis of a HR STEM image (Fig. 1) was performed, to determine which ironoxide phases are present. A careful analysis of the diffractogram acquired in the middle of the NP (Fig. 1c) suggests the presence of the Wüstite phase. A second diffractogram, obtained near the edge, can be indexed according to either Magnetite or Maghemite. Since both phases have the same crystal space group and a very similar lattice parameters, HR imaging or electron diffraction is not sufficient to distinguish between both phases.
A characteristic that can be used to differentiate between the different phases is the valency of iron, which can be determined by the fine structure of monochromated EELS. Fig. 2 shows EELS spectra acquired in the middle and near the edge of the NP respectively. Both spectra contain features suggesting the presence of Fe+2 and Fe+3, but the peak corresponding to Fe^{+3} is more significant near the edge of the NP. Both spectra can be considered as 2D averages of the overlapping core and shell. To determine if the shell only contains Fe^{+3} (Maghemite) or Fe^{+2} and Fe^{+3} (Magnetite) it is essential to combine EELS with tomography. By using the so-called direct spectroscopic tomography technique, a reconstruction of voxels containing Fe^{+2} and a reconstruction with the voxels that contain Fe^{+3} were obtained. The result, illustrated in Fig. 3, reveals a core/shell morphology. Slices through the reconstructions demonstrate that the core of the NP only contains Fe^{2+}, in agreement with the Wüstite structure. At the edge of the NP only Fe^{3+} can be observed. From this result, we can conclude that the shell of the NPs corresponds to Maghemite.
Conclusion: In this study we demonstrated that HR HAADF-STEM and EELS tomography are suitable techniques to determine the phase of ironoxide NPs.

References:
[1] Khurshid, H.; *Nanoscale* **2013**, 5, 7942-52
[2] Ortega, D.; *Philos Trans A Math Phys Eng Sci* **2010***,* 368, 4407-18
[3] Goris, B.; *Ultramicroscopy* **2016**, 171, 55-62
[4] Goris, B.; *ACS Nano* **2014**, 8, 10878–10884

The authors acknowledge financial support from the Research Foundation Flanders (FWO, Belgium) through Project No. G038116N. S. Bals and N. Winckelmans acknowledge funding from the European Research Council (ERC Starting Grant 335078-COLOURATOMS).

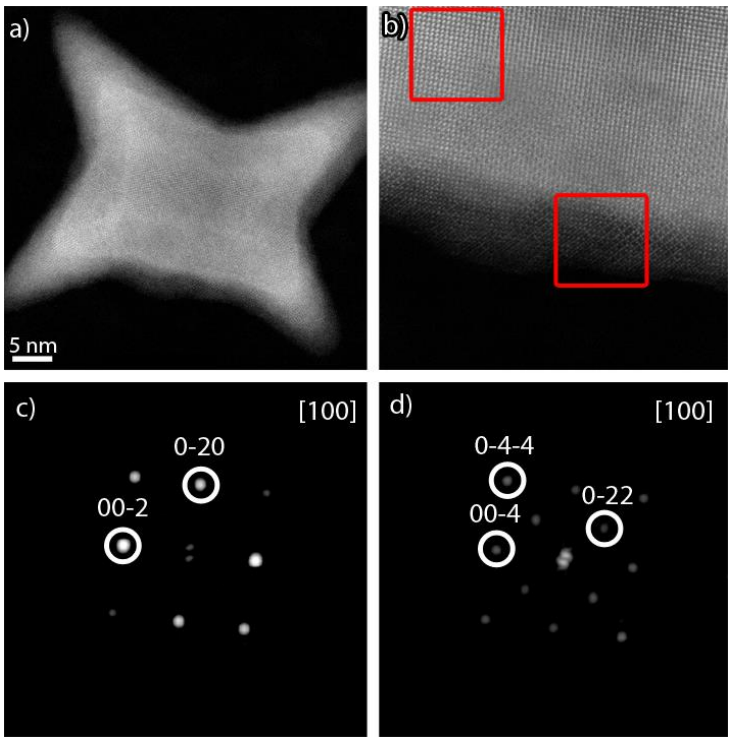

Figure 1. a) HR HAADF-STEM image of an octapod shaped NP. b) Zoom in of image a. c-d) FFT of regions indicated by red squares in image b.

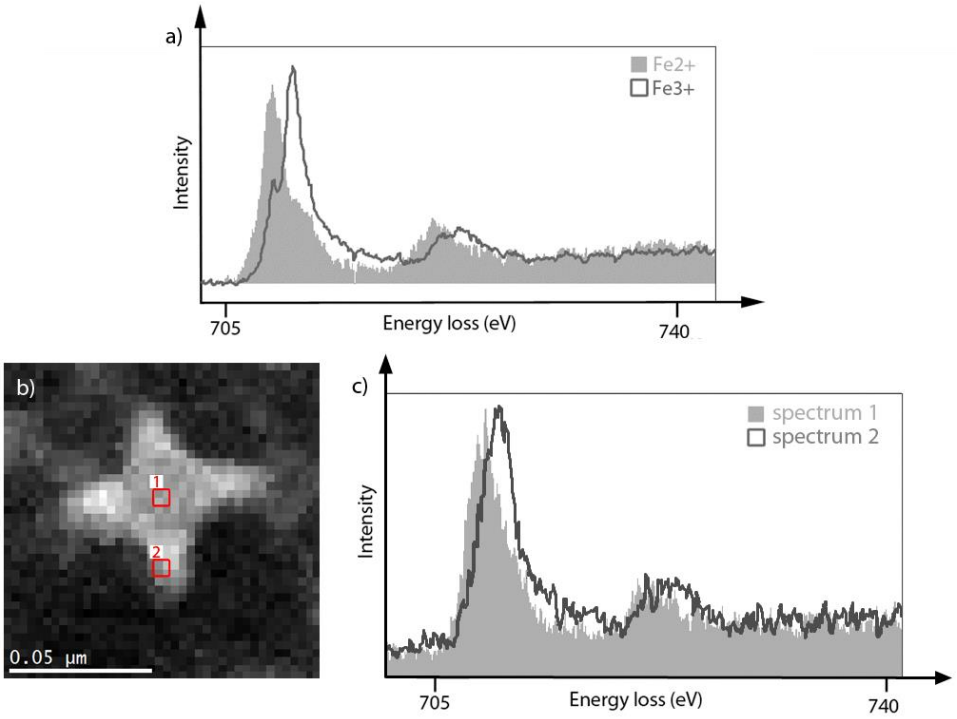

Figure 2. a) Reference: spectra of Fe^{2+} and Fe^{3+}. b) 2D HAADF-STEM image of the region on which EELS is performed. c) EELS spectra of regions indicated in image b.

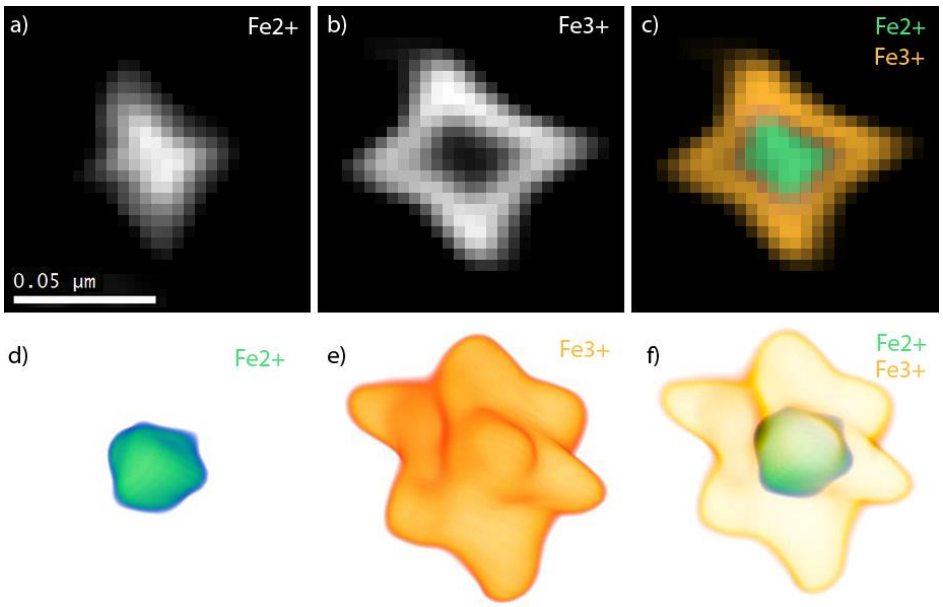

Figure 3. a-c) Slice through the reconstruction of Fe^{2+}, Fe^{3+} and the overlap of both slices respectively. d-f) 3D reconstruction of Fe^{2+}, Fe^{3+} and the overlap of both reconstructions respectively.

MS4.004
Sulphur-induced embrittlement of copper

T. Meiners[1], Z. Peng[2], C. Liebscher[1], G. Dehm[1]

[1]Max-Planck-Institute für Eisenforschung GmbH, Structure and Nano- /Micromechanics of Materials, Düsseldorf, Germany
[2]Max-Planck-Institut für Eisenforschung GmbH, Microstructure Physics and Alloy Design, Düsseldorf, Germany

meiners@mpie.de

The segregation of impurity atoms to grain boundaries (GBs) can have significant influence on the cohesive properties, atomic arrangements and the mechanical properties of such interfaces. Sulphur – induced embrittlement in copper (Cu) is a longstanding problem, but due to the limited availability of high resolution characterization techniques, the detailed mechanisms are still unclear. For the Cu-S system, a drop in ductility was observed to occur at very low sulphur (S) concentrations, because of the low solubility (0.0005 wt.% at 600°C) [1].
In numerous studies, Auger electron spectroscopy (AES) and secondary ion mass spectroscopy (SIMS) were used to detect S enrichments at fractured GBs [2]. The major disadvantage of these techniques is that only fractured surfaces of GBs can be analyzed, which mainly works for brittle materials and cleavage can introduce structural and chemical defects. Furthermore, it is in principle impossible to gain any information about the structure and nature of the segregated atoms due to the limited lateral resolution of the latter techniques [3]. In our study, we aim to systematically study the segregation and precipitate formation in model Cu alloys in dependence of the S concentration by aberration corrected scanning transmission electron microscopy (STEM) and to correlate these results to the mechanical properties.
As material, we use three different Cu alloys with different S concentrations (14, 27 and 7920 at. ppm). The embrittlement effect is demonstrated in our study by macro – sized tensile tests. The macroscopic / microscopic local structure is investigated by optical light microscopy (OLM) and scanning electron microscopy (SEM). The atomic structure and segregation of S are characterized by aberration-corrected STEM in combination with analytical techniques including energy-dispersive X-ray spectroscopy (EDX) and electron energy loss spectroscopy (EELS).
Tensile tests for the three alloys demonstrate the embrittlement in dependence of S concentration and temperature. The higher the S concentration and temperature, the lower the fracture elongation, but the ultimate tensile strength increases. SEM results show that with increasing S impurities, the amount and size of precipitates increases (fig. 1). These precipitates are located within the grains and at the GBs (fig. 1b). For 7920 ppm, a dendritic structure is found and the precipitates are several µm in size (fig. 1c). No direct evidence for S segregation to the mainly random GBs is found by atomic resolution high angle annular dark field (HAADF) – STEM in combination with analytical techniques in the samples with low S contents (fig. 2). These measurements are supported by atom probe tomography. The structure of precipitates is determined to low chalcocite (Cu2S) by HAADF – STEM imaging and selected area diffraction (fig. 3).
Our study shows that the embrittlement of Cu is mainly attributed to the formation of nano to micro scaled monoclinic Cu2S precipitates. The size and size distribution largely depends on the S content of the alloy. No direct evidence of S segregation to the GBs was found by STEM – EDS and – EELS.

References:
[1] D.T.L. Van Agterveld, G. Palasantzas, J.T.M. De Hosson, Effects of precipitates in Cu upon impact fracture: an ultra-high-vacuum study with local probe Scanning Auger/Electron Microscopy, Acta Mater. 48 (2000) 1995–2004.
[2] H. Fukushima, H.K. Birnbaum, High resolution saes and sims studies of grain boundary segregation of S and Cl in Ni, Scr. Metall. 16 (1982) 753–757.
[3] P. Lejcek, Grain Boundary Segregation in Metals, Springer Berlin Heidelberg, Berlin, Heidelberg, 2010. http://link.springer.com/10.1007/978-3-642-12505-8 (accessed November 9, 2016).

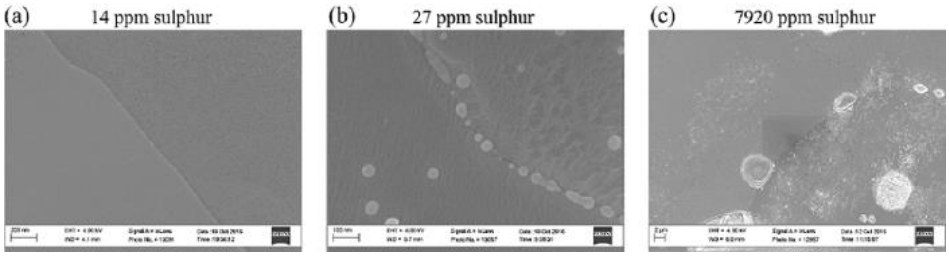

Figure 1. SEM micrographs of the copper alloys showing the local microstructure.

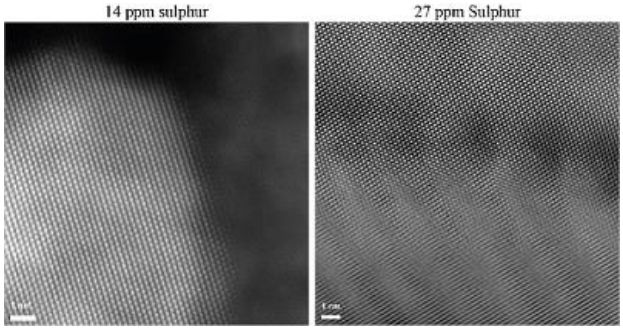

Figure 2. HAADF images of the GBs from the two alloys with low S contents.

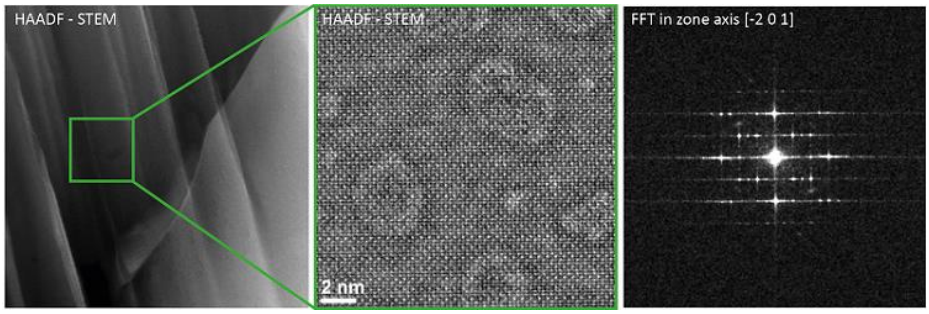

Figure 3. (a) HAADF image of the phase boundary between the copper matrix and a µm sized Cu2S precipitate from the alloy with 7920 ppm S. (b) HAADF image of the atomic structure of the precipitate and accompanying FFT (c).

MS4.005
Complex study of thermally induced phase decomposition in magnetron sputtered Cu-Cr thin films

A. Sologubenko[1], A. Wyss[1], R. Spolenak[1]

[1]ETH Zürich, Material Science, Zürich, Switzerland

alla.sologubenko@scopem.ethz.ch

The development of thermally and structurally stable Cu-based Cu-Cr thin film material with good electro-mechanical performance for flexible electronic applications is the goal of current work.
The effect of Cr-content on the microstructure and phase evolution upon thermally induced phase decomposition in 500 nm thick Cu-x at.% Cr (x=0 - 30) thin films on viscoelastic (Kapton® E) and rigid (Si-wafer) substrates is studied by a combination of techniques: transmission electron microscopy (TEM) and reflectance anisotropy spectroscopy (RAS). RAS tests in a combination with concurrent electrical resistance measurements are carried out as a function of tensile straining of the film. The correlated data set allows the characterization of the microstructure - property relationship in the system and is complemented by the post-mortem TEM analyses of the films.

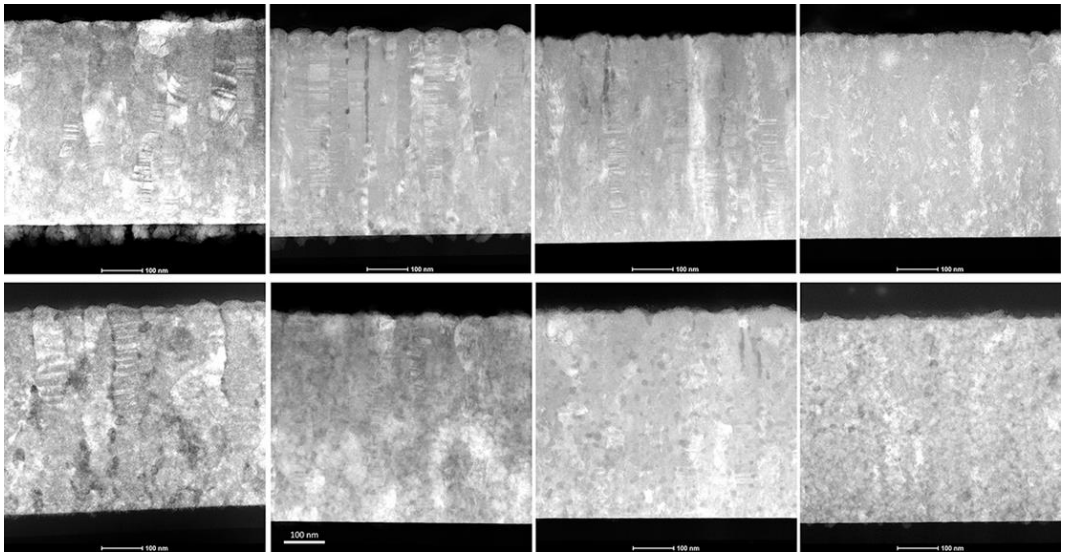

Figure 1. HAADF STEM micrographs of TEM lamellae prepared by FIB milling from Cu-x at.% Cr (x=3, 7, 11, 15) thin films sputter-deposited on a rigid substrate. The upper raw of images presents the films in an as-deposited and the lower row in an annealed at 300oC for 24h states. Columnar grain morphology is distinct in the films of all compositions and all thermal states. It is found to become more pronounced upon Cr-addition. Addition of Cr stabilizes the grain size and increases the film density.

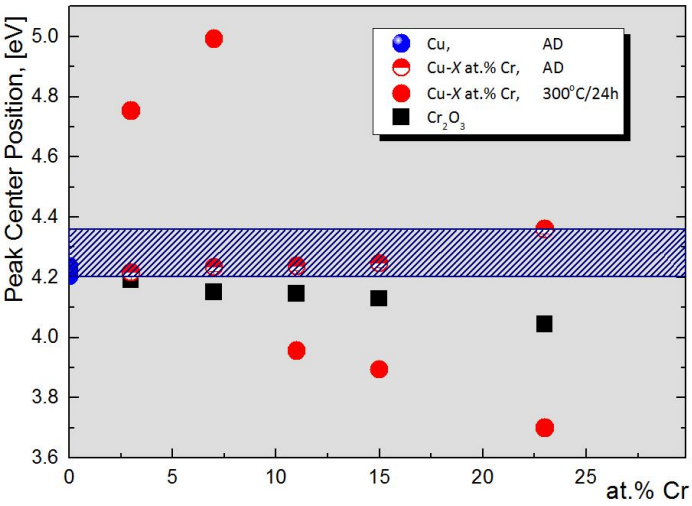

Figure 2. The RAS peak center position in as-deposited and annealed films as a function of Cr-content. The data for pure Cu-films of differnet thicknesses and for the deconvoluted Cr2O3 peak is also shown.

MS4.006
Local structures of crystalline $Ge_2Sb_2Te_5$ phase-change alloy

A. Lotnyk[1], U. Ross[1], I. Hilmi[1], X. Sun[1], B. Rauschenbach[1]

[1]Leibniz Institute of Surface Modification (IOM), Leipzig, Germany

andriy.lotnyk@iom-leipzig.de

Introduction: Phase change materials, such as Te-based $Ge_2Sb_2Te_5$ (GST) alloy, are of high interest due to their technological eminent optical and electronic properties. Technological relevant phases of GST are an amorphous phase, a metastable (cubic) phase and a stable trigonal phase. The metastable GST phase (phase I) possess a cubic rock-salt like structure with ordered anion sublattice and disordered cation sublattice. Although theoretical calculations predict the existence of a cubic phase with ordered vacancy layers (phase II), such cubic phase has not been confirmed or studied experimentally. The overall structure of stable layered GST alloy consists of rocksalt-type building blocks periodically separated from each other by intrinsic vacancy layers (VLs). However, local atomic arrangement in layered GST alloy is controversial and still under discussion.
Objectives: Following the problems stated above, this work aims to give new insights into local structure of the cubic and trigonal GST phases prepared as thin films by pulsed laser deposition, employing atomic-resolution Cs-corrected STEM supported by theoretical image simulations.
Materials and Methods: Metastable GST phases were obtained either by laser irradiation of amorphous GST films or grown as epitaxial thin films [1,2]. The trigonal GST phase was prepared by ex-situ heating of an amorphous GST thin film [3]. TEM specimens were prepared using a combination of FIB and focused low-energy Ar ion milling [4]. HRSTEM studies were performed with a probe Cs-corrected Titan^3 G2 60-300 microscope operated at 300 kV.
Results: The outcomes of this work reveal the existence of distinct crystal structures of cubic GST phases. The crystal structure of phase I is described by a distorted rock-salt like structure with vacancies randomly distributed on the Ge/Sb sublattice [1], whereas the crystal structure of GST phase II consists of rock-salt type building blocks with alternating Te and mixed Ge/Sb layers separated by intrinsic VLs [2]. Concentration of Sb atoms in the cation layers next to the VLs was found to be higher than in the middle of building blocks [3]. Similarly to the phase II, the trigonal GST phase is made up of building blocks separated by VLs. However, the building blocks in trigonal GST structure are systematically shifted against each other in [1-100] direction by $a_{(100)}/3$. The sensitivity of HAADF image intensities to thermal displacement parameters in the layered GST structure at Te sites allowed experimental access to the local atomic arrangement and to identify favorable structure model for the GST compound. The comparison with image simulations reveals a disordered cation sublattice with pronounced local lattice distortions [3]. This result is also supported by atomic resolution EDX mapping.
Conclusion: The results of this work show the existence of at least three disordered crystalline structures of GST which should be considered during phase transformations. The crystal structures of these phases are conceptually similar to each other, but clear distinctions can be made based on the lattice symmetry, local distortions and disorder in the mixed cation sublattice.

[1] A. Lotnyk, S. Bernütz et al., Acta Mater. 105, 1-8 (2016)
[2] I. Hilmi, A. Lotnyk et al., Materials & Design 115, 138-146 (2017)
[3] A. Lotnyk, U. Ross et al., Sci. Rep. 6, 23843 (2016)
[4] A Lotnyk, D. Poppitz et al., Microelectronics reliability 55 (9), 2119-2125 (2015)

We thank Mrs. A. Mill for assistance in the FIB preparation.

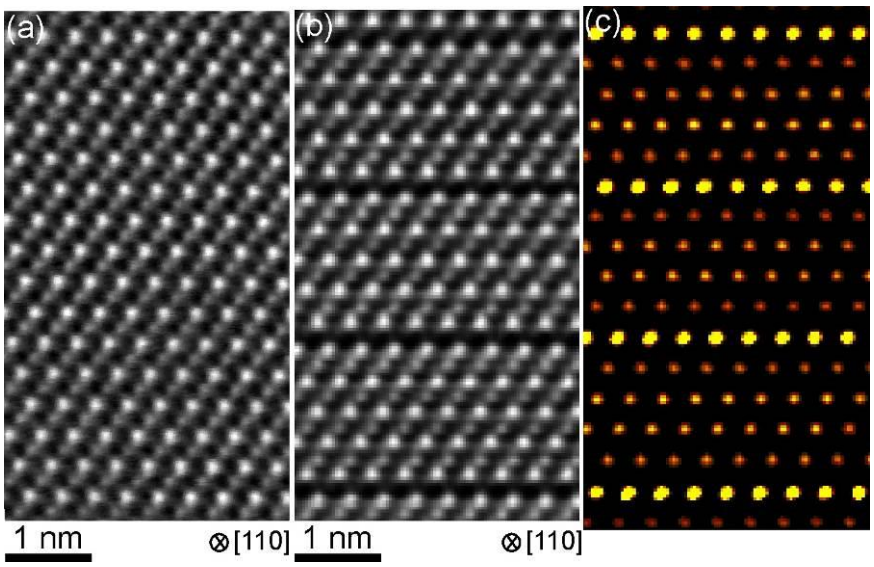

Figure 1. Cs-corrected HAADF-HRSTEM images of (a) GST phase I and (b) GST phase II. The dark lines in (b) are vacancy layers (van der Waals gaps). (c) Te/GeSb intensity ratios map.

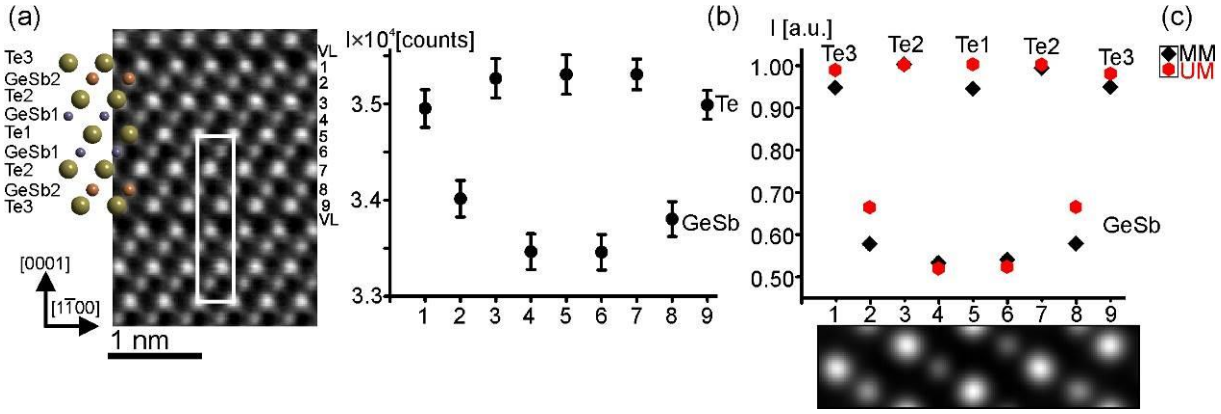

Figure 2. (a) Cs-corrected HAADF-HRSTEM micrograph of trigonal GST lattice. (b) Experimental averaged intensity maxima from Te and GeSb rows. (c) Simulated intensity maxima using GST crystal structures with Matsunaga model (MM) (-Te3-$Ge_{0.44}Sb_{0.56}$2-Te2-$Ge_{0.56}Sb_{0.44}$1-Te1-) and Urban model (UM) (-Te3-$Ge_{0.32}Sb_{0.68}$2-Te2-$Ge_{0.68}Sb_{0.32}$1-Te1-).

MS4.007
Atomic resolution microscopy of cage materials

R. Ramlau[1], Y. Grin[1]

[1]MPI für Chemische Physik fester Stoffe, Chemische Metallkunde, Dresden, Germany

ramlau@cpfs.mpg.de

The clathrates comprise representatives being chemically completely different: gas hydrates, clathrasiles, intermetallic phases, and even elemental polymorphs as Ge(*cF*136) [1, 2]. The clathrates-I, as a subgroup, constitute a distinct structure type (*cP*54). Large (tetrakaidecahedral) and small (dodecahedral) cages are closely packed to form the "host" framework. Within the cages usually "guest" atoms or molecules are situated. Among the intermetallic clathrates-I, $K_7B_7Si_{39}$ and $K_{2.73}Rb_{3.93}B_{6.78}Si_{39.5}$ are the only borosilicides known [3]. Other representatives, the barium germanide aurides $Ba_8Au_xGe_{46-x-y}Vac_y$ are promising for thermoelectric applications [4, 5]. In the case of the borosilicides, there are less guest atoms than cages. Together with the possible ordering of boron at the host framework, this raises the question of order/disorder phenomena. In the case of germanide aurides only the host framework contains defects in different quantities and ratios: vacancies and/or Au substitutes. X-ray data and measurement of physical properties indicate extraordinary disorder.
The Dresden Grand ARM [6] is a double-C_S-corrected JEOL ARM 300F, with unique resolution power of 50 pm in STEM and 50 -70 pm in TEM – the latter depending on the criterion applied. It is the appropriate instrument to investigate clathrates-I, where projected interatomic spacings go down to 47 pm (Fig. 1).
For both borosilicides long-range ordering could not be found (with one exception for the ternary compound). This holds for the guest atoms, K or/and Rb (Fig. 2), as well as for B at the Si dominated host framework. In the case of the investigated germanide aurides, there is no long-range ordering of Au and/or vacancies (Vac) either (Figs. 3 and 4). However, the resulting disordered state includes short-range order between the host and guest substructures. For instance, the occupation of the 6*c* site by Ge, Au or Vac changes the interspace between neighboring Ba(6*d*)–Ge(24*k*) considerably: 61, 63, or 89 pm. This indicates distortion of the large, tetrakaidecahedral cages and displacement of Ba guest atoms out of the cage center. There is virtually no translational periodicity any longer, and the terms "ideal" and "real structure" lose their distinction.

[1] G. S. Nolas, (Ed.): "The Physics and Chemistry of Inorganic Clathrates", Springer, Dordrecht, 2014.
[2] A. M. Guloy *et al.,* Nature **443** (2006) 320.
[3] W. Jung *et al.*, Angew. Chem. Int. Ed. **46** (2007) 6725.
[4] H. Zhang *et al.,* Inorg. Chem. **50** (2011) 1250.
[5] H. D. Nguyen and M. Baitinger, private communication.
[6] R. Ramlau, Y. Grin and H. Sawada, JEOL News **51** (2016) 2.

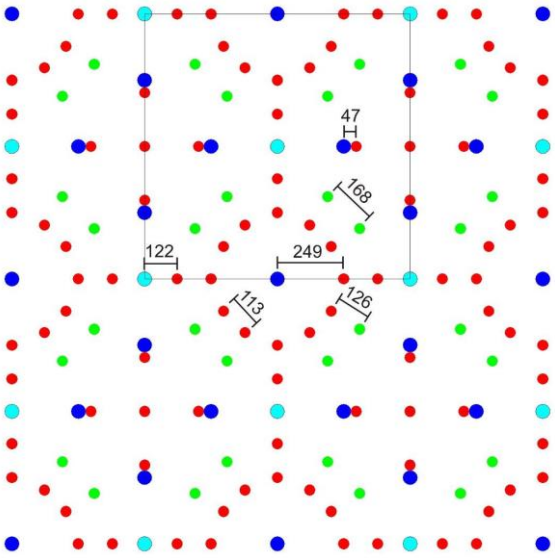

Figure 1. Projected structure (SG *Pm*-3*n*) of $K_7B_7Si_{39}$ and $K_{2.73}Rb_{3.93}B_{6.78}Si_{39.5}$, resp., in [100] direction. Unit cell and selected atomic interspaces in pm are indicated. Green: Si/B at 16*i*, red: Si at 24*k* and 6*c*, light-blue: K at 2*a* (center of the small cage) and dark-blue: K/Rb at 6*d* (center of the large cage). The projected interspaces between the 6*d* and the 24*k* sites, *e.g.* K and Si, are as small as 47 pm–making the borosilicides good test specimens for (S)TEM resolution.

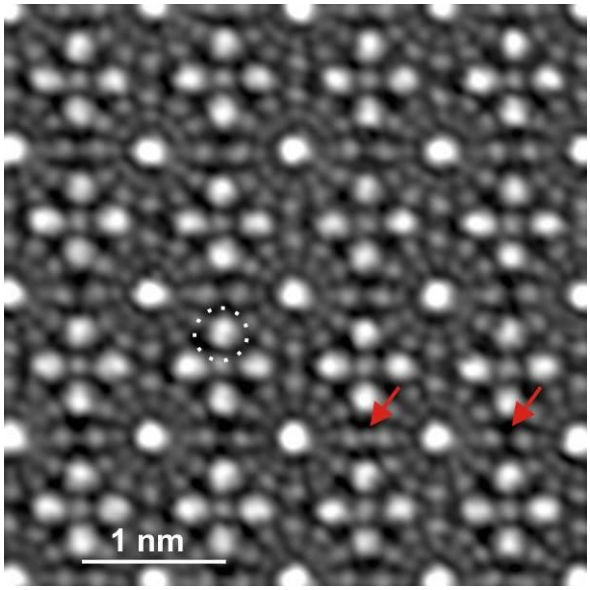

Figure 2. HAADF-STEM of $K_{2.73}Rb_{3.93}B_{6.78}Si_{39.5}$. Arrows indicate K at 2*a* with different occupancies. Projected "pairs" of atoms, K–Si and/or Rb–Si, are encircled. Their interspace is 47 pm following to x-ray investigations. These pairs are almost resolved in the STEM images (band-pass filtered and rectified) illustrating the excellent performance of the Dresden "Grand ARM".

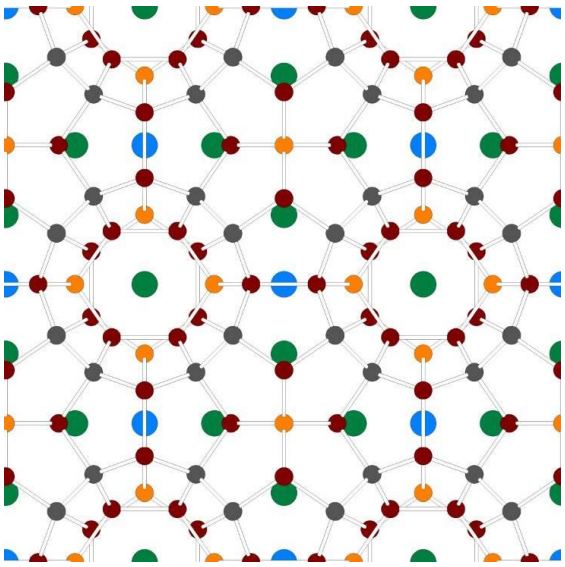

Figure 3. Projected structure (SG *Pm*-3*n*) of $Ba_{8-\varepsilon}Au_{5.33-0.67\varepsilon}Ge_{40.67+0.67\varepsilon}$ ($\varepsilon < 0.2$) in [100] direction with framework bonds displayed. Grey: Ge at 16*i*, dark-red: Ge at 24*k*, yellow: Au/Ge at 6*c*, blue: Ba at 2*a* (small cage) and green Ba at 6*d* (large cage). Compare with Fig. 1.

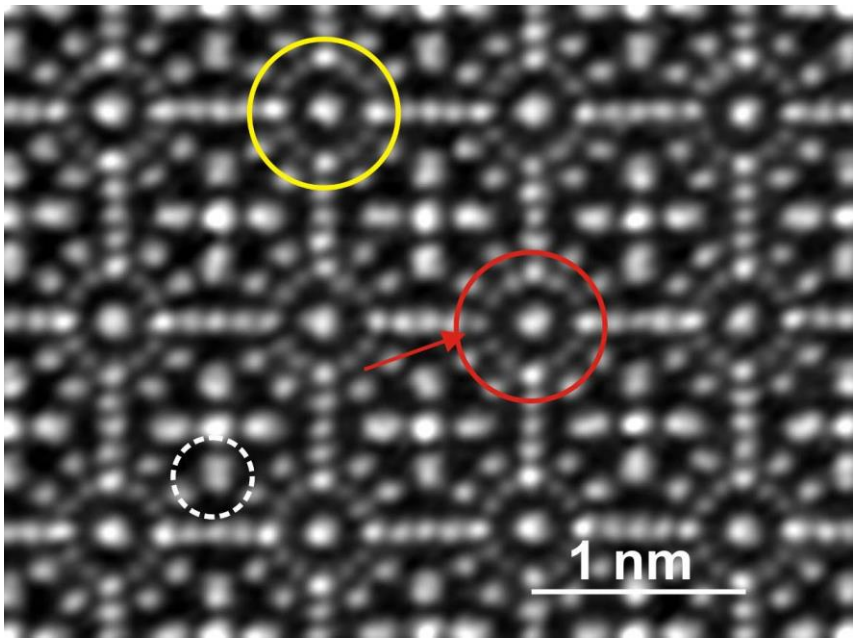

Figure 4. HAADF-STEM of $Ba_{8-\varepsilon}Au_{5.33-0.67\varepsilon}Ge_{40.67+0.67\varepsilon}$ ($\varepsilon < 0.2$). The region encircled yellow shows full occupancy of Au at the four 6*c* sites. The region encircled red shows zero occupancy of Au at one of the four 6*c* sites. Encircled in white are completely resolved Ba–Ge "pairs" with projected interspaces of 61 - 63 pm.

MS4.008 invited
Quantified (S)TEM and electron diffraction results on various metallic systems

D. Schryvers[1], H. Idrissi[2], M. Nishida[3], S. van Aert[1]

[1]University of Antwerp, Physics, Antwerp, Belgium
[2]UCL, Materials, Louvain-la-Neuve, Belgium
[3]Kyushu University, Materials, Kyushu, Japan

nick.schryvers@uantwerpen.be

Introduction: With the development of monochromated guns, aberration corrected lens systems, ultra-fast cameras and MEMS designs for in-situ experiments, electron microscopy has entered the era of quantification. In most cases, however, oxides or semiconductors are used as model systems to provide proof of ultimate resolution and precision.
Objectives: In this contribution we will review some examples of dedicated quantification of experimental data on alloy systems.
Materials and Methods: The materials include $L1_0$ ordered Co-Pt, B2 and B19" Ni-Ti(-Nb) and thin film Zr-Ni metallic glass. The techniques used include atomic resolution in TEM and Z-contrast HAADF-STEM, both supported by statistical parameter estimation to quantify the images, nanobeam electron diffraction (NBED) and diffuse scattering quantification, in-situ nanomechanical testing and orientation imaging microscopy (OIM).
Results: In L10 ordered Co-Pt the existence of anti-phase boundaries (APB) can disturb the local magnetic moment relevant for memory applications. Using quantified HAADF-STEM we were able to show that the width of the boundary was smaller or equal than 2 atomic layers (Figure 1), which implies that the boundaries do not severely influence the magnetic behaviour of the material [1].
After comparing average HAADF-STEM intensities from the two sublattices in Ni-Ti samples with and without Nb, it was found that separate intensity histograms for Ti and Ni in Ni-Ti overlap in the matrix containing Nb atoms, indicating that Nb substitutes for Ti, confirming DFT calculations (Figure 2) [2].
The Type I $(11\text{-}1)_{B19"}$ twin in Ni-Ti was shown to reveal no local strain in AC HRTEM, although it is supposed to be formed as a response to two coalescing martensite plates. In those cases the use of statistical parameter estimation was instrumental to determine the intensity resp. position of the atom column points with a 90% precision interval. Using OIM the sub-grain structure of B2 austenite in cold compressed and annealed Ni-Ti could be quantified revealing aspect ratios related to the earlier martensite plate configuration from which the subgrains are formed. Using cluster theory short <111> Ni strings are found to be at the origin of diffuse scattering in low temperature annealed Ni-Ti (Figure 3) [3].
NBED has shown the evolution of the local atomic order in thin film Zr-Ni metallic glass with increasing tensile strain, yielding a decrease of about 50% of the atomic order with 12% induced tensile strain (Figure 4).
Conclusion: It can be concluded that, although metallic, intermetallic as well as alloy systems often do not provide the clean image or diffraction datasets available from, e.g., layered oxide heterostructures, careful microscopy and data treatment can provide detailed quantification of the investigated atomic structures, elementary deformation and other processes.

[1] H. Akamine et al., Journal of Alloys and Compounds 644 (2015) 570–574
[2] H. Shi et al., Acta Materialia 74 (2014) 85–95
[3] S. Pourbabak et al., Functional Materials Letters 10 (2017) 1740005

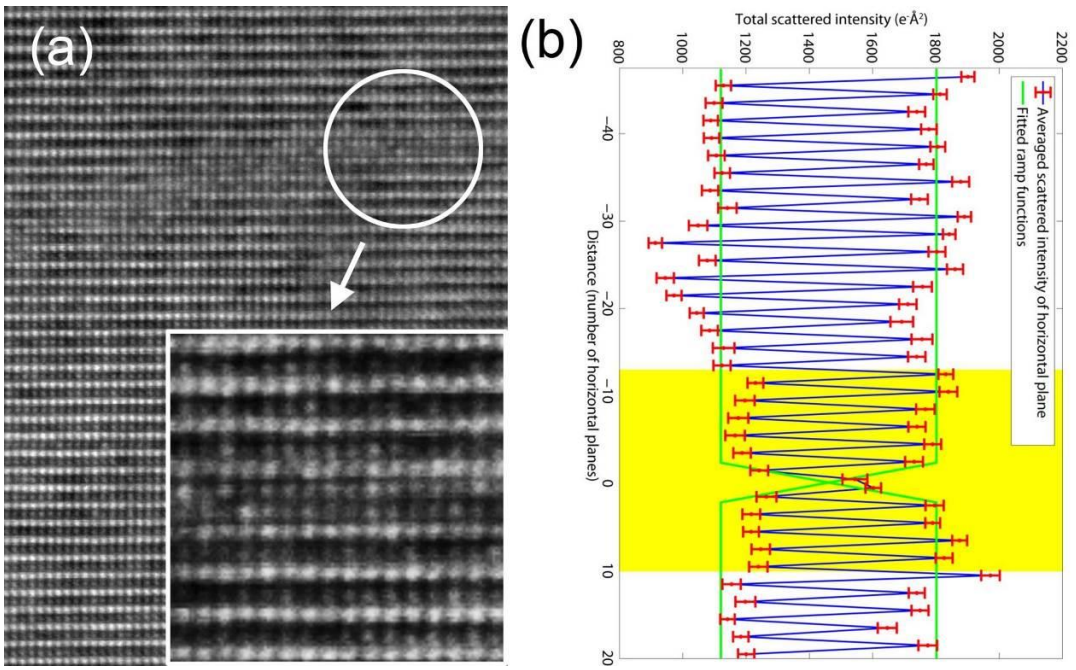

Figure 1. (a) $[100]_{L10}$ HAADF-STEM image of a curved APB in Co-Pt with (b) the averaged intensities of the planes parallel to the APB showing a width of maximum 2 planes.

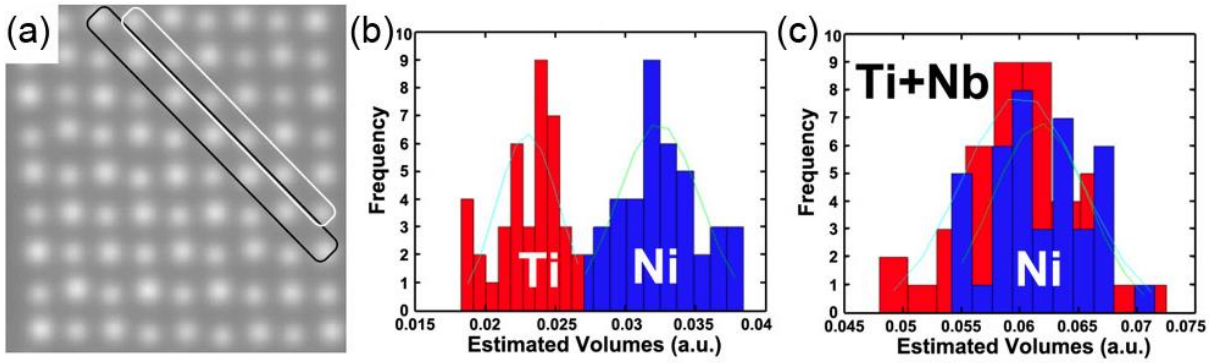

Figure 2. (a) Refined parameterized empirical model image of an $[001]_{B2}$ HAADF-STEM image of Ni-Ti. (b,c) Histograms of total scattered column intensities in (a) and a corresponding model for Ni-Ti-Nb, resp. The white and black boxes in (a) represent the Ti and Ni atom columns, resp.

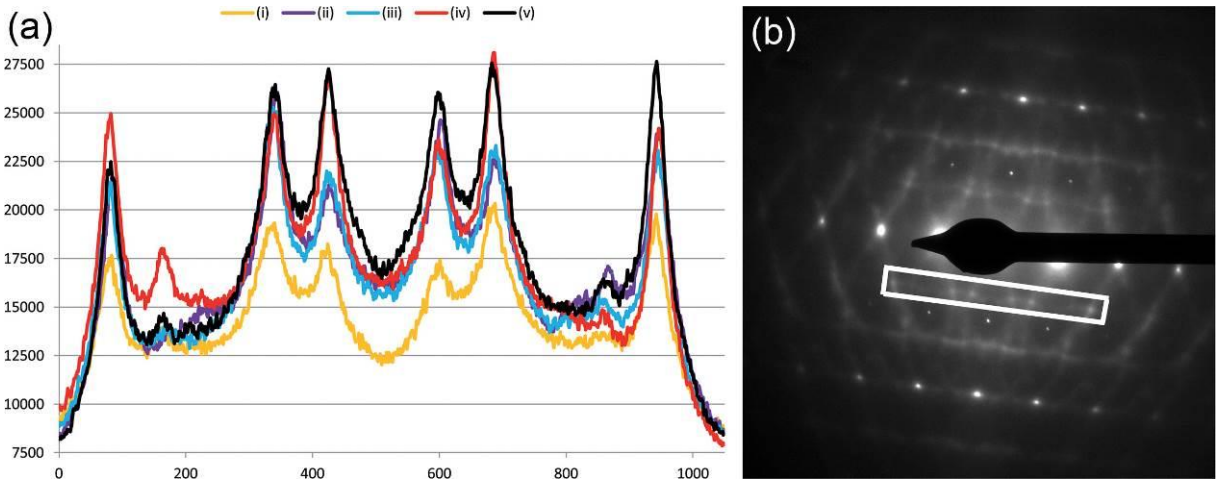

Figure 3. (a) Rectangular averaged profiles of the same region in $[112]_{B2}$ SAED patterns as in (b) of samples with various treatments.

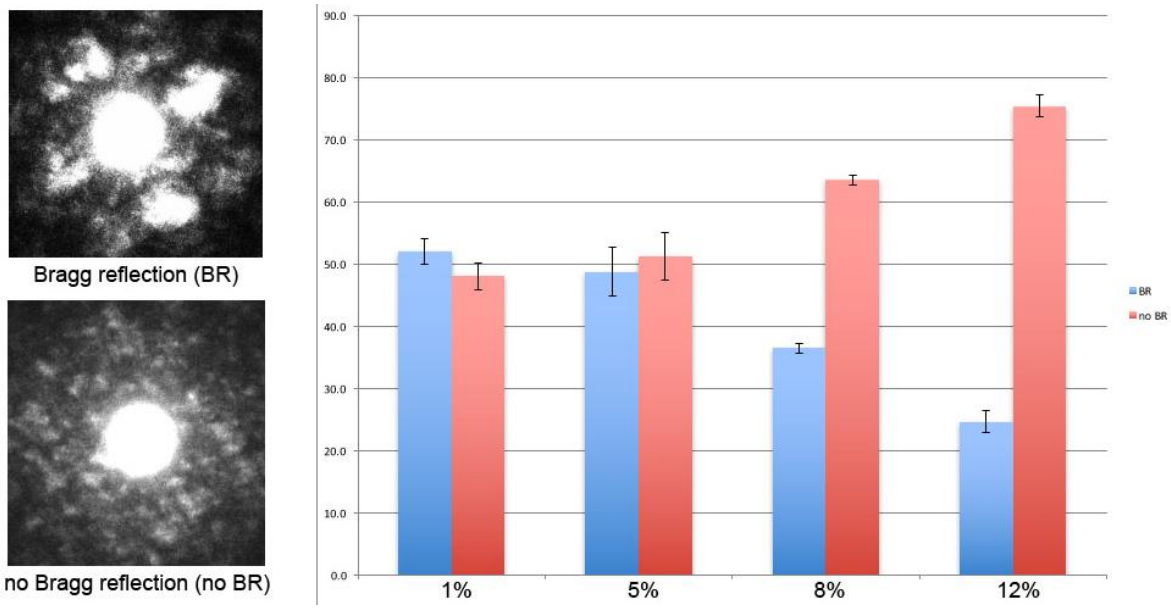

Figure 4. Examples of NBD patterns with and without Bragg reflections in thin film Zr-Ni metallic glass and the respective fraction measures after various strains.

MS4.009
Early-stage biocorrosion of magnesium-based alloys studied by TEM

M. Cihova[1], K. von Petersdorff-Campen[1], R. Schäublin[1,2], D. Deiana[3], P. J. Uggowitzer[1], P. Schmutz[4] J. F. Löffler[1]

[1]Laboratory of Metal Physics and Technology, ETH Zurich, Department of Materials, Zurich, Switzerland
[2]Scientific Center for Optical and Electron Microscopy, ETH Zurich, Zurich, Switzerland
[3]Centre Interdisciplinaire de Microscopie Electronique, EPFL, Lausanne, Switzerland
[4]Laboratory of Joining Technologies and Corrosion, EMPA, Dübendorf, Switzerland

martina.cihova@mat.ethz.ch

Thanks to their biodegradation ability, magnesium (Mg)-based alloys are attractive as temporary implant materials for e.g. osteosynthesis. A newly developed lean alloy with a composition Mg-Zn1.0-Ca0.3 (in wt.%), referred to as ZX10, is promising as it combines good mechanical properties with an appropriately slow degradation rate [1]. Its properties strongly depend on sub-micrometer sized intermetallic precipitates (IMPs) that are present as finely dispersed particles in the size range 50 to 200 nm. They are either the Mg_2Ca Laves phase or the ternary IM1 phase, with a composition $Ca_3Mg_xZn_{15-x}$ ($4.6 \leq x \leq 12$, in at.%) [2]. Due to the different electrochemical potential of the IMPs relative to the Mg matrix, Mg alloys containing secondary phases are highly susceptible to localized corrosion. An in-depth understanding of the IMPs role in the corrosion mechanisms is therefore fundamental to ensure a predictable and therewith safe biodegradation behavior of this new implant material in the human body.
Transmission electron microscopy (TEM) proves to be a powerful tool to study the initial corrosion events as a function of the underlying microstructure. *Ex situ* corrosion analysis of heat-treated ZX10 was performed allowing the comparison of the same area before and after immersion in a simulated body fluid (SBF). In order to address the role of IMP type, heat-treatment parameters were worked out to obtain ZX10 specimens with only one type of IMPs. Standard 3mm discs were prepared and electron transparency was obtained via ion milling at LN_2 temperature using PIPS II®. Prior to their immersion, regions of interest containing IMPs were identified and their microstructure evaluated by EDS. The IMPs position in the thin foil was determined via stereo imaging therewith identifying those that are in the surface and can contribute to the corrosion reactions. STEM imaging and energy-dispersive X-ray spectroscopy (EDX) for chemical mapping were obtained on a FEI Talos® equipped with a Super-X EDS detector and operated at 80kV to avoid irradiation damage. Atomistic structural information of the IM1 phase was obtained on an FEI Themis® (at CIME/EPFL).
The desired heat treatment-induced microstructure containing only one type of IMPs was verified with STEM/EDS chemical maps pre-immersion. The IMPs appeared to be mainly at the grain boundaries and non-coherent with the matrix. Furthermore, elemental segregation of Zn and Ca at the grain boundaries was observed. The direct comparison of the same area before and after immersion in SBF (Fig. 1.a and 1.b) allowed correlating the elemental distribution with the evolving morphological and compositional changes upon corrosion. The post-immersion investigation of ZX10 with IM1-type IMPs revealed strong preferential matrix dissolution at the grain boundaries, whereas no dissolution of the IMPs was observed (Fig. 1b). EDS maps further allowed identifying a microstructural-dependent oxidation pattern with significantly lower oxidation at sites of the IMPs suggesting their cathodic activity (Fig. 1c).
This study does not only open new insights into the acting mechanisms of localized corrosion in ZX10 but also supports determining the experimental conditions for real *in situ* corrosion studies of Mg-based materials.

[1] J. Hofstetter, M. Becker, E. Martinelli, A. M. Weinberg, B. Mingler, H. Kilian, S. Pogatscher, P. J. Uggowitzer, J. F. Löffler, *JOM* **66** (2014) 566 – 572.
[2] J. Hofstetter, S. Rüedi, I. Baumgartner, H. Kilian, B. Mingler, E. Povoden-Karadeniz, S. Pogatscher, P. J. Uggowitzer, J. F. Löffler, *Acta Mater.* **98** (2015) 423 – 432.

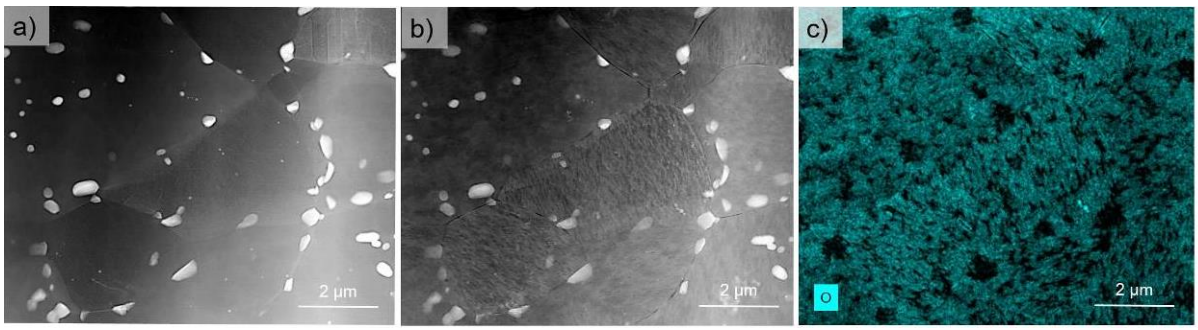

Figure 1. STEM images and corresponding STEM/EDS chemical map of Mg-Zn1.0-Ca0.3 with ternary IM1 phase: same area (a) before and (b,c) after immersion in simulated body fluid.

MS4.010
Assessing time-dependent compositional changes at planar faults in Co-base superalloys using TEM and APT

M. Lenz[1], Y. Eggeler[1], J. Müller[1], C. Zenk[2], S. Neumeier[2], P. Felfer[2], M. Göken[2], P. Wollgramm[3]
G. Eggeler[3], E. Spiecker[1]

[1]Institute of Micro- and Nanostructure Research & Center for Nanoanalysis and Electron Microscopy (CENEM), Department for Material Science and Engineering, Erlangen, Germany
[2]Institute for General Material Properties, Department for Material Science and Engineering, Erlangen, Germany
[3]Institute for Materials, Department for Engineering, Bochum, Germany

malte.lenz@fau.de

Co-based superalloys with a composition of Co-9Al-9W exhibit a γ/γ' microstructure at 900°C [1] well-known from Ni-based superalloys. Shifting the basis of alloys from nickel to cobalt has promising benefits, such as a higher melting point of Co and a positive lattice misfit between the γ- and γ'-phase. Recent investigations have shown that planar fault formation is a dominant deformation mechanism during creep and common for different Co- and CoNi-based superalloys [2,3].
In the present work a single crystalline Co-based superalloy, referred to as ERBOCo-1, was creep deformed in tension and compression under 400 MPa along the [001]-direction at 850 °C. The alloy contains high amounts of Co (44.5 at%), Ni (32 at%), Al (8 at%), Cr (6 at%), W (5 at%) and four minor alloying elements (Ti, Ta, Si and Hf). After heat treatment ERBOCo-1 exhibits cuboidal γ'-precipitates ($L1_2$) coherently embedded in a solid solution γ-matrix (fcc). The precipitates have an average edge length of 610±125 nm and a projected area fraction of 84 %.
After creep testing TEM samples were prepared and the defects were characterized by means of conventional transmission electron microscopy (CTEM) and scanning transmission electron microscopy (STEM) in combination with energy dispersive X-ray spectroscopy (EDXS). In tension a/2<112>-shear is found to be the predominant mechanism governing early creep deformation. Two partial dislocations with Burgers vectors a/3<112> and a/6<112> cut through the γ'-phase leaving behind a ASA-defect (APB-SISF-APB) where superlattice intrinsic stacking faults are fully enclosed by an anti-phase boundary as shown in figure 1. In contrast to previous work, we investigated two stages of tensile creep at plastic strains of 0.3 % and 5 %. The segregation behavior at more than 10 SISFs in both samples was investigated using a SuperXDetector for EDXS to assure high counting rates and statistical accuracy. For the ASA-fault formation in Co-based and for microtwinning in Co- and Ni-based alloys, a deformation mechanism with coupled displacive and diffusive processes has been proposed [2,4,5]. In the present work, STEM-EDX analysis of SISFs show that the planar faults formed during the early stages of creep show no or marginal local compositional changes, as can be seen in the vertically integrated line scans in figure 3. This suggests a diffusion-independent ASA formation process. A longer exposure to temperature and stress increases the segregation of Co, Cr and W and the depletion of Ni and Al as shown in figure 4. In order to confirm the findings of STEM-EDXS a site-specific preparation of single defects for atom probe tomography (APT) has been established (c.f. figure 2) and will be used to independently assess the 3D-chemical composition at SISFs.
Further investigations will be carried out to identify the rate-controlling steps during creep deformation and to identify characteristic deformation mechanisms for Co- and Ni-base alloys with the goal to improve alloy development and provide experimental data for the simulation of planar defect energies and segregation effects.

Acknowledgement
The authors gratefully acknowledge financial support by the DFG via the collaborative research center SFB-TR 103 and the Cluster of Excellence EXC315.

[1] Sato et al., Science (2006).
[2] Eggeler et al., Acta Materialia (2016)
[3] Titus et a., Science Advances (2016)
[4] Kovarik et al., Progress in Material Science (2009)
[5] Freund et al., Acta Materialia (2017)

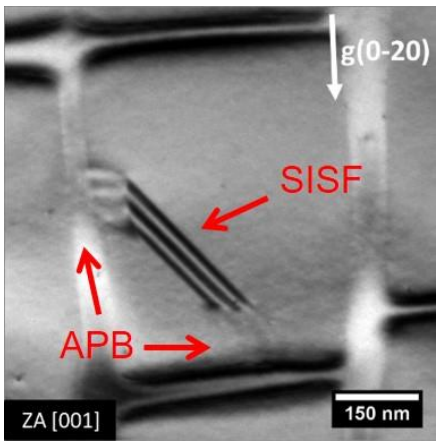

Figure 1. BF-TEM micrograph showing an ASA-defect where a SISF is enclosed in an APB. This mechanism is predominant in the early stages of tensile creep.

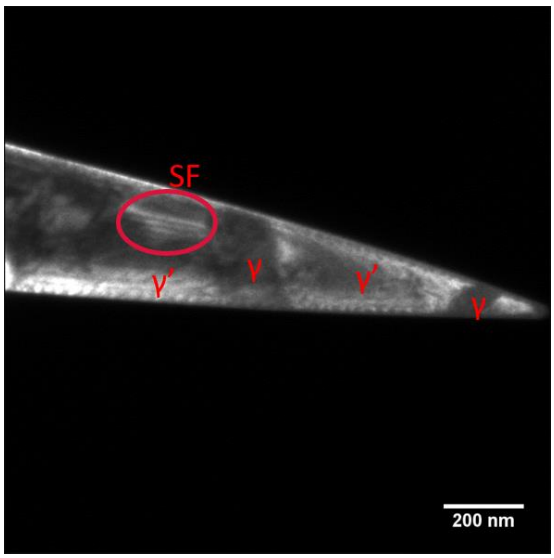

Figure 2. Site-specific preparation of an APT-tip. The sample contains multiple γ/γ'-interfaces and a single SISF.

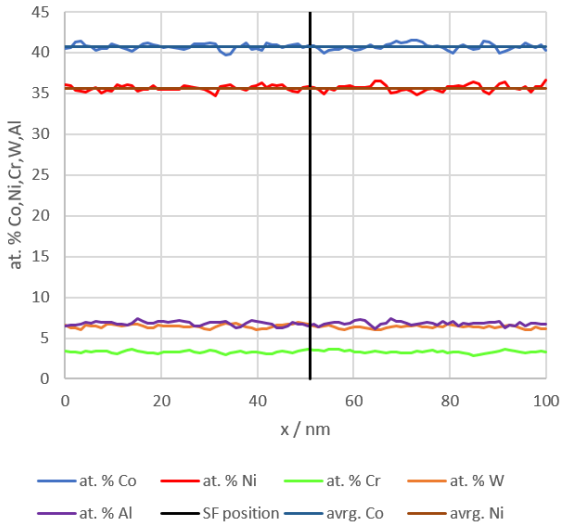

Figure 3. EDXS linescan across a SISF (in edge-on orientation, not shown) in the 0.3 % strained sample (400 MPa, 850 °C) showing no segregation at the fault plane.

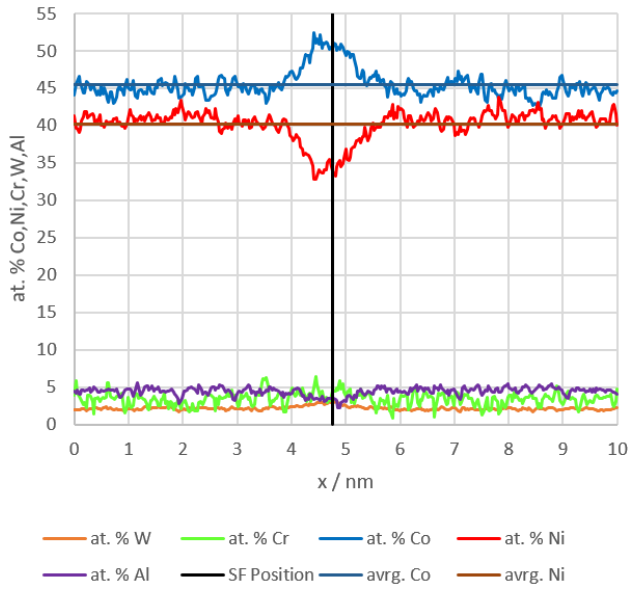

Figure 4. EDXS linescan across a SISF in the 5 % strained sample (400 MPa, 850 °C) revealing the segregation of Co, Cr and W at the fault plane and depletion of Ni and Al.

MS4.011
Limiting factors of deformation-induced supersaturation

Z- Zhang[1], P. Ghosh[1], R. Pippan[1]

[1]Erich Schmid Institute of Materials Science, Leoben, Austria

karoline.kormout@oeaw.ac.at

Introduction: Metals, usually immiscible in thermodynamic equilibrium at room temperature, can be forced into a supersaturated metastable state by severe plastic deformation [1,2]. However, although intensively investigated the mechanisms behind deformation-induced supersaturation are still controversial [2]. The respective materials properties of the immiscible elements, in particular the mechanical properties like hardness or yield strength, govern the dominating deformation mechanisms and as a consequence determine if and to what degree supersaturation takes place. Strain localization, especially the formation of shear bands, plays a key role since it possibly hinders structural homogenization. Other potential key factors for the supersaturation process are the respective lattice structures and the level of the positive heat of mixing.
Objectives**:** The aim of the present study was to correlate deformation-induced supersaturation with the dominating deformation mechanisms and identify the limiting factors for supersaturation. Additionally, detailed microstructural analyses should help to get insights into the underlying mixing mechanisms. For this purpose Cu-Ag and Ni-Ag were used as model systems because both exhibit a positive heat of mixing. But while Cu and Ag have low hardness and yield strength, Ni is relatively hard compared to Ag. This leads to different deformation behaviors during HPT processing.
Materials and Methods**:** The used HPT process, see Figure 1a, offers the opportunity to easily vary processing parameters such as applied strain or temperature. Experiments were performed on several Cu-Ag and Ni-Ag powder blends. The evolving microstructures were studied by SEM and TEM and combined with XRD measurements to verify the formation of supersaturated solid solutions on large probe volumes. To evaluate the impact of shear bands, samples were additionally processed by a two-step HPT process. In a two-step HPT process the shear direction is changed for about 90° from the first HPT process to the second one, which means that also the shear band orientation is rotated with respect to the HPT shear plane, see Figure 1b. Additionally, quasi *in-situ* experiments were performed by a split sample technique, see Figure 1c.
Results**:** The experiments show, that alloys with a higher Ag content (~20at%) are in general prone to shear band formation, see Figure 2. However, shear bands do not necessarily hinder homogenization of the microstructure. Only in some cases single dominant shear bands take over the major part of plastic deformation, causing a development of inhomogeneous multi-phase composites. A change in shear plane orientation realized by a two-step HPT process does not hinder the formation of such shear bands. Shear bands accommodate very high strains, this is associated with extreme phase refinement resulting in the formation of a single-phase supersaturated state, see Figure 2.
Conclusion**:** The dominating deformation mechanisms, in particular strain localization in the softer phase as in Ni-Ag or in form of shear bands, can strongly limit the degree of supersaturation by simply hindering homogenization of the alloy. Elevated deformation temperatures can suppress shear band formation, but simultaneously thermodynamic driving forces promote phase separation leading to dual-phase structures. The present results indicate that the fundamental mixing mechanism is not necessarily the same in system with two soft phases (Cu-Ag) and systems with a relatively hard second phase (Ni-Ag).

[1] C. Suryanarayana, *Prog. Mater. Sci.* **2001**, *46*, 1.
[2] K.S. Kormout, R. Pippan, A. Bachmaier, *Adv. Eng. Mater.* **2016**, 1.

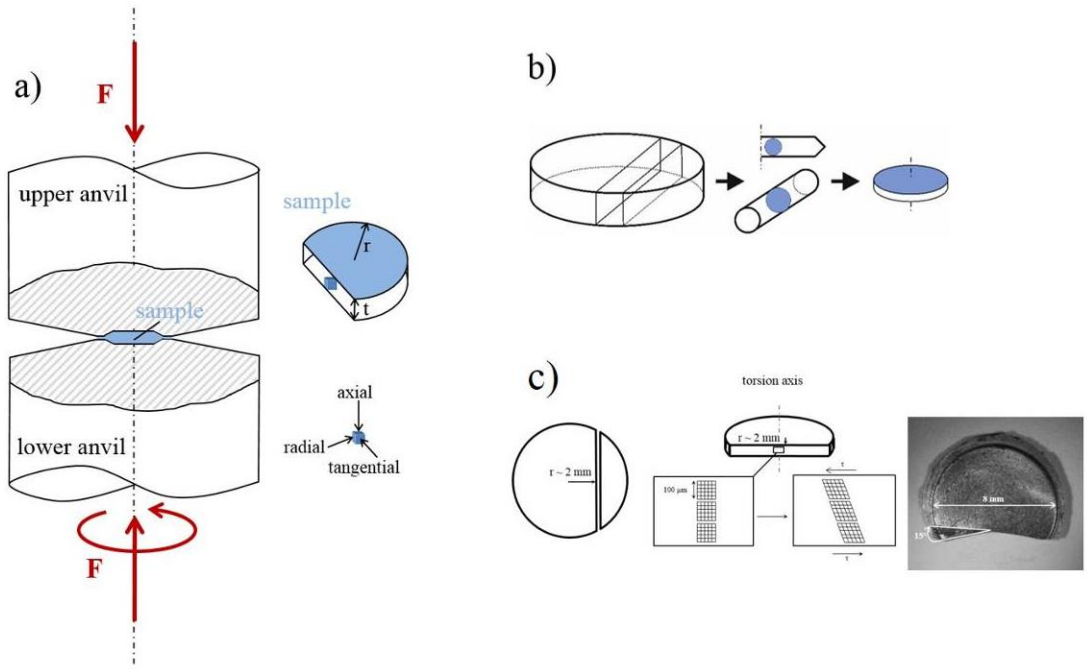

Figure 1. Schematics of a) the HPT process, b) the two-step HPT process and c) the split sample technique.

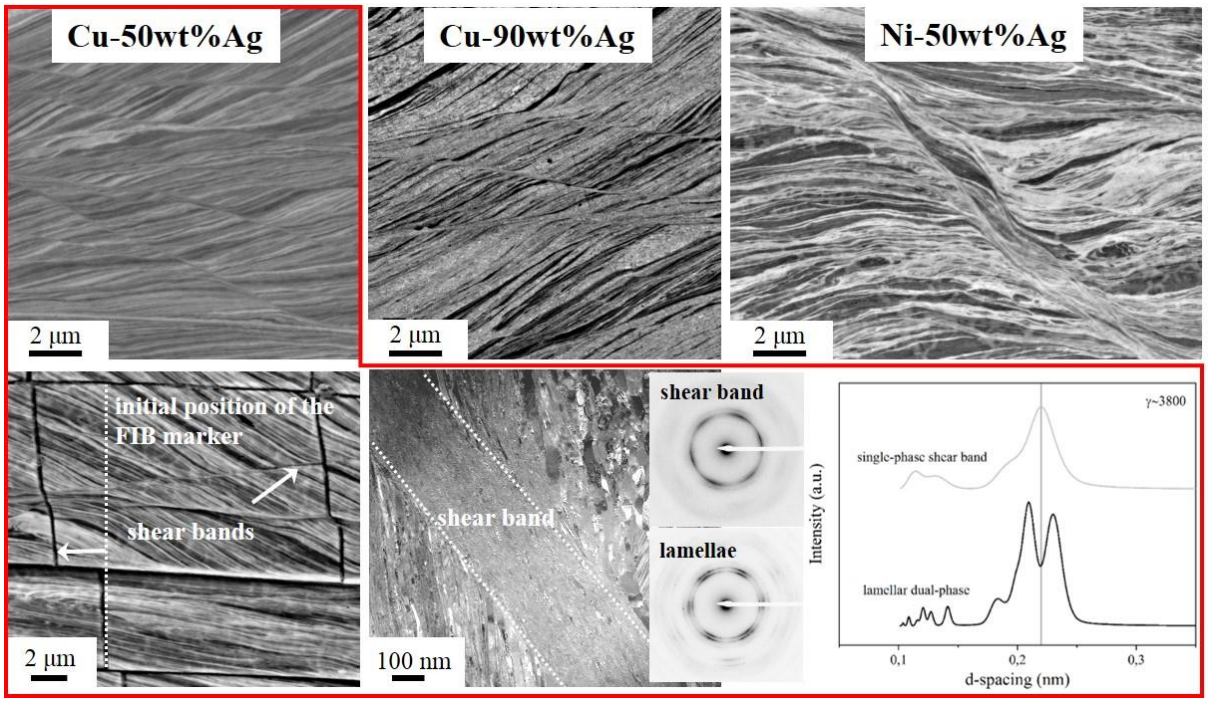

Figure 2. Formation of shear bands in different composites. Extremely high strains are accommodated in single shear bands as revealed by a split sample experiment. Inside the shear bands a supersaturated solid solution is formed as confirmed by diffraction analysis.

MS4.012
Structural characterization of PdSi metallic glass and corresponding nanoglass

A. Ahmadian[1], X. Mu[1,2], T. Scherer[1,3], S. H. Nandam[1,4], R. Schwaiger[5], S. Schlabach[3,5], D. Wang[1,3]
C. Kübel[1,2,3]

[1] Karlsruhe Institute of Technology, Institute of Nanotechnology, Eggenstein-Leopoldshafen, Germany
[2]Karlsruhe Institute of Technology, Helmholtz-Institute Ulm for Electrochemical Energy Storage, Ulm, Germany
[3]Karlsruhe Institute of Technology, Karlsruhe Nano Micro Facility, Eggenstein-Leopoldshafen, Germany
[4]Technische Universität Darmstadt, KIT-TUD Joint Research Laboratory Nanomaterials, Institute of Materials Science, Darmstadt, Germany
[5]Karlsruhe Institute of Technology, Institute for Applied Materials, Eggenstein-Leopoldshafen, Germany

ahmadian.ali@partner.kit.edu

Metallic glasses (MGs) are non-crystalline metals, which exhibit at the same time higher strengths, larger reversible deformations but lower ductility than their crystalline counterparts [1]. This is mainly due to the absence of dislocation mechanism and the appearance of shear banding. One way to improve the ductile flow of MGs is to introduce interfaces between glassy grains (unlike crystalline metals where the introduction of grain boundaries decrease the ductility). Such kind of metals have been discussed as nanoglasses [2]. The differences in the mechanical properties can be explained by examining the atomistic structure of nanoglasses and corresponding MGs. This is quite challenging as they do not contain any long-range order.
In this work, we investigated the microscopic structures of thin film nanoglass, bulk nanoglass and the corresponding melt-spun ribbon of PdSi using transmission electron microscopy (TEM). The thin film nanoglass was synthesized by simultaneously sputtering pure Pd and Si onto a carbon TEM-grid and the bulk nanoglass was prepared by consolidation of amorphous PdSi nanoparticles prepared by inert gas condensation (IGC). We applied electron diffraction measurements to the samples, and analyzed them by radial distribution function (RDF) [3,4] to get short- and medium-range information about the atomic ordering (Fig.1). For that the diffraction patterns were averaged azimuthally to obtain intensity profiles. Structure factors were determined by normalizing the intensity profiles with single atomic scattering factor. The RDFs were obtained by Fourier-transform of the structure factors. The nanoglasses exhibit similar short-range order to the MG-ribbon but differ in the medium-range order (Fig.1c). In addition, EDX-maps were acquired to correlate chemical and structural properties for a more comprehensive understanding of the nanoglasses (Fig.2).

References:
[1] C. A. Schuh et al., *Acta Materialia*, **2007**, *55*, p. 4067.
[2] H. Gleiter, *Journal of Applied Crystallography*, **1991**, *24*, p. 79.
[3] X. Mu et al., *Ultramicroscopy*, **2016**, *168*, p. 1.
[4] D.J.H Cockayne, D.R. Mckenzie, *Acta Crystallographica Section A*, **1988**, *44*, p. 870.

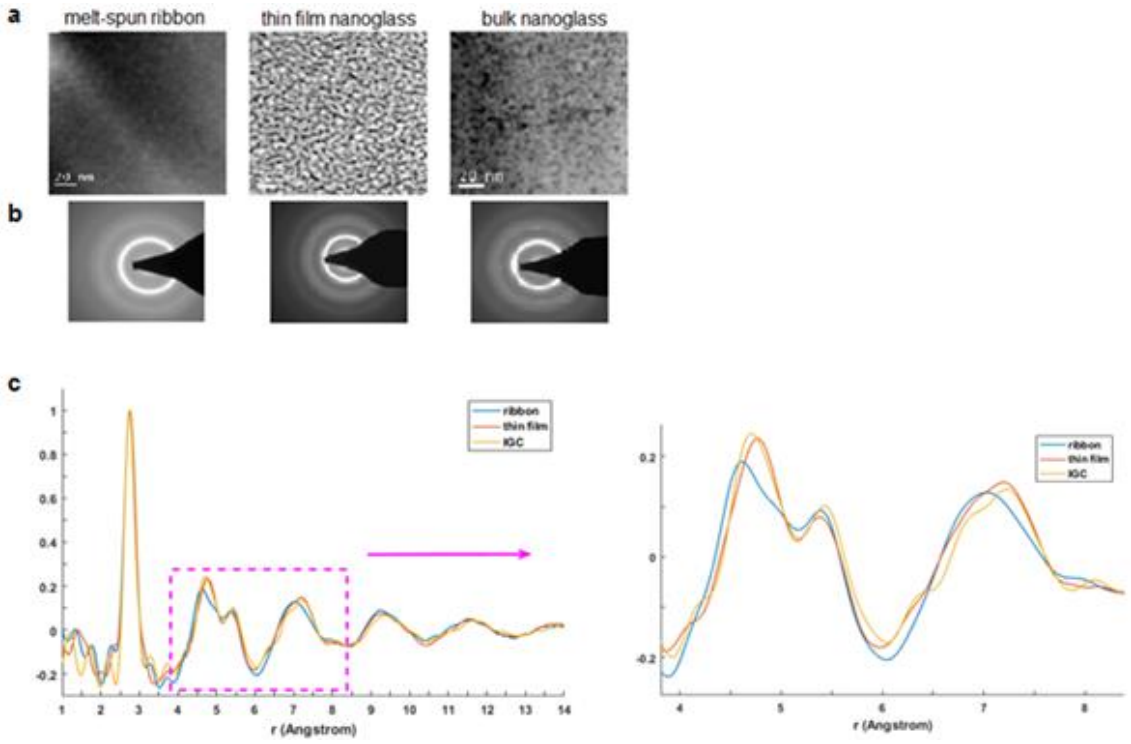

Figure 1. STEM-HAADF images (a) and typical diffraction patterns (b) of the different glasses. The diffraction spots in the bulk nanoglass originate from the sample preparation using focused ion beam. (c) RDFs of melt-spun ribbon, thin film nanoglass and IGC nanoglass.

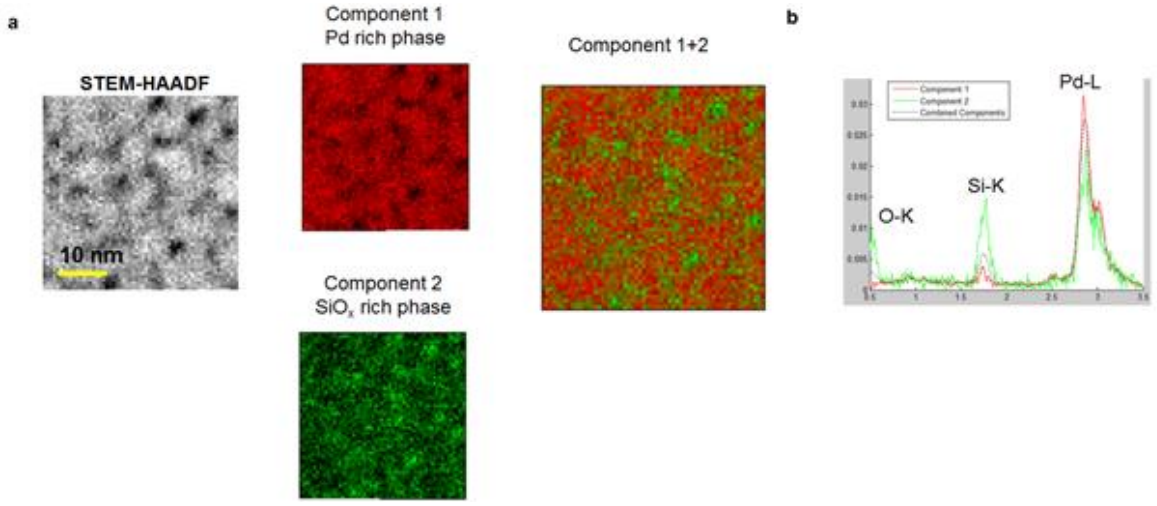

Figure 2. Elemental distribution analysis in the thin film nanoglass: (a) STEM-HAADF image and EDX elemental maps processed by multivariate curve resolution analysis. (b) The corresponding spectra show an enrichment of Si and O at the interface (component 2).

MS4.013
Flash-annealed CuZr based bulk metallic glass studied by electron microscopy

C. Müller[1], C. Gammer[2], K. Kosiba[3], S. Pauly[3], C. Rentenberger[1]

[1]University of Vienna, Faculty of Physics, Vienna, Austria
[2]Österreichische Akademie der Wissenschaften, Erich Schmid Institute of Materials Science, Leoben, Austria
[3]IFW Dresden, Institute for Complex Materials, Dresden, Germany

christoffer.mueller@univie.ac.at

Introduction: Bulk metallic glasses (BMGs) are amorphous materials showing attractive physical and mechanical properties due to their unique atomic structures. Despite the lack of a long-range order, still topological and chemical short-range and medium-range order are expected to occur. Although being amongst the strongest engineering materials known, they exhibit a disappointingly low plastic deformability.
Objectives**:** To circumvent this limited ductility the concept of implementing a heterogeneous microstructure by the formation of composites has recently been used [1]. One way to achieve such a structure is thermal treatment of the BMG. This work deals with the structure of flash-annealed CuZr based BMGs.
Materials and Methods: During the flash-annealing process the atomic structure of the $Cu_{44}Zr_{44}Al_8Hf_2Co_2$ BMG is modified by rapid heating to different target temperatures above glass transition temperature (712 K) and the subsequent cooling in a water bath. The samples were heated to 817 K, 898 K and 916 K with a mean rate of 67 K/s and studied using a Zeiss Supra 55VP scanning electron microscope (SEM) at 20 kV as well as a Philips CM200 transmission electron microscope (TEM) operating at 200 kV.
Results: Using back-scattered electrons the SEM observation of the sample heated to 916 K reveals both an amorphous and a crystalline part each taking up about half of the sample with spherical crystallites of different size in between. Figure 1 illustrates a TEM image of a FIB lamella taken from one of the crystallites embedded in the amorphous structure. The corresponding diffraction pattern (DP) contains superlattice reflections indicating the presence of the B2 ordered structure. This is interesting as in crystalline CuZr based materials, devitrified from the amorphous structure, $Cu_{10}Zr_7$ and $CuZr_2$ structures are expected to occur.
In order to analyse and compare the structures of the fully amorphous samples flash-annealed to 817 K and 898 K as well as the amorphous part of the sample heated to 916 K, variable resolution dark field (DF) fluctuation electron microscopy (FEM) was applied. Figure 2a shows a DP with integrated intensity using the software PASAD [2] indicating the amorphous structure. Figure 2b illustrates a tilted DF image taken with a given scattering vector k showing intensity variations in the form of speckles due to local structural correlations. Fluctuations of DF image intensity reveal structural ordering at the medium range. Acquiring a series of DF images at different vectors k and azimuthal angles φ provides the mean intensity and normalized variance as a function of k. The normalized variance is defined as $V(k) = (\langle I(k,r)^2\rangle / \langle I(k,r)\rangle^2) - 1$, with I being the image intensity and <> meaning the average over sample position r.
Figure 3 illustrates the mean intensity and variance curves of the differently treated samples, calculated from 320 images each, using an aperture size of 10 µm. It is interesting to compare the profile of the normalized variance to the 4 most intense peaks in the X-ray spectrum of B2 structured CuZr, as they show remarkable similarities.
By changing the aperture size and thus varying the spatial resolution the correlation length, a length scale for medium-range order, can be derived from the pair persistence model [3]. Figure 4 compares the correlation lengths of the flash annealed amorphous samples to the as-cast state showing an increase in medium-range order with increasing target temperatures.
Conclusion: Based on our results flash-annealing of CuZr based BMGs facilitates the formation of B2 ordered crystalline structure. The profile of the normalized variance is similar to the position and intensity of the most intense peaks in the X-Ray spectrum of the B2 structure. The correlation length, as a measure for medium-range order, increases with the target temperature for flash-annealing.

We kindly acknowledge financial support by the Austrian Science Fund (FWF): [I1309, J3397].

References:
[1] J. Eckert, J. Das, S. Pauly, C. Duhamel, Journal of Materials Research 22, 285 (2007).
[2] C. Gammer, C. Mangler, C. Rentenberger, H. P. Karnthaler, Scr Mater 63, 312 (2010).
[3] J.M. Gibson, M.M.J. Treacy, P.M. Voyles, Ultramicroscopy 83, 169 (2000).

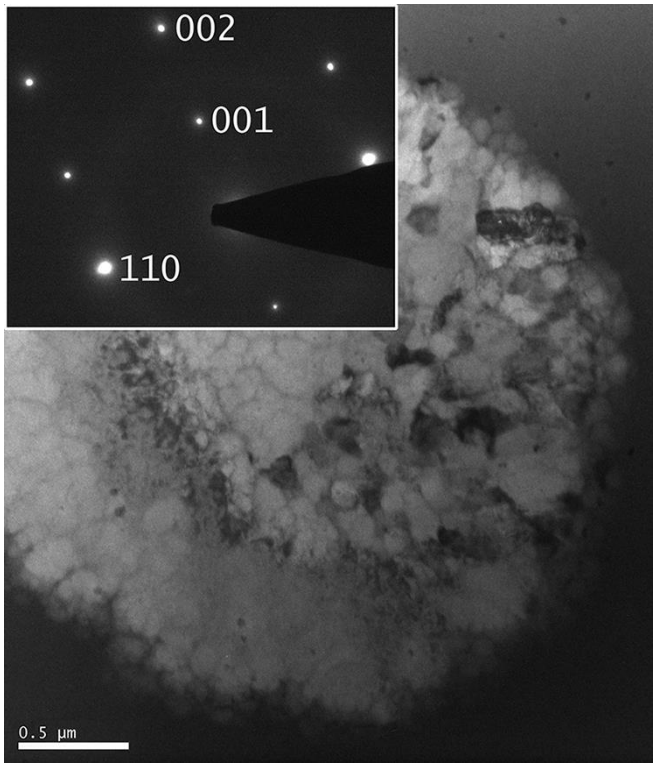

Figure 1

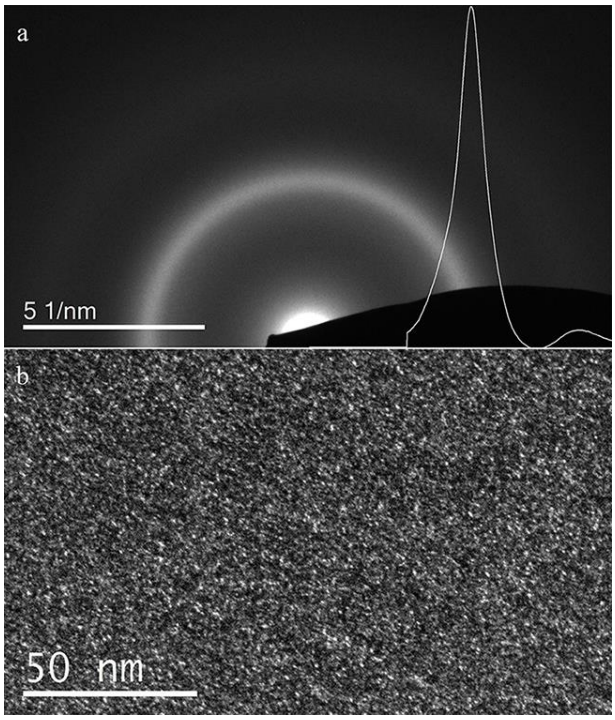

Figure 2

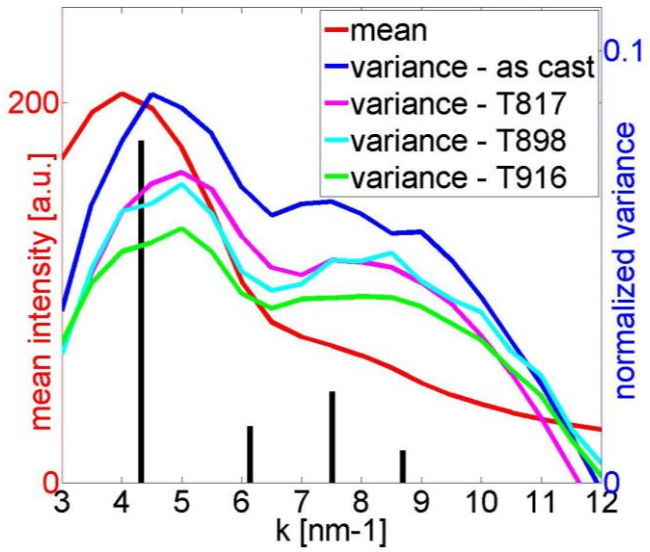

Figure 3

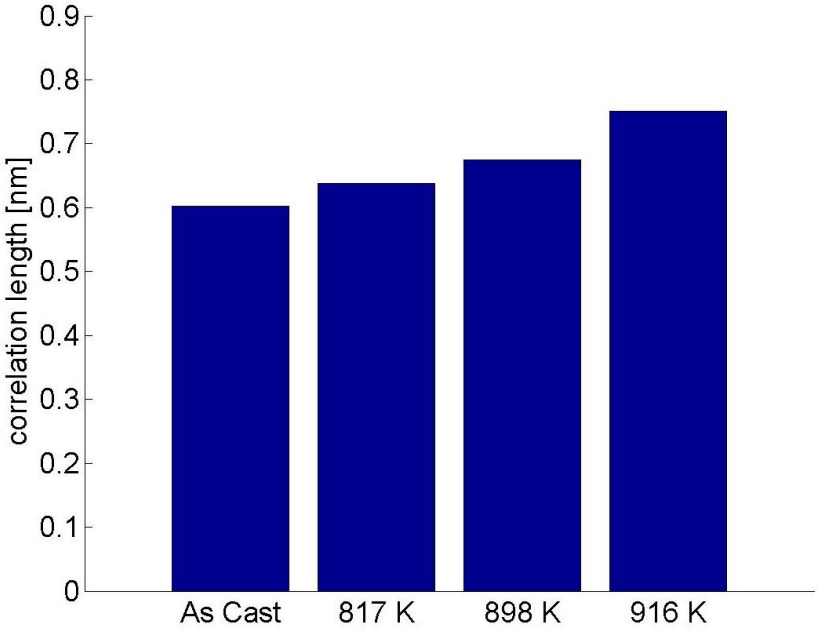

Figure 4

MS4.014
S-phase growth and coarsening in alloy 2618A during ageing

C. Rockenhäuser[1], B. Skrotzki[1]

[1]Bundesanstalt für Materialforschung und -prüfung (BAM), Experimentelle und modellbasierte Werkstoffmechanik, Berlin, Germany

christian.rockenhaeuser@bam.de

The aluminium alloy 2618A is designed for long-term operation at elevated temperatures for applications in transportation and aerospace industries (e.g. for radial compressor wheels). It is an Al-Cu-Mg alloy which is part of the 2xxx series of age-hardenable alloys. The fine S-phase precipitates formed from Guinier-Preston-Bagaryatsky (GPB) zones within the matrix control the desired properties, e.g. creep behavior and hardness. It is well-known that due to the overageing of the rod-shaped S-phase precipitates (Al2CuMg) and the conversion of the GPB zones into the stable equilibrium S-phase the strength of the material declines during exposition to elevated temperatures [1]. In this work several coarsening parameters were quantitatively investigated to improve the understanding of the overageing process of alloy 2618A at application relevant temperatures.
To systematically investigate the coarsening process, the precipitate size distribution and volume fraction of the S-phase has to be determined for different ageing conditions. To this purpose cross-section samples were fabricated from circular blanks of the peak hardened alloy in the T61 condition and after heat treatments of 1000 h and 8760 h. The Al2CuMg precipitates were selectively imaged by DFTEM. The precipitates form as rods along the α direction of the α-Al matrix. Therefore, the samples were oriented in the [001]α direction for the TEM investigations. Dark-field images of the Al2CuMg precipitates are shown in Fig. 1a) and b). The oriented rods penetrating the image plane result in a roughly circular contrast. The longer line shaped contrasts are caused by rods oriented orthogonal to the incident electron beam and look similar to the precipitates in the 2618 alloy investigated by Nový et al. [2,3]. The initial T61 condition contains numerous small and several large precipitates (Fig 1a)) and after 1000 h of ageing at 190 °C mainly large precipitates remain (Fig. 1 b)). Precipitate radii distributions were obtained from multiple images in a multi-step procedure leading to the distributions shown in Fig. 2a). A lognormal distribution fits the data very well and the resulting average radii are shown in Fig. 2b). The radii distributions show that with increasing average precipitate radius the initially narrow distribution (T61) broadens during isothermal heat treatments with increasing duration and the distribution maximum moves to higher radii. The coarsening process cannot be described as Ostwald ripening of the precipitates from the determined radii. In addition to the DFTEM images high-resolution TEM (HRTEM) images were acquired from the initial state and the sample heat treated at 190 °C for 8760 h and are shown in Fig. 3a) and b). Comparing these to Charai et al. [4], who investigated the S-phase precipitation sequence, the small precipitates in Fig. 3a) can be identified as GPB zones, whereas only large S-phase precipitates remain in heat treated samples (Fig. 3b)).
The authors suggest that the fast coarsening during the initial 1000 h of ageing elapses due to the combined coarsening of the S-phase precipitates and transformation of GPB zones into S-phase precipitates. The lognormal distributions of the initial state and 1000 h of ageing show a significant decrease of small precipitates (1-2 nm diameter), which supports the transformation of GPB zones into S-phase precipitates. After about 1000 h only S-phase precipitates remain and the coarsening process slows down. To confirm this hypothesis and to determine an exact ageing model additional parameters of the precipitates have to be evaluated. First investigations show an increase in S-phase volume fraction during ageing.

[1] Styles et al., Act. Mat. **60** (2012) p6940
[2] Nový et al., J. Alloy Compd. **487** (2009) p146
[3] Nový et al., Int. J. Mat. Res. **103** (2012) p688
[4] Charai et al., Act. Mat. **48** (2000) p2751

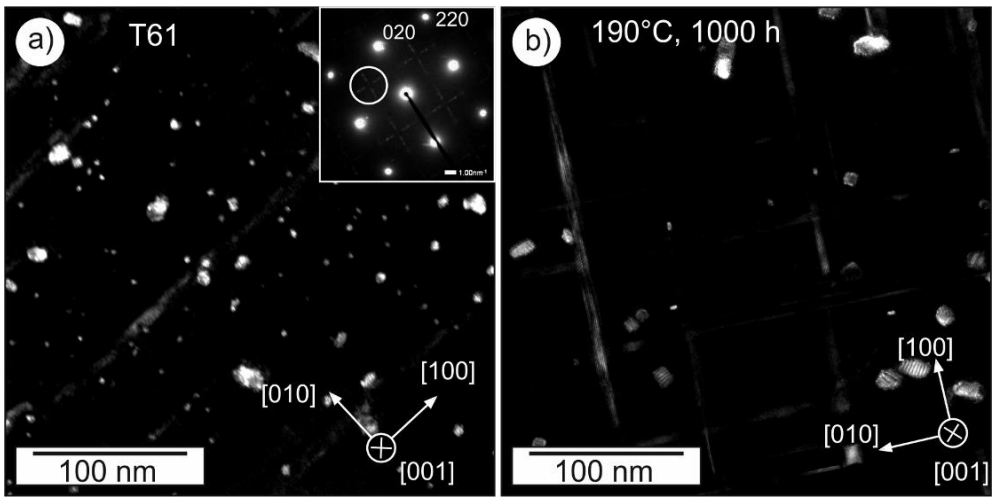

Figure 1. Dark-field images ([001]α zone axis) of the Al2CuMg precipitates for a) the initial T61 condition, b) aged sample state (1000 h, 190 °C).

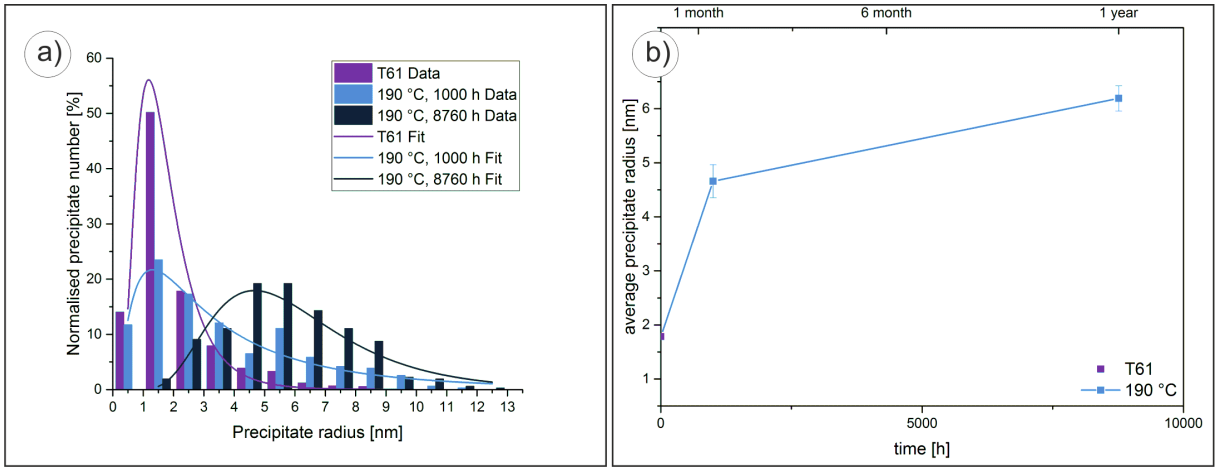

Figure 2. a) Lognormal distribution fits of the radii distributions acquired from the initial state and two heat treated samples and b) average precipitate radii of the investigated samples.

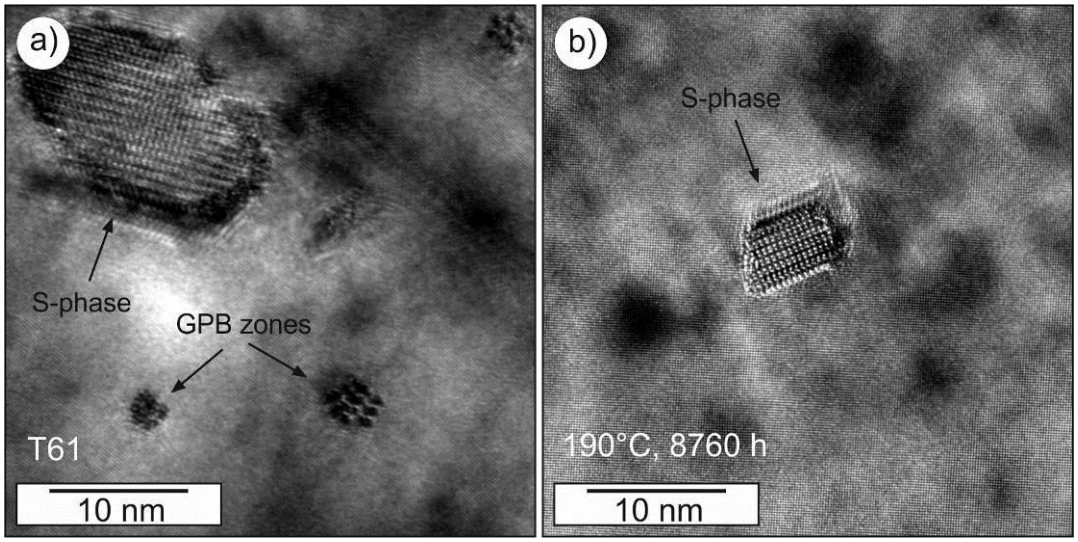

Figure 3. HRTEM images ([001]α zone axis) of a) S-phase precipitate and GPB zones in T61 condition and b) S-phase precipitate after heat treatment (8760 h/190 °C).

MS4.P001
Influences of Dy content and heat treatments on the formation of hydrides in Mg-Dy alloys

Y. Huang[1], L. Yang[1], N. Hort[1]

[1]Helmholtz-Zentrum Geesthacht, MagIC-Magnesium Innovation Centre, Geesthacht, Germany

yuanding.huang@hzg.de

Owing to their suitable mechanical properties and acceptable corrosion resistance, Mg-RE (rare earths) alloys were recently regarded as one of the most potential degradable biomaterials [1]. From their preparations to their final applications these magnesium alloys are subjected to the environments containing hydrogen (H). It is of particular interesting to investigate the possible interactions between RE and H. Yang et al. reported that NdH2 was formed in Mg-2wt.% Nd alloy with T4 treatment [2]. The formation of NdH2 was attributed to the reaction of Nd with the previously dissolved hydrogen during casting. In the recent, another different explanation was suggested by Peng et al. [3]. They suggested that the formation of hydride in Mg-Gd alloys can also proceed during sample preparations or mechanical deformation if subjected to H-containing environment. The hydride could be formed even at room temperature by interacting with the external H-agents such as water vapour or water.
The present work investigates the influences of alloying element Dy and heat treatments on the formation of hydrides in Mg-Dy alloy. The alloys with different contents of Dy were prepared by permanent mould direct chill casting. The heat treatments such as T4 or T6 were performed. The samples for the observations of optical microscopy and scanning electron microscopy (SEM) were machined and polished with water or without water. The X-ray diffraction (XRD) was used to identify the phases on the surfaces of samples.
Figure 1 shows SEM micrographs of Mg-20Dy alloy with T4 treatment. Lots of hydride particles are observed on its surface when the sample was wet machined and mechanical polished with water. In contrast, the hydride particles are hardly found on the surface of the sample with dry machined and electropolished. The formed hydrides have a cuboid morphology with a size of 2 to 5 micrometers. XRD results indicate that the content of Dy influences the formation of hydrides (Figure 2(a)). With the increment of Dy content, the amount of hydrides increases. In addition, the amount of hydrides is also affected by the heat treatment (Figure 2(b)). The maximum amount of formed hydrides can be determined on the surface of the sample with T4 treatment. On the surfaces of the samples with as-cast or T6 treatment, XRD test cannot identify the existence of hydrides, indicating that the amount of hydrides is very less.
In conclusion, the formation of hydrides in Mg-Dy alloys is affected by Dy content and heat treatment. Their formation mechanism is attributed to the surface reaction of Mg-Dy alloys with water. The part of Dy in solid solution plays an important role in influencing the formation of hydrides.

References:
[1] Hort N, Huang Y, Fechner D, Störmer M, Blawert C, Witte F, Vogt C, Drücker H, Willumeit R, Kainer KU and Feyerabend F (2010). *Magnesium alloys as implant materials - principles of property design for Mg-RE alloys*. Acta Biomaterialia, 6, 1714-1725.
[2] Yang Y, Peng L, Fu P, Hu B and Ding W (2009). *Identification of NdH2 particles in solution-treated Mg-2.5%Nd (wt.%) alloy*. Journal of Alloys and Compounds, 485, 245-248.
[3] Peng Q, Huang Y, Meng J, Li Y and Kainer KU (2011). *Strain induced GdH2 precipitate in Mg-Gd based alloys*. Intermetallics, 19, 382-389.

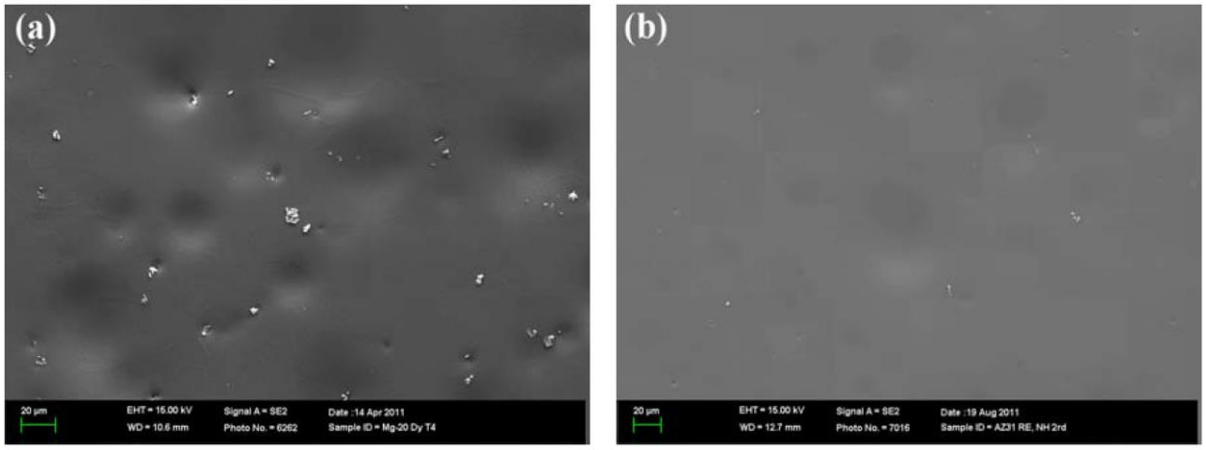

Figure 1. SEM micrographs of Mg-20Dy alloy with T4 treatment, (a) machined and polished with water, and (b) dry machined and electropolished.

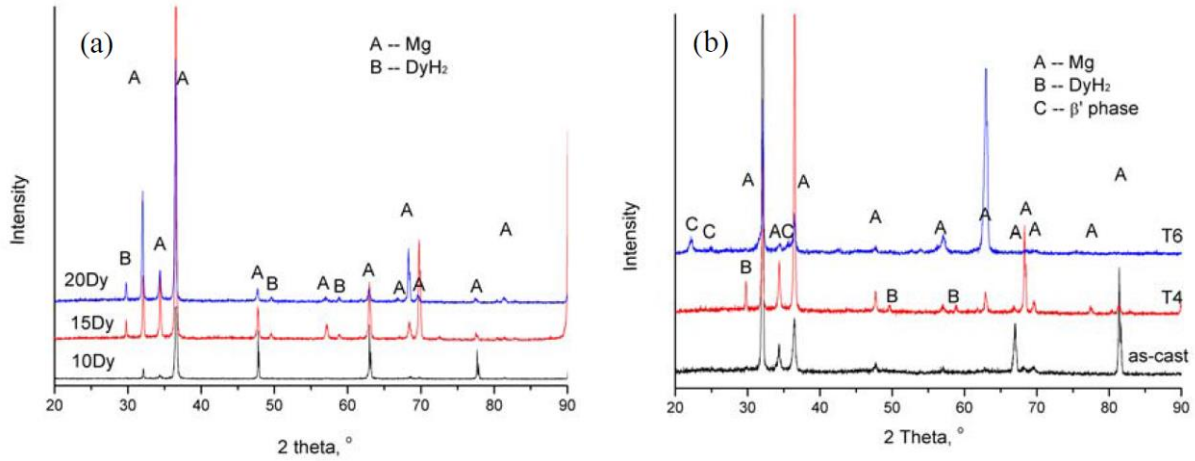

Figure 2. X-ray diffraction patterns showing the phases, (a) effects of Dy content and (b) effects of heat treatments.

MS4.P002
Characterization of α_2/O-phase domains in a γ-based lamellar Ti-Al-Nb alloy

H. Gabrisch[1], U. Lorenz[1], F. Pyczak[1], M. Rackel[1], A. Stark[1]

[1]Helmholtz-Zentrum Geesthacht, Metal Physics, Geesthacht, Germany

heike.gabrisch@hzg.de

γ-based intermetallic TiAl-alloys exhibit a combination of excellent high-temperature strength, low density and good corrosion resistance, which qualifies them for the use in structural components in aero-engines. To a certain extent, the alloys' properties can be tuned via their microstructures that depend on composition and processing route. For example the best room temperature ductility is measured in near γ or duplex microstructures while lamellar (α_2+γ) microstructures provide better high-temperature strength [1]. Furthermore, alloying with niobium improves the alloys' high temperature yield stress and room temperature ductility [2].
Recently the orthorhombic O-phase was identified in a niobium containing alloy Ti-42Al-8.5Nb using high energy X-ray diffraction (HEXRD) [3]. In-situ heating HEXRD experiments verified that the O-phase forms from the hexagonal α_2 phase. The orthorhombic O-phase has been reported before for Al-lean, niobium-rich α_2-based alloys where it forms in grains of α_2 and/or β_o phase [4]. The finding in γ-based TiAl-alloys is new. In the present study, the spatial arrangement of α_2 and O-phase within the alloy's microstructure is characterized by transmission electron microscopy techniques and the site occupancy of niobium is investigated.
The alloy Ti-42Al-8.5Nb was produced by a powder metallurgical route followed by heat treatments to promote the formation of orthorhombic phases as described in [3, 5]. After compacting the powder by hot-isostatic pressing (200MPa, 1250°C) the alloy consists of the major phases α_2 (hexagonal, D019) and γ (tetragonal,L10) that form lamellar colonies surrounded by seams of γ phase and a few small ω_o grains, Fig. 1. The alignment of α_2 and γ phases within the lamellar colonies is (0001)α_2//{111}γ and <1-210>α_2//<110>γ (Blackburn-relationship) [6]. During annealing at 550°C to 650°C, the lamellar morphology is unaltered. Transformations are observed inside the α_2 lamellae where small shifts of atom positions along α_2-<11-20> directions lead to the formation of orthorhombic domains. As a result, the volume of former α_2 lamellae is replaced by α_2/O-phase compounds. In α_2-[0001] projection the α_2 and O-phase domains take on a faceted shape, Fig. 2. Combining the information of projections parallel and perpendicular to the α_2 basal plane allows to determine the three dimensional shape of the domain structure. Imaging of the α_2/O-phase compounds in atomic resolution by ChemiSTEM [7] showed that niobium shares sites with titanium but not with aluminum.

References:
[1] Y.-W. Kim, Acta metall. mater. 40 1121-1134 (1992).
[2] F. Appel, M. Oehring, and R. Wagner, Intermetallics 8 1283-1312 (2000).
[3] M.W. Rackel, et al., Acta Materialia 121 343-351 (2016).
[4] D. Banerjee, et al., Acta metall. 36 871-882 (1988).
[5] R. Gerling, H. Clemens, and F.P. Schimansky, Advanced Engineering Materials 6 23-38 (2004).
[6] M.J. Blackburn, Science, Technology, and Application of Titanium 633-643 (1970).
[7] J.o.l.-s.r.f.A. http://dx.doi.org/10.17815/jlsrf-2-68., (2016).

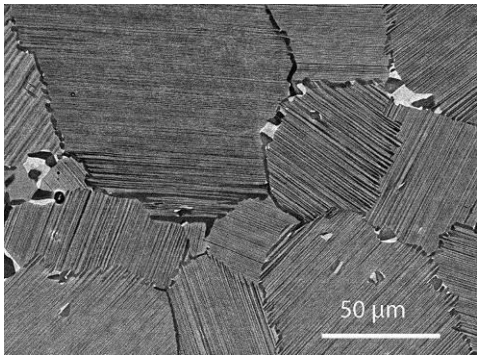

Figure 1. Overview showing lamellar (α_2+γ) colonies by SEM imaging.

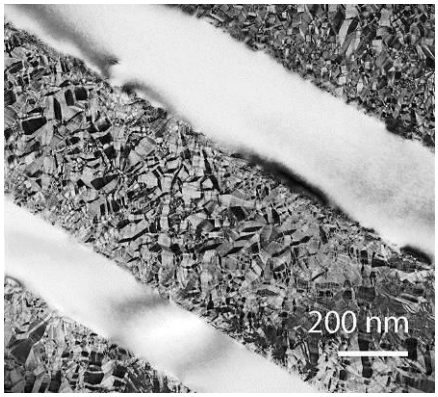

Figure 2. Planar view of a transformed lamellar ($\alpha_2+\gamma$) colony (α_2-[0001]-projection).

MS4.P003
TEM study of the decagonal Al–Cr–Fe phase

R. Li[1], K. A. Khor[1], Z. Dong[1]

[1]Nanyang Technological University, Singapore, School of Materials Science and Engineering, Singapore

zldong@ntu.edu.sg

Introduction: Quasicrystals (QCs) have drawn a lot of attention from researchers due to their ordered but non-periodic atomic arrangement and thus unique properties [1-3]. Al–Cr–Fe QCs are commercially available, but their structures and properties still lack comprehensive studies. Therefore, more systematic research on their structures is needed to further understand their physical properties.
TEM has been playing a very important role in the study of QCs, as it can provide information on their point group, space group, thickness, strain, dislocations, etc. [4, 5]. In most cases, QCs coexist with crystals. This makes TEM the only feasible method to determine its symmetry and atomic arrangement. Decagonal QCs can be described as a periodic stack of quasiperiodic planes [6]. Due to their two-dimensional character, their atomic arrangement can be analyzed through the diffraction patterns along their tenfold and twofold symmetry axes [7, 8]. In our study, we aim to study the microstructure and space group of decagonal Al–Cr–Fe using TEM.
Objective: The objective of the research is to obtain a comprehensive understanding of the structure of decagonal Al–Cr–Fe using TEM, including grain size, morphology space group etc.
Materials and Methods: The Al70Cr20Fe10 powders were purchased from Saint Gobian, France. They were consolidated using SPS apparatus (Sumitomo Coal Mining Company Ltd., Tokyo, Japan). 1g of Al–Cr–Fe powders was loaded into the graphite mold with an inner diameter of 10 mm. The sintering was conducted at 800 ˚C with a constant holding time of 30 min with a pre-sinter constant heating rate of 100 ˚C/min under an applied pressure of 50 MPa in vacuum (<10 Pa).
TEM samples were prepared by mechanical polishing, dimpling and ion milling. a JEOL 2100F transmission electron microscope (TEM) was used to study the microstructure and space group of decagonal Al–Cr–Fe phase.
Results: A typical bright-field TEM image of decagonal Al–Cr–Fe is shown in Fig. 1. The quasicrystal has a polygonal morphology and its size is in the micrometer scale.
The CBED pattern shows that the aperiodic planes have a five-fold rotational axis (Fig. 2a). Fig. 2b, taken along axis A, shows two mirror symmetry planes: one is parallel and the other is perpendicular to the five-fold axis. On the other hand, the CBED pattern taken along another characteristic orientation (Axis B) that is perpendicular to the five-fold axis and 18º away from axis A (Fig. 2c) shows that there is no mirror plane parallel to the five-fold rotation axis. This means that the space group is consistent with non-centrosymmetric P-10m2.
Conclusions: TEM study shows that in the spark plasma sintered sample, the grain size of decagonal Al–Cr–Fe is in the micrometer range and it has a polygonal morphology. The CBED pattern analysis indicates that this phase has a space group of P-10m2.

Acknowledgments
This project was financially supported by the Nanyang Technological University Tier 1 Grant Novel Metal Matrix Quasicrystal Composites with Strong Interface Chemical Bonding for Advanced Applications.

References:
[1] Y. Tian, H. Huang, G. Yuan, W. Ding, Journal of Alloys and Compounds, 626 (2015) 42-48.
[2] D. Shechtman, I. Blech, D. Gratias, J.W. Cahn, Physical Review Letters, 53 (1984) 1951.
[3] B.A. Silva Guedes de Lima, R. Medeiros Gomes, S.J. Guedes de Lima, D. Dragoe, M.-G. Barthes-Labrousse, R. Kouitat-Njiwa, J.-M. Dubois, Science and Technology of Advanced Materials, 17 (2016) 71-79.
[4] C. Patiño-Carachure, J. Flores-Chan, A.F. Gil, G. Rosas, Journal of Alloys and Compounds, 694 (2017) 46-50.
[5] J. Liu, Z. Yang, H. Ye, Journal of Alloys and Compounds, 621 (2015) 179-188.
[6] E. Abe, Chemical Society Reviews, 41 (2012) 6787-6798.
[7] M. Tanaka, K. Tsuda, M. Terauchi, A. Fujiwara, A. Tsai, A. Inoue, T. Masumoto, Journal of Non-Crystalline Solids, 153 (1993) 98-102.
[8] K. Tsuda, Philosophical Magazine Letters, 73 (1996) 271-278.

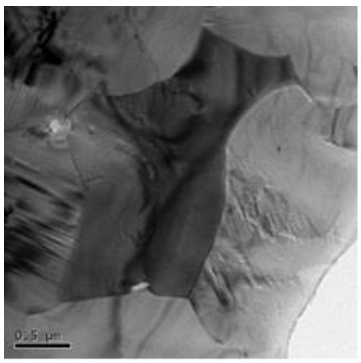

Figure 1. Bright field TEM image of decagonal Al–Cr–Fe.

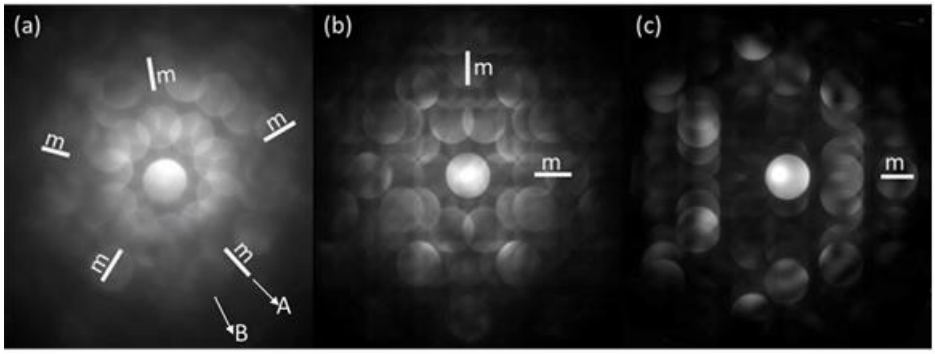

Figure 2. CBED pattern along (a) five-fold axis, (b) axis A, and (c) axis B.

MS4.P004
TEM study on the metallic microstructure of a neolithic copper axe

U. Schürmann[1], C. Horn[2], A. Högberg[3], K. Brink[4], L. Grandin[5], L. Kienle[1]

[1]University Kiel, Institute for Materials Science, Kiel, Germany
[2]University Kiel, Institute of Pre- and Protohistoric Archaeology, Kiel, Germany
[3]Linnaeus University, Department of Cultural Sciences, Kalmar, Sweden
[4]Sydsvensk Arkeologi, Vintrie, Sweden
[5]Statens historiska museer, Arkeologerna, Uppsala, Sweden

usc@tf.uni-kiel.de

Introduction: The interdisciplinary examination of archeologic findings can reveal new insights into the production and processing of tools and weapons. Techniques of Materials Science, namely Scanning Electron Microscopy (SEM) and Transmission Electron Microscopy (TEM), were used to study the element distribution on the surface and inside a Neolithic copper axe.
Objectives: Previous chemical analyses on the axe give the result of a composition of oxidized copper and another metal component that was revealed as silver. This work should clarify by means of electron microscopy if the for the Late Neolithic Scandinavia unexpected silver is coated afterwards on the copper axe probably as decoration or if it was an integral component of the origin material during the production.
Materials and Methods: The late Neolithic metal axe was found in autumn 2015 at Eskilstorp in south-west Scania near Malmö, Sweden. [1] The surface of the axe was studied by means Energy Dispersive X-Ray (EDX) Spectroscopy in a SEM (FEI Dualbeam Helios Nanolab). TEM and High Angle Annular Dark Field (HAADF) Scanning TEM (STEM) was performed on lamellae prepared from the surface of the axe into a depth of ca. 10 µm via Focussed Ion Beam (FIB). EDX point measurements and elemental maps were performed in STEM mode. Electron diffraction pattern were recorded to get information about the crystalline structure. TEM studies were performed in a FEI Tecnai F30 G² STwin equipped with an EDX detector (Si/Li, EDAX).
Results**:** SEM elemental maps of the surfaces reveal that a relative thick layer (up to one mm) on one side of the axe consists of iron compounds. This is probably the outcome of the one-sided contact with the drained bog in which the axe was found. The free copper layer is covered with isolated microscopic silver beads sometimes with additional spiral structures. FIB lamellae taken out of regions with a silver bead as well as on a clean area were analyzed with TEM techniques. The oxidized copper matrix contains nanoscopic silver crystallites distributed inside this matrix documented by EDX elemental maps and electron deepraction. These Ag precipitates show different sizes and shapes, some of them euhedral. The micrometer sized Ag bead is restricted on the surface. Also pure Cu crystals were found. Additional structures rich on the elements Fe, Ca, and P were found near the surface.
Conclusion**:** Silver precipitations with different shapes were found on the surface as well as inside the copper axe. This result is a hint that the silver was not a post production coating but was already a part of the starting material during the formation. The different shapes and sizes of the silver precipitations make it difficult to easily conclude on the history of the production process.

Acknowledgements
The authors want to thank Cristin Szillus for the preparation of the FIB lamellae.

[1] Högberg, A., Brink, K., Grandin, L., Horn, C. (2016). A silver-coated copper axe from Late Neolithic Scania: initial analyses. *Fornvännen*, *111*(4), 258-264.

Figure 1. Iron free side of the Neolithic copper axe.

MS4.P005
The application of scanning electron microscope (SEM) in the studies of phase and texture in the aluminium rolled products

L. Savioz[1], P. Nolan[2], Z. Liang[3], A. Despois[1], C. Bezencon[1]

[1]Novelis Inc, R&D Center Sierre, Sierre, Switzerland
[2]Novelis Inc, R&D Center Kennesaw, Kennesaw, GA, United States of America
[3]Novelis Inc, R&D Center Göttingen, Göttingen, Germany

liliana.savioz@novelis.adityabirla.com

The specific properties of the aluminium rolled product is achieved by optimum controls of deformation and thermal treatment in the rolling processes. The microstructure and texture of the alloy changes significantly from the casting to rolling and finally determines some of the most important properties, such as strength, formability, corrosion resistance, toughness and conductivity. In order to study the development of the microstructure through the process route, different methods in SEM are often used. In this work, the advanced use of Scanning Transmission Electron Microscopy (STEM), Electron Backscatter Diffraction (EBSD) and Transmission Kikuchi Diffraction (TKD) to study grain size, texture and the identification of intemetallics and precipitates in different conditions of the rolled aluminium product is introduced. Later two specific examples will be highlighted: (1) the impact of dispersoids on precipitation during quenching and (2) the role of grain texture distribution on formability (roping issues).

MS4.P006
Structural and phase composition of austenitic ODS steel

D. Litvinov[1], L. Strassberger[1], J. Aktaa[1]

[1]Karlsruhe Institute of Technology, Eggenstein-Leopoldshafen, Germany

litvinov@kit.edu

Transmission electron microscopy (TEM) was applied to study the structure of oxide dispersion strengthened (ODS) austenitic steel (16 wt.% Cr, 14 wt.% Ni, 1 wt.% W) produced by two-step milling technique. The microstructure was analyzed using Tecnai 20 FEG microscope. High angle annular dark field (HAADF) scanning TEM (STEM) with energy-dispersive X-ray (EDX) spectroscopy for the determination of the composition, conventional TEM with selected area diffraction SAD and high resolution TEM (HRTEM) with fast Fourier transformation (diffractogram) analysis for the crystallographic investigations were applied.

Figure 1a-b shows HAADF STEM images of the sample. The grain sizes of the steel are in the range of 300-1000 nm. As shown in Figure 1b, the typical observed defects in the sample are dislocations (D) or twins (TW), but many grains are without defects. By arrows in Figure 1a, bright regions with a high Cr concentration are marked, as show EDX analysis. The sample contains precipitates with mainly a dark contrast (up to 70 nm in diameter), distributed as well inside the grains and at the grain boundaries. The detail EDX analysis of Y/Ti relationship in many ODS particles combined with HRTEM analysis shows that they have mainly a composition of $Y_2Ti_{2-x}O_{7-2x}$. EDX investigation of the complex particles with different contrast in HAADF STEM image in Figure 1b combined with analysis of diffractograms from HRTEM images demonstrates that very small particles with a dark contrast consist of Y_2O_3 with *bcc* structure and a lattice parameter of ~ 1.06 nm.

The HRTEM image in Figure 2 shows an $Y_2Ti_2O_7$ particle (region 1) with size of ~ 3 nm having pyrochlore *fcc* structure with a lattice parameter of ~ 1.01 nm close to [110]-zone axis embedded in γ-Fe (region 2) having simple *fcc* structure with a lattice parameter of ~ 0.36 nm close to [110]-zone axis as shown by the obtained diffractograms. Analysis of corresponding diffractogramms from regions 1 and 2 in Figure 2 shows the full coherence relationship between the ODS particles and the matrix: <001> $Y_2Ti_2O_7$ II <001> Fe, <111> $Y_2Ti_2O_7$ II <111> Fe. This can be explained that misfit between lattice planes (002) and (111) of $Y_2Ti_2O_7$ and corresponding lattice planes (006) and (333) of γ-Fe is about 6 %. As shows filtered with reflection only from particle image in insert of Figure 2, the shape of $Y_2Ti_2O_7$ particle is close to hexagon.

Figure 3 shows HAADF-STEM image with elemental EDX maps of complex precipitate with the size of ~ 60 nm. The dark contrast in the STEM image (right-bottom) corresponds to Y-rich and O-rich region (probably Y_2O_3). The center of precipitate consists of Y-Ti-Cr-O (probably $Y_2Ti_2O_7$ + Cr), and left part of precipitate have Cr-Ti-O-enriched composition. Note, that Cr rich regions are observed at the grain boundaries in Figure 1a. It means that Cr has a tendency to segregate in the investigated austenitic steel.

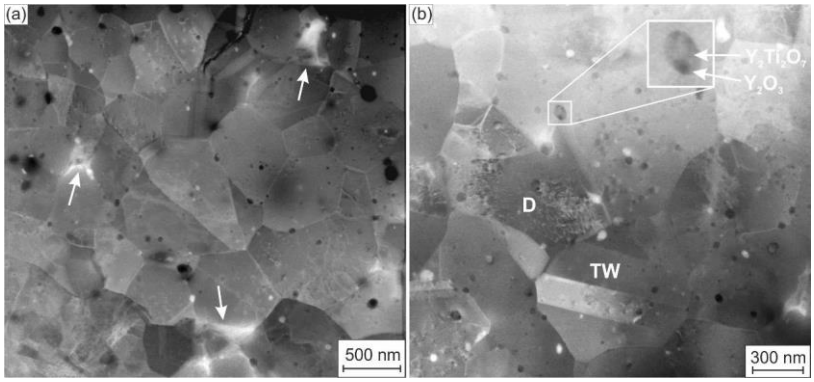

Figure 1

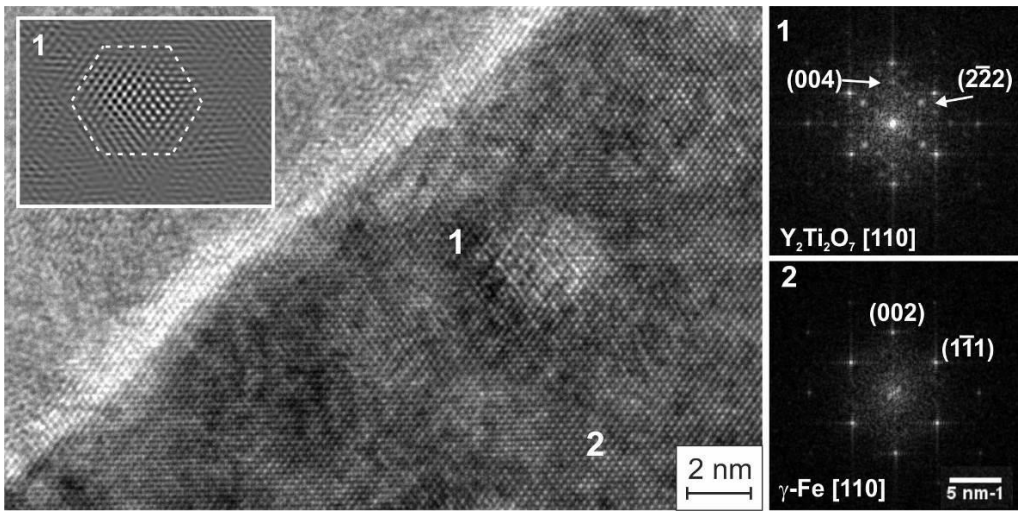

Figure 2

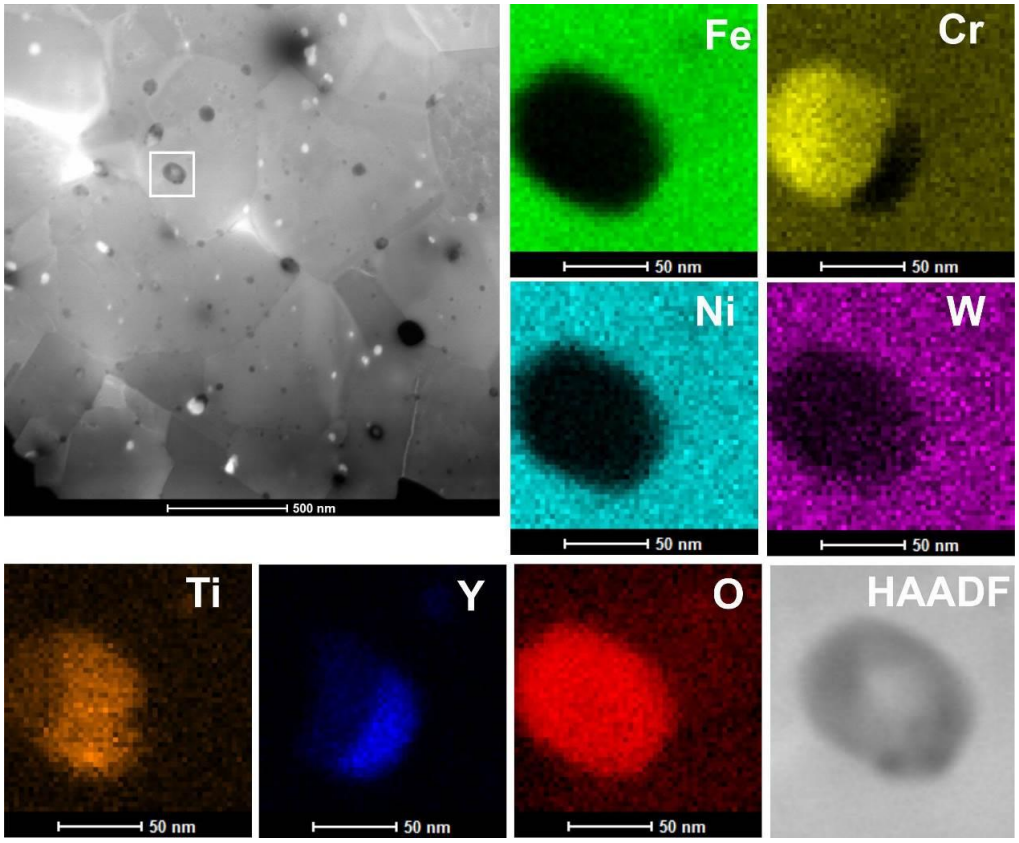

Figure 3

MS4.P007
Investigation of the techniques of the gilding and silvering on Bohemian medieval painting

M. Kmoníčková[1], R. Šefců[1], Ů Chlumská[1]

[1]The National Gallery in Prague, Prague, Czech Republic

martina.kmonickova@ngprague.cz

Introduction: The investigation was carried out on Bohemian panel paintings of 14th and beginning of 15th century from collections of the National Gallery in Prague. During the investigation various techniques of gilding or silvering and several types of preparative layers for plating were found. Among them black poliment was detected, this rare material occurs mostly with paintings of overwhelming importance. It was identified for example in most important artworks of Master of the Třeboň Altarpiece (active in the last third of the 14th century) and in Votive Panel of Jan Očko of Vlašim (Prague, before 1371).
Objectives: The aim of the investigation was to explore materials used for gilding and silvering, to analyze exact elemental composition, percentage representation of gold and silver (if found together) and also to describe structure proprieties of metallic leaves. Another intention was to explore preparative layer under metallic leaves.
Materials and Methods: Cross-sections from Bohemian paintings of 14th and beginning of 15th century were used like samples for further survey. Optical microscopy was applied to observe cross sections and proprieties of preparative layer for plating. Scanning electron microscope JEOL JSM-6460 LA with energy dispersive spectrometer was used to determine chemical composition and to observe structure and execution of metallic leaves. Analysis of individual points and mapping of chemical composition were effectuated in back-scattered electrons mode in low vacuum and accelerating voltage 20 keV. The identification of pigments in the preparing layer under metal leaves was made by micro-Raman spectrocopy using a dispersive Raman microscope Nicolet DXR (Thermo Scientific). Analyses were performed using 532 and 780 nm excitation lasers.
Results: Simple layers of gilding and silvering and also superposition of these layers was revealed. Thickness of each metal layer was determined. Thickness of silver layer passed about 1.36 µm and thickness of gold leaves was figured out between 0.44 and 1.82 µm. Thickness of all metal leaves might be attenuated due to degradation. Special technique of zwishgold was identified and quantity relation of gold and silver was figured out. The content of gold and silver was very variable even at panels appurtenant to the same workshop. Content of gold varied from 30 % to around 65 %, thickness of zwishgold was figured out between 0.63 and 1.5 µm. Zwishgold is a unique technique used in 14th and beginning of 15th century and it´s very rarely found in panel painting. In case of Bohemia paintings this technique consists on use of two metal plates (thinner leave of gold for upper and silver for down layer) beaten together and applied to a preparative layer for plating. In preparative layer there were found mixtion, chalk ground layer, red bole and also unique black poliment. In black poliment carbon based black was identified and in some cases described as vine black.
Conclusion: There were found several modes of gilding and silvering including valuable technique of zwishgold. Metal leaves were deposited on divers preparative layers including rare black poliment. Obtained data facilitated deeper understanding of described precious materials used for metal plating and allowed in particular an insight into technological practice of medieval decorative techniques.

This work has been financially supported by the project of the Ministry of Culture of the Czech Republic: Historical technologies and modern methods of research. The interpretative possibilities of the specialized methods of research of medieval artworks using innovative technologies (DF 13P010V010).

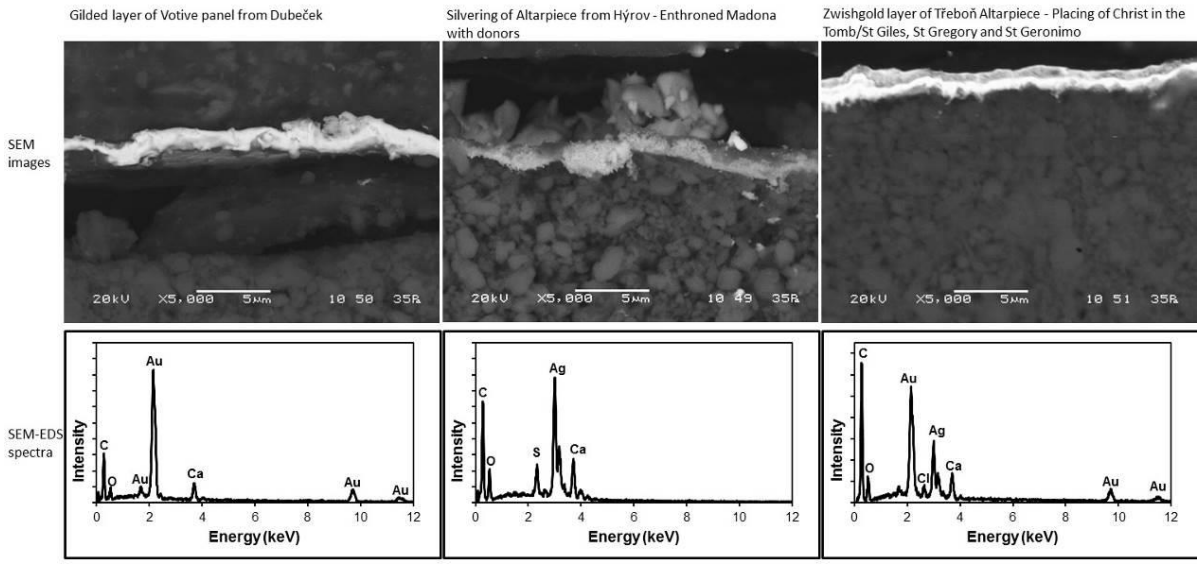
Gilded layer of Votive panel from Dubeček
Silvering of Altarpiece from Hýrov - Enthroned Madona with donors
Zwishgold layer of Třeboň Altarpiece - Placing of Christ in the Tomb/St Giles, St Gregory and St Geronimo
SEM images
SEM-EDS spectra
Intensity
Energy (keV)
C
O
Au
Ca
Ag
S
Cl

Figure 1

MS4.P008
Investigation of the stability of defects in hydrided/dehydrided nanocrystalline Palladium films using in situ TEM

G. Lumbeeck[1], B. Amin-Ahmadi[2], H. Idrissi[1,3], T. Pardoen[3], D. Schryvers[4]

[1]University of Antwerp, Physics, Antwerpen, Belgium
[2]Colorado School of Mines, Mechanical Engineering, Golden, CO, United States of America
[3]Université catholique de Louvain, Louvain-la-Neuve, Belgium
[4]University of Antwerp, Physics, Antwerp, Belgium

gunnar.lumbeeck@uantwerpen.be

Question: Palladium (Pd) has been known as an enabling material for future hydrogen (H) technology such as H purification and sensing applications. However, the mechanical stability and response to H pressure of Pd thin films is still insufficiently understood. It is already reported that in nanocrystalline (nc) Pd films, intrinsic or extrinsic stacking faults (SFs), Shockley partial loops and 9R phase are formed after hydriding to β-phase indicating a clear effect of H on the stacking fault energy (SFE) of Pd [1]. In the present research, the effect of the hydriding induced defects on the mechanical properties and the corresponding nanoplasticity mechanisms is investigated. In-situ high resolution (HR) TEM nanomechanical testing was performed on a Pd film containing SF loops and 9R phase (after hydriding to β phase). Furthermore, Automated Crystal Orientation Mapping (ACOM) TEM was used to study mechanical twinning and grain boundary processes under tensile deformation.
Methods: The Pd films were sputter-deposited until a thickness of 150 nm was reached. The hydriding cycles to β phase were performed with an imposed H_2 pressure of 97.5 mbar. After hydriding, the system returns to ambient conditions, i.e., atmospheric pressure and room temperature. Cross-sectional TEM specimens are prepared ex situ using Focused Ion Beam (FIB) thinning with the lift-out procedure and mounted on a push-to-pull (PTP) grid [2]. In-situ tensile test experiments were performed using a Hysitron TEM PicoIndentor instrument [2]. Conventional and high resolution (HR) TEM characterizations were used to record selected defects before deformation, in between and after the final loading/unloading cycle. ACOM TEM was performed with the ASTAR system from Nanomegas [3] to map the crystal orientation and phase using TEM spot diffraction patterns.
Results: From HR TEM images, a 9R area was seen to shrink during the consecutive loading/unloading cycles. Furthermore, it was shown that single SFs transform into a nanotwin. Additionally, gradual loss of TB coherency was found (Figure 1). The occurrence of twinning/detwinning was confirmed from the ACOM TEM data, on the one hand through grain boundaries dissociating into TBs and by removal of twins within the grains (Figure 2).
Conclusions: The deformation mechanisms can be categorized into two classes, depending on the initial defect before deformation. Firstly, deposition-induced growth twins lose their coherency. Secondly, H-induced defects such as the 9R and SFs transform respectively by the collapse of SFs and twin expansion due to the nucleation of new SFs. The twin related effects were confirmed with ACOM TEM. Although the exact occurring deformation mechanisms depend highly on the exact preparation method and site in the sample (grain size, orientation, etc.), it has been shown that some of these mechanisms are related with the H-induced defects.

[1] B. Amin-Ahmadi *et al*, Act. Mat. 111 (2016), 253-261.
[2] A. Kobler, et al, Ultramicroscopy 128 (2013) 68–81.
[3] NanoMEGAS, website http://www.nanomegas.com/ .

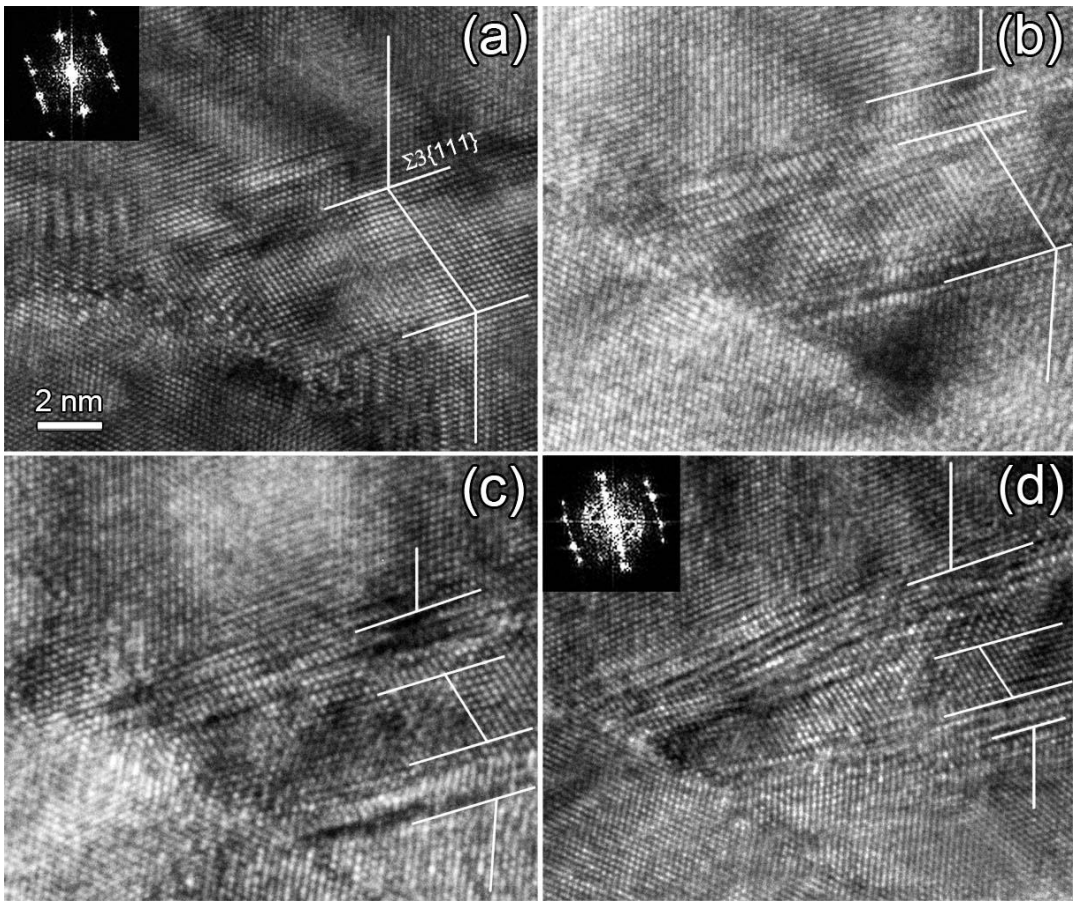

Figure 1. (a) <110> HR TEM image of a twin in the Pd matrix after hydriding, before deformation. (b) after applying 30 µN loading/unloading tensile force in vertical direction, (c) after 80µN and (d) after 160µN. The gradual loss of TB coherency is clear.

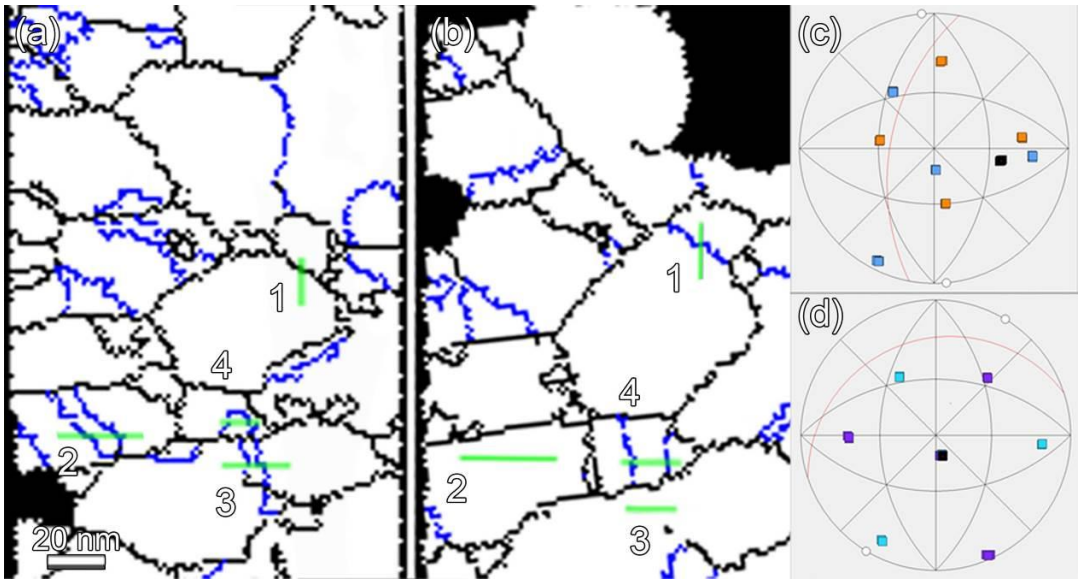

Figure 2. Twin boundary map of (de)hydrided cross-sectional film of Pd (a) before deformation and (b) after deformation. All lines indicate boundaries with black for normal rotation boundaries and blue for Σ3{111} coherent twin boundaries. (c) Inverse pole figures from a line profile drawn over the green marker of index 1 before deformation and (d) after deformation indicating the chance in boundary character.

MS4.P009
Precipitates morphology in CuCr0,6 alloy after the repetitive corrugation process

T. Jung[1], W. Kwaśny[1], Z. Rdzawski[2], W. Głuchowski [2], K. Matus[1], M. Pawlyta[1]

[1]The Silesian University of Technology, Faculty Of Mechanical Engineering, Gliwice, Poland
[2]Institute of Non-Ferrous Metals, Metals Processing Department, Gliwice, Poland

Tymoteusz.Jung@polsl.pl

Introduction: Nowadays, materials engineering is increasingly focusing on the development of methods which can offer economic opportunities and, above all, continuous production of materials with and nanometric structure. In the modern group of metalworking techniques very promising is repetitive corrugation and straightening (RCS), which main advantage is the opportunity to plan the order of use of individual rolls in the process of deformation. In the case of precipitation hardening alloys after severe plastic deformation, a large influence on the mechanical properties have precipitations.
Objectives: The aim of our study was to determine the effect of the repetitive corrugation process on the chromium precipitates occurring in the CuCr0,6 alloy after 30 predefined cycles deformation. The main interest was to determine the influence of intensive plastic deformation process on the localisation and shape of the precipitates and their coherence with the copper matrix.
Materials and Methods: The study was carried out on copper chromium alloy strips; the test material was obtained from copper waste through the process of recycling hence its chemical composition contains a 0.6% of chromium. Prepared material was melted and cast into moulds. It was then rolled into a 3mm thickness sheets. After mechanical removal of the oxides from the surface, sheets were cold rolled down to 0,1 mm of thickness, cut to dimensions: 20 mm x 120 mm and annealed in a resistance furnace in a protective atmosphere of argon at 650 °C during one hour. The material was subjected to the repetitive corrugation process using the 30 cycles of deformation consisting in repetitive bending by toothed and grooved rolls and final straightening using conventional rolls.
Studies have been performed primarily using scanning and transmission electron microscopy. Back-Scattered Electron (BSE) and electron backscatter diffraction (EBSD) was primary research technique, supported by energy-dispersive X-ray spectroscopy (EDX). The research was conducted in a scanning electron microscope Zeiss Supra 35 with field emission gun. TEM investigations were performed in a probe Cs-corrected S/TEM Titan 80-300 FEI microscope equipped with EDAX EDS.
Results: The results of BSE and EBSD allowed to determine the positions of the formed chromium precipitates and determine the privileged place of their occurrence. It has been discovered the high impact of intensive deformation process on fragmentation occurring precipitates as well as their tendency to agglomerate. Studies performed with transmission electron microscopy allowed us to determinate the coherence of formed chromium precipitates relative to the copper matrix.
Conclusion: Our findings confirm the impact of the RCS process on precipitates of chromium in examined copper alloy. The process of deformation affects mainly the localisation of formed precipitates.

MS4.P010
"Inverse-nanoglasses" formation via severe plastic deformation processing of amorphous TiNiCu alloy.

E. Ubyivovk[1], E. Boltynuk[2], D. Gunderov[2,3,4], V. Pushin[5], O. Vyvenko[1], R. Valiev[2,3]

[1]St. Petersburg State University, Department of Physics, St. Petersburg, Russian Federation
[2]St. Petersburg State University, Department of Mathematics and Mechanics, St. Petersburg, Russian Federation
[3]Ufa State Aviation Technical University, Ufa, Russian Federation
[4]Institute of Molecule and Crystal Physics, Ufa Research Center RAS, Ufa, Russian Federation
[5]Ural Division of Russian Academy of Sciences, Institute of Metal Physics, Ekaterinburg, Russian Federation

ubyivovk@gmail.com

Nanoglasses are a new type of amorphous structure. In nanoglasses amorphous clusters are divided by amorphous boundaries with increased free volume. Such type of structure provides the unique properties of nanoglasses: reduced density, enhanced ductility, biocompatibility and catalytic activity. Presently there are few ways of nanoglasses synthesis – inert gas condensation (IGC) with further consolidation and magnetron sputtering (MS). However nanoglasses produced by such techniques have few disadvantages: some residual porosity, relatively small specimens sizes, that limited attractive applications. It is known, that by means of severe plastic deformation (SPD) it is possible to introduce high density of shear bands into the processed material and modify its structure and therefore properties. In this regard, SPD is a perspective way of nanoglasses formation without limitations mentioned above. In nanoglasses produced by SPD shear bands must operate as cluster boundaries with increased free volume.

The objective of our study is to investigate structural features of $Ti_{50}Ni_{25}Cu_{25}$ specimens processed by high pressure torsion (HPT) under different regimes and compare these states with nanoglasses produced by IGC and MS methods.

$Ti_{50}Ni_{25}Cu_{25}$ amorphous ribbons with a width of 2 mm and thickness of 40 μm were fabricated by rapid quenching of melt. Ribbons were HPT processed at pressure of 6 GPa for 10 revolutions at temperatures of 20°C and 150°C. Disc shaped samples with diameters of 10 mm and thicknesses of 0.25 mm were produced. Structural investigations were performed by means of transmission electron microscopy (TEM) Zeiss Libra 200 FE. Samples for TEM studies were prepared by two schemes. First scheme: mechanical thinning with following polishing on precise ion polishing system on Gatan PIPS (plan view specimens). Second scheme: focused ion beam (FIB) lamella preparation on Zeiss Auriga (cross section).

Initial ribbons show typical for amorphous alloys "salt-paper" contrast (in TEM). It was found, that HPT at temperature of 150°C leads to formation of predominantly nanosized cluster-type amorphous structure in addition to "salt-paper" (Fig. 1). FIB-lamellas were prepared with the aim to determine nature of contrast localization (Fig. 2). Three types of contrast/structure were observed on lamella sample (Fig. 3): 1) shear bands with nanocrystallization inside; 2) areas with cluster-type amorphous structure around "large" shear bands and 3) featureless amorphous structures distant from shear bands were observed. Plan view and cross section samples did not exhibit chemical separation (EDX spectra). No difference in the chemical composition between the areas with different types of the contrasts could be detected with EDX both on plan-view and cross sectional samples.

Cluster-type amorphous structure of second type of areas could be compared with nanoglasses-type structure mentioned above. However, opposite tendency was observed: low density amorphous clusters separated by boundaries with increased density in comparison with nanoglasses. Therefore such observations we called "inverse- nanoglasses". Detailed discussion of the results will be presented at the conference.

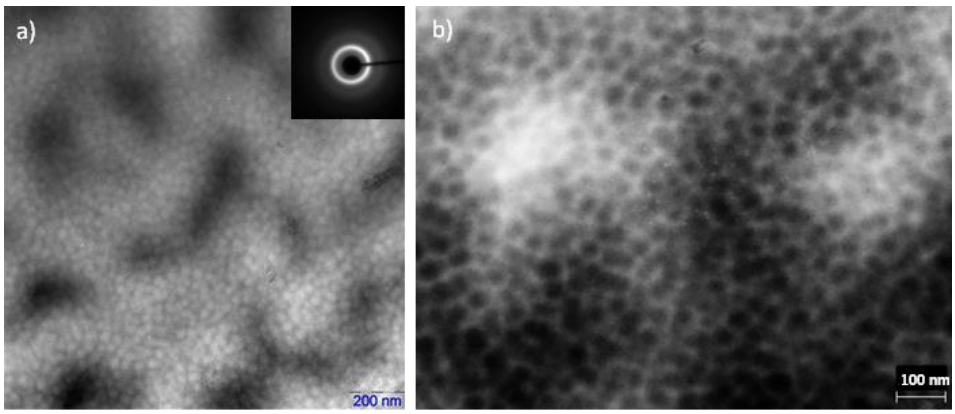

Figure 1. Images of cluster-type contrast in $Ti_{50}Ni_{25}Cu_{25}$ subjected to HPT at temperature of 150°C: a) TEM image, SAED pattern; b) STEM-HAADF image.

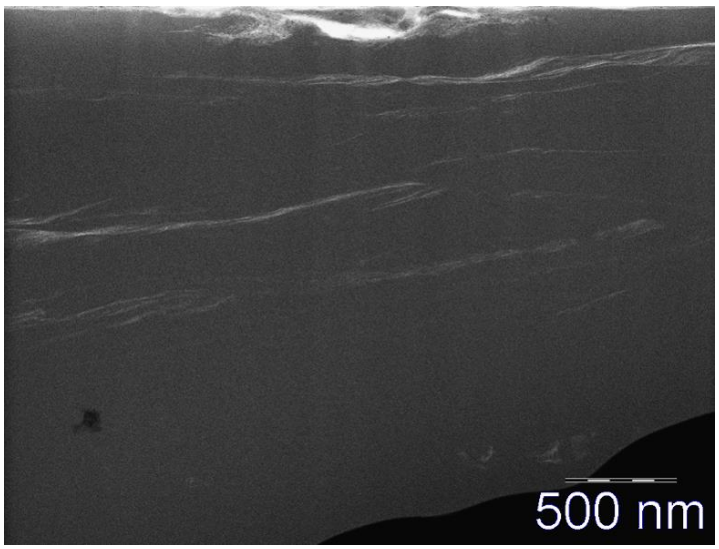

Figure 2. STEM-BF image of FIB-lamella $Ti_{50}Ni_{25}Cu_{25}$ subjected to HPT at temperature of 150°C (in cross section). Low-magnification cross-sectional STEM-BF image of $Ti_{50}Ni_{25}Cu_{25}$ ribbon subjected to HPT at temperature of 150°C.

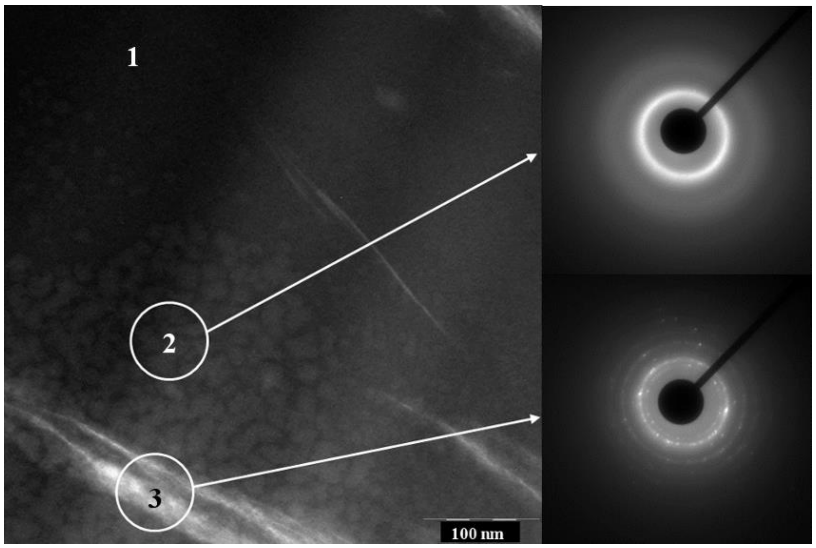

Figure 3. TEM image of FIB-lamella $Ti_{50}Ni_{25}Cu_{25}$ subjected to HPT at temperature of 150°C. Three states of different structure could be distinguished: featureless structure of amorphous matrix (1); cluster-type amorphous structure – "inverse-nanoglass" (2); shear bands with nanocrystals (3) (in cross section view). On the right side SAED patterns of 2 and 3 states are presented.

MS4.P011
Simultaneous magnetic domain and microstructure TEM imaging in oriented magnetic shape memory Co-Ni-Ga single crystals

A. Zak[1], W. Dudzinski[2], G. Gerstein[3], H. J. Maier[3]

[1]Wroclaw University of Science and Technology, Faculty of Mechanical Engineering, Wroclaw, Poland
[2]Wroclaw University of Science and Technology, Faculty of Technology and Engineering, Wroclaw, Poland
[3]Leibnitz Universitat Hannover, Institut für Werkstoffkunde (Materials Science), Garbsen, Germany

andrzej.zak@pwr.edu.pl

Introduction: Magnetic shape memory alloys are currently intensively developed. Alloys of this type feature a martensitic or austenitic state, and the temperature of the phase transformation can be different from the temperature of the ferromagnetic to paramagnetic transition. Simultaneous magnetic and microstructural imaging can be a powerful tool to shed light on the underlying phenomena and their interaction.
Objectives: The aim of the study was to observe the magnetic structure of a Co-Ni-Ga alloy in the martensitic and austenitic state. For details on the mechanical properties of this material, see Ref. [1]. The current study focused on the observation and description of the magnetic domain formation in the martensitic structure and their evolution upon application of an external magnetic field.
Materials and Methods**:** The Co49Ni21Ga30 alloy was prepared from pure Co, Ni and Ga by melting in a high frequency induction furnace under high vacuum conditions. Single crystals were then obtained using the Bridgman method.
Samples for TEM observations were prepared using mechanical thinning down to a thickness of 100 µm, followed by electrolytic polishing and then ion polishing The samples were observed using a Hitachi H-800 transmission electron microscope operated at an accelerating voltage of 150 kV. The microscope was equipped with conventional side-entry pole piece, instead of a low-field Lorenz pole piece. The sample was tilted to obtain different magnetic fields in the plane of the sample. To confirm the size of the magnetic domains, additional observations with the objective lens turned off were performed. Most of the observations was conducted with manual control of the lens current.
Results: Co49Ni21Ga30 in the martensitic state shows a magnetic structure, which is finely associated with the grain structure. In figure 1, the magnetic domain boundaries are visible as dark lines that intersect at an angle of 90 degrees. At the intersections an unusual contrast with curved contours was observed. The contrast changed as a function of the sample tilt, as tilting varied the magnetic field in the plane of the sample. Micro twinning in the martensite grains was still visible together with the magnetic domain boundaries.
Higher magnification images recorded in the thicker areas of the sample allowed for observation of a tweed magnetic effect in the slightly defocused condition (fig. 2). The tweed, grid-like patterns confirm the presence of strain fields, resulting from the martensitic transformation. The presence of magnetic tweed contrast is not been fully explained in the literature [2] and the description of this phenomenon will be the subject of further work.
Conclusion**:** The imaging of the magnetic domains and the internal microstructure with grain boundaries and micro twins in Co-Ni-Ga Heusler alloys is possible using a conventional side-entry pole piece by manual controlling the lens current. Tilting of the sample allows for applying different magnetic fields in the plane of the sample. Methods of the precise distinction of the magnetic, phase and scattering contrast should be the subject of further research.

Acknowledgments
Financial support of this study by German Research Foundation (DFG grant: MA 1175/61-2) is gratefully acknowledged.

References:
[1] J. Dadda, H.J. Maier, I. Karaman, Y. Chlumlyakov, High-temperature in-situ microscopy during stress-induced phase transformations in Co49Ni21Ga30 shape memory alloy single crystals, Int. J. Mater. Res.: Vol. 101, No. 12, pp. 1503-1513 (2010).
[2] A. Planes, M. Porta, T. Castan, A. Saxena, Magnetostructural tweed in ferromagnetic Heusler shape-memory Alloy, Mater. Sci. Eng. A: Vol. 438–440, pp. 916-918 (2006).

MS4.P012
Ex situ and in situ TEM analysis of the microstructure evolution during heat treatment of a titanium alloy (BT14)

L. S. Mantha[1,2], A. Mazilkin[1], X. Mu[1], M. H. Fawey[1], A. K. Vesangi[3], R. K. Gupta[3], C. Kübel[1,4]
V. S. K. Chakravadhanula[1], A. K. Kanjarla[2]

[1]Karlsruhe Institute of Technology, Institute of Nanotechnology, Karlsruhe, Germany
[2]Indian Institute of Technology Madras, Metallurgical and Materials Engineering, Chennai, India
[3]Vikram Sarabhai Space Centre, Materials and Mechanical Entity, Trivandrum, India
[4]Karlsruhe Institute of Technology, Karlsruhe Nano Micro Facility, Karlsruhe, Germany

lakshmisravani07@gmail.com

Titanium alloys are extensively used as structural materials in aerospace applications due to their excellent combination of specific strength, workability and corrosion resistance. Titanium exists as a hexagonal close-packed (HCP) crystal structure upto 882 ˚C beyond which it undergoes an allotropic transformation into body centered cubic (BCC) crystal structure. Due to this allotropy, depending on the alloying elements, titanium alloys exhibit a wind range of microstructures ranging from near a, a+b, near-b, stable b alloys. In addition to the alloying elements, the type of thermo-mechanical treatment the material is subjected to also affect the resulting microstructure. The morphological features of the phases and the crystallographic textures in the microstructures play a significant role in determining the macroscopic properties.
The titanium alloy Ti-5Al-3Mo-1.5V (BT14) is a a+b alloy that is used in the fabrication of critical engine and pyro components for space application [1]. The alloy was subjected to different heat treatments: a) homogenizing above the b transformation temperature, followed by air (Fig. 1) and water quenching (Fig. 2) b) solutionizing+aging (Fig. 3). The phase transformation characteristics were investigated using different characterization techniques. A detailed microstructure analysis was carried out with optical microscopy and Electron Back Scattered Diffraction (EBSD-SEM) to gain insights into the variant selection during transformation. Automated Crystal Orientation Mapping (ACOM) in STEM mode combined with Electron Energy Loss Spectroscopy (EELS) and Energy Dispersive Spectroscopy (EDS) was performed to understand the effect of cooling rate on transformation texture and elemental segregation at the phase boundaries. *In situ* TEM thermal experiments were performed to understand the transformation characteristics at the nanoscale using ACOM-STEM.

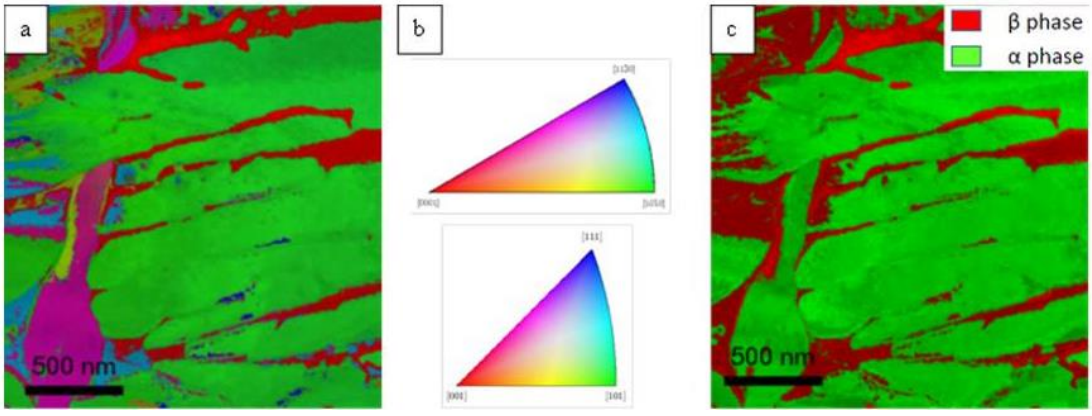

Figure 1. STEM-ACOM a) orientation map, b) IPF color coding, c) phase map for 980°C-air cooled specimen.

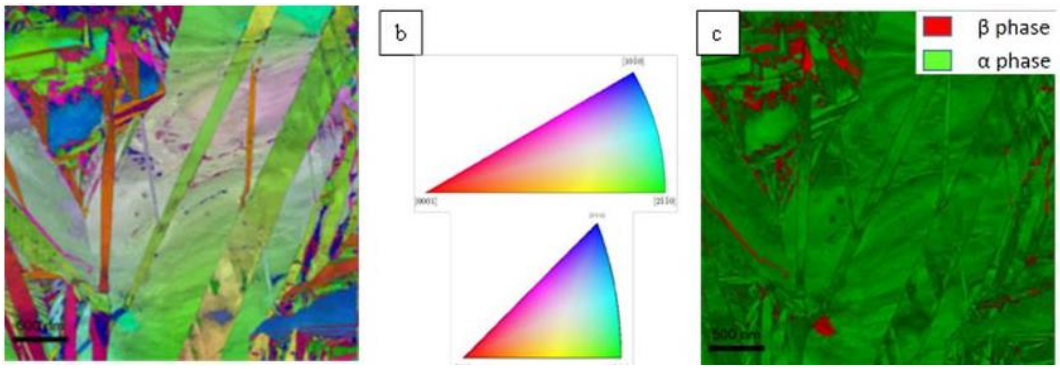

Figure 2. STEM-ACOM a) orientation map, b) IPF color coding, c) phase map for 980°C-water quenched (WQ) specimen.

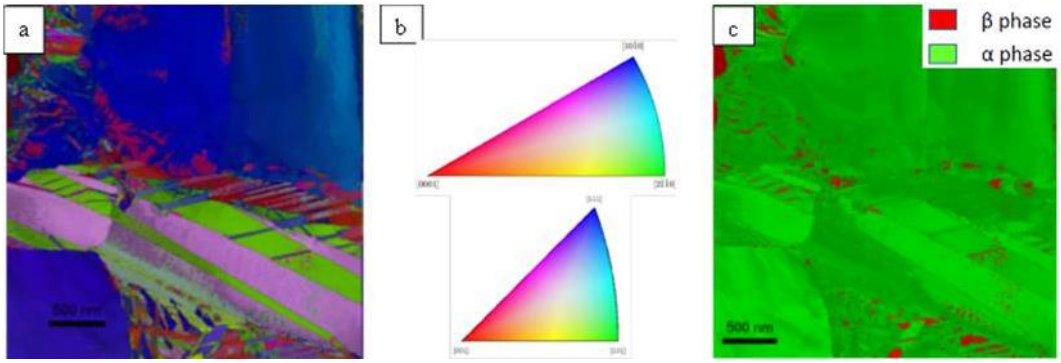

Figure 3. STEM-ACOM a) orientation map, b) IPF color coding, c) phase map for 900°C-WQ-540°C-aged specimen.

MS4.P013
Atomic structure and deformation behavior of an κ-strengthened Fe-Mn-Al-C lightweight steel

M. Lipinska-Chwalek[1,2], M. Jao[3], E. Welsch[3], C. Liebscher[3], D. Ponge[3], C. Scheu[3], J. Mayer[1,2]

[1]RWTH Aachen, Central Facility for Electron Microscopy (GFE), Aachen, Germany
[2]Forschungszentrum Jülich GmbH, Ernst Ruska-Centre for Microscopy and Spectroscopy with Electrons (ER-C), Jülich, Germany
[3]Max-Planck-Institut für Eisenforschung GmbH, Düsseldorf, Germany

m.lipinska@fz-juelich.de

Introduction: High Mn steels evoke large interest due to their exceptional combination of high strength and ductility. Addition of Al makes high Mn steels even more attractive, due to reduced density, but also improved resistance against oxidation and hydrogen-induced failure. Last but not least, it promotes formation of nanosized $(FeMn)_3AlC$ κ-carbides, which effectively influence mechanical properties of the alloy.
Objectives: The aim of this study is to get insight into the structure of the alloy at the atomic level and identify mechanisms controlling the deformation behavior of Fe-30Mn-8Al-1.2C (wt. %) steel. For these purposes, aberration-corrected high resolution scanning transmission electron microcopy (HRSTEM) was employed.
Materials and Methods: The lightweight steel Fe-30Mn-8Al-1.2C (wt. %) was fully austenitic in as-received state (for heat treatment details, see [1]). Precipitation of k-carbides proceed upon subsequent aging at 600 °C. Room temperature (RT) tensile deformation was carried out on cylindrical samples.
The atomic structure was investigated with the aid of an aberration-corrected FEI Titan G2 80-200 Cs probe-corrected STEM operated at 200 kV[2]. An high angle annular dark field detector (HAADF) was used for imaging. Electron transparent TEM specimens were prepared by electropolishing in a Struers Tenupol twin jet device or as lamellas cut with the focused ion beam (FIB) using a dual beam FEI Helios Nano-Lab 600i instrument.
Results: The austenitic steel Fe-30Mn-8Al-1.2C (wt. %) subjected to the 600°C aging exhibits intensive precipitation of κ-carbides already at very short treatment. In 1 h-aged samples, a network of homogenously distributed κ-carbides with an average size of 5 to 10 nm is present in the austenitic matrix. Upon extended aging, size of the existing carbides increases and reach maximum of 20 ± 10 nm after 24h. Comparison HAADF HRSTEM images of 1h- and 24h-aged steel are shown in Fig. 1. In both samples, the κ-carbides possess coherent interfaces to the surrounding g-matrix.
Fig. 1: HAADF HRSTEM of Fe-30Mn-8Al-1.2C after 1h- (A, B) and 24h- aging at 600 °C (C).
Strengthening of the material takes place with the increase of aging time (with max. strength of 1,4 for 24h-aged material). Stable hardening rate observed, indicates presence of single, dominant deformation mechanism. Very thin slip bands (thickness of an interatomic distance) formed during deformation in {111} planes are an evidence of dislocation movement (Fig.2).
Fig. 2: HAADF HRSTEM of 24 h-aged Fe-30Mn-8Al-1.2C after 5% tensile deformation. Slip band in {111} planes crosses diagonally the image in (A). Magnified view of a slip band cutting through the carbides (indicated with an arrow) (B). Atomic structure of the slip plane (C).
Density of the slip bands increases proportionally to deformation progress. The subsequent bands emerge equally distanced between existing bands. As a result, a continuous decrease of the mean slip band spacing and effectively, refinement of the material structure takes place.
Conclusion: Microstructural evolution of lightweight steel Fe-30Mn-8Al-1.2C (wt. %) upon RT tensile straining was investigated. Aberration-corrected HRSTEM was employed to track structure development at the atomic level. Deformation is mediated by slip of dislocations confined to {111} planes, resulting in the structure refinement.

References:
[1] E. Welsch, D. Ponge, et al., Acta Materialia 116 (2016) 188
[2] Ernst Ruska-Centre for Microscopy and Spectroscopy with Electrons, Journal of large-scale research facilities 2 (2016) A43

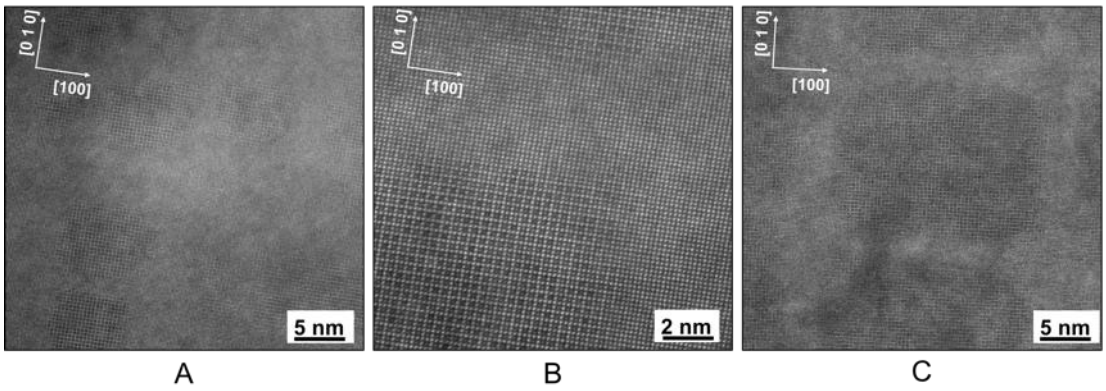

Figure 1. HAADF HRSTEM of Fe-30Mn-8Al-1.2C after 1h- (A, B) and 24h- aging at 600 °C (C).

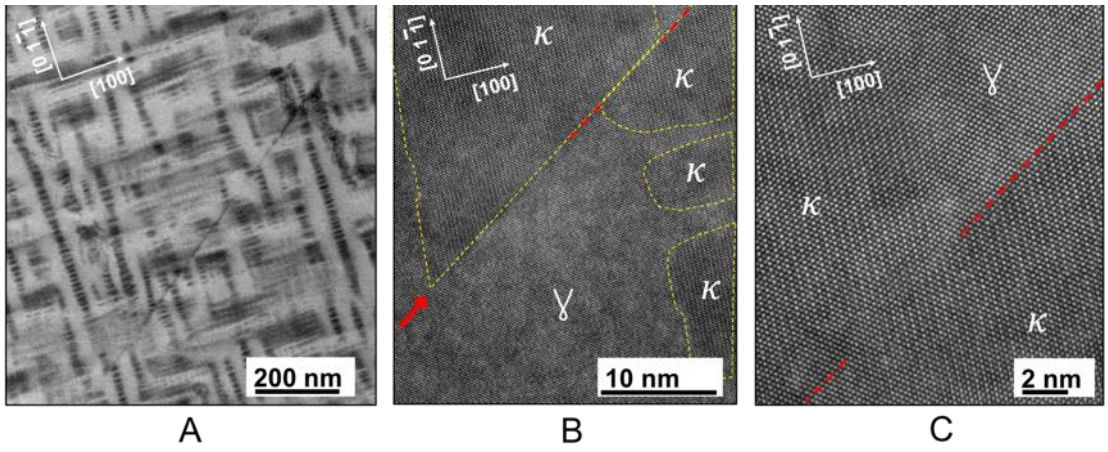

Figure 2. HAADF HRSTEM of 24 h-aged Fe-30Mn-8Al-1.2C after 5% tensile deformation. Slip band in {111} planes crosses diagonally the image in (A). Magnified view of a slip band cutting through the carbides (indicated with an arrow) (B). Atomic structure of the slip plane (C).

MS4.P014
Segregation and precipitation in twin-roll cast Al-Mg-Sc-Zr alloy

M. Cieslar[1], J. Bajer[1], M. Šlapáková[1], O. Grydin[2], M. Zimina[3]

[1]Charles University, Faculty of Mathematics and Physics, Prague, Czech Republic
[2]University of Paderborn, Faculty of Mechanical Engineering, Paderborn, Germany
[3]Research Center Rez, Husinec-Rez, Czech Republic

cieslar@met.mff.cuni.cz

Introduction: Excellent weldability, satisfactory corrosion resistance and possibility of superplastic forming make Al-Mg-based alloys a frequent material used in the aerospace industry. Their potential might be enhanced by alloying with Sc and Zr due to the presence of a fine dispersion of strengthening Al3(Sc,Zr) precipitates with the structure of the L12 type [1,2]. However, similarly to other Mg-containing Al alloys, rolled sheets or extruded profiles suffer from the exfoliation corrosion associated primarily with grain boundaries (or subgrain boundaries) microstructure (see Fig. 1) and microchemistry.
Objectives: Twin-roll casting (TRC) is a typical example enabling directly cast strips with the thickness requested for semi-finished product with rather equiaxed grains. However, no information concerning the preparation and properties of TRC materials containing Zr and Sc are available. In the present contribution the microstructure of a model Al-Mg-Sc-Zr alloy prepared by TRC is described.
Materials and Methods: A model Al-3.24wt.%Mg-0.19wt.%Sc-0.14wt%Zr alloy was prepared by TRC with a vertical operational plane. In order to investigate the changes of microstructure at elevated temperatures and their influence on mechanical properties samples were annealed in an isothermal heating scheme at 300, 350 and 400 °C. Vickers microhardness measurements HV 0.1 with the load of 100 g at QNESS 10A, light optical microscopy (LOM) (Olympus GX51) and transmission electron microscopy (TEM) (JEOL JEM 2000FX) observations including in-situ TEM in a heating stage were used for the material characterization.
Results: TRC produces strips containing equiaxed grains significantly differing from flat grains observed in direct chill (DC) cast and rolled materials of the same thickness (Fig. 2). Hardening of the TRC material is most pronounced in specimens annealed at 300 °C and persists even after 8 hours of annealing. At higher annealing temperatures (350 and 400 °C) this hardening is weaker followed by a partial degradation of mechanical properties at longer annealing times (Fig. 3). TEM observations clearly proofs that similarly to DC cast and rolled materials the precipitation of fine dispersion of Al3(Sc,Zr) phase is responsible for the maximal age-hardening of the TRC material at 300 °C. Lower microhardness values measured in specimens annealed at higher temperatures, and following overaging is caused by a lower density of precipitated particles and their coarser size (Fig. 4).
Conclusions: Strips of twin-roll cast Al-Mg-Sc-Zr alloy were prepared and characterized by TEM, LOM and microhardness measurements. Dispersion of fine Al3(Sc,Zr) particles precipitates at 300 °C and results in a remarkable hardening of the material and stabilization of grains. Coarsening and lower number density of Al3(Sc,Zr) particles is responsible for overaging of the alloy.

Acknowledgements
The financial supports of project of the Czech Science Foundation 16-16218S is gratefully acknowledged.

References:
[1] Vlach M, Stulíková I, Smola B and Žaludová N 2010 Mater. Charact. 61 1400.
[2] Fuller C B, Seidman D N and Dunand D C 2003 Acta Materialia. 51 4803
[3] Liao M, Bellinger N C, Komorowski J P 2003 Int. J. Fatigue 25 1059
[4] Oguocha I N A, Adigun O J and Yannacopoulos S 2008 J. Mater. Sci. 43 4208

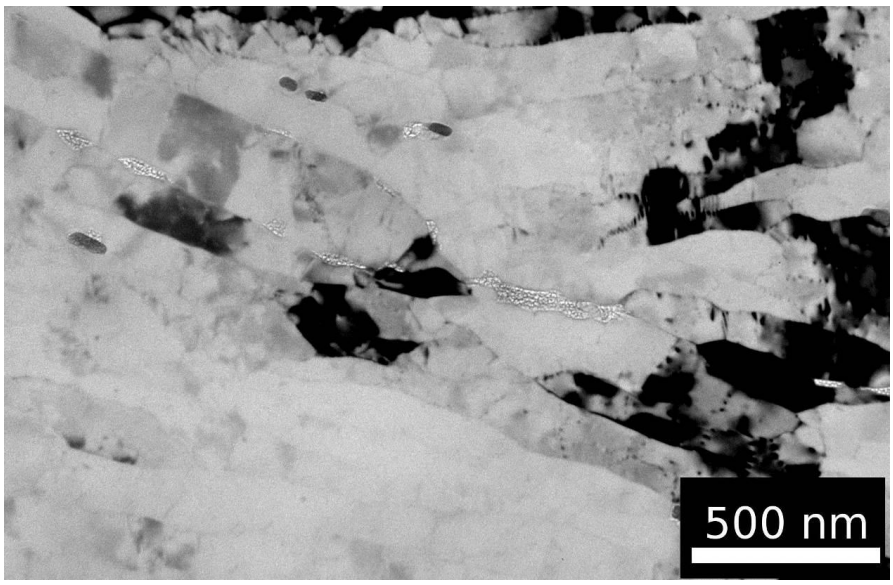

Figure 1. Formation of Mg-rich layer near subgrain boundaries in rolled Al-Mg-Sc-Zr alloy after annealing at 120 °C for 250 h.

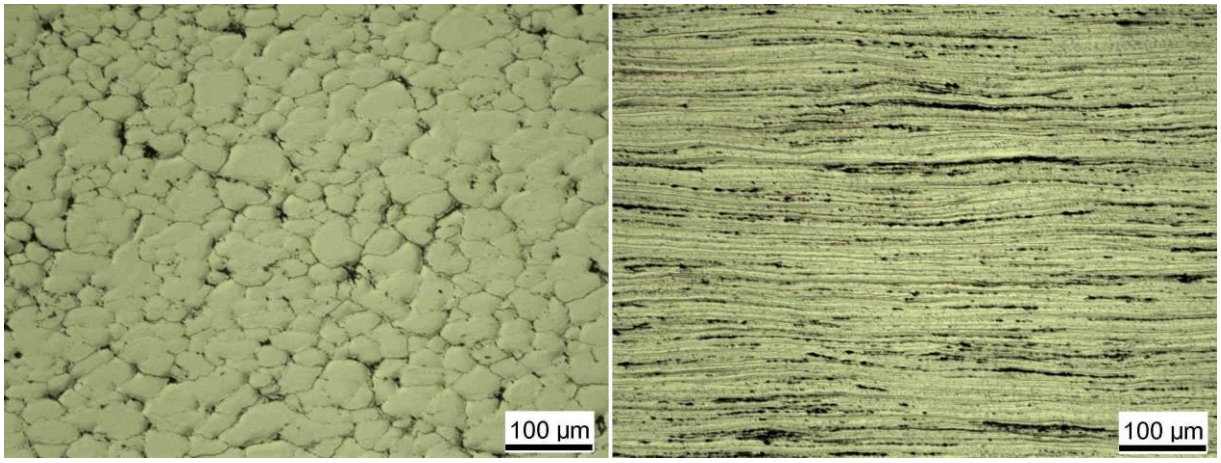

Figure 2. Comparison of equiaxed grains in TRC material (left) and flat grains produced by conventional technology including rolling (right).

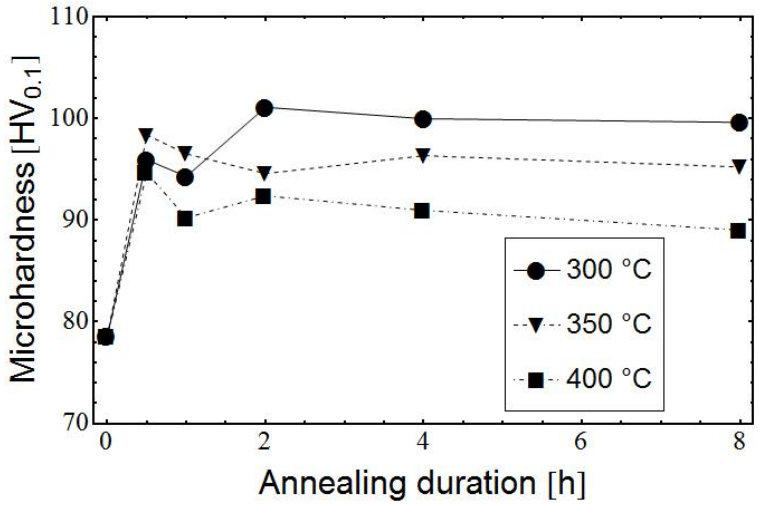

Figure 3. Evolution of microhardness during isothermal annealing.

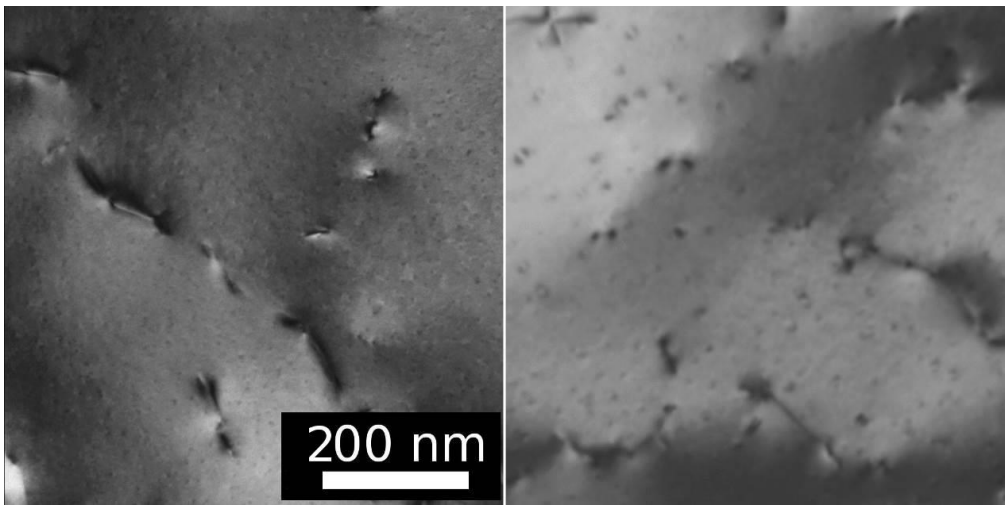

Figure 4. Al3(Sc,Zr) in TRC material annealed for 8 h at 300 (left) and 400 °C (right).

MS4.P015
On-line monitoring of steel microsturcture changes within tensile testing

M. Bystriansky[1], L. Kucerova[1], J. Prochazka[1]

[1]University of West Bohemia, Regional Technological Institute, Pilsen, Czech Republic

mbyst@rti.zcu.cz

Microstructure of steel determines its mechanical properties. Deformation stage MTI/Fullam compatible with scanning electron microscope was used for both microstructure and mechanical observation. Low alloyed steels with 0.2 to 0.5 % (w) C, 0.5 to 1.5 % (w) Mn and 1.7 to 2.0 % (w) Si were used and prepared either mechanically for crack development observation or electrochemically for grain deformation observation by electron-backscatter difraction analysis.

MS4.P016
Evaluation of dissimilar metals welds joints – SA 533 – Alloy 82 – SA 36

L. Zamora Rangel[1], J. A. Aguilar Torres[1]

[1]Instituto Nacional de Investigaciones Nucleares, Materials of Technology, La Marquesa, Ocoyoacac, Edo. de México, Mexico

luis.zamora@inin.gob.mx

The Alloy 82 has been widely used as filler metal to joints the low – alloy steel reactor pressure vessel (RPV) and pressure vessel nozzles to both components in light water rector by manual metal arc welding. In the case of components have suffered cracking interdendritic (ID)/ intergranular (IG) and usually confined to the weld metal of alloy 82 [1]. For the better understanding of heat affected zones (HAZs) usually present in dissimilar metals welds along the fusion lines are particular susceptible to cracking, it was important investigated behavior in the transition regions.
For this study, two plates, the steel SA 533 and A36, the physical dimensions of these samples were 7.62 X 5.08 X 1.90 cm. The weld metals of particular interest were those prepared as multilayer by arc welding process using electrodes ERNiCr3 to 3.175 mm of diameter. The chemical compositions of different materials were given in the table 1 (figure 2). The non-destructive evaluation (NDE) of materials such as visual inspection, applied during each of stages of steps of welds made of figure 1. The microstructural characterization was performed by scanning electron microscopy (SEM). Additionally, Vickers microhardness measurements performed using Shimadzu, Mod HMV-G-20DT, microhardness mark beginning on the base metal, to the HAZ and weld, the test was applying a load of 100 gf for 15 seconds.
The results of the application of NDE in the SA 533- Alloy 82 – A36 based on the criteria of ASME Code, was in all cases no relevant indications. The microstructural aspects after to welding are shown in figure 2. The microstructure can be observed in the base metal steel SA 533 their structures austenite and distinguishing martensite, bainite and ferrite (figure 3)[2]. The Alloy 82 had a peak microhardness in 298 HV was usually observed in the region of weld metal, the hardness in the HAZ was usually close to the fusion line and below 247 HV and the metal base tended to slightly decrease until 228 HV with increasing distance to the fusion line, the values were characteristics of these joints (figure 4)[3].

References:
[1] L. Griffing (Ed.), Welding Handbook, AWS, Vol. 1 y 4, US 1972.
[2] Tsung-Kuang Yeh, Guan-Ru Huang, Mei-Ya Wang, Chuen-Horn Tsai. Progress in Nuclear Energy 63, 7- 11 (2013).
[3] Zamora L., et al. 2015, Dissimilar Welds:in the System: SA533-E309-E308L-Alloy 82-Alloy 182 B168, Microscopy Conference 2015, George-August-University Göttingen, 6-11 September 2015.}

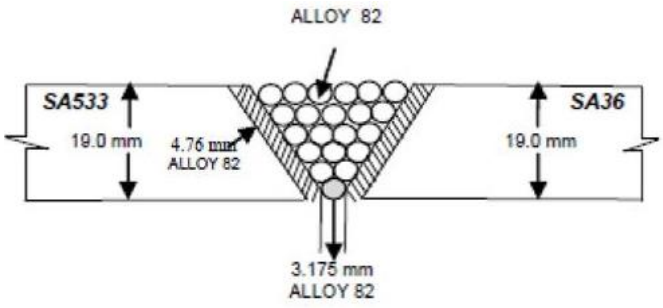

Figure 1. SA 533 – Alloy 82 – SA 36 system.

Materials	C	Si	Mn	P	S	Ni	Cr	Fe
Steel A-36[1]	0.13	0.07	0.63	0.00	0.10	0.00	0.00	Bal.
Steel A-533[1]	0.10	0.20	1.15	0.00	0.02	0.73	0.09	Bal.
ERNiCR-3[2]	<0.05	<0.40	4.0	0.00	0.00	Bal.	19.5	<4.0

[1] Chemical analysis making in ININ.
[2] Chemical composition of Thermanit Nicro 82.

Figure 2. The chemical compositions of different materials (table 1).

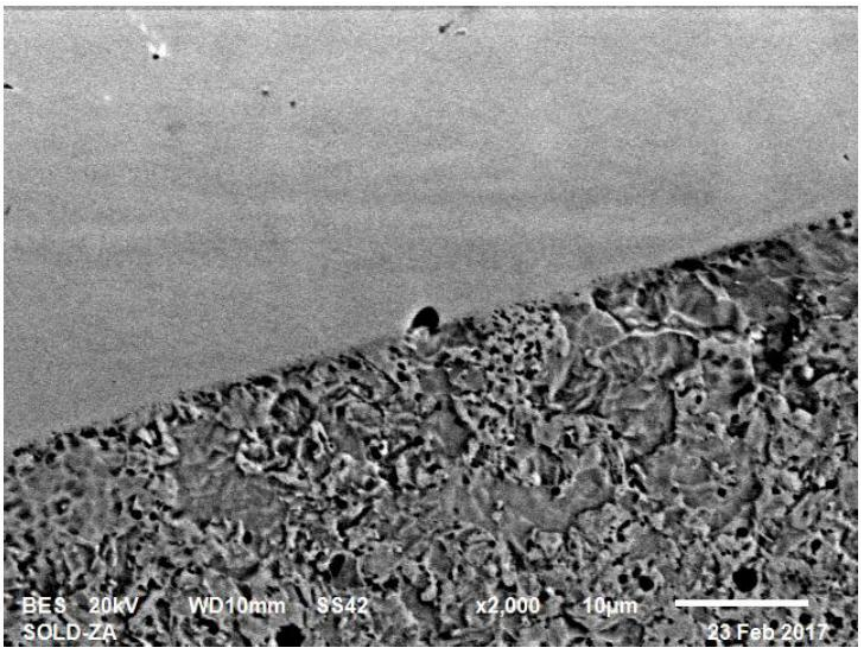

Figure 3. Interfaces microstructures SA 533 – Alloy 82.

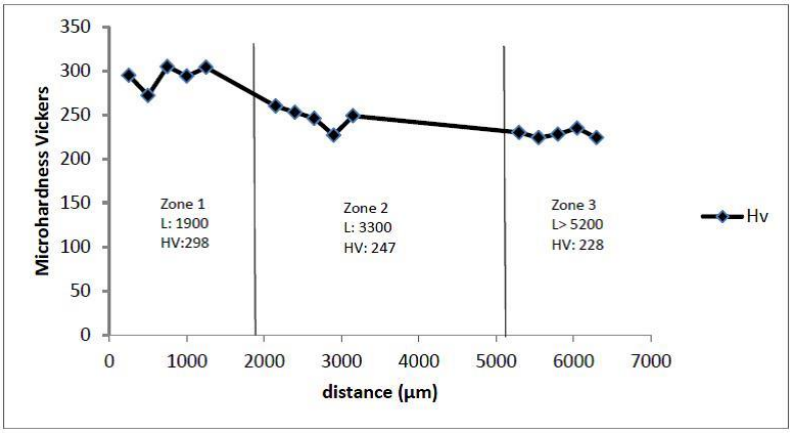

Figure 4. Profile of Microhardness at interfaces.

MS4.P017
Mechanical properties and microstructure observation of Al-1.0mass%Mg_2Ge alloys with different alloying elements

T. Kataoka[1], T. Sato[1,2], S. Seungwon[3], S. Ikeno[4], K. Matsuda[3,4]

[1]University of Toyama, Graduate School of Science and Engineering for Education, Toyama-shi, Japan
[2]University of Toyama, Graduate School of Science and Engineering for Education, Toyama, Japan
[3]University of Toyama, Graduate School of Science and Engineering for Research, Toyama-shi, Japan
[4]University of Toyama, Professsor of Emeritus, Toyama-shi, Japan

tomoya3@live.jp

Introduction: Matsuda *et al.* reported that Ge could be good substitutional or better element for Si in Al-Mg-Si alloy. In Al-Mg-Ge alloy, it showed a better age-hardenability at the high aging temperatures and a different precipitation sequence when it compares to Al-Mg-Si alloy[1]. It is worth to research the effect of alloying element to precipitation sequence and mechanical properties for use of industrial purpose, however, only few reports are available.
Objectives: The aim of this research is to understand the effect of alloying elements on age-hardening behavior and mechanical property variation of Al-Mg-Ge alloy.
Materials and Methods: The chemical compositions of the alloys are in shown in Table 1. Alloys were fabricated using casting, then, they were subjected to homogenization treatment before extrusion. During extrusion, alloys were deformed from 30mm of bar to 1mm thickness of plate. Solution treatment was conducted at 873K for 3.6ks. Aging treatment was carried out at the temperatures of 473K and 523K. Vickers microhardness measurement and tensile test were conducted to estimate the mechanical properties of alloys. To observe microstructure, TEM and SEM were used. TEM samples were prepared electron-polishing using 10% $HClO_4$ and 90% ethanol solution at 243K. TEM observation was conducted using Topcon, EM-002B with accelerated voltage of 120kV
Results: Fig.1 shows age-hardening curves aged at 473K. Every alloy with Cu containing, maximum hardness increased compared to base alloy. With Ag addition, hardness increased quickly at the initial stage of aging. In the case of Ag-Cu-Cr-Si added alloy shows the highest hardness values. With microstructure observation, of Ag-Cu-Cr-Si added alloy showed the higher density of precipitation than base. Also, it showed the highest ultimate tensile strength, yield strength and the elongation.
Conclusion:

1) The hardness of Ag-Cu-Cr-Si added alloy aged 473K was the highest of the this research.
2) Alloying Ag, Cu, Cr and Si on Al-Mg-Ge alloy is effective to enhance its mechanical property and to form more precipitates at the peak aging condition.

Reference:

[1] Matsuda, T. Munekata, T. Kawabata, Y. Uetani and S. Ikeno: Journal of Japan Institute Light Metals, 56, 680-684, 11 (2004).

	Mg	Ge	Ag	Cu	Cr	Si	Al
base	0.43	0.20	-	-	-	-	bal.
Ag added	0.47	0.23	0.23	-	-	-	bal.
Cu added	0.44	0.19	-	0.18	-	-	bal.
Cr added	0.46	0.20	-	-	0.20	-	bal.
Si added	0.49	0.19	-	-	-	0.39	bal.
Ag-Cu added	0.45	0.21	0.19	0.20	-	-	bal.
Ag-Cu-Cr added	0.51	0.20	0.19	0.19	0.18	-	bal.
Ag-Cu-Cr-Si added	0.47	0.20	0.18	0.19	0.19	0.38	bal.

Figure 1. The chemical composition of alloys (at. %).

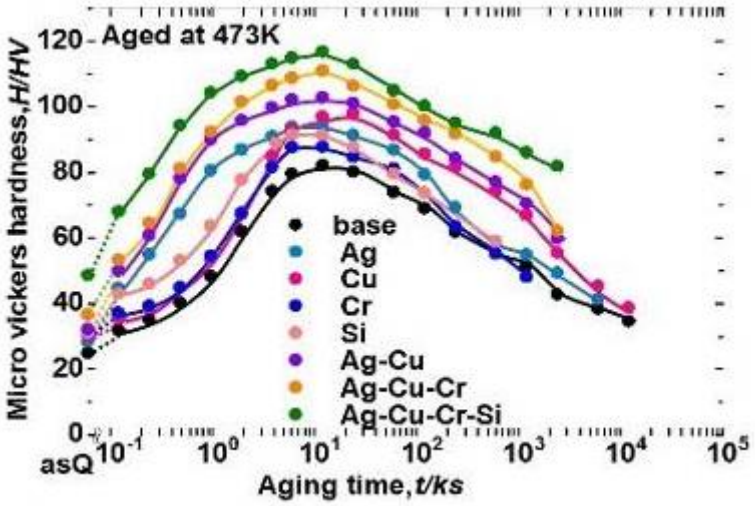

Figure 2. Age-hardening curves aged at 473k.

MS4.P018
Thermal stability of Eurofer 97 during long term thermal treatment

M. Klimenkov[1], U. Jäntsch[1], J. Hoffmann[1], M. Rieth[1]

[1]Karlsruhe Institute of Technology, Institute for Applied Materials - Applied Materials Physics, Eggenstein-Leopoldshafen, Germany

michael.klimenkov@kit.edu

High-performance reduced-activation ferritic–martensitic steels (EUROFER 97) with 9%Cr (WMnVTa) content have been envisaged for application as a structural material for operations at up to 650°C in future fusion reactors as well as in Generation IV fission reactors [1]. The steel exhibits several properties required for such applications: reduced void swelling, good resistance to radiation damage, high mechanical strength even at high temperatures, and reasonable ductility. The thermal stability of the EUROFER97 microstructure is achieved by the formation of M23C6, TaC, and VN precipitates on the grain and lath boundaries [1]. Annealing temperatures from 450°C to 650°C for up to 108.000 h hours leads to the significant changes in the original microstructure, including lath widening, coarsening of precipitates and formation of new phases. Transmission Electron Microscopy (TEM) with Electron Energy Loss Spectroscopy (EELS) has been used for identification and to study the lath structure as well as morphology and chemical composition of new precipitates.

TEM analysis of material after long term thermal treatment were focused on identification and detailed characterization of new precipitate phases, e.g. Laves and Z- phases, which were not present in original material. Formation W-rich Laves-phase precipitates with (FeCr)2W composition was observed in the specimens treated at 550°C and 500°C for the time longer than 32.000h. The Laves phase can be clearly identified in elemental maps based on its higher W concentration compare to M23C6 phase. The Laves phase is mainly situated on the grain and lath boundaries next to M23C6 precipitates. In some cases the phases tend to form complex precipitated with TaC core which possibly serve as a nucleation site for Laves phase. The fraction of this phase increases continuously with annealing time for up to 108.000h (Fig. 1). Laves phase was also detected in the specimen annealed at 500°C for 53.000h and longer.

Formation Z-phase precipitates with Cr(TaV)N composition was detected only at 600° and after annealing for more than 20.000h. Fig. 2 shows a distribution of main compositional elements in a specimen annealed at 600°C for 35000 h. The investigated area is marked by a square in the HAADF image (Fig. 2). Fig. 2b presents a coloured map of these three compositional elements. Cr concentration is high in M23C6 precipitates, which is indicated by the red colour, the Ta map in blue colour reflects the location of TaC precipitates, and V in yellow colour shows the distribution of the few VN precipitates. The Z-phase is imaged in light blue and light green colours as a combination of these elements (Fig. 2). Based on these analytical results, it was found that the Z-phase can be differentiated well from other phases, which also may contain Cr, V, and Ta or a combined composition of these elements [2].

In the material annealed at 650°C for up to 17.000h no formation of Z- or Laves phase could be detected. Investigations shown in the Fig. 3 demonstrate coarsening of M23C6, VN and especially TaC particles.

The results demonstrate that precipitation mechanism of secondary phases changes in the temperature range between 450°C and 650°C. Formation Z-phase precipitates with Cr(TaV)N composition was detected only at 600° after annealing for more than 30.000h. The annealing at lower temperatures leads to the coarsening of existed phases and formation of Laves phase.

[1] M. Klimenkov, et. al Progress in Nuclear Energy 57 (2012) 8-13
[2] H. K. Danielsen Ph.D. thesis (2007) Technical University of Denmark

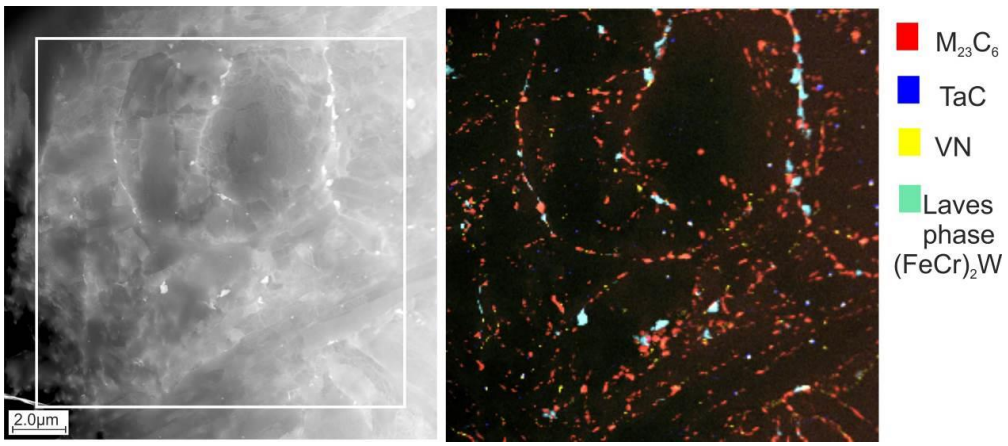

Figure 1. HAADF image and colour mix image which demonstrates distribution of Laves phase in material treated at 550°C for 108.000h.

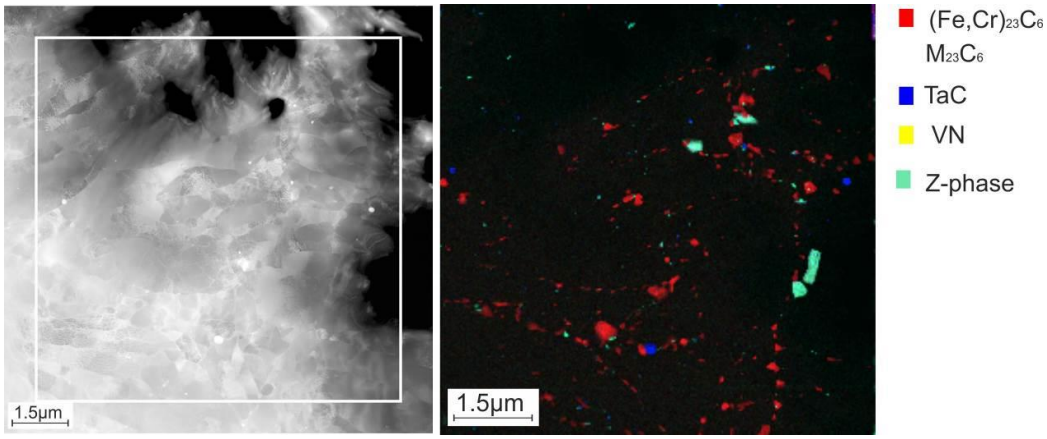

Figure 2. HAADF image and colour mix image which demonstrates distribution of Z-phase in Eurofer97 treated at 600°C for 76.000h.

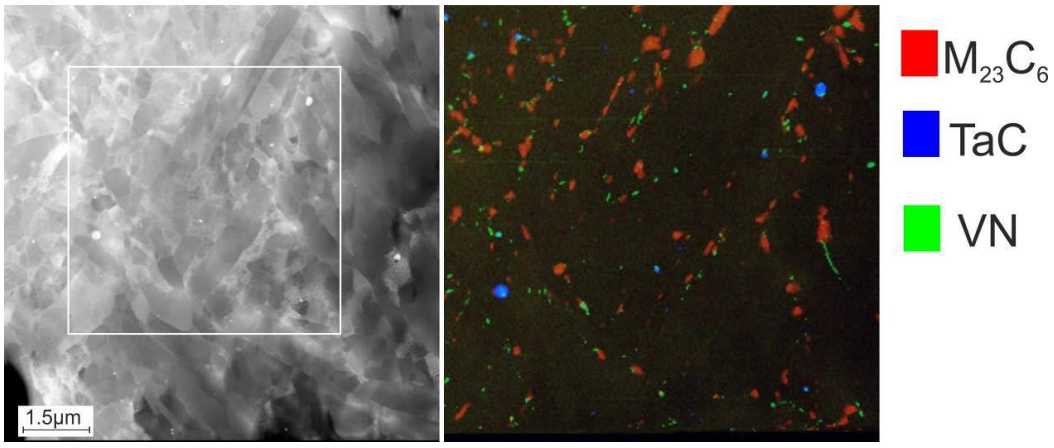

Figure 3. HAADF and colour mix EDX images which demonstrate coarcening of M23C6 and TaC precipitates in Eurofer 97 treated at 630°C for 17.000h.

MS4.P019
Microstructure observation of Ni, Zr added 60/40 brass with annealing

H. Goto[1], T. Miura[1], S. Lee[2], S. Ikeno[3], K. Matsuda[2]

[1]University of Toyama, Graduate School of Science and Engineering for Education, Toyama, Japan
[2]University of Toyama, Graduate School of Science and Engineering for Research, Toyama, Japan
[3]University of Toyama, Professor of Emeritus, Toyama, Japan

rachrub1025@outlook.com

Introduction: 60/40 Cu-Zn alloys decompose to α-phase from the β single phase during annealing, and hardness value increases with phase decomposition. Decomposition sequence of 60/40 Cu-Zn alloys has been reported as: $\beta \rightarrow \alpha_{9R} \rightarrow \alpha_{fcc}$. Several reports are available that addition of alloying elements for understanding the decomposition mechanism of 60/40 Cu-Zn alloy [1, 2]. However, the decomposition sequence of Cu-Zn-X alloy is not unclear, yet.
Objectives: The aim of this study is to clarify the phase decomposition sequence of Ni, Zr contained Cu-Zn alloys by means of hardness measurement, SEM and TEM observations.
Materials and Methods: Cu-41.7wt.%Zn alloy (base alloy), Cu-41.7%Zn-1.0%Ni alloy (Ni containing Alloy) and Cu-41.7%Zn-0.1%Zr alloy (Zr containing alloy) in wt.% were fabricated by casting. Samples were sliced to 10mm thickness, and hot-rolled to 4mm, then cold-rolled to 2mm of thickness. The alloys were kept at 1103K for 0.6ks in the single-phase region of β phase, and then quenched into chilled water. The samples were subsequently annealed at 523K. Microhardness measurement was carried out using Mitutoyo (HM-101, load: 2.94N, holding time: 15s) and microstructure observation was conducted by scanning electron microscopy (SEM, Hitachi S-3500) and transmission electron microscopy (TEM, JEOL 4010T).
Results: Fig. 1 shows the annealing hardening behaviors of alloys. Annealing for 24ks led to peak hardness in all alloys and Ni containing alloy showed the maximum hardness value. In peak annealing, number density of plate-like α-phase showed maximum density in all alloys. In TEM observation, striations of three layers in 9R structure were observed in decomposed α-phase. Maximum number of striations was obtained in the early stage of annealing, the number of striations were decreased as annealing time increasing. At the annealing for 24ks (peak- annealed), SAED patterns from α-phase both base alloy and Zr containing alloy showed fcc structure that was changed from 9R structure. When fcc structure changed from 9R structure, the number of striations decreased in all alloys. Particularly, Ni containing alloy had a high-density striation at over-annealed condition, and it showed a higher hardness than other alloys in over-annealing. It is considered that these striations are responsible for strengthening of Cu-Zn alloy.
Conclusion:

- 1.0 wt.% of Ni addition to Cu-Zn alloy influenced positively about the number density of α-phase, hardness.
- 1.0 wt.% of Ni addition to Cu-Zn alloy delayed the change of α_{9R} to α_{fcc}.
- Hardness variation is related to the number density of striation in the α-phase.

Reference:
[1] S. Ikeno, K. Matsuda, T. Kawabata, Y. Uetani: Journal of the JRICu, Vol. 41 (2002), 25-28.
[2] S. Ikeno, K. Matsuda, Y. Nakamura, T. Kawabata, Y. Uetani: Journal of the JRICu, Vol. 43 (2004), 26-30.

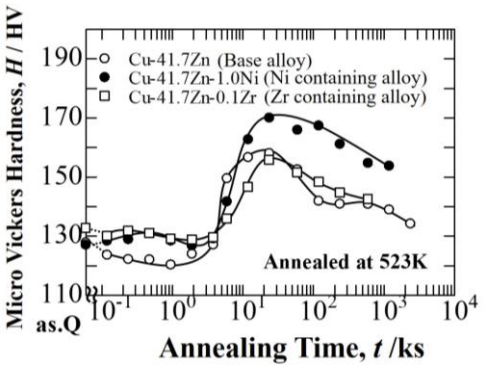

Figure 1. Hardness variation of alloys.

MS4.P020
Microstructure observation of Al-7wt.%Si-0.3wt.%Mg casting alloy aged at 473K

Y. Makita[1], Y. Kuroda[1], S. Lee[2], S. Saikawa[2], S. Ikeno[3], K. Matsuda[2]

[1]Univercity of Toyama, Graduate School of Science and Engineering for Education, Toyama, Japan
[2]Univercity of Toyama, Graduate school of Science and Engineering for Research, Toyama, Japan
[3]Univercity of Toyama, Professor of Emeritus, Toyama, Japan

maki1.2.1.239@gmail.com

Introduction: Al-Si alloys have been used as casting materials for automobile parts. Mg addition to Al-Si alloys enhance its ductility and castability due to formation of metastable phase (Mg_2Si). Moreover, it is effective for increasing both strength and corrosion resistance with Mg addition . However, precipitation sequence is not clear in T5 (casting + aging treatment) process.
Objectives: The aim of this research is to estimate mechanical properties and to classify precipitates by micro Vickers hardness measurement and transmission electron microscopy (TEM) of Al-7%Si-0.3%Si (wt.%) alloy in T5 condition.
Materials and Methods: Al-7%Si-0.3%Si alloy was fabricated by casting using Cu Y-block mold, then, alloy was cooled in the mold as is to 773K, and quenched into cold water. Specimens were taken from mold bottom were used in this research. After casting, artificial aging was carried out at 473K. Micro Vickers hardness measurement was conducted using Mitutoyo HV-101 (load: 0.98N, duration time:15s). Microstructure observation were conducted the samples of aged for 7.2ks using scanning ion microscopy (SIM, HITACHI FB-2100), SEM (HITACHI S-3500H) and TEM (TOPCON EM-002B operated at 120kV). TEM samples were prepared using electro polishing using 10vol.% perchloric acid- 90vol.% ethanol solution.
Result: Fig.1 shows the age-hardening curve of Al-7%Si-0.3%Mg alloys at 473K. Microhardness increases with increase of aging time, it reaches the peak hardness at 6.0ks, then, gradually dropped. Eutectic Si and α-Al matrix were observed by SIM. In the matrix, white particles were observed and the particles were not observed near eutectic Si. A closer inspection of TEM bright field images that aged at 473K for 7.2ks, it was possible to classify the particles with shape and size; rod-shape precipitates, coarsened rod-shape precipitates parallel to <001>Al and granular-shape precipitates. The lengths of rod-shape precipitates become longer with increase of distance from eutectic Si in matrix. The granular precipitates were confirmed as Si phase by analysis of selected area diffraction pattern (SAED)
Conclusion: Al-7Si-0.3Mg showed a good aging hardening ability. TEM observation of samples aged at 473K for 7.2ks shows rod shape precipitates, coarser rod shape precipitates and coarser precipitate. Length of rod shape precipitates in matrix varied along the distance from eutectic Si.

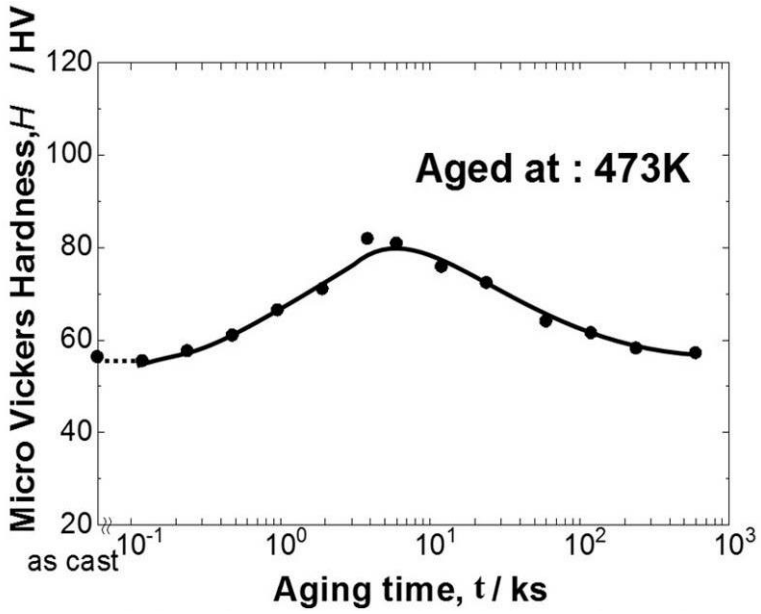

Figure 1. Age-hardening curve of Al-7Si-0.3.

MS4.P021
Aging behavior of Al-Zn-Mg(-Cu) alloys with different Cu concentration

T. Yasumoto[1], R. Arita[1], S. Lee[2], K. Matsuda[2], S. Nishikawa[3], T. Yoshida[3], S. Murakami[3], S. Ikeno[4]

[1]University of Toyama, Science and Engineering for Education, Toyama, Japan
[2]University of Toyama, Science and Engineering for Research, Toyama, Japan
[3]AISIN KEIKINZOKU Co., LTD, Imizu, Japan
[4]University of Toyama, Professor of Emeritus, Toyama, Japan

y.tksmaiktth@gmail.com

Introduction: Al-Zn-Mg alloys (7xxx series alloys) are known as the strongest aluminum alloy and, have been traditionally strengthened by dispersed fine precipitates through aging treatment. The precipitation sequence is reported like: S.S.S.S. -> G.P.zone -> η' -> η($MgZn_2$) [1]. The η' phase has been referred as the main hardening phase in Al-Zn-Mg alloys. Watanabe *et al*. reported that Cu addition in Al-Mg-Zn-Si alloy can increase the hardness at the initial stage of aging and peak aging [2].
Objectives: The aim of this research is to understand the effect of Cu addition on Al-Zn-Mg alloy of using transmission electron microscopy and to estimate the mechanical properties.
Materials and Methods: All samples have the ratio of Zn/Mg is 2.0 prepared by casting. The chemical compositions of the alloys are shown in Table 1. Solution heat treatment was conducted at 748K for 3.6ks, and then quenched in cold water. The alloys were subjected to artificial aging at 423K using oil bath. Micro-vickers hardness was measured using Mitutoyo HM-101 (load: 0.98 N, holding time 15s). Tensile test was performed using peak-aged samples with the strain rate of 1.0 X 10-3s^{-1} at room temperature using Instron type tensile machine. Fractured surfaces were observed by scanning electron microscopy (SEM, HITACHI S-3500). Transmission electron microscopy (TEM, Topcon EM-002B) observation was conducted under the accelerated voltage of 120kV.
Results: Fig.1 shows age-hardening curves of all alloys aged at 423K. The peak hardness increased with increasing of Cu concentration. Result of tensile tests, Ultimate tensile strength and yield strength increased with increasing concentration of Cu. While, elongation decreased with increasing concentration of Cu. In SEM observation, all alloy"s fracture mode show mainly transgranular fracture and a part of fractured specimen were intregranular fracture.
Close inspection of TEM bright field images from peak-aged alloys at 423K, fine precipitates were well dispersed on grain inside in all alloys. The shape of precipitates was granular and elongated. The precipitates of Cu addition alloys were finer than that of Cu free alloy. In grain boundary,grain boundary precipitates and precipitate free zone (PFZ) was observed in all alloys. The grain boundary precipitates were coarser than precipitate of grain inside. The width of the PFZ became narrow with addition of Cu.
Conclusion:

- Hardness, tensile strength and yield strength increased at peak-aged condition with increase of Cu contents.
- The fracture surfaces of all alloys showed a typical intergranular fracture.
- When the Cu addition to alloys, the precipitates were finer and the width of the PFZ became narrow than that of Cu free alloy

Reference:
[1] L. F. Mondolfo, N. A. Gjostein, D. W. Levinson: Transactions of American Institute of Mining and Metallurgical Engineers, 206 (1956) 1378-1385.
[2] K. Watanabe, K. Matsuda, T. Yoshida, S. Ikeno: Journal of the Japan institute of Light Metals, 64 (2014) 413-417.

alloy	Zn	Mg	Cu	Al	Zn+Mg	Zn/Mg
ZM42	3.4	1.9	-	Bal.	5.3	1.8
ZM42C	3.3	1.8	0.2	Bal.	5.1	1.8
ZM42HC	3.7	1.8	1.0	Bal.	5.5	2.0

Table 1. Chemical composition of alloys (at. %).

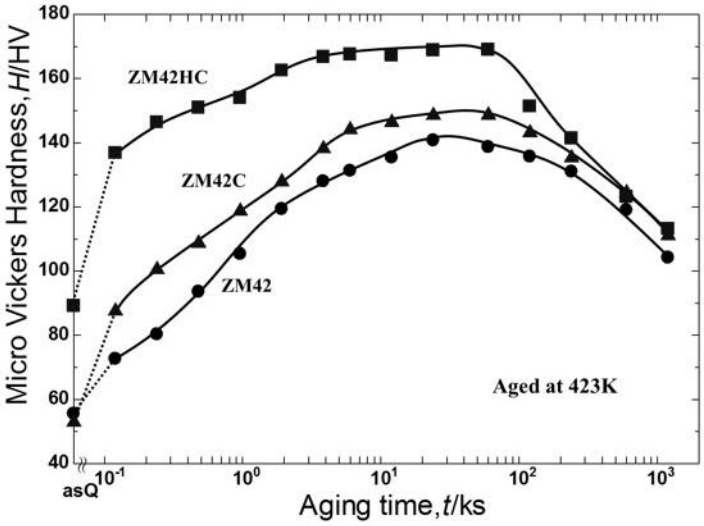

Figure 1. Age-hardening curves of alloys aged at 423K.

MS4.P022
TEM observation of two-step aged Al-Mg-Si (-TM) alloys

Y. Kuroda[1], L. Seungwon[1], S. Ikeno[1], K. Matsuda[1]

[1]University of Toyama, Toyama, Japan

oyhetbzkq@yahoo.co.jp

Introduction: Al-Mg-Si alloys (6xxx series) are one of age-hardenable aluminum alloys and they are widely used as structural materials and vehicle parts due to a good combination of strength-to-density. However, it is generally known that the mechanical properties of 6xxx series are not good when it compares to 2xxx and 7xxx series alloys because the amount of solute atom is much less than 2xxx and 7xxx series alloys. It is worth to investigate the effect of alloy element, especially, transition metals because an addition of small amount of alloying element can increase the mechanical properties, also, there are several reports about Cu, Fe addition on 6xxx series alloy [1, 2]. Furthermore, some reports are available about two-step aging for increasing aging-hardenability and its mechanical properties [3].

Objectives: Aim of this work is to understand the effect of alloying elements, V, Co and Ni on Al-Mg-Si alloys and to investigate the precipitate sequence of Al-Mg-Si alloys using TEM.

Materials and Methods: Four kinds of alloys were fabricated by casting, 1) Al-0.7%Mg-0.35%Si (Base alloy) , 2) A-l-0.7%Mg-0.35%Si-0.1% V (V-added alloy, 3) Al-0.7%Mg-0.35%Si-0.1Co (Co-added alloy) and 4) Al-0.7%Mg-0.35%Si-0.1Ni (Ni-added alloy, at.%) Alloys were subjected to homogenization treatment after casting at 848K for 36ks, then quenched into cold water. Solution treatment was conducted at 848K for 3.6ks. After solution treatment, samples were undergone the aging treatment at 473K as single-step aging process. Also, samples were pre-aged at the temperature of 298K or 343K for 6ks, 60ks, or 600ks, then aged at 473K as two-step aging treatment. Micro Vickers hardness measurement was conducted on mirror-like polished surface using a load of 0.98N for 15s of duration time. Samples were ground to a thickness of 0.07mm and punched out with 3mm diameter, then thinned using a twin-jet electro-polishing facility using a 33 vol. % HNO_3 and 67 vol. % CH_3OH solution at 258K. Microstructure observation was conducted by using a TOPCON 002B (TEM) operating at 120 kV to avoid to damage to samples by electron beam.

Result: In single-step aging, all TM-added alloys showed higher peak hardness than that of Base alloy. Especially, Ni-added alloy showed the highest peak hardness level among four alloys. Ni- and Co-added alloys increased hardness in the early stage of aging. In TEM observation at peak aged condition, rod- or needle-shaped precipitates and their cross sections were observed in all alloys. TM-added alloys have higher number density of cross sectional precipitates per $\mu m^2$and shorter average length of precipitates than Base alloy.

In two-step aging, all alloys showed higher each value of peak hardness than that of single-step aging (positive effect) when they were pre-aged at 343K. Remarkably, V-added alloy drastically increased peak hardness. On the other hand, Base, V-, and Co-added alloys showed negative effect when we conducted pre-aging at 298K and final-aging at 473K. But, Ni-added alloy kept the peak hardness level compared to single-step aging.

Conclusion:

(1) TM-added alloys increase mechanical property and have finer distribution of precipitates than Base alloy.
(2) Ni- and Co-added alloys show quick response on precipitation in single-step aging.
(3) In two-step aging, Base, V-, and Co-added alloys alter each peak hardness level by different pre-aging temperature compared to single-step aging. But, Ni-added alloy clearly reduce negative effect when pre-aging temperature is 298K.

References:

[1] T. Saito, C.D. Marioara, S.J. Andersen, W. Lefebvre, R. Holmestad, Philosophical Magazine 94 (2015) 520-531.
[2] S. Wang, K. Matsuda, T. Kawabata, T. Yamazaki, S. Ikeno, Journal of Alloys and Compounds 509 (2011) 9876-9883.
[3] Y. Aruga, M. Kozuka, Y. Takaki, and T. Sato, Metallurgical and Materials Transactions A 45 (2014) 5906-5913.

MS4.P023
The effects of double annealing on medium manganese steel

T. Truglas[1], C. Commenda[2], M. Arndt[2], D. Krizan[2], H. Groiß[1,3]

[1]CEST Competence Centre for Electrochemical Surface Technology, Wiener Neustadt, Austria
[2]voestalpine Stahl GmbH, Linz, Austria
[3]Johannes Kepler University, Center of Surface and Nanoanalytics, Linz, Austria

tia.truglas@jku.at

The mechanical properties of batch or continuously annealed medium manganese steel grades with an ultrafine-grained α + γ microstructure make them a promising candidate for the third generation of advanced high strength steels. In the present study the effects of advanced continuous annealing processes were investigated for a 0.1C6Mn2.2Al medium manganese steel with various electron microscopy techniques, whereby a full microstructure analysis with EBSD and TEM was done after single and double annealing. Compared to the former heat treatment the latter one contained an additional annealing step using full austenitization and subsequent quenching prior to the final intercritical annealing. EBSD phase maps revealed a fully α + γ microstructure with fine grain diameters of around 400 nm for both steel types, whereas the simple annealed steel still contained larger ferrite grains and a higher amount of low-angle grain boundaries (<15°). The double annealed steel contained tendentially more retained austenite, which was also confirmed by XRD measurements.
Because of the ultrafine grain structure the limits of the EBSD methods were reached. Thus grain sizes were also measured using the line intercept method on STEM bright field micrographs and the phases of individual grains were determined by selected area diffraction. Generally, the TEM showed a higher dislocation density in the simple annealed steel and a more recrystallized structure in the double annealed one. Extended EDX investigation showed a similar partitioning of manganese to the different phases for both annealing types, whereas the partitioning of aluminium to ferrite was more pronounced in the double annealed steel. The presence of manganese carbides in the simple annealed steel in contrast to the precipitate-free microstructure of the double annealed one, constituted another significant difference between the results of the two annealing processes. Their crystal structure and chemical composition were determined by high resolution TEM, selective area diffraction and EDX (see figs. 1 and 2).

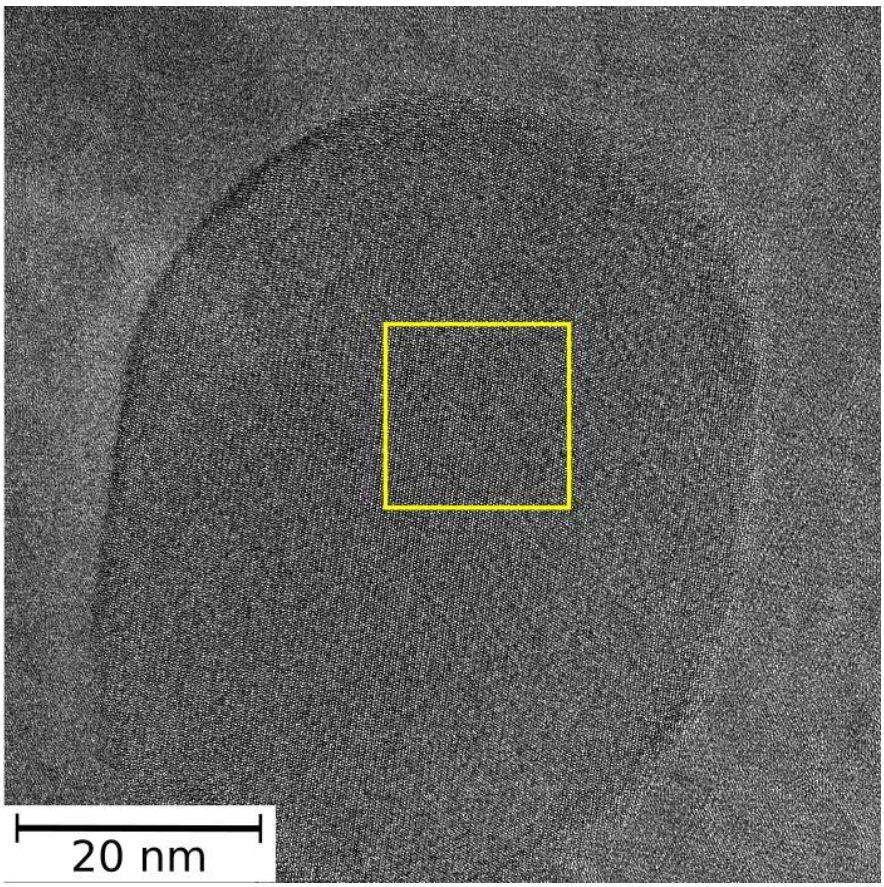

Figure 1. High resolution TEM micrograph of a manganese carbide.

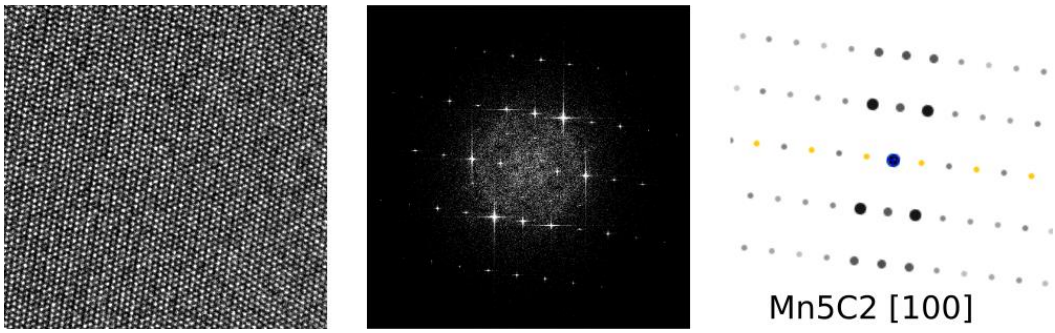

Figure 2. The Fourier transformation of the image section highlighted in fig. 1 together with the simulated diffraction pattern of Mn_5C_2 orientated in the [100]-direction allow the determination of the carbide type.

MS4.P024
Microstructure observation of Y or Nd contained Mg alloys

S. Lee[1], T. Hamaguchi[1], Y. Tomuro[1], S. Saikawa[1], S. Ikeno[1], K. Matsuda[1]

[1]University of Toyama, Toyama, Japan

swlee@eng.u-toyama.ac.jp

Introduction: Mg alloys have been used as structural materials and vehicle parts for weight reduction because Mg is lighter than conventional structural materials, i.e. Fe, Al. With addition of rare earth element on Mg, it is possible to improve its strength or high temperature resistance due to the formation of precipitates [1,2]. Several reports are available about Mg-Gd alloys, and precipitation sequence is suggested like: S.S.S.S. (super saturated solid solution) → β phase (D019) → β phase (cbco) → β1phase (fcc)→β phase (fcc) [3]. However, the precipitation sequence or mechanical property dose not clearly reveal the effect of another rare-earth elements on Mg alloys.
Objectives: The aim of this research is to estimate mechanical property and to understand the precipitation sequence of Y or Nd added Mg alloys by means of hardness measurement and TEM observation, respectively.
Materials and Methods: Three kinds of alloys (Mg-1.7%Y alloy, Mg-0.5Nd alloy, Mg-1.4Y-0.5Nd alloy, in at. %) were fabricated by casting using Y-shape mold. Alloys were subjected to homogenization treatment after casting, then, they were undergone hot-rolling to destroy dendritic structure. Solution treatment at 823K for 1h at Ar atmosphere and quenched into room temperature water. Artificial aging was carried out at 473K. Micro Vickers hardness measurement was conducted using Mitutoyo HV-101 (load: 0.98N, duration time:15s). Microstructure observation were conducted using TEM (TOPCON EM-002B operated at 120kV). TEM samples were prepared using twin-jet electro polishing using 10vol.% perchloric acid- 90vol.% ethanol solution.
Result: In hardness measurement, hardness increased with increasing of aging time, Mg-1.4Y-0.5Nd alloy showed the maximum hardness level among alloys. In TEM microstructure observation aged for 921.6ks, needle like precipitates were observed with diffused diffraction pattern in Mg-1.7%Y alloy. In Mg-0.5Nd alloy, rod shape precipitates were observed with streak diffraction pattern. In the case of Mg-1.4Y-0.5Nd alloy, mixed microstructure of both Mg-1.7%Y alloy and Mg-0.5Nd alloy was observed. In HRTEM images, it was possible to observe the mono layered structure in Mg-1.7%Y alloy, the chain structure and some β phase in Mg-0.5Nd alloy, mono layered structure, pre- βphase, chain structure in Mg-1.4Y-0.5Nd alloy.
Conclusion: The precipitate sequence was different with addition of rare-earth elements on Mg alloy. Mg-1.4Y-0.5Nd alloy showed better maximum hardness with formation of 3 types precipitates.

References:
[1] Y. Negishi, S. Iwasawa, S. Kamado, Y. Kojima, and R. Ninomiya, Journal of the Japan Institute of Light Metals, 44 (1994) 555-561.
[2] W. Yuan, R. S. Mishra, R. DcLorme, B. Davis, R. A. Howell, K. Cho, Materials Science and Engineering A, 530 (2011) 28-35.
[3] X. Gao, S. M. He, X. Q. Zeng, L. M. Peng, W. J. Ding, J. F. Nie, Materials Science and Engineering A, 431 (2006) 322-327.

MS4.P025
Microstructure observation of Cu added Al-Mg-Ge alloy with aging

T. Sato[1,2], L. Seungwon[3], K. Matsuda[3], S. Wenner[4], C. D. Marioara[5], R. Holmestad[4], S. Ikeno[6]

[1]University of Toyama, Graduate School of Science and Engineering for Education, Toyama-shi, Japan
[2]University of Toyama, Graduate School of Science and Engineering for Education, Toyama, Japan
[3]University of Toyama, Graduate School of Science and Engineering for Research, Toyama, Japan
[4]NTNU, Department of Physics, Trondheim, Norway
[5]SINTEF, Department of Materials and Nanotechnology, Trondheim, Norway
[6]University of Toyama, Professsor of Emeritus, Toyama-shi, Japan

m1671509@ems.u-toyama.ac.jp

Introduction: Al-Mg-Ge alloy is one of an age-hardenable aluminum alloy after solution heat treatment. In the periodic table, Ge and Si is belong to 14 group, however Ge and Si is belong to period 4 and 3, respectively. It was difficult to investigate the crystalstructure of precipitates in Al-Mg-Si alloy by using X-ray diffraction because of the similarlity of atomic number Al, Mg and Si. Ge can exchange to Si in Al-Mg-Si alloy, so Al-Mg-Ge alloys was used to understand the microstructure of precipitates Al-Mg-Si alloy[1)]. Al-Mg-Ge alloys are treated as Al-Mg_2Ge quasi-binary alloy like Al-Mg_2Si alloy. Needle or rod-like shape precipitates were observed in microstructure both Al-Mg-Ge and Al-Mg-Si alloys [2)]. Al-Mg-Ge alloys showed a good age-hardenability despite the amount of solute is lower than Al-Mg-Si alloys. It is known that Al-Mg-Si alloys can be improved the mechanical properties by addition of Cu in Al-Mg-Si alloys because of formation of pre-Q' and Q' phase [3-5)]. However, no paper is available about precipitate and precipitation sequence of Cu added Al-Mg-Ge alloys.
Objectives: The aim of this research is to understand the effect of Cu addition on Al-Mg-Ge alloy by means of microstructure observation using TEM.
Materials and Methods: In this study, two types of Al-Mg-Ge alloys were investigated; Al-0.43%Mg-0.20%Ge (at. %, Base alloy) and Al-0.44%Mg-0.19%Ge-0.18%Cu (at. %, Cu-added alloy). Samples were subjected to homogenization treatment at 623K for 21.6 ks after casting. After the homogenization process, alloys were extruded to the thickness of 1.5mm plate at 723K. Solution treatment was conducted at 873K for 3.6 ks and quenched into ice water. Artificial aging treatment was conducted at the temperatures of 423K and 523K. Vickers hardness measurement was conducted after different ageing treatment using Mitutoyo HM-101 (load: 0.98N, duration time: 15s). TEM samples were prepared by electropolishing using perchloric acid (10 vol. %) and ethanol (90 vol.%) solution at 273K. Microstructure of Al-Mg-Ge(-Cu) alloys was observed by using TOPCON EM-002B (TEM, 120kV) and JEOL ARM-200F (STEM, 200kV).
Results: In the results of Vickers hardness measurement, Cu-added alloy showed the higher peak hardness than Base alloy. In the results of TEM observation in peak aged alloys, needle or rod-like shape precipitates that along with $_{Al}$ was observed. In Cu-added alloy, the cross section of some needle or rod-like shape precipitates was elongated. It is known that the contrast of HAADF-STEM images is proportional to the squared number of atomic number Z. In the results of HAADF-STEM observation of Cu-added alloy, the contrast of Cu atoms was observed at the precipitate-matrix boundary or inside of precipitates.

References:
[1] Lutts: Acta Metallurgica, Vol. 9, No. 6 (1961) p. 577-586.
[2] Matsuda, T. Munekata, T. Kawabata, Y. Uetani and S. Ikeno: Journal of Japan Institute of Light Metals, Vol. 56, No. 11 (2004) p. 680-684.
[3] Matsuda, D. Teguri, Y. Uetani, T. Sato and S. Ikeno: Scripta Materialia, Vol. 47, (2002), p. 833-837.
[4] Matsuda, D. Teguri, T. Sato, Y. Uetani and S. Ikeno: Materials Transactions, Vol. 48, No. 5 (2007) p. 967-974.
[5] Nakamura, K. Matsuda, A. Furihata, K. Niwa, T. Kawabata and S. Ikeno: Journal of Japan Institute of Light Metals, Vol. 60, No. 4 (2010) p. 164-169.

MS4.P026
Effect of Cu addition on electron diffraction at the early stage of aging in Al-Mg-X (X=Si, Ge, Zn) alloys

K. Matsuda[1], S. Lee[1], C. D. Marioara[2], S. Wenner[3], K. Nishimura[1], T. Matsuzaki[4], N. Nunomura[1]
T. Sato[5], R. Holmestad[3], S. Ikeno[1]

[1]University of Toyama, Toyama, Japan
[2]SINTEF, Trondheim, Norway
[3]NTNU, Trondheim, Norway
[4]RIKEN, Wako, Japan
[5]Tokyo Institute of Technology, Tokyo, Japan

matsuda@eng.u-toyama.ac.jp

Introduction: Traditionally, 2xxx, 6xxx and 7xxx series have been strengthened by dispersion of fine precipitate through aging heat treatment. There are numerous reports are available about precipitation hardening and sequence with addition of alloy element. However, in the case of early stage of aging, there are argument about formation of cluster, GP zones including GP(I), GP(II), GPB and GPBII when alloying elements are added, i.e. Si, Ge, Zn, Cu. However, it is not easy to observe directly these early stage precipitates due to their small size and random structures.
Objectives: The aim of this research is to understand the extra diffraction spots that appear in SAED patterns and the common zones/precipitates that have been discovered during the early stage of aging using age-hardenable Al alloys containing Mg and Cu with added Si, Zn, or Ge.
Materials and Methods: Nine kinds of age-hardenable alloys, denoted AlCuMg, AlZnMg, AlZnMg42, AlZnMgCu, AlZnMgCu42, AlMgSi, AlMgSiCu, AlMgGe, AlMgGeCu were fabricated to estimate the effect of Cu addition and ratio of Zn-to-Mg by casting in air, as shown in Table 1 [1]. The ingots were hot-extruded and cold-rolled into 1-mm-thick sheets. These sheets were solution heat-treated at 848 K for 3.6 ks for the AlMgSi and AlMgSiCu alloys, at 873 K for 3.6 ks for the AlMgGe and AlMgGeCu alloys, at 748 K for 3.6 ks for the AlZnMg and AlZnMgCu alloys, and at 773 K for 3.6 ks for the AlCuMg alloy to obtain single-phase solid solutions. After quenching in 273 K chilled water, the sheets were aged under several different conditions in a silicone oil bath. The micro Vickers hardness was measured using a Mitutoyo HV-101 hardness tester (load: 0.98 N, holding time: 15 s). The aged sheets were electrolytically polished using a mixture of perchloric acid and ethanol (1:9), or nitric acid and methanol (1:3), to prepare thin samples for TEM observation. Accelerating voltages of 120 kV and 200 kV were used to observe these samples by TEM (TOPCON 002B) and high-angle annular dark-field (HAADF-STEM) imaging (Hitachi HD7200), respectively.
Result: Figure 1 [1] shows SAED patterns obtained peak-aged samples. With close inspection of SAED patterns, extra diffracted spots were observed in all Cu added alloys marked with arrows in Fig. 1. Also, in the early stage of aging, extra diffracted spots were observed on Cu added alloys, too. It is suggested that the same precipitates (including clusters) exist in the Cu-containing alloys from initial stage of aging regardless chemical composition of alloys. Cu-free AlMgSi and AlZnMg alloys in Fig. 1 (e), (f) do not exhibit extra spots in their measured SAED patterns. I can be concluded that MgSiMg clusters cannot include Cu inside their structures, and probably depends on the chemical compositions of the alloys.
Conclusion

1. Alloys containing Cu exhibited extra diffraction spots in their SAED patterns for precipitates and the Al matrix, while alloys without Cu did not.
2. The initial cluster, which is based on the β-phase in Al-Mg-Si alloys, has been proposed as MgSi(/Ge)Mg, CuMgSi(/Ge), AlCuMg, and AlZnMg.
3. Based on simulated diffraction patterns, it has been suggested that second clusters, which consist of three initial clusters including short-range order with an APB, exist in the Cu-containing alloys. The initial MgSi(/Ge)Mg cluster cannot grow into a second cluster, and the AlZnMg cluster can contain Zn or replace it with Cu.

Reference:
[1] K. Matsuda et. al, Mater. Trans., 58(2017) pp.167-175.

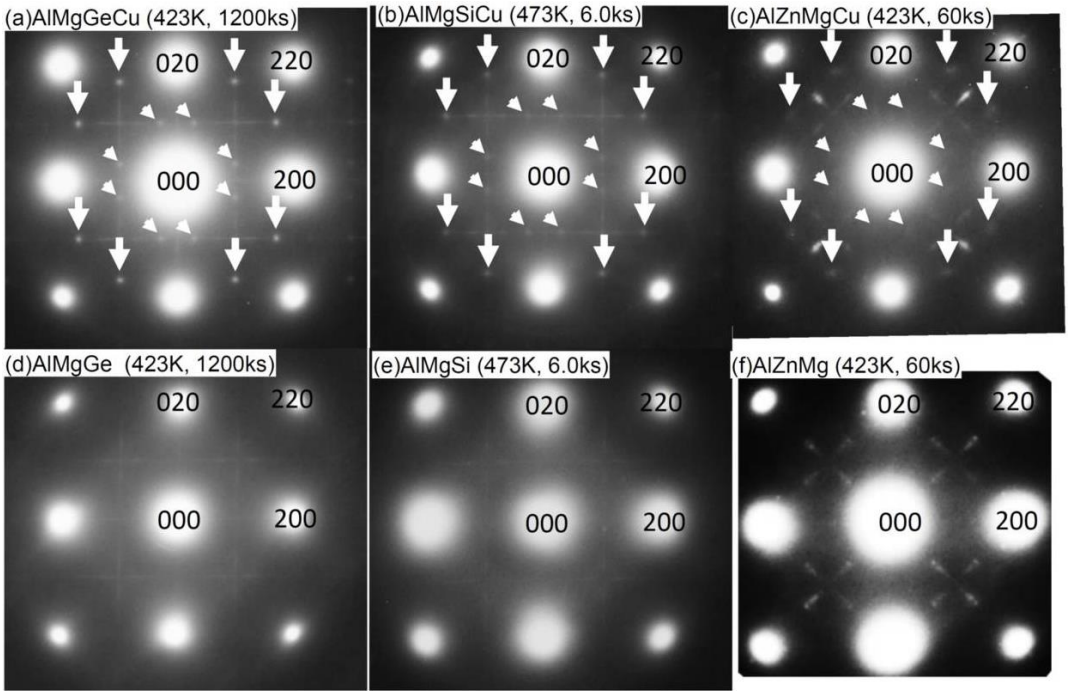

Figure 1. SAED patterns obtained for Cu added and Cu free alloys. (a) AlMgGeCu (423K,1200ks), (b) AlMgSiCu (473K, 6.0ks), (c) AlMgZnCu (423K, 60ks), (d) AlMgGe (423K,1200ks), (e) AlMgSi (473K, 6.0ks) and (f) AlMgZn (423K, 60ks) alloys.

alloys	Mg	Si	Cu	Zn	Ge	Ti	Al
AlCuMg	1.2	-	0.98	-	-	-	bal.
AlZnMgCu	3.20	-	0.20	2.70	-	0.01	bal.
AlZnMg	2.80	-	-	2.60	-	0.01	bal.
AlZnMgCu42	1.80	-	0.24	3.30	-	-	bal.
AlZnMg42	1.90	-	-	3.40	-	-	bal.
AlMgSiCu	1.12	0.37	0.2	-	-	-	bal.
AlMgSi	1.10	0.37	-	-	-	-	bal.
AlMgGeCu	0.44	-	0.18	-	0.19	-	bal.
AlMgGe	0.43	-	-	-	0.22	-	bal.

Table 1. Chemical compositions of alloys (at.%).

MS4.P027
Characterization of 3003-type aluminium alloy processed by constrained groove pressing

J. Bajer[1], M. Cieslar[1], M. Šlapáková[1], M. Zimina[2]

[1]Charles University, Faculty of Mathematics and Physics, Prague, Czech Republic
[2]Research Center Rez, Husinec-Rez, Czech Republic

janbajer69@seznam.cz

Introduction: Sheets produced by Twin-roll casting (TRC) exhibit fine-grained structure with high solid solution supersaturation. Properties can be improved by severe plastic deformation (SPD). Constrained groove pressing (CGP) is one of few SPD methods which preserve original thickness of the material and also seems to be the most promising of those methods.
Objectives: Objectives of this experiment are to investigate effects of CGP method on mechanical properties and structure of Twin-Roll cast EN AW3003 aluminium alloy strip and to compare results obtained from light optical microscopy (LOM), transmission electron microscopy (TEM), EBSD mapping and from microhardness measurement.
Material and Methods: Standard EN AW3003 aluminium alloy with small addition of Zr (0.17 wt. %) and Cr (0,07 wt. %) was used in the experiment. TRC alloy was processed by CGP method. Two cycles were performed (see Fig.1). Microhardness measurement was done in order to examine distribution of microhardness and its inhomogeneity. The same sample was observed with the light optical microscope so that grain structure could be compared with microhardness map. Samples for TEM were prepared from the hardest and from the softest areas of the cross-section of the sample according microhardness map. EBSD mapping was performed on the same places of cross-section in order to compare grain structure of the harder and softer areas.
Results: The twin-roll casting produced grain structure with grains elongated in the rolling direction and inhomogeneous mechanical properties along normal direction [1]. Constrained groove pressing suppresses this inhomogeneity and creates wavy grain structure (see Fig. 2) [2].It forms new inhomogeneous distribution of mechanical properties. Microhardness measurement reveals alternating areas with higher and lower microhardness (see Fig. 2). This alternating corresponds to the periodicity of grooves of the deformation dies. It is qualitatively in accordance with finite element method simulation of stored deformation energy [2].
The high dislocation density and grain fragmentation was observed in TEM (See Fig. 3). According to TEM observation and EBSD measurement harder area exhibits more pronounced grain fragmentation [3]. It suppresses dislocation movement which manifests as higher microhardness despite lower dislocation density in comparison with softer areas.
Conclusion: CGP method eliminates original grain structure of parallel elongated grains and inhomogeneity of mechanical properties in the normal direction. It produces material with the high dislocation density and pronounced grain fragmentation. Due to inhomogeneous distribution of stored deformation energy it forms alternating harder and softer areas with periodicity corresponding to the groove periodicity of deformation dies. Harder areas exhibit stronger fragmentation and lower dislocation density in comparison with softer areas.

Acknowledgements
The financial supports of project GAUK 134715 is gratefully acknowledged.

References:
[1] Ben Q. Li. Producing thin strips by twin-roll casting - part I: Process aspects and quality issues. JOM, 1995, Volume 47, Number 5, Page 29
[2] Lee, J. W., Park, J. J. Numerical and experimental investigations of constrained groove pressing and rolling for grain refinement. Journal of Materials Processing Technology. 2002, Volumes 130–131, Pages 208–213.
[3] Zrnik, J., Kovarik, T., Novy, Z., Cieslar, M. Ultrafine-grained structure development and deformation behavior of aluminium processed by constrained groove pressing. Materials Science and Engineering: A. 15 March 2009, Volume 503, Issues 1–2, Pages 126–129.

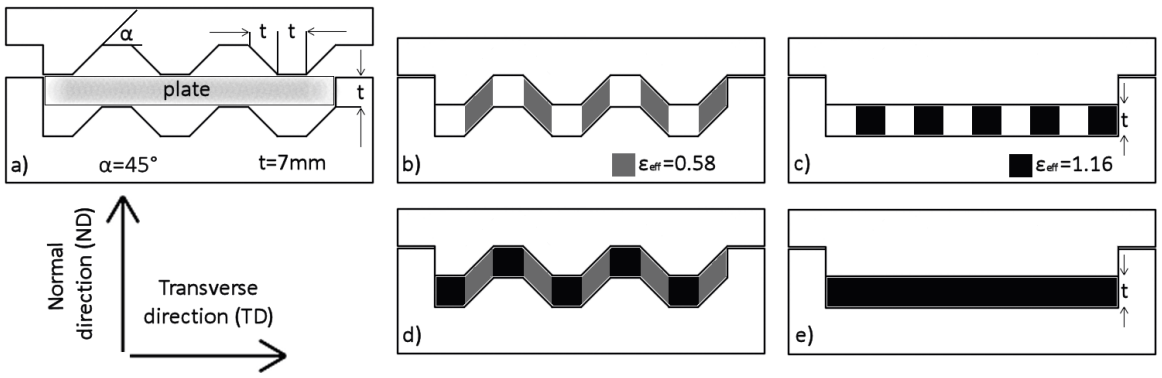

Figure 1. Schematic of one CGP cycle.

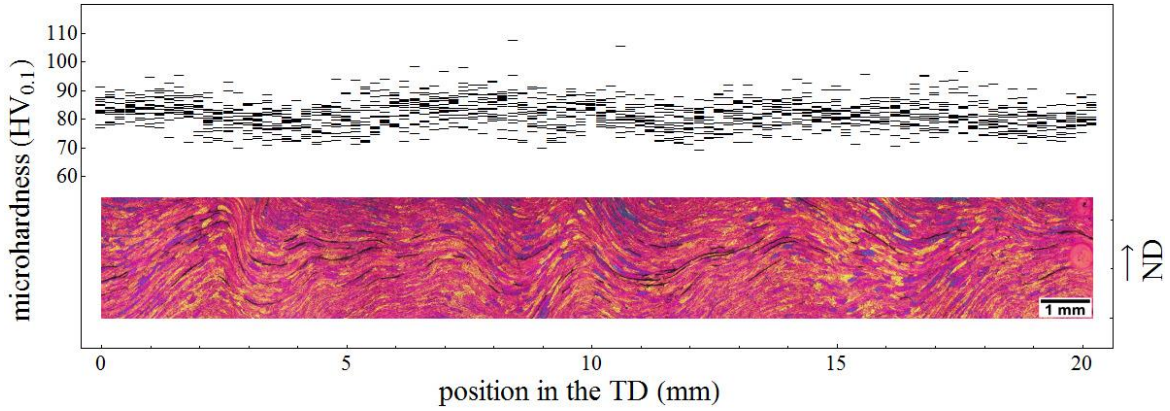

Figure 2. Microhardness distribution along TD compared with LOM image of the same sample.

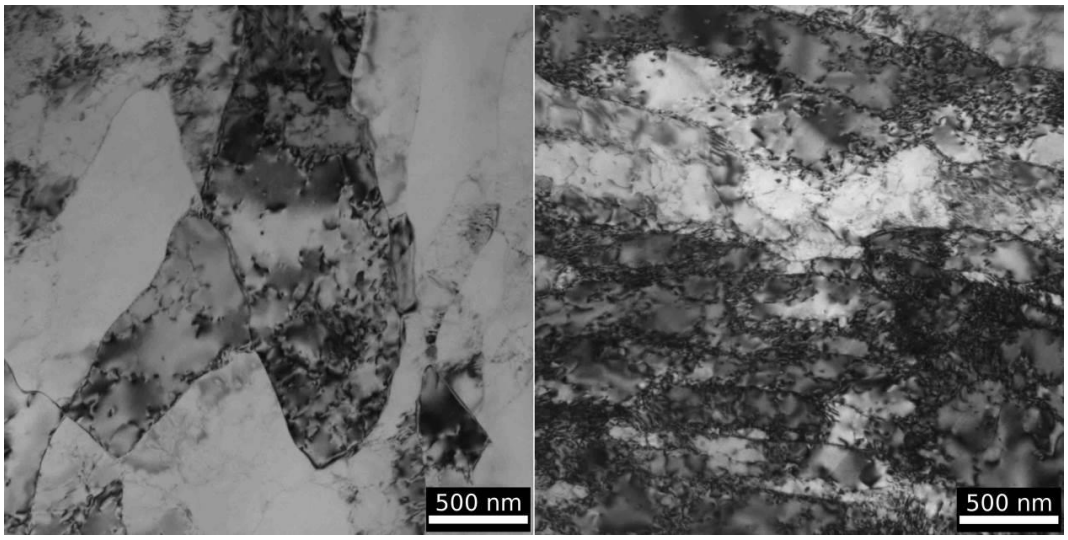

Figure 3. Comparison of subgrain structure of the harder area (left) and the softer area (right) of the cross-section.

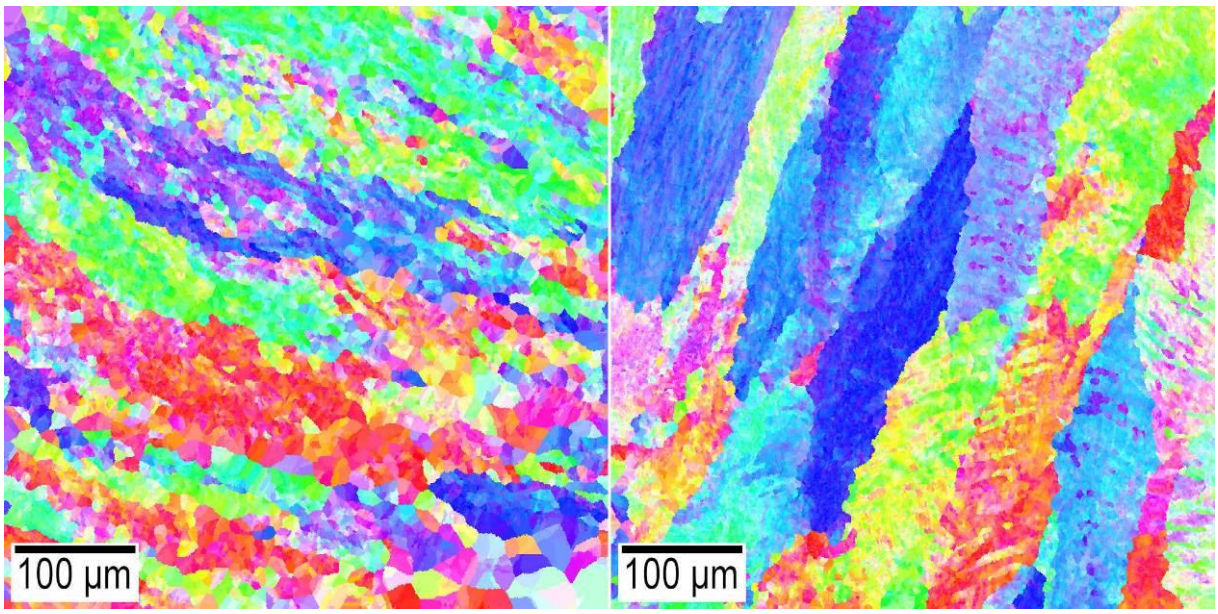

Figure 4. EBSD orientation maps comparing grain structure of the harder area (left) and the softer area (right) of the cross-section.

MS4.P028
Cyclic stress behavior and dislocation substructure at different temperatures in Modified 9Cr-1Mo steel

P. Verma[1], N. C. S. Srinvas[2], V. Singh[2]

[1]National Institute of Technology Jamshedpur, Materials Science and Technology, Jamshedpur, India
[2]Indian Institute of Technology (Banaras Hindu University), Department of Metallurgical Engineering, Varanasi, India

preeti.rs.met12@itbhu.ac.in

Introduction: Modified 9Cr-1Mo steel, with minor additions of V and Nb in conventional 9Cr-1Mo steel, is widely used for steam generators of nuclear reactors. It possesses higher thermal conductivity, lower thermal expansion coefficient, higher tensile and creep strength, better weldability, microstructural stability and higher resistance to stress corrosion cracking in water-steam systems in comparison to those of low Cr-Mo steel, conventional 9Cr-1Mo steel and austenitic stainless steels. During service, the components of steam generators are often subjected to repeated thermal stresses as a result of temperature gradients occurring from heating and cooling during start-up and shutdown operations. These transient thermal stresses induce cyclic strains and cause low cycle fatigue (LCF) damage in the material. Low cycle fatigue at elevated temperatures is known to be influenced by time dependent processes like dynamic strain ageing (DSA), creep, oxidation and microstructural degradation. DSA has been found deleterious for tensile ductility, LCF life and creep resistance of structural components. Little attention has been paid on microstructure resulting from LCF damage in this material, in particularly related to effects of DSA and higher temperature.
Objective: The objective of the present paper is to understanding the deformation substructural changes with the temperature in modified 9Cr-1Mo steel in the normalized and tempered condition at room temperature, 300 ℃ (where the material exhibit DSA) and 600 ℃ (the material intended application temperature).
Experimental Methods**:** Low cycle fatigue tests, in normalised and tempered condition, were conducted under total strain controlled mode at three different temperatures room temperature, 300 °C & 600 °C, at different strain amplitudes of ±0.25%, ±0.31%, ±0.375%, ±0.42% and ±0.50% at two different strain rates 10^{-2} s^{-1} and 10^{-3} s^{-1}. Dislocation substructure was analyzed after fatigue testing using TEM.
Results: Irrespective of strain amplitude, strain rate, and temperature cyclic stress response showed initial mild hardening followed by cyclic softening till failure. Dislocation cell structure rotation of the grains was observed at all the temperature, strain rate and strain amplitude. Transition from non-Masing to Masing behavior was observed at ±0.375% strain amplitudes at room temperature and 300°C is mainly due to change in equiaxed cell structure to elongated cell structure. Inverse effect of strain rate was observed on cyclic stress response, fatigue life, fatigue crack propagation at 300°C due to dynamic strain ageing. Dynamic recovery and recrystallization as well as coarsening of precipitates and oxidation of the steel was observed at 600°C.
Conclusions: The cyclic softening in the modified 9Cr-1Mo steel is strongly dependent on the strain amplitude and temperature. The observed cyclic softening at room temperature was attributed to the transformation of lath martensitic structure into cell structure. In addition to the cell structure, recovery of dislocation cell structure was observed at 300 °C. At 600 °C, several phenomena are contributing for the occurrence of cyclic softening such as dislocation cell structure, annihilations of array of dislocations, grain rotation, coarsening of carbides and dynamic recovery/recrystallization.

MS4.LBP01
Investigating the kinetics of atomic diffusion processes by ultra-fast heating and quenching of single crystal Ni-base superalloy specimens

M. Fuhr[1], Y. Eggeler[1], E. Spiecker[1]

[1]University of Erlangen-Nürnberg, Institute for Micro- and Nanostructure Research, Erlangen, Germany

yolita.eggeler@fau.de

Single crystal Ni-base superalloys exhibit outstanding high temperature properties and are used as turbine blade material of modern turbojet engines, withstanding mechanical loads at high temperatures in harsh environments. Superalloys are designed to be multicomponent systems comprised of a variety of alloying elements. Their high temperature properties emerge from the alloy´s complex two-phase γ/γ' microstructure consisting of cuboidal γ' precipitates (ordered L12 crystal structure) coherently embedded in a solid solution strengthened face centered cubic γ matrix [1]. The γ' cubes exhibit average edge lengths of 400 nm and typical volume fractions of approx. 80 %. To enable strengthening by precipitation hardening at temperatures relevant to turbojet engine turbine applications (700 – 1100 °C), the stability of the γ/γ' phases and therefore the inter-phase diffusion is of fundamental importance [1].
This work makes a new approach to resolve the kinetic diffusion processes across the γ/γ' interface in Ni-base superalloys using state of the art MEMS based heating chips [2]. In order to promote diffusion processes in complex materials systems, heating and quenching steps are applied to both superalloy thin films (see figure 1a) and µ-bulks (see figure 1b). The ultra-fast heating and quenching (heating/quenching rates up to 1500 K/s [2]) of a specimen from room temperature to an elevated temperature and vice versa enable the initiation of transient diffusion phenomena and their quantitative analysis. These diffusion processes are driven by the temperature dependent change in the equilibrium concentration of alloying elements and the simultaneous alteration of the γ and γ' phase volume fraction. To avoid an undesired influence of surface oxidation on the measurements of the element distribution during heating, the specimen geometry was optimised from thin foils to µ-bulks, compare figure 1(a) and (b). These cuboidal shaped samples exhibit edge lengths of 10 to 50 µm and enable the study of the diffusion kinetics at γ/γ'-interfaces sufficiently apart from oxidized surface regions.
Kinetic processes were studied using the single crystal Ni-base superalloy ERBO1 [3]. A homogenisation heat treatment of the as-aged material was performed for 100 hours at 850 °C with a subsequent water quenching to ensure a freezing of the thermodynamic high temperature state. The thin foil as well as the µ-bulk were extracted from electrolytically polished TEM samples were transferred to a DENSsolutions Wildfire D3 in-situ TEM chip using a FEI Helios NanoLab DualBeam 660 FIB-SEM. The heating experiments were then performed in a double corrected FEI Titan Themis3 300 equipped with a high-efficiency Super-X EDX detector in a high vacuum environment. The kinetic processes in the thin film samples were studied in short-term (maximum accumulated holding time at elevated temperatures: 10 minutes) and long-term heating experiments (maximum accumulated holding time at elevated temperatures: 200 minutes).
EDX profiles were extracted across a γ-channel including the two adjacent γ/γ'-interfaces following every heating and quenching step, see dotted white rectangle in figure 2a. Using the element Chromium (Cr) as example (figure 2b) the diffusion towards the γ/γ' interface can be nicely demonstrated and corresponds well to theoretical predictions [4]. Furthermore, the saturation of diffusion in long-term experiments forecasted by simulations was confirmed. The µ-bulks reproduce the findings of the thin foil experiments and hold the opportunity to expand the maximum heating time. A detailed investigation of the effect of surface oxidation on the diffusion phenomena in thin foils and µ-bulks is under way.

[1] R. C. Reed, Superalloys, Cambridge University Press (2006)
[2] F. Niekiel et al., Ultramicroscopy 176 (2017)
[3] A. B. Parsa et al., Advanced Engineering Materials 17(2) (2015)
[4] C. E. Campbell et al., Acta Materialia 50 (2002)

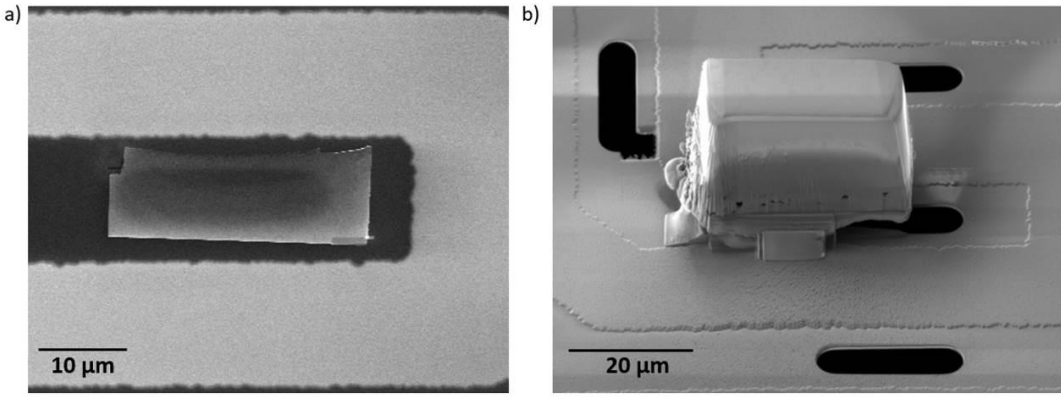

Figure 1. FIB-prepared single crystal Ni-base superalloy specimens attached to a MEMS-based DENSsolutions Wildfire D3 in-situ TEM chip for ultra-fast heating and quenching experiments. a) Thin foil, b) µ-bulk.

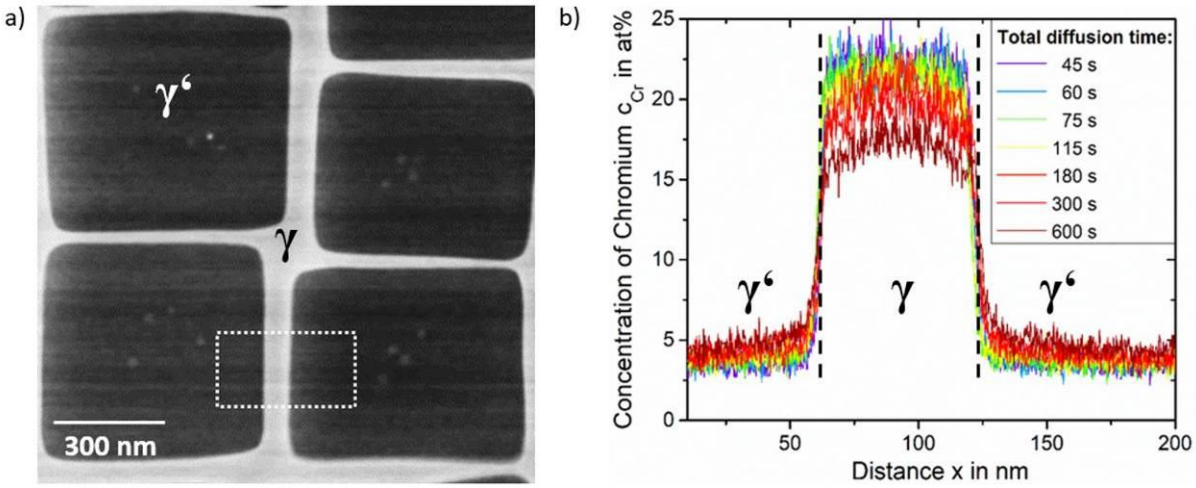

Figure 2. a) Initial γ/γ‘ microstructure of a Ni-base superalloy. The white rectangle marks the region of the EDX ChemiSTEM measurement. b) Temporal evolution of the Cr concentration profiles observed in short term heating experiment conducted at 900 °C.

MS4.LBP02
Quantitative electron diffraction study of γ and γ' lattice parameters in a model Co- based superalloy.

C. Hell[1], Y. Eggeler[1], E. Spiecker[1]

[1]Institute for Micro- and Nanostructure Research, Material Science and Engineering, Erlangen, Germany

christoph.martin.hell@gmail.com

Co-based superalloys, of a composition of Co-12Al-9W, form a stable two phase γ/γ' microstructure at 900°C [1]. This microstructure is morphologically identical to the microstructure of well-studied Ni-based superalloys which find their application as blade material in the combustion chamber of turbines for airplanes and power plants. Ni-based superalloys withstand high mechanical loads at temperatures close to 80% of their melting point in harsh environments [2]. These unique high temperature properties rely on their two phase γ/γ' microstructure, where cuboidal γ' precipitates consisting of the $L1_2$ crystal structure are coherently embedded in a solid solution fcc γ matrix. In contrast to Ni-based superalloys, Co-based superalloys exhibit a larger γ' phase lattice constant than the one of the γ matrix corresponding to a positive lattice misfit δ.
In this study a cobalt based superalloy (ERBOCo) with a purposely engineered γ' volume fraction of 20 % containing Ta is investigated [3]. The γ' phase distributes itself in three characteristic ways, as shown in Figure 1. A γ' phase predominated region (green), a γ phase prevailing region (blue) and regions where γ and γ' phases show a quasi-lamellar arrangement (red).
The inhomogeneous distribution of the γ' phase within the sample can be exploited for an independent measurement of γ and γ' lattice parameters. For this the hypothesis is made that in regions where γ' prevails (green), the average lattice parameter is close to the one of the pure γ' phase ($a_{\gamma'}$), whereas γ phase regions (blue) adopt the lattice parameter of the pure γ phase (a_{γ}).
The unconstrained lattice misfit is evaluated by means of SAED by measuring in the characteristic regions of the microstructure. In regions with quasi-lamellar arrangement of the γ and γ' phases (red), an intermediate state is obtained. Here, lattice coherency results in tetragonal distortion of the respective unit cells perpendicular to the γ/γ'-interface, as schematically sketched in Figure 1b. Accordingly, SAED patterns show splitting of Bragg reflections (e.g. {002}) in the corresponding (reciprocal) direction (Figure 2b-d). In the perpendicular direction only little splitting is observed (not shown). This could be either due to contributions from the narrow γ channels in the γ' band or due to partial relaxation of coherency strain in the γ and γ' lamellae facilitated by the thin TEM foil.
The purpose of this study is to directly measure the γ and γ' lattice parameters of a particular Co-based superalloy taking advantage of its unique microstructure. In order to analyze the strain distribution inside the microstructure SAED will be complemented by strain mapping using convergent beam electron diffraction or nano beam diffraction. This model alloy has potential for *in situ* heating experiments aiming for determination of γ/γ' misfit at elevated temperatures which is an important parameter in alloy designing.

[1] Sato et al., Science 7 (2006) pp. 90-91.
[2] R. C. Reed, Superalloys, Cambridge University Press (2006)
[3] C. Zenk, Dissertation, to be submitted, Friedrich-Alexander-Universität Erlangen-Nürnberg, (2017)

Acknowledgement
The authors gratefully acknowledge C. Zenk and S. Neumeier for supplying and engineering the sample material as well as financial support by the DFG via the collaborative research center SFB-TR 103 and the Cluster of Excellence EXC315.

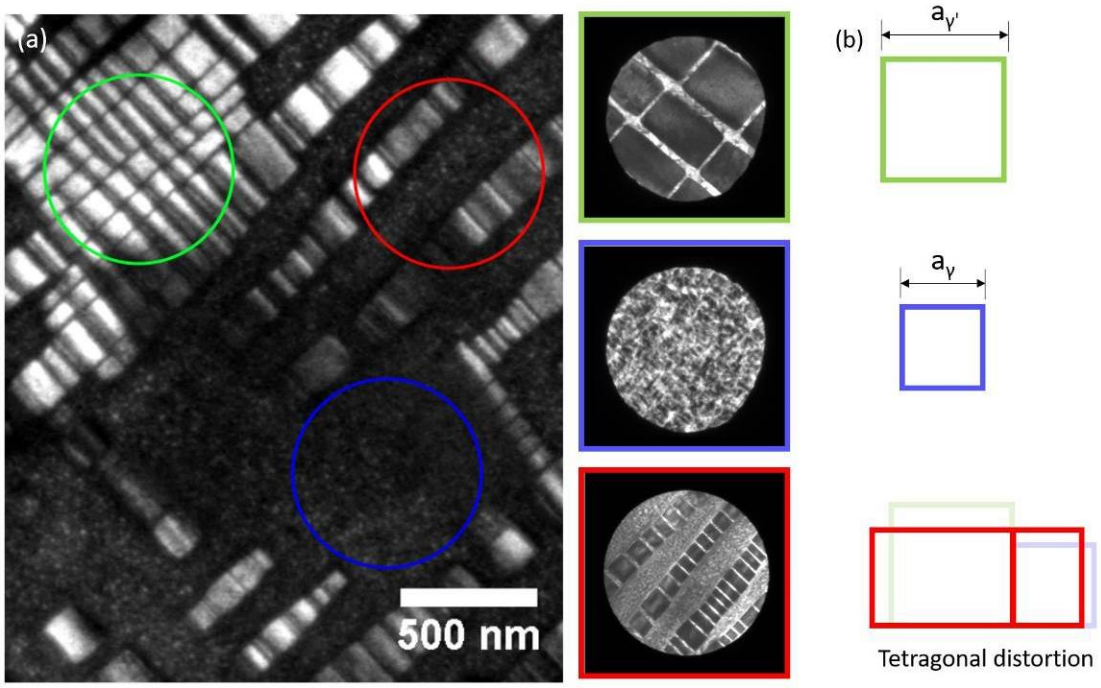

Figure 1. a) Overview of the three characteristic regions of the γ/γ' microstructure (red, blue and green) and the belonging selected area micrographs. (b) Schematic illustration of the tetragonal distortion of the γ' and γ unit cells.

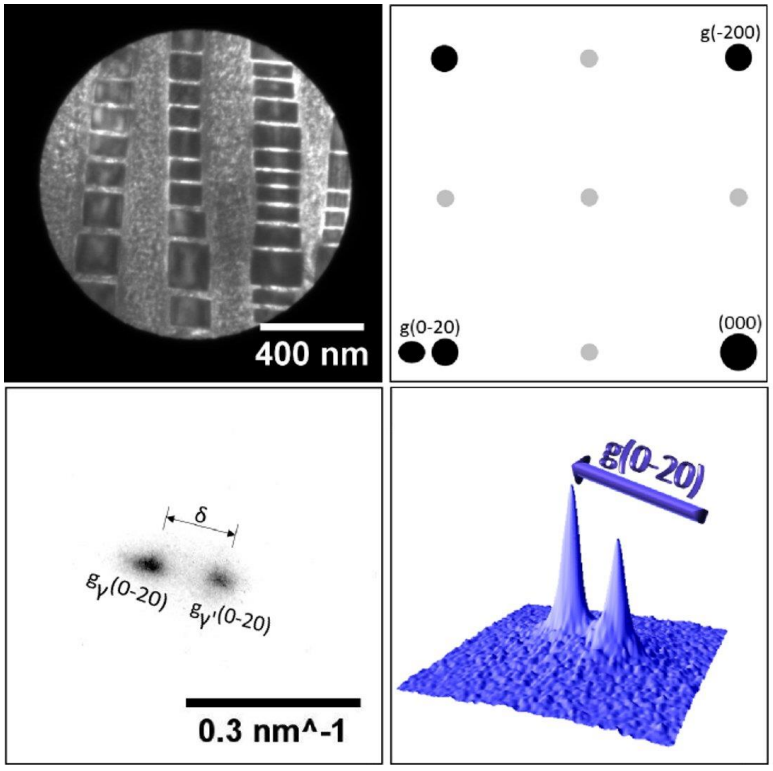

Figure 2. (a) Bright-field TEM image of several γ'- bands; (b) Schematic of diffraction pattern of a lamellar γ/γ' arrangement; (**c)** SADP of the g(0-20) diffraction spot showing pronounced splitting due to tetragonal distortion (camera length 6.7 m); (d) 3D illustration of the intensity distribution in (c).

MS5.002
Atomic level insights into the structure and dynamics of vacancies and dopants in graphene

J. H. Warner[1]

[1]Department of Materials, University of Oxford, Oxford, United Kingdom

jamie.warner@materials.ox.ac.uk

Vacancies in graphene are studied at the atomic level using aberration corrected transmission electron microscopy. The detailed structure and dynamics of mono, di, and larger vacancy clusters in graphene will be presented. The transition of many vacancy forms by the rotation of C-C bonds is examined along with the impact of adatom bonding and incorporation into defective structures. Using an in-situ heating holder within a TEM enables the observation of partial dislocations with carbon bridging atoms that help stabilize the system and reduce out of plane buckling, revealing the important balance between sp2 bonding and buckling. Finally I will present results on the surface interactions and bonding between graphene and metal atoms and clusters, showing planar formation of gold sheets on graphene at high temperature and their rapid phase transitions.

MS5.002
Probing vibrational and plasmonic modes and molecule-plasmon interactions in chemically functionalized metal particles using EELS

P. Abellan[1], P. El-Khoury[2], F. Hage[1], J. Cottom[3], A. Joly[2], W. Hess[2], R. Brydson[3], Q. Ramasse[1]

[1]SuperSTEM Laboratory, Daresbury, United Kingdom
[2]Pacific Northwest National Laboratory, Physical Sciences Division, Richland, WA, United States of America
[3]University of Leeds, School of Chemical and Process Engineering, Leeds, United Kingdom

pabellan@superstem.org

Metal nanostructures can be used to detect, image, and identify molecules with high sensitivity and selectivity using tools of (non-)linear optical spectroscopy [1]. Slight nanometric variations in the morphology and distribution of metal particles can completely alter the plasmonic response of the local electric field interacting with nearby molecules. Indeed, the interplay and coupling of molecules to plasmons is known to be complex and the exact mechanisms behind a plethora of phenomena of mixed molecular-metallic/plasmonic origin are not well understood. In this regard, the commonly adopted practice of correlating structural/topographic images of plasmonic nanostructures with near-field optical spectra is often insufficient.
Using electrons in a Cs-corrected scanning transmission electron microscope (STEM), unrivalled spatial resolution for measuring the plasmonic response of nanoparticles is achieved. Furthermore, electron energy loss spectroscopy (EELS) has already provided spectral evidence of charge transfer (CT) states and classical/quantum plasmonic resonances in dimers of cubic metal particles containing an organic dielectric junction.[2] In this work, we demonstrate the use of monochromated EELS in a Nion UltraSTEM 100MC Hermes microscope [3], to simultaneously visualize the local electric fields associated with plasmonic excitation and to probe aromatic thiols in chemically-functionalized metal particles. We will present our latest results aimed at finding experimental conditions for identifying molecular signatures (e.g. 4,4-dimercaptostilbene, C14H12S2, DMS – see Fig. 1A). We will also explore the interaction between molecules and plasmons on the nanoscale and discuss some of the limitations we have found for such simultaneous spectral recording and mapping of vibrational and plasmonic modes (see Fig. 1B and 1C). [4].

References:
[1] Pettinger *et al*., N. Annu. Rev. Phys. Chem. **63** (2012) 379; Le Ru & Etchegoin, Annu. Rev. Phys. Chem. **65** (2012) 65
[2] Tan *et al.* Science **343** (2014) 1496
[3] Krivanek et al. Nature Letter **2014**, 514, 209-212; R. Brydson, Nature **2014,** 514, 177-178
[4] SuperSTEM is the UK EPSRC National Facility for Aberration-Corrected STEM, supported by the Engineering and Physical Science Research Council. PZE acknowledges support from the Laboratory Directed Research and Development Program at Pacific Northwest National Laboratory (PNNL). WPH and AGJ are supported by the US Department of Energy (DOE), Office of Science, Office of Basic Energy Sciences, Division of Chemical Sciences, Geosciences & Biosciences.

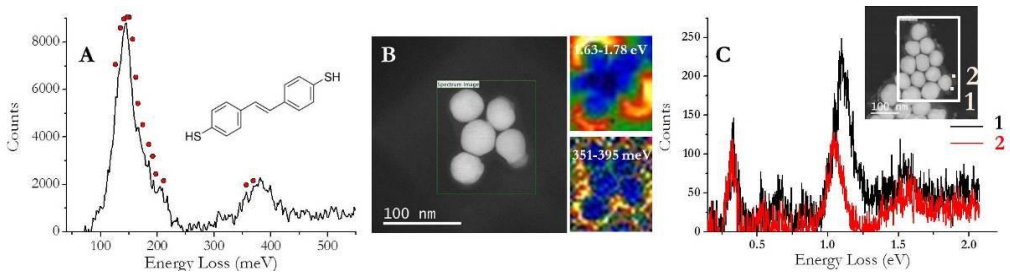

Figure 1. A) Vibrational modes of DMS, with vibrations (IR and Raman active) indicated by red circles. The most intense peak is assigned to the C-S stretching (134meV) and aromatic C-H in-plane rocking (147meV) vibrations. B) Simultaneous mapping of aromatic C-H (360meV) from surface bonded molecules and Ag nanoparticle surface plasmon modes. C) Vibrational response and plasmonic resonances measured in aloof geometry from locations 1 and 2 (see inset). The energy resolution was 12 meV (full-width at half-maximum of the zero-loss peak through the support).

MS5.003
Host-guest interactions and spatial orientation in charge density wave materials intercalated with organic molecules.

M. Kinyanjui[1], J. Holzbock[2], J. Köster[1], M. Linden[2], U. Kaiser[1]

[1]University of Ulm, Electron Microscopy group of Materials Science, Ulm, Germany
[2]University of Ulm, Institut für Anorganische Chemie II, Ulm, Germany

michael.kinyanjui@uni-ulm.de

Charge density waves (CDW) are periodic modulations of charge density in low-dimensional metals which are observed as a function of temperature, doping and pressure.1 Due to electron phonon coupling, CDW are also accompanied by a periodic lattice distortion (PLD) which is characterized by a periodic modulation of the atomic positions. While CDW can be directly probed using Scanning Tunnelling Microscopy (STM) 2, electron diffraction and imaging techniques such as HRTEM are sensitive to the corresponding structural distortions (PLD).
Quasi two-dimensional (2D) transition metal dichalcogenides including 1T/2H-TaSe2, 1T/2H-TaS2, 1T-TiSe2, 2H-NbSe2 are some of the low-dimensional metals that exhibit strong CDW distortions whose transition temperature and commensuration varies mainly with temperature.1 The transition temperature can however be also affected by dimensionality, pressure, and doping or intercalating with ion or organic molecules. The objective of this present work is to determine the structure of the CDW materials intercalated with organic molecules.
We have investigated the electronic and atomic structures of CDW- material 1T-TiSe2, and 1T-TaS2 intercalated with Pyridine (C5H5N), Bipyridine (C10H8N2), and Triethylenediamine (C6H12N2). Using momentum-resolved valence electron energy loss spectroscopy (MREELS), we have determined the nature and dispersion of the plasmon and interband excitations along different directions of the Brillouin zones and at different CDW states. In addition we have determined the orientation of the intercalated C5H5N and C6H12N2 molecules within the 1T-TaS2 layers through orientation dependent EELS at the C-K and N-K edges.
Figure.1(a) displays the electron diffraction of 1T-TaS2 at 350 K showing the super-lattice spots due to the nearly-commensurate CDW distortion. The electron diffraction of 1T-TaS2 intercalated with C6H12N2 is shown in Fig.1 (b). The complex electron diffraction pattern of the C6H12N2 intercalated sample is a result of structural transformation from 1T-TaS2 structure to the 4Hb-TaS2 structure and the subsequent rotation of two commensurate CDW. The CDW in corresponding layers are therefore rotated with respect to each other. In Fig 1(c) we display the C-K edge of 1T-TaS2 intercalated with C6H12N2 showing the (i) peak due to $1s \rightarrow \pi^*$ and peak feature (ii) due to $1s \rightarrow \sigma^*$ transition. The intensity of the peak (i) is related to the orientation of the molecules in the crystal lattice. The molecules are oriented perpendicular to the dichalcogenide layers.
In conclusion we have used electron diffraction and electron energy loss spectroscopy to determine the interaction of intercalated organic molecules with charge density wave materials. We have shown that the organic molecules change the structure of the host structure with subsequent changes in character of the charge density waves. Electron energy loss spectroscopy shows that the organic molecules are oriented perpendicular to the layers.

[1] J. Wilson, F. D. Salvo, and S. Mahajan, Adv. Phys. 24, 117 (1975).
[2] H. Dai, and C. Lieber, Annu. Rev. Phys. Chem. 44, 237 (1993)
[3] T. Ishiguro and H. Sato,Phys. Rev. B 52, 759 (1995).

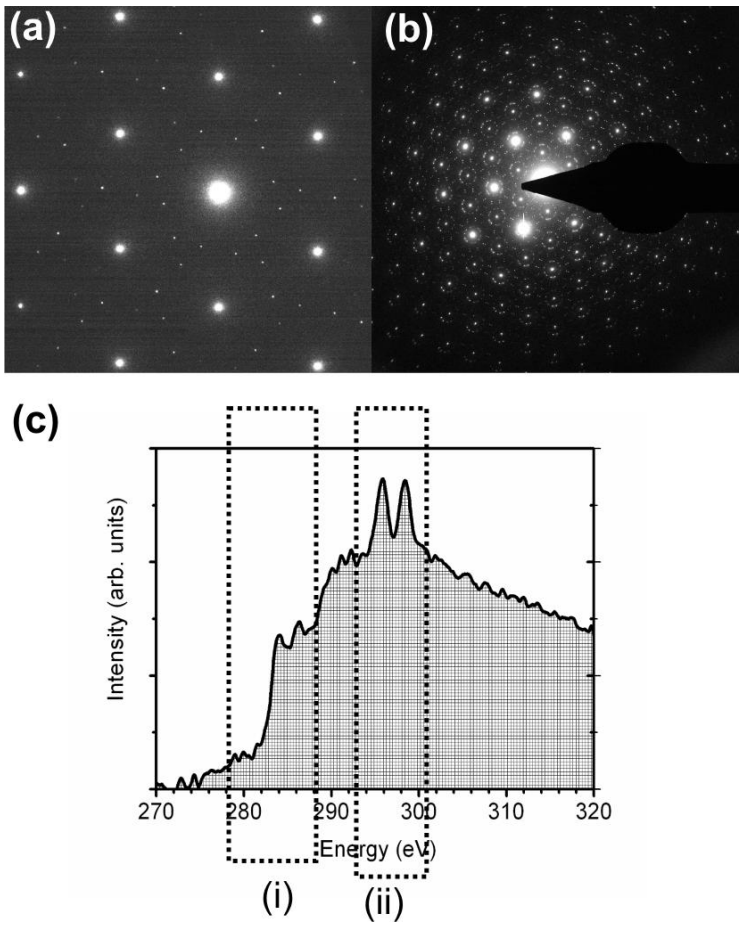

Figure 1. Electron diffraction of (a) 1T-TaS2 at 350 K showing the superlattice spots due to CDW distortion (b) 1T-TaS2 intercalated with C6H12N2 (c) C-K edge of 1T-TaS2 intercalated with C6H12N2 showing the (i) peak due to 1s→ π* and peak feature (ii) due to 1s→ σ* transition.

MS5.004
Three-dimensional reconstruction of soft materials by array tomography with fiducial markers.

Y. Konyuba[1], T. Haruta[1], H. Nishioka[1], M. Kato[2], M. Suga[1], T. Higuchi[3], H. Jinnai[3]

[1]JEOL Ltd., TOKYO, Japan
[2]Yamagata Research Institute of Technology, Yamagata, Japan
[3]Tohoku University, Miyagi, Japan

ykonyuub@jeol.co.jp

In recent years, three-dimensional (3D) reconstruction using serial slice scanning electron microscopy (SSSEM) is attracting much attention, and many applications in biological cells and tissues have been reported. SSSEM allows 3D reconstruction for a wide region (ranging over several hundreds of μm2) with high spatial resolution (within several nm). The array tomography is one type of SSSEM: ultrathin slices are cut sequentially using ultramicrotome, which are scooped in sequential order on a flat surface such as a silicon substrate or a conductive glass substrate. A series of 2D images from each slice are imaged by SEM with back scattered electron detector [1-2]. Array tomography has several advantages compared to the other SSSEMs: The samples are not destroyed by the observation; thus, the slices are successively and repeatedly observable under different observation conditions. Spatial resolution in xy-plane is the highest among its analogous methods, because working distance between the objective lens and the sample can be minimized and the substrate bias is easily applicable. In addition, initial cost for the introduction of the instrument can be minimum, since there is no need of a focused ion beam column or a ultramicrotome module inside a SEM. Note that the spatial resolution in z(depth)-direction is limited by the thickness of the slices (> 40 nm).

Although very effective and high-resolution, the array tomography may be difficult if samples do not have particular structural features, or if they have highly periodic structures. In such cases, lateral arraignment, i.e., registration, of each 2D image at different depth can be difficult. Our solution to this difficulty is to introduce fiducial makers to soft materials (see Fig. 1 below for details). Here, we used a multi-component polymeric specimen called ABS resin that is one of the most commonly used "plastic" materials today. Actual experimental procedure is the following: (1)ABS was stained by OsO4 (B part is selectively stained), (2)fiducial markers, quadrangular pyramids, were impressed to the ABS resin using a diamond indenter, (3)ABS with fiducial markers were sliced by ultramicrotome, (4)ribbons of serial slices were scooped on a silicon substrate, (5)each serial slice was observed by SEM, and (6)individual images were registered by using the fiducial markers to stack them in a sequential order to reconstruct a 3D volume.

Figure.1 shows a back-scattered electron image of OsO4 stained ABS resin on a silicon substrate with fiducial markers. By forming fiducial markers, the sample positions of each slice can be easily identified and working time to find a field of view is significantly reduced with much better alignment. Consequently, we have successfully made a 3D reconstruction (Fig. 2) with higher accuracy and shorter time than before.

[1] Micheva, Kristina D., and Stephen J. Smith. "Array tomography: a new tool for imaging the molecular architecture and ultrastructure of neural circuits." Neuron 55.1 (2007): 25-36.
[2] Wacker, I., and R. R. Schroeder. "Array tomography." Journal of microscopy 252.2 (2013): 93-99.

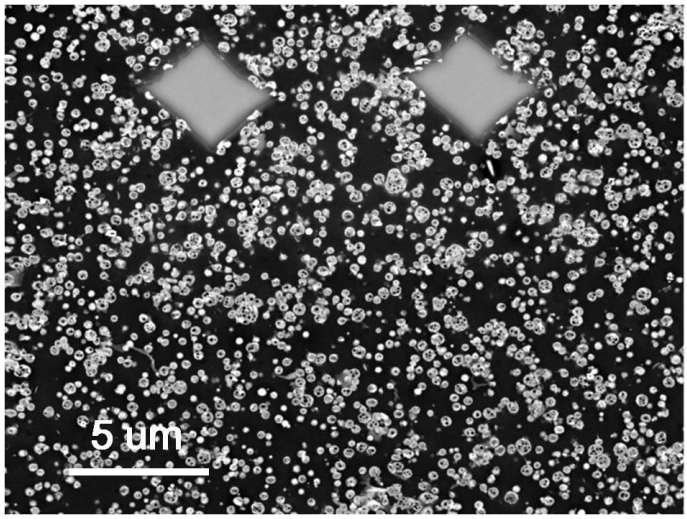

Figure 1

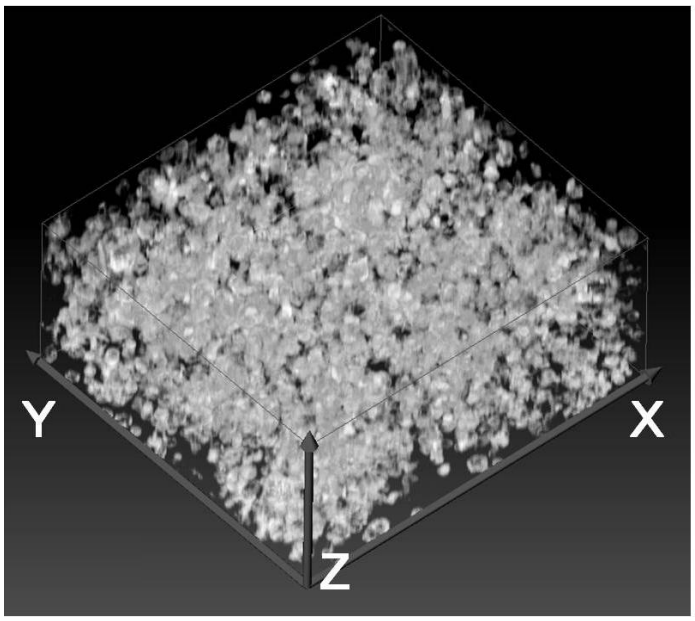

Figure 2

MS5.005
Properties of amorphous carbon for phase plates in transmission electron microscopy

P. Hermann[1], M. Dries[1], S. Hettler[1], D. Gerthsen[1]

[1]Karlsruhe Institute of Technology, Laboratory for Electron Microscopy, Karlsruhe, Germany

peter.hermann@partner.kit.edu

Thin-film phase plates (PPs) are used in transmission electron microscopy (TEM) to obtain phase contrast for weak-phase objects. PPs introduce an additional phase shift between unscattered and scattered electrons, which results in an improved contrast transfer especially for small spatial frequencies [1]. A standard material for thin-film PPs is amorphous carbon (aC). Unfortunately, thin-film PPs experience irreversible aging after a short time of usage, which leads to charging, uncontrollable phase shifts and artifacts in PP TEM imaging [2]. However, it is not clear up to now if structural and/or chemical changes lead to these effects.

To analyze possible reasons for aC-degradation we have fabricated aC-films with three different deposition techniques. Film thicknesses were between 10 and 40 nm. Aging was simulated by illumination of the aC-films with a defined electron dose. High resolution TEM and electron diffraction was used to verify the amorphous structure of the aC-films. Electron energy loss (EELS) spectroscopy was applied to measure the local sample thickness and fraction of sp^2- and sp^3-coordinated C-atoms by exploiting the fine structure of the C-K ionization edge. Quantification of the sp^2-fraction was performed according to the procedure described in [3]. The fraction of sp^2-coordinated C-atoms is considered as an indicator of the electronic properties of the material, which is expected to change under electron illumination. Possible charging of an aC-film was assessed by off-axis electron holography using a Möllenstedt biprism.

Fig. 1 shows the measured sp^2-fraction of four aged specimens as a function of the electron dose up to $3 \cdot 10^{10}$ e/nm^2. All specimens are made from the same aC-film which was fabricated by electron beam evaporation. Aging was performed with a parallel beam for different dose rates given in Fig. 1. Starting from an initial sp^2-fraction of 72±3 at%, aging depends on the dose rate. Large dose rates lead to a significant reduction of the sp^2-fraction whereas only minor changes are observed for small dose rates. During aging, the film thickness decreased slightly (significantly) for high (low) dose rates.

Analogous experiments were performed under focused-beam conditions in the scanning (S)TEM mode. EELS spectra were continuously acquired, while carbon contamination built up on the aC-film. Fig. 2 shows the sp^2-fraction as a function of the dwell time of the focused beam. All differently fabricated aC-films are initially characterized by a rather high sp^2-fraction of 72±3 at% despite different fabrication techniques. With rising dwell times, the contamination becomes thicker and the sp^2-fraction approaches the sp^2-fraction of the contamination. Contamination seems to contain carbon with a higher sp^2-fraction than the underlying aC-film. Electron holography shows no significant charging of aC-films with an increasing amount of contamination.

All differently fabricated non-aged and non-contaminated aC-films showed roughly the same sp^2-fraction of 72±3 at%. A significant decrease of sp^2-fraction could be observed for aC-films, which were aged using a parallel electron beam with a dose rate of $3.6 \cdot 10^6$ e/(nm^2 s). This could partially explain the aging of thin-film PPs fabricated from aC-films.

[1] R. Danev and K. Nagayama, Ultramicroscopy 88 (2001), p. 243.
[2] R. Danev et al., Ultramicroscopy 109 (2009), p. 312.
[3] X. Zhang et al., Carbon 102 (2016), p. 198.

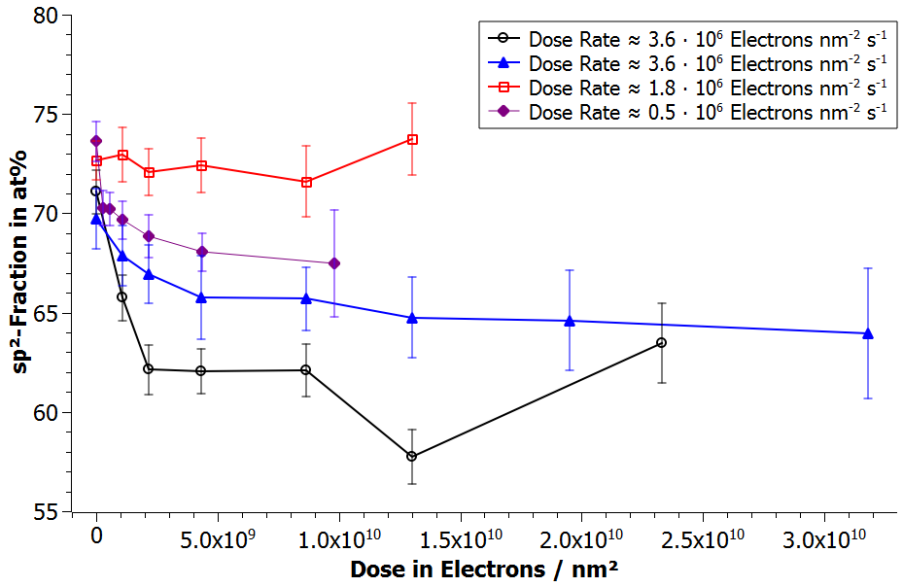

Figure 1. sp²-fraction of four specimens of an aC-film fabricated by electron beam evaporation as a function of the electron dose. Different dose rates were applied as indicated in the legend.

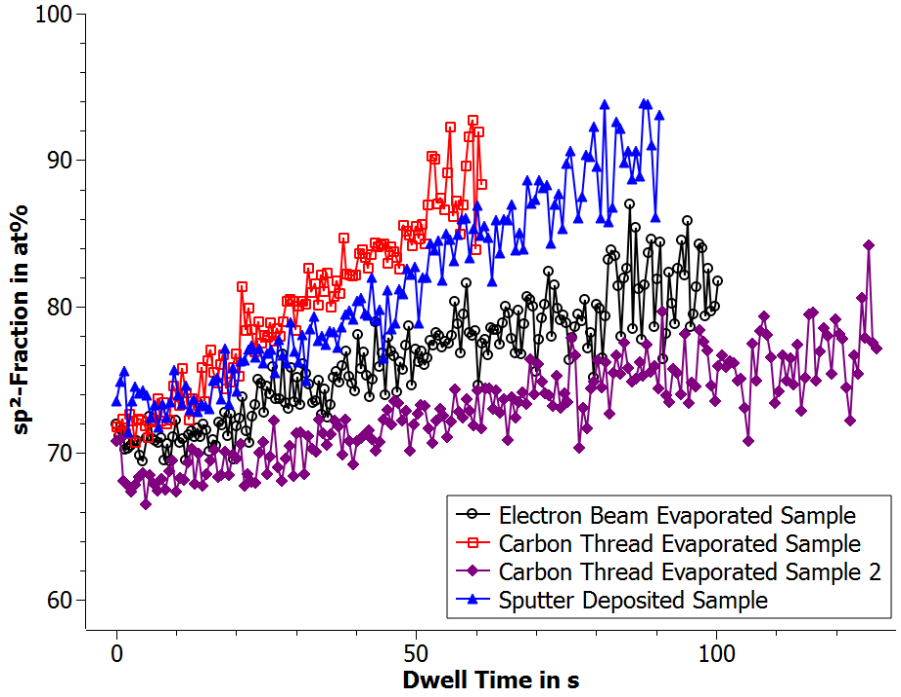

Figure 2. Fraction of sp²-coordinated C-atoms as a function of illumination time under focused-beam conditions in STEM mode. Samples were produced by different fabrication techniques as indicated in the legend.

MS5.006
Understanding graphitization and growth of free-standing nanocrystalline graphene using in situ transmission electron microscopy

C. N. Shyam Kumar [1,2], V. S. K. Chakravadhanula[1,3], A. Riaz[1,2], S. Dehm[1], W. Di[1], M. Xiaoke[1]
R. Krupke[1,2], C. Kübel[1,3,4]

[1]Karlsruhe Institute of Technology, Institute of Nanotechnology, Eggenstein-Leopoldshafen, Germany
[2]Technische Universität Darmstadt, Department of Materials and Earth Sciences, Darmstadt, Germany
[3]Helmholtz Institute Ulm, Ulm, Germany
[4]Karlsruhe Nano Micro Facility, Karlsruhe, Germany

shyam.neelakandhan@partner.kit.edu

Catalyst free synthesis by the graphitization of polymers is an effective way to synthesize nanocrystalline graphene on different substrates with tunable shape, thickness and properties [1]. The catalyst free synthesis results in crystallite sizes on the order of few nanometer, significantly smaller compared to commonly prepared polycrystalline graphene [2]. Even though this method provides the flexibility of graphitizing polymer films on different substrates, substrate free graphitization of freestanding polymer layers has not been studied yet. We report the first time the thermally induced graphitization and domain growth of free standing nanocrystalline graphene thin films using *in situ* TEM techniques. High resolution transmission electron microscopy (HRTEM), selected area electron diffraction (SAED) and electron energy loss spectroscopy (EELS) techniques were used to analyze the graphitization and the evolution of nanocrystalline domains at different temperatures by characterizing the crystallinity and domain size, further supported by *ex situ* Raman spectroscopy.
Commercially available microposit S1805 photo resist was spin coated onto a MEMs based heating chip (Protochips Inc.) The chip was initially heated *ex situ* at a temperature of 600 °C and 10-7 mbar pressure for 5 hours. The Raman signature of the free standing film (peak positions and ID/IG ratio) formed across the holes of the supporting film on the heating chip, is almost identical to the substrate supported graphitization on a SiO2 terminated Si wafer (figure 1). This confirms that graphitization without any catalytic support of the substrate yields very similar materials. These free standing films were the starting point for a detailed *in situ* TEM graphitization study at temperatures up to 1200 °C. *In situ* TEM analysis showed that the growth of the nanocrystalline domains (figure 1) in the intermediate temperature range of 600 °C – 1000 °C mainly proceeded by consuming amorphous carbon present around the domains. After heating to 1000°C, essentially only sp2 carbon is left in the [001] texture dominated film (figure 2). Further growth of the domains at higher temperatures (1000-1200 °C) was facilitated by the merging of small crystalline domains forming bigger ones. The amorphous carbon transforms in two ways, one by attaching on to the active edges of the domains and by the catalyst free transformation on the top of graphitic layers. This catalyst free transformation forms new small graphitic structures which are highly mobile and get attached to the edges, extending the edges. However, both mobile and stationary (pinned) structures with varying size and shape were observed. HRTEM images showed the formation of extended graphene domains stacked on top of each other. The partially stacked graphene layers exhibit a preferential misorientation of 22° (figure 2).

References:
[1] Z. Zhang, B. Ge, Y. Guo, D. Tang, X. Wang and F. Wang, *Chem. Commun.*, 2013, **49**, 2789.
[2] A. Riaz, F. Pyatkov, A. Alam, S. Dehm, A. Felten, V. S. K. Chakravadhanula, B. S. Flavel, C. Kübel, U. Lemmer and R. Krupke, *Nanotechnology*, 2015, **26**, 325202.
[3] Shyam Kumar Chethala Neelakndhan greatly acknowledge PhD funding from Deutscher Akademischer Austauschdienst (DAAD)

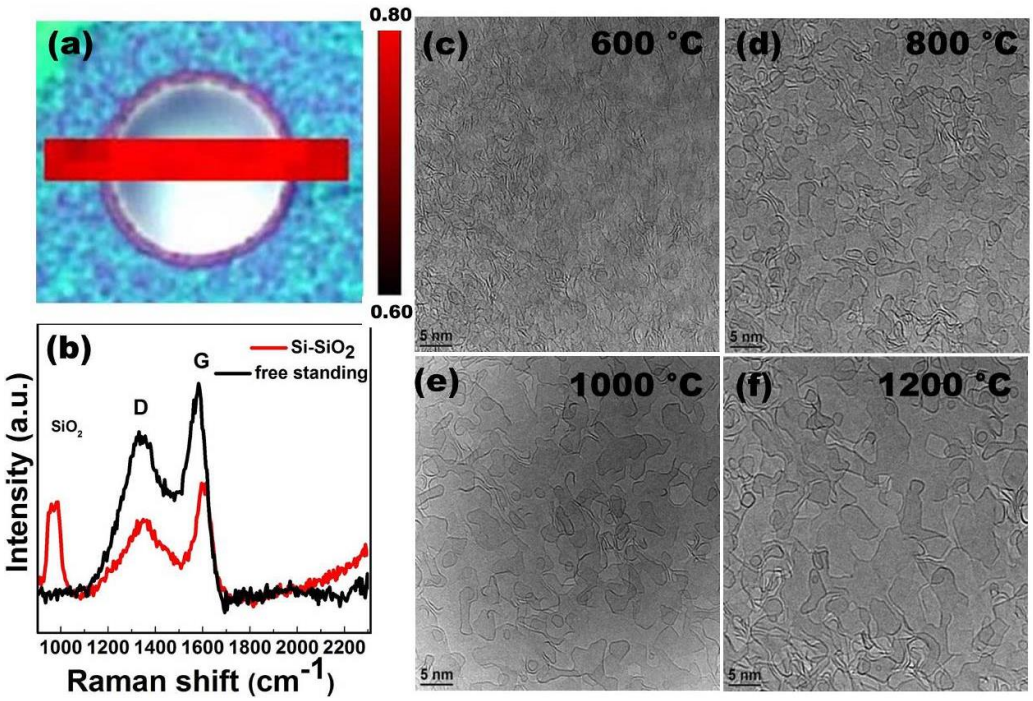

Figure 1. (a) ID/IG ratio map of a free standing film over a hole on the heating chip, (b) Raman spectra of free standing and SiO2 supported film at 600 °C and (c-f) evolution of nanocrystalline domains with temperature.

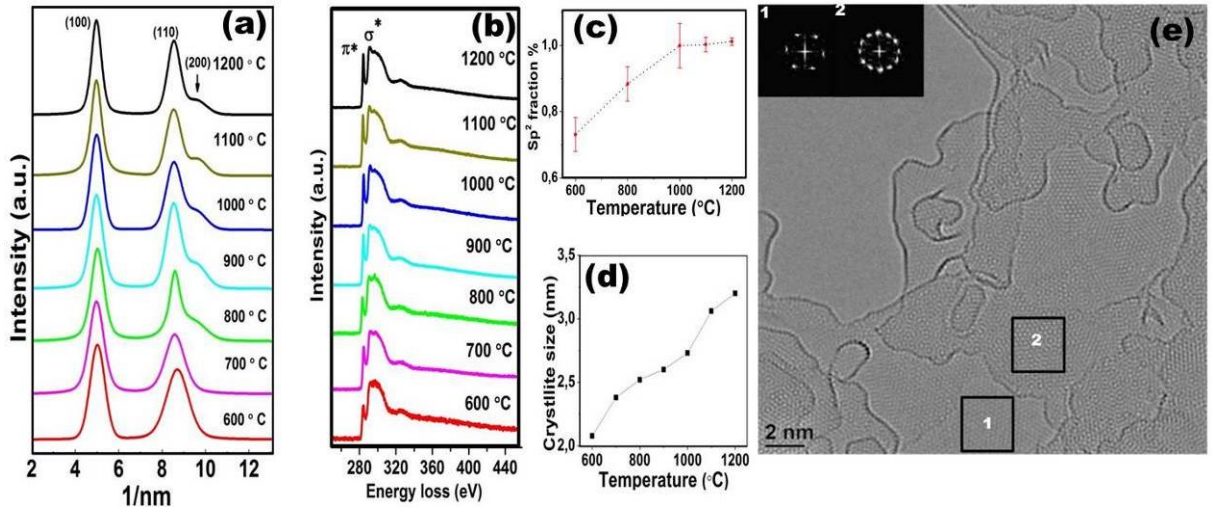

Figure 2. (a) SAED intensity profiles, (b) carbon core loss EELS edge, (c) crystallite size evolution and (d) sp2 fraction at different temperatures and (e) HRTEM image of the graphitized layers, FFT from the marked regions showing a misorientation of 22° is given in inset.

MS5.007
Aberration-corrected TEM/ETEM-based research on single-walled carbon nanotubes

H. Jiang[1], Y. Tian[1], M. He[1], E. Kauppinen[1]

[1]Aalto University, Department of Physics, Espoo, Finland

hua.jiang@aalto.fi

In this contribution, we will review methods of chiral structure analysis of single-walled carbon nanotubes (SWNTs) by electron diffraction (ED) technique. With that as a basis, we have established an approach using ED as a means to evaluate the validity of Raman spectroscopy for quantification of concentrations of metallic SWNTs (M%) or of semi-conducting tubes (S-SWNT%). Chirality distribution maps of SWNTs produced by CVD methods with Fe nanoparticles as catalysts at various synthesis conditions have been analyzed with electron diffraction. HRTEM observation has disclosed the structure relationship between catalyst nanoparticles and SWNTs. We also demonstrate that structural control of SWNTs is achievable by fabricating nanoparticle catalysts with a defined structure on crystalline substrates via epitaxial growth techniques. *In situ* time-resolved environmental transmission electron microscope (ETEM) observation at atomic resolution of nanoparticle formation and SWNT growth are accomplished.

MS5.P001
Graphene and polyaniline composited fibers prepared by wet-spinning

D. Zhang[1], Z. Zhang[1], H. Lin[1], Y. Chen[1]

[1]Soochow University, College of Textile and Clothing Engineering, Suzhou, China

dszhang@suda.edu.cn

Graphene, a two dimensional (2D) carbon nanostructure, has demonstrated fascinating properties, such as electron mobility, large surface area, high mechanical, thermal and chemical stability, which has attracted a persistent attention [1]. The macroscopic, functional structures for practical applications based on graphene or graphene oxide have been designed and produced, such as film, fiber, sponge, and other composited materials. Polyaniline is a typical conducting polymer that has been widely studied since its excellent properties, including high conductivity and optical activity [2]. In this study, graphene oxide and polyaniline composited fibers (GO/PANI-F) were firstly and largely spun by wet-spinning method. Graphene and polyaniline composited fibers (G/PANI-F) were prepared through reducing the GO/PANI-F.

Macroscopic and neat GO/PANI-F was continuously spun by wet-spinning method. Figure 1a shows the photograph of dried GO/PANI-F. The morphologies of axial external surface and cross-section of GO/PANI-F were observed by SEM which showed in figure 1b to 1d. Many order grooves along with the fiber axis direction exhibited on the external surface which results from drastic contraction in the diameter direction during the drying process. The broken section shows PANI particles dispersed between close packed GO sheets, clearly visible from the high-resolution image. Figure 2 reveals the Energy Disperse Spectroscopy (EDS) of GO/PANI-F. Figure 2b, 2c and 2d were C, N, O element mapping of GO/PANI-F corresponding to figure 2a. N element, which comes from PANI, mapping consisted with C and O mappings, indicating the uniform distribution of PANI along GO/PANI-F.

The GO/PANI-F was then reduced using hydroiodic acid to prepare G/PANI-F. The changes of structure and mechanical properties of them were measured. Figure 3 shows Raman spectra of GO/PANI-F and G/PANI-F. The intensity values of the characteristic D and G bands (ID/IG) of G/PANI-F increase compared to GO/PANI-F, indicating the decrease of average size of sp2 domains after reduction process. Figure 4 shows typical strain-stress curves of GO/PANI-F and G/PANI-F. The tensile strength of G/PANI-F increased from 20.81 MPa to 25.55 MPa after reduction. However, the elongation decreased from 14.92% to 5.57%. It indicated that graphene sheets became more densely stacking after reduction.

In this study, a new GO/PANI-F was largely prepared through wet-spinning method. The G/PANI-F was produced by the following reducing process. This graphene-based composited fibers will have a wide range of applications such as smart clothing and electronic textiles.

References:

[1] X. Wan, G. Long, L. Huang, Y. Chen. Adv. Mater., 23, 5342-5358 (2011).
[2] J. Huang, S. Virji, B. H. Weiller, R. B. Kaner. J. Am. Chem. Soc., 125, 314-315 (2003).

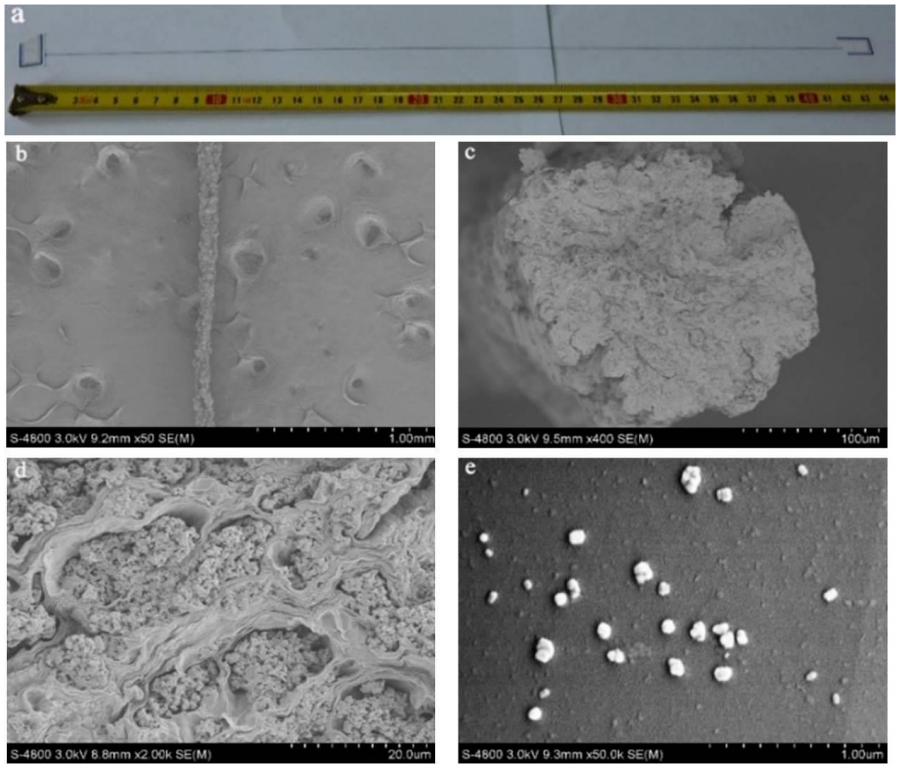

Figure 1. Morphology of GO/PANI-F and PANI. (a) A photograph of GO/PANI-F. (b) The axial external surface SEM image of GO/PANI-F. (c and d) The cross-section SEM images of GO/PANI-F with different magnifications. (e) SEM image of PANI particles.

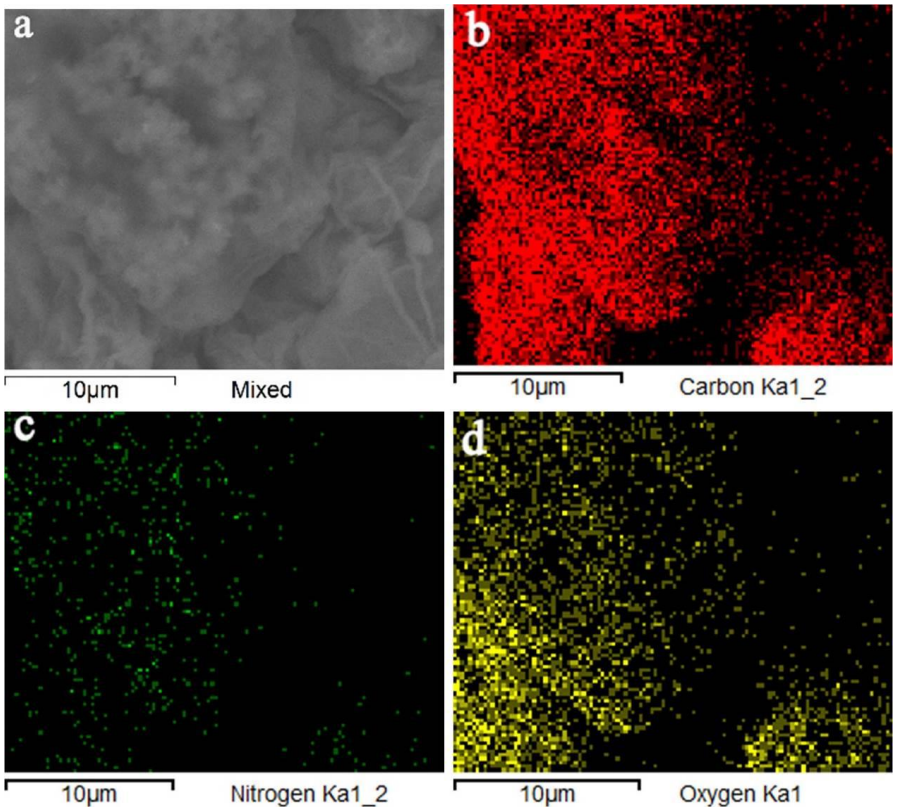

Figure 2. EDS of GO/PANI-F. (b-d) C, N, O elemental mappings of (a) determined by EDS.

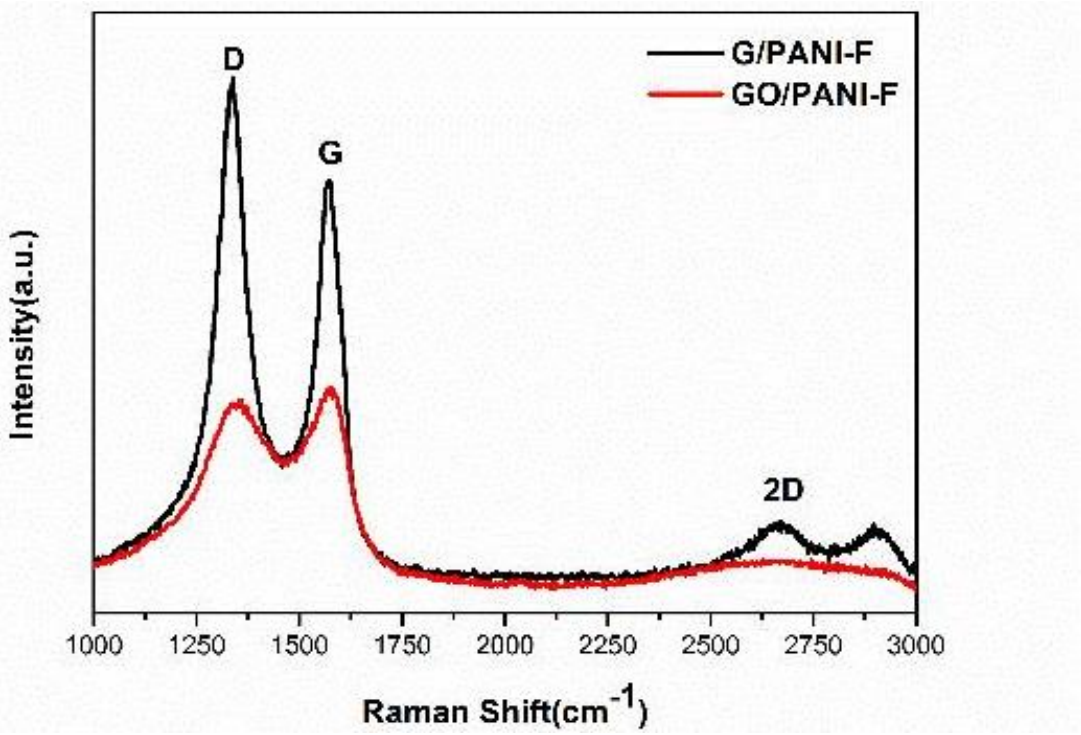

Figure 3. Raman spectra of G/PANI-F and GO/PANI-F.

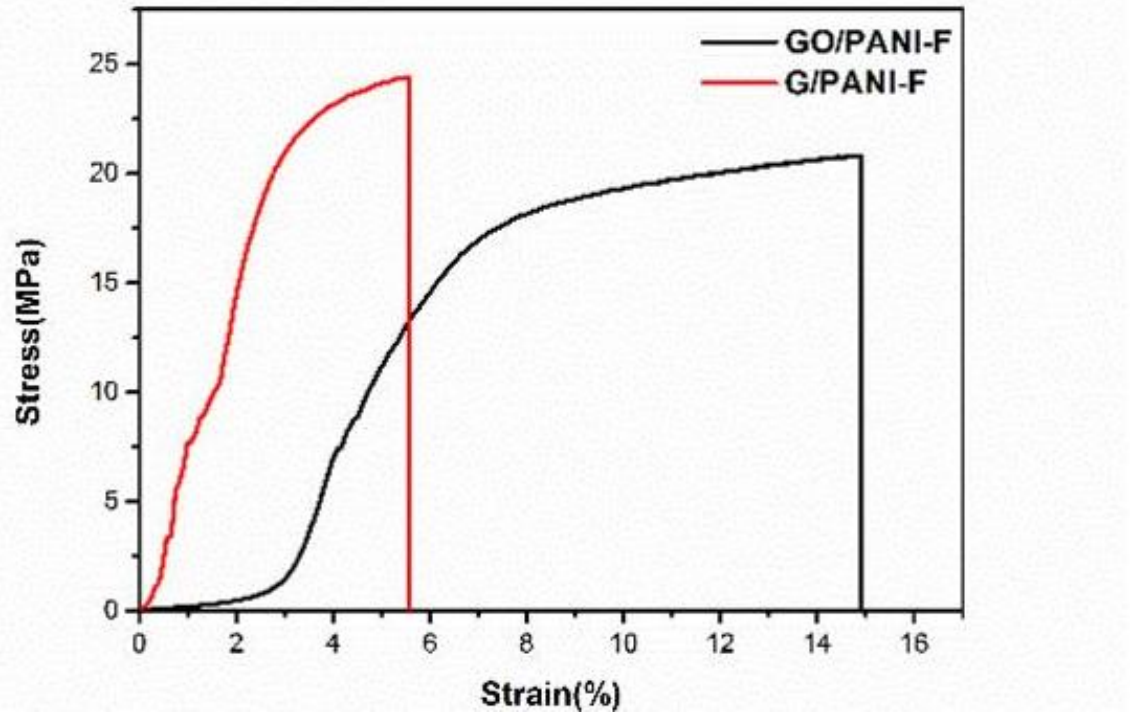

Figure 4. Typical strain-stress curves of GO/PANI-F and G/PANI-F.

MS5.P002
Temperature and time dependence of graphene growth on stainless steel by thermal chemical vapor deposition

A. Ruammaitree[1], D. Phokharatkul[2], A. Wisitsoraat[2]

[1]Thammasat University, Physics, Prathumthani, Thailand
[2]National Electronics and Computer Technology Center, Prathumthani, Thailand

ruammaitree@gmail.com

Graphene is an allotrope of carbon, in which carbon atoms are arranged into a one-atom-thick honeycomb lattice. The growth of graphene on stainless steel can enhance corrosion resistance and conductance of the stainless steel surface. These advantages make the application range of stainless steel wider. In this report, we have investigated the growth of graphene on stainless steel by thermal chemical vapor deposition as a function of growth temperature and time. The results showed that graphene growth and coverage depended on growth temperatures and times, respectively. Although at higher growth temperature (1000°C) graphene could be grown on stainless steel, at low growth temperature (<1000 °C), its growth was hindered due to the surface being covered with iron oxides. In addition, the grain size of graphene was very small (~50 nm in diameter). According to time dependence of graphene growth, coverage of graphene on the stainless steel obviously increased with growth time.

MS5.P003
Massive production of nanofibers via an improved free surface electrospinning

L. Xu[1], Z. Shao[1]

[1]Soochow University, Suzhou, China

lanxu@suda.edu.cn

Electrospinning has been recognized as a simple and efficient technique for the fabrication of polymer nanofibers, which have excellent properties, such as high surface area, high surface energy, and high surface activity et al. These electrospun polymer nanofibers can be used in a wide variety of applications such as drug delivery, composites, sensorics, filtration, tissue engineering, and so on [1,2]. Conventional single-needle electrospinning inhibits the application of nanofibers to commercial applications due to its low production [3]. It is desirable to obtain massive production of quality nanofibers to broaden the applications of nanofibers. Many efforts have concentrated on enhancing the production of the electrospinning technique.
In our studies, an improved free surface electrospinning using a cone shaped air nozzle combined with a solution reservoir made of copper tubes was presented to obtain mass production of quality nanofibers based on the bubble electrospinning [4]. The nozzle combined with the solution reservoir made of copper tubes was used to generate multiple jets on the solution surface to initiate the electrospinning process. The effects of the applied voltage on nanofiber quality and production were systematically investigated, and the results showed the quality and production of nanofibers were improved with the increase of applied voltage. Compared with the bubble electrospinning, the improved free surface electrospinning could produce nanofibers under a much higher applied voltage which would result in decreasing the nanofiber diameter, enhancing the diameter distribution, and improving the nanofiber throughput.

References:
[1] T. Jiang, E.J. Carbone, K.W.H. Lo, C.T. Laurencin, Prog. Polym. Sci. 46 (2015) 1.
[2] R. Nakhowong, Mater. Lett. 163 (2016) 222.
[3] J.S. Varabhas, G.G. Chase, D.H. Reneker, Polymer. 49 (2008) 4226.
[4] R.X. Chen, Y.Q. Wan, N. Si, et al., Therm. Sci. 19 (2015) 1141.
[5] The authors kindly acknowledge the financial supports through the National Natural Science Foundation of China (Grant No. 11672198) and Natural Science Foundation of the Jiangsu HigherEducation Institutions of China (Grant No. 14KJA130001).

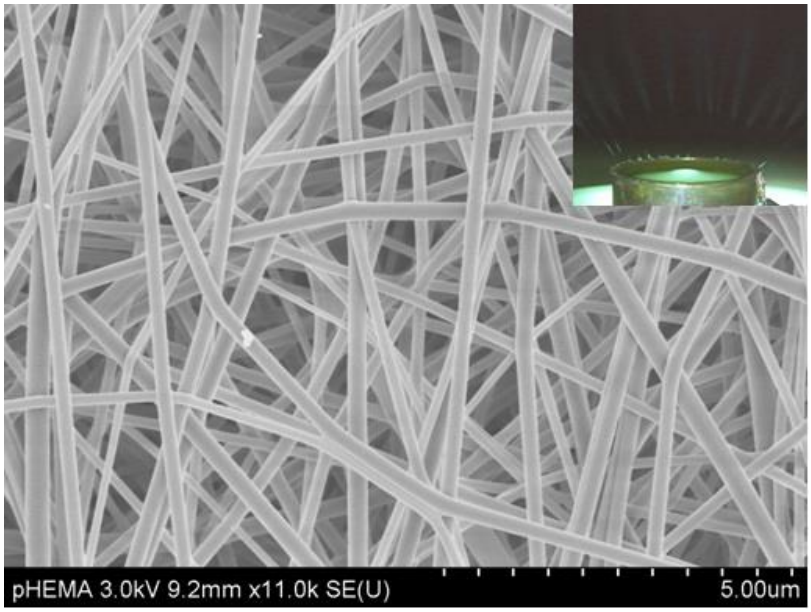

Figure 1. SEM picture of the PVA nanofibers obtained by the improved free surface electrospinning, Inset: a photograph of the electrospinning process.

MS5.P005
Quantitative crystallographic analysis of individual carbon nanofibers using high-resolution transmission electron microscopy and electron diffraction

M. Seyring[1], A. Simon[2], I. Voigt[2], U. Ritter[3], M. Rettenmayr[1]

[1]Friedrich Schiller University, Otto Schott Insitute of Materials Research, Jena, Germany
[2]Fraunhofer Institute for Ceramic Technologies and Systems (IKTS), Hermsdorf, Germany
[3]Technical University Ilmenau, Institute of Chemistry and Biotechnology, Ilmenau, Germany

martin.seyring@uni-jena.de

Introduction: High resolution transmission electron microscopy (HRTEM) and electron diffraction allow for a thorough crystallographic characterization of carbon nanofibers (CNF) leading to a more profound understanding of growth conditions and the resulting cup stacked structure. Up to now, the crystallographic interpretation of CNF structures has focused on orientation and shape of the (0 0 2) reflections in diffraction patterns [1-2]. The appearance of higher order reflections has not been interpreted, and consequently specific structural features of CNFs such as their turbostratic character have not yet been characterized in detail. The shape of reflections provides valuable and quantitative information about CNF structure, but this has so far not been exploited.
Objectives: Structural parameters of single CNFs are extracted by a newly developed method for quantitative analysis of diffraction pattern and power spectra of HRTEM images [3]. The performance of the method yields new insight into structural variations during growth and their relationship with processing parameters [3-5].
Method: The method is based on the quantitative analysis of radial and azimuthal profiles extracted from selected area electron diffraction (SAED) patterns, nano beam electron diffraction (NBED) patterns or power spectra of HRTEM images. The precise quantification of structural parameters, in particular cone apex angle 2θ, interlayer spacing d_{hkl}, undulation of graphene layers $\Delta\theta$ and average size of the coherently scattering domains L is described in Fig. 1 (see also Ref. [3]).
Results: The SAED patterns of the sides of the fiber axis in Fig. 2 display only (h k 0) and (0 0 2l) reflections, indicating the turbostratic character of the CNF. According to the graphitic stacking, the parallel alignment of the (1 0 0) and (1 1 0) reflections reveals a rotational disorder between successive graphene layers. The continuous intensity distribution of the (1 0 0) and (1 1 0) reflections implies a random rotation between successive graphene cones, suggesting a cup stacked instead of a helical wound structure. Fig. 3 displays the change of structural parameters along the axis of a single CNF. A clear trend of increasing interlayer spacing d_{002} and decreasing domain size *L* along the fiber axis is found, which may be related to the decrease of the catalysts performance during CNF growth [4].
Conclusion: Quantitative structural analysis of single CNFs is carried out in an automated procedure. For the first time a profound interpretation of CNF diffraction patterns is given, proving the rotational disorder of the turbostratic structure with a random rotation between successive graphene cones. A continuous increase of the interlayer spacing along CNF is found. Quantified structural parameters may serve to understand and optimize growth conditions for CNFs and to relate their resulting properties to their structural characteristics.

References:
[1] Kiselev et al. Carbon 42 (2004) p 149
[2] Van Gulijk et al. Carbon 44 (2006) p 2950
[3] Seyring et al. Carbon 116 (2017) p 347
[4] Simon et al. Carbon 90 (2015) p 25
[5] Simon et al. submitted

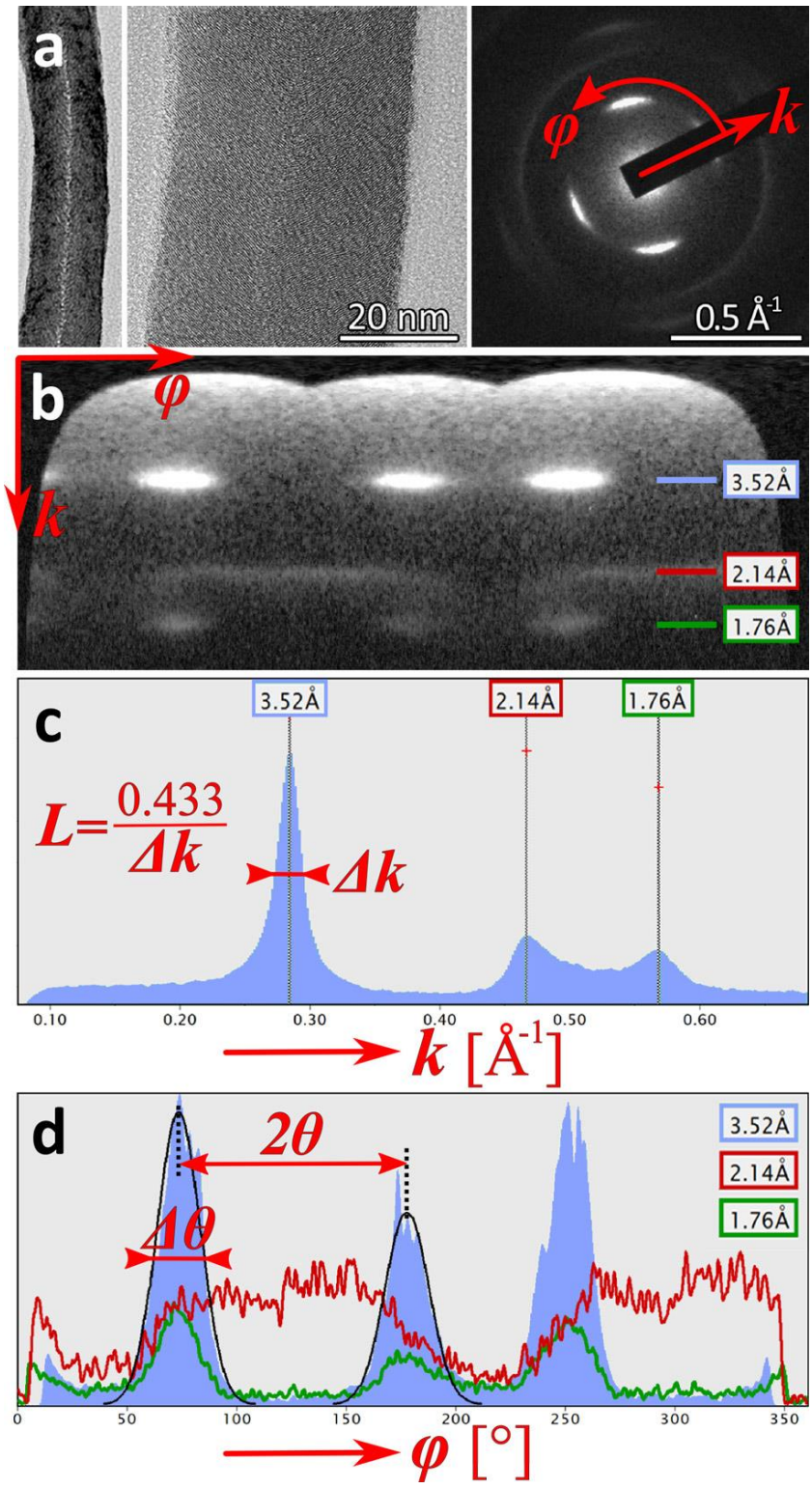

Figure 1. Principles of the diffraction pattern analysis: (a) bright field and HRTEM image together with SAED pattern including diffraction vector k and azimuthal angle φ, (b) azimuthal projection, (c) radial intensity profile with identified reflections and corresponding d_{hkl}, (d) azimuthal profiles of the identified reflections. The domain size L is calculated from the full width at half maximum of the reflections in (c) applying the Scherrer equation. Apex angle 2θ and azimuthal width Δθ are determined by Gaussian fits of the azimuthal profile.

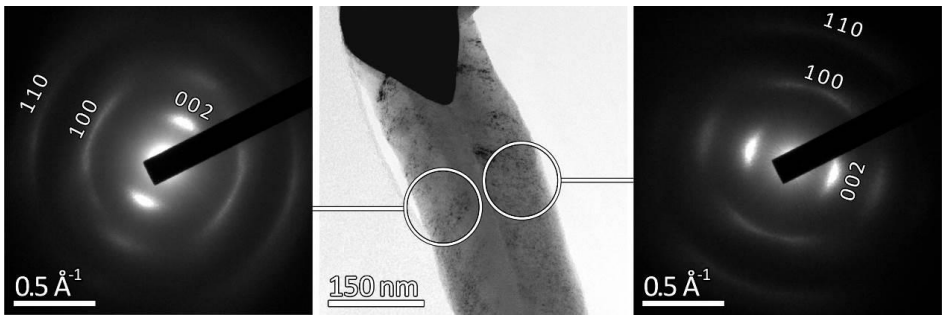

Figure 2. Detailed diffraction analysis of a single CNF: SAED pattern of left and right CNF side and bright field image of the corresponding probed areas.

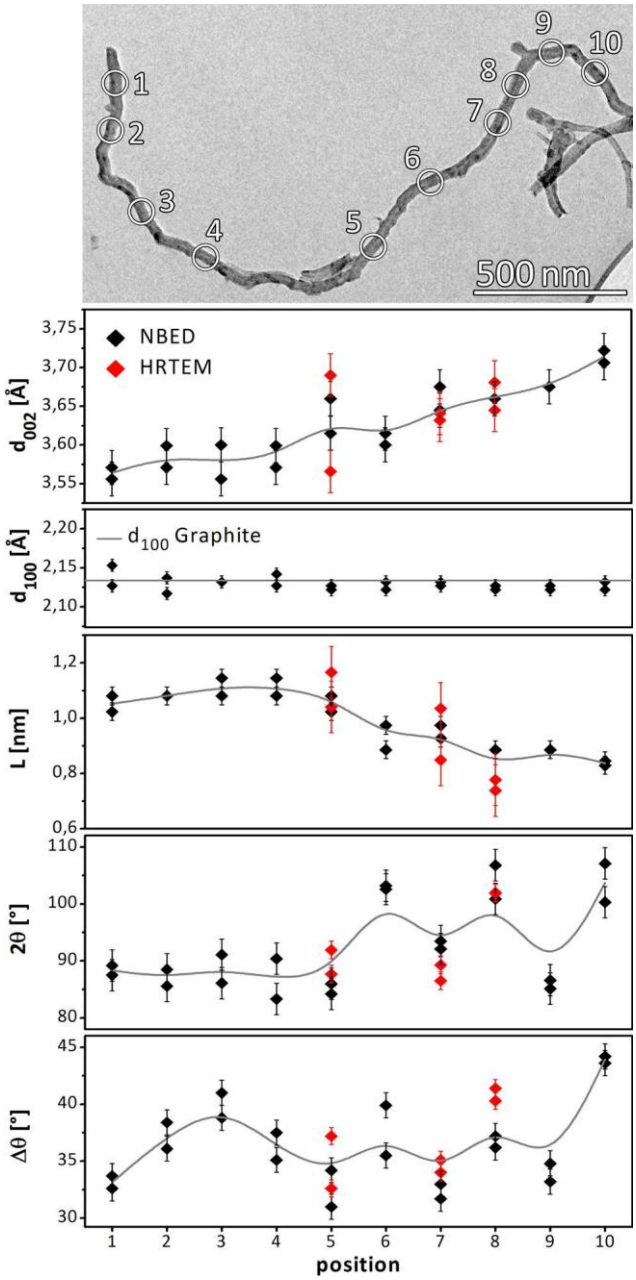

Figure 3. Variation of structural parameters along the axis of a single CNF: bright field image, interplanar spacing d_{002} and d_{100}, domain size L, apex angle 2θ and azimuthal width Δθ. The areas probed by NBED and HRTEM are numbered corresponding to position axis.

MS5.P006
In situ electrical probing of chains of carbon atoms in the TEM – on the way to the ultimate 1D conductor

F. Banhart[1], F. Ben Romdhane[1], A. La Torre[2], O. Cretu[3]

[1]University of Strasbourg, IPCMS, Strasbourg, France
[2]University of Nottingham, School of Chemistry, Nottingham, United Kingdom
[3]National Institute of Materials Science, MANA, Tsukuba, Japan

florian.banhart@ipcms.unistra.fr

The integration of an STM tip for electrical probing into a TEM specimen stage allows the measurement of the electrical properties of selected objects while they can be observed at high spatial resolution. Ultimately, such a system can be used to measure electrical currents through single-atom contacts. By establishing metal contacts at graphenic materials, welding the contacts at high current, and slowly retracting the contact tips, chains of carbon atoms can be unraveled from graphene layers (fig. 1) [1]. These carbon chains constitute the elementary building blocks of carbyne, which is the *sp1* hybridized one-dimensional phase of carbon [2]. Theoretical work has predicted that carbon chains are unusual conductors that may occur either as metallic cumulene with double bonds or as semiconducting polyyne with alternating single and triple bonds. Now, as it became possible to characterize them electrically in the TEM, these two electronic configurations can be distinguished.
Detailed studies have been undertaken to measure current-voltage characteristics of carbon chains under different contact geometries and different strain states [3]. Cumulene with ohmic behaviour as well as semiconducting polyyne were identified [4]. The comparison of the measured electrical characteristics with quantum conductance calculations showed that transport through narrow resonant states limits the conductivity clearly below 2G0 = 4e2/h as would be expected for two degenerate conduction channels with unit transmission. At increasing bias, sudden rises in current occur, showing the presence of conduction channels in certain energy windows.
By straining the chains, a transition from metallic cumulene to semiconducting polyyne was found (fig. 2), confirming a recent theoretical prediction, namely that the Peierls distortion, which would stabilize polyyne, is suppressed by zero-point vibrations in an unstrained chain. In the presence of strain, however, polyyne is favored by the Peierls instability. In non-symmetric contact configurations, i.e., between a carbon and a metal contact or between two carbon contacts of different type, a rectifying behavior is observed so that atomic carbon chains can act as diodes [4].
Further studies show that carbon chains have high current carrying capabilities (fig. 3) of several microamperes. By observing the rebounding of contacts after rupture, it is found qualitatively that carbon chains have an exceptionally high mechanical strength.

Acknowledgement:
Financial support by the LABEX program "Nanostructures in Interaction with their Environment", project ANR-11-LABX-0058 NIE is gratefully acknowledged.

References:
[1] O. Cretu, A. R. Botello-Mendez, I. Janowska, C. Pham-Huu, J.-C. Charlier, F. Banhart, *Nano Lett.* 13, 3487 (2013).
[2] F. Banhart, *Beilstein J. Nanotech*. **6**, 559 (2015).
[3] A. La Torre, F. Ben Romdhane, W. Baaziz, I. Janowska, C. Pham-Huu, S. Begin-Colin, G. Pourroy, F. Banhart, *Carbon* **77**, 906 (2014).
[4] A. La Torre, A. Botello-Mendez, W. Baaziz, J.-C. Charlier, F. Banhart, *Nature Comm*. **6**, 6636 (2015).

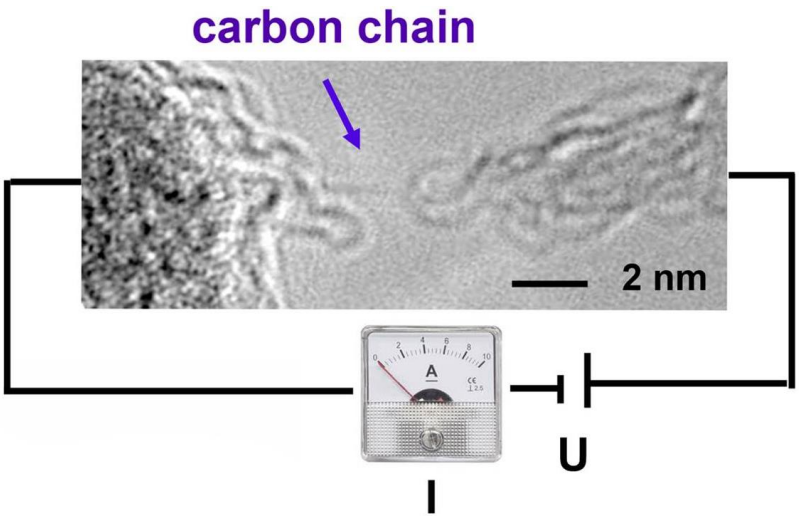

Figure 1. Principle of the experiment: the current through a carbon chain is measured at an applied voltage. The TEM image shows a typical carbon chain.

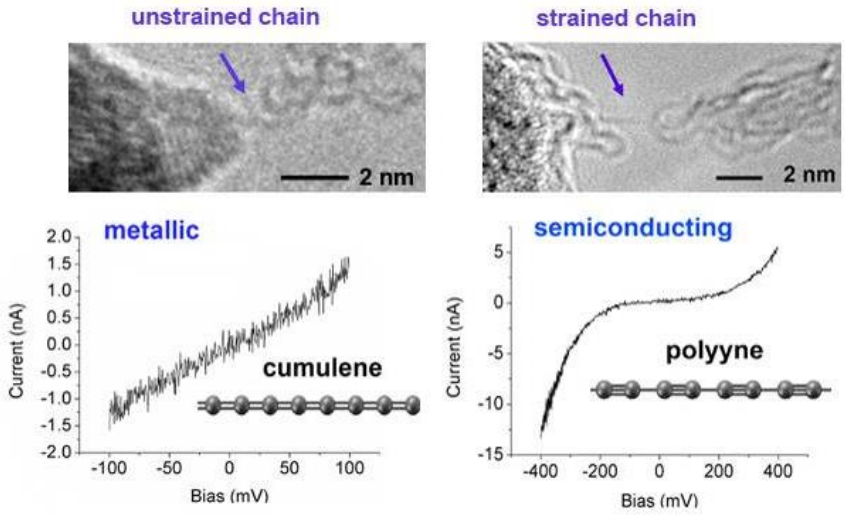

Figure 2. Current-voltage measurements of an unstrained cumulene chain with metallic behaviour (left) and a strained polyyne chain with semiconducting behaviour (right).

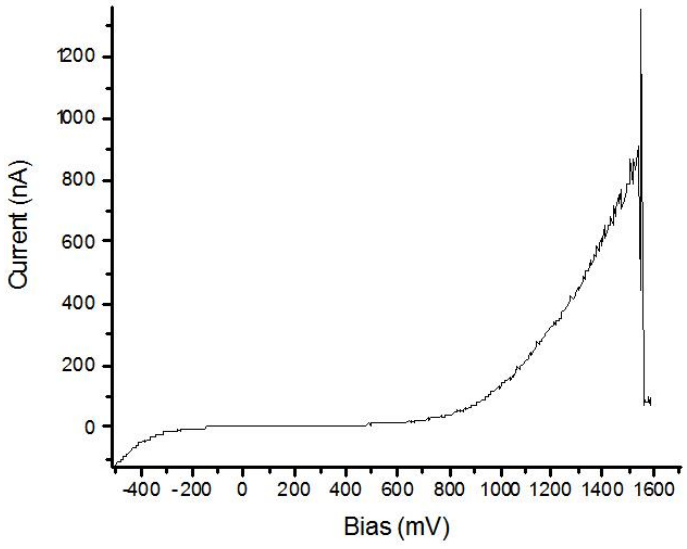

Figure 3. Current-voltage curve of a carbon chain that ruptured at a current of approximately 1.5 µA.

MS5.P007
Polymer fracture – 3D reconstructions as an analysis tool

M. Nachtnebel[1], C. Mayrhofer[2], P. Poelt[1]

[1]Graz University of Technology, Institute of Electron Microscopy and Nanoanalysis, Graz, Austria
[2]Graz Centre for Electron Microscopy, Graz, Austria

peter.poelt@felmi-zfe.at

Introduction: Rubber particle modified polymers are widely used materials for already a long time. Nevertheless, the fracture behaviour of such polymers is still a heavily discussed topic. Wu claimed already in 1988 that the transition between tough and brittle behaviour of rubber blends depends mainly on the surface-to-surface interparticle distance [1]. This was contested by many other researchers.
Objectives: Most of the microscopic investigations in connection with the fracturing of polymers are restricted to the imaging of the fracture surface after the sample is completely fractured. But from such images it is difficult to extract which microscopic processes were mainly responsible for the fracturing and which rather tend to prevent crack growth. In the investigations presented here the focus was put on the very early stages of the fracturing process, at forces / stresses far below the yield, where the formation of crazes / cracks / voids has just started. From 3D reconstructions of the fracture zone after tensile tests it should be possible to get correlations between e.g. particle distributions, interparticle distances and crack / void formation.
Materials and Methods: The fracture behaviour of three different types of polymeric blends was investigated. The matrix of all three consisted of polypropylene (PP), with the second phase being around 20 wt% of either ethylene-propylene-rubber (EPR) or linear low density polyethylene (LLDPE) filler particles (specimens by courtesy of Borealis Polyolefine GmbH, Linz, Austria). The tensile tests were stopped at 25% or 50% yield respectively. After staining of the samples an ultramicrotome 3View® (Gatan, Pleasanton, USA), mounted in the specimen chamber of an environmental scanning electron microscope Quanta FEG 600 (FEI, Eindhoven, NL), was used to perform serial sectioning and imaging. The 3D reconstructions of the cracks and filler particles (software: Avizo Fire, FEI, Eindhoven, NL) provide information about the crack surfaces and the position of the cracks related to the distribution of the rubber particles. A detailed description of the whole procedure can be found in [2].
Results: Whereas in EPR modified samples cracks / crazes appeared, in the LLDPE modified samples debonding of the particles from the matrix and void formation took place. To figure out whether the particle distribution and the surface-to-surface interparticle distance had any influence on the crack formation, 3D particle distance maps were calculated. The distribution of the interparticle distances gained from the 3D reconstructions differed substantially from those provided by just a few single 2D images (Fig. 1). Correlation of the distance maps with the position of the cracks proved that, at least at these early stages of fracturing, both the cracks and voids were formed preferentially between particles with short interparticle distances (Fig. 2). The reason could be strong stress enhancement between such particles [3].
Conclusion: 3D reconstructions of fracture zones of polymer blends can provide information about their fracture behaviour not directly accessible from single 2D images.

References:
[1] S. Wu, J. Appl. Polym. Sci. 35 (1998), 549-561.
[2] M. Nachtnebel, doctoral thesis, Graz University of Technology, 2017
[3] G. H. Michler, F. J. Baltá-Calleja, Nano- and Micromechanics of Polymers. Carl Hanser Verlag GmbH & Co KG, München 2012.

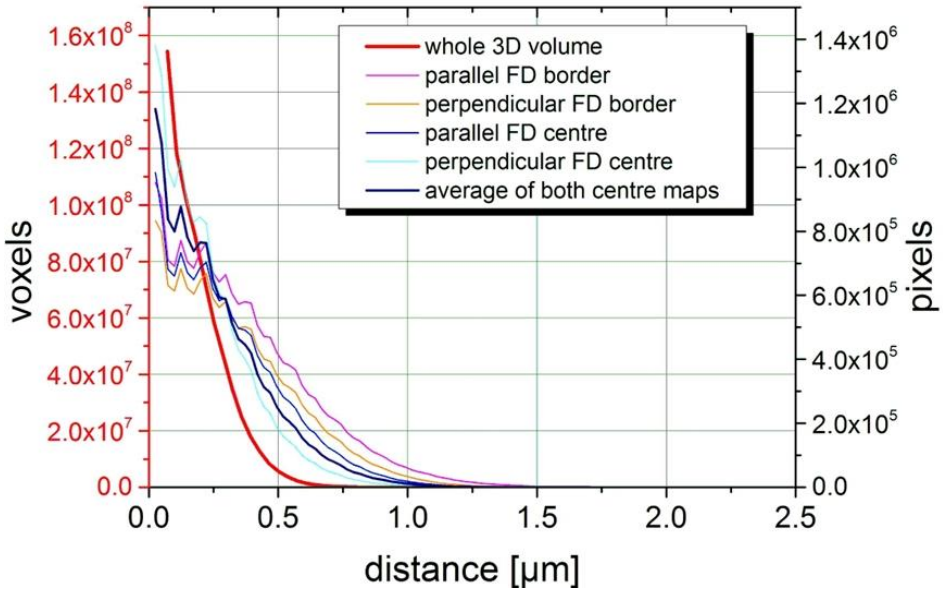

Figure 1. Number of pixel / voxel outside the particles as a function of the distance of these pixels / voxels to the nearest particle surface calculated from both 2D images and 3D reconstructions for an EPR modified sample. These are substitutes for the distribution of the interparticle distances.

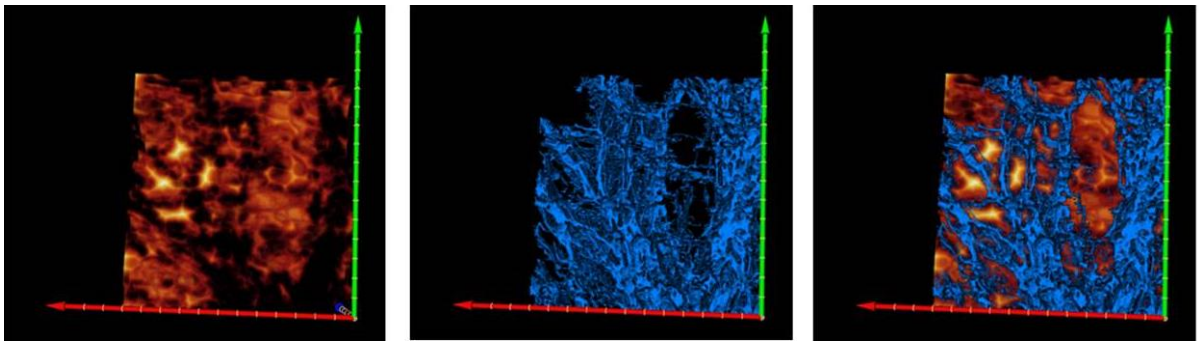

Figure 2. EPR modified sample, tensile test stopped at a force of 50% yield; left: 3D interparticle distance map, the higher the brightness, the larger the interparticle distances; centre: 3D map of the cracks; right: distance map and cracks merged (30.0x31.0x8.5 µm³).

MS5.P008
Polyethylene nanocrystals in aqueous dispersions

M. Krumova[1], S. Mecking[1]

[1]University of Konstanz, Department of Chemistry, Konstanz, Germany

marina.krumova@uni-konstanz.de

Aqueous polymer dispersions are widely used as paints or adhesives, being an environmentally friendly alternative to products which contain organic solvents. By aqueous catalytic polymerization, polyethylene (PE) can be obtained in the unusual morphology of nanoscale single crystals. The resulting stable nanocrystal dispersions are a unique and versatile system with a high potential for the development of new materials and represent at the same time an ideal model system for fundamental understanding of the particle formation and crystallization mechanisms.
Unprecedentedly small, hexagonally shaped nanoparticles of linear polyethylene of about 6 nm thickness and 25 nm lateral extension were obtained via catalytic polymerization of ethylene with water-soluble Ni(II)-complexes at very mild conditions (15°C, 40 atm). Crystallization thus occurs more than 100°C below the melting point of polyethylene. This extreme supercooling is not accessible by any other method used so far for the crystallization of PE. The single crystal nature and unique single lamellar structure of the particles was illustrated by cryo-TEM and SAXS analysis. The exceptionally high degree of order is thought to arise from the particular formation process: the growing chain is deposited on the crystal growth front, leaving no opportunity for entanglements or other disorder.
Larger polyethylene crystals formed by crystallization from dilute solution at low undercooling are known to have a diamond (lozenge) shape. To get insights into the mechanism of growth of the polymer nanocrystals enormous chemical effort for modifications of the catalyst complexes and control of their activity was required. A pressurizable sampling chamber was used to draw samples during the polymerization and enabled the analysis and monitoring of the particle formation in a time range of 30 sec to 24 h. We report here our TEM observations on the evolution of the particle shape from platelet-like hexagons via truncated lozenges into much larger lozenges, or more likely hollow pyramids.
To provide nanoparticles with defined shape and surface chemistry, also a novel concept based on the direct encoding of the crystal thickness via the polymer molecular structure was considered. A precise placement of hydrophilic groups in constant distances along the polymer chain can induce regular arrangement of the hydrocarbon chain segments. Carboxylic acid groups were chosen as branching groups, since these groups are bulky enough to be completely excluded from the crystalline segments and furthermore enable self-stabilization of nanoparticles in aqueous dispersions, when deprotonated with a base. The thicknesses of 5-6 nm and ca. 3 nm of the obtained nanoparticles with platelet-like shape correspond well with the defined distances of 44 and 20 methylene units between carboxy branches in the corresponding precisely functionalized polymers. Shape and thickness of the particles were evaluated from cryo-TEM images.

MS5.P009
Fabrication of amorphous diamond by ion implantation and thermal annealing

S. Rubanov[1], P. Olivero[2,3], A. Battiato[3], F. Scaffidi Muta [2], F. Picollo[2,3]

[1]University of Melbourne, Bio21 Institute, Melbourne, Australia
[2]University of Torino, Physics Department and "NIS" Inter-Departmental Centre, Torino, Italy
[3]National Institute of Nuclear Physics (INFN), Torino, Italy

sergey@unimelb.edu.au

Fig. 1. a) bright field cross-sectional TEM image and b) corresponding diffraction pattern of disordered carbon channel in diamond after 1 MeV He+ implantation.
The carbon K-edge EELS spectra from implanted channel and bulk diamond are shown in Fig. 2a. The prominent peak at 285 eV (π* peak) indicates the presence of sp2 bonded carbon in implanted channel after ion implantation. Thus, despite the suppression of swelling in disordered channels and large internal strain there is transition of some sp3 to sp2 bonds during amorphisation of diamond.
Fig. 2 EELS spectrum of carbon K-edge in implanted channels and bulk diamond after a) ion implantation and b) thermal annealing.
TEM study of implanted diamond after thermal annealing showed no change in structure of channels – they remained amorphous in structure without any traces of graphitisation. However EELS study of carbon K-edge revealed the absence of peak at 285 eV (Fig.2b). The disappearance of π* peak indicates the complete conversion to σ bonds and the formation of an amorphous 100 % sp3 bonded carbon.

References:
[1] N.R. Parikh et al., Single-crystal diamond plate liftoff achieved by ion implantation and subsequent annealing, Appl. Phys. Lett. 61 (1982) 3124-3126.
[2] R. Kalish et al., Ion-Implantation-Induced Defects in Diamond and Their Annealing: Experiment and Simulation, Phys. Stat. Sol. (a) 1974 (1999) 83.
[3] D.P. Hickey, K.S. Jones, R.G. Elliman, Amorphization and graphitization of single-crystal diamond - A transmission electron microscopy study, DRM 18 (2009) 1353.
[4] S. Rubanov and A. Suvorova, Ion implantation in diamond using 30 keV Ga+ focused ion beam, DRM 20 (2011) 1160.
[5] P. Olivero et al., Characterisation of three-dimensional microstructures in single-crystal diamond, DRM 15 (2006) 1614-1621.
[6] F. Picollo et al., Fabrication and electrical characterization of three-dimensional graphitic microchannels in single crystal diamond, New J. of Phys. 14 (2012) 053011.
[7] V.P. Popov et al., High-quality single-crystal diamond-graphite-diamond membranes and devices, Int. J. Nanotechnol., 12 (2015) 226.

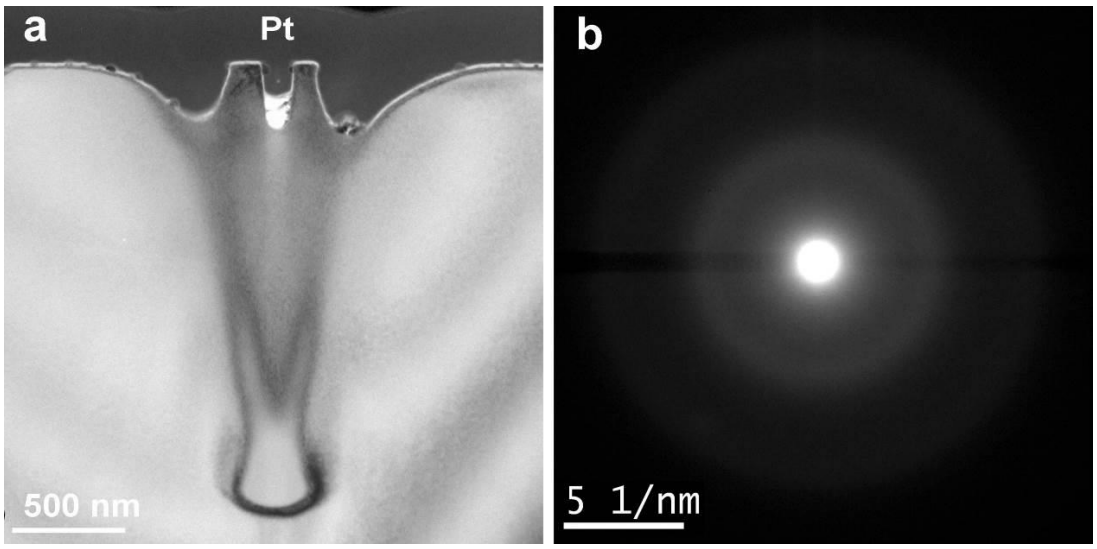

Figure 1. a) Bright field cross-sectional TEM image and b) corresponding diffraction pattern of disordered carbon channel in diamond after 1 MeV He+ implantation.

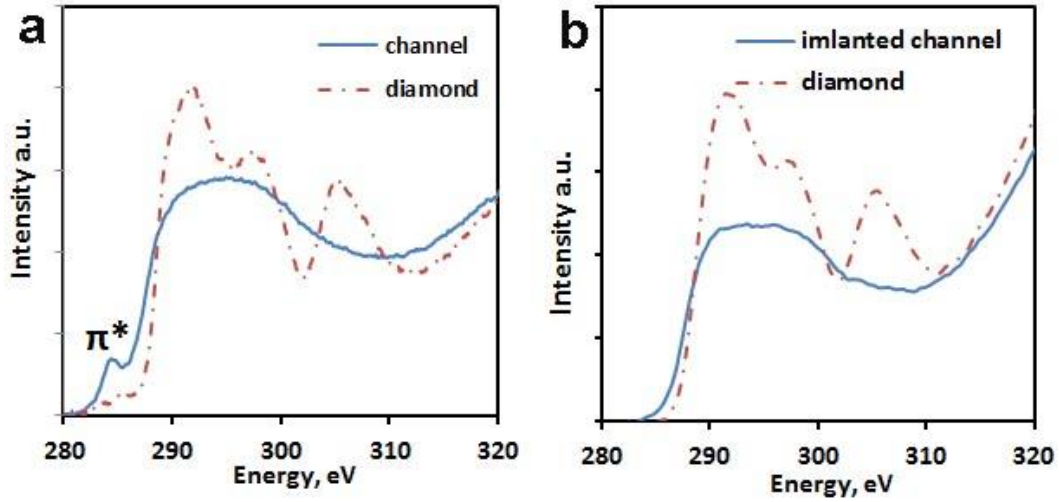

Figure 2. EELS spectrum of carbon K-edge in implanted channels and bulk diamond after a) ion implantation and b) thermal annealing.

MS5.P010
Compatibilization of polypropylene – polyethylene blends

E. Tocha[1], S. Vervoort[1], K. Jeltsch[2]

[1]Dow Benelux B.V., Terneuzen, Netherlands
[2]Dow Europe GmbH, Horgen, Switzerland

eatocha@dow.com

Introduction: Many plastic waste recycle streams are blends of various types of polypropylene (PP) and polyethylene (PE). When reprocessing these blends into products it is difficult to obtain good mechanical and optical properties due to the immiscibility of the components. Blend morphology is one of the governing factors for these properties. Therefore, morphology control is a key challenge when turning plastic waste into valuable materials.
Objectives: In this work, the effect of a novel PP-based olefin block copolymer compatibilizer on the morphology of PP – PE blends was investigated. SEM analysis was key to systematically study the effect of polypropylene compatibilizer on phase morphology over a broad range of compositions.
Materials and Methods: Two homopolymer PPs and polyethylene-co-octene (POE) based blends were examined in this study. The homopolymer PP were from Braskem selected to vary viscosity ratios. The polyolefin elastomers (POE) and the compatibilizer were from The Dow Chemical Company. The POE loading was studied between 10 wt% and 40 wt%. Blend morphology was characterized using SEM imaging of RuO_4 stained polished block surfaces at low accelerating voltages by means of backscattered electron (BSE) detector. This is an alternative characterization method to conventional TEM that allows easy and fast preparation of large sample cross-sections. Image analysis was performed on a large particle population in the range of 3000 to 15000 particles per sample.
Results: SEM analysis of compression-molded plaques showed that finer dispersions were obtained when adding even a small amount of compatibilizer. As an illustration, two examples of POE in PP dispersions are shown in Figure 1. At blend ratios up to 30 wt% dispersed phase, a droplet-in-matrix morphology was observed, while the blend with 40 wt% minor phase had a more co-continuous morphology. In both cases, the dispersed domains became smaller when the compatibilizer was added to the formulation. Moreover, study of coalescence demonstrated that presence of compatibilizer stabilized the phase dispersion and reduced coalescence.
Conclusion: A new propylene-based polymeric compatibilizer was used in blends of PP and POE. SEM study on the blends demonstrated that addition of the compatibilizer resulted in finer blend morphologies for droplet-matrix and co-continuous systems. The compatibilizer suppressed coalescence of droplets in PP/elastomer blends and helped stabilizing a fine morphology. Low compatibilizer level was sufficient for significant improvement. This is a very effective way to create valuable materials out of mixed recycle waste streams.

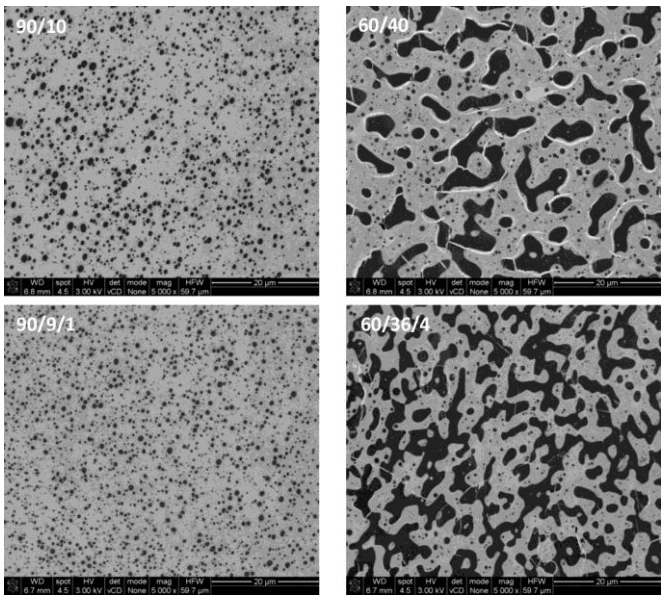

Figure 1. SEM micrographs of two series of PP/POE blends without (top row) and with (bottom row) polymeric compatibilizer.

MS5.P012
TEM morphological analysis of polyethylene and polyethylene-EPDM blends

A. Priante[1], M. Vighi[1]

[1]Versalis SpA, Mantova, Italy

alessia.priante@versalis.eni.com

Introduction: Image contrast in Transmission Electron Microscopy (TEM) is the result of variations in electron density between the phases or the structures of the specimen under test. Most polymers are composed of low atomic number elements, and thus they exhibit little variation in electron density. This variation is often not sufficient to provide an acceptable contrast in the image. [1] The primary methods that have proved useful in contrast enhancement are staining, generally by the addition of heavy atoms to specific structures. Staining involves the chemical or physical incorporation of electron dense atoms into one or more specific components of the polymer, in order to increase the density and thus enhance contrast. Staining agents depend on the type of polymer and of the properties investigated.
Kakugo, Sadatoshi H. and M. Yokoyama were among the first to successfully implement selective contrast of saturated olefin rubbers in polyolefins for TEM analysis, applying it specifically to binary blends of polypropylene (PP) / Ethylene - Propylene Rubber (EPR) and ternary PP/EPR/PE (Polyethylene) [2]. They implemented a technique that involves two steps: the use of a staining agent (OsO_4) and of an adjuvant (1,7 - octadiene).
In the present work the method developed by Kakugo et al. has been suitably modified and applied to the study of the morphology of pure PE samples crystallized under different processing conditions and to the analysis of blend of Very Low Density Polyethylene (VLDPE) and Ethylene Propylene Diene Monomer Rubber (EPDM). The blends were prepared by melt mixing of two different PE and EPDM and using different EPDM concentrations (wt.%).
Objectives: The development of innovative staining method for TEM analysis was performed in order to analyze the distribution of the elastomeric component in PE matrix and to investigate the morphology of the crystalline phase and the amorphous phase distribution in pure PE subjected to different processings.
Materials and Methods: VLDPE/EPDM blends with several rubber content were prepared at Basic Chemicals and Plastics Research Centre of versalis SpA in Mantova using a twin screw extruder. Two PE matrix with different melt flow rate and two EPDM with different molecular weight and Mooney viscosity were used. Pure PE samples were realized by film blowing and compression molding.
The method of Kakugo et al. has been modified by varying the adjuvant and its immersion/drying times, the concentration of the aqueous solution of OsO_4 and its method of use (exposure to vapors instead of immersion).
Results: After applying the innovative staining, TEM analysis at different magnifications was carried out. EPDM rubbers can be easily identified, their morphology is clearly distinguished and the relevant particle size can be measured. It is also possible to analyze their dispersion quality in the two matrices, identifying the best combination of PE/EPDM.
The method adopted, moreover, allows to investigate the crystalline morphology of pure PE and to identify the variation of the distribution of the crystalline part and amorphous part of the polymer processed with different techniques.
Conclusion: The staining method specially developed was particularly useful for the analysis of PE/EPDM blends and can be applied to saturated and amorphous olefinic rubbers. TEM micrographs show that the staining is successful: the rubber particles are clearly visible and distinguishable. Thanks to this technique, it is also possible to appreciate the morphological structure of polyethylene (distribution of crystalline/amorphous phase).

References:
[1] Linda C. Sawyer, David T. Grubb, Polymer Microscopy, Springer Netherlands, 2008.
[2] Kakugo M., Sadatoshi H. and Yokoyama M., Journal of Polymer Science Part C: Polymer Letters, Volume 24, Issue 4, pages 171–175, (1986).

MS5.P013
Correlative TEM-raman spectroscopy study of damage formation due to ion irradiation in MWCNT

S. Eswara[1], J. N. Audinot[1], T. Wirtz[1], P. Philipp[1]

[1]Luxembourg Institute of Science and Technology (LIST), Advanced Instrumentation for Ion Nano-Analytics (AINA), MRT Department, Belvaux, Luxembourg

santhana.eswara@list.lu

Targeted tuning of the structure and properties of carbon nanotubes (CNT) using ion irradiation is very attractive for technological applications. To understand the damage formation and evolution due to ion irradiation in multiwalled (MW) CNT, we used 25 keV Ne^+ and He^+ ion irradiation of controlled dose (10^{14} to 10^{18} ions/cm^2) and subsequently investigated the irradiated areas by TEM imaging and Raman spectroscopy. A new methodology (see Fig. 1) involving Au TEM grids was developed to ensure compatibility across the different techniques. The experimental results indicate a significant difference in the damage evolution between He^+ and Ne^+ irradiation. Furthermore, the sample thickness was found to play an important role in determining the extent of damage. TEM imaging suggests that the thicker areas are significantly amorphized, while thin areas (t < 10 nm) were found to be relatively undamaged with only very minor changes in comparison to pristine samples. For Ne^+ ion bombardment, no amorphisation can be observed probably because the damage is sputtered away from the top and bottom sides as fast as it accumulates. Raman spectroscopy (532 nm laser, spot size ~ 0.7 µm) of the ion irradiated areas was used to interpret the average overall damage in relation to the dose and the ion species. The experimental results were then compared with the Monte-Carlo (MC) simulations of ion-solid interaction by approximating the sample to a thin carbon membrane. In this presentation, we will describe the new correlative methodology that was developed for this study and discuss the experimental results from correlative TEM-Raman analysis of MWCNT under He^+ and Ne^+ irradiation together with insights drawn from MC simulations.´

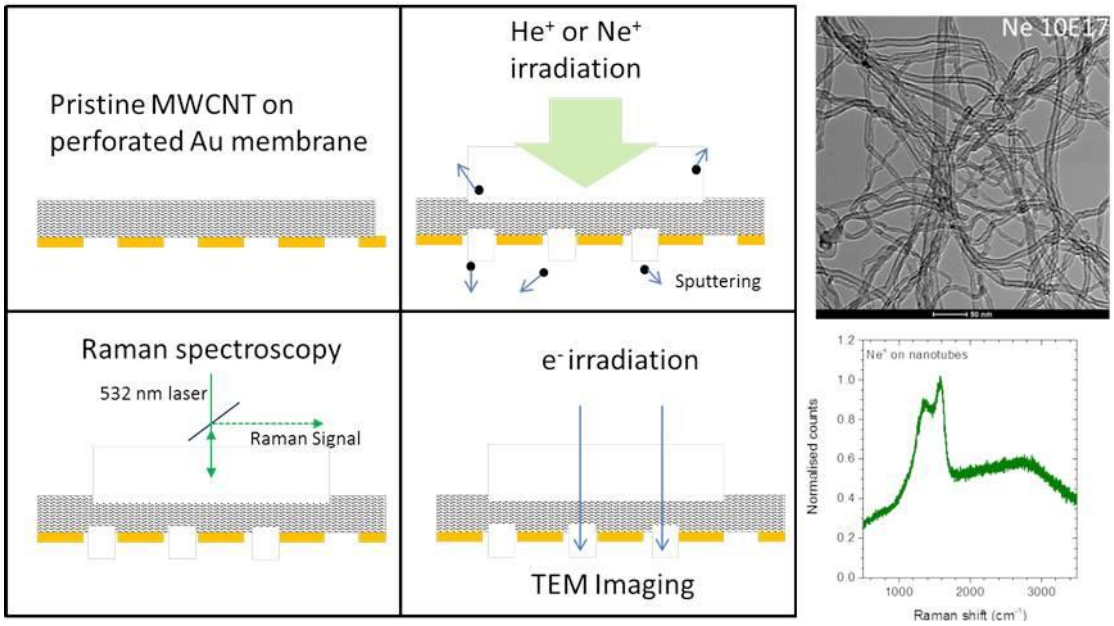

Figure 1. Schematic illustration of the analysis methodology alongside a TEM image and a Raman spectrum of region irradiated with NE° dose of 10^{17} ions/cm^2.

MS5.P015
Catalytic growth of carbon nanotubes on atomic layer deposited nickel layers – a FIB/SEM, EDX and ToF-SIMS study

P. Kshirsagar[1], B. Schröppel[1], D. Hähnel[2], A. Mohr[2], T. Wirtz[3], S. Eswara[3], C. J. Burkhardt[1]

[1]The Natural and Medical Sciences Institute (NMI) at the University of Tübingen, Reutlingen, Germany
[2]Plasma Electronic GmbH, Neuenburg, Germany
[3]Advanced Instrumentation for Ion Nano-Analytics (AINA), , Luxembourg Institute of Science and Technology (LIST), 41 rue du Brill, MRT Department, Belvaux, Luxembourg

pranoti.kshirsagar@nmi.de

Introduction: Scanning electron microscopy (SEM), focused ion beam (FIB), energy-dispersive X-ray spectroscopy (EDX) and secondary ion mass spectroscopy (SIMS) are powerful tools which altogether offer the opportunity for excellent correlative analysis. SEM enables imaging of the substrates at high magnification which is essential in studying nano- and micro-structures such as carbon nanotubes (CNTs). FIB-together with SEM, allows preparation and visualization of the cross section of samples in detail. EDX provides elemental analysis either by point spectrum or linescan or mapping. SIMS enables imaging of 3D elemental distributions with detailed information of the layered systems.
In this work correlative FIB / SEM, EDX and Time-of-Flight (ToF) SIMS analysis is performed to understand the indium tin oxide (ITO) modification during CNT growth process. CNTs are grown by thermal chemical vapour deposition (CVD) on atomic layer deposited (ALD) deposited Ni layers.
Materials and Methods: ITO is deposited on 1 mm thick float glass which is subsequently coated with a photoresist. Photolithography yields squares of ITO where Ni is deposited (see Figure 1) by means of plasma enhanced ALD (PEALD). Bis(ethylcyclopentadienyl) nickel(II) is used as Ni precursor which is subsequently oxidized (water plasma) and reduced (hydrogen plasma). The deposition is carried out at room temperature (< 50 °C) and at an increased temperature of 150 °C. The Ni thicknesses varied between 3 nm and 8 nm. Lift off is employed to obtain squares of Ni catalyst on ITO/float glass as base substrate. The CNT process involves two steps, namely, annealing of the catalyst and CNT growth [1]. Annealing is done in presence of ammonia for 10 min at 550 °C. After annealing, acetylene is introduced in the process chamber for 10 min.
Samples are analyzed with SEM / FIB, EDX and ToF SIMS before and after CNT growth. Selected results are included in the next section.
Conclusion: A thin ALD nickel was successful deposited on ITO. The Ni acted as catalyst for CNT growth with acetylene as carbon source in presence of ammonia at 550 °C. The reducing atmosphere and the high temperature resulted in decomposition of the ITO layer. This was confirmed by FIB/SEM, ToF-SIMS and EDX. ToF-SIMS also showed bottom growth of the CNTs.
These findings pave way towards understanding the layered system and the mechanism of catalytic growth of CNTs.

Acknowledgements:
This work is supported by the Federal Ministry of Education and Research (BMBF), PTKA-PFT, grant 02P14Z200 (M-ERA NET project C4HEALTH).

References:
[1] P. Kshirsagar et. Al., *Carbon-based transparent electrodes*, Carbon, 2017, Submitted
[2] S. Boxer et. Al*., Advances in imaging secondary ion mass spectrometry for biological samples*, Annu. Rev. Biophys. 38: 53-74, 2009.

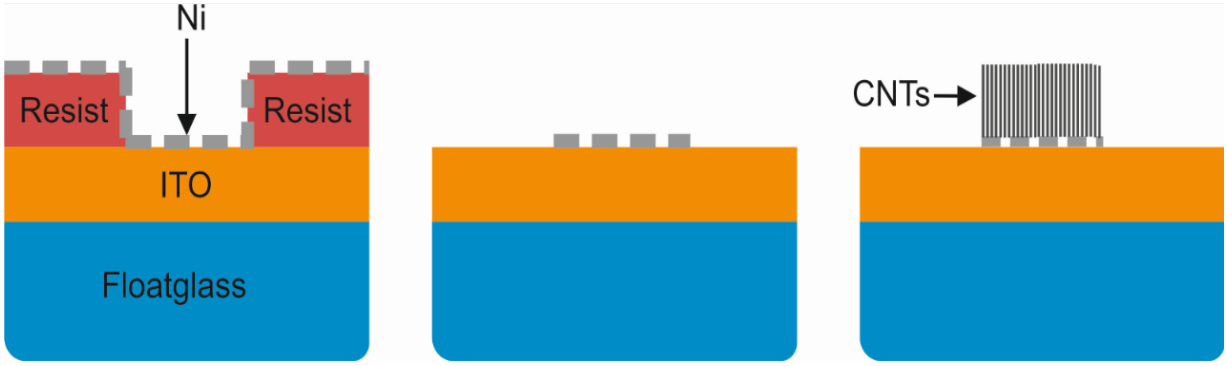

Figure 1. Schematic depicting the layered system. ALD Ni is deposited over the substrate and subsequently removed by lift off. CNTs are grown on the retained Ni. 1 SEM and FIB, sample 1.

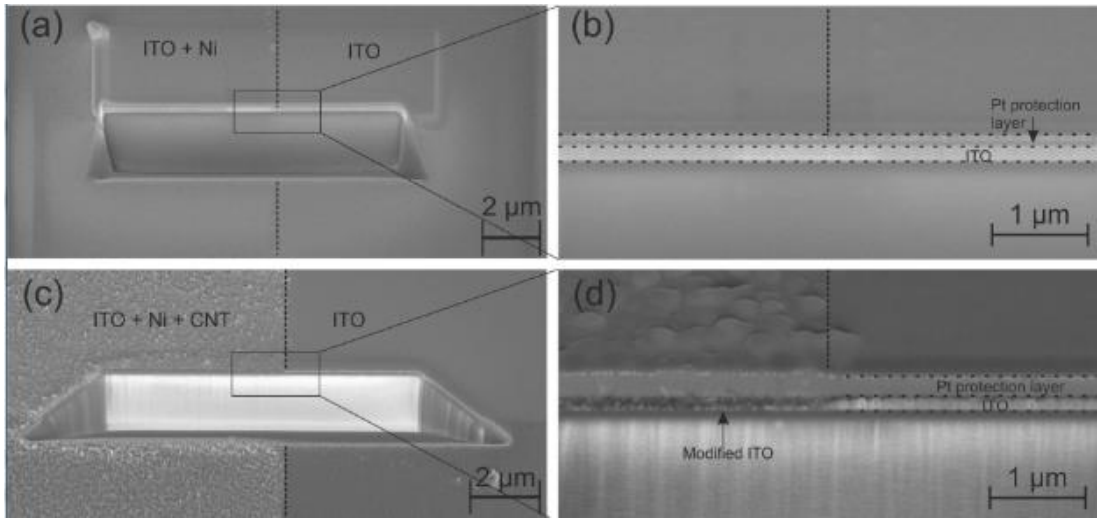

Figure 2. (a) FIB-cut made prior to CNT growth where the dashed line indicates the edge of the Ni square on ITO. **(b)** Higher magnification image of the region indicated in Figure 1 (a). Here the presence of ITO (bright layer) is clearly visible. **(c)** FIB-cut after CNT growth where the edge between regions with and without CNTs is distinct. **(d)** Higher magnification image of the region indicated in (c). On the left CNTs appear smudged due to the deposition of platinum protection layer, ITO appears to be modified beneath Ni and CNTs. 2 ToF-SIMS, sample 1.

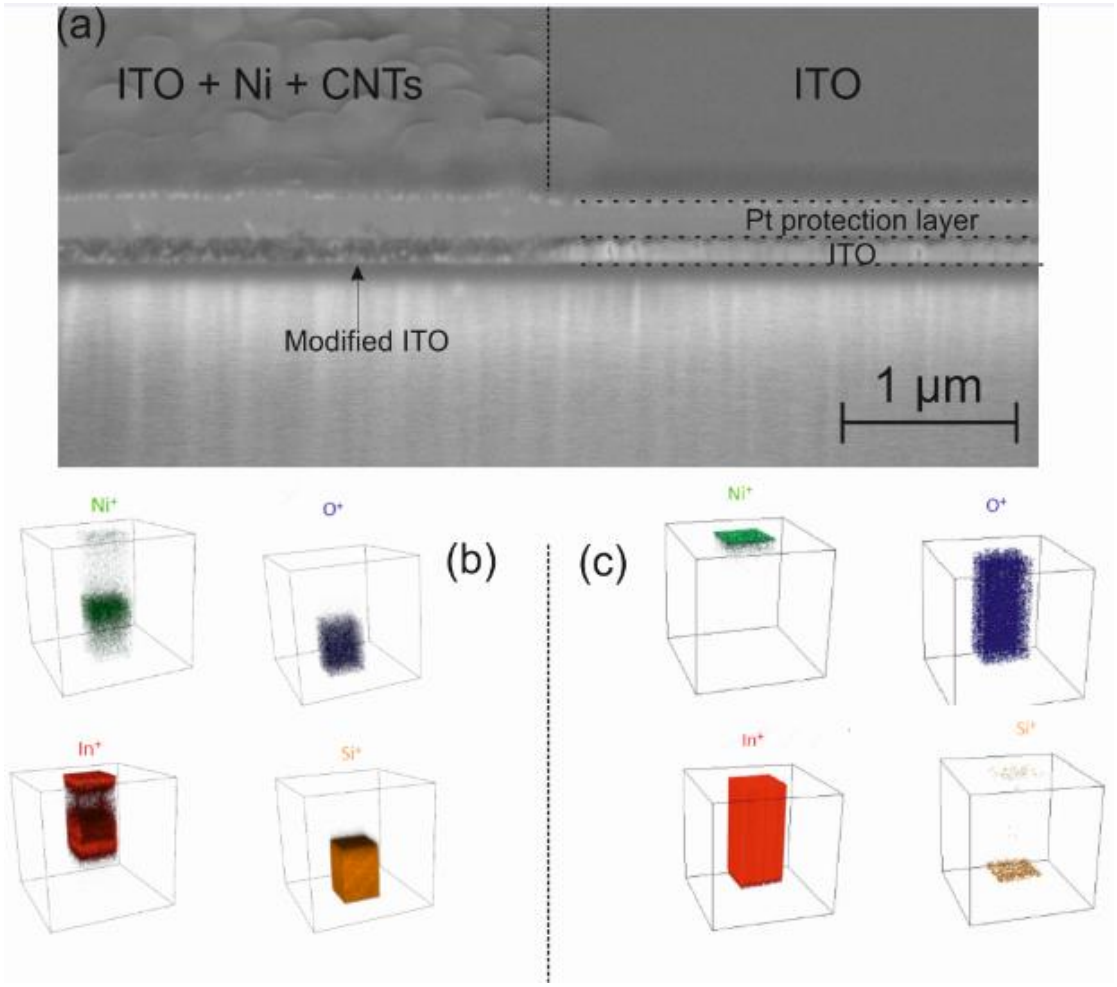

Figure 3. (a) FIB seen in figure 2 (d). Here the modification of ITO is clearly visible beneath Ni + CNTs. **(**b) and (c**)** are 3D tomograms of Ni+, O+, In+, Si+ of regions with and without Ni + CNTs, respectively. Field of view is 200 µm x 200 µm and the area nalysed is 60 µm x 60 µm. The Ni signal in panel (b) indicates the bottom growth mechanism of CNTs.

MS5.P017
Unraveling the structure of 2D polymers by low-dose imaging and diffraction

H. Qi[1], K. Liu[2], R. Leiter[1], Z. Zheng[2], X. Feng[2], U. Kaiser[1]

[1]Ulm University, Electron Microscopy Group of Materials Science, Ulm, Germany
[2]Dresden University of Technology, Center for Advancing Electronics Dresden and Department of Chemistry and Food Chemistry, Dresden, Germany

haoyuan.qi@uni-ulm.de

Introduction: Two-dimensional (2D) covalent crystals, which are laterally infinite, one to a few atom- or monomer-unit thin and freestanding, are promising candidates for next-generation electronics, optoelectronics, sensors, and membranes. Organic synthesis opens up an emerging route to the realization of novel 2D covalent crystals, i.e., crystalline 2D polymers (2DPs). Through self-assembly of well-defined building blocks, the crystal structure of the 2DPs can be engineered at the molecular- or even atomic-level [1]. However, the elucidation of the molecular structures of the synthetic 2DPs remains challenging due to the interaction of the imaging electrons with the specimen.
Objectives: In this work, low-dose selected-area electron diffraction (SAED) and aberration-corrected high-resolution transmission electron microscopy (AC-HRTEM) have been applied to investigate the crystallinity and to resolve the molecular structures of the synthetic 2D polyimide.
Materials and Methods: The 2D polyimide film was synthesized through Schiff-base condensation reaction at the air-water interface and subsequently transferred onto copper TEM grids for further characterization. Figure 1 shows the atomic structure of the 2D polyimide derived by functional-based tight binding (DFTB) calculation. It consists of a square lattice with lattice parameters of 3 nm. AC-HRTEM imaging and diffraction experiments were conducted on an image-side *C*s-corrected FEI Titan 80-300 microscope operated at 300 kV. Low-dose technique was applied to preserve the pristine structure of the 2DP. The electron dose rate for AC-HRTEM and SAED were as low as 200 $e^-/ Å^2 \cdot s$ and 0.15 $e^-/ Å^2 \cdot s$, respectively. For AC-HRTEM imaging, the spherical aberration coefficient C_s has been tuned to approx. -15 µm and the images were acquired using overfocus conditions.
Results: Figure 2 shows a bright-field TEM image of the 2D polyimide film. The crystalline domains appear dark on a bright background and the single-crystalline domain size is approx. 1µm. The SAED pattern reveals a square symmetry with the nearest reflections at 0.33 nm-1, corresponding to a square unit cell with lattice constants of 3 nm (Fig. 3). The molecular structure determined by SAED is in good agreement with the atomic model shown in Fig. 1. The positions of all reflections in Fig. 3 coincide wit$\sqrt{(h/d)^2+(k/d)_2}$, where *h* and *k* integers and *d* = 3nm, demonstrating the single-crystalline nature of the synthetic 2DP. The molecular structure of 2D polyimide was further confirmed by AC-HRTEM imaging (Fig. 4), from which the square lattice with 3 nm periodicity is clearly visible.
Conclusion: By using low-dose TEM techniques, the molecular structure of the synthetic 2D polyimide has been unambiguously determined. Atomic-resolution imaging of beam-sensitive 2DP, on the other hand, remains challenging and warrants further investigation.

Reference:
[1] H. Sahabudeen, H. Qi, B.A. Glatz, D. Tranca, R. Dong, Y. Hou, T. Zhang, C. Kuttner, T. Lehnert, G. Seifert, U. Kaiser, A. Fery, Z. Zheng and X. Feng, *Nature Communications*, 7 (2016) 13461

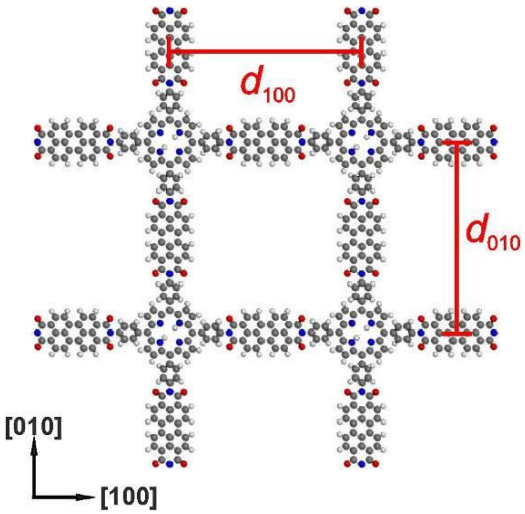

Figure 1. Atomic model of 2D polyimide. The 2DP shows a square lattice in [001] projection with d_{100} = d_{010} = 3nm.

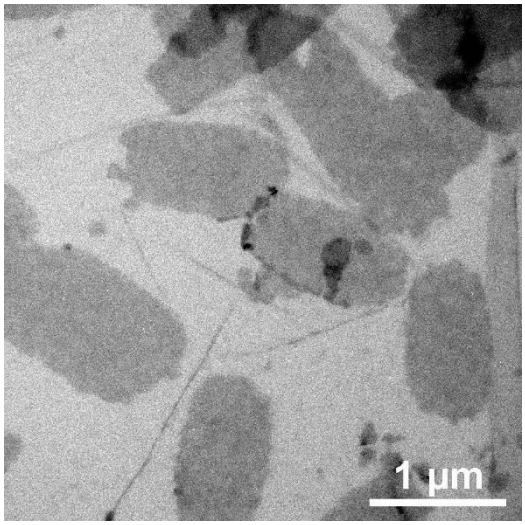

Figure 2. Bright-field TEM image of the free-standing polyimide film suspended over a copper grid. The crystalline domains appear dark on a bright background.

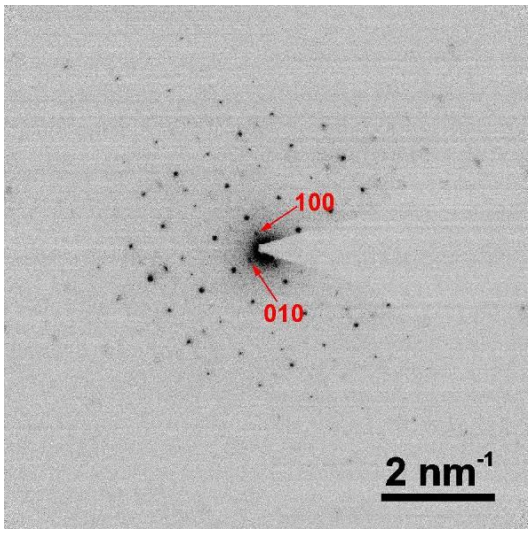

Figure 3. SAED pattern from the crystalline domain. The (100) and (010) reflections are at 0.33 nm^{-1}. Total electron dose: 1.5 e$^-$/ Å^2.

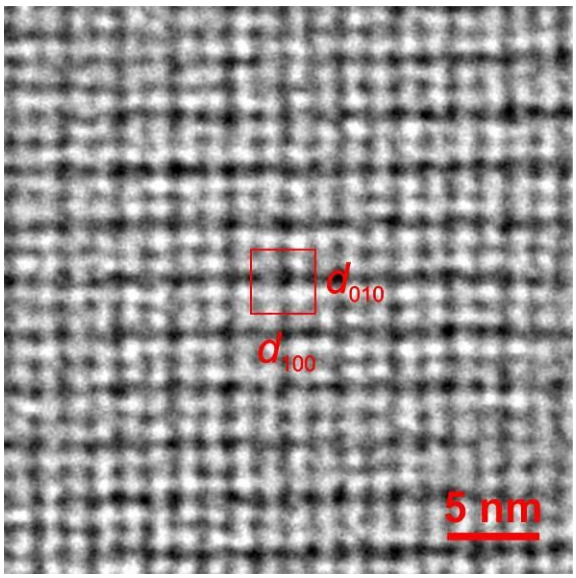

Figure 4. AC-HRTEM image acquired in [001] projection. Average background subtraction filtering was applied to remove noise. The square unit cell is indicated by the red box. Total electron dose: 1000 e^-/ $Å^2$.

MS5.P018
Optical microscopy and spectroscopy of ultrathin subsurface layer of organic polymer with nanometer resolution in the axial direction

Y. Vainer[1], Y. Sobolev[1], L. Kador[2]

[1]Institute of spectroscopy of the Russian academy of scienies, Molecular spectrocopy department, 142190, Russian Federation
[2]University of Bayreuth, Institute of physics and BIMF, Bayreuth, Germany

vainer@isan.troitsk.ru

We developed a new method of optical fluorescence microscopy of organic disordered solids (polymers, molecular glasses, etc.) with ultrahigh spatial resolution in axial direction. It is based on the detection of individual fluorescence images and optical spectra of single fluorescent molecules incorporated to subsurface layers of sample. For this purposes we developed a procedure for the controlled introduction of fluorescent molecules or directly upon the surface or into the immediate surface layer of sample under study on controllable depth (of nanometers and smaller).
We present the first results of our experimental study of spectral dynamics of subsurface layers of amorphous polyisobutylene. The fluorescent *tetra-tertbutylterrylene* molecules were used as spectral nanoprobes. The individual spectra and spectral histories of single fluorescent molecules embedded into the subsurface layer were recorded at 4.5 K as a function of diffusion depth.
In the case of probe molecules located directly on the surface, only broad-band fluorescence excitation spectra of ensemble fluorescent molecules was found. No zero-phonon lines (ZPLs) were observed closer to the polymer surface than 0.5 nm. At very small distances from the surface (< 1 nm), ZPLs became be detectable. The individual linewidths of ZPLs of fluorescent molecules near the surface were unusually large and strongly dependent on the distance from the surface. The temporal evolution of these spectra looked more random than in the case of molecules in the bulk of polymer. With increasing depth, the ZPLs become narrower and theirs temporal evolutions change to the behavior typical in the bulk. We found that this deviation becomes noticeable at distances less than about 20 nm from the surface.
The obtained results clearly demonstrate the existence near the surface of polymer ultrathin layer with faster and richer than in the case of bulky material dynamics. Possible physical reasons of the observed phenomena are discussed.

MS5.P019
Fabrication and characterization of nanofluidic devices for DNA analysis using a FIB-SEM instrument

P. Bayat[1], R. Blick[1], T. Volkenandt[2], F. Perez-Willard[2]

[1]UHH, CHyN, Hamburg, Germany
[2]Carl Zeiss Microscopy, Oberkochen, Germany

ifernand@physnet.uni-hamburg.de

Introduction: DNA optical mapping allows visualizing the genomic structure of individual molecules of DNA with high throughput [1]. For this, the molecules need to be stretched and elongated, for example inside nanochannels with lateral dimensions in the sub-100 nm range. These nanochannels have to be integrated in micro/nanofluidic devices, which are often complex systems with multi-scale structures of different sizes and depths. Large microchannels, typically several microns deep and wide, transport the fluids from reservoirs to the nanochannels. Nanochannels with dimensions in the sub-100 nm range (both depth and width) serve to stretch the single DNA molecules. And, to minimize the entropic barrier due to size mismatch, 3D funnel-like transient inlets are designed at the entrance of the nanochannels. These inlets pre-stretch the DNA molecules and prevent clogging. The fabrication of these multi-level devices requires multiple lithography-plus-etching steps, making the production expensive and very time consuming.
Objectives: Here, we propose a rapid prototyping method, by making a hard silicon stamp by focused ion beam (FIB), and using it for molding a polymer by UV-nanoimprint lithography (UV-NIL). Direct milling by FIB allows defining three dimensional structures with multiple lateral sizes and depths in a single step, without using resists. Once the stamp is ready, the complete fluidic devices are made in one single UV-NIL step [2]. In addition, the imprinted devices (polymer on glass) can be easily characterized in by SEM without coating them using charge neutralization techniques. This allows for non-destructive detailed nanochannel characterization prior to sample using in DNA experiments.
Materials and Methods: A cross-beam 550 from Zeiss has been used for sample fabrication and device inspection. A UV-nanoimprint tool from EVG has been used for sample replication. A UV-curable hybrid polymer (Ormostamp, from micro resist technology GmbH) has been used for device fabrication.
Results: Since the prototyping is fast and flexible, different channel sizes and configurations have been fabricated and tested, as shown in Figure 1 and Figure 2. Figure 1 shows short (5 um), very narrow (<100 nm) nanochannels combined with wider nanostructures for very fast optical mapping. Figure 2 shows meander-shaped nanochannels to allow for stretching of very long molecules [3]. The nanochannels imprinted on a polymer on glass substrate can be inspected by SEM using N2 charge compensation as shown in Figure 2 (b) and (c). Channels as small as 80 nm x 80 nm can be easily seen (Figure 2 (c)), and the samples can be used afterwards. The DNA molecules are driven through the channels by electrophoresis, and visualized in an inverted microscope, using a UV-fluorescent lamp and an ultra-high sensitivity CCD camera.
Conclusion: A method for rapid prototyping of multidimensional fluidic structures using a focused ion beam has been shown. The same instrument can be used for non-destructive polymer structure visualization.

References:
[1] E.T. Lam, Nature Biotechnology 30, 771–776 (2012)
[2] I. Fernandez-Cuesta et al., J. Vac. Sci. Technol. B29, 06F801 (2011).
[3] C. Freitag, Biomicrofluidics 9, 044114 (2015)

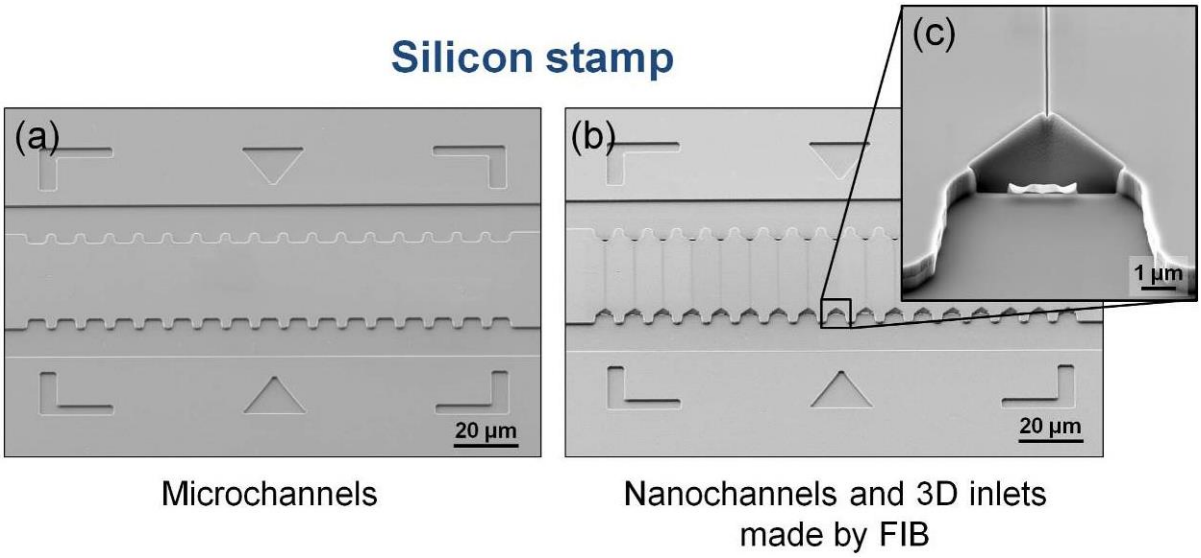

Figure 1. Fabrication of a silicon stamp. The microchannels are made, for example, by photolithography and reactive ion etching (a). Then, the nanochannels with different widths and depths, together with 3D funnel-like inlets are made by focused ion beam in one single step (b).

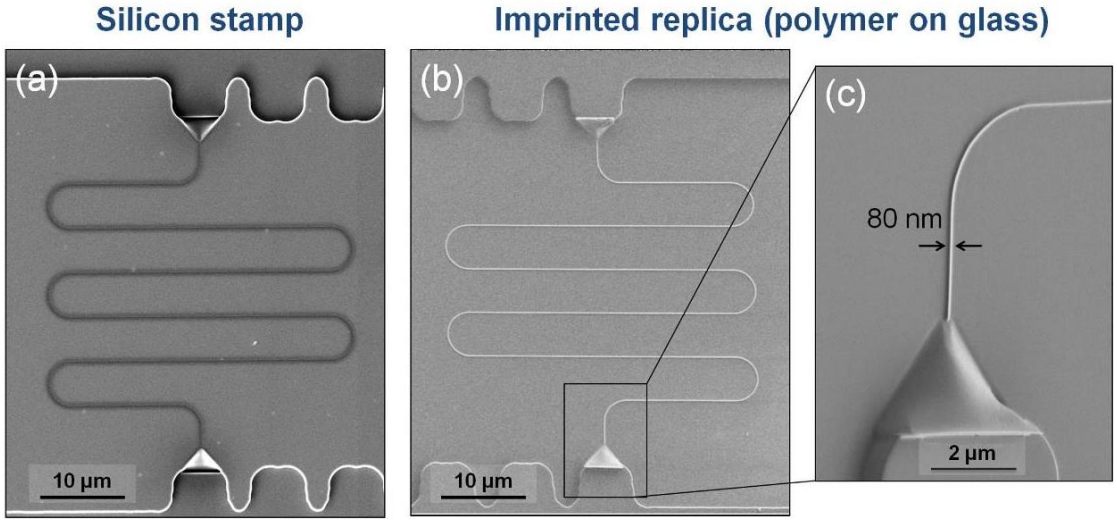

Figure 2. Non-destructive sample inspection and characterization using SEM and charge neutralization. A silicon stamp with meander nanochannels (a) is replicated by nanoimprint lithography (b, c). The imprinted sample consists of a polymer – Ormostamp – on a 3 mm thick glass or polycarbonate substrate. The nanochannels can be very easily imaged and visualized prior to DNA experiments.

MS5.P020
Nanoparticles for modification of vesicles

Z. P. Guven[1], F. Stellacci[1]

[1]EPFL, Materials Science, Lausanne, Switzerland

zekiye.guven@epfl.ch

Vesicles that are formed by self-assembly of lipids and certain polymers (called liposomes and polymersomes respectively) are used in several fields including drug-delivery, diagnostics, and storage. Liposomes are fragile and challenging to modify chemically, polymersomes on the contrary are too robust to have desired permeability. Recently, amphiphilic gold nanoparticles (NPs), having binary ligands (octanethiol (OT) and 11-mercaptundecanoic sulfonate (MUS)) on the surface in an ordered molecular arrangement, have been shown to penetrate lipid membranes following non-endocytotic pathways both experimentally and computationally.1,2 Additionally, the same NPs can transport a third type of molecule that is accommodated within the monolayer into the cell by employing the same pathway to cross the cell membrane.3

In this project, as inspired by the membrane proteins, we propose to introduce NPs into the membranes of vesicles as modification sites on the membranes. We aim to design NP-vesicle hybrid systems in which we perform chemical reactions and exchanges on the NPs present within the membranes.

Several NPs with different sizes, ligand types, and ratios on the surface have been synthesized to check their interaction with vesicles. We monitor the interaction of NPs with liposomes made of a zwitterionic lipid, dioleoylphosphatidylcholine (DOPC) after introduction of NPs by incubation. We use Cryo-electron microscopy (Cryo-EM) in order to assess whether an interaction between NPs and vesicles had taken place, qualitatively. To evaluate the interaction quantitatively, Flow Cytometry is used.

To determine the role of NP type on vesicle interaction, several NPs incubated with liposomes have been monitored in Cryo-EM. The images point that existence of negatively charged sulfonate group on the surface seems like the key element for NPs to interact with vesicles, regardless of NP size. To characterize the interaction in the system, we acquired multiple images of the sample with different tilting angles. Doing so, we could locate the NPs more precisely. Generally we observed that they locate on the surface of the membrane or in-between of multiple vesicles, Fig.1.

To investigate these NPs deeper, tomograms have been acquired and 3D reconstruction of tomogram showed the insertion of MUS:OT (30% OT) particles with a diameter of 5 ± 0.8 nm into DOPC bilayer, Fig.2.

We have also observed different arrangements of NPs during interacting, including formations of 'facet' and 'ring'. Fig, 3 shows the closed pack alignments of NPs in between or on the surface of vesicles. This behaviour was observed with various different kinds of NPs.

NPs show different kinds of interaction with vesicles depending on their size and ligand ratio. Having demonstrated that penetration of NPs into the bilayer depends on certain size and ligand ratio, the next step is to use these NPs to control inner environment of artificial vesicles through chemical reactions that happen at the NPs inserted in the membranes.

References:

[1] Verma, A. et al. Surface-structure-regulated cell-membrane penetration by monolayer-protected nanoparticles. Nat. Mater. 7, 588–595 (2008).

[2] Van Lehn, R. C. et al. Lipid tail protrusions mediate the insertion of nanoparticles into model cell membranes. Nat. Commun. 5, 4482 (2014).

[3] Jewell, C. M. et al. Oligonucleotide delivery by cell-penetrating striped nanoparticles. Angew. Chemie - Int. Ed. 50, 12312–12315 (2011).

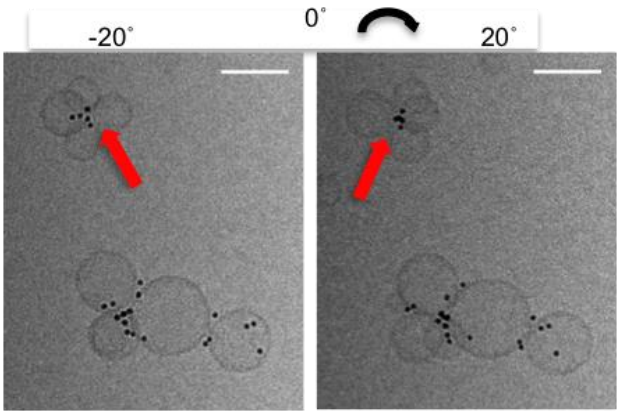

Figure 1. Cryo-EM images of tilting series of MUSOT (10%OT) particles with a diameter of 3.2 nm. showing NPs are in between of vesicles. The scale bars are 100 nm.

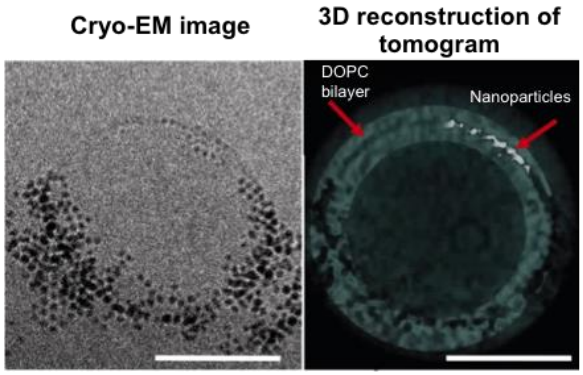

Figure 2. Cryo-EM image of DOPC vesicles with MUS:OT (30% OT) particles of 5 ± 0.8 nm diameter (left). A snapshot from 3D reconstruction of the tomogram of the same vesicle-nanoparticle system. (right) DOPC bilayer (black line inside green area) and NPs embedded in the membrane(lighter areas inside black bilayer) are indicated with arrows. The scale bar is 100 nm.

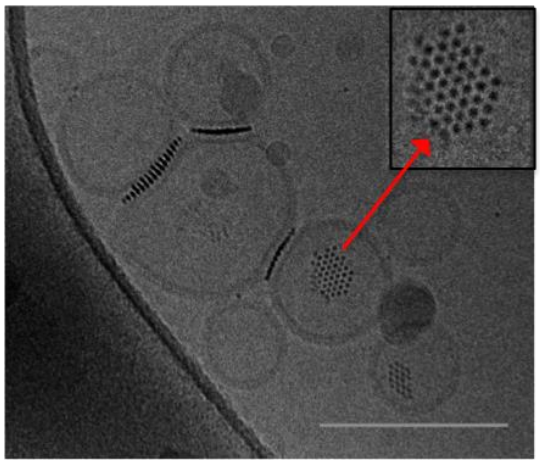

Figure 3. All Mercapto-ethanol sulfonate particles incubated with DOPC vesicles. The scale bar is 100 nm.

MS 6: Nanoparticles, 2D materials, nanocomposites and catalysts

MS6.001 invited
Growth Dynamics, stacking sequence and interlayer coupling in few-layer graphene revealed by in situ SEM

Z. J. Wang[1], R. Schlögl[1,2], M. G. Willinger[1,2,3]

[1]Fritz-Haber-Institut der Max-Planck-Gesellschaft, Anorganische Chemie, Berlin, Germany
[2]MPI für Chemische Energiekonversion, Heterogene Reaktionen, Mülheim an der Ruhr, Germany
[3]MPI für Kolloid- und Grenzflächenforschung, Kolloidchemie, Potsdam, Germany

zhujun@fhi-berlin.mpg.de

To date, the most widely applied method for the production of single-layer graphene (SLG) and vertically stacked few-layer graphene (FLG) is based on metal catalyzed chemical vapor deposition (CVD) growth. However, due to the difficulties that are related with the observation of atomically thin films growing at temperatures of around 1000 °C, there is a lack of information regarding the dynamics of graphene growth on metal catalysts under relevant catalytic CVD conditions.
We use a slightly modified commercial environmental scanning electron microscope (ESEM) in order to perform *in situ* investigations on chemical vapor deposition (CVD) growth of graphene on different metal catalysts. Since the experiments are performed in the chamber of the microscope, it is possible to observe complete CVD processes starting from substrate annealing through graphene nucleation and growth and, finally, substrate cooling in real time at nanometer-scale resolution without the need of sample transfer. The nucleation and growth of single layer graphene can be investigated at temperatures of up to 1000 °C, while at the same time, surface dynamics of the active metal catalyst can be studied. Growth on polycrystalline substrates reveals grain orientation dependent growth dynamics and catalytic activity [1]. Due to the high sensitivity of the secondary electron signal to changes in the work function and charge transfer at the surface, we are able to visualize different degrees of graphene-substrate coupling [2].
In the case of graphene growth on copper substrates, we present detailed investigations on the growth dynamics during different stages of growth as well as the effects of grain dependent substrate dynamics. In the case of graphene growth on platinum substrates, we will discuss growth kinetics of different layers in few-layer graphene. Real-time imaging under well-controlled atmosphere enables the observation of the response of in-plane dynamics in few-layer graphene to changes in the chemical potential of the atmosphere. By switching between graphene growth and hydrogen etching we were able to distinguish between graphene layers that are inserted underneath or forming on top of the initial layer. It is thus possible to abstract information about the stacking behavior of 2D materials directly from the observation of in-plane dynamics [3].
It will be shown how layer dependent etching rates can be used to determine the relative strength of the graphene-graphene and graphene-substrate interaction. Using anisotropic etching rates extracted from the evolution of the shape of islands and vacancy islands (holes) we were able to judge the strength of the interaction between graphene edges and steps at the Pt surface.
Finally, it will be highlighted that *in situ* scanning electron microscopy completes the spectroscopic data that is provided by complementary *in situ* techniques that provide spectroscopic information, such as ambient pressure X-ray and Raman spectroscopy. It adds the visual information and provides unprecedented and direct insights about the complex interplay between environment, catalyst and formed product.

References:
[1] Z.-J. Wang et al., ACS Nano **9** (2015), p. 1506.
[2] P. R. Kidambi et al., Nano Lett. **13** (2013), p. 4769
[3] Z.-J. Wang et al., Nature Communications **7**, Article number: 13256 (2016).

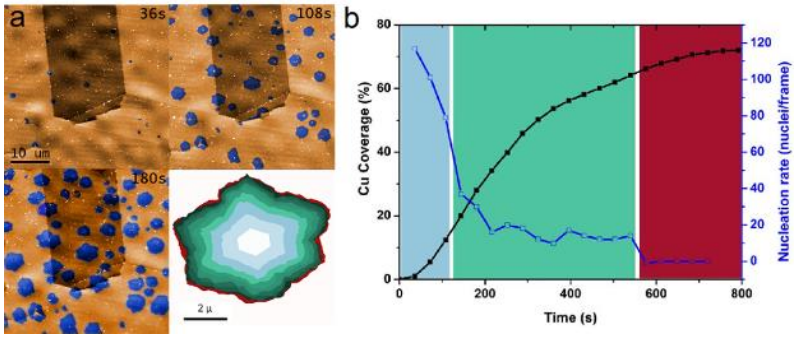

Figure 1. (a) Colorized snapshots taken during low-pressure CVD growth of graphene on copper at 1000°C. The growth and nucleation behavior can directly be abstracted from the recorded images as shown in (b).

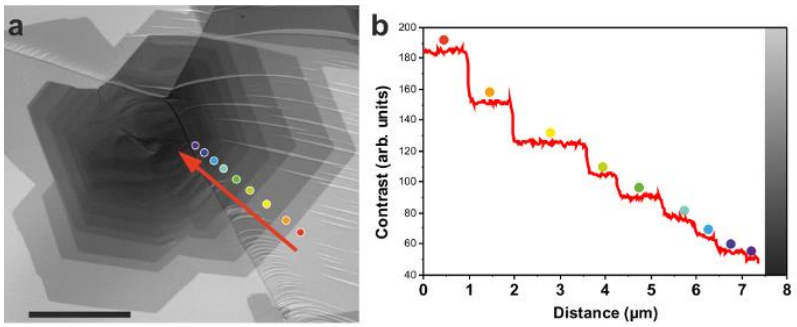

Figure 2. (a) Images of a few-layer graphene stack recorded during CVD growth. Up to 9 individual layers can be differentiated by their contrast (b). It is thus possible to study layer dependent growth kinetics.

MS6.002
Structural properties of nanoporous magnesium nitride aggregates

O. Wenzel[1], V. Rein[2], R. Popescu[1], C. Feldmann[2], D. Gerthsen[1]

[1]Karlsruhe Institute of Technology (KIT), Laboratory for Electron Microscopy (LEM), Karlsruhe, Germany
[2]Karlsruhe Institute of Technology (KIT), Institute for Inorganic Chemistry (AOC), Karlsruhe, Germany

olivia.wenzel@kit.edu

Magnesium nitride (Mg3N2) is a frequently used catalyst and has recently been pushed into the spotlight due to its potential use for hydrogen storage as well as in nuclear fuel recovery [1]. Despite its widespread use and recent growth in interest, there is a lack of experimental data concerning its physical properties [2]. Especially structural characterizations of porous Mg3N2 are needed in order to evaluate catalytic efficiency and hydrogen storage potential. The lack of data stems primarily from the difficulty in synthesizing a porous Mg3N2 and the high reactivity of the material with H2O.
This works focuses on structural and chemical characterizations of porous Mg3N2 aggregates, which were synthesized with a liquid –crystalline phase with liquid ammonia pioneered by Gyger et al. [3].
Electron microscopic techniques comprising high-resolution and scanning transmission electron microscopy (HRTEM, STEM), high-angle annular dark-field imaging (HAADF-STEM) and energy dispersive X-ray spectroscopy (EDXS) were performed to determine structure, morphology as well as chemical composition. The electron microscopy studies were supplemented by X-ray powder diffraction (XRD) to assess larger sample volumes. These studies were accompanied by gas adsorption measurements to characterize the pore structure and surface area. Synthesis and sample preparation took place under argon atmosphere with a Schlenk line, in a glove box and with the aid of a transfer TEM holder to protect the material from oxidation.
Fig. 1a shows the globular shape and the wavy boundaries of the aggregates. The average Mg/N ratio is 1.3 from quantitative EDXS analysis close to the stoichiometric composition of Mg3N2. The aggregate sizes ranges from approximately 45 nm up to 330 nm. The aggregates consist of small crystallites with an average size of 2.7 nm, as determined from HRTEM images (see Fig. 1b). Fast Fourier transform (FFT) analysis of HRTEM images (Fig. 1c) as well as XRD found the dominant phase to be Mg3N2 with an antibixbyite crystal structure (Ia-3) [4]. In HAADF-STEM, the aggregates appear to have a cloud-like structure, which may be an indication of nm-sized pores. In an approach to assess pore sizes, the distance between nanocrystallites in aggregates were measured and found to be between 0.5 and 6 nm with a median at 1.6 nm (Fig. 2b). A similar pore-size distribution was observed by gas adsorption measurements (Fig. 2a) which yield micropores and mesopores < 8 nm as shown in Fig. 2a with a large surface area of 176 m2/g.
This comprehensive study shows that the novel approach by Gyger et al. [3] produces high quality, nanoporous Mg3N2 aggregates, which have favorable properties for a variety of applications. The electron microscopic investigations are in accordance with gas adsorption measurements and XRD analysis, which validates these methods. Moreover, compositional and structure analysis with HRTEM, XRD and EDXS shows that the sample was successfully protected from contact with air during preparation and characterization.

References:
[1] L. Mei, J.-T. Li, Scr. Mater. 60 (2009) 141–143.
[2] K. Toyoura, T. Goto, K. Hachiya, R. Hagiwara, Electrochim. Acta. 51 (2005) 56–60.
[3] F. Gyger, P. Bockstaller, D. Gerthsen, C. Feldmann, Angew. Chemie. 125 (2013) 12671–12675.
[4] D.E. Partin, D.J. Williams, M. O'Keeffe, J. Solid State Chem. 132 (1997) 56–59.

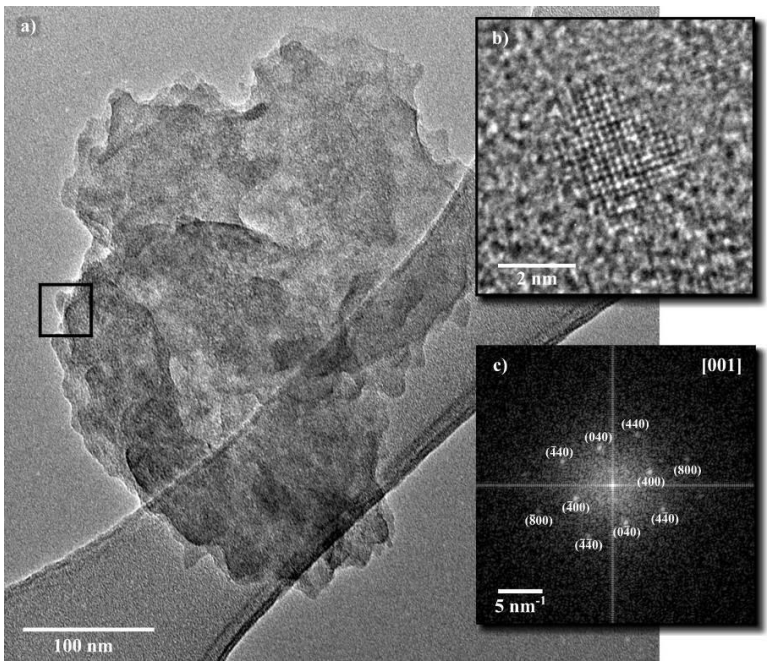

Figure 1. a) Overview TEM image of a Mg3N2 aggregate with a black square marking the magnified region shown in b). c) FFT of crystallite shown in b) with Miller indices for [001] zone-axis orientation.

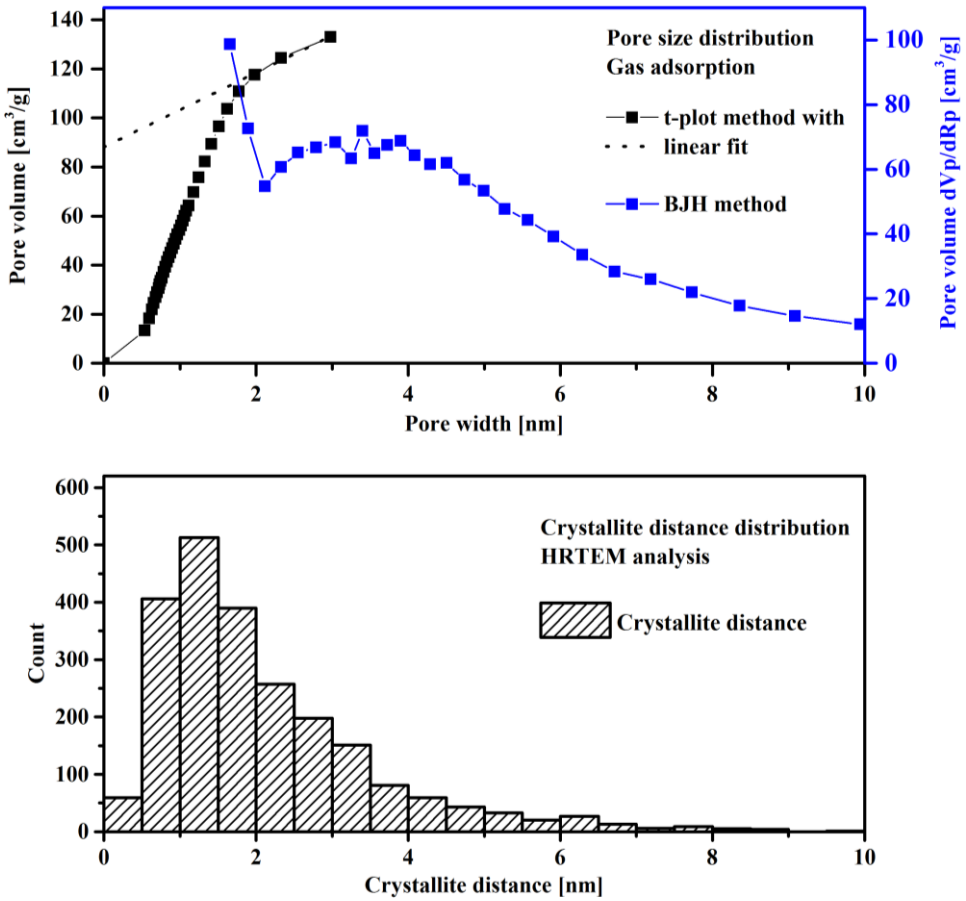

Figure 2. a) Pore-size distribution determined with gas adsorption using the t-plot (black) and BJH (blue) method. b) Distribution of crystallite distances measured from HRTEM images.

MS6.003
Analytical investigation of magnetic iron nitride nanoparticles by electron microscopy

M. Duerrschnabel[1], A. M. Zieschang[2], J. D. Bocarsly[3], H. J. Kleebe[1], R. Seshadri[3], B. Albert[2]
L. Molina-Luna[1]

[1]TU Darmstadt, Material- and Geosciences, Darmstadt, Germany
[2]TU Darmstadt, Eduard-Zintl-Institute of Inorganic and Physical Chemistry, Darmstadt, Germany
[3]University of California, Department of Chemistry & Biochemistry, Santa Barbara, CA, United States of America

duerrschnabel@geo.tu-darmstadt.de

Introduction: The search for alternative magnetic materials without rare earths has regained attention after the rare-earth crisis[1,2]. Iron nitrides exhibit exceptional physical properties[3-6], which are of use for several applications, e.g. magnetic recording media[6,7], catalysis[8], and biomedical applications[9]. These applications demand control over the particle size and corresponding magnetic properties on the nanometer scale. Iron nitride nanoparticles are cheap, exhibit a high saturation magnetization and a large magnetic moment[5,7]. The investigation of their magnetic properties is hampered due to the difficulty to prepare pure phases in sufficiently large quantities. A recent review discusses the synthesis and properties of iron nitrides at reduced dimensions[10]. The most important ferromagnetic iron nitrides are α''''-$Fe_{16}N_2$, ε-Fe_3N_{1+x} and γ''-Fe_4N. Analytic electron microscopy is of crucial importance for establishing structure-property correlations in these materials.
Objectives: A new approach was used to produce iron nitride (ε-Fe_3N_{1+x}) nanoparticles: the reduction of iron(II) bromide with elemental sodium in liquid ammonia at -78 °C, followed by annealing at 573 K[11]. As can be seen from Fig. 1 it is crucial to use the right annealing temperature otherwise a non-ferromagnetic phase is produced. The challenge was to characterize the nanoparticles in an oxygen-free environment by electron microscopy (Fig. 2a,b), since they are easily oxidized if exposed to ambient air. Core-shell iron nitride nanoparticles were prepared by slow oxidation and visualized using STEM-EELS (Fig. 2c). Afterwards, the particles were magnetically characterized[11] to establish together with the microscopic data a structure-property correlation.
Materials and Methods: A 200 kV Jeol JEM 2100F (scanning) transmission electron microscope (STEM) was used to determine the microstructure using a Gatan transfer specimen holder model 648. Electron energy-loss spectroscopy (EELS) was done using a Jeol ARM 200F microscope equipped with a Gatan Enfina EELS spectrometer. Further details can be found in [11].
Results: See Figures 1 and 2.
Conclusion: We succeeded in characterizing pure iron nitride (ε-Fe_3N_{1+x}) nanoparticles by electron microscopy, which were synthesized via an innovative method. Using the right annealing temperature was crucial for obtaining the correct ferromagnetic phase (ε-Fe_3N_{1+x}). A combination of STEM-EELS and magnetic measurements was used to establish structure-property correlations of iron nitride/iron oxide core-shell nanoparticles showing their exchange bias behavior.

References:
[1] Bourzac, Technol. Rev. **114** (2011), 58 – 63
[2] Kuz"min et al., J. Phys.: Condens. Matter **26** (2014), 064205
[3] Takahashi et al., Acta Mater. **60** (2012), 2054-2060
[4] Coey et al., J. Magn. Magn. Mater. **200** (1999), 405-424
[5[Kim et al., Appl. Phys. Lett. **20** (1972), 492-494
[6] Suzuki et al. IEEE Trans. Magn. **17** (1981), 3017-3019
[7] Matar et al., IEEE Trans. Magn. **26** (1990), 60-62
[8] Kramm et al., Phys. Chem. Chem. Phys. **14** (2012), 11673-11688
[9] Namiki et al., Acc. Chem. Res. **44** (2011), 1080–1093
[10] Bhattacharyya, J. Phys. Chem. C **119** (2015), 1601-1622
[11] Zieschang et al., Chem. Mater. **29** (2017), 621–628
[12] Jack Acta Crystallogr. **5** (1952), 404-411

The authors thank the LOEWE project RESPONSE funded by the Ministry of Higher Education, Research and the Arts of the Hessen state.

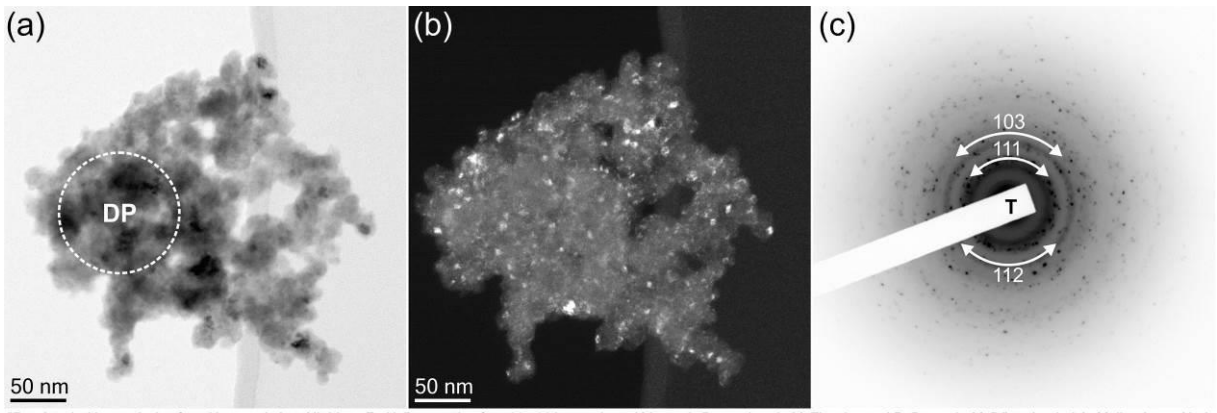

Figure 1. Diffraction contrast TEM images of a representative Fe_2N agglomerate annealed at 473 K: (a) bright-field and (b) dark-field. (c) Selected area diffraction pattern indexed according to the structure model of Fe_2N[12].

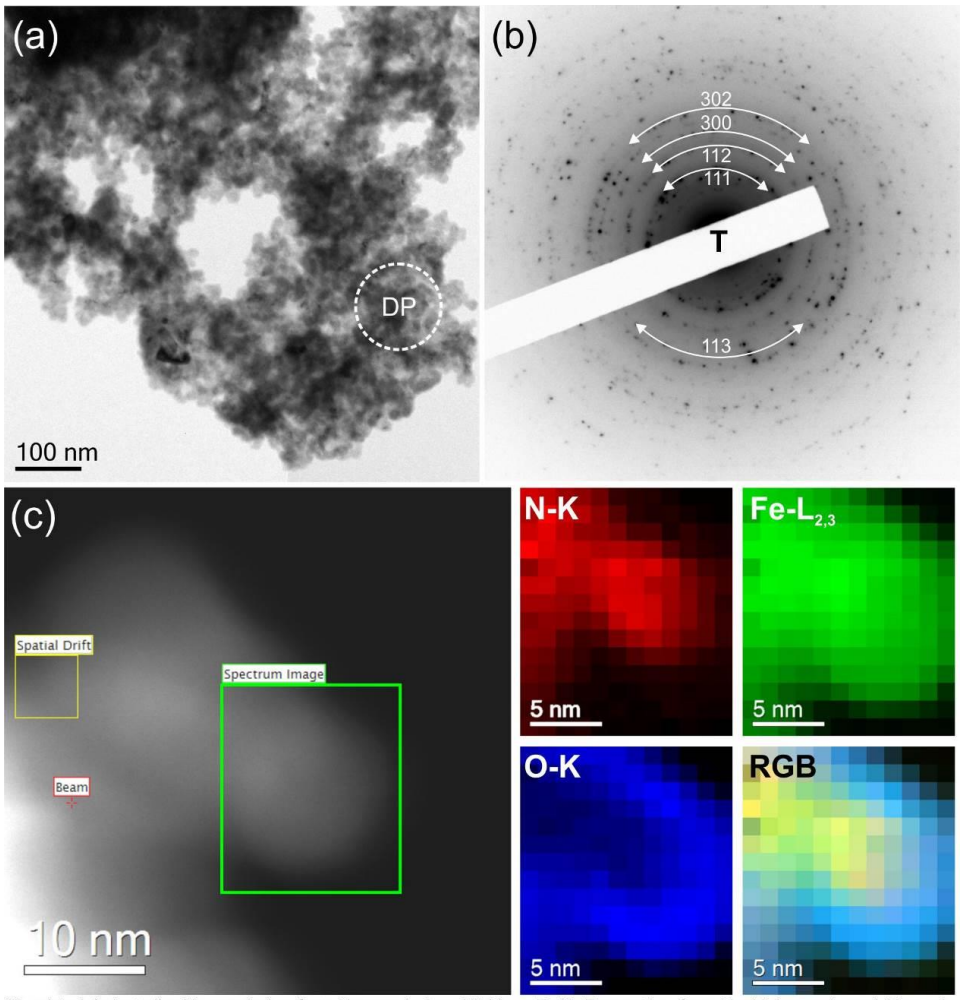

Figure 2. (a) TEM bright-field image of ε-Fe_3N_{1+x} nanoparticles. (b) Selected area diffraction pattern with rotationally averaged intensity in the inset. (c) STEM high-angle annular dark-field (HAADF) image with the mapped area being indicated by the green rectangle. The corresponding STEM-EELS elemental maps using the N-K, O-K and Fe-$L_{2,3}$ ionization edges are shown on the right in false color. Furthermore, a RGB map (red: N-K, green: Fe-$L_{2,3}$, blue: O-K) is shown.

MS6.004
Encapsulated calcium sulfate between graphene sheets studied by aberration-corrected HRTEM

T. Lehnert[1], M. Kinyanjui[1], G. Algara-Siller[1,2], F. Börrnert[1], U. Kaiser[1]

[1]Ulm University, Electron Microscopy Group of Materials Science, Ulm, Germany
[2]Fritz-Haber-Institut der Max-Planck-Gesellschaft, Department of Inorganic Chemistry, Berlin, Germany

tibor.lehnert@uni-ulm.de

Aqueous solutions between graphene offer the capability to study samples in a liquid environment in a Transmission Electron Microscope (TEM) [1]. Despite recent research [2, 3], the formation conditions of crystals in so-called graphene pockets in a TEM are still not fully understood. Here, we report about the crystallization of encapsulated $CaSO_4$ from a solution into the AII phase, studied by aberration-corrected high-resolution transmission electron microscopy (HRTEM).We describe the formation process with respect to the estimated pressure and temperature in a graphene pocket.
The samples were prepared with a drop of a $CaSO_4$ solution on top of a monolayer of chemical vapor deposited (CVD) graphene which was transferred to a TEM grid. Then a second grid with CVD graphene was placed on top of the first grid and let to dry, so that the graphene layers came into contact and encapsulate the remaining liquids in the graphene pockets.
We observed the in-situ crystallization of the quasi 2-dimensional $CaSO_4$ in the AII phase from a solution in the high vacuum (10^{-5} Pa) of a TEM, the prediction of van-der-Waals pressure for liquids encapsulated within graphene pockets is supported [2, 3] because pressures in the range of 10^6 Pa are necessary that the anhydrite can form [4].
Furthermore, the effect of temperature on nanoscale is discussed with respect to the crystallization of anhydrous $CaSO_4$. A temperature of 100 - 150 °C for the crystallization of $CaSO_4$ in the AII phase [4] is not likely, due to the efficient heat dissipation on graphene [5]. But it was predicted from theoretical calculations and confirmed with experimental data, that the transition temperatures decrease with smaller nanocrystal sizes [6, 7] Therefore it can be concluded that the transition temperature for the crystallization to the AII phase on the nanoscale is shifted to approximately room temperature, which is a typical temperature in the TEM.

References:
[1] H.-G- Liao and H. Zheng; Annu. Rev. Phys. Chem. 2016. 67:719-47
[2] E. Khestanova, F. Guinea, L. Fumagalli, A.K. Geim and I.V. Grigorieva; Nature Communications, 7:12587, 2016
[3] K.S. Vasu, E. Prestat, J. Abraham, J. Di, R.J. Kashtiban, J. Beheshtian, J. Sloan, P. Carbone, M. Neek-Amal, S.J. Haigh, A.K. Geim and R.R. Nair; Nature Communications, 7:12168, 2016
[4] P.W. Mirwald; J. Chem. Phys. 128, 074502 (2008)
[5] A.A. Balandin, S. Ghosh, W. Bao, I. Calizo, D. Teweldebrhan, F. Miao, C.N. Lau, Nano Letters, vol. 8, no. 3, pp 902-907, (2008)
[6] H. Li, P.D. Lan, X.B. Zhang, M. Li; Materials Chemistry and Physics 137, 1007-1011 (2013)
[7] H. Jiang, K. Moon, H. Dong, F. Hua, C.P. Wong; Chem. Phys. Lett. 429, 492-496 (2006)

MS6.005
Exploring and tailoring MXenes – a new family of 2D materials

P. Persson[1], I. Persson[1], J. Palisaitis[1], J. Rosén[1]

[1]Linköping University, Department of Physics, Linköping, Sweden

per.persson@liu.se

Introduction: The discovery of 2D materials is now one of the strongest generators for new research in the field of materials science. Besides Graphene, there is a large number of other 2D materials such as h-BN, MoS2 and WS2. Essentially, all of these materials are derived from thinned down or delaminated versions of layered bulk structures. Beyond these materials a new family of 2D solids were discovered a few years ago; MXenes1,2. MXenes originate from a large family of naturally nanolaminated materials known as MAX phases, where *M* is a transition metal, *A* a group A element and *X* is either C or N, following the general formula Mn+1AXn. The MXenes are best described as *2D-conductive clays*3, and can be produced as thin films or in bulk, and exhibit a significant potential for applications in electrochemistry, water filtration, hydrogen storage etc.
Objectives: While MXenes are already finding their way towards applications, little is known on their fascinating structural versatility and further functionalization and modification by adatoms and molecules. With this contribution, the purpose is to highlight the status of current research at the atomic level.
Materials and Methods: MAX samples were produced either by high temperature furnace annealing (1500°C) of transition metal/ carbide powders in a vacuum environment, or by PVD sputtering from elemental targets at UHV conditions on alumina substrates. MXenes were produced from the powders and films by chemical etching using HF. Electron microscopy of the resulting materials were performed on the Linköping double corrected Titan3 60-300, predominantly using HAADF-STEM, in combination with simulations using Dr. Probe.
Results: The presentation comprises results from the large array of tailored structures that were formed by *intentional* manipulation of the inherent MXene structure, including out of plane and in plane ordering of different transition metals or vacancies. Additionally, the surface functionalization by single O and F adatoms and their thermal properties were investigated. The investigation shows a preferred site competition between adatom species, as well as surface ordering and adatom desorption at elevated temperatures.
Conclusion: It is shown that the MXene family constitute a highly versatile 2D structure, with a significant potential for intentional tailoring and property tuning. In parallel, the surface functionalization of MXenes is similarly flexible and enables further tuning of the material properties.

References:
[1] M. Naguib, M. Kurtoglu, V. Presser, J. Lu, J. Niu, M. Heon, L. Hultman, Y. Gogotsi, M.W. Barsoum, Adv. Mater. 23, 4248 (2011).
[2] M. Naguib, V. N. Mochalin, M. W. Barsoum, Y. Gogotsi, Adv. Mater. 26, 992 (2014).
[3] M. Ghidiu, M. R. Lukatskaya, M. Q. Zhao, Y. Gogotsi, M. W. Barsoum, Nature 516, 78 (2014).

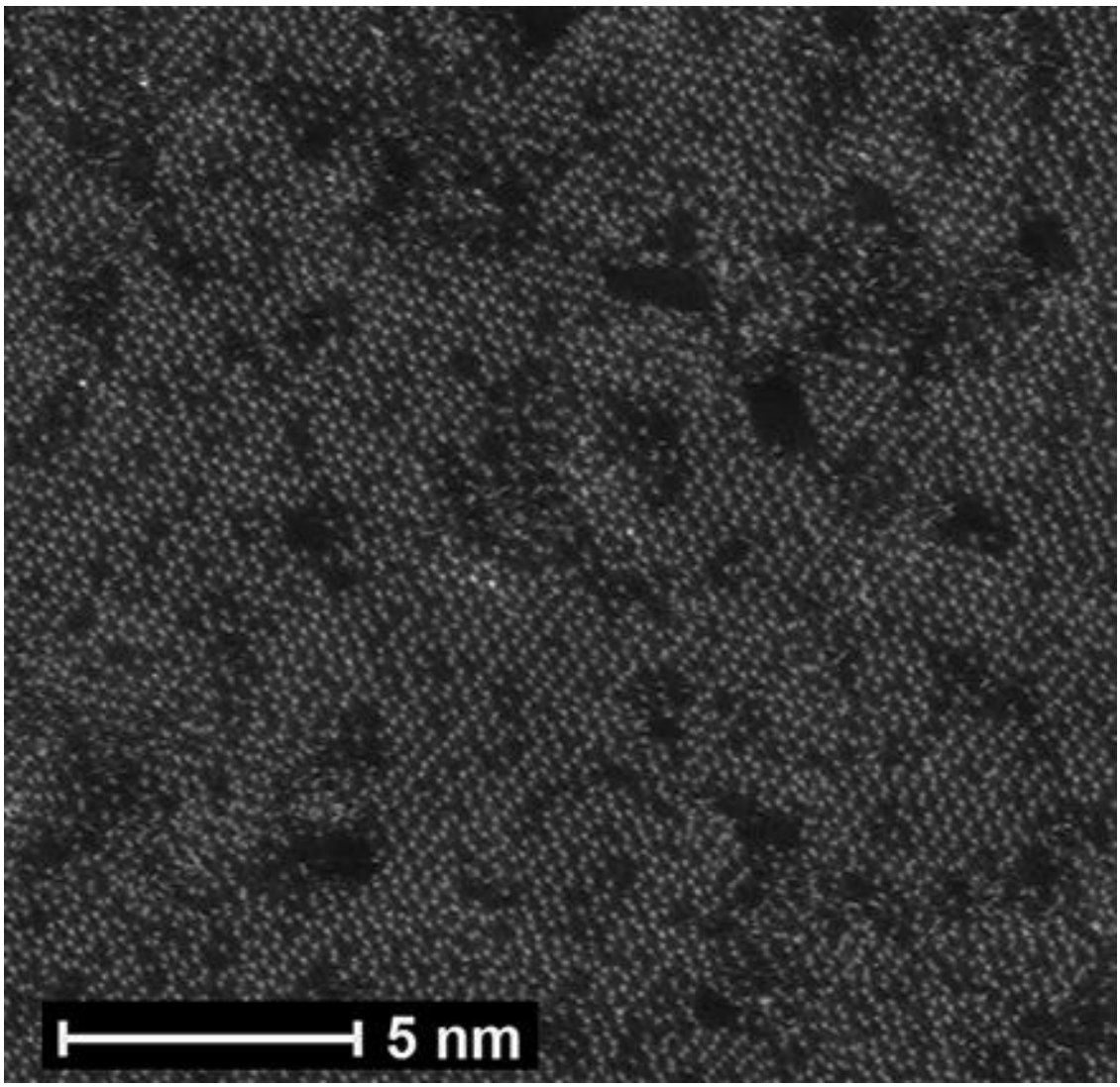

Figure 1. HAADF-STEM image of 2:1 MXene subject to prolonged etching, resulting in significant point defect formation.

MS6.006
Residual silver in dealloyed nanoporous gold – quantitative spatial distribution and influence on structure and catalytic performance

C. Mahr[1], P. Kundu[2], A. Lackmann[3], D. Zanaga[2], M. Schowalter[1], M. Schwan[3], S. Bals[2], A. Wittstock[3] A. Rosenauer[1]

[1]Universität Bremen, Institute of Solid State Physics, Bremen, Germany
[2]University of Antwerp, EMAT, Antwerp, Belgium
[3]Universität Bremen, Institute of Applied and Physical Chemistry, Bremen, Germany

mahr@ifp.uni-bremen.de

The residual silver left in dealloyed nanoporous gold (npAu) after corrosion of a gold-silver alloy has been shown to play a key role in the catalytic support of different chemical reactions.[1] NpAu is a particularly interesting catalyst because of its non-toxic nature, its stable structure as compared to gold nanoparticles and its ability to support chemical reactions at low temperatures. Similar to Raney-Nickel npAu is a completely unsupported nanoporous bulk catalyst, hence it is also predestined to study the catalytic activity of almost pure gold without any (oxidic) support. Although the ambiguous influence of the residual silver on the catalytic performance is known for a while information about the quantitative spatial silver distribution is lacking.

In this contribution we present quantitative energy dispersive X-ray spectroscopy tomography measurements of npAu.[2] Samples have been prepared by stopping the dealloying process of gold-silver alloys (70at% Ag) in nitric acid after different times providing samples with different residual silver concentrations. For measurements in the transmission electron microscope thin, electron transparent slices or needles have been prepared using a focussed ion beam. The tomography reconstructions have been obtained with the method explained by Zanaga et al. [3] including an elemental quantification using the zeta-factor method.[4]

Figure 1 shows that the silver is distributed irregularly within the sample. Silver rich clusters are located either inside or on the surface of the ligaments forming the porous structure. Two samples with different average silver concentrations of 8 at% (Fig.1a-c) and 11 at% (Fig.1d-f) are depicted, showing that the silver concentration within the cluster is larger for the sample with lower average silver concentration whereas the silver concentration in the regions between silver clusters is higher for the sample with higher average concentration, indicating that clusters form during dealloying. Some clusters show silver concentrations that are even larger than in the start alloy

Also structural properties of npAu are different if more silver remains in the sample. We apply a method proposed by Fujita and Chen [5] to show that ligaments and pores are smaller if more residual silver is left in the sample. This can be seen in Figure 2, where the characteristic length of npAu as a function of the residual silver concentration is shown.

Characterisation of the samples is completed by a measurement of the density of low coordinated surface atoms. The catalytic activity depends on this density as the adsorption of reactive atoms or molecules is favoured at these sites. Figure 3 shows the percentage of low coordinated surface atoms as a function of the residual silver concentration. Although ligament and pore sizes change with silver concentration the density of low coordinated surface sites stays constant within the margins of error, resulting in a value that is comparable to values that can be obtained for nanoparticles.[6]

References:
[1] A.Wittstock et al., Phys. Chem. Chem. Phys. **12** (2010), p.12919.
[2] C. Mahr et al., submitted
[3] D. Zanaga et al., Part. Part. Syst. Charact., **33** (2016), p.396.
[4] M. Watanabe and D. B. Williams, J. Microsc., **221** (2006), p.89.
[5] T. Fujita and M.W.Chen, Jpn. J. Appl. Phys., **47** (2008), p.1161.
[6] T. Fujita et al., Nat. Mater., **11** (2012), p.775.

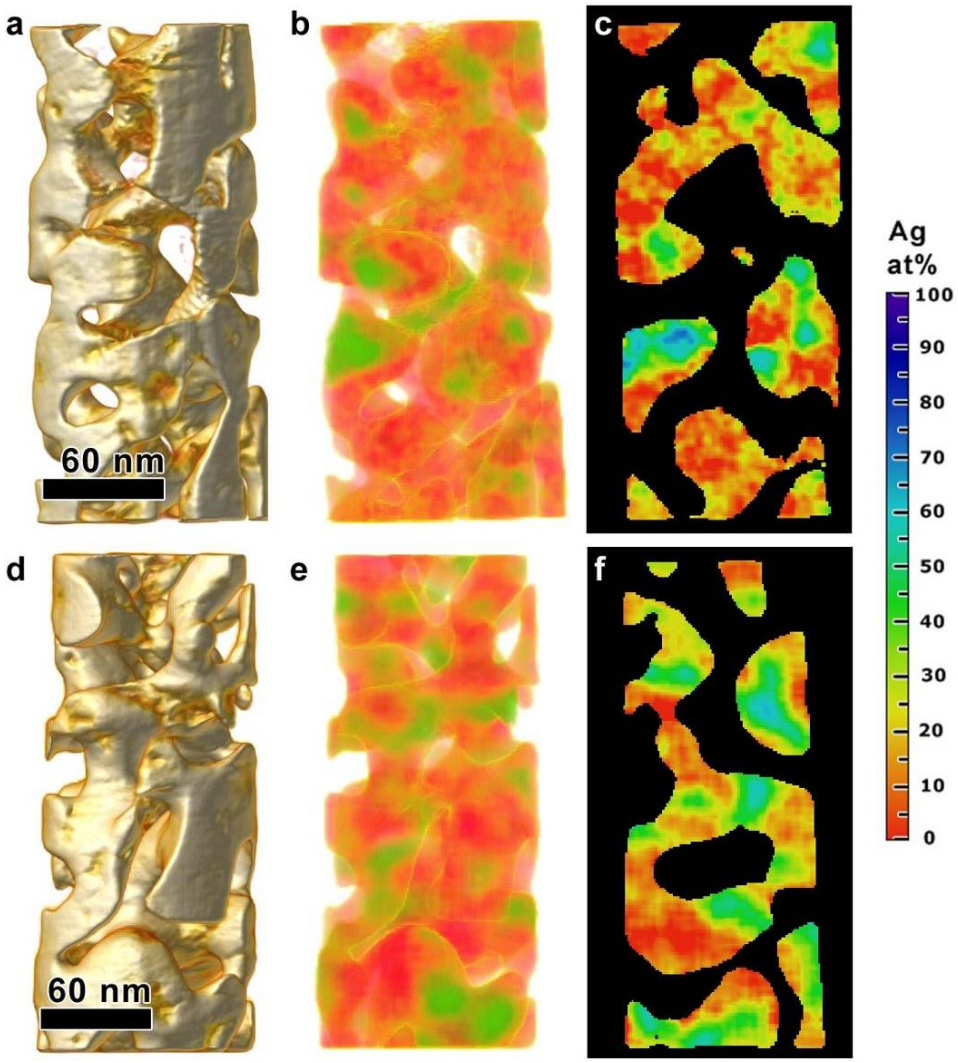

Figure 1. Tomographic reconstruction of the elemental distribution in nanoporous gold. (a), (d) volume reconstructions, (b), (e) quantified elemental reconstructions, (c), (f) single slices of the reconstructed quantified elemental distributions. (a) - (c) average Ag concentration of about 8 at%, (d) - (f) average Ag concentration of about 11 at%. Silver enriched regions are distributed irregularly, both on the surface and inside the ligaments.

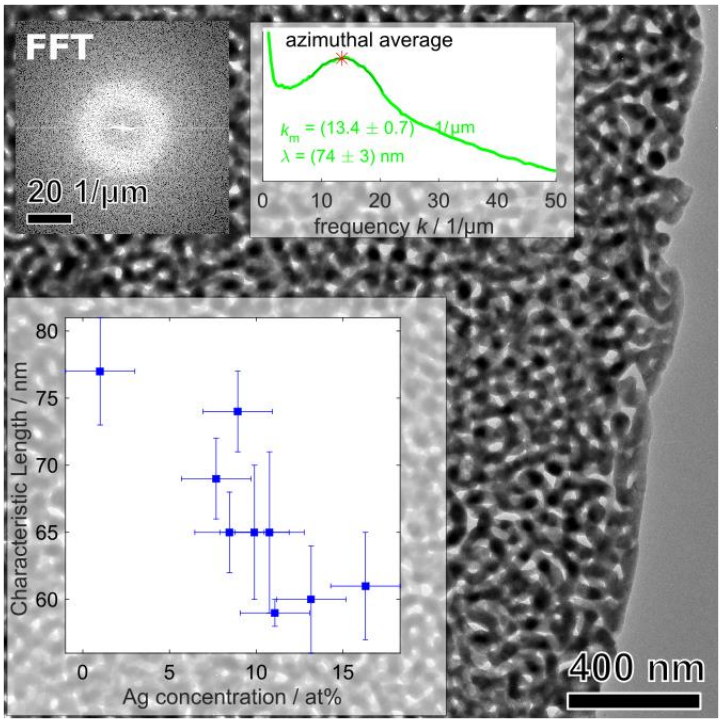

Figure 2. Characteristic length as a function of the residual silver concentration showing that ligaments and pores are smaller for increasing residual silver concentrations.

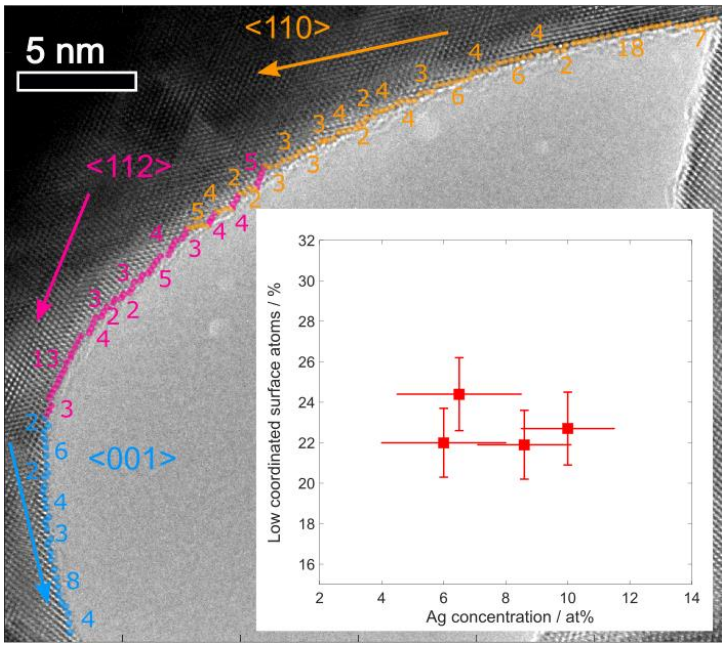

Figure 3. Percentage of low coordinated surface atoms as a function of the residual silver concentration. No relationship towards the residual silver concentration can be found.

MS6.007
Direct synthesis of molybdenum dioxide nanowires from MOS_2 nano-flakes

L. Vogl[1], P. Schweizer[1], E. Spiecker[1]

[1]Institute of Micro- and Nanostructure Research & Center for Nanoanalysis and Electron Microscopy (CENEM), Friedrich-Alexander Universität Erlangen-Nürnberg, Erlangen, Germany

lilian.vogl@fau.de

Molybdenum oxide nanowires are very promising for many technical applications, ranging from energy storage to micromechanics [1]. However, the synthesis of such nanowires with a uniform diameter remains challenging. Additionally, for wide-spread application the cost of production is a crucial factor. Using widely available raw materials, such as the natural-occurring molybdenite is a very promising way to reduce costs.

In this work we introduce a novel method of producing metal oxide nanowires directly from Molybdenum Disulfide (MoS_2). In contrast to other syntheses, this method offers the direct formation of molybdenum dioxide nanowires from MoS_2 nanoflakes using the naturally occurring prevalent mineral molybdenite as starting material.

Figure 1a shows the preparation process of the direct synthesis of molybdenum dioxide nanowires. The first step is the dispersion of MoS2 nanoflakes on a Cu TEM grid. Using a TEM grid as a substrate enables the direct characterization of the synthesized structures using electron microscopy. Alternatively, other subtrates such as sapphire can be used as well.

The MoS2 nanoflakes were produced by mechanical cleavage from bulk MoS_2. After that a thin homogenous layer of platinum is sputtered on the sample surface. Now the prepared sample is heated up to 700 °C under a constant nitrogen flow. During the temperature treatment, molybdenum based nanowires are formed on the MoS2 flake surface area.

The diameter of the synthesized nanowires is typically between 15 to 250 nm with a length of up to several micrometers. The growth of the wires is highly directional and follows crystallographic directions of the MoS2 flakes compare to Figure 1c.

To determine the nanowire morphology, TEM was used (see figure 2). Figure 2a shows a BFTEM image of two wires. Additionally, a cross-section TEM lamella was prepared by *in situ* liftout using a Focused Ion Beam (FIB). An overview Bright-field Scanning Transmission Electron Microscopy (STEM) image of the lamella can be seen in figure 2b. Figure 2c shows a High Resolution Transmission Electron Microscopy (HRTEM) image. Electron diffraction and electron energy loss spectroscopy have been performed to analyze the chemical composition and crystallographic structure of the nanowires.

In the future *in situ* heating experiments are planned to elucidate the growth mechanism of the nanowires as well as the role that platinum plays during the synthesis.

References:

[1] Liqiang Maia, Fan Yanga, Yunlong Zhaoa, Xu Xua, Lin Xua, Bin Hua, Yanzhu Luoa, Hangyu Liua: Molybdenum oxide nanowires: synthesis & properties, Volume 14, Issues 7–8, 2011, pp. 346–353

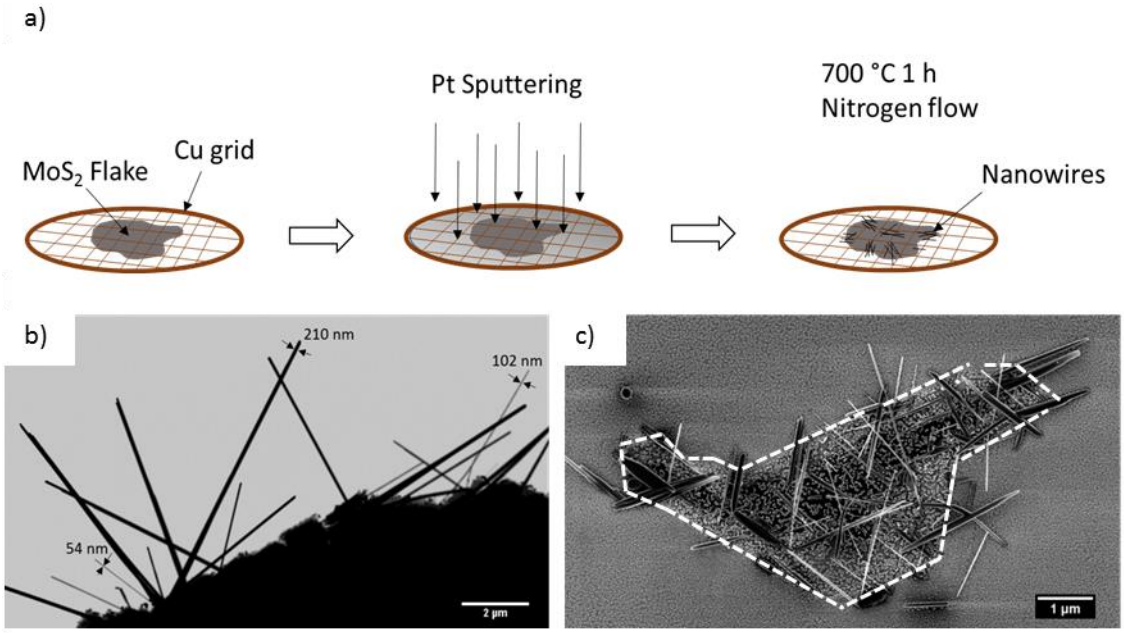

Figure 1. a) preparation process b) BFSTEM image of the nanowires with diameters in the range of 50 to 250 nm c) Wires made from a MoS2 nanoflake, the line shows the original scope of the MoS2 Flake.

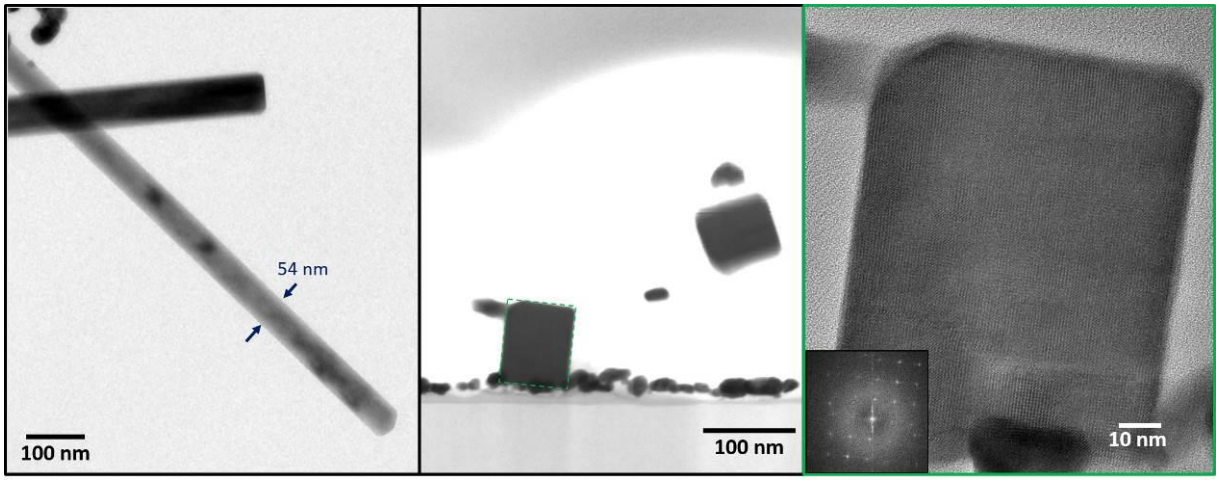

Figure 2. a) BFTEM image of molybdenum dioxide nanowires b) cross sectional BF STEM image. A HRTEM image of the marked area can be seen in c). The FFT (inset) shows the symmetry of the wires.

MS6.P001
Application of SEM in the study of Ziegler-Natta catalyst

Z. Liang[1], W. Huang[1]

[1]SINOPEC Beijing Research Institute of Chemical Industry, Beijing, China

masterlzw@yeah.net

Since Ziegler and Natta obtained polyethylene and polypropylene using titanium catalyst in the early 50s of last century, Z-N catalyst (Ziegler-Natta catalyst) is still the most important catalyst in the production of polyolefin resin after nearly 60 years of development, accounting for 70 % of total amount of catalysts. As a typical heterogeneous catalyst, Z-N catalyst's physical structure (crystal pattern, stacking mode of crystals and pore structure, etc.) has a key impact on the performance of the catalyst. Since Z-N catalyst is sensitive to air and humidity, detailed observation of its physical structure is always a problem for catalyst researchers. This paper introduced several applications of Scanning Electron Microscope (SEM) technologies and sampling methods in the research of the unique physical structure of the catalyst and the structural changes during the preparation process.

It is possible to obtain both topographic and compositional information of sample from backscattered electron (BSE) image. As for Z-N catalyst, there is significant atom number difference between Ti and Mg, which helps observe distribution of these two elements in catalyst. Fig. 1 is a BSE image of a typical Z-N catalyst under research in our lab. It is clear that Ti-Mg of the catalyst formed a distribution pattern similar to that of island structure. The dark region (Mg-Cl) formed a continuous phase and the bright region (Ti compound) was evenly distributed therein, which has never been observed in previous research.

Fig. 2 shows images of the same region of catalyst using backscattered and secondary electrons, respectively. It can be clearly seen that the chips with distinct edges and corners are dark, and that with irregular shape are bright. The Energy Dispersive Spectroscopy (EDS) results show that the main elements in both dark and bright region are Mg, Ti and Cl, but the content of Ti in the bright area is higher and the content of Mg in the dark area is higher. It can be inferred that the particles with distinct edges and corners were based on magnesium chloride microchips with titanium chloride coordination on surface, and irregularly shaped particles were mainly titanium alkoxyl compounds formed by the reaction of titanium chloride with ethanol.

Fig. 3a shows morphology of another catalyst's final product. In the image, the microspheres are intermixed with irregular fine particles, which was hard to explain and once confused Z-N catalyst researchers. After that, by continuously improving sampling methods, SEM images of different stages of catalyst preparation have been obtained as Fig. 3b and Fig. 3c. By these results, the understanding of catalyst forming process could be improved.

In summary, through the development of new technologies in recent years, SEM can provide more information on physical structure for Z-N catalyst development.

Reference:

[1] S. Pirinena, K. Jayaratneb, P. Deniflb, T. T. Pakkanen, J. Mol. Catal. A.: Chem. 395 (2014) 434-439
[2] 2. T. Taniike, T. Funako, M. Terano, J. Catal. 311 (2014) 33-40
[3] Z. Guo, W. Chen, J. Zhou, H. Yang, Chinese J. Chem. Eng. 17 (3) 530-534
[4] V. D"Anna, S. Norsic, D. Gajan, K. Sanders, A. J. Pell, A. Lesage, V. Monteil, C. Copéret, G. Pintacuda, P. Sautet, J. Phy. Chem. C 120 (2016) 18075-18087

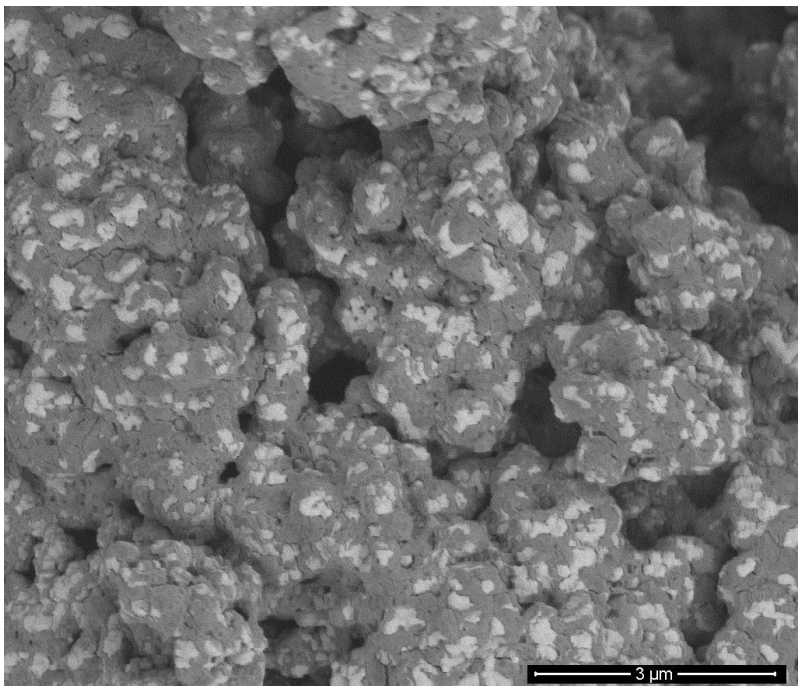

Figure 1. BSE image of a typical Z-N catalyst.

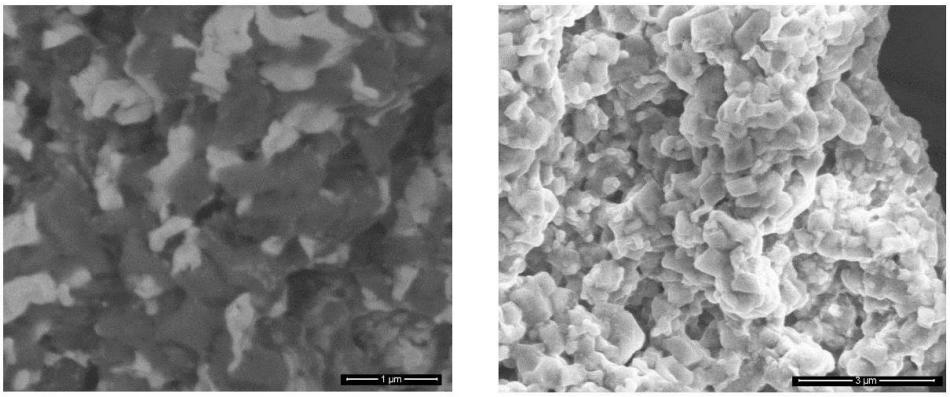

Figure 2. Images of the same region of Z-N catalyst using backscattered (a) and secondary (b) electrons.

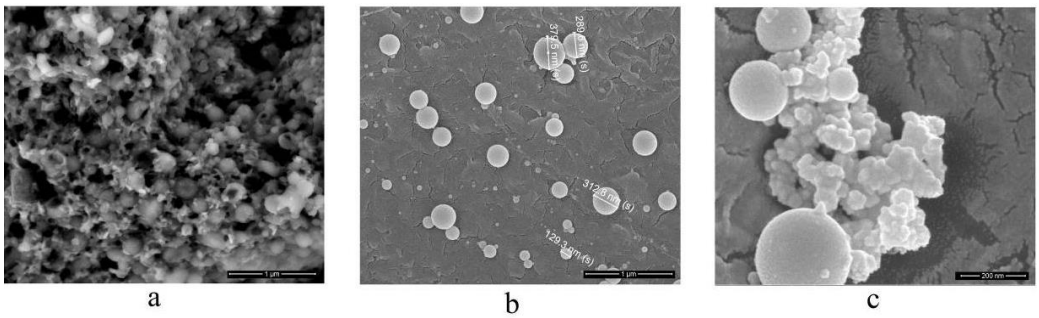

Figure 3. SEM images of different stages (a, internal structure of final product; b, initial stage of catalyst formation; c, middle of catalyst formation) of Z-N catalyst preparation.

MS6.P002
Transfer hydrogenation of carbonyl compounds catalyzed by natural phosphate supported nickel

A. Baba[1], H. Ouahbi [1], J. Sebti[1], A. Hassine[1], L. Laasri[1], S. Sebti[1]

[1]Laboratory of Physical Chemistry Catalysis and Environment, University of Hassan 2 Casablanca, Chemistry, Casablanca, Morocco

baba.abderrahim@yahoo.fr

The natural phosphate represents an important mining wealth for Morocco. Several studies have been carried out to develop this resource. Within this objective, development of phosphates as a catalyst has been carried out in our laboratory. Thus, it has been shown that phosphates, especially natural phosphate, have very interesting catalytic proprieties. This has permitted the development of a family of efficient catalysts able to perform well with both acid and basic syntheses. The combination of phosphates with metals produced a new generation of efficient catalysts that allow the broadening of the application field of catalytic phosphates. Newer phosphate-based performing catalysts have been developed, allowing the production of many transformations such as Suzuki-Miyaura, reforming of methane and other organic reactions. Furthermore, amongst several catalytic reactions used in industrial processes and general organic synthesis, hydrogenation allows the production of a considerable number of basic intermediate reactions. In this study, we are especially interested in the hydrogenation of carbonyl compounds. This transformation permits the production of alcohols in a specific manner. First, we prepared a NP doped with nickel catalyst (Ni/NP) using nickel chloride in an aqueous medium. Evaporation and calcination produced the sought material. Then we tested the Ni/NP catalyst in the catalytic hydrogenation of some aldehydes and ketones. The development of the conditions of the reaction was used to assess the performance of this catalyst. In this work, we will present the results obtained in this reaction.

Keywords*:* Naturel phosphate; Catalysis, Doping, Nickel, Carbonyl, Transfer hydrogenation.

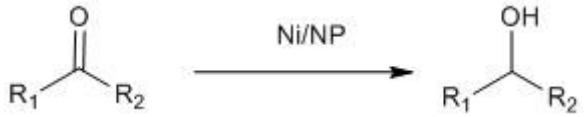

Figure 1

MS6.P003
TEM study of the transformation of massive InO(OH) nanoparticles into hollow In_2O_3 nanoparticles

R. Popescu[1], L. Schliker[2], A. Gurlo[2], D. Gerthsen[1]

[1]Karlsruher Institut für Technologie, Laboratorium für Elektronenmikroskopie, Karlsruhe, Germany
[2]Technische Universität Berlin, Institut für Werkstoffwissenschaften und -technologien, Berlin, Germany

radian.popescu@kit.edu

Introduction: In_2O_3 is a prototype material for several emerging applications, e.g. photovoltaics, spintronics, touch displays and gas sensors. Therefore, controllable synthesis of In_2O_3-based nanomaterials is of great interest for improving device functionalities. In this context, synthesis routes towards InO(OH) and rh-In_2O_3 with controllable crystal structure and morphology are studied. It is shown that solvothermal synthesis [1] results in monocrystalline InO(OH) nanospheres with orthorhombic structure, which transform into rhombohedral In_2O_3 hollow nanospheres upon calcination at 350 °C in air.
Materials and Methods: For the structural and chemical characterization, high-resolution (HR) transmission electron microscopy (TEM) and high-angle annular dark-field scanning TEM (HAADF STEM) combined with energy-dispersive X-ray spectroscopy (EDXS) was used. The TEM samples are prepared by deposition of nanoparticles (NPs) dispersed in methanol on an amorphous carbon film at room temperature. Samples were investigated by performing HRTEM with an aberration-corrected FEI Titan^3 80-300 microscope at 300 kV and HAADF-STEM/EDXS with an FEI Osiris ChemiSTEM microscope at 200 kV.
Results: InO(OH) NPs with an average diameter of D=18±4 nm are synthetized by a solvothermal synthesis route. The single NP shown in the HRTEM image (Fig. 1a) is a monocrystalline InO(OH) NP. Crystal structure analysis is performed by comparing its 2-dimensional Fourier transformation (FT) and the calculated diffraction pattern (Fig. 1b). Good agreement is obtained on the basis of the bulk orthorhombic InO(OH) structure (space group P21nm, space group number 31 [2]) in the the [133] zone axis. Quantitative EDXS analysis was performed using the In-L series and O-Ka1 line, which yields an average chemical composition of $In_{33.7\pm3.0}O_{66.3\pm2.0}$, which is consistent with the InO(OH) composition, i.e. $In_{33}O_{67}$.
A phase and morphological transformation takes place upon heat treatment of initial InO(OH) NPs at 375 °C for 30 min in air, which results in the formation of hollow spherical particles (HPs) with a rhombohedral In_2O_3 structure. The ring-like feature observed on the HRTEM image shown in Fig. 1c) is characteristic for the 2-dimensional projection of HPs on the image plane. Histograms of the outer (D) and inner (d) diameter distribution of HPs result in average diameters of D=18±4 nm and d=8±2 nm. The HP in Fig. 1c is a monocrystalline In_2O_3 NP, as indicated by the good agreement between its FT and the calculated diffraction pattern of bulk rhombohedral In_2O_3 (space group R-3cH, space group number 167 [3]) in the [661]-zone axis (Fig. 1d). Quantitative EDXS yields an average chemical composition of $In_{38.0\pm3.0}O_{62.0\pm3.0}$, which corresponds well with the composition of bulk In_2O_3, i.e. $In_{40}O_{60}$.
Conclusion: Monocrystalline orthorhombic InO(OH) NPs are obtained by using the solvothermal synthesis route. A phase- and morphological transformation takes place upon heat treatment of initial InO(OH) NPs and results in the formation of monocrystalline hollow nanoparticles particles with a rhombohedral In_2O_3 structure.

References:
[1] L. Schlicker, M. F. Bekheet and A. Gurlo, *Z Kristallogr*. **232** (2017) 129.
[2] M. S. Lehmann et al., Acta Chem Scand **24** (1970) 1662.
[3] C. T. Prewitt et al., Inorganic Chemistry **8** (1969) 1985.

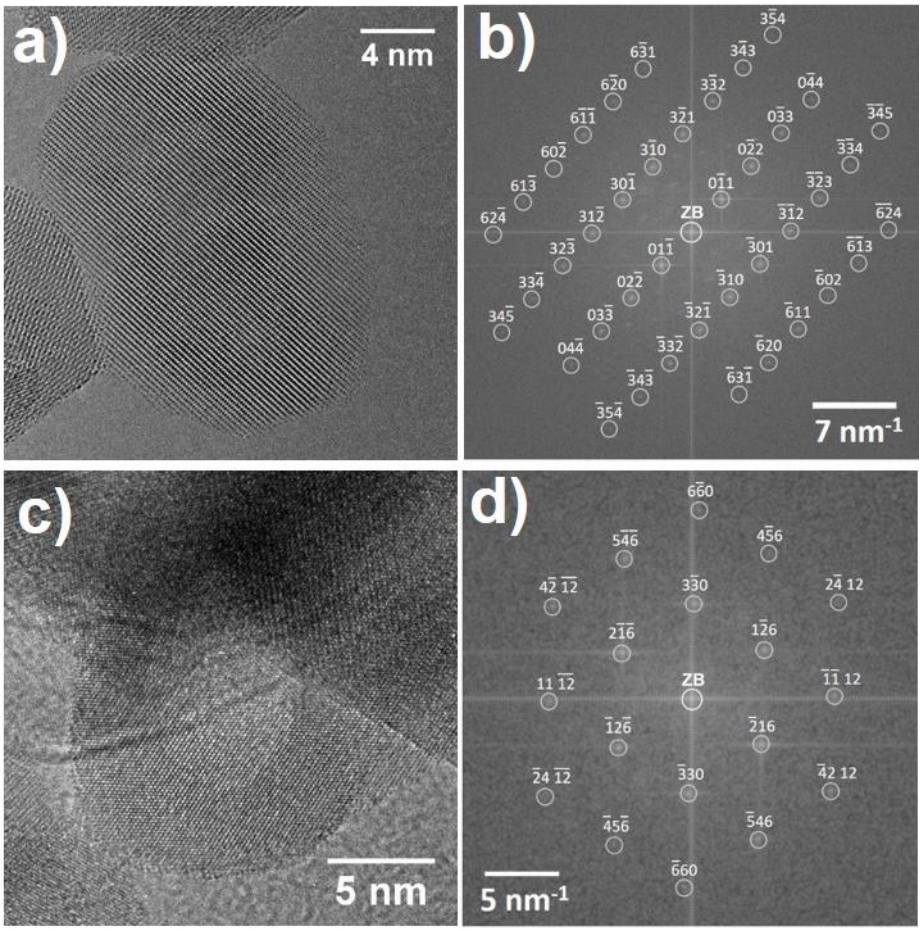

Figure 1. a) HRTEM image of InO(OH) NPs; b) FT of the NP in a) and calculated diffraction pattern with Miller indices for the orthorhombic InO(OH) structure in the [133]-zone axis (gray circles). The white circle indicates the zero-order beam (ZB); c) HRTEM image In_2O_3 HPs; d) FT of the HP in c) and calculated diffraction pattern with Miller indices for the rhombohedral In_2O_3 structure in the [661]-zone axis (gray circles).

MS6.P004
TEM analysis of laser-generated iron gold core shell nanoparticles

M. Kamp[1], A. Tymoczko[2], U. Schürmann[1], C. Rehbock[2], J. Jakobi[2], S. Barcikowski[2], L. Kienle[1]

[1]Technical Faculty of the Christian-Albrechts-University of Kiel, Institute for Materials Science, AG-Synthesis and Real Structure, Kiel, Germany
[2]University of Duisburg-Essen, Technical Chemistry and Center for Nanointegration (CENIDE), Duisburg-Essen, Germany

maka@tf.uni-kiel.de

Introduction: The combination of elements in multiphase alloy nanoparticles reveals a wide field of applications. Therefore iron and gold are merged in one nanoparticle combining functionality like biocompatibility, functionalization by thiolated biomolecules, magnetic properties as dual contrast agent and magnetic thermotherapy [1], [2]. Biphasic crystalline nanoparticles with gold shell and iron core (Fe@Au) represent an outstanding ultrastructure to achieve these multifunctional properties within one nanoparticle.
Objectives: The aim of the research is a controlled synthesis of core shell nanoparticles with iron core and a protective gold shell by pulsed laser ablation in liquid. Though parameters affecting the resulting ultrastructure like the solvent, target composition and the laser pulse duration are analyzed to investigate the formation mechanism. The influence of the bulk target composition on the ultrastructure is decisive. In addition thermal stability and oxidation resistance of the synthesized nanoparticles is significant.
Materials and Methods: The one-step synthesis of Fe@Au nanoparticles by pulsed laser ablation in liquids (PLAL) generates core shell, intermetallic alloy and multicore nanoparticles from bulk Fe-Au alloy targets. The Investigation of its ultrastructure is performed by transmission electron microscopy applying versatile methods, like high resolution phase and Z-contrast imaging, accompanied by quantitative nanoprobe EDX elemental mapping. The thermal stability of the ultrastructure and their changes upon thermal treatment was studied by *in situ* TEM examinations. The chemical reactivity against oxidation and Fe ion release was investigated *ex situ* by suspending the nanoparticles to concentrated acids and EDTA solution.
Results: The bulk target composition during synthesis has been varied from gold rich to iron rich systems. X-ray spectroscopy over large quantity of nanoparticles revealed that the composition of the target is well recovered by the average composition of the nanoparticles. Depending on the target composition different ultrastructures are formed. Gold rich compositions result in intermetallic alloy nanoparticles, while core shell and multicore shell particles are formed from iron rich targets. These results are based on a wide range of statistical data, including size distribution, nanoparticles hydrodynamic diameter, structure and shell width. A target composition of 50 at.% Au gives a high fraction of Fe@Au core shell nanoparticles with mean diameter of 20 nm containing iron cores of 17 nm and dense gold shell. Treatment with concentrated hydrochloric acid and EDTA approved the completeness and stability of the gold shell by the protection of the Fe core against these agents. Subsequently, the thermal stability of the ultrastructure up to 250 °C has been demonstrated by an *in situ* TEM measurement.
Conclusion: The one-step synthesis of iron gold nanoparticles by PLAL is controllable by the surrounding solvent medium and the target composition. Thus the particle internal phase and resulting properties can be regulated to receive a Fe@Au core shell ultrastructure. Its thermal stability and excellent oxidation resistance is a prerequisite for long-term multifunctional application.

References:
[1] H. Liao, A. Fisher, and Z. J. Xu, "Surface Segregation in Bimetallic Nanoparticles: A Critical Issue in Electrocatalyst Engineering," *Small Weinh. Bergstr. Ger.*, vol. 11, no. 27, pp. 3221–3246, Jul. 2015.
[2] P. Wagener *et al.*, "Solvent-surface interactions control the phase structure in laser-generated iron-gold core-shell nanoparticles," *Sci. Rep.*, vol. 6, p. 23352, Mar. 2016.

MS6.P006
In vivo study of biphasic calcium phosphate bone graft material

S. M. Masudi[1], N. Sukminingrum[2]

1Lincoln University College, Fac. Dentistry, Restorative Dentistry, Petalin, Malaysia
[2]University Sains Malaysia Dental School, Human Biology, Kubang Kerian, Malaysia

masudi1904@yahoo.com

Introduction: Calcium Hydroxyapatite [Ca10 (PO4)6 (OH)2, HA] ceramics are very bioactive and biocompatible, allowing a strong bond with neighboring bone when they were implanted at bone-defect site (Bucholz, 2002). However, non-biodegradability of synthetic HA ceramics limited their clinical uses since it hinders natural bones to completely replace artificial ones.
Among other Ca-P based ceramics, tricalcium phosphate [Ca3(PO4)2, TCP] ceramics are shown to be biodegradable as well as bioactive (Petrov *et al*., 2001). The dense HA ceramics when used as bone implant is almost non-resorbable and bio-inert. However in TCP, the biodegradation rate is much higher than the growth rate of natural. These problems have led to the study on BCP ceramics, which are expected to show optimal biodegradation behavior for medical/dental application, such as dental implant, root canal sealer, bone repair and bone augmentation. (Daculsi *et al.,* 2003).
A mixture of 60wt% HA and 40wt% TCP provides very good bioactivity and scaffold matrix for implant (Daculsi *et al*., 2003). These previous studies used highly reactive, nano-sized, and calcium-deficient hydroxyapatite powders prepared by the wet chemical method. The advantage of the BCP is its bioresorbability and/or bioactivity, which depends on the solubility of HA and β-TCP. BCP substituted or doped with lanthanides helps in further improving the biological activity compared to unsubstituted products (Meor Yusoff and Masliana, 2007).
Objectives: This *in vivo* study was conducted to assess the host tissue reaction around the BCP powder implanted into the rabbit bone.
Materials and Methods: In this study 12 mature male New Zealand White rabbits 4-5 kg, and approximately 6 months in age were used. They were divided into two group were used for microscopic study. A defect was created at both sides body of mandible, the right side received BCP powder. The left side was left empty to act as control. Three rabbits from each groups were sacrificed at 1, 2, 4 weeks and three rabbits were sacrificed at 12 weeks post implantation. Each sample from each group was prepared for light microscopic and SEM study respectively.
Results: Light and scanning electron microscopy revealed complete and good osteo-integration between implant materials and host bone in addition to new bone formation in the mandible defects implanted with BCP powder form.
Conclusions: This study suggested that both the BCP powder showed favorable tissue response. Microscopically, the powder BCP induced higher fibro-vascular in-growth and colonization of cells and fibers.

References:
[1] Bucholz, R.W. (2002). Nonallograft osteoconductive bone graft substitutes. *Clin. Orthop. Res.* 395, 44.
[2] Petrov, O.E., Dyulgerova, E., Petrov, L., Popova, R. (2001). Characterisation of calcium phosphate phases obtained during the preparation of sintered biphase Ca-P ceramics. *Mat. letters* 48, 162-167.
[3] Daculci, G, Laboux, O., Mallard, O, Weiss, P. (2003). Current state of the art of biphasic Calcium phosphate bioceramics. *J. Mater. Sci. Mater. Med.* 14, 195.
[4] Meor Yusoff, M.S. and Masliana, M. (2007). Synthesis of functional biomaterial from Organic based phosphoric acid. *Proceed. Int. Conf. of Adv.of Mat. and Nanotech. 2007.*

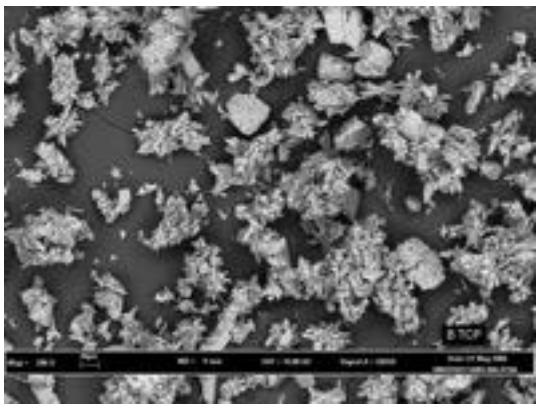

Figure 1. Biphasic Calcium Phosphate: SEM 200x.

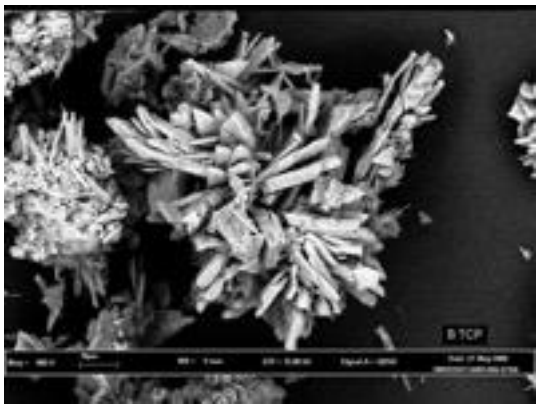

Figure 2. Biphasic Calcium Phosphate: SEM 800x.

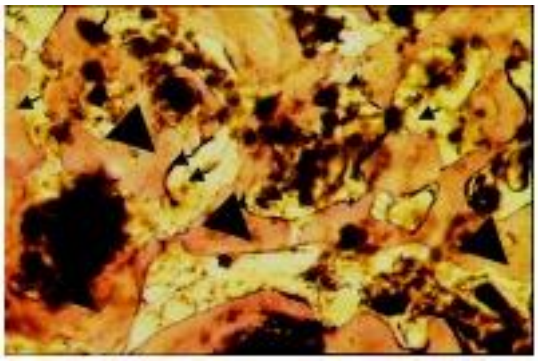

Figure 3. Photomicrograph of the histological section of BCP powder group, at 12 week shows BCP powder particles with active resorption process, invaded with osteoblasts (Arrows). BCP were replaced with new bone formation coalesce together (Arrow heads). [HE, Original magnification, x 10].

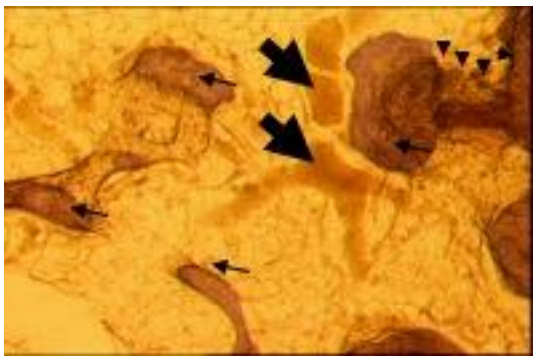

Figure 4

MS6.P007
Characterization of calcium phosphate zirconia bio-composite material

S. M. Masudi[1], N. Sukminingrum[1]

[1]University Sains Malaysia Dental School, Human Biology, Kubang-Kerian Malaysia

masudi1904@yahoo.com

Introduction: Calcium phosphate, Ca3(PO4)2 is the name given to a family of minerals containing calcium ions (Ca2+) together with orthophosphates (PO43-), Calcium phosphate ceramics have gained wide-spread attention due to their compositional and structural similarity to the mineralized constituent in hard tissues (Hench, L.J., 1991). However, due to their relatively low strength and toughness, susceptibility to physiological attack, and poor fatigue properties, the biomedical uses of calcium phosphate ceramics are limited to non-load bearing applications. One of the most promising approaches to increase the strength in ceramics is through transformation toughening based on the tetragonal-monoclinic transformation of zirconia. A ceramic with dispersed tetragonal zirconia can be used to enhance the strength and toughness. In this case study, zirconia and calcium phosphate powders were used to produce a bio-composite.
Objectives of this study were to determine the characterization of CaPZr by Scanning Electron Microscope-Energy Dispersive X-ray (SEM-EDX), Transmission Electron Microscope (TEM) and Fourier Transform Infrared (FTIR) X-ray Diffraction (XRD) techniques.
Materials and Methods: CaPZr powder was prepared using organic diethyl hexyl phosphoric acid (DEHPA) as the source for phosphate. Zirconyl chloride octahydrate was mixed with DEHPA. Calcinations were performed in the furnace at 1000°C for 3 hours and BCP powder was collected. Energy Dispersive X-ray (EDX) spectrum imaging has been performed in a SEM on a CaPZr to characterize the elemental distribution near the interface. The analysis was performed in a Leo Supra 50 VP Field Emission SEM equipped with Oxford INCA 400 energy dispersive x-ray microanalysis system. Transmission Electron Microscope (TEM) analysis was performed using following technique: Place a droplet of the suspension on a carbon film coated 400 mesh copper grid for 1-3 minutes. The drop was pipetted out after the larger particles have settled to the bottom of the sample tube. The droplet is then wicked to dryness using pieces of filter paper. Place the grid in a filter paper lined petri dish until it can be examined. Clean the fine forceps used with ethanol / filter paper before storing it away. The CaPZr powder was poured into mortar and mixed with potassium bromide to produce pellet from the grind powder and analyzed using Fourier Transform Infrared (FTIR).
Results: The result shows that some crystal structure changes occurred with the addition of Zr that resulted in formation CaPZr powder. Zr shows to be exists in monoclinic, tetragonal and cubic polymorphs. Advantages of Zr-doped Ca(PO4) synthesized from this method are strong bonding between Zr and the Ca(PO4) without having loss of Zr and more homogenous Zr distribution.
Conclusions: The result of this study indicates that the structure of CaPZr powder is positively influences by addition of Zirconia and could improve physical strength of BCP.

References:
[1] Daculsi, R., Grellier, M., Remy, M., Bareille, R., Pierron, D., Fernandez, P. & Bordenave,
[2] (2008). Unusual transduction response of progenitor-derived and mature endothelial cells exposed to laminar pulsatile shear stress. *J Biomech,* 41 (12), 2781-5.
[3] Hench, L.L. (1998). Bioceramics. *J. Am. Ceram. Soc*. 81, 1705.
[4] LeGeros RZ. (2002). Properties of osteoconductive biomaterials: calcium phosphates. *Clin. Orthop. Rel. Res*, 395,81–95.
[5] Masudi, S.M., Farea, M., Masudi A.F., Sulaiman M.Y.M., Rajion, Z.A., Mohamad, D. and Pameijer, C.H. (2011). Synthesis and characterization of Biphasic Calcium Phosphate Doped with Zirconia. *J. Mater. Sci Eng. B,* 1(1), 34-42.

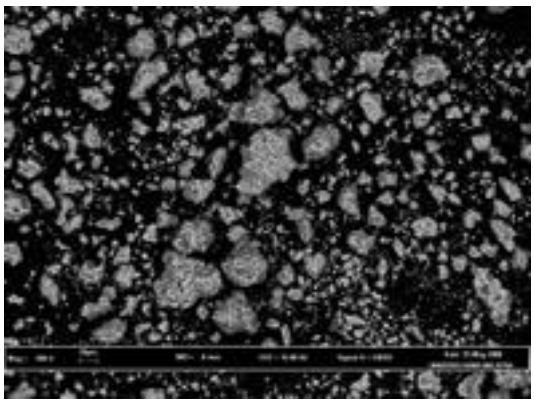

Figure 1. Scanning Electron Microscope-Energy Dispersive X-ray (SEM-EDX) images at 200 x Mag.

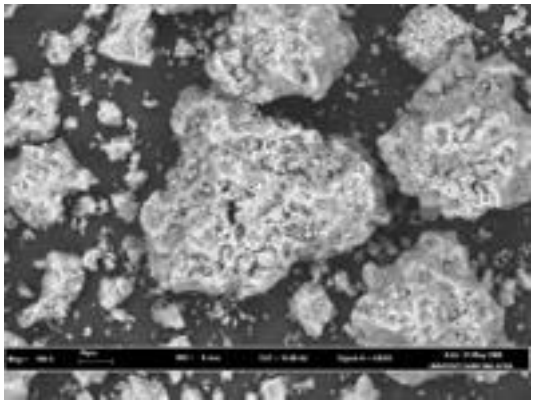

Figure 2. Scanning Electron Microscope-Energy Dispersive X-ray (SEM-EDX) images at 800x Mag.

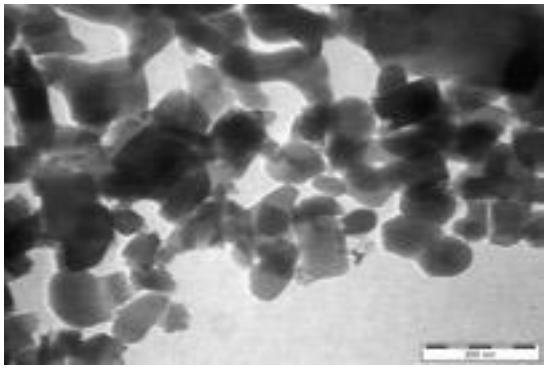

Figure 3. Transmission Electron Microscope (TEM) images of CaPZr in low magnification.

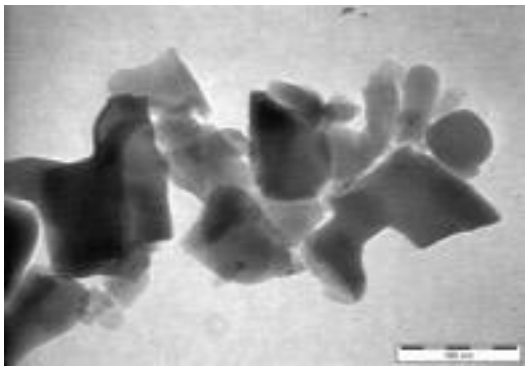

Figure 4. Transmission Electron Microscope (TEM) images of CaPZr in high magnification.

MS6.P008
SEM study on morphology and distribution of active components in supported hydrogenation catalysts

W. Huang[1], Z. Liang[1]

[1]Beijing Research Institute of Chemical Industry, SINOPEC, Analytical Research Division, Beijing, China

huangwendy@sina.com

In the field of petrochemical industry, most of unsaturated hydrocarbon hydrogenation catalysts are supported solid catalysts, i.e., active metal components are supported on carriers with high specific surface area such as Al_2O_3, SiO_2 and so on. The properties of catalyst, such as metal dispersion, distribution and surface acidity, have a great influence on performance of catalyst.

The morphology and distribution of the surface species on catalyst can be studied by secondary electron images on scanning electron microscope (SEM) coupled with EDS for microzone analysis. However, due to the limited spatial resolution of EDS, this method is not suitable for the characterization of nanometer and sub-micrometer-sized active metal (or metal oxide) on catalyst surface. In this paper, we overcame the shortcomings of methods above by SEM using backscattered electron signals at low accelerating voltages, and studied the morphology and distribution of two kinds of active metal oxides in an unsaturated hydrocarbon hydrogenation catalyst.

The results of pulse chemisorption show that CO adsorption capacity of catalyst A was less than that of B, which conformed by SEM images. Besides, Fig. 1B shows that there is no correlation between the distribution of NiO and RuO_2 on surface of the carrier, so less interaction between NiO and RuO_2 is very clear.

The distribution depth of active metal on catalyst supports directly affects performance of the catalyst. In general, the more superficial distribution of active metal on surface of the catalyst, the easier it is to contact gaseous molecules in gas phase reaction and the higher activity of the catalyst. Fig. 2 is a sectional elemental profile of catalyst particle showing a substantially uniform distribution of Ni within the catalyst particles while Ru is distributed in depth of 10 μm away from the surface. A number of experiments on catalysts with different Ru contents showed that the distribution depth of Ru was approximately proportional to its content.

In summary, we can obtain the information of morphology and distribution of active metal components on catalyst carrier by SEM and EDS. It can be used to predict the activity of catalyst before evaluation, which will save much reaction time.

Figure 1: Backscattered electron images of hydrogenation catalyst containing Ni (A) and Ni, Ru (B) with acceleration voltage of 5 kV, respectively.

Reference:

[1] Y. Lv, F. Hao, P. Liua, S. Xiong, H. Luo, J. Mol. Catal. A.: Chem. 426 (2017), 15-23
[2] S. Irmak, B. Meryemoglu, B. K. Ozsel, A. Hasanoglu, O. Erbatur, Int. J. Hydrogen Energ. 40 (2015) 14826-14832
[3] H. Zhao, J. Xu, T. Wang, Appl. Catal. A: Gen. 502 (2015) 188-194

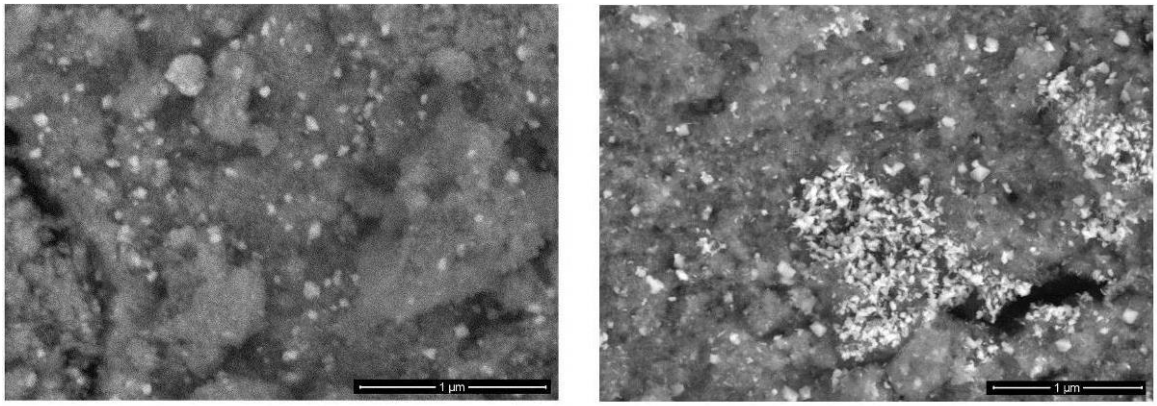

Figure 1. Shows backscattered electron images of an unsaturated hydrocarbon hydrogenation catalyst containing Ni (A) and Ni, Ru (B) under SEM with accelerating voltages 5 kV, respectively. It is clear that all the metal oxide particles shown in the image are in nanometer scale. In both Fig. 1A and Fig. 1B, the octahedral crystals are NiO, and in Fig. 1B, a kind of rod-like crystals can be observed. X-ray diffraction (XRD) results show that the particular crystals in Fig. 1B are rutile-phase RuO2. Based on comprehensive analysis of Fig. 1A and Fig. 1B, NiO uniformly distributed whereas RuO2 partly agglomerated and covered NiO.

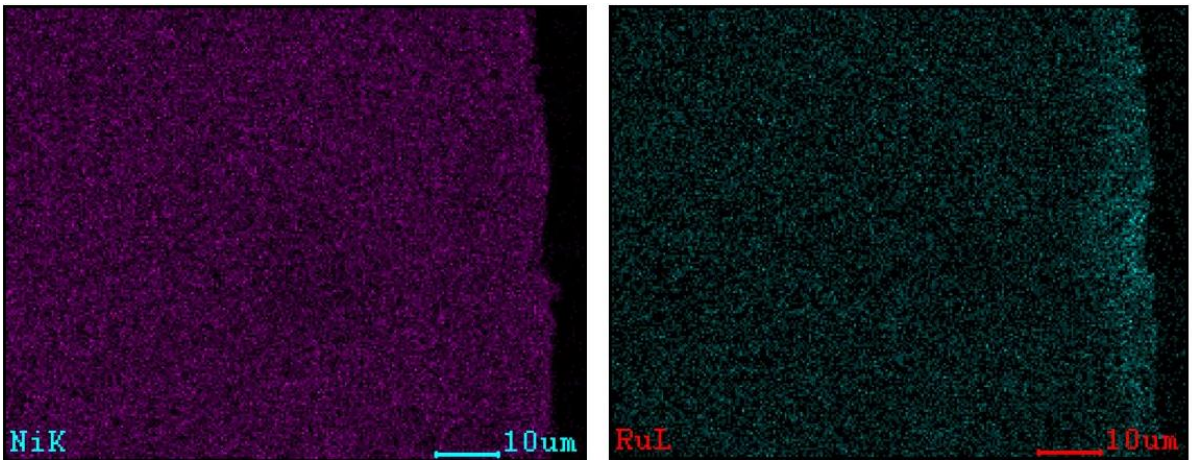

Figure 2. Distribution profile of Ni and Ru on the cross-section of a catalyst particle.

MS6.P010
Thickness determination of plate-like nanoparticles by HAADF-STEM

P. Mueller[1], T. Wieczorek[1]

[1]BASF SE, Material Physics and Analytics, Ludwigshafen am Rhein, Germany

philipp.mueller@basf.com

TEM is considered as most promising analytical technique for size distribution measurement of nano-materials according to the nano-definition by the European Commission (EC) [1]. While TEM will act as confirmative technique in the proposed strategy for nano-particle size determination [2] the method is affected by one significant flaw. Plate-like particles usually align with the TEM carrier substrate obscuring the smallest dimension of the particles in standard bright-field TEM (Figure 1; left). While electron tomography gives access to the thickness of plate like particles, it is time consuming and reconstruction artefacts hinder an automated image evaluation while covering only a small sample region. Preparation of cross-sections through embedded particles helps to estimate the thickness of the plates but the method is prone to significant errors due to a skewed cutting angle (Figure 1; right). Furthermore, cross-sections also cover only two dimensions of the particles.
Image contrast in HAADF mode in STEM as well as TSEM (transmission SEM) is proportional to the sample thickness, given a single-phase material and a thickness sufficiently small (~1µm for Z=13; 200kV) to prevent multiple scattering events.
In the present study we demonstrate that thickness-calibrated imaging combined with automated image evaluation are a viable method for particle size determination in 3 dimensions according to the EC recommendation and are able to fix the main limitations of bright-field TEM.
The detector signal can either be calibrated by comparison to simulations of the thickness-dependent signal like e.g. described by Katz-Boon et al. [3] or by measurement of a well-defined calibration sample of the same material [4]. Simulations require detailed knowledge of the sample composition, crystal structure and density as well as detector geometry and performance parameters. Information that is often not available in an industrial context.
In the present work we describe strategies for an implementation of particle thickness determination of plate-like materials of high industrial relevance like kaolin clay. While thickness calibration employing a FIB-prepared wedge [4] is a straight-forward approach for bulk materials like silicon, industrial particles require different approaches. Tracer particles give access to local thickness in tilt experiments. Furthermore, electron etching can be employed to drill holes in the particles which can also be gauged by tilting. Several local thickness measurements combined with the corresponding HAADF-STEM signal result in a calibration curve by a linear fit.

References:
[1] European Commission, Commission Recommendation of 18 October 2011 on the definition of nanomaterial, Official Journal of the European Union. 2011/696/EU (2011) p.38.
[2] The NanoDefine project (www.nanodefine.eu)
[3] Katz-Boon et al. Ultramicroscopy 124, 61–70, 2013 doi: 10.1016/j.ultramic.2012.08.009
[4] Volkenandt et al. Microsc. Microanal. 20, 111–123, 2014 doi:10.1017/S1431927613013913

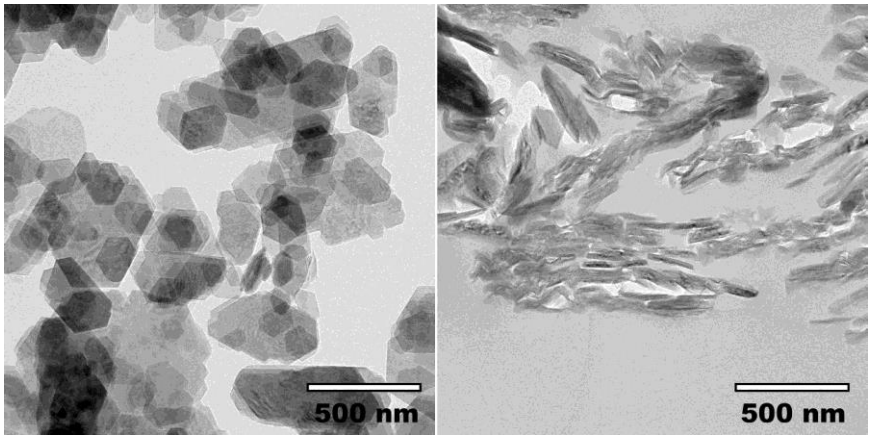

Figure 1. TEM bright-field image of kaolin clay (left); ultramicrotomy cross-section through particles embedded in resin (right).

MS6.P011
A simple way to count and measure polymer stabilized nanoparticles in (S)TEM images

E. Suvorova[1], D. Shvedchenko[1]

[1]A.V. Shubnikov Institute of Crystallography, Moscow, Russian Federation

suvorova@ns.crys.ras.ru

Introduction and Objectives: The total market for composites with nanoparticles is expected to grow. The relevant methods for analysis of such materials are required. The work is motivated by the practical need to develop the simple, reliable, and fast tool to analyze metal (non-metal) particles formed in water polymer solutions for biomedical use. The comparative size distribution analysis performed for Ag nanoparticles born and stabilized in aqueous solutions of polymers (2-(dimethylamino)ethyl methacrylate and 2-deoxy-2-methacrylamido-D-glucose homopolymers and their copolymers) was the basis of Ag nanoparticle growth model taking into account the structure of the copolymers and the amount of reducing centers per monomer [1].
The problem on the ratio safety–efficiency–cost of biomaterials has to be solved. The control of particle sizes by using polymers with different structure allows us to obtain less toxic, probably less expensive and still efficient materials. In order to find the direction for some optimal solution, we had to analyze particles in various polymer environments, to study the (S)TEM contrast of particles and develop the software.
Method: The majority of computer algorithms for particle recognition and diameter measurements are based on image thresholding: distinguishing pixels of a halftone image, which correspond to objects or background by grayscale thresholding.
The idea underlying our method is to combine thresholding and fitting procedures in the same software: thresholding is used for particle recognition while measurements of particle sizes and size distributions is performed by fitting the calculated grayscale distribution to the real one in (S)TEM images. The problem of background noise reduction is solved by applying the preliminary image treatment: blurring or smoothing or despeckling. This operation can be crucial for TEM images having significant noise due to speckles from amorphous carbon film, which can be defined as interference pattern from randomly packed carbon atoms and density fluctuations in thick polymer films. Some groups of background pixels can be recognized as a particle. Uneven background is treated with the Rolling ball algorithm. The calculated grayscale–thickness function $g(t)$ has to be suited to the main requirement of statistical analysis - to gather reliable statistics for a short time. Therefore the calculation of the grayscale distribution in the vicinity of the nanoparticle was proposed to make using polynomial grayscale-thickness relationship: $g(t)=g0+g1\ t+g2\ t2+\cdots$.
Thus, thresholding method is used for particle recognition and fitting procedure is suited for size measurements in original images. The preliminary image treatment does not have any impact on particle sizes. These two methods are in the basis of the program **AnNa** (Analyzer of Nanoparticles)
The program was successfully tested in systems with Ag nanoparticles in TEM and BF-DF STEM images. The example of Ag particle analysis in HAADF STEM image is shown in Fig. 1.
Program AnNa is available at website of the Institute of Crystallography: http://crys.ras.ru/struktura-instituta/nauchnye-podrazdeleniya/otdel-elektronnoj-kristallografii/laboratoriya-elektronografii.
Conclusion: The new method provides an opportunity to overcome difficulties for processing high noise (S)TEM images and the need to express the result by an integer number of pixels, and to open the valid information contained in variations of grayscale from pixel to pixel.

References:
[1]. D. O. Shvedchenko, T. N. Nekrasova, O. V. Nazarova, P. A. Buffat, E. I. Suvorova. J. Nanoparticle Res. 17(2015) 275.

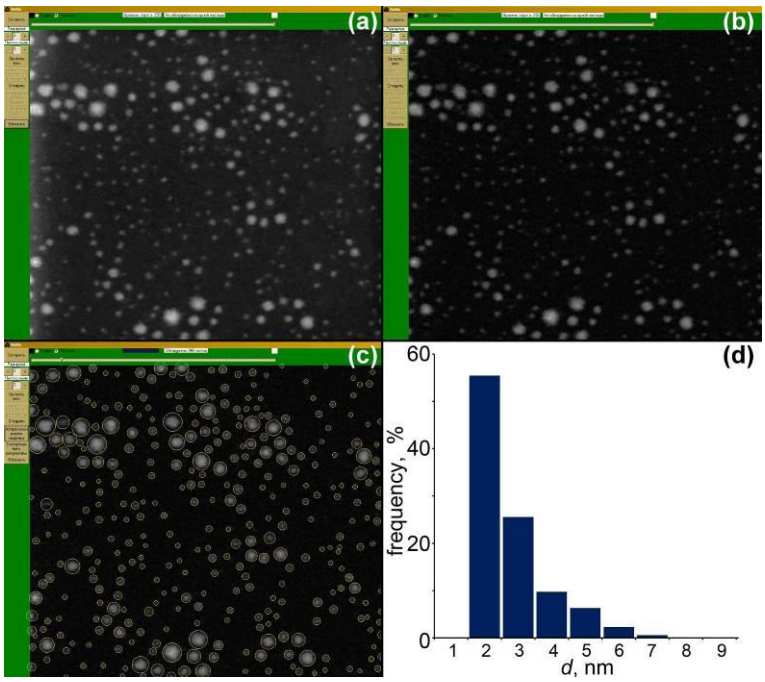

Figure 1. Loaded original HAADF STEM image (bmp format) with uneven background (a), background correction (b), recognition (685 particles) and size measurements (c), histogram – particle size distribution (c).

MS6.P012
Effect of chelating process on the size controlling of $CoFe_2O_4$ magnetic nanoparticles synthesized by coprecipitation method

S. F. Shams[1], M. R. Ghazanfari[2], M. Kashefi[2], C. Schmitz-Antoniak[1]

[1]Juelich Research Center, Peter Gruenberg Institute (PGI6), Juelich, Germany
[2]Ferdowsi University Of Mashhad, Materials Science and Engineering, Mashhad, Islamic Republic of Iran

sfs.academic@gmail.com

In last decades, the magnetic nanoparticles have been extremely employed in many applications such as electronic devices, sealing technology, and biomedical usages like MRI contrast agent, magnetic targeted drug delivery, and magnetic hyperthermia. On the other hand, the particle size can be known as a critical property of powders in all applications especially in biomedical ones. In present research, the effects of different chelating agents on the final size of synthesized $CoFe_2O_4$ nanoparticles during coprecipitation method were investigated. In order to achieve these aims, the citric, acetic, and stearic acids were utilized in situ as chelating agents. The studies of particles hydrodynamic size were done by dynamic light scattering (DLS) analyses. Moreover, the structural, microstructural, and magnetic properties of particles were evaluated by X-ray diffraction (XRD), transmission electron microscopy (TEM), and vibration sample magnetometer (VSM) techniques. The results show that the utilization of chelating agents can be caused to limitation of particles growth and control of their size in nanometric scales. Furthermore, although the stearic acid agent can be led to lower size of particles due to more effective chelating process, these particles show relatively lower crystallinity degree and saturation magnetization (M_s) compared to coated particles by citric acid.

MS6.P013
In situ study of highly active PtNi octahedral ORR electrocatalysts at the atomic scale

M. Shviro[1], M. Gocyla[1], M. Heggen[1], R. Dunin-Borkowski[1]

[1]Forschungszentrum Jülich GmbH, Ernst Ruska-Centre for Microscopy and Spectroscopy with Electrons and Peter Grünberg Institute, Jülich, Germany

m.shviro@fz-juelich.de

PtNi octahedral nanoparticles (NPs) represent an evolving class of electrocatalysts, which are expected to show improved oxygen reduction reaction (ORR) activities. A full understanding of such reactions requires a knowledge of the structural and chemical evolution of the NPs. In situ techniques are increasingly important for closing this gap in material characterization. In particular, in situ transmission electron microscopy (TEM) can now be performed using specimen holders that are based on micro-electro-mechanical systems (MEMS) technology and allow catalysts to be analysed under controlled conditions. Previous studies have shown that PtM (M = transition metal) NPs demonstrate enhanced catalytic performance after thermal annealing. This improvement is thought to result from the creation of specific surface atomic configurations.[1],[2] For shaped NPs, high temperature thermal annealing can result in undesired morphological shapes, as reported in previous TEM studies on the thermal annealing of shaped Pt nanoparticles..[3] A recent study by Pan et al.[4] reported changes in Ni content at the surfaces of octahedral NPs during heating, while Gan et al.[5] showed that octahedral PtNi NPs largely maintain their octahedral shapes during annealing up to 500 °C. Here, we use a MEMS-based *in situ* specimen holders to observe structural and compositional changes of active PtNi octahedral catalysts under controlled reducing and oxidizing conditions using high-resolution TEM, high-angle annular dark field scanning TEM (HAADF-STEM) and energy dispersive x-ray spectroscopy (EDX). We follow the dynamic evolution of NP morphology, faceting and elemental segregation under working conditions. We successfully follow changes to the octahedral catalysts from segregated structures (Fig. 1a) to alloy configurations and finally shapeless structures (Fig. 1b) at different temperatures under reducing and oxidizing conditions.

References:

[1] S. Chen, P. J. Ferreira, W. Sheng, N. Yabuuchi, L. F. Allard, Y. Shao-Horn, *J. Am. Chem. Soc.* 2008, *130*, 13818.
[2] C. Wang, G. Wang, D. van der Vliet, K.-C. Chang, N. M. Markovic, V. R. Stamenkovic, *Phys. Chem. Chem. Phys.* 2010**,** *12*, 6933.
[3] Z. L. Wang, J. M. Petroski, T. C. Green, M. a. El-Sayed, *J. Phys. Chem. B* **1998**, *102*, 6145.
[4] Y. Tin Pan, J. Wu, X. Yin, H. Yang , *AIChE J.* 2015, *62*, 399.
[5] L. Gan, M. Heggen, C. Cui, P. Strasser, *ACS Catal.* 2016, *6*, 692.

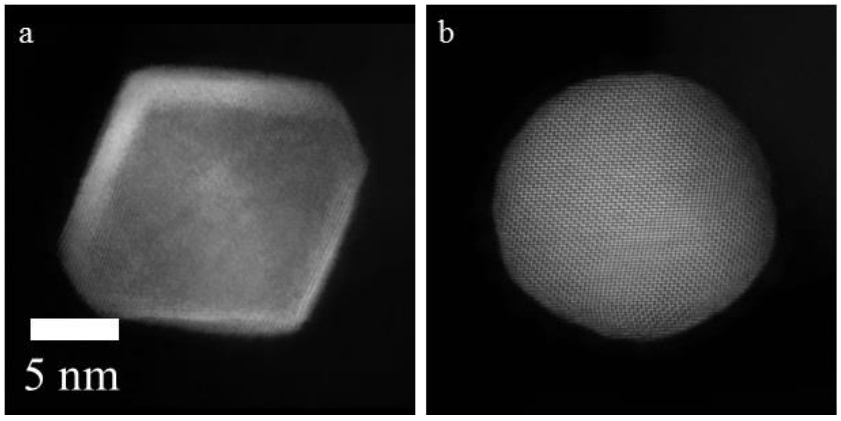

Figure 1. HAADF-STEM images of (a) an octahedral PtNi NP with a segregated structure under reducing conditions at 300 °C; (b) the same NP shapeless after examination at 600 °C under reducing conditions.

MS6.P014
Description and quantification of defects in orthorhombic (Mo,V)O_x mixed oxide

L. Masliuk[1], M. Heggen[2], A. Trunschke[1,2], K. Hermann[1], M. G. Willinger[1,3], R. Schlögl[1,4]
T. Lunkenbein[1]

[1]Fritz-Haber-Institut der Max-Planck-Gesellschaft, Inorganic Chemistry, Berlin, Germany
[2]Forschungszentrum Jülich GmbH, Ernst-Ruska Centre, Jülich, Germany
[3]Max Planck Institute of Colloid and Interphases, Golm, Germany
[4]Max Planck Institute for Chemical Energy Conversion, Department of Heterogeneous Reactions, Mülheim a.d. Ruhr, Germany

liumasliuk@fhi-berlin.mpg.de

Defects in catalysts modify the reaction pathway and influence the outcome. Thus, a detailed knowledge of the real bulk and surface structure of the catalytic material is extremely important. Unfortunately, these local structural heterogeneities can easily be overseen by common sample averaging techniques such as X-ray diffraction (XRD) or X-ray photoelectron spectroscopy (XPS). Here transmission electron microscopy (TEM) imaging allows to investigate the structure at a local, atomic scale and provides, therefore, new insights in heterogeneous catalysis research.[1]
Besides many active selective oxidation catalysts, molybdenum and vanadium based orthorhombic mixed-metal oxides crystallize in the so-called M1 structure are promising candidates for the partial oxidation of light alkanes. Ternary (Mo,V)O_x mixed oxides are often used to study the structural influence on selective oxidation reactions.[2,3] While their ideal bulk and surface structures are investigated in detail reports focusing on an in-depth defect description are scarce.[4-5] Here we provide a quantitative and qualitative analysis of local structure deviations in an orthorhombic (Mo,V)Ox mixed oxide using the concept of tiling based on scanning transmission electron microscopy (STEM). This allows us to reveal new structural connectivities of the pentagonal {(Mo)Mo_5O_{27}} building blocks.
Our local and statistical TEM investigation shows that orthorhombic (Mo,V)O_x mixed oxide exhibits an average defect concentration of 2.3%, which is not detectable by XRD. We apply tiling for a facile separation of local regions that deviate from the ideal bulk structure (Figure 1). Our local structure analysis reveals new linear and triangular motifs that can be expressed by a re-connectivity of the {(Mo)Mo_5O_{27}} pentagonal building blocks, intergrowth, interstitial regions, and inclinations. We distinguish between five linear (mirrored, translated, shared, twinned, and rotated) and two triangular structural motifs, respectively, which can co-exist at interphases and/or surface regions. More complex structural arrangements deviating from the ideal orthorhombic structure, such as intergrowth and interstitial regions usually include the structural motifs mentioned above (Figure 1).
In conclusion, we have investigated orthorhombic (Mo,V)O_x mixed metal oxide by means of local high resolution STEM imaging. The defects can be classified as linear (connection of two pentagonal building blocks) and triangular structural motifs (connection of three pentagonal blocks), respectively, intergrowth, interstitial regions, and inclinations. The quantitative defect analysis may allow new structure-activity correlations.

References:
[1] Qing-Hua, Z.; Dong-Dong, X.; Lin, G., *Chin. Phys. B* 2016**,** *25* (6), 066803.
[2] Schlögl, R., *Top. Catal.* 2011**,** *54* (10-12), 627-638.
[3] Konya, T.; Katou, T.; Murayama, T.; Ishikawa, S.; Sadakane, M.; Buttrey, D.; Ueda, W., *Catal. Sci. Technol.* 2013**,** *3* (2), 380-387.
[4] Lunkenbein, T.; Girgsdies, F.; Wernbacher, A.; Noack, J.; Auffermann, G.; Yasuhara, A.; Klein-Hoffmann, A.; Ueda, W.; Eichelbaum, M.; Trunschke, A.; Schlogl, R.; Willinger, M. G., *Angew. Chem., Int. Ed.* 2015**,** *54* (23), 6828-6831.
[5] Vogt, T.; Blom, D. A.; Jones, L.; Buttrey, D. J., *Top. Catal.* 2016, 1-7.

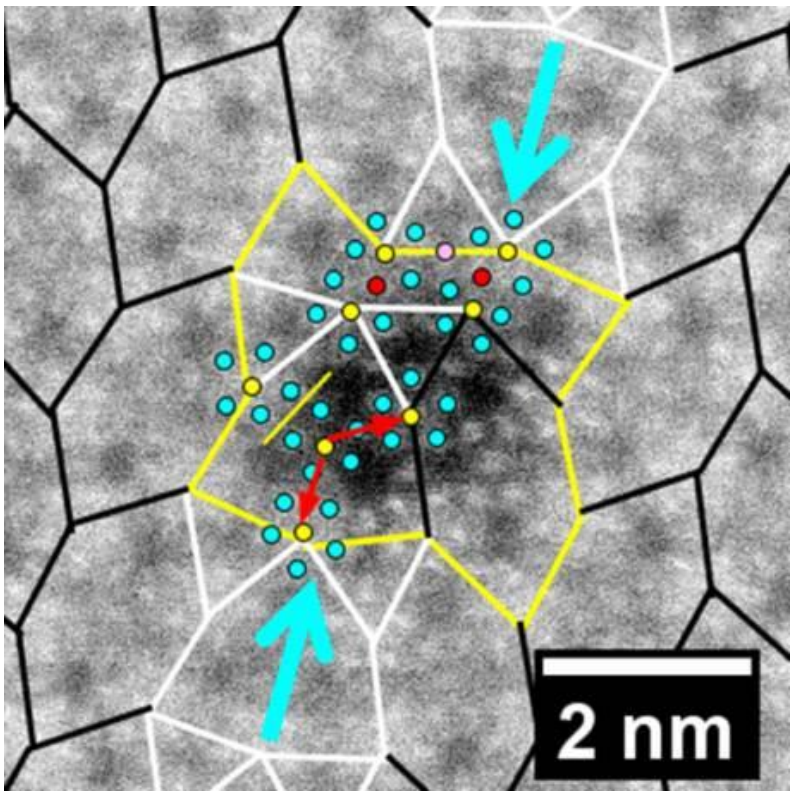

Figure 1. HAADF-STEM image of orthorhombic (Mo,V)O_x mixed oxide viewed along [001] highlighting an interstitial region (yellow polygon) and the pseudo-trigonal intergrowth (white tiles) processing through the orthorhombic bulk (black tiling), the interstitial region contains two translation motifs (marked by red arrows), a mirror motif (mirror plane is denoted by yellow line), two shared motifs (shared cations are highlighted red) and a rotated motif (the respective cation is marked pink), the yellow and cyan circles highlight the central and side cations of the standard pentagonal building blocks.

MS6.P015
TEM investigation on misfit layer compounds of the system LaSe-VSe_{2-x}

T. Dankwort[1], U. Ross[2], M. Falmbigl[3], G. Mitchson[4], D. Hamann[4], D. Johnson[4], A. Lotnyk[2], L. Kienle[1]

[1]Christian-Albrechts-Universität, Technische Fakultät, Kiel, Germany
[2]IOM , Leipzig, Germany
[3]Drexel University, Philadelphia, PA, United States of America
[4]University of Oregon, Eugene, Germany

td@tf.uni-kiel.de

Introduction: Recently, van der Waals heterostructures have been recognized as a powerful concept to tailor new types of materials1. Within this concept individual building blocks of two-dimensional layers of e.g. dichalcogenides can be stacked on top of each other in any desired sequence to gain new architectures and properties. However, the number of building blocks for realization of ultrathin heterostructures is limited to materials which exhibit van der Waals gaps in the bulk structure.
Objectives: Our recent study focuses on the synthesis and characterization of misfit layer compounds of the system LaSe-VSe_{2-x}. For these materials layered VSe_{2-x} building units are confined between LaSe double-layers separated by non-epitaxial incommensurate interfaces. A combination of state of the art X-ray and electron microscopy techniques was applied to identify and quantitatively describe the complex structural phenomena.
Materials and Methods: The compounds were prepared using a diffusion constrained, kinetically controlled synthesis approach facilitating an amorphous precursor. Therefore, alternating layers with precise stoichiometry of the pure elements were deposited on a silicon substrate. The as obtained amorphous precursors were annealed *ex situ* to initiate the crystallization. Structural and chemical information were retrieved by probe corrected Transmission Electron Microscopy investigations and X-ray diffraction Rietveld refinements.
Results: Crystallization of the amorphous precursor results in layers of LaSe and VSe_{2-x} separated by non-epitaxial incommensurate interfaces. The films were *c*-axis oriented and the adjacent building blocks exhibit incommensurate (in plane) and turbostratic disorder. Quantitative HRSTEM investigation of the VSe_{2-x} layers revealed the formation of the V_3Se_4 phase while also nanodomains of VSe and VSe_2 were present. Rietveld refinements corroborate these findings.
Conclusion: The synthesis approach described above offers the opportunity to extend the field of potential building blocks of complex layered materials to candidates, which do not naturally exhibit a van der Waals gap in their bulk structure and thus significantly increases the number of possible combinations for van der Waals heterostructures. HRSTEM data is a critical tool in determining the atomic structure and local chemical composition of these heterostructures, which although highly *c*-axis oriented show complex disorder along the interface.

References:
[1] Geim, A. K. & Grigorieva, I. V. Van der Waals heterostructures. *Nature* **499,** 419–425 (2013).

MS6.P016
Outperforming magneto-electrical properties of cobalt−carbon nanogranular deposits locally written by focused-electron-beam-induced deposition

I. Utke[1], Y. Zhang[2], X. Maeder[3], C. Guerra-Nuñez[4], J. P. Best[3], M. V. Puydinger dos Santos[3,1]
M. Velo[1], R. D. Domingos[1], F. Beron[1], K. Pirota[1], J. A. Diniz[1], S. Moshkalev[1]

[1]University of Campinas, Campinas, Brazil
[2]Empa, Dübendorf, Switzerland
[3]Empa, Thun, Switzerland
[4]Empa, Zürich

ivo.utke@empa.ch

Introduction: Non-noble metal containing deposits directly written with gas-assisted focused-electron-beam-induced deposition (FEBID) always suffered from the lack of an effective purification method not oxidizing the metal.
Objective: We developed an effective post-growth annealing approach. It represents a novel and reproducible method for tuning the magneto-electrical transport properties of directly written nanogranular Co−C deposits.[1,2]
Materials, Methods and Results: The metal content and electrical properties of Co−C−O nanodeposits obtained by electron-induced dissociation of volatile $Co_2(CO)_8$ precursor adsorbate molecules were reproducibly tuned by applying postgrowth annealing processes at 100 °C, 200 °C, and 300 °C under pressures below 5 x 10^{-5} mbar for 10 min. Advanced thin film EDX analysis showed that during the annealing process predominantly oxygen is released from the Co−C−O deposits, yielding an atomic ratio of Co:C:O = 100:16:1 (85:14:1) with respect to the atomic composition of as-written Co:C:O = 100:21:28 (67:14:19) (Figure 1a). In-depth Raman analysis (Figure 1b) suggests that the amorphous carbon contained in the as-written deposit turns into graphite nanocrystals with size of about 22.4 nm with annealing temperature. Transmission electron microscopy (TEM) analysis showed reduction of the hexagonal-closed-packed (hcp) Co_3O_4 nanocrystals into metallic face-centered-cubic (fcc)/hcp Co during annealing. Remarkably, these microstructural changes allow for tuning of the electrical resistivity of the deposits over 3 orders of magnitude from 26 mΩ cm down to 26 μΩ cm (Figure 2), achieving a residual resistivity of $\rho 2\ K/\rho 300\ K = 0.56$ (Figure 3), close to the value of 0.53 for pure Co films with similar dimensions.[3] In addition, the magnetoresistance (MR) signal found in our FEBID granular nanocomposites are about one order of magnitude larger than those found in pure Co with similar dimensions defined by electron beam lithography.
Conclusions: The outperforming properties of the nanogranular Co-C directly written by gas assisted focused electron beam induced deposition make this material interesting and advantageous for applications such as advanced scanning-probe systems, magnetic memory, storage, and ferroelectric tunnel junction memristors.

References:
[1] Fernández-Pacheco, A., *et al*., 2009, *J. Phys. D: Appl. Phys.* 42, 055005.
[2] Puydinger dos Santos, M. V., *et al*., 2016, *ACS Appl. Mater. Interfaces* **8**, 32496.
[3] De Vries, J. W. C., 1988, Thin Solid Films 167, 25.

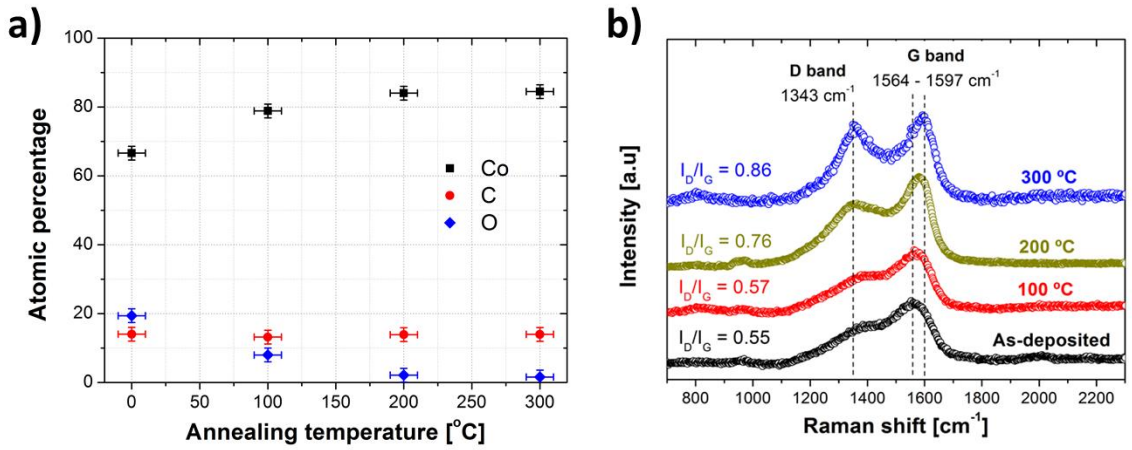

Figure 1. (a) Thin film corrected atomic composition analysis by EDX and (b) Raman spectra in the carbon range (disordered carbon band, D (1350 cm^{-1}), and graphitic band, G (1580 cm^{-1}) are present) as a function of the postgrowth annealing temperature.

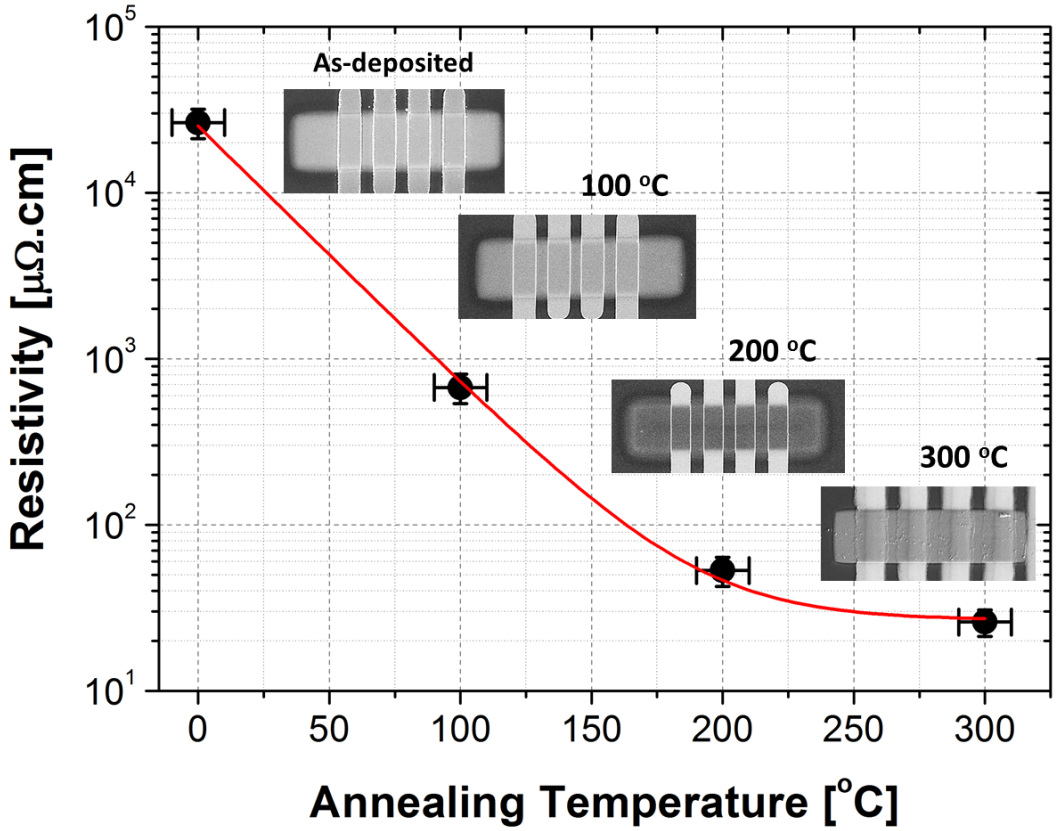

Figure 2. Resistivity of Co FEBID material as a function of postgrowth annealing temperature, measured for five different samples at each temperature. Insets show top view SEM images of the four-point platinum electrodes taken at 3 keV.

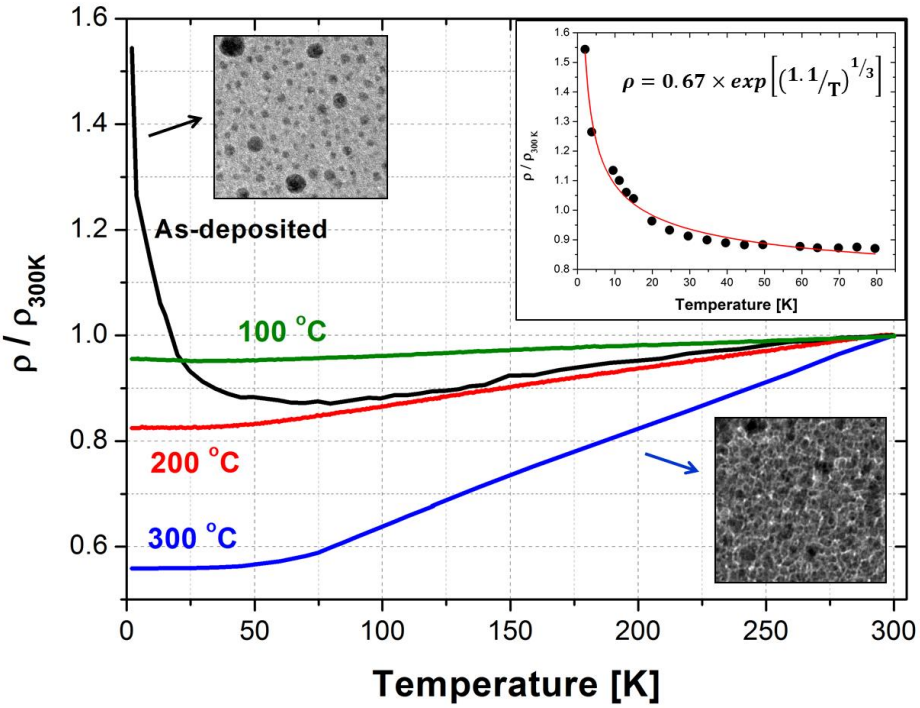

Figure 3. Normalized electrical resistivity of Co-FEBID deposits as a function of the temperature during cooling from 300 K to 2 K of the as-deposited as well as the annealed samples at 100 °C, 200 °C, and 300 °C. *Inset*: Normalized resistivity during the cooling process for the as-deposited Co−C FEBID material. Mott"s variable-range hopping mechanism fits our experimental data and gives a bi-dimensional thin film deposit.

MS6.P017
Challenges in imaging and characterization of CsPbBr3 QDs/AlOx nanocomposites

A. Loiudice[1], S. Saris[1], E. Oveisi[1], D. T. L. Alexander[1], D. Laub[1], R. Buonsanti[1]

[1]EPFL, Lausanne, Switzerland

anna.loiudice@epfl.ch

In the last year, all-inorganic perovskite quantum dots (CsPbX3 QDs with X=Br,I,Cl) have emerged as a new class of semiconductor nanocrystals with improved optical properties compared to the well-studied cadmium based QDs [1,2]. For their implementation in optoelectronic devices and for exploring their properties, one of the issues that still remains to be addressed is their lack of stability with respect to temperature, moisture, and light exposure. To combat this, we have successfully developed a low temperature process for atomic layer deposition (ALD) of a thin layer of metal oxide on a film of CsPbBr3 QDs that 1) protects the perovskite QDs from water and high temperature, and 2) prevents dissolution of the bottom layer or anion exchange in a multi-layering process.
Preparing samples for transmission electron microscopy (TEM) characterization of perovskite QDs is usually a big challenge. Their instability in several solvents as well as to temperatures above 50ºC hinders the use of traditional sample preparation techniques for TEM cross-section analysis (mechanical polishing and/or ion beam milling with a broad or focused beam). This has spurred us to develop the new approach presented here based on the ultramicrotomy of a nanocomposite of QDs deposited on a soft polymer substrate.
Different electron microscopy techniques, in particular STEM-HAADF, EDX, and EELS were performed for structural analysis of the microtomed nanocomposite, as shown in Fig. 1. Together the results allowed us to confirm the complete infilling of the ALD deposited alumina across the entire thickness of the nanocomposite film. The alumina coating further conferred stability to the QDs under the electron beam, even enabling high-resolution imaging without special low-dose techniques. The obtained nanocomposite shows exceptional stability against exposure to air (over 45 days), to irradiation under simulated solar light (over 8 hours), to thermal treatment (up to 200 ºC in air), and finally to immersion in water [3]. However, ALD alumina is susceptible to hydrolysis by long term exposure to water, particularly for films deposited at low temperature. With this in mind, we are exploring the possibility to further improve the long-term stability of CsPbBr3 QD film by fabricating ALD nanolaminates, specifically alumina/zirconia [4].

References:
[1] D. Bera, *et al., Materials,* 2010, 3, 2260.
[2] L. Portesecu, *et al., Nano Letters*, 2015, 15, 3692.
[3] A. Loiudice *et al.,* submitted.
[4] A. H. Ip *et al.*, *Appl. Phys. Lett.*, 2013, 103, 263905.

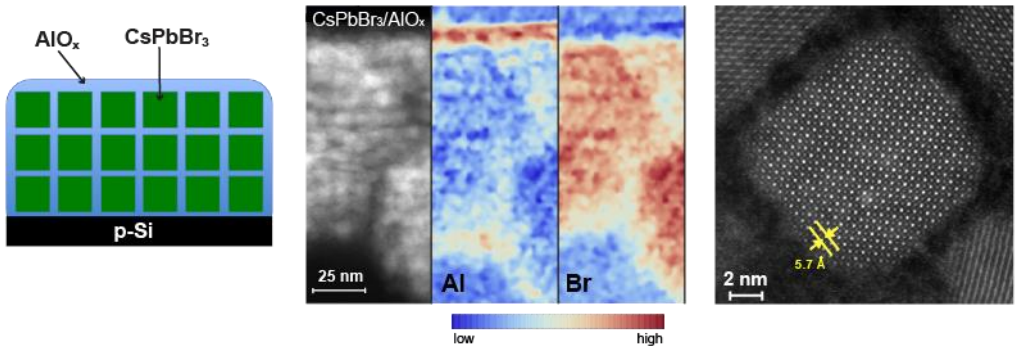

Figure 1

MS6.P018
Fluid catalytic cracking catalysts – a microscopic perspective

F. Krumeich[1], J. Ihli[1,2], W. C. Cheng[3], Y. Shu[3], J. van Bokhoven[1,2]

[1]ETH Zürich, Department of Chemistry and Applied Biosciences, Zürich, Switzerland
[2]Paul Scherrer Institut, Villigen, Switzerland
[3]W. R. Grace Refining Technologies, Columbia, MD, United States of America

krumeich@inorg.chem.ethz.ch

Fluid catalytic cracking (FCC) is a chemical conversion process of industrial relevance, providing the majority of the world's gasoline. In this process porous composites composed of zeolite, clay and minor additives are used to crack the heavy fractions in crude oil into gasoline and light olefins. A significant decrease of the catalytic activity of these composites is observed during long-term operation, necessitating their continuous fractional replacement. As major refineries require several tons of fresh FCC catalysts on a daily basis, there is a strong need to extend the lifetime of such catalysts. To realize this it is essential to understand the structural changes that are behind the observed catalyst deactivation.

A three-dimensional model of individual catalyst particles and its pore architecture derived by different X-ray 3D imaging techniques recently highlighted structural changes on the micrometer scale, >300 nm [1]. In this contribution, we present and discuss electron microscopy results obtained from both pristine and industrially deactivated FCC catalysts characterizing structural changes on the nano scale.

The FCC catalysts investigated are spherical in appearance (diameter 50 - 100 micrometer). Cross-sections of these particles, used to investigate their internal structure, were prepared following well-established procedures [2]. The samples were embedded in a resin and fixed in a Cu tube. After hardening of the resin, the tube was cut into thin slices. For TEM and STEM investigations, these slices were mechanically thinned and finally ion-milled.

SEM images of these cross-sections recorded with back-scattered electrons (BSE) reveal a porous and partly fibrous interior structure (Fig. 1). The whole particle is surrounded by a dense envelope (Fig. 1a) which is iron rich according to EDX spectroscopy (Fig. 1b). HAADF-STEM images, (Fig. 2a), taken at the edge of such a particle reveal that this envelope is two to five micrometer thick and consists mainly of silicon oxide with little amounts of aluminum and iron (Fig. 2b-c). Furthermore, EDXS mapping allowed the identification of zeolite and clay fractions consisting either mainly of Si and La or Si and Al. In addition to these main components iron rich particulates, introduced from the feedstock, appear to be homogenously distributed in the core of the particle and concentrated in the edge of the particle. Current theories suggest that these feedstock introduced impurities cause the formation of the aforementioned dense, iron-rich amorphous silicon oxide phase during unit operation, triggering a loss of porosity in the outermost layer and eventual a decrease in the catalysts activity. Whether the observed incorporation of these particles is truly causing this layer formation is part of the current investigations. [3]

References:
[1] J. C. da Silva et al. ChemCatChem **2015**, *7*, 413–416.
[2] E. Müller and F. Krumeich, Ultramicr. **2000**, *84*, 143-147.
[3] Electron microscopy was performed at the Scientific Center for Optical and Electron Microscopy (ScopeM) of ETH Zurich.

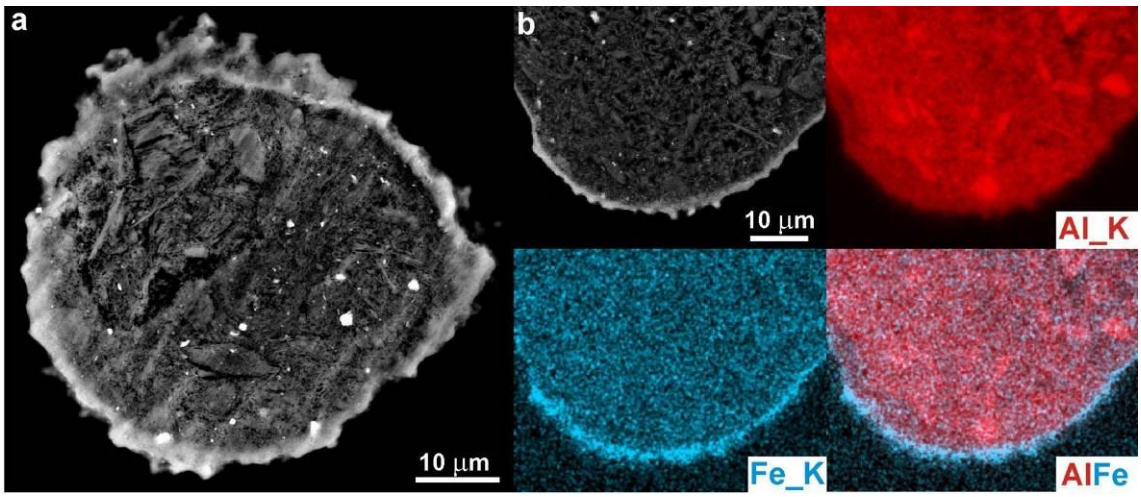

Figure 1. BSE-SEM images of cross-sections of a complete sphere (a) and of a fraction (b) along with the corresponding Al and Fe EDXS maps and a combined map for both elements. (Quanta 200 (FEI)).

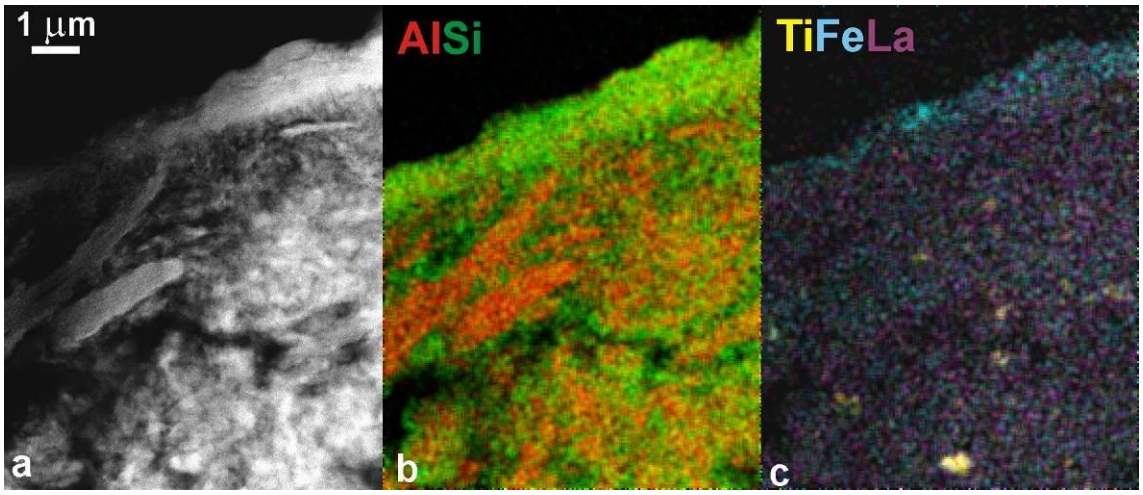

Figure 2. Thin area close to the rim of a spheres cross-section. (a) HAADF-STEM image, (b) and (c) combined EDXS maps for Al and Si as well as for Ti, Fe and La (HD2700CS (Hitachi)).

MS6.P019
Observation of charge density waves in single-layer 1T-$TaSe_2$ at room temperature.

P. Börner[1], M. Kinyanjui[1], T. Lehnert[1], J. Köster[1], U. Kaiser[1]

[1]Ulm University, Electron Microscopy Group of Materials Science, Ulm, Germany

pia.boerner@uni-ulm.de

Following the discovery of the exceptional electronic and physical properties of the two-dimensional (2D) material graphene, and thanks to hard-ware aberration correction in TEM, a new research area has emerged namely on the atomic structure of 2D transition metal dichalcogenides (TMDs). Depending on their composition they have diverse properties as semiconductors, metals, or superconductors. Metallic TMDs like 1T/2H-TaSe2, or 2H-NbSe2 can produce — depending on temperature, doping and pressure — so-called charge density waves (CDWs) [1]. These superstructures are characterized by a periodic modulation of the charge density accompanied by a periodic lattice distortion (PLD). Already since the 1970s it is known that bulk 1T-$TaSe_2$ shows a commensurate (C)CDW/PLD at temperatures below 473 K [1] and the CCDW/PLD is characterized by a $\sqrt{13}\ a_0 \times \sqrt{13}\ a_0$ superstructure. Owing to the layered structure of the TMD materials, nowadays single layers of these materials can be mechanical exfoliated. However, so far it is not much known about the stability and the characteristics of CDWs/PLDs in single-layer TMDs.
Here we present the experimental characterization of PLDs in single-layer 1T-$TaSe_2$ using aberration-corrected high-resolution transmission electron microscopy (AC-HRTEM) and selected area electron diffraction (SAED). Experimental observations of PLDs in single-layer 1T-$TaSe_2$ are a challenge due to difficulties in sample preparation and due to electron beam damage occurring during the TEM experiment. Thus 1T-$TaSe_2$ - graphene heterostructures are investigated instead of a freestanding 1T-$TaSe_2$ monolayer. In this heterostructure graphene is used as a support material for imaging a few micrometer large exfoliated 1T-$TaSe_2$ monolayer and to reduce radiation damage effects [2]. Our TEM experiments were performed at room temperature at an accelerating voltage of 80 kV. Figure 1 shows that PLDs are formed in a monolayer 1T-$TaSe_2$ - graphene heterostructure. Figure 1 (a) shows a simulated AC-HRTEM image of a 1T-$TaSe_2$ monolayer with the $\sqrt{13}\ a_0 \times \sqrt{13}\ a_0$ superstructure and (c) shows a simulated kinematic electron diffraction pattern of this structure. The experimental AC-HRTEM image of a single 1T-$TaSe_2$ layer - graphene heterostructure is shown in Figure 1 (b) and in (d) the corresponding Fourier transformation is depicted. In addition we will present our first experiments obtained with the new spherical and chromatic aberration-corrected SALVE instrument operating in the range between 20 kV and 80 kV at exceptionally high-resolution. Results proving better understanding of electron-sample interaction will be also discussed. [3]
To conclude our results, CDWs/PLDs are stable in monolayer 1T-$TaSe_2$ and have the expected $\sqrt{13}\ a_0 \times \sqrt{13}\ a_0$superstructure.

References:

[1] J. A. Wilson, F. J. Di Salvo, and S. Mahajan, Advances in Physics 24.2 (1975): 117-201.
[2] G. Algara-Siller, S. Kurasch, M. Sedighi, O. Lehtinen, & U. Kaiser, Applied Physics Letters 103.20 (2013):203107.
[3] The authors acknowledge funding from the German Research Foundation (DFG) and the Ministry of Science, Research and the Arts (MWK) of the federal state Baden-Württemberg, Germany in the frame of the SALVE (Sub-Angstroem Low-Voltage) project.

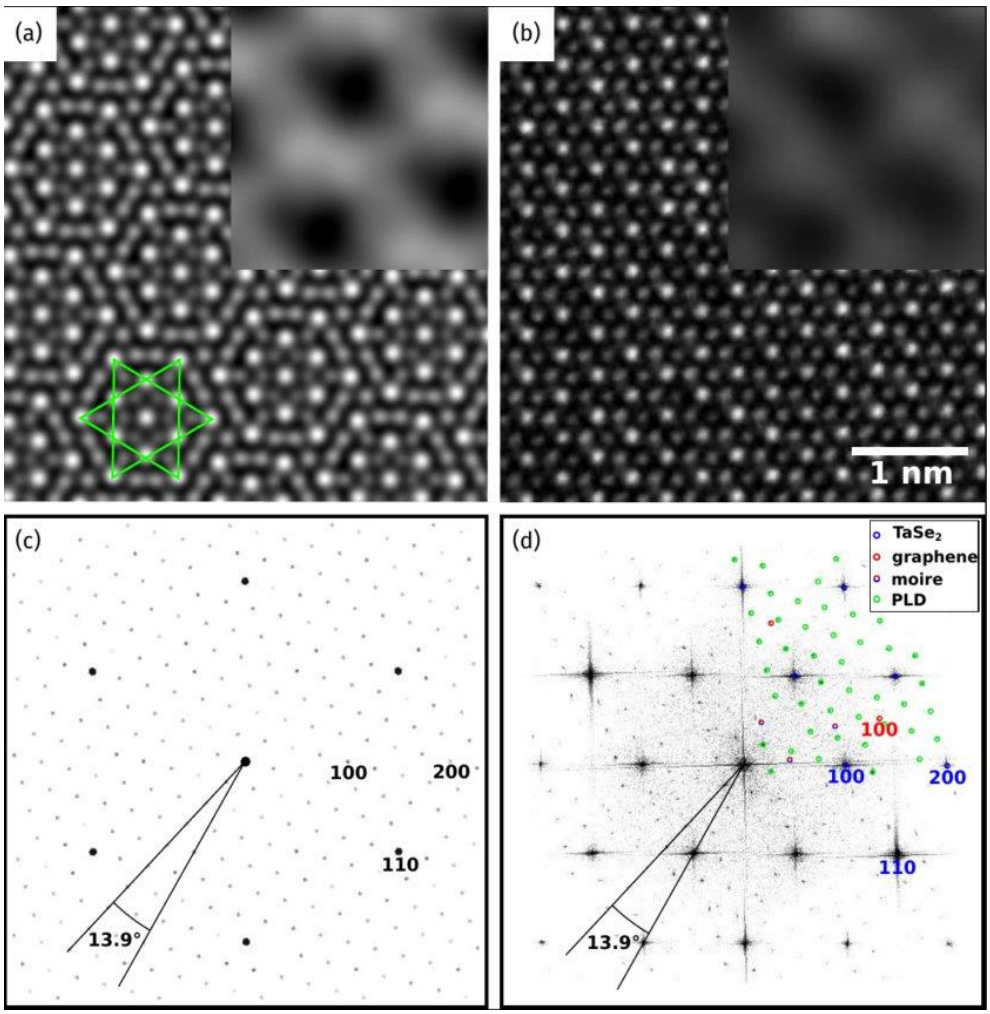

Figure 1. (a) Simulated AC-HRTEM image of a 1T-TaSe2 monolayer with the $\sqrt{13}\,a_0 \times \sqrt{13}\,a_0$ superstructure and (c) simulated kinematic electron diffraction pattern of this structure. On parts of (a) a Gaussian blur is applied to show a low frequency contrast variation. (b) Experimental AC-HRTEM image of a single 1T-TaSe2 layer - graphene heterostructure showing the same contrast variation as the simulation (a). (d) Fourier transformation of the experimental image (b) showing the expected satellite spots.

MS6.P021
Characterization of multiply twinned and single-crystalline hexagonal close-packed Au@Pt core-shell nanocrystals

A. C. Swertz[1], J. Knossalla[1], C. W. Lehmann[1], N. Pfänder[2], F. Schüth[1]

[1]Max-Planck-Institut für Kohlenforschung, Mülheim an der Ruhr, Germany
[2]Max-Planck-Institut für Chemische Energiekonversion, Mülheim an der Ruhr, Germany

swertz@kofo.mpg.de

Introduction: Metallic nanoparticles, especially gold, are known to offer a wide range of different shapes of single-crystalline or multiply twinned particles.[1,2] Bimetallic nanoparticles show even more complex structures as different distributions of the two elements within the particles, like core-shell or alloy, are possible. The equilibrium shape of these particles is not only depending on parameters like reaction temperature and reducing agents but also on the atomic size and ratio of the used elements.[3]
Objectives: The Aim of this work was the analysis of Au core Pt shell nanoparticles regarding their shape and crystal structure. The observed structures of these particles were compared to the structures of pure gold nanoparticles synthesized under similar reaction conditions to investigate the influence of the formation of the platinum shell.
Materials and Methods: The analyzed Au@Pt particles were prepared via stepwise reduction of Au and Pt ions to form the core-shell structure. The characterization of the nanocrystals was carried out using a CS-corrected FEI Titan 80-300 operated at 300 kV for high-resolution transmission electron microscopy (HR-TEM) and selected area electron diffraction (SAED). The elemental distribution of Au and Pt within the bimetallic particles was analyzed with elemental mappings performed with an CS-corrected Hitachi HD-2700 dedicated STEM operated at 200 kV equipped with an EDAX Octane Ultra W EDX-detector.
Results: For the Au@Pt particles a great variety of different shapes could be observed. Common shapes of single-crystalline nanoparticles are truncated cubes and cuboctahedrons. The multiply twinned particles with clearly visible twin boundaries appear with decahedral and icosahedral shape with a five- or six-fold symmetry. The observed particles show comparable shapes as known from gold particles synthesized in a similar way. The distribution of gold and platinum within the particles was analyzed using EDX. The elemental mappings clearly evidence the expected Au core and Pt shell structure. The crystal structure of single-crystalline Au@Pt particles was analyzed using SAED patterns. The recorded patterns have a six-fold symmetry with 60°angles between adjacent reflections. Assuming an fcc-structure patterns with this symmetry correspond to an [111]-orientation of the crystal. However no reasonable lattice constant for a cubic structure could be determined from the SAED patterns. The calculated lattice constant diverges from the constants of Au and Pt by a factor of approx. $\sqrt{3}$. To explain this discrepancy a theoretical hcp-cell for Au and Pt was designed to compare calculated and measured lattice spacings. Diffraction patterns with a six-fold symmetry of an hcp-crystal correspond to an orientation along [0001] zone axis. The measured lattice spacings from the patterns are in good agreement with the theoretical spacings for hcp crystals of Au and Pt. So the structure of these Au@Pt particles is expected to be hcp rather than fcc.
Conclusion: The analyzed Au@Pt core-shell particles show comparable shapes as observed with pure gold nanoparticles synthesized in a similar way. However the crystal structure of single-crystalline particles is much different. For Au@Pt all analyzed particles seem to have a hexagonal close-packed rather than the expected face-centered cubic structure. To understand this observation the influence of the platinum shell-formation will be further investigated. Therefore the role of parameters like the reducing agent and the reaction temperature will be further studied.

References:
[1] Huang, R., et al., *RCS Adv.* 4, 7528-7537 (2014).
[2] Yacaman, M., J., et al., *J. Vac. Sci. Technol. B* 19, 1091-1103 (2001).
[3] Yun, K., et al., *Acta Materialia* 60, 4908-4916 (2012).

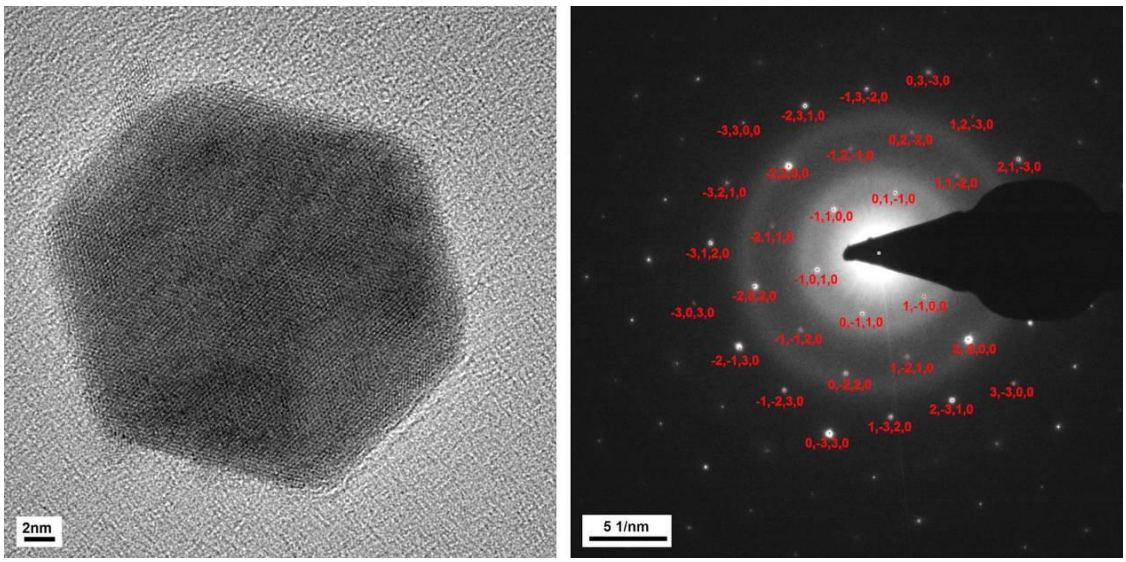

Figure 1. HR-TEM image and SAED pattern of an Au@Pt particle. The reflections are indexed for the [0001]-orientation of a hcp crystal.

MS6.P022
Study of magnetic nanoparticles using new dispersion technique and differential phase contrast in STEM

B. K. Park[1], S. H. Lee[1], D. Y. Kim[1], J. I. Son[1], K. J. Choi[1], C. H. Rhee[1], W. J. Moon[2]

[1]Thermo Fisher Scientific, Materials & Structural Analysis (formerly FEI), Suwon-si, Gyeonggi-Do, South Korea
[2]Korea Basic Science Institute, Gwangju, South Korea

byungkyu.park@fei.com

In the TEM specimens prepared with general sampling method, it is very difficult to avoid aggregation of nanoparticles even though dispersant is added. Especially, this aggregation occurred more prominently in magnetic particles. In this work, we tried to apply new dispersion technique which can be extensively applied to diverse nanoparticles. The technique was developed by improving the conventional formvar support film method.
Magnetic particles with magnetization properties have been extensively studied by various analysis tools [1-4] and TEM and STEM are a powerful tool to research the crystallographic and chemical properties [5]. Especially, differential phase contrast (DPC) in STEM is an attractive function for characterization of magnetic or electric properties.
We present results using DPC technique to give information about magnetic domain contrast and its vector direction in magnetic particles. This technique uses sensitivity direction detectors to measure quantitatively the deflection of the electron beams when they are influenced by magnetic field [6-7].
The magnetic particles were prepared by solvo-thermal method. The magnetic properties of these magnetic particles were characterized using STEM installed DPC detectors. The crystal structures were investigated using SAED pattern in TEM. The chemical compositions of magnetic particles were analyzed by EDS Spectrum, mapping.

References:
[1] Burda C, Chen X and Narayanan R, Chem.Rev. (2005), **105**, p. 1025-1102.
[2] Frank Caruso, Andrei S. Susha and Michael Giersig, Adv. Mater (1999), **11**, No 11.
[3] Yin Y., Alivisatos A.P., Nature (2005), 437, 664-670.
[4] Qing Song and Z.John Zhang, J.Am.Chem.Soc. (2012), 134, p.10182-10190.
[5] Williams, David B in "Transmission Electron Microscopy", (Publisher, Springer-Verlag US) p.3.
[6] M.R.McCartney, P Kruit and A.H.Buist, Ultramicroscopy (1996), 65, p.179-186.
[7] Matthias Lohr, Ralph Schregle and Michael jetter, Ultramicroscopy (2012), 117, p.7-14.

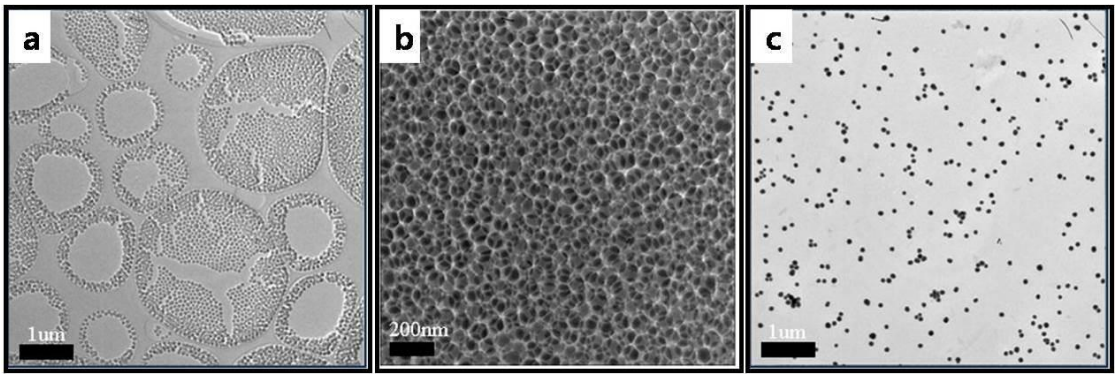

Figure 1. TEM micrographs of silica nano-particles prepared by each different dispersion method. TEM micrographs taken from the specimen prepared with general method((a) and (b)) and new dispersion technique(c).

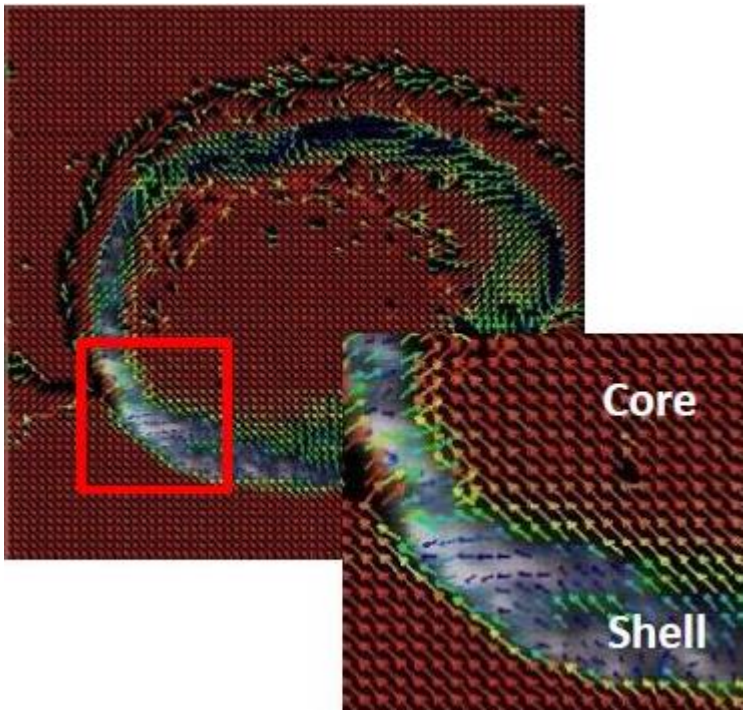

Figure 2. Magnetic field in vector diagrams in CoFe2O4@MnFe2O4 magnetic particle. CoFe2O4 area is mostly observed has one magnetic direction and MnFe2O4 area is observed as the arrows toward to core material.

MS6.P024
Structural studys of flat golc nanoparticles using zone axes processiin diffraction and diffraction pattern simulation

M. C. Mendoza Ramirez[1], M. Avalos-Borja[1]

[1]Instituto Potosino de Investigación Científica y Tecnológica, Advanced Materials, San Luis Potosí, Mexico

miriam.mendoza@ipicyt.edu.mx

Introduction: Design nanoparticles with well-defined shapes and uniform size is a fundamental priority on materials research. Despite significant advances, there are still questions regarding the mechanisms that govern particle growth.
Some authors have suggest that presence or absence of structural defects could form a crucial role in the morphology of the final product [1]. The presence of anomalous crystalline structure and defects is the central topic of this work.
In particular, we will refer to defects found in "nanoplates". This particles had attracted interest owing to "forbidden reflections" observed by electron diffraction [2].
Our novel methodology using PED (Precession Electron Diffraction) technique allowed us to obtain detailed structural information about a secondary structure found inside nanoplates, overcoming the limitations of the conventional techniques of structural elucidation (DRX and SAED).
Objectives: To analyze the secondary phase in Au nanoplates acquiring zone axes PED patterns and to compare them with simulated patterns.
Materials and Methods: Nanoprism were synthetized according to C. Wang [3] methodology. Microscopy was performed on a Tecnai F-30 TEM FEI microscope. PED patterns were acquired using an analogic Spinningstar unit from Nanomegas [4]. Kinematical diffraction patterns were simulated using MacTempas and CrystalKit [5].
Results: Au nanoplates were synthetized using surfactants; Triangular and hexagonal nanoplates were the majority obtained product (Figure 1). Nanoplates revel well defined bending contours, evidencing good crystallinity. SAED patterns show 1/3{422} forbidden reflections as well PED patterns (Figure 2).
Conclusions: Wang´s procedure was reproduced successfully. Particles show well defined bending contours and excellent crystallinity. Acquired patterns show "weak" reflections in most of its orientations. By using MacTempas and CrystalKit all acquired patterns were reproduced. The nature of the crystal"s inner defect(s) will be discussed.

References:
[1] Germain V., Li J., Ingert D., Wang Z. L., y Pileni M. P. "Stacking Faults in Formation of Silver Nanodisks" (2003). J. Phys. Chem. B, Vol. 107, No. 34.
[2] Kirkland, A. I.; Jefferson, D. A.; Duff, D. G.; Edwards, P. P.; Gameson, I.; Johnson, B. F. G.; Smith, D. J. Proc."Structural Studies of Trigonal Lamellar Particles of Gold and Silver" (1993). R. Soc. London A, 440, 589-609.
[3] Wang C., Kan C., Zhu J., Zeng X. , Wang X., Li H., y Shi D. (2010). "Synthesis of High-Yield Gold Nanoplates: Fast Growth Assistant with Binary Surfactants". Nanomaterials Volume 2010, 1-9.
[4] http://www.nanomegas.com/.
[5] http://www.totalresolution.com/.

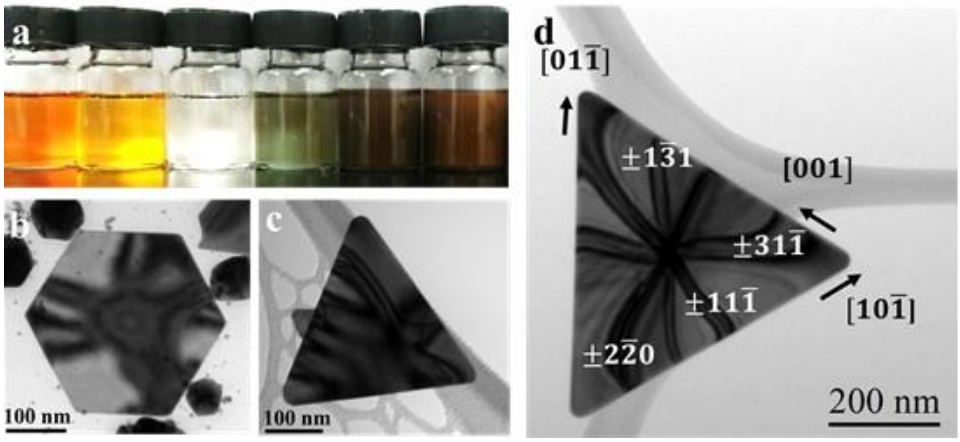

Figure 1. (a) Color change of reaction (from 1 to 30 min). (b, c and d) Bright Field micrograph of hexagonal and triangular particles showing bending contours

PED patterns were acquired in at least seven different zone axes. Additional reflections and anomalous patterns were found. In Figure 2 a comparison between an acquired pattern and a simulated pattern is made.

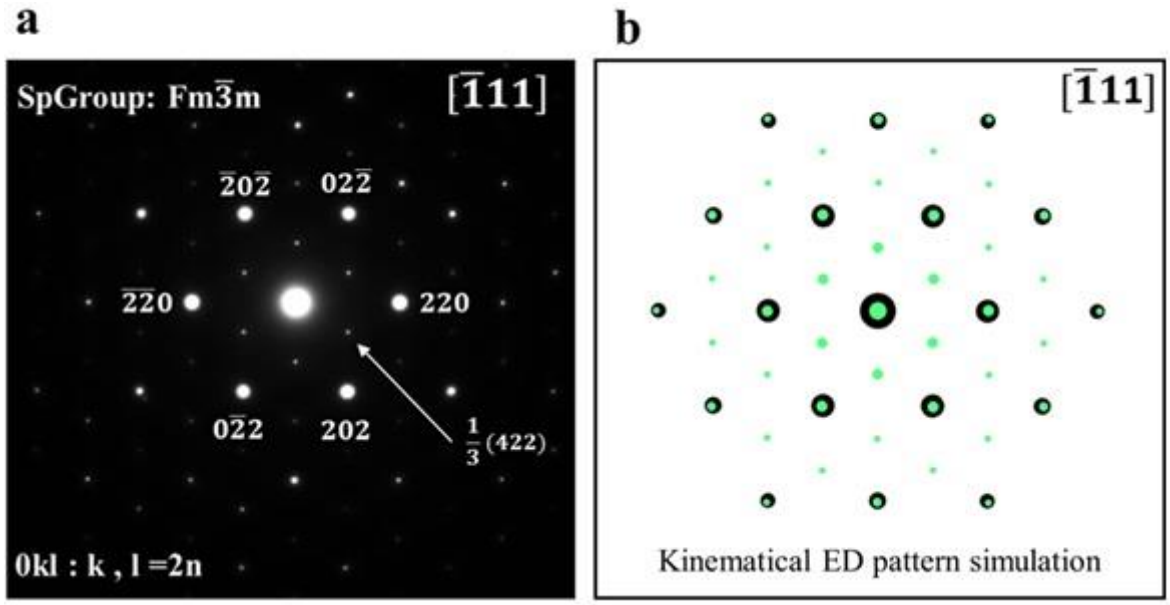

Figure 2. (a)An electron diffraction pattern acquired using PED and indexed as [. (b) Simulated Electron Diffraction Pattern using CrystalKit on MacTempas.

On Figure 2, black spots correspond to a perfect Cubic F crystal, while green spots are "secondary phase" diffraction.

MS6.P025
Enhanced visible-light photocatalytic oxidation of salicylic acid driven by the hydrogenated TiO_2 nanotubes arrays decorated with Ag nanoparticles

M. Plodinec[1,2], I. Grcic[3], A. Gajovic[2], X. Huang[1], M. G. Willinger[1,4]

[1]Fritz-Haber Institute der Max-Planck-Gesellschaft , Inorganic Chemistry Department, Berlin, Germany
[2]Rudjer Boskovic Institute, Division of Material Physics, Zagreb, Croatia
[3]University of Zagreb, Faculty of Chemical Engineering and Technology, Zagreb, Croatia
[4]Max Planck Institute of Colloids and Interfaces, Department of Colloid Chemistry, Potsdam, Germany

mplodinec@fhi-berlin.mpg.de

Since the black TiO_2 nanostructures show advanced performances in photocatalysis and water splitting reactions[1,2], we prepared a novel form of the black TiO_2-based photocatalyst for waste water purification. The photocatalytic efficiency was studied on the real contaminant from the pharmaceutical company, salicylic acid, listed as a pollutant in precipitation, surface waters and as a constituent of humic material in drinking waters. The novel photocatalyst was formed by the hydrogenation of TiO_2 nanotube arrays additionally decorated with Ag nanoparticles. Prepared nanotubes arrays synthesized by this procedure are strongly attached on Ti foils. In this way, after the catalytic reaction, there is no nanoparticles released in purified waste water as in the case of powder catalysts.
The influence of nanotube array decoration with silver nanoparticles and annealing in a hydrogen atmosphere on the photocatalytic activity, using visible and solar simulated radiation, will be presented. TiO_2 nanotube arrays were synthesized by simple, routine, anodization process and decorated by silver nanoparticles using photoreduction process. The study of structure, phase transition and optical properties change before and after modification will be shown. The structural and phase change were studied by Raman spectroscopy, scanning and transmission electron microscopy techniques (SEM and TEM). Additionally, optical characteristic was investigated by UV-vis spectroscopy and photocatalytic activity in flow cell reactor.
HAADF STEM images of cross-section performed on the TiO_2 NT's@Ag sample, that TiO_2 nanotubes have an outer diameter (87±10) nm with nanotube wall thickness 14 nm.and length of around 2100 nm. The silver nanoparticles have an average size of 6 nm and uniform distribution along whole nanotubes wall length (Fig 1a. and 1b.). Figures 1c. and 1d. shown that on the outer surface of the nanotube wall is formed amorphous thin layer due to the reduction in the hydrogen atmosphere. The confirmation of Ti^{3+} in a disordered layer will be studied by EELS spectroscopy.
Photocatalytic measurements show the best photocatalytic performances for TiO_2 nanotube arrays decorated with Ag nanoparticles and subsequently annealed in the hydrogen atmosphere. The enhancement in the photocatalytic efficiency, particularly under visible light irradiation, can be explained by synergetic effects of surface plasmon resonance effect of Ag and creation amorphous layer with Ti^{3+} and oxygen vacancies states at nanotubes surfaces. Also, the silver nanoparticles can act as a dissociation factor of hydrogen molecules during the reduction process creating highly active hydrogen species The findings are well supported by the complex kinetic model which allowed a separate study of contribution from salicylic acid photolysis, photocatalysis in UVB, UVA and visible part of applied simulated solar irradiation on overall degradation rate.
The obtained results in this research are promising for large-scale application of these photocatalysts and the development of more efficient photocatalytic reactors, due to novel design that allows easy usage of prepared material.

References:
[1] M. Plodinec, A. Gajović, G. Jakša, K. Žagar, M. Čeh, J. Alloy. Compd., 591, (2014) 147-155.
[2] X. Chen, L. Liub, F. Huang, Chem. Soc. Rev. 44, (2015), 1861.

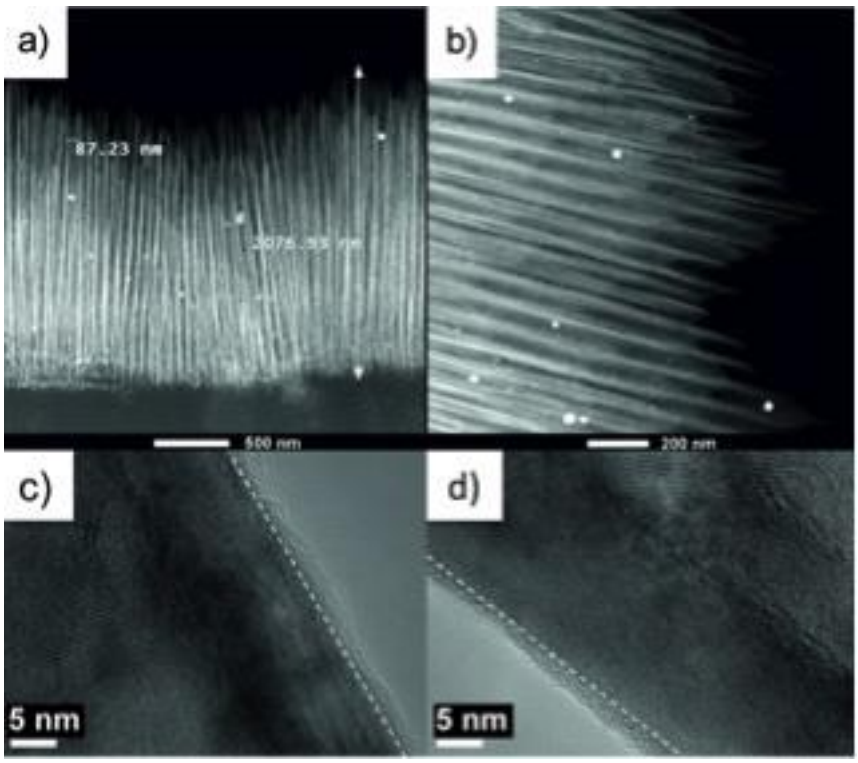

Figure 1. a) and b) HAADF STEM images of cross-section TiO_2 NT's@Ag sample, c) and d) HRTEM of TiO_2 NT's@Ag-HA.

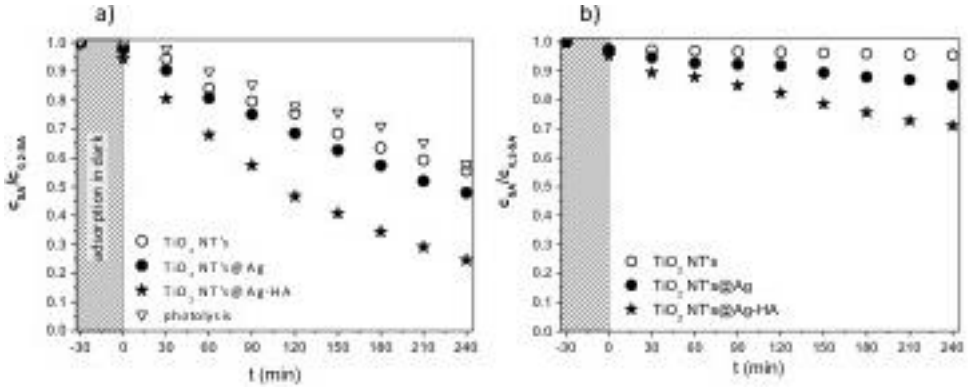

Figure 2. Kinetics of photolysis and photocatalytic degradation of SA under full-spectrum solar irradiation a) and visible irradiation (photolysis was negligible), b) using TiO_2 NT's, TiO_2 NT's@Ag and TiO_2 NT's@Ag-HA as photocatalysts (C0, SA = 0.2 mmol dm-3, pH 4).

MS6.P026
Catalytic reaction of thin Ni films with diamond studied by SEM and TEM

S. Tulić[1], V. Skákalová[1], T. Waitz[1], G. Habler[2], M. Varga[3], A. Kromka[3], M. Čaplovičová[4], V. Vretenár[4] M. Kotlár[4]

[1]University of Vienna, Faculty of Physics, Vienna, Austria
[2]University of Vienna, Department of Lithospheric Research, Vienna, Austria
[3]Czech Academy of Sciences, Institute of Physics, Prague, Czech Republic
[4]Slovak University of Technology, Centre for Nanodiagnostics, Bratislava, Slovakia

semir.tulic@univie.ac.at

The aim of our work is to study the formation of graphene via a Ni-catalyzed transformation of diamond surface layers. Our interest is focused on the interactions at the diamond-graphene interface.
The catalytic transformation of the diamond surface layers was studied by using two different structures: thin films of nanocrystalline diamond (NCD) with an average grain size of about 200 nm grown on Si substrates, and commercially available monocrystalline diamond (MCD) substrates with (100) orientation. Samples NCD and MCD were coated with a Ni layer of 20 nm thickness by magnetron sputtering deposition (specimens denoted NCD-20 and MCD-20, respectively). In addition, samples NCD were coated with a rather thick Ni layer (specimens denoted NCD-500, the film contains columns of Ni of about 500 nm in thickness and 300 - 400 nm in width). The Ni-coated diamond specimens were annealed at 900 °C for 10 min. under a forming gas atmosphere (95% Ar/5% H_2). In the case of the specimens NCD-20 and MCD-20, residuals of the Ni catalyst were removed chemically using a solution of 10% HNO_3. In contrast, the residual Ni catalyst of the specimens NCD-500 was not removed. The specimens were analyzed by scanning electron microscopy (SEM) using a Zeiss Supra 55 VP operated at 10 kV, and transmission electron microscopy (TEM) using a Philips CM200 and an aberration-corrected JEOL JEM-ARM200F operated at 200 kV. TEM specimens were prepared in a cross-sectional geometry by focused ion beam (FIB) thinning using protective layers of Au and Pt. In addition, the specimens were characterized by Raman spectroscopy.
The annealing of the NCD-500 specimens results in the formation of a thick graphite layer. TEM cross-sectional images show that the graphite has formed on columns of $NiSi_2$ (Fig. 1). With increasing distance from the $NiSi_2$ the structure of graphite becomes gradually disordered, finally yielding amorphous C (a-C) (Fig. 2). It is concluded that the graphite is formed by a catalytic reaction of the Ni with diamond by allowing C to diffuse along the boundaries of the Ni-columns towards the surface [1]. As a consequence of the C diffusion, the Ni penetrates through the NCD reacting with the Si to form $NiSi_2$; Si also reacts with the NCD forming SiC. During the heating, the initially present NCD film is completely consumed by catalytic reactions with Ni and Si. In the case of the specimens NCD-20, annealing yields isolated Ni nanoparticles formed by dewetting of the thin Ni film. The nanoparticles cause the formation of grooves in the NCDs by a catalytic etching process related to the solid state C-Ni reaction. Raman investigations conducted after annealing indicate that both diamond and graphite are present. However, the cross-sectional TEM image shows a continuous layer of a-C on top of the NCD (Fig. 3). Similar results are obtained for the MCD-20 specimens. After annealing, the originally flat surface contains catalytic etch pits with a geometry of a four-sided truncated pyramid. The orientation of the sides of the pyramid corresponds to that of {111} planes of the diamond. While the Raman investigations indicate the presence of graphite on top of the diamond substrate, a continuous layer of a-C on the MCD is observed in the TEM cross-section images (Fig. 4).
To summarize, in the case of samples NCD-500 the graphite gradually changes to a-C with decreasing distance to the free surface. In the case of NCD-20 and MCD-20, only a-C is present while graphite could not be observed in the TEM. Since the catalytic reaction of Ni and C is expected to yield the formation of graphite [1], in the present case the a-C might have formed by radiation damage during the specimen preparation via FIB [2].

References:
[1] H. Mehedi, J.C. Arnault, D. Eon, C. Hébert, D. Carole, F. Omnes, E. Gheeraert, *Carbon*, 59, 448-456, 2013.
[2] R. Colby, Q. Yu,H. Cao,S.S. Pei,E.A. Stach,Y.P. Chen, *Diamond and Related Materials*, 19, 143-146, 2010.

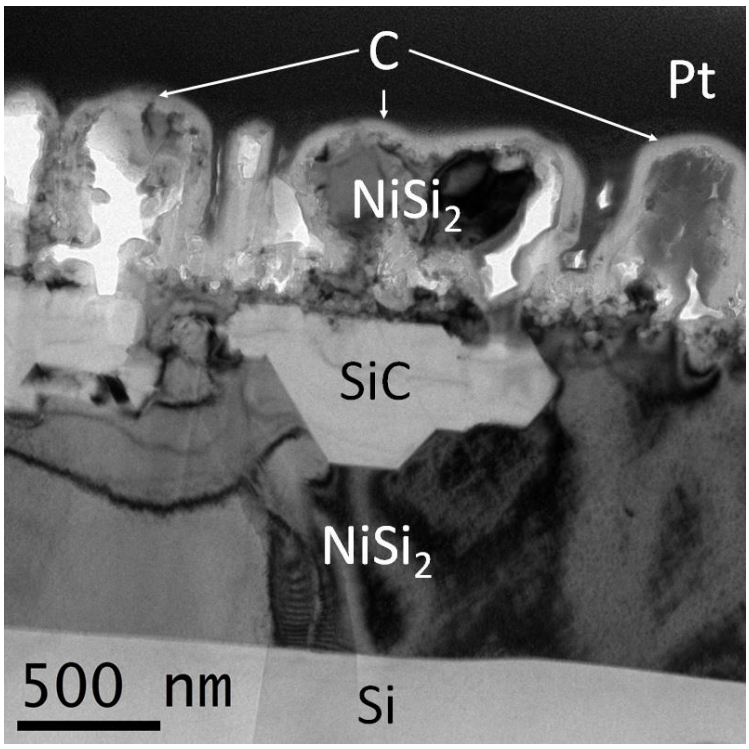

Figure 1. NCD-500. TEM images of C/$NiSi_2$/SiC/Si reaction nanostructures.

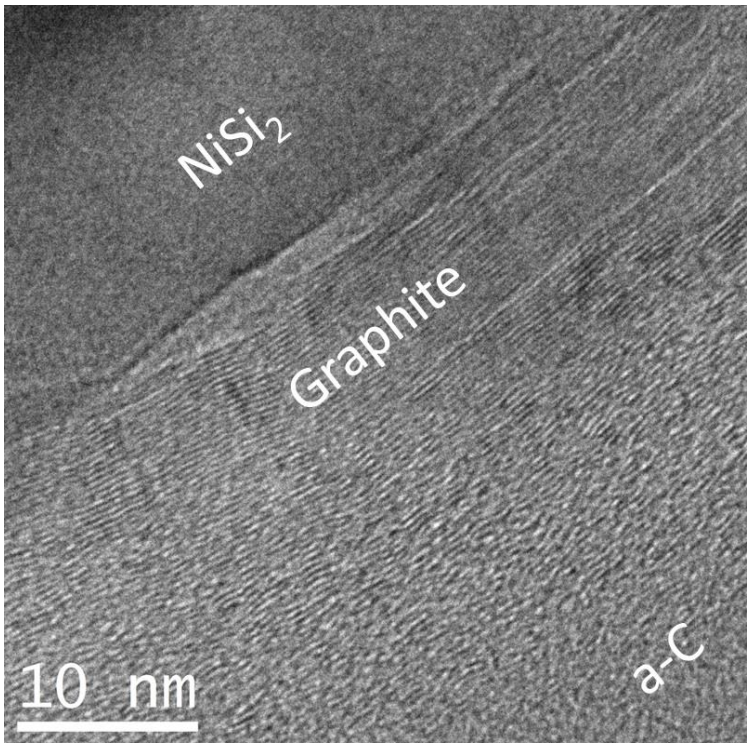

Figure 2. NCD-500. TEM image of graphite gradually changing to amorphous C with decreasing distance to the free surface.

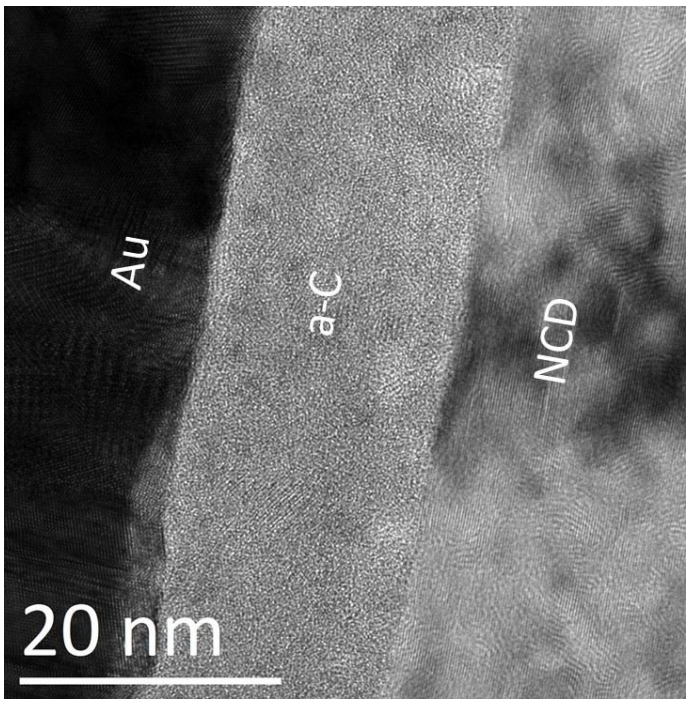

Figure 3. NCD-20. TEM image of Au/a-C/NCD interface.

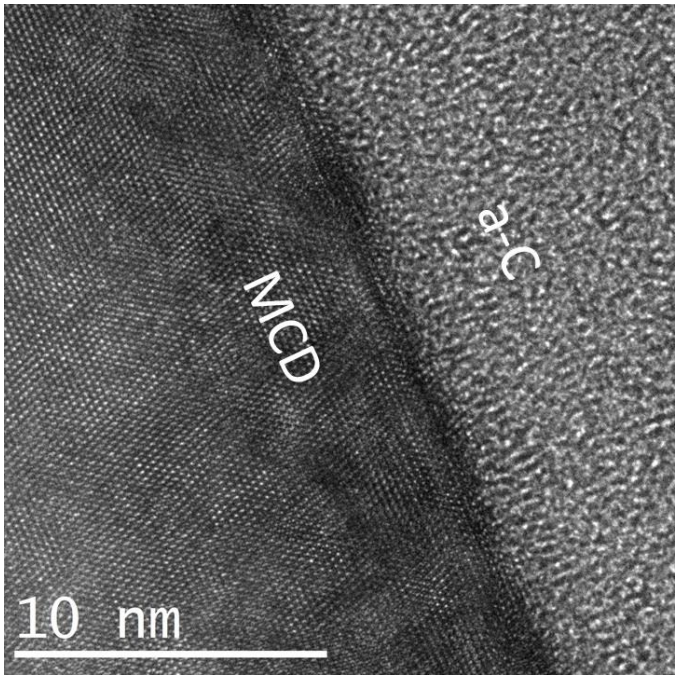

Figure 4. MCD-20. TEM image of a-C/MCD interface.

.

MS6.P027
Following the atomic nanostructure of Pt skin $PtCu_3$/C nanoparticles with IL-TEM after electrochemical activation

F. Ruiz-Zepeda[1], M. Gatalo[1,2], N. Hodnik[3], A. Pavlišič[3], M. Bele[1], G. Drazic[1], M. Gaberšček[1,2]

[1]National Institute of Chemistry (Slovenia), Department of Materials Chemistry, Ljubljana, Slovenia
[2]University of Ljubljana, Faculty of Chemistry and Chemical Technology, Ljubljana, Slovenia
[3]National Institute of Chemistry (Slovenia), Department of Catalysis and Chemical Reaction Engineering, Ljubljana, Slovenia

francisco.ruizzepeda@ki.si

Currently the main challenge in the field of energy conversion for improving fuel cell efficiency is the sluggish kinetics and low stability of catalysts [1]. Among many important issues that need to be solved dealloying stability is of high importance since it takes the catalyst nanoparticles to the active state. And since a connection between the geometry and oxygen reduction reaction (ORR) activity of surface atomic sites has been suggested to play an important role in designing a better catalyst [2], a study of the surface of such catalyst is needed. In this work, we use identical location Transmission Electron Microscopy (IL-TEM) as a method to study the morphological and nanostructural features that arise as a consequence of electrochemical activation of $PtCu_3$/C nanoparticles used for ORR in polymer electrolyte membrane fuel cells (PEMFC). IL-TEM is now well stablished and has provided new insights in previous studies [3]. Aberration corrected scanning transmission electron microscopy (AC-STEM) is performed before and after activation in identical locations on the TEM sample grid, allowing to track the morphology and nanostructure of identical nanoparticles. An IL-TEM protocol was used for this procedure [4]. By comparing before and after electrochemical activation, IL-TEM results showed that nanoparticles shrink in size from 15 to 20%. Additionally, certain facets are observed to develop faster than others, reshaping and restructuring the nanoparticle (Figure 1). It was found that {111} facets were more stable than {110}. In summary, Pt skin $PtCu_3$/C nanoparticles are observed before and after being submitted to an electrochemical process by using high resolution IL-TEM. Finding that nanoparticles shrink and that electrochemical etching is plane selective.

References:
[1] J. Greeley, I. E. L. Stephens, A. S. Bondarenko, T. P. Johansson, H. A. Hansen, T. F. Jaramillo, J. Rossmeis, I. Chorkendorff, and J. K. Nørskov, Nature Chemistry, 1 (2009) 552 – 556.
[2] F. Calle-Vallejo, M. D. Pohl, D. Reinisch, D. Loffreda, P. Sautetcd, and A. S. Bandarenka, Chem. Sci., 8 (2017) 2283-2289.
[3] N. Hodnik, G. Dehm, and K. J. J. Mayrhofer, Acc. Chem. Res., 49 (2016) 2015–2022.
[4] N. Hodnik, M. Zorko, M. Bele, S. Hočevar, and M. Gaberšček, J. Phys. Chem. C, 116 (2012) 21326–21333.

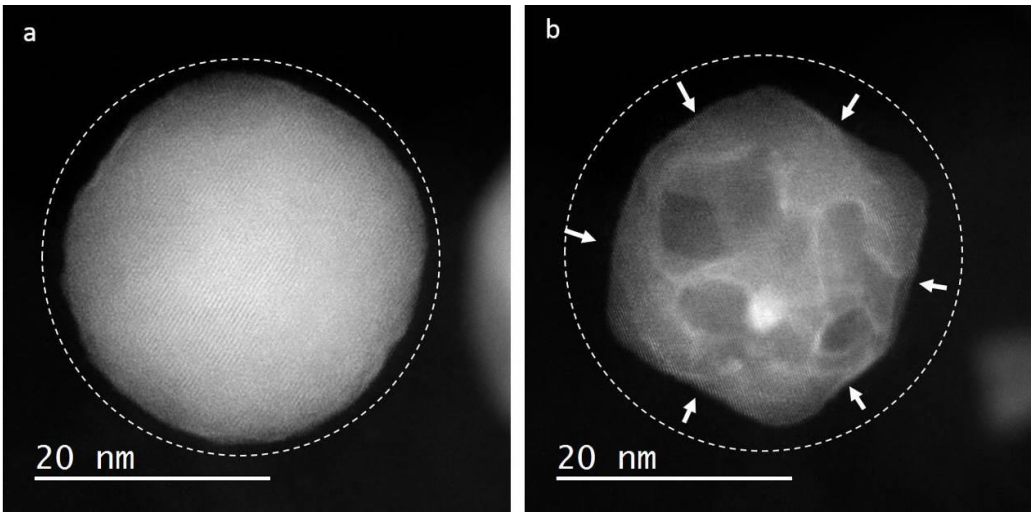

Figure 1. IL-STEM ADF image of (a) before (as-prepared) and (b) after electrochemical activation.

MS6.LBP02
Surface plasmon modes in nanoparticles chains observed by low-loss EELS spectrum-imaging

P. Potapov[1], D. Pohl[1], J. Schultz[1], M. Mayer[2], A. Lubk[1], T. Koenig[2]

[1]Leibniz Inst. for Solid State and Materials Research, Dresden, Germany
[2] Leibniz Inst. for Polymer Research, Dresden, Germany

p.potapov@ifw-dresden.de

Linear chains composed of gold nanoparticles provide an interesting object for plasmonics, e.g., facilitating the directional transfer of optical signals in a confined nanogeometry. To design suitable devices and to optimize the signal transfer, a precise understanding of the surface plasmonic modes including their dissipative behavior is indispensable. Here we present the results of EELS STEM spectrum-imaging of gold chains with varying number of gold nanoparticles carried out on the monochromated probe-corrected FEI Titan[3] microscope. The low-loss spectra were recorded at 300 kV acceleration voltage employing the accelerating mode of the Wien monochromator. Subsequently, an extensive data treatment involving the removal of the zero-loss peak, fitting the background and denoising by the Principal Component Analysis (PCA) has been applied to improve the quality of the data and hence the interpretation.
The principle dipolar surface plasmon mode with an excitation energy of about 2.3eV is visualized as a halo around the particles surfaces independent of the chain length (Fig. 1). On top of that, a coupling among particles results in additional plasmon modes at lower energies. These lower-energy modes show various geometrical configurations depending on the number of particles in a chain (Fig. 2). In longer chains, the modes are shifted into the intraband dissipative regime with accordingly reduced spectral weight. As a result, characteristic spatial field distribution composed from the high-node modes might eventually emerge.
We acknowledge funding from the European Research Council (ERC) under the European Unions Horizon 2020 research and innovation programme (grant agreement No 715620).

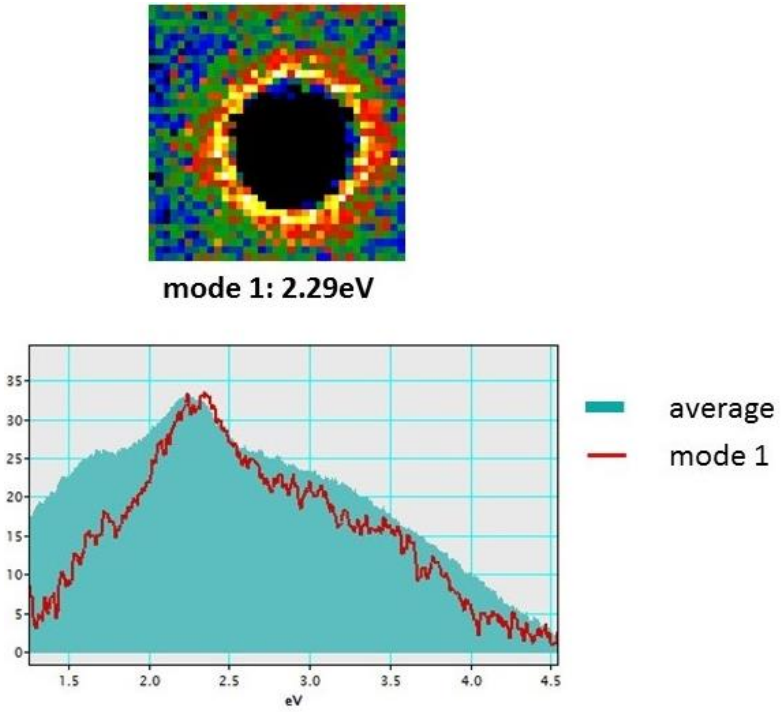

Figure 1. Plasmon mode of a singular gold particle.

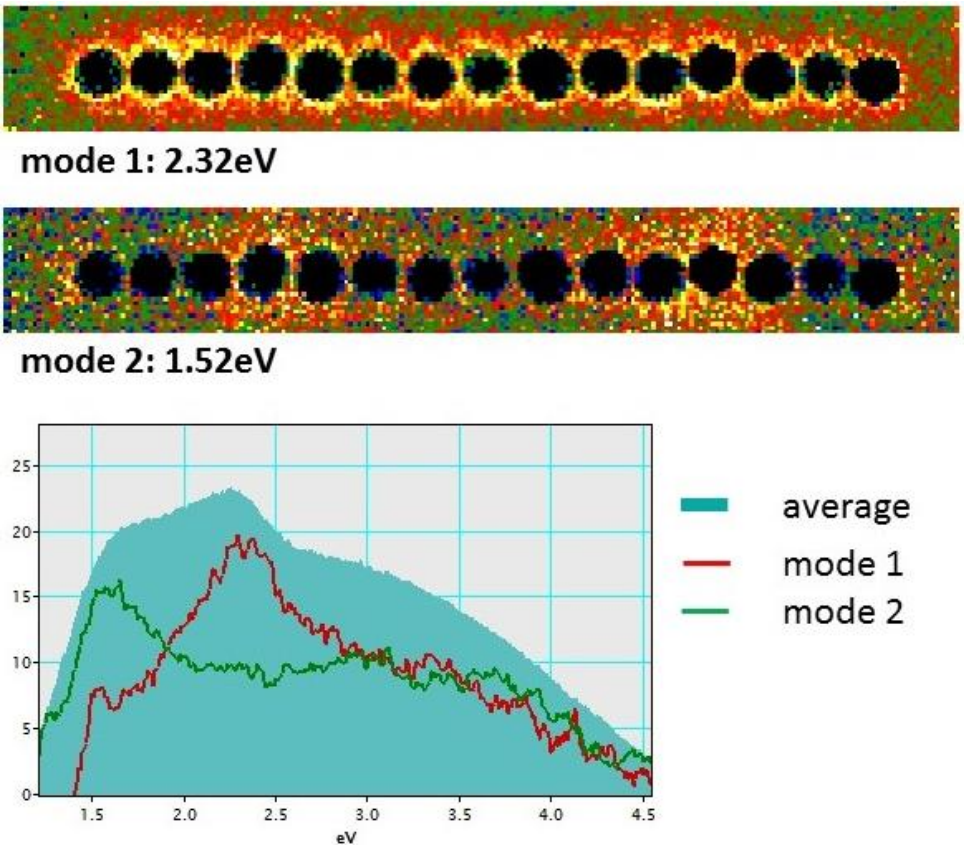

Figure 2. Plasmon modes of a 15-particles chain.

MS 7: Ceramics, oxides and minerals

MS7.001 invited
Replacement reactions at the atomic scale – exsolution of rutile on oxidation of ilmenite

A. Rečnik[1], N. Stanković[1], N. Daneu[1]

[1]Jožef Stefan Institute, Nanostructured Materials, Ljubljana, Slovenia

aleksander.recnik@ijs.si

The mechanism of rutile/ilmenite replacement reaction occurring during controlled oxidation was studied on partially transformed ferrian–ilmenite samples from Mwinilunga (Zambia) and by firing of natural ilmenite samples from Zagi Mt. (Pakistan) in air. Rutile/ilmenite pseudomorphs from Mwinilunga were investigated by complementary electron microscopy methods in order to resolve a sequence of topotaxial reactions. Electron diffraction and high–resolution transmission electron microscopy (HRTEM) analysis of equilibrium rutile/hematite interfaces showed a new exsolution–host relation $[010]_R\{401\}_R||[001]_H\{170\}_H$, dictated by the formation of $\{170\}_H|\{401\}_R$ interfaces leading to 12 possible directions of rutile exsolution within a hematite matrix and 144 different incidences between the intergrown rutile crystals. The resulting rutile–rutile interfaces could be classified to four classes: (i) non–crystallographic contacts at 60°and 120°, (ii) {101} twins with incidence angles of 114.44° and their complementaries at 65.56°, (iii) {301} twins at 54.44° with complementaries at 125.56° and (iv) low–angle tilt boundaries at 174.44°and 5.56°. Except for non–crystallographic contacts, all other rutile–rutile interfaces were confirmed in these samples. Using high–angle annular dark–field scanning TEM (HAADF–STEM) with energy dispersive X–ray spectroscopy (EDS) remnants of ilmenite lamellae were identified in a vicinity of rutile exsolutions, which are an important indication of high–T formation of the primary ferrian–ilmenite. The overall composition of our samples indicates that ratio between ilmenite and hematite in parent ferrian–ilmenite crystals was close to $Ilm_{67}Hem_{33}$, typical for Fe–Ti rich differentiates of mafic magma. The presence of ilmenite lamellae indicates that the primary solid solution passed miscibility gap at ~900°C. Subsequent exsolution processes were triggered by surface oxidation of ferrous iron and remobilization of cations within the common oxygen sublattice. Based on nanostructural analysis of the samples we identified three successive exsolution processes: (i) exsolution of ilmenite lamellae from the primary ferrian–ilmenite crystals, (ii) exsolution of rutile lamellae from ilmenite and (iii) exsolution of hematite precipitates from Fe–rich rutile lamellae (Fig. 1). All observed topotaxial reactions appear to be a combined function of temperature and oxygen fugacity (f_{O2}).

The progress of ilmenite oxidation in air (high f_{O2}) was studied in temperature range between 600–900°C. The samples were cut from the single Mn–ilmenite crystal in two special orientations, $[001]_{ILM}$ and $[110]_{ILM}$, that allowed determination of crystallographic relations among the reaction products. Mn–ilmenite with the pyrophanite: ilmenite ratio of ~40:60 was used to understand the role of divalent cation diffusion during the topotaxial reaction processes. Using electron microscopy techniques we determined that the ilmenite–to–rutile and hematite transformation is triggered by surface oxidation of divalent cations (Fe, Mn) from the starting ilmenite and their crystallization in the form of hematite and bixbyite on the surface of the single crystal. Out–diffusion of Fe(II) and Mn(II) cations opens paths for exsolution of rutile within the pseudo–hexagonal oxygen sublattice of the parent ilmenite, following a simple orientation relationship: $[100]_R\ \{010\}_R\ ||\ [210]_I\{001\}_I$. With this transformation, pathways for out–diffusion of divalent cations to oxidation surface are opened along the c–axis of the rutile structure, whereas the volume difference of reaction products causes cracking of the single crystal opening additional free surfaces for accelerated oxidation (Fig. 2). The main driving force for ilmenite–rutile transformation is surface oxidation that triggers subsequent topotaxial processes such as exsolution of rutile within the ilmenite matrix. The results of this study contribute to better understanding of topotaxial reactions during oxidation of ilmenite.

References:

[1] Rečnik A, Stanković N, Daneu N. *Topotaxial reactions during the genesis of rutile/hematite intergrowths from Mwinilunga (Zambia)*. Contrib Mineral Petrol **169** (2015) 19. & Stanković N, Rečnik A, Daneu N. *Topotaxial reactions during oxidation of ilmenite single crystal*. J Mater Sci **51** (2016) 958–968.

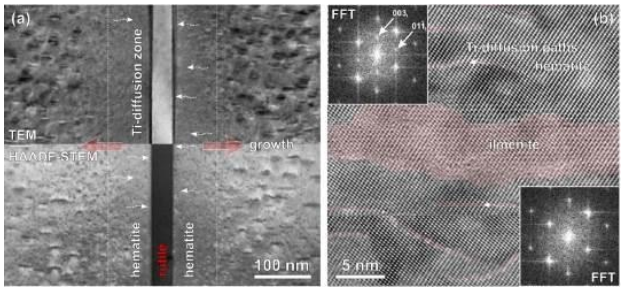

Figure 1. Rutile/hematite exsolution viewed along $[100]_H$ projection. (**a**) Composed TEM/HAADF-STEM image of the $(030)_H|(301)_R$ interface. White arrows indicate fast diffusion paths for Ti-ions. (**b**) A close-up from Ti-diffusion zone indicated in (a). In the vicinity of the rutile lamella only the Ti-diffusion paths, roughly lined along the hematite basal planes, can be seen (below). Fast-Fourier transforms (FFT) from the two regions show the presence or the absence of ilmenite reflections, respectively.

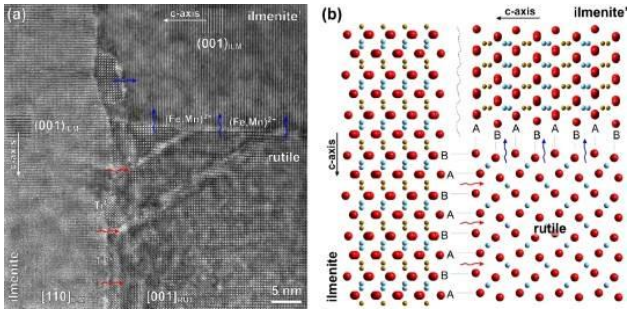

Figure 2. Exsolution of rutile during oxidation of ilmenite under 800 °C. (**a**) HRTEM image of parent ilmenite (left), exsolved rutile (centre) and secondary ilmenite' (above). (**b**) Structural relations between the exsolved phases. First, rutile is exsolved from parent ilmenite forming a coherent $(110)_I$ | $(100)_R$ interface.

MS7.002
Titanium oxide inclusions with different phases in corundum – an atomic structure investigation via STEM

C. Li[1], L. C. Baldwin[1], T. J. Pennycook[2], C. Mangler[2], J. Meyer [2], G. Habler[1], R. Abart [1]

[1]University of Vienna, Department of Lithospheric Research, Vienna, Austria
[2]University of Vienna, Faculty of Physics, Vienna, Austria

lichen0320@gmail.com

Inclusions in natural minerals can provide rich information on the environmental conditions during crystal growth. Rutile (TiO_2)[1], as one of the most common inclusions in minerals, has often been found in quartz[2], garnet[3,4], and corundum[5], and commonly with a needle-like shape. In single crystal corundum (α-Al_2O_3) from the Siebengebirge volcanic field in Germany, needle-shape rutile inclusions have been observed with the long axes parallel with corundum (0001) basal planes. It has also been observed that inclusions show different densities and shapes in different chemical zones in corundum. In Nb-rich regions, the inclusions appear in high densities and small sizes of about 10-50 nm. In regions low in Nb the inclusions have a lower density but larger size (>50 nm). In order to figure out the nature of these different phases, we have employed scanning transmission electron microscopy (STEM) to investigate their atomic structure, as well as their crystallographic orientation relationship to the host corundum.
Beside the normal needle-shape rutile, titanium oxides inclusions with different phases have been found. Some of the nano-inclusions in the Nb-rich area have a "butterfly"-shape (Fig. 1(a)). Atomic resolution imaging shows that they are rutile structures, each with a single central twin boundary (Fig. 1(b)). The twinning planes are occupied by heavy elements, revealed by the higher intensity in STEM Z-contrast image. Away from the Nb-rich zones, another phase of titanium oxide inclusions have been found with rectangular shapes (Fig. 2(a)). Electron energy loss spectroscopy (EELS) shows Ti and O in the rectangular inclusions, and further atomic resolution imaging reveals that this phase inherits the corundum structure. Bright columns that indicate heavy impurity atoms have been found at the inclusion/corundum interfaces parallel with Crn (10-10) facets (Fig. 2(b)). However, rather than being part of the inclusions, they appear to be "dangling" outside them as shown in Fig. 2(c). The chemical information of these impurities will be studied.[6]

References:
[1] Meinhold, G. Rutile and Its Applications in Earth Sciences. *Earth Science Reviews* **2010**, *102*, 1–28.
[2] Li, X.; Rusk, B.; Wang, R.; Morishita, Y.; Watanabe, Y.; Chen, Z. Rutile Inclusions in Quartz Crystals Record Decreasing Temperature and Pressure During the Exhumation of the Su-Lu UHP Metamorphic Belt in Donghai, East China. *American Mineralogist* **2011**, *96*, 964–973.
[3] Proyer, A.; Habler, G.; Abart, R.; Wirth, R.; Krenn, K.; Hoinkes, G. TiO2 Exsolution From Garnet by Open-System Precipitation: Evidence From Crystallographic and Shape Preferred Orientation of Rutile Inclusions. *Contrib Mineral Petrol* **2013**, *166*, 211–234.
[4] Hwang, S. L.; Shen, P.; Chu, H. T.; Yui, T. F.; Iizuka, Y. Origin of Rutile Needles in Star Garnet and Implications for Interpretation of Inclusion Textures in Ultrahigh-Pressure Metamorphic Rocks. *Journal of Metamorphic Geology* **2015**, *33*, 249–272.
[5] Demaesschalck, A. A.; Oen, I. S. Fluid and Mineral Inclusions in Corundum From Gem Gravels in Sri-Lanka. *Mineralogical Magazine* **1989**, *53*, 539–545.
[6] This research was funded by the EU Marie Skłodowska-Curie grants No. 656378 – Interfacial Reactions (CL) and the Austrian Science Fund (FWF) I1704-N19 (GH).

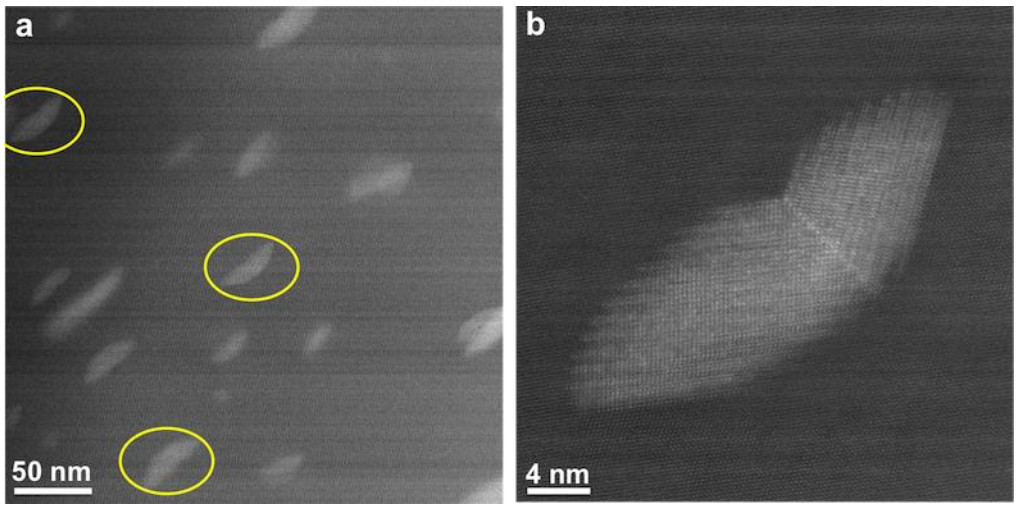

Figure 1. STEM images show (a) "butterfly-shape" Nb-rich rutile inclusions marked by yellow circles, (b) with heavy element doping at twining plane.

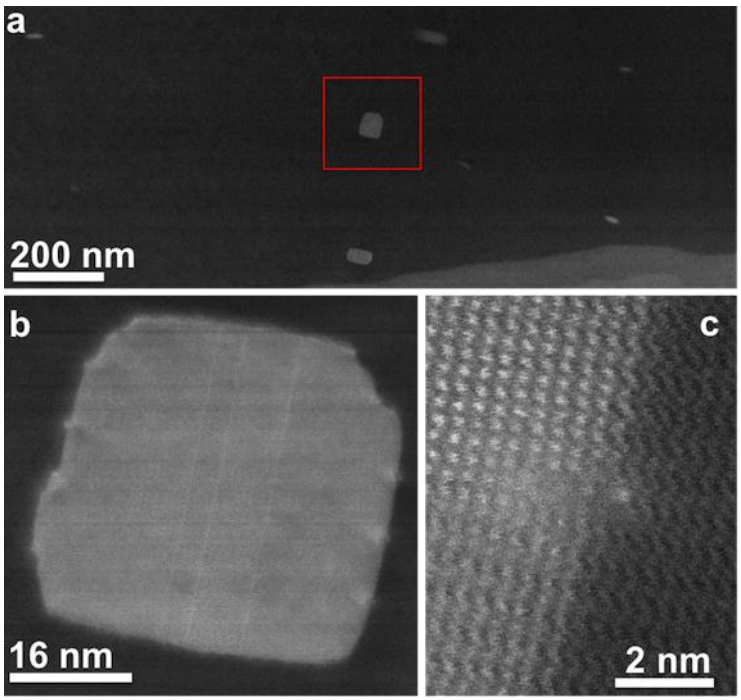

Figure 2. STEM images show rectangle-shape titanium oxide inclusions with heavy columns "dangling" outside of the inclusion.

MS7.003
Characterization of inclusions in extraterrestrial diamond

F. Nabiei[1,2], J. Badro[1,3], T. Dennenwaldt[2,4], E. Oveisi[2], M. Cantoni[2], C. Hébert[2,4], A. El Goresy[5]
P. Gillet[1]

[1]Ecole Polytechnique Fédérale de Lausanne, Earth and Planetary Science Laboratory (EPSL), Lausanne, Switzerland
[2]Ecole Polytechnique Fédérale de Lausanne, Interdisciplinary Center for Electron Microscopy (CIME), Lausanne, Switzerland
[3]Sorbonne Paris Cité, Institut de Physique du Globe de Paris, Paris, France
[4]Ecole Polytechnique Fédérale de Lausanne, Electron Spectrometry and Microscopy Laboratory (LSME), Lausanne, Switzerland
[5]Universität Bayreuth, Bayerisches Geoinstitut, Bayreuth, Germany

farhang.nabiei@epfl.ch

Ureilites are achondritic meteorites with high carbon concentration. Carbonaceous materials consisting of graphite and diamond appear as veins between olivine and pyroxene grains in ureilites[1]. Transformation of graphite to diamond during the shock impact, CVD growth of diamond in solar nebula and diamond growth under static high pressure are three mechanisms suggested for the origin of diamond in these meteorites. Previous studies on Almahata Sitta MS-170 showed large diamond grain size (up to ~100 µm) in this particular meteorite which could only be explained by the diamond formation under static pressure[2]. Diamond inclusions in natural terrestrial diamonds are the major source of information on the origin and formation of diamonds. However, no inclusion in meteoritic diamonds has been reported before.

Five thin sections (~100 nm in thickness) were prepared by focused ion beam (FIB) from diamond grains in Almahata Sitta MS-170 for transmission electron microscopy (TEM) analysis. Energy dispersive X-ray (EDX) spectroscopy and electron diffraction techniques were used for chemical and structural characterization of minerals in diamond matrix. Moreover, to study the morphology of inclusions as well as to determine the position of inclusions in the thin section, tilt-series of high-angle annular dark-field (HAADF) images were acquired from different regions of the sections with a tilt increment of 2° over the ranges -72° to 72° and -54° to 54°.

Three different inclusions were found in diamonds. Most of the inclusions showed Fe-S-rich composition (figure 1). These inclusions had two major phases namely: kamacite (Fe, Ni) and troilite (FeS). They also contained phosphorous which segregated to the grain boundaries or made a separate $(Fe,Ni)_3P$ phase. However, all of these phases were enclosed together in well-defined polyhedral shapes suggesting that they were formed as single crystals (figure 1). Chemical analysis of the complete and uncut inclusions of this type showed that the total composition agrees with the high pressure $(Fe,Ni)_3(S,P)$ phase. The presence of this phase in the core of planetary bodies has already been predicted[3]. But since this phase is only stable above 21 GPa, no natural evidence of its formation has been found[3]. In addition, we have detected two other rare inclusions, characterized as chromite (Cr_2FeO_4) and Ca-Fe-Na phosphate. Absence of Mg in the composition of chromite grains indicates that they have formed in an iron-rich region of the parent body. Mg-free chromite and Ca-Fe-Na phosphate were only seen in iron meteorites or pallasites (stony-iron meteorites). Our observations lead us to conclude that diamonds in Almahata Sitta MS-170 were formed in the core (or core-mantle boundary) of their parent body under the pressure of at least 21 GPa. The minimum size for ureilite parent body (UPB) to generate this pressure at its center is ~4000 km in diameter.

References:

[1] Goodrich, C. A. Ureilites: A critical review. *Meteoritics* **27,** 327–352 (1992).
[2] Miyahara, M. *et al.* Unique large diamonds in a ureilite from Almahata Sitta 2008 TC3 asteroid. *Geochim. Cosmochim. Acta* **163,** 14–26 (2015).
[3] Fei, Y., Li, J., Bertka, C. M. & Prewitt, C. T. Structure type and bulk modulus of Fe3S, a new iron-sulfur compound. *Am. Mineral.* **85,** 1830–1833 (2015).

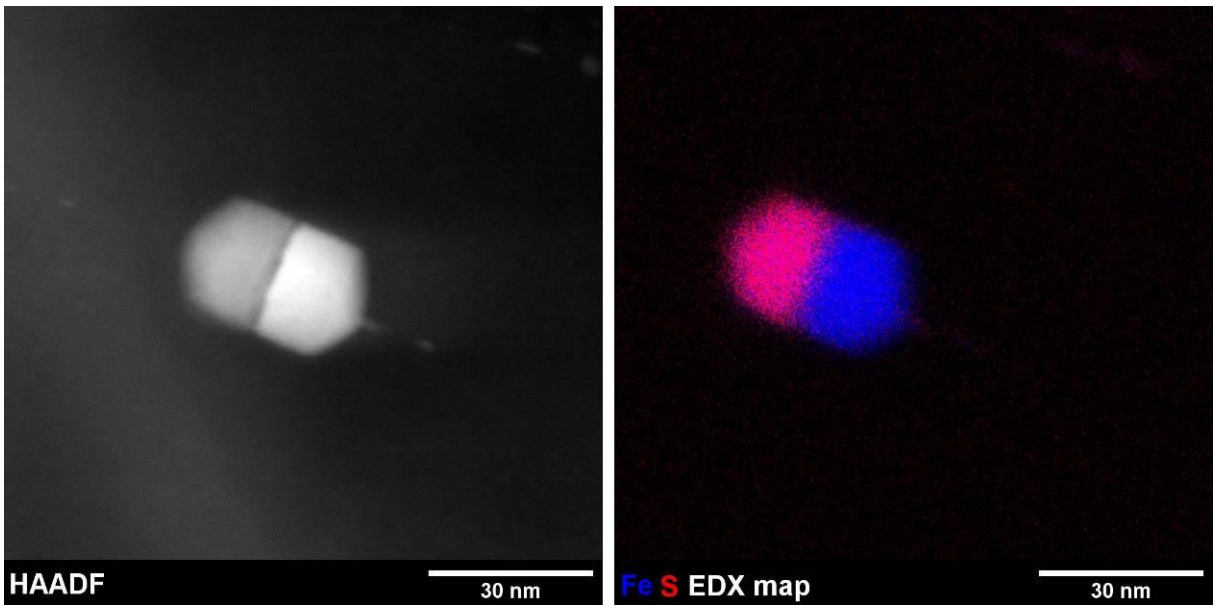

Figure 1. HAADF image (left) and corresponding EDX map (right) of an inclusion in diamond matrix which is consisted of troilite (FeS) and kamacite (Fe, Ni) phases.

MS7.004
Investigation of natural and artificial mineral structures by electron energy-loss spectroscopy

T. Dennenwaldt[1,2], F. Nabiei[3,1], H. Piet[3,4], D. T. L. Alexander[1], J. Badro[3,5], P. Gillet[3], C. Hébert[1,2]

[1]EPFL, CIME, Lausanne, Switzerland
[2]EPFL, LSME, Lausanne, Switzerland
[3]EPFL, EPSL, Lausanne, Switzerland
[4]Arizona State University, School of Earth and Space Exploration, Tempe, AZ, United States of America
[5]Sorbonne Paris Cité, Institut de Physique du Globe de Paris, Paris, France

teresa.dennenwaldt@epfl.ch

The electron energy-loss near edge structures (ELNES) of core loss ionization edges, recorded in TEM, carry information about the electronic structure and the bonding behavior of the corresponding elements, and so can act as fingerprints for a material. Both the chemical shift in the edge onset and the shape of the ELNES carry information about the valence state or bonding coordination or behavior of a material. As such, the ELNES can be used to distinguish between various structures of similar composition but different electronic structure.
For instance, the carbon K-edge exhibits diverse ELNES features depending on its hybridization state (sp^2- or sp^3-bonded) and can be used to quantify the sp^2/sp^3 ratio of materials ranging from diamond structure (pure sp^3) to graphite structure (pure sp^2). Furthermore, the iron $L_{2,3}$-edge can be used to determine the ratio of ferrous and ferric iron concentrations in e.g. lower mantle minerals.
Acquiring electron energy-loss spectra (EELS) at magic angle conditions (MAC) allows one to cancel the orientation dependence of ELNES intensities in anisotropic materials [1] and is therefore necessary to precisely analyze the carbon sp^2/sp^3 ratios of different carbonaceous phases irrespective of the orientation of possible graphitic-type substructures relative to the incident electron beam. Here, we show how reliable acquisition conditions can be set up in scanning TEM mode, benefitting from the flexible condenser optics of the FEI Titan Themis platform, and how this allows acquiring of spatially-resolved ELNES data on the carbon K-edge of mineral samples under MAC. By comparing the samples to Reference: material, we use the chemical shift, white-line ratio and shape of the ELNES to correlate the hybridization and oxidation states of the minerals to their EELS data.
The Almahata Sitta 2008 TC3 asteroid [2] containing both diamond and graphite inclusions is investigated. We found a clear separation between the two phases with no real mixture of the sp^2/sp^3 hybridization in the different regions of the specimens (Fig. 1). The lower mantle minerals samples are composed of calcium perovskite (CaPv, $CaSiO_3$), bridgmanite (Brg, $(Mg,Fe)SiO_3$) and ferropericlase (Fp, (Mg,Fe)O) which is the composition of the lower mantle. As the valence state and partitioning of iron have a strong impact on the physical and chemical properties [3,4], samples consisting of a Brg (amorphous) and Fp (crystalline) mineral assemblage have been previously synthesized from Al-rich olivine composition at different temperatures and pressures. Their $Fe^{3+}/\sum Fe$ has been studied with EELS (Fig. 2) [5] to understand the correlation between the distribution and oxidation states of iron.
Challenges that occur during acquisition will be discussed, e.g. beam damage of the materials or electron-beam-induced oxidation of iron.

References:
[1] C. Hébert et al., Ultramicrosc. **106** (2006) 1139.
[2] P Jenniskens et al., Nature **458** (2009), 485.
[3] J Badro, et al., Science **300** (2003), 789.
[4] C Prescher, et al., Earth and Planetary Science Letters **399** (2014), 86.
[5] H Piet, et al., Proceedings of the National Academy of Sciences **113** (2016), 11127.

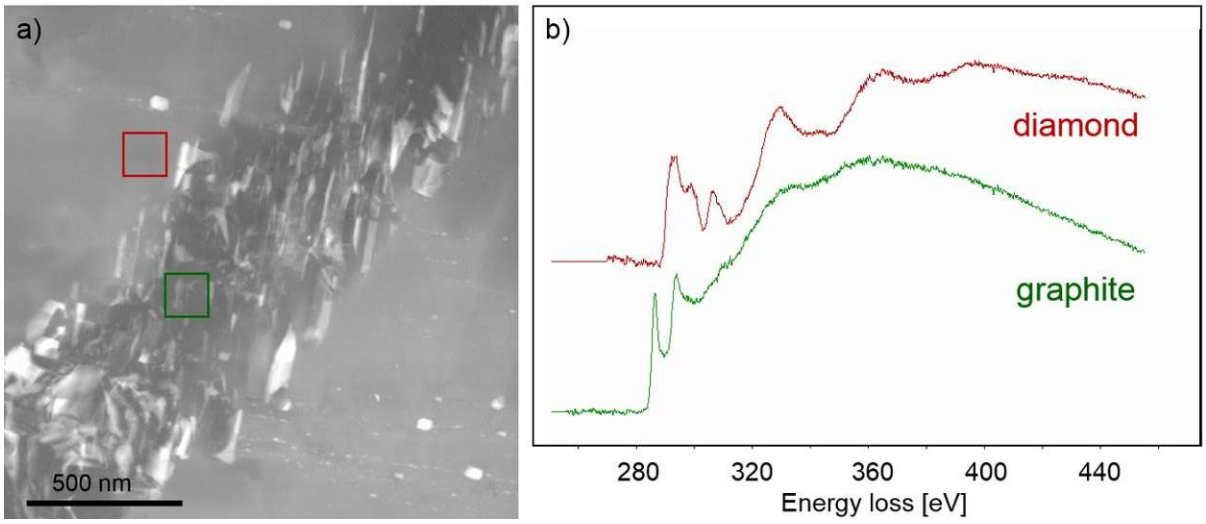

Figure 1. a) HAADF-STEM image of a meteorite sample. b) EEL spectra of the C K-edges of the diamond phase (red) and the graphite phase (green) showing a significant difference in the ELNES.

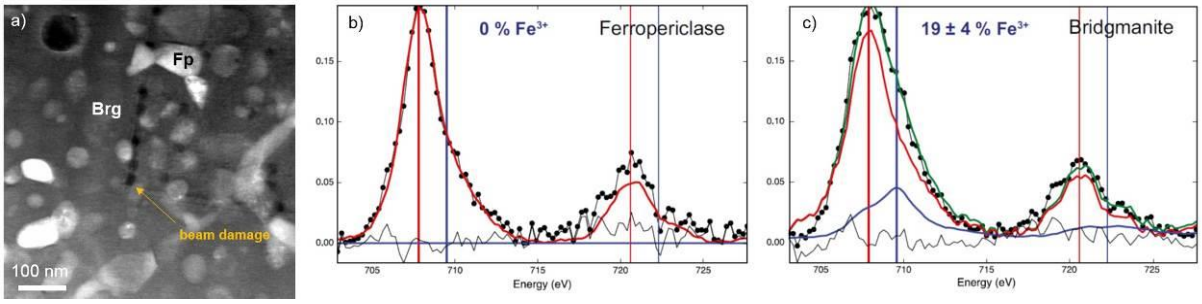

Figure 2. a) HAADF-STEM images showing beam damage, especially of the amorphous Brg matrix, b) and c) valence state analysis of the two phases Fp and Brg. The black dots are measurements on the sample, the red (Fe^{2+}) and blue (Fe^{3+}) curves are from the standards (chemical shift of 1.5 eV). The green curve is the calculated spectrum using the two standards. The thin black line is the residual of the fit. Fp shows no Fe^{3+} (b), while Brg has a Fe^{3+} /ΣFe value of 0.19± 0.03 (c).

MS7.005
Plastic deformation of nanostructured Al_2O_3 at room temperature

E. Frankberg[1], L. Joly-Pottuz[2], F. Garcia[3], T. Salminen[4], J. Kalikka[5,6], S. Koneti[2], L. Roiban[2]
T. Douillard[2], B. Le Saint[2], J. Akola[5,6], E. Levänen[1], F. Di Fonzo[3], K. Masenelli-Varlot[2]

[1]Tampere University of Technology, Laboratory of Materials Science, Tampere, Finland
[2]Université de Lyon, INSA-Lyon, MATEIS, Villeurbanne, France
[3]Istituto Italiano di Tecnologia, Center for Nano Science and Technology, Milano, Italy
[4]Tampere University of Technology, Optoelectronics Research Center, Tampere, Finland
[5]Tampere University of Technology, Department of Physics, Tampere, Finland
[6]Aalto University, COMP Centre of Excellence, Department of Applied Physics, Aalto, Finland

karine.masenelli-varlot@insa-lyon.fr

Recent TEM *in situ* mechanical experiments on single alumina nanoparticles have shown unexpected plasticity in room temperature alumina [1, 2]. These results push the theoretical boundaries of ceramics mechanical ductility towards comparable levels with metals. The important questions for materials science now are: *(i)* whether the plastic behaviour can be transferred into polycrystalline, continuous material; *(ii)* what is the microstructure of such plastic material and *(iii)* what is the mechanism behind the hypothetical plasticity of the material. Relatively cheap and abundantly available engineering ceramic, such as alumina, with room temperature plasticity would be a breakthrough in the engineering ceramics field.

This work deals with the study of room temperature plasticity on alumina thin films produced by pulsed laser deposition. Alumina produced this way has an exotic, nanocrystalline microstructure and is a strong candidate for having the capability for room temperature plasticity. For this purpose, pulsed laser deposition (PLD) of alumina thin films was done on various substrates including sapphire and sodium chloride. TEM samples were obtained by several methods: first by dissolving the PLD coated NaCl crystals and depositing the free-standing PLD alumina film onto a TEM grid, secondly using FIB lift-out method taken from a PLD coated film on a silicon single crystal wafer and thirdly by directly depositing a film on an electron transparent sapphire substrate. For in situ TEM mechanical testing, the sample was placed on a special tool which was then compressed using a diamond indenter. . The in situ tests were conducted using Nanofactory and Hysitron PI95 in situ TEM sample holders with JEOL 2010F and FEI Titan microscopes, respectively. In the test, the PLD alumina film was compressed between a sapphire substrate and a diamond tip (see Figure 1) and the deformation process was filmed in situ together with synchronized strain and force measurement.

We show the latest results of our *in situ* TEM studies and atomistic simulations that are focused on analysing and explaining the material"s mechanical response (strain, dislocation activity, fracture etc.) to compression and indentation forces and look for evidence of the mechanism behind the mechanical response. The structure of the PLD Al_2O_3 depends on the sample preparation method, which indicates that the structure is metastable. The as received structure is mostly amorphous, but contains partly crystallized areas (see Figure 2). Critical dose of electron irradiation causes as-deposited amorphous areas to fully crystallize into dominantly gamma-phase with a sub-micrometer grain size. The in situ TEM mechanical testing gives us understanding how amorphous Al_2O_3 behave at strains up to 100%, which is not achievable in macroscale tests due to flaw distribution inside the sample leading to fracture. The results are compared to atomistic simulations to understand the mechanical behaviour and deformation mechanisms of PLD Al2O3 at high strain and high stress situations [3].

References:

[1] E. Calvié et al. Journal of European ceramic society, Vol. 32, No. 10, p. 2067-2071, 2012
[2] E. Calvié, et al. Materials Letters, Vol. 119, p. 107-110, 2014
[3] The authors acknowledge the Consortium Lyon Saint-Etienne de Microscopie (CLYM) for the access to the electron microscopes.

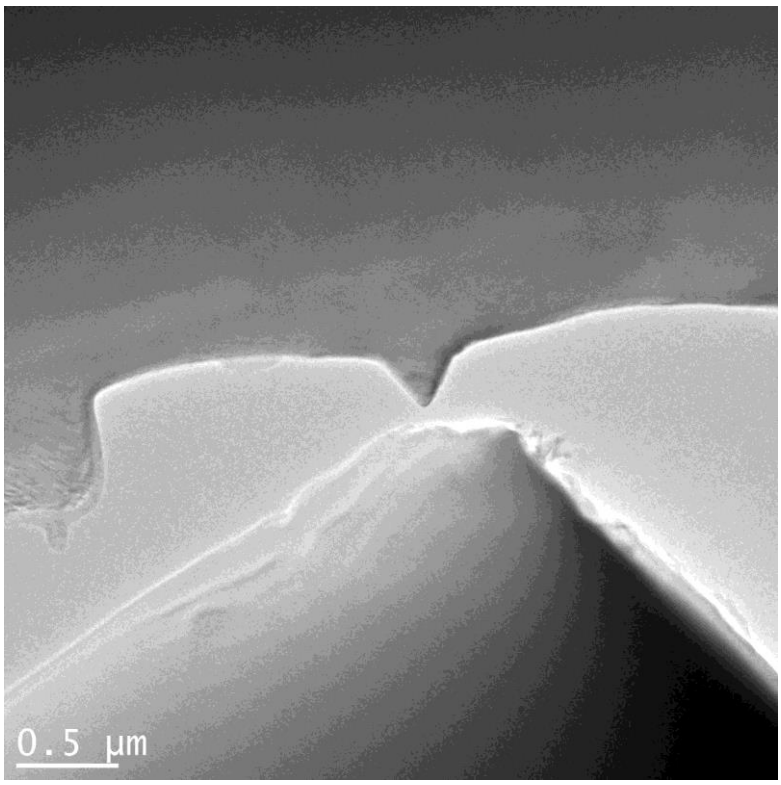

Figure 1. Set-up used for the in situ TEM nanocompression tests.

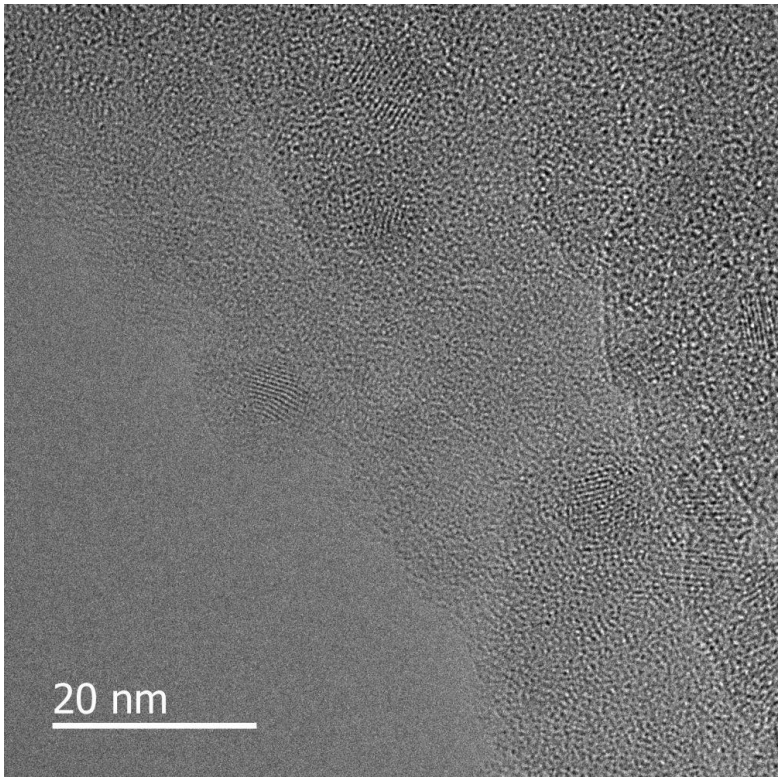

Figure 2. TEM image of a pulsed laser deposited alumina film with nanometer-sized crystals embedded in an amorphous matrix.

MS7.006
Automated 3D mapping using serial mechanical polishing – advances and benefits for studies of mineral and oxide systems

T. Griffiths[1], S. Zaefferer[1]

[1]Max Planck Institute for Iron Research, Department for Microstructure and Alloy Design, Düsseldorf, Germany

t.griffiths@mpie.de

Practically all phenomena studied in materials and rocks are the result of processes that occur in three dimensions and result in 3D microstructures. Measurement in 2D leads to significant loss of information and some parameters simply cannot be obtained from a 2D section. Scanning electron microscopes (SEMs) provide a wealth of information at sub-micrometer spatial resolutions, but are restricted to 2D scans. Destructive 3D measurement using a focused ion beam (FIB) to cut away successive slices is well-established, but limited to volumes smaller than ~50 µm to a side. Ceramics, oxides and minerals commonly have larger grainsizes and have therefore been excluded from high resolution 3D study.
We aim to use mechanical polishing to serially section samples and generate 3D maps from successive 2D SEM datasets. Specifically, we aim to completely automate the process of repeated polishing, cleaning and scan acquisition in order to transform this technique from a time-consuming pursuit into a routine analysis method.
The setup consists of a Zeiss Merlin SEM with an automated chamber door and a programmable, highly adaptable polishing station (ATM Saphir X-change) that can automatically polish and clean a sample (25mm diameter x 18mm height) using up to 16 interchangeable disks and 5 different polishing suspensions per program. A robotic arm and gripper transfers the sample between the microscope and polishing station. The microscope is equipped with a stage attachment that allows extraction and replacement of the sample with high reproducibility of position. A specially designed polishing head is also necessary to allow automatic loading and re-levelling of the sample.
The automated setup reliably produces scratch-free, EBSD-quality surfaces for metal samples. Absolute slice thickness is determined by polishing type, pressure, and time. The amount of material removed by a polishing step can be measured to a precision of approx. ± 70 nm using inclined pairs of marker trenches FIB-milled into the sides of samples (before embedding). Using multiple marker sets the change in inclination of the polished surface can be measured with a precision of approx. ± 0.1°. We are able to polish off slices with a thickness reproducible to within ± 100 nm and with surface inclination changes below the error limit. We present automated 3D scans of metal samples with 2D grain sizes > 50µm as proof of concept. After processing in the QubeTM software, we obtain the full 5 parameter grain boundary character distribution for each grain boundary in the scan volume, comprising many hundreds of grains.
Serial sectioning via polishing is the only way to generate 3D datasets from coarser-grained materials while still taking advantage of the excellent resolution and variety of analytical techniques offered by the SEM. It offers other advantages over FIB milling, including greater flexibility in depth resolution, the ability to adapt the polishing sequence to each new material, and the elimination of milling artefacts. This technique also allows several ways to mitigate charging, e.g. coating outside the microscope or measurement at elevated chamber pressures. Ceramic, oxide and mineral research will benefit considerably from automated 3D serial sectioning due to the common presence of larger grainsizes and non-conductive samples. The ability to scan a 3D volume of up to 1 mm^3 over one weekend will allow the study of microstructures in 3D at SEM resolution to become a routine tool in materials and earth sciences.

MS7.P001
Synthesis, crystal structure and vibrational studies of the monoclinically distorted double perovskite, $Sr_2Mn_{1-x}Ni_xTeO_6$

A. Zaraq[1,2], B. Orayech[3], J. M. Igartua[2], A. El Bouari[4]

[1]University Hassan II Casablanca, Chimestry, Casablanca, Morocco
[2]Zientzia eta Teknologia Fakultatea, Euskal Herriko Unibertsitatea, Fisika Aplikatua II Saila, Bilbao, Spain
[3]Universidad del Pais Vasco, Fisica de la Materia Condensada, Bilbao, Spain
[4]Université Hassan Ii Casablanca, Chimestry, Casablanca, Morocco

assmaa.zaraq@gmail.com

Double perovskites $Sr_2Mn_{1-x}Ni_xTeO_6$ with x= 0.25, 0.5 and 0.75 were prepared by solid state reaction. The structural and vibrational properties of these materials were studied by means XRPD, Raman and IR spectroscopy. It has been proven that all the materials show typical double perovskite sturcutres with a monoclinic space group. The obtained cell parameters are in accordance with the ones of the two exteme pure Mn and Ni. Taking into account the parameters reported by Ortega et al. we have observed that Vegard Law is satisfied. In-situ XRPD measuremenents have shown that the materials suffer three phase transition from low to high temperature, according to the phase-transition sequence: P21/n-I2/m-I4/m-Fm3m.
Keywords: New Materials, double perovskites; Raman spectroscopy; infrared spectroscopy; crystal structure.

References:
[1] A. Souidi, S. Bentata, W. Benstaali, B. Bouadjemi, A. Abbad, T. Lantri, *J. Material Science in* Semiconductor Processing *43* (2016).
[2] Y. Tamraoui, Bouchaib Manoun, F. Mirinioui, R. Haloui, P. Lazor, *JALCOM* 30808 (2014).

MS7.P002
Temperature and composition induced phase transitions in $Sr_2Co_{1-x}Ni_xTeO_6$ (x = 0.25, 0.5 and 0.75) double perovskite

A. zaraq[1], Y. Bouch[1], B. Orayech[2], J. M. Igartua[3], A. El Bouari[1]

[1]Université Hassan II Casablanca, Chimestry, Casablanca, United Kingdom
[2]CICenergigune, Albert Einstein , Miñano, Alava, Spain
[3]Zientzia eta Teknologia Fakultatea, Euskal Herriko Unibertsitatea, Fisika Aplikatua II Saila, , Bilbao, Spain

assmaa.zaraq@gmail.com

Structures of $Sr_2Co_{1-x}Ni_xTeO_6$ (x = 0.25, 0.5 and 0.75) double perovskites have been studied by the profile analysis of X-ray diffraction data and Raman spectroscopy at room temperature. This series adopts a monoclinic symmetry with P21/n as space group. These results were confirmed by the observed tolerance factor calculated from the distances obtained from the Rietveld refinements. Clear changes in the Raman modes centered at 600, 610 and 620 cm^{-1} and the FWHM of O-Te-O bending vibrations, centered at 738 cm^{-1}. Furthermore, Raman spectroscopy studies at high temperature were done for this series. Considerable changes in the temperature dependence of the modes were well illustrated.
Keywords*:* New Materials*,* double perovskites; Raman spectroscopy; infrared spectroscopy; crystal structure, phase transition.

MS7.P003
Composition and structure analysis of nephrite from Tieli, China

S. Gao[1], G. Heide[1], F. Bai[2]

[1]Institute Mineralogy, TU Bergakademie Freiberg, Freiberg, Germany
[2]China University of Geosciences (Beijing), Beijing, China

gaoshijia19890915@gmail.com

Introduction: In the recent two decades, the demand for nephrite continuously increases, and many nephrite deposits have been discovered. The close attention of present paper is on nephrite deposit in Tieli, Heilongjiang province, China (Fig. 1a), which is one of the newly discovered nephrite deposits, and it appears that there is few research of this deposit so far.
Mineralogical characteristics of nephrite samples and surrounding rocks are measured, in order to preliminary identify the samples. Furthermore, the results of Raman spectroscopy, SEM and EPMA indicate the chemical composition and micro-structure of samples. Analyzing all the data, the forming process can be presumed.
Methods: We selected out 6 pieces' nephrite samples and 10 pieces' surrounding rocks from two mines in Tieli (Fig. 1b) as experimental objects.
Raman spectra of samples were determined by Renishaw System-2000 confocal Raman spectroscopy in Institute of Mineral Resources, Chinese Academy of Geological Sciences. A scanning electron microscope (SEM) helps to recognize crystals in μm level. The used instrument was ZEISS-EVO18 at University of Science and Technology, Beijing. To analyze the result of JXA-8230 Electron probe micro-analyzer (EPMA) in Institute of Mineral Resources, Chinese Academy of Geological Sciences, chemical composition of major element was calculated.
Results: The Raman spectrum of samples is respectively showed in Fig. 2. After peaks assignment, they consistent with the standard spectrum of tremolite, indicating the main mineral composition of samples is tremolite. (F. Casadio et al., 2007; T.-H. Chen et al., 2004; Z. Zhu et al., 1981)
Under SEM, these two kinds of micro-structure are also observed as expected: microscopic fibroblastic structure (Fig. 3a) and microscopic schistose structure (Fig. 3b).
According to the calculation of EPMA data, 18/22 test points are amphibole, the others are calcite. $Mg/(Mg+Fe^{2+})>0.982$ can determine that these are tremolite. (S. Li, 2008; B. E. Leake, 1978; T. Zoltai, 1981) Except for amphiboles, the minerals in surrounding rocks are diopside, serpentine, plagioclase, chlorite, sphere, apatite, calcite, dolomite and quartz.
Combined with EMPA data, the back-scattered electrons images (BSE) of surrounding rocks are analyzed. There are flaky tremolite (Tr) and radial fiber serpentine (Srp) in large grains of calcite. (Fig. 4a) Quartz (Qtz) and calcite (Cal) contact with each other. (Fig. 4b) Diopside (Di) contains apatite (Ap) and dolomite (Dol) particles. (Fig. 4c) Calcite (Cal), dolomite, apatite particles and flaky chlorite (Chl) are situated in cryptocrystalline flaky tremolite. (Fig. 4d)
Conclusion: The major mineral composition of samples is tremolite, they show felt-like microstructure and microscopic fibroblastic structure. All the data provide the first evidence to identify nephrite from Tieli. Combining the mineral composition of surrounding rocks, it helps to indicate the forming process.

References:
[1] B. E. Leake. 1978. Nomenclature of amphiboles[J]. American Mineralogist, 63(11-12): 1023–1052.
Francesca Casadio, Janet G. Douglas, Katherine T. Faber. 2007. Noninvasive methods for the investigation of ancient Chinese jades: an integrated analytical approach[J]. Analytical and Bioanalytical Chemistry, 387(03):791-801.
[2] P. Li. 2008. Crystallography and Mineralogy[M]. Beijing: Geological Publishing House. 232. (in Chinese) T.-H. Chen, T. Calligaro, S. Pag`es -Camagna, etc. 2004. Investigation of Chinese archaic jade by PIXE and μRaman spectrometry[J]. Applied Physics A- Materials Science & Processing, 79(02):177-180.
[3] Tibor Zoltai. 1981. Amphibole asbestos mineralogy[J]. Reviews in Mineralogy and Geochemistry, 9:237-278.
[4] Z. Zhu, Y. Fang. 1981. Laser Raman spectroscopy(II) [J]. Chinese Journal of Organic Chemistry, 5:377-380. (in Chinese)

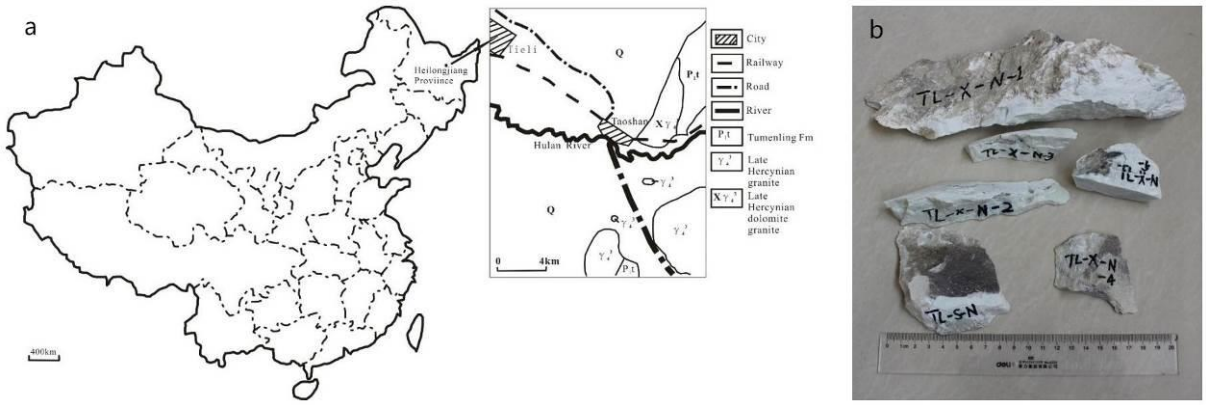

Figure 1. Geographic position of Tieli (a) and fotos of samples (b).

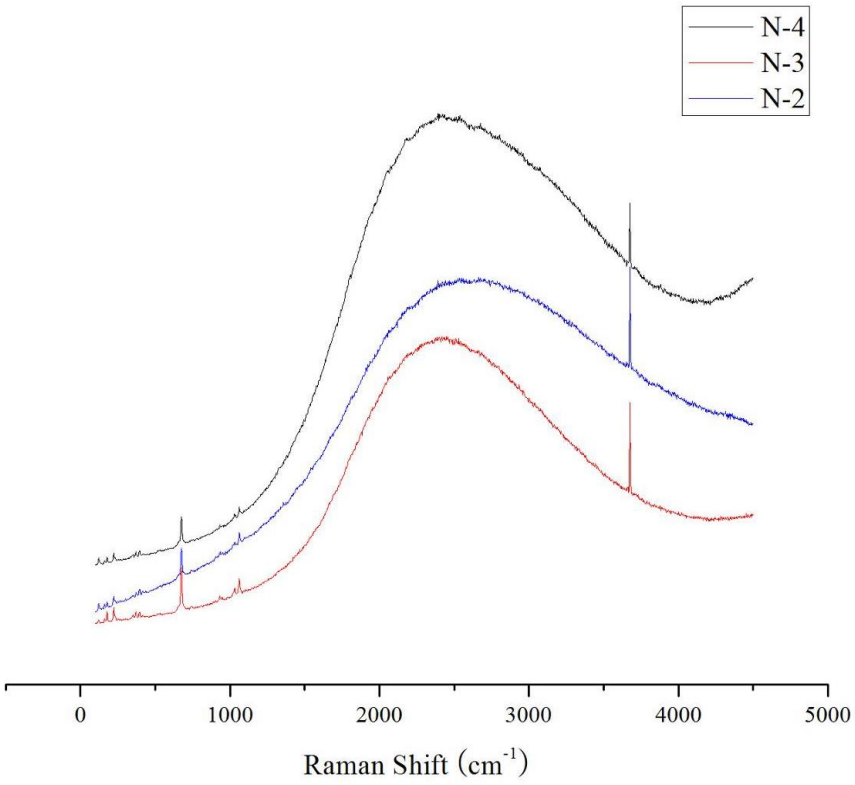

Figure 2. Raman spectrum of samples.

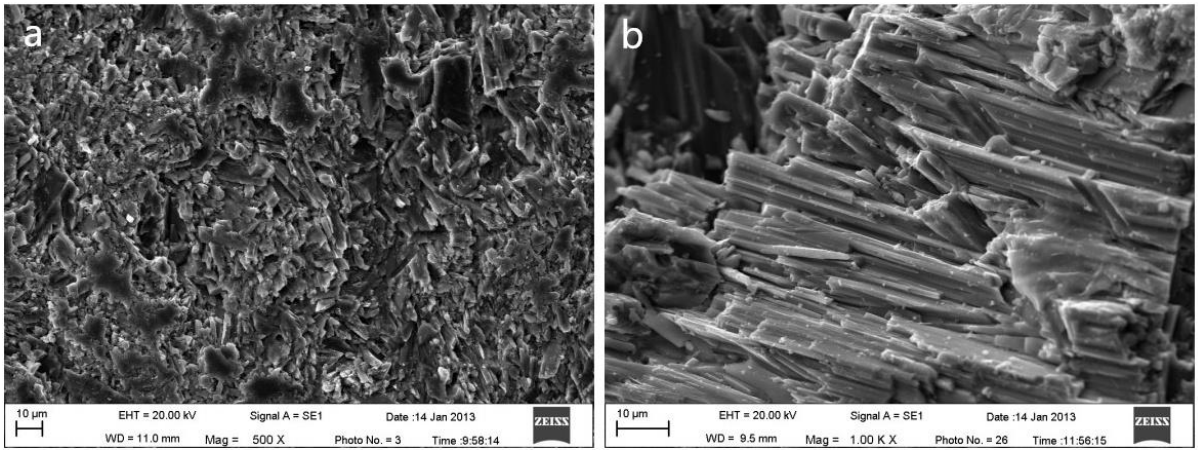

Figure 3. Micro-structure of samples.

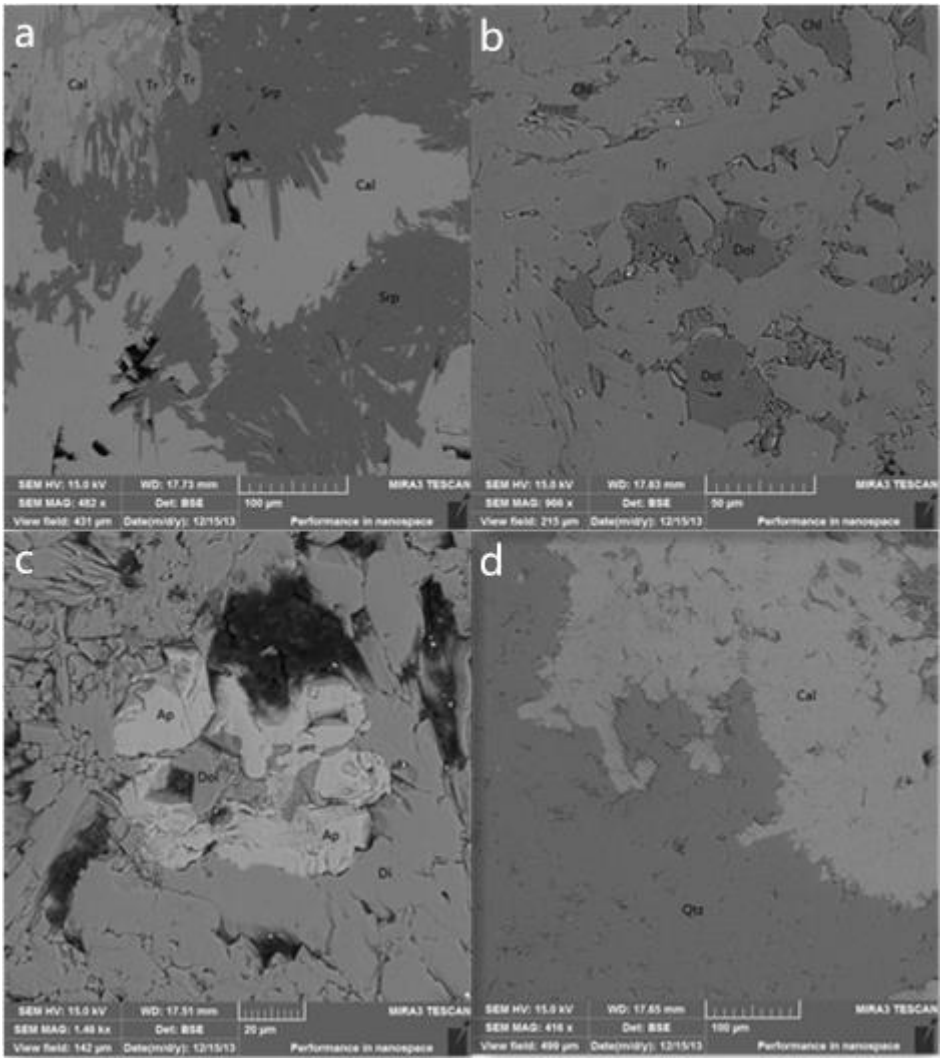

Figure 4. BSE images of surrounding rocks.

MS7.P004
Textural analysis and identification of sub-microscopic laumontite in andesites and volcanoclastic rocks from central Chile.

A. Bravo[1,2], U. Kelm[2], O. Jerez[2], M. Poblete[3]

[1]TU Bergakademie Freiberg, Institut für Mineralogie, Freiberg, Germany
[2]Universidad de Concepción, Instituto de Geología Económica Aplicada (GEA), Concepción, Chile
[3]Universidad Católica de la Santísima Concepción, Concepción, Chile

geoarturobravo@gmail.com

Drill cores from the very low grade metamorphic altered andesites and volcanoclastic rocks from Central Chile, showed detachments of shotcrete in a tunnel exposed to periodic water flow with expandable clay phases apparently responsible for the observed failure.
However, when conducting an analysis of the phases on the samples, small amounts of clays, and a notable abundant presence of laumontite was found. Literature often refers to laumontite that when hydrated and dried, goes through an expansion-contraction process of its lattice in response to the aforementioned cyclical process. This can render a weakening of the adjacent material which could be the cause of said detachments.
Based on this information and considering the ample distribution in deposits along Chile with the presence of altered andesitic rocks, it is relevant to identify accurately and exhaustively the presence of laumontite. This research work is under review by "Clay Minerals" to be published.
Laumontite was identified by optical microscopy, semi-quantitative x-ray diffraction and automated mineralogical analyzer. The main goal was compare the different semi-quantitative techniques analyzed by Qemscan® (Quantitative Evaluation of Minerals by Scanning Electron Microscopy) and X-ray diffraction (XRD) semi-quantification, using Autoquan 2.1.6 version software.
Thin sections were analyzed by Qemscan® considering a visualization of laumontite in false colours to detect any directionality in its distribution as well as to evaluate this method as a means for microchemical semi-quantification of laumontite abundance. In order to detect laumontite, the microchemical Reference: database of the automated mineral analyzer had to be partially adjusted to ensure a differentiation from the compositionally similar plagioclases.
The identification of zeolites by optical microscopy is only possible for large crystals, which are not a regular occurrence in the very low temperature altered andesites of central Chile. XRD analysis permits the easy identification of the zeolite, but restrains itself to obtain the information on any preferred orientation of laumontite.
However, semi-quantitative Rietveld modeling will include any very fine-grained – submicroscopic – laumontite. To obtain greater textural information, an automated microchemical analysis was tested as a possibility to visualize the distribution of laumontite down to a resolution of 2 µm.
When evaluating both techniques, it is concluded that a combination of the two semi-quantitative methods are considered recommendable to obtain information on the presence of sub-microscopic laumontite as well as gaining a visual impression of the textural arrangement of the zeolite in the rock.
Acknowledgements: The help of technical staff at the GEA Institute (Universidad de Concepción) at all stages of sample preparation is acknowledged. I would like to thank to TU Bergakademie Freiberg for the financial support for the conference's participation

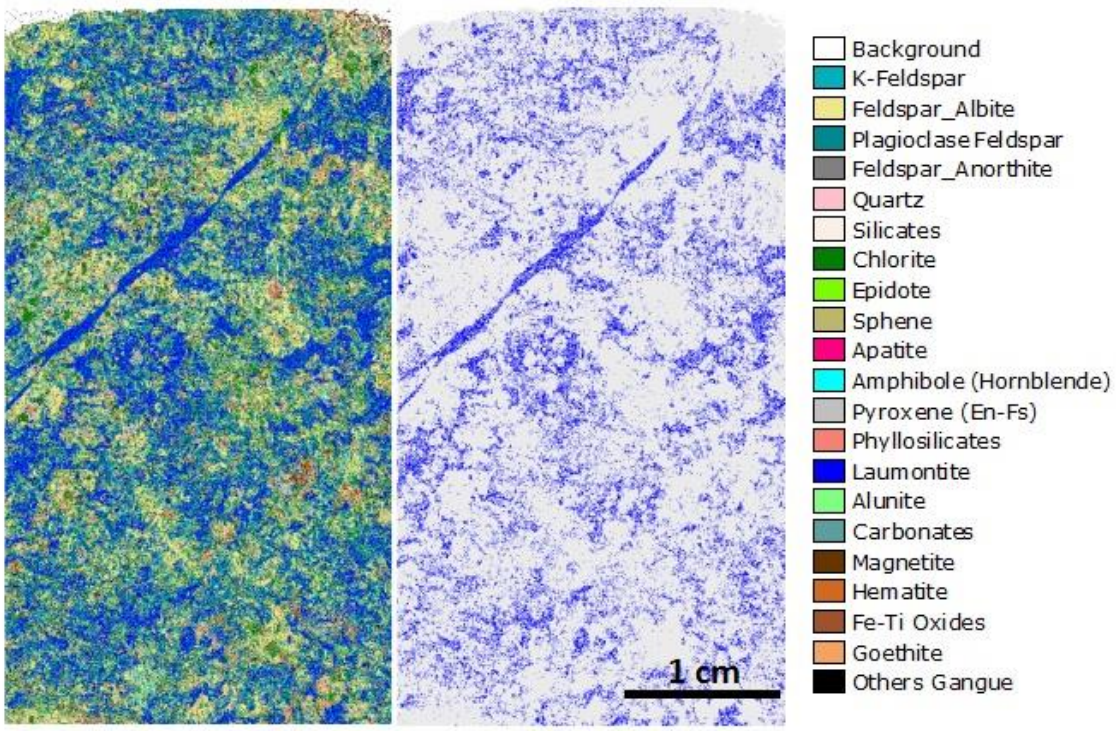

Figure 1. Example of setting for the Qemscan® system and thin section with patchy, but pervasive laumontite distribution.

MS7.P005
In situ electron microscopy studies of electric field assisted sintering of oxide ceramics

D. Schwarzbach[1], V. Roddatis[1], C. A. Volkert[1]

[1]Georg-August-Universität Göttingen, Institut für Materialphysik, Göttingen, Germany

dschwarzbach@ump.gwdg.de

A wide range of studies show a dramatic effect of applied electric fields or currents on the sintering behavior of oxide ceramic powders. However, the mechanisms accounting for these strong effects remain elusive despite the wide application potential.
By using in-situ scanning and in-situ transmission electron microscopy, material changes during sintering of model oxide ceramics (e.g. ZnO) will be directly observed. The evolution of microstructure and morphology, including grain/void morphology, segregation, and precipitation, will be tracked, both with and without applied fields and currents. The results will be compared with models to determine the dominant driving forces and mechanisms for sintering, and how these are affected by fields and currents. In-situ high resolution and electron holography studies, EELS, and in-situ studies will be performed under oxidizing and reducing atmospheres to gain insight into the atomic origins of sintering behavior, as well as of high conductivity states that occur in conjunction with flash events during field-assisted sintering. In order to catch the specimen in such a high conductivity state in the middle of a flash event, experiments will be performed while imposing a current limit. This is essential to gain enough time to search for processes or microstructural changes in the sample, which are specific to field-assisted or flash behavior. The main focus of this poster is to present the research plan and methods and to provide an overview of the current state of research in the literature. Nevertheless, some initial results from our own studies are expected.

Support through the Priority Program (SPP 1959) "Manipulation of matter controlled by electric and magnetic fields: Towards novel synthesis and processing routes of inorganic materials" of the DFG is gratefully acknowledged.

MS7.P006
RISE microscopy – correlative raman SEM imaging of geological samples

U. Schmidt[1], X. Bourrat[2], P. Ayasse[1], G. Wille [2], O. Hollricher[1]

[1]WITec GmbH, Ulm, Germany
[2]BRGM, Orleans, France

ute.schmidt@witec.de

Introduction: The characterization of geological samples greatly benefits the combination of different analytical methods. The interconnection of data from the separate methods can deliver the comprehensive understanding often thought. SEM (Scanning Electron Microscopy) equipped with various accessories and detectors (SE – secondary electrons, BSE – backscattered electrons) and with microanalysis tools (EDS, CL) is a powerful tool for geo-scientific inquiry, providing information on morphology, elemental composition and crystallography. Confocal Raman imaging of geological samples reveals the chemical composition of minerals as well as polymorphisms, stress states and anisotropies.
Objectives: A combination of SEM and confocal Raman imaging in a single instrument – the RISE microscope - enables the analysis and correlation of images from various investigated techniques of the same region of interest on a geological sample [1,2].
Materials and Methods: RISE microscopy was used to study nanometeric fibers in rocks, and also pearls produced from a natural bio-mineralization process.
Results: Natural nanometric fibers in rocks are a hazard for the mining industry and a public health concern [3]. Of interest are their morphology, chemistry and crystallography. SEM provides the morphological information, whereas confocal Raman imaging gives information about the chemistry of the fibers and surrounding rocks. Furthermore, the confocal setup of the Raman microscope enables the 3D distribution of such fibers in the host material to be determined. Fig. 1a shows a 3D Raman image of actinolite fibers in moganite, a polymorph of quartz [4]. The Raman spectra are shown in Fig. 1b and the RISE image of the top surface of the sample is shown in Fig. 1c.
Natural pearls consist of polymorphs of calcium carbonate. The regular form of pearl mineralization is aragonite, an orthorhombic polymorph of calcium carbonate which produces the associated pearlescent sheen. This structure can be visualized with the SEM. Sometimes, pearls show a biomineralisation defect characterized by reduced iridescence (also called "milky pearl"). These defects are related to the change in the mineralization form, from orthorhombic aragonite to hexagonal vaterite. Such a defect was studied with RISE microscopy. The crystallographic structures of the two polymorphs were detected with the SEM and confirmed by the chemical bond-sensitivity of Raman imaging (Fig 2a). Furthermore small changes in relative Raman peak intensities highlight anisotropies in the aragonite phase in the vicinity of the vaterite polymorph (Fig. 2b).
Conclusions: The two examples described in the paragraph above highlight the power of RISE microscopy for the analysis of geological materials.

References:
[1] J. Jiruse, M. Hanicinec, M. Havalec, O. Hollricher, W. Ibach, P. Spizig, J. Vac. Sci. Tech. B 32 (2014) 2166.
[2] U. Schmidt, K. Hollricher, P. Ayasse, O. Hollricher, Microscopy and Analysis May/June (2015), 24.
[3] F Rey, C Boutin, J Steinbauer, Viallat, P Alessandroni, P Jutisz, D Di Giambattista, MA Billon-Galland, P Hereng, P Dumortier. European Respiratory Journal 6 (1993) 978.
[4] P. Schmidt, L. Bellot-Gurlet, V. Lea, P. Sciau, Eur. J. of Mineral (2012)

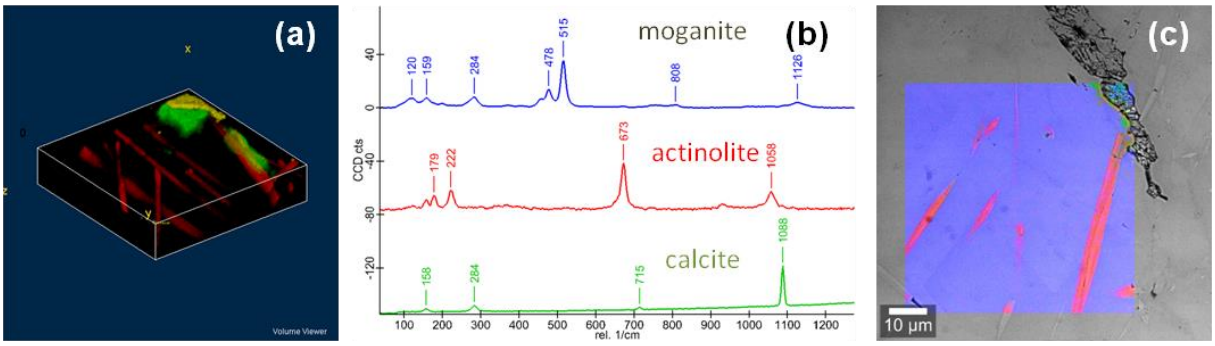

Figure 1. (a) Color coded 3D confocal Raman image of actinolite fibers in a moganite host (imaging parameter: 60 x 60 x 20 µm^3, 120 x 120 x 20 pixels, integration time 0.1 s/spectrum), (b) color coded Raman spectra, and (c) RISE image of the surface of the region of interest.

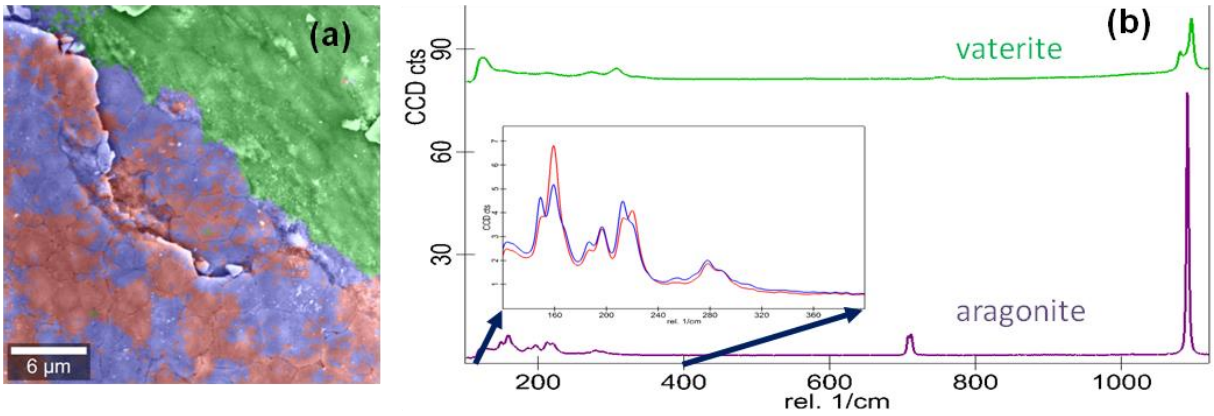

Figure 2. (a) RISE image of the border of a milky pearl and (b) color coded Raman spectra of vaterite and aragonite. The inset shows the changes in Raman band intensities of the Ca-lattice vibrations associated with anisotropies in the aragonite phase.

MS7.P007
Analysis of dependence of conductive and reflective properties on structure and composition in nanostructured carbonaceous geomaterials on the based microscopic data

E. Golubev[1], I. Antonets[2]

[1]Institute of Geology of Komi SC of RAS, Laboratory of crystallography, Syktyvkar, Russian Federation
[2]Syktyvkar State University, Physycs, Syktyvkar, Russian Federation

golubev@geo.komisc.ru

Introduction: Disordered carbonaceous geomaterials (DCGM) at a high degree of metamorphism have an almost pure carbon composition and a three-dimensional disordered structure with nanoscale domains from graphene stacks. One of the more intriguing types of DCGM occurs in the shungite rocks of Karelia (Russia) [1]. Shungite occurs in both dispersed and in pure forms in sedimentary and volcanic rocks. The dispersed form of shungite, occurring as an impregnation in various rocks, represents natural composite from carbon matrix and mineral impurities (mostly quartz) with different carbon content. Shungite has a great application potential in various fields of technology [2]. Electromagnetic properties are of special interest, first of all for shielding of electromagnetic radiation.
Nanoscale structure of DCGM and distribution of dielectric impurities have a significant impact on their electromagnetic properties [3]. The most effective approach of the DCGM study is methods of microscopy. This work reports the results of the modeling of electromagnetic properties of shungites on the basis of data about nanostructure, conductive properties of surface and elemental mapping.
Materials and Methods: The samples were collected from various deposits of carbonaceous materials in Karelia. We investigated samples with carbon content (wt. %) of 3%, 24%, 30%, 35%, 52%, 62% and 95%. The static conductivity was measured using two-probe method. Microwave spectra of reflection and transmission were obtained for samples, representing the schungite plates of thick 20 microns, pasted to glass plates of thick 1 mm. The reflection and transmission coefficients of the microwave signal from shungites at normal incidence were measured in the frequency bands 26-38 GHz. HRTEM for structural description, SEM/EDS for mapping of chemical elements and scanning spreading resistance microscopy (SSRM) to evaluate the distribution of conductive properties of the surface were used.
Results: It is found that the dependence of reflection coefficient versus frequency for samples with low-carbon content (up to 30%) is largely determined by the properties of the substrate (reflection from the glass is 0.55-0.60). With increasing of carbon content the reflection in the whole frequency range sharply increases from 0.55 (for content 24%) to 0.96 (for content 62%) and further practically does not change.
As a part of the model of 3D network from carbon ribbons with different thicknesses surrounding the dielectric regions, a quantitative evaluation of influence of size of the dielectric regions and thickness of the carbon ribbons (as conductive bridges) between the dielectric regions on static and dynamic electrical conductivity of shungites was carried out. Average thickness of the bridges and size of the dielectric regions were determined from the maps of chemical elements (Fig.) and conductivity maps.
In conclusion, for a carbon content up to 52% the width of the conductive bridges and size of the dielectric regions (SEM/EDS and SSRM data), and for a carbon content is greater than 60% the width and length of the carbon nanoribbons (HRTEM data) play a key role for modeling of conductive properties.

This work was supported by RFBR (grant 15-05-04369).

References:
[1] Kovalevski, V.V., Buseck, P.R., Cowley, J.M. (2001): *Carbon*, 39, 243–256.
[2] Melezhik, V.A, Filippov, M.M, Romashkin, A.E. (2004): *Ore Geol. Rev.,* **24,** 135–154.
[3] Golubev, E.A. (2013): *Physics Solid State*, **55**, 1078–1086.

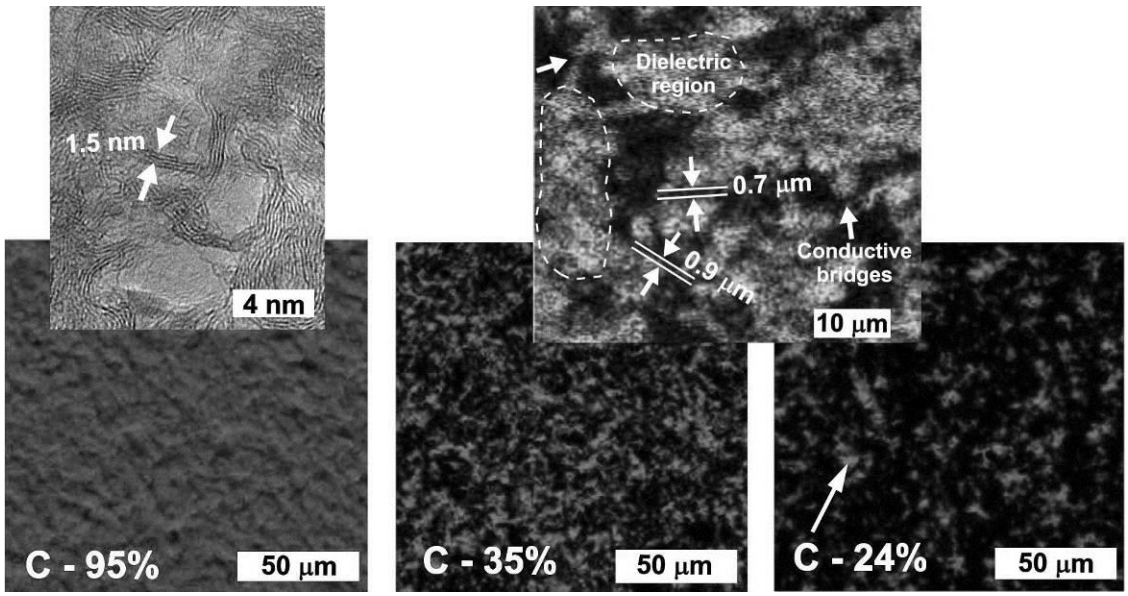

Figure 1. Energy dispersive elemental maps of shungite samples with different carbon content. Carbon nanoribbons on HRTEM-image and conductive bridges on ED elemental maps are shown as insets.

MS7.P008
Aberration corrected STEM imaging of domain walls in complex oxides

N. Alem[1,2], D. Mukherjee[1,2], V. Gopalan[1,2]

[1]Pennsylvania State University, Materials Science and Engineering, University Park, PA, United States of America
[2]Pennsylvania State University, Materials Science, State College, PA, United States of America

nasimalem@gmail.com

Introduction: Domain walls in complex oxides can host structural distortions that can perturb the local charge distribution further leading to ferroelectricity, photovoltaic behavior, and two dimensional electron gas (2DEG). The richness in the crystal chemistry and structure of complex oxides has led to many compounds with polar domain walls within an insulating matrix. Among the family of complex oxides, polar metals offer new multifunctional materials with emergent phenomena such as anisotropic thermoelectric responses and magnetoelectric multiferroics enabling the design of new generation of devices with simultaneous electrical, magnetic and optical functions.
Objectives: LiNbO3 is a ferroelectric crystal at room temperature with a spontaneous electrical polarization [1-3]. With a high Curie temperature, electrical polarization, LiNbO3 has applications as diverse as pyroelectric sensors, ferroelectric memory, quasi-phase matched second harmonic generators, optical switching etc. A multitude of these applications depend on the precise manipulation and control of domain walls in LiNbO3. The exact structure of the domain wall is however a subject of ongoing controversy on whether it is a pure Ising wall, or has a mixed Ising-Neel-Bloch nature [4]. In this work, we image domain walls with atomic resolution to quantify the atomic displacements and polarization across the domain walls.
Materials and Methods: A periodically poled congruent LiNbO3 (PPLN) crystal with 6.7μm wide y-wall 180o domains is chosen for this study. The domain walls were imaged using an aberration-corrected TEM with a beam voltage of 200kV from the [010] pseudocubic orientation using annular dark field (ADF) and annular bright field (ABF) detectors simultaneously.
Results: The origin of ferroelectricity in classical ferroelectrics like LiNbO3 is due to second order Jahn-Teller distortions with the B-site atom, niobium, displacing from the center of the oxygen cage [5]. Here we probe the structural distortions and relaxation effects resulting from Jahn-Teller effect across the domain walls in LiNbO3 by imaging both oxygen and B-site atoms. While the ABF image (Fig. 1a) shows both the niobium (yellow) and the oxygen atoms (green), the simultaneously obtained ADF image (Fig. 1b) shows just the niobium atoms from the same region. The niobium atom positions obtained from the ABF and the ADF images are cross-Reference:d with each other, while the oxygen atom positions are obtained from the ABF image. The combined atom positions are then used to measure the Jahn-Teller distortions and the spatial extent of the domain wall.
Conclusion: Our measurement shows the Ising character of the wall with Nb-O spacing to undergo a displacement in the y-direction (displacement parallel with the domain wall), while in the x-direction Nb-O spacing shows a Neel character (displacement parallel with the domain wall) as previously predicted. Such distortions lead to polarization across the domain wall in the sample and give rise to a ferroelectric behavior.

References:
[1] G. A. Srzolenski *et. al.* Phys. Stat. Sol. **13** (1966), p. 309
[2] A. Savage, J. Appl. Phys. **49** (1978), p. 3071
[3] M. L. Bortz, L. A. Eyres, and M. Fejer, Appl. Phys. Lett. **62** (1993), p. 2012
[4] D. Lee *et. al.* Phys. Rev. B. **80** (2009), p. 060102-1
[5] I.B. Bersuker, Ferroelectrics, **164** (1995), p. 75

Figure 1. a) ABF image of the domain wall, with the wall marked with white lines. The inset shows how the Nb rows marked in yellow bend across the wall (marked by the white dashed line), while the O rows marked in green do not. b) ADF image showing the Nb atoms across the domain wall. The blue arrows refer to the polarization directions in the respective domains.

MS7.P009
Determination of the local conductivity of ceramic composites by electron microscopy

K. Sempf[1], P. Gnauck[2]

[1]IKTS Dresden FhG, Sachsen, Dresden, Germany
[2]Carl Zeiss Microscopy, Oberkochen, Germany

kerstin.sempf@ikts.fraunhofer.de

Introduction: The electrical conductivity in ceramic composite materials can be tailored by combining a conductive and non-conductive phase. Typical applications of these materials are heating elements such as glow plugs or evaporator boats. Another large area are current collector in solar panels or sensor devices. An additional advantage of conductive ceramic composites is the ability to easily generate complex shapes by electro discharge machining.
Objectives: In order to generate a certain electrical conductivity in the composite ceramic the conducting phase needs to build up a percolated three-dimensional network.
The conductivity strongly depends on the fraction and grain size of the conducting phase and the homogeneity of the distribution, especially near the percolation threshold.
A change of the microstructure of the composite has a big influence on the conductivity. During operation of the device contacts between grains can be changed or even interrupted and therefore change the electrical properties. Therefore, a detailed analysis of the microstructure of such materials is a precondition for a clear understanding of the electrical properties and the aging behaviour.
Materials and Methods: BN/TiB2 was chosen as a typical example for a composite ceramic consisting of a non conducting (BN) matrix and a conductive phase (TiB2). By adjusting the volume content and the interconnectivity the conductivity of the whole composite can be adjusted.
The information concerning the local conductivity can be derived by using the inlens detector of a FESEM (Fig. 1) . The results were verified by means of Helium Ion Microscopy and 3D-FIB imaging.
Results: The results of the two and three dimensional investigations of the microstructure showed, that the in-lense signal is sensitive to the connectivity of the TiB2 grains. Therefore the FESEM can be used to characterise the local conductivity and the degree of percolation of the electrical conductive phase of ceramic composites. The results of the SEM investigation were be verified by direct three dimensional analysis of the network by using a focused ion beam FIB.
The result determined on the BN/TiB2 composite could be also verified on other ceramic composite materials.
Conclusion: Using ceramographic preparation and FESEM analysis the distribution, volume content and size of the conducting components can be determined. By analysing the grey levels in the secondary electron signal percolated and non-percolated parts of the conducting phase could be distinguished and the conductive network can be visualized.

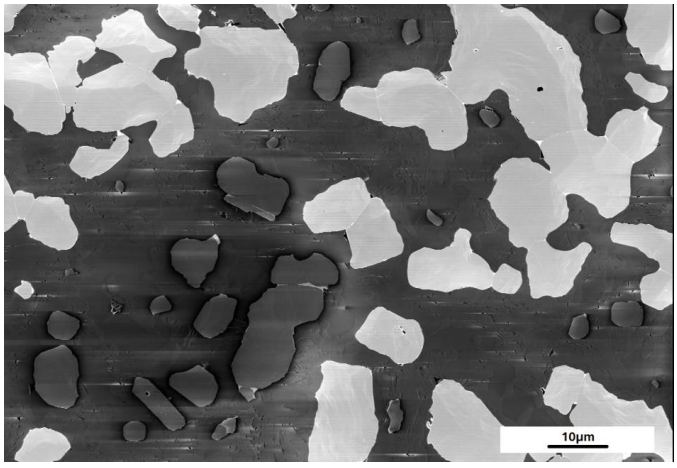

Figure 1. Inlens image of a BN/TiB2 composite ceramic. TiB2 Particles that are in the percolation appear bright. Isolated TiB2 particles appear dark.

MS7.P010
3D Information on glasses and glass ceramics by X-ray microscopy

M. Krause[1], A. Barascu[2], S. A. H. Sander[3], C. Thieme[1,4], G. Schusser[1], C. Rüssel[4], S. T. Kelly[5]
T. Höche[1]

[1]Fraunhofer IMWS, Fraunhofer Center for Applied Microstructure Diagnostics, Halle, Germany
[2]Leipzig University, 2 Institute for Technical Chemistry, Leipzig, Germany
[3]Martin Luther University Halle Wittenberg, Institut of Physics, Halle, Germany
[4]Friedrich Schiller University, Otto Schott Institute for Materials Research, Jena, Germany
[5]ZEISS Group, 5Carl Zeiss Microscopy, LLC, Pleasanton, CA, United States of America

thomas.hoeche@imws.fraunhofer.de

Recently, X-ray microscopy (XRM), the high-resolution counterpart of X-ray tomography has moved from synchrotron sources into labs, facilitating the accelerated and knowledge-based development of glasses and glass ceramics close to the location of their synthesis. The outstanding characteristics of XRM include two major points:

- Non-destructive, three-dimensional screening of the interior of relatively large objects (between a few 10 and up to a few 100 µm edge lengths) at a spatial resolution of as good as 50 nm.
- Favorable volume-to-surface ratio allowing for studying one and the same sample at different stages of microstructure development.

Due to these features, the *Carl Zeiss Xradia 810 Ultra* X-ray microscope that will become available in Halle by summer 2017 has the potential to significantly foster the development of new nanostructured glasses and glass ceramics. The latter materials are very well suited from the point of view of absorptions length for the Cr-K X-radiation used.
After briefly introducing the advantages of laser-based sample preparation using Gatans microPREP, experimental results obtained at porous silica glasses (Figs. 1 & 2) as well as multiphase glass ceramics (Fig. 3) [1] will be discussed to illustrate the capabilities of this novel method bridging the gap between knowing everything about nothing (TEM) und knowing too little about everything (SEM). Based on three-dimensional datasets, conclusions about attainable quantification and spatial arrangement of phases will be drawn.

References:
[1] A. Keshavarzi, W. Wisniewski, and C. Rüssel, ACS Appl. Mater. Interfaces 5 (2013) 8531.

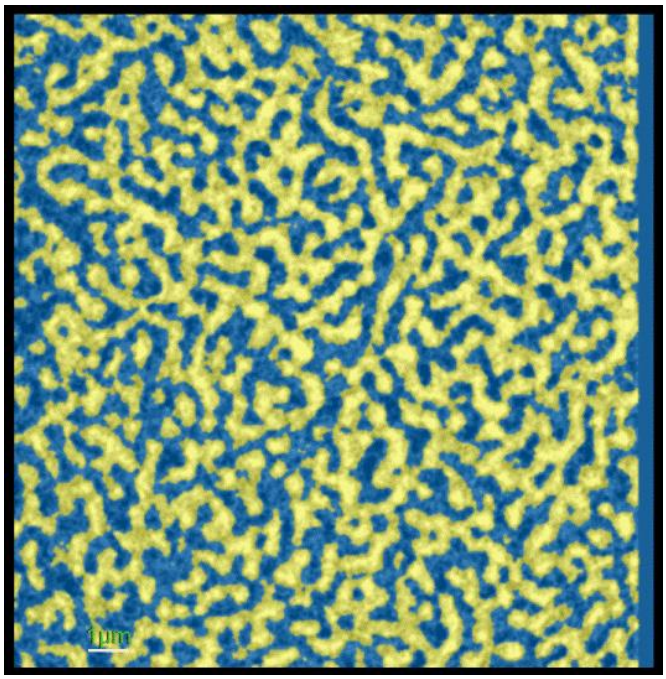

Figure 1. Leached sodiumborosilicate glass possessing an average pore diameter of 400 nm, absorption- contrast data displayed in false colors [Yellow = Silica glass scaffold, Blue = Pores].

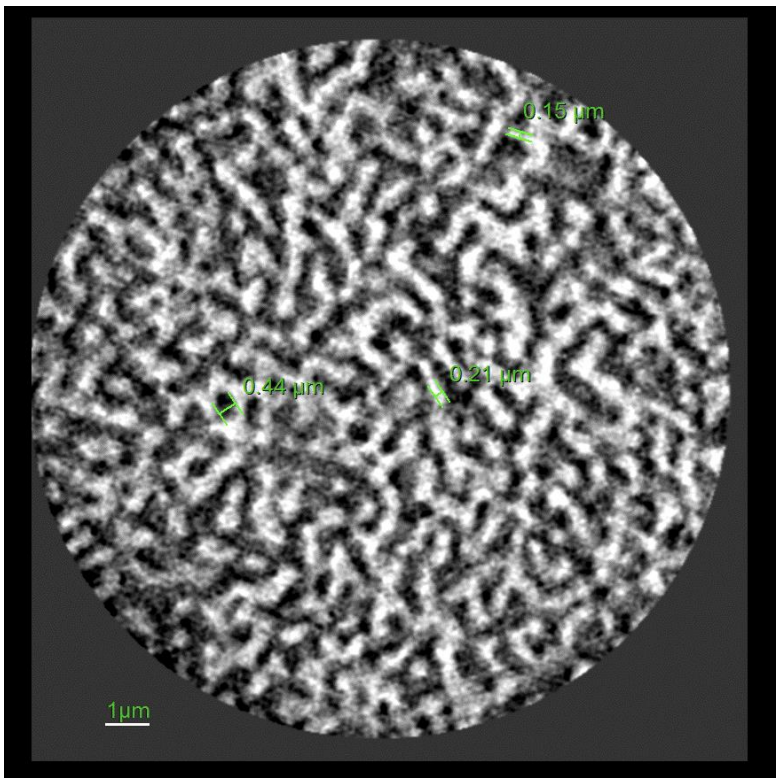

Figure 2. Leached sodiumborosilicate glass possessing an average pore diameter of 400 nm, 2D section through high-resolution data.

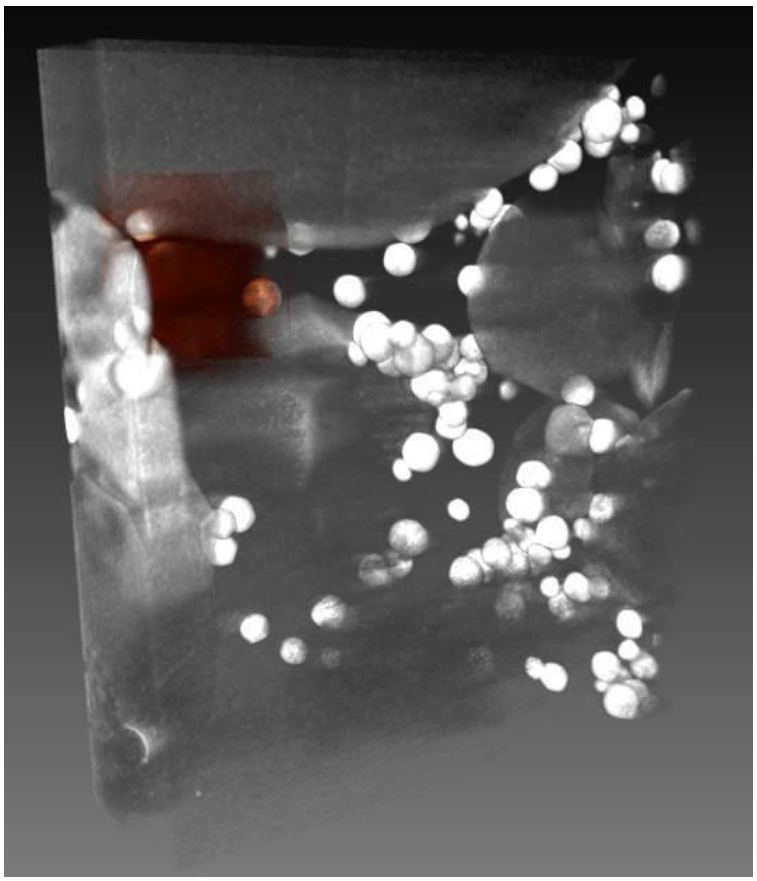

Figure 3. Crystallized 23.82 Y_2O_3·39.82 Al_2O_3·28.50 SiO_2·2.91AlF_3·4.95 ZrO_2 glass ceramics (field of view: 64 x 64 µm²) possessing white Y-stabilized zirconia (YSZ) precipitates as well as grey YAG, and $Y_2Si_2O_7$.

MS7.P011
Microstructure and texture of a natural spinel corona on a corundum single crystal – an SEM-EBSD and EMPA study

L. C. Baldwin[1], G. Habler[1], C. Li[1], R. Abart[1]

[1]University of Vienna, Department of Lithospheric Research, Vienna, Austria

lisa.baldwin@univie.ac.at

A natural, c. 20 mm sized single-crystal corundum (Al_2O_3) xenocrystal reacted with the hosting alkaline basaltic melt to form a concentric c. 0.3 mm wide ferroaluminate spinel ($(Mg,Fe)Al_2O_4$) layer at the contact to basaltic melt. The single-crystal nature of corundum (Crn) allows investigating the dependence of the spinel (Spl) layer microstructure and texture on different reaction front orientations with respect to the precursor Crn lattice. The study allows testing the representativeness of results from experimentally produced Spl layers (Keller et al 2010; Jeřábek et al 2014) for natural Spl formation. Secondly, remarkable oscillatory inclusion size distribution zoning of the precursor Crn crystal provides information on how the microstructure and texture of the polycrystalline Spl layer is influenced by the presence and nature of preexisting (ultra-)fine grained Ti-oxide inclusions, as well as their behavior during host decomposition.

Based on optical microscopy several SEM methods (SE-, BSE-, FSE imaging, EBSD-, EDX-analysis) as well as FEG-EMPA analyses have been applied to various Crn domains and Spl rim segments with different reaction front orientations in order to investigate i) the Spl layer microstructure, texture and grain boundary characteristics, ii) the reaction front geometry, iii) the Ti-oxide phases and their distribution, size and geometry within Crn and the Spl layer, as well as at the Crn/Spl interface, and iv) compositional variations of Crn and the Spl layer.

The resulting data indicate that Spl has a topotactic crystallographic orientation relation (COR) with Crn that is independent of the reaction front orientation and consistent with observations from experiments. Spinel {111} twin boundaries have straight trace segments with preferred orientations parallel to the precursor Crn (0001) planes, which induces a shape preferred orientation of the Spl-twin individuals when the reaction front is oriented at an angle with respect to the Crn (0001) plane. Only for a special interface orientation subparallel to Crn (0001) Spl twin boundaries are curved and interlobate. General grain boundaries and Σ3 boundaries generally show curved boundary traces separating grains with low aspect ratio. There was no remarkable microstructural and textural difference of the Spl layer found when comparing rim sections with reaction front traces subparallel to either n{2 2 -4 3} or ω{14 14 -28 3} planes of Crn, which are the most prominently developed Crn/Spl interface trace orientations at the millimeter scale. Still, at the micrometer scale the Crn/Spl interface trace shows steps with spikes towards Spl at points where Spl grain boundaries impinge the reaction front. At the grain scale Spl grain boundaries therefore cause retardation of the reaction front propagation compared to segments bounding single crystal Spl.

Inclusions in Crn are either c. 10 – 50 nm sized ilmenorutile ($(Nb,Ti,Fe)O_2$) nanocrystals, or c. 200 – 500 nm sized rutiles (TiO_2), showing an oscillatory size-distribution zoning, which, in turn, correlates with Ti and Nb trace element compositional zoning in Crn. During host decomposition, ilmenorutiles recrystallize to larger but fewer grains at the reaction front and are incorporated into the Spl rim. Contrastingly, in rutile-dominated Crn areas, inclusions coarsen at the reaction front where they are dragged along during reaction propagation, whereas the Spl rim remains inclusion free. Therefore, the ilmenorutile-distribution in the Spl rim correlates with the former inclusion distribution in precursor Crn.

We conclude that the compositional zoning, inclusion nature and crystal orientation of the precursor Crn controls the Ti-oxide inclusion behavior at the reaction front and the texture and microstructure of the spinel rim formed. Except of a special interface orientation parallel to Crn (0001) the reaction front orientation with respect to the Crn lattice has subordinate influence on the Spl microstructure formation.

References:

[1] Keller et al (2010) Am Mineral 95: 1399-1407

[2] Jeřábek et al (2014) Am J Sci 314: 940–965

MS7.P013
X-ray diffraction, electron microscopy and density functional theory study of (130) twins and rutile precipitates in chrysoberyl from Pratinhas, Brazil

S. Drev[1], M. Komelj[1], M. Mazaj[1], N. Daneu[1], A. Rečnik[1]

[1]Jožef Stefan Institute, Nanostructured Materials, Ljubljana, Slovenia

aleksander.recnik@ijs.si

We studied V-shaped twins of chrysoberyl ($BeAl_2O_4$) from Rio das Pratinhas near Arataca in the Bahia state of Brazil. The local structure of the twin boundaries was determined using powder X-ray diffraction analysis (XRD), transmission electron microscopy (TEM) methods and density functional theory (DFT) calculations. The chrysoberyl structure was first studied by Bragg and Brown (1926). It crystallizes in the olivine-type structure, a hexagonal close-packed (*hcp*) analogue of cubic (ccp) spinel ($MgAl_2O_4$) structure. Chrysoberyl has a slightly distorted *hcp* O-sublattice with Al^{3+} and Be^{2+} ions partially occupying octahedral (½) and tetrahedral (¼) interstices. Current strutural reports do not differ much in the cell parameters as they do in the axial setting of the orthorhombic unit cell leading to a space groups variants: Pnma, Pbnm, Pmnb, *etc.* due to different choice of crystallographic setting. In our setting the unit cell was oriented in accordance to the spinel archetype structures. *hcp* planes of the O-sublattice were thus oriented normal to the crystallographic c-axis so that (001) planes of chrysoberyl correspond to (111) planes of spinel, with the a-axis aligned parallel to the [110] axis of spinel, allowing direct comparison between the spinel, taaffeite and chrysoberyl structures. The structure was refined by Rietveld analysis (Topas-Academic V4) using experimental XRD data: *s.g*. Pmnb (62); a = 5.4825, b = 9.4163, c = 4.4308 and Rwp = 7.8%.

Refined structure was used for interpretation of electron diffraction patterns and lattice images obtained by TEM. The specimens were investigated in [001]-projection, where the (130) twin boundaries are viewed edge-on. The twin boundary is coherent, making occasional steps. The periodicity along the twin boundary is accomplished at ~ 1.9 nm, roughly corresponding to 4·[110] distances. HRTEM images recorded at the defocus value of -60 nm show characteristic undulating pattern following the O atomic columns, and remains stable in the thickness range from 5-20 nm. This condition is very sensitive to the positions of Be-atoms, which alternate form one to another side of the chain (Fig. 1). This translation of crystal domains is reproduced by mirror-twin operation across (130) plane. Image simulations, based on a simple mirror-twin model, perfectly match the contrast of bulk crystal parts, while the interface is not reproduced and needs reconstruction. Two characteristic atomic clusters are observed at the interface. DFT calculations using pseudo-potential method suggested that atomic Cluster-I undergoes a significant relaxation of interfacial Be^{2+} and O^{2-} positions, whereas in Cluster-II the interfacial Be2+ sites are shifted to neighboring tetrahedral interstices, further away form the boundary. Local charge balance involved with this operations remains preserved. T he contrast of the simulated image based on the DFT relaxed atomic model, shows correct tendency in the interface contrast compared to experimental HRTEM.

In addition to the twin boundaries, bulk chrysoberyl contains numerous nanosized TiO2 precipitates with a distorted rutile structure, following orientation relationship of $[001]_{Ch}\{120\}_{Ch}||[010]_R\{103\}_R$. The increase of Ti at the twin boundaries and the formation of rutile-type TiO_2 precipitates in chrysoberyl suggest a transient Ti-exsolution that took place after the twin formation. Nanostructural analysis of rutile exsolutions has shown that the c-axis of rutile is oriented in such a way that the channels along this direction are providing shortest pathways for cation diffusion that allow their lateral growth after nucleation as long as Ti^{4+} ions continue to segregate from the host chrysoberyl matrix. On further cooling, elastic accommodation of the rutile, was driven by temperature dependent contraction of chrysoberyl lattice, followed by Ti^{4+} exsolution in form of rutile, which helps to better understand the dynamics of geochemical processes during the crystallization of chrysoberyl.

Reference:

[1] Drev S, Komelj M, Mazaj M, Daneu N, Rečnik A. *Structural investigation of (130) twins and rutile precipitates in chrysoberyl crystals from Rio das Pratinhas in Bahia (Brazil)*. Am Mineral **100** (2015) 861-871.

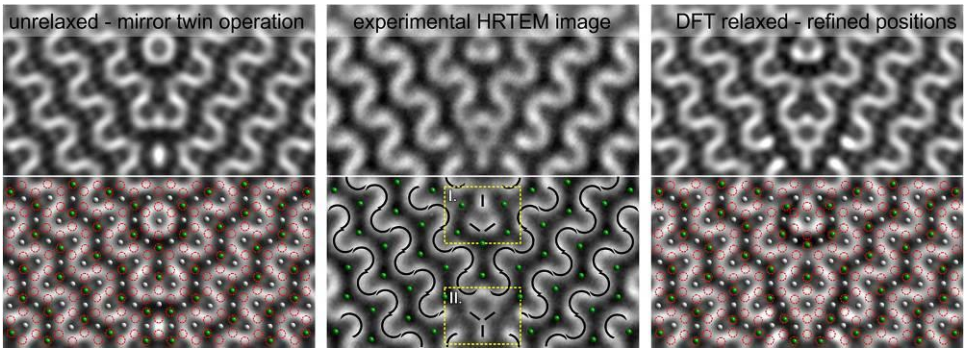

Figure 1. HRTEM study of (130) twin boundary in chrysoberyl from Pratinhas.

MS7.P014
Diffraction mapping of the verwey transition at magnetite

P. L. B. Ho[1], L. Jin[2], A. Kovács[2], Z. A. Li[3], Z. Wang[1], J. Mayer[2,4], R. Dunin-Borkowski[2], X. Zhong[1]

[1]Tsinghua University, National Center for Electron Microscopy in Beijing, Key Laboratory of Advanced Materials (MOE), The State Key Laboratory of New Ceramics and Fine Processing, School of Materials Science and Engineering, Beijing, China
[2]Research Centre Jülich, Ernst Ruska-Centre for Microscopy and Spectroscopy with Electrons and Peter Grünberg Institute, Jülich, Germany
[3]Chinese Academy of Science, Institute of Physics, Beijing, China
[4]RWTH Aachen, Gemeinschaftslabor für Elektronenmikroskopie (GFE), Aachen, Germany

hbl15@mails.tsinghua.edu.cn

Introduction: Ferromagnetism shows various phenomena at low temperature. The story of the Verwey Transition in magnetite has been investigated over a period of about one century. In 1941, Verwey et al. found for the first time that Magnetite undergoes a rapid rising of heat capacity at the temperature of less than 125 K, and also its magnetization and resistivity varies significantly [1]. Along with the development of advanced materials characterization methods, more research groups have a new interpretation to explain the magnetic performance of magnetite such as Jahn–Teller distortions, coupled distribution of a minority-spin electron and Trimeron distribution in the low-temperature magnetite structure [2].
Objectives: This report focuses on the immobile select electronic diffraction by nano-beam and dynamical evolution of crystallographic structure of magnetite during magnetic phase transitions at low temperatures.
Materials and Methods: Lamellar specimens of magnetite were cut along the <001> and <011> zone axes by focused ion beam milling. The changes in morphology and diffraction patterns were continuously recorded around Verwey temperature by in-situ transmission electron microscopy. The heating effect of electron beam was also confirmed in the in-situ experiments. The nano-beam provides us the high spatial resolution for diffraction mapping, despite the HAADF detector cannot acquire the image on charge ordering twins efficiently. It is a method to extract the local information by Bright Field in scanning transmission electron microscope during High-speed camera captures.
Results: About 96 K, the stripes of twin can be captured on the magnetite lamellae, these observation is generally consistent with previous studies of Verwey phase transition. Investigating the different regions of contrast, the orientation relationship of crystal demonstrates the imperceptible select electronic diffraction pattern. Furthermore, the super-lattice diffraction spots had disappeared after electron irradiation damaged on the surface immediately, whereas the stripe still existed on the region of spot size.
Conclusion: One encouragement is that the result evidences relationship between crystallographic structural phase transition and charge-ordering, which exist the phase coexisting region during the Verwey Transition of magnetite. The aim of the present study is to generate the charge ordering twins without internal diffractive dynamics, which builds upon correct various statements of physical mainstream.

References:
[1] Verwey E. J. W., Haayman P. W., Physica, 8 (979), 1941.
[2] Mark S. Senn et al., Nature, 481, 173-176 ,
[3] Juan de la Figuera et al., Phys. Rev. B, 88 (161410), 2013.

MS7.P015
$InGaO_3(ZnO)_{0.5}$ – synthesis, structure and cation distribution

G. Schaan[1], W. Assenmacher[1], H. Schmid[2], N. Kimizuka[3], N. Miyakawa[4], A. Kamai[4], W. Mader[1]

[1]University of Bonn, Inorganic Materials Research, Bonn, Germany
[2]MPI, Solid State Research, Stuttgart, Germany
[3]Universidad de Sonora, Dept. de Investigaciones en Polimeros y Materiales, Hermosillo, Mexico
[4]Tokyo University of Science, Dept. of Applied Physics, Tokyo, Japan

s6dolahr@uni-bonn.de

Transparent and conducting materials are indispensable elements, e.g., of flat panel and touch displays. MOS transistors using indium gallium zinc oxides (IGZO) have shown extremely low off-state current and high optical transparency, and are used in smart phone displays [1]. IGZOs are compounds of the homologous series $InGaO_3(ZnO)_m$ which have layered crystal structures. Up to now, IGZO compounds with integer m = 1, 2, 3, 4, etc. have been synthesized and characterized [2-5]. Motivation of the present work is the synthesis and structural characterization of the m = 0.5 phase, $InGaO_3(ZnO)_{0.5}$.

Single crystals of $InGaO_3(ZnO)_{0.5}$ were grown by the optical floating-zone method using a mirror furnace where halogen lamps are used as heat source. X-ray diffraction on $InGaO_3(ZnO)_{0.5}$ yielded a hexagonal crystal system ($P6_3/mmc$; No. 194) isostructural to $Yb_2Fe_3O_7$ [6]. Structure refinement from single crystal XRD data (a = 3.3137(1) Å; c = 29.523(1) Å) revealed a structure which consists of three different alternating layers: (i) layer of edge-sharing InO_6 octahedra, (ii) a pair of two layers of corner-sharing $(Ga/Zn)O_4$ tetrahedra corresponding to wurtzite structure type, and (iii) a layer of $(Ga/Zn)O_5$ trigonal-bipyramids (tbp). Ga^{3+} and Zn^{2+} are indistinguishable by XRD and thus, yield a mixed occupation. The polyhedra of layers (ii) and (iii) share corners with the InO_6 octahedra, resulting in inverted orientations of the two $(Ga/Zn)O_4$ layers in the wurtzite type region (Fig. 1).

HAADF and BF/ABF STEM imaging at high resolution as well as spectroscopic analyses were performed using an advanced analytical TEM/STEM system (JEOL JEM-ARM 200CF equipped with a cold FEG, probe Cs corrector, X-ray (JEOL Centurio) and electron spectrometer (GATAN GIF Quantum ERS) attachments) [7].

Elemental distributions of the cations were mapped by X-ray spectroscopic imaging with a line resolution sufficient to resolve the cation layers. The extracted elemental maps confirm that indium exclusively occupies the octahedral sites, in agreement with XRD. The Ga map provides a convincing insight to the occupation of the tbp-sites, showing that these sites are occupied by Ga ions only. Moreover, in the dual layers the maps reveal a mixed occupation by Ga and Zn on tetrahedral sites (Figs. 2, 3).

Cation columns, which are well resolved in the HAADF image (Fig. 3), coincide with the structure model derived from XRD (shown in overlay). Due to atomic number dependence, In gives rise to the highest HAADF signal. The layer of Ga in-between the two layers of In appears more intense than the pair of Ga/Zn layers. This would be explicable either by crosstalk from the adjacent In atoms and/or by the shape of the electron probe. The extracted X-ray line scan profiles in Fig. 3 perfectly align with the HAADF intensities and prove the assignment of the cation distribution for the octahedral (In), tetrahedral (mixed Ga/Zn) and tbp (Ga) sites.

References:

[1] S. Yamazaki, T. Tsutsui (Editors), Physics and Technology of Crystalline Oxide Semiconductor CAAC-IGZO: Application to Displays. **2017** Wiley, U.K.
[2] M. Nakamura, N. Kimizuka, T. Mohri, *J. Solid State Chem*., **1991**, *93(2)*, 298–315.
[3] M. Nespolo, A. Sato, T. Osawa, H. Ohashi, *Cryst. Res. Technol.*, **2000**, *35(2)*, 151-165.
[4] I. Keller, W. Assenmacher *et al*., *Z. Anorg. Allg. Chem.*, **2009**, *635(12)*, 2065-2071.
[5] I. Keller, W. Mader, *Z. Anorg. Allg. Chem.*, **2010**, *636*, 1045-1049.
[6] K. Kato *et al.*, *Z. Krist.*, **1976**, *143*, 278-284.
[7] H. Schmid, E. Okunishi, W. Mader, *Ultramicrosc*., **2013**, 127, 76-84.

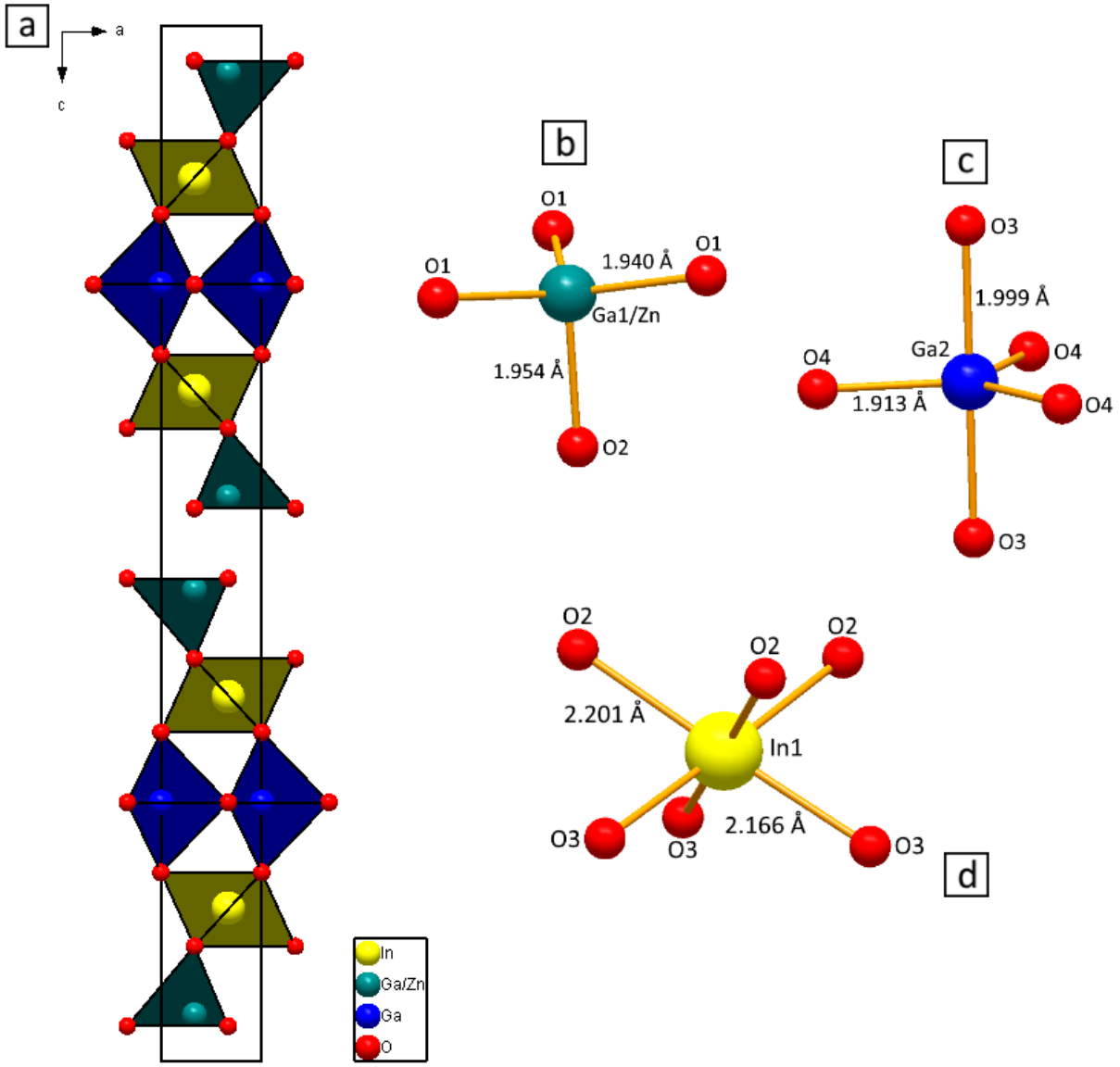

Figure 1. Structure of $InGaO_3(ZnO)_{0.5}$ viewed along (a). Coordination of Ga^{3+}/Zn^{2+} (b), Ga^{3+} (c) and In^{3+} (d).

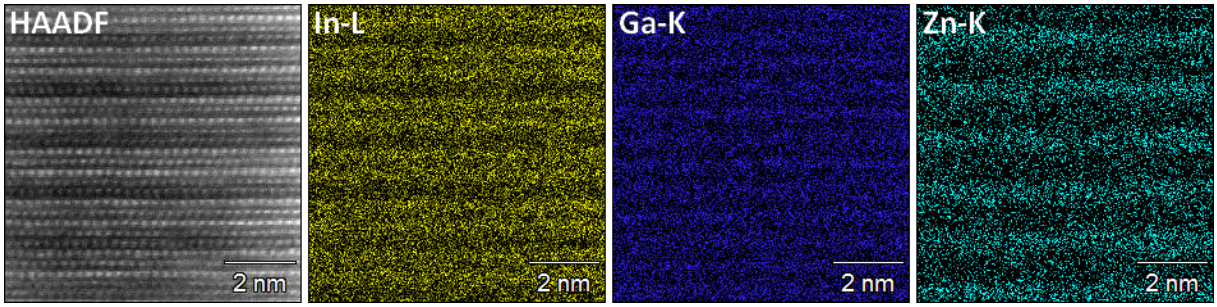

Figure 2. HAADF image and associated EDX-maps of In-L (yellow), Ga-K (blue) and Zn-K (cyan).

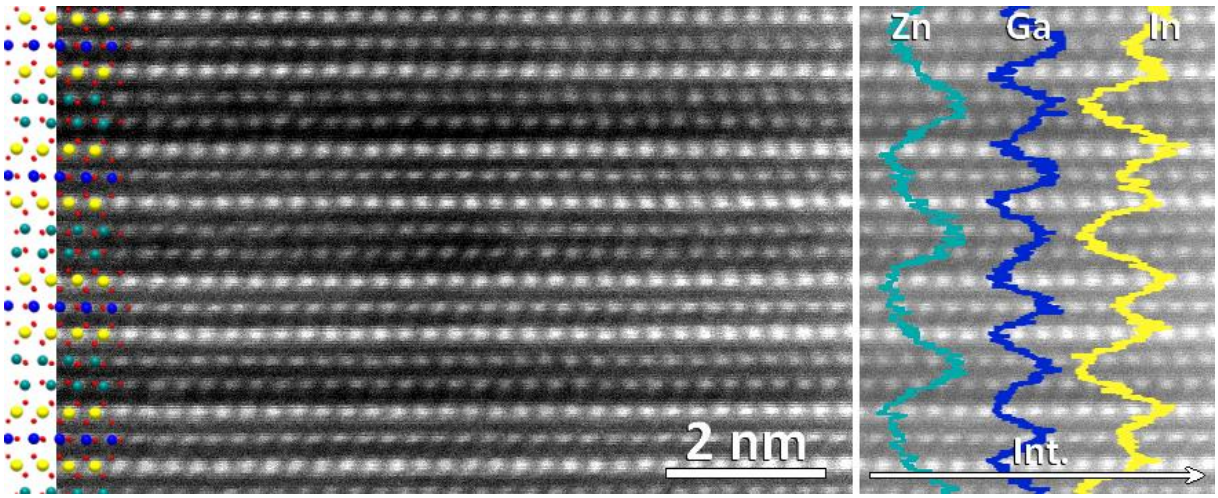

Figure 3. HAADF image showing the crystal structure of $InGaO_3(ZnO)_{0.5}$ (left) and extracted EDX line-scan profiles for In-L (yellow), Ga-K (blue) and Zn-K (cyan) (right).

IM 1: Advances in instrumentation & methods

IM1.001 invited
Compressed sensing in (S)TEM – imaging materials with reduced electron dose

A. Béché[1], H. Vanrompay[1], W. Van den Broek[2], S. Bals[1], J. Verbeeck[1]

[1]EMAT - University of Antwerp, Antwerp, Belgium
[2]Humboldt-Universität zu Berlin, Institut für Physik, Berlin, Germany

armand.beche@uantwerpen.be

Question: Electron beam damage is one of the predominant issues encountered in the characterization of materials by transmission electron microscopy (TEM). Limiting the incoming electron dose one of the main strategies to avoid, or at least limit, the appearance of such damage. However, this often leads to loss of performance of the instrument and increases the signal to noise ratio in the recorded images. Here, we discuss the experimental use of compressed sensing [1,2], a technique issued from signal processing, as a way to reduce beam damage during scanning TEM (STEM) investigations.
Methods: Compressed sensing consists of acquiring a limited amount of pixels of an image at random. The missing information is later reconstructed based on the natural sparsity present in the experimental images with the core algorithm relying on the solution of an l1-norm minimization problem [3]. To implement compressed sensing in a STEM, we developed an electromagnetic beam blanker inserted in the condenser aperture of the microscope [4]. This beam blanker is synchronized to the STEM scan engine using a specific control unit which allows illuminating the sample at random positions. Our setup can now acquire images with a dwell time down to 5 ms, matching the conventional experimental conditions used in STEM imaging.
Results: As displayed in Figure 1, compressed sensing was successfully applied in high resolution high angle annular dark field imaging (HAAD-HRSTEM) with only 20% of the pixels illuminated. More beam sensitive materials are under investigation such as metal organic frame (MOF) materials and zeolite (Figure 2). The effect of compressed sensing in electron tomography, a typically high electron dose technique, is also investigated (Figure 3).
Conclusion: Compressed sensing is successfully applied in STEM for different type of materials and compared. Theoretical aspects of compressed sensing depending on the electron dose and Poisson noise will also be discussed. [5]

References:
[1] Candes E. J., Romberg J. K. and Tao T., Communications on Pure and Applied Mathematics, 59, 1207-1223 (2006).
[2] Donoho, D., IEEE Transactions on Information Theory, **52,** 1289-1306 (2006).
[3] Van den Berg E., Friedlander M. P., SIAM J. Scient. Comp., **31,** 890-912 (2008).
[4] Béché A., Goris B., Freitag B. And Verbeeck J., APL 108, 093103 (2016).
[5] A.B. and J.V. acknowledge the FWO project G093417N. H.V. acknowledges funding from FWO-SB. W.V.d.B. acknowledge the DFG projects BR 5095/2-1 and KO 2911/7-1. S.B. acknowledges funding from the ERC-Starting Grant 335078.

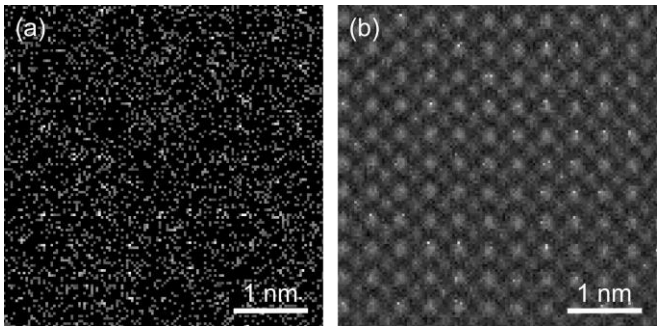

Figure 1. (a) Experimental high resolution STEM image of SrTiO3 in [001] zone axis with only 20% of the pixels acquired. (b) Image (a) reconstructed using the SPGL1 algorithm.

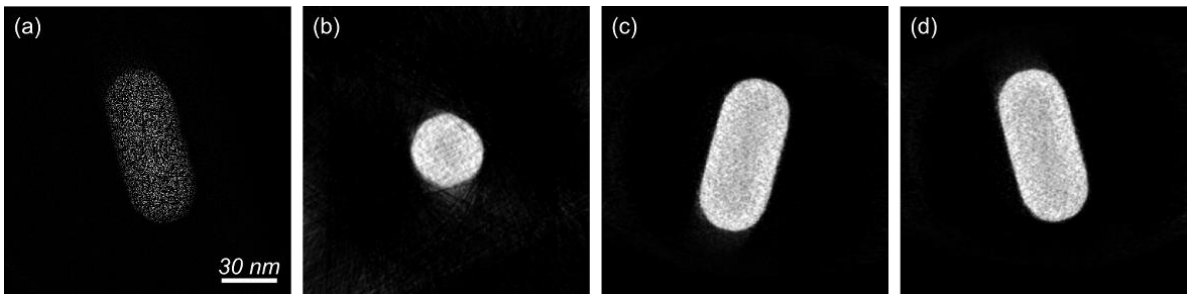

Figure 2. (a) Experimental image of a medium scale tomography series of a gold nanoparticle with 20% of the pixels acquired. (b-d) Orthoslices of the reconstructed nanoparticle in 3D using the TVM algorithm.

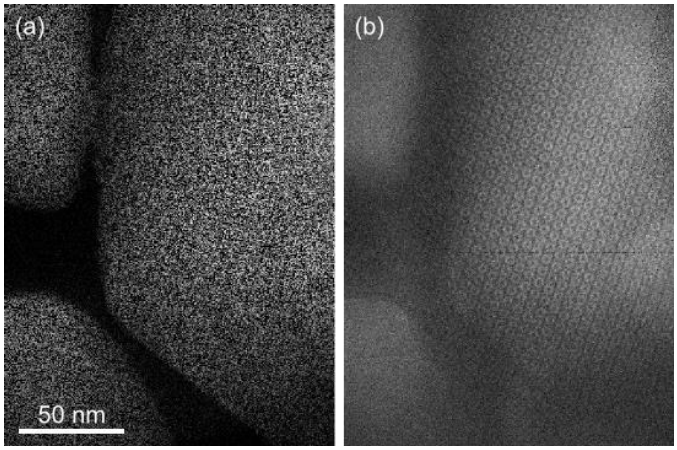

Figure 3. (a) Experimental high resolution image of a MOF MIL 101 with 50% of the pixels acquired and (b) its reconstruction using the SPGL1 algorithm.

IM1.002
Automated image acquisition for low-dose STEM imaging

A. Mittelberger[1], C. Kramberger[1], C. Hofer[1], C. Mangler[1], J. Meyer[1]

[1]University of Vienna, Faculty of Physics, Vienna, Austria

andreas.mittelberger@univie.ac.at

With todays aberration corrected machines, atomically resolved (scanning) transmission electron microscopy (TEM/STEM) has become a standard characterization technique for nanoscaled materials, especially in the evolving field of 2D-materials. However, a big limitation is beam damage because of the high required dose of energetic electrons. While reducing the acceleration voltage to 80 kV or below can prevent beam damage in pristine graphene [1], defects, functional groups or molecules on the surface are still strongly affected by energetic electrons. Therefore, we have developed an automated acquisition of large-area, low-dose data sets with atomic resolution, and a maximum likelihood reconstruction algorithm that can recover frequently occurring deviations from the periodic lattice [2, 3]. We demonstrate that the stage mechanics of the Nion UltraSTEM, combined with an intelligent algorithm to move the sample, allow the automated acquisition of atomically resolved images from micron-sized areas of a graphene substrate. Furthermore, we show the successful reconstruction of defects in a graphene lattice from automatically acquired low-dose data [4].

References:

[1] J. C. Meyer *et al.*, Accurate Measurement of Electron Beam Induced Displacement Cross Sections for Single-Layer Graphene, *Phys. Rev. Lett.*, vol. 108, no. 19, p. 196102, May 2012.

[2] J. C. Meyer, J. Kotakoski, and C. Mangler, Atomic structure from large-area, low-dose exposures of materials: a new route to circumvent radiation damage., *Ultramicroscopy*, vol. 145, pp. 13–21, Oct. 2014.

[3] C. Kramberger and J. C. Meyer, Progress in structure recovery from low dose exposures: Mixed molecular adsorption, exploitation of symmetry and reconstruction from the minimum signal level, *Ultramicroscopy*, vol. 170, pp. 60–68, 2016.

[4] A. Mittelberger *et al.*, Automated image acquisition for low-dose STEM at atomic resolution, *Micrsocopy & Microanalysis*, submitted, Feb. 2017

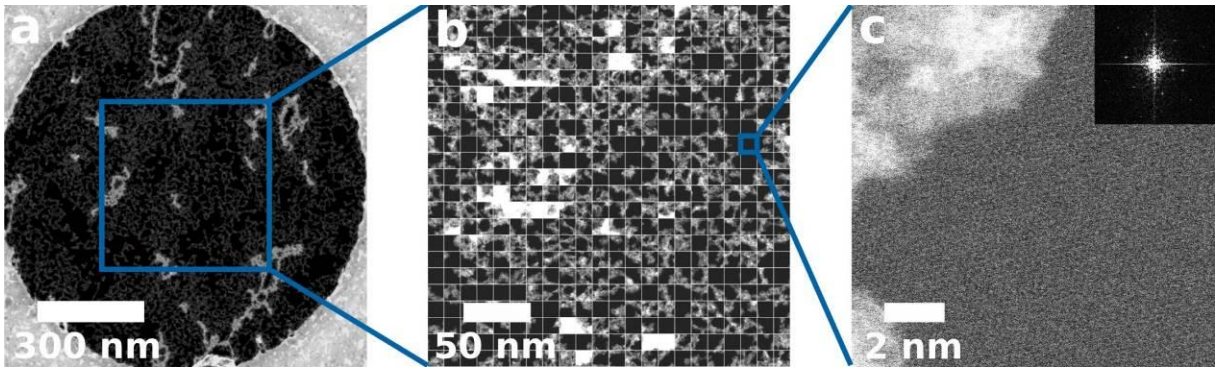

Figure 1. Montage of a low-dose map consisting of 22x22 images. The total mapped area is about 0.1 µm². (a) Overview image of a hole in the Quantifoil support film covered with monolayer graphene. (b) Montage of low-dose images acquired from the highlighted region in (a). (c) Single low-dose image. The graphene lattice is not directly visible, but the typical reflections are still present in the FT.

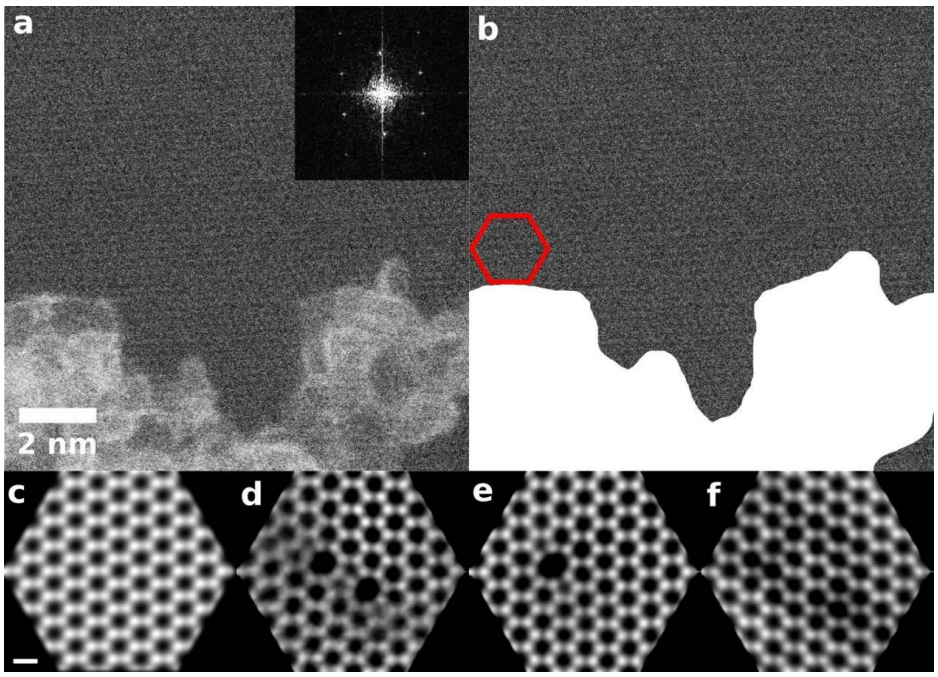

Figure 2. Reconstruction of point defects in graphene from low-dose data. (a) One raw data frame. Inset: FT of the image. Although the noise level in the image is too high to directly see the graphene lattice, the presence of the 12 typical spots in the FT indicates that the imaging conditions are excellent. (b) The same image as in (a) but with the contamination masked. The red hexagon shows how the data is cut into data cells before feeding it into the reconstruction algorithm. (c) The sum of ~90,000 data cells shows a perfect and noise-free graphene lattice. (d-f) Result of the reconstruction. The models are optimized in parallel and show frequently appearing features in the raw data. The scale bar for (c-f) is 0.25 nm.

IM1.003
Three-dimensional electron imaging and reconstruction of dislocations from a single acquisition

E. Oveisi[1,2], A. Letouzey[3], P. Fua[3], C. Hébert[1,2]

[1]EPFL, Interdisciplinary Centre for Electron Microscopy (CIME), Lausanne, Switzerland
[2]EPFL, Electron Spectrometry and Microscopy Laboratory (LSME), Lausanne, Switzerland
[3]EPFL, Computer Vision Laboratory (CVLab), Lausanne, Switzerland

emad.oveisi@epfl.ch

Three-dimensional (3-D) visualisation of crystal dislocations reveals pivotal information, otherwise inaccessible, about their network geometry and interaction mechanisms[1-4]. Conventional tomographic techniques in transmission electron microscopy (TEM) can provide such information from a series of images that are acquired at regular intervals within a relatively large tilt-arc[5,6]. Not only is this time-consuming and subject to prolonged electron exposure, but changes in diffraction contrast during tilting can significantly complicate the reconstruction and can even render the technique inapplicable for challenging (e.g. magnetic) specimens.
Here, an innovative method is presented that provides a reliable assessment of the 3-D configuration of dislocation lines using data acquired from just one sample tilt and a single acquisition[7]. In this technique, we benefit from the convergent probe of the scanning TEM to create virtual incident beam tilts while maintaining a constant diffraction condition over stereoscopic image pairs. For a crystal orientation where a systematic row of reflections is excited, a variation of the incidence angle perpendicular to the direction of the diffracted beams corresponds to the same excitation condition. Such an angle of incidence, which is part of the un-diffracted disc, contributes to image formation. With a segmented STEM detectors that allow the two counterparts of the un-diffracted disk be acquired simultaneously, single-acquisition stereo imaging can be realized (Fig. 1). The resulting bright-field stereo micrographs are then treated with an innovative approach based on an in house reconstruction algorithm, yielding a 3-D reconstruction of the dislocation arrangement[7,8].
Besides its speed and efficiency, this 3-D imaging method offers important advantages for investigations of radiation-sensitive materials. With the single-acquisition approach that we introduce, real-time 3-D electron imaging can be envisaged, for instance for the in-situ observation of defect dynamics in crystalline materials.

References:
[1] Clark, J.N. *et al.* Three-dimensional imaging of dislocation propagation during crystal growth and dissolution. *Nat. Mater.* **14**, 780-784 (2015).
[2] McNally, P.J. 3D imaging of crystal defects. *Nature* **496**, 37-38 (2013).
[3] Liu, G.S. & Robertson, I.M. Three-dimensional visualization of dislocation-precipitate interactions in a Al-4Mg-0.3Sc alloy using weak-beam dark-field electron tomography. *J. Mater. Res.* **26**, 514-522 (2011).
[4] Chen, C.C. *et al.* Three-dimensional imaging of dislocations in a nanoparticle at atomic resolution. *Nature* **496**, 74-77 (2013).
[5] Weyland, M. & Midgley, P.A. Electron tomography. *Mater. Today* **7**, 32-40 (2004).
[6] Midgley, P.A. & Dunin-Borkowski, R.E. Electron tomography and holography in materials science. *Nat. Mater.* **8**, 271-280 (2009).
[7] Oveisi, E. *et al.* Tilt-less 3-D electron imaging and reconstruction of complex curvilinear structures. *Submitted to Scientific Reports* (2016).
[8] Oveisi, E *et al.* Stereo-vision three-dimensional reconstruction of curvilinear structures imaged with a TEM. *Submitted to Ultramicroscopy* (2017).

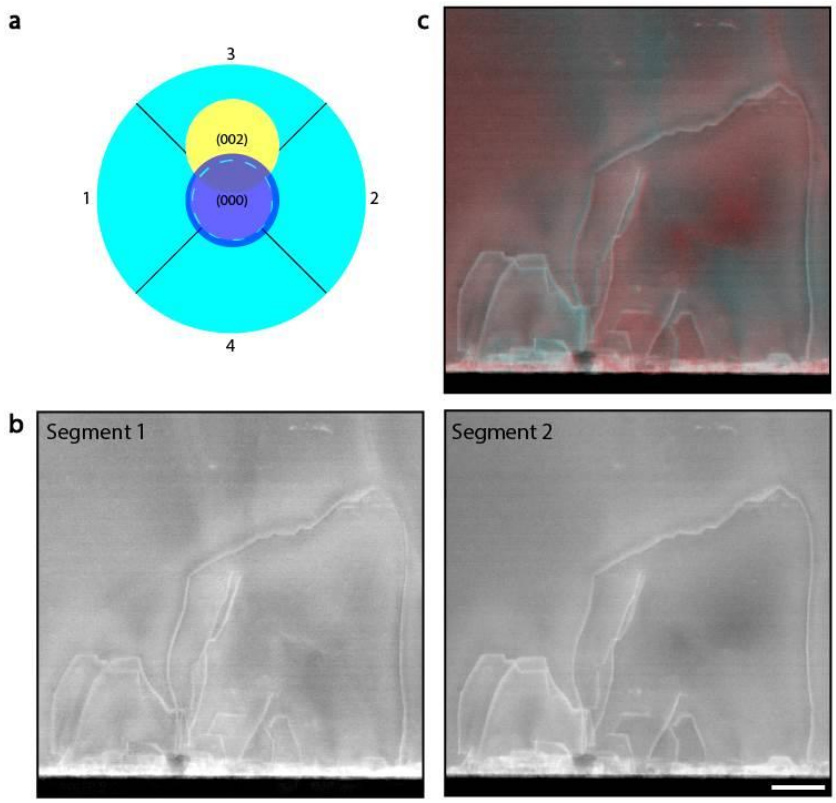

Figure 1. 3-D electron imaging of dislocations in the GaN layer of an ultrathin InAlN/GaN-based heteroeptaxial membrane. **a,** Schematic illustration of the CBED pattern and a segmented STEM detector. **b,** BF-STEM micrographs (inverted contrast) were obtained using the intensity of the edges of the (0 0 0) disc overlapping the two opposite channels (channels 1 and 2) of the detector. **c,** Anaglyph illustrating the 3-D configuration of dislocations. Scale bar: 100 nm.

IM1.004
Quantitative single-particle analysis correlation of structure and mass via scanning transmission electron microscopy

S. Tacke[1,2,3], C. Zaubitzer[1], V. Krzyzanek[4], L. Lecoq[5], U. Keller[3], A. Böckmann[5], R. Wepf[6], B. Meier[2]

[1]ETH Zürich, Scientific Center for Optical and Electron Microscopy, Zürich, Switzerland
[2]ETH Zürich, Departmanet of Chemistry and Applied Biosciences, Zürich, Switzerland
[3]University of Münster, Institute of Medical Physics and Biophysics, Münster, Germany
[4]Czech Academy of Sciences, Institute of Scientific Instruments, Brno, Czech Republic
[5]CNRS/University of Lyon, Molecular Microbiology and Structural Biology, Lyon, France
[6]University of Queensland, Centre for Microscopy and Microanalysis, Brisbane, Australia

sebastian.tacke@scopem.ethz.ch

The correlation of structure and function is of key interest in structural biology. Typically, x-ray crystallography, nuclear magnetic resonance or single-particle cryo-electron microscopy are utilized to resolve biological macromolecules at highest possible resolution. Especially, single-particle cryo-EM became increasingly popular in the last decade [1]. The preferred instrument for this approach is the transmission electron microscope (TEM) but recently it was shown that also scanning TEM (STEM) could potentially be used to image soft matter samples at atomic resolution [2]. Compared to TEM, the image interpretation in STEM is typically simpler since contrast and detection efficiency are defined by the geometry of the monolithic detectors. Beyond imaging, STEM could also be used for mass determination of nano-scaled structures like cell organelles or protein complexes. Besides the global mass determination, it is also possible to correlate structure and mass of individual domains within the protein-complex [3].
The aim of the present study is to fuse quantitative STEM (qSTEM) and single-particle analysis. For this purpose, the scope of the project includes developments in sample preparation, hardware and software instrumentation. Finally, the potential of this novel approach is demonstrated by several proof-of-principle experiments, where TMV, virus capsids, HPI layer and other protein complexes will be used as test cases. Herewith, the authors want to pave the way for a quantitative single-particle analysis via STEM.
Samples were vitrified by plunge-freezing and partially or totally freeze-dried. To guarantee a contamination free transfer between the preparation device and microscope, a high-vacuum cryo-transfer system was developed [4]. All experiments where performed on a scanning electron microscope (Hitachi, S-5000) with a nominal spot size of 0.7nm at an acceleration voltage of 30kV. The microscope was equipped with a (homemade) annular dark-field (ADF) detector, capable of single electron counting [5]. Imaging was performed at low temperatures (-120°C) and at low-dose conditions (300 e- per nm2). The following software packages were used for data analysis: MONCA [6], MASDET [7] and RELION [8].
Figure 1 shows the conceptional workflow of the proposed technique. In the first phase of the project, the qSTEM technique and related preparation tools were designed, built and tested. Thereafter, proof-of-principle measurements were performed successfully on mass standards like TMV and F-Actin, see figure 1. In the current phase, software tools are developed to analyse the qSTEM data in the framework of the single-particle analysis approach. Having these tools in hand, preparation routines can be modified to achieve a maximal structural preservation and therefore to achieve the highest possible resolution.
With this novel approach, we believe to add a new dimension to the field of single-particle analysis. Quantitative information about classes may improve reconstructions since broken particles could be excluded due to their missing mass. Additionally, the accuracy of the mass determination will be improved by the fusion of both techniques. Particles, that result in high-resolution averages could be extracted and analysed separately.

[1] W. Kühlbrandt. Science **343** (2014), p. 1443.
[2] C. Ophus et al. *Nature Communications* **7** (2016), p. 10719.
[3] A. Engel et al. *Proceedings of the National Academy of Sciences* **79** (1982), p. 4050.
[4] S. Tacke et al. *Biophysical Journal* **110** (2016), p. 758.
[5] V. Krzyzanek and R. Reichelt. *Microscopy & Microanalysis* **13** (Suppl. 3) (2007), p. 80.
[6] V. Krzyzanek and R. Reichelt. *Microscopy and Microanalysis* **9** (Suppl. 3) (2003), p. 110.
[7] V. Krzyzanek et al. *Journal of Structural Biology* **165** (2009), p. 78.
[8] S.H.W. Scheres. *Journal of Structural Biology*, **180** (2012), p. 519.

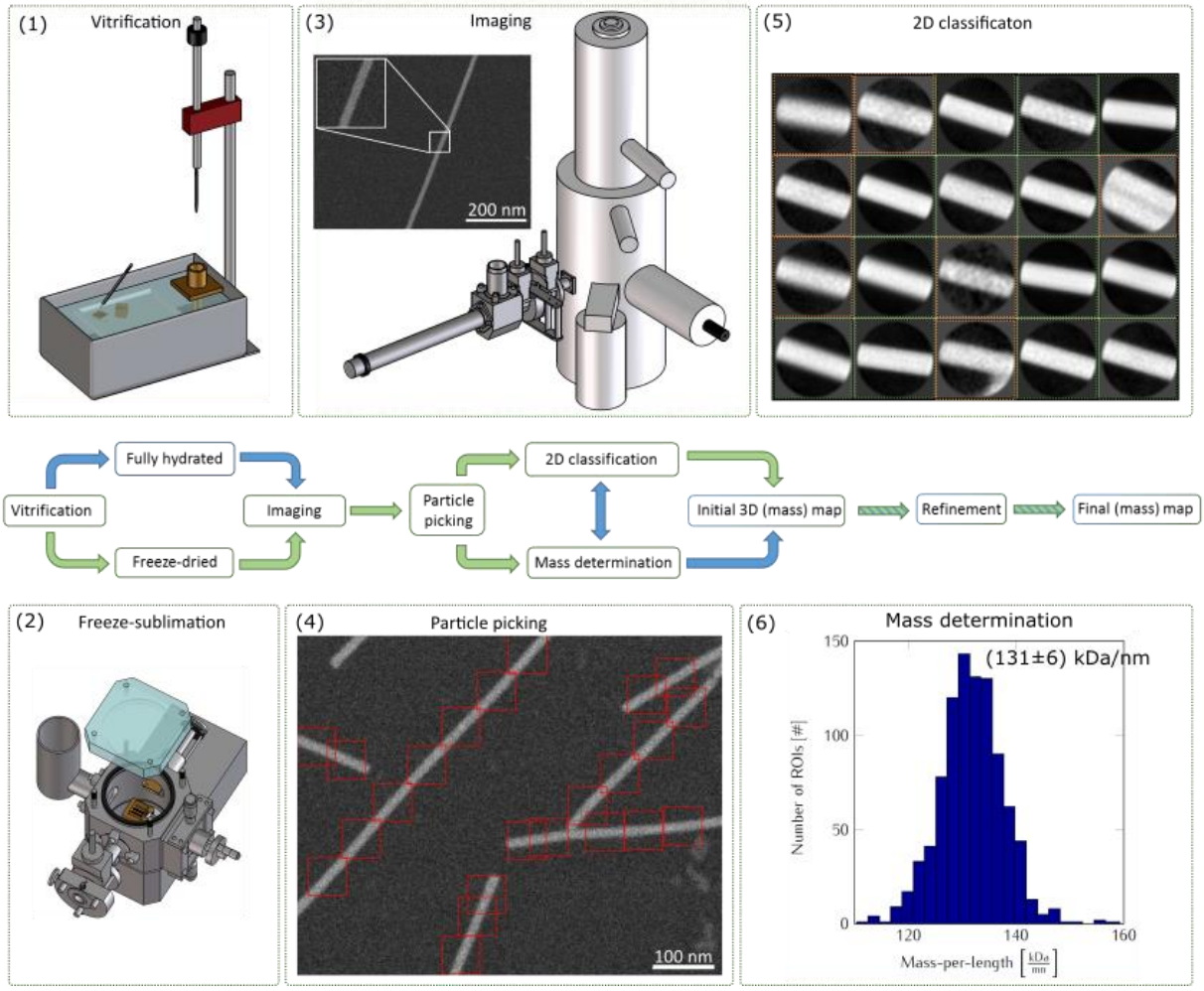

Figure 1. Intended workflow of the quantitative single-particle approach. (1) The sample material is vitrified by plunge-freezing. (2) Thereafter, the samples are partially/totally dehydrated by freeze-sublimation and transferred via high-vacuum cryo-shuttle to the microscope. (3) Imaging is performed at low temperatures and under low-dose conditions. (4) Class averages are calculated after automatic region-of-interest identification. (5) Particles from high-resolution averages are extracted and analysed quantitatively (6). The established steps are highlighted in green.

IM1.005
Advanced 4D STEM imaging with the pnCCD (S)TEM camera

M. Huth[1], M. Simson[1], R. Ritz[1], J. Schmidt[1], H. Soltau[1], H. Yang[2], P. D. Nellist[2], R. Sagawa[3], Y. Kondo[3] H. Ryll[4], L. Strüder[4,5]

[1]PNDetector GmbH, Munich, Germany
[2]University of Oxford, Oxford, United Kingdom
[3]JEOL Ltd., Tokyo, Japan
[4]PNSensor GmbH, Munich, Germany
[5]University of Siegen, Siegen, Germany

martin.huth@pndetector.de

Introduction: Inspired by advancements in pnCCD detector technology, there has been increasing interest in the technique of four dimensional scanning transmission electron microscopy (4D STEM). Typically, a focused electron beam is applied to a sample in a two dimensional (2D) raster pattern. At each point, a 2D image is captured which intrinsically contains bright field (BF), dark field (DF), and high angle annular dark field (HAADF) signals. In total, a 4D dataset is recorded allowing a comprehensive analysis and enabling a number of techniques such as strain analysis, magnetic domain mapping, scanning electron diffraction, TEM tomography, and electron ptychography.
Objectives: Two example 4D STEM techniques demonstrate the possibilities of the pnCCD (S)TEM camera, meeting the following key requirements: (i) Fast acquisition of data to minimize effects of beam and sample drift, and sample damage; (ii) a large number of pixels; and (iii) a sufficiently radiation hard detector compatible with high electron rates used in diffraction experiments.
Materials and Methods: Using a direct detecting, radiation hard pnCCD with 264x264 pixels, the pnCCD (S)TEM camera provides ultra-fast acquisition of 2D camera images [1]. Routinely, the readout speed is 1000 frames per second (fps) in full frame mode and can be further increased up to 8000 fps by binning and windowing. By operating the camera in one of three predefined operation modes [2], namely the single electron, imaging and anti-blooming mode with energies ranging from 20 keV to 300 keV, optimum results are guaranteed for a wide range of experimental conditions. The pnCCD (S)TEM camera is a complete system including a data acquisition computer and software allowing a versatile live visualization and full raw data access.
Results: Using electron ptychography, the reconstruction of the electron phases allows to image beam sensitive complex nanostructures containing light and heavy elements with atomic resolution (Fig. 1a-d) [3]. Lens aberrations can be corrected postacquisition allowing to maximize the phase image contrast. Further, the pnCCD allows precise determination of the deflection a magnetic sample imposes on a traversing electron beam by measuring shifts of the bright field disc. (Fig. 1e-g) [1].
Conclusion: The outstanding capabilities of the pnCCD (S)TEM camera were demonstrated in many experiments at various TEMs, and showed the numerous new scientific applications made possible with that detector.

References:
[1] Ryll, H., Simson, M., et al A pnCCD-based, fast direct single electron imaging camera for TEM and STEM, Journal of Instrumentation 11 (2016)
[2] J. Schmidt, R. Hartmann et al Journal of Instrumentation 11 (2016)
[3] Yang, H., Rutte, R.N. et al Simultaneous atomic-resolution electron ptychography and Z-contrast imaging of light and heavy elements in complex nanostructures, Nature Communications 7 (2016)

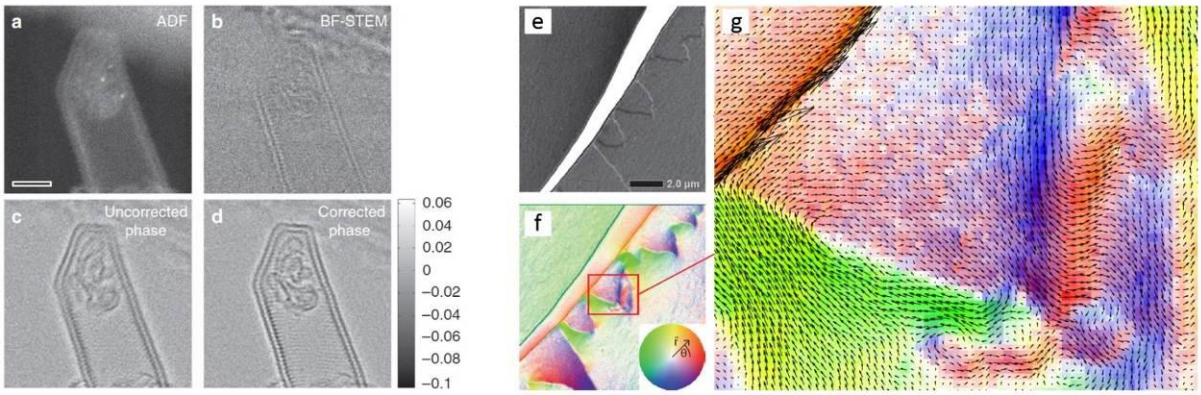

Figure 1. Double wall carbon nanotube. Comparison of (a) ADF image, (b) simultaneous BF image, and the phase image (c) before and (d) after correcting residual aberrations. (b-d) were calculated from a 4D-STEM dataset acquired with the pnCCD (S)TEM camera on a JEOL JEM-ARM200F. Figure from [3]. (e) Visualization of magnetic domain boundaries of a magnetic Ni sample using standard Lorentz TEM. (f) Same area imaged with the pnCCD on a JEOL JEM-2800 using 4D-STEM imaging. (g) Zoom into marked region in (f). Figure from [1].

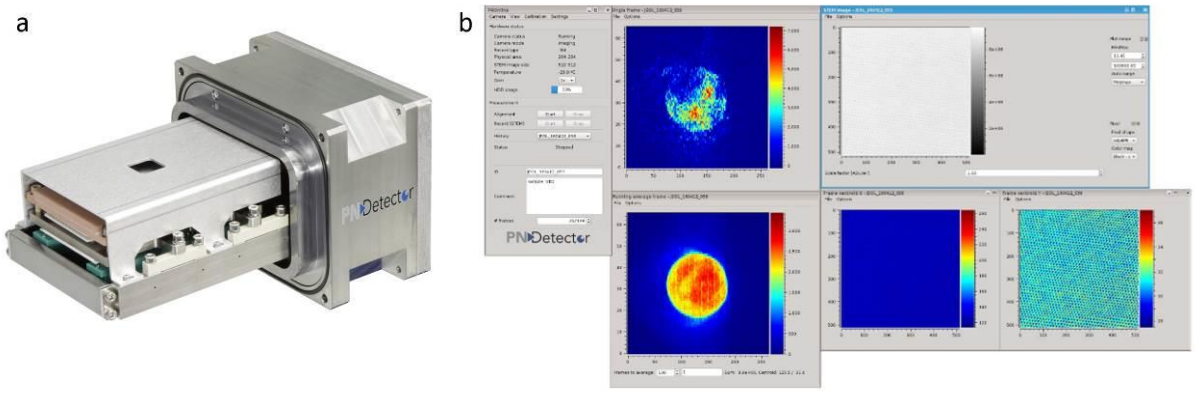

Figure 2. (a) pnCCD (S)TEM camera. (b) PNOnline data acquisition and camera control software.

IM1.006
A comparative study on DPC using a sectored annular and the EMPAD pixelated detector

J. Zweck[1], B. Freitag[2], E. Yücelen[2], H. Rohrmann[3], C. Falub[3]

[1]Universität Regensburg, Physik, Regensburg, Germany
[2]FEI Company, Eindhoven, Netherlands
[3]Evatec AG, Trübbach, Switzerland

josef.zweck@ur.de

Introduction: Traditionally, differential phase contrast (DPC) uses a four quadrant annular detector for electrons to record minute deflections of the diffraction disk. With the advent of atomic resolution DPC and ptychography, the need for pixelated detectors arose. These detectors are capable to capture a multi-pixel image of the diffraction disk per image pixel scanned at a frame rate of several 100s of frames per second (fps). We report on the first results of an EMPAD detector [1], mounted on an image corrected Titan microscope, operated at 300 kV and with a frame rate of 550 fps (128 x 128 pixels).
Objectives: The goal of this study was to compare STEM images, taken under different conditions (HRSTEM, LMSTEM), with different detector set-ups. We used the center-of-mass (COM) evaluation and conventional annular detectors. If the beam is subject to a field that is homogeneous across its diameter, it will be shifted sideways in the detector plane. On the other hand, if the probe diameter becomes comparable to inter-atomic distances or even smaller, it will experience an inhomogeneous field geometry, depending on its relative position with respect to the nuclei. In this case, the beam will not be shifted, but a redistribution of the intensity leads to a non-uniform intensity pattern. The COM of the intensity pattern will then be affected, which can be explained by an average lateral momentum transfer per electron due to the experienced field landscape [2].
Materials and Methods: For the experiments, two different specimens were used: a GaN/InGaN/GaN quantum well (QW) structure with intrinsic defects (i.e. dislocations) and a $[FeCoB/AlN]_N$ multilayer. Both specimens were investigated using different camera lengths and microscope modes (GaN: HRSTEM; FeCoB: HRSTEM and LMSTEM). The acquired images of up to 4 GB in size were analyzed using the COM method and by using virtual annular detector segments, meaning that only those areas of the diffraction disk that fall onto a (real) detector quadrant were used for the evaluation.
Results: HRSTEM images of the QW structure show strong contrasts fringing the dislocation (Fig. 1a). High resolution is preserved, the observable contrast regions around the dislocation extend over approximately 7 atomic distances on both sides. The simulated annular detectors often give a very similar result (Fig. 1b), with a little loss in resolution. Unfortunately, this is not always the case.
For magnetic imaging we observe a dramatic improvement in signal-to-noise (S/N) ratio (Fig. 2a), while for a conventional evaluation with annular segments we observe the same features, but with inferior S/N (Fig. 2b).
Conclusion: The performance of the EMPAD camera is superior to the conventional annular quadrant detector. A pixelated detector is mandatory for atomic resolution DPC imaging, while medium resolution can be achieved with annular detectors.

[1] Mark W. Tate et al, Micr.&Microanal. 22(1) (2016), pp 237 - 249
[2] K. Mueller et al, Nat Commun. 5 (2014) p. 5653

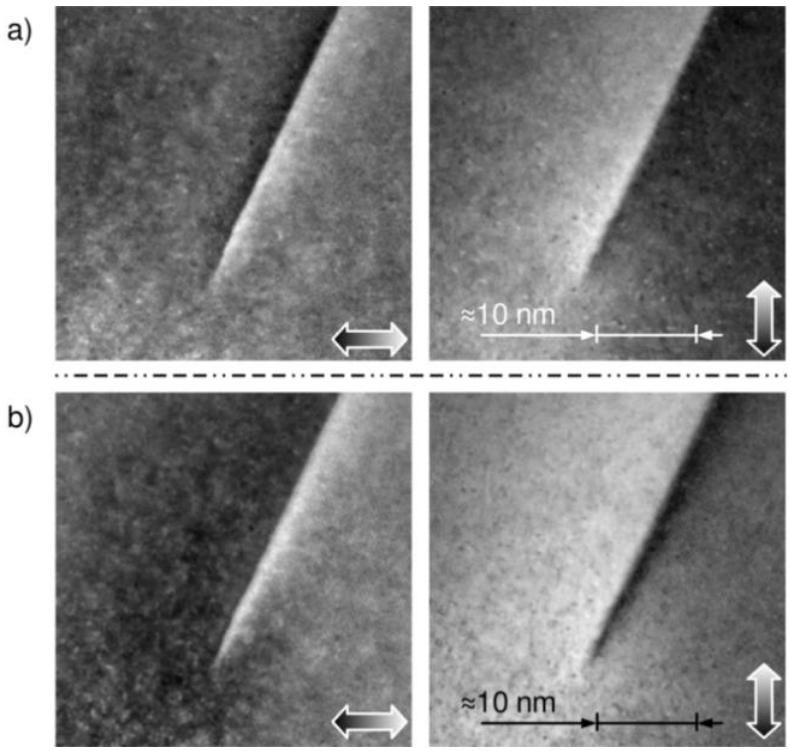

Figure 1. DPC image of a dislocation in GaN (directionality indicated by arrows). Results from a) COM, b) annular detector.

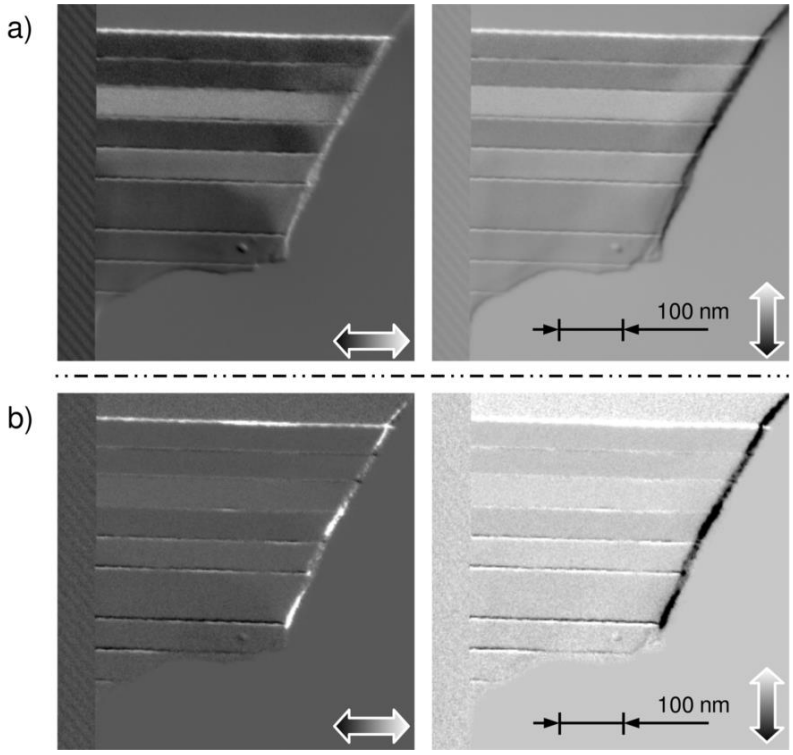

Figure 2. DPC imaging of magnetic domains in a $[FeCoB/AlN]_N$ magnetic multilayer. Results from a) COM, b) annular detector (massively enhanced in contrast).

IM1.007
First results with a non-pixelated and fast centre of mass detector for differential phase contrast microscopy (DPC)

F. Schwarzhuber[1], P. Melzl[1], J. Zweck[1]

[1]Institute for Experimental and Applied Physics, University of Regensburg, Regensburg, Germany

felix.schwarzhuber@ur.de

Introduction: DPC in a STEM can be used to image and analyse potential differences at atomic resolution [1-3]. As for those experiments the potential gradient across the electron probe is not constant, a diffractive redistribution of intensity within the diffraction disk is observed. This was shown by MacLaren [4] for DPC measurements on grain boundaries in polar materials. For atomic DPC the annular DPC detector is replaced by one capable of measuring the centre of mass (COM) of the diffraction disks intensity distribution. To do so pixelated detectors such as fast CCD or MOSFET cameras are usually utilized.
Objective: As these cameras require about 1 ms to acquire the diffraction pattern for one pixel, they are slow when compared to solid state detectors (1-10 µs). For measurements where the knowledge about the COM is sufficient and the precise overall intensity distribution can be neglected, we present a non-pixelated and fast COM-detector based on a commercially available duo-lateral position sensitive diode (PSD). A PSD is a high resistive silicon pin-diode with a resistive layer and a pair of electrodes on top and bottom (see Fig.1). With this device, it is possible to obtain the position of the COM of the diffraction disk by measuring the ratio of the photo current through opposing electrodes. Our objective was to test such a device for its applicability as a COM-DPC detector.
Results: First tests with a PSD showed sufficient signal strength and good responsivity to movements of the electron beam. Fig. 2 shows the result of a measurement where the electron beam was deflected by defined electric fields, leading to a shift of the diffraction disk on the PSD, mainly along the y-direction. Since we find the expected linear dependence between signal and increasing field strength, our PSD is suitable for DPC measurements. We determined the minimum detectable shift on the detector to be 1.6 µm and therefore comparable to annular DPC detectors [5].
As proof of concept we also acquired first DPC images showing the x- and y-components of the magnetic induction (Fig. 3a/b) of a domain structure in a thin film cobalt specimen. As the SNR of the images is still quite low we will discuss the reasons and will present solutions to further improve the imaging capabilities of this detector including simulations on signal formation.
Conclusion: Our tests showed that DPC measurements with a PSD are possible and with further improvements could be a promising alternative for pixelated detectors, especially for measurements where only the position of the COM of the diffraction disk is of interest.

[1] K. Müller et al, Nat Commun, vol. 5, 5653, 2014
[2] N. Shibata et al, Nature Physics, vol. 8, pp. 611-615, 2012
[3] K. Müller-Caspary et al, Ultramicroscopy, 10.1016/j.ultramic.2016.05.004, 2016
[4] I. MacLaren et al, Ultramicroscopy, vol. 26, pp. 57-63, 2015
[5] F. Schwarzhuber et al, Ultramicroscopy, 10.1016/j.ultramic.2017.02.005, 2017

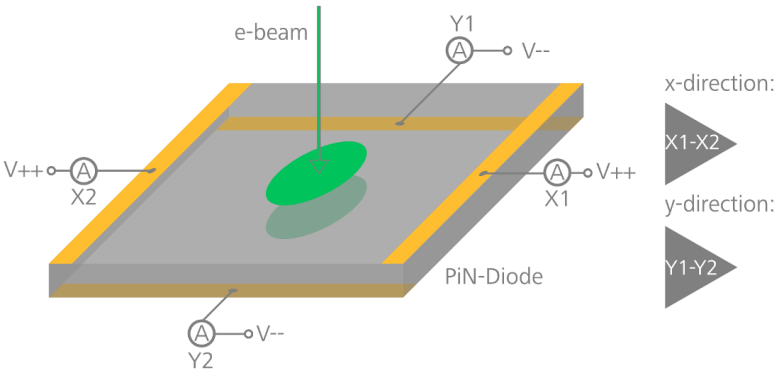

Figure 1. Reverse biased duo-lateral PSD. The position of the COM is defined by the signal differences of the upper/lower electrode pairs.

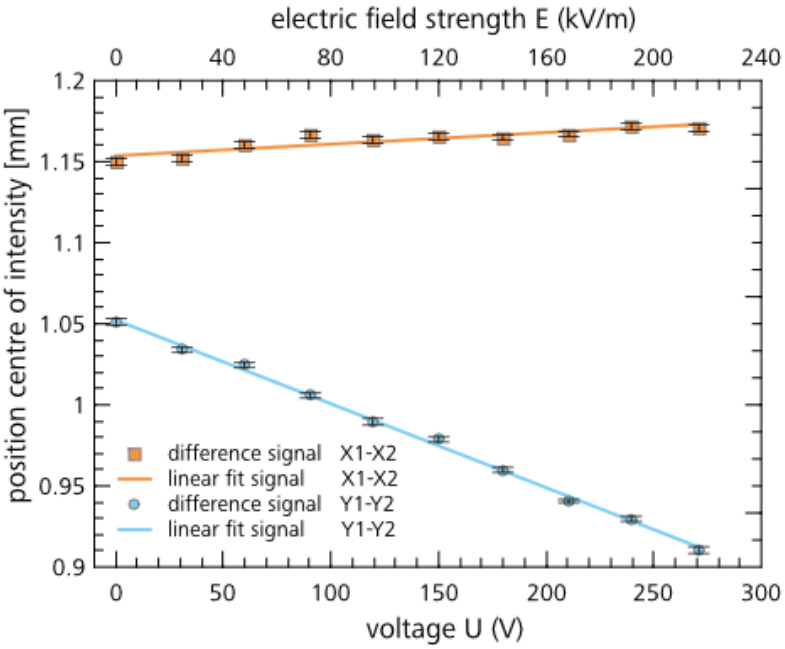

Figure 2. Result of a measurement with defined electric fields. The x- and y-signals show linear behavior.

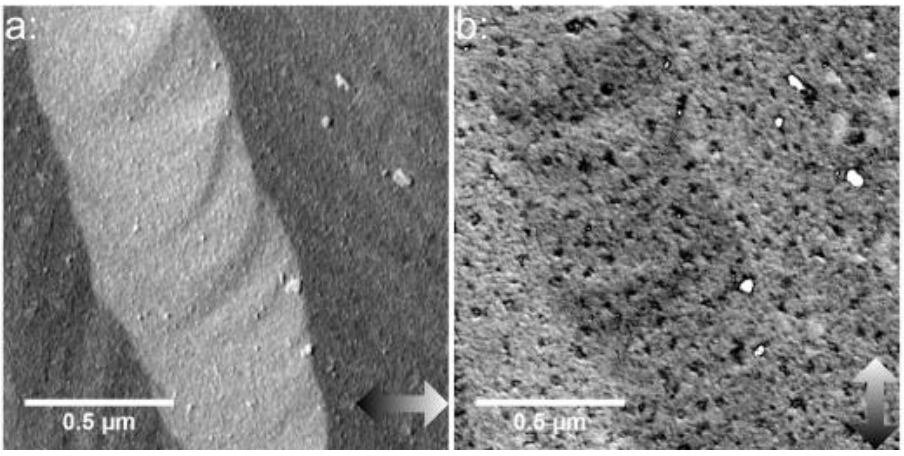

Figure 3. First images captured with a PSD showing the x- and y-component of the magnetic induction of a cobalt domain structure.

IM1.008 invited
Advances in microfluidic cryofixation for correlative light and electron microscopy

M. Fuest[1], G. M. Nocera[1], M. Modena[1], D. Riedel[1], T. P. Burg[1]

[1]Max Planck Institute for Biophysical Chemistry, Goettingen, Germany

marie.fuest@mpibpc.mpg.de

Introduction**:** Correlative light and electron microscopy (CLEM) is a promising approach to study cellular functions across length scales. CLEM uses light microscopy to perform live imaging at the cellular level (~µm scale) which is then correlated with the ultrastructure of the relevant subcellular components (~nm scale) through electron microscopy (EM). The time resolution of this correlation is generally limited by the sample preparation procedures for EM[1,2]. Cryofixation immobilizes the sample in a near-native frozen-hydrated state for EM within milliseconds, but typically requires transfer of the sample from the light microscope to a dedicated instrument for rapid freezing, such as a high pressure or plunge freezer. Due to this transfer step, studying dynamic processes such as synaptic transmission, membrane trafficking, or wound healing with millisecond time resolution remains a challenge.
Objectives**:** The objective of this work is to demonstrate a full CLEM workflow that allows uninterrupted visualization of a sample before, during, and after cryofixation. Til date, our group has developed a microfluidic cryofixation system for fast freezing of biological samples in the field of view of an optical microscope[3]. We seek to integrate this microfluidic cryofixation method into a complete CLEM workflow that includes sample transfer, sample preparation, and finally electron microscopy using *Caenorhabditis elegans* as a model system.
Materials and Methods**:** Figure 1 shows a conceptual schematic of the microfluidic system used to cryofix the sample. *C. elegans* were suspended in M9 with 10%w/w sucrose as a cryoprotectant then loaded into a PDMS microfluidic channel. The microchannel was mounted on a thin film resistive heater which was in thermal contact with a liquid nitrogen cooled heat sink. The heater maintained the sample at room temperature during live imaging. When the heater was switched off, the *C. elegans* were cryofixed. Following fixation, the channel/heater/heat sink system was transferred to a liquid nitrogen dewer for disassembly and recovery of the fluidic chip under liquid nitrogen. The *C. elegans* was then freeze substituted and resin embedded. The embedded sample was sectioned into ~100 nm thick sections with an ultramicrotome in preparation for TEM.
Results**:** Figure 2 shows *C. elegans* before and after cryofixation within the microfluidic device. The images were taken using reflected-light differential interference contrast. The cryofixed sample remained in contact with the copper heat sink during transfer from the optical microscope to the liquid nitrogen dewar. The temperature of the microfluidic cryofixation system remained below -190°C during transfer, well below the threshold for recrystallization of -140°C.
Figure 3 shows TEM images of *C. elegans* after freeze substitution, resin embedding, and sectioning. To our knowledge this is the first demonstration of a CLEM workflow that includes light microscopy with *in situ* cryofixation, sample transfer, and electron microscopy.
Conclusions**:** A microfluidic system was implemented to cryofix *Caenorhabditis elegans* in the field of view of an optical microscope, allowing continuous imaging of the sample during freezing. The microfluidic cryofixation device further allows transfer and preparation of the fast frozen sample for electron microscopy, enabling correlation between live imaging, cryo light microscopy, and electron microscopy. The time resolution of this new technique is limited only by the sample cooling rate to millisecond time scales.

[1] Koning, R.I. *et al*; (2014). *Ultramicroscopy*, **143**, 67-76.
[2] Caplan, J.; Neither, M.; Taylor, R. M; Czymmek, K.; (2011). *Curr. Opin. Struct. Biol.*, **21**, 686–693.
[3] Meija, Y.X.; Feindt, H.; Zhang, D.; Steltenkamp, S.; Burg, T.P.; (2014), *Lab Chip*, **14**, 3281-3284.

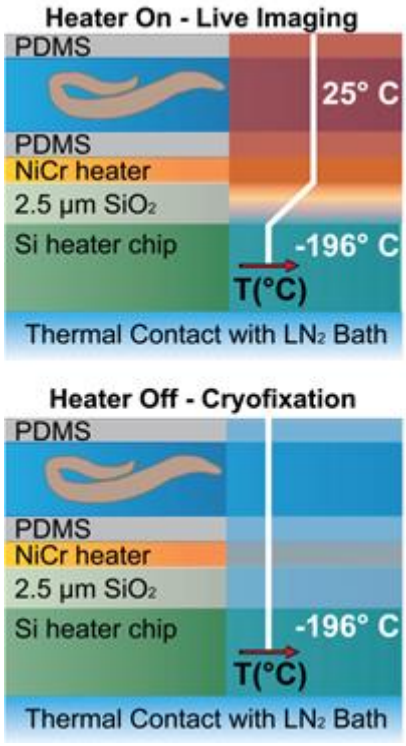

Figure 1. Cryofixation of *C. elegans* within a microchannel.

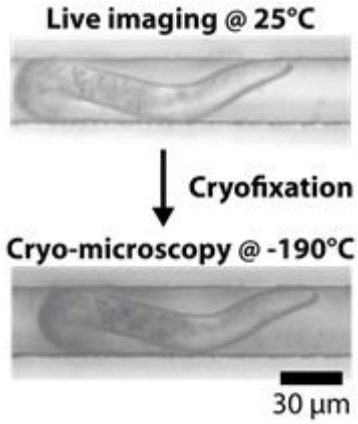

Figure 2. *C. elegans* within a PDMS microchannel during live imaging and after cryofixation.

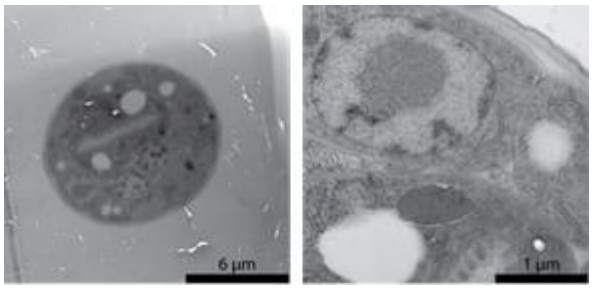

Figure 3. TEM images of *C. elegans* following microfluidic cryofixation, freeze substitution, resin embedding, and sectioning.

IM1.009
New in situ techniques for correlative microscopy –TEM-SIMS and HIM-SIMS

S. Eswara[1], D. Dowsett[1], L. Yedra[1], J. N. Audinot[1], T. Wirtz[1]

[1]Luxembourg Institute of Science and Technology (LIST), Advanced Instrumentation for Ion Nano-Analytics (AINA), MRT Department, Belvaux, Luxembourg

santhana.eswara@list.lu

Development of innovative characterization tools is of paramount importance to advance the frontiers of science and technology in nearly all areas of research. In order to overcome the limitations of individual techniques, correlative microscopy has been recognized as a powerful approach to obtain complementary information about the investigated materials. High-resolution imaging techniques such as Transmission Electron Microscopy (TEM) or Helium Ion Microscopy (HIM) offer excellent spatial resolution. However, the analytical techniques associated with TEM such as Energy Dispersive X-ray spectroscopy (EDX) or Electron Energy-Loss Spectroscopy (EELS) are inadequate for the analysis of (i) isotopes, (ii) trace concentrations (< 0.1 at. % or < 1000 ppm) and (iii) light elements (H, Li, B). Likewise, for the case of HIM, until recently there was no direct possibility to perform elemental mapping because sub-30 keV He+ or Ne+ ion irradiation do not excite X-ray emission. Secondary Ion Mass Spectrometry (SIMS), on the other hand, has several advantages such as the possibility to analyze elements and isotopes of all elements of the periodic table while also providing high-sensitivity to detect even trace concentrations. However, the main drawbacks of SIMS are (i) difficulty in quantification and (ii) lateral resolution of SIMS imaging is fundamentally limited by ion-solid interaction volume to ~10nm (the resolution of commercial SIMS instruments is limited to 50nm because of the brightness of the used primary ion source technology). Owing to the complementary strengths of SIMS imaging, we developed new instrumentations for correlative microscopy combining in-situ (i) TEM-SIMS and (ii) HIM-SIMS.

The octagon of a FEI Tecnai F20 TEM was modified to attach a FIB column and to mount the SIMS extraction nozzle around the objective lens pole-piece gap [1]. The configuration is such that with the TEM sample holder tilted to 68°, the FIB axis is at 45° to the sample surface while the SIMS extraction nozzle is perpendicular to the sample surface. The secondary ions are analyzed in a magnetic-sector mass spectrometer that was completely designed and developed in-house. A special TEM sample holder in which the sample can be biased to +/- 4.5 kV was also produced to enable in-situ TEM-SIMS analysis.

Similarly, a SIMS add-on for HIM was also designed and developed in-house [2] to enable direct chemical imaging in HIM which was previously not possible. The secondary ions sputtered by He^+ or Ne^+ primary ion bombardment are extracted and injected into a magnetic-sector mass spectrometer and counted in a parallel detection configuration.

In this presentation, we will discuss the instrumentation development aspects of the TEM-SIMS and HIM-SIMS techniques. With examples from materials science, we will show the powerful correlative microscopy possibilities that emerge due to these new in-situ methods.

[1] L. Yedra, S. Eswara, D. Dowsett, T. Wirtz, In-situ Isotopic Analysis at Nanoscale using Parallel Ion Electron Spectrometry: A Powerful New Paradigm for Correlative Microscopy, Sci. Rep. 6, 28705, 2016

[2] P. Gratia et al, Intrinsic Halide Segregation at Nanometer Scale Determines the High Efficiency of Mixed Cation/Mixed Halide Perovskite Solar Cells, J. Am. Chem. Soc. 138 (49) 15821–15824, 2016

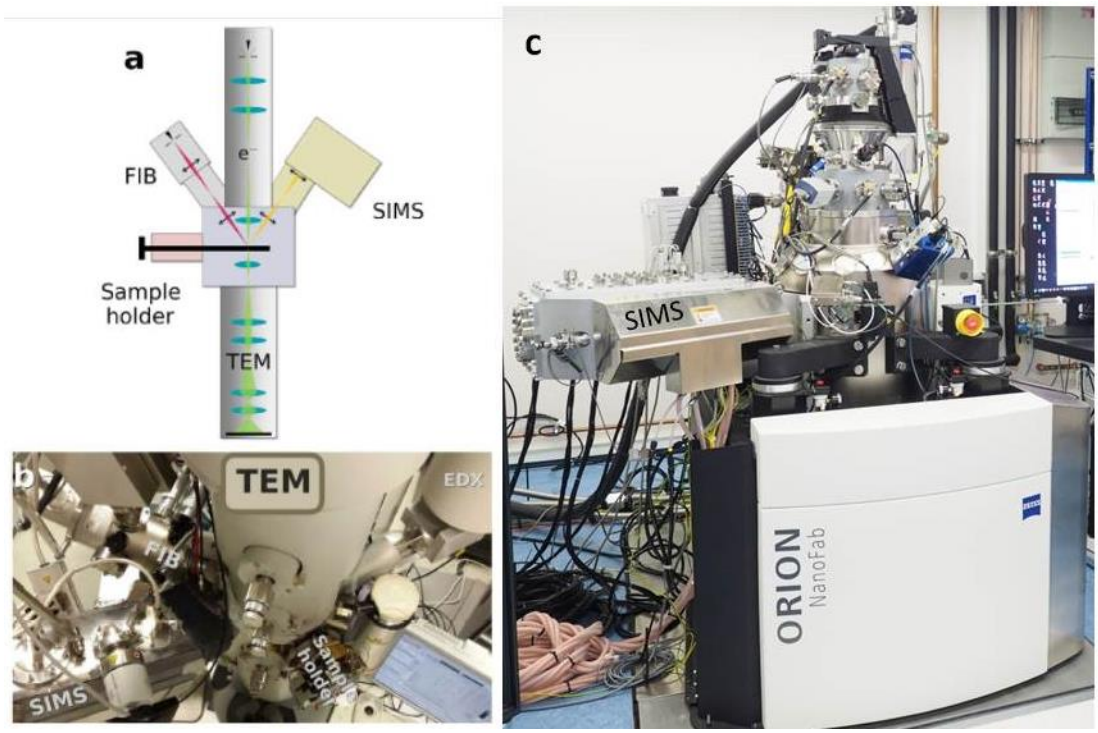

Figure 1. (a) Schematic and (b) a photo of the TEM-SIMS instrument, adapted from our work [1]. (c) Photo of the HIM-SIMS instrument.

IM1.010
Development of a SEM-EDS analyzer utilizing superconducting-tunnel-junction array x-ray detector toward realizing nanometer-scale elemental mapping

M. Ukibe[1], G. Fujii[1], S. Shiki[1], M. Ohkubo[1]

[1]AIST, Nanoelectronics Research Institute, Tsukuba, Japan

ukibe-m@aist.go.jp

Light elements (B, C, N, O …) have a big influence on performances of advanced functional and structural materials, such as next generation compound-semiconducting materials and heat-resistance steels. Usually in those materials, the light elements exist as many kinds of compounds and have many different forms, which are often nanometer size. Thus, to improve those properties, it is very important to evaluate amounts and the spatial distribution of light elements in there by those qualitative elemental mappings with a nanometer scale.
An EDS analyser combined with a SEM is suitable to obtain spatial and quantitative information on the elemental composition of a sample non-destructively. In particular, in order to perform the nanometer scale elemental mapping, it is necessary to operate a SEM at lower accelerating voltage less than 1 keV, because electron ranges and interaction volumes in samples become significantly small (< several 10 nm) at accelerating voltage of 1 keV.[2,3]
However, the elemental analysis at the low accelerating voltage (< 1 keV) mode is fairly difficult because in this condition, only K-lines of light elements with atomic numbers less than 10 (Ne), L- and M-lines of the other elements can be used for the analysis but SDDs or Si(Li) detectors equipped in the conventional EDS analysers can"t clearly distinguish the K-lines of the light elements from the L- and M-lines of various elements.
In contrast, energy-dispersive X-ray detectors based on arrays of superconducting-tunnel-junctions (STJs) have simultaneously exhibited excellent energy resolution of <10 eV, relatively large detection area of >1 mm^2, and high counting rate capability of >500 kcps for soft X-rays less than 1 keV [4,5]. We have been developing a SEM-EDS analyser utilizing an STJ array (SC-SEM), in order to realize analysis of light elements in structural or functional materials with nanometer scale [6].
In this work, we performed elemental analysis of the 9% Cr steel to demonstrate a peak separation capability of SC-SEM at low-acceleration-voltage.
Figure 1 shows a cross-sectional schematic illustration of SC-SEM. SC-SEM consisted of an SEM with a tungsten filament and the STJ array detector. The STJ array was cooled to 0.31 K on a cold stage of a cryogen-free ^{3}He cryostat. In order to improve the collection efficiency, a polycapillary collimating X-ray lens was installed in the system. The overall collection efficiency of SC-SEM was 0.34 msr so far.
Figure 2(a) shows a SEM image of the 9% Cr steel. The acceleration voltage was 5 kV. The black and white inclusions of sub-micrometer size can be seen in the SEM image. To evaluate the difference in the elemental composition between point 1 and 2(the black inclusion), X-ray spectra of two points were measured. The spectra were displayed in figure 2(b). The measurement time was 3600 s. In the spectrum of point 1, Fe-*L*, Cr-*L*, and O-*Kα* peaks were observed, and Cr-*L*l (500 eV) and O-*Kα* (525 eV) peaks can be clearly separated. A full width at half-maximum value for the peaks was about 10 eV, which was about 5 times higher than that of the SDDs. In contrast, in the spectrum of point 2, the N-*Kα* peak was observed in addition to peaks observed in the spectrum of point 1 and the intensity of O-*Kα* peak was about 3 times higher than that in the spectrum of point 1. As a result, it is found that the black inclusion is the steel containing a lot of oxygen and a little nitrogen.

[1] M. Taneike, et. al., Nature **424** (2003) 294.
[2] R Wuhrer et. al., IOP Conf. Ser.: Mater. Sci. Eng. **109** (2016) 012019.
[3] J R Michael, et. al., Microsc. Microanal. 15 (Suppl. S2) (2009) 660.
[4] S. Friedrich, et. al., J. Low. Temp. Phys. **176** (2014) 553.
[5] M. Ukibe, et. al., J. Low. Temp. Phys. **184** (2016) 200.
[6] G. Fujii, et. al., submitted in X-ray spect.

A part of this work was supported by Cross-ministerial Strategic Innovation Promotion Program - Unit D66 - Innovative measurement and analysis for structural materials (SIP-IMASM) operated by the cabinet office. The sample of the 9% Cr steel was provided by F. Abe of the National Institute for Materials Science (NIMS).

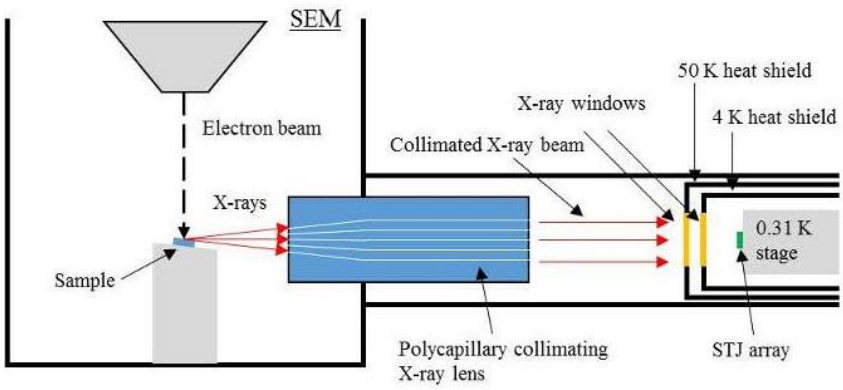

Figure 1. Cross-sectional schematic illustration of the SC-SEM:

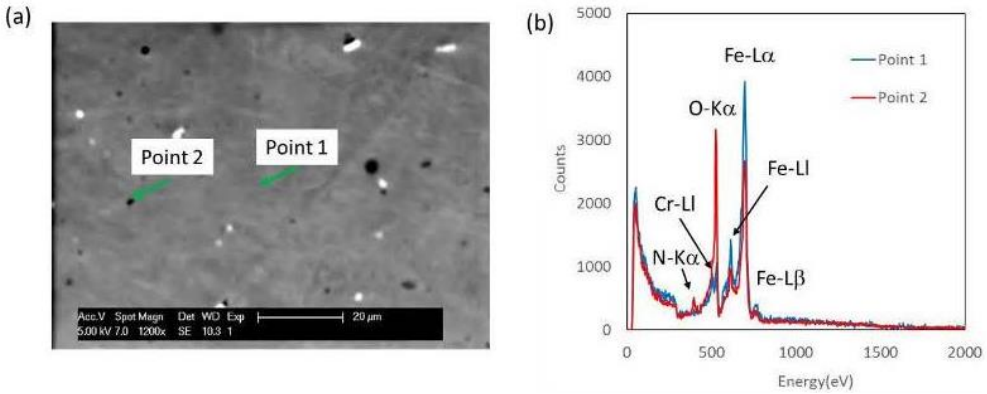

Figure 2. (a) SEM image and (b) X-ray spectra for the 9% Cr steell.

IM1.011
Optical performance and first experimental results of a liquid he cryogenic transmission electron microscope

F. Kern[1], S. Sturm[1], F. Börrnert[2], A. Lubk[1]

[1]Leibniz-Institut für Festkörper- und Werkstoffforschung, Institut für Festkörperforschung, Dresden, Germany
[2]Universität, Materialwissenschaftliche Elektronenmikroskopie, Ulm, Germany

f.l.kern@ifw-dresden.de

For a large class of materials interesting solid state physics phenomena, such as superconductivity, frustrated magnetism, or charge density waves, occur at very low temperatures, which requires liquid He cooling to be analyzed in the lab. For the understanding of these phenomena, however, the materials intrinsic electrostatic and magnetic fields as well as their structure and chemical composition are crucial. (Holographic) transmission electron microscopy (TEM) is a method which probes all of these material properties down to nanometer length scales. However, in order to facilitate liquid He cooling within a transmission electron microscope (TEM) one needs to dispense of sufficient space for a cryostat at the specimen position, which is typically not available due to the small pole piece gap of the objective lens required for highest resolving power.
In our dedicated double-corrected cryogenic JEOL 2010F TEM we sacrifice resolving power for more space at the specimen position by removing the pole pieces completely, which results in about 7cm longitudinal and 18cm lateral usable space in the object plane (Fig. 1). The released space is used for a continuous-flow liquid He cryostat that enables cooling down to ca. 7K for days and approaching any temperature above 7K by a counter heating device.
Here we report on the optical performance of this cryogenic TEM in terms of geometric aberrations, chromatic aberration coefficient and other spatial resolution limiting factors (e.g., mechanical noise) limiting the optical performance at low temperatures. To that end we performed Young fringes tests, measured Cc and determined the holographic fringe contrast at various biprism voltages. All of these measurements were conducted in the cooled (at ca. 7K) and in the uncooled state, using an acceleration voltage of 80kV and 200kV. Accordingly, we were able to resolve up to 4nm at 200kV and 5nm at 80kV in the Young fringes test. The measured aberrations suggest that the resolution is not limited by the electron optical system but rather by the microscopes stability, a problem which we are addressing at the moment. We report on various experiments demonstrating the low temperature capabilities. As an example, the diffraction pattern in Fig. 2 reveals a phase transition of 2H-$TaSe_2$ into a charge density wave state at ~120K.

[1] This project has received funding from the European Research Council (ERC) under the European Union"s Horizon 2020 research and innovation programme (grant agreement No 715620).

Figure 1. Redesigned specimen chamber with removed objective lens. The ISO-K 63 ports allow the lock in of a continuous-flow He cryostate.

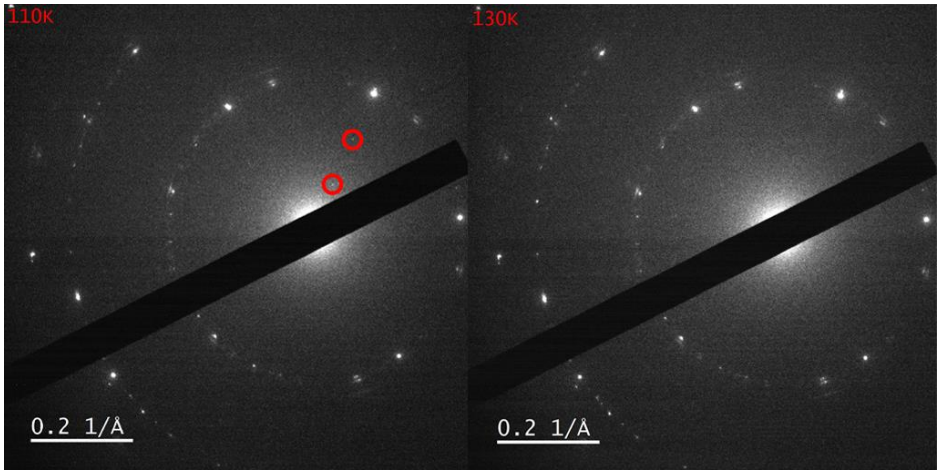

Figure 2. Diffraction pattern of 2H-$TaSe_2$ observed at 130K and 110K revealing the emergence of a charge density superstructure over 3 lattice constants.

IM1.012
Universal pressure scanning electron microscopy (UPSEM) – electron microscopy from high vacuum to atmospheric pressure

J. Rattenberger[1], T. Achtsnit[2], H. Fitzek[2], H. Schroettner[1,2], F. Hofer[1,2]

[1]Graz Centre for Electron Microscopy (ZFE), Graz, Austria
[2]Graz University of Technology, Institute of Electron Microscopy and Nanoanalysis (FELMI), Graz, Austria

johannes.rattenberger@felmi-zfe.at

Commercially available Scanning Electron Microscopes (SEM) can be divided into High Vacuum-, Low Vacuum- (up to a few 100 Pascal chamber pressure) and Environmental SEMs (up to a few thousand Pascal chamber pressure). High Vacuum microscope are usually used for high resolution applications, low vacuum microscopes to analyze insulting samples and environmental SEMs for wetting experiments or for samples which should not outgas during imaging process.
Unfortunately these high pressure applications in the kPa regime are limited by poor image quality which is caused by electron scattering processes and insufficient secondary electron detection. The imaging gas inside the chamber suppresses charging and outgassing of the sample but it also decreases the signal to noise ratio with increasing chamber pressure [1]. As a result these experiments must be done at high electron energies, long dwell times and large electron beam currents.
Recent publications on high pressure capabilities of state of the art microscopes have shown that they are working far away from physical limits and that there is plenty of room for improvements [2].
The key to high image quality at high pressures is to reduce scattering of the primary beam electrons inside the imaging gas as far as possible while maintaining ideal operation conditions for the SE-detector [3].
In the FEI Quanta 600 ESEM the gaseous environment in the sample chamber is separated by a differential pumping system and two Pressure Limiting Apertures (PLA) from the high vacuum inside the electron column. Nevertheless, a lot of gas streams through the PLA upwards and a significant amount of scattering takes place even before the electron beam is entering the sample chamber [2]. Based on the insights of Monte Carlo and finite element simulations a new aperture holder was designed that significantly reduces this gas flow and therefore also the primary beam scattering.
By replacing the position and modifying the shape of the secondary electron detector it can be optimized for high pressure applications. Nearby a needle detector with very small tip radius ($R < 10$ µm) the electric field is strong enough for SE amplification even at very high chamber pressure and by positioning the needle on the sample table it operates at ideal conditions regardless of pressure and working distance. The distance sample to PLA and sample to detector is no longer coupled. A by-product of this design is that the conventional position of the backscatter electron detector (BSE) at the end of the column is no longer blocked by the SE detector.
With this optimized high pressure design the limits of conventional ESEM technology can be crossed. Imaging at higher chamber pressures up to one atmosphere (see figure 1, copper wire specimen), of living organisms (see figure 2, captured images from a movie of a living mite) and backscatter electron imaging at high pressure (see figure 3, gold nanoparticles in oil at 10 kPa chamber pressure) are possible.

[1] Danilatos, G.D, Foundations of environmental scanning electron microscopy, Advances in Electronics and Electron Physics Vol. 71, 109-250, 1988
[2] Danilatos, G.D., Rattenberger, J., Dracopoulos, V., Beam transfer characteristics of a commercial environmental SEM and a low vacuum SEM, Journal of Microscopy Vol. 242, 166-180, 2011
[3] Fitzek H., Schroettner H., Wagner J., Hofer F., Rattenberger J., High-quality imaging in environmental scanning electron microscopy – optimizing the pressure limiting system and the secondary electron detection of a commercially available ESEM, Journal of Microscopy, DOI: 10.1111/jmi.12347

Figure 1. Copper wire specimen.

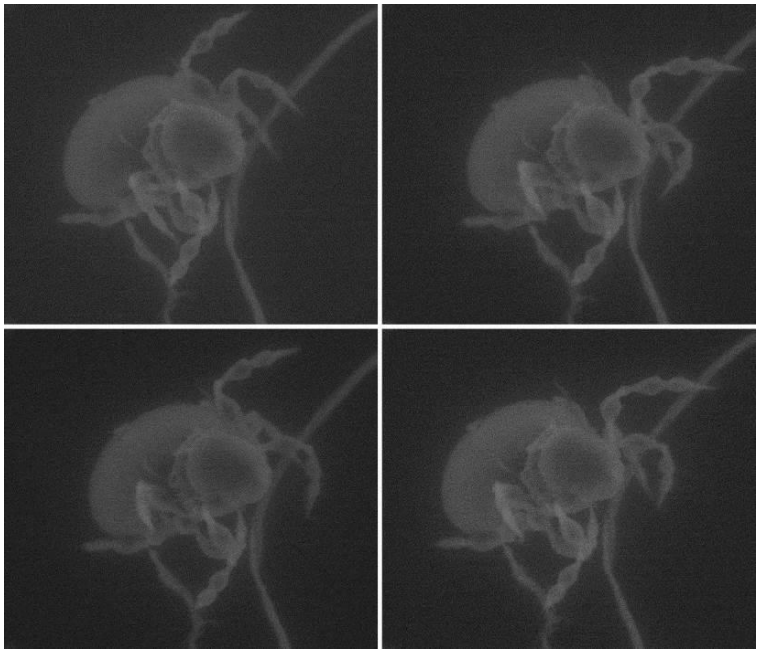

Figure 2. Captured images from a movie of a living mite.

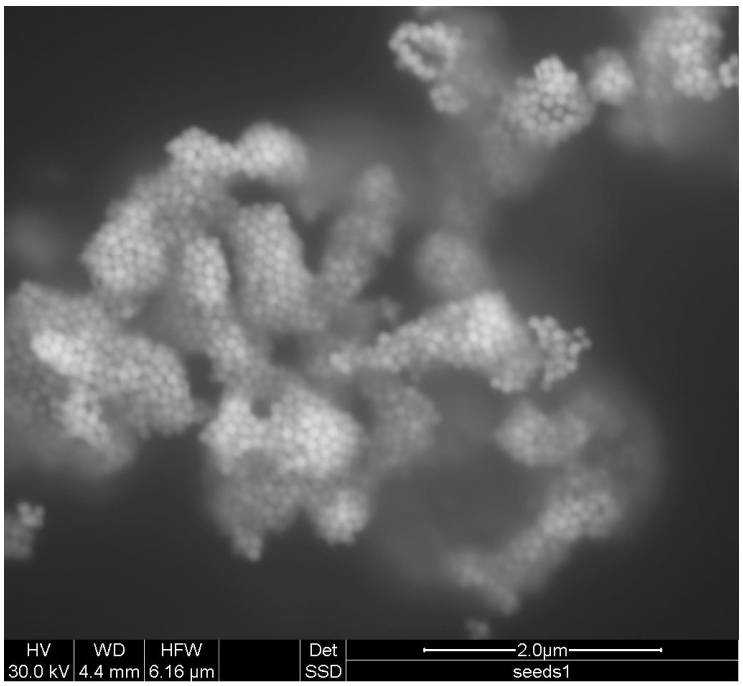

Figure 3. Gold nanoparticles in oil at 10 kPa chamber pressure.

IM1.013
X10 microscopy – multi-coloor imaging at a resolution of 25-30 nm on conventional epifluorescence microscopes

S. Truckenbrodt[1], M. Maidorn[1], D. Crzan[1], S. Kabatas[1], S. Rizzoli[1]

[1]University Medical Center Göttingen, Institute for Neuro- and Sensory Physiology, Göttingen, Germany

sventruckenbrodt@gmail.com

Introduction: Super-resolution light microscopy has so far overcome the diffraction limit of light by separating the signal from fluorophores in the sample in time (STED/STORM). Expansion microscopy has taken a different approach, by embedding the sample in a swellable hydrogel to isotropically increase the distance between fluorphores and achieve a separation in space (Chen et al., 2015). This allows multi-colour super-resolution imaging on conventional epifluorescence microscopes.
Objective: However, the resolution of expansion microscopy has so far been limited to ~70 nm, as the best expansion factor achieved to date has been ~4x. The resolution increases linearly with the expansion factor, which prompted us to further develop this method in an effort to achieve a higher expansion of biological samples. This would significantly further the spread of super-resolution imaging in biology, as no dedicated STED or STORM microscopes and specially trained personnel to operate them would be required, and material costs would be very low.
Materials and Methods: We adapted recently described hydrogels, engineered to provide exceptional stability during extreme swelling, for use in expansion microscopy to achieve multi-color imaging (3-4 imaging channels) of biological samples on conventional epifluorescence microscopes. The method is compatible with standard immunostaining protocols of biological samples.
Results: We present here X10 microscopy, which increases the expansion factor from 4x to 10-11.5x, achieving a resolution of 25-30 nm. This rivals the resolution of conventional STED and STORM setups and, in contrast to these techniques, allows multi-colour imaging at equal resolution across channels without any added effort compared to single-colour imaging. X10 microscopy can be applied to a wide array of biological samples, from various cell types (neurons, cell lines) to tissues (brain slices). We investigated, among other cellular structures, microtubuli networks and the ultrastructure of synapses, where we could resolve individual microtubules (25 nm diameter, Fig. 1A) and synaptic vesicles (40 nm diameter, Fig 1B). We could further investigate the ultrastructure of postsynaptic densities and presynaptic active zones. To demonstrate that distortions during isotropic expansion are not a detrimental factor for ultra-structural investigations of sub-cellular protein assemblies, we successfully replicated previous studies on nanometer-scale distance measurements (e.g. on pre-/postsynapse alignment, inset in Fig. 1B).
Conclusion: All investigations we performed have perviously only been possible with major investments in equipment and personnel training (STED/STORM). Multi-colour imaging in super-resolution microscopy has thus far usually been particularly difficult and required a major additional effort compared to single-colour imaging. Multi-colour imaging, however, is a basic requirement for most ultra-structural investigations of sub-cellular structures and molecular assemblies. These factors have hampered the wide-spread application of super-resolution techniques in biology. The low cost, low requirements in personnel training and equipment, and the triviality of multi-colour imaging for X10 microscopy will greatly extend the use of super-resolution techniques in biology and thus further advances in basic research.

References:
[1] Chen, F., Tillberg, P., Boyden, E. Expansion microscopy. Science. 347:543-548 (2015).

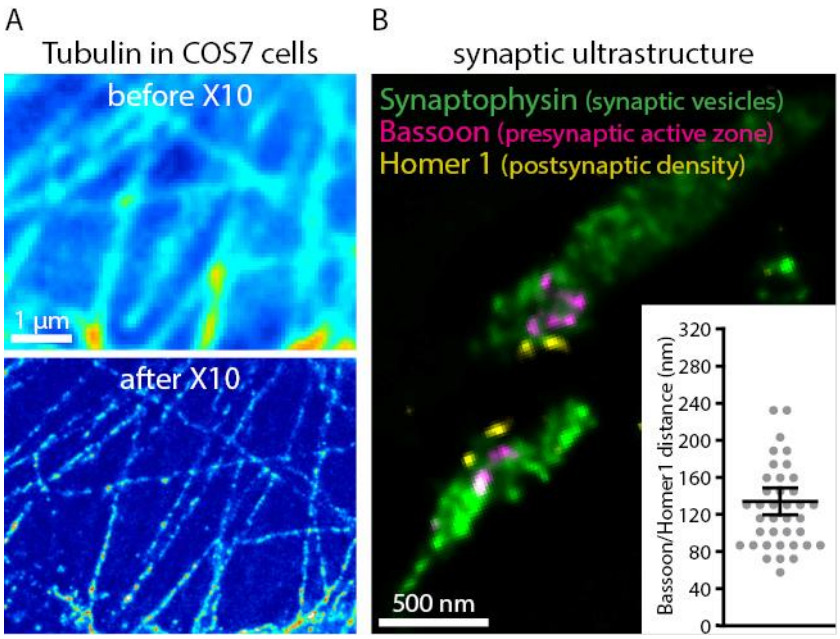
A
Tubulin in COS7 cells
before X10
1 µm
after X10
B
synaptic ultrastructure
Synaptophysin (synaptic vesicles)
Bassoon (presynaptic active zone)
Homer 1 (postsynaptic density)
500 nm
Bassoon/Homer1 distance (nm)
320
280
240
200
160
120
80
40
0

Figure 1

IM1.014
Application of the 20–80 kV SALVE TEM to graphene

F. Börrnert[1], J. Biskupek[1], U. Kaiser[1]

[1]Universität Ulm, Ulm, Germany

felix.boerrnert@uni-ulm.de

Modern aberration-corrected transmission electron microscopy is able to routinely image sample structures with true atomic resolution with a resolution better than 1 Å. Unfortunately, light-element materials suffer severe damage via the knock-on mechanism at electron energies commonly used for high resolution imaging [1]. To avoid this kind of sample damage, imaging at lower acceleration voltages of 60–80 kV became popular to undercut the threshold for knock-on damage. Thanks to geometric aberration correction, an image resolution of below 2 Å can still be maintained. One interest when performing atomic resolution microscopy of thin and/or light-element materials lies in interfaces and defects and there, the aforementioned damage threshold is significantly lowered, thus, calling for even lower imaging electron energies [2].
In TEM at acceleration voltages of 40 kV and lower, in addition to the geometric aberration, the chromatic aberration coefficient of the imaging lens limits the information transfer. The chromatic aberration can be corrected by using a C_c/C_s corrector [2, 3] or its effects can be minimized by employing a monochromator for the primary electrons [4]. In the latter case, most of the electrons coming from the electron source are blocked and do not contribute to the imageforming process, thus the signal-to-noise ratio decreases severely.
Here, we demonstrate the use of our new chromatic and geometric aberration-corrected SALVE microscope [3] with examples of various point defects in graphene imaged at 20 kV to 80 kV with so far unprecedented high resolution. For example, figure 1 shows a single vacancy with a clear Jahn-Teller distortion and figure 2 a substitute atom in the graphene lattice. Additionally, we discuss the contrast transfer with a special focus on the effects of chromatic aberration correction on the contrast dampening and information limit.

[1] J. C. Meyer et al. (2012), Physical Review Letters 108, 196102.
[2] U. Kaiser et al. (2011), Ultramicroscopy 111, 1239.
[3] M. Linck et al. (2016), Physical Review Letters 117, 076101.
[4] S. Morishita et al. (2016), Applied Physics Letters 108, 013107.

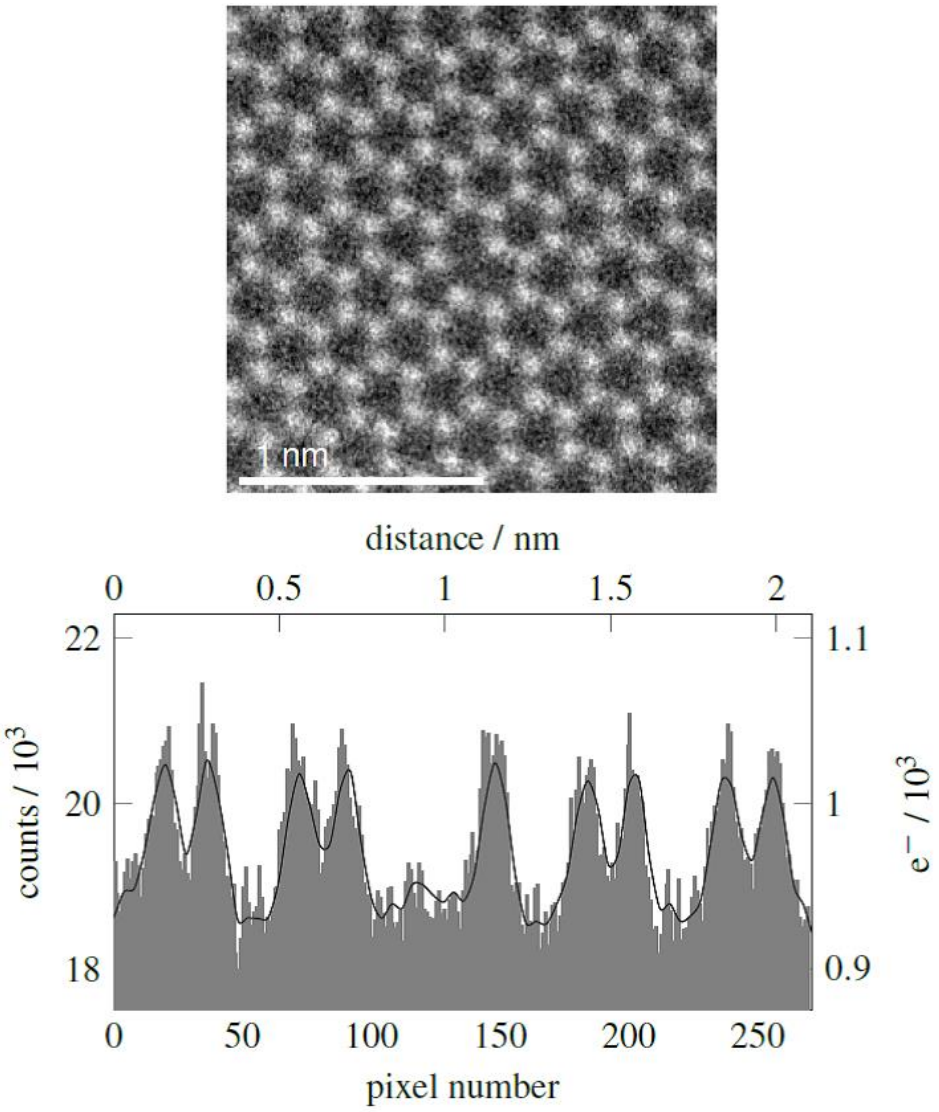

Figure 1. Raw micrograph showing a single vacancy. Note that the vacancy is not symmetric, this is due to the Jahn-Teller distortion. The plot below shows a line profile over the defect in two-o'clock direction as a histogram with a line width of one pixel. An indicating line is omitted in favor of clarity in the micrograph. Overlaid is a smoothed intensity profile along the same line in the same micrograph binned four times.

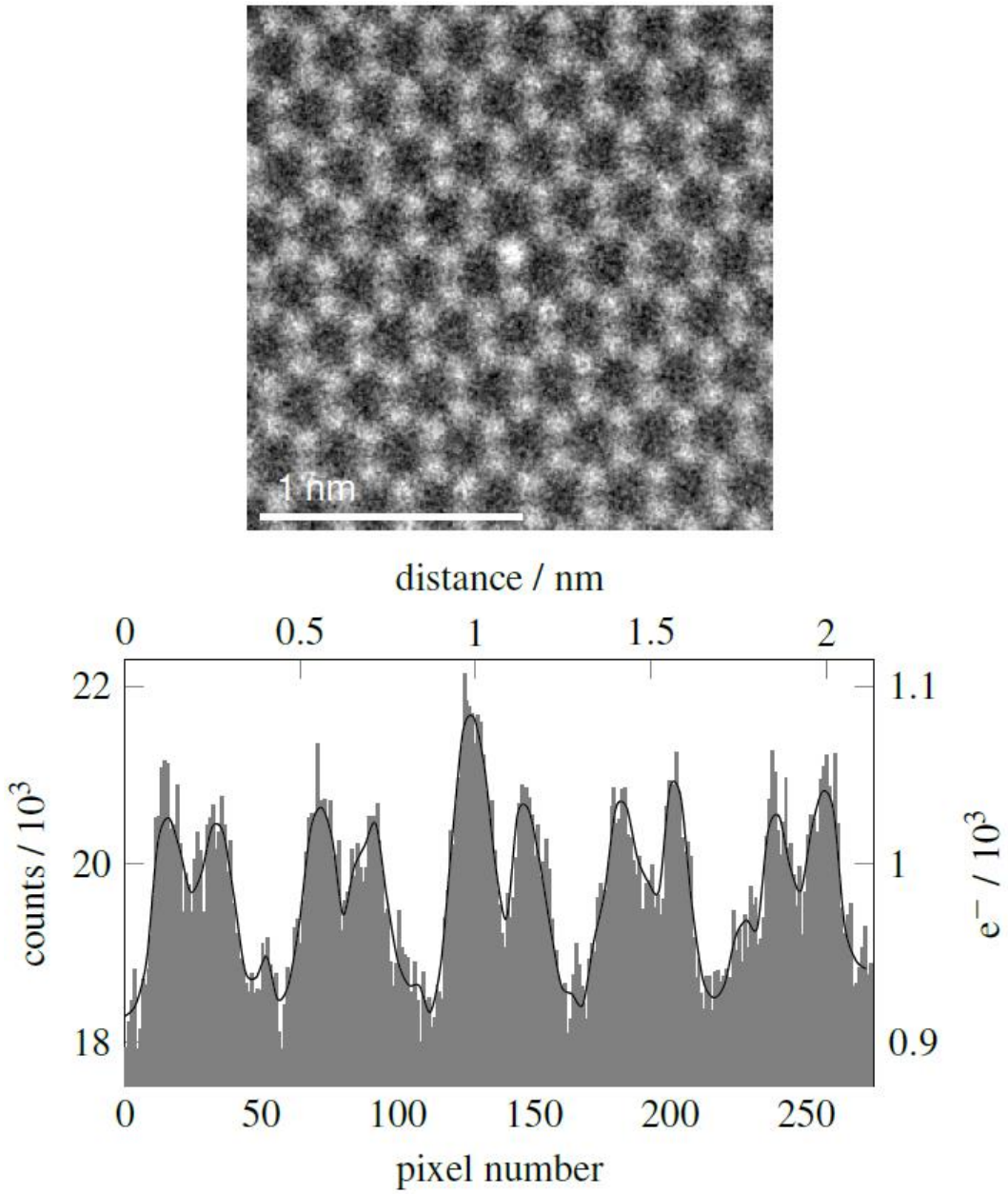

Figure 2. Raw micrograph showing a substituting atom of a heavier element. The plot below shows a line profile over the defect in two-o'clock direction as a histogram with a line width of one pixel. An indicating line is omitted in favor of clarity in the micrograph. Overlaid is a smoothed intensity profile along the same line in the same micrograph binned four times.

IM1.P001
Combination of real and reciprocal space observation methods – complementary use of small-angle scattering and scanning electron microscope-

S. Koizumi[1]

[1]Ibaraki Univ, College of Engineering, Tokai, Japan

satoshi.koizumi.prof@vc.ibaraki.ac.jp

In order to investigate hierarchical structure of materials, we attempt to combine scanning electron microscope (SEM) and small-angle scattering (SAS). Secondary electron image (SE) obtained by SEM is sensitive to surface topology, giving a projection map. SE image is influenced by local inclination of surface (edge effect). With larger inclination angle, brighter image is obtained. Small-angle neutron scattering (SANS), on the other hand, is sensitive to fine structures such as fluctuations in concentration at interface or inside domains. In this study, we perform two-dimensional Fourier transform of SE image to obtain power spectrum curve and compare to scattering curves as a function of wave number *q* obtained by SANS.

To establish the combined method, first we examine a test specimen of SiO2 particles, which are mono-dispersed in size. We established calibration procedures according to bright & dark converging and background subtraction. It was found that two-dimensional Fourier transform of the calibrated SE image is identical with a scattering curve as a function of *q*.

Second, we applied the combined method to the catalyst for polymer electrolyte fuel cell, which is composed of carbon-supported platinum (Pt) nanoparticles implanted on carbon block powder and covered with ionomer thin layer. By quantitatively comparing scattering q-profiles obtained by SANS and Fourier transform of SE images, we found a significant difference in decay behaviors in *q* in a small lenght scale limit (~nm). After careful analysis on the difference in q-behavior, the structural parameters were determined; ionomer thin layer thickness (~3nm) and volume fraction of voids in a carbon particles (~50%).

IM1.P002
Temperature dependence of saturation magnetostriction of a ferromagnetic film

S. U. Jen[1], W. T. Tsai[1]

[1]Academia Sinica, Institute of Physics, Taipei, Taiwan

physjen@gate.sinica.edu.tw

In the past, there did not exist many studies on the temperature (T) dependence of saturation magnetostriction (λ_S) in a ferromagnetic material. Moreover, most of the studies were using a sample in a bulk or ribbon form [1, 2]. If the sample is in a thin-film form, the relevant study rarely exists.
In this study, ferromagnetic $Fe_{62}Co_{19}Ga_{19}$ film, 110 nm in thickness, was deposited on a thin Si(100) substrate, 110 mm in thickness, by the dc magnetron sputtering method at room temperature (RT). An integrated system, including a digital holographic microscope, electromagnet, infra-red camera, high-temperature sample stage, and vacuum chamber, was employed to measure the temperature dependence of saturation magnetostriction (λ_S) of the $Fe_{62}Co_{19}Ga_{19}$/Si(100) film. Because in the thin-film magnetostriction measurement [3], the film-substrate sample has to be clamped at one end of the sample length, two additional effects need to be considered: i.e., the thermal expansion and the non-uniform temperature (ΔT) effects. Thus, the following auxiliary experiments were also performed: e.g., to measure the T dependence of Young"s moduli (E) and thermal expansion coefficients (α) of $Fe_{62}Co_{19}Ga_{19}$ and Si(100). The theoretical T dependence of λ_S, based on the single-ion model [4], has been calculated for the $Fe_{62}Co_{19}Ga_{19}$ film. For comparison, the experimental T dependence of λ_S agrees with the theoretical prediction in the T range from RT to 140℃. At a higher temperature, e.g., T=180℃, the large difference between theoretical and experimental $\lambda_S(T)$ is due to the following effects: e.g., the thermal expansion difference between the film and substrate, non-uniform T-distribution (ΔT) along the sample length, reduction of Ga content, and surface oxidation effects, respectively.

[1] A. E. Clark, M. Wun-Fogle, J. B. Restorff J B, K. W. Dennis, T. A. Lograsso, and R. W. McCallum, J. Appl. Phys. **97** 10M316(2005).
[2] R. C. O"Handley, Phys. Rev. **B18** 930(1978).
[3] S. U. Jen, C. C. Liu, and S. T. Chen, IEEE **MAG-50**, 600404(2014).
[4] E. R. Callen and H. B. Callen, Phys. Rev. **129**, 578(1963).

Keywords: Ferroagnetic Thin Film; Saturation Magnetortriction; Temperature Dependence

IM1.P003
A simple and rapid scanning electron microscope preparative technique for observation of biological samples.

I. Piroeva[1], S. Atanasova-Vladimirova[1], L. Dimowa[2], R. Rusev[2], B. Ranguelov[1], B. Shivachev[2]

[1]IPC-BAS, Laboratory of Electron Microscopy and Microanalysis, Sofia, Bulgaria
[2]IMC-BAS, Sofia, Bulgaria

piroeva@abv.bg

Biological samples e.g. bacteria, DNA, proteins, contain significant amounts of water and exhibit low conductivity. Normally, such samples cannot be observed directly by conventional scanning electron microscope (SEM) because the surface and subsurface water quickly evaporates under the high vacuum conditions necessary for electron microscopy observation [1, 2]. Thus different preparative techniques have been developed to preserve sample integrity. Our aim has been to adapt a protocol that will reduce significantly the processing time of such samples without significant loss of observation quality. The adapted protocol provides a fast alternative for biological samples preparation and can be used for rapid assessment of samples shapes, structural morphology etc. Although that there are many conditions to be met for "ideal" sample preparation for electron microscopy observation the most important and necessary condition is to maintain the integrity of the biological sample during sample preparation and subsequent work in the electron microscope [3]. Materials which are used in this preparation protocol are inexpensive and are located in every laboratory (agar, ethanol, tweezers, incubator etc.)[4]. The processing is relatively rapid and may be completed for one day. The SEM visualization and data quality allows sufficient detail for samples that are bigger than 1 μm while for smaller size a contrast enhancement is suited (Fig. 1). Compared to classical procedures the developed one is cost and time effective with minimal loss of data quality (mainly contrast lost).

References:
[1] T. Ogura, 1. *Biochem. Biophys. Res. Comm*., **391** (1), 198 (2010).
[2] F. Iwata, Y. Mizuguchi, H. Ko, T. Ushiki, *J.* El. Microscopy, **60** (6), 359 (2011).
[3] S. Susan, W. Tai, M. Tang, Journal *of Scanning Microscopies*, **23**, 267 (2001).
[4] Piroeva, I., Atanassova-Vladimirova, S., Dimowa, L., Sbirkova, H., Radoslavov, G., Hristov, P., Shivachev, B.L., Bulg. Chem. Commun. **45**, 510–515 (2013).

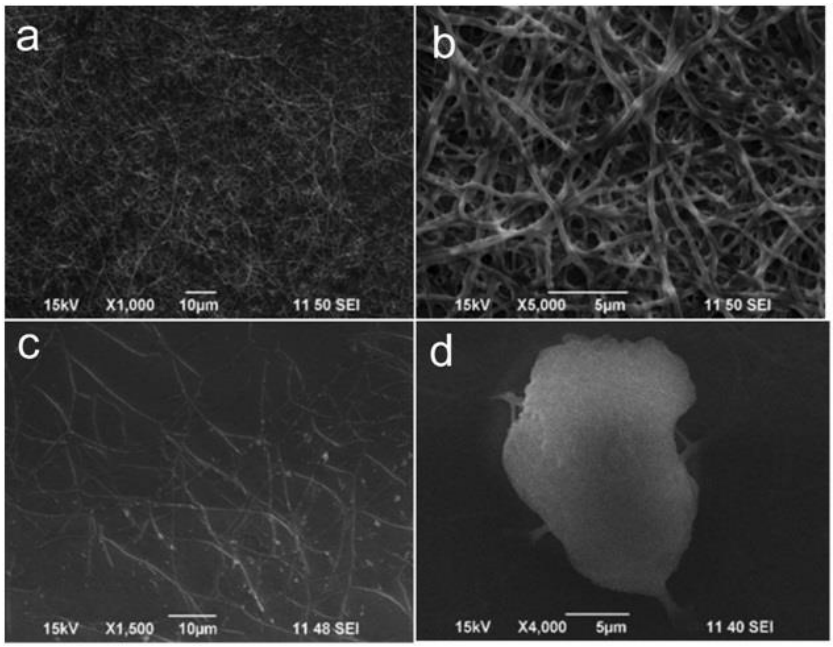

Figure 1. SEM images of *Thermobispora bispora* with different concentrations of bacteria a) and b) after centrifugation of 3×1.5 ml while c) and d) are samples centrifuged 1×1.5 ml.

IM1.P004
Study of phase and composition contrast of nanomaterials with LL-BSE imaging

X. Liu[1]

[1]Carl Zeiss Microscopy GmbH, Oberkochen, Germany

xiong.liu@zeiss.com

The surface and interface dominate the both materials properties and the performance of semiconductor devices with continuously shrinking the size and structure. The advanced nanofabrication technology is able to engineer well-defined materials structures down to a few nanometers. This requires scanning electron microscope (SEM) as a most conventional technical method in material characterization and analysis not only to visualize and resolve such nanostructures with the secondary electron imaging at a low landing energy to reveal real surface information but also to analyze the tiny compositional differences like doping contrast, oxidation states of elements, small phases, hybrids or function group in polymers etc., which are not available via the classical backscattered electron imaging or other Energy-dispersive X-ray spectroscopy methods. Although the classical backscattered electron (BSE) imaging are from the multiple inelastic scattering process which could provide density related contrast like channeling contrast at high landing energy, the backscattering coefficient shows non-linear behavior and get very complicated at low landing energy range[1].

In the conventional backscattering process (Rutherford scattering), the backscattered electrons are mainly from the scattering of the high energy primary electrons with the nucleus charge or inner electron shells of the material. In such a case the contrast or brightness of the BSE imaging scale with material density, atomic number (Z). However the scattering between the primary beam with the outer electron shells of the materials at low impact energy (below 2 kV) region is not any more negligible which even becomes more dominant where the surface plasma resonance and ionization loss could happen and contribute to in the total contrast mechanism [2]. Such backscattered electrons undergone a single inelastic scattering process with low energy loss are rebounded back along the primary electron beam which involve unique properties of the analyzed materials.

The unique electron beam booster inside the Gemini® column not only maintains the brightness of the primary electron beam but also reduced the aperture diffraction at low energy. The recently appeared new Nano-Twin Lens has a tremendous improvements in lens aberration correction and electron signal separation on the basis of the well-known Gemini® lens technology. The integration of the Nano-Twin Lens and beam booster technology means, on one hand a further reduction of the beam probe size for both low kV and high kV, and on the other, the dispersion of generated electron signals backward into the column has been enhanced. It means that the secondary electrons and backscattered electrons with a small energy and angle differences could be amplified and separated through the Nano-Twin Lens in real time and space without converting the signals or applying stage bias. The separated backscattered electrons undergoes energy filtering by an energy filtering grid and are projected back into the corresponding detector. The multiple inelastic scattered electrons could be filtered out by setting an appropriate threshold potential to the filtering grid. Only the backscattered electrons with a specific energy low loss (energy larger than the gird potential) could go through the grids window into the detector for imaging. At low landing energy condition, such backscattered electrons are called energy low loss backscattered electrons which bring some characteristic properties and scattering information of the specimen. This idea design allows microscopists to gain not only a better resolution but more unique contrast information in low kV applications.

Herein, we will present the band gap difference induced contrast in ZnO nanocrystals imaging (ref. Figure 1) and different phases ferrite, austenite, marensite in steel as shown in Figure 2 by LL-BSE imaging.

[1] L. Reimer, Scanning electron microscopy, 2nd edition. Springer-Verlag, 1998, Berlin Heidelberg New York.

[2] H. Jaksch, Contrast mechanisms of low loss backscattered electrons in field emission SEM, EMAS conference, May 2011, France.

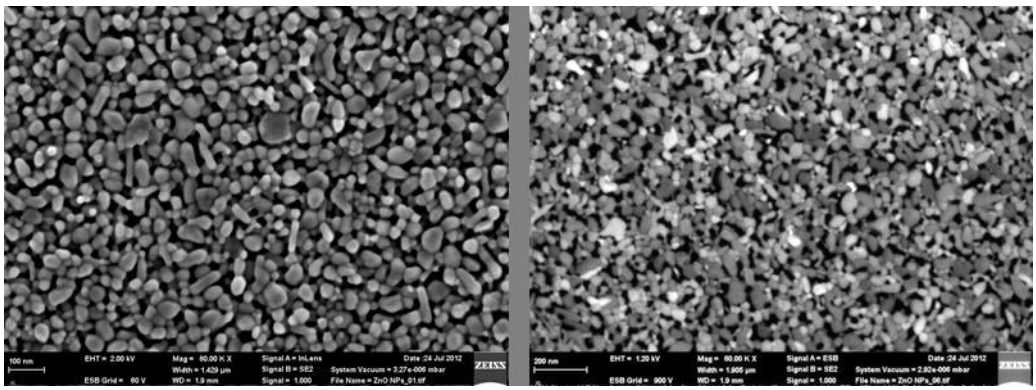

Figure 1

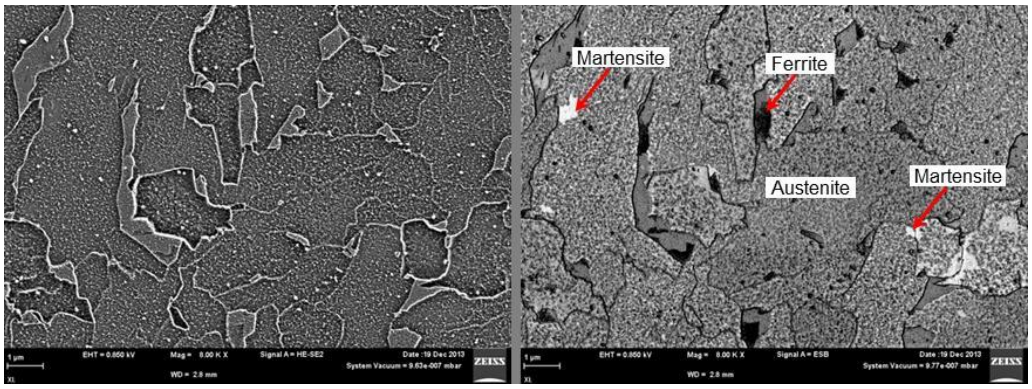

Figure 2

IM1.P005
Are electrons the new photons?

S. De Carlo[1]

[1]Dectris Ltd, Business Development EM, Baden, Switzerland

sacha.decarlo@dectris.com

Hybrid photon-counting detectors have caused a major breakthrough in macromolecular crystallography. The new EIGER detectors for synchrotron applications feature a pixel size of 75 µm and continuous read-out at frame rates of up to 3000 Hz. In its first year in regular operation at MX beamlines, EIGER has already contributed to several outstanding publications. A few selected examples will be discussed.
Since EIGER was designed for noise-free single-event counting, we wondered how it would perform with electrons instead of X-rays. Better performing detectors are considered a key to further improvements in the resolution of cryo-electron microscopy [1]. To find out how EIGER compares, we characterized an EIGER X 1M in a Philips CM200-FEG transmission electron microscope.
Using the knife-edge method [2], we determined the edge spread function and the modulation transfer function (MTF) of the EIGER X 1M detector. Processing the data in single-event mode and using noise binning [3], we then calculated the detective quantum efficiency (DQE, see figure) of EIGER. At energies of 80 and 100 keV, the DQE curves are very near the theoretical limit across all spatial frequencies.
EIGER turns out to be close-to-ideal for counting electrons with energies up to 120 keV. To push the limits further, DECTRIS designed a new ASIC, called IBEX, that will allow higher frame rates than EIGER and the counting of electrons with energy resolution and sub-pixel accuracy as a result of the time-over-threshold (ToT) acquisition mode.

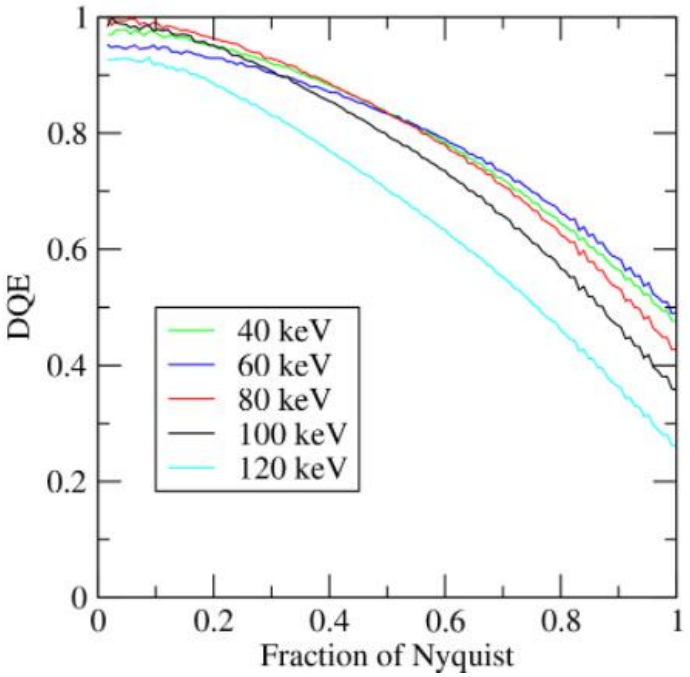

Figure 1. Detective quantum efficiency of EIGER X 1M. The DQE of EIGER X 1M is shown for electron energies between 40 and 120 keV.

IM1.P006
Method development to determine the dependence of oxidation on the crystal surface orientation of tungsten

M. Balden[1], K. Schlueter[1,2], S. Elgeti[1], T. F. da Silva[1,3]

[1]Max-Planck-Institut für Plasmaphysik, Garching, Germany
[2]Technische Universität München, Fakultät für Maschinenwesen, Garching, Germany
[3]University of Sao Paulo, Physics Institute, Sao Paulo, Brazil

karsten.schlueter@ipp.mpg.de

Many material properties depend on the crystal orientation in respect to the surface. The orientation resolved properties are often important for basic understanding of phenomena. Examples of such properties are the physical sputtering by ion bombardment and the oxidation rate.
In order to determine the correlation between a property and the crystal surface orientation for many grains, a measurement strategy and evaluation tools must be developed which can then be applied on different material properties of interest.
Tungsten is envisaged as plasma-facing material in future fusion power plants and its oxidation behavior got attention due to safety studies on potential accident scenarios. Due to the lack of data on the surface orientation resolved oxidation of tungsten, its oxidation was studied in the temperature range 720-870 K.
Confocal laser scanning microscopy (CLSM) and electron backscattering diffraction (EBSD) in a scanning electron microscope (SEM) were applied on recrystallized tungsten samples with grains of about 20 µm in order to get a large variety of surface orientations in one experiment. The pre-characterized samples were oxidized in a thermobalance in dry air (20% O_2, 80% Ar). The variation of the thickness of the oxide layer for the different crystal on the previous flat surface was studied by CLSM determining the height differences and by SEM on focused ion beam prepared cross-sections for absolute thickness measurement. A manual method was developed and applied to overlay the EBSD orientation maps with the height maps exploring only grains close to the low index surface orientation. The automated method evaluating all appearing orientations on the samples is under development.
As a result, it is found that the oxidation rate varies by a factor of 2 with the surface orientation. The {100} surface has the highest rate and the {111} belong to those with the lowest rates.
In conclusion, the measuring and evaluation strategy has been proven on the oxidation behavior of tungsten and are applied now on other for the fusion research important properties, i.e., physical sputtering and the so-called "blistering" of tungsten under hydrogen bombardment.

IM1.P007
Correlative X-Ray-Microscopy – FIB/SEM workflow to determine impurities in additively manufactured parts

T. Schubert[1], L. Hunter[2], S. Freitag[3], T. Bernthaler[1], G. Schneider[1]

[1]Hochschule Aalen, Institut für Materialforschung, Aalen, Germany
[2]Carl Zeiss X-Ray Microscopy, Inc., Pleasanton, CA, United States of America
[3]Carl Zeiss Microscopy GmbH, München, Germany

tim.schubert@hs-aalen.de

Introduction: Additive manufacturing (AM) is a key technology for the fabrication of attractive material-, energy- and resource-efficient products for a future competitive mechanical engineering market as well as sustainable mobility and power-engineering. It furthermore is a high potential technology to implement industrial internet standards and a digitized production chain. AM however requires extensive R&D work in understanding process and materials characteristics as well as quality and reliability of produced parts. To deepen the understanding of process influences on the manufactured part such as impurities in the base material, a correlative microscopic workflow combining high resolution X-Ray-Microscopy with FIB/SEM-Technology for further analysis is introduced using the example of an additively manufactured gear part.
Objectives: In powder based additive manufacturing (in this case laser assisted powder bed fusion) even the slightest contamination of the powder (e.g. by residual powder from a prior build-job) can lead to impurities in the finished part which have major influence on the overall properties. The objective of the conducted investigation was to non-destructively determine impurities in additively manufactured parts and by the presence of such using a correlative workflow to target-prepare these distinctive features for further analytical investigation.
Materials and Methods: The correlative workflow is shown on an additively manufactured gear-part made from an aluminum-silicon-alloy (AlSi10Mg). The investigations were carried out on a ZEISS Xradia Versa 520 submicron X-ray-microscope (XRM) for the high-resolution non-destructive scan of the whole part and on a ZEISS Crossbeam 540 FIB/SEM for the correlative analysis of inspected discontinuities. To correlate the XRM-dataset with the Crossbeam 540 for further investigation the specific software application Fibics Atlas 5 was used. The chemical composition was furthermore determined using an Ametek EDAX EDS-System.
Results: The volume rendering of the XRM-scan of the gear-part shows some distinct pore formation throughout the whole part and a single bright discontinuity with approx. 50 µm size (Fig. 1). Bright spots in an X-ray-scan always imply higher absorbing material so having an impurity there is very likely. As the feature is located deeply under the parts surface, a sole FIB-preparation is not suitable to reach the location. To overcome this issue a materialographic target-preparation was done to remove surplus material. The correlation of the XRM-volume with the FIB/SEM-image using Atlas 5 allows very precise preparation and imaging of the distinct feature. The microstructure of the feature deviates from the surrounding material and EDS-analysis shows a high iron-content as well as chromium and Molybdenum (Fig. 2). The peculiarity observed in the XRM-scan turned out to be a steel powder-particle (approx. 50 µm) from a prior build-job derived from insufficient cleaning of the manufacturing device.
Conclusions: The investigations show that high-resolution submicron X-ray-microscopy is an excellent way to non-destructively determine failures in additively manufactured parts such as pores and impurities and that the combination of XRM-scans with FIB/SEM preparation/analysis via a correlative workflow provides a quick and easy way to find out what distinct features consist of and what is their origin. Not only does the correlative XRM-FIB/SEM-workflow play an important role in quality control and quality assurance of additively manufactured parts but it also improves the understanding of process-property-correlations.

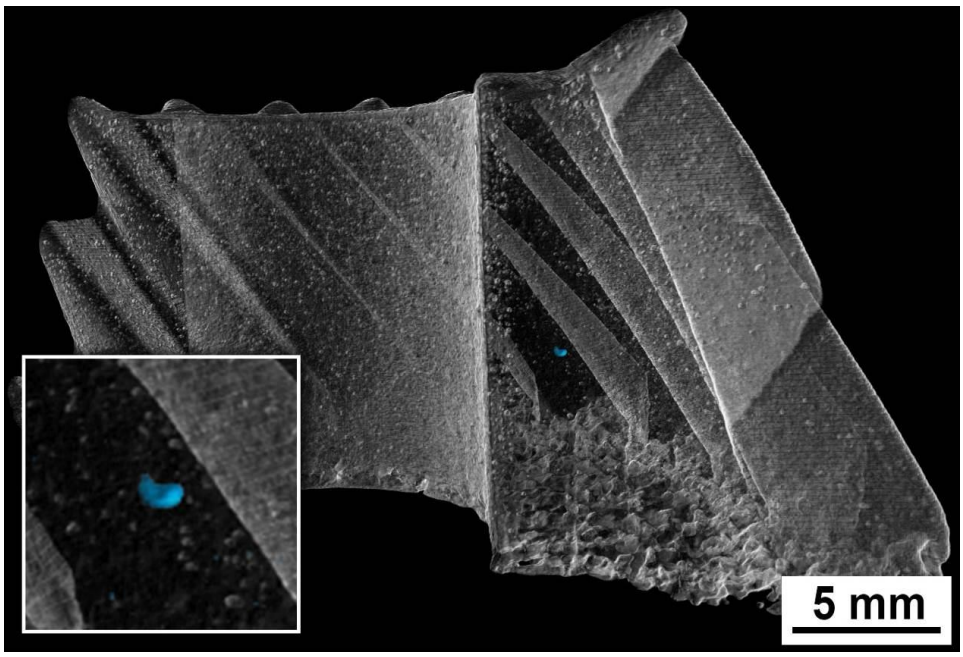

Figure 1. XRM-volume of gear-part, highlighted in blue is the feature with higher X-ray absorbance.

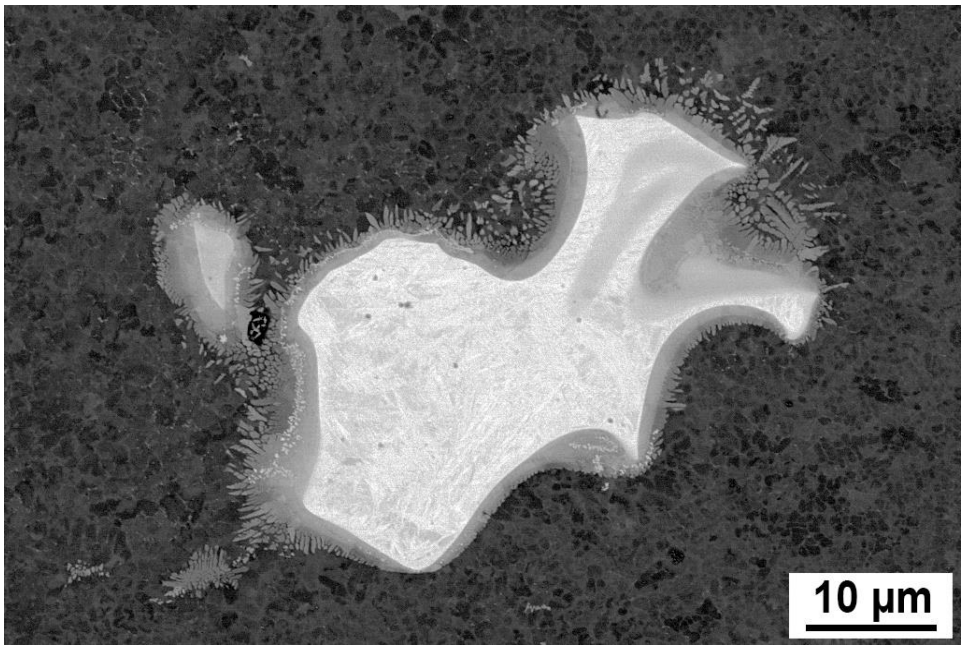

Figure 2. FIB crossection of distinctive feature, molten steel powder particle of approx. 50 µm, BSE-contrast.

IM1.P008
Determination of grain size and grain size distributions of nanocrystalline materials – a comparative study including t-EBSD, TEM and XRD

J. Schmauch[1], C. Braun[1], R. Birringer[1]

[1]Universität des Saarlandes, Experimentaphysik, Saarbrücken, Germany

schmauch@nano.uni-saarland.de

Physical properties of crystalline materials often strongly depend on the grain size of the crystallites. Mechanical properties like the yield strength may be the most prominent ones but also electrical and magnetic properties can be strongly influenced by grain boundaries [1]. Only in very rare cases one has a single grain size throughout the sample. Depending on their synthesis route, polycrystalline materials generally have a more or less pronounced distribution of grain sizes. In general, the related distribution of grain sizes will affect the properties of the investigated material.
In the limit of very small grain sizes (D < 50-100 nm), i.e. the case of a real nanocrystalline structure, wide-angle x-ray scattering is a common method for the determination of the average grain size of the microstructure. Advanced methods like the Warren-Averbach analysis [2] allow the determination of a volume and an area averaged mean grain size and so enable to calculate the width of the grain size distribution whenever its general functional shape, usually a lognormal distribution, is known. An alternative traditional approach to determine the grain size distribution is based on analysing dark field images captured in a TEM.
A few years ago, transmission EBSD (t-EBSD) has been established as a new method to quantitatively analyse average grain sizes and grain size distributions [3]. In contrast to conventional EBSD measurements, the t-EBSD configuration has the advantage of an improved spatial resolution in the range of a few nanometers. It is the aim of this study to show that t-EBSD is a suitable tool to determine grain size and grain size distribution of nanocrystalline materials at the low end of the nanoscale. Exemplarily, we use an inter-gas condensed PdAu-sample with a grain size of about 10-20 nm. Fig. 1 shows the inverse pole figure recorded in t-EBSD in a JEOL 7000 F SEM equipped with an EDAX Trident EBSD analysis system (Fig. 2).
To compare our results with traditional methods and to highlight the advantages of t-EBSD, we also determined the mean grain size and grain size distribution of the same sample using XRD and TEM. Dark field images were performed by a JEOL 2011 TEM and for XRD measurements we used a Panalytical XpertPro diffractometer. But care must be taken when comparing average grain sizes measured by different methods. The mean grain size evaluated by x-ray diffraction is a volume average while the data measured by t- EBSD and TEM represent an average over a cross-sectional area, i.e. it is an area averaged value. In contrast to x-ray diffraction, t-EBSD and TEM yields direct evidence of the grain-size distribution and thus offers the possibility to calculate all moments of the distribution function [4]. All these aspects will be discussed in this contribution.

[1] Arzt, Acta Mater. 46, p5611 (1998).
[2] E. Warren, X-ray diffraction, Chapter 13, p251, (Dover Publications, New York, 1990).
[3] R. Keller and R.H. Geis, Journal of Microscopy, Vol. 245, Pt 3 2012, pp. 245–251
[4] E. Krill and R. Birringer, Philos. Mag. A **77**, p621 (1998).

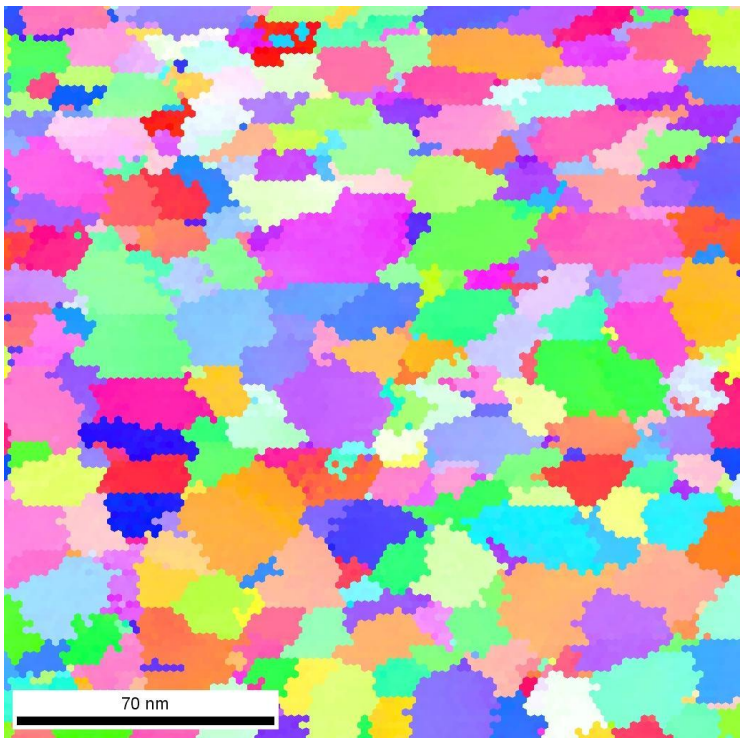

Figure 1. t-EBSD scan (Inverse Pol Figure) of the nanocrystalline PdAu-sample.

Figure 2. Configuration for t-EBSD in the JEOL 7000 F SEM.

IM1.P010
Detection of atomic columns from noisy STEM images

J. Fatermans[1,2], K. Müller-Caspary[1], A. J. den Dekker[2,3], S. van Aert[1]

[1]University of Antwerp, Electron Microscopy for Materials Science (EMAT), Antwerp, Belgium
[2]University of Antwerp, Vision Lab, Antwerp, Belgium
[3]Delft University of Technology, Delft Center for Systems and Controls, Delft, Netherlands

jarmo.fatermans@uantwerpen.be

Structure parameters from scanning transmission electron microscopy (STEM) images are commonly determined by using a physics-based model describing the image data. More precisely, the atomic column positions and intensities are estimated by performing a model-fitting approach. Such an approach is generally referred to as statistical parameter estimation [1,2]. Hereby, the number of atomic columns needs to be specified beforehand. This number can be estimated by visual inspection of the image when the signal-to-noise ratio (SNR) is sufficiently high.
In case of noisy STEM images a visual inspection is unreliable and may lead to wrong structure information. Therefore, a selection procedure is needed to make a better decision on the number of atomic columns which are present in the image data. In this work, the maximum a posteriori (MAP) probability rule is proposed as a model-order selection method to detect atomic columns from STEM images, making use of a Bayesian framework [3]. An analytical expression for the MAP rule is derived and it is tested whether this rule can retrieve the correct number of atomic columns present in experimental STEM data.
In order to test the MAP probability rule, it has been used to detect the number of atomic columns when imaging a material with known structure, $SrTiO_3$, using high-angle annular dark-field (HAADF) STEM. Images with both low and high SNR have been recorded by using the X-Ant-EM, a probe corrected FEI Titan, operated at 300 kV. The HAADF regime has been selected by using a semi-convergence angle of 21.3 mrad and detector collection range of 58-197 mrad.
Figure 1(a) shows part of a low SNR image of $SrTiO_3$ with an incoming electron dose of $(1.08 \pm 0.05)\cdot 10^4$ $e^-/Å^2$. By using MAP selection, the probabilities of different numbers of atomic columns present in the image can be calculated. The obtained probabilities are compared to each other in a relative way and visualized in figure 1(b) as a probability curve as a function of the number of columns. The curve reaches its maximum for 13 atomic columns, indicating that a configuration consisting of 13 columns, shown in figure 1(c), is most probable to be present in the image. A recorded high SNR image of the same material with an incoming electron dose of $(9.1 \pm 0.4)\cdot 10^5$ $e^-/Å^2$ is illustrated in figure 1(d). The obtained most probable configuration is in agreement with the recorded high SNR image in figure 1(d), which shows that the MAP probability rule has retrieved the correct structure of $SrTiO_3$ from a low SNR image.
The MAP probability rule is able to retrieve the expected number of atomic columns in a recorded HAADF STEM image of $SrTiO_3$ with low SNR. It is expected that MAP selection can be especially useful to detect atomic columns from images of beam sensitive materials where the electron dose should be kept to a minimum in order to avoid damage to the specimen, from images of weakly scattering materials or from images of materials with a random structure, such as small nanoclusters. The proposed method overcomes the limits set by just a visual interpretation of such images.

References:
[1] A. J. den Dekker et al. (2005), *Ultramicroscopy*, 104, 83-106.
[2] S. Van Aert et al. (2016), *International Union of Crystallography Journal*, 3, 71-83.
[3] P. Stoica & Y. Selen (2005), *IEEE Signal Processing Magazine*, 21(4), 36-47.

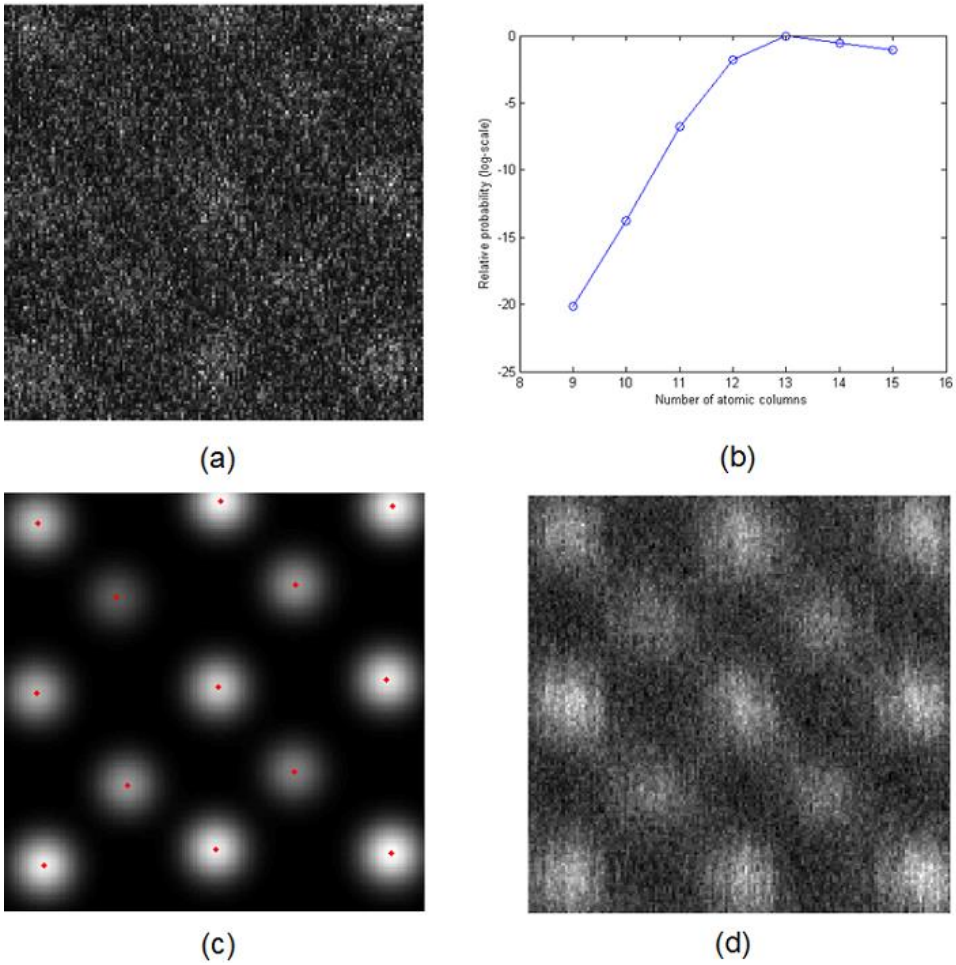

Figure 1. (a) HAADF STEM image of $SrTiO_3$ [100] with an incoming electron dose of $(1.08 \pm 0.05) \cdot 10^4$ $e^-/Å^2$. (b) Probability curve as a function of the number of atomic columns calculated by applying the MAP probability rule on the data shown in (a). (c) Most probable configuration consisting of 13 atomic columns from (a) corresponding to the maximum of the probability curve in (b). (d) HAADF STEM image of $SrTiO_3$ [100] with an incoming electron dose of $(9.1 \pm 0.4) \cdot 10^5$ $e^-/Å^2$.

IM1.P011
A newly developed 120 kV transmission electron microscope for diverse range of users from biomedical to material

T. Fujii[1], K. Tamura[1], H. Mise[2], I. Nagaoki[1], K. Kageyama[2], A. Wakui[3], M. Shirai[3], H. Matsumoto[3]
M. Konomi[4], T. Yaguchi[1]

[1]Hitachi High-Technologies Corporation, Electron Microscope System Design 2nd Dept., Hitachinaka, Ibaraki, Japan
[2]Hitachi High-Technologies Corporation, Electron Microscope Solution System Design Dept., Hitachinaka, Ibaraki, Japan
[3]Hitachi High-Technologies Corporation, Application Development Dept., Hitachinaka, Ibaraki, Japan
[4]Hitachi High-Technologies Corporation, Marketing Dept., Tokyo, Japan

takashi.fujii.uj@hitachi-hightech.com

Introduction: Transmission electron microscopy operated at low acceleration voltage is widely used for investigation not only of biological specimens but also soft materials. We have developed a new 120 kV transmission electron microscope (TEM) relevant to a diverse range of applications.
Objectives: In order to meet the various needs of users and make it possible to observe specimens covering a wide field from biomedical to materials we have developed two types of lens for the 120 kV TEM. The external view of the newly designed TEM is shown in Fig. 1.
System software of the TEM is also improved. The graphical user interface of the software allows easy operation by novice users. In addition, the newly developed software function for TEM image navigation greatly improves visual field search operations.
Method: Improvement of TEM image contrast and reduction of electron beam irradiation damage are especially important for observing a low contrast and beam-sensitive biological specimen. The new TEM achieves this by incorporating a high-contrast objective lens which has a long focal length.
The other new development is a high-resolution objective lens [1] which has a short focal length designed for observing nanomaterials. A single-crystal LaB_6 cathode which provides an electron source of high brightness enables TEM observation at high magnification.
Results: TEM observation with high scattering contrast is achieved through the combination of the objective lens and a small objective aperture which provides a small scattering angle of transmitted electrons for forming a TEM image. Figure 2 shows an image of mouse kidney (unstained section) observed with the new high contrast type lens. Moreover, a high-sensitive CMOS camera used for fluorescent screen observation makes it possible to obtain a TEM image with low electron beam irradiation and capable of observing the whole specimen area.
Another new high resolution type lens provides lattice resolution of 0.19 nm with on-axis illumination at 120 kV. Figure 3 shows a TEM image of Si (100) which was obtained by the new TEM (high resolution type). An automatic operation for acquiring the selected-area electron diffraction (SAED) patterns at the plural analysis positions is available at the TEM [2].
The STEM images of electro catalyst of fuel cell are captured with a LaB6 cathode. As shown in fig. 4, a distribution of metal particulates is clearly observed. The STEM image resolution of the high resolution type at 120 kV is 1 nm. A large-size (100 mm^2) energy dispersive X-ray (EDX) analyzer can be mounted for high-sensitivity elemental composition analysis.
Conclusion: Two types of objective lens have been developed for a new 120 kV TEM. Using a high contrast type lens, unstained biological specimens can be clearly observed. Whilst with the high resolution type lens, 0.19 nm lattice image can be obtained.
Explanations will be provided regarding the details of the instrument and application results.

References:
[1] Kubo, T., et al, 2013. Microsc. Microanal. 19 (Suppl 2), 1328.
[2] Kamino T., et. Al, Proc. of IMC 18, Prague, Czech Republic (2014) IT-6-P-1552.

Figure 1. The newly designed Hitachi Transmission Electron Microscope.

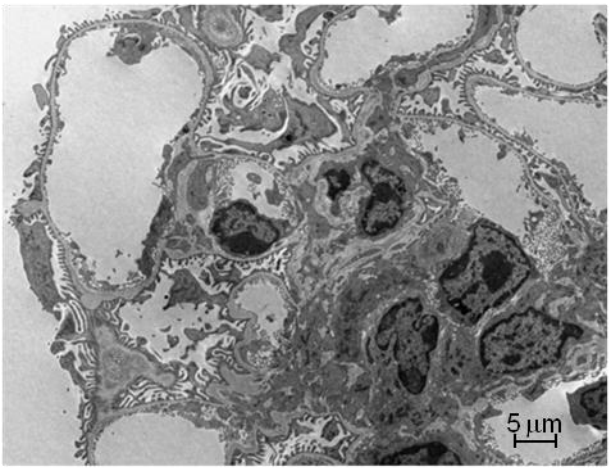

Figure 2. TEM image of mouse kidney (unstained section) obtained by the new 120 kV TEM (high contrast type) for the biomedical field. Acceleration voltage is 80 kV.

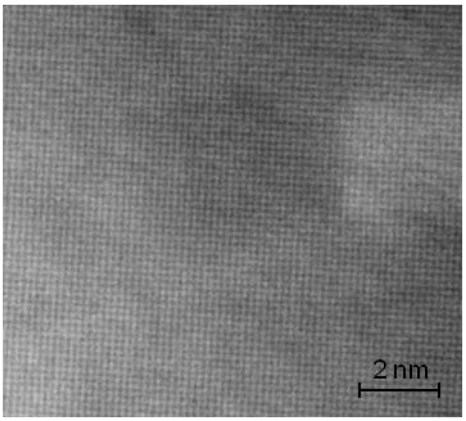

Figure 3. TEM image of Si(100) with the new 120 kV TEM (high resolution type) for the material field. Acceleration voltage is 120 kV.

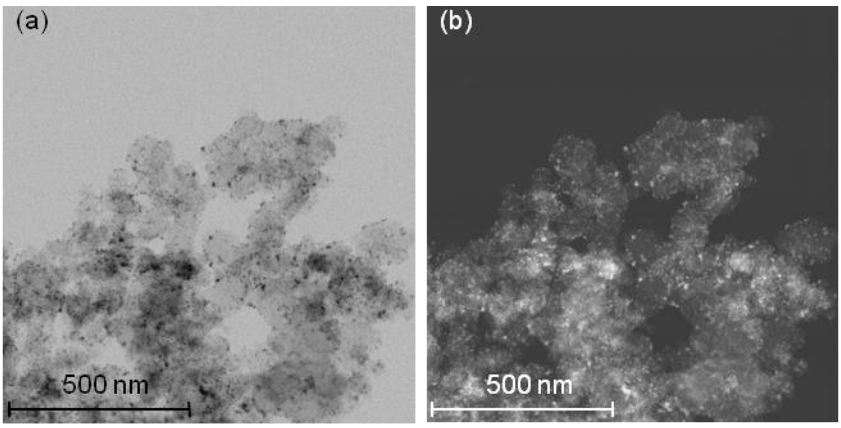

Figure 4. STEM image of materials for a fuel cell with the new 120 kV TEM (high resolution type). (a): bright field image, (b): dark field image.

IM1.P012
Application of high resolution imaging using the voltage-tunable SALVE microscope to study low dimensional materials

J. Biskupek[1], K. Cao[1], T. W. Chamberlain[2,3], C. Stoppiello[2], A. Khlobystov[2], U. Kaiser[1]

[1]Universität Ulm, ZE Elektronenmikrokopie, Materialwissenschaftliche Elektronenmikroskopie, Ulm, Germany
[2]University of Nottingham, School of Chemistry, Nottingham, United Kingdom
[3]University of Leeds, School of Chemistry, Leeds, United Kingdom

johannes.biskupek@uni-ulm.de

We are going to present applications of the dedicated SALVE (sub-Ångstrøm low voltage electron microscopy) instrument. This TEM is equipped with a geometric and chromatic aberration corrector and is voltage-tunable between 20 to 80 kV [1,2]. SALVE delivers corrected phase plates of more than 60 mrad [3].
As many low-dimensional materials have knock-on damage thresholds around 80 kV or lower, we tune the SALVE-TEM below this threshold to image the structures in ultra-high resolution in their pristine states [2]. Figure 1, in which C_{60} molecules filled in single walled carbon nanotubes are imaged at electron beam energies of 80 kV and 30 kV, clearly demonstrates the advantages of low voltage imaging. At 80 kV, the molecules are damaged during electron irradiation while at 30 kV they remain unchanged after imaging with the same dose.
Furthermore, if the voltage-tunable SALVE TEM is operated slightly above the damage threshold it is possible to study structural transformations with much higher resolution than standard instruments. As an example we were able to image the electron beam driven reaction of perchloro-coronene (PCC) molecules transforming in a chlorine terminated graphene nanoribbon with atomic resolution [4].
He we report several further examples including; graphene, boron nitride and functionalized carbon nanotubes, imaged at low voltage revealing unprecedented details about the properties of these low dimensional materials.

References:
[1] http://www.salve-project.de
[2] Kaiser U, Biskupek J, Meyer JC, Leschner J, Lechner L, Rose H, Stöger-Pollach M, Khlobystov AN, Hartel P, Müller H, Haider M, Eyhusen S, Benner G "Transmission Electron microscopy at 20kV for Imaging and spectroscopy", Ultramicroscopy 111 (2011), 1239-1246
[3] Linck M, Hartel P, Uhlemann S, Kahl F, Müller H, Zach J, Haider M, Niestadt M, Bischoff M, Biskupek J, Lee Z, Lehnert T, Börrnert F, Rose H, Kaiser U "Chromatic Aberration Correction for Atomic Resolution TEM Imaging from 20 to 80 kV" Phys. Rev. Let. 117 (2016) 076101
[4] Chamberlain TW, Biskupek J, Skowron ST, Markevich AV, Kurasch S, Reimer O, Walker K, Rance GA, Müllen K et al. "Stop-frame filming and discovery of reaction at the single-molecule level by transmission electron microscopy" ACS Nano (2017) doi: 10.1021/acsnano.6b08228

Acknowledgment
We acknowledge the support of the German Research Foundation (DFG) and the Ministry of Science, Research and the Arts (MWK) of Baden-Wuerttemberg within the frame of the SALVE (Sub Angstrom Low Voltage Electron microscopy) project, ERC Consolidator Grants and EPSRC for financial support.

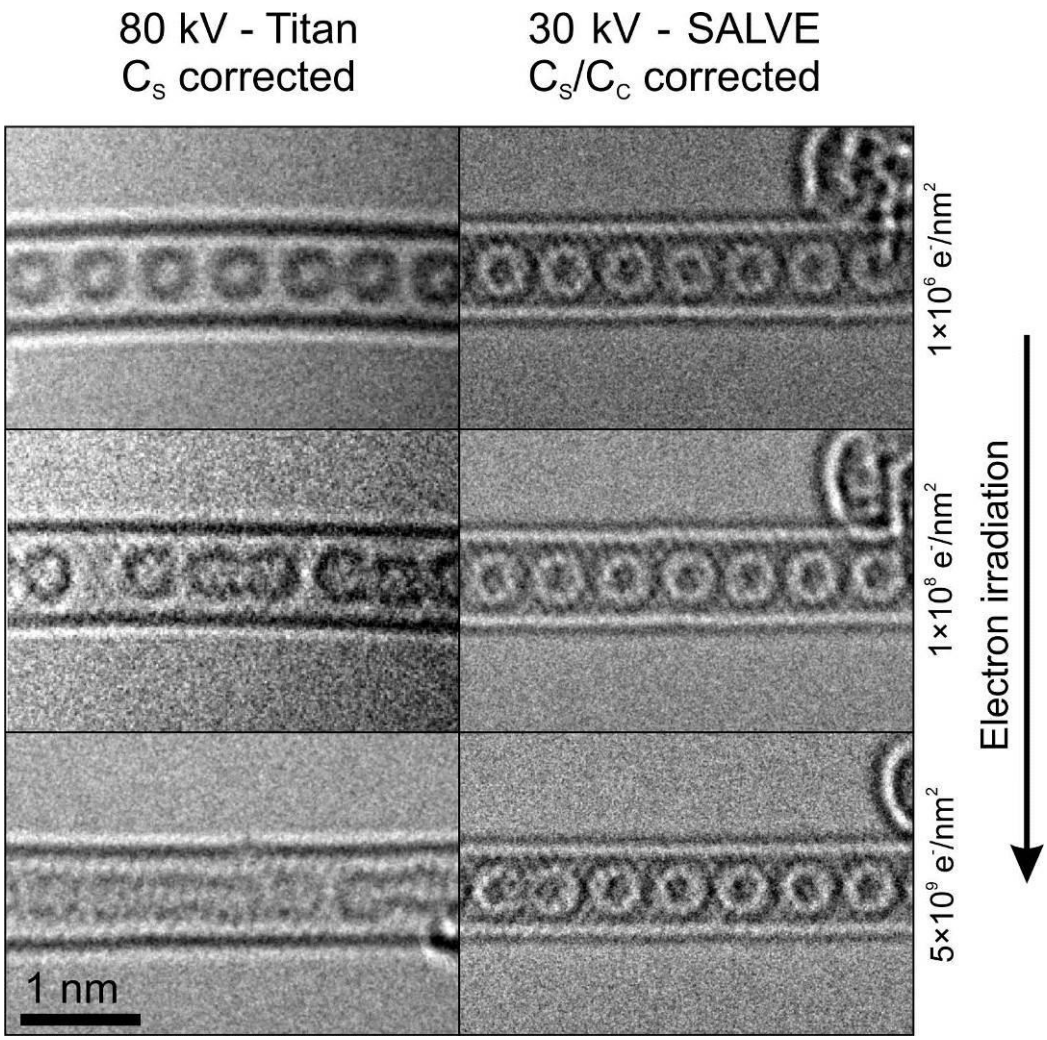

Figure 1. Comparison of the effect electron irradiation of C_{60} molecules in single walled carbon nanotubes at 80 kV and 30 kV (SALVE TEM Cs/Cc corrected).

IM1.P013
A new model-based two-stage classifier for airborne particles analyzed with automated SEM/EDX

J. Rausch[1,2], M. Meier[1,2], R. Locher[3], D. Jaramillo Vogel[1,2], T. Zünd[1], E. Bieler[4], K. Kammer[5]

[1]Particle Vision GmbH, Fribourg, Switzerland
[2]University of Fribourg, Department of Earth Sciences, Fribourg, Switzerland
[3]Zurich University of Applied Sciences (ZHAW), Institute of Data Analysis and Process Design (IDP), Winterthur, Switzerland
[4]University of Basel, Swiss Nanoscience Institute (SNI), Basel, Switzerland
[5]Federal Office for the Environment (FOEN), Bern, Switzerland

juanita.rausch@particle-vision.ch

Particulate Matter (PM) is an important air quality parameter due to its environmental and health impact. Scanning Electron Microscopy (SEM) coupled with Energy Dispersive X-ray spectroscopy (EDX) is able to produce detailed chemical and morphological data of a significant number of single particles, which can be used for source apportionment studies. However, a major issue of this method is the time consuming data treatment and interpretation.

To deal with this issue we developed a particle classifier able to classify homogenous and mixed particles based on their chemical composition. It was trained with SEM/EDX results of > 55000 single particles from different environments (83 samples). The sampling was performed with the Sigma-2 passive sampler [1] on carbon pads and actively on polycarbonate filters. Analyses were run with a FEI XL30 SFEG using an acceleration voltage of 20 keV. Compositional data were ZAF corrected. For particle classification a two stage procedure was applied. The first stage is a rule-based filter grouping particles consisting of the same elements with a content ≥ 5 wt.% into main classes (Fig. 1). In the second stage, a robust model-based clustering method using the R package tclust is applied to each main class resulting in subclasses. The training delivered 465 subclasses within 227 main classes. The subclasses were manually verified and assigned to known substances [2].

The performance of the classifier was tested in different case studies showing that it is a powerful tool for source apportionment studies. We present the results of a project aiming to characterize/quantify PM emitted from the road and railway traffic in the Reuss Valley (Altdorf, Switzerland). This valley is of paramount interest because it is a major north-south freight traffic artery through the Alps. In order to protect the environment and population the freight traffic has been increasingly shifted from the road to the railway. However, a detailed differentiation and quantification of PM from both pollution sources was lacking.

At two emission and two immission sites, located on a transect between the A2 highway and the AlpTransit railway line, samples were taken actively and passively during 4 weeks with sampling periods of 1 week. All 32 samples were analyzed by SEM/EDX and the particles measured were classified as described above. Concentrations of each subclass were plotted along the transect (Fig. 2), showing its potential origin and its dispersion. The transect measurements revealed that the coarse particles (2.5 - 10 µm) from both sources have a small contribution to the immission sites. However, under specific meteorological conditions (e.g. high wind velocities in a prevalent direction) this fraction can be dispersed over much longer distances. In contrast, particles ≤ 2.5 µm are finely dispersed in the air independent of the wind conditions. Thus, the fine fraction measured away from the source mainly represents a background concentration.

This study shows that particles emitted by railway and road traffic are partially similar (e.g. Fe-rich particles derived from railway, wheel, vehicle and/or brake wear). However, road traffic emissions are by far more heterogeneous consisting of at least 47 different chemical subclasses. Many of them can be apportioned to heterogeneous mixtures of tire wear (Figs. 2 and 3).

References:

[1] VDI, VDI2119:2013-06, Beuth Verlag, 10772, Berlin, Germany, 2013

[2] This work was financially supported by the Swiss Commission for Technology and Innovation (CTI project 16675.1 PFIW-IW).

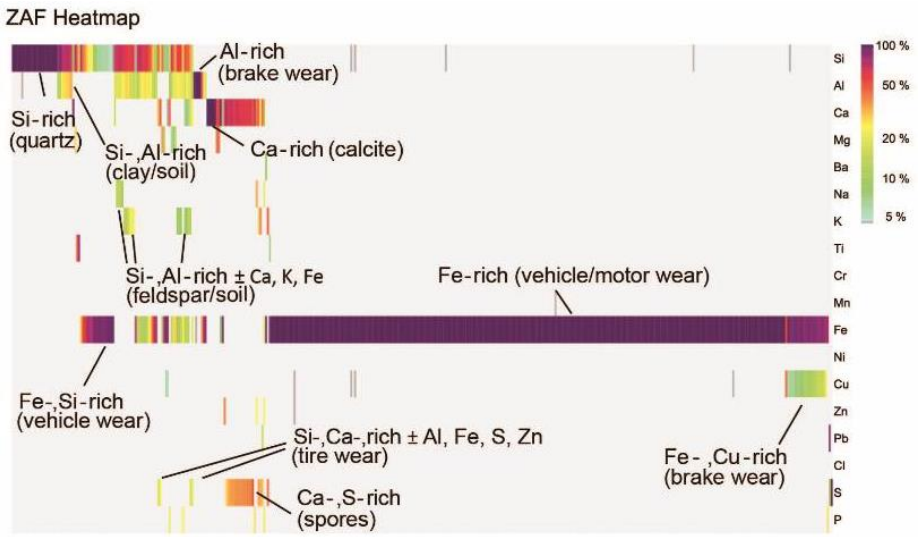

Figure 1. Heatmap showing typical classes and subclasses for a road traffic site.

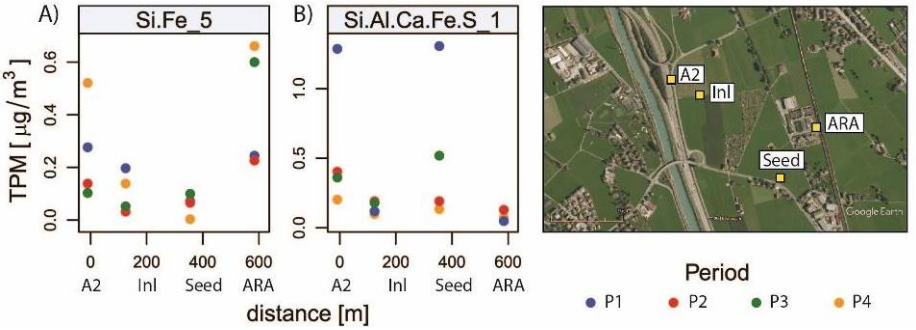

Figure 2. A) Total PM transect plot of the subclass Si.Fe_5 (railway, wheel and vehicle wear) and B) Si.Al.Ca.Fe.S_1 (tire wear). Inset map: location of sites.

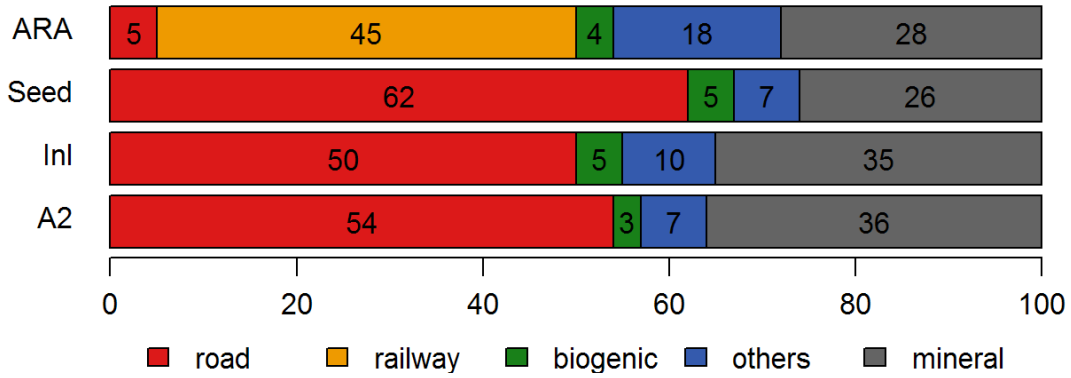

Figure 3. Bar diagram showing the particle number concentration of the main sources (i.e. mineral, biogenic, road, railway traffic and others) at the 4 studied sites averaged for the 4 periods.

IM1.P014
Ultra-low dose STEM via compressed sensing without rapid beam blanker

J. Spiegelberg[1], J. C. Idrobo[2], J. Hachtel[2], J. Rusz[1]

[1]Uppsala University, Physics and Astronomy, Uppsala, Sweden
[2]Oak Ridge National Laboratory, Center for Nanophase Materials Sciences, Oak Ridge, TN, United States of America

jakob.spiegelberg@physics.uu.se

Compressed sensing (CS) techniques offer a perspective to reconstruct images from undersampled input images with potentially large undersampling rates, i.e., few active pixels ([1],[2]). In the context of STEM imaging applications, CS can be applied to, e.g., drastically reduce the dose needed for the acquisition of the image, to increase the field of vision or to decrease the acquisition time for a STEM image of given size, all of which pushes the limits of todays STEM. However, an experimental realization of CS experiments is more challenging as hysteresis loops in the micrscopes scanning coils prohibit rapid changes of the scanning directions needed to acquire a randomly sampled image. Alternatively, a rapid beam blanker needs to be installed into the beam line to block the beam whenever a dark pixel on a pre-defined, random scanning grid is approached [2].
From an experimental perspective, it would, however, be advantageous to avoid the random sampling pattern altogether. Using a regular sampling grid, images with $1/n^2$ % active pixels can easily be measured by decreasing the magnification by a factor of n. Thus, if a CS algorithm could cope with a regular scanning grid, this algorithm would allow CS-STEM measurements to be performed on any standard STEM instrument.
In this talk, we present a new CS algorithm, dictionary local low rank CS (d-LLR-CS) [3], which does not require random sampling. Hence, d-LLR-CS overcomes the needs of dedicated beam blanker allowing c-LLR-CS to be measured on a standard STEM. Moreover, we demonstrate how d-LLR-CS is able to correctly recover simulated and experimental STEM images with as few as 4% of active pixels (corresponding to an undersampling of 96%), which is the highest reported undersampling within microscopy to our knowledge.
In conclusion, our findings not only push the limits of CS-STEM, but bring the technique to thousands of laboratories worldwide.

[1] H. S. Anderson et al., Proc. SPIE 8657 (2013).
[2] A. Béché et al., Appl. Phys. Lett. 108 (2016).
[3] J. Spiegelberg et al., Manuscript.

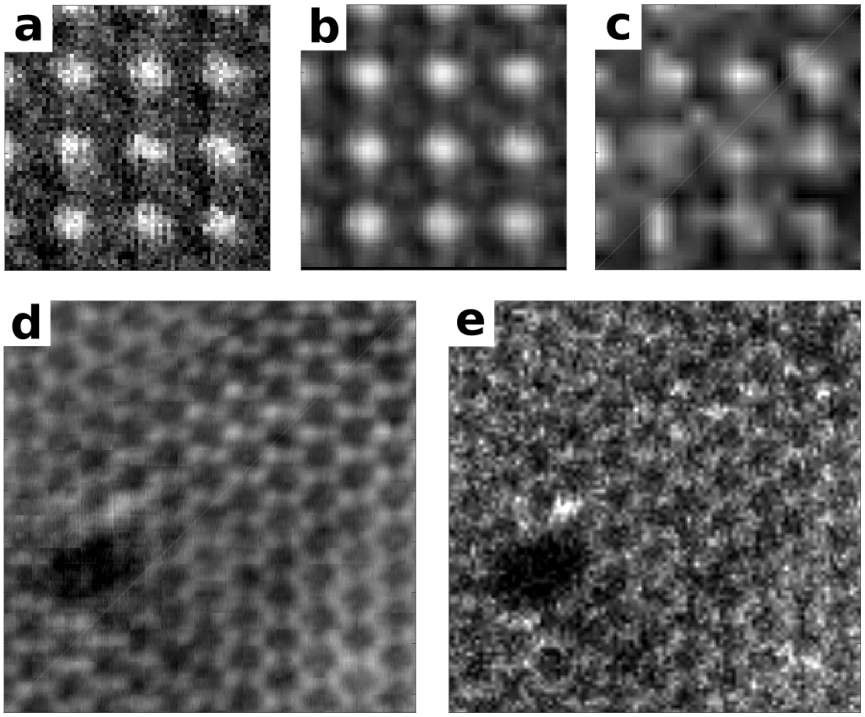

Figure 1. (a) Section of an experimental STEM image of a LaMnAsO crystal from which an undersampled image using only 4% of the pixels was created. (b) Reconstructed image using d-LLR-CS. (c) Reconstructed image using linear interpolation. (d,e) Sections of reconstructed images of an experimentally undersampled STEM image (6.25% active pixels) of a $MoWSe_2$ single layer with defect. The reconstrructions were performed using d-LLR-CS (d) and linear interpolation (e).

IM1.P015
Low-energy scanning transmission electron microscopy for high-resolution characterization of solid-state and soft-matter samples

C. Sun[1], E. Müller[1], H. Blank[1], T. Vystavel[2], D. Gerthsen[1]

[1]Karlsruhe Institute of Technology, Laboratory for Electron Microscopy, Karlsruhe, Germany
[2]Thermo Fisher Scientific, Brno, Czech Republic

cheng.sun@kit.edu

Scanning transmission electron microscopy at electron energies ≤ 30 keV (low-keV STEM) in a scanning electron microscope (SEM) is promising for the study of a large variety of materials. It is particularly interesting for beam-sensitive samples because knock-on damage is inherently reduced. Another advantage of low-keV STEM is the enhanced material contrast in the high-angle annular dark-field (HAADF)-STEM mode especially for materials with low atomic number or similar material densities. Carbonaceous materials, like organic solar cells, exhibit high contrast compared to using transmission electron microscopy (TEM) [1].

The results of the study of various samples are presented in this work to demonstrate application range of low-keV STEM. It is important to note that low-keV STEM can be combined with SEM which yields additional valuable information. Two DualBeam instruments, a FEI Strata 400S and a FEI Helios G4 FX, equipped with multi-segmented STEM detector were used.

Imaging magnetic materials is challenging in TEM where the specimen is situated in the magnetic field of the objective lens while it is straightforward by low-keV STEM in the field-free mode. Fig. 1a shows low-magnification SEM image of a strongly magnetic FeNiC steel sample which shows the grain structure of the chemically etched specimen. It facilitates reliable size measurements of large grains by SEM imaging of large surface regions. The bright-field (BF)-STEM image Fig. 1b from the electron-transparent specimen region shows diffraction contrast from dislocations.

Low-keV STEM is particularly suited to image nanoparticles with an inherent small specimen thickness. This is demonstrated by Fig. 2a which shows a HAADF-STEM image of CeO2 nanoparticles surrounded by a carbon-contamination layer. Fig. 2b shows a BF-STEM image of a multi-walled carbon nanostructure surrounding a catalyst particle, lattice fringes corresponding to planes with spacing 0.34 nm are clearly resolved.

Fig. 3 shows a 15 keV HAADF STEM image of a thin section of a HT29 colon carcinoma cell, which was incubated with SiO2 nanoparticles. OsO4 was used for fixation of the cell during the TEM specimen preparation. Membranes of the mitochondrion (M) and multivesicular body (MB) containing SiO2 nanoparticles are seen with high contrast and good resolution although poststaining was omitted in the specimen preparation procedure.

Low-keV STEM in combination with SEM is well suited to study a large variety of solid-state and soft-matter samples. Diffraction contrast can be used for defect analysis. Strong material contrast in life-sciences samples is obtained by HAADF-STEM. The application of low-energy STEM will become even more attractive with the new generation of scanning electron microscopes where lattice-fringe resolution is possible [2].

[1] M. Pfaff et al., Micros. Microanal. 18, 1380 (2012).
[2] We acknowledge funding of the project by the Deutsche Forschungsgemeinschaft (DFG) and thank Prof. Dr. Doris Marko (University of Vienna) for providing the HT-29 specimen.

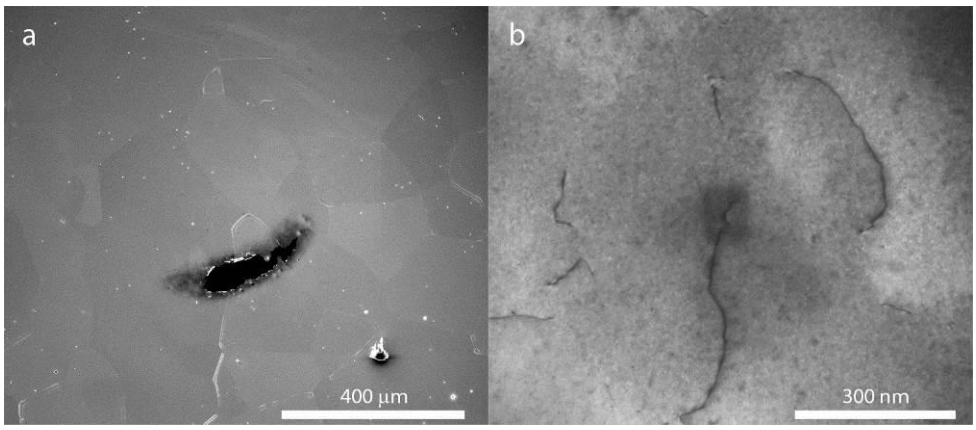

Figure 1. (a) 10 keV low-magnification SEM image of the surface topography of a magnetic steel sample and (b) 25 keV BF-STEM image from the electron transparent specimen region.

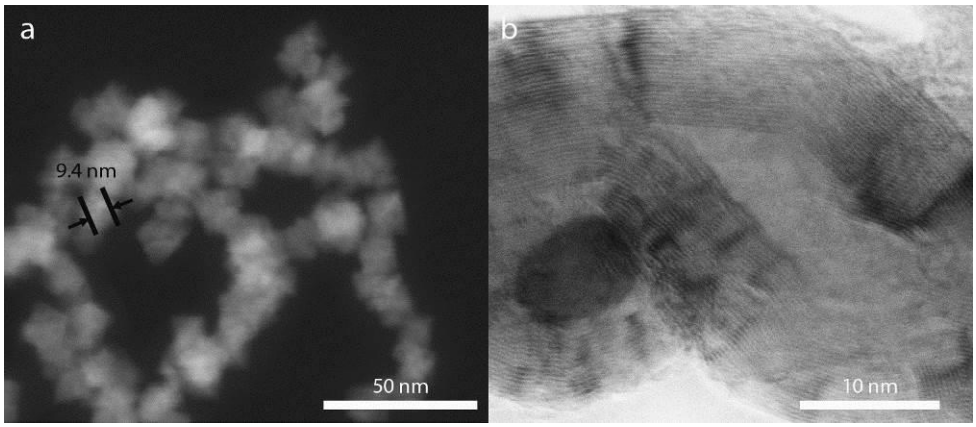

Figure 2. (a) 30 keV HAADF-STEM image of CeO2 nanoparticles and (b) 30 keV BF-STEM image of a section of a multi-walled carbon nanostructure surrounding a metallic catalyst particle.

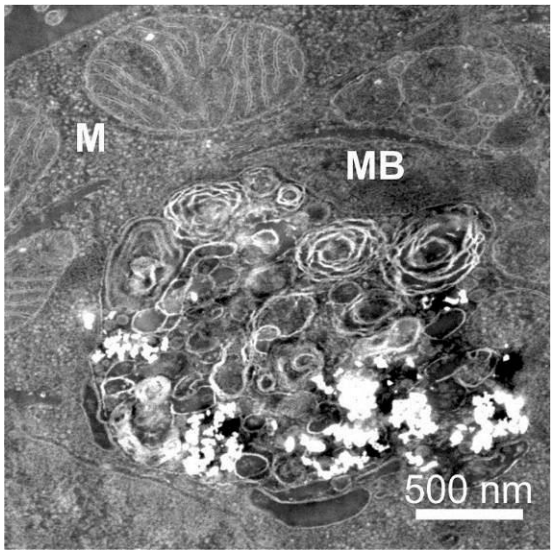

Figure 3. 15 keV HAADF-STEM image of a thin section of a HT-29 colon carcinoma cell with strong membrane contrast.

IM1.P016
Nanoscale thermal conduction analysis of thermoelectric $CuFeS_2$ by using nanothermocouple in STEM

N. Kawamoto[1], Y. Kakefuda[1], I. Yamada[1], N. Tsujii[1], M. Mitome[1], Y. Bando[1], T. Mori[1], D. Golberg[1,2]

[1]National Institute for Mateials Science (NIMS), MANA, Tsukuba, Japan
[2]Queensland University of Technology (QUT), Brisbane, Australia

kawamoto.naoyuki@nims.go.jp

Much attention has been given to simultaneous analysis of advanced microstructures and their physical properties, such as electrical, mechanical, and magnetic ones by using probing techniques in a transmission electron microscope (TEM). For instance, *in-situ* TEM observations using a scanning tunneling microscopy (STM)–TEM holder with piezodriven mechanics have revealed electrical properties of individual carbon nanotubes (CNTs) [1], graphene [2], BN nanoribbons [3], and nanowires [4]. Also, using STM-TEM holders, the lithiation processes of Li ion batteries using nanowire electrodes were uncovered [5], [6]. Besides, it is expected that thermal properties of advanced nanoscale materials may be studied in TEM. Especially, it is highly desirable to develop an advanced technique for simultaneous observation of a microstructure, such as its lattice defects, grain boundaries, and impurities which induce phonon scattering, and its thermal conductivity in order to reveal thermal transport at nanoscale.
In this study we developed STEM-based thermal analytical microscopy (STAM) by combining nanoscale temperature measurements using a three-dimensionally controllable nanothermocouple and a scanning heat input through focused electron beam irradiation using scanning transmission electron microscopy (STEM) mode in a 300 keV JEM-3100FEF microscope. In order to make non-magnetic constantan (Cu-Ni) and chromel (Cr-Ni) nanoprobes [7], [8] used for the nanoscale thermocouple, constantan and chromel wires, whose diameters were 200 μm, were sharpened by an electrochemical etching method [9] to diameters below 10 nm. A TEM specimen was prepared by using a focused ion beam (FIB) system under accelerating voltage of 30 kV. The specimen thickness was controlled to be about 300 nm to input a sufficient heat by a focused electron beam in STEM.
As shown in a high-angular annular dark field (HAADF)-STEM image of Figure 1(a), the nanoscale thermocouple was attached to the corner of a TEM specimen at the point M for temperature measurement. A STAM image in Fig. 1(b) of the same area as in Fig. 1(a) was obtained by using a heat input from the scanning electron beam of a constant current. The STAM image shows a two-dimensional temperature map acquired at the point M using the thermocouple. From the HAADF-STEM image in Fig. 1(a), it is seen that the homogeneous $CuFeS_2$ layer *I* and inhomogeneous $CuFeS_2$ layer *II* are stacked on an impurity layer/glass substrate. In the STAM image temperature gradient within the layer *I* in the direction parallel to a blue dotted line was acquired, Fig. 1(b); the temperature is gradually decreasing with increasing the distance from the M point thus following the Fourier"s Law. In the presentation, we will discuss the thermal analysis of the local area around the inhomogeneous $CuFeS_2$ layer.

[1] Z. L. Wang, P. Poncharal, and W.A. de Heer, J. Phys. Chem. Sol. **61**, (2000), p. 1025.
[2] A. K. Schaper, H. Hou, M. S. Wang, Y. Bando, and D. Golberg, Carbon **49**, (2011), p. 1821.
[3] H. Zeng, C. Y. Zhi, Z. H. Zhang, X. L. Wei, X. B. Wang, W. L. Guo, Y. Bando, and D. Golberg, Nano Lett. **10**, (2010), p. 5049.
[4] Z. Xu, Y. Bando, W. L. Wang, X. D. Bai, and D. Golberg, ACS Nano **4**, (2010), p. 2515.
[5] X. Wang, D. M. Tang, H. L, W. Yi, T. Zhai, Y. Bando, and D. Golberg, Chem. Commun. **48**, (2012), p. 4812.
[6] N. Kawamoto, D. M. Tang, X. Wei, X. Wang, M. Mitome, Y. Bando, and D. Golberg, Microscopy **62**, (2013), p. 157.
[7] N. Kawamoto, Y. Kakefuda, T. Mori, K. Hirose, M. Mitome, Y. Bando, and D. Golberg, Nanotechnology **26**, (2015), p. 465705.
[8] N. Kawamoto, M. S. Wang, X. Wei, D. M. Tang, Y. Murakami, D. Shindo, M. Mitome, and D. Golberg, Nanotechnology **22**, (2011), p. 485707.
[9] R. Kasshing, and E. Oesterschulze, Proceedings of the NATO Advanced Study Institute (Sesimbra, Portugal), (1996), p. 35.

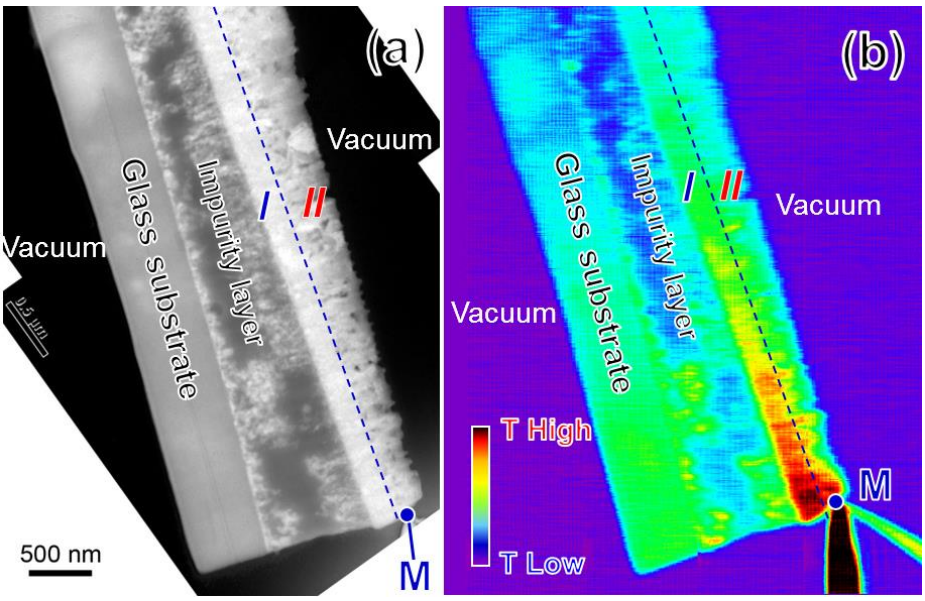

Figure 1. (a) HAADF-STEM image of a cross-sectional complex specimen of $CuFeS_2$/impurity layer/glass with a thermocouple attached to the corner of $CuFeS_2$ portion (M-point) (b) STAM image of the same area as in (a).

IM1.P017
A new tool for high-contrast STEM imaging of biological samples

S. Zachej[1], M. Petrov[1], J. Dluhos[1], M. Bilik[1], J. Dumkova[2], A. Hampl[2], M. Buchtova[3]

[1]TESCAN Brno, R&D Applications, Brno, Czech Republic
[2]Faculty of Medicine, Masaryk University, Department of Histology and Embryology, Brno, Czech Republic
[3]Czech Academy of Science, Institute of Animal Physiology and Genetics, Brno, Czech Republic

samuel.zachej@tescan.com

Introduction: Life science research increasingly uses ultra-thin biological specimens, nanomaterials and their combinations to study morphology and function of biological structures. Scanning transmission electron microscopy (STEM) has become a widely-used method because of its universality and the ability to study various specimens inside a single scanning electron microscope (SEM).
Routine STEM imaging in bright field (BF), dark field (DF) or high-angle dark field (HADF) mode may not be sufficient for light-element biological specimens. High-energy electrons are scattered only into low angles by biological samples that are almost electron-transparent. Thus, a major portion of the contrast information is hidden in the bright field signal. Signal filtering masks and limiting apertures enable image formation from electrons scattered only at very low angles, which leads to the enhancement of structural and material contrast [1].
Objectives: The goal of the study is to demonstrate the improvement in contrast information gathered from low-scattering structures, using different bright-field selection apertures. In addition, limitation of the bright field signal should lead to contrast enhancement mainly on thin biological sections [2]. The difference is demonstrated on carbon nanotubes (CNTs) and resin-embedded sections of various thicknesses.
Materials and Methods: A new versatile detection approach by TESCAN was used to enhance image contrast in the bright field signal by using a bright field selection aperture (Fig. 1a - BF selection aperture in the TESCAN STEM detector). Changing the sample position with respect to the STEM detector (using a compatible STEM sample holder) allows the user to optimize image contrast by selecting a suitable angular distribution of the detected electrons (Fig. 1b - Angular distribution of forward-scattered electrons in a non-immersion system).
The STEM-BF mode with a 30 keV primary beam was used to observe a suspension of CNTs on a standard 3 mm TEM grid. Apertures with different sizes were used to compare the contrast in the obtained images. In addition, thin sections of resin-embedded tissues with various thicknesses were prepared to study the contrast on membranous structures.
Results: CNTs used in the experiment were observed with different BF selection apertures. The resulting contrast enhancement is presented in Fig. 2 - Contrast improvement for low scattering CNTs with different bright field apertures: 50 mrad (left), 25 mrad (middle) and 5 mrad (right). Equipment used: TESCAN MAIA 3 model 2016 (30 kV). The smaller the aperture size, the more significant improvement of the contrast of low scattering CNTs. Tiny surface structures not visible e.g., with the 50 mrad aperture, were highlighted using the small BF aperture.
Conclusion: Filtration of the bright field signal using selective apertures enhances the capabilities of the standard STEM system, enabling life scientists to explore light-element specimens with reasonable structural and material contrast. This was successfully demonstrated on low-contrast CNTs and thin sections with different thicknesses, where significant enhancement in contrast was observed.

References:
[1] J. Holm, R.R. Keller, Ultramicroscopy 167 (2016), 43-56
[2] J. Nebesářová et al., Microscopy Research and Technique 79 (2016), 512-517

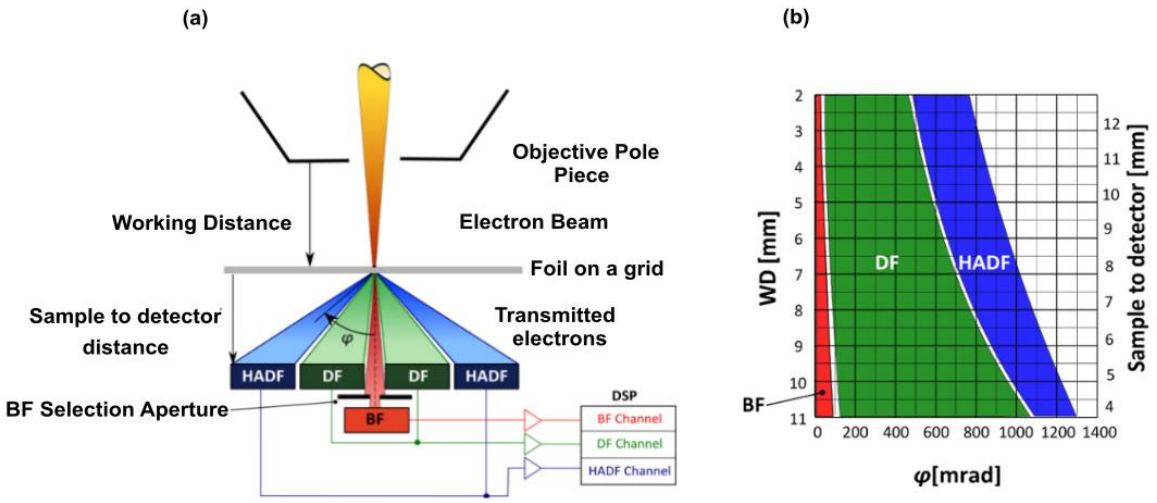

Figure 1. (a) BF selection aperture in the TESCAN STEM detector. (b) Angular distribution of forward-scattered electrons in a non-immersion system.

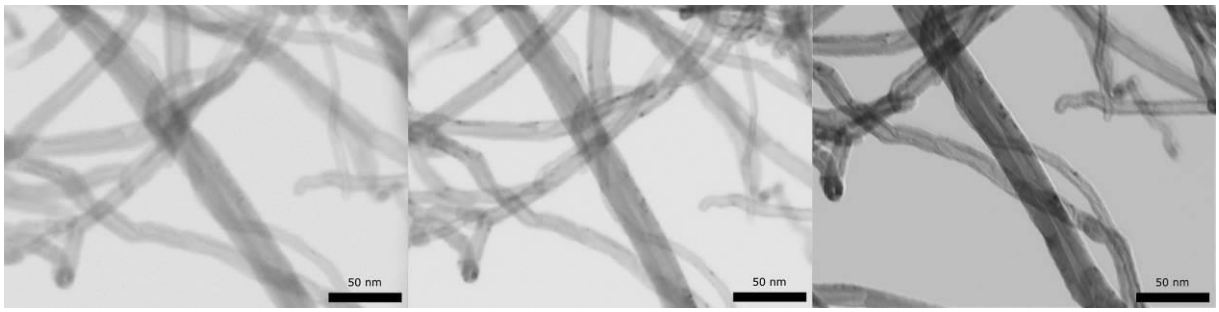

Figure 2. Contrast improvement for low scattering CNTs with different bright field apertures: 50 mrad (left), 25 mrad (middle) and 5 mrad (right).

IM1.P018
Composition determination of multinary III/V semiconductors via STEM HAADF multislice simulations.

L. Duschek[1], A. Beyer[1], J. O. Oelerich[1], K. Volz[1]

[1]Philipps-Universität Marburg, Materials Science Center and Faculty of Physics, Marburg, Germany

lennart.duschek@physik.uni-marburg.de

The composition determination for any multinary semiconductor material is an important field in material sciences. For compound semiconductors with more than three atomic species involved, there is no well-established characterization method for composition determination yet, such as high resolution x-ray diffraction (HRXRD) for ternary materials.
In this work, we describe a procedure to determine the composition of multinary III/V semiconductors at atomic resolution using high angle annular dark field (HAADF) multislice scanning transmission electron microscopy (STEM) simulations for the example of Ga(NAsP).
The method presented here follows the approach to compare HAADF STEM intensities, with a set of STEM multislice simulations and thereby to quantify the elemental composition at atomic resolution. Hereby the intensity is split into group III, V and background (BG) positions, i.e. the positions between the atomic columns. The set contains 150 simulations with systematically varied N and P composition for the chosen example of Ga(NAsP). The N as well as the P atoms were distributed randomly on the group V lattice positions of a GaAs matrix and the resulting cell was relaxed via a valence force field (VFF) routine [1], minimizing the total energy. The numerical simulations were performed with the STEMsalabim software package [2] based on the multislice algorithm of Kirkland [3] on a high performance computing cluster.
The main goal of the presented algorithm is to find the smallest deviation between input values $\bar{I}^{\,\mathrm{exp}}_{III,V,BG}(\theta_{in-out})$ and *composition maps* $I_{III,V,BG}(\theta_{in-out})$, built from the multislice simulation set. The *composition maps* represent the integrated STEM intensity with a fixed radius *r* on distinct spatial positions, i.e. group III, V and the background positions as a function of N and P composition. With this, individual *deviation maps* $I^{\Delta}_{III,V,BG}(\theta_{in-out})$ can be formed via:

$$I^{\Delta}_{III}(\theta_{in-out}) = \frac{|I_{III}(\theta_{in-out}) - \bar{I}^{\,\mathrm{exp}}_{III}(\theta_{in-out})|}{I_{III}(\theta_{in-out})}.$$

These normalized maps represent the deviation between the input values and the *composition maps* as a function of N and P composition. By combining the information gained from the individual *deviation maps* to a *total deviation map* via:

$$I^{\Delta}_{\mathrm{total}} = \frac{\sum_{j=1}^{M} I^{\Delta}_{III}(\theta_j) + I^{\Delta}_{V}(\theta_j) + I^{\Delta}_{BG}(\theta_j)}{3 \cdot M},$$

where the used detector ranges are represented by $\theta_1 \ldots \theta_M$. We can now identify the global minimum of all individual maps at once which gives us the N and P concentration with the best agreement between input values and individual *deviation maps.* To check if the algorithm is self-consistent, a sanity check with two exemplarily chosen simulated Ga(NAsP) alloys was performed, with the results of $\mathrm{I}^{\Delta}_{\mathrm{total}}$ depicted in Figure 1.
With the sanity check we could show that the presented algorithm is perfectly self-consistent. Furthermore, we applied the method to an experimental HAADF STEM image and determined the composition. With this we presented that it is possible to determine the concentration of a quaternary semiconductor alloy via STEM images at atomic resolution without further information from any additional method. This method has great potential to be implemented in the standard workflow when investigating semiconductor alloys with STEM.

[1] P. N. Keating, *Phys. Rev.*, vol. 145, no. 2, pp. 637–645, 1966.
[2] J. O. Oelerich, L. Duschek, J. Belz, A. Beyer, S. D. Baranovskii, and K. Volz, *Submitted to Ultramicropscopy.*, 2016.
[3] E. J. Kirkland, *J. Appl. Cryst*, vol. 32, pp. 378–379, 1999.

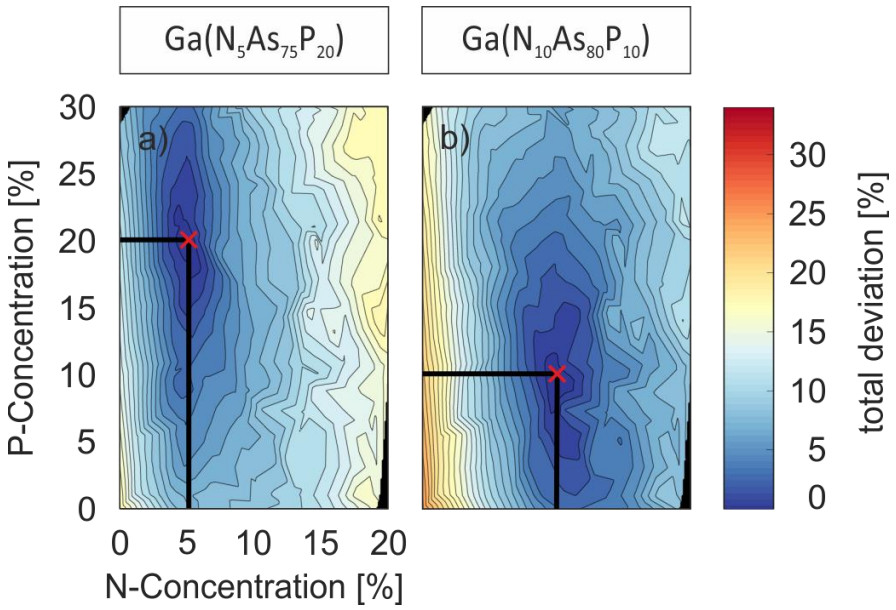

Figure 1. Sanity check of the algorithm with two different input compositions. The total deviation maps show a minimum area of total deviation around the input composition. The red cross marks the global minimum of the map and thus the calculated N-P composition. The black lines separates plateaus with 1 % error steps. The composition axes from subfigure (a) applies to all subfigures in the figure.

IM1.P019
Newly developed heavy-duty stage for high resolution imaging and analysis of 10kg-samples in a scanning electron microscope with focused ion beam

S. Elgeti[1], M. Balden[1], R. Neu[1]

[1]Max-Planck-Inst. f. Plasmaphysik, E2M, Garching, Germany

stefan.elgeti@ipp.mpg.de

In the research for future fusion power plants large experimental devices are used which generate hydrogen plasmas at several million degrees Celsius. A cage of magnetic fields confines the plasma and minimizes the contact with the plasma facing material (PFM) protecting the wall of the vacuum vessel. Nevertheless, the PFM is loaded by particle flux, heat and radiation. In particular regions the plasma is even guided to the PFM (so called divertor) to exhaust the impurities from the plasma. The PFM-tiles or PFM-components have the dimensions of tens of centimeters, particularly if they are actively cooled. They consist of different materials as carbon, steel, and tungsten, alloyed or coated.
In this contribution analyses using scanning electron microscope (SEM) with focused ion beam (FIB) are applied to study in various projects the erosion, deposition, and transformation of the morphology at the surface and near-surface on the tiles and components. In our new SEM-device, the maximal sample size is limited laterally to 44 cm and for the weight to 10 kg. A sample area of 10x23 cm can be reached for imaging and analysing by lateral stage movement and tilting of 60°. The sample height can extend up to 6 cm with full rotation, and 10 cm without the ability of rotation. The imaging resolution achieved is better than 5 nm. With this new heavy-duty stage developed by Kammrath&Weiss together with ZEISS tiles can be analysed without previous cutting and iterative studies of exposure and imaging/analyzing become possible (Fig.1).
FIB cross-sections are prepared and a multiple gas injection system with N_2, XeF_2, C, Pt, W allows analyzing insulated materials, chemical assisted FIB-cutting and coating of different marker for erosion measurements, respectively. Energy and wavelength dispersive x-ray spectroscopy (EDS/WDS, Bruker) allow mapping of the elemental distribution before and after exposure. By using a low energy beam (3-5 keV) small features can be investigated by assisted WDS maps to separate clearly x-ray lines in the low energy range (<3keV).
As one example of the first investigation with the heavy-duty stage fig. 2 shows the surface (a) of a plasma loaded PFM-tile (5 kg) made of tungsten powder (50 µm) sintered in a Fe/Ni-matrix, the element distribution is color coded in the EDS-map (b) Ni red, C yellow, W blue. The width of image frame (WIF) is 570 µm. The morphology in near surface region shows fig. 3, (a) the surface (WIF 300 µm) with marked position of the shown cross section (b) (WIF 40 µm). On the surface are lamellas of tungsten with Ni/Fe (dark) deposits. At higher loaded regions of this tile, the roughness of the surface considerably increased probably by arc burning during plasma exposure. A high magnification image (WIF 2.3 µm) strongly sloped and with bubbles fine structured surface is shown in fig. 4.
This heavy-duty stage proves that heavy samples up to 10 kg can be handled by standard microscopes and software. The high resolution imaging and analyses are achievable, the vibrations and weights can be controlled. With this technique new experiments becomes possible like iterative loading and imaging, and sensitive surfaces can be analysed without danger of damage of the surface by sample preparation as cutting.

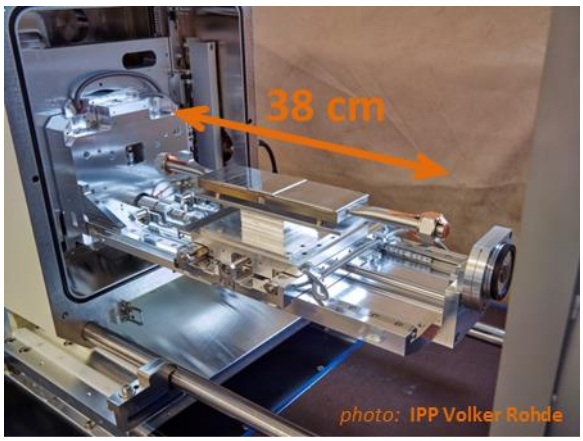

Figure 1. Heavy-duty stage with PFM test-tile with connections for water cooling.

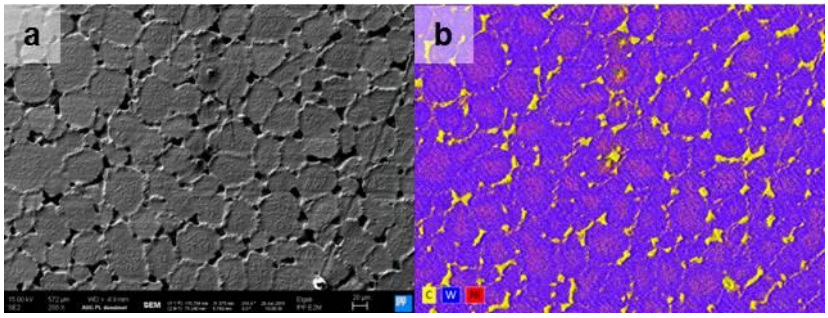

Figure 2. WIF 570 µm, plasma loaded surface of Fe/Ni sintered W, a) SEM image, b) EDS-map of C, W, Ni.

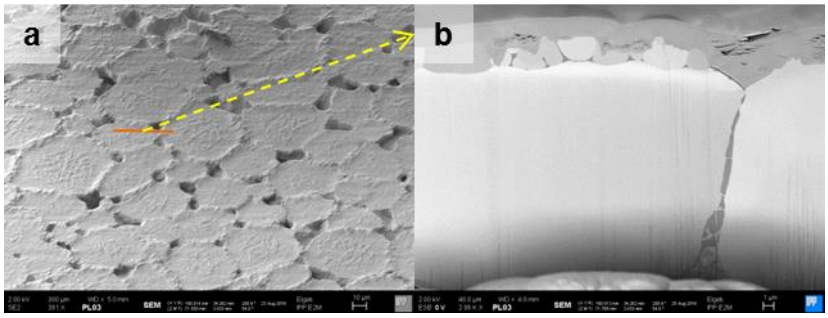

Figure 3. WIF 300 µm, PFM test-tile, a) plasma loaded surface with marked position of the FIB cut, b) cross section of the FIB cut.

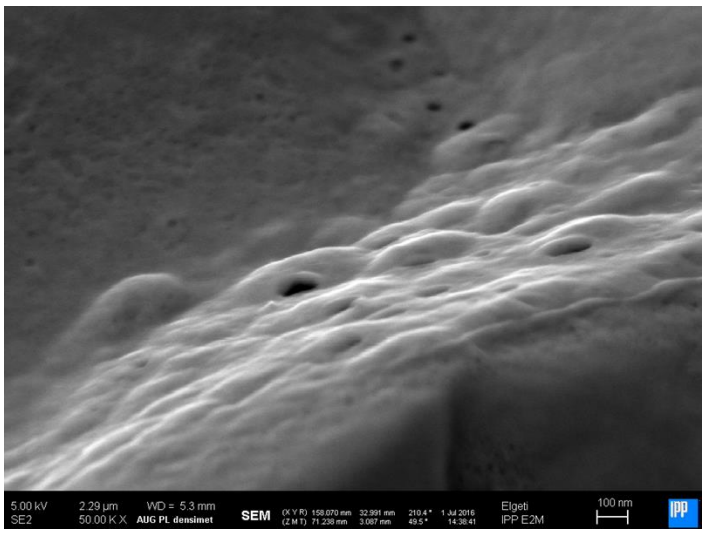

Figure 4. WIF 2.3 µm, SEM-image with high magnification of a plasma loaded region with high roughness and fine structured surface by arc burning.

IM1.P020
Sub 30meV energy resolution in the monochromated Themis transmission electron microscope

B. Freitag[1], P. Tiemeijer[1]

[1]Thermo Fisher Scientific, Eindhoven, Netherlands

Sorin.Lazar@fei.com

When the FEI monochromator was introduced in 2001 [1], the main application in material sciences was unravelling the fine structure in EELS core losses. To this end, its design was optimized for an energy resolution of 0.1eV at HT= 200kV and probe current >100pA. Since then, applications of the monochromator have diverged to a wider range, such as bandgap measurements [2], reduction of chromatic blur [3], and plasmon mapping [4]. Improving the resolution of our monochromator to 0.05eV (for plasmon mapping) or reducing it to 0.2eV (for reduction of chromatic blur) was possible since the dispersion of our monochromator, being based on the Wiener filter principle, can be varied continuously. However, stimulated by the recently generated interest for observing phonons in the electron microscope [5], which requires an even better energy resolution, we revisited the optics of our monochromator. We optimized the system (without compromising on standard performance of the Themis) to circumvent the resolution limits previously set by instabilities and aberrations. This resulted in an energy resolution between 25meV and 30meV at 60kV acceleration voltage. Figure 1 shows BN phonon peaks observed using this improved optics.

References:
[1] P.C. Tiemeijer et al., Microscopy and Microanalysis 7, suppl 2 (2001) 1130
[2] S. Lazar et al., Ultramicroscopy 96 (2003) 535
[3] C. Girit et al., Science 323 (2009) 1705
[4] D. Rossouw et al., Nano Letters 11 (2011) 1499
[5] O. Krivanek et al., Nature 514 (2014) 209

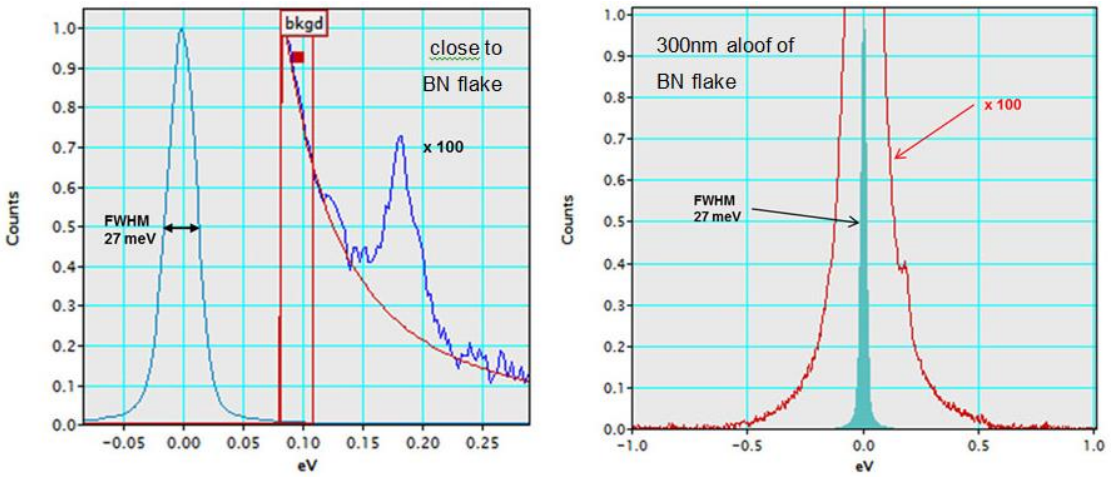

Figure 1. Sub-30meV with a monochromated Themis with Quantum 966 at 60kV. Left: BN phonon peak with FWHM of the ZLP and phonon peaks of 27meV; collection time 25ms. The phonon peak is magnified 100 times**.** Right: ZLP recorded in vacuum 300nm aloof of the specimen; the BN phonon is still observable. The spectrum is magnified 100x to show the tails of the ZLP. Collection time 300ms.

IM1.P021
Calculation of topography independent backscattering coefficient from 4 quadrant BSE detector

D. Berger[1], M. Hemmleb[2]

[1]Technische Universität Berlin, Zentraleinrichtung Elektronenmikroskopie ZELMI, Berlin, Germany
[2]m2c, Potsdam, Germany

dirk.berger@tu-berlin.de

In scanning electron microscopy (SEM), segmented backscattered electron (BSE) detectors with four different detection angles (4Q) enable the reconstruction of the three-dimensional surface topography of various samples, i.e. catalysts, fractured surfaces and micro-devices [1]. An efficient shape from shading reconstruction algorithm is applied to the BSE signals to extract the surface topography with high accuracy in two main steps: calculation of the surface orientation for each sampling point and processing of the digital surface model. The reconstruction is very fast and needs no sample tilting since the surface topography is calculated from the four simultaneous recorded BSE images.
The capabilities of the algorithm go beyond the reconstruction of the sample topography: since the intensity of the backscattering images depends on the local element composition as well. The algorithm determines the backscattering coefficient (i.e. the mean Z-number) with high lateral resolution at the same time. The advantage is on one hand, that the reconstruction of the element composition is free of any influence of the local surface topography, allowing a better element characterization of the sample compared to a single backscattering image.
One the other hand is the formerly mentioned surface topography model independent from any element distribution.
To demonstrate the capabilities of the reconstruction algorithm we used a calibration sample with Pt-deposited structures on a silicon wafer. The sample consists of a three step pyramid with flat planes and flanks with about 45° inclination. A standard SEM (Hitachi SU520) equipped with a segmented (4Q) BSE detector from point electronic GmbH was applied for imaging with different high voltages at a magnification of 1500x. For the calculation of the backscattering coefficient, the explained shape from shading algorithm was applied. For comparison, Fig. 1 shows the mean value image of all four BSE-images and is comparable to a standard BSE-image and therefore shows Z- and surface-inclination-contrast. The Si-Wafer has lowest intensity (blue). The Pt base plate is thinner than the range of electrons and its intensity is given by the mean Z of the film system (orange). The Pt pyramid has the intensity of a thick Pt layer (red). The flanks of the pyramid have a middle intensity due to the surface inclination, which is compensated in the calculated backscattering coefficient image (Fig. 2) only. Now the inclined flanks have the same intensity as the plateaus of the pyramid. The inclination image (Fig. 3) displays the normalized length of the surface gradients without any Z-contrast. Therefore, all flat surfaces have the same color (blue) and the color of the flanks corresponds to their steepness. The height model of the sample (Fig. 4) is calculated from the surface gradients and shows a slight sample tilt, which is not visible in Fig. 3 (length of surface gradients). Nevertheless, the height model is free of any element dependence as well.
The 3d reconstruction from the signals of a 4 quadrant BSE detector not only enables the three-dimensional analysis of the sample topography, but also the correct calculation of the backscattering coefficient independent from topographical effects. In future, this element contrast will be enhanced by the use of energy filtered BSE-signals since the rate of elastically backscattered electrons depends more strongly on the atomic number.

References:
[1] Hemmleb et al.: 3D surface reconstruction with segmented BSE detector: New improvements and application for fracture analysis in SEM, Proc. EMC 2016, pp.489-490.

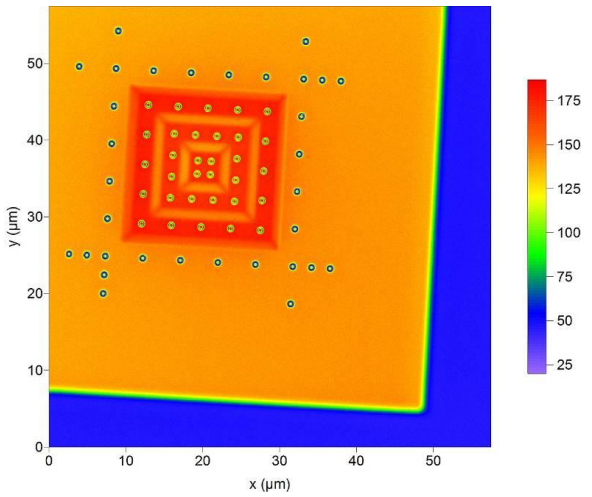

Figure 1. Mean values from 4Q BSE image data (20 kV, grey values are color coded). Background (Si) is blue, Pt-deposited material is orange to red.

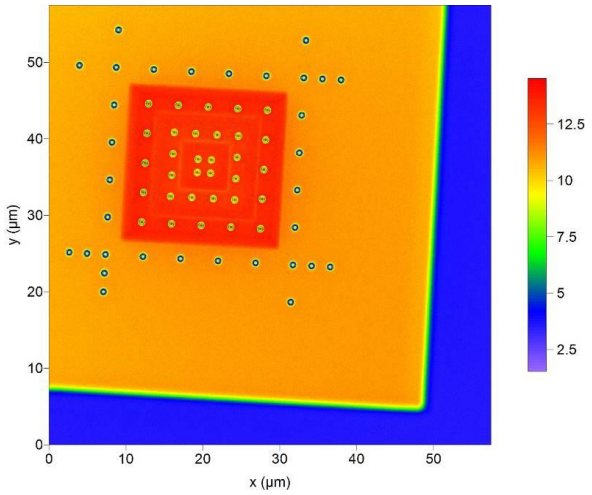

Figure 2. Calculated backscattering coefficient from 4Q BSE reconstruction (20 kV, backscattering coefficient is color coded).

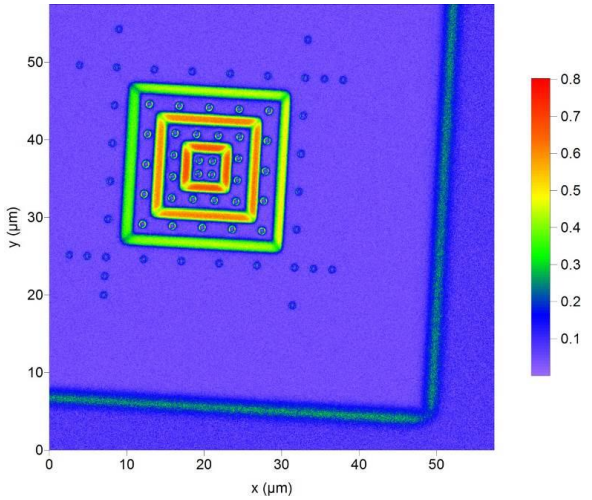

Figure 3. Calculated surface inclination from 4Q BSE reconstruction (20 kV, absolute values from surface gradients, color coded).

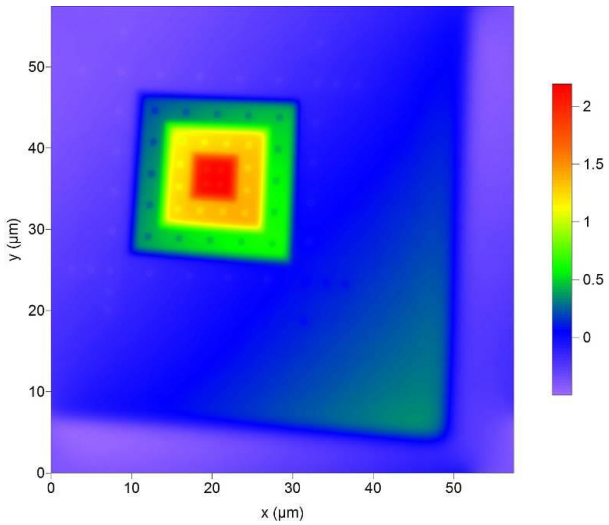

Figure 4. Calculated surface height from 4Q BSE reconstruction (20 kV, heights in µm).

IM1.P022
Measurement of enormous spatial distribution of scattered electrons in scanning electron microscope

S. Nishimura[1]

[1]Osaka Instatitute of Tecnology, Electronic Information and Communication Engineering, Kobe City, Japan

dance1225s@gmail.com

Keywords: electrostatic force microscopy, charging of insulators, surface potential distribution, bias potential applied to specimen

Electron beam (EB) can be focused in nanometers, and it is an indispensable tool for nanoscale observation and processing etc. However, examining the electron scattering behaviour in detail, it has been found that electrons are not only present in the vicinity of the electron beam irradiation point but also spread to a wide range of several cm from the electron beam irradiation point. These electrons are produced by multiple backscattering events between the specimen and electrode at the bottom of the objective lens, which is facing opposite to the specimen. We call those electrons as fogging electrons (FGEs).
In order to measure the spatial spread of FGEs, we use electron beam resist coated photomask as a specimen. By measuring the surface potential distribution of the resist, it is possible to know the distribution of electrons accumulated on the surface or inside. The potential distribution is measured by a home-made electrostatic force microscope (EFM). The configuration of the EFM is as shown in Fig.1. After the EB irradiation, the probe is approached and the stress is monitored while the bias voltage applying to the specimen is swept, and then, the surface potential is determined by the null method.
In the present study in particular, to know the energy and spatial distribution of FGEs in vacuum, an EB was irradiated while applying a positive bias voltage to the photomask specimen. As shown in the illustration in Fig. 2, by applying a positive voltage to the photomask it is possible to attract electrons flying over the surface. Electron charge distribution sucked and accumulated on the resist on the surface forms a negative potential distribution. By changing the bias voltage to be applied, it is possible to adsorb fogging electrons with different energies, so we can expect to know the energy distribution of fogging electrons from the difference in potential distribution.
Figure 3 shows the potential distribution up to 21 mm from the EB irradiation point. Three kinds of conditions are shown by changing the distance between the sample surface and the bottom electrode of the objective lens, that is, the working distance (WD) and the bias voltage to the specimen. In this combination of WD and bias voltage shown here, the electric field above the sample is constant. FGEs with less than 10 eV returns to the specimen surface at bias of 10 V. In the figure it is obvious that more FGE is being adsorbed with a larger bias with a distribution of 10 V to 50 V, but no significant difference was seen among them. From this fact, it was found that there are not so many electrons having 10 eV or more as FGE energy.

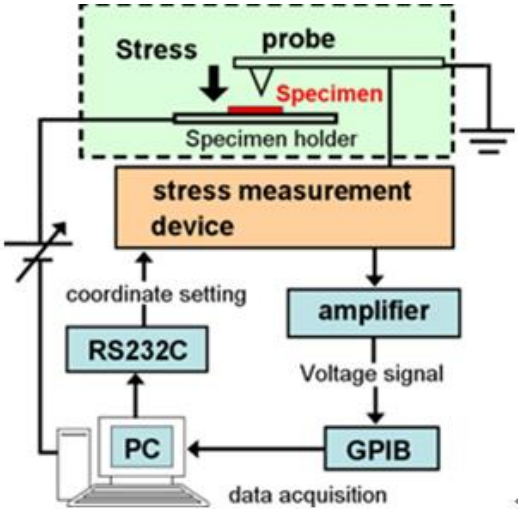

Figure 1

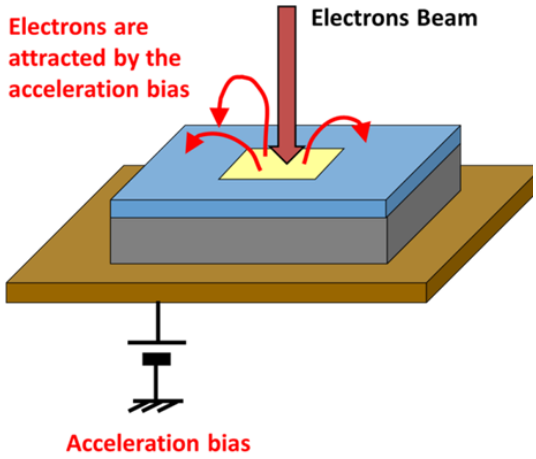

Figure 2

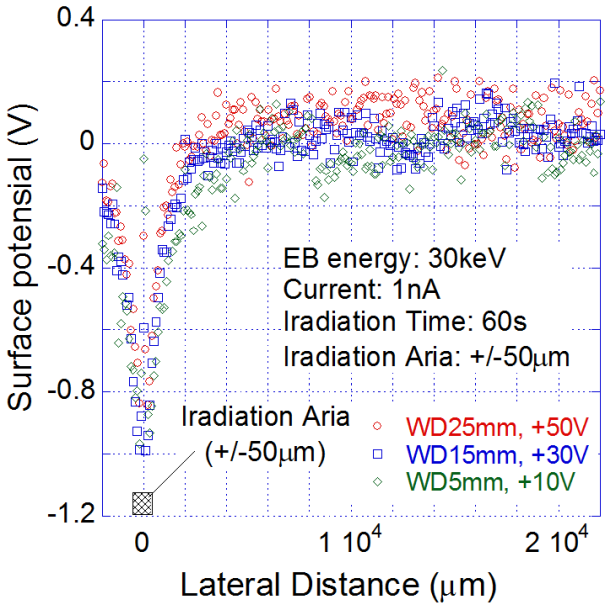

Figure 3

IM1.P023
Advanced TEM-lamella preparation with FIB/SEM

D. Berger[1], S. Selve[1], U. U. R. Hömpler[2], L. Meissner[2]

[1]Technische Universität Berlin, Zentraleinrichtung Elektronenmikroskopie ZELMI, Berlin, Germany
[2]Technische Universität Berlin, Institut für Optik und Atomare Physik IOAP, Berlin, Germany

dirk.berger@tu-berlin.de

FIB/SEM has become a standard tool for the target preparation of TEM lamellas. Nevertheless, individual tool- and problem-specific solutions are required for advanced preparation methods including transfer of the lamella to specialised holders like heating holders or for lamellas with specified crystallographic orientations. This contribution presents some solutions found in our laboratory.

1) Lift-off spacers

The advanced TEM-lamella preparations presented here require a lift-off procedure from specimens tilted to 50° - 60°. The usual recipes can be used if the lamella is cut at the edge of a specimen. Otherwise a free space for the transfer needle is needed to approximate its tip to the pre-prepared lamella. Since the needle has a diameter of up to 500 µm, the ion beam milling of this free space is very time consuming. Any ion-beam sharpening of the needle would be very lengthy as well. Therefore, we suggest an alternative method by increasing the distance between the transfer needle and the specimen surface: ion beam induced deposition of platinum bars on top of the lamella. A spacers cross section of 0.5 µm x 0.5 µm is sufficient if the stacked-rocks-shape, which is typical for ion beam induced Pt deposition, is steadied by electron induced Pt deposition from the perpendicular direction, see Fig. 1.

2) Adapted lift-off procedure of TEM-lamellas for in-situ heating experiments

For in-situ heating experiments, the TEM-lamella has to be placed flat onto the membrane of a heating holder. Then the lamella is fixed and finally thinned. For this purpose, an adapted recipe has been developed and implemented. First, the lamella is conventionally prepared with the specimen surface perpendicular to the ion beam. For the lift-off, the specimen is further tilted to at least 57°. To be able to approximate the transfer needle to the lamella, a free space, a lift-off spacer (see sect. 1) or both are used. The heating holder is then mounted on a 33° pretilted specimen holder, to guarantee that the ion beam is nearly parallel to the membrane. Then the lamella is placed flat on top of the membrane, fixed by Pt deposition and then further thinned, see fig. 2. Since the surface of the membrane is tilted, special care has to be taken before the Pt GIS is inserted especially because it shakes when the valve is opened.

The same recipe has been used for putting down lamellas onto aperture stripes [1] and for in-situ-biasing experiments with electrically contacted TEM-lamellas [2].

3) Preparation of TEM-lamella with 45° inclination with respect to the surface

Typically, TEM-lamellas are cut perpendicular to the specimen surface. In some applications it is necessary to prepare TEM-lamellas with a specified inclination to the surface, e.g. strain analysis with dark field holography [3]. For this aim, an adapted recipe has been developed and implemented which first produces a cross section surface perpendicular to the aimed inclination of the lamella and second prepares a lamella perpendicular to this cross section surface. The recipe regards a Pt protection layer to preserve the specimen surface, a free space for the transfer needle and a lift-off spacer. As an example, Fig.3 shows the preparation of a 45°-inclined TEM-lamella before the lift-off. Finally, the lamella is attached to a support grid in usual way for the final thinning and the transfer to the TEM.

In conclusion the presented recipes demonstrate that advanced TEM-lamella preparation is feasible with FIB/SEM.

[1] S. Selve, D. Berger *Manufacturing and application of a 2 µm dark field aperture in TEM* EMC2016 Lyon
[2] U. Hoempler et al*. Towards on-chip in-situ biasing of FIB/SEM-prepared TEM-lamellas* these proceedings
[3] L. Meissner et al. *Strain analyses of InGaAs/GaAs quantum dots* these proceedings

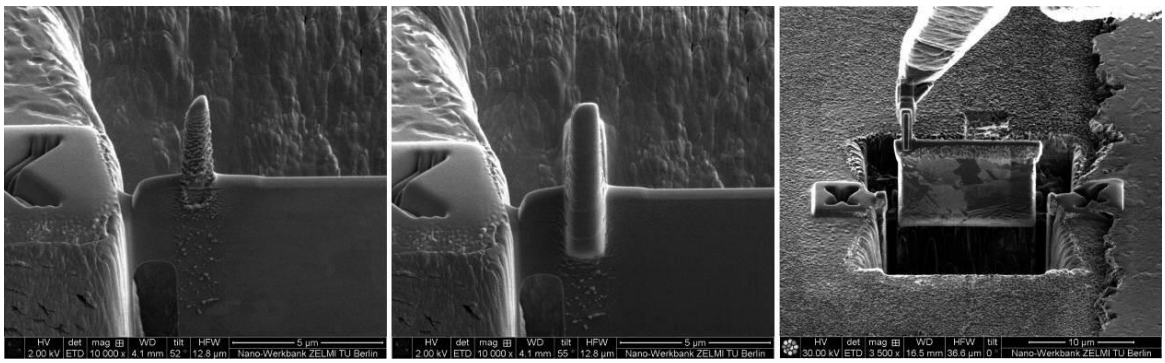

Figure 1. Lift-off spacer produced by ion and electron induced Pt deposition and lift-off example.

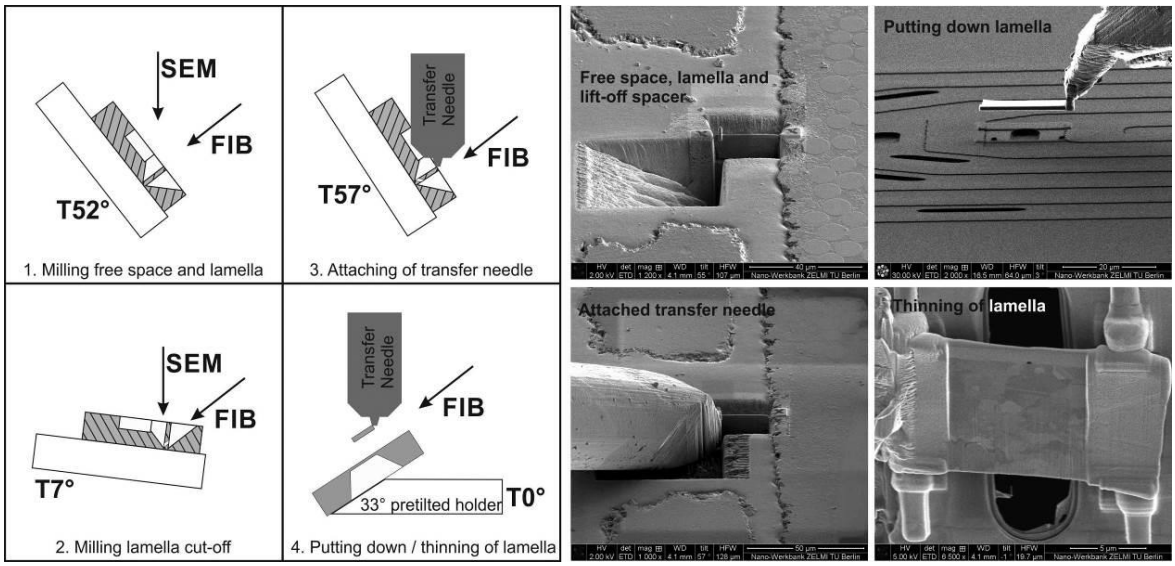

Figure 2. Main steps of a recipe for milling and transfering TEM lamellas onto a DENSsolution NANO-chip for in-situ heating and biasing measurements.

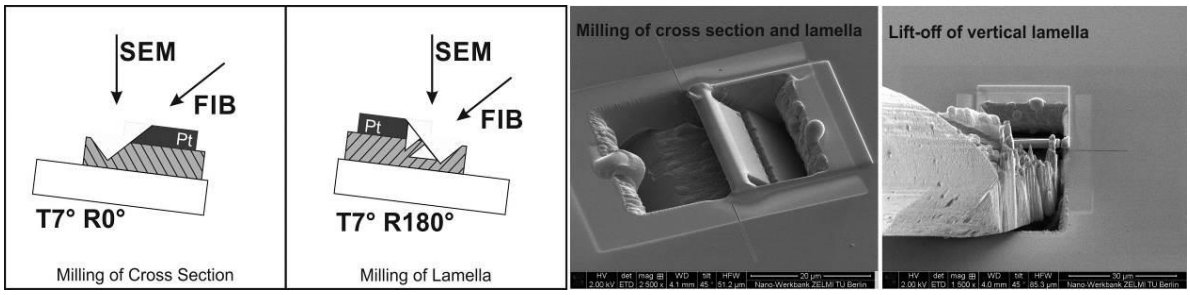

Figure 3. Main steps of a recipe for preparation of TEM lamellas with 45° inclination to the specimen surface.

IM1.P024
Relocation of defined sample positions with an automated stage navigation tool for SEM

J. Moré[1], N. Dziurowitz[1], C. Thim[1], M. Hemmleb[2], D. Berger[3]

[1]Bundesanstalt für Arbeitsschutz und Arbeitsmedizin, Gruppe 4.5 "Partikelförmige Gefahrstoffe, Innovative Materialien", Berlin, Germany
[2]m2c microscopy measurement and calibration, Potsdam, Germany
[3]Technische Universität Berlin, Zentraleinrichtung Elektronenmikroskopie ZELMI, Berlin, Germany

more.john@baua.bund.de

For various applications in Scanning Electron Microscopy (SEM), the relocation of defined sample positions is very advantageous, i.e. for time dependent re-measurement of special features or investigations with different electron beam analyses techniques. For this reason we developed a software tool, which enables the relocation of sample positions with the help of defined Reference: marks. It allows repeated measurements at defined sample positions at different times as well as with different SEMs by control of the SEM sample stage. A special application is the high resolution measurement of nanomaterials ([1], fig. 1). The acquired images are used to detect and classify fibers with an automated software approach.
The introduced sample navigation tool (TiNa, fig. 2) is based on the manual measurement of four Reference: marks. For this reason, the corners of a silicon chip or a sampler holder are applied. For advanced applications, i.e. with highest relocation accuracy, also special FIB marks are used. The software tool allows the registration of the stage positions of the Reference: marks, the transformation of already measured sample positions into the stage coordinate system and the control of the stage for the relocation of the positions of interest.
It was developed especially for the application of nanomaterial detection, which requires SEM images with a field of view of 42.2 µm x 31.7 µm with a pixel size of 8.2 nm at random sample positions. The aim is to do an automated statistical based detection and classification of nanomaterials as harmful to health. For its evaluation, a special test chip was designed and application tests were performed on three different SEMs.
The silicon test chip has the size of the usually applied samples for nanomaterial collection. We used FIB etching for the creation of four Reference: marks and a grid of nine control marks in the sample center. The marks consist of a finder cross and a circle structure in the center, which enables manually and automated geometric measurements with highest precision (fig. 3). The Reference: sample was measured with three different SEMs (Hitachi SU8030, SU8230 and FEI Helios NanoLab 600) at different times. After the re-measurement of the positions of the Reference: marks, the sample navigation tool reproduces the previously defined test positions. The remaining positioning errors were measured in the SEM images, which were acquired at these positions.
The developed stage navigation tool was successful applied for the measurement and archiving of different nanomaterial samples. The accuracy of repeated relocation of the marks was investigated with the test sample; it is 1-5µm at the same SEM (SU8230), also with a remounted sample (fig. 4). The comparison with measurements on the second used SEM (SU8030) shows the relocation accuracy within the same size in that case.
The performed test showed the easy-to-handle and precise functionality of the stage navigation tool. The relocation of special fibers at a magnification of 3000x is possible.
Further work is planned for an automated determination of the stage accuracy of different SEMs.

References:
[1] Plitzko, S., Dziurowitz, N.: Charakterisierung und Messung von ultrafeinen Partikeln (Nanomaterialien). Immissionsschutz (4), pp. 369-381.

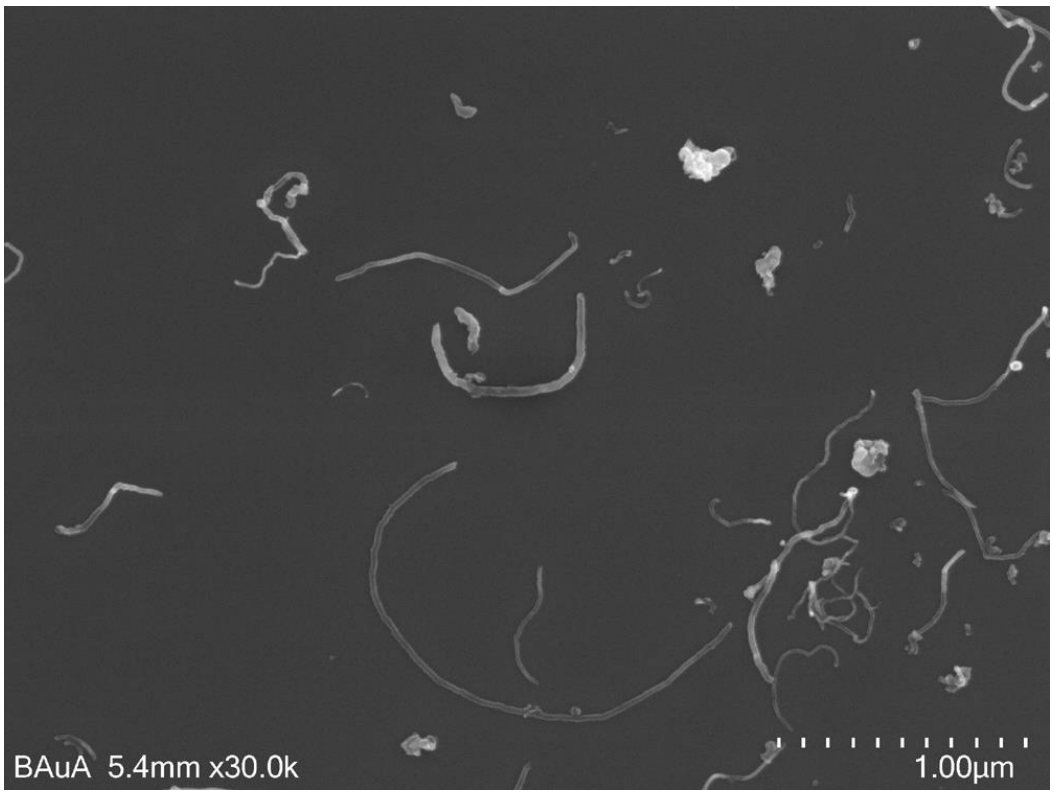

Figure 1. SEM image of nanomaterials.

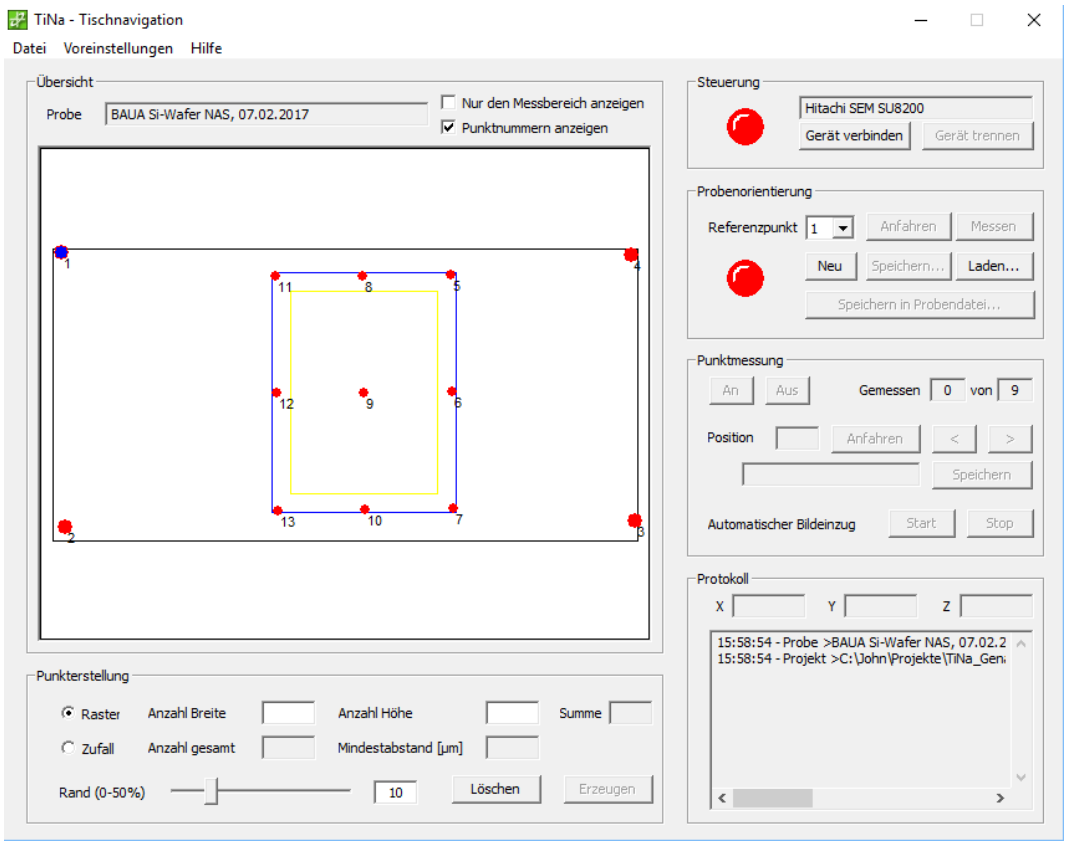

Figure 2. Screenshot of stage navigation software with layout of test sample.

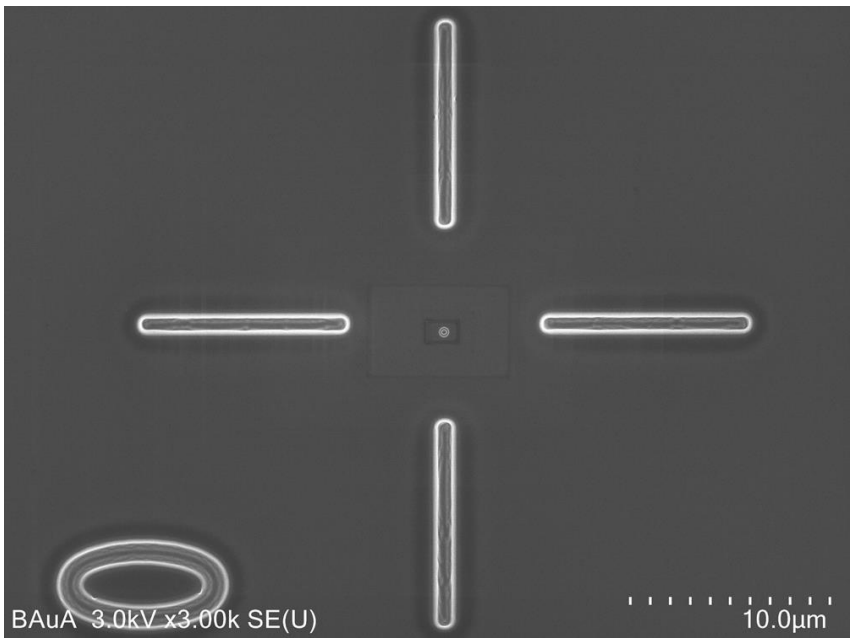

Figure 3. SEM image of control mark on test sample.

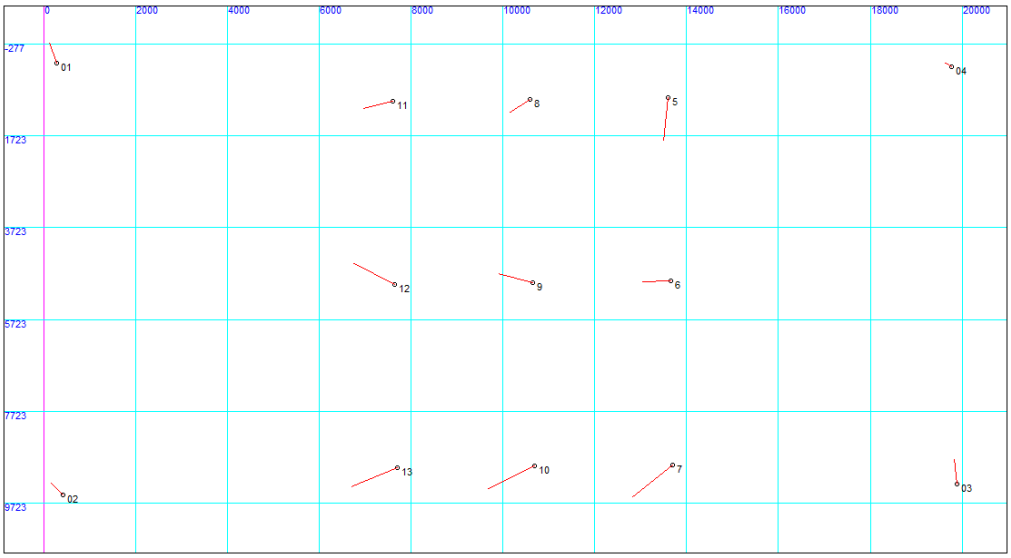

Figure 4. Diagram with remaining deviations (vectors are 200 times scaled).

IM1.P025
Noise reduction by improving dark-reference images

T. Heil[1], G. Tatlock[2]

[1]Max Planck Institute of Colloids and Interfaces, Colloid Chemistry, Potsdam, Germany
[2]University of Liverpool, School of Engineering, Liverpool, United Kingdom

tobias.heil@mpikg.mpg.de

Introduction and Objectives: The quality of TEM CCD images is not only influenced by the investigated sample and the utilised instrument, but also by the noise that is acquired together with the signal, which becomes especially apparent when dealing with a low signal-to-noise ratio. One way to improve the signal-to-noise ratio is to acquire several similar images and to merge them into one, thus ideally increasing the signal while flattening the random noise at the same time.
However, systematic noise can become a severe problem in this case, since its influence on the final image will be increased as well. One considerable source for systematic noise is the dark-Reference: image, which is automatically subtracted from the raw CCD acquisition in order to compensate for the dark current of the CCD chip. Especially for images that are merged drift-corrected, noise in the dark-Reference: image can be the cause of significant artefacts (figure 1). In order to generate the best results, it is therefore important to ensure that the dark-Reference: image is free of any excessive noise.
Methods and Results: A first and simple option to increase the quality of the dark-Reference: image is to use an image created by averaging over several mages instead of the regular single one. This way the noise can already be reduced significantly, even if just a small number of images are used for averaging.
Having access to a stack of dark-Reference: images offers further the possibility of a more sophisticated way of noise reduction. With a routine that checks for differences between the individual images, it becomes possible to separated intense one-shot noise like cosmic rays or x-ray spikes from wanted features like hot pixels. This information allows to remove the one-shot noise from the merged image altogether, instead of only diminishing it by the merging alone (figure 2).
Conclusion: A significant amount of artefacts in CCD images can be successfully removed when the quality of the dark-Reference: image is improved. This can be done by averaging over several images and by using a routine to identify and remove intense one-shot noise.
While this routine is only applied to dark-Reference: image so far, it should also be possible to utilise it to improve the quality of other series of CCD acquisitions, like gain-Reference: images, multi-frame EELS acquisitions or drift-corrected images of static objects.

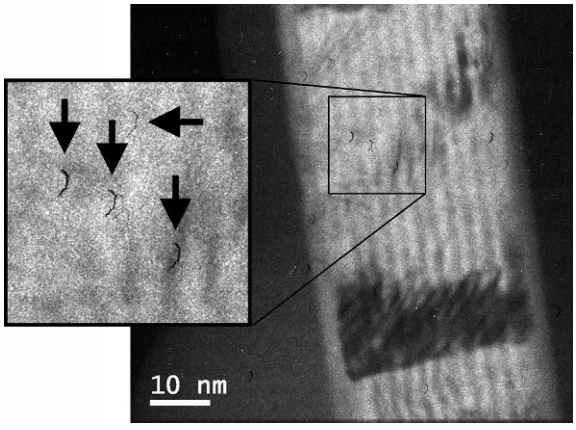

Figure 1. Artefacts caused by dark-Reference: image noise in a drift-corrected multi-frame EFTEM image. The artefacts can easily be recognised as similar shaped clusters of darker pixels.

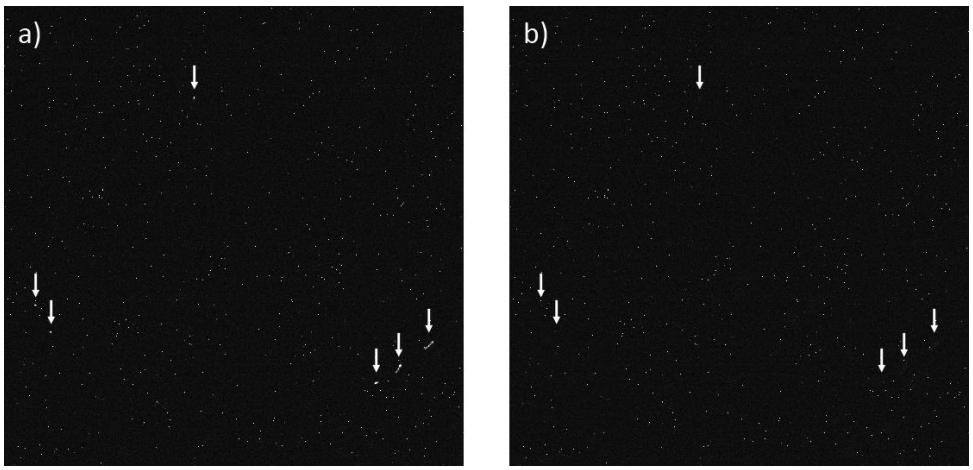

Figure 2. Section of a dark Reference: image created by averaging over 3 images without (a) and with (b) using one-shot noise correction. Note that the indicated one-shot events are removed, while the hot pixels are preserved.

IM1.P026
Improvement of depth resolution by low-voltage aberration-corrected TEM with monochromator

S. Morishita[1], Y. C. Lin[2], K. Suenaga[2]

[1]JEOL Ltd., Akishima, Japan
[2]National Institute of Advanced Industrial Science and Technology (AIST), Tsukuba, Japan

shmorish@jeol.co.jp

Determination of three-dimensional (3D) atomic structures is important for material analysis. In the techniques for the 3D analysis such as tomography proposed so far, the depth resolution is insufficient for determining atomic positions in 3D. Although atomic-level 3D analysis has been performed by using exit wave reconstruction [1], it needs many images and post processing for the 3D reconstruction. In this paper, we demonstrate the improvement of the depth resolution by utilizing a high-resolution low-voltage TEM, toward atomic resolution 3D observation without complicated post processing.

Low-voltage transmission electron microscopy (TEM) and scanning-TEM (STEM) are important for observing damageable materials such as graphene, because the electron energy should be below the knock-on threshold energy of a sample to reduce the damage. In addition to the damage reduction, low-voltage TEM is suitable for high depth-resolution imaging. In TEM, a contrast transfer function (CTF) is expressed as $e^{-f(k)}\sin(\pi \lambda\, df\, k^2)$, where λ is wavelength, df is defocus, and k is wave number. This expression shows that a large evolution of CTF is induced by a long wavelength at a low voltage when the damping function $e^{-f(k)}$ is constant.

For obtaining atomic resolution images at low voltage, we used a TEM equipped with Delta correctors and a monochromator consisting of double Wien filters [2]. The Delta correctors are used for correct geometrical aberrations up to fifth-order including six-fold astigmatism [3]. The monochromator is used for reduce the effect of chromatic aberration. Since a narrow energy spread provided by the monochromator decreases the defocus spread, the resolution degradation caused by the chromatic aberration is reduced. By using this TEM, damageable materials have already been imaged with atomic lateral-resolution at 15 – 60 kV [4,5].

Figure 1 shows simulated images of bilayer graphene at 200 kV and 60 kV. Simulation parameters such as defocus, C_c, and energy width are adjusted to have similar CTF in both voltages. Although the contrasts of the atoms in upper layer and lower layer are different in both images, the contrast difference at 60 kV is larger than that at 200 kV. This result suggests that lower voltage is suitable for improving the depth resolution, when the damping function at the low voltage is same with that at the high voltage. According to this simulation, it is also confirmed that the atoms in lower layer show darker contrast than upper layer does when the defocus is negative around 0 to – 2 nm.

Figure 2 shows an experimental image of the bilayer graphene with defocus of – 1 nm. Carbon atoms in upper and lower layers have been imaged with different contrasts. The atoms indicated by red circles show brighter contrast, indicating that they are located on the upper layer. The atoms indicated by blue circles show darker contrast, indicating that they are on the lower layer. We have demonstrated that the height difference of 0.34 nm, which corresponds to layer spacing of graphene, is distinguishable using the advanced low-voltage TEM. This TEM would be possible to use for 3D analysis of various materials utilizing its high depth resolution.

[1] J.R. Jinschek, *et al*., Carbon 49, 556-562 (2011).
[2] M. Mukai, *et al*., Ultramicroscopy 140, 37-43 (2014).
[3] H. Sawada, *et al*., J. Electron Microsc. 58, 341-347 (2009).
[4] S. Morishita, *et al*., Appl. Phys. Lett. 108, 013107 (2016).
[5] S. Morishita, *et al*., Phys. Rev. Lett. 117, 153004 (2016).

This work was supported by the JST under the Research Acceleration Program (2012–2016).

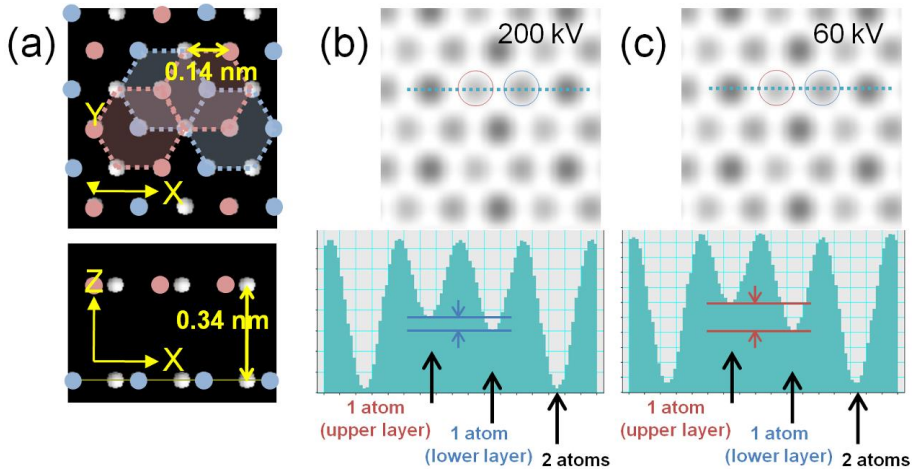

Figure 1. (a) Bilayer graphene structure model for image simulation. (b) Simulated TEM image of bilayer graphene at 200 kV. df = -1.5 nm, C_c = 1.2 mm, dE = 0.75 eV. (c) Simulated image at 60 kV. df = -0.8 nm, C_c = 0.8 mm, dE = 0.2 eV. Intensity profiles along the dotted lines in the simulated images are also shown.

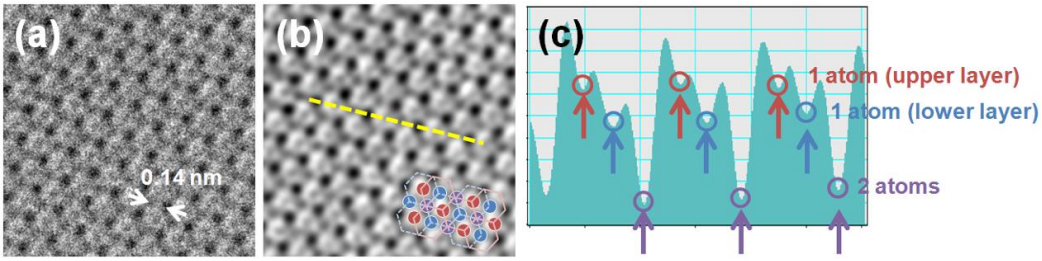

Figure 2. (a) Row TEM image of bilayer graphene at 60 kV with the energy width of 0.2 eV. (b) Low-pass filtered image of (a) produced by the convolution of the Gaussian distribution. (c) Intensity profile along the dotted line in (b).

IM1.P027
Combination of pulsed laser and focus ion beam preparation for an efficient microstructural analysis of pristine and aged Li-ion battery materials

D. Zeibig[1], U. Golla-Schindler[1], T. Bernthaler[1], G. Schneider[1]

[1]Aalen University, Materials Research Institute, Aalen, Germany

daria.zeibig@hs-aalen.de

Introduction: Since many years Lithium-ion batteries (LiB) are effectively used as power sources in electronic devices. One major aim for future research is to improve the cell quality, since the demands for the latest applications show a significant increase regarding safety and costs compared to earlier uses. [1, 2]
For a better understanding of the processes occurring inside of the batteries, such as morphology changes of active materials due to processing and cycling, a parameter study with a pulsed laser in combination with Focused-Ion-Beam (FIB)-technology will be presented. With this approach we will demonstrate the increase of analysis efficiency, and on the other hand the benefit to obtain more statistics in evaluating microstructural effects.
Objectives: Aim of this study was to prepare a relatively large area of a battery electrode foil using a laser in order to get a representative insight into the microstructure of the material. The prospects and limits of the laser ablation pre-preparation technique are analyzed. The preparation quality is optimized by modifying different parameters, so that a fast post-polishing with the FIB can be carried out.
Materials and Methods**:** In this case study a lithium-ion pouch-cell (Li-rich NMC/graphite; 32 mAh), has been cut open, washed with dimethylcarbonate to remove the electrolyte, and dried at room temperature. Afterwards pieces of the cathode and anode foil were cut out and attached on a specimen holder for further analysis. The investigation has been conducted in a ZEISS Crossbeam 540 FIB/SEM with an integrated TRUMPF TruMark 6330 pulsed laser (Wavelength: 355 nm in the UV-range). Windows with 380 µm x 380 µm were cut into the battery materials. Each window was prepared with varying laser parameters, such as power, velocity, pulse frequency and increment angle. Subsequent FIB preparations were performed with standard parameter settings to remove heat affected and damaged zones to develop the microstructure of the battery materials.
Results: Different laser sections with a variance in the power for the anode as well as for the cathode material have been carried out. For the cathode material a power of 60 %, a pulse frequency of 15 kHz, a velocity of 150 mm/s and an incremental angle of 20 ° enables a relatively smooth surface area. However, as exemplarily shown in figure 1a), the heat affected zone in the cathode material is considerably more distinguishable than in the anode foil (Fig. 1c)). However via post-preparation with the FIB, a well-polished surface was achieved after approx. 4 µm ion milling (Fig. 1b)). For the anode foil, acceptable results were achieved with a power of 70 %, a velocity of 150 mm/s, a pulse frequency of 15 kHz and an incremental angle of 18 °. A subsequent cross-section through the anode (Fig. 1d)) shows good results for the post-preparation with the FIB.
Conclusion: The combination of the FIB technology with the integrated pulsed laser is a very efficient method for cutting cross-section. The cutting time could be reduced from 6,5 h (only FIB) to 45 min (laser assisted). This time includes the final FIB polishing of a selected area at 7 nA. The microscopic analysis enables a better understanding of the occurrence of aging effects in a larger submicroscopic scale. Further laser parameter variations must be carried out for better pre-polishing results with less thermal damage, especially for the cathode material.

[1] T. Waldmann, et al., in J. Power Sources 262, 129–135, 2014
[2] G. Pistoia, Lithium-ion batteries: Advances and Applications: Advances and applications, first ed, 2014.
[3] J. Fehrenbach, et al., IEEE Transactions on Image Processing, 4420–4430, 2012.

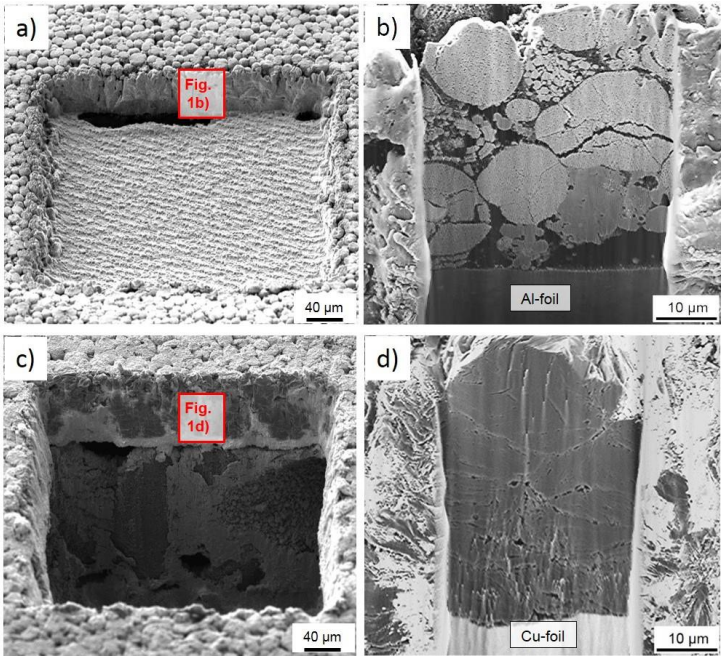

Figure 1. a) Laser section of the NMC cathode. Image acquisition with 200x magnification and a SESI detector. b) FIB-cross section of the laser pre-preparated cathode-foil. Image acquisition with 1.000x magnification and a SESI detector, improved images via VSNR [3] c) Laser section of the anode foil. Image acquisition with 200x magnification and a SESI detector. d) FIB-cross-section of the laser pre-preparated anode. Image acquisition with 1.000x magnification and a SESI detector, improved images via VSNR [3].

IM1.P028
A backscattered electron detector dedicated to high speed imaging and defect inspection

M. Schmid[1], A. Liebel[1], R. Lackner[1], D. Steigenhöfer[1], A. Niculae[1], H. Soltau[1]

[1]PNDetector GmbH, München, Germany

maximilian.schmid@pndetector.de

Introduction: Pattern analysis and defect detection is an important field of quality control in modern semiconductor production. High device densities, small structures and increasingly complicated process operations demand for fast but reliable wafer inspection. At the same time the influence on the specimen should be kept to a minimum to ensure damage-free process control. Defect and pattern analysis algorithms are capable of fulfilling this demand. However, the capabilities of these software tools depend on fast detection systems providing high speed and high quality images.
Objectives: Here, we show a BSE detector dedicated to imaging with pixel dwell times down to 10 ns without degradation in quality. This allows ultra fast detection resulting in minimal exposure time of the specimen.
Materials and Methods: To support the high speeds of the BSE-Chip, the diode and the preamplifier board form one unit placed in a flat aluminum housing. The close connection of the BSE-Diode to the preamplifier board ensures minimum stray capacities between the signal generation and amplification. In addition, the design of the amplifier is geared to the diode which enables the BSE detector to realize signal rise times down to 10 ns. Figure 1 shows the BSE detector module. The device is compatible with high vacuum conditions inside SEM and the materials are selected carefully to not influence the electron beam. With its thickness of only 2.5 mm, it can be placed directly under the pole piece of an SEM. At this position it offers small working distances (WD) with high Geometric Collection Efficiencies (GCE) for the BSE.
Results: Figure 2 shows the step response of the BSE detector module. The edge was simulated by an ultra fast switching LED with switch on times around 7 ns. Corresponding to this input, our BSE detector module shows a rise time of about 10 ns to 15 ns at an amplification factor of 10^4 V/A. As an example, an image of 1000 x 1000 pixels can be taken within 10 ms, highlighting the outstanding speed of the BSE detector module and the minimal interaction time between the electron beam and the specimen. The high GCE values of up to 60% enable high signal outputs in order to maintain high signal to noise ratios at these high scan speeds. Figure 3 shows two SEM images of a defect recorded with the BSE detector module at 100 ns dwell time at 4 keV beam energy and 120 pA beam current. The advantage of BSE over SE detection in defect analysis becomes visible since the composition as well as the topographic structure of the specimen can be monitored very precisely. Figure 3(a) is a compositional image with pure material contrast and figure 3(b) the corresponding topographical image. Since the BSE detector module provides each signal of the four segments of the diode separately, different signal combinations can be monitored in a simultaneous scan. This advantage further decreases the exposure time of the specimen to the electron beam.
Conclusion: In conclusion, we have shown a BSE detector module dedicated to high speed imaging. It is designed to achieve rise times down to 10 ns with a geometric collection efficiency up to 60%. This ensures ultra fast imaging with minimal influence on the specimen.

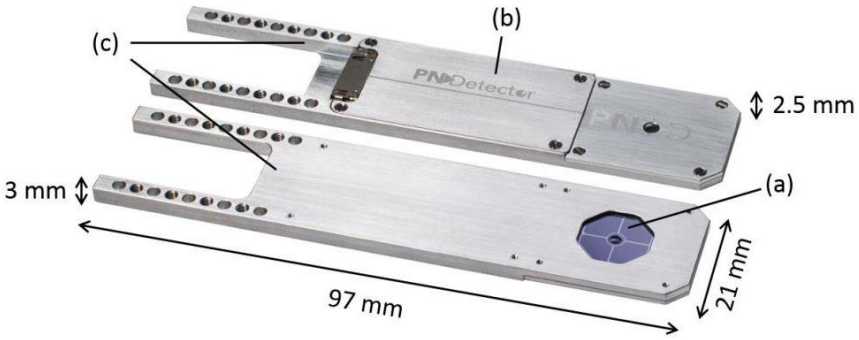

Figure 1. Front and backside view of the PN-Detector high speed BSE detector module: (a) 4 Quadrant BSE Diode, (b) 4 channel preamplifier, (c) ultra flat aluminum housing.

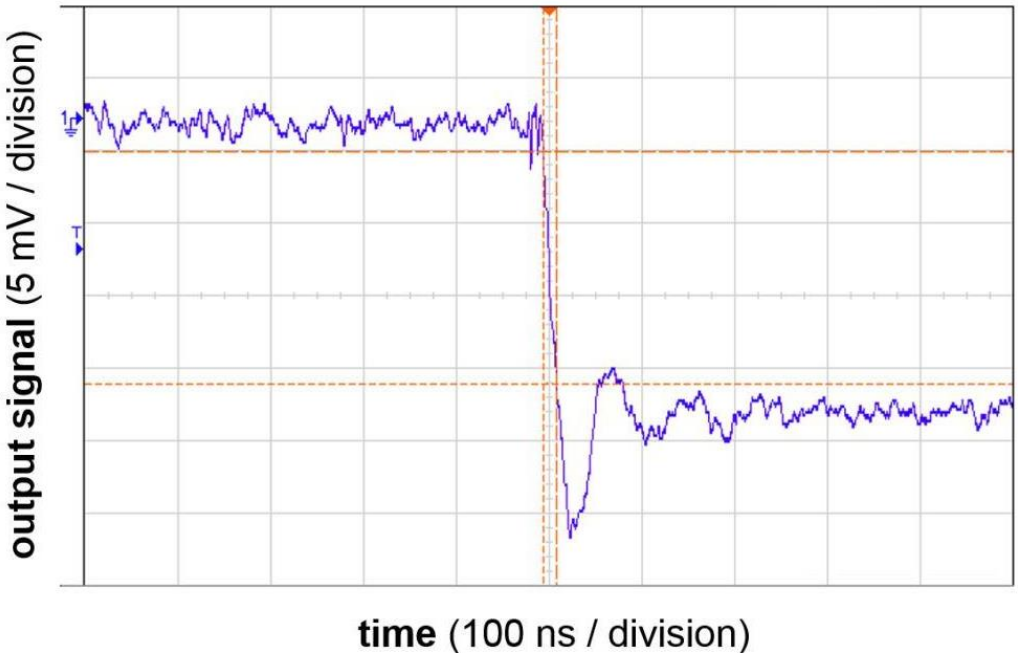

Figure 2. BSE detector module output vs. time. Signal rise time of 10 to 15 nsec measured by illuminating the BSE-detector with a high speed LED pulser with a switch on rise time of 7 ns.

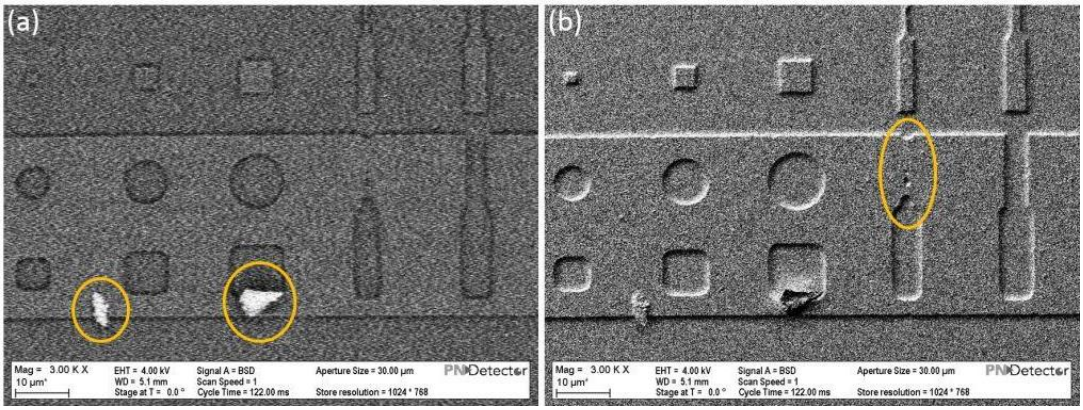

Figure 3. SEM images of a structured Al layer on a Si wafer. Image taken at a beam energy of 4 keV with a beam current of 120 pA at a WD of 5.1 mm and a pixel dwell time of 100 ns. (a) Compositional contrast, high Z particle contamination highlighted. (b) Topographical contrast, structural defect highlighted.

IM1.P029
Novel in situ heating and EBSD inspection using microelectromechanical system (MEMS)-based micro heating device in FIB/SEM systems

M. Wu[1], L. Novák[1], T. Vystavěl[1]

[1]Thermo Fisher Scientific, Brno, Czech Republic

min.wu@fei.com

Direct real-time observation of microstructure evolution at elevated temperatures in electron microscope has a crucial impact on understanding underlying principles of thermally active processes, such as recrystallization, grain growth and phase transformation. Traditional way is to use in chamber bulk "furnace type" heating stages in a low vacuum environment. Although this valuable approach contains various undeniable merits, new state-of-the-art experiments come with new demands, for instance rapid changes in temperature, high-vacuum operation to maximize experiment cleanliness, ultra-high resolution SEM imaging and on top of it adaptable geometry for quantitative crystallographic and composition investigation. Conventional bulk heating stages have limitations to meet these new challenges mainly owing to their slow thermal response (maximum heating rate of 5 degrees per second) and large thermal mass capacity[1]. The slow ramping impedes experiments requiring critical fast temperature change such as quenching, and may allow undesirable microstructure change during ramping. Their large thermal mass gives rise to significant amount of infrared (IR) radiation during heat change, thereby degrading the quality of the electron diffraction patterns at elevated temperatures (above 600°C). Despite some efforts have been made to minimize the thermal electron emissions (such as applying an extra IR filter in EBSD detectors[2]), it might require certain expensive implementation of special apparatus. These seemingly unavoidable drawbacks, however, can be eliminated by employing a novel microelectromechanical system (MEMS)-based micro heating device in combination with *in-situ* sample preparation in SEM/FIB system.

This miniaturized MEMS heating chip provides new opportunities for convenient, fast and reliable high temperature *in-situ* annealing experiments under high vacuum conditions. It is capable of providing a rapid heating/cooling rate in the order of 10^5 degrees per second and a maximum temperature of 1200°C. The localised heating and small thermal mass capacity brings distinguished advantages such as uniform temperature distribution over the heating area, high stability even during operations above 1000°C, minor sample displacement and drift stablilization[3]. *In-situ* imaging of samples placed on the MEMS microheater during heating can be obtained using all types of detectors including STEM, EBSD and EDS. We present work of a sequential EBSD analysis of a slightly deformed Ti6Al4V sample obtained during *in-situ* heating at 1100°C on MEMS Heating System in an FEI DualBeam FIB/SEM Helios G4 work station equipped with standard EBSD detector. The chunk sample of size 50x30x20µm^3 was fabricated using FIB milling from the bulk, subsequently *in-situ* lifted out and welded onto the MEMS chip by an in-chamber micromanipulator (Figure1). As an option the sample surface can be cleaned on the MEMS chip with low energy ion to improve SEM and EBSD pattern quality. The sample was *in-situ* heated at a rate of 10^3 degrees per second to 1100°C. During the isothermal treatment at 1100°C, EBSD maps were sequentially acquired at 20kV and 26pA with a step size of 100nm. The average hit rate (indexing percentage) for the maps are above 80% and did not decrease during the heating.

The results of the experiment in Figure2 show a successful *in-situ* heating (1100°C) experiment facilitated by novel MEMS microheatingplate coupled with *in-situ* sample mounting and EBSD detector. Dynamic grain boundary migration and grain morphology evolution are observed and characterized using EBSD analysis.

References:

[1] N. Bozzolo, *et al.*, *Mater. Charact.*, vol. 70, pp. 28–32, 2012.
[2] H. S. Ubhi, J. Parsons, *J. Phys. Conf. Ser.*, vol. 522, p. 12011, 2014.
[3] L. Mele *et al.*, *Microsc. Res. Tech.*, vol. 79, no. 4, pp. 239–250, Apr. 2016.

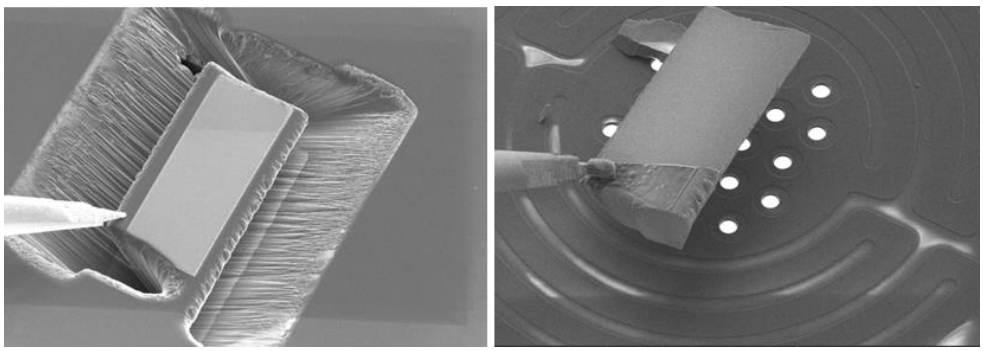

Figure 1. The Ti6Al4V chunk sample fabricated in bulk and *in-situ* lifted out by FEI "Easylift" micromanipulator and attached to MEMS heating chip. The HFW is 150µm.

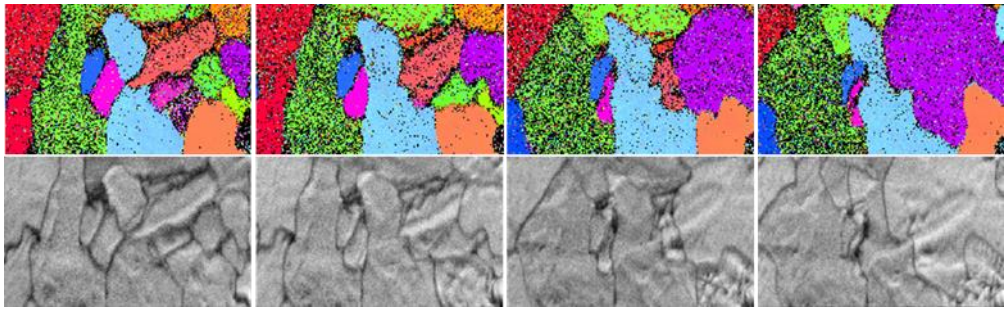

Figure 2. Sequence of 4 EBSD IPFZ images (top row) and corresponding IQM (bottom row) of deformed Ti6Al4V alloys, taken at 1100°C using *in-situ* MEMS heating. The first three columns of images were taken in 15 minutes intervals, while the last column of images was taken after 60 minutes. The HFW is 20µm.

IM1.P030
FIBTOFSIMS, AFM, SEM integration into a single instrument to for 3D chemical imaging at the nanoscale

L. Pillatsch[1,2], F. Östlund [2], I. Utke[1], M. V. Puydinger dos Santos[1], J. Michler[1]

[1]EMPA, Thun, Switzerland
[2]TOFWERK AG, Thun, Switzerland

lex.pillatsch@empa.ch

Atomic Force Microscopy (AFM) is a well-known tool for investigation of surface roughness and 3D imaging at the nanoscale. FIBTOFSIMS is a new technique that allows for analysing secondary ions (SI) generated by a focussed ion beam instrument by means of a time of flight mass spectrometer (TOFSIMS). During TOFSIMS imaging in a FIB quantitative depth profiling can be achieved by sequential acquisition of FIBTOFSIMS images. A full 3D image of the sputtered volume can in principle be recorded with a complete mass spectrum with a material dependent voxel size in the range of 50nm. The problem is the evolving roughness of the sputtered surface and the lack of accurate sputter depth data during sequential FIB imaging. For this purpose a high vacuum compatible AFM has been developed and installed in a FIBSEM instrument (Figure 1) [1]. In combination with a ToF-SIMS installed on the FIBSEM instrument, chemical information obtained from sputtered crater are located laterally and depth corrected. With these combined analysis method, 3D reconstruction of the chemical composition of a sputtered volume is performed.
We demonstrate the instrument performance on a multilayer thin film structure of a vertical cavity surface emitting laser where we investigated the chemical structure as well as the thickness of the different layers. The combination of FIBSIMS, SEM and AFM [1] was also used to analyse a Co deposit produced by focused electron beam induced deposition (FEBID) [2]. The shape of the deposit was visualised with the SEM and analysed with the AFM. Possible contamination from the deposition process, modifying the magnetic properties of the Co deposit has been analysed by FIBSIMS (Figure2).

[1] J.A. Whitby et al, Advances in Materials Science and Engineering, 2012, article ID 180437
[2] Marcos V. Puydinger dos Santos, Murilo F. Velo, Renan D. Domingos, Yucheng Zhang, Xavier Maeder, Carlos Guerra-Nuñez, James P. Best, Fanny Béron, Kleber R. Pirota, Stanislav Moshkalev, José A. Diniz, and Ivo Utke, Annealing-Based Electrical Tuning of Cobalt−Carbon Deposits Grown by Focused-Electron-Beam-Induced Deposition, ACS Appl. Mater. Interfaces (2016), DOI: 10.1021/acsami.6b12192

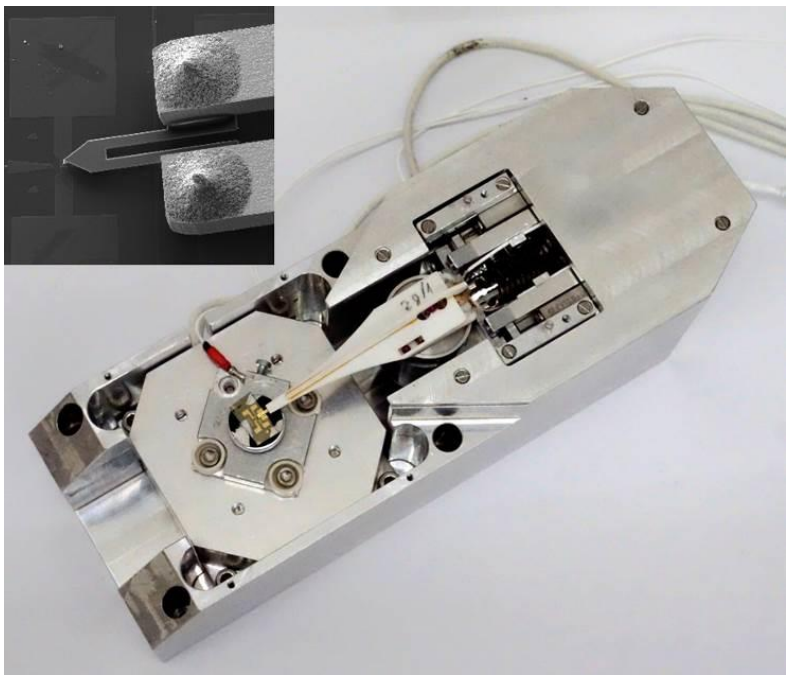

Figure 1. High vacuum AFM setup with the sample installed on the 10x10 mm range scanning table. The adjustment of the tip height is done by a piezo manipulator below the tip. Coarse motion of the tip to position the tip at the area of interest is realized by slip stick nanomanipulators. The inset picture shows an SEM image of the tip close to the surface.

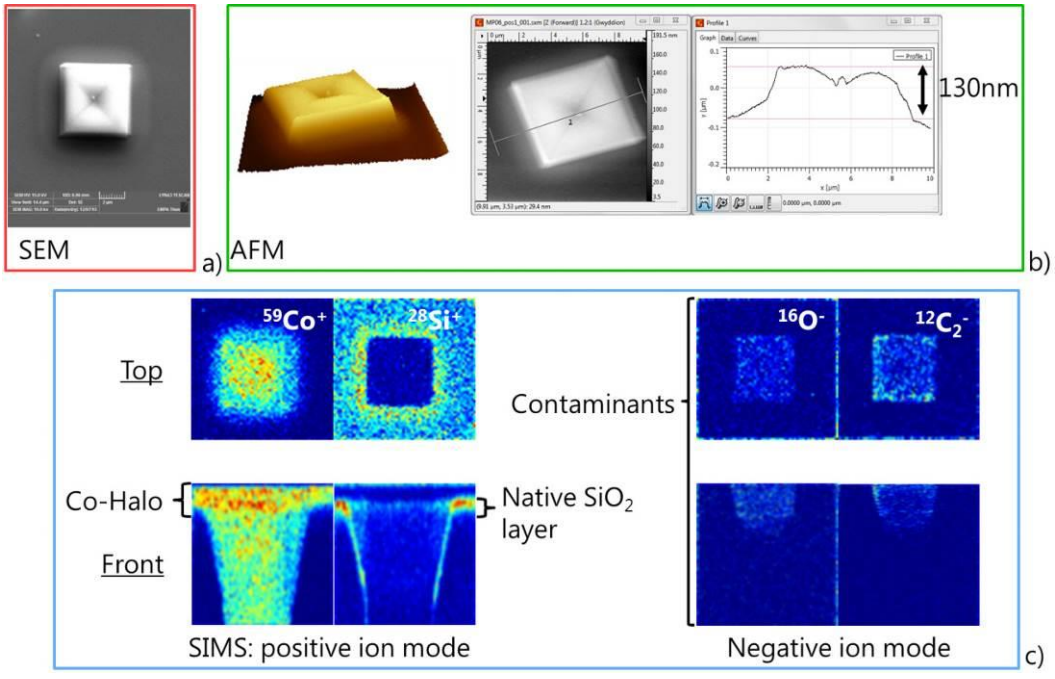

Figure 2. Analysis of a Co-deposit by SEM, AFM and FIBSIMS. a)The structure was visualized by SEM b)and the height was measured by AFM. c) Oxygen and carbon contamination from the deposition process were measured by FIBSIMS.

IM1.P031
A high frame rate, large field of view pillar defelction tracking setup using minimal oversampling

F. Margadant[1], X. Xu[1], X. Hu[1], B. Yang[1], M. Sheetz[1]

[1]MechnoBiology Institute, MBI, Singapore, Singapore

felix@margadant.ch

Introduction: PDMS pillars of well controlled shape and rigidity have been used to map the forces generated and experienced by spreading cells for more than a decade. If the pillars are small and dense enough to match the focal adhesion dimensions of mammalian cells, collaborative sensing and subsequent adhesion growth can be observed [1], figure 1 (deflection plot of early spreading fibroblast).
Objectives: The goal is to observe single protein force sensing and contractile unit steps. This is achieved by searching for the fine pinching movement of two neighboring pillars [2]. Fast event observation is achievable with conventional sources through averaging and high empty magnification [3]. Our modifications are introduced to allow exact time stamp and whole-cell observation.
Materials and Methods: The light path through the specimen is shared by an epi-fluorescent system for the wavelength range from 360nm through 630nm and a far-red, high intensity tracking system for 650nm and above that operates either by transmitted light or backscattered imaging, figure 2 (backscatter vs. oblique transmission, at 120mW and 30mW respectively and 5ms exposure). The tracking light is segregated out earlier in the path by a short-pass (642nm or 665nm) thick, flat dichroic and an emitter and is hence of higher optical quality then the fluorescent system that passes through two dichroics and two emitters before being focused onto the camera. The two cameras (Photometrics Prime95 B for fluorescent, PointGrey Grasshopper 3 for the tracking) run completely asynchronously.
Results: In order to assess the repeatability of the localization, we compare the apparent movement of a single pillar relative to the ensemble of all central pillars. In order to account for inhomogeneity in illumination, we step the piezo stage by pixel distances for 1K frames. AT 200fps better than 1.4nm average stability is achieved, pixel-centered pillars are tracked more accurately, figure 3 (tracking standard deviation for 110 pillars in a FOV).
Conclusion: The current flux of 665nm light of 500mW through a FOV of 50mm square allows for observation periods of minutes without altering the physiological spreading of the cells. Neither does the frequency of the contractions diminish nor does the spreading rate slow other than by steric hindrance. Figure 4 (a migration plot over 5 minutes at the same scale as figure 1, 4, blue encoding the early frames, red the late ones. The 37 degree water bath transports the excess heat quite efficiently. For transmitted light tracking, power levels as low as 150mW proved sufficient for tracking at 600fps. The lowered efficiency in backscattering mode requires the higher setting though if the accuracy needs to be better than 5nm. These power settings and frame rates are still insufficient to observe the motor protein step which can be detected but not resolved. The step is believed to be completed within 2ms and will require quadrupling the current frame rate.
Higher fps CMOS sensors are available but they come – even at significant cost – a quantum efficiency drop from >70% down to <50%. This is still does not to justify the reduced dynamic range and temporal blur of an image intensifier. To cope with the expected 6 fold increase in flux, we see no way but to limit both the observation time and the field of view to a region and period of interest.

[1] Gupta, M. *et al*. Adaptive rheology and ordering of cell cytoskeleton govern matrix rigidity sensing. *Nat. Commun.* (2015)
[2] Yang Bo.*et al*, Mechanosensing Controlled Directly by Tyrosine Kinases, *Nano Lett.* 16(9):5951-61 (2016)
[3] Haguy Wolfenson.*et al*. Tropomyosin Controls Sarcomere-like Contractions for Rigidity Sensing and Suppressing Growth on Soft Matrices. *Nature Cell Biology*, 18, 33–42 (2015)

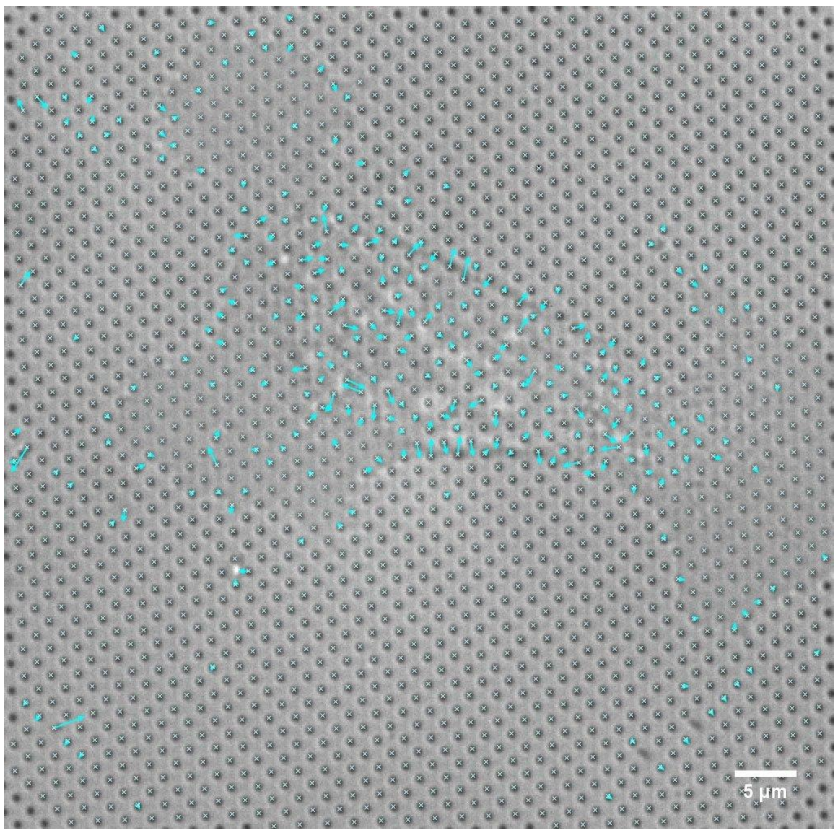

Figure 1. Deflection plot of early spreading fibroblast.

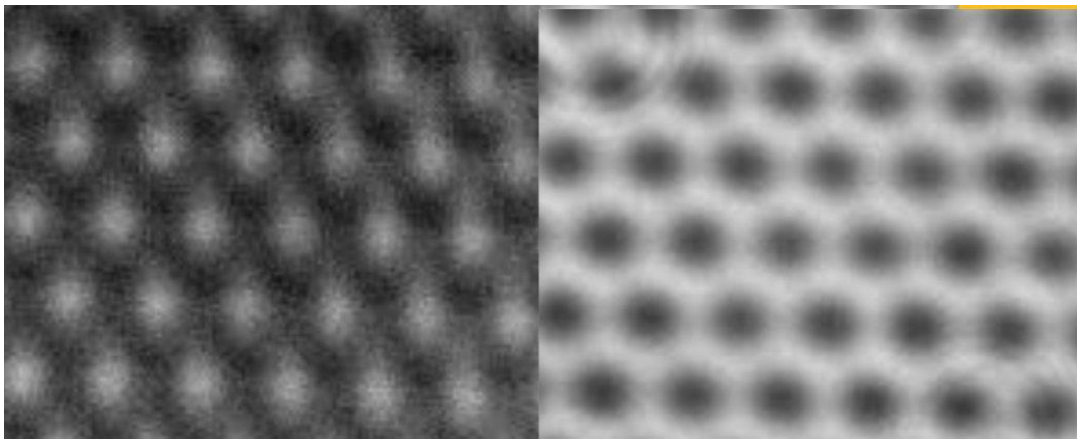

Figure 2. Backscatter vs. oblique transmission, at 120mW and 30mW respectively and 5ms exposure.

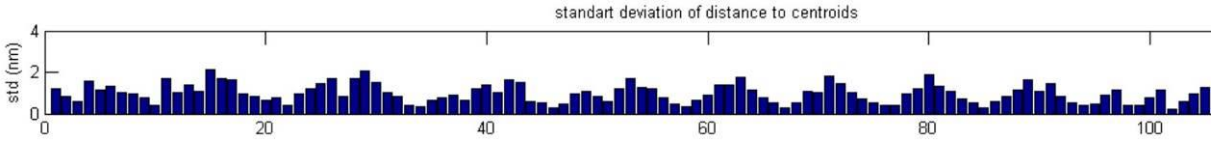

Figure 3. Tracking standard deviation for 110 pillars in a FOV.

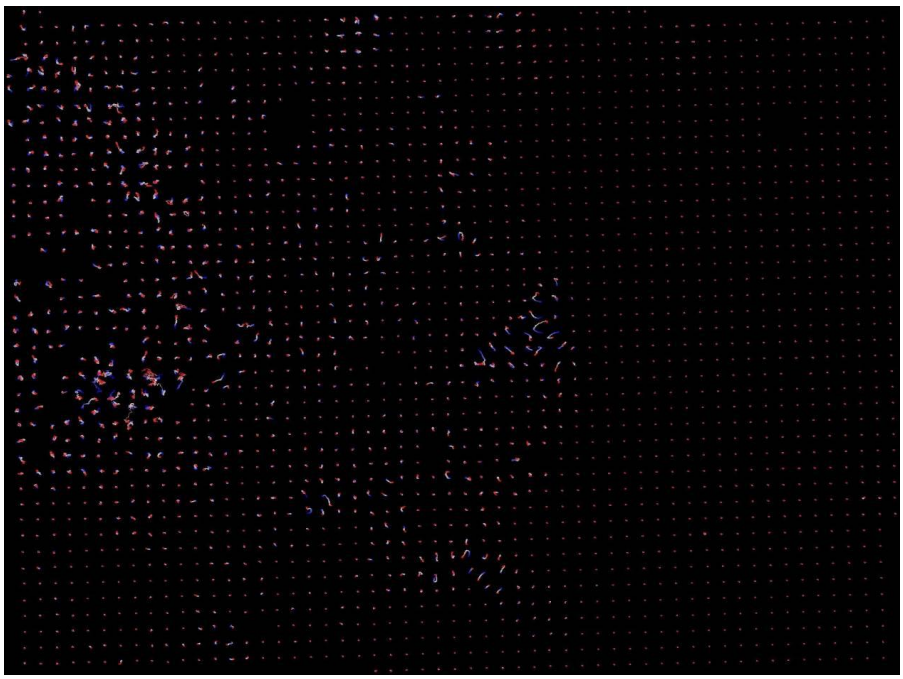

Figure 4. A migration plot over 5 minutes at the same scale as figure 1, 4, blue encoding the early frames, red the late ones.

IM1.P032
Combined in situ mechanical testing and scale-bridging 3D analysis of nanoporous gold

T. Przybilla[1], E. Thiess[1], F. Niekiel[1], B. Winter[1], M. Mačković[1], P. Schweizer[1], Z. Xie[2], J. Guénolé[2] A. Prakash[2], S. T. Kelly[3,4], H. Bale[3], E. Bitzek[2], E. Spiecker[1]

[1]Institute of Micro- and Nanostructure Research & Center for Nanoanalysis and Electron Microscopy (CENEM), Department of Materials Science and Engineering, Friedrich-Alexander Universität Erlangen-Nürnberg, Erlangen, Germany
[2]Institute I, Department of Materials Science and Engineering, Friedrich-Alexander-Universität Erlangen-Nürnberg, Erlangen, Germany
[3]Carl Zeiss X-ray Microscopy, Pleasanton, CA, United States of America
[4]Carl Zeiss X-ray Microscopy, Pleasanton, CA, United States of America

thomas.przybilla@fau.de

In situ micromechanical testing of nanoporous gold (npg) offers insights into deformation mechanisms of nanoscale metal networks. Au ligaments act together as a three-dimensional open porous network of interconnected nanostruts resulting in high mechanical strength under compression and nanoindentation [1, 2]. With decreasing ligament size stresses close to the theoretical shear strength of Au have been reported in compression and nanoindentation experiments [2-4]. As the material is easy to process and the ligament size can be tailored within the nm-µm range without changing the relative density of the foam itself, npg can be regarded as a model material for studying size effects on nanoscale porous structures [5]. The objective of this study is to understand the deformation behaviour of nanoporous metal networks, in particular the interplay between the size of single struts, the nanoporous network morphology and the defect structure.
Here we present results on *in situ* small scale testing of nanoporous gold (npg) in scanning electron microscopy (SEM) (cf. Figure 1) and transmission electron microscopy (TEM) (cf. Figure 2). By combining nano- and micromechanical testing of pillar structures with advanced tomographic imaging, a 3D characterization of the plastic deformation process in different states of deformation is achieved. For small ligament sizes (~ 30 nm) 360° electron tomography (ET) is applied enabling high quality reconstructions of the 3D morphology of npg without missing-wedge artefacts (cf. Figure 2). Combining the geometric information with mechanical data from *in situ* testing in SEM and TEM the yield strength is precisely determined. Furthermore, the experimentally derived 3D data are used as input for large-scale molecular dynamics (MD) and finite element simulations in order to understand the role of strain localization and identify predominant defect processes.
For larger ligament sizes (~ 300 nm), mechanical testing and 3D structure analysis of npg pillars are carried out by *in situ* SEM and high-resolution X-ray tomography (XT), respectively (cf. Figure 3). Image correlation analysis applied to *in situ* SEM image series reveals the evolution of local strain gradients during deformation (cf. Figure 1a) and, in particular, local yielding in the very early stages of deformation. The yield strength strongly depends on strut size revealing a clear size effect. The scale-bridging approach is complemented by *in situ* nanomechanical testing of single struts in TEM.

References:
[1] C. A. Volkert, E. T. Lilleodden, D. Kramer, J. Weissmüller, Appl. Phys. Lett., 89, 2006.
[2] A. M. Hodge, J. Biener, J. R. Hayes, P.M. Bythrow, C. A. Volkert, A. V. Hamza, Acta Mater., 55, 2007.
[3] J. Biener, A. M. Hodge, J. R. Hayes, C. A. Volkert, L. A. Zepeda-Ruiz, A. V. Hamza, F. F. Abraham, Nano Lett., 6, 2006.
[4] M. Hakamada, M. Mabuchi, Scr. Mater., 56, 2007.
[5] E. Seker, M. L. Reed, M. R. Begley, Materials, 2, 2009.

Acknowledgment
The authors gratefully acknowledge the financial support of the German Research Foundation (DFG) within the research training group GRK 1896 In-situ Microscopy with Electrons, X-rays and Scanning Probes, the priority program SPP 1570 (project SP 648/4) and the Cluster of Excellence EXC315 Engineering of Advanced Materials. They further thank Dr. Colin Ophus (NCEM, Berkeley) for helpful discussion on Bézier surface fitting.

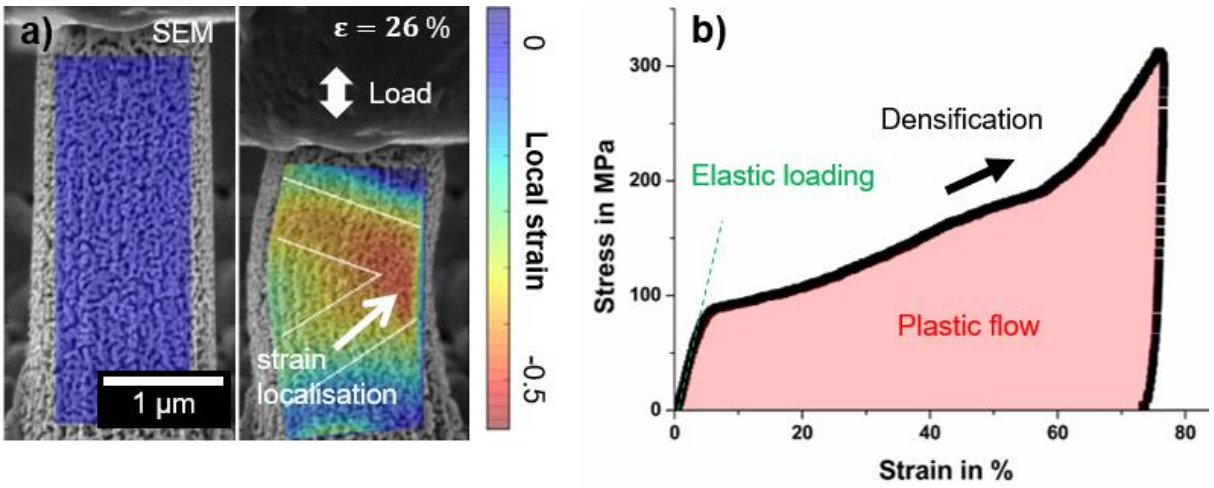

Figure 1. Investigation of strength, plasticity and failure by SEM *in situ* compression testing. a) Evolution of local strain upon deformation. b) Corresponding stress-strain diagram revealing initial elastic loading, plastic yielding and densification of the porous network.

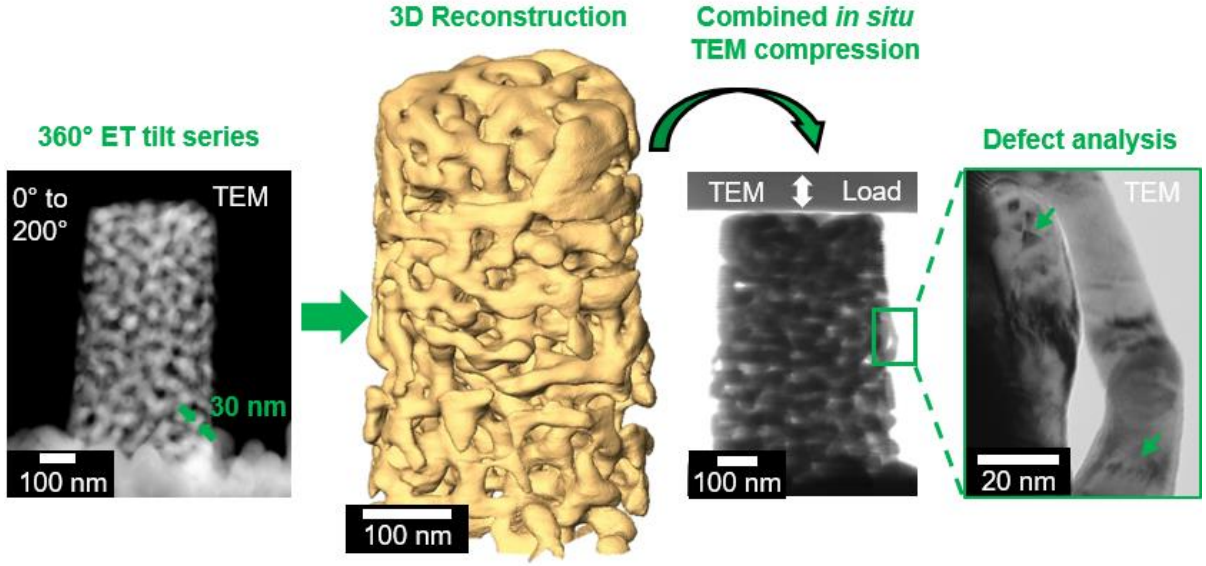

Figure 2. Advanced 3D characterization of the deformation process on orientation-specifically prepared npg pillars by combining *in situ TEM* nanomechanics and 360° ET followed by subsequent defect analysis in the TEM.

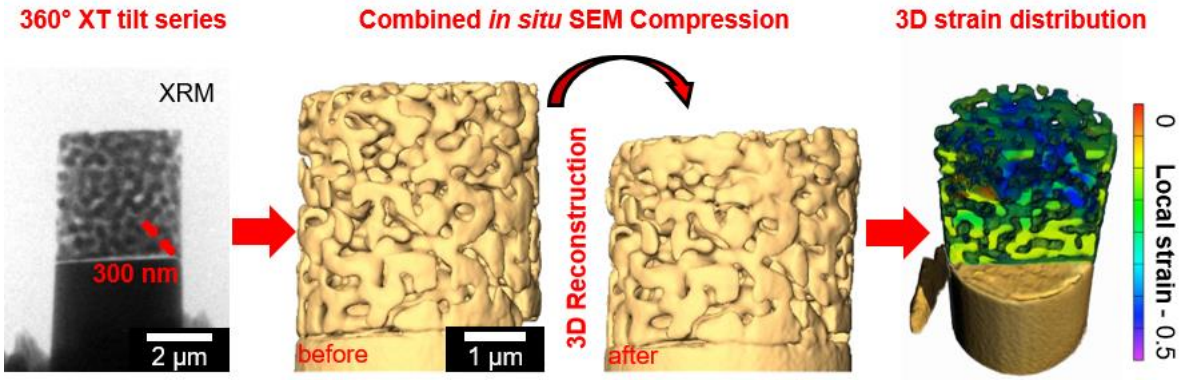

Figure 3. Scale-bridging 3D analysis of coarser npg pillars by means of *in situ SEM* nanomechanics and 360° XT revealing the distribution of plastic strain after deformation.

IM1.P033
SEM / EDX with silicon nitride window: better surface sensitivity and new analytical capabilities

U. Gernert[1], D. Berger[1]

[1]Technische Universität Berlin, Zentraleinrichtung Elektronenmikroskopie ZELMI, Berlin, Germany

ulrich.gernert@tu-berlin.de

20 years ago, the first silicon drift detector (SDD) for use with an SEM was placed on the market. It's main advantage is the property, to process much higher input count rates than the established Si(Li)-detector. Thus, high-resolution quantitative mappings became possible. The latest generation of SDDs gives the additional possibilities to detect usable lines below 200 eV and to do highly surface-sensitive EDX analyses at low excitation energies with a good lateral resolution at the same time. Even insulating samples can be analyzed without changing its surface by coating. The low energy EDX analyses fits very well to the outstanding lateral resolution and high surface sensitivity of recent high-end SEMs operated at low acceleration voltages of 1 kV and below. This contribution considers new capabilities of low acceleration voltage EDX analyses with the new SDD types.

The investigations were carried out with an Octane-A Plus SDD from EDAX mounted on a Hitachi SU8030 SEM. The SDD is equipped with an Amptek module, including a low noise preamplifier and an 80 nm silicon nitride window. Comparative measurements were done with an EDAX Apollo XP SDD equipped with a conventional SDD module and a 300 nm polymer window (Moxtek AP3). As test samples silicon carbide (SiC), titanium (Ti), chrysoberyl ($BeAl_2O_4$), aluminium oxide (Al_2O_3) and a layered aluminium-silicon sample (Al-Si) were selected.

The refined detector module of the Octane-A has a higher sensitivity for energies below 1 keV and enables the detection of X-ray energies down to about 70 eV. The spectrum of SiC, measured with the Octane-A SDD shows a strong Si-Ll-Line [Fig. 1]. Thus, SiC could be analyzed with high surface sensitivity by reducing the accelerating voltage below 1 kV. In contrast, the Apollo XP SDD does not detect the Si-L_l-line. To excite the Si-K-line the accelerating voltage has to be increased to at least 2.5 kV and the surface sensitivity as well as the lateral resolution would be much lower.

A second example for the high surface sensitivity of the Octane-A at low excitation energy is given in figure 2. The L-lines from Al and Si are well separated, therefore thin Al-layers on Si or vice versa can be analyzed. The information depth of Al-L is determined by Monte Carlo simulation to 20 nm, which gives an idea of the achievable depth resolution in analyzing thin coatings.

Another application of the soft X-ray detection is shown in figure 3, by comparison of a chrysoberyl ($BeAl_2O_4$)- to an Al_2O_3-spectrum. Obviously, the Octane-A detector is not only able to detect the Be-K-line (109 eV) but also to separate it from the Al-L_l-line (69 eV). However, the peak deconvolution is imprecise in this energy region and thus the identification of 7 wt% Be in $BeAl_2O_4$ is close to the detection limit.

The SiC-spectra in figure 1 show that the sensitivities of both detectors are close together for the C-K-line, but for the Ti-L_l-line the sensitivity of the Octane-A is two times higher [Fig. 4]. The reasons are the different absorption properties of the windows. The same applies for the analysis of nitrogen, whose K-line (392 eV) has nearly the same energy as Ti-Ll (395 eV). The higher sensitivity of the Octane-A for low energy lines is enabled by both, the detector module and the silicon nitride window.

In conclusion it can be said that the latest SDDs with silicon nitride window allow for a useable detection of low energy lines in the range of 70 eV to 2 keV, e.g. K-lines of Be to N, or L_l-lines from Al, Si, Ti or corresponding M- and N-lines of heavier elements. This enables for the first time the useful detection of Be and the EDX analyses with low acceleration voltages for highest lateral resolution and surface sensitivity. To gain quantitative evidence, the peak deconvolution has to be improved and because of strong absorption effects within the sample material the usage of standards is mandatory.

We kindly acknowledge fruitful discussions with M. Schleifer and F. Eggert from EDAX.

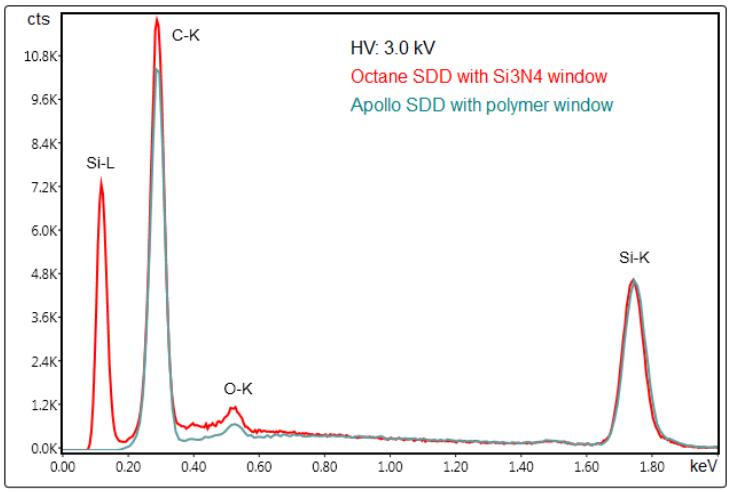

Figure 1. EDX spectrum of SiC for different SDDs.

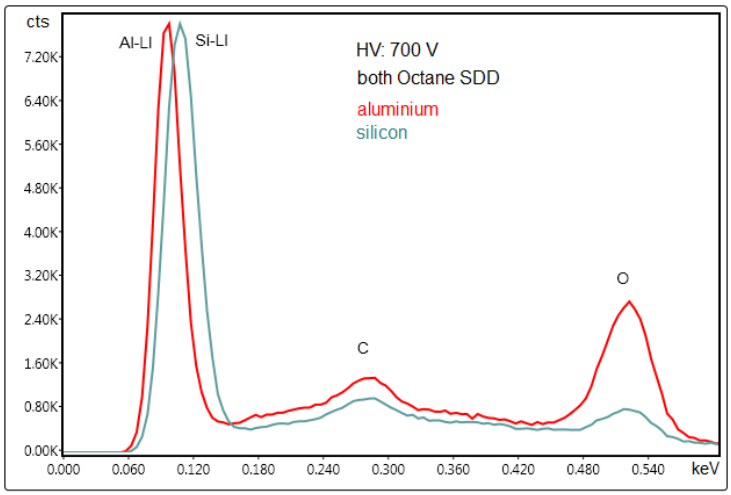

Figure 2. EDX spectra of Al and Si.

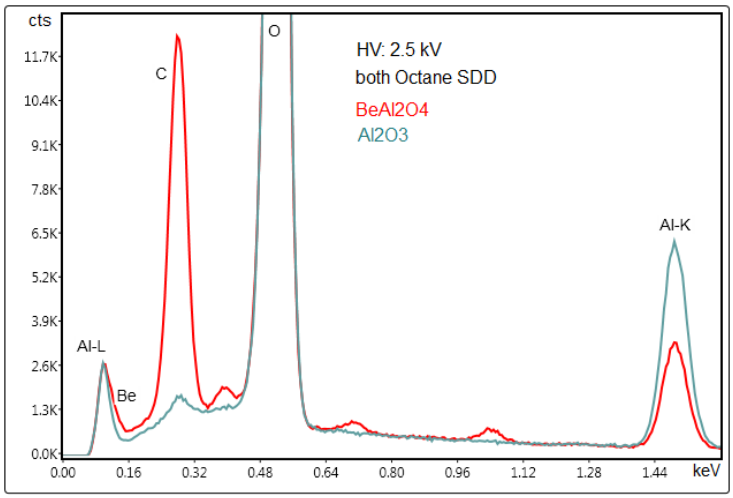

Figure 3. EDX spectra of $BeAl_2O_4$, and Al_2O_3.

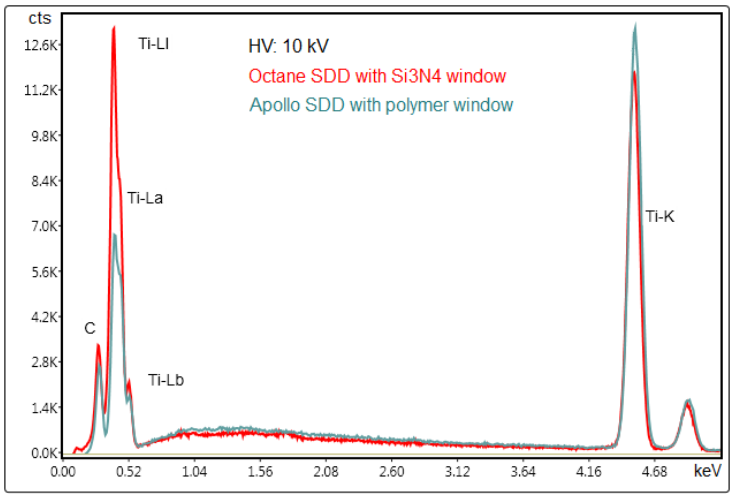

Figure 4. EDX spectrum of Ti for different SDDs.

IM1.P034
Exploring the full potential of ultra-low-energy electron microscopy – LEND and SEM-STEM

C. Dolle[1], P. Schweizer[1], E. Spiecker[1]

[1]Institute of Micro- and Nanostructure Research, Erlangen, Germany

christian.dolle@fau.de

Current trends in electron microscopy point towards low-voltage applications [1,2]. The reduction of beam energy offers several benefits like reduced beam damage and higher scattering cross sections, especially beneficial for the investigation of light elements. Widely recognized examples of light element-materials are graphene and carbon nanotubes, which have been thoroughly investigated by electron microscopy demanding primary beam energies below 80 keV to exclude knock-on damage.
While dedicated low-voltage TEMs are only slowly entering the commercial market, scanning electron microscopes already use primary electron energies of 0.5-30 keV and thus offer an easy access to low-voltage microscopy.
The SEM is a highly versatile tool for the investigation of novel materials by offering a complex set of applicable techniques, less spatial limitations compared to a TEM, high throughput and the possibilities to use a wide range of available add-on tools (e.g. manipulators, GIS, *in situ* equipment) while still maintaining resolution in the nm-range and high material contrast [3].
Besides the well-established imaging of surfaces by secondary electrons and chemical contrasts/composition by backscattered electrons and X-Ray spectroscopy, a SEM gives access to ultra-low-voltage transmission SEM (SEM-STEM). State-of-the-art STEM detectors are very versatile and even allow for the retrieval of crystallographic information of ultra-thin specimens like graphene.
To address crystallographic questions and to understand the contrast formation mechanisms in dark field SEM-STEM, electron diffraction is inevitable. So far, only few SEMs are equipped with dedicated CCD cameras to explore convergent beam electron diffraction patterns, therefore we will show a portable setup to record Low Energy Nanobeam Diffraction (LEND) patterns of graphene in a SEM at low primary electron energies. The path of diffracted beams, depending on the beam energy and working distance, is elucidated and the contrast formation in SEM-STEM imaging is explained. The combination of two independent adjustment parameters, working distance and primary beam energy give access to a wide range of imaging conditions.
Diffraction patterns are sequentially acquired in a FEI Helios NanoLab 660 FEGSEM by commercially available Ditabis imaging plates which are evaluated *ex situ* (see fig. 1). The LEND patterns are used to characterize the convergence angles and, more importantly FEI's own immersion mode. This mode boosts the microscopes resolution down to 0.7 nm by applying a magnetic field around the objective pole piece which increases the effective numerical aperture. The applied field has a severe impact not only on the probe formation but also on the path of the diffracted electrons behind the sample. However, by acquiring series of diffraction patterns we can deduce the effect of the magnetic field on the scattering angles reaching the segmented STEM detector and can adjust the imaging parameters for maximum contrast images.
With the gathered knowledge, we will present qualitative and quantitative investigations of graphene by SEM-STEM imaging and Nanobeam diffraction. With SEM-STEM imaging using dark field (DF) detectors we will show how to reliably discriminate between mono- and bilayer graphene, as well as, in the case of bilayer graphene, the assignment of Bernal AB-stacking versus turbostratically rotated stacking. Finally, topographic information and defect contrasts in bilayer graphene will be shown by application of SEM-DF-STEM at ultra-low primary electron energies of 2 keV and below (see fig. 2).

[1] U. Kaiser *et al.*, Ultramicroscopy 111, **2011**, 1239
[2] T. Sasaki et al., J. Electron Microsc. 59, **2010**, s7–s13
[3] V. Kochat *et al.*, J. Appl. Phys. 110, **2011**, 014315

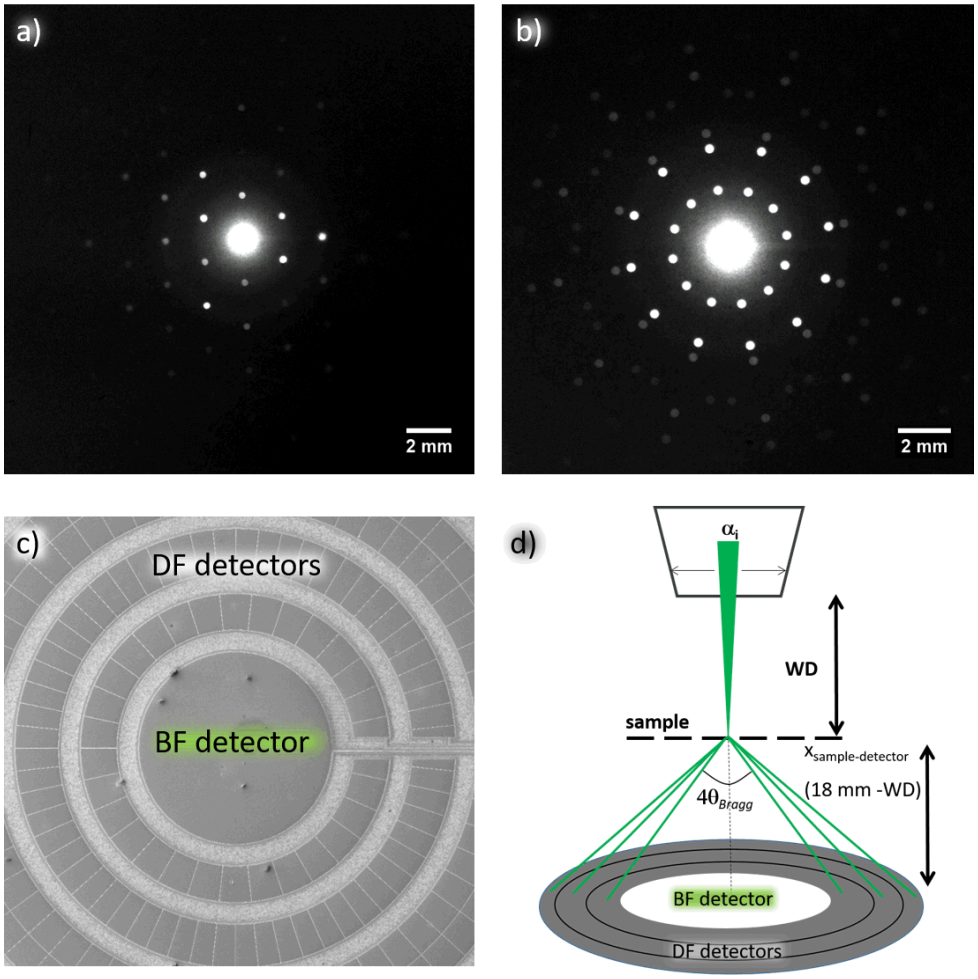

Figure 1. LEND patterns aquired in SEM. AB-bilayer graphene at 20 kV (a) and rotated bilayer graphene at 30 kV (b), setup of the FEI STEM III detector (c), schematic beam path of electrons in STEM-SEM (d).

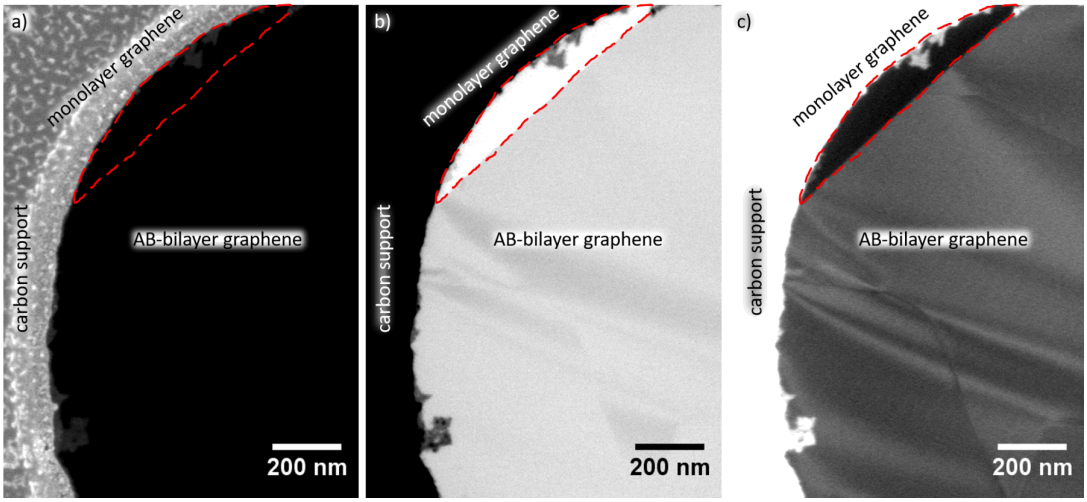

Figure 2. Ultra-low-energy (2keV) images of AB stacked bilayer graphene. SE (a), BF (b) and HAADF image (c).

IM1.P035
High throughput TEM and SEM – automated loading of multiple liquid samples onto a single grid

A. Sweet[1], W. Weigel[1]

[1]SCIENION AG, Berlin, Germany

asweet@scienion.de

Automate and miniaturise loading of your transmission and scanning electron microscopy samples onto grids using sciTEM, SCIENION"s picolitre dispenser.
Analysis of nanoparticles by TEM is a useful characterization method. However, by nature of TEM instrument design placing sample grids under high vacuum, the number of samples that measured in a given time period is limited.
For over 15 years, SCIENION"s picoliter liquid dispensing technology has been used to deposit arrays of different sample solutions onto a wide variety of substrates. Applying this well-proven technology to dispense multiple liquid samples as colloidal suspension of nanoparticles onto a single TEM grid is an obvious extension.
Our technology can be applied to dispense multiple different samples of nanoparticles and a range of other substances onto a single TEM sample grid. This application will enable high-throughput analyses and experimentations that were previously not possible.

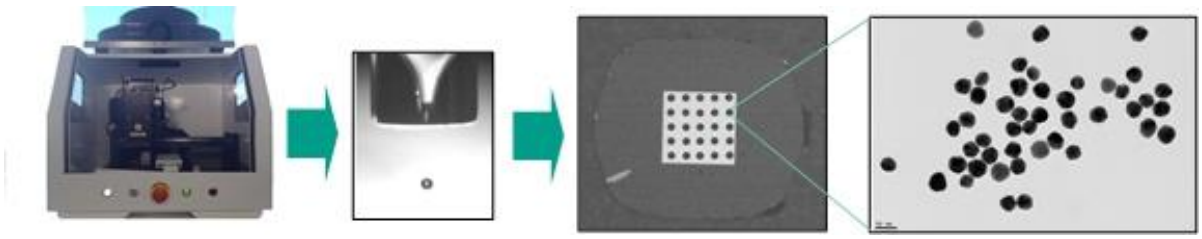

Figure 1. Printed 5x5 array of 100 pL solutions of nanoparticles using a piezoelectric drop generation with a sciTEM system. TEM image shows distribution of 40 nm Au nanoparticles within a single spot.

IM1.P037
Comparison of LVEM5, LVEM25 and standard TEM

E. Coufalová[1], E. Pavlova[2], M. Šlouf[2], P. Štěpán[1], M. Drštička[1], V. Kolařík[1], P. Hozák[3]

[1]Delong Instruments a.s., Research&Development, Brno, Czech Republic
[2]Institute of Macromolecular Chemistry , Prague, Czech Republic
[3]Institute of Molecular Genetics, Prague, Czech Republic

eva.coufalova@delong.cz

Introduction: The same specimen of Ag nanospheres and Pd nanocubes has been observed in three microscopes, LVEM5 (the accelerating voltage of 5 kV)[1], LVEM25 (25 kV)[2], and standard TEM (120 kV).
Objectives: The reason is to verify/demonstrate if the low voltage microscopy can be applied for shape differentiation of nanoparticles used for multiple immunolabeling. The LV TEM microscopes are characterized by reduced instrument size, low demands on laboratory conditions, and enhanced contrast in the images. On the other hand it is necessary to use appropriate sample preparation, specially the thinnest possible support films, namely in the case of the 5keV TEM.
Materials and Methods: The specimen for testing contained Ag nanospheres (approximately spherical silver nanocrystals with average size of ~10 nm) and Pd nanocubes (cubic palladium nanocrystals with average size of ~15 nm). The nanoparticles were prepared according to procedures described elsewhere [3,4, 5] and deposited in the form of a thin homogeneous layer formed by means of ruthenium tris(bipyridyl) [6] on a thin, electron transparent carbon film covered by poly(lysine). One sample was prepared by simple deposition on clean very thin carbon film. The support carbon films were placed on standard TEM grids.
Comparison of the results from all three microscopes is shown in Fig. 1. The micrographs have been resized so that the real-width-of-image and aspect ratios of all three micrographs were exactly the same. Brightness and contrast for all four micrographs (including the Fig.2) has been adjusted by the same (automatic) procedure in ImageJ.
Results: The images show that the shape discriminability remains applicable at the low energies, but in the case of 5 keV the choice of supporting film is crucial. The same can be expected in the case of application of these particles as markers in thin tissue sections.
Conclusion: The LV TEM technique is applicable for shape differentiation of nanoparticles used for multiple immunolabeling, the method of sample preparation is crucial at the energy as low as 5 keV.
The voltage of 5 keV is certainly well applicable for such tasks as nanoparticles preparation technology checks.
The voltage of 25 keV in comparison with the standard TEM might have the advantage of higher contrast and suppression of phase and crystallographic contrast features in the images for the particles discrimination and possible automated image recognition.

References:
[1] Delong, K. Hladil, V. Kolařík and P. Pavelka, Low voltage electron microscope I. – Design, Proc. EUREM 12, I197
[2] E. Coufalova, M. Mynar, P. Stepan, M. Drsticka, V. Kolarik, Low voltage TEM from 10 kV to 25 kV, Proc. MCM2015 and MC2015
[3] Hozak P, Slouf M, Nebesarova J, Mosa M, Krivjanska M: Soubor vzájemně rozlišitelných nanočástic, způsob jejich přípravy a jejich použití pro vícenásobné ultrastrukturální značení Czech patent CZ 304250. (2010)
[4] Slouf M, Hruby M, Bakaeva Z, Vlkova H, Nebesarova J, Philimonenko AA, Hozak P: Preparation of stable Pd nanocubes for multiple immunolabeling. Colloid Surf. B-Biointerfaces, 100 (2012) 205–208.
[5] Philimonenko VV, Philimonenko AA, Sloufova I, Hruby M, Novotny F, Halbhuber Z, Krivjanská M, Nebesarova J, Slouf M, and Hozak P: Simultaneous detection of multiple targets for ultrastructural immunocytochemistry. Histochem Cell Biol 141 (2014) 229–239.
[6] Sloufova I, Prochazka M, Vlckova B: Identification of two Ag-2,2′:6′,2″-terpyridine surface species on Ag nanoparticle surfaces by excitation wavelength dependence of SERS spectra and factor analysis: evidence for chemical mechanism contribution to SERS of Ag(0)–tpy*J. Raman Spectrosc.* 46 (2015) 39–46.

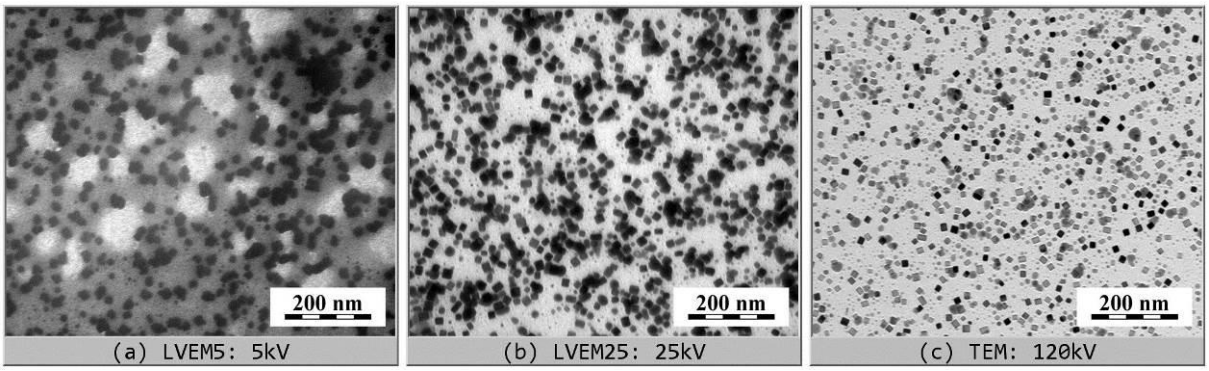

Figure 1. TEM micrographs showing mixture of Ag nanospheres and Pd nanocubes, which have been obtained with three different microscopes at the accelerating voltage of (a) 5 kV, (b) 25 kV, and (c) 120 kV.

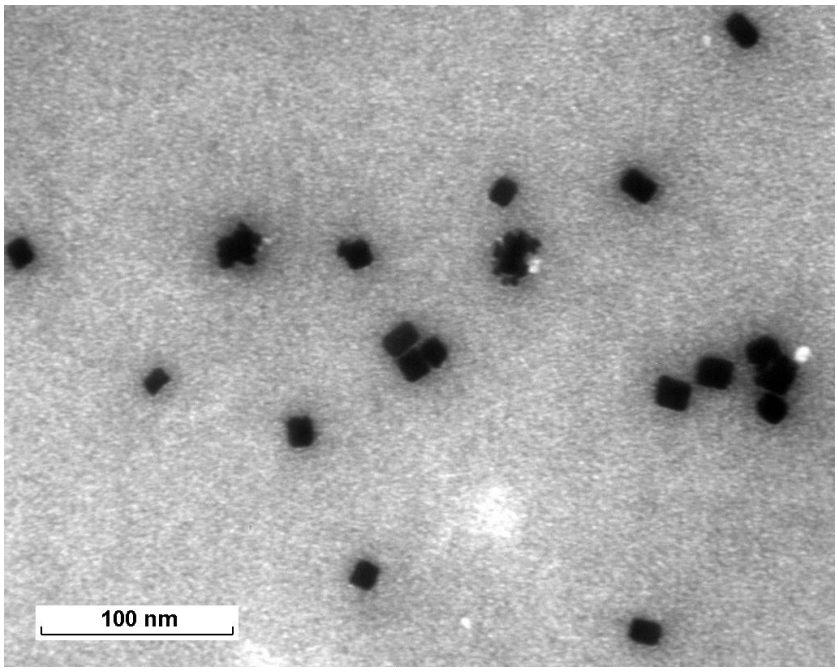

Figure 2. TEM micrograph detail of the same nanoparticles deposited on a clean carbon film taken at the accelerating voltage of 5 kV.

IM1.P038
A novel ultra-high resolution SEM column with a combined magnetic-electrostatic lens and flexible scanning

P. Sytar[1], A. Zavodny[1]

[1]TESCAN Brno, s.r.o., R&D Physics, Brno, Czech Republic

jaroslav.jiruse@tescan.cz

Introduction: The main propertiescritical parameters of the a scanning electron microscope (SEM) optical system are determined by the technology of the objective lens (altering the resolving power) and the configuration of the scanning elements (altering the field of view). A significant advance was made towardsin universality by was the introduction of Wide Field OpticsTM technology incorporating two objective lenses located below and above the double-stage scanning deflectors [1]. This configuration provides several display modes which delivers both high resolution imaging and a large field of view using optimizationing of the position of the scanning pivot-point position and an advanced engine for correction of correcting optical distortion. The technology further allows a mode with controlled depth of focus and a rocking beam mode with the pivot point on the sample. However, conventional lenses do not cannot provide high resolution at low beam beam-energies. Another technology uses An alternative to achieve ultra-high resolving power with is to use immersion optics, but the resolution in the magnetic-field-free mode is lower [2].
Objectives: Our main goal is to deliver an ultra-high resolution SEM column in the field-free mode while preserving all aspects of the Wide Field Optics like large field of view as well as channeling and other options. The detection system is an integral part of the column.
Materials and Methods: The column combines a high-potential tube with magnetic-electrostatic objective lens. The electrostatic part is located inside the magnetic polepieces with only a negligible portion of both the magnetic and electrostatic fields getting through to the sample. Thus the resolution at low beam energies is improved without restricting sample tilt which is especially critical for analytical applications or focused ion beam (FIB) milling.
Results: The column reaches the a resolution of 1.7 nm at 1 kV in field-free mode and 1 nm at 15 kV. The probe current can be as high as 400 nA. Channeling patterns are obtained by rocking the beam by up to 8 degrees. Requirements The requirements for extra extra-wide field of view, channeling or and live navigation were solved met by various varying scanning modes, see Fig. 1 - 4. In this way all these features, usually contradicting incompatible with each other, may be presentare possible in the same SEM column by switching between modes. A new detection system inside the SEM column was developed for advanced control of image contrast and low-kV operation. The in-column detectors allow the filtering of secondary electrons, energy filtering of back-scattered electrons and angular BSE selection.
Conclusion: Versatility of the SEM column was the key for the design. As a result, a unique combination of field-free resolution, wide-angle rocking beam and a wide field of view for live sample navigation has been achieved in the category of UHR SEM and FIB-SEM.

References:
[1] Wide field optics description at www.tescan.com
[2] J Jiruše, M Havelka and J Polster, Microsc. Microanal. 22 (Suppl 3), 2016, p. 578-579

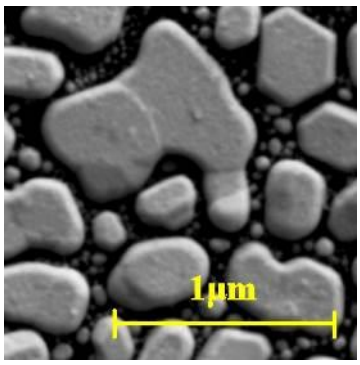

Figure 1. High magnification image of gold on carbon at 1 kV (at working distance of 6 mm).

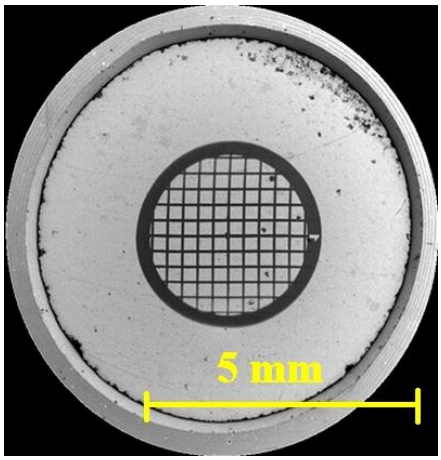

Figure 2. Minimal magnification without distortion at 1 kV (at working distance of 6 mm).

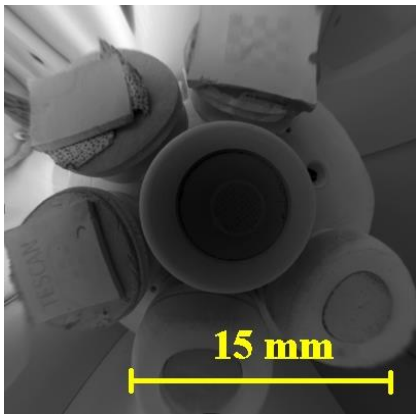

Figure 3. Live sample navigation with a slight distortion in the corners; field of view as large as 30 mm can be obtained at a WD of only 6 mm (image taken at 200 V).

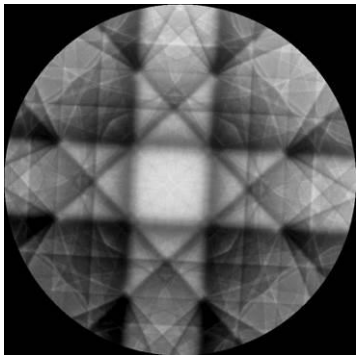

Figure 4. Channeling pattern with obtained by rocking the beam angles to by 6 degrees at 20 kV.

IM1.P039
Development of magnetic field free objective lens for atomic resolution imaging

Y. Kohno[1], S. Morishita[1], N. Shibata[2]

[1]JEOL Ltd., Akishima, Japan
[2]The University of Tokyo, Institute of Engineering Innovation, Tokyo, Japan

yukohno@jeol.co.jp

Ordinary STEM/TEM objective lens for high resolution imaging realizes short focal length and small chromatic aberration by putting a specimen in strong magnetic field, which works as electron lenses with principal planes close to the specimen. Therefore, it is difficult to observe samples at high resolution in Lorentz mode, where the specimen is placed out of magnetic fields. An addition of a spherical aberration corrector shows one way to improve the resolution in Lorentz mode. The improved resolution of 0.6 nm was reported with no excitation of the objective lens, located near a sample, using the spherical aberration corrector in combination with a monochromator that reduces the chromatic aberration [1]. Another example realized 0.24 nm resolution with spherical aberration corrected ultrahigh voltage microscope operated at 1.2 MV, using an objective lens located apart from the sample and no magnetic field at the sample [2]. However, the short focal objective lens is indispensable for realizing higher resolution imaging in Lorentz mode at regular accelerating voltages.
There were attempts to realize short focal length by using an objective lens pole piece which had magnetic poles to shield the sample from the magnetic field [3]. It is difficult, however, to realize the focal length less than 5 mm because the magnetic poles were necessarily thick for shielding. Therefore, we have been developing a new type magnetic-field-free objective lens as schematically shown in Figure 1. This lens composed of two round lenses: the Front Objective Lens (FOL) located in front of the specimen and the Back Objective Lens (BOL) located in back. The magnetic poles and coils of FOL and BOL are symmetric with respect of the specimen plane. However the polarities of their excitations are opposite, resulting in anti-symmetric magnetic field distributions. In this configuration, the z component of the fields of FOL and BOL at the specimen plane is canceled out. In addition, the radial component of the field is small near the optic axis for a round lens. This configuration can realize the objective lens which has short focal length and small magnetic field at the sample.
Figure 2 shows the experimental results on the characteristics of the BOL acquired at 180 kV. The focal length of the BOL was estimated to be 3.1 mm from its magnification, assuming the BOL works as a thin lens. We calculated the BOL magnification from the difference of magnifications of sample and the selected area aperture shown in Fig. 2(a). The chromatic aberration coefficient Cc* was estimated to be 2.9 mm from the gradient of the graph shown in Fig. 2(b), which plots focus variation depending on the accelerating voltage shift. The TEM lattice resolution of this system was estimated to be 0.2 nm from the image of gold foil shown in Fig. 2(c). The optical characteristics of FOL are almost the same as the BOL because of the symmetric design. The magnetic field strength in the region around the sample, where the radius from the optic axis is less than 0.3 mm and the z-direction length from the specimen is less than 0.1mm, was measured to be 0.3 mT using a magnetic field survey holder under the same condition as the above evaluations.
In conclusion, we developed the new magnetic field free STEM/TEM objective lens, which has small focal length and Cc*. We plan to use this objective lens in combination higher order aberration corrector [4], which may realize atomic resolution STEM/TEM imaging in Lorentz mode.

Acknowledgment: This development was supported by SENTAN, JST.

[1] T. Nagai, et al, Microscopy **64** suppl_1(2015), i112, doi:10.1093/jmicro/dfv275
[2] Y. Takahashi, et al, Microscopy and Microanalysis **21** Suppl. 3(2015), p 1865
[3] K. Shirota, et al, J. Electron Microsc., **25**(1976), p 303
[4] H. Sawada, et al, J. Electron Microsc., **58**(2009), p 341

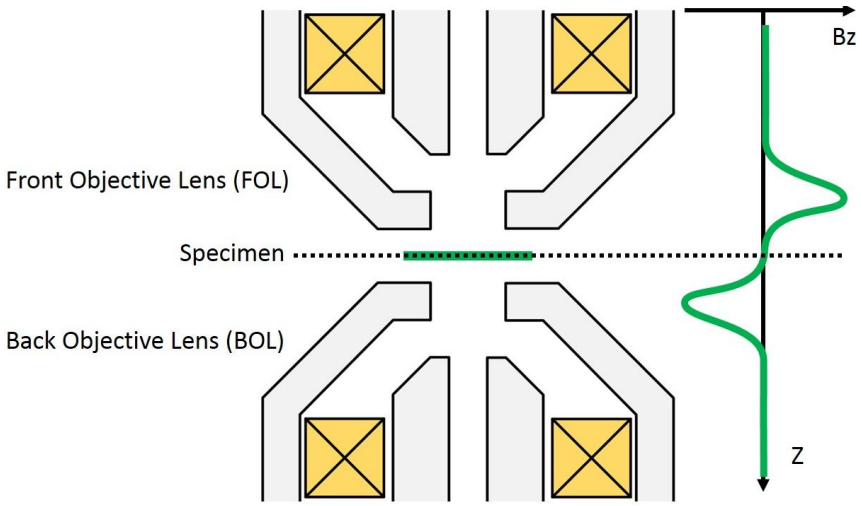

Figure 1. Schematic and z-field distributions of the new objective lens.

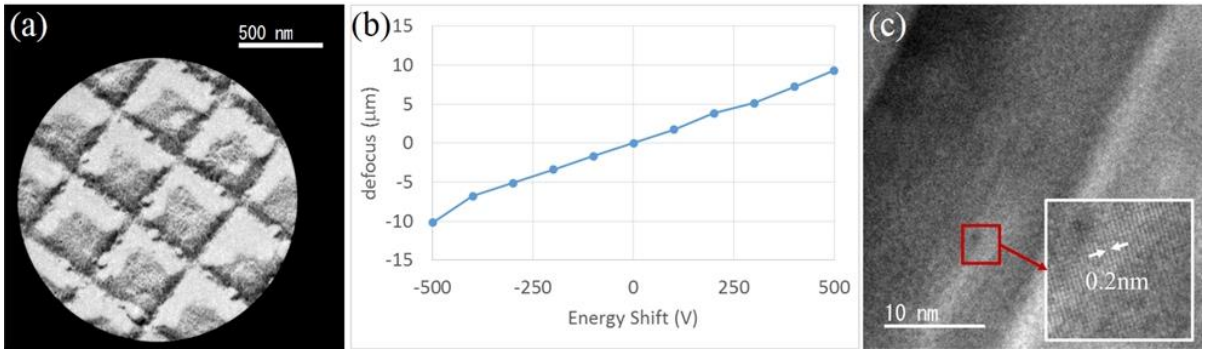

Figure 2. The experimental results of the measurements of optical parameters at 180kV. (a) an image of a grating replica with shadow of selected area aperture, (b) focus change depending on the energy shift, (c) TEM image of gold thin foil.

IM1.P040
Development of a reference material for image sharpness evaluation in scanning electron microscopy – the evaluation of second prototype

K. Kumagai[1], A. Kurokawa[1]

[1]National Institute of Advanced Industrial Science and Technology, Research Institute for Material and Chemical Measurement, Tsukuba, Japan

quaz.kumagai@aist.go.jp

Introduction: Similarly to other microscopies, the spatial images resolution is also one of biggest interests in scanning electron microscopy (SEM) for both of instrument manufacturers and users, as the resolution is an important indicator for the performance of an SEM instrument. At present, in the typical practice of specifying the resolution of SEM images, of measuring the smallest visible gap between two particles in an image, there still is poor repeatability and ambiguity owing to the selecting of the smallest gap by human operator. Thus, the technical committee on microbeam analysis in the international standards organization, ISO/TC202, has been developing a standard for the quantitative determination of image sharpness in SEM images based on derivative (DR) method [1,2].
Objective: Since the image formation in SEM has material dependence, Reference: materials (RMs) play important role in practical use of the image sharpness evaluation. For instance, there are needs of RMs to make a diagnosis of instrument and inter-instrument comparison. To meet these demands, we have been developing a Reference: material designed for image sharpness evaluation [3]. This paper presents the recent progress on our prototype of the RM.
Materials and Methods: According to the procedures for DR method [1], specimens for image sharpness determination should (1) consist of particles on background (2) show enough contrast between the particles and the background (3) have no contrast anomalies such as charging effect or strong edge effect.
Based on our previous study [3], the second prototype of RM was newly designed and fabricated by semiconductor process. As illustrated in Fig. 1, this prototype consists of arrays of W cylinder embedded in Si substrate, which appears as dot-array in SEM images. The prototype has three domains of dot-array with different diameters (60, 100 and 300 nm, respectively,) enabling us to choose the optimum dot size according to observing magnification. The depth of cylinder is designed to be 100 nm. We observed the prototype at various observing conditions to study the variation in and the contrast of W dots and image sharpness. The dot pitch d is measured by DUV diffraction to offer a capability to calibrate magnification with this prototype. To elucidate the quality of the prototype, the cross-section of W cylinders was evaluated by using SEM and transmission electron microscopy. Surface morphology of the dot-array was observed with atomic force microscopy.
Results: As shown Fig. 2, W dots were observed in bright contrast against background in SE images. The contrast is sufficient for the image sharpness determination. The W dots stably showed bright contrast over an accelerating voltage range of conventional SEM. The image sharpness values sensitively responded to the difference of the observing condition. The analyses on the detail structure showed that the prototype was fabricated almost as designed.
Conclusion: The authors have developed new prototype of RM for image sharpness evaluation. The SEM observations and analyses on the prototype revealed that the prototype is a promising candidate of the RM for image sharpness evaluation.

Acknowledgements
A part of this study was conducted as one of the activities in Japan Research Industries and Industrial Technology Association supported by JKA Foundation (FY2016). The authors are grateful to the staffs in super clean room facility (SCR) in AIST for their kind technical support in the fabrication of the prototype.

References:
[1] ISO/TS 24597:2011 Microbeam analysis – Scanning electron microscopy – Methods of evaluating image sharpness (2011)
[2] M Matthews and J Shah, Microsc. Microanal. **21** (2015) p. 2239.
[3] K Kumagai and A Kurokawa, Microsc. Microanal. **22** (suppl 3) (2016) p. 448.

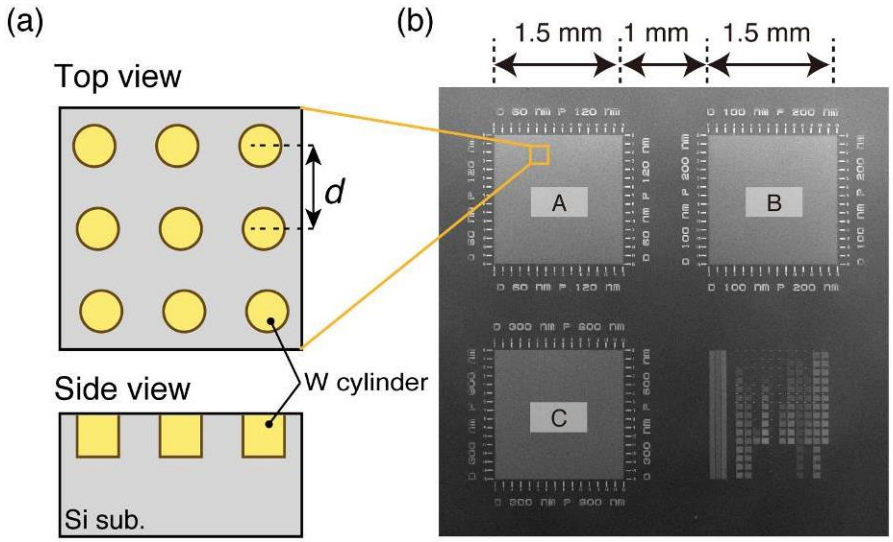

Figure 1. Schematics of the prototype of the Reference: material, which consists of W dot array embedded in Si substrate (a), and an SE image of the prototype (b).

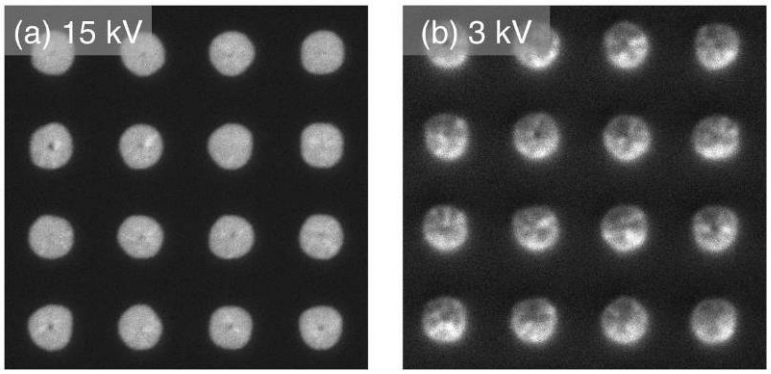

Figure 2. Typical SE images of the prototype (dot-pitch: 60 nm) taken by FE-SEM at accelerating voltages of (a) 15 kV, and (b) 3 kV.

IM1.P041
Advantages of nonstandard imaging methods in TEM and STEM

Z. Lee[1], U. Kaiser[1], H. Rose[1]

[1]University of Ulm, Ulm, Germany

zhongbo.lee@uni-ulm.de

Several nonstandard phase-contrast techniques have been proposed for TEM and STEM in 1977 at a time when aberration correction was not yet available [1]. Due to the revolutionary development of aberration correctors in the last decade, the methods can now be realized. Our calculations demonstrate that the resolution limit for bright-field (BF) imaging in a low-voltage Cc/Cs-corrected electron microscope can be appreciably improved by applying these methods.

In order to illustrate the advantages of nonstandard imaging, we have chosen $BaSO_4$ as an example (Fig.1a). The length of S-O bond is 1.49Å, and in [001] direction the projected bond length is 0.87Å. The point resolution of the SALVE C_c/C_s-corrected TEM with C_5 = 4mm operating at 50kV is 1.02Å for parallel illumination. In this case, it is impossible to resolve the S-O bond in [001] projection (Fig.1b). Compared with parallel illumination, hollow-cone bright-field illumination improves both the resolution limit and increases the signal-to-noise ratio of the image. The suitable illumination cone angle is obtained by adjusting appropriately the aberration coefficients C_1 and C_3. As a result, the resolution limit is lowered from 1.02Å to 0.7Å, which is more than sufficient to resolve the S-O bond in [001] projection (Fig.1c).

Standard STEM-BF imaging with a small disc detector produces the same phase contrast image as a TEM with parallel illumination. However, even in the BF mode the contrast of light atoms like sulfur and oxygen is very low compared with that of heavy atoms like barium(Fig.1d). Differential phase contrast methods offer a solution to reduce this problem, either by employing a Fresnel phase plate and a ring detector (DPC) [2] or by using the integrated signal of a split detector (IDPC). In both cases the nonlinear information is largely removed combined with an improved phase contrast. The enhanced phase contrast is especially sensitive to light atoms (Figs. 1e and 1f).

Summarizing, the results of our calculations demonstrate that nonstandard BF-imaging is in many cases more suitable than conventional BF-imaging using parallel illumination in TEM or a small central disc detector in STEM. The proposed methods offer the possibility to explore the nanoworld with a significantly improved gain of information.

[1] H. Rose. Ultramicroscopy 2(1977) 251-267.
[2] C. Ophus, J. Ciston, J. Pierce et al. Nat. Commun. 7(2016) 10719.
[3] We would like to acknowledge the financial support of DFG (German Research Foundation) and the Ministry of Science, Research and the Arts (MWK) of Baden-Württemberg in the frame of the (Sub-Angstrom Low-Voltage Electron microscopy) (SALVE) project.

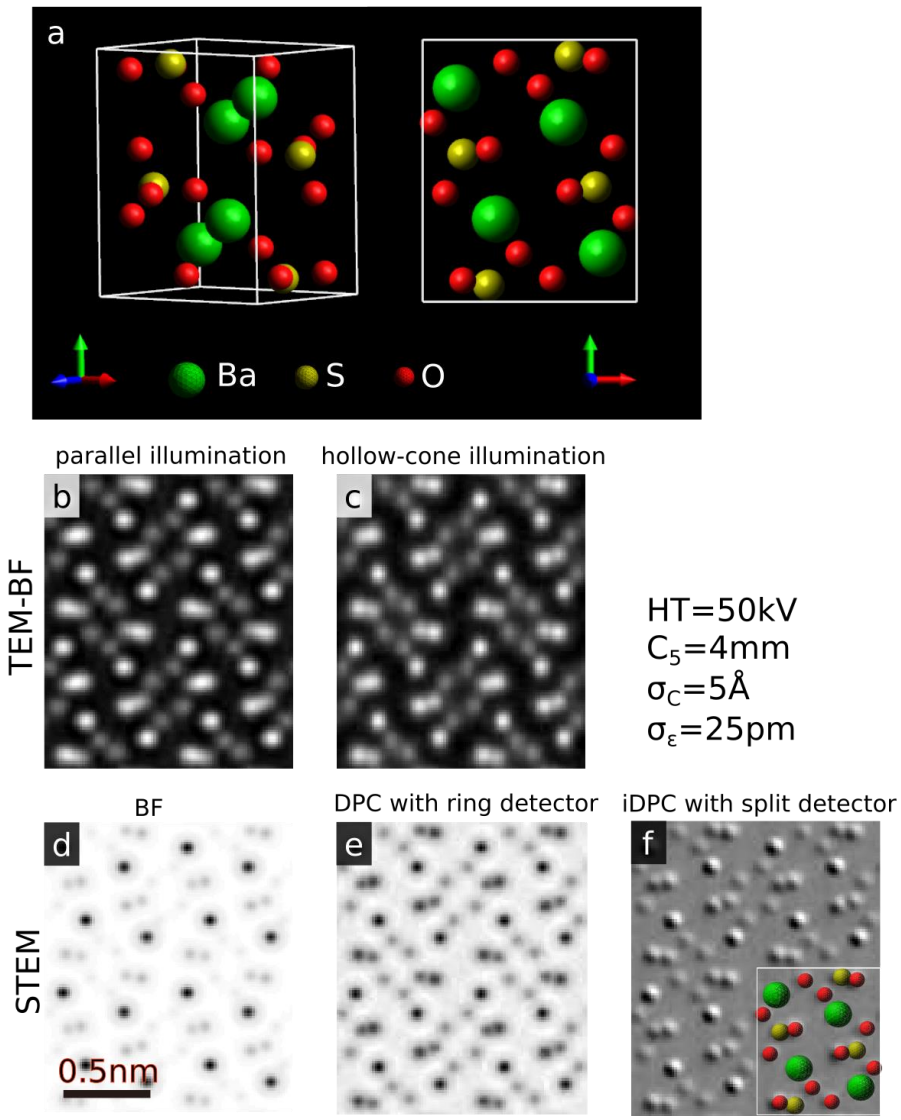

Figure 1. Calculated images for $BaSO_4$ with conventional and nonstandard (S)TEM at 50kV. a) The structure of $BaSO_4$. The S-O bond is 0.87Å in [001] projection. 2nd row: TEM-BF image of $BaSO_4$ with parallel illumination (b) and hollow-cone illumination (c). 3rd row: STEM image of $BaSO_4$ in BF mode (d), in DPC mode recorded with ring detector (e) and in DPC mode recorded with split detector (f).The 5th – order spherical aberration is set to 4mm for the calculation, and a residual focus spread of 5Å and an image spread of 25pm are taken into account.

IM1.P042
A detection system with controlled surface sensitivity for a novel UHR SEM

P. Sytar[1], J. Paral[1]

[1]TESCAN Brno, s.r.o., R&D Physics, Brno, Czech Republic

jaroslav.jiruse@tescan.cz

Introduction: Control of the surface sensitivity of the detected signal electrons is beneficial for modern scanning electron microscopy. Conventional methods include observing with secondary electrons (SE) which are created at the vicinity of the sample surface or with backscattered electrons (BSE) whose interaction volume inside the sample surface depends on the energy of the electron beam. As these two basic SEM signals provide different types of contrast, finer control of the surface sensitivity of both SE and BSE images can be advantageous for specific applications.
Objectives: A new ultra-high resolution SEM with an extended detection system has been designed with emphasis on detection with low beam-energies and advanced filtering of the signal electrons for better control of the contrast type.
Materials and Methods: The tested SEM combines a high-potential tube with a magnetic-electrostatic objective lens delivering ultra-high resolving power in the field-free mode and two-stage flexible scanning with an extra wide field of view. It can also be combined with a focused ion-beam column.
To achieve the most surface-sensitive SE images, the portion of SE signal located in the vicinity of the optical axis of SEM column can be detected simultaneously with main SE signal using two specially designed detectors inside the column.
A straightforward approach to control the surface sensitivity of BSE is energy filtration. The penetration depth of BSE into the sample surface is already decreased at low beam energies [1]. High-pass BSE energy filtering may be used for even smaller interaction volumes [2]. The BSE detector has been designed incorporating a filtering grid that can be biased up to 6 kV. The detector provides low-loss BSE image or BSE image in which sample charging artefacts are reduced.
At high acceleration voltages, the energy-filtering grid would need too high a potential to be sufficiently insulated in practice. In these cases, angular BSE filtration can control the type of contrast. Increased surface sensitivity can be seen in the images acquired with BSE particles with low take-off angles measured from the sample [3], [4] or with the axial part of BSE signal.
Results: A sample of gold on silicon with surface contamination with a 3.0 µm field of view was used for initial testing. Micrographs created with the axial portion of SE or BSE electrons and with BSE electrons with very low take-off angles measured from the sample show enhanced surface-sensitivity (see Fig. 1 and 3). The increased surface sensitivity of the low energy BSE image was achieved using energy filtration of BSE electrons (see Fig.2).
Conclusion: A new SEM column with field-free ultra-high resolution, a detection system for low-kV operation and advanced filtering of secondary and backscattered signal electrons is presented. Using this system, high magnification images with variable contrast types and controlled surface sensitivity was achieved.

References:
[1] L Reimer in Scanning Electron Microscopy, ed. H K V Lotsch, (Springer Verlag, Berlin) p.142.
[2] H Jaksch, Proceedings of EMAS 2011 (2011), p. 255.
[3] T Luo and A Khursheed, Journal of Vacuum Science & Technology B 25, 2007, p.2017
[4] T Aoyama, M Nagoshib and K Satoc, Surface and Interface Analysis, 2014, 46, p.1291

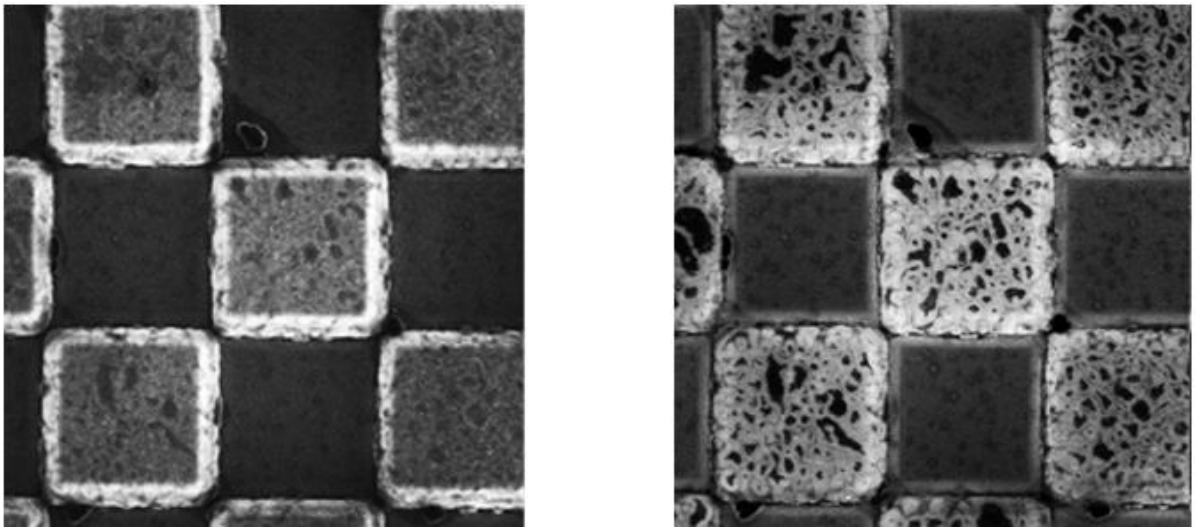

Figure 1. SE image of gold on silicone at 0.5 kV acceleration voltage (left) and image using the axial part of the SE signal with enhanced surface sensitivity (right).

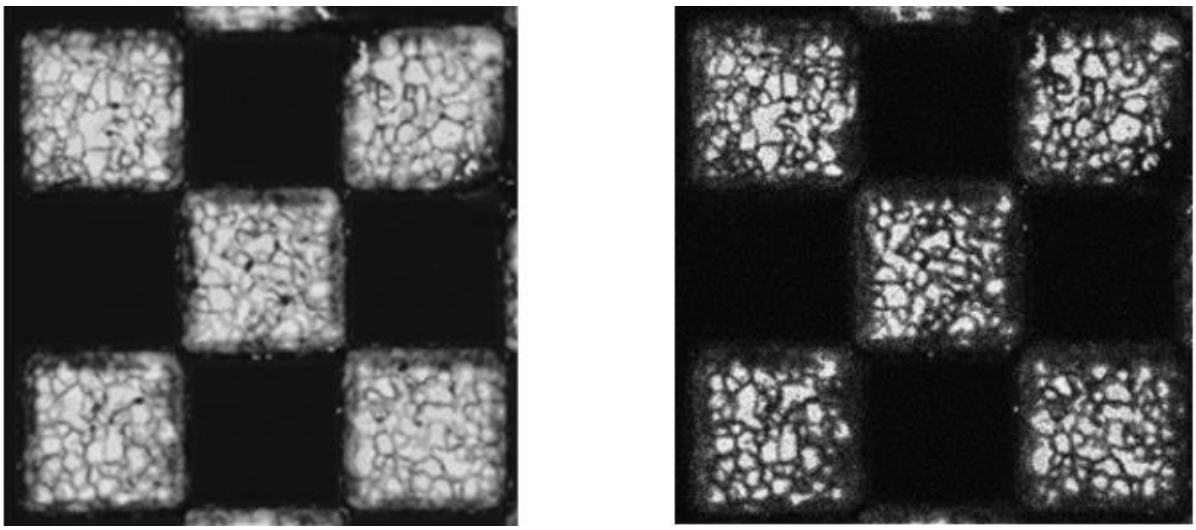

Figure 2. BSE image of gold on silicone at 2 kV acceleration voltage (left) and image using the energy filtered part of BSE signal in the 1900 eV- 2000 eV range with enhanced surface sensitivity (right).

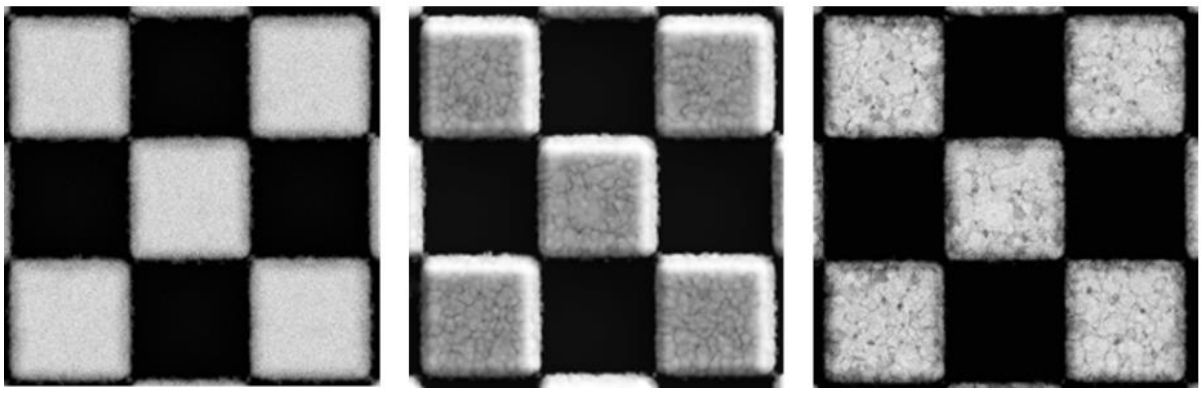

Figure 3. BSE image of gold on silicone at 10 kV acceleration voltage (left). Enhanced surface sensitivity using the wide-angle part of the BSE signal (center) and the axial part of the BSE signal (right).

IM1.P043
Method of manufacturing samples with the use of fib for the identification of nano-dimensional phase components in steels

L. Kutuzov[1], S. Fedotova[1], A. Frolov[1], G. Zhuchkov[1]

[1]NRC "Kurchatov Institute", Kurchatov Nuclear Technological Complex, Moscow, Russian Federation

kutuzov_lv@nrcki.ru

Atomic-probe tomography (APT) studies imply manufacturing of needle-shaped samples. Basically, metal samples are made by electrochemical polishing. However, in some cases (if the volume of the material under investigation is limited or if it is necessary to investigate certain places of the sample such as the grain or interphase boundaries, etc.), electrochemical polishing is not applicable. The focused ion beam method (FIB) is usually used to solve such problems.

Method of manufacturing samples for atomic probe tomography

Samples of irradiated weld metal steel (WWER-1000 steel SV-10KhGNMAA) were made by two techniques:

- Electrochemical polishing. This method is used for producing of both the samples itselves and the bases for the needle tips manufactured by FIB method.
- The method of focused ion beam.

This method enables preparing of the needles from an extremely limited volume of the material and choosing the place for the analysis. It also allows one to compare the data on the phase composition obtained by different methods (for example, TEM and APT) to each other.

Choosing the same sample is the key condition of correct comparison of the results obtained by APT and TEM methods ensuring no influence of heterogeneity in chemical or phase composition. The place for manufacturing of APT sample is selected next to the central hole of the TEM sample. This, first, accelerates the production of the blank, and, secondly, ensures the identity of the investigated section of the material.

Etching of FIB sample

The technique was tested on a two-beam Helios NanoLab 650 (FEI, US) system. The cuts were etched by the ion beam until a membrane was obtained. Then the needle was welded to the micromanipulator and cutted off from the sample by the ion beam. Steel blanks prepared by electrochemical method were used as the bases.

Cutting off small sections on both the right and left sides of the tip with a gradual rotation around its vertical axis, allowed us to achieve a cylindrical shape of the tip with a cross section of ~1 μm^2. Then the sample was tilted perpendicular to the ion beam axis and a tip was produced by a radial etching with a gradually decreasing radius until it was sharpened (Fig. 1). The modes of ion beam sharpening were chosen based on the optimal quality of the obtained needle tips.

After achieving the acceptable geometry the tip image was stored to be used later for reconstruction of the data obtained by the method of atomic-probe tomography.

Data acquisition and processing of the samples prepared by electrochemical polishing and FIB. The samples produced by the two methods were studied by APT using the Cameca LEAP 4000 HR atomic probe.

12 datasets of a total volume ~$6x10^{-21}$ m^3 were analyzed for the samples obtained by both the electrochemical polishing method and FIB.

Table 1 shows the average concentrations of the matrix and precipitates elements. Figure 2 demonstrates the 3D distribution of precipitates in the sample.

Analysis of Table 1 and Figure 2 shows:

- An inhomogeneous distribution of copper was demonstrated in the investigated model alloy (Fig. 2);
- The experimental results obtained on the samples made by the two methods overlap within the error limits

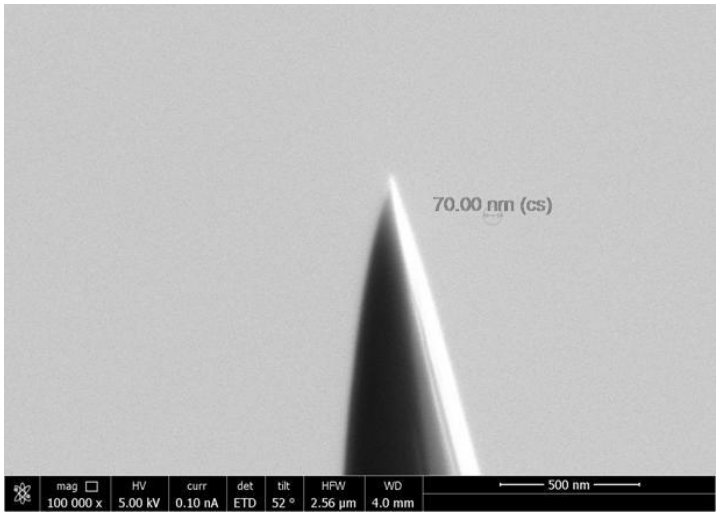

Figure 1. The sharpened needle tip.

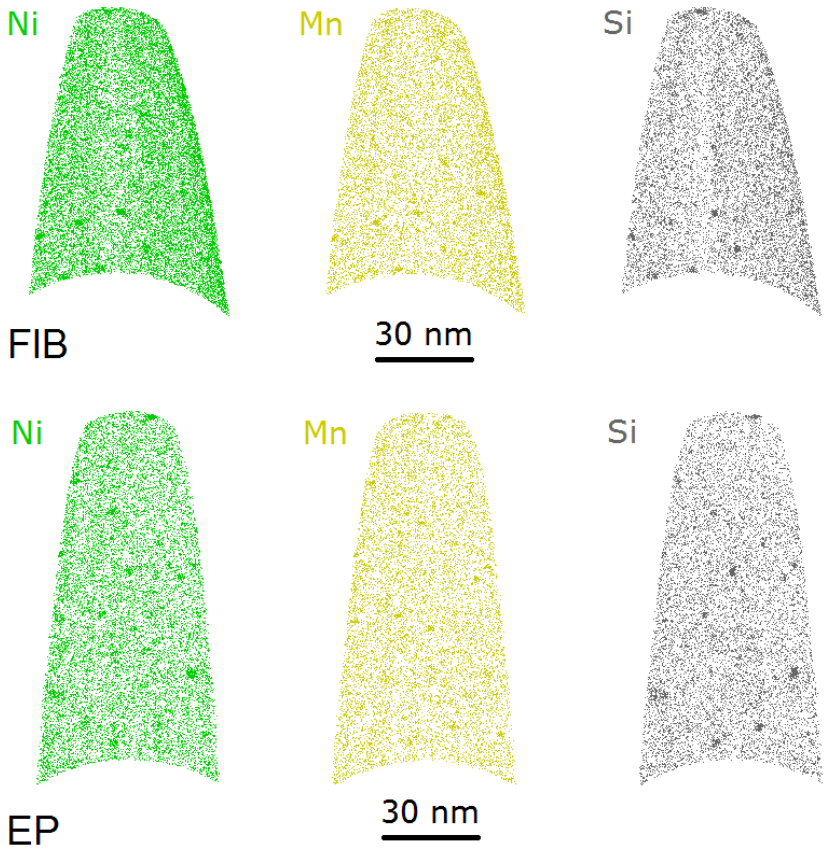

Figure 2. 3D distribution of key elements in the samples of the studied material manufactured by two techniques.

Technique		Composition, at%						
	Element	Fe	C	Si	Mn	Ga	Ni	Cr
Electrochemical polishing	Matrix	bal	0.07	0.69	0.67	-	1.64	1.83
	Precipitate	bal	0.03	13.6	6.9	-	17.7	0.2
FIB	Matrix	bal	0.07	0.72	0.76	**<0.01**	1.63	1.95
	Precipitate	bal	0.04	14.2	6.5	**<0.01**	18.5	0.21

Table 1. APT data on average compositions of matrices and precipitates.

IM1.P044
High performance PEGylated glass cover slides for optical microscopy

I. von der Hocht[1], T. Züchner[1], R. Ledesch[1], A. Albarghash[2], J. Fitter[2]

[1]Forschungszentrum Jülich, ICS-5, Jülich, Germany
[2]RWTH Aachen, 1. Physikalisches Institut, Aachen, Germany

i.von.der.hocht@fz-juelich.de

Fluorescence based single-molecule spectroscopy techniques offer the possibility to study individual (macro)molecules. These techniques facilitate to observe conformational states, conformational dynamics, and activity of single biological molecules unmasked by ensemble averaging and without the impossible requirement to synchronize all the molecules in the ensemble. A challenge using single molecule imaging techniques is the need to immobilize molecules of interest in the native state on a glass cover slide and to suppress any fluorescent background by blocking unspecific binding of especially proteins to the glass surface.
So we aimed to develop a cover slide coating that masks the glass surface and efficiently blocks adsorption of DNA and proteins. Furthermore the surface should allow the specific binding of functionalized DNA or proteins in the native state. Immobilization would offer the possibility to multiply the concentration of the molecule of interest locally and would expand the possible observation time.
In line with other published protocols on surface PEGylation [1,2] we first extensively cleaned and activated the glass slides. The NHS-ester functionalized PEG is then covalently bound to the surface via an amine functionalized silane. Densitiy of biotin anchors is adjusted by admixture of certain amounts of biotinylated PEG molecules in the PEGylation step. We use Piranha and plasma cleaning to clean and activate the sides, which is much cheaper and less toxic than the solvent based cleaning of the published protocols.
For the first time the blocking and specific binding properties of the PEG-coated glass slides were tested quantitatively and compared for DNA, soluble proteins, a solubilized membrane protein and ribosomes. The PEGylated slides block the adsorption of proteins up to a concentration of 200 nM. This is several orders of magnitude better than the blocking of e.g. a BSA coated glass cover slide.
We report on the preparation of PEGylated glass surfaces, which efficiently block the unspecific binding of DNA and proteins as well as ribosomes. These surfaces might be functionalized with e.g. biotin anchors to bind specifically via streptavidin or neutravidin a certain number of biotinylated DNA or protein molecules.
Eukaryotic cells also might grow well on these surfaces. So also life cell fluorescence imaging might benefit from using these surfaces having lower fluorescence background from adsorbed media components on the surface.

[1] Ha *et al*. Initiation and re-initiation of DNA unwinding by the *Escherichia coli* Rep helicase. *Nature*, **419**, 638-641 (2002).
[2] Tanner *et al*. Visualizing Single-molecule DNA replication with Fluorescence Microscopy. *J. Vis. Exp.*, **32**, e1529 (2009).

IM1.P045
3D Scanning in SEM – practical geometry and signals

G. Moldovan[1]

[1]point electronic GmbH, Halle, Germany

grigore.moldovan@pointelectronic.de

Introduction: Scanning Electron Microscopes (SEM) are instruments that produce 2D images of objects on the nanoscale; 3D scanners are instruments that produce 3D models of objects on the mm-scale. Is it possible to use an SEM as a high-resolution 3D scanner? What is required for a robust 3D scanning technique?
3D scanners an optical imaging system with a rotating sample stage, which mirrors common SEM configurations - an electron-optical imaging system with a 5-axes sample stage. 3D scanning includes algorithms for automated 3D reconstruction, and similarly, there have been attempts at developing 3D reconstruction algorithms for SEM, including photogrammetry [1-2] and stereo-photogrammetry [3], however no SEM software is available.
To help navigate terms across fields, any SEM method that produces 3D surface model will be termed here 3D scanning.
Objectives: The limitations of standard SEM stubs on standard stages axes present a barrier for practical 3D scans - for example maintaining a useful working distance. A new geometry is required to overcome this, as well as to enable automation.
Difficulties in reconstruction arise not only from the artefacts specific to SEM, such as charging, but more importantly from the shadows that highlight topography. Whilst this is beneficial for visual interpretation, it prevents the automatic reconstruction. Signals with minimum shadowing are required.
Method: The following we added to the standard SEM workflow:

(A) a nanotip was used to match stage axes, and to provide a wider range of angles.
(B) BackScattered Electron (BSE) and Electron Beam Absorbed Current (EBAC) signals were used as they contain less shadowing.
(C) Simultaneous acquisition was employed, such that additional textures may be built.

Uncoated cement was selected as a test sample and loaded onto the Tungsten nanotip. This was placed vertically on the sub-stage of an ZEISS DSM982 FEG SEM upgraded by point electronics GmbH. The needle was tilted so that the electron beam had a 60° incidence. 360° rotation was possible whilst maintaining the working distance, and the sample was rotated with 15° steps.
Relatively low resolution images of only 1,024x1,024 at 12µs/pixels were acquired. SE micrographs show strong charging artefacts, as the particles are not coated. BSE micrographs appear to be free of charging artefacts as the detector is insensitive to electrons of energy less than ~2keV.
3D scan data was loaded into Agisoft PhotoScan, where scale was entered manually. Reconstruction followed the automated workflow of aligning, building dense cloud points, meshing and texture.
Results: Reconstruction from this SE and IL dataset was not successful. Charging artefacts did reduce the number of useful data points, however further limitation arise from shadowing (not shown here), and the higher IL noise associated with the long working distance.
BSE and EBAC data produced a very dense mesh and detailed texture, thus showing that they provide more robust reconstructions than SE and IL. Further,
- BSE contains information on composition, and its available in most SEMs.
- EBAC signal is independent from the working distance and accelerating voltage, it does not have the resolution limiting factors of BSE, and it has a lower cost.
Conclusions: The work lays out the simplest and most robust approach to 3D scanning in SEM to date. The standard stub is replaced with a nanoprobing needle. BSE and EBAC signals are shown to give photogrammetric reconstruction where SE and IL fail. Short reconstruction time and simple sample geometry are suitable for automated live reconstruction.

[1] A Boyde and H F Ross, The Photogrammetric Record 8 (1975) p. 408
[2] L C Gontard et al., Ultramicroscopy 169 (2016) p. 80
[3] F Marinello et al., Measurement Science and Technology 19 (2008) 065705
[4] M Hemmleb at al., European Microscopy Congress (2016) p. 489

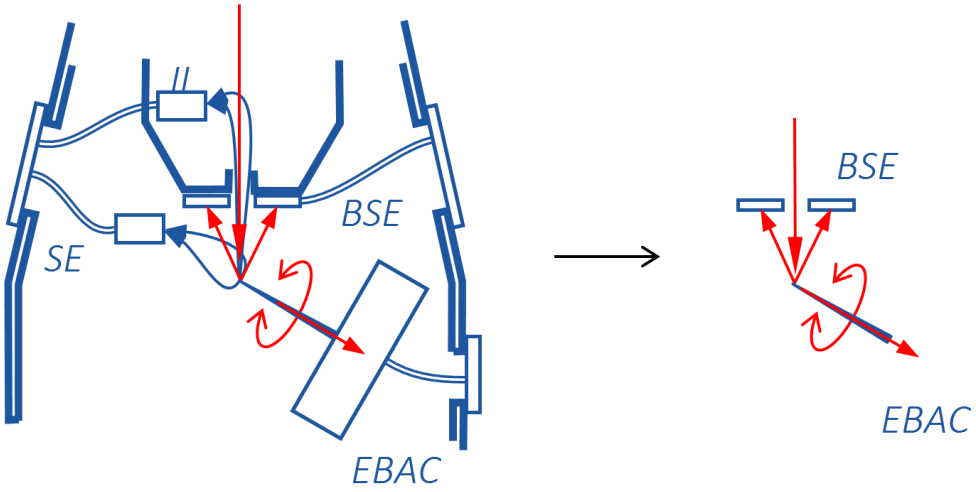

Figure 1. Detailed (left) and simplifier (right) diagram of 3D scanning in SEM.

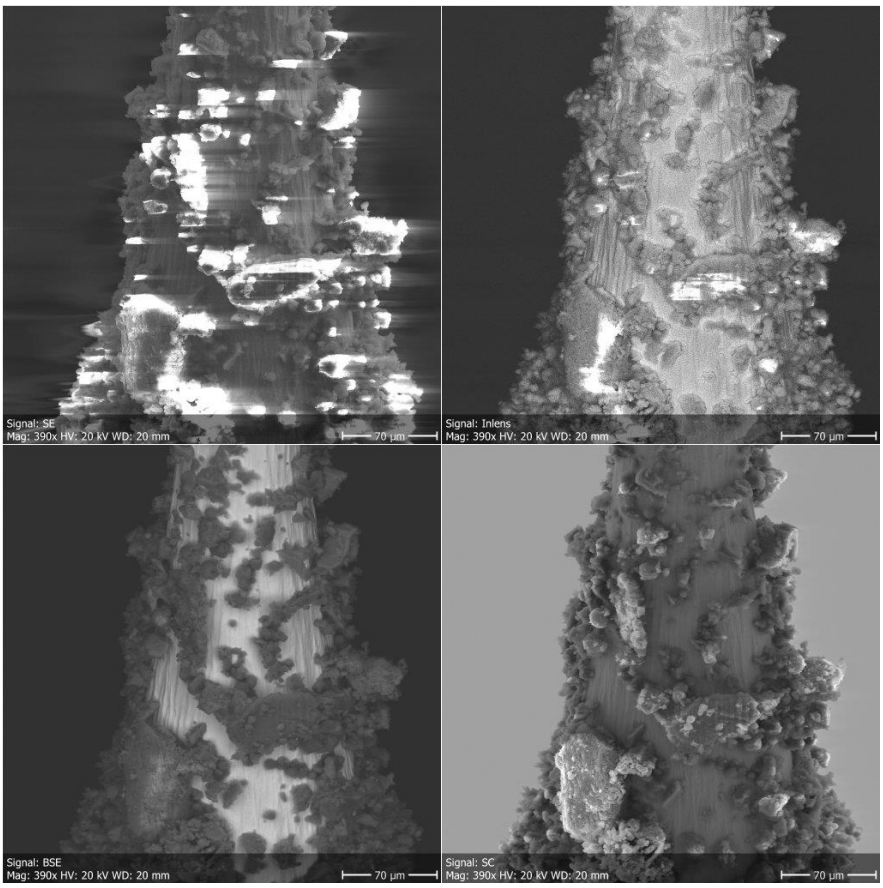

Figure 2. Typical SE (top left), IL (top right), BSE (bottom left) and EBAC (bottom right).

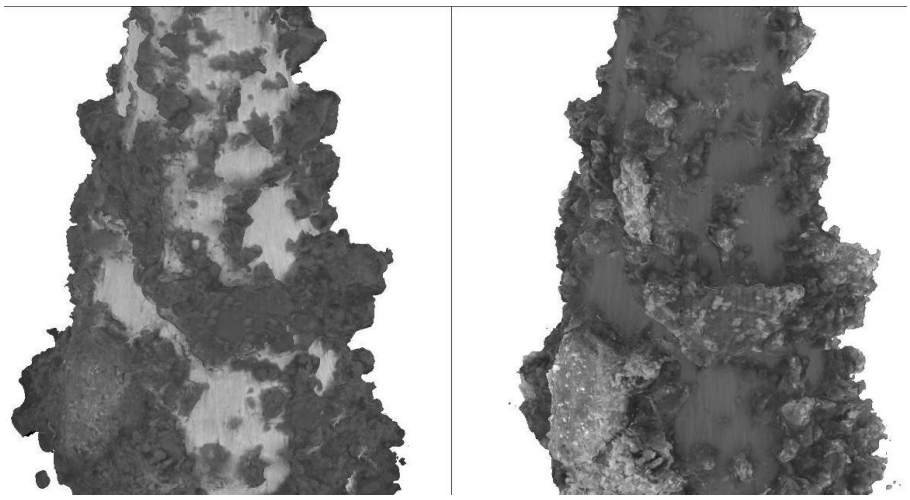

Figure 3. View of textured 3D models from BSE (left) and EBAC (right) data.

IM1.P046
Correlative in situ AFM & SEM & EDX analysis of nanostructured materials

M. Winhold[1], M. Leitner[1], A. Lieb[2], P. Frederix[2], F. Hofbauer[1], T. Strunz[1], G. Fantner[3], J. Sattelkov[4] H. Plank[4], C. Schwalb[1]

[1]GETec Microscopy GmbH, Vienna, Austria
[2]Nanosurf AG, Liestal, Switzerland
[3]EPFL, Institute for Bioengineering, Laboratory for Bio- and Nano-Instrumentation, Lausanne, Switzerland
[4]Graz University of Technology, Institute for Electron Microscopy and Nanoanalysis, Graz, Austria

marcel.winhold@getec-afm.com

During the last decade, the combination of different microscopic and spectroscopic methods into one instrument gained increasing importance due to the simultaneous acquisition of complementary information. Especially highly localized probing of mechanical, electrical and chemical properties on the lower nanoscale represents a key success factor for gaining new insights in the micro- and nanoworld. Correlating these complementary information is an indispensable task for further technological developments.

In this work, we present a unique atomic force microscope (AFM) – the AFSEM™ - designed for seamless integration into scanning electron microscopes (SEM) or other host systems (e.g. dual beam microscopes). Its open design allows to simultaneously operate SEM and AFM inside the vacuum chamber and perform correlative *in-situ* AFM/SEM/EDX analysis of nanostructured materials. For the first time, this allows direct in-situ combination of complementary techniques - SEM imaging, chemical information by EDX, real 3D topography, phase information, mechanical and electrical properties by AFM. This is rendered possible by eliminating the need for optical detection and implementing novel low-noise self-sensing cantilever probes [1].

For AFM measurements, the AFSEM™ was used in contact and AC mode using self-sensing cantilevers. These cantilevers are equipped with a deflection sensor that directly measures the cantilever signal electrically, therefore removing the space consuming requirement for optical readout. In addition, we use a 3D nanoprinting technology (focused electron beam induced deposition, FEBID) for a variable tip modification of the cantilever structures to achieve electric conductive nanoprobes with final tip radii of 15 nm and below.

We present a broad variety of case studies for correlative analysis of nanostructured materials. We demonstrate results for *in-situ* electrical characterization of nanostructures by combining SEM and conductive AFM measurements for nanoscale dose-dependent conductivity measurements of nanogranular Pt(C) structures after focused electron beam induced processing. In addition, we use the AFM capability inside the vacuum environment of the SEM for the analysis of ultrathin structures concerning roughness, real 3D topography, and electrical properties (e.g. Black Silicon, plasma treated surfaces). We show the first interactive AFM/SEM/EDX analysis that enables the direct correlation of (sub)nanometer topography, electrical and chemical information at the exact same sample position without the need of air exposure or sample transfer (Figure 1). Finally, we present correlative AFM/SEM imaging of graphene films as well as free-standing graphene membranes in the SEM. We show how the SEM allows to quickly identify areas of interest while the AFM enables high resolution analysis even in highly insulating regions (Figure 2).

Based on the broad variety of applications regarding the characterization of semiconductor materials and devices we anticipate the AFSEM™ to be the driving characterization tool for correlative SEM/AFM/EDX analysis in the future.

[1] M. Dukic, J.D. Adams and G.E. Fantner, Scientific Reports **5** (2015) 16393

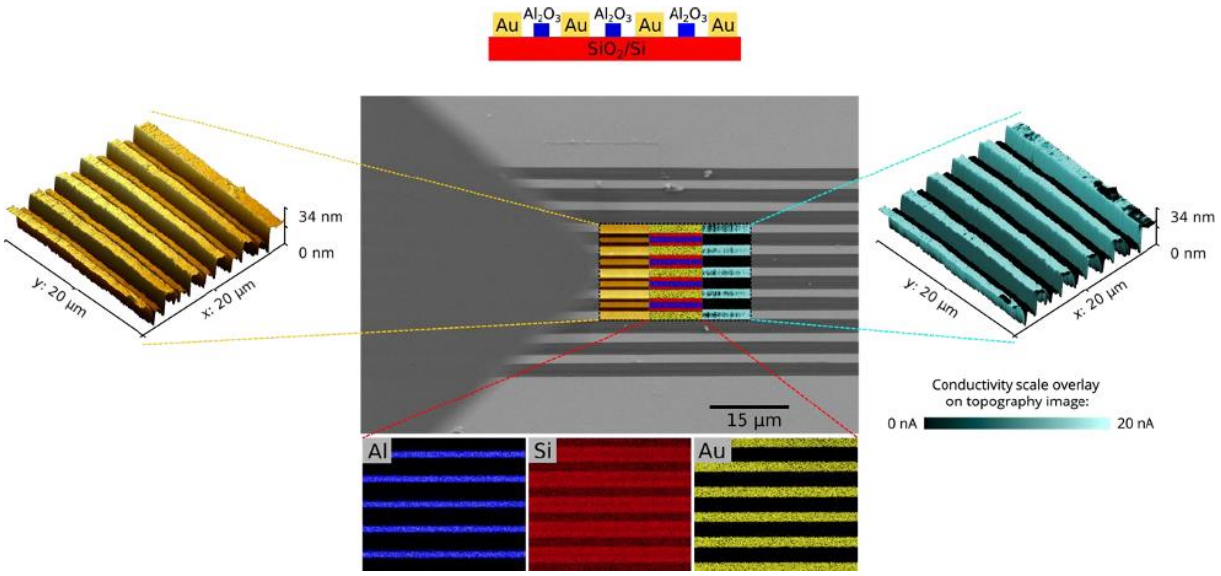

Figure 1. Combined in-situ SEM imaging, chemical analysis by EDX, AFM topography, and conductivity analysis.

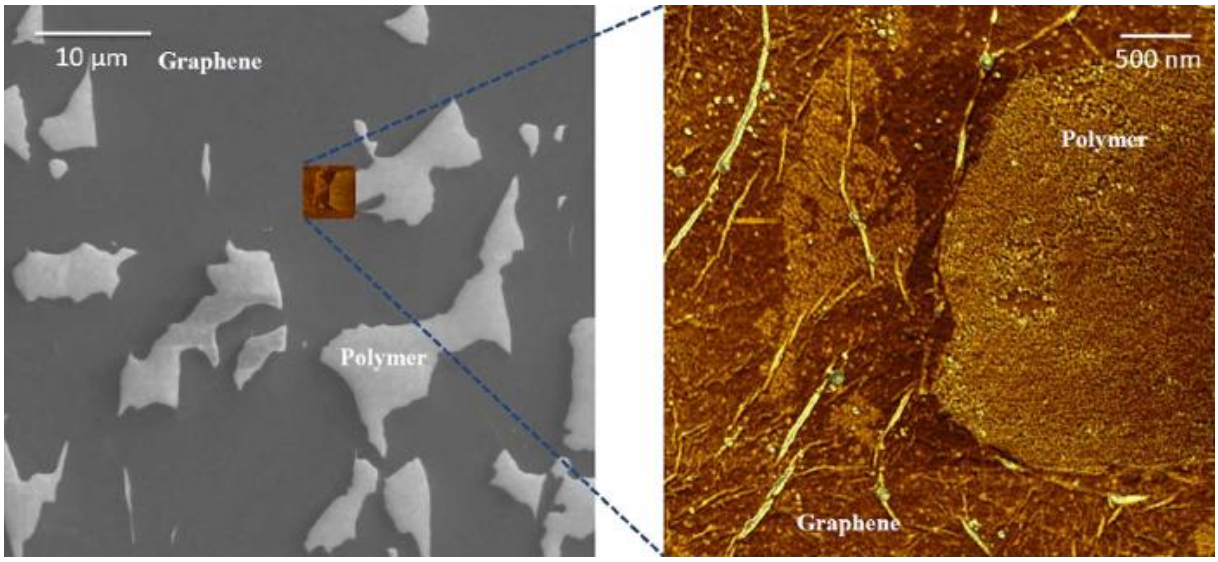

Figure 2. Correlative SEM (left) and AFM (right) in-situ analysis of graphene layers and undesired polymer residues after transfer process to an insulating substrate.

IM1.P047
Aberration corrected analytical scanning and transmission electron microscope for high-resolution imaging and analysis for multi-user facilities

F. von Cube[1], H. Inada[2], Y. Taniguchi[2], T. Yotsuji[2], K. Watanabe[2], H. Muto[2], W. Shimoyama[2]
H. Matsumoto [2], M. Konno[2]

[1]Hitachi High-Technologies Europe GmbH, EMB, Krefeld, Germany
[2]Hitachi High-Technologies Corp., Science & Medical Systems Business Group, Hitachinaka, Japan

hiromi.inada.yd@hitachi-hightech.com,

Introduction and Objectives: In recent years the revolution in aberration correction technology has made ultrahigh resolution imaging and analysis routinely accessible on TEM and STEM. We have developed a new analytical 200 kV cold field emission S/TEM equipped with a probe-forming aberration corrector, the Hitachi HF5000 (Figure 1).
Materials and Methods: Regarding the atomically resolved analytical capability, one of the key demands is to achieve high performance at a multi-user facility. To meet this demand, the Hitachi HF5000 is designed to be user friendly and at the same time handle most requirements from users in the fields of material science, materials fabrication, and device industry. The probe-forming aberration corrector with automated correction of up to third order aberrations allows users to obtain aberration-free STEM illumination optics with minimized effort.
Results: Figure 2 shows the result of the aberration correction. The Ronchigram pattern of the amorphous specimen shows an approximately 32 mrad half angle flat region, corresponding to the optimal aperture condition for aberration-free STEM imaging. While TEM and STEM imaging usually probe the bulk structure of specimens, the SE imaging helps understanding the surface structure. It is important to note that the SE image can be acquired simultaneously with BF and DF images and therefore both, surface and bulk structures are revealed side-by-side at the same time, even at atomic resolution [1]. Such a triple imaging capability on one microscope column is very unique and critical in studying heterogeneous materials such as catalysts. For modern analytical TEM, the most desirable features are high spatial resolution, high signal detection sensitivity, and sufficient specimen tilting angle range. A new pole-piece is therefore designed for HF5000 which enables sub-angstrom resolution DF-STEM imaging and a large specimen tilt angle of +/-35 degrees. Figure 3 shows a high-angle annular DF (HAADF)-STEM image of a silicon thin film at the <112> zone-axis direction, Si dumbbells with a 78 pm separation between adjacent Si columns are resolved. To make X-ray analysis highly sensitive, increasing solid angle of the Energy Dispersive X-ray spectroscopy (EDX) detector is essential. Two 100 mm2 silicon drift detectors (SDDs) are installed on the HF5000, the distance between detector and specimen (*l*) is carefully managed to maximize the solid angle (Figure 4). In order to increase peak to background ratio (P/B), the SDDs are positioned as high as possible relative to specimen surface. The large take-off angle (*q*) reduces X-ray absorption and continuum X-rays which radiates with an angular intensity distribution [2]. The improvement of resolving power is also related to the increased long term stability. High voltage circuits are carefully designed, and the stability for the power supply of lenses and deflection coils is enhanced.
Conclusion: With the development of the new 200kV HF5000 FE-TEM, Hitachi seeks to offer a Sub-Å high-resolution imaging and high-sensitivity analysis microscope, to a broad range of users, including high-end users.

Figure 1. Overview of newly designed Hitachi HF5000, stabilized cold field emission gun equipped analytical scanning / transmission electron microscope.

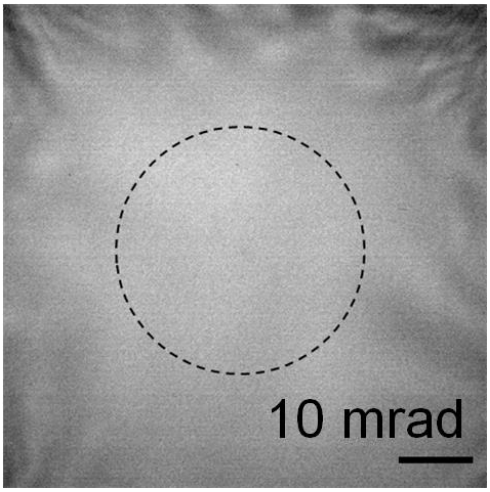

Figure 2. Aberration corrected Ronchigram of amorphous silicon nitride thin film. The size of the dot-line circle corresponds to 32 mrad half angle aberration-free region.

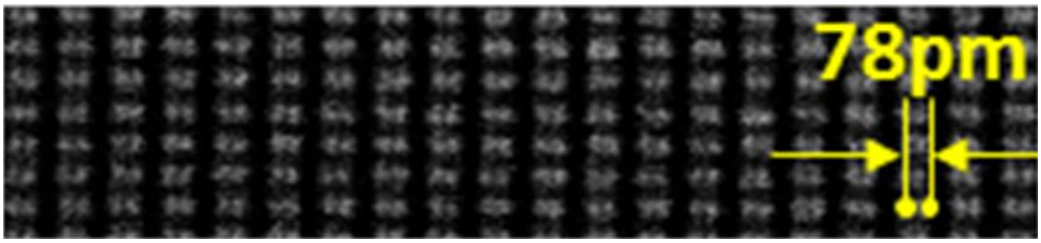

Figure 3. Aberration corrected HAADF-STEM image for a silicon <211> thin film, acceleration voltage of 200 kV and convergence angle of 25 mrad were employed.

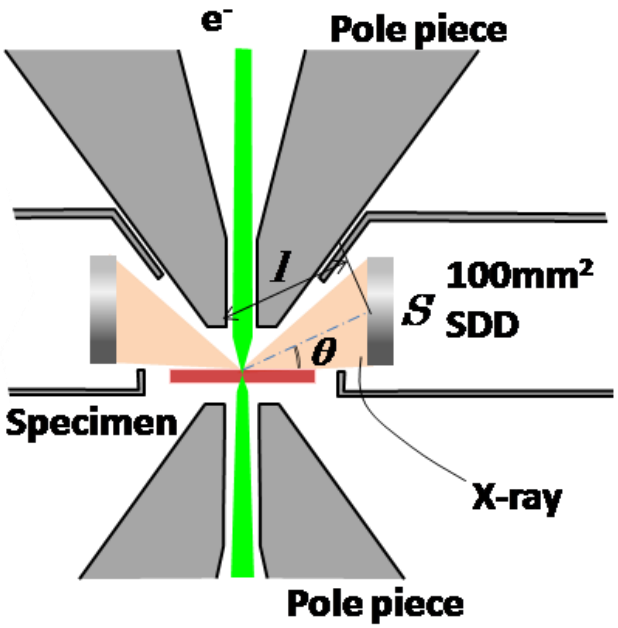

Figure 4. Illustration of the 100 mm2 SDD and TEM specimen in the objective lens pole piece.

IM1.P048
Novel techniques for improvement of EDS mapping resolution of low voltage FE-SEM

Y. Yamamoto[1], Y. Nakajima[1], Y. Yamaguchi[1], N. Kikuchi[1], T. Nokuo[2]

[1]JEOL Ltd., SMBU SM Application , Akishima, Tokyo, Japan
[2]JEOL Ltd., SM Business Unit, Akishima, Tokyo, Japan

yyamamot@jeol.co.jp

Introduction: Energy Dispersive X-ray Spectrometry (EDS) combined with an SEM is very popular for elemental analysis of bulk materials. Recently, windowless EDS detector which is designed to detect low energy characteristic X-rays, such as those from Li, without any absorption and large area Silicon Drift Detector (SDD) have been developed to efficiently detect characteristic X-rays. With these detectors and utilizing low voltages, EDS analysis for nano-scale areas close to the surface in a bulk sample is becoming possible.
Generally, low voltage is used for nano-scale analysis to reduce interaction volume of the primary beam. However, high electron probe current is required to generate characteristic X-rays from a specimen for EDS analysis, resulting in the larger diameter of electron beam, and it causes degradation of resolution.
At this time, we have tested some methods for resolution improvement of SEM image at low voltages and clarified the correlation between the SEM image resolution and the EDS mapping resolution for the low voltage EDS analysis.
Objective: The objective of this study is to see whether the techniques for low voltage imaging are also effective for EDS analysis under the analytical condition.
Materials and Methods: The system for this test consists of a Schottky FE-SEM, JEOL JSM-7800FPRIME, in combination with 100 mm2 SDD window-less EDS detector, Oxford Instruments X-Max Extreme. An electron beam deceleration mode with a maximum specimen bias of -5 kV can be applied in this SEM to achieve high spatial resolution at low voltages. This can be combined with the EDS system. The objective lens of JSM-7800FPRIME is a Super Hybrid Lens, which consists of a magnetostatic field overlapped with an electrostatic field. Reducing the chromatic and spherical aberrations improves the resolution at low voltages. This effect can be expected at short working distance (WD), for example less than 4.5 mm.
Test 1: To check the effect of changing the diameter of electron beam by SEM condition, line analysis for the boundary between Cu and Ni was performed, and the distance between the positions where the intensity decreases by 75% and 25% from the top of Cu-L line profile in Fig.1. Test conditions were set at an incident voltage of 3 kV with an electron probe current of 300 pA, 2 kV with 750 pA and 1.5 kV with 870 pA, respectively. At 3 and 2 kV, WDs of 10, 7 and 4.5 mm were used. At 1.5 kV, WD of 7 and 4.5 mm were used and beam deceleration was also used at each WD. Test 2: To check the correlation between the SEM image resolution and the EDS mapping resolution, EDS mapping of Au particles on a carbon block at an incident voltage of 3 kV and an electron probe current of 300 pA was performed. This was carried out at WD 7 and 4.5 mm with or without beam deceleration.
In Test 3, we compared the spatial resolution of EDS Maps taken for a BeCuCo alloy under different conditions. One of the EDS Maps was taken at an incident voltage of 1.5 kV with an electron probe current of 870 pA, and WD 7 mm. Different condition was WD 4.5 mm with beam deceleration.
Results: Table 1 shows the results of test 1. According to the results, EDS spatial resolution can be improved at a shorter WD using combination of a magnetic-lens and an electrostatic-lens. This has a profound effect, especially at an incident voltage of 1.5 kV, and beam deceleration is also effective to improve the resolution. Figure 2 shows the result of Test 2. The result suggests good correlation between the SEM image resolution and the EDS mapping resolution. Figure 3 is the result of test 3. Upper images are taken at WD 7mm, and the lower images are taken at WD 4.5mm with beam deceleration. According to this result, using the condition for high spatial resolution of SEM images at low voltages, the resolution of EDS maps are also found to be improved, and the distribution of light elements in nano-scale area can be clearly observed.
Conclusion: Low voltage SEM techniques, with a combination of magnetic-lens and an electrostatic-lens, and beam deceleration, are suitable for the EDS analysis at low voltage.

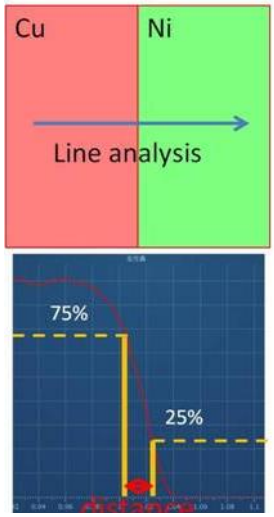

Figure 1. Line analysis of Cu Ni boundary.

Incident voltage	WD	Distance of 75%–25%	
3kV	10 mm	20 nm	
	7 mm	17 nm	
	4.5 mm	14 nm	
2kV	10 mm	60 nm	
	7 mm	40 nm	
	4.5 mm	24 nm	
1.5kV	7 mm	100 nm	
	7 mm	16 nm	Beam Deceleration
	4.5 mm	16 nm	
	4.5 mm	13 nm	Beam Deceleration

Table 1. Results of line analysis for Cu Ni.

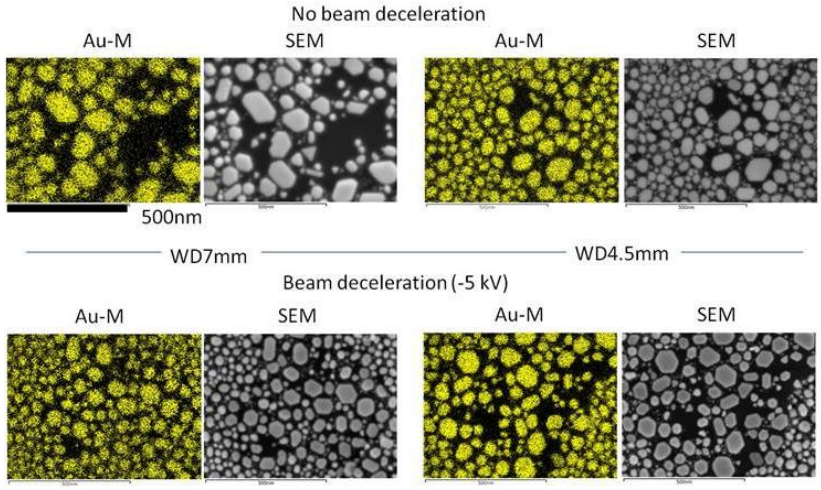

Figure 2. SEM images and EDS Maps of Au particles taken under different conditions.

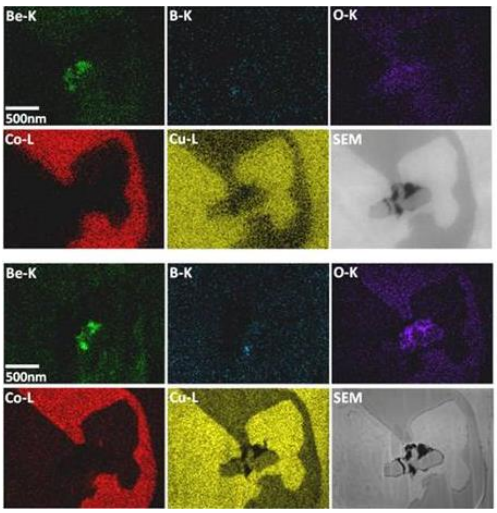

Figure 3. Comparison between EDS Maps of a BeCuCo alloy taken with different spatial resolution.

IM1.P049
Improving spatial resolution of EDX-microanalysis in a FIB-SEM

T. Krekeler[1], M. Ritter[1]

[1]Hamburg University of Technology, Electron Microscopy Unit, Hamburg, Germany

krekeler@tuhh.de

Introduction: Current scanning electron microscopes (SEM) can image specimen with a spatial resolution below 0.8 nm using surface sensitive detectors, low accelerating voltages and aberration corrected electron optics or a combination thereof. EDX-microanalysis (EDXMA), in contrast, requires sufficiently high excitation voltages and beam currents, which results in distinct beam spreading in the bulk material (Fig. 1) and in worse spatial resolution compared to electron images.
A common approach to increase the spatial resolution of EDXMA in SEM is to optimize the beam voltage and current and, hence, to put up with suboptimal excitation of desired X-ray lines, chromatic aberration and space charge effects[1]. EDXMA in transmission electron microscopes (TEM), on the other hand, disregards issues like beam spread as the specimen is very thin and the beam voltage is very high, leading to spatial resolutions down to the atomic level[2]. One promising approach is using a FIB-SEM equipped with a STEM-holder and an EDX-detector to prepare thin foils from sample materials for subsequent microanalysis. This procedure has already shown to reduce the EDXMA "resolution gap" between SEM and TEM[3].
Objective: In this work, we describe the potentials and limits of EDXMA on thin foils using a certified Reference: material and a state-of-the-art FIB-SEM. The spatial resolution for EDXMA as a function of microscope parameters and specimen thickness is experimentally determined and compared to MC simulations.
Materials and Methods: The Reference: material consists of a nanoscale stripe pattern consisting of alternating GaAs/$Al_{(0.7)}Ga_{(0.3)}$As layers with certified periodicities and distances (BAM L-200)[4] (Fig. 2). Thin foils of the stripe pattern with various thicknesses were prepared and analyzed using a FEI Helios G3 UC FIB-SEM equipped with an Oxford X-Max^N 80 EDX detector. The achieved spatial resolution is determined by using a generalized Rayleigh criterion, showing an intensity drop to 81.1% between peak and valley of Al K-α EDX-linescans. Simulated EDX-linescans and electron trajectories were calculated for comparison with the software MC X-Ray[5].
Results: Exemplary results show (Fig. 3) that the spatial resolution of EDX-linescans is significantly enhanced just by reducing the specimen thickness to 100 nm relative to measurements on the bulk material and by keeping the parameters for beam voltage and current constant. While the 23 nm spacing cannot be resolved in the bulk material, the same experiment on a 100 nm thick sample displays two resolved peaks for the 23 nm spacing plus nearly fulfilling the 81.1% criterion for the 17.5 nm spacing. Additionally, the P/B ratio increases by a large margin due to the reduction of bremsstrahlung.
Conclusion: These initial findings emphasize the potential for increasing the resolution limits in microanalysis on nanostructured materials in FIB-SEM by adjusting the specimen thickness with corresponding adjustment of microscope parameters.

References:
[1] J. Orloff, *Handbook of Charged Particle Optics*, CRC Press, Boca Raton FL/USA, 1997.
[2] A. J. D'Alfonso, B. Freitag, D. Klenov, L. J., Allen *Phys. Rev., B* 81, 100101(R), 2010.
[3] C. Notthoff et al., *Ultramicroscopy,* 129, 30–35, 2013.
[4] M. Senoner et al., *Anal. Bioanal. Chem.,* 407, 11, 3211, 2015.
[5] R. Gauvin and P. Michaud, *Microscopy and Microanalysis*, 15, 488-489, 2009.

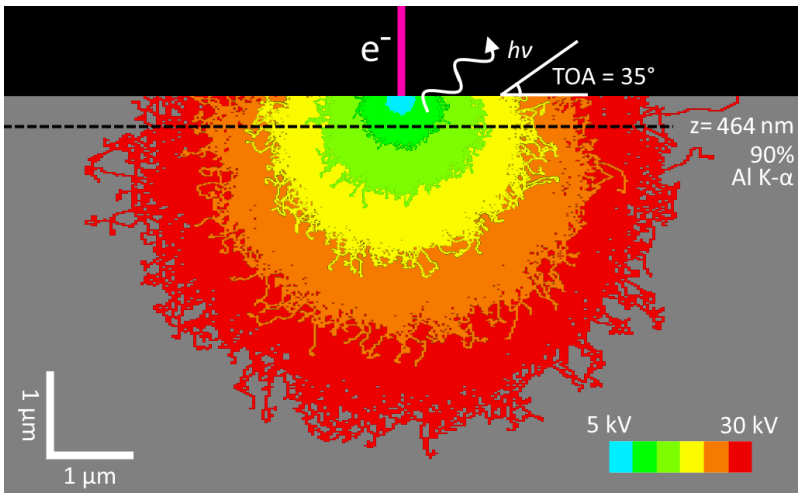

Figure 1. Simulated excitation volumes in GaAs calculated for various electron beam voltages. Dashed line indicates depth of 90% attenuation for 1.49 keV Al K-α X-rays.

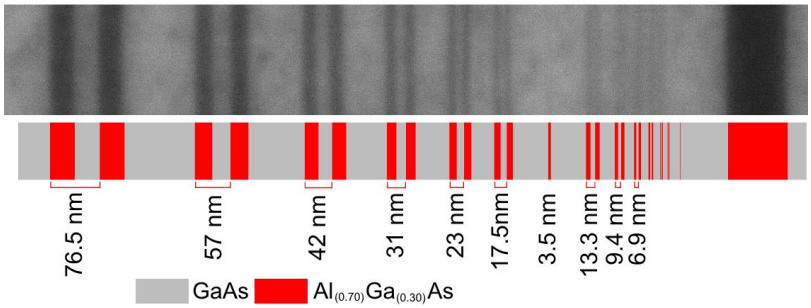

Figure 2. SEM Image of BAM L-200 stripe pattern including schematic of alternating GaAs/$Al_{(0.7)}Ga_{(0.3)}As$ layers including layer spacing.

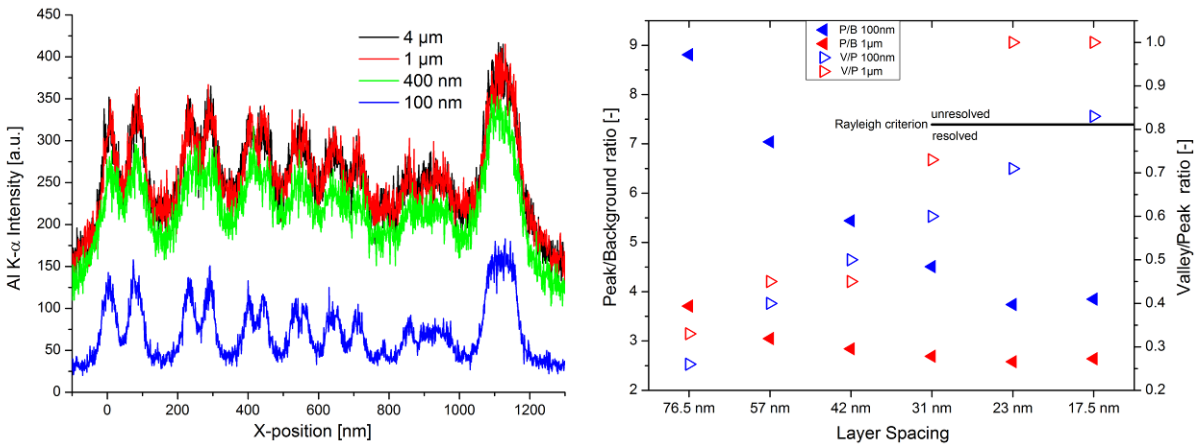

Figure 3. Left: Al K-α EDX-linescan of various lamella thicknesses. Parameters: 15 kV / 0.8 nA / FWTM 22.5 nm. Right: Values for peak to background (P/B) (closed triangles) and valley to peak (V/P) (open triangles) determined on EDX-linescans of a 100 nm and a 1 µm thick lamella.

IM1.P050
Past and recent trends in energy- and/or angular filtration of SEs in SEM

S. Mikmekova[1], M. Takano[1], D. Tsukiori[1], R. Arai[1], M. Nagoshi[1], H. Nakamichi[1]

[1]JFE Steel Corporation, Kawasaki, Japan

sarka@isibrno.cz

Secondary electrons (SEs) are one of the most important image signal in a scanning electron microscope (SEM). Modern SEMs are equipped with extraordinary sophisticated multiple detection systems allowing the simultaneous read-out of all detectors and enabling effective energy- and/or angular- separation of the signal electrons [1-7].
The aim of this study is to compare the SE micrographs collected from an identical specimen using range of SE detectors styles (including in-column, in-lens, trough-the-lens and out-lens type of detector) on a variety of SEMs (both older and modern models of instruments). Detection flexibility of the instruments is tested via systematical study of the imaging parameters effect on the collected signal.
Material under inversigation is a locally corroded nickel-platted copper disc (Pelco; SEM low magnification ruler disc, No. 631). The circular corroded areas consist of Cu oxides and hydroxides and decorate the kerfs. A schematic sketch of the instruments used in this study is shown in Fig. 1. The SE micrographs were collected at 1 keV landing energy of the primary beam and a working distance (WD) of 5 mm.
A first set of SE images was collected by the FEIs instruments having a different concept of the SEM column technology (Fig.2). Detection of the low kinetic energy SEs is presented by the dark contrast of the corroded areas. This phenomenon is caused by reattracting of the slow SEs to the surface as a consequence of a positive charge presence.
Sharing of the SEs by in-column, in-lens and out-lens detectors located in the last generation of SEMs is demontrated in Fig. 3. The micrograph collected by the T3 Trinity detector (Scios) exhibits unique phenomenon, namely a bright halo effect around the corroded areas. The images taken by the EsB detector and the T3 detector show the contrast inversion between the original surface and the areas situated inside the kerfs.
The interesting contrasts and phenomena will be discussed in detail and their origin explained by the SE energy- and angular- filtration.

References:
[1] Griffin B J (2011): Scanning 33, p. 162-173
[2] Kazemian P et al. (2007): Ultramicroscopy 107, p.140-150
[3] Kumagai K and Segikuchi T (2009): Ultramicroscopy 109, p. 368-372
[4] Rodenburg C et al. (2010) Ultramicroscopy 11, p. 1185-1191
[5] Cazaux J (2012): Journal of Electron Microscopy 61, p. 261-284
[6] Nagoshi M et al. (2016) Surface and Interface Analysis 48, p. 470-473
[7] Konvalina I et al. (2016) Proceedings of the 15th International Seminar on Recent Trends in Charged Particle Optics and Surface Physics Instrumentation, p. 28-29

Acknowledgments
The presentation is based on results obtained from pioneering project commissioned by the New Energy and Industrial Technology Development Organization (NEDO).

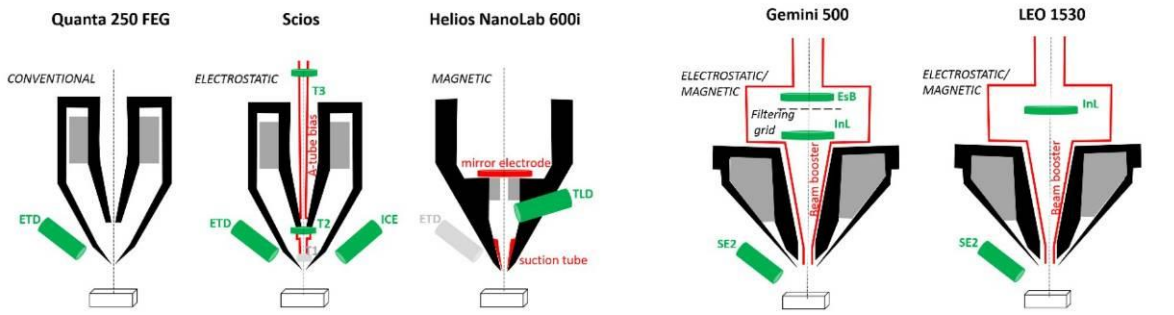

Detector (SE)	out-lens	in-lens	in-column	trough-the-lens	variable imaging parameters
Quanta 250 FEG	ETD	x	x	x	WD, stage bias (0V -> - 4kV)
SCIOS	ETD & ICE	T2	T3	x	WD, A-tube bias (0V -> 8 kV), stage bias (+50V -> -4 kV)
Helios 600i	ETD	x	x	TLD	WD, suction tube voltage, mirror bias, stage bias (0V -> -4 kV)
Gemini SEM 500	SE2	x	InL, EsB	x	WD, beam booster bias (0V –> 10 kV), specimen bias (0V -> - 5kV)
Leo 1530	SE2	x	InL	x	WD, beam booster bias, (0V -> 8 kV)

Figure 1. Schematic cross-section of the optical columns, together with the detector geometry and relative location of SE detectors. Variable imaging parameters for each instrument are mentioned in the table below.

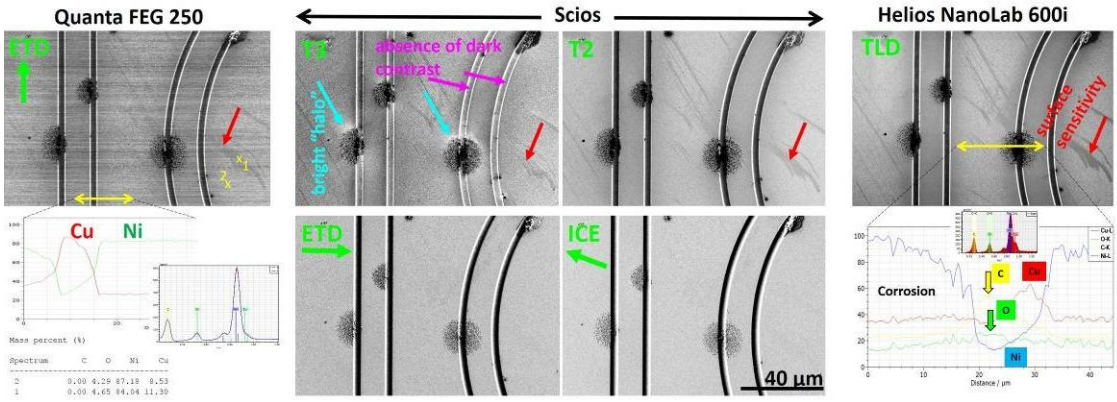

Figure 2. SE images of the same point of view on the specimen surface obtained at 1 keV primary beam energy and WD of 5 mm, together with corresponding EDS data. (Scios: A-tube 8 kV, simultaneous read-out of all detectors; Helios NanoLab 600i: immersion mode, suction tube +70V, mirror -15V).

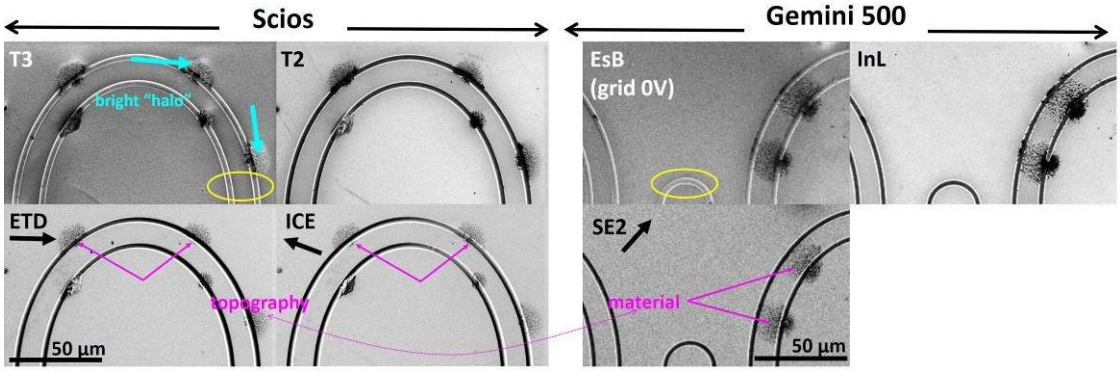

Figure 3. SE images of the specimen acquired by the Scios and the Gemini SEM 500 instruments. The micrographs were collected simultaneously at 1 keV landing energy of the primary beam and WD was fixed at 5 mm.

IM1.P051
Drastic enhancement of BSE signal from ultrathin nanostructured metal film revealed by low-voltage scanning electron microscopy

V. Mikhailovskii[1], Y. Petrov[1], O. Vyvenko[1]

[1]Saint-Petersburg State University, Saint-Petersburg, Russian Federation

v.mikhailovskii@spbu.ru

Low voltage scanning electron microscopy (LVSEM) is widely used in many fields of modern research. It is well known that the role of inelastic scattering of electrons in mechanism of image contrast formation grows as energy of primary electrons decreases [1]. This fact results in some imaging features that are specific for LVSEM, the best known of them is inversion of Z-contrast. These imaging features may change conventional SEM contrasts [2], and produce some new contrasts specific only for LVSEM[3].
We recently observed with LVSEM enhancement of signal of backscattering electrons(BSE) from thin metal granular films(TGF) consisted of separated gold nanoparticles. TGF were prepared by evaporating of gold through shadow mask onto silicon surface. At the edge of shadowed region of Si surface stripe-like TGF was formed. Gold nanoparticles with mean diameter of 7 nm were separated with the gaps of about 5-10 nm (see Fig. 1C).
The detection of BSE signal was performed with in-lens detector of BSE (Zeiss *EsB* detector). This detector provides energy filtration of BSE signal and collects BSE emitted at very low angles to the surface normal [3]. We observed that at certain low values of accelerating voltage(EHT) BSE signal from TGF dramatically increases and exceeds BSE signals both from massive gold film and from silicon substrate (see Fig. 2B) , while secondary electrons (SE) signal doesn"t change significantly(see Fig. 2A). The effect of BSE signal enhancement was observed at EHT below 450 V. BSE images taken at high magnification showed that most of enhanced BSE signal was produced by gaps between nanoparticles (see Fig 1D).
Here we report about the observation of similar effect in another plasmonic nanostructure which contains so called "gold nanocells". The nanocells were prepared with focused ion beam(FIB) technique. The square 5*5 um2 of 80 nm gold film on Ge surface was continuously irradiated by 30 keV Ga+ focused ion beam with the dose ~102 uC/cm2. This irradiation resulted in formation of cellular-like structure of gold nanowires (see Fig 2A). Inside the larger cells with the sizes of about 100-200 nm ten times smaller cells were created (see Fig. C).
At values of EHT in the ranges from 350 V to 600 V BSE signal from the region with gold nanocells significantly exceeded BSE signal from continuous 80 nm gold film (bright square in Fig. 2B). The most intense BSE signal stemmed both from the thin and thick nanowires, obviously, from their most thin parts (Fig. 2D).
The enhancement of BSE signal both on the TGF and the nanocells prepared on glass was not observed indicating that the high permittivity of semiconductor plays an important role in the formation of such phenomenon. It seems to be due to the transfer of a part of electron momentum, and accordingly, of their energy to interface plasmons aligned parallel to the surface [4]. In this way only BSE having tangential velocity component can lose their energy stretching, thus, BSE angular distribution along the normal to the surface. More narrow angular distribution increases the ratio of BSE signal collected by *EsB* detector. Though the suggested explanation of the drastic enhancement of BSE signal of ultrathin metal films on semiconductor substrate detected with an in-lense BSE detector is rather qualitative yet the effect opens a new way of investigation of such nanostructures. A new accurate theory needs to be developed to retrieve quantitative information from the experimental data.
All experimental results were obtained in IRC for Nanotechnology, Research Park of SPbU.

[1] Fitting, H. J. // *Journal of Electron Spectroscopy and Related Phenomena*, *136*(3), 265–272, (2004)
[2] Cazaux, J., Kuwano, N., Sato, K. // *Ultramicroscopy,* v. 135, pp 43-49, (2013).
[3] Jaksch, H. // *Microscopy and Microanalysis,* 18 (Suppl 2), (2012)
[4] Mikhailovskii, V., Petrov, Y., Vyvenko, O. //*AIP Conference Proceedings*, 1748, art. no. 020005, (2016)

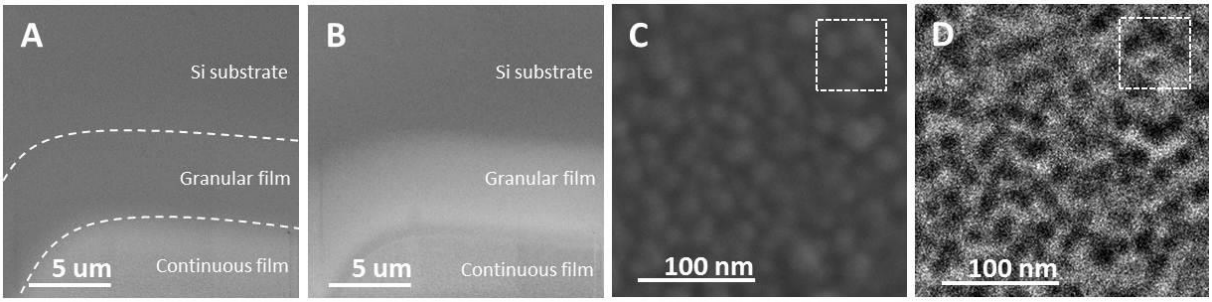

Figure 1. LVSEM images of TGF. EHT=400 V. A,C – SE image, B,D – BSE image.

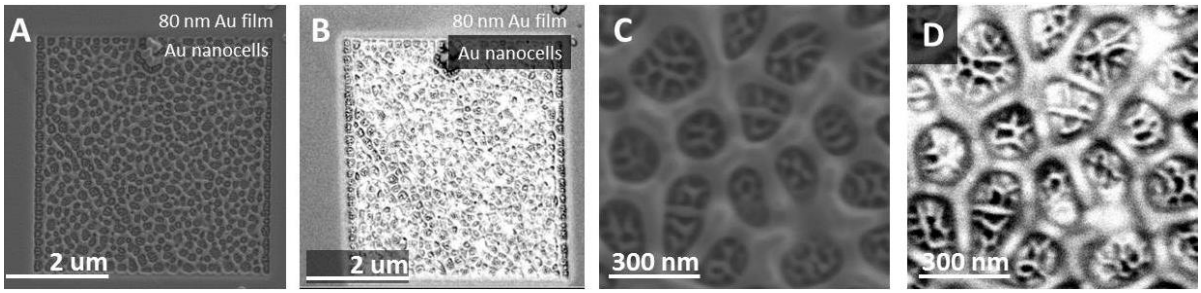

Figure 2. LVSEM images of gold nanocells. EHT=450 V. A,C – SE image, B,D – BSE image.

IM1.P052
PFIB and microCT innovations provide multi-scale 3D pore information in battery cathode material

D. Phifer[1], H. Lemmens[1]

[1]Thermo Fisher Scientific, Eindhoven, Netherlands

daniel.phifer@thermofisher.com

Introduction: Many materials have features crossing several length scales which make it difficult to select the correct technique to fully characterize structure as it relates to properties and function. In developing instrumentation to image samples for 3D modeling, it would be interesting to know how well the overlap of the information can close the gap in available techniques to eliminate much of the "blind spot" with some length scales. As an example, the microstructure of battery electrodes has a significant impact on the transport properties and is hence key to understand ionic and electronic transport.
Objectives: The goal of this presentation is to investigate the relationship to the length scales in the new Xe based DualBeam (FIB-SEM) and compare/combine this to data from microCT techniques employing helical scanning technology for energy storage materials to fully estimate the pore structure.
Materials and Methods: In this study we have used a plasmabeam for sectioning and an electron beam for imaging. The plasmabeam allows to expand the field of view to hundreds of micrometers; whilst preserving the high resolution of the electron beam. A first attempt is made to reproduce the results from the above mentioned multi-scale workflow by a single experiment. 3D reconstruction of the anode (Field of View 200micrometer) and the cathode (Field of View 100 micrometer) are presented.
Results: The 3D analysis of the composite electrode is typically a combination of microCT imaging and FIB-SEM imaging; where the microCT provides the representative volume and the FIB-SEM provides stochastical input to the fine structure in the microCT volume. In this way the lack of resolution of the microCT is offset by the higher resolution of the FIB-SEM; which itself has too small Field of View to be representative.
Segmentation of the pore space is demonstrated (Fig 1.) to come to a pore network model from which transport properties over a representative volume can be calculated. It appears the two techniques can indeed be combined to give a better picture of the structure from the macro to micro scale which affects both the properties and function.
Conclusion: Segmentation of the pore space is demonstrated to come to a pore network model from which transport properties over a representative volume can be calculated with a high degree of confidence by combining data from the PFIB and microCT techniques.

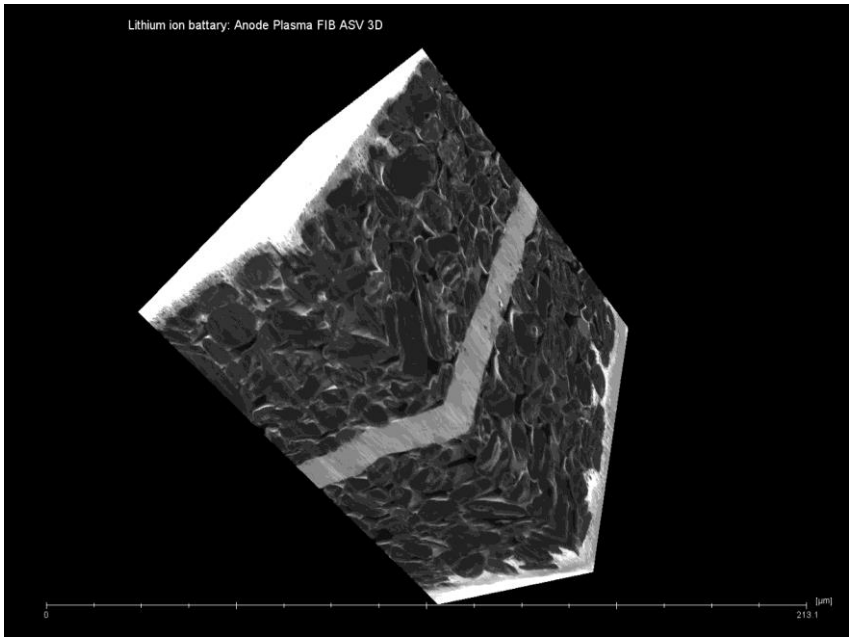

Figure 1. 3D model showing the pore network in lithium-ion battery cathode. Scale bar for this model is approximately 213 um.

IM1.P053
Beam induced polishing system and its application on a dual-beam microscope

J. Huang[1], M. Löffler[1], J. Mulders[2], P. Trompenaars[2], E. Zschech[3]

[1]Technische Universität Dresden, Dresden Center for Nanoanalysis, Dresden, Germany
[2]FEI Company, Eindhoven, Netherlands
[3]Fraunhofer IKTS, Dresden, Germany

jin.huang@tu-dresden.de

Introduction: There has been increasing needs to prepare ultra-thin lamellae typically below 20 nm in thickness. This enables high resolution transmission electron microscope (HRTEM) imaging and elemental analysis, which is required in the state-of-art material science research and industrial applications. Focused Ion Beam is the most common preparation technique for electron transparent specimen thanks to its site-specific milling capability. However, it inevitably creates damage to the original material. Broad argon-ion milling on the other hand provides an alternative thinning method. It is of great interest to combine these two techniques together to achieve a better HRTEM sample preparation approach. In this work, a Beam Induced Polishing System (BIPS) was introduced as an accessory to a dual-beam microscope.
Objectives: The objective of this work is to proof the feasibility of the functioning of a Beam Induced Polishing System as an accessory to a commercial available dual-beam microscope. Broad argon-ion milling devices have been available as standalone sample preparation equipment. Although the milling principles are the same, mechanical configuration that generates the argon-ion from a continuous gas supply system and afterwards incorporates into the existing Focused Ion Beam specimens needs to be re-engineered.
Materials and Methods: Compressed liquid argon is used as resource for ion generation. Before being ionized by the electron beam inside the microscope chamber, argon gas is guided through a liquid nitrogen cold trap for purification. Purified argon is then ionized in a special engineered volume and targeted onto the specimen. Two types of silicon specimen were tested: silicon substrate with native oxide and silicon substrate with thin platinum coating layer.
Results: Most of the efforts was spent on configuring the parameters of the hardware outside of the chamber because of the differences from its laboratory prototype in terms of dimensions and limitations imposed by infrastructure. A specific BIPS spot pattern shall be formed on the specimen surface after ion milling. The spot shape and size depend on the operation parameters such as time or ionization energy. When purified argon is achieved and proper argon-ions are generated, ion beam is targeted onto the specimen on varies locations with different milling time. Three series of spots with different sizes were created on three specimens.
Conclusions: A Beam Induced Polishing System is successfully installed and tested on a commercial dual-beam microscope as an accessory. The BIPS system uses a continues argon supply and generates argon-ions with the electron beam in the chamber for the polishing purpose. The ion beam is targeted on to three specimens and three series of signature spots are formed. Such system has been demonstrated to be able to perform polishing function on a FIB sample in a dual-beam microscope.

IM1.P054
High-throughput characterization of nanoparticles by TEM

W. Weigel[1], A. Sweet[1], G. BAred[1], H. Eickhoff[1]

[1]SCIENION AG, Berlin, United Kingdom

weigel@scienion.de

Analysis of nanoparticles by TEM is a very useful characterization method. However, by nature of TEM instrument design placing sample grids under high vacuum, the number of samples that measured in a given time period is very limited. Indeed, for each sample placed on a TEM grid, the TEM has to undergo a complete cycle of losing and re-establishing vacuum conditions. Having the capability to insert multiple samples at once inside the TEM and then acquiring all images without breaking vacuum for each one, would result in a tremendous increase in the number of samples that can be analyzed per hour.
For over 10 years, SCIENIONs picoliter liquid dispensing technology has been used to deposit arrays of different sample solutions onto a wide variety of substrates. Applying this well-proven technology to dispense multiple liquid samples as colloidal suspension of nanoparticles onto a single TEM grid is an obvious extension.
Non-contact dispensing preserves the integrity of the sensitive grid films. Wetting properties of substrates that can be critical for the assembling of the nanomaterials can be tailor-made by specific surface functionalization techniques.
This technology can be applied to dispense multiple different samples of nanoparticles and a range of other substances onto a single TEM sample grid. This application will enable high-throughput analyses and experimentations that were previously not possible.

[1] R.Tannenberg, H. Eickhoff, W. Weigel *Imaging Microscopy* **2016**, 33–35

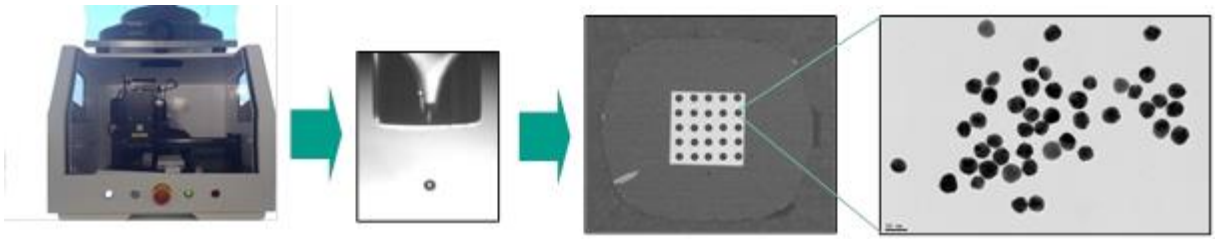

Figure 1. Printed 5x5 array of 100 pL solutions of nanoparticles using a piezoelectric drop generation with a sciTEM system. TEM image shows distribution of 40 nm Au nanoparticles within a single spot.

IM1.P055
Robust structure factor retrieval from large-angle rocking-beam electron-diffraction (LARBED) patterns

F. Wang[1], C. T. Koch[1]

[1]Humboldt-Universität zu Berlin, Department of Physics, Structure Research and Electron Microscopy Group, Berlin, Germany

feng.wang@physik.hu-berlin.de

Introduction: Structure-factor refinement by quantitative convergent-beam electron diffraction (QCBED) [1] has been able to reveal the charge distribution responsible for the bonding between atoms [2]. However, to fit a set of complex structure factors by matching dynamical electron diffraction simulations to the contrast within CBED discs, the sample must typically be roughly 100 nm thick, and the lattice parameters should not exceed 1 nm.
Large-angle rocking-beam electron diffraction (LARBED) [3] data can be acquired for arbitrarily large unit cell structures and reveals features that are clearly due to dynamical electron diffraction even at specimen thicknesses below 10 nm. A successful ab-inito reconstruction method [4] is able to handle a nonlinear optimization problem, without assuming additional information such as atomicity or chemical composition.
Objectives: Reconstruction algorithms have in common that they try matching the experimental and simulated diffraction data by minimizing either the least squares distance or the R-value. Electron diffraction data from a very thin sample contains only weak dynamic features in the observed intensities while for a thick sample a lot of dynamic effects will be present. This difference is also reflected in the behaviour of reconstruction algorithms using different figures of merit. Fig. 1 shows the case when the SrTiO3 sample is very thin (5 nm in this case), the performance of the potential reconstruction by minimizing the R-value is very poor. Fig. 2 shows when the specimen is thick (40 nm) – the reconstruction by minimizing least squares gets stuck in a local minimum. Our goal is to design a generic target function to handle both types of situations equally well.
Materials and Methods: We design a convex homotopy function H taking the advantages of the least-square function χ^2 and the R-value function R,
$H(\lambda) = \lambda \chi^2 + (1-\lambda) R$.
By minimizing the homotopy function H with an adjustable but fixed factor λ, the structure factor retrievement for SrTiO3 was successful throughout all thicknesses.
Results and Conclusion: In Fig. 3, the reconstruction using a convex homotopy merit function shows good robustness and generally outperforms reconstructions using either the least-square function or the R-value function in each case throughout all thicknesses from 5 nm to 40 nm.

References:
[1] C. Deininger, G. Necker, J. Mayer, Ultramicroscopy 54 (1994) 15-30
[2] J.-M. Zuo, M. Kim, M. OKeefe, J.C.H. Spence, Nature 401 (1999) 49
[3] C.T. Koch, Ultramicroscopy 111 (2011) 828 – 840.
[4] Wang, F., Pennington, R.S., Koch, C.T., 2016. Phys. Rev. Lett. 117, 15501.

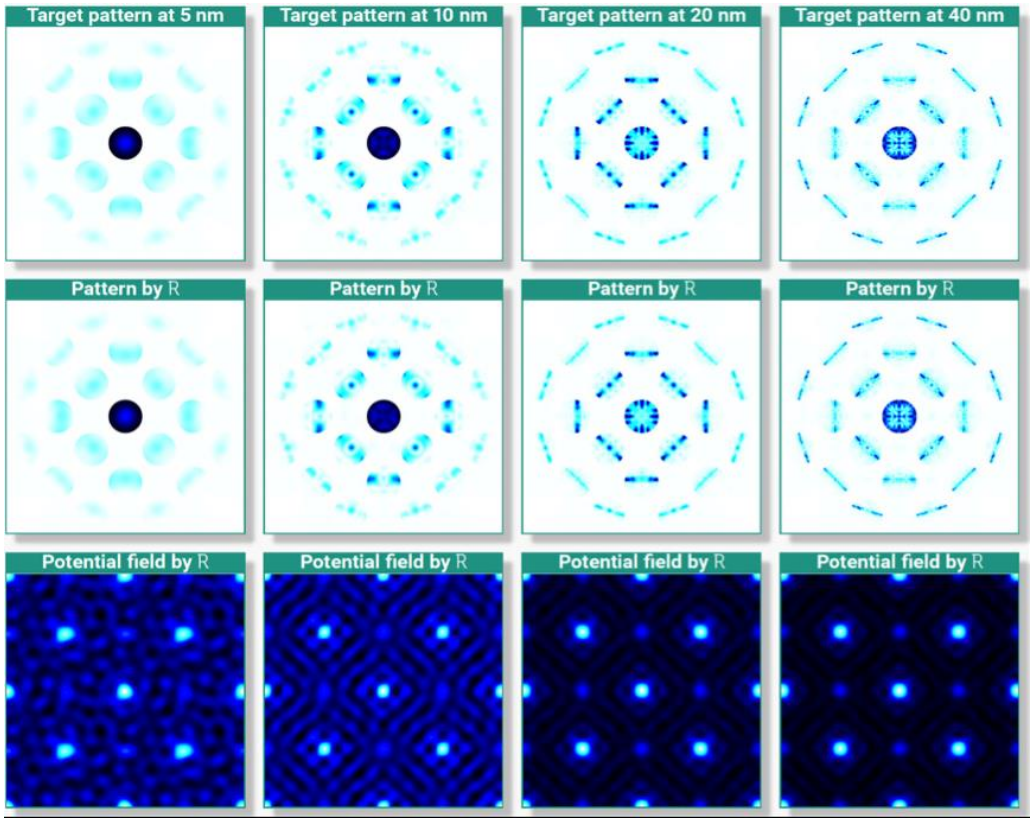

Figure 1

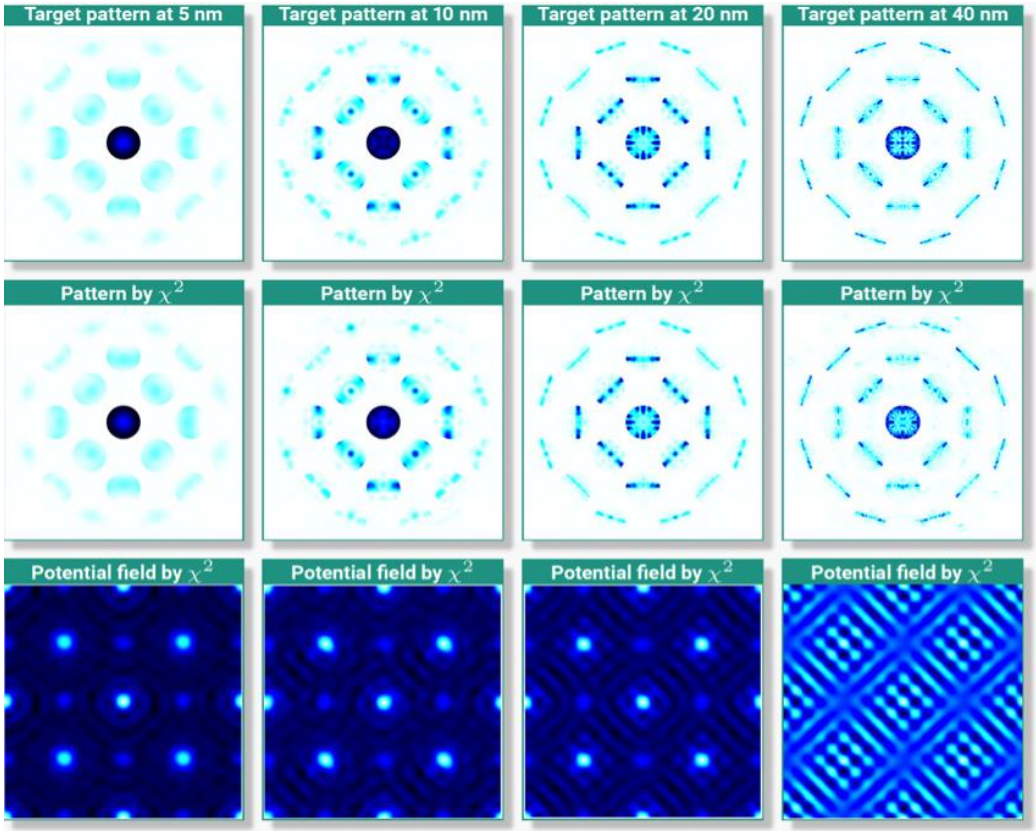

Figure 2

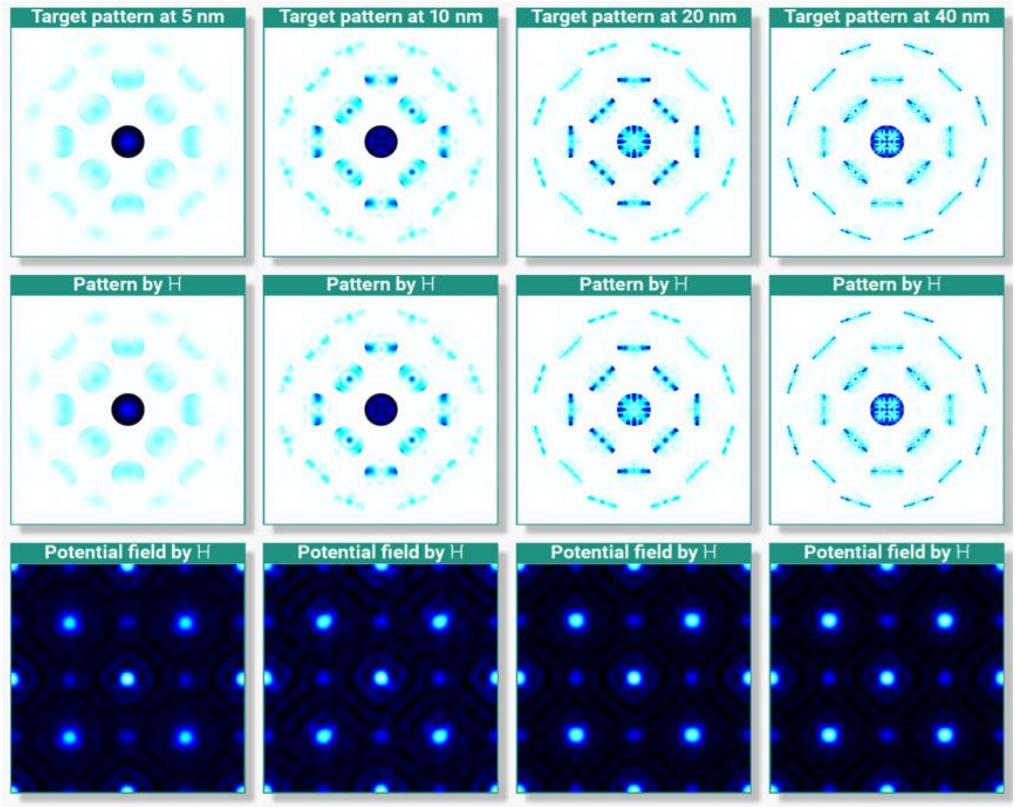
Target pattern at 5 nm
Target pattern at 10 nm
Target pattern at 20 nm
Target pattern at 40 nm
Pattern by H
Pattern by H
Pattern by H
Pattern by H
Potential field by H
Potential field by H
Potential field by H
Potential field by H

Figure 3

IM1.P056
A novel technique for in-vivo phase imaging of retinal cells

D. Carpentras[1], T. Laforest[1], M. Künzi[1], C. Moser[1]

[1]EPFL, LAPD, Ecublens (VD), Switzerland

dino.carpentras@epfl.ch

Light entering the eye needs to pass through several transparent layers before reaching the photodetectors. These layers contain many different types of cell responsible of the correct functioning of the eye process and their observation can provide information of the development of eye disease at early stages. However, due to their transparency, these bodies cannot be observed with standard imaging techniques.
Novel techniques based on obliquely scattered light use a laser scanning system through the pupil to provide phase gradient contrast, which allows to image retinal translucent bodies [1]. This technique has yet to show high contrast images in vivo due to the optical power safety limit. Outside the field of ophthalmology new microscopy techniques for phase imaging have been demonstrated. Mertz et al. [2] showed how light backscattered from the deep layers of a biological media can be used to back-illuminate top layers in a transmission-like system. In a different work Waller et al. showed how a microscope with incoherent oblique illumination can be used for providing phase imaging of thin samples [3].
In this work we show a novel technique based on transcleral illumination that allows for the observation of translucent bodies in the living human retina.

[1] Rossi et al., Imaging individual neurons in the retinal ganglion cell layer of the living eye, PNAS 114(2016).
[2] Giese et al., Fast volumetric phase-gradient imaging in thick samples, Opt. Express 22(2014).
[3] Tian et al., Quantitative differential phase contrast imaging in an LED array microscope, Opt. Express 23(2015).

IM1.P057
Precipitation imaging in alloy 718 using an electron microscope pixel array detector

C. A. Wade[1,2], E. Yücelen[2], S. Sluyterman[2], B. Freitag[2], G. Burke[1]

[1]The University of Manchester, Materials Performance Centre, Manchester, United Kingdom
[2]Thermo Fisher Scientific, Materials & Structural Analysis , Eindhoven, Netherlands

austin.wade@manchester.ac.uk

Successful additive manufacturing of metallic components requires the complete characterization of the microstructure of the printed parts to determine the suitability of these techniques for replacement of more expensive traditional processing methods. Precipitation hardening in Alloy 718 may occur during additive manufacturing of components. The main precipitates present in Alloy 718, forming semi-coherently in the γ matrix, are γ" (ordered - L12) and γ" (ordered - DO22). In order to eliminate comparatively more expensive manufacturing techniques the distribution of γ" and γ" must be shown to be consistent, in large part, with microstructures in traditionally prepared material ideally displaying a microstructure similar to that of thermally treated Alloy 718 when in the as printed condition. To assess the distribution of these precipitates in Alloy 718, scanning transmission electron microscopy (STEM) imaging of the distribution of phases was accomplished using an instrument equipped with an electron microscope pixel array detector (EMPAD).

Developed by Cornell University, the EMPAD is currently under commercial development with the Materials & Structural Analysis Department of Thermo Fisher Scientific [1]. The sensor may operate from 20 to 300kV and consists of 128x128 pixels of 150 microns. The EMPAD records an image frame in less than a millisecond, and can detect from 1 to 10,000,000 primary electrons per pixel per second at 200 kV allow the entire unsaturated diffraction pattern to be recorded in scanning mode. Image reconstructions from the complete electron scattering information incident to the detector may be used to form images by masking particular areas of the data, essentially providing the user with complete control of what areas of the back focal plane are used to form images.

A thin foil of Alloy 718 was imaged in STEM with data acquired at each pixel in the scanned area on an EMPAD. Figure 1a and 1b show reconstructed STEM bright-field (BF) and STEM annular bright-field (ABF) images of the Alloy 718 microstructure. These images, particularly the BF image, show location of precipitates throughout the microstructure. In an attempt to distinguish between γ" and γ" STEM dark-field (DF) images may be formed. Two orientations of γ" can easily be distinguished in DF STEM imaging though significant overlap in diffraction information between γ"/γ" [001] exists. Figure 2 displays the effect of this overlap where γ" cannot readily be seen as separate from any γ" present. The inability to distinguish diffraction information from γ"/γ" [001] precipitates requires additional analysis. Though these two orientations of precipitates may provide near identical diffraction the chemical information from each of these phases may be exploited to observe their distributions through the microstructure independently. This may be accomplished through the choice of a shorter camera length when acquiring the EMPAD data. A change of camera length from one useful in reconstructing BF, ABF, and DF images to one useful for high-angle annular dark-field (HAADF) imaging can be seen in Figure 3. The γ" phase contains an increase in Al and a decrease in Nb content when compared to γ". This change in chemistry provides different contrast in HAADF imaging. The efficacy of obtaining and comparing low and high camera length EMPAD acquisitions is investigated as a means of complete determination of phase distributions in additively manufactured Alloy 718.

References:

[1] M. W. Tate et al., *Microsc. Microanal.* 22 Issue 1 (2016), p. 237.

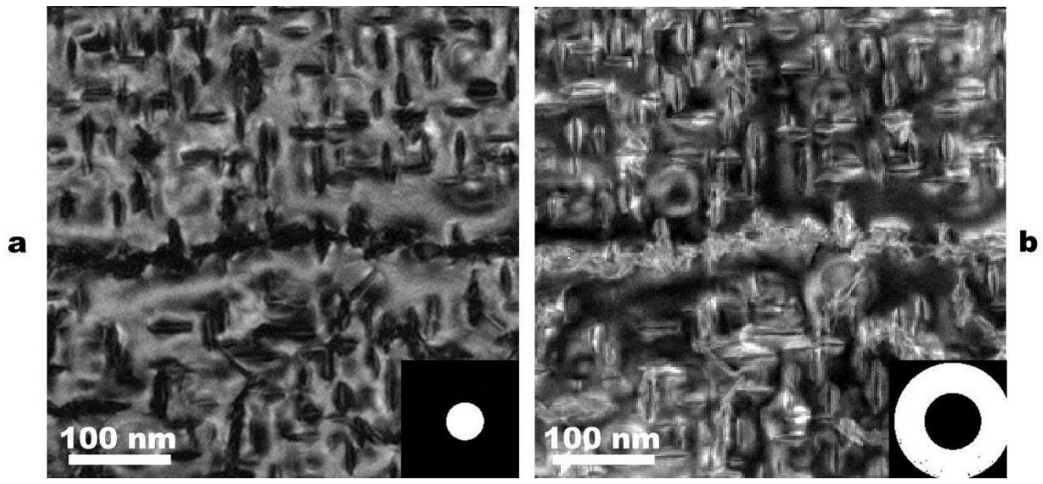

Figure 1. BF STEM image (a) and ABF image (b) with insets showing masks used to reconstruct images.

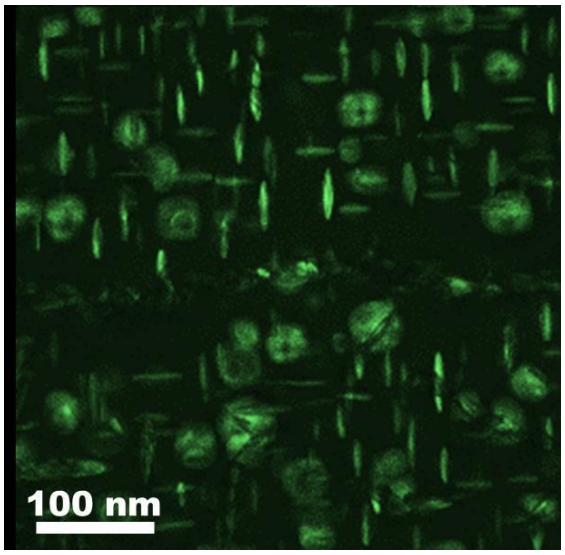

Figure 2. Reconstructed DF image showing common location of γ''/γ'' [001] precipitates in Alloy 718 showing significant contribution of contrast from nearly all γ'' and γ'' precipitates.

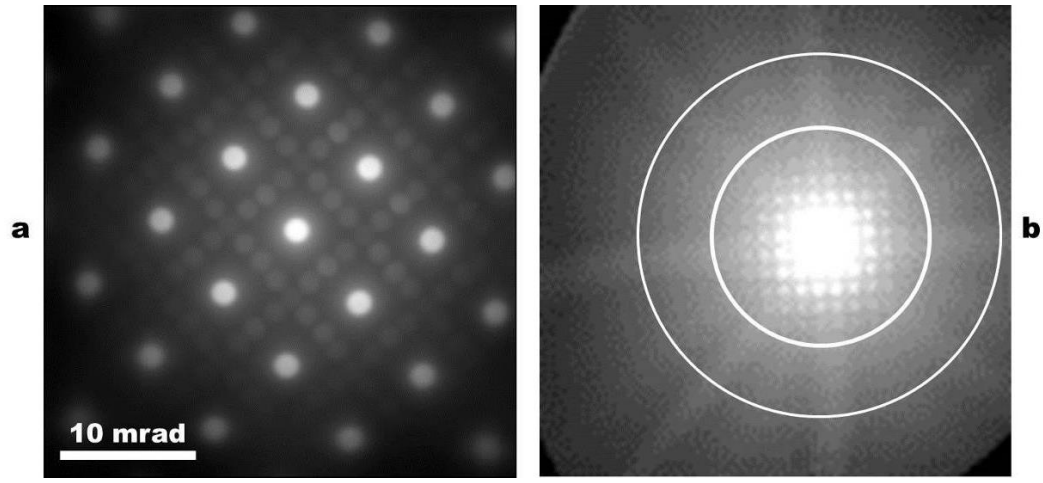

Figure 3. Sum diffraction pattern acquired at a camera length suitable for dark-field and bright-field image reconstructions (a) and a sum diffraction pattern taken at a much smaller camera length suitable for HAADF imaging (b) with circles of 40 and 70 mrad, respectively.

IM1.P058
Calibration and quality control of modern fluorescence microscopes

G. Papon[1]

[1]Argolight, Pessac, France

g.papon@argolight.com

Although quality control of fluorescence microscopes is a topic that appeared more than fifteen years ago in academic laboratories [1] and national regulatory agencies [2], it is still topical as it was for example in the program of the Core Facility Satellite Meeting of the 15th international ELMI meeting in 2015. Due to the increasing complexity of the instrumentation used for confocal and high-end wide-field fluorescence imaging microscopy, national metrology institutes [3], microscope manufacturers [4], and more recently core facilities [5] have gotten involved in identifying,
making and/or testing different tools, both hardware and software, to assess the numerous aspects of fluorescence microscopes.
In particular, quality control is important: (i) for core facilities, to assure the performances of the microscopes they make available to the end users; (ii) for microscope manufacturers, to guarantee the microscopes specifications and to improve maintenance; (iii) for end users to remove the bias introduced by the microscopes in their experiments. In this talk, the context and issues of quality control will be first outlined; the mostly used tools will be then presented and their advantages and drawbacks will be discussed; finally, examples of quality control of fluorescence confocal and high-end wide-field microscopes with Argolight solutions will be shown.

[1] R. I. Ghauharali et al., Fluorescence photobleaching-based shading correction for fluorescence microscopy, Journal of Microscopy 192, 99-113 (1998).
[2] R. M. Zucker and O. T. Price, Practical Confocal microscopy and the evaluation of system performance, Methods 18, 447- 458 (1999).
[3] U. Resch-Genger et al., How to Improve Quality Assurance in Fluorometry: Fluorescence-Inherent Sources of Error and Suited Fluorescence Standards, Journal of Fluorescence 15, 337-362 (2005).
[4] A. Dixon et al., Standardization and Quality Assurance in Fluorescence Measurements II, Chapter 1. (Springer-Verlag, Berlin Heidelberg, 2008).
[5] R. W. Cole et al., Measuring and interpreting point spread functions to determine confocal microscope resolution and ensure quality control, Nature Protocol 6, 1929-1941 (2011).

IM1.P059
Rapid and localized ion-beam etching of surfaces using initial notches

R. Busch[1], M. Krause[1], S. Coyle[2], T. Höche[1]

[1]Fraunhofer Institute for Microstructure of Materials and Systems IMWS, Halle, Germany
[2]Gatan Inc., Pleasanton, CA, United States of America

richard.busch@imws.fraunhofer.de

Ion beam erosion is an important tool for the preparation of high-quality samples, as required by many microstructure investigation techniques. In particular, large and plan-parallel, electron transparent lamella with a thickness of not more than 100 nm are needed for transmission electron microscopy. Besides focused ion beam (FIB) thinning, broad Ar^+-ion beam (BIB) erosion at glancing angles is commonly used for thinning or as a final processing step to remove damaged material layers incurred during preceding sample treatment. However, with typical beam diameters in the order of mm, lateral accuracy is low, making this technique unsuitable for target preparation. Furthermore, erosion rates are small at glancing angles.

We present a novel method that allows for rapid BIB erosion with a high degree of control over erosion position and depth. Notches (iNotches™, [1]) are created on the sample, causing a locally altered angle of ion incidence upon subsequent BIB erosion. Thus, preferential erosion occurs at the flanks of the notches, leading to the formation of a terrace structure with a well-defined depth jump (Fig. 1). Advantages include increased throughput and sample stability.

Experiments were conducted on (100)-Si substrates. Notches were created using the novel Gatan microPREP™ laser ablation tool, equipped with an ultra-short pulsed solid-state laser. A Gatan PIPS broad ion beam tool equipped with two Penning ion guns was used for BIB erosion. The experiments were conducted at ion energies ranging from 2 keV to 4 keV and ion incidence angles from 4° to 10° to the sample surface. The resulting surface was characterized by means of scanning electron microscopy and optical profilometry. Additionally, simulations have been performed, based on a two-dimensional model and the assumption of deterministic material removal caused by angle-dependent sputtering [2].

The experiments confirmed the formation of a terrace structure with well-defined depth jump (Fig. 2). The height difference is proportional to the width of the notch and decreases as gracing ion incidence is approached. The erosion dynamics are also dependent on the incidence angle, with both terrace formation and time-dependent expansion being more rapid at lower glancing angles. Simulation results were in accordance with these findings. The surface roughness was found to be dependent on both notch quality and width and can be reduced by oscillation milling within an arc segment around the vertical incidence direction w.r.t. to the notch. Utilizing a workflow consisting of laser ablation sample cutting and pre-thinning as well as notch creation, followed by BIB erosion, electron transparent Si samples with µm target accuracy could be obtained within two hours. Preliminary results also indicate that this method can be extended to notches created with plasma FIB instruments, yielding high quality surfaces with little roughening.

In summary, iNotches™ allow for fast and localized surface erosion, opening up new vistas for sample preparation procedures for TEM as well other techniques with high demands on surface quality, such as EBSD.

The authors acknowledge financial support of Fraunhofer Internal Programs under Grant No. Attract 692 280.

[1] M. Krause, R. Busch, Th. Höche, and G. Schusser, EP 15188587.8, patent pending.
[2] R. Busch, M. Krause, S. Coyle, T. Höche, Ultramicroscopy, under review.

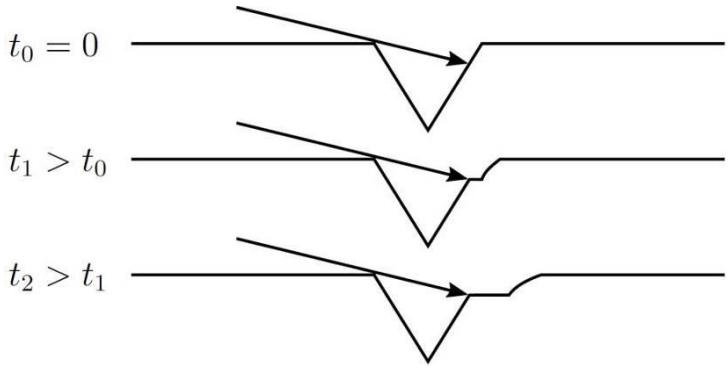

Figure 1. Principle of surface erosion utilizing iNotchesTM. Surface cross-sections across a notch at three consecutive points of times.

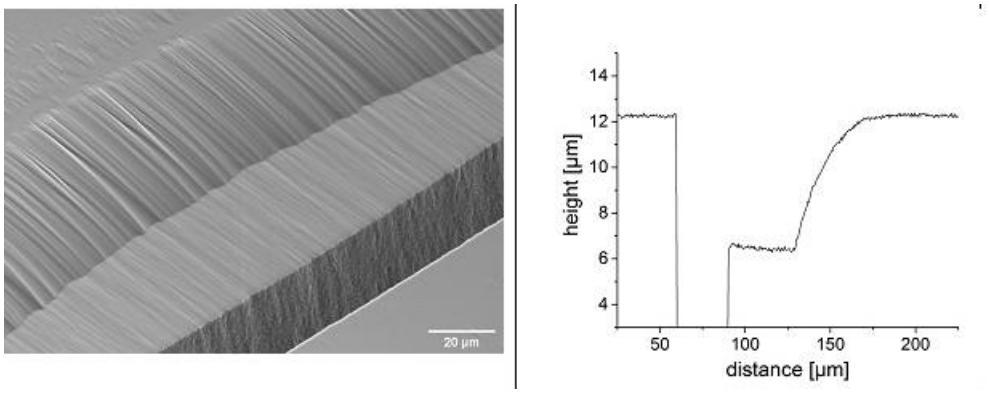

Figure 2. SEM micrograph (a) of an iNotchTM after broad ion beam erosion and height profile (b) perpendicular to the notch.

IM1.P060
Performance of the SALVE III energy filter for low-voltage energy-filtered TEM

M. Mohn[1], J. Biskupek[1], U. Kaiser[1]

[1]University of Ulm, Central Facility of Electron Microscopy, Ulm, Germany

michael.mohn@uni-ulm.de

The SALVE (Sub-Ångstroem Low-Voltage Electron Microscopy) instrument is corrected for geometric and chromatic aberrations and equipped with an imaging energy filter [1, 2]. According to these properties the instrument provides the possibility to form high-resolution images by inelastically scattered electrons of different energy losses [2].
Here we characterize the performance of our C_C/C_S-corrected EFTEM system and show first experimental results. In particular, we (a) discuss the effects of chromatic aberrations induced by the imaging energy filter in the voltage range between 20 kV and 80 kV and (b) show first atomically-resolved experimental images of 2D materials such as graphene and boron nitride obtained by plasmon-loss electrons and by high-energy-loss electrons.
In order to characterize the filter performance, we analyze two different effects of chromatic distortions in the imaging filter: (1) We observe the energy variations across the field of view. In EFTEM images, this non-isochromaticity locally changes the actual energy losses that contribute to the formation of the images. This effect is most clearly visible when recording energy-filtered images with small energy windows and sharp features in the energy-loss spectrum.
(2) Another distortion is caused by a non-achromatic behavior of the imaging energy filter. Depending on the energy loss, EFTEM images undergo a lateral shift. As a consequence, the very different energy losses within a large energy window will form a blurred image.
In this work, the two distortion effects of the imaging filter are quantified in terms of absolute energy shifts and relative lateral shifts within the images. These numbers define the filter performance for energy-filtering TEM and thus also the limits for experiments.
As first applications we present images formed by electrons which have excited the carbon K-edge (graphene) and the Ti $L_{2,3}$ edge (TiO_2, $TiSe_2$), respectively.
Regarding the general performance of the present energy filter, we find that for EFTEM at low voltages, different filter alignments may be necessary to achieve the best possible performance for a certain task. In energy-filtered TEM with atomic resolution however, we can state that we are mostly limited by the low signal-to-noise ratio of core loss signals. Our analysis may pave the way for future low-voltage energy filter developments. [3]

[1] U. Kaiser et al. (2011). *Ultramicroscopy*, 111(8), 1239–1246.
[2] M. Linck et al. (2016). *Physical Review Letters*, 117(7), 1–5.
[3] We acknowledge financial support by the German Research Foundation (DFG) and the Ministry of Science, Research and Arts (MWK) of the state Baden-Württemberg within the Sub-Angstrom Low-Voltage Electron Microscopy Project (SALVE).

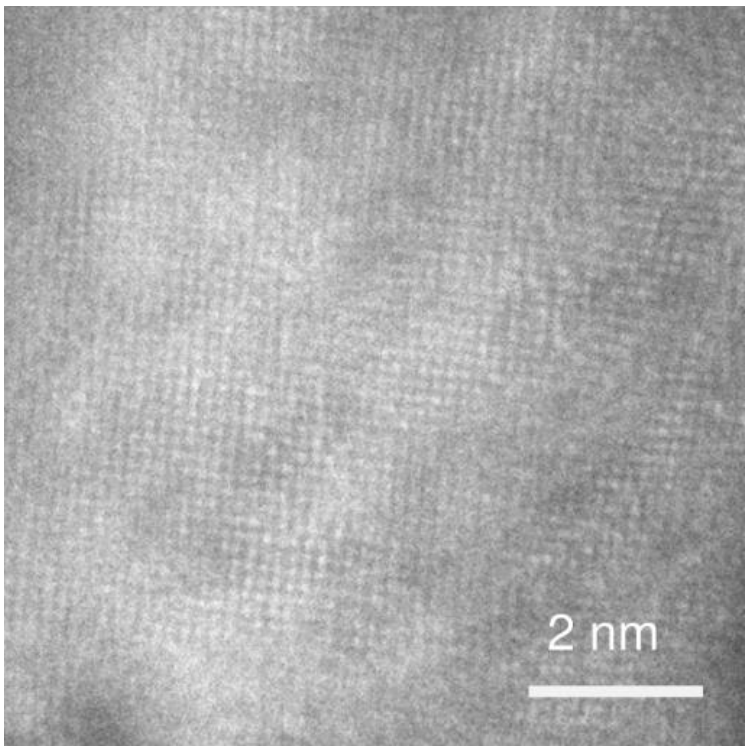

Figure 1. 80 kV C_C and C_S corrected energy-filtered TEM image of TiO_2 at an energy loss of 463 eV using an 8 eV energy window.

IM1.P061
Recent advancements in 3D correlative microscopy – from X-rays to electrons

J. Gelb[1], T. Volkenandt[2], F. Perez-Willard[2], A. Merkle[1]

[1]Carl Zeiss Microscopy, Pleasanton, CA, United States of America
[2]Carl Zeiss Microscopy, Oberkochen, Germany

jeff.gelb@zeiss.com

Introduction: In a typical characterization laboratory, many types of instruments are available. These may include structural techniques, spectroscopic analyzers, or more specialized instrumentation. Each tool is capable of capturing a unique type of data that exists at or across a specific range of length scales. A typical material system, likewise, exists across a range of length scales: there may be interesting macroscopic features, such as large fractures in the bulk structure, as well as atomic scale features, such as point defects, all of which may be of relevance within a characterization workflow.
Thus, classically it is the role of the scientist or engineer to select the appropriate tool or tools to achieve the necessary insight. This includes the instrument selection, sample preparation, tool setup, data acquisition, and the final interpretation of the results. Properly characterizing a material may require using several characterization instruments, due to the unique data produced by each tool, and getting all tools working together in a correlative manner is considered by some to be the present-day grand challenge of microscopy.
Objectives: Here, we present a novel correlative microscopy environment capable of integrating data from a variety of sources, using each result to build on the previous and inform the next step in the study. The initial developments have focused on linking 3D X-ray micrographs into a scanning electron microscope coupled to a focused ion beam (FIB-SEM), allowing the X-ray microscope (XRM) to produce a 3D (or 4D) survey of a material system and guide higher-resolution imaging by FIB-SEM.
Materials and Methods: In the present study, a correlative microscopy software environment has been created, which takes any image data as input and merges it together with other image data from the same sample in a common workspace. The results of one technique may then be used to inform a subsequent experiment, resulting in straightforward, accessible correlative microscopy interface. To test the routine, several specimens have been examined using correlative XRM and FIB-SEM. First, an aluminum alloy (type 7075) was non-destructively surveyed in 3D on the XRM, which provided a large-scale map of the inclusions within the material. A representative region was selected and enlarged using correlative FIB-SEM tomography, providing a high-resolution nano-scale characterization of the grains, grain boundaries, and precipitates. Next, a magnesium alloy was surveyed with 3D XRM and studied non-destructively as it corroded in situ (a so-called "4D" imaging experiment). When the corrosive attack was evident from the images, the corrosion process was stopped and a representative region was physically extracted for nano-scale XRM and, finally, examined using FIB-SEM tomography. The results enabled a multi-scale view into the corrosion dynamics of the magnesium alloy, as well as a high-resolution characterization of the localized microstructure. Further examples of characterizing a carbon fiber reinforced composite and lithium-ion battery will be presented as time permits.
Results: The results indicate the unique power of using multi-scale characterization in a series of real-world materials science studies. By combining techniques within a common workspace, all datasets are kept registered to each other and may be enabled/disabled as needed. Furthermore, correlative data acquisition with the electron microscope becomes much more straightforward in this environment, delivering quantitative results on the microstructure, guided by 3D XRM results. This allows easy access to correlative data without spending significant amounts of time on dataset alignment or ROI localization.
Conclusion: Correlative microscopy is a key characteristic of the modern materials characterization laboratory. By creating a common workspace capable of housing a multitude of results, characterization studies become more cooperative with each other, facilitating multi-scale characterization, multi-modal analysis, and collaboration amongst researchers.

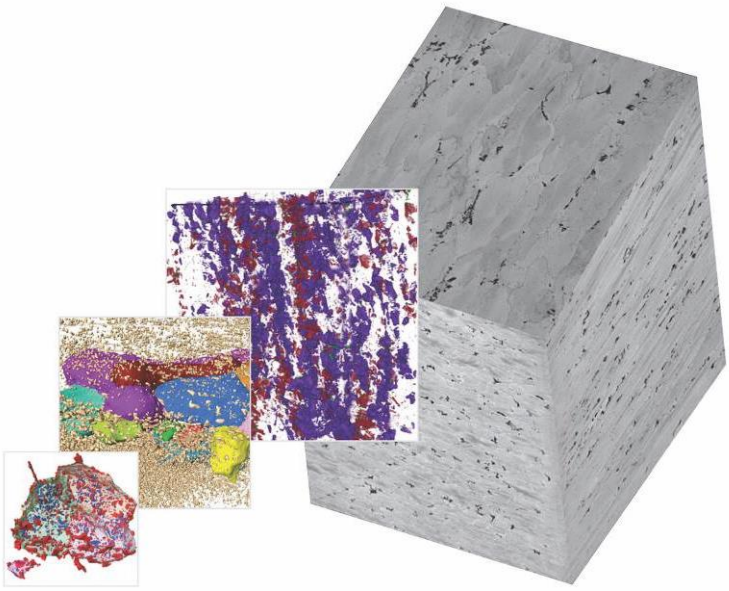

Figure 1. Multi-scale correlative analysis of an aluminum alloy, type 7075. Images courtesy of Prof. Nikhilesh Chawla, Arizona State University, USA.

IM1.P062
SEM or TEM for the characterization of nanoparticles?

R. Schmidt [1], V. D. Hodoroaba[2]

[1]Hitachi High-Technologies Europe GmbH, Krefeld, Germany
[2]Bundesanstalt für Materialforschung und –prüfung (BAM), Berlin, Germany

roland.schmidt@hht-eu.com

Scanning Electron Microscopy (SEM) or Transmission Electron Microscopy (TEM) ? This is a question, nowadays discussed in EM labs of research and industry involved in the characterization and metrology of nanoparticles (1). The Scanning principle is adapted to TEM, the Transmission mode is adapted to Ultra High Resolution SEM. Can modern SEM replace TEM, reach atomic resolution even without Cs corrector or nm lateral resolution for energydispersive X-ray spectroscopy (EDX)?
Due to the development of a New Cold Field Emission (NCFE) electron source Hitachi SEMs SU9000 and SU8200 can deliver routinely sub-nm image resolution and EDX mappings at very high count rates and a lateral EDX resolution of a few nm (2), (3), (4) . A TiO2 sample (Fig. 1) provided by BAM was analysed at 30kV using low kV STEM – simultaneously with the Through-the-lens (TTL) SE detector, the Bright Field transmitted and Dark Field transmitted signals. By this method a pixel precise information of the particles surface using SE, its chemical nature using DF-STEM and its crystalline structure using Bright Field signal is given in one 40sec scan. The advantage of this observation mode compared to Ultra Low Voltage imaging is outlined.

References:
[1] www.setnanometro.eu
[2] The latest innovation on FE-SEM and its applications, H. Sato et.al., poster at MC2013
[3] New developments for Low Voltage STEM with in-lens CFE-SEM, R. Schmidt, poster at MC2015
[4] Characterization of nanoparticles by means of high-resolution SEM/EDX in transmission mode, Hodoroaba, et al., IOP Conf. Series: Material Science and Engineering 109 (2016) 012006 doi: 10.1088/1757-899X/109/1/0 12006

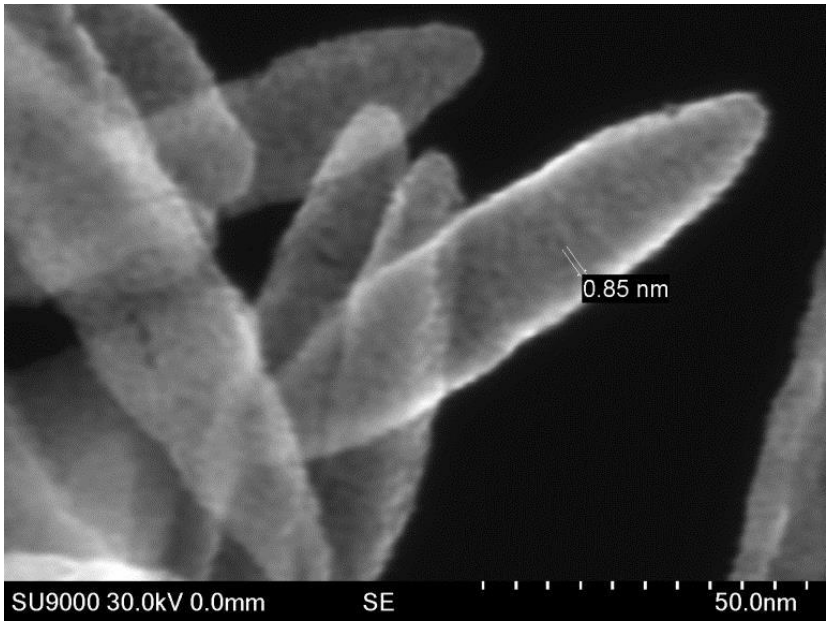

Figure 1. SE image at 30kV of a TiO2 nano-particulate sample mounted on TEM grid.

IM1.LBP01
Visualization of mitochondrial oxidative stress during apoptosis – time-resolved fluorescence microscopy approach

V. Huntosova[1], L. Koptasikova[2], S. Sokolova[2], M. Misuth[2], P. Miskovsky[1]

[1]P.J. Safarik University in Kosice, Center for Interdisciplinary Biosciences, Kosice, Slovakia
[2]P.J. Safarik University in Kosice, Department of Biophysics, Kosice, Slovakia

veronika.huntosova@upjs.sk

Cell metabolism can be affected by different stimuli. Apoptotic death pathway can be regulated *via* several of them: reactive oxygen species (ROS), phosphorylation of protein kinases, Bcl-2 family proteins or caspases activation. Fluorescence imaging helps determine localization and distribution of important molecules active in apoptosis, mostly by immunofluorescence or labeling with specific fluorescent probes, directly in cells. Time-resolved fluorescence imaging (FLIM), furthermore, offers information about surrounding and interactions of detected molecule with other molecules during apoptosis. Fluorescence lifetime is a unique parameter of fluorescent probe, which is concentration independent but strongly depends on the environment. FLIM enables detection and estimation of protein-protein interactions, intracellular changes of microenvironment (ROS production), the impact of pro-/anti-apoptotic agents on organelles morphology and signaling pathway in cancer cells. In our recent studies, we have followed drug distribution by Förster resonance energy transfer (FRET), mitochondrial stress and phosphorylation of protein kinase C δ in glioma cells treated with light-activated molecule during photodynamic therapy. Our results demonstrated that fluorescence lifetime is not only complementary but often compulsory parameter that helps precisely describe processes in cells.

Acknowledgment
This work was supported by Slovak grant agency APVV-15-0485 and a grant of FS UPJS in Kosice VVGS-2017-272.

IM1.LBP02
Simultaneous e-field and strain mapping by precession electron diffraction

B. Haas[1,2], D. Cooper[1], J.-L. Rouvière[1]

[1]CEA / Univ. Grenoble Alpes, Minatec, Grenoble, France
[2]Humboldt-Universität zu Berlin, Institut für Physik, Berlin, Germany

Introduction: Measuring electric fields by means of a scanning electron probe has recently gained a lot of momentum [1-3]. While techniques that rely on segmented detectors are based on oversimplified models [1-2], pixelated detector based methods that were proposed so far require very thin specimens [3].
Objectives: In this abstract, we demonstrate a new method to reliably measure the electric field and the strain of a specimen simultaneously from the same data set (patent pending). By combining a nano-beam setting (convergence angle of around 2 mrad) with precession of the beam in a hollow cone, the E-field can be measured avoiding diffraction artifacts even for thick specimens with a probe size of less than 1 nm. The capabilities of this technique are investigated on piezoelectric specimens, where the simultaneous measurement of strain and E-field are especially interesting.
Materials and Methods: Using the prototype FEI Epsilon software in a Titan Themis microscope together with a FEI Ceta CMOS camera, scanning nano-beam precession diffraction patterns are acquired with typically 2 mrad convergence angle, 0.3º precession angle, 100 pA beam current and 150 ms exposure time as 512² pixel images. The images are subsequently analyzed with a homemade DigitalMicrograph plugin. It determines the strain from the distance of diffraction discs as extracted by means of auto-correlation. The E-field is measured from tracking of the central diffraction disc. By repeating the scan in vacuum and subtracting the result, parasitic movement of the discs due to imperfect pivot point alignment can be eliminated. By precessing the beam and then tracking the movement of the homogeneous disc, the measured shifts really correspond to the beam deflection from E-fields. Artifacts from multiple scattering are suppressed by precessing the beam and by tracking its position by means of template-matching of the central disc in the diffractograms. This turns out to be more effective than measuring the center-of-mass.
Two samples are investigated with this technique; an InGaN/GaN LED structure (30% In) to test the reliability and spatial resolution, and a-plane grown AlN/GaN layers that exhibit dislocations.
Results: In Fig. 1 (a) an HR-HAADF image of a InGaN/GaN LED sample is shown. A single diffraction pattern from the acquired nano-beam precession series is given in (b). The vertical strain and E-field components (in growth direction) are shown in (c) and (d) respectively. A piezoelectric field of 3.9 MV/cm could be detected.The precision of the E-field measurement as determined from the rms value at the nominally field-free regions is 0.2 MV/cm. The horizontal E-field component, displayed in (e) shows only small fluctuations, where none are to be expected, giving confidence in the method.
Fig. 2 (a) shows an HAADF image of a-plane grown AlN/GaN layers observed in [0001] ZA. Fig. (b) is a virtual image (constructed from digital apertures placed in the diffraction patterns of the series), showing the mapped area. Fig. (c) and (d) are the horizontal components of the strain and E-field, respectively, revealing individual dislocations at the interfaces and their influence on strain relaxation of the layers and resulting piezoelectric fields.
Conclusion: We demonstrated a new reliable method to simultaneously measure E-field and strain even for thick specimens and with spatial resolution of below 2 nm. Thus, enabling e.g. the observation of strain and E-fields of individual defects in piezoelectric materials.

Acknowledgements
Precession maps were acquired using the Epsilon acquisition package developed by FEI within the CEA Grenoble/FEI common lab. The authors thanks the FEI company (now part of Thermo Fisher Scientific) and especially Max Otten and Mark Williamson for their help. Benedikt Haas acknowledges funding from Deutsche Forschungsgemeinschaft (KO 2911/12-1). The authors thank Bruno Daudin for providing samples.

References:
[1] M. Lohr et al., *Ultramicroscopy* 117, 7 (2012).
[2] N. Shibata et al., *Scientific Reports* 5, 1 (2015).
[3] K. Müller et al., *Nature Comm.* 5, 5653 (2014).

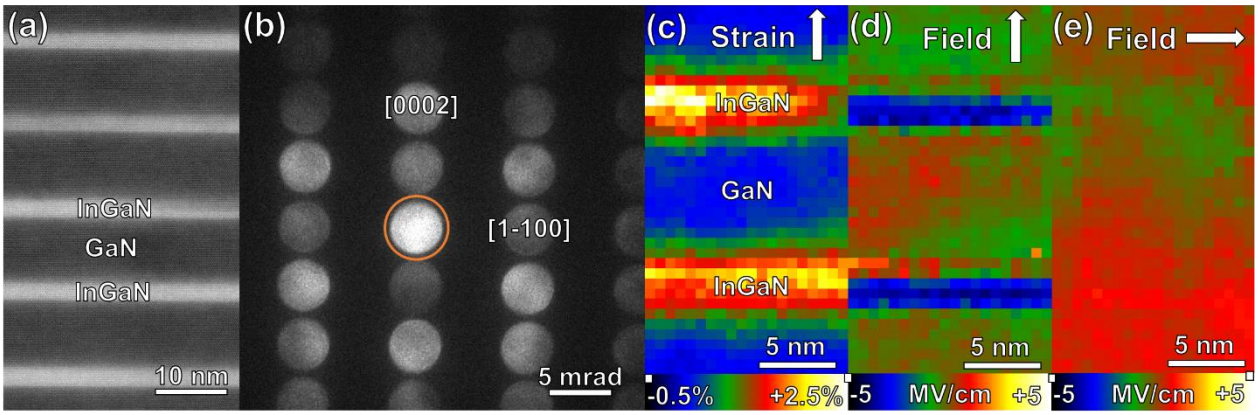

Figure 1. (a) Overview HAADF image of InGaN/GaN LED sample. (b) Individual nano-beam precession diffraction pattern of the series. (c) Vertical strain component (growth direction). (d) Vertical E-field component showing a piezoelectric field in the quantum wells. (e) Horizontal E-field component.

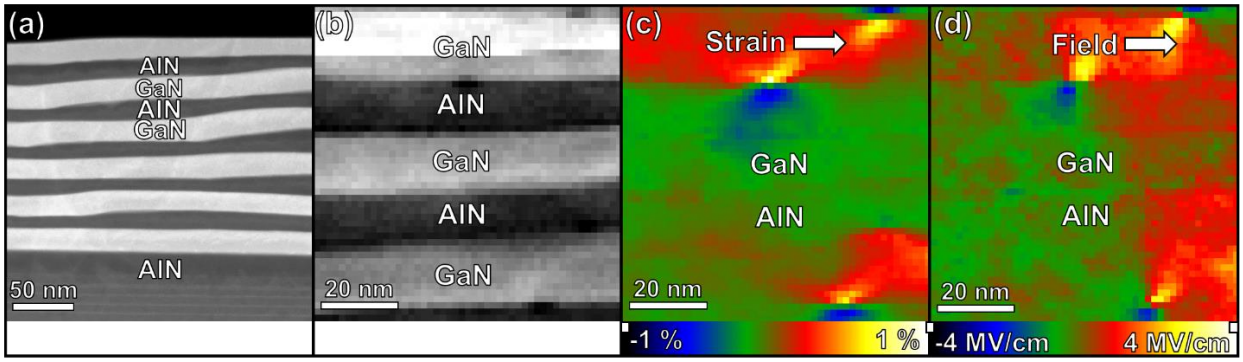

Figure 2. (a) HAADF image of a-plane grown AlN/GaN layers imaged along c-axis. (b) Virtual image created from diffraction patterns showing the mapped region. (c) Horizontal strain component, revealing dislocations at interfaces. (d) Horizontal E-field component showing piezoelectric fields associated with the dislocations.

IM2.001
Direct observations of interactions between water and single WS_2 nanotubes – in situ SEM and AFM studies

O. Goldbart[1], I. Kaplan-Ashiri[2], S. R. Cohen[2], A. Enyashin[3], P. Glazyrina[3], H. D. Wagner[1], R. Tenne[1]

[1]Weizmann Institute of Science, Materials and Interfaces, Rehovot, Israel
[2]Weizmann Institute of Science, Chemical Research support, Rehovot, Israel
[3]Institute of Solid State Chemistry, Ekaterinburg, Russian Federation

ohad.goldbart@weizmann.ac.il

The wetting of nanoparticles by molten polymers is a key factor in the field of nanocomposites as it will affect their properties and performance. The wetting of a solid surface by a liquid is a process being controlled by many factors, for instance: surface morphology, liquid droplet size and shape, energetics of both liquid and solid surfaces and their interface. Exploring these events at the nanoscale is of great importance for the study of molecular basis of wetting, and will enable a better design of nanocomposites.
The objective of this work is to study the wetting phenomena at the nanoscale. Specifically, to measure the interaction between a single WS_2 nanotube and water by means of wetting angle and the force required to pull out the nanotube from water.
In this work, we present a methodology that was developed to measure the interactions between individual nanotubes and different liquids using environmental scanning electron microscope (ESEM) and atomic force microscope (AFM). The experimentations are based on pullouts of single nanotubes from water films and other liquids, and were conducted both in Wet mode SEM and AFM. These measurements strategies allow the correlation between the WS2 nanotubes morphology and structure and the measured interaction strength with different liquids.
The results demonstrate that the interaction energy/cross-section area of the nanotubes falls-off dramatically with the diameter of the nanotubes (30-70 nm) and then levels-off. These differences are currently attributed to the capillary interaction of the small hollow core nanotubes and the water molecules. MD simulations show that the highly confined space results in large interaction energy between the water molecules and the inner core of the nanotubes. This interaction leads to imbibition of the water molecules into the nanotube"s hollow core. These effects and the impact of the nanotubes surface chemistry on the interaction energy will be presented and discussed.
From these experiments, as well as from theoretical simulations, it follows that the morphology of the WS2 nanotube has a significant effect on the interaction of the nanotubes and the surrounding media.

IM2.002
Capturing the aggregation dynamics of ϒS Crystallin with in-liquid electron microscopy

S. Azim[1], G. Kassier[1], S. Keskin[1], S. Manz[1], R. Bücker[1], A. Casandruc[1], E. Schulz[1], K. Roskamp[2]
R. W. Martin[2,3], D. V. Rojas[4], H. K. Trieu[4], R. J. D. Miller[1,5]

[1]Max Planck Institute for the Structure and Dynamics of Matter, Atomically Resolved Dynamics Department, Hamburg, Germany
[2]University of California Irvine, Department of Chemistry, CA, United States of America
[3]University of California Irvine, Department of Molecular Biology and Biochemistry, CA, United States of America
[4]Hamburg University of Technology , Institute of Microsystems Technology, Hamburg, Germany
[5]University of Toronto, Department of Chemistry, Toronto, Canada

sana.azim@mpsd.mpg.de

Introduction**:** βϒ-Crystallins are structural proteins, responsible for maintaining the refractive index gradient of the lens in the eye. Any small variations in these proteins can lead to congenital cataracts. Depending on the conditions under which the aggregates are formed, they can be classified under two categories, amorphous aggregates and crystalline aggregates (amyloid fibrils) [3]. Insight into the morphology and dynamics of the aggregation process is very important in order to find causes of and treatments for cataracts.
Objectives**:** The aim of this work is to observe UV-B (285 - 315 nm) radiation induced morphology and real time aggregation dynamics in samples of wild-type human ϒS – Crystallin and its more aggregation-prone variant, G18V ϒS – Crystallin.
Materials and Method**:** We use transmission electron microscopy (TEM) at 200 kV with stained dry and in-liquid specimen preparation modalities. Initial morphological studies were conducted on samples drop cast onto Carbon/Formvar grids and treated with 1% Uranyl acetate acting as contrasting agent. For in-liquid electron microscopy, samples were prepared by drop casting the aggregate suspension on custom fabricated silicon nitride on silicon chips with a window thickness of 50 nm, a lateral size of about 50x50 µm and a spacer thickness of 100 nm between the two windows[1,2]. The assembled liquid cell was then loaded in a custom in situ TEM probe arm featuring in situ UV irradiation capability.
Results: Wild type ϒS Crystallin exhibits sphere-like aggregates, confirmed by both in-liquid (Fig. 1) and negative stain (Fig. 2) microscopy. The negative stain images reveal a propensity towards linear cluster formation of the small (30 nm) sphere-like aggregates. In addition, isolated amyloid fibrils with a width of about 20 nm and a length of several microns can be seen. The amyloid fibrils in the lysozyme control specimen can be clearly seen with the negative stain TEM technique. The structure of the UV irradiated G18V aggregates appear slightly different as compared to the WT sample, with the aggregates similar in size as WT (15 – 30 nm), but rather more irregular in shape, as confirmed by both in-liquid (Fig. 3) and negative stain (Fig. 4) TEM.
Conclusions**:** It is possible that the linear clusters of spherical aggregates, observed in case of WT ϒS Crystallin, could be precursors to the formation of amyloid fibrils, a process that could eventually be observed dynamically in situ. In case of G18V no amyloid fibrils could be found. However, there appears to be a tendency to the formation of linear aggregate clusters. Individual strands have a thickness of about 12 nm; the networks/bundles appear much thicker, in the range of 40 – 100 nm. These results have also been verified by Cryo electron microscopy. We discuss the morphological features of the observed UV-B induced aggregation states in our WT and G18V ϒS – Crystallin samples with emphasis on their relevance in elucidating possible aggregation mechanisms.

References:
[1] Keskin, S., Besztejan, S., Kassier, G., Manz, S., Bücker, R., Riekeberg, S., Trieu, H.K., Rentmeister, A. and Miller, R.J.D, J. Phys. Chem. Lett. 2015, 6, 4487-4492.
[2] Besztejan, S., Keskin, S., Manz, S., Kassier, G., Bücker, R., Venegas-Rojas, D., Trieu, H.K., Rentmeister, A. and Miller, R.J.D., Microscopy and Microanalysis, pp. 1–10. doi: 10.1017/S1431927616012708.
[3] Jiang, J., Golchert, K.J., Kingsley, C.N., Brubaker, W.D., Martin, R.W., and Mukamel, S., J. Phys. Chem. B 2013, 117, 14294-14301.

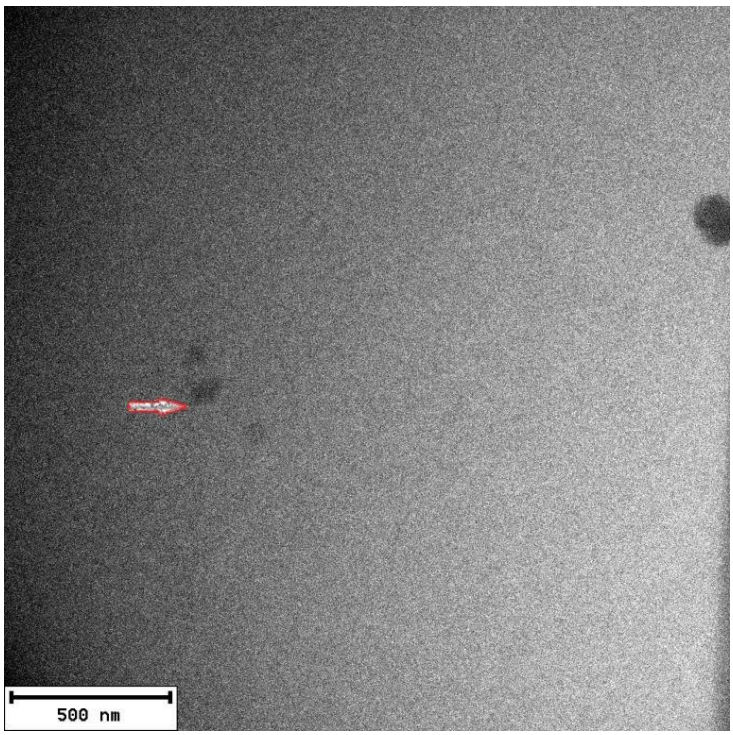

Figure 1

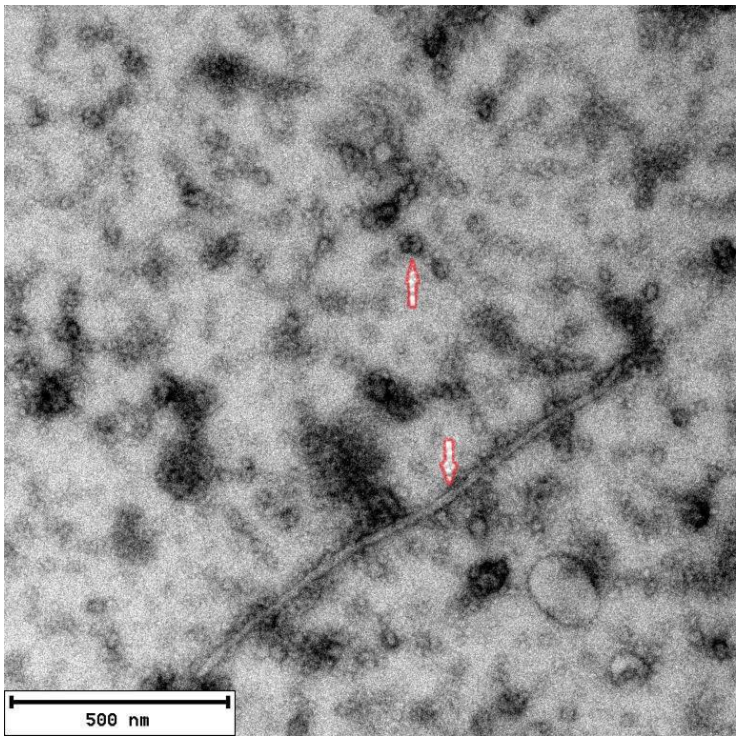

Figure 2

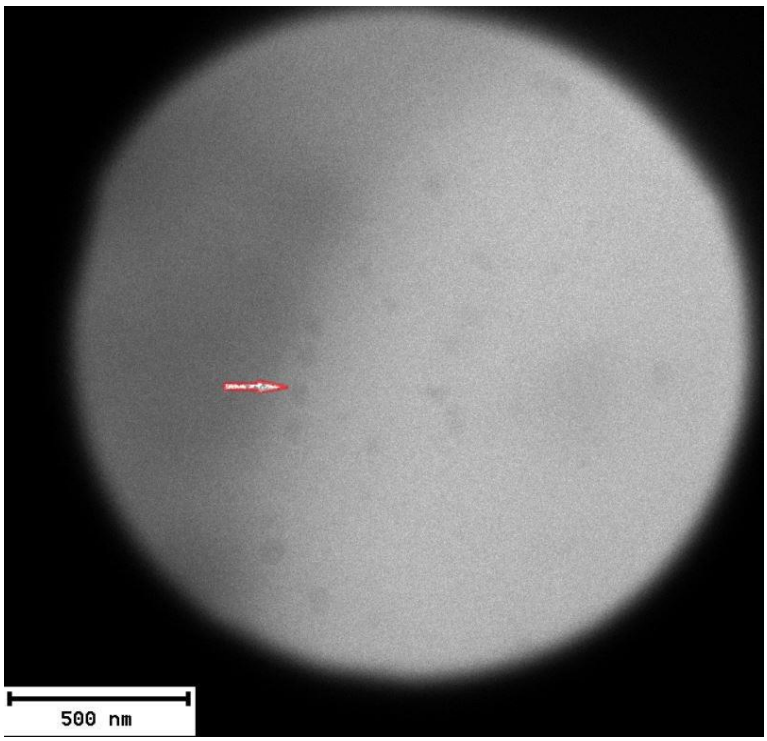

Figure 3

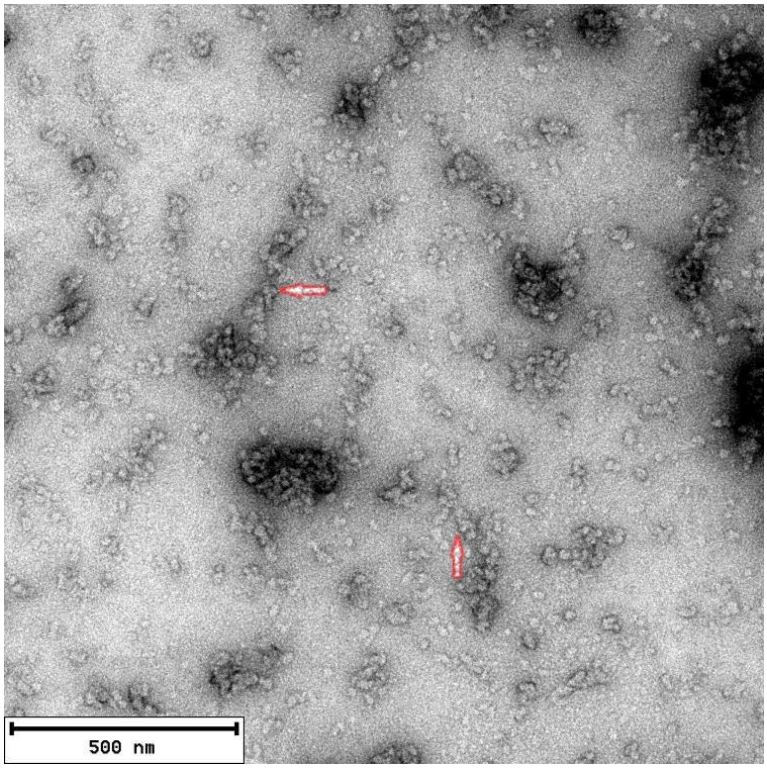

Figure 4

IM2.003 invited
Perspectives on in situ chemical analysis using nanosecond EELS measurements

T. LaGrange[1], K. Bücker[2], M. Picher[2], F. Banhart[2]

[1]École Polytechnique Fédérale de Lausanne, Interdisciplinary Centre for Electron Microscopy, Lausanne, Switzerland
[2]Université de Strasbourg, Institut de Physique et Chimie des Matériaux (IPCMS), Strasbourg, France

thomas.lagrange@epfl.ch

A limiting factor for in-situ measurements has been the acquisition rate of recording media, which has been limited to video rate that is too slow to capture most salient dynamics of nanomaterial systems. Though recent innovations in camera technology have pushed acquisition rates to the a few ms, the current (~50nA) of conventional electron sources ultimately limits the acquisition speed to 100s of microseconds. The immergence of time-resolved TEMs, such as the femtosecond, ultrafast TEM at Caltech and nanosecond dynamic TEM (DTEM) at Lawrence Livermore National Laboratory have overcome the signal limitations of conventional electron sources but using laser induced electron emissions, producing much higher peak currents (mAs). Such high instantaneous beam currents come at a cost; electrons are closer in space and scatter off each other, increasing energy spread and decreasing spatial and temporal coherence, i.e., increased Boersch effects. The femotosecond to picosecond stroboscopic approach overcomes the Boersch effects by limiting number of electrons per pulse and integrating billons of probe events to form an image or EELS spectrum [1]. However, for most experiments, processes are either irreversible or reset times between sample excitation and its return to the ground state are typically longer than 1µs, and thus, it is practically difficult to operate in the "one-electron per pulse" mode as it results in effective exposure times of several minutes, as the specimen and spectrometer drift greatly reduce resolution during long exposures. With specific electron optical configurations, time-resolution can be traded-off for increased signal while maintaining an energy spread below 1.5 eV in the stroboscopic setup [2], which is sufficient to perform EELS experiments.
Spectroscopy with the single-shot approach used in the DTEM microscope at LLNL was speculated to be too challenging to yield meaningful results [3]. The single-shot approach can explore irreversible events in materials by taking "snap-shot" images using electron pulses that have a bunch length of 5ns to 100s of nanoseconds and contain billons of electrons. With such high currents (1-100mA), Boersch effects are the dominant limitation to this technique, especially near the cathode where electrons have a low energy. Usually, signal is traded –off to increase electron pulse coherence and improve spatial resolution. Ultimately, for short, ns pulses, spatial resolution is limited by the electron trajectory changes in the crossovers of the objective lens. However, we found that for conventional DTEM electron sources, the Boersch effects and resulting chromatic aberrations are the dominant limitation.
To obtain sufficient signal on the detector, we need to use electron pulses containing >$5x10^7$ electrons which results in energy spreads of >50eV (See Figure 1). The coherence length is very short, being only a few nanometers, and thus, spatial coherence and resolution are low. From recent experiments at UTEM facility in Strasbourg, we believe that the Boersch effects near the cathode, even under optimized conditions, result in chromatic aberrations limiting resolution in single shot mode. Moreover, the meaningful EELS measurements at energy spread shown in is not possible. However, by optimization the electron optical configuration and using the wehnelt and fixed apertures in the acceleration as a crude monochromator, the energy spread can be greatly reduced while maintaining enough signal to perform core loss EELS, e.g. we have measured the carbon K-edge (See Figure 2). Given these preliminary results and with further optimization of the cathode geometry, it may be possible to improve signal without increasing the energy spread.

References:
[1] V. A. Lobastov, R. Srinivasan, and A. H. Zewail, P Natl Acad Sci USA **102**, 7069 (2005).
[2] K. Bücker, M. Picher, O. Cregut, T. LaGrange, B. W. Reed, S. T. Park, D. J. Masiel, and F. Banhart, Ultramicroscopy **171**, 8 (2016).
[3] T. LaGrange *et al.*, Appl Phys Lett **89** (2006).

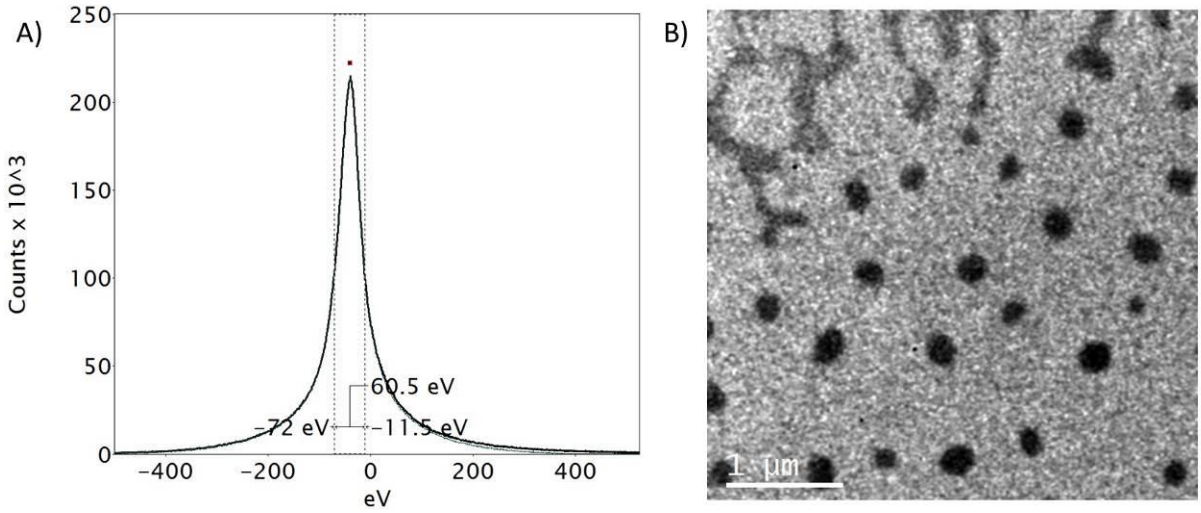

Figure 1. A) Zero loss peak showing a FWHM of ~60 eV measured at the microscope setting optimized for single-shot imaging using 7ns electron pulses, B) a 7ns, single-shot image of gold particles on a carbon films obtained with an energy spread of 60 eV.

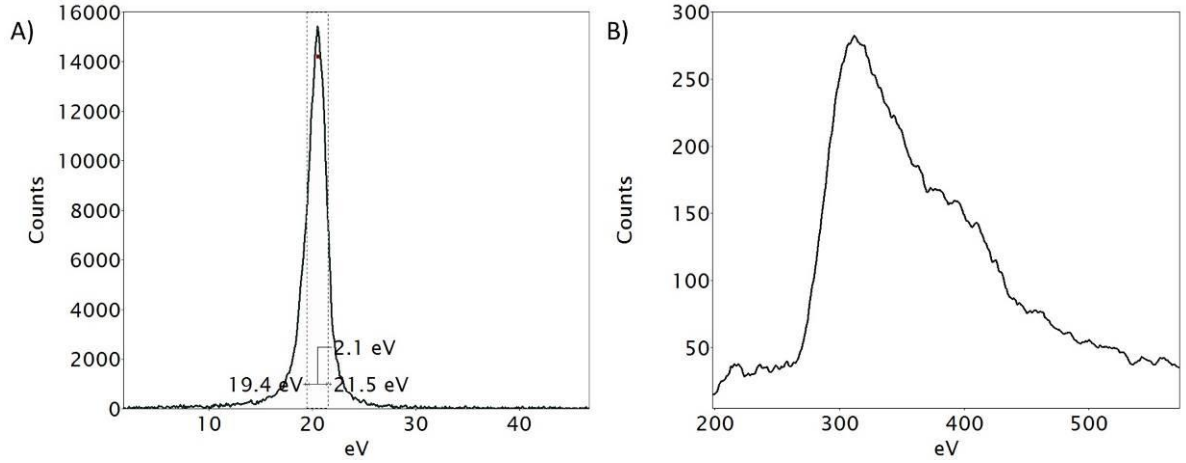

Figure 2. A) Zero loss peak showing a FWHM of ~2 eV measured at the microscope setting optimized for single-shot EELS using 7ns electron pulses, B) single-shot EELS measurement of the carbon K-edge.

IM2.004
Quantitative analysis of block copolymer vesicle formation by in situ liquid phase transmission electron microscopy

H. Wu[1], J. P. Patterson[1], A. Ianiro[1], A. Keizer[1], H. Friedrich[1], R. Tuinier[1], C. Esteves[1], N. Sommerdijk[1]

[1]Eindhoven University of Technology, Department of Chemical Engineering and Chemistry, Eindhoven, Netherlands

h.wu@tue.nl

Introduction: Recent advances in liquid phase transmission electron microscopy (LP-TEM) have provided unique capabilities for *in situ* probing of material formation processes on different time and length scales, and thus unravelling growth mechanisms [1-2]. However, so far, most LP-TEM studies have focused on metallic and inorganic materials, with only few reports on organic soft matter [3-4], mainly due to their low contrast and beam sensitivity. Block copolymer vesicle formation processes have been well-studied both experimentally and theoretically [5-8], yet little is known about the dynamics of assembly in real time and real space.
Objectives: To image block copolymer vesicle formation in-situ with good contrast and resolution using developed low dose protocols; 2) To automate quantitative image analysis via Matlab scripts;
Materials and Methods: PEO-b-PCL (polyethylene oxide-b-polycapralactone) block copolymer system was used to investigate self-assembly via the solvent switch protocol.
Liquid phase TEM experiments were carried out on an FEI Tecnai 20 (type Sphera) TEM microscope operated with a 200 keV LaB_6 filament and a 1K × 1K Gatan CCD camera, by using a commercial liquid cell holder (Ocean) provided by DENSsolutions.
In house automated algorithms written via Malab Mathworks were used to implement the automated analysis.
Results: Here we show the first observation of block copolymer vesicle formation via the solvent switch process using LP-TEM (Figure 1). In the early stages of vesicle formation we see particle growth, which is followed by an increase in particle contrast and an increase in membrane thickness during the late stages of formation. Comparing to previous literature, it appears that the vesicles form via the so called "mechanism II" [7] which is a process that has not previously been observed experimentally. Moreover, our real-time direct observation of the membrane formation process clearly shows that during formation the vesicle membranes are not continuous and of uniform intensity, but are consisting of different patches with various intensities. This allows us to investigate the local formation processes within a single vesicle and we show that local differences in membrane thickness are related to the formation mechanism.
Conclusions: Our findings illustrate the ability of liquid phase electron microscopy to implement quantitative visualization of the block copolymer vesicles formation process to reveal the mechanism of formation on an individual particle level. The formation processes of polymer vesicles are different for individual vesicles, and the local formation of the membrane within a single vesicle is dependent on the formation process. We therefore anticipate a promising future for the use of LP-TEM to study the dynamics of low-contrast soft matter in solution.

References:
[1] J. De Yoreo, N. Sommerdijk, Nature Reviews Materials **1**, 16035 (2016).
[2] P. J. M. Smeets *et al*, Nature Materials **14**, 394-399 (2015).
[3] M. T. Proetto *et al*, Journal of the American Chemical Society **136**, 1162-1165 (2014).
[4] J. P. Patterson *et al*, Journal of the American Chemical Society **137**, 7322-7328 (2015).
[5] D. E. Discher, A. Eisenberg, Polymer vesicles. Science **297**, 967-973 (2002).
[6] B. M. Discher *et al*, Science **284**, 1143-1146 (1999).
[7] X. H. He *et al*, Macromolecules **39**, 2654-2662 (2006).
[8] J. H. Huang *et al*, Journal of Chemical Physics **131**, (2009).

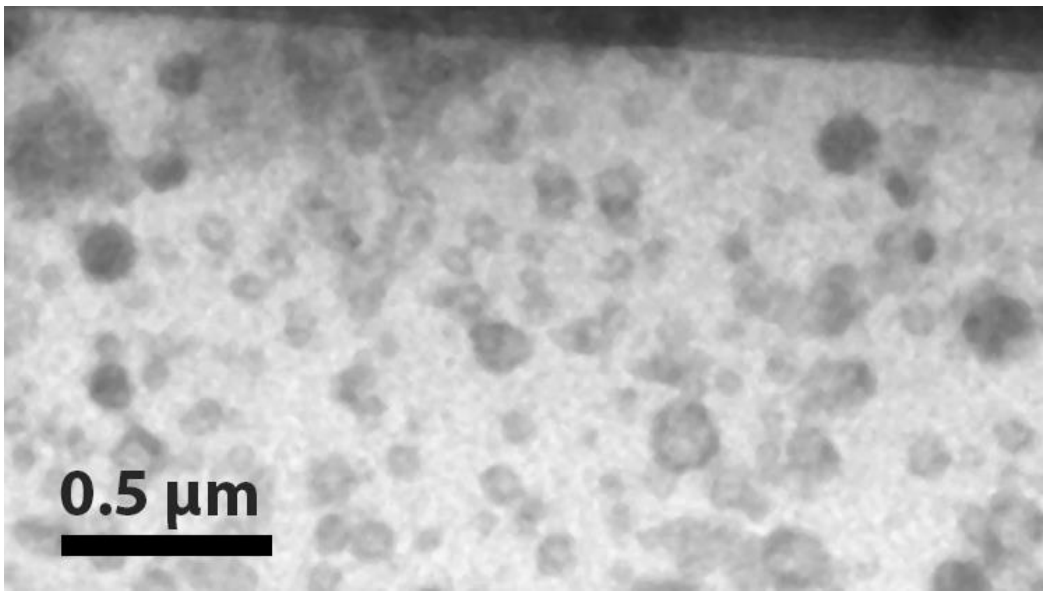

Figure 1. Snapshot from LP-TEM movie illustrating the formation of PCL-b-PEO vesicles via solvent switch process.

IM2.006
Revealing the inner workings of atomic friction using correlative in situ electron microscopy

P. Schweizer[1], C. Dolle[1], E. Spiecker[1]

[1]Institute of Micro- and Nanostructure Research & Center for Nanoanalysis and Electron Microscopy (CENEM), Friedrich-Alexander-Universität Erlangen-Nürnberg, Erlangen, Germany

peter.schweizer@fau.de

The topic of Friction between two atomically flat crystalline surfaces has seen increasing interest in the recent years due the discovery of a novel, near-frictionless state called superlubricity [1]. This effect occurs if two crystalline surfaces are incommensurate with respect to each other and has been shown to exist for many materials including rotated graphite flakes [2]. Depending on the rotation angle, different values for the friction force have been measured. This principle of ultra-low friction due to a rotational misorientation can be extended to other layered materials such as the transition metal dichalcogenides. However, the experimental observation of the dynamic processes on a microstructural level during rotation and sliding remain elusive so far.

In this work we demonstrate a novel approach, based on correlative *in situ* Scanning Electron Microscopy (SEM) and Transmission Electron Microscopy (TEM) experiments, to unravel the processes happening in an atomically flat crystalline interface during translation and rotation. Figure 1 A) and B) show the general experimental approach: Using Focused Ion Beam (FIB) pillars are cut into a bulk layered crystal. The pillars are subsequently sliced into small discs using a micromanipulator and pushed partially over the sample edge to make them visible in the TEM. In a consequent step using *in situ* TEM the slices can be rotated and pushed around while looking at the microstructure. Frames from the slicing procedure are shown in Figure 1 C) and D). The slices precisely follow the basal planes of the crystal and can be produced with thicknesses of below 80 nm.

Figure 2 shows Experimental Data from the Transmission Electron Microscopy experiments. A) and B) are two frames from a large field-of-view *in situ* STEM experiment, that shows the rotation around a certain pair of slices. Apart from rotations, translations are also possible. Going to TEM and a higher magnification (Figure 2 C and D) reveals a distinct Moiré pattern, that not only gives us a direct measure of the relative rotation of the slices but can also be used to characterize defects in the interface.

In future experiments the *in situ* TEM experiments will be combined with force measurements to correlate certain changes in the interfacial defect structure with characteristics in the friction force curve.

References:

[1] M. Hirano, K. Shinjo; Physical Review B (1990)

[2] M. Dienwiebel, G. Verhoeven, N. Pradeep, J. W. M. Frenken, J. Heimberg, H. W. Zandbergen; Physical Review Letters (2004)

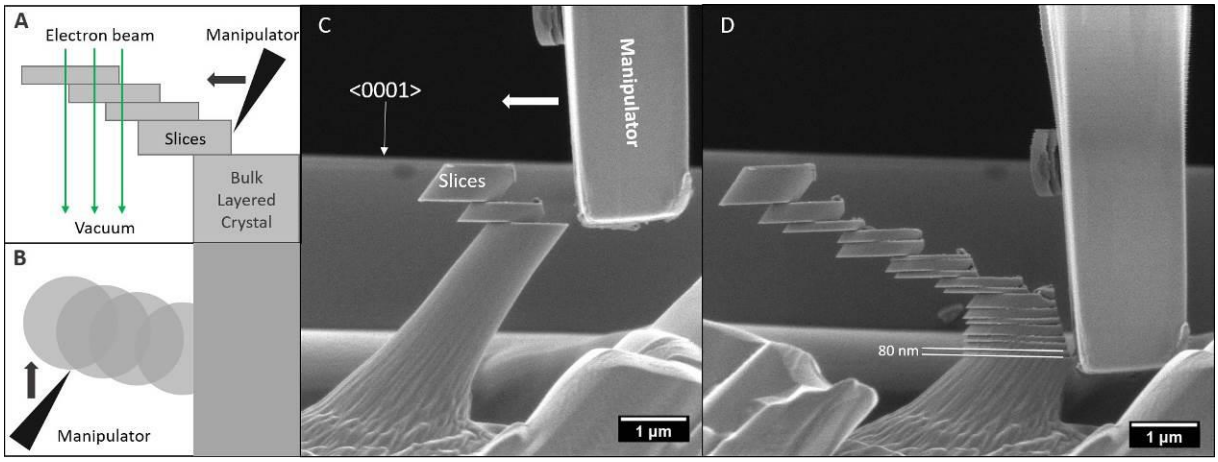

Figure 1. A) Side-view schematic of the slicing approach. B) Top-view of the experimental setup for the in situ TEM experiments. C), D) Frames from an in situ video showing the sequential slicing of a FIB-prepared structure along the basal planes of the layered material.

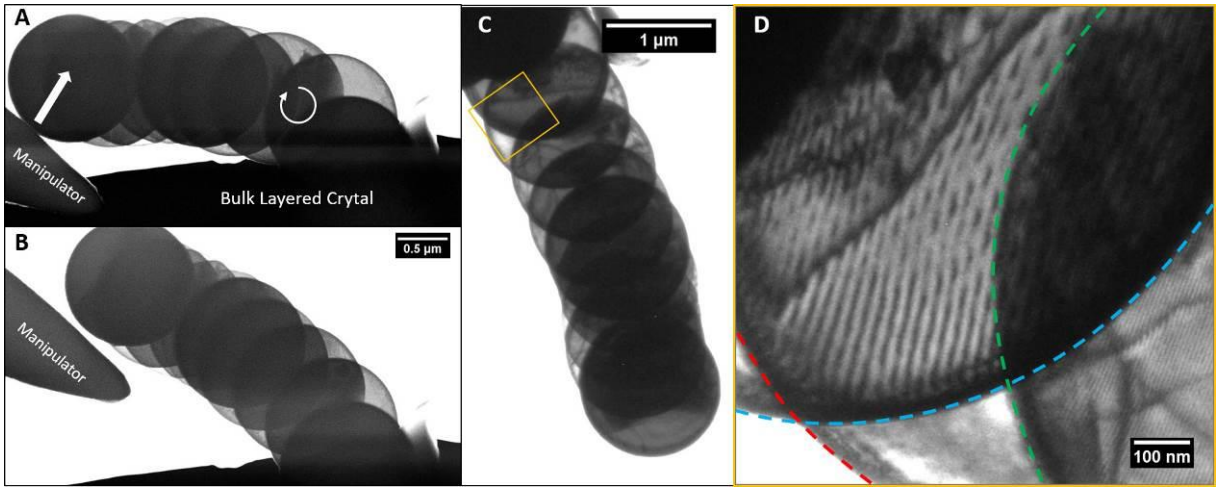

Figure 2. A), B) Different Stages during an in situ STEM rotation experiment. C) BF TEM overview image of a manipulated stack of slices. A higher magnification of the marked area showing distinctive Moiré patterns can be seen in D). The dashed colored lines show the edges of the different slices.

IM2.007
Ex situ and in situ SEM/TEM investigation of plasticity/fatigue mechanisms of single and bi-crystal Ni samples by using micro/nano-mechanical testing

V. Samaeeaghmiyoni[1], M. Wenk[2], R. Schwaiger[2], H. Idrissi[1,3], D. Schryvers[1]

[1]University of Antwerp, physiscs, Antwerp, Belgium
[2]Karlsruhe Institute of Technology, Institute for Applied Materials , Karlsruhe, Germany
[3]Université catholique de Louvain, Louvain-la-Neuve, Belgium

vahid.samaeeaghmiyoni@uantwerpen.be

Introduction: Recent advancements of nano-mechanical instruments have enabled the investigation of mechanical properties, like fatigue, of small-scale materials which is important and helpful in designing of small-scale components as micro-electro-mechanical-systems (MEMS) and micro-electronics.
Objectives: The specific objective of this study was to investigate either compressive or tensile fatigue properties of small-scale single crystal and bi-crystal nickel samples and to correlate the observed fatigue properties to the dislocation structural evolutions.
Materials and Methods: For monotonic and cyclic compression experiments, the single crystal and the bi-crystal micropillars (2um*2um*6um) of pure nickel were prepared by Focused Ion Beam (FIB) and experienced cyclic compressive tests by the Nanomechanics InSem1. In addition of conventional ex-situ TEM techniques, advanced Precession Electron Diffraction (PED), Automated Crystal Orientation Mapping in TEM (ACOM-TEM) and TopSpin were used to determine the local orientation and strain maps.
To prepare tensile samples (1200nm*600nm*120nm) a novel combination of twin-jet electro-polishing (TJEP), FIB and in-situ TEM heating was used to obtain damage-free nickel samples proper for quantitative in-situ TEM tensile test experiments, Fig 1. Then monotonic and cyclic tensile deformation tests were carried out using the Hysitron PicoIndenter holder and a special MEMS device, Push-To-Pull (PTP), designed for performing tensile tests [1].
Results: The mechanical results and TEM investigation of the micropillars revealed the correlation between the accumulated strain and formation of dislocation walls. It was also observed that grain boundaries (GBs) can postpone formation of dislocation walls in the structure of bi-crystal mircopillars. Orientation maps revealed sharp misorientations by crossing the dislocation walls and strain maps showed the prevalent character of dislocation types in the walls.
In addition, in-situ TEM cyclic tensile deformation of single crystal samples showed that the governing mechanism is a combination of dislocation interactions and dislocation starvation. Surprisingly the fracture stress was very high and the crack initiated from the surface, parallel to the highly activated slip plane.
Conclusion: In micropillars, interaction of dislocations and formation of new dislocation sources are the dominant governing mechanisms of fatigue, but in smaller samples, such as a tensile sample, dislocation starvation is also an important mechanism.

[1] Samaeeaghmiyoni, V., et al., *Quantitative in-situ TEM nanotensile testing of single crystal Ni facilitated by a new sample preparation approach.* Micron, 2017. **94**: p. 66-73.

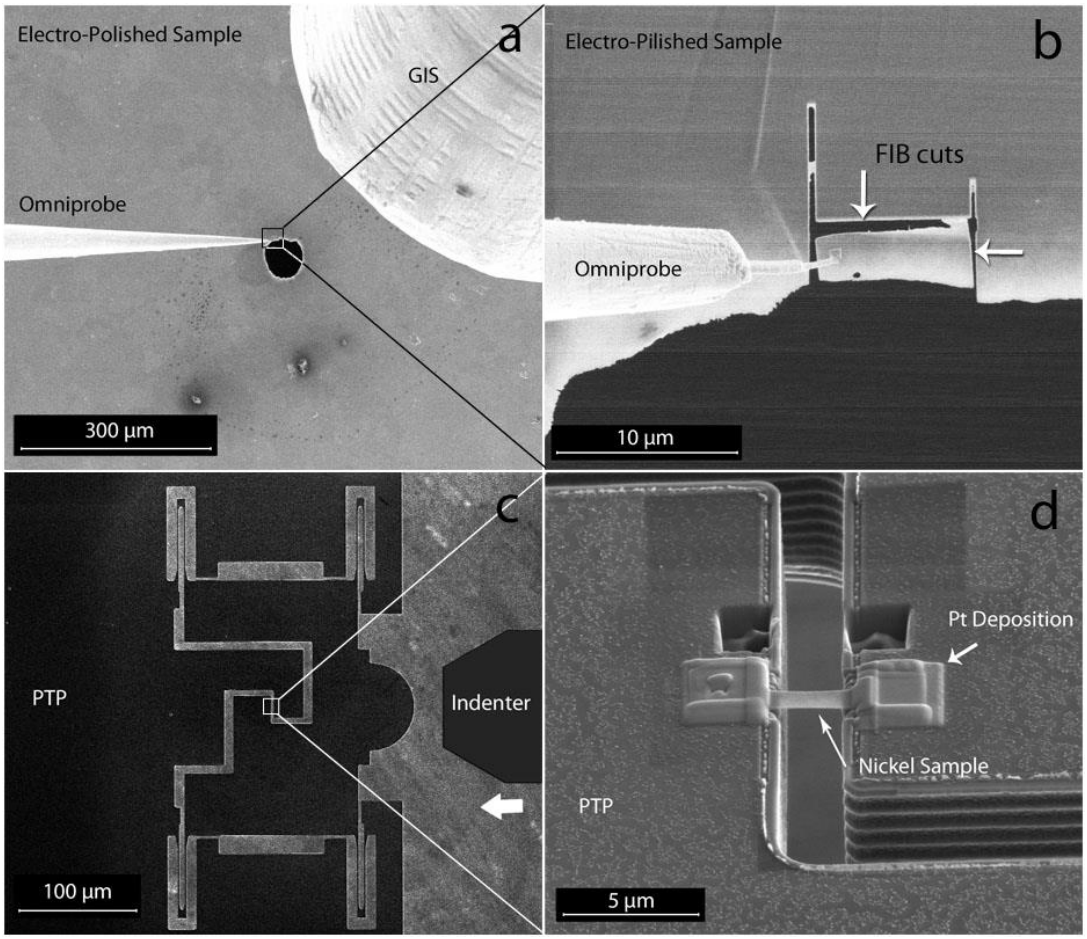

Figure 1. SEM images showing the sequence of sample preparation steps, (a) a low mag. view of the electro-polished foil, (b) FIB cut from the thin edge of the hole, (c) the PTP device, and (d) final configuration of the sample on PTP.

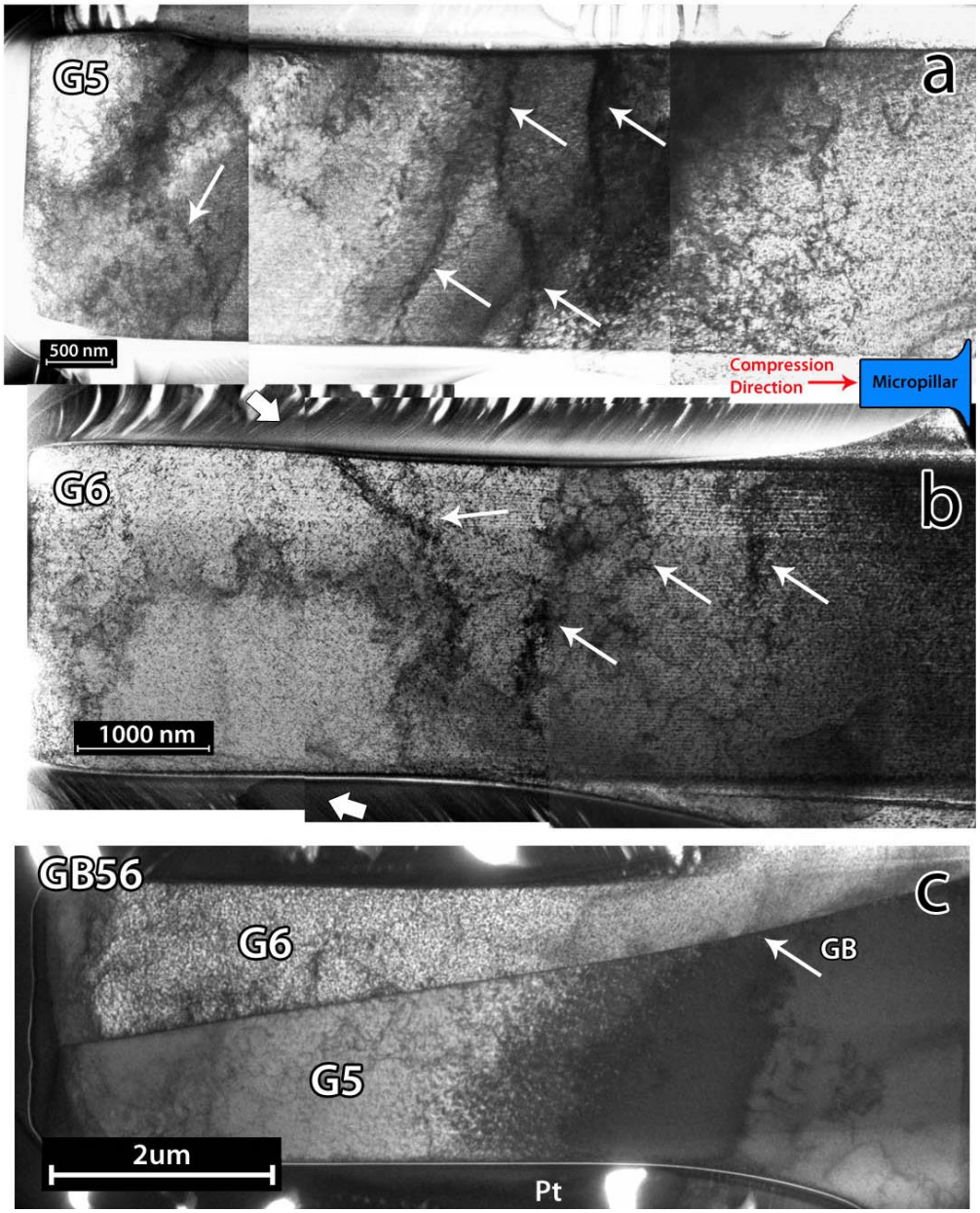

Figure 2. The BF micrographs of 2 single crystal micropillars (a) and (b) and a bi-crystall micropillar (c). The white arrows in (a) and (b) show the dislocation walls in the structure.

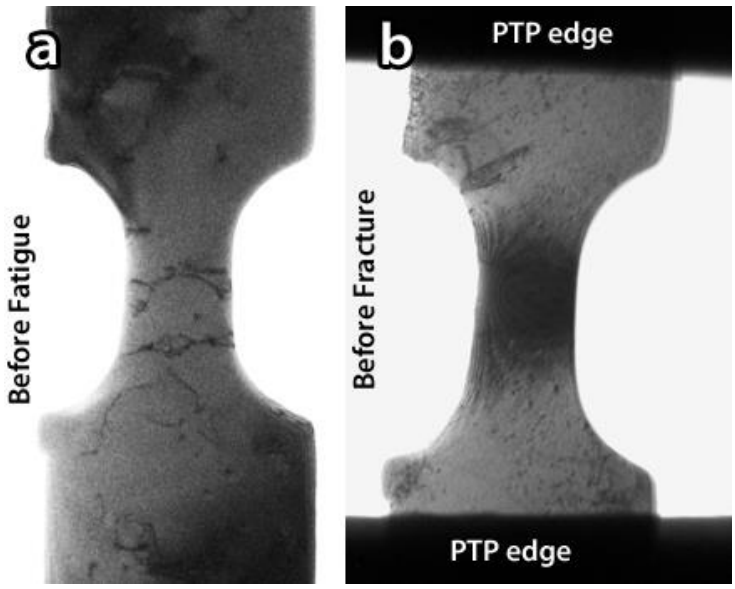

Figure 3. BF images of the tensile sample (a) before fatigue which shows completely FIB defect free sample and (b) before the last cycle of fatigue which shows dislocation free structure.

IM2.008
Time resolved Lorentz-TEM measurements of dynamical skyrmion lattice defects in Cu_2OSeO_3

S. Pöllath[1], J. Wild[1], L. Heinen[2], T. Meier[1], M. Kronseder[1], L. Tutsch[1], A. Bauer[3], H. Berger[4]
C. Pfleiderer[3], J. Zweck[1], A. Rosch[2], C. Back[1]

[1]University of Regensburg, Physics, Regensburg, Germany
[2]University of Cologne, Physics, Köln, Germany
[3]Technical University Munich, Physics, München, Germany
[4]Crystal Growth Facility, Lausanne, Switzerland

simon.poellath@ur.de

Introduction: The particle-like properties of the skyrmion, a new type of topological protected soliton, are believed to lead to major advances in high-density data storage and spintronics devices. The chiral magnet Cu_2OSeO_3 exhibits a skyrmion lattice phase in a finite temperature-, magnetic field range [1, 2]. Using Lorentz Transmission Electron Microscopy (LTEM), this hexagonal lattice can be observed in real space at temperatures below 50K [3].
Objectives: In this work, imperfect skyrmion lattices are studied [5-7]. The structural and dynamic properties of skyrmion lattice defects are evaluated and similarities to hard sphere models of atomic crystals are evidenced.
Materials and Methods: Time resolved non-stroboscopic cryo-LTEM is used to record real-time videos of fluctuating skyrmion domains. The fluctuation is driven by the magnon current originating from the temperature gradient introduced to the system by the electron beam [7]. The mechanically thinned Cu_2OSeO_3 single crystals have an approximate thickness of 100nm. To model the experimental findings classical 2D Monte-Carlo Simulations, as well as particle simulations are performed.
Results: The analysis of the structure and dynamics of domain boundaries and defects in the skyrmion lattice shows that it predominantly uses the so-called 5-7 defect for stress compensation. Furthermore, grain boundaries of differently oriented skyrmion domains are found and consist of 5-7 defects. The defect density along the grain boundary with respect to misorientation angle follows the classical Frank equation. The findings are well described by 2D classical Monte Carlo-, as well as skyrmion particle simulations.
Conclusion: The particle character of individual skyrmions in the hexagonal skyrmion lattice phase of the material Cu_2OSeO_3 is confirmed by the findings. Like atomic lattices the spin lattice shows defects and the defect density along the grain boundary follows a classical formula.

References:
[1] Mühlbauer, S., et al. "Skyrmion lattice in a chiral magnet." *Science* 323.5916 (2009): 915-919.
[2] Yu, X. Z., et al. "Real-space observation of a two-dimensional skyrmion crystal." *Nature* 465.7300 (2010): 901-904.
[3] Seki, Shinichiro, et al. "Observation of skyrmions in a multiferroic material." *Science* 336.6078 (2012): 198-201.
[4] Matsumoto, Takao, et al. "Direct observation of Σ7 domain boundary core structure in magnetic skyrmion lattice." *Science advances* 2.2 (2016): e1501280.
[5] Rajeswari, Jayaraman, et al. "Filming the formation and fluctuation of skyrmion domains by cryo-Lorentz transmission electron microscopy." *Proceedings of the National Academy of Sciences* 112.46 (2015): 14212-14217.
[6] Nagao, Masahiro, et al. "Real space observation of skyrmion polycrystallization and its domain boundary behavior in FeGe1− xSix." *Applied Physics Express* 8.3 (2015): 033001.
[7] Mochizuki, Masahito, et al. "Thermally driven ratchet motion of a skyrmion microcrystal and topological magnon Hall effect." *Nature materials* 13.3 (2014): 241-246.

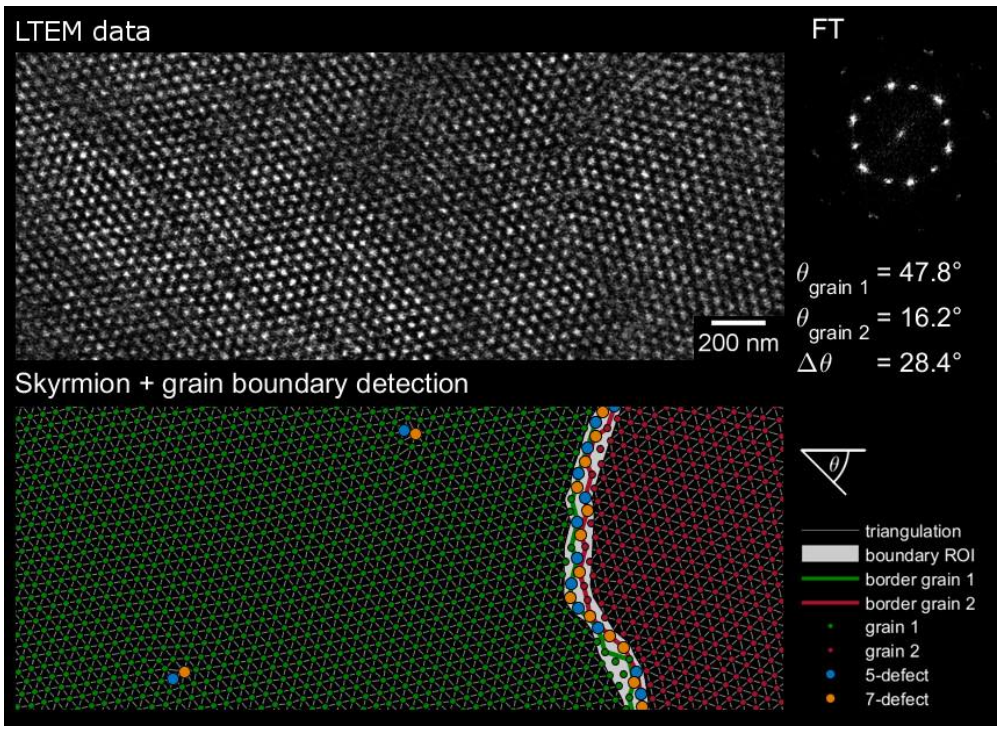

Figure 1. Defects and grain boundaries in the skyrmion lattice. The upper panel shows background subtracted LTEM data. In the Fourier transformation (FT) the presence of two skyrmion domains is evident. The lower panel shows the evaluated image showing two grains, a grain boundary and single 5-7 defects.

IM2.009
Self-arrangement of latex particles in water studied in 3D using STEM-in-SEM

J. Xiao[1], L. Roiban[1], G. Foray[1], S. Descartes[2], K. Masenelli-Varlot[1]

[1]Université de Lyon, INSA-Lyon, MATEIS, Villeurbanne, France
[2]Université de Lyon, INSA-Lyon, LaMCoS, Villeurbanne, France

karine.masenelli-varlot@insa-lyon.fr

The analysis of liquid suspensions has recently been pushed forward thanks to two major developments. On the one hand, specific sample holders can be used in transmission electron microscopes (TEM) operating under vacuum and have been used to study nanoparticle motion, growth and electrochemical processes at the nanoscale [1]. On the other hand, in dedicated environmental electron microscopes, a certain partial pressure of gas can be introduced around the sample. Environmental scanning electron microscopy has proven to be an efficient method to study liquids when observing the sample in transmission (STEM-in-SEM mode) under specific conditions of gas partial pressure and sample temperature [2]. Moreover, 3D characterizations can be made possible using a rotating STEM-in-SEM stage [3]. However, one can wonder whether the results obtained are representative of the suspension, as the particles in liquid might be affected by both the presence of the supporting membrane and the surface tension at the liquid surface.
In this work, we will present results obtained on SBA-PMMA (copolymer derived from styrene and metacrylic acid esters) latex particles in aqueous solution. These particles exist only in suspension in water. Upon evaporation, the particle form a compact arrangement and then form a homogeneous film [4]. The suspensions are characterized in 3D using a home-made device fitting in a FEI XL30-FEG Environmental Scanning Electron Microscope working in transmission (STEM-in-STEM mode). Observations are also performed in cryo-SEM using a FEI Quanta FEG 250 equipped with a cryo-transfert system Alto 2500 from Gatan.
We will first show series of tilted images that are acquired on solutions. Reconstructed volumes are obtained using the image processing softwares *etomo* and *Fiji* (see Figure 1) and the resolution is calculated using Fourier Shell Correlation (FSC). The influence of irradiation damage on the reconstructed volumes is discussed. The particle arrangement, including the lattice type and grain size, will then be compared with the results from cryo-SEM (see Figure 2).

References:
[1] Ross, F. (Ed.) Liquid cell electron microscopy (advances in microscopy and microanalysis) Cambridge University Press (2016)
[2] Bogner, A., Ultramicroscopy 104, 290-301 (2005)
[3] Masenelli-Varlot, K., Malchère, A. Microscopy and Microanalysis, 20, 366-375(2014)
[4] Chevalier, Y., Colloid & Polymer Science 27, 806-821 (1992)
[5] The authors acknowledge the Consortium Lyon Saint-Etienne de Microscopie (CLYM) and the Centre Technologique des Microstructures (CTμ) for the access to the electron microscopes.

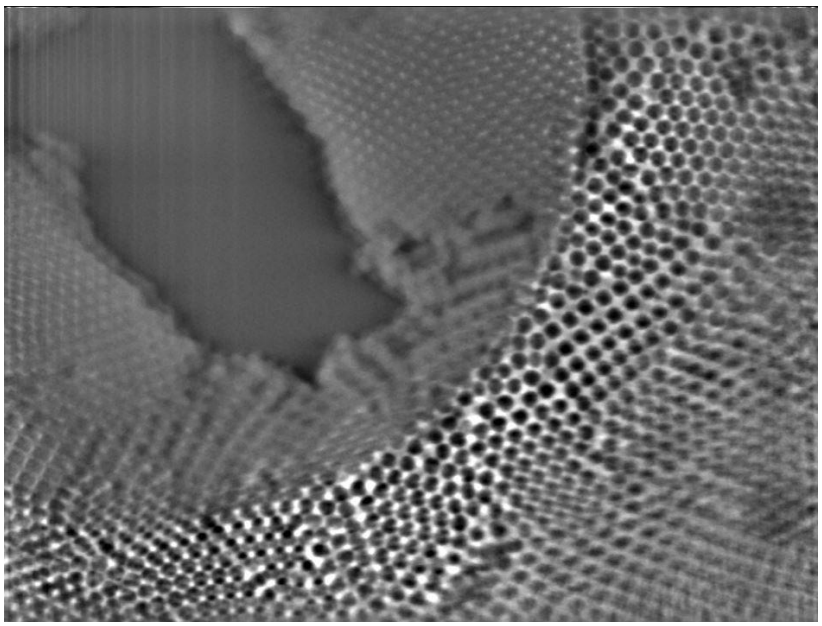

Figure 1. XY slice of the reconstructed volume of a suspension of latex particles in water, obtained by STEM-in-SEM.

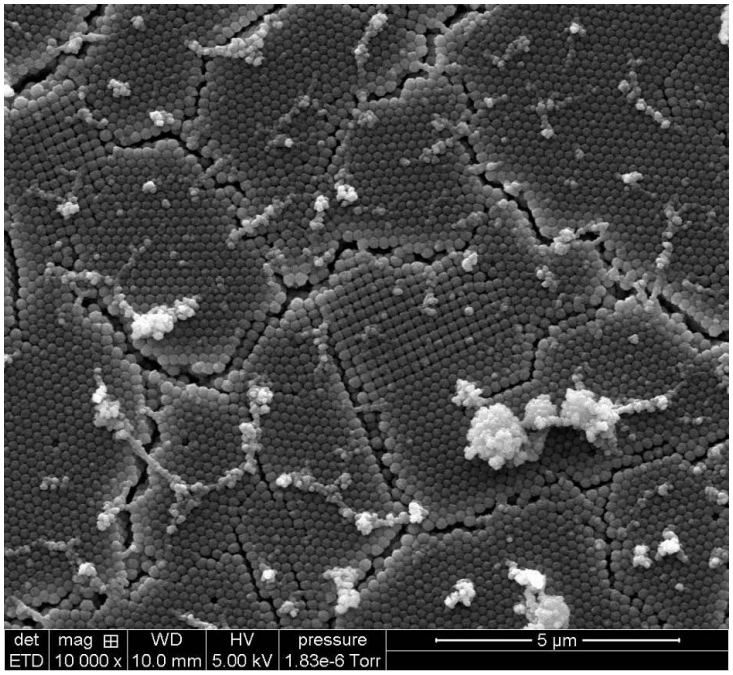

Figure 2. Secondary electron image of a frozen suspension of latex particles in water, obtained by cryo-SEM.

IM2.010
Time-resolved nanoscale mapping of strain tensor fields in ultrafast transmission electron microscopy

A. Feist[1], N. Rubiano da Silva[1], W. Liang[2], C. Ropers[1], S. Schäfer[1]

[1]University of Göttingen, 4th Physical Institute, Göttingen, Germany
[2]Huazhong University of Science and Technology, Wuhan National Laboratory for Optoelectronics, Wuhan, China

sschaef5@gwdg.de

Introduction: Time-resolved diffraction techniques using ultrashort electron pulses [1] yield precise and quantitative information on the average ultrafast atomic re-arrangement in photoexcited homogenous crystalline samples. Despite substantial progress in the field of ultrafast transmission electron microscopy (UTEM) [2-7], localized ultrafast processes governed by nanoscale inhomogeneities, such as phase boundaries, interfaces, surfaces, and defects, remain particularly difficult to address.
Objectives: Here, we demonstrate the quantitative spatio-temporal mapping of ultrafast nanoscale structural dynamics at the edge of a single-crystalline graphite membrane (Fig. 1a) [8].
Materials and Methods: We employ sub-picosecond electron pulses focused to 20-30 nm diameters in the Göttingen UTEM instrument [5,9], to stroboscopically record transient large-angle convergent beam electron diffraction (CBED) pattern for varying probing positions relative to the edge of a graphite membrane.
Results: After optical excitation of the graphite membrane, we observe pronounced angular shifts of multiple Bragg lines (Fig. 1b-d), with a picosecond temporal behavior depending on the Bragg line index and the electron probing position. Exemplary delay-dependent Bragg line profiles corresponding to <4-22> lattice planes are shown in Fig. 1b,c, recorded at a probing distance of 500 nm relative to the membrane edge (Fig. 1c), as well as far away from the edge (Fig. 1b). Considering the shift in multiple Bragg lines, we reconstruct the temporal evolution of the dominant components of the local strain tensor (Fig. 1e,f) at the electron probing position. Far away from the membrane edge, we find the optically triggered structural distortion to be dominated by a high-amplitude acoustic membrane breathing mode (1e,f, red curve). However, close to the membrane edge, the Bragg line profiles display a more complex, multi-frequency behavior (Fig. 1c). The extracted strain tensor components (Fig. 1e,f, black curves, extracted from average line shift) reveal the generation of an additional coherent acoustic shear mode, which is launched by an in-plane shock wave originating from the sample edge. The resulting inhomogeneous strain distribution within the film thickness causes a substantial reshaping of the Bragg line profiles, as visible in Fig. 1c. Finally, ultrafast CBED traces acquired at varying sample positions allow us to track the ballistic propagation and dephasing of the optically induced phonon modes with nanoscale spatial resolution, yielding a comprehensive picture of the optically induced acoustic phonon dynamics.
Conclusion: More generally, we believe that the quantitative experimental access to the local structural distortions demonstrated here offers new opportunities to develop tailored nanophononic fields, which may be utilized in advanced phonon blocking devices or for achieving phonon-controlled phase transitions.

References:
[1] R. J. D. Miller, *Science* **343**, 1108 (2014).
[2] A. H. Zewail, Science **328**, 187 (2010)
[3] L. Piazza, D. J. Masiel, T. LaGrange, B. W. Reed, B. Barwick, F. Carbone, *Chem. Phys.***423**, 79 (2013).
[4] K. Bücker, M. Picher, O. Crégut, T. LaGrange, B. W. Reed, S. T. Park, D. J. Masiel, and F. Banhart, *Ultramicroscopy***171**, 8 (2016).
[5] A. Feist, N. Bach, N. R. da Silva, T. Danz, M. Möller, K. E. Priebe, T. Domröse, J. G. Gatzmann, S. Rost, J. Schauss, S. Strauch, R. Bormann, M. Sivis, S. Schäfer, C. Ropers, *Ultramicroscopy*, advanced online (2016).
[6] A. Yurtsever and A. H. Zewail, *Proc. Natl. Acad. Sci.***108**, 3152 (2011).
[7] D. R. Cremons, D. A. Plemmons, and D. J. Flannigan, *Nat. Commun.* **7**, 11230 (2016).
[8] A. Feist, N. Rubiano da Silva, W. Liang, C. Ropers, S. Schäfer, in preparation.
[9] A. Feist, K. E. Echternkamp, J. Schauss, S. V. Yalunin, S. Schäfer, C. Ropers., *Nature* **521**, 200 (2015).

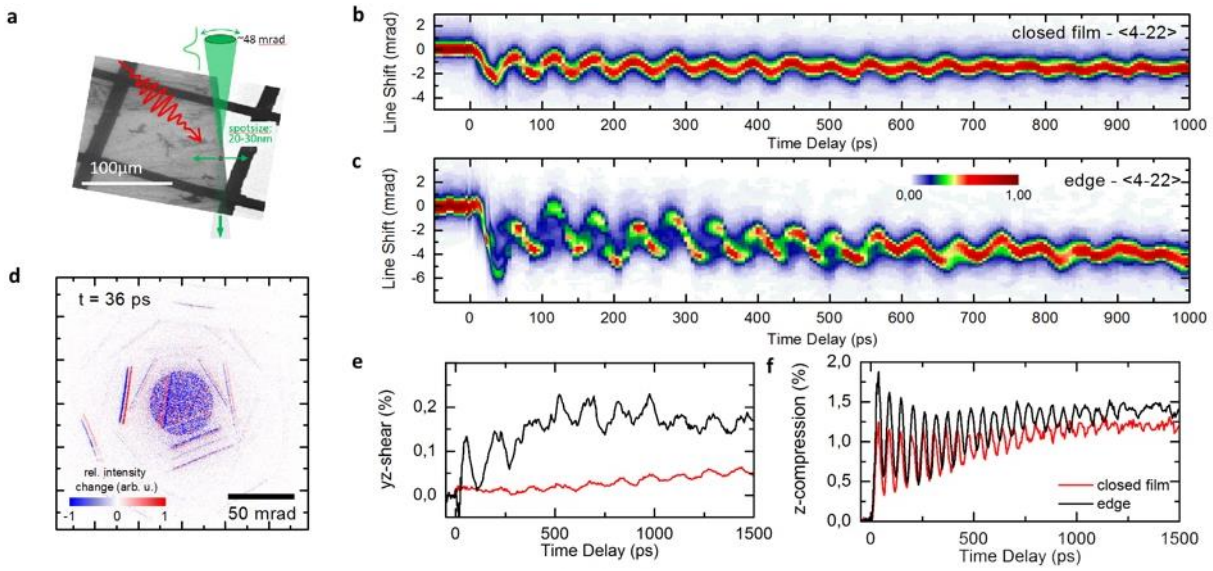

Figure 1. (a) Ultrafast CBED with 30-nm spatial resolution recorded at the edge of a single-crystalline graphite membrane. (b,c) Delay-dependent change in the <4-22> Bragg line profile probed far away from the membrane edge (b) and at a distance of 500 nm from the edge (c). (e,f) Reconstructed local strain components for the probing positions employed in (b,c).

IM2.011
In situ electron microscopy – insights in solid state dewetting of epitaxial Al thin films on sapphire

S. Hieke[1], M. G. Willinger[2], Z. J. Wang[2], G. Richter[3], G. Dehm[4], C. Scheu[1]

[1]Max-Planck-Institut für Eisenforschung GmbH, Nanoanalytics and Interfaces, Düsseldorf, Germany
[2]Fritz-Haber-Institut der Max-Planck-Gesellschaft, Berlin, Germany
[3]Max-Planck-Institut für Intelligente Systeme, Stuttgart, Germany
[4]Max-Planck-Institut für Eisenforschung GmbH, Structure and Nano-/ Micromechanics of Materials, Düsseldorf, Germany

s.hieke@mpie.de

Solid state dewetting is a topic of current research [1]. Besides its benefits for targeted patterning, solid state dewetting may cause degradation or failure of thin film devices. Thermal induced hole or hillock formation of Al based interconnections on Si was reported decades ago [2]. An in-situ observation of aluminium void formation by optical microscopy has been carried out by Sugano et al. [3]. We performed in-situ annealing using an environmental scanning electron microscope (ESEM) to investigate the void formation mechanism in detail.
Molecular beam epitaxy was used to deposit a defined model system of Al thin films on single crystalline (0001) sapphire (α-Al_2O_3). The microstructure and epitaxial orientation relationships of the as-deposited and the annealed Al films were analysed by SEM and transmission electron microscopy (TEM) methods including electron backscatter diffraction (EBSD) and C_s-corrected atomic column resolved scanning TEM (STEM). The as-deposited Al films form a mazed bicrystalline microstructure consisting of the two twin-related growth variants exhibiting the following orientation relationship: {111} Al || (0001) α-Al_2O_3 with ±<-110> Al || <10-10> α-Al_2O_3 (OR a/b). A high angle annular dark field (HAADF) STEM image of a Σ3 twin boundary is presented in Fig. 1.
Annealing in oxidizing (O_2, ~30 Pa) atmosphere at temperatures up to 550°C lead to the formation and growth of faceted voids which was observed in-situ by SEM (Fig. 1). In addition to the growth of existing voids to a certain size, new voids are forming. Complementary experiments in reducing atmosphere (67% H_2/33% N_2, ~50 Pa) showed no void formation.
Post mortem EBSD analysis showed no change in (111) texture (Fig. 2). Site-specific cross-sections prepared by focused ion beam (FIB) sectioning confirmed the expected presence of drum-like voids in the Al film covered by a thin oxide layer (Fig. 3). The native oxide in the as-deposited films suppresses Al surface diffusion, thus it is assumed that interface and grain boundary diffusion dominate [4] in contrast to the classical solid state dewetting model [1, 4, 5]. The void formation can be described by film retraction [6] below the surface scale. Further in-situ SEM annealing experiments are planned to investigate the dewetting phenomena in more detail.

Keywords
Thin films; metal-ceramic interface; solid state dewetting; in-situ SEM; microstructural evolution

References:
[1] C. V. Thompson, *Annu. Rev. Mater. Res.* **2012**, *42*, 399-434.
[2] N. Kristensen, F. Ericson, J.-Å. Schweitz, U. Smith, *Thin Solid Films* **1991**, *197*, 67-83.
[3] Y. Sugano, S. Minegishi, H. Sumi, M. Itabashi, *26th Annu. P. Rel. Phys. Sym. 1988*, **1988**, 34-38.
[4] D. Amram, L. Klinger, N. Gazit, H. Gluska, E. Rabkin, *Acta Mater.* **2014**, *69*, 386-396.
[5] W. Kaplan, D. Chatain, P. Wynblatt, W. C. Carter, *J. Mater. Sci.* **2013**, *48*, 5681-5717.
[6] S. Dutta, J. M. Biser, R. P. Vinci, H. M. Chan, *J. Am. Ceram. Soc.* **2012**, *95*, 823-830.

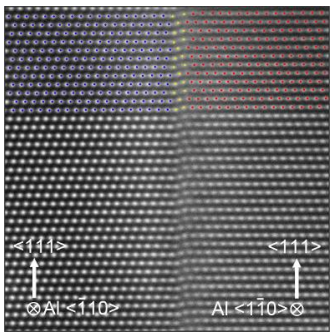

Figure 1. C_s-corrected HAADF STEM micrograph of an exemplary Σ3 Al twin boundary of the as-deposited films.

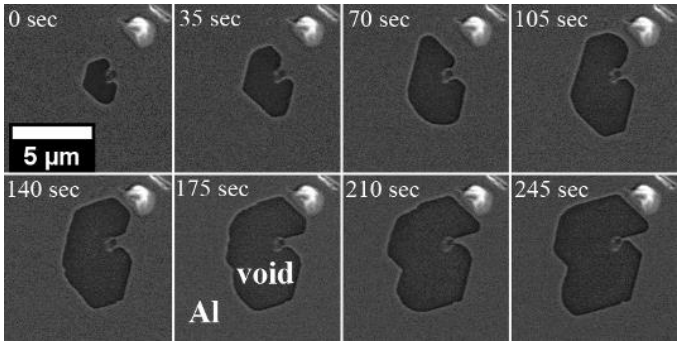

Figure 2. Void growth with time observed in-situ at ~500 – 550°C in O_2 atmosphere by plan-view SEM micrographs.

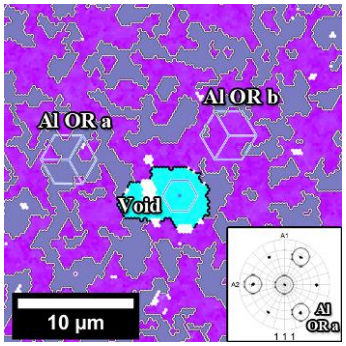

Figure 3. Post annealing EBSD orientation map showing the mazed microstructure of both Al twin variants (OR a in grey, OR b in purple, twin boundaries in white, white area not indexed) surrounding a faceted void (bright blue). The normal grain orientation is indicated by the cube overlays (inlet: {111} pole figure).

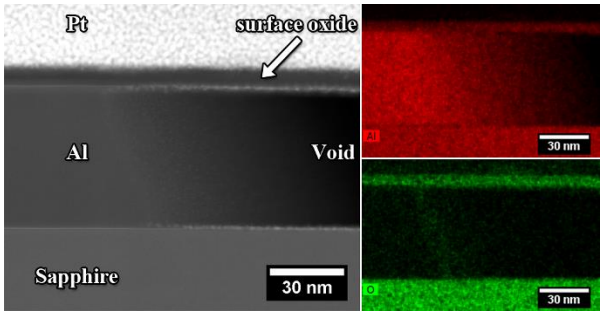

Figure 4. Cross sectional STEM HAADF micrograph showing the void/remaining Al film/sapphire substrate triple phase boundary after annealing and void formation (prepared by FIB). The still existing surface oxide layer covering the void and the film is clearly visible in the EDS maps of Al and O.

IM2.012 invited
Multi-scale observation of catalyst dynamics under reactive conditions

M. G. Willinger[1,2,3], R. Farra[1], J. Cao[1], Z. J. Wang[1], A. Rinaldi[1], E. Willinger[2], X. Huang[2], M. Greiner[2]
R. Schlögl[1,2]

[1]Fritz-Haber-Institut der Max-Planck-Gesellschaft, Anorganische Chemie, Berlin, Germany
[2]MPI für Chemische Energiekonversion, Heterogene Reaktionen, Mülheim an der Ruhr, Germany
[3]MPI für Kolloid- und Grenzflächenforschung, Kolloidchemie, Potsdam, Germany

willinger@fhi-berlin.mpg.de

Electron microscopy plays an important role in the characterization of catalysts and their precursors. Atomically resolved images of catalyst particles serve as Reference: for theoretical modelling and have influenced the way in which we depict active sites. However, since high-resolution imaging and local compositional analysis is generally performed under vacuum and close to room temperature, the obtained atomistic details concern an equilibrium state that is of limited relevance if the active state of a catalyst is in the focus of the investigation. Indeed, heterogeneous catalytic reactions are highly non-linear chemical processes that are operated far from thermodynamic equilibrium. *In situ* electron microscopy has clearly demonstrated that the interaction with the gas phase induces changes of shape, composition and chemical dynamics [1,2].
Structural dynamics of catalysts are strongly depending on the chemical potential of the gas phase. Specific processes require a certain chemical potential in order to be initiated. Slowing down the reaction rate and observation under quasi-equilibrium conditions does not reveal the full complexity of hierarchical multi-scale processes involving collective phenomena such as mass- and heat transport. Our aim is thus to investigate catalysts in their active state, under conditions in which catalytic conversion can be detected.
We use environmental scanning electron microscopy (ESEM) for the investigation of larger-scale dynamics on surfaces [3] and commercially available gas-flow holders for *in situ* experiments on nanostructured catalyst particles in a commercial TEM. Both setups are equipped with home-built gas-feeding stations and mass spectrometers (MS) for analysis of the gas-phase composition and detection of catalytic conversion.
By combining *in situ* SEM and TEM, we are able to cover a pressure range from 10^{-4} to 10^{3} mbar and a spatial resolution ranging from the mm to the sub-nm scale. The multi-scale approach allows us to embed local processes that occur on the nanometre scale in a larger picture, in with collective processes, which involve fast movement of large numbers of atoms, play a role.
We will present structural dynamics that are observed during oscillatory red-ox reactions on nickel, copper and platinum catalysts (such as Figures 1, 2 and 3). It will be shown that the ability of observing the adaption of an active surface to changes in the chemical potential of the surrounding gas phase in real-time potentially offers new and direct ways of optimizing catalysts and applied reaction conditions. Under relevant catalytic conditions, the observed metals show rich structural dynamics, oscillatory phase changes, catalyst sintering and splitting. Factors affecting shape, faceting and size of particles will be discussed. The ability to directly image the active catalyst and associated morphological changes at high spatial resolution enables us to refine the interpretation of spatially averaged spectroscopic data that was obtained under otherwise similar reaction conditions, for example, during near-ambient-pressure *in situ* XPS measurements [4].

References:
[1] P. L. Hansen et al., Science **295** (2002), p. 2053
[2] S. B. Vendelbo et al., Nature Materials **13** (2014), p. 884
[3] Z.-J. Wang et al., Nature Communications **7** (2016), Article number: 13256
[4] M. T. Greiner et al., Phys.Chem.Chem.Phys. **17**, (2015), p. 25073

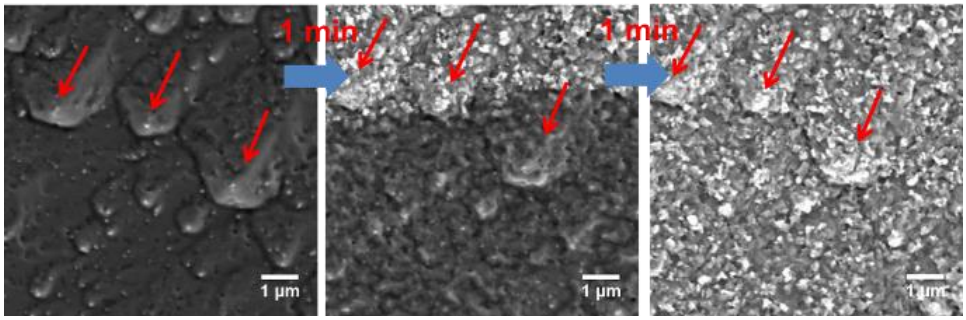

Figure 1. In situ ESEM observations of thermo-kinetic oscillations during hydrogen oxidation on a Ni foil. The surface shows rich dynamics and periodic changes from an oxide (bright) to a metallic state (dark).

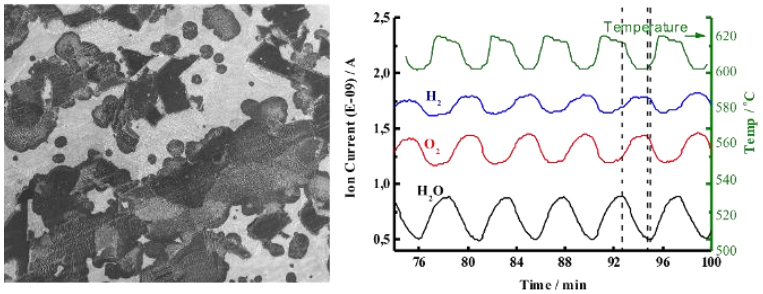

Figure 2. Overview image recorded during in situ observation of redox dynamics of Ni. Changes in contrast due to oxidation and reduction of the Ni are correlated to changes in activity detected in the MS.

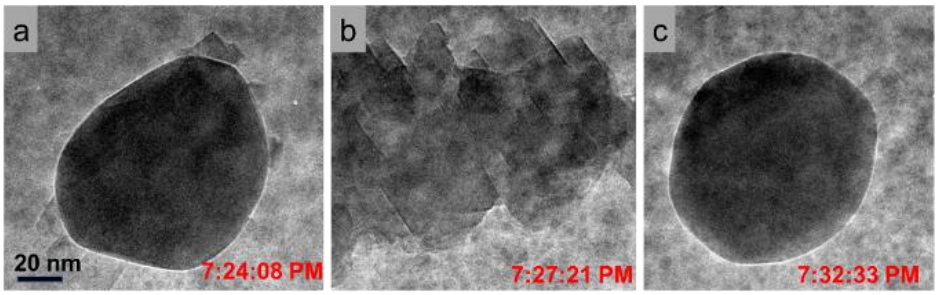

Figure 3. Corresponding in situ TEM observations showing a Ni particle oscillating between metallic (a and c) and oxide state (b) during hydrogen oxidation at 700 °C.

IM2.013
Studying the dynamics of atomic clustering in 3D by HAADF-STEM

T. Henninen[1], R. Erni[1], M. D. Rossell[1]

[1]Empa, Electron Microscopy Center, Dübendorf, Switzerland

trond.henninen@empa.ch

The formation of solid matter is typically modelled by classical nucleation theory. This model assumes the solid forms a spherical nucleus. However, during the initial phase at sub-nm, non-spherical atomic clusters form with atomic structures deviating from the stable bulk crystal. Thus understanding the dynamics of this regime requires considering individual atoms. Understanding and control of this initial cluster formation, enables improved control of nanomaterial fabrication and potentially the creation of new materials. The aim of this work is to study the atomic dynamics of cluster formation, from single atoms of Pt combining to form clusters sized ~1 nm.

Aberration corrected scanning transmission electron microscopy (STEM) has the spatial resolution required to directly image this system. However, STEM images are 2D projections, and 3D reconstruction must be done to recover the 3D geometry of the clusters. Using high-angle annular dark field STEM (HAADF-STEM) imaging, the contrast is proportional to the atomic number $Z^{\sim 1.7}$, making even single atoms of Pt (Z=78) distinctly visible compared to the nearly invisible C (Z=6) of the support film. Further, the contrast is linearly proportional to the number of atoms stacked in a column (up to >10 atoms). This enables 3D reconstruction of these clusters through atom counting. The atomic dynamics of the clusters are affected by the e-beam, as have been studied for clusters of Ge and Si [1,2]. However, to study cluster formation in-situ, the effect of the e-beam should be minimized. By using a heating stage, we evaluate the effect of the e-beam on the clusters, and have thermal effects dominating the system.

Samples were made by plasma sputtering (Leica ACE200) Pt onto Protochips Fusion thermal chips. The chips were homogeneously covered by single atoms of Pt and small clusters up to ca 2 nm. HAADF-STEM was done using a probe corrected FEI Titan Themis at 300 and 80 kV. Heating experiments were performed using a Protochips Fusion heating holder, from room temperature up to 500°C. Image series were recorded at 512x512, 50 fps, or 256x256, 100 fps. 3D reconstruction was done by atom counting, using Matlab code based on StatSTEM [3].

Preliminary data shows the clusters at room temperature appeared amorphous below 2 nm in size, while quasi-molten crystalline above 2 nm. The amorphous clusters disassociated to single atoms over minutes due to the high energy e-beam, while the crystalline particles were more resistive, enduring imaging for more than an hour. Heating promotes crystallinity and clustering. At above 300°C single atoms were observed to combine, forming metastable (for minutes) amorphous clusters ranging from less than 10 atoms up to ~1 nm (ca 50 atoms). 1 nm clusters were also observed to turn quasi-molten at 350°C, with crystalline structures distinctly changing in every few 10s of frames. In contrast, amorphous clusters showed significant changes in structure for every frame. Atomic scale Ostwald ripening was observed when clusters came into contact, but also due to individual atoms crossing a gap between particles of up to a few nanometers (fig 1a). 3D reconstruction of particles and clusters showed that clusters form a flatter structure than the more spherical crystalline particles (fig. 2).

To conclude, HAADF-STEM was used to study atomic dynamics of Pt atoms and clusters. When heated, atoms were observed to form amorphous clusters sized up to 1 nm. At 350°C, 1 nm clusters were observed to become quasi-molten. Ostwald ripening was observed by single atoms moving between clusters.

References:
[1] S. Bals, et al., Nat. Commun. 3:897, (2012)
[2] J. Lee, et al., Nat. Commun. 4:1650, (2013)
[3] A. De Backer et al., Ultramicroscopy 171, (2016)

We acknowledge funding from the European Research Council (ERC) under EU"s Horizon 2020 program (grant agreement No. 681312).

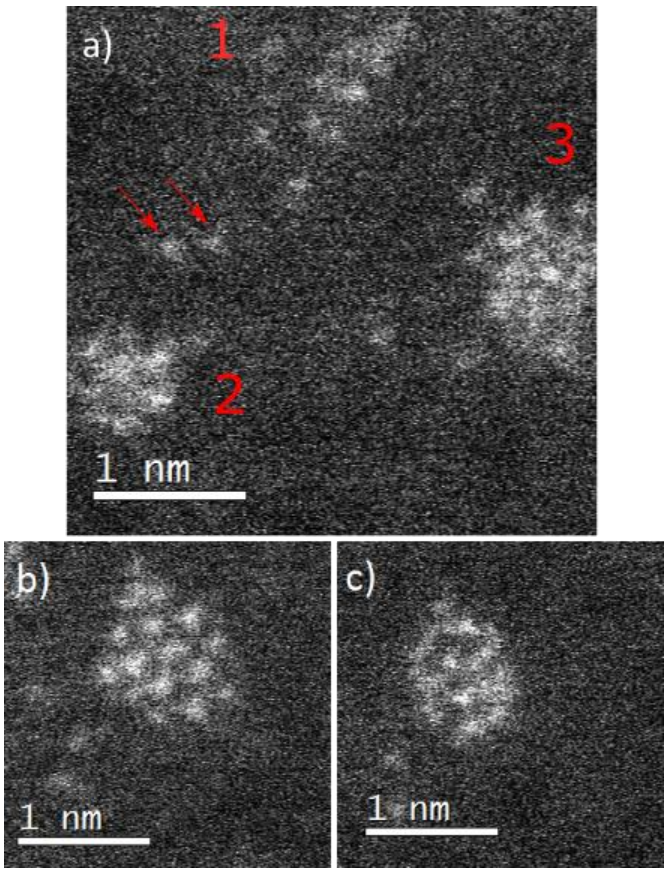

Figure 1. a) Three clusters at 350°C. Marked atoms were moving from cluster 1 to 2. b) Crystalline structure of cluster 3. c) Structure of cluster 3 2.36 s later.

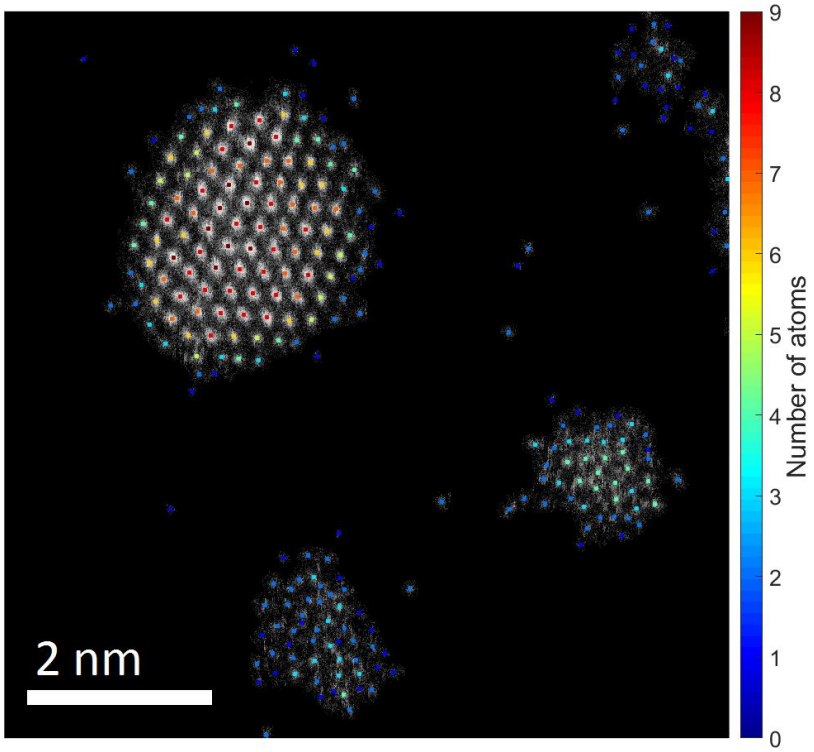

Figure 2. 3D reconstruction of atomic columns from 1 to 9 atoms, overlaid a noise-filtered HAADF-STEM image of a nanoparticle and three clusters.

IM2.014
Hydride precipitates in zirconium alloys – dissolution and precipitation by in situ TEM thermal cycling correlated to global approach investigations

E. Conforto[1], X. Feaugas[1]

[1]University of La Rochelle, LaSIE UMR 7356 CNRS-ULR, La Rochelle, France

egle.conforto@univ-lr.fr

Introduction: The fast and spontaneous hydrogen diffusion in zirconium alloys used in the nuclear industry leads to the hydride precipitation which is often pointed as causing embrittlement and rupture. The crystallographic coherence between HCP substrates (as Zr, Ti and their alloys) and hydride precipitates is fairly high. In previous works, TEM analyses allowed the identification of four particular epitaxial orientation relationships (OR) [1-5] between the HCP substrate and both the FCT γ-ZrH, and the FCC δ-$ZrH_{1.66}$ hydrides. Thermodynamic parameters play a crucial role in the dissolution/precipitation mechanism and on the thermal stability of hydride phases in Zr alloys. The activation energy, the entropy and enthalpy have been measured for these processes in different Zr alloys [4-7] at a global approach (over a large density of hydrides). However, only few data are available at a local approach (over a single hydride precipitate) to explain the energies values and the mechanism acting close to the hydride/substrate interface during hydride dissolution and reprecipitation. Moreover, no information is available on the OR stability after many dissolution/reprecipitation cycles.
Objectives: To compare energies values obtained at global and local approaches correlated to misfit dislocations and microstructure evolutions as ORs after many *in-situ* dissolution / reprecipitation cycles.
Materials and Methods: Small tubes of Zircalloy-4 (here after labeled "Zr-4") were charged with 112 wppm and 356 wppm in hydrogen. TEM analyses were performed with a JEOL JEM 2011 microscope at 200 kV using a GATAN double-tilt heating holder for i*n-situ* cycling.
Results: Figure 1 shows the in-situ dissolution of a γ-hydride precipitate in Zr-4 containing 112 wppm in H which takes place in a temperature range comparable to that indicated in the Heating rate vs T curve at global approach by Differential Scanning Calorimetry (DSC). Figure 2 shows the same type of precipitate before (at left) and after (at right) dissolution, where a misfit dislocation depinning is observed. It drives H atoms far from the precipitation region, and they are no more available to re-precipitate. Figure 3 shows a γ-hydride in OR1 with the Zr-4 substrate, which was submitted to 2 thermal cycles between 300 and 680 K. During the first cycle the dissolution is partial, and the γ-hydride reprecipitates close to the initial OR1, but slightly misoriented. During the second cycle (not shown) the hydride dissolution is almost complete. The main part of H atoms migrate towards a grain boundary at right in the image, and reprecipitate incoherently. Similar results were obtained for δ-$ZrH_{1.66}$ precipitates in Zr-4 samples containing 356 wppm in H.
Conclusions: Hydrides dissolution temperature observed in local approach is in good agreement with that observed in global approach. Hydride re-precipitation is possible only if H atoms are not driven away during heating by misfit dislocations depinning. A hydride initially in an OR reprecipitates close to the primitive orientation. The memory of its previous OR includes also crystalline defaults, which are probably responsible for memory effects.

[1] Numakura H, Koiwa M (1983) *Acta Metall* 32: 1799-1807
[2] Conforto E, Caillard D (2007) *Acta Materialia* 55: 785–798
[3] Feaugas X, Conforto E (2009) *PlastOx 2007* (EDP Sciences):161-178
[4] Conforto E, Feaugas X (2015) *Proceedings PTM2015*:231-238
[5] Conforto E et al. (2017) *Mat Sci Forum* 879 :2330-2335
[6] Fukai Y, The metal-hydrogen system: basic bulk properties. New York: Springer; 2005
[7] Vizcaino P, Rios RO, Banchik AD (2005) *Thermochimica Acta* 429:7-11

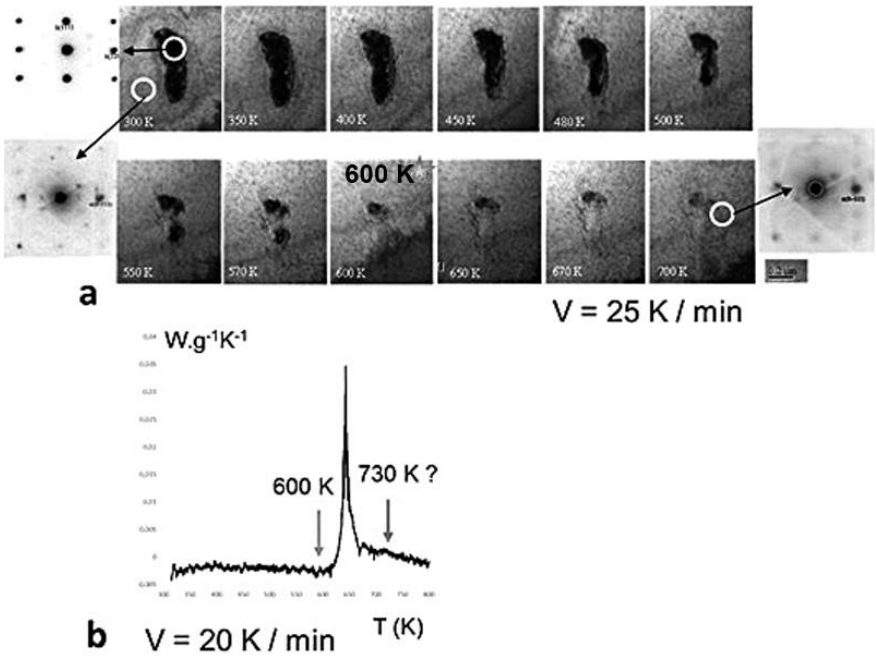

Figure 1. In-situ TEM dissolution of a γ-hydride precipitate in Zr-4 compared to the temperature range indicated in the heating rate vs T curve by DSC (global approach).

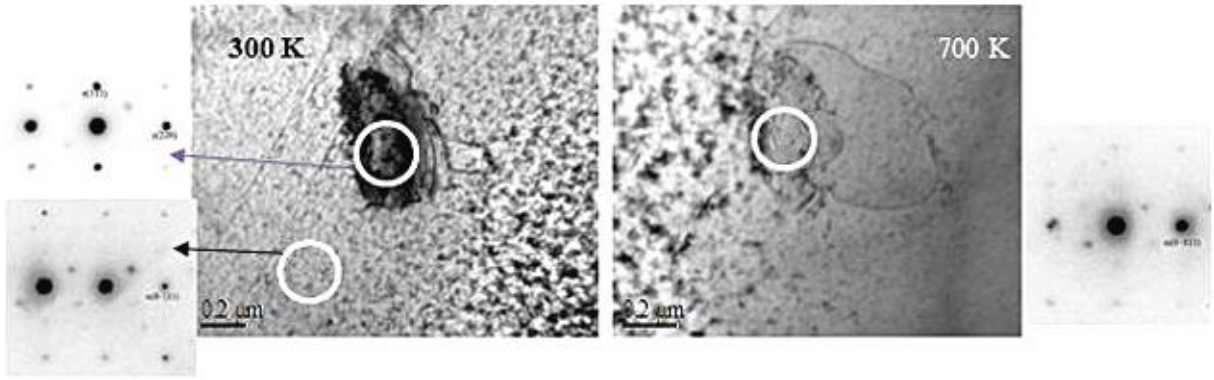

Figure 2. A γ-hydride precipitate before (at left) and after (at right) in-situ dissolution, in which a misfit dislocation depinning is shown.

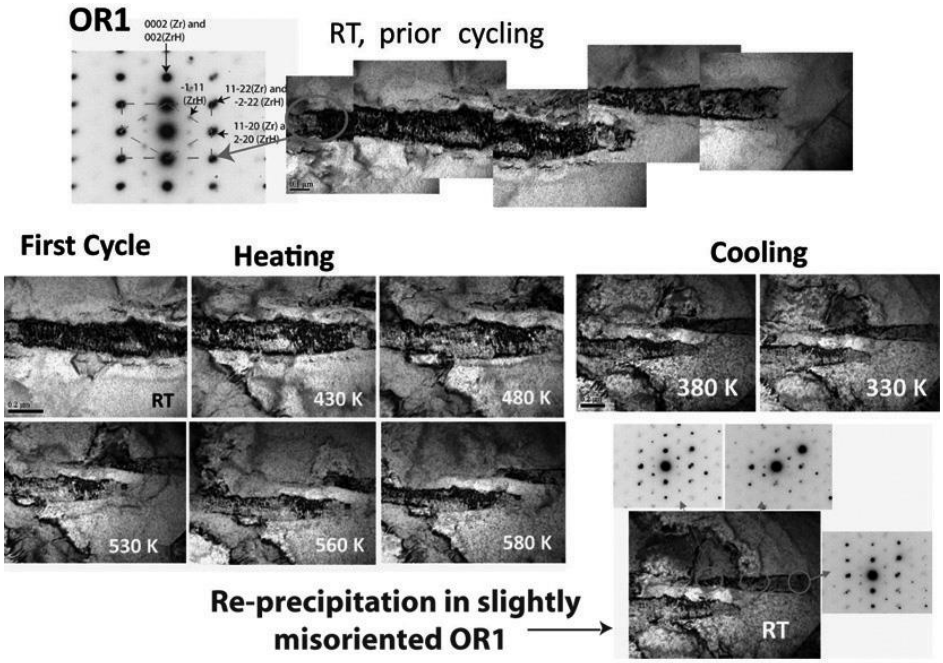

Figure 3. First thermal cycle in the 300 – 580 K temperature range. The γ-hydride precipitate, initially in OR1, reprecipitates with a slight misorientation.

IM2.P001
In situ studies of high-purity mono- and bimetallic nanostructures in experiment and simulation

D. Knez[1,2], M. Schnedlitz[3], M. Lasserus[3], G. Kothleitner[1,2], A. Hauser[3], W. Ernst[3], F. Hofer[1,2]

[1]Graz University of Technology, Institute for Electron Microscopy and Nanoanalysis, Graz, Austria
[2]Graz Centre for Electron Microscopy, Graz, Austria
[3]Graz University of Technology, Institute of Experimental Physics, Graz, Austria

daniel.knez@felmi-zfe.at

Metallic nanostructures have attracted more and more interest in recent years as they exhibit completely new physical and chemical properties compared to bulk materials. This is especially true for low-dimensional structures whose sizes approach only a few nanometres in at least one dimension, such as thin nanowires or clusters [1]. For the application of such structures, knowledge about their thermodynamic properties and thermal stability is of paramount importance. To this end, we performed in situ heating experiments using metallic nanowires and bimetallic clusters using aberration corrected scanning transmission electron microscopy (STEM).

The nanoparticles used for our investigations were synthesized within superfluid helium nanodroplets (composed of 10^3 to 10^{10} helium atoms) at around 0.4 K, under ultra-high vacuum (UHV) conditions [2]. This approach provides exceptional advantages over conventional methods, like sequential addition of a wide range of materials without the use of ligands and stabilizers. Thus, nanoparticles can be synthesized with any composition and different structures, with extremely high purity, which cannot be achieved by other known methods [3].

For in situ heating experiments, we used a DENSsolutions Wildfire D6 holder in a probe corrected FEI Titan^3 60-300 microscope. This microscope is equipped with a Super-X detector (EDX) and a Gatan Quantum energy filter for EELS.

Nanowires with diameters of less than 10 nm and a length of 100-200 nm were placed on a heating chip backed with a 5 nm amorphous carbon film. The wires were comprised of either Au, Ag, Ni or Cu. In all cases we observed Rayleigh-breakup as a consequence of surface diffusion processes. The degradation of the nanowires was analysed over time and temperature via STEM high angle annular dark field (HAADF) image series. We compared the results from these heating experiments with simulations based on cellular automata. Figure 1a shows an Au nanowire in its initial state and after breakup at 300°C, with corresponding simulation results. The regions where the wire starts to segregate are predicted correctly (red circles).

In similar experiments, we investigated the alloying of carbon supported Ni-Au core-shell clusters at elevated temperatures. We observed the intermixing between Ni and Au via atomically resolved STEM HAADF image series over time and temperature. Figure 1b shows two clusters in their initial state at room temperature. The darker Ni core can clearly be distinguished from the bright Au shell. At a temperature of 400°C, all particles were found to be alloyed.

The separation of beam induced sample changes from purely thermally driven processes is often challenging during in situ experiments, especially with nanostructures that possess a high percentage of low-coordinated atoms. Therefore, a deeper understanding of the observed dynamics is necessary and this was achieved by comparing the experimental data (transient STEM HAADF image sequences) with a theoretical description using molecular dynamics and Monte Carlo algorithms. Figure 2 shows such simulations exemplary for an elongated core-shell particle, with Au@Ag (a) and Ag@Au (b) configuration. Both geometries exhibit significant changes in morphology. In case of Au@Ag selective surface sputtering of Ag atoms leads to a considerable change in composition during electron beam exposure, while Ag@Au particles retain their chemical composition. Such beam induced processes can have a high impact on the results, obtained via in situ heating experiments in a STEM.

References:

[1] F. Baletto, R. Ferrando, *Rev. Mod. Phys.* **2005**, *77*, 371.
[2] A. Volk, P. Thaler, M. Koch, E. Fisslthaler, W. Grogger, W. E. Ernst, *J. Chem. Phys.* **2013**, *138*, 214312.
[3] P. Thaler, A. Volk, F. Lackner, J. Steurer, D. Knez, W. Grogger, F. Hofer, W. E. Ernst, *Phys. Rev. B* **2014**, *90*.

Acknowledgements
Our research is supported by the Federal Ministry of Science, Research and Economy with the project Infrastrukturförderung 2015 and by the Austrian Research Promotion Agency (FFG) in the project SOLABAT (853627).

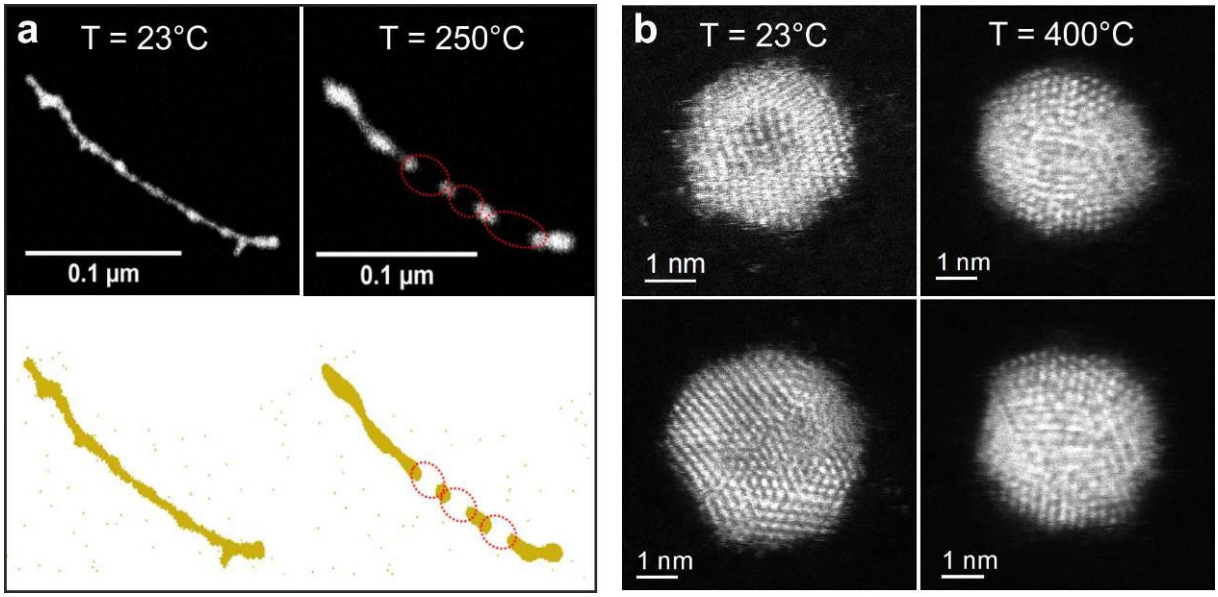

Figure 1

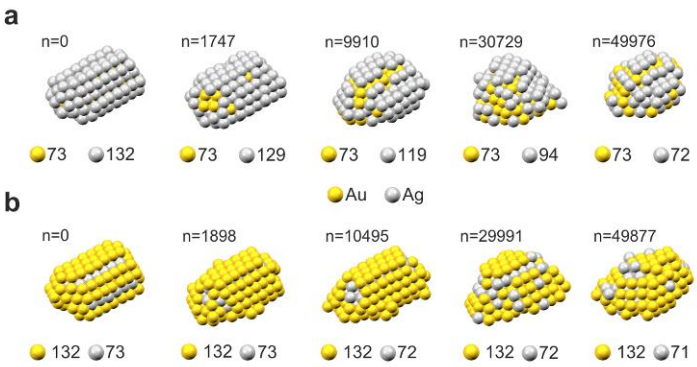

Figure 2

IM2.P002
X-ray elemental analysis of in situ heated sample using large sized silicon drift detector with Be window in transmission electron microscope

I. Ohnishi[1], K. Fukunaga[1], K. Miyatake[1], M. Morita[1], S. Kawai[1], E. Okunishi[1]

[1]JEOL Ltd., Tokyo, Japan

ionishi@jeol.co.jp

In-situ experiments under various conditions such as cooling, heating, and gas environment have been conducted even in a conventional transmission electron microscope (TEM) by special specimen holders developed by recent MEMS technology. Energy dispersive X-ray spectroscopy (EDS) and electron energy loss spectroscopy (EELS) under the conditions of the in-situ experiments give important evidences for in-situ study of chemical reaction or processes accompanied with compositional change of samples [*e.g.,* 1, 2]. However, when a sample is heated, infrared radiation from the heated sample increases the background noise and degrades energy resolution of EDS detector. So far, the maximum allowable temperature of the measurement, by using a silicon drift detector (SDD) with no window, was reported to be 525 ℃, when they used a MEMS-based heating specimen holder, by Zaluzec et al. [3].
Recently, we have developed a new SDD with a large-sized sensor (100 mm^2 in area) with a Be window in order to reduce the infrared radiation from heated samples. The maximum allowable temperature of in-situ elemental analyses is improved to be ~1000 °C with the SDD and MEMS-based heating specimen holder, since some portion of the infrared radiation is absorbed by the Be window. For test results in this paper, we used the SDD installed on the 200 kV field emission TEM (JEOL, JEM-F200) and the MEMS-based heating specimen holder (Protochips, Aduro500). Figure 1 shows a series of X-ray elemental maps of Pd/Au nano particles at 25, 300, 400, 600 °C, when the sample was heated up to 800 °C step-by-step. At 25 °C, the particles show core-shell structure: A core is made of Au covered with Pd. They were intermixing as the sample temperature was raised and became homogenous in chemical composition at 600 °C. The new SDD with the Be window can provide in-situ elemental analyses at higher temperature than ever before. Thus, it can probably expand the range of in-situ experiments with chemical analysis.

References:
[1] E. Prestat *et al*, Micros. Microanal. **21. Suppl. 3** (2015) p.247-248.
[2] S. Sceilling *et al*, Micros. Microanal. **21. Suppl. 3** (2015) p.1291-1292.
[3] N.J. Zaluzec *et al*, Micros. Microanal. **21. Suppl. 3** (2015) p.961-962.

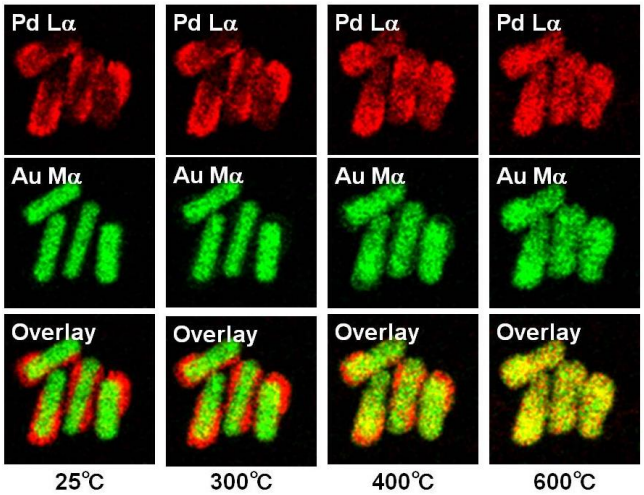

Figure 1. In-situ X-ray elemental maps of Pd/Au nano particles at temperatures: 25, 300, 400, 600 °C, obtained by JEM-F200 with Be-window SDD.

IM2.P003
Evaluation of the metabolic contribution of cytosolic and mitochondrial NAD(P)H during insulin secretion

A. Zbinden[1,2], D. Carvaja-Berrio[1], S. Hinderer[1,2], K. Schenke-Layland[1,2,3]

[1]University of Tübingen, Women´s health , Tübingen, Germany
[2]Fraunhofer Institute for Interfacial Engineering and Biotechnology (IGB), Cell and Tissue Engineering, Stuttgart, Germany
[3]University of California in Los Angeles, Dept. of Medicine/Cardio, Los Angeles, CA, United States of America

aline.zbinden@igb-extern.fraunhofer.de

Introduction: Diabetes mellitus is a chronic disease that occurs either when the pancreas is not able to produce (T1) or properly respond (T2) to insulin. Although oral therapeutics are available to stimulate insulin secretion, many T2 patients and nearly all T1 patients require intensive therapies such as constant blood glucose monitoring and repeated injections of exogenous insulin. A greater understanding of the mechanisms involved in beta cell glucose stimulated insulin secretion (GSIS) may enable the development of new Diabetes therapies.
Objectives: It has been described that GSIS is coupled to the metabolic state of beta cells. Briefly, after being transported into the cell, glucose is phosphorylated and directed into glycolysis, leading to a general increase in metabolic flux, Ca^{2+} influx and insulin release. This change in metabolic state can be monitored by NAD(P)H autofluorescence, which is a coenzyme produced during glycolysis and by the Krebs cycle. The metabolic contribution from both cellular compartments is essential for a proper GSIS response, but not yet fully understood. To gain a better insight into the metabolic contribution between cytosolic NAD(P)H generated by glycolysis (free NAD(P)H) and mitochondrial NAD(P)H (bound NAD(P)) from the Krebs cycle, we used fluorescence lifetime microscopy (FLIM) in combination with multiphoton imaging (MP) on a rat insulinoma (INS-1E) cell line.
Materials and Methods: We used a 5D MP microscope developed by JenLab GmbH (Jena, Germany), which can switch between MP and FLIM acquisition mode. MP images were collected with a total acquisition time of 23 seconds (Jenlab Image) at a laser power of 25 mW and wavelength of 710 nm (MaiTaiControl). Acquisition time for FLIM was of 180 seconds. A bi exponential decay fitting was used to analyze the FLIM data. Based on the emission maxima at 470nm from NAD(P)H, we used a filter with 425-509 nm range. All recording settings were adjusted in the software SPCM and DCC (Becker&Hickl). INS-1E cells were cultured as adherent monolayer on glass bottom dishes for 72h. Pre-incubation of the cells with Krebs 1x buffer was performed for 15 minutes before the baseline measurements (MP & FLIM). Then, 16.7 mmol/L glucose was applied to the culture and measurements taken after 30 minutes pre-incubation (MP & FLIM).
Results: MP imaging and quantification showed a significant increase in overall NAD(P)H intensity between the Krebs solution and glucose conditions. Indeed, the glucose stimulates the insulin secretion mechanism by increasing its general metabolic activity. Using the difference in fluorescence lifetime from free and bound NAD(P)H, we were able to observe an increase in the α1 ratio by adding glucose. The shift toward a higher α1 ratio corresponds to an increase in the glycolysis contribution to the overall metabolism.
Conclusion: In this study, we were able to track the metabolic changes during glucose stimulation of INS-1E cells. We demonstrated an overall increase in metabolic activity, as well as a shift toward a higher glycolysis contribution when glucose is applied.

IM2.P004
Charge dynamics in aluminum oxide thin film revealed by ultrafast scanning electron microscopy

V. Sala[1,2], M. Zani[1], G. Irde[1,2], S. M. Pietralunga[2,3], G. Cerullo[1,3], G. Lanzani[1,2], A. Tagliaferri[1,2]

[1]Politecnico di Milano, Physics, Milano, Italy
[2]Istituto Italiano di Tecnologia, Center for Nano Science and Technology@PoliMi, Milano, Italy
[3]CNR, IFN, Milano, Italy

vittorio.sala@polimi.it

Introduction: Optical properties in the visible and near UV of wide bandgap insulators are influenced by defects that act as electron traps;lifetime and energy of excited trap states have been studied by time resolved photoluminescence [1]. The possibility to set and read optically single electrons excited states makes insulators a unique playground with applications in a variety of fields from Electronicsand Photonics to Quantum computing [2].
Objectives: From cathodoluminescence measurements, it is known that defects may be excited also by the electron beam of a scanning electron microscope (SEM) [3]. Our goal is to evaluate the excitation dynamics of the color center in an insulator from the secondary electron contrast typical of the SEM images.
Materials and Methods: We report about a time resolved measurement of electron dynamics in an aluminum oxide film on silicon done by Ultrafast Scanning Electron Microscopy (USEM). This novel technique aims to join the time resolution typical of fs lasers to the spatial lateral and depth resolution of electron microscopy in a single tabletop tool [4]. In our pump-probe setup, the sample is excited both by an UV fs laserpulse and by a delayed electron pulse, triggering the emission of low energy electrons to the detector.
Results: On alumina, the laser-induced electronic contrast shows a relevant CW contribution, that we attribute tentatively to the photo-inducedcarriers within the insulator. Nonetheless, by employing lock-in detection of secondary electrons, it is possible to observe also a fast dynamics with components ranging from hundreds of picoseconds to few nanoseconds. We observed an enhancement of secondary electron emission rising at zero delay and vanishing for positive delay with a time constant of tens of nanoseconds attributed to the excitation of an oxygen vacancy by the laser beam. It was possible to observe a depletion mechanism acting at positive delay and decaying with a tau of tens of picoseconds that was attributed to laser induced surface charging [5]. A third enhancement acting at negative delay and decaying with a time constant of few nanoseconds was attributed to the photoemission of electrons from color centers excited by the electron beam.
Conclusions: Time resolved SEM images, already known to be sensitive to electron dynamics in semiconductors, has shown to be sensitive also to electron dynamics of defects in alumina. Furthermore, time resolution proved to be fundamental to disentangle the effects contributing to the count of low energy electrons to the detector.

[1] B.D. Evans, G.J. Pogatshnik and Y. Chen, Nuclear Instruments and Methods in Physics Research B, 91, 258-262 (1994), Optical properties of lattice defects in α-Al_2O_3
[2] M.S. Akselrod, A.E. Akselrod, S.S. Orlov, S. Sanyal and T.H. Underwood, Journal of Fluorescence, 13, 503-511 (2003), Fluorescent Aluminum Oxide Crystals for Volumetric Optical Data Storage and Imaging Applications
[3] E.C. Kouroukla, I.K. Bailiff, I. Terryand L. Bowen, Radiation Measurements, 71, 117-121 (2014), Luminescence characterisation of alumina substrates using cathodoluminescence microscopy and spectroscopy
[4] O.F. Mohammed, D.S. Yang, S.K. Pal, and A.H. Zewail, Journal of the American Chemical Society, 133, 7708 (2011), 4D Scanning Ultrafast Electron Microscopy: Visualization of Materials Surface Dynamics
[5] R. Stoian, A. Rosenfeld, D. Ashkenasi, I.V. Hertel, Phyical Review Letters 88, 097603 (2002) Surface Charging and Impulsive Ion Ejection During Ultrashort Pulsed Laser Ablation

IM2.P005
Shape memory alloy grids for in situ straining in the TEM

N. Wolff[1], U. Schürmann[1], C. Chluba[1], D. Smazna[1]
R. Lima de Miranda[1], P. Junker[1], R. Adelung[1], E. Quandt[1], L. Kienle[1]

[1]Christian-Albrechts-Universität zu Kiel, Institute of Material Science, Kiel, Germany

niwo@tf.uni-kiel.de

Introduction: In the recent years, the urge for materials characterization via *in situ* experiments on the nanoscale is pushing the field of modern transmission electron microscopy (TEM) to provide dedicated/advanced solutions[1]. The realization of examinations under temperature variation, electrical biasing, chemical environment modification, electron beam induced reactions as well as mechanical testing require novel and sophisticated setups, often based on MEMS devices and/or special sample holders[2]. More feasible solutions are therefore of high demand. The presented approach for *in situ* straining experiments is based on functional TEM grids[3] composed of the shape-memory alloy NiTi[4] and is applicable on a common heating holder.
Objectives: The functional grid technology is a cost effective alternative to available MEMS and AFM based solutions to perform tensile testing experiments by applying moderate temperature in common TEM heating holders. Morphological changes, phase transformations, straining effects, defect propagation, fracture and other mechanically induced phenomena could be observed after dedicated sample preparation. The working principle is demonstrated for different grid designs and tensile tests were performed on a 3D tetrapodal ZnO network.
Materials and Methods: Functional TEM grids of the shape memory alloy Nickel Titanium were fabricated by MEMS technology. Micro tensile testing experiments were performed to determine the forces at the pre-straining and to measure the forces applied during *in situ* TEM experiments. Computational simulation using the finite element method were performed to provide assistance to understand the evolving phase transitions and indicate parts of the specimen under maximum stress/load-with respect to the martensitic microstructure during pre-straining and force - displacement curves during subsequent heating. Matters for visualization of *in situ* straining experiments in the TEM were a 3D tetrapodal ZnO network.
Results: *In situ* TEM heating experiments show a linear behaviour of the displacement with temperature beginning at the austenite start temperature. The velocity of gap broadening is strongly dependent on the grid design. Straining experiments on the 3D ZnO material show rotation of tetrapodal flexible network and bending of wires to unexpected high angles under applied strain. The applied forces of up to 0.6 N (by simulation) are large enough to treat samples with a small cross-sectional area like TEM samples.
Conclusion: The feasibility of functional TEM grids for *in situ* mechanical tests has been evaluated and demonstrated on a 3D tetrapodal ZnO network exploiting the shape memory properties of NiTi alloy. The realization of various actuator designs is supported by a thin film technological process and numerical FEM simulation. By optimization of grid designs also cycling processes and *in situ* electrical measurements should be realizable in future.

Acknowledgements
This work was funded by the German Research Foundation (DFG) as part of the Collaborative Research Center 1261–Magnetoelectric sensors from composite materials to biomagnetic diagnostics (SFB 1261).

[1] R. Ramachandramoorthy, R. Bernal, H. D. Espinosa, Pushing the envelope of in situ transmission electron microscopy, ACS Nano 9(5) (2015) 4675–4685.
[2] H. D. Espinosa, R. A. Bernal, T. Filleter, In situ TEM electromechanical testing of nanowires and nanotubes, 8(21) (2012) 3233-3252.
[3] R. Lima de Miranda, Probenträger zum Halten von Proben für die Bearbeitung und/oder Untersuchung in einem Elektronenmikroskop; Verfahren zur Heilung derartiger Probenträger und Verfahren zur Lastbeaufschlagung von Proben (German Patent - DE102013103985)
[4] R. Lima de Miranda, C. Zamponi, and E. Quandt, Micropatterned Freestanding Superelastic TiNi Films, Adv. Eng. Mater. 15(1–2) (2013) 66–69.

IM2.P006
In situ TEM setup for the safe usage of toxic and pyrophoric gases with the example of thermal annealing of III/V semiconductor heterostructures

R. Straubinger[1]

[1]Philipps-Universität Marburg, Materials Science Center and Faculty of Physics, Marburg, Germany

rainer.straubinger@physik.uni-marburg.de

This study presents the extension of the Protochips Inc. *in-situ* TEM setup for the safe usage of toxic and pyrophoric III/V semiconductor precursors. Post growth annealing has proven to be an effective way to reduce crystal defects in order to improve the layer quality, and accordingly the performance of devices such as lasers.
The test Ga(NAsP)/Si samples for this study were grown by MOVPE. The samples were prepared for the *in-situ* annealing STEM investigation using a focused ion beam (FIB, JIB 4601 F, JEOL) system. A double Cs-corrected JEOL JEM-2200 FS operating at 200 kV in combination with the gas cell holder was used for the TEM observations. The images were recorded in high angle annular dark field (HAADF) mode.
First, quantitative thermal annealing experiments both with and without group V stabilization are compared to prove the functionality of the system used. The STEM images in Figure 1a) to c) show the structure during the unstabilized thermal annealing experiments in a 10 hPa nitrogen environment. Figure 1a) shows the intact quantum well structure at 400°C, with the single layers in the sample annotated on the left hand side. By comparing images a) and b) one can already see a significant degradation of the structure at 600 °C. This degradation is caused by incongruent evaporation of group V constituents. Figure 1c) shows the same area of the sample at 700 °C, in which the quantum well structure has been completely destroyed. Figures 1d) to f) show a different lamella of the same material. However, the annealing experiment was carried out in 140 hPa tertiarybutylphosphine (TBP) without additional carrier gas in the system. In this P-rich environment the P in the structure is prevented from incongruent evaporation. By comparing Figures 2d), e) and f), one is not able to see any degradation of the structure.
The present disordering in the structure can be quantified by the change in the intensity distribution σ_i. Figure 2a) shows the σ_i divided by the mean intensity in the quantum well region as function of the annealing temperature. An increase in compositional inhomogeneity within the quantum well with increasing temperature is clearly visible. Figure 2b) shows the intensity of the group V columns along the lower Ga(NAsP)/GaP interface normalized to their mean intensity in the Ga(NAsP). The orange-colored data points represent the group V column intensity at room temperature. This measurement was done in a conventional double tilt holder before the sample was placed on the thermal e-chip. The STEM image shown in the background of the plot is also recorded in the double tilt holder at room temperature. By taking a closer look at the orange-colored data points it is possible to observe a nearly abrupt interface between the quantum well and the surrounding GaP material after growth. This can be seen by the group V intensity dropping within two group V layers by a factor of 5. Compared to that the red- (250°C), green- (300°C), magenta- (350°C) and cyan- (450°C) colored data points represent the group V intensity with increasing annealing temperature. This series shows a significant increase in the group V column intensity within the GaP close to the Ga(NAsP)/GaP interface. This increase in the intensity indicates that As diffuses from the quantum well into the surrounding material and replaces P in the group V columns during the annealing process.
In summary, this study proves that it is possible to investigate thermal annealing processes like material desorption and diffusion *in-situ* in the TEM at atomic resolution conditions under the safe supply of toxic and pyrophoric gases.

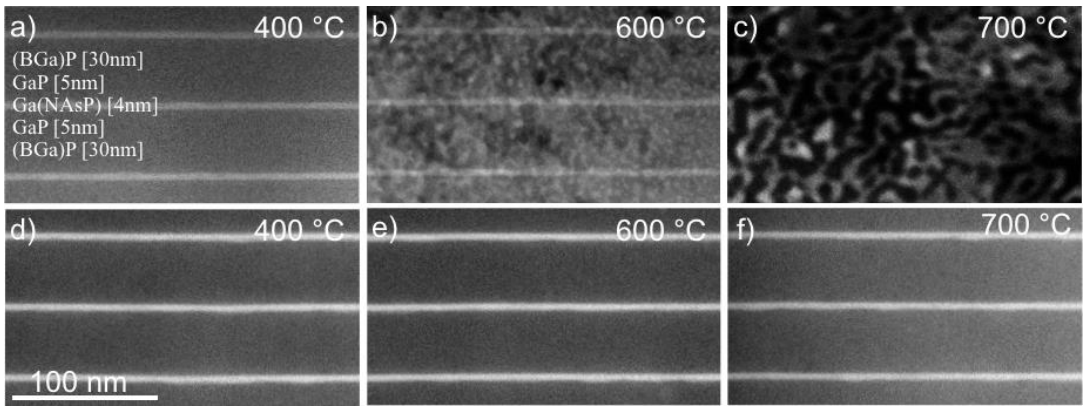

Figure 1. STEM images of the quantum well structure during the unstabilized thermal annealing process in 10 hPa N_2 environment (a-c). In image a), annotated single layers can be seen. Images (d-f) show the annealing process in 140 hPa TBP environment.

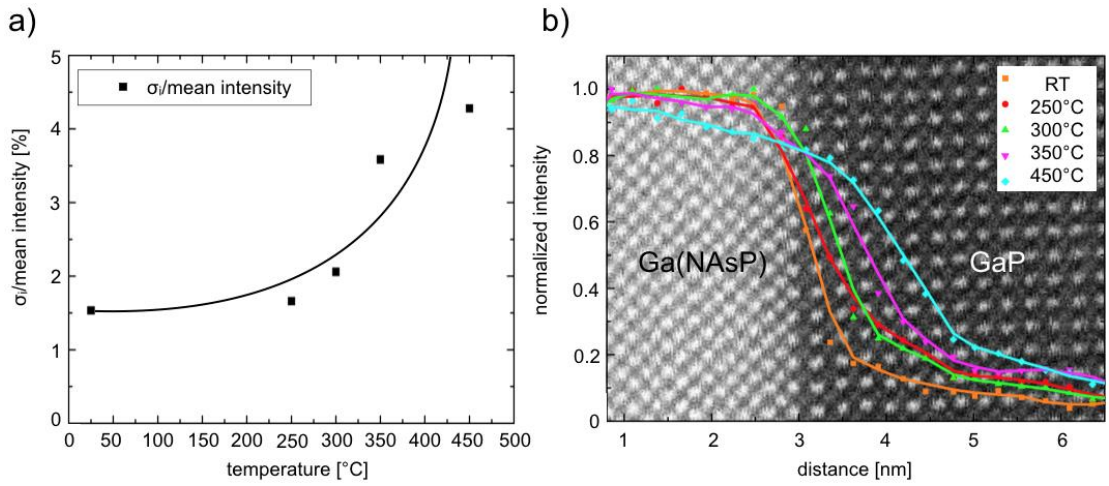

Figure 2. Plot a) shows the standard deviation divided by the mean intensity of the group V column within the quantum well over the temperature range investigated. Plot b) shows the normalized intensity of the group V columns along the Ga(NAsP)/GaP interface.

IM2.P007
Combining in situ SEM with high sensitivity analytical TEM for understanding the oxidation of metallic interconnects in SOFC

S. Poitel[1], Z. J. Wang[2], C. Hébert[1], M. G. Willinger[2], J. Van herle[3]

[1]Ecole Polytechnique Fédérale de Lausanne, Centre Interdisciplinaire de Microscopie Electronique, Lausanne, Switzerland
[2]Fritz Haber Institute of the Max Planck Society, Department of Inorganic Chemistry, Berlin, Germany
[3]Ecole Polytechnique Fédérale de Lausanne, Group of Energy Materials, Sion, Switzerland

stephane.poitel@epfl.ch

Solid Oxide Fuel Cells (SOFC) are very effective energy converters. They allow obtaining electricity and heat from fuels like natural gas or hydrogen and will play a key role in the energy transition.
Among the critical components of SOFC, interconnects are coated steel plates. Their main roles are to collect current, separate the gases and to ensure mechanical stability of the stack. The main problem is that at 700-800°C (SOFC working temperature), the chromium present in the steel to prevent its oxidation tends to evaporate and contaminate other parts of the stack [1]. Hence coatings are necessary to protect chromium from evaporation. Several SOFC metallic interconnect coatings are based on cobalt, which is efficient to prevent chromium evaporation and to maintain the contact resistance low after prolonged exposure [2]. The addition of a very thin cerium layer beneath the Co coating seems to reinforce its properties [3]. The oxidation of such coated SOFC FeCr steels, which contain a considerable number of alloy additives, becomes difficult to interpret.
Getting insight into the degradation mechanisms of interconnects is crucial to be able to design reliable elements that will perform over the lifetime of the SOFC. Here we report on the combined use of in-situ scanning electron microscopy in an in-house modified FEI Quanta 200 environmental SEM (ESEM) and post mortem analytical TEM of sample extracted by FIB from the in-situ oxidized specimens.
The sample was a Sanergy SSHT steel with Ce-Co coating, frequently used as interconnect material. It was observed at high temperature (900°C) under an oxygen flow, in ESEM, for durations from 0 to60.
In order to be close to operation conditions, one should heat the sample under vacuum to 900°C and then introduce oxygen and record images. Due to the gas introduction at high temperature (and hence switch from high vacuum mode to ESEM mode), the beginning of the reaction is challenging to record. To record the beginning of the experiment, it was tried to heat at slower rate, heat under hydrogen and introducing the oxygen at a slower rate but all these modifications induce different final morphology.
In-situ observation of the oxidation shows grain growth and coarsening for the first 10 hours. Then a change in morphology appears. The symmetry of the crystal seems to evolve from cubic to another structure.
TEM lamellae are then extracted from the in-situ observed areas using a focused ion beam (FIB). This allowed to evaluate the final composition of the oxidation layers of the steel by scanning transmission electron microscopy (STEM) and energy dispersive x-ray analysis (EDX) (figure 2).
We observe a complex migration of species, especially, the diffusion of manganese towards the cobalt coating to form a cobalt-manganese spinel oxide layer. Under this top layer, chromia scale forms. The very thin cerium layer does not prevent the diffusion of other elements from the steel. Niobium and titanium form oxidized precipitates in the steel just below the chromia scale.
Results from shorter exposure/observation times present a time-lapse picture of the initial oxidation for a more detailed understanding. Ex-situ experiments complement the results.

References:
[1] Fergus, J. W. Effect of cathode and electrolyte transport properties on chromium poisoning in solid oxide fuel cells. International Journal of Hydrogen Energy 32, 3664–3671 (2007).
[2] Froitzheim, J. & Svensson, J.-E. Multifunctional Nano-Coatings for SOFC Interconnects. ECS Trans. 35, 2503–2508 (2011).
[3] Harthøj, A., Holt, T. & Møller, P. Oxidation behaviour and electrical properties of cobalt/cerium oxide composite coatings for solid oxide fuel cell interconnects. Journal of Power Sources 281, 227–237 (2015).

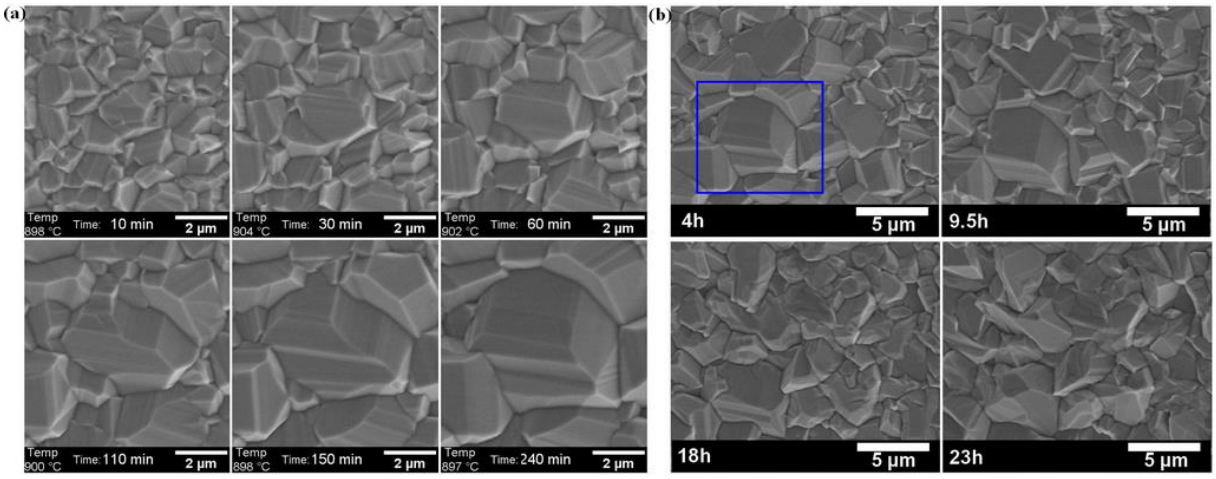

Figure 1. (a) grain growth at the surface of the sample at 900°C under 30Pa of O2. (b) Morphology change after 4-23h exposure to same condition (blue rectangle highlight the grain that growth is showed on (a)).

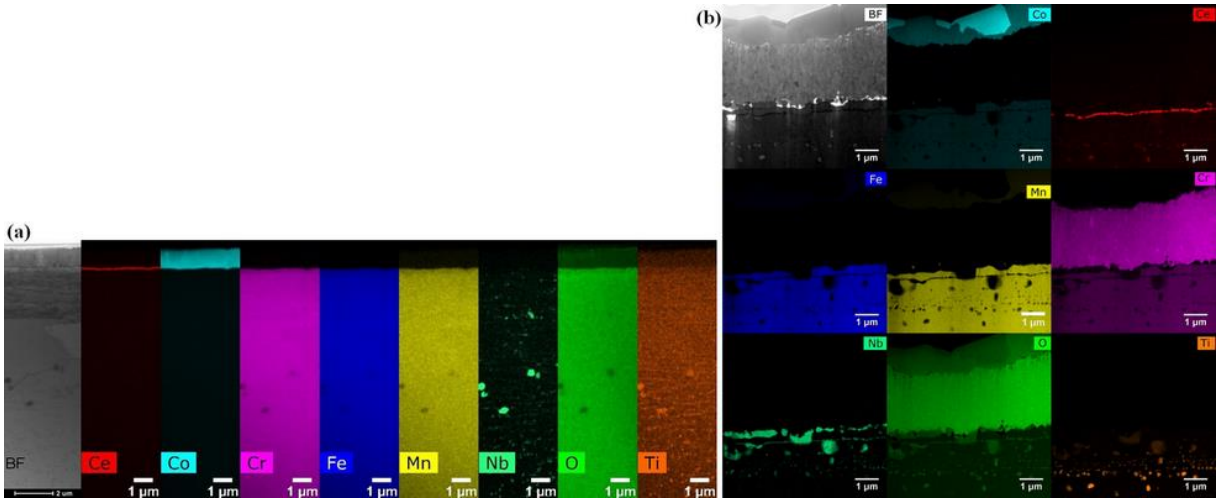

Figure 2. STEM EDX of the cross section of the surface of the coated steel (a) before oxidation and (b) after 48 hours oxidation at 900°C under 30Pa O2.

IM2.P008
Charge carrier dynamics at doped silicon surface by ultrafast scanning electron microscopy

V. Sala[1,2], S. M. Pietralunga[3,2], M. Zani[1], G. Irde[1,2], C. Manzoni[3], G. Isella[1], G. Cerullo[1], G. Lanzani[1,2] A. Tagliaferri[1,2]

[1]Politecnico di Milano, Physics, Milano, Italy
[2]Istituto Italiano di Technologia, CNST, Milano, Italy
[3]CNR, IFN, Milano, Italy

alberto.tagliaferri@polimi.it

Introduction: Ultrafast Scanning Electron Microscopy (USEM) aims at combining the temporal resolution of femtosecond laser spectroscopy and the nanometer spatial resolution of scanning electron microscopy to characterize the dynamics of photo-induced processes at surfaces and in ultra-thin films. The temporal evolution of SE contrast as a function of the relative pump-probe delay provides information on the charge transport and its timescales within a few nm thick layer at the sample surface. Silicon crystals and *p-n* junctions have been already investigated by USEM showing evolution down to the ps timescale, which was attributed to intra- and inter-band relaxation [1].
Objectives: This work aims at investigating the photo-generated charge carrier dynamics at Silicon surface as a function of the doping, and at highlighting the role of the surface, both in affecting the charge carrier dynamics in its proximity and in determining the contrast of the secondary electron probe exploited in USEM.
Materials and Methods: Single crystalline *p* and *n* doped Silicon samples, with resistivity ranging from 10^{-3} to 10^{3} Ohm cm, were accurately cleaned and introduced in the ultra-high vacuum chamber of our USEM apparatus. Time resolved imaging is achieved in pump-probe mode, exploiting a field-emission electron source coupled to a femtosecond 1030 nm laser. The UV third harmonic laser pulses are used as the optical pump at the sample, while the fourth harmonic beam photoemits the ultrafast electron pulses from the SEM tip generating the probe beam. The SE signal from the sample is detected by an Everhart-Thorley detector. The pump-probe relative delay is tuned with sub-ps resolution by a mechanical delay stage, allowing to freeze the dynamics of repeatable phenomena at a selected time after the pump trigger. The setup allows to achieve ultrafast temporal resolution as originally demonstrated by A. H. Zewail and coworkers [2], with a signal rise time of about 10 ps in our apparatus.
Results: The intense UV optical pumping adopted brings the material in a nearly degenerate injection state with highly excited charge carriers and defects, allowing to investigate a wide range of generation and recombination processes at the silicon wafer surface. The Charge carrier timescales are addressed in a range from few tens of ps up to tens of ns. We show that the SE contrast depends dramatically on the bulk material doping level, similarly as shown previously in GaAs [3], and also on the surface states and defects. Based on our USEM results, the modeling of the charge carrier dynamics needs to account for both the evolution of the energy distribution and of the momentum distribution, which has not been considered in so far.
Conclusions: Secondary electron contrast in USEM allows to access charge carrier dynamics with a thickness resolution of few nm or less from the surface. We show that intense UV pumping of Silicon gives access to high injection states, whose dynamics evolves over a large time range. Several timescales are found from tens of ps to tens of ns, which depends on a subtle interplay between the bulk and surface electronic structures. These results demonstrate the potential of USEM in the investigation of nanostructured materials for light emission and energy harvesting applications.

References:
[1] J. Sun, A. Adhikari, B.S. Shaheen, H. Yang, and O.F. Mohammed, J. Phys. Chem. Lett. **7**, 985 (2016).
[2] O.F. Mohammed, D. Yang, S.K. Pal, and A.H. Zewail, J. Am. Chem. Soc. **133**, 7708 (2011).
[3] J.W. Cho, T.Y. Hwang, and A.H. Zewail, Proc. Natl. Acad. Sci. U. S. A. **111**, 2094 (2014).

IM2.P009
Controlled silver-shell growth on gold nanorods studied by in situ liquid cell TEM techniques

A. Hutzler[1], R. Branscheid[2], T. Schmutzler[3], M. P. M. Jank[4], L. Frey[1,4], E. Spiecker[2]

[1]Chair of Electron Devices, Friedrich-Alexander University Erlangen-Nuremberg, Erlangen, Germany
[2]Insitute of Micro- and Nanostructure Research & Center for Nanoanalysis and Electron Microscopy, Friedrich-Alexander University Erlangen-Nuremberg, Erlangen, Germany
[3]Chair for Crystallography and Structural Physics, Friedrich-Alexander University Erlangen-Nuremberg, Erlangen, Germany
[4]Fraunhofer Institute for Integrated Systems and Device Technology, Erlangen, Germany

andreas.hutzler@leb.eei.uni-erlangen.de

Liquid cell transmission electron microscopy (LCTEM) enables the observation of dynamic processes at the place of the event in real time that is *in situ*. An early concept of this method has already been suggested in 1944 by Abrams and McBain [1] and could be realized nearly 60 years later in 2003 by Williamson *et al.* [2]. Since that, much effort has been put into characterizing various reactions in material, biological, and electrochemical systems.
Anisotropic core-shell nanostructures are highly attractive for plasmonic applications like e.g. sensors, light guiding or labeling, because their plasmon resonance frequency can be variably adjusted over a wide spectral range via a simple variation of the shell thickness as already shown by Becker *et al.* [3]. Here we apply LCTEM to induce and to investigate the growth of silver-shell from aqueous silver nitrate ($AgNO_3$) solution on cetrimonium bromide (CTAB) stabilized gold nanorods. For this purpose, a new, simplified liquid cell design is utilized, which is not only capable being used for conventional, but also for analytic TEM techniques like energy dispersive x-ray spectroscopy (EDXS) and electron tomography. To achieve that, the fluid is enclosed between a structured silicon nitride membrane and a second few layer graphene membrane, leaving one side of the cell plane, as shown elsewhere [4]. For the experiments, a conventional TEM specimen holder is used together with a Philips CM 30 and a FEI Titan³ Themis, both operated at 300 kV.
It could be shown that silver bromide (AgBr) is forming, which components are originating from CTAB and $AgNO_3$. AgBr is subsequently being reduced by solvated electrons acting as reducing agent. These free electrons are generated intrinsically by electron beam irradiation of the aqueous solution. The silver atoms can then nucleate and crystallize at different nucleation centers. One possible nucleation center is the surface of the present gold nanorods, where an epitaxial, defect free growth of a silver shell can be observed (cf. Fig. 1 and Fig. 2). The whole process is slowed down compared to bulk reactions because of the confinement of the solution to a narrow channel and thus because of a higher liquid viscosity hindering diffusion. Nevertheless, the growth rate of silver perpendicular to the longitudinal direction of the nanorods is considerably higher compared to the growth rate in the parallel direction. Furthermore, a dose dependent and reversible layer-by-layer dissolution of AgBr particles, acting as silver sources, is observable (cf. Fig. 3). Here, the reduction, and thus the annihilation of solvated silver ions at higher electron dose rate conditions shifting the solubility product to nonequilibrium state, so that AgBr dissolves to restore this equilibrium. In contrast to this process, counter reactions prevail at lower dose conditions. Here, the formation of silver ions is favored until the solubility is being exceeded and crystallization of AgBr takes place.
The experiments done within this study show that this new liquid cell design is appropriate for solving material scientific issues. In particular, the planar surface of the liquid cell as well as the large viewing areas allow for improved performance of analytical TEM techniques like EDXS and electron tomography making the cell architecture capable of more comprehensive investigations into complex material systems.

References:
[1] I. M. Abrams and J. W. McBain., Science 1944, **100** (2595), 273−274
[2] M. J. Williams *et al.*, Nat. Mater. 2003, **2** (8), 532−536
[3] J. Becker *et al.*, Nano Lett. 2008, **8** (6), 1719−1723
[4] A. Hutzler *et al.*, Microsc. Microanal. 2016, **22** (S5), 78–79

Acknowledgment
Financial support by the DFG via the Research Training Group GRK1896 is gratefully acknowledged.

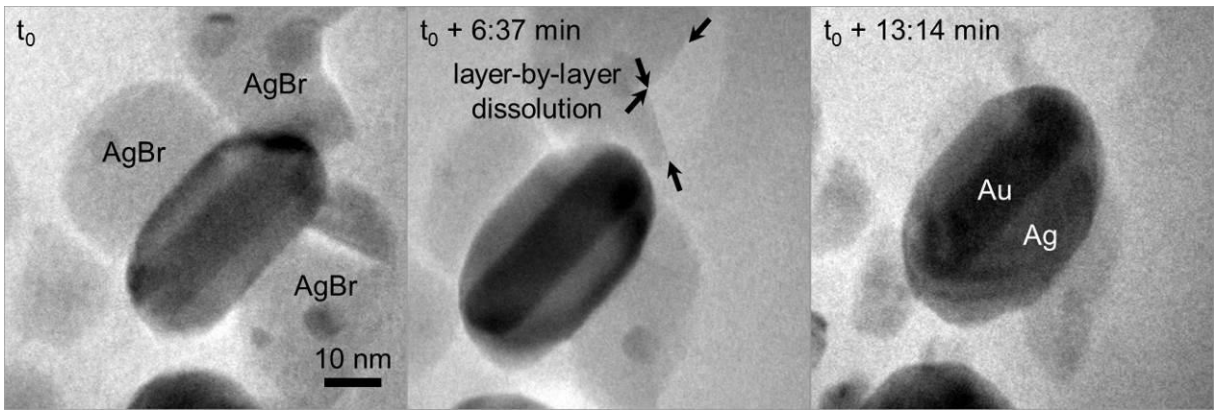

Figure 1. Bright field TEM image series of epitaxial growth of a silver shell on a gold nanorod with adjacent AgBr particles acting as silver source.

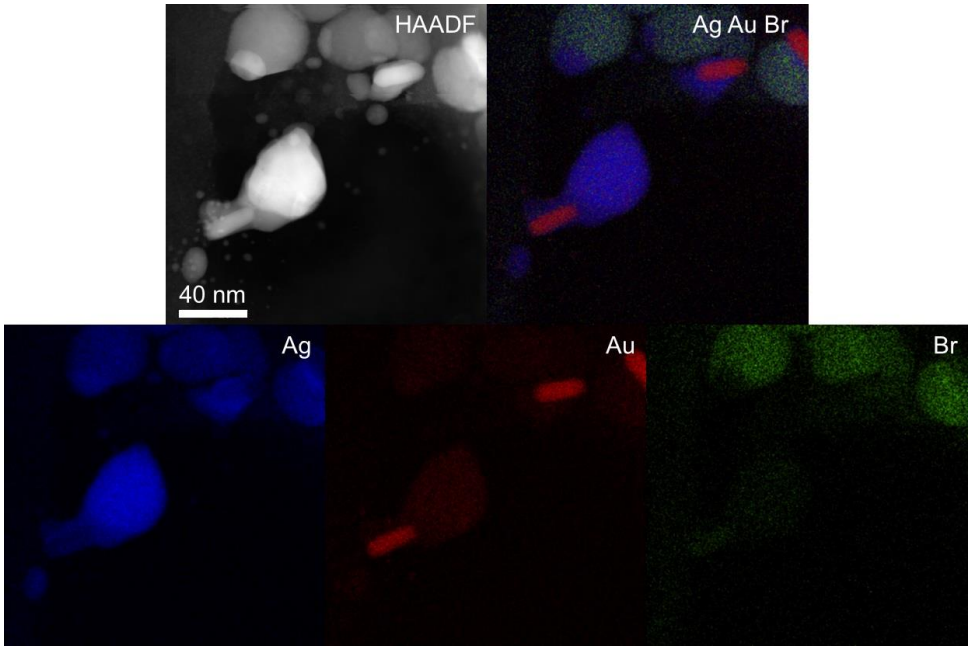

Figure 2. EDXS mapping of a silver coated gold nanorod.

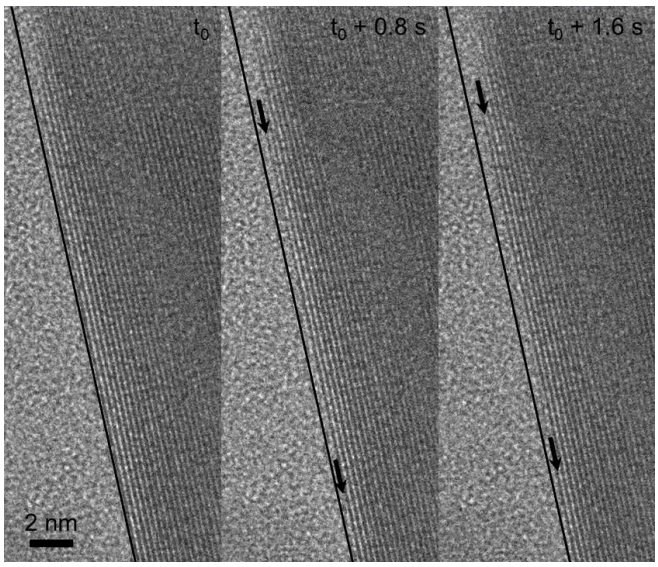

Figure 3. Bright field TEM image series of layer-by-layer dissolution of a AgBr particle.

IM2.P010
Observation of nucleation and growth processes of Au nanoparticles at high dose rates

D. Keller[1], Y. Zhang[1], R. Erni[1]

[1]Empa - Swiss Federal Laboratories for Materials Science and Technology, Electron Microscopy Center, Dübendorf, Switzerland

debora.keller@empa.ch

The shape-controlled synthesis of nanoparticles has been considerably improved in the last few years but there is still very limited knowledge about the mechanisms that initially trigger nucleation and growth of nanoparticles and finally determine their morphology. Liquid-cell transmission electron microscopy (LC-TEM) therefore offers a new and very useful tool to study such dynamic processes in a liquid environment and at a high lateral and temporal resolution. Metal precursors in liquid can be reduced by the electron beam which provides a direct and local control of the reduction reaction via the electron dose rate. In previous studies two different nanoparticle growth mechanisms were distinguished, i.e. the reaction-limited growth resulting in well-shaped plates or facetted 3D particles and the diffusion-limited growth resulting in less facetted spherical and dendritic structures. The two growth mechanisms could directly be triggered by choosing either a low or a high electron dose rate [1,2].
In the present work we aim at extending the knowledge about different growth mechanisms by studying gold nanoparticle growth at dose rates beyond the reported range and in concentrated precursor solutions.
LC-TEM experiments were performed on a Poseidon holder from Protochips. Two 550 x 50 μm^2 windows were used in parallel alignment and separated by a 150 nm flow spacer. The cell was flooded with a 20 mM $HAuCl_4$ precursor solution. The experiments were performed on a FEI Titan Themis at 300 kV in scanning (S)TEM mode whereas different beam currents between 17 to 226 pA were applied, corresponding to dose rates of 3.2 - 41.9 $e^-/Å^2s$.
The nucleation and growth process was recorded under different high dose rate conditions. Fig. 1 shows the growth progress after 10, 60 and 120 seconds of irradiation under four different conditions. Flower-shaped, dendritic structures grew at comparably low dose rates (3.2 -6.1 $e^-/Å^2s$, Fig. 1a-b) whereas the growth of spherical and facetted 3D particles became predominant at higher dose rates (8.1 $e^-/Å^2s$, Fig. 1c). The nucleation and growth processes decelerated and finally ceased when the dose rate was further increased. The threshold above which no particle growth was observed anymore was reached at ~41.9 $e^-/Å^2s$ (Fig. 1d). Besides the difference in morphology the results also indicate that fewer particles are formed with increasing dose rate.
Based on the previously described growth models, a shift from reaction-limited to diffusion-limited growth is expected with increasing dose rate [1,2]. The low-dose scenario described in this work matches the diffusion-limited (high-dose) growth regime reported in literature in respect to both, the absolute dose rate applied and the resulting dendritic structures obtained [1]. However, when the dose rate is even further increased we observe another switchover back again to a reaction-limited growth type that leads to facetted 3D structures. As the growth rate decreases and eventually ceases towards very high dose rates, we suspect that the high dose creates an etching environment that slows down the growth. In contrast to the low dose nucleation threshold due to a lack of precursors, the high dose threshold would then rather reflect an equilibrium condition between particle growth and dissolution. However, further investigations are needed to clarify the mechanisms responsible for particle growth dynamics under high dose rates. Also, the impact of the dose rate on the local pH value and temperature needs to be analyzed, as these factors are known to play a crucial role in ex situ particle synthesis too [3].

[1] D. Alloyeau et al., Nano Lett. 15, 2574–2581 (2015).
[2] T. J. Woehl et al., ACS Nano. 6, 8599–8610 (2012).
[3] N. T. K. Thanh et al., Chem. Rev. 114, 7610–7630 (2014).
[4] This project has received funding from the European Research Council (ERC) under the EU's Horizon 2020 (grant agreement No 681312)

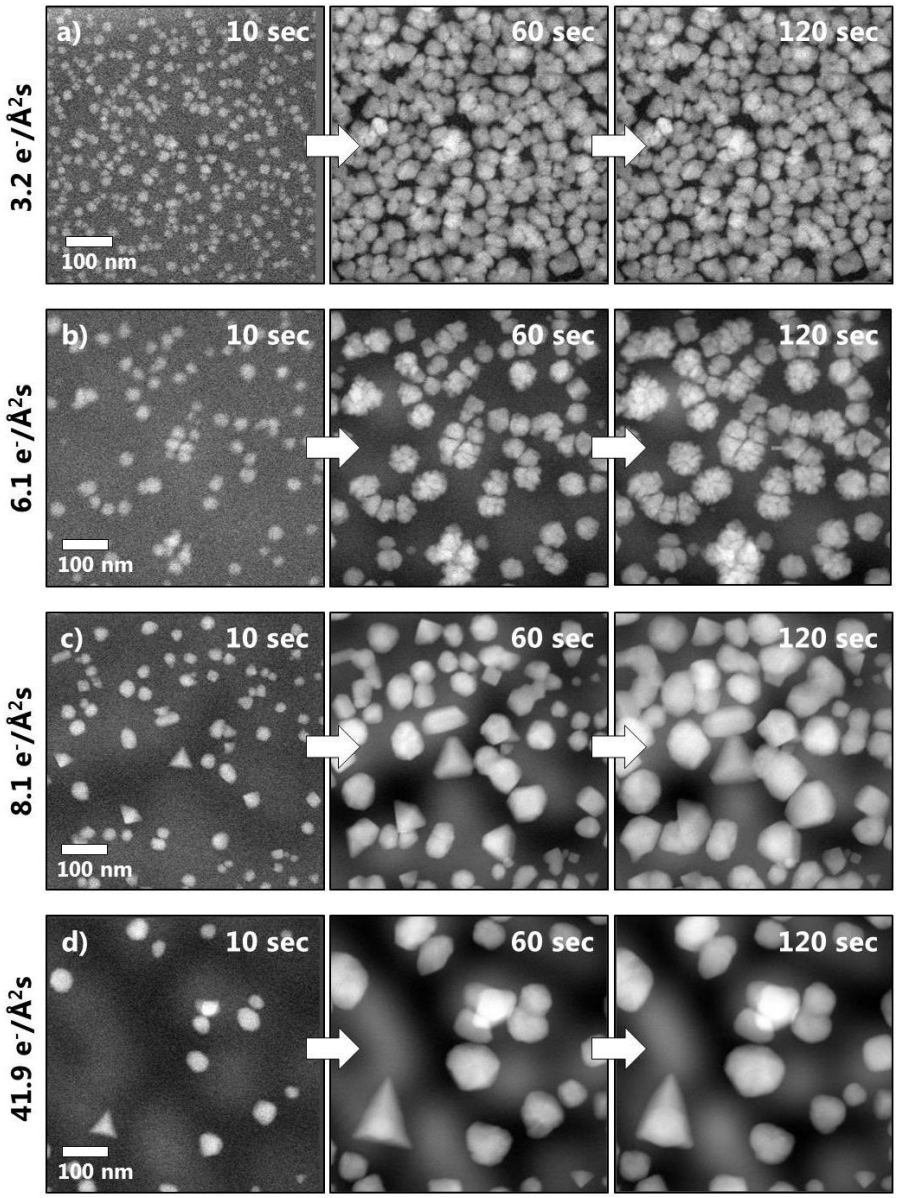

Figure 1. Gold nanoparticle growth process captured after 10, 60 and 120 seconds of electron irradiation of a 20 mM $HAuCl_4$ solution at the different electron dose rates a) 3.2, b) 6.1, c) 8.1 and d) 41.9 $e^-/Å^2s$.

IM2.P011
Structure manipulation of a manganite using environmental TEM

V. Roddatis[1], D. Mierwaldt[1], M. E. Abrishami[1], C. Jooss[1]

[1]Universität Göttingen, Institut für Materialphysik, Göttingen, Germany

vroddatis@ump.gwdg.de

During the last decades transmission electron microscopy has been used as a very powerful method to investigate atomic and electronic structure of materials with unprecedented spatial, energy and temporal resolution. Many technical improvements and breakthroughs including development of correctors of spherical and chromatic aberration, environmental TEM (ETEM), gaseous, liquid, electrical, and heating/cooling specimen holders allowed for demonstration of ETEM as an instrument, which can create nanostructures or modify them at nanoscale. These impressive examples include growth of carbon nanotubes with metallic conductivity using an H_2O rich atmosphere [1], formation of nanobridges [2] and nano 3D-printing [3]. All these achievements resulted in the proposal of using an electron microscope operated in STEM mode as a tool in which three vitally important parameters, namely: control of the beam position, monitor and feed back in real time, and improved theory and modelling, all are necessary to achieve this goal [4]. Here, we apply an ETEM operated in TEM mode to demonstrate that another additional parameter – environment or gas atmosphere – can be used to influence and control the structure of materials. In order to demonstrate this, we have used Ruddelsden-Popper $Pr_{1-x}Ca_{1+x}MnO_4$ (RP-PCMO) powders prepared by wet chemistry methods using calcium nitrate tetrahydrate $Ca(NO_3)_2$ $4H_2O$ (99%), manganese nitrate tetrahydrate $Mn(NO_3)_2$ $4H_2O$ (99.5%), praseodymium nitrate hexahydrate $Pr(NO_3)_3$ $6H_2O$ (99.9%) and gelatin precursors, as well as subsequent high temperature calcination with CaO powder. The RP-PCMO nanoparticles were pressed into pellets and specimens for the ETEM measurements were prepared by use of mechanical thinning followed by Ar+ ion milling. The structure of samples was studied using a FEI ETEM Titan 80-300 equipped with Cs-image corrector. During the ETEM experiments the gas pressure of oxygen (O_2), inert gas (He) and its mixture with O_2, as well as H_2O vapor was varied between $1 \cdot 10^{-6}$ mbar and 1 mbar.
The study of RP-PCMO revealed that the material is stable against electron irradiation of a dose below 14000 $e^-/(A^2s)$. Due to the presence of residual water molecules in high vacuum conditions a dose of about 30000 $e^-/(A^2s)$ causes reconstruction of material"s surface. At the amorphous free surface of particles exposed to O_2 pressures up to 1 mbar strong cation movement was detected but the structure remained unchanged (Figure 1a, b). The electron beam illumination of flat terraces gives rise to the epitaxial growth of perovskite structure from amorphous material formed during TEM specimen preparation (Figure 1c, d).

[1] A.R. Harutyunyan, G. Chen, T.M. Paronyan, E.M. Pigos, O.A. Kuznetsov, K. Hewaparakrama, S.M. Kim, D. Zakharov, E.A. Stach, G.U. Sumanasekera, Science 326 (2009), 116.
[2] C.Chen, Z. Wang, F. Lichtenberg, Y. Ikuhara, and J.G. Bednorz, Nano Lett. 15 (2015) 6469−6474.
[3] S. Jesse, A.Y. Borisevich, J.D. Fowlkes, A.R. Lupini, P.D. Rack, R.R. Unocic, B.G. Sumpter, S.V. Kalinin, A. Belianinov, and O.S. Ovchinnikova, ACS Nano 10 (2016) 5600−5618.
[4] S.V. Kalinin, Al. Borisevich and S. Jesse, Fire up the atom forge, Nature 539 (2016) 485.

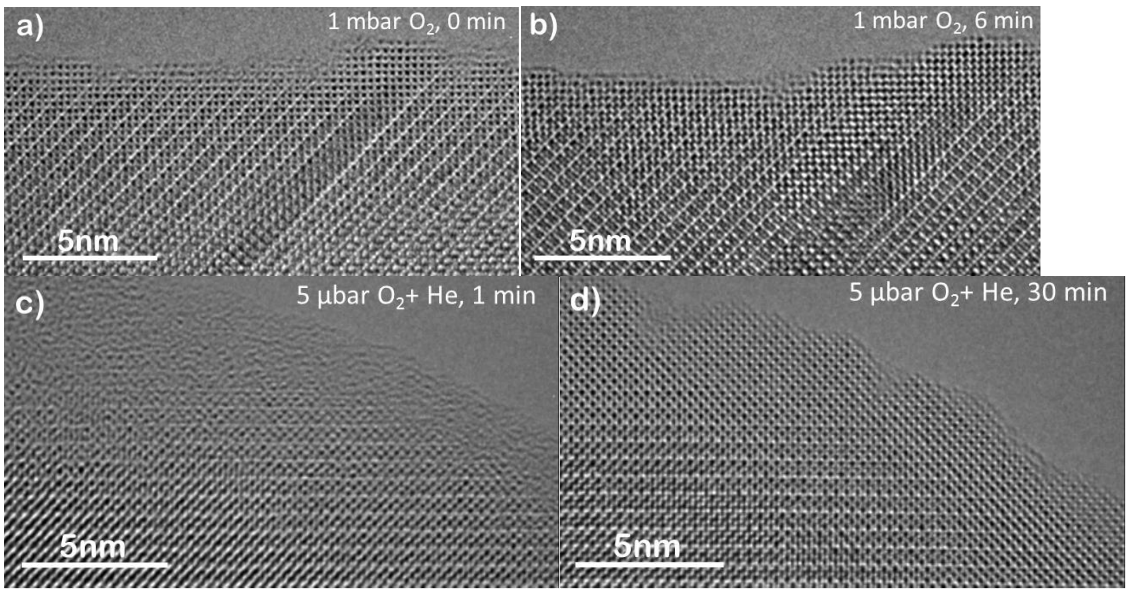

Figure 1. High resolution TEM images of RP-PCMO in oxygen at the very beginning (a) and after 6 min. RP-PCMO in a mixture of O_2 and He after 1 min (c) and after 30 minutes (d).

IM2.P012
A functional ultrafast transmission electron microscope in Strasbourg

M. Picher[1], K. Bücker[1], F. Banhart[1], T. LaGrange[2], S. T. Park[3], D. Masiel[3], B. W. Reed[3]

[1]CNRS, IPCMS, Strasbourg, France
[2]EPFL, Lausanne, Switzerland
[3]IDES, Pleasanton, CA, United States of America

matthieu_picher@yahoo.fr

Question: High temporal resolution transmission electron microscopy techniques have shown significant progress in recent years. Using photoelectron pulses induced by ultrashort laser pulses on the cathode, these methods can probe ultrafast materials processes and have revealed numerous dynamic phenomena at the nanoscale. Most recently, the technique has been implemented in standard thermionic electron microscopes that provide a flexible platform for studying material's dynamics over a wide range of spatial and temporal scales. In this study, the electron pulses in such an ultrafast transmission electron microscope are characterized in detail.
Methods: The microscope is based on a thermionic gun with a Wehnelt electrode and is operated in a stroboscopic photoelectron mode. An infrared laser beam is focused onto the specimen and excites the material. After an adjustable delay, a UV pulse is focused onto the photocathode of the TEM gun in order to generate electron pulses via photoelectric effect, which probe the specimen by forming a TEM image, a diffraction pattern or an electron energy-loss spectrum (EELS) (fig.1). Stroboscopic mode is achieved by operating the laser at a repetition rate in the MHz range. Reversible processes can then be investigated through the accumulation of millions of low-intensity electrons pulses (1-1.000 electrons, duration of few ps).
Results: Comparable image resolution can be obtained in the thermionic mode and in the stroboscopic photoelectron mode (0.23 nm) and lattice resolution of metals can be observed with photoelectrons. The shortest electron pulses obtained were 1.5 ps long and the energy resolution in the photoelectron mode is 0.7 eV, enabling high resolution stroboscopic studies in imaging, diffraction and EELS modes. (fig.2) However, maximizing the signal to noise ratio requires a high number of electrons per pulse, thus favoring electron-electron interactions which generates spatial, temporal and energy broadening of the electron packets. This is the key phenomenon limiting the UTEM capabilities. It essentially occurs at the photocathode surface (while electrons are not accelerated yet, i.e. space charge) and in the crossovers (where many electrons are condensed in a narrow volume, i.e. Boersch effect).
It is shown that the Wehnelt bias has a decisive influence on the temporal and energy spread of the picosecond electron pulses. Depending on the shape of the cathode and the cathode-Wehnelt distance, different emission patterns with different pulse parameters are obtained. The energy spread of the pulses is determined by space charge and Boersch effects, given by the number of electrons in a pulse. However, filtering effects due to the chromatic aberrations of the Wehnelt electrode allow the extraction of pulses with narrow energy spreads. The temporal spread is governed by electron trajectories of different length and in different electrostatic potentials. High temporal resolution is obtained by excluding shank emission from the cathode and aberration-induced halos in the emission pattern. By varying the cathode-Wehnelt gap, the Wehnelt bias, and the number of photoelectrons in a pulse, tradeoffs between energy and temporal resolution as well as beam intensity can be made as needed for experiments. Based on the characterization of the electron pulses, the optimal conditions for the operation of ultrafast TEMs with thermionic gun assembly are elaborated. [1]

[1] Electron beam dynamics in an ultrafast transmission electron microscope with Wehnelt electrode. K. Bücker, M. Picher, *et al.* Ultramicroscopy 2016

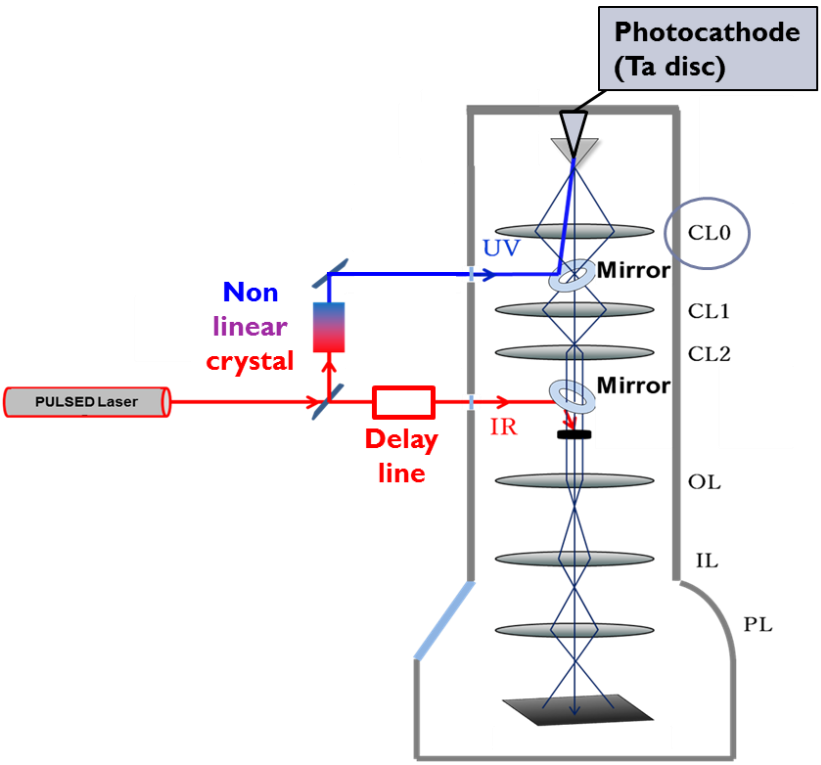

Figure 1. Simplified schematic drawing of an ultrafast TEM.

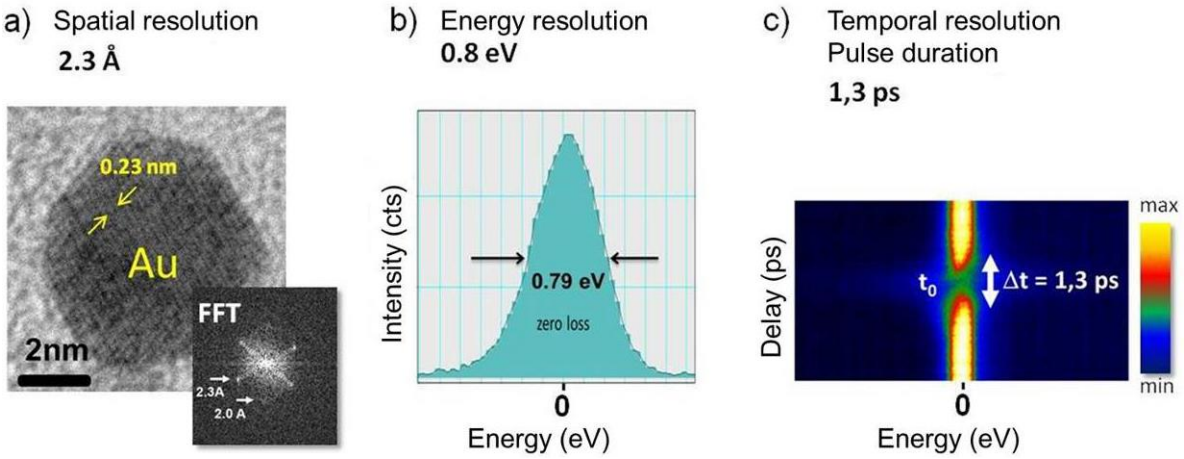

Figure 2. Resolution tests in stroboscopic mode a) Atomic resolution obtained with a gold nanoparticle b) Zero-loss peak showing the EELS resolution c) Pulse duration obtained via the photo-induced near field microscopy (PINEM) method [1].

IM2.P013
Investigation of solid state dewetting of Pt thin films by in situ transmission electron microscopy

C. Wiktor[1], F. Niekiel[1], L. Vogl[1], E. Spiecker[1]

[1]Friedrich-Alexander Universität Erlangen-Nürnberg, Institute of Micro- and Nanostructure Research & Center for Nanoanalysis and Electron Microscopy (CENEM), Erlangen, Germany

christian.wiktor@fau.de

Solid state dewetting of thin metal films describes their gradual transition into nanosized particles at temperatures well below the melting temperature of the metal.[1] It can be detrimental for electronic or magnetic devices,[2] but can also be used as a synthetic route to generate defined nanoparticle arrays.[3] Despite its importance there are only a few *in situ* studies about the dynamics of the process which could help in the design of more stable metal films for increasingly small devices or in the synthesis of highly defined nanoparticle/support structures.
Recently *in situ* Transmission Electron Microscopy (TEM) emerged as a powerful tool to gain insight into the kinetics of solid state dewetting and the underlying microscopic processes, including edge retraction, grain coarsening and texture evolution.[4,5] High quality TEM data can be obtained with the help of chip based heating systems featuring highly reduced sample drift compared to conventional TEM heating holders.
In this contribution we will focus on the solid state dewetting of thin Pt films which exhibit a strong tendency to develop a [111] texture upon dewetting. Our experiments prove this tendency to be dependent on the chosen temperature for the dewetting process. Figure 1 shows high angle annular dark field scanning TEM (HAADF-STEM) images of an initially continuous Pt thin film and of corresponding films after 15 min annealing at 500 °C, 600 °C and 700 °C (a-d), respectively. Below the HAADF-STEM images electron diffraction (ED) patterns of the respective samples are depicted (e-h). While the different degree of coverage with Pt is the intuitive result of the temperature dependent kinetics of the dewetting process, the ED patterns reveal differences in the developed texture. After treatment at 600°C almost all intensity in the pattern can be found in the reflections associated with {220} planes pointing to an almost exclusive [111] texture of Pt. At both lower and higher temperature a significant amount of intensity remains in reflections corresponding to {200} planes, pointing to a much less pronounced [111] texture.
As part of a general in depth characterization of the dewetting of Pt thin films, but in particular to study this unexpected texture development we combine *in situ* ED, HAADF- and ADF-STEM, hollow cone dark field TEM, and HRTEM. Based on a detailed statistical analysis we will present new insights into the kinetics of solid state dewetting and into the dynamic growth of crystal domains and its role in texture evolution.

[1] Thompson, C.V. Annu. Rev. Mater. Res., 42, 399-434 (2012), doi:10.1146/annurev-matsci-070511-155048.
[2] Han, G.C. and Wu, Y.H. and Luo, P. and Qiu, J.J. and Chong, T.C., Solid State Communications, 126, 479-484 (2003), doi:10.1016/S0038-1098(03)00182-0.
[3] Wang, D. and Schaaf, P., Phys. Status Solidi A, 210, 1544-1551 (2013). doi:10.1002/pssa.201200895.
[4] F. Niekiel, P. Schweizer, S.M. Kraschewski, B. Butz, E. Spiecker: Acta Materialia, 90, pp. 118-132, (2015), DOI: 10.1016/j.actamat.2015.01.072
[5] Niekiel, F. and Kraschewski, S.M. and Schweizer, P. and Butz, B. and Spiecker, E.: Acta Mater., 115, 230-241 (2016), doi:10.1016/j.actamat.2016.05.026.

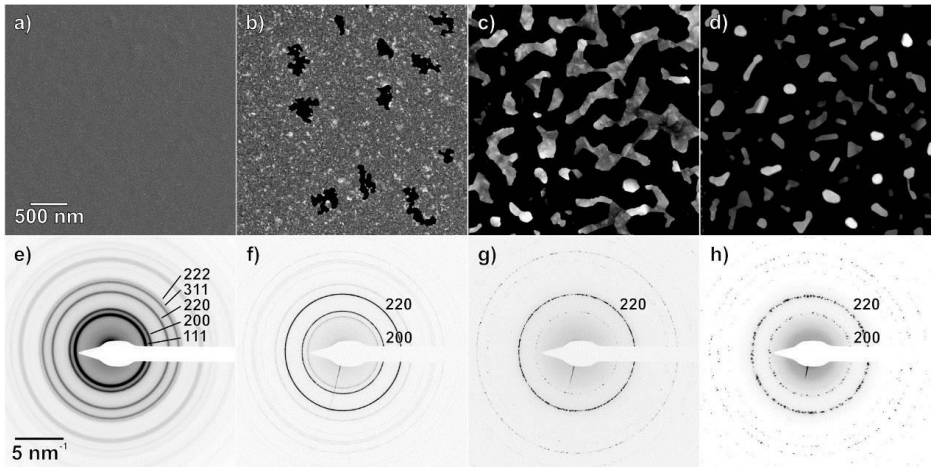

Figure 1. HAADF-STEM images of Pt thin films as synthesized (a) and after dewetting for 15 min at 500 °C (b), 600 °C (c), and 700 °C (d). e-h) Electron diffraction patterns of the respective Pt thin films.

IM2.P014
In situ HR-EBSD characterization during micro-mechanical testing

X. Maeder[1], J. Ast[1], Y. Guo[1], J. Michler[1]

[1]Empa, Thun, Switzerland

xavier.maeder@empa.ch

Introduction: The constant progress in miniaturization of micro-mechanical parts brings the necessity to assess and understand the deformation mechanism of materials at small scale. SEM in-situ nanoindentation has widely emerged as the technique of choice since it allows routine testing of small volumes of materials in a highly controlled fashion and with high data resolution. It has been adapted for compression, shearing and bending tests of various micron-sized sample geometries to study size effects, time dependent plasticity, fracture toughness and host of other mechanical properties. We recently developed the technique in order to do in-situ electron backscatter diffraction (EBSD) during micro-mechanical testing. Combined with cross-correlation technique (HR-EBSD), the strain/stress field and the GNDs distribution can be mapped at several steps during progressive deformation [1-2].
Objectives: We applied in-situ HR-EBSD during micropillar compression in titanium in order to understand how local stress field and dislocation distribution influence twin formation and evolution. In-situ HR-EBSD was also applied to microcantilever bending in order to understand the scale effect in bending strength and fracture toughness.
Materials and Methods: The in-situ mechanical tests were done with an in-house developed Alemnis indenter in a FIB-FEGSEM Tescan Lyra microscope. Micropillars of 5 x 5 x 15 µm have been fabricated in polycrystalline titanium for compression. For bending and fracture toughness experiments, both notch and un-notch cantilevers were fabricated with dimensions of ca. 5-7 µm in width and height and ca. 25 µm in length in single crystal tungsten.
Results: The local shear stress on the active twin variant has been determined and compared to the global shear stress determined by the pillar compression. The results show that the active twin variant that forms during compression doesnt have the highest global shear stress but a higher local shear compared with other twin variants. The experiments show that elongation of the active twin involves a competition between local shear stress and dislocation density in front of twin tip, which leads to a discontinuous elongation process.
Results on un-notched tungsten cantilevers bending experiments show that the stress measured by HR-EBSD compared well with the beam bending theory in the elastic regime. With further deformation, locally increased yield and flow stresses were linked to pronounced stress gradients on {110} and {112} slip planes. It is shown that dislocations tend to pile-ups at the neutral axes of the beam, where the stress is zero. The experiments on notched cantilever show dislocation emission from the crack tip on {110} planes already shortly prior to crack propagation (Fig.1). These dislocations were found to leave the specimen at the free surfaces and their contribution to efficient crack tip shielding is therefore negligible. With further deformation and stable crack propagation, dislocations were progressively generated at the crack tip, shielding the crack from propagating.
Conclusions: In-situ HR-EBSD during mechanical testing is a powerful technique to assess the microstructure, the local stress and the dislocation distribution evolution in materials at different deformation steps. All these information can give new insights to understand small scale deformation mechanisms in materials. It can be applied to different materials system and geometries such as pillars, beams, tensile and shear specimen.

[1] Guo, Y., Schwiedrzik, J., Michler, J., Maeder, X., Acta Materialia 120, 292-301, (2016).
[2] Ast, J., Mohanty, G., Guo, Y., Michler, J., Maeder, X., Materials & Design 117, 265-266, (2017).

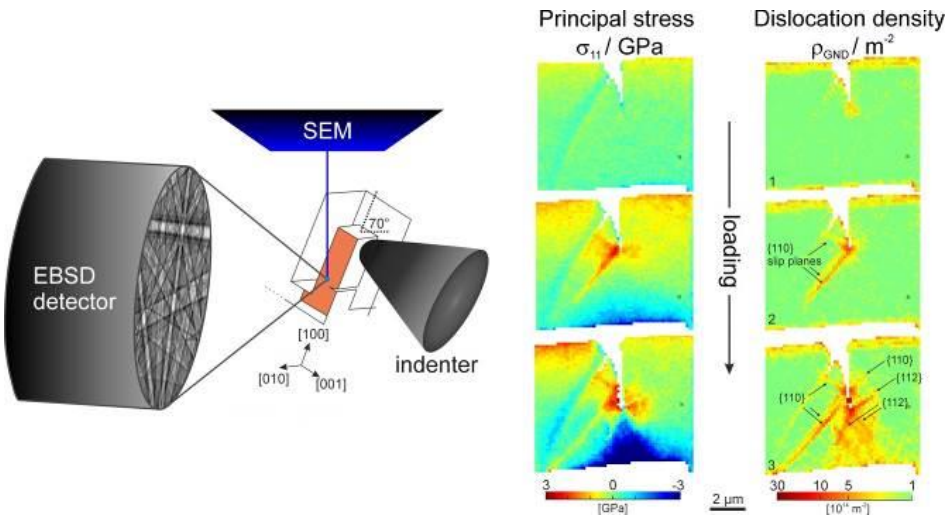

Figure 1. Left: Schematic illustration of the in-situ EBSD setup for notched cantilever bending. Right: EBSD stress and GND density maps around the crack tip at different deformation steps, respectively, unloaded state, right prior to crack propagation and after crack propagation.

IM2.P015
Towards on-chip in situ biasing of FIB/SEM-prepared TEM-lamellas

U. U. R. Hömpler[1], D. Berger[2], T. Niermann[1], M. Lehmann[1]

[1]TU Berlin, IOAP, Berlin, Germany
[2]TU Berlin, Zentraleinrichtung Elektronenmikroskopie ZELMI, Berlin, Germany

hoempler@physik.tu-berlin.de

Electron holography, a special TEM technique, gives access to the phase of the electron wave, which is directly related to the electrostatic potential and the sample thickness [1]. Especially in combination with FIB, TEM-lamellas with a constant sample thickness over a wide area are realizable [2]. The band bending in semiconductors (e.g. p-n junctions) is caused by several contributions: defects, current, doping, electron-hole-pair generation by the incident electron beam, or external bias. Retrieving the potential drop from the phase is not trivial. By manipulating the junction by an electrical bias, the potential drop at the p-n junction can be distinguished from other phase contributions.
First attempts were made with an electron transparent lamella at the edge of a piece of wafer [3]. The macroscopic sample size of 1 mm x 1 mm however does not guarantee a current flow through the lamella itself. Another approach is the in-situ microprobe needle contact [4].
Here, a TEM-lamella is placed on a chip and contacted by Pt-deposition. The base for the experiment is a MEMS chip from DENSsolutions. The electrical circuit of the chip was opened by a 5 µm wide gap by FIB. Afterwards the insulating surface layer was removed. Resistance measurements confirm two insulated contacts ($R = (2.0 \pm 0.1)\ G\Omega$). The lamella was cut out of a silicon wafer with a symmetric n-p junction [5, 8]. An advanced FIB/SEM-preparation recipe for tilted lift-off has been developed [6]. The n and p side of the sample were fixed at the contacts by ion beam deposited platinum (fig. 1). By means of the ion beam, the platinum contaminated area around the sample was removed and the surface of the lamella was polished. The edge of the sample between the contacts was thinned under a small angle. The following TEM-investigations were done at 300 kV acceleration voltage.
In the reconstructed phase (fig. 2a) the different layers (e.g. n-p junction) are clearly visible. The phase difference between biased and unbiased conditions is shown in figures 2b/c. Direction and slope of the phase gradient depend on the sign and the magnitude of the applied voltage. The corresponding IV-curve is presented in figure 3. The cause for the non-visibility of the junction in figures 2b/c could be problems with the electrical contact. In addition, the shape of the IV-curve indicates further current paths which can bypass the diode.
Platinum contamination on or implanted gallium ions in the surface of the TEM-lamella are possible sources for the bypass. Manufacture of better electrical contacts and reduction of additional current paths will be faced. Approaches like wet chemical etching [7], ion milling, and annealing [5] will be investigated in respect to demonstrate a bias dependence inside the n-p junction of the TEM-lamella.

[1] H. Lichte & M. Lehmann, Advances In Imaging And Electron Physics **123**, 2002
[2] M. H. F. Overwijk et al., Journal of Vacuum Science & Technology B **11**, 1993
[3] A.C. Twitchett et al., Phys. Rev. Lett. **88**, 2002
[4] K. He et al., Nanotechnology **24**, 2013
[5] D. Cooper et al., Journal of Applied Physics **104**, 2008
[6] D. Berger et al., Advanced TEM-Lamella Preparation with FIB/SEM, these proceedings.
[7] Z. Han et al., Nanotechnology **26**, 2015
[8] We thank David Cooper (CEA, Leti) for providing the samples.
[9] We kindly acknowledge the support from the DFG within the Collaborative Research Center 787, project A4.

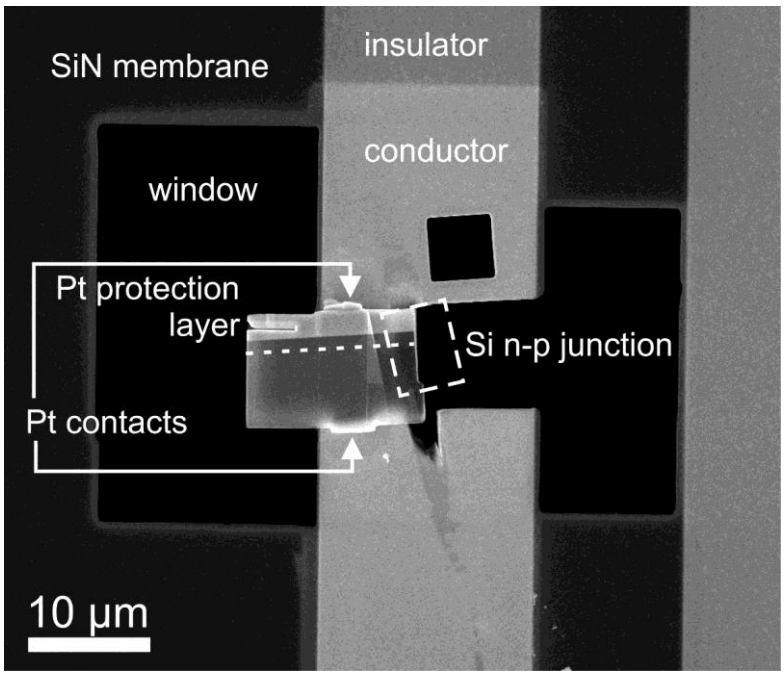

Figure 1. SEM image of an electrical contacted TEM-lamella on a modified MEMS chip.

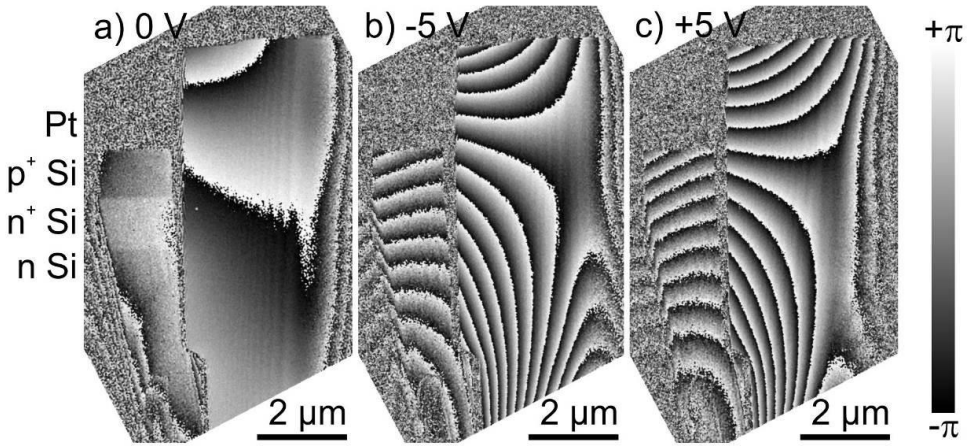

Figure 2. a) The reconstructed phase of a symmetric silicon n-p junction without an applied bias. The phase difference between 5 V b) reverse / c) forward biased and unbiased conditions.

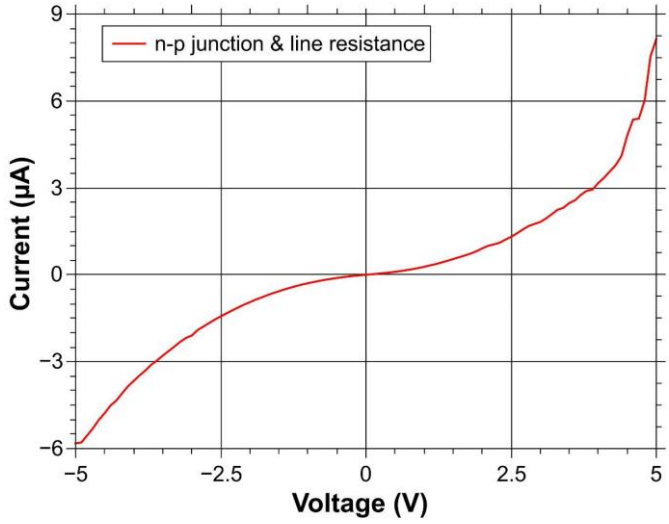

Figure 3. Measured macroscopic current in dependence of the applied voltage.

IM2.P016
An optimized methodology to analyze biopolymer capsules by environmental scanning electron microscopy

E. Conforto[1], N. Joguet[2], P. Buisson[3], J. E. Vendeville[4], C. Chaigneau[4], T. Maugard[2]

[1]University of La Rochelle, LaSIE UMR 7356 CNRS-ULR, La Rochelle, France
[2]University of La Rochelle, LIENSS UMR 7266 CNRS-ULR, La Rochelle, France
[3]INNOV'IA, La Rochelle, France
[4]INNOV'IA, IDCAPS R&D, La Rochelle, France

egle.conforto@univ-lr.fr

Introduction: Encapsulation is used in food, feed, cosmetic and pharmaceutics industries to protect various bioactive molecules like vitamin, peptide, aromas or pigments from the environment, acting as a barrier. The development of a successful encapsulation process is based on the properties of the material used for coatings and on the control of the delivery capability. SEM analyses of non-conductor capsules under high vacuum requires the deposition of a metallic film on the surface to avoid the accumulation of electrical charges and to prevent heat damage. However, metallization is not suitable in many cases because it recovers roughness and porosities of the coating surface, and masks important information as micro-cracks. Environmental scanning electron microscopy (ESEM) has been recently used as an alternative to observe non-conductors and/or hydrated samples [1-3] without any preparation, by introducing a low pressure of water vapor, gas or air in the specimen chamber. Analyses can be performed at high accelerating voltage with good resolution in images and Energy Dispersive Spectroscopy (EDS) spectra, without peaks from the metal coverage. In the literature SEM images often aim to show morphological aspects of capsules as shape and size, with few information on sample preparation and/or observation parameters [4,5]. No study correlating these parameters to results was found, in spite of its importance to correctly evaluate capsule characteristics.
Objectives: An optimized methodology using ESEM is proposed, which is able to provide information on the adequacy of capsule fabrication process and the functionality of its original surface.
Materials and Methods: Capsules containing garlic extract in hydrogenated vegetable oil (labeled « A ») and capsules constituted of sodium chloride coated by gelatin or by hydrogenated vegetable oil ("B") have been observed by ESEM using a FEI Quanta 200 ESEM/FEG equipped with an EDAX-Genesis EDS, in the 3.5–20 kV accelerating voltage range. The water vapor pressure was varied between 0.9 and 2.0 mbar. Thin gold films were sputtered on some samples to be observed in high vacuum mode for comparison.
Results: In the left column of Fig. 1, the cross-section of a "A" capsule before metallization is compared to images after metallization, in the column at right. These latter show some smoothed roughness, some artificial shadows and contrasts, and partially or completely recovered cavities and filaments.
Figures 2a, b show the morphology of uncoated "B" salt capsules which is not affected by the water vapor from the ESEM mode. In Figure 2c, d, BSE images of the salt coated with gelatin allows evaluating the coating permeability and the coating-core interactions. The same information is shown in Figs. 2e, f where capsules were covered by fat. Fine details of gelatin and mainly of fatty coatings can be observed. For some stable fatty molecules like stearic acids, C/O ratio has been successfully measured by environmental EDS through a careful choice of analysis parameters. The same procedure is in progress for other fats and sugars.
Conclusion: This methodology provides a reliable evaluation of the parameters used in capsule elaboration for research and industrial applications, as well as that of capsule functionality which is essential for the technological progress in this domain.

[1] James B (2009), Trend *Food Sci. Technol*. 20:114–124.
[2] Muscariello L et al. (2005), *J. Cell. Physiol*. 205:328–334.
[3] Conforto E et al. (2015) Mat. Sci. Eng. C 47 :357-366
[4] Bugra O (2012) *J. Environ. Manag*. 100: 22–28.
[5] Paques JP, van der Linden E, van Rijn CJM, Sagis LMC (2013), *Food Hydrocoll*. 31:428–434.

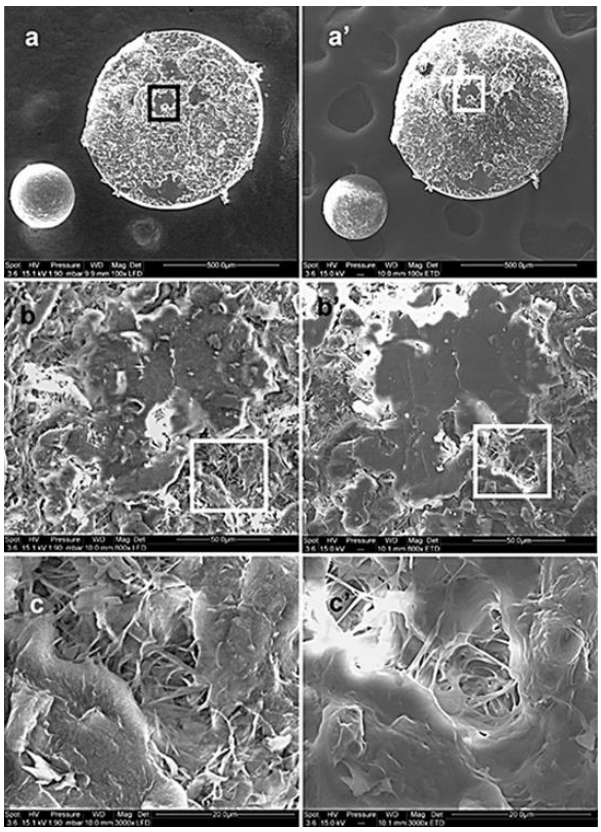

Figure 1. "A" capsules in cross-section. Column at left: ESEM images before metallization. Column at right: secondary electron (SE) images in high vacuum mode after metallization, where some parts are partially or completely recovered.

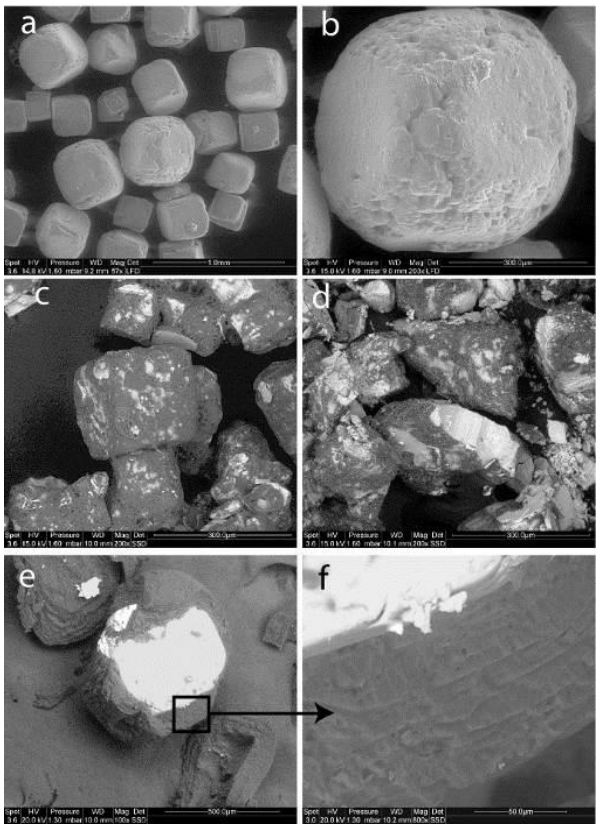

Figure 2. ESEM images of "B" salt capsules. a, b) SE images of uncovered capsules; Backscattered Electron images of the same capsules covered with: gelatin (c, d); and fat (e, f).

IM2.P017
In situ aberration-corrected TEM observations of carbon nanotube based molecular motors at low voltages

K. Cao[1], J. Biskupek[1], T. Zoberbier[1], C. Stoppiello[2], R. McSweeney[2], T. W. Chamberlain[2,3]
A. Khlobystov[2], U. Kaiser[1]

[1]Ulm University, Central Facility for Electron Microscopy, Ulm, Germany
[2]University of Nottingham, School of Chemistry, Nottingham, United Kingdom
[3]University of Leeds, School of Chemistry, Leeds, United Kingdom

kecheng.cao@uni-ulm.de

Question: Single-walled carbon nanotubes (SWNTs) are promising materials to realize the controllable transport of molecules due to their narrow cylindrical cavities. Time-resolved in-situ transmission electron microscopy (TEM) imaging with atomic resolution enables direct visualization of molecular motion in SWNTs. The back and forth translations of a carbon capsule, a LaC_2 nanocrystal, and C60 molecules in SWNTs have been recently reported.[1-3] However, understanding of the driving force and mechanisms of such nanoscale molecular motion is still incomplete and requires substantial further work in order to control and harness it for real-life applications.
Methods: In this study, SWNTs were filled with ferrocene molecules,[4] and subsequently converted into Fe nanoparticles and Fe-carbon compounds in the lumen of the SWNTs by electron beam irradiation. The atomic structure of the formed nanoparticles as well as their motion are captured and recorded by a spherical (C_S)-corrected FEI Titan 80-300 at 80 kV and a spherical/chromatic (C_S/C_C)-corrected SALVE (Sub Angstrom Low Voltage Election Microscope) TEM[5,6] at 30 and 40 kV.
Results and Conclusion: The characteristic shuttling motion of the Fe clusters, amorphous carbon and their composite stimulated and recorded at different low voltages are shown in Figure 1. The reciprocating motions of the nanostructures at lower voltages (40 kV and 30 kV, Figure 1B and 1C) are much faster than the motion at higher voltage (80 kV, Figure 1A). In addition, some specific SWNT based molecular motors are expected to oscillate forever when irradiated by a constant electron beam, such as the motion of the Fe cluster shown in Figure 1B. We demonstrate that electrostatic repulsion due to ionization of the nanoparticles by the electron beam may be the most likely force propelling the nanoparticles during their translational motion. These SWNT based molecular motors show the possibility to be applied to assemble nanodevices.

References:
[1] Hiroshi Somada *et al. Nano Lett.* **2009**, *9*, 62-65.
[2] Jamie H. Warner *et al. ACS Nano.* **2009**, 3, 3037-3044.
[3] Ke Ran *et al. ACS Nano.* **2011**, 5, 3367-3372.
[4] Thilo Zoberbier *et al. Small.* **2016**, 12, 1649–1657.
[5] Martin Linck *et al. Phys. Rev. Let.* **2016**, 117, 076101.
[6] www.salve-project.de

Acknowledgment
We acknowledge the support of the DFG and the Ministry of Science, Research and the Arts (MWK) of Baden-Wuerttemberg within the frame of the SALVE project, China Scholarship Council (CSC), ERC Consolidator Grants and EPSRC for financial support.

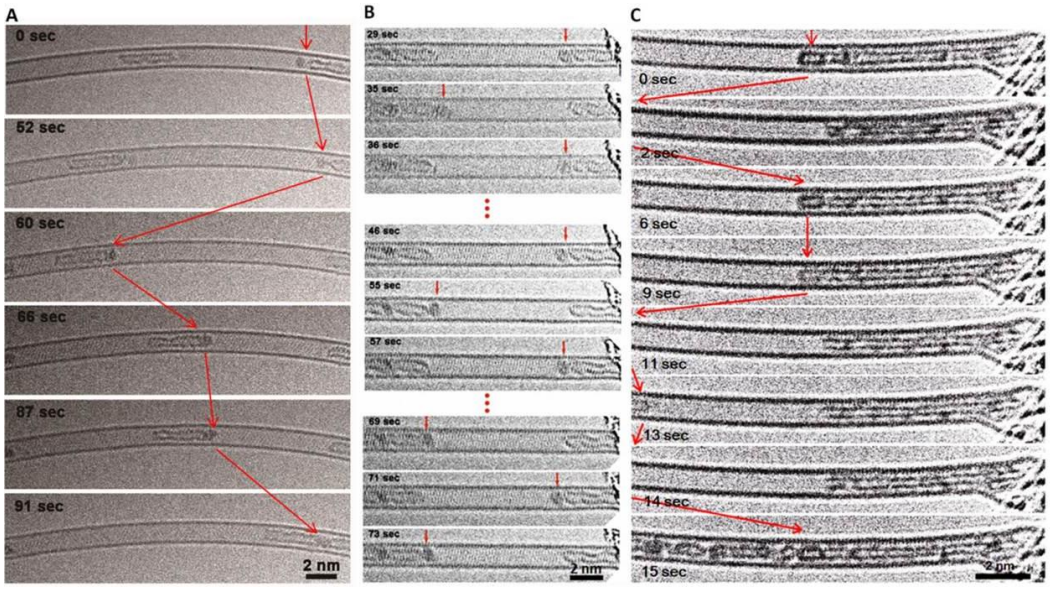

Figure 1. HRTEM time series showing SWNT based molecular motors. (A) The Fe cluster and the Fe-carbon nanostructure translate in the SWNT during irradiation by the election beam at 80 kV. (B) A Fe cluster shuttles back and forth in the SWNT during irradiation by the 40 kV electron beam, the motion lasts over 73 seconds. (C) The carbon nanostructures move back and forth in the SWNT during irradiation by the 30 kV electron beam.

IM2.P018
In situ SEM mechanical testing under biaxial stress conditions using a newly developed deformation rig

M. Smid[1], E. Polatidis[1], W. N. Hsu[1], S. Van Petegem[1], H. Van Swygenhoven[1,2]

[1]Paul Scherrer Institut, Photons for Engineering and Manufacturing, Villigen PSI, Switzerland
[2]Ecole Polytechnique Federale de Lausanne, Neutrons and X-rays for Mechanics of Materials, Lausanne, Switzerland

miroslav.smid@psi.ch

Introduction: Industrial processing of metal sheets usually consists of several forming steps during which a sheet undergoes uniaxial, biaxial straining or strain path changes. Moreover, these abrupt changes of straining direction can lead to different mechanical behavior depending on previous deformation history [1,2]. Materials properties are predominantly measured under uniaxial conditions. Therefore, mechanical models based solely on results from uniaxial tests are not able to predict accurately properties under biaxial or strain path loading conditions.
In situ techniques are capable of bringing insight into the deformation mechanisms under complex loading conditions. Despite the devices enabling *in situ* testing on a synchrotron instruments or in a SEM are complicated to design and have some instrumental limitations (i.e. small loading capacity, geometrical restrictions etc.), these techniques motivate research groups worldwide to construct their own multiaxial testing systems [3, 4].
In order to enable in-situ SEM or Synchrotron X-ray Diffraction (SXRD) tests, a new biaxial testing rig has been developed recently [5]. After application of a speckle pattern on the specimen surface, SEM images were subsequently analysed by digital image correlation (DIC) in order to obtain full-field strain maps. This analysis can precisely describe the heterogeneous distribution of the plastic strain on a selected area of interest. This contribution will present the design of the biaxial rig, the optimization of the cruciform shaped specimens, the application of DIC and the first results conducted on superelastic NiTi alloys.
Objectives: The aim of the newly developed biaxial rig is to enable *in-situ* SEM and SXRD mechanical testing of materials under a wide range of in-plane stress states which will help understanding multiaxial strains during processing or service conditions.
Materials and Methods: The investigated material was superelastic NiTi alloy acquired by Memry GmbH (Germany) in form of 80 µm sheets. Initial structure of material consist of strongly textured grain structure with average grain size of 27 µm. Grains are fragmented into very fine subgrain structure with average size approximately 40 nm. The geometry of the cruciform shaped specimens was optimized with respect to the mechanical properties of NiTi. *In situ* tests were conducted on a FE-SEM Carl Zeiss ULTRA 55 by employing the above mentioned deformation rig. Digital image correlation analysis was done using NCorr software [6].
Results: The specimen geometry was optimized by finite element analysis in order to avoid stress concentrations outside the studied central region of the cruciform that could promote undesired failure. Fabrication of the specimens has been done by employing a picosecond laser ablation. The superelastic NiTi alloy specimens were subjected to deformation under uniaxial and strain path change while SEM images were obtained for DIC analysis. Full-field strain maps revealed the traces of stress-induced martensite. The localization of the transformation was followed and the variant selection was correlated to the loading condition.
Conclusions: First results of the new biaxial rig indicate great possibilities of *in situ* SEM mechanical testing for various metals under complex stress states. The results show the importance of application of this technique, particularly, on phase transformation materials for revealing the localization of the martensitic transformation and its variant selection under different loading states or strain path changes.

This research is performed within the ERC Advanced Grant MULTIAX (339245).

References:
[1] J.H. Schmitt et al. *Mater Sci Eng A* **75** (1991) 143.
[2] F. Barlat et al. *Acta Mater* **48** (2000) 2123.
[3] C.C. Tasan et al. *Exp Mech* **52** (2011) 669.
[4] Van Petegem et al. *Acta Mater* **105** (2016) 404.
[5] S. Van Petegem et al. *Exp Mech* (2017), in press, DOI: 10.1007/s11340-016-0244-0.
[6] J. Blaber et al. *Exp Mech* **55** (2015) 1105.

IM2.P019
Coherent control of free-electron beams for temporal shaping on the attosecond time scale

C. Rathje[1], K. E. Priebe[1], S. V. Yalunin[1], A. Feist[1], T. Hohage[2], S. Schäfer[1], C. Ropers[1]

[1]IV. Physical Institute - Solids and Nanostructures, University of Göttingen, Göttingen, Germany
[2]Institute for Numerical and Applied Mathematics, University of Göttingen, Göttingen, Germany

rathje@ph4.physik.uni-goettingen.de

Ultrafast transmission electron microscopy (UTEM) combines the femtosecond temporal resolution of ultrafast laser systems with the nanometer spatial resolution of a TEM. Besides being a powerful tool for studying ultrafast dynamics, UTEM allows for the coherent manipulation of free-electron quantum states by inelastic electron-light scattering. The light-field imprints a sinusoidal phase modulation on the electron wavefunction which gives rise to the formation of photon sidebands in the electron kinetic energy spectrum [1, 2]. The Göttingen UTEM features a nanoscale Schottky field-emitter providing highly spatially coherent electron beams which allows for strongly localized probing [3]. This is crucial to revealing the quantum coherent characteristics of the electron-light interaction, which are otherwise masked by spatial averaging effects.
Recently, we demonstrated that the electron-light scattering exhibits field-dependent multi-level Rabi-oscillations in the population of photon sidebands, illustrating the quantum coherence of the process [2]. By utilizing intense tailored optical near-fields, the electron-light interaction can be precisely controlled, enabling the manipulation of single-electron quantum states [2, 4].
In a recent study, we investigated the reversibility of the electron-light interaction [4]: By illuminating a tailored nanostructure, we created two spatially-separated optical near-fields acting on the electron beam. Realizing a Ramsey-type dual interaction, we observed a final kinetic energy distribution that strongly depends on the relative phase of these two near-fields. Furthermore, we studied the electron quantum state employing two-color phase-controlled near-fields [5], probing and reconstructing the single-electron quantum state.
In this contribution, we review these recent works and discuss the possibility to use the control of the free-electron quantum state for a manipulation of the time-dependent electron density (see fig. 1). After a first interaction, dispersive propagation in free space leads to self-compression of the electron density, which results in the formation of an attosecond pulse train [2]. By probing the quantum state with a second near-field, we will be able to retrieve the temporal shape of the electron density. Finally, we describe our progress towards experimentally demonstrating temporal focusing of the free-electron beam.
More generally, the quantum coherent interaction of electrons with light is a promising approach for the temporal structuring of free-electron beams, which may find application in optically phase-resolved electron imaging, diffraction and spectroscopy with attosecond precision.

[1] Barwick et al., Nature 462, 902 (2009)
[2] Feist et al., Nature 521, 200-203 (2015)
[3] Feist et al., Ultramicroscopy (2016)
[4] Echternkamp et al., Nat. Phys. 12, 1000-1004 (2016)
[5] Priebe et al., in preparation

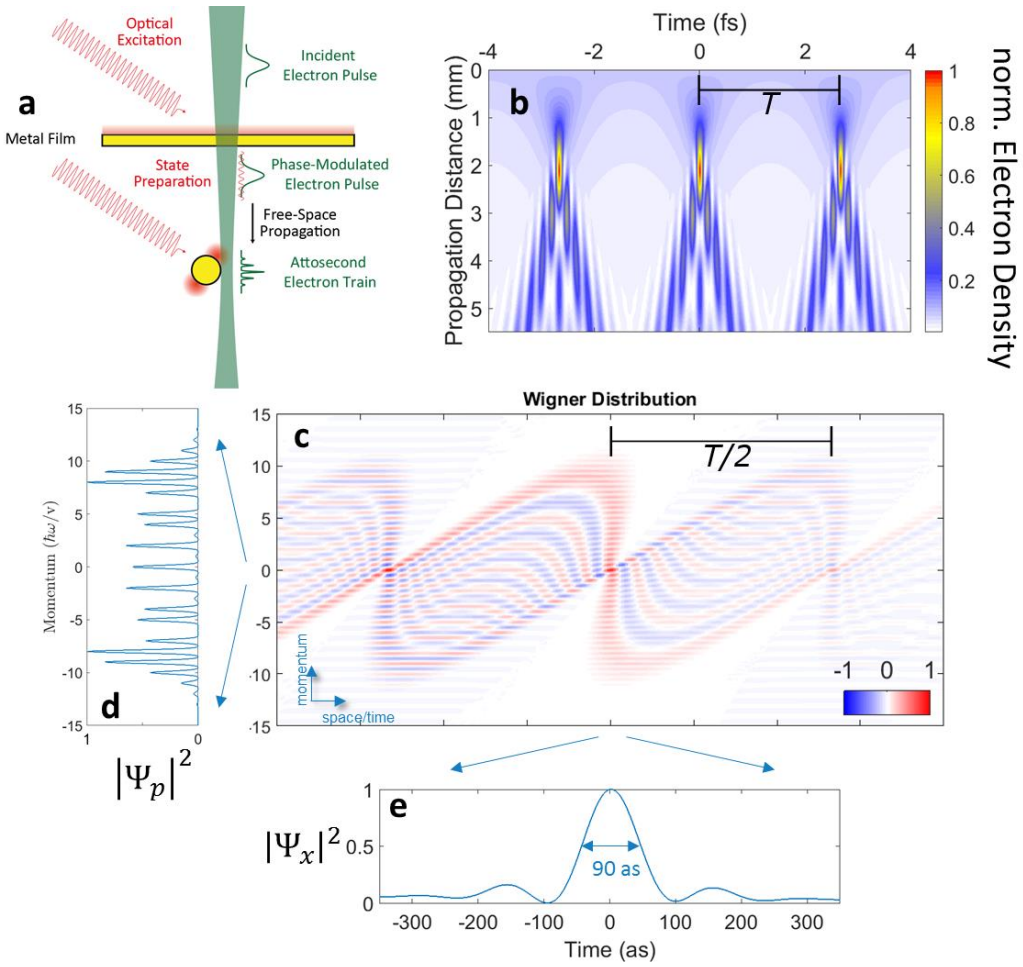

Figure 1. a) A highly coherent electron pulse sequentially interacts with two optical near-fields. The first interaction prepares a coherent superposition of momentum states. Dispersive propagation leads to a temporal reshaping of the electron density probed by a second interaction. b) Formation of a train of attosecond spikes in the electron density, separated by the optical period *T*. c) The Wigner function represents the quantum state for 2.15 mm propagation distance (temporal focus). d) The projection onto the momentum axis corresponds to the electron energy spectrum after the first interaction. e) The projection onto the time axis results in peaks of about 90 as FWHM duration. b)-e) adapted from ref. [2].

IM2.P020
A novel approach for site-specific preparation and quantitative in situ tensile testing of thin silica glass membranes in the TEM

M. Mačković[1], T. Przybilla[1], C. Dieker[1], P. Herre[2], S. Romeis[2], H. Stara[1], N. Schrenker[1], W. Peukert[2] E. Spiecker[1]

[1]Institute of Micro- and Nanostructure Research and Center for Nanoanalysis and Electron Microscopy, Department of Materials Science and Engineering, Erlangen, Germany
[2]Institute of Particle Technology, Department of Chemical and Biological Engineering, Erlangen, Germany

mirza.mackovic@fau.de

The mechanical properties of glasses in the micro- and nanometer regime increasingly gain importance in nowadays modern nanotechnology. However, suitable small scale preparation and mechanical testing approaches for a reliable evaluation of the mechanical properties of glasses are currently lacking. In particular in case of silica glass, *in situ* micromechanical testing in the scanning electron microscope (SEM) is reported for specimens in pillar geometry [1,2]. Moreover, *in situ* micro- and nanomechanical testing of vitreous silica spheres is demonstrated in the SEM and transmission electron microscope (TEM) [3,4]. The objective of the present work was to develop a reliable method for the preparation and *in situ* tensile testing of silica glass, and, hence, to establish a way to assess its mechanical behavior at nanometer scale.
To achieve this, dog bone shaped silica glass tensile specimens are prepared by advanced focused ion beam (FIB) techniques on push-to-pull (PTP) devices (Fig. 1) and *in situ* tensile testing was performed with the PI95 TEM Picoindenter (Hysitron, Inc., USA) inside the Titan3 Themis 300 (FEI Company, Netherlands) [5]. *In situ* tensile testing of silica glass membranes under electron beam (e-beam) irradiation results in distinctive elongations confirming the phenomenon of superplasticity (Fig. 2) [5], previously shown for sol-gel derived amorphous silica fibers in the TEM [6]. E-beam-induced ductility of nanoscale silica spheres was reported from *in situ* compression testing inside the TEM [7,8]. The silica glass membrane pulled under e-beam irradiation exhibits a Young"s modulus (*E*) of 49 GPa, which is clearly below values known for bulk fused silica [9], and most probably caused by e-beam-induced softening of the silica network structure, both, reducing its rigidity and promoting plastic flow [5]. The switching off the e-beam during initial *in situ* tensile testing of a silica glass membrane under e-beam irradiation (Fig. 3) directly evidences the impact of the e-beam on the mechanical behavior of nanoscale silica glass. Under e-beam irradiation the silica glass membrane shows an elastic/plastic deformation behavior, which switches to purely elastic starting from the point where the e-beam is blanked. At beam off conditions, the membrane exhibits an E = 78 GPa, which is in the range of bulk fused silica [9] and silica nanowires with comparable dimensions [10].
In conclusion we have presented a novel approach combining advanced FIB preparation and quantitative *in situ* tensile testing of silica glass, and obtained valuable insights into its nanomechanical behavior.

References:
[1] R. Lacroix et al., *Acta Mater.* 2012, *60*, 5555.
[2] G. Kermouche et al., *Acta Mater.* 2016, *114*, 146.
[3] J. Paul et al., *Powder Techn.* 2014, *270*, 337.
[4] S. Romeis et al., *Scr. Mater.* 2015, *108*, 84.
[5] M. Mačković et al., *Front. Mater.* 2017, *4*:10. doi: 10.3389/fmats.2017.00010
[6] K. Zheng et al., *Nature Commun.* 2010, *1*, 24.
[7] M. Mačković et al., *Acta Mater.* 2014, *79*, 363.
[8] M. Mačković et al., *Scr. Mater.* 2016, *121*, 70.
[9] T. Adachi et al., *J. Mater. Sci.* 1990, *25*, 4732.
[10] E.C.C.M. Silva et al., *Small* 2006, *2*, 239.

Acknowledgments
Financial support by the Deutsche Forschungsgemeinschaft (DFG) through the SPP1594 "Topological Engineering of Ultra-Strong Glasses", Cluster of Excellence EXC 315 "Engineering of Advanced Materials" and GRK1896 "In situ microscopy with electrons, X-rays and scanning probes" is gratefully acknowledged.

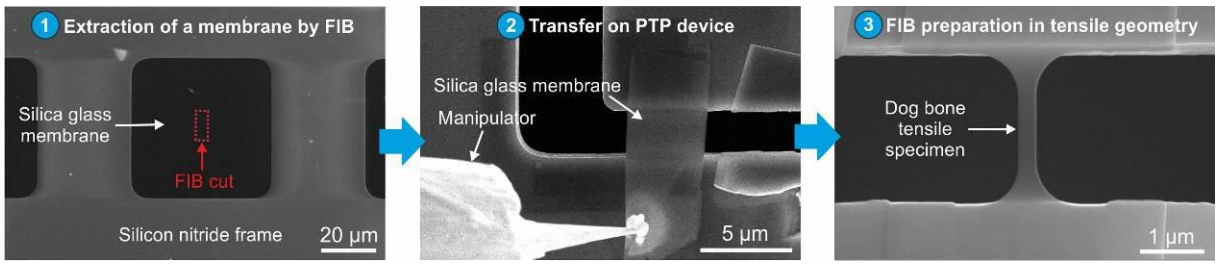

Figure 1. FIB-based approach for site-specific preparation of silica glass membranes on PTP device suitable for *in situ* tensile testing inside the TEM. Reprinted from [5], Copyright Frontiers in Materials.

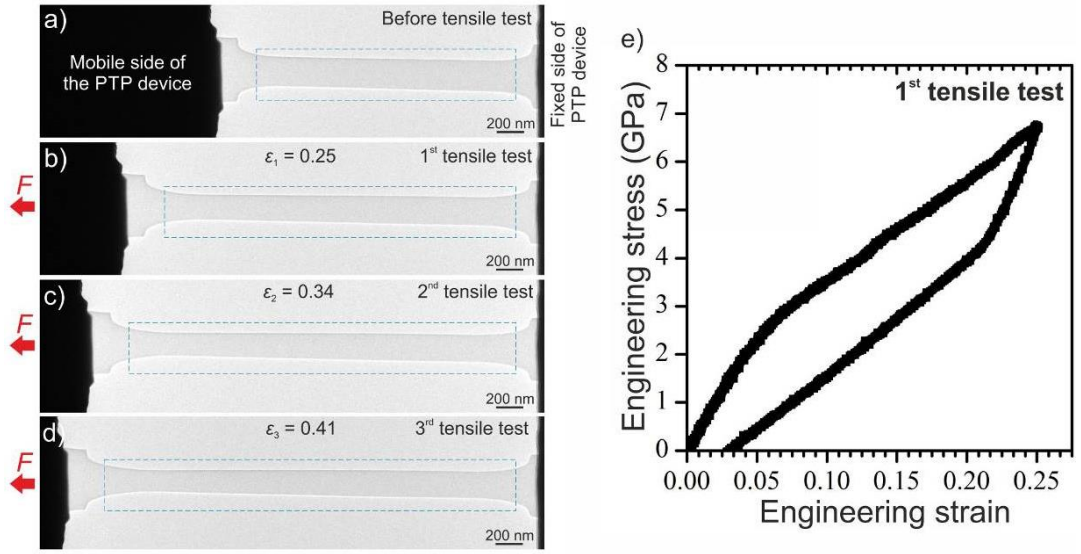

Figure 2. *In situ* tensile testing of a silica glass membrane under e-beam irradiation in the TEM. The specimen is pulled interruptedly to different strains (a-d). In e) the stress-strain response of the silica glass membrane is shown. Reprinted from [5], Copyright Frontiers in Materials.

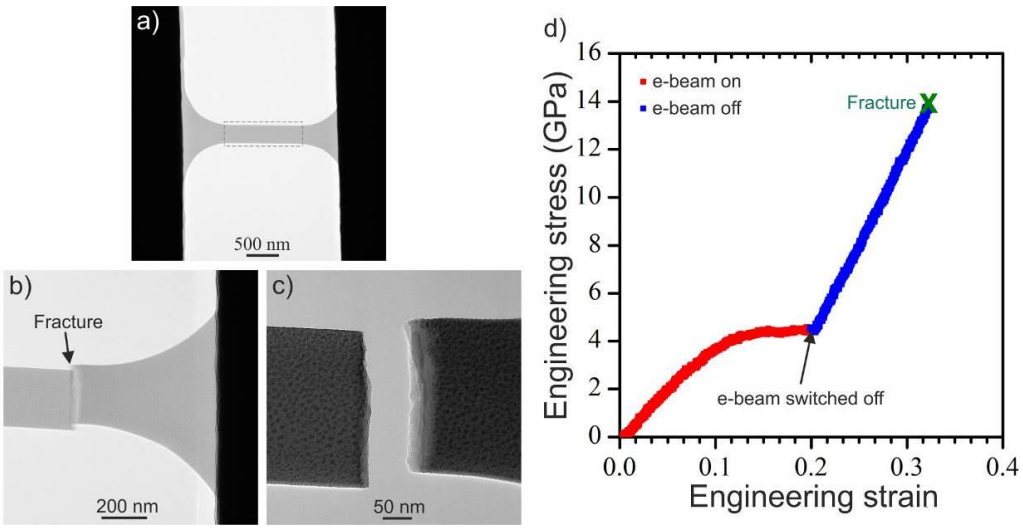

Figure 3. *In situ* tensile testing of a silica glass membrane under initial e-beam irradiation and at beam off conditions. TEM images show the membrane a) before, and b) and c) after the tensile test. In e) the mechanical properties of the membrane are shown. Reprinted from [5], Copyright Frontiers in Materials.

IM2.P021
Site-specific preparation and in situ mechanical testing of nanoscale fused silica pillars in the TEM and SEM

M. Mačković[1], T. Przybilla[1], P. Herre[2], S. Romeis[2], J. Paul[2], N. Schrenker[1], W. Peukert[2], E. Spiecker[1]

[1]Institute of Micro- and Nanostructure Research and Center for Nanoanalysis and Electron Microscopy, Department of Materials Science and Engineering, Erlangen, Germany
[2]Institute of Particle Technology, Department of Chemical and Biological Engineering, Erlangen, Germany

mirza.mackovic@fau.de

Although the advancement of modern nanotechnology increasingly pushes glasses to an improved mechanical reliability, the assessment of their mechanical properties, in particular on smaller scales, still remains a big challenge. While on the micrometer scale *in situ* mechanical testing of silica glass pillars [1] and vitreous silica spheres [2] was demonstrated in the scanning electron microscope (SEM), data on the mechanical behavior of glasses in the submicron regime are largely lacking. Extensive *in situ* mechanical testing of nanoscale, sol-gel derived and vitreous silica spheres was reported in the SEM and the transmission electron microscope (TEM) [3-7]. The objective of the present work was to develop a method for site-specific preparation of nanoscale fused silica in pillar geometry, suitable for *in situ* mechanical testing in the TEM and SEM, and on which bases quantitative mechanical data can be obtained on nanoscale.
Nanoscale fused silica pillars are prepared by focused ion beam (FIB) in combination with a charge neutralizer system, leading to pillar structures with a reproducible geometry suitable for *in situ* mechanical testing (Fig. 1 and Fig. 2). *In situ* nanomechanical testing was performed with the PI95 TEM Picoindenter (Hysitron, Inc., USA) in the TEM and a micromanipulator system inside the SEM. The combinatorial application of these two systems allows for scale-bridging *in situ* mechanical testing in electron microscopes. A pillar compressed at smaller strains and beam off conditions in the TEM exhibits a fully elastic deformation behavior without fracture (see Fig. 1). While the Young"s modulus of 78 GPa is in the range, the compressive strength of ≥ 8 GPa clearly exceeds values known for bulk fused silica [8] and microscale amorphous silica pillars [9]. *In situ* compression testing of fused silica pillars to larger strains in the SEM results in an elastic/plastic deformation behavior and finally leads to fracture of the pillars (see Fig. 2). *In situ* compression experiments on pillars in the TEM and SEM are currently carried out, with the aim to explore their overall size-dependent mechanical behavior in direct relation to our previous work on nanoscale glass spheres [5]. In addition, Raman spectroscopy is performed on samples before and after FIB preparation, with the aim to evaluate possible damage induced by ion beam irradiation and its impact on mechanical properties of fused silica. Just recently we have shown that ion beam irradiation causes densification of silica glass during FIB preparation of tensile specimens suitable for *in situ* tensile testing in the TEM [10].
In conclusion, we have presented an approach, which allows fabrication of nanoscale fused silica pillars, suitable for *in situ* nanomechanical testing in the TEM and SEM.

References:
[1] G. Kermouche et al., *Acta Mater.* 2016, *114*, 146.
[2] S. Romeis et al., *Scr. Mater.* 2015, *108*, 84.
[3] S. Romeis, *Rev. Sci. Instr.* 2012, *83*, 95105.
[4] S. Romeis et al., *Part. Part. Syst. Char.* 2014, 31, 664.
[5] J. Paul et al., *Powder Technol.* 2015, *270*, 337.
[6] M. Mačković et al., *Acta Mater.* 2014, *79*, 363.
[7] M. Mačković et al., *Scr. Mater.* 2016, *121*, 70.
[8] R.F. Cook, G.M. Pharr, *J. Am. Ceram. Soc.* 1990, *73*, 787.
[9] R. Lacroix et al., *Acta Mater.* 2012, *60*, 5555.
[10] M. Mačković et al., *Front. Mater.* 2017, *4*:10. doi: 10.3389/fmats.2017.00010

Acknowledgements
Financial support by the Deutsche Forschungsgemeinschaft (DFG) through the SPP1594 "Topological Engineering of Ultra-Strong Glasses", Cluster of Excellence EXC 315 "Engineering of Advanced Materials" and GRK1896 "In situ microscopy with electrons, X-rays and scanning probes" is gratefully acknowledged.

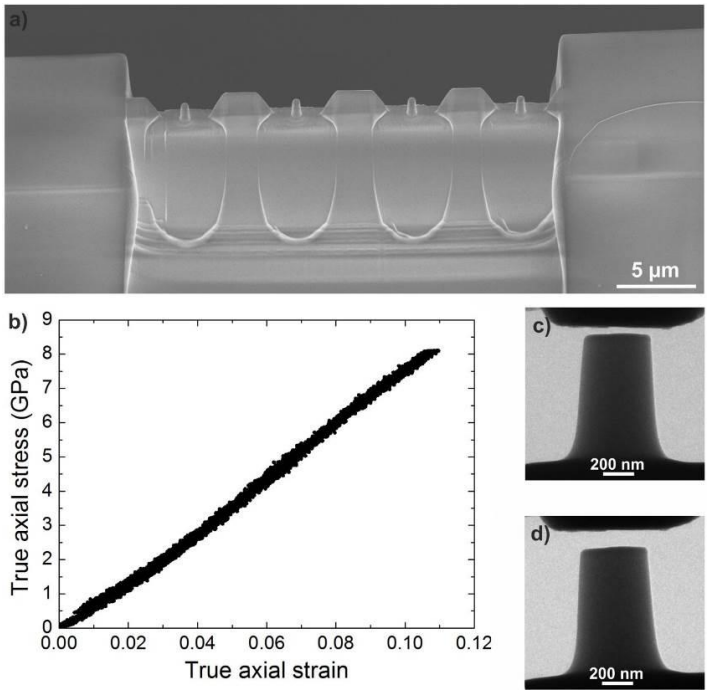

Figure 1. *In situ* compression testing of fused silica pillars in the TEM: a) overview SEM image of pillars prepared by FIB; b) mechanical data of a pillar compressed in the TEM; c) and d) are TEM image of a pillar before and after compression, respectively.

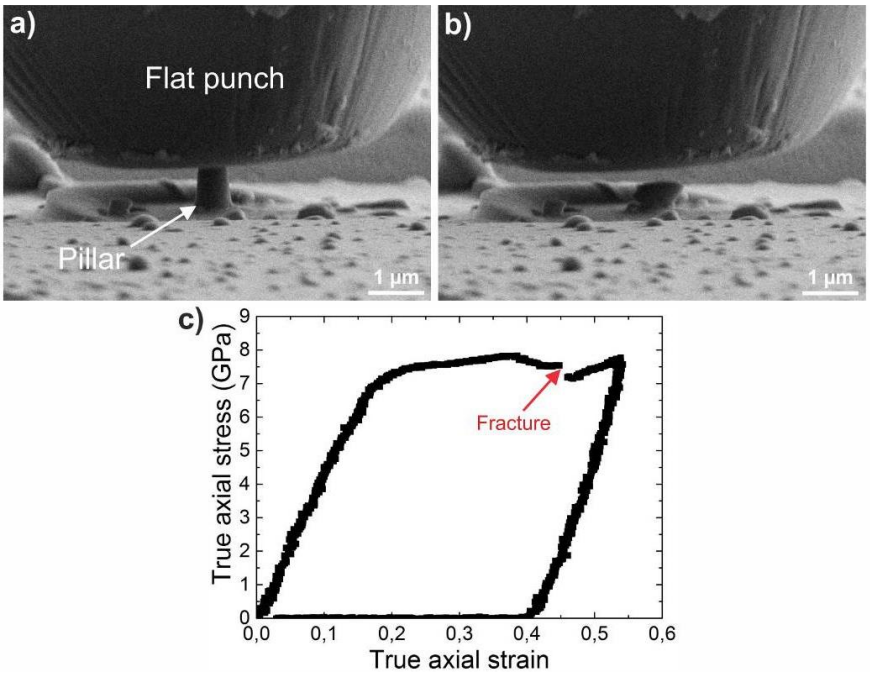

Figure 2. *In situ* compression testing of fused silica pillars in the SEM: a) and b) are SEM images showing a pillar before and after compression, respectively, while c) shows mechanical data of the pillar compressed in the SEM.

IM2.P022
Direct observation of oxygen vacancy-driven structural and resistive phase transition in $La_{2/3}Sr_{1/3}MnO_3$

L. Yao[1], S. Inkinen[1], S. van Dijken[1]

[1]NanoSpin, Department of Applied Physics, Aalto University School of Science, Espoo, Finland

lide.yao@aalto.fi

Oxygen defects can have a profound effect on the physical properties of transition metal oxides. Electric-field driven migration of oxygen vacancies provides a viable mechanism for the formation, rupture and reconstruction of conducting filaments in insulating oxides, an effect that is used in nanoscale resistive switching devices [1,2]. In complex oxides where magnetic, ferroelectric and superconducting phases emerge from strong correlations between localized transition metal valence electrons, oxygen vacancies can radically alter a plurality of intrinsic properties via valance changes and structural phase transitions [3]. The ability to reversibly control the concentration and profile of oxygen vacancies in oxide nanostructures would thus open up comprehensive prospects for new functional ionic devices. Advancements in this direction require experimental techniques that allow for simultaneous measurements of oxygen vacancy dynamics, atomic-scale structural effects and macroscopic physical properties. In this presentation, we report on deterministic voltage control of three structural phases with distinctive resistance states in $La_{2/3}Sr_{1/3}MnO_3$ (LSMO) epitaxial films by in-situ transmission electron microscopy (TEM) [4].

In our experiments, we used aberration-corrected TEM and a double-tilt probing holder with a piezo-controlled metal tip. The samples, consisting of a 20 nm thick LSMO film on a conducting Nb-doped $SrTiO_3$ (STO) substrate, were grown by pulsed laser deposition and prepared into cross-sectional TEM wedges by mechanical polishing and Ar ion milling. Electrical contacts to the STO side of the sample were made by placing one of the wedges on a half Cu grid. After mounting the TEM sample into the microscope, we brought the electrically grounded tip into contact with the LSMO film. This produced an effective contact area with a diameter of about 30 nm. We continuously monitored the electrical resistance and simultaneously recorded scanning TEM (STEM) images with high-angle annular dark field (HAADF) contrast after the application of short triangular voltage pulses to the STO side of the specimen. Our in-situ TEM measurements (Fig. 1) demonstrate reversible switching between low- and high-resistance states. The resistive switching events directly correlate with uniform structural transition between perovskite and brownmillerite phases in the LSMO film. Detailed STEM analyses of domain growth during switching, electron energy loss spectroscopy on the LSMO/STO contact area, and electro-thermal simulations indicate that horizontal and reversible migration of oxygen vacancies in LSMO, driven by combined effects of Joule heating and bias voltage, predominantly causes the transitions. A transition to an oxygen-deficient perovskite phase with intermediate resistance occurs at even larger voltage pulses (not shown in Fig. 1). Our findings open new prospects for ionotronic devices based on dynamic control of physical properties in complex oxide nanostructures.

References:
[1] R. Waser and M. Aono, Nature Materials 6, 833 (2007).
[2] J.J. Yang, D.B. Strukov, and D.R. Stewart, Nature Nanotechnology 8, 13 (2013).
[3] S. Kalinin and N.A. Spaldin, Science 341, 858 (2013).
[4] L. Yao, S. Inkinen, and S. van Dijken, Nature Communications 8, 14544 (2017).

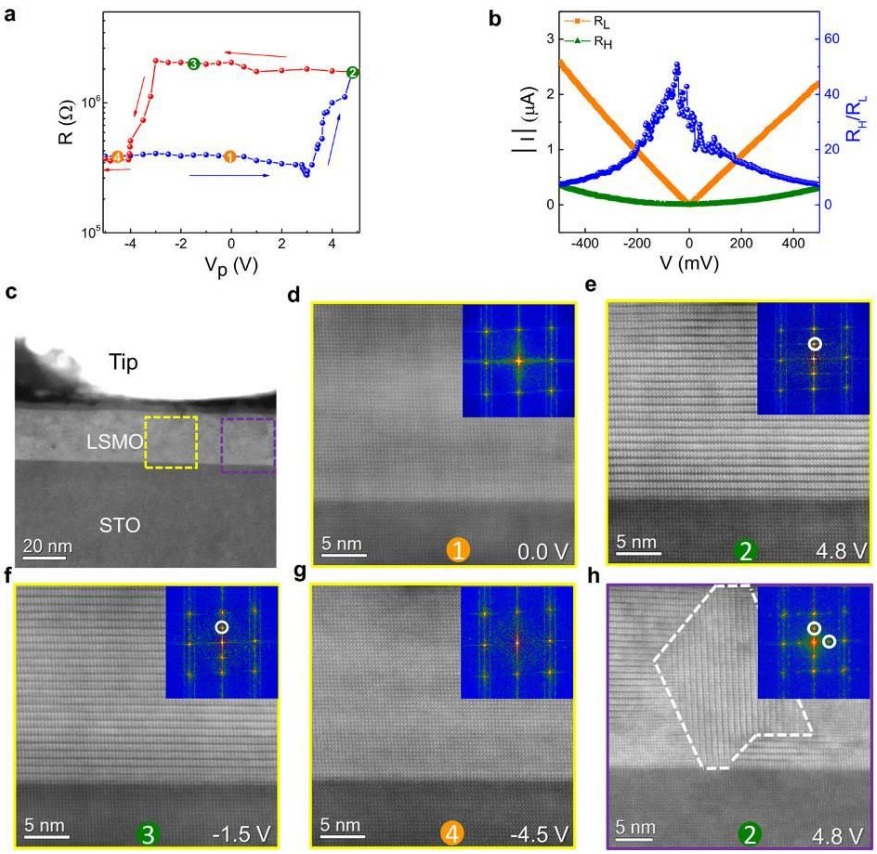

Figure 1. (a) In-situ TEM resistive switching curve for a LSMO film on top of a conducting STO substrate. The resistance is measured at V_m= 0.5 V after the applications of triangular voltage pulses with maximum voltage V_p and a duration of 100 ms. (b) I–V curves for the same film, measured after switching to the low (orange squares) and high (green triangles) resistance states. The blue data points indicate the resistance ratio as a function of bias voltage. (c) Cross-sectional STEM image of the contact between the metal tip and the LSMO film. (d)-(h) STEM-HAADF images and corresponding fast Fourier transform (FFT) patterns of the sample within the contact area, as indicated by the dashed boxes in c, at several stages of the resistive switching process. The images in (d)-(h) and data in (a) were collected simultaneously (colored dots indicate matching measurements). In some areas (see (h)), the horizontal brownmillerite phase coexists with a vertical brownmillerite structure.

IM2.P023
In situ microscopy of formation of nickel-based bimetallic nanoparticles

C. D. Damsgaard[1]

[1]Technical University of Denmark, DTU Cen and DTU Physics, kgs. Lyngby, Denmark

cdda@cen.dtu.dk

Introduction: Nickel based catalysts are well-known heterogeneous catalysts for hydrogenation and reforming reactions. Furthermore, nickel is a good and less expensive alternative to much less abundant materials such as palladium and platinum active for similar reactions. As nickel based catalysts may change their morphology and catalytic performance with respect to the environment, it is essential for the fundamental understanding to investigate the materials under conditions similar to conditions applied during the catalyst lifecycle e.g. calcination, nanoparticle (NP) formation, and catalytic reaction conditions. This study will focus on the NP formation process of Ni-M (M=Cu[1], Ga[2], and Fe[3]) alloys.
Objectives: The important NP characteristics i.e. crystal structure, morphology, uniformity, and size are investigated for Ni-M (M=Cu, Ga, and Fe) alloys. The characteristics are monitored on the single NP scale as well as over an ensemble of NPs in the same sample. Furthermore, the NP formation process in an intermetallic Ni-M system (M=Ga and Fe) is compared to a substitutional alloy (M=Cu) regarding especially crystal phase composition and purity.
Materials and Methods**:** The studied material systems were synthesized by incipient wetness impregnation method using aqueous solutions of metal nitrate salts as precursor. In the case of NiFe system the impregnation was further developed by using glycerol as solvent.
Dedicated complementary techniques were applied to investigate the material systems. In situ X-ray diffraction (XRD) and X-ray absorption spectroscopy (XAS) were used to follow the average catalyst"s structural and electronic changes during formation and reaction conditions[1,2]. High resolution environmental TEM (ETEM) was used to follow the dynamics of the catalysts on the nanoscale (sintering, crystallinity)[1,2]. Spatially resolved information on the meso scale (50 nm–1 µm) was obtained by X-ray microscopy[3,4].
Results: At high Ni contents, Cu–Ni samples predominantly form a homogeneous solid solution of Cu and Ni. At lower Ni contents Cu and Ni are partly segregated and form metallic Cu and Cu–Ni alloy phases.
For the Ni-Ga system, highly dispersed Ni(II) nanocrystallites serve as centres for further reduction of the nickel and gallium oxides and metallic gallium is incorporated into the nickel crystal lattice to form an intermetallic phase (Fig. 1).
SEM-EDX and X-ray micro tomography confirmed even distribution of the active Fe-Ni phase throughout the entire volume of the catalyst (Fig. 2). By use of TEM Fe and Ni alloyed nanoparticles with approximately 5 nm were measured.
Conclusion: This study illustrates how the formation of NP in Ni-based catalyst have been investigated by in situ diffraction, imaging and spectroscopic methods. The phase purity of the Ni-based NPs in an entire ensemble depends highly on the Ni-M ratio and the complexity of the phase diagram. The results clearly underlined the need for complementary techniques and highlight the potential of these for application in catalysis.

[1] Wu, Q. *et al.* In Situ Observation of Cu-Ni Alloy Nanoparticle Formation by X-Ray Diffraction, X-Ray Absorption Spectroscopy, and Transmission Electron Microscopy: Influence of Cu/Ni Ratio. *ChemCatChem* 6, 301–310 (2014).
[2] Sharafutdinov, I. *et al.* Intermetallic compounds of Ni and Ga as catalysts for the synthesis of methanol. *J. Catal.* 320, 77–88 (2014).
[3] Silva, H. *et al.* Synthesis and characterization of Fe-Ni/γ-Al_2O_3 egg-shell catalyst for H2 generation by ammonia decomposition. *Appl. Catal. A Gen.* **505,** 548–556 (2015).
[4] Baier, S. *et al.* In Situ Ptychography of Heterogeneous Catalysts using Hard X-Rays: High Resolution Imaging at Ambient Pressure and Elevated Temperature. *Microsc. Microanal.* 22, 178–188 (2016).

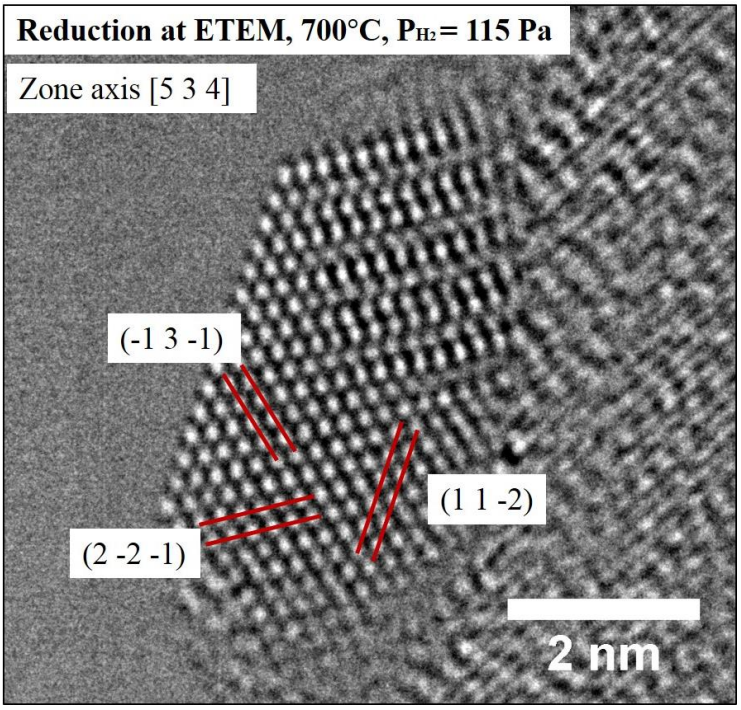

Figure 1. High-resolution TEM image of a Ni_5Ga_3 (δ-phase) nanoparticle acquired in the ETEM under reduction conditions (700°C, 1.15 mbar H_2).

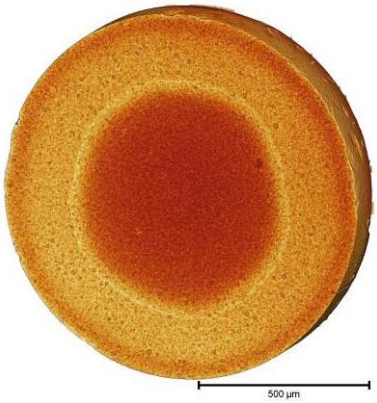

Figure 2. Computed X-ray micro tomography image of reconstructed 3D volume of the Ni-Fe catalyst on a γ-Al_2O_3 sphere.

IM2.P024
In situ TEM fracture experiments on single crystal silicon beams at RT

I. Issa[1], D. Kiener[1]

[1]Erich Schmid Institute, Leoben, Austria

inas.issa@hotmail.com

Fundamental understanding of the mechanical behavior of single crystalline 3-dimentional micro and nano-objects (micropillars, nanowires and nanoparticles, etc.) provides useful pieces of information and design guidelines in many fields concerned with nano-objects as based-components (electromechanical devices, NC ceramics, etc.). Advances in experimental setups provide this field to achieve new limits in mechanical behavior investigations at low scale, such as direct observation of different dislocations processes *in situ* in TEM correlated to quantitative mechanical tests. Among the high strength and elastic limit that materials gain when decreasing its volumes, they exhibit large plastic deformation under high load. This was not expected for certain materials (highly brittle at bulk). Many studies are dedicated on the origin of this high plastic deformation. Mechanisms proposed are mainly size, among other parameters, dependent.
However, fewer studies are dedicated on the size scale effect on fracture properties and DBT of brittle materials. A good knowledge of the critical size and temperature for DBT of materials allows better design guideline of more fracture resistant and tough materials and avoid its brittle failure. Silicon is still the most used material in modern technological devices. In this work, we aim to investigate the size scale effect on the fracture behavior of single crystal Si *in situ* in TEM and SEM.
An increase of the fracture toughness of Si micro beams, tested in SEM, is observed above 300°C [*Jaya et al. 2016)*]. No sharp DBT is observed but a change in cracking mechanisms and authors relate this to a change in cracking mechanisms (plasticity) above 300° C (< DBTT of macro Si). No clear size scale effect can be extracted from previous work on Si, knowing that thermal energy play an important role in activating/nucleating dislocations and thus increase KIC. Even though some experimental compression tests report an increase of Si fracture resistance at RT [*Deneen et al. 2006)*] or at elevated temperatures [*Korte et al. 2011)*]. But compression tests are well known to prevent fracture of small enough samples [*Kendall, Nature 1978*].
Herein, we present bending tests on notched Si beams, of thickness range [70 - 380] nm, *in situ* in TEM and SEM at RT. TEM images correlated to force-time/displacement curves will allow us to monitor a possible plasticity near the crack tip and investigate dislocation processes.
Si beams oriented along [110] and typical aspect ratio of ~1*1*5 for thickness, width and length respectively, are fabricated using FIB milling. Sharp notches, of 1 to 5 nm curvature radius, are introduced in TEM, by condensing the 200 kV electron beam on the samples, see Figure 1. Finally, to get rid of dislocations and especially those introduced during the FIB process, samples are annealed at ~ 645 °C (0.54*Tmelting of Si), *in situ* in TEM.
Si bending beams in the thickness range 250 nm and above show pure brittle behavior with KIC around 1MPa.m1/2 in accordance to literature. *In situ* SEM test on 75 nm thickness, presented in Figure 2, reveals plasticity after few cycles of loading unloading accompanied with an increase of KIC. Further results on the transition behavior of smaller samples coupled with TEM observations will be presented.

References:
[1] Deneen et al. (2006). In situ deformation of silicon nanospheres. *Journal of Materials Science*, *41*(14),
[2] Jaya et al. (2016). Microscale Fracture Behavior of Single Crystal Silicon Beams at Elevated Temperatures. *Nano Letters*,
[3] Korte et al. (2011). Deformation of silicon - Insights from microcompression testing at 25-500 °C. *International Journal of Plasticity*, *27*(11).
[4] Kendall (1978) « The Impossibility of Comminuting Small Particles by Compression ». *Nature 272-n 56555.*

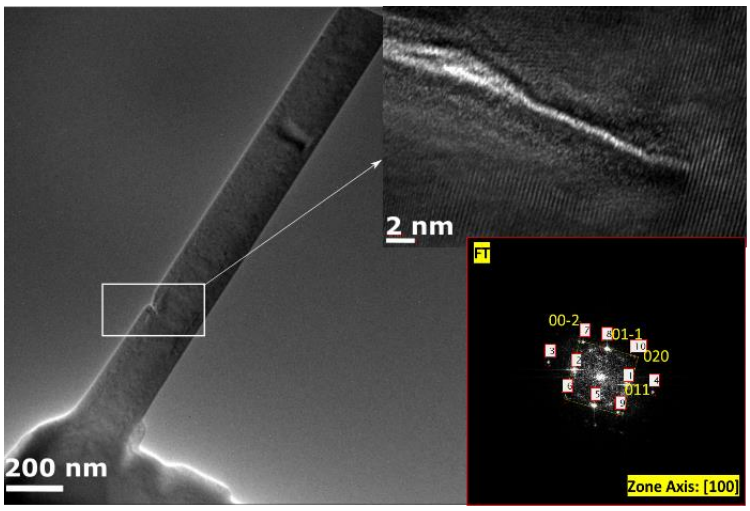

Figure 1. TEM image of a Si Bending beam. HRTEM of the notch introduced in TEM and DP of the zone near the notch tip.

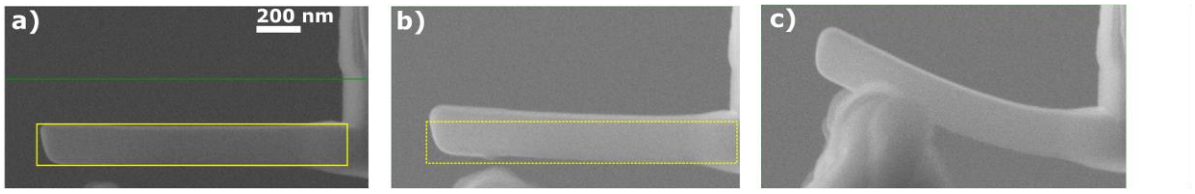

Figure 2. In situ SEM bending tests of Si beam of T:75 nm, W:180 nm and L: 1300 nm. a) At zero load. b) at zero load after 3 cycles of loading unloading (lines indicate plasticity). C) at highest load before Failure.

IM2.P025
Monitoring the dynamics of heterogeneous catalysts by electron microscopy

R. Farra[1], M. Greiner[1], J. Cao[1], R. Schlögl[1], M. G. Willinger[1]

[1]Fritz Haber Institute of the Max Planck Society, Inorganic Chemistry, Berlin, Germany

farra@fhi-berlin.mpg.de

Introdcution and Objectives: It is known that the shape of metal catalysts adapts to the chemical potential of the surrounding atmosphere and that the active surface evolves dynamically under reaction conditions [1-3]. Different photon-based characterization techniques were improved and implemented to probe the active state of catalysts *in situ*. However, such techniques lack the spatial resolution as they provide information averaged over a macroscopic scale, which is much larger than the catalytic active nanostructures.
In situ Scanning Electron Microscopy (SEM) and Transmission Electron Microscopy (TEM) have proven to be powerful techniques for the study of atmosphere and temperature induced morphological or compositional changes of catalysts at micrometer- to atomic resolution scale [4,5]. Furthermore, *in situ* SEM and TEM can be used as complementary methods from the point view of applicable pressure range and the obtainable resolution. Hence, pressure gap impact on the catalysts activity can be assessed using these techniques. On the other hand, collective (SEM) and individual (TEM) phenomena on the surface of active catalysts in the micro- to nanometer scale can be compared and correlated to the reactivity.
In this contribution we present *in situ* TEM and SEM results of the catalytic oxidation of hydrogen on Copper. Aside from the fundamental importance of this catalytic system, the investigation of copper redox chemistry is of great importance for decisive future energy related catalytic processes as methanol synthesis or water gas shift reaction.
Materials and Methods: *In situ* SEM experiments were conducted in the chamber of a modified commercial environmental scanning electron microscope. The instrument is equipped with a home-built heating stage and attached to a gas feeding system and a mass spectrometer for product analysis.
In situ TEM experiments were carried out using a Protochips, Inc. gas flow holder equipped with an environmental cell (a nanoreactor). The holder is combined with a home built gas feeding and a mass spectrometer for gas analysis. The environmental TEM cell allows monitoring gas-solid interactions under relevant catalytic conditions.
Results and Conclusions: Metal catalysts were prepared *in situ* by decomposing the catalyst precursor in an oxidative atmosphere and subsequent reduction in hydrogen (figure 1). As the resulting metal catalysts were exposed to a reductive gas mixture (H_2 in He) that contains a little amount of molecular oxygen, the catalytic reaction starts to proceed, as proved by the gas analysis of products which shows a concomitant increase of water and decrease of oxygen MS-signals (figure 2). The catalyst at work is very dynamic and shows continuous and erratic morphological changes, provided that the Wulff construction of crystals was preserved most often over time. The interpretation of this dynamic behavior of catalysts under working conditions needs much further elaborated studies that can control or slow down the kinetics of the reactions, and hence make it possible to exploit other TEM analysis techniques as *in situ* EELS and diffraction. Nevertheless, these results may evoke strong debates about the assumptions that were published in the catalysis literature on the basis of TEM observations made in vacuum.
In this contribution we will outline how the implementation of complementary *in situ* electron microscopy techniques can enrich our understanding of the dynamic behavior of the active catalysts.

References:
[1] P.L. Hansen, *et al.*, Science, **2002**, 295, 5562, 2053-2055
[2] T. Lunkenbein, *et al.*, *Angew. Chem.-Int. Ed.* **2015**, *54*, 4544–4548.
[3] J. R. Jinschek, *Chem. Commun.* **2014**, *50*, 2696–2706.
[4] Z.-J. Wang, G., *et al*., *ACS Nano* **2015**, *9*, 1506–1519.
[5] S. B. Vendelbo, *et al*., *Nat. Mater.* **2014**, *13*, 884–890.

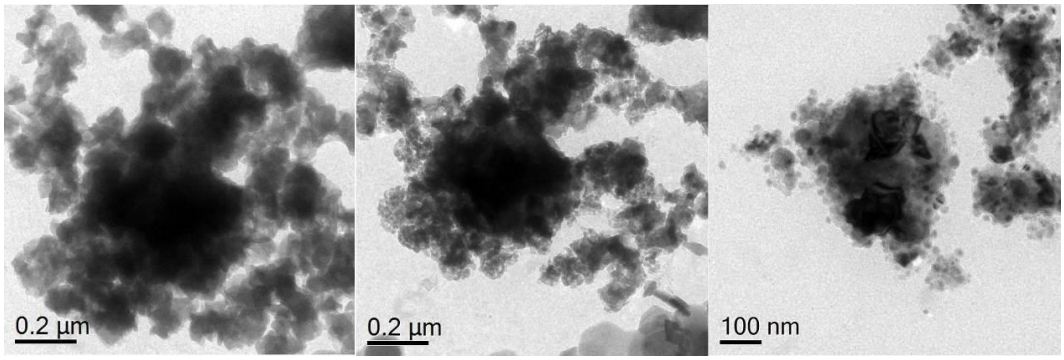

Figure 1. Sequential steps of catalyst preparation *in situ* (from left to right): Copper oxalate before oxidation, Copper oxide after calcination and Copper after reduction.

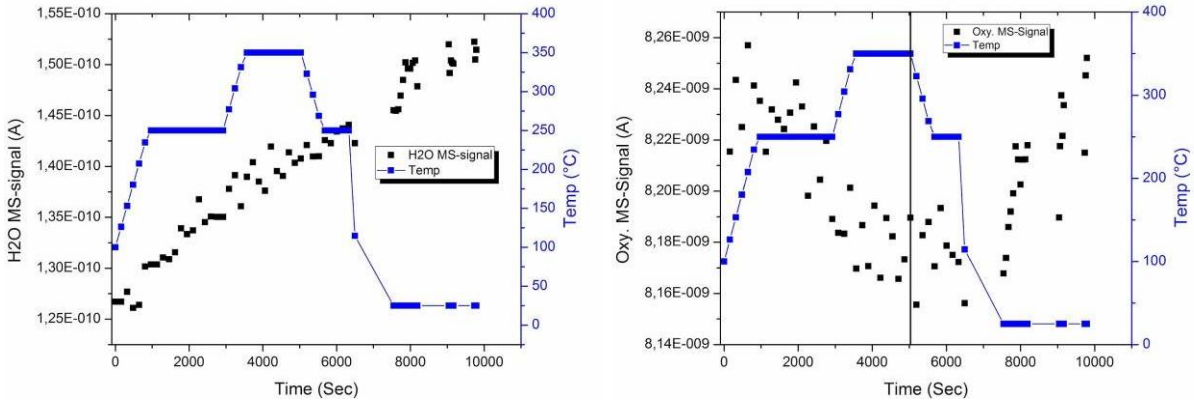

Figure 2. On-line mass spectroscopy signals of water (left) and Oxygen (right) at different reaction temperatures. Gas mixture flow was 0.1 ml/min, pressure inside the nanoreactor was 200 mbar.

IM2.P028
Ultrafast transmission electron microscopy applied to phase transitions in correlated materials

T. Danz[1], N. Rubiano da Silva[1], A. Feist[1], K. Rossnagel[2], V. Moshnyaga[3], S. Schäfer[1], C. Ropers[1]

[1]University of Göttingen, 4th Physical Institute, Göttingen, Germany
[2]University of Kiel, Institute for Experimental and Applied Physics, Kiel, Germany
[3]University of Göttingen, 1st Physical Institute, Göttingen, Germany

thomas.danz@uni-goettingen.de

Introduction: Ultrafast transmission electron microscopy (UTEM) is a promising approach to investigate ultrafast processes with nanometer spatial resolution [1]. Using the versatile imaging, diffraction, and spectroscopy capabilities of such an instrument, we investigate structural, electronic, and magnetic dynamics in a laser pump/electron probe scheme [2]. Here, we apply the Göttingen UTEM in the probing of phase transitions in correlated materials, including vanadium dioxide (VO2) and tantalum disulphide (1T-TaS2). We address both structural and electronic degrees of freedom using different contrast methods such as ultrafast diffraction and electron energy loss spectroscopy (EELS).
Objectives: Although the ultrafast metal-insulator transition close to 70°C in VO2 has been under investigation for quite some time, its origin and the coupling between the electronic and structural changes remain of considerable interest. Using UTEM, we are able to simultaneously gain insight into the structural and electronic components of the phase transition on a femtosecond timescale, and to disentangle both components. The transition metal dichalcogenide 1T-TaS2, on the other hand, owes its rich electronic phase diagram to the reduced dimensionality of quasi two-dimensional materials. It exhibits an electronic superstructure in its charge-ordered phases (charge density wave, CDW) that is apparent from a periodic lattice distortion observed in diffraction. Both widely studied material systems serve as model systems to be investigated by UTEM.
Materials and Methods: The Göttingen UTEM instrument is based on a conventional field emission TEM, which was modified to allow for both optical excitation of the specimen and photoemission from a nanometric tip emitter. At the sample position, we obtain sub-nm electron focal spot sizes with 0.6 eV spectral width and 200 fs pulse duration. Thin films of VO2 and 1T-TaS2 are conventionally prepared from monocrystalline VO2 grown via metalorganic aerosol deposition (MAD) on sapphire and using ultramicrotomy of bulk crystals, respectively [3].
Results: In the experiments, we characterize both the thermal and optically-induced phase transitions in the materials investigated. In particular, we address the issue of reversibility of the transition at high pump-probe repetition rates, and discuss possible strategies to reduce average thermal load on the specimen. Alongside stroboscopic pump-probe studies, we also study optically-induced domain changes in the nearly commensurate (NC) CDW phase in 1T-TaS2 exposed to intense individual laser pulses. In the thin films investigated, the associated transition to the incommensurate (IC) CDW phase is not fully reversible, as evidenced by shot-to-show changes in the distribution of both symmetry-equivalent NC CDW phases φR and φL in Fig. 1(a). This is evident from the movement of the anti-phase boundary schematically depicted in (b). Corresponding diffraction patterns of the NC CDW phase are shown in (c). While bright spots indicate structural reflections, weaker spots are induced by the CDW.
Conclusion: In conclusion, we present the current status of our work on applying UTEM in the simultaneous probing of structural and electronic components of phase transitions in correlated materials. In the future, we expect our approach to provide for unique femtosecond and nanometer views of the spatiotemporal dynamics associated with structural phase transitions.
References:

[1] A.H. Zewail, Science 328, pp. 187-193 (2010)
[2] A. Feist *et al.*, in press, Ultramicroscopy (2016)
[3] Th. Danz *et al.*, J. Phys.: Condens. Matter 28**,** 356002 (2016)

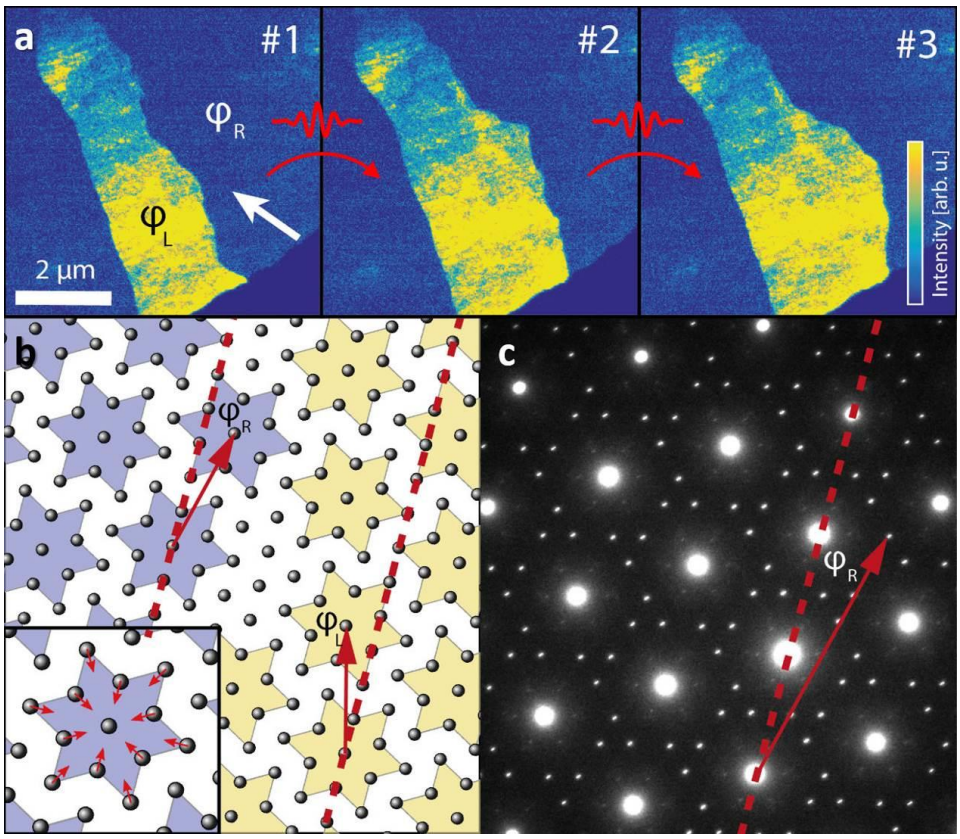

Figure 1. (a) TEM dark-field micrographs of an anti-phase (φR/φL) boundary in the NC CDW phase of 1*T*-TaS2. Between each frame, an individual intense laser pulse has driven the specimen into the IC CDW phase. Note the irreversible variations in the domain boundaries after cooling. **(b)** Atomic lattice of 1*T*-TaS2 in the NC phase with anti-phase boundary. **(c)** TEM diffraction of NC phase. Bright spots: lattice reflections, weaker spots: CDW.

IM2.P029
A streak camera setup for time resolved and spectroscopic measurements in the TEM

H. Ali[1], J. Eriksson[2], H. Li[1], S. H. M. Jafri[1], M. S. S. Kumar[1], J. Ögren[2], V. Ziemann[2], K. Leifer[1]

[1]Uppsala University, Electron Microscopy and Nano-Engineering, Applied Materials Science, Department of Engineering Sciences, Uppsala, Sweden
[2]Uppsala University, Department of Physics and Astronomy, Uppsala, Sweden

klaus.leifer@angstrom.uu.se

For the observation of time dependent processes, a priori, we would not like to impose that the observable shows a temporary periodicity or a repeatable evolution. Many time resolved experiments with time resolution in the nanosecond range and faster rely on pump probe methods. Pump probe methods are extremely powerful and have, in the field of electron microscopy, widened our knowledge about the dynamic behavior of physical and chemical phenomena over the past decades [1–9]. Yet, non-repeatable dynamic processes such as melting and a range of phenomena relying on collective excitations need single shot experiments. Such experiments have been successfully built and used by the groups [10–13]. Some of the key elements of these experiments are intense electron bunches and sensitive detectors. More recently, in pump probe experiments, EELS spectroscopy started to be used. Here, the typical experimental strategy consists in the acquisition of the signal, mostly low loss events, at a well-defined delay time and the full time series is acquired by taking the signal at various delay times. An alternative consists in rapidly sweeping the electron beam across a CCD camera such that one axis is time, the other one is, for example, spectroscopy. This streak camera approach has been used in normal imaging mode by the Bostanjoglo group [14] to acquire fast time series of real space images. Here, we propose an experimental setup based on a streak camera approach inside an energy filter to measure time resolved properties of materials in the transmission electron microscope (TEM). In order to put in place the streak camera, a beam sweeper was built inside an energy filter. After exciting the TEM sample, the beam is swept across the CCD camera of the energy filter. We describe different parts of the setup at the example of a magnetic measurement as well as testing of the components. This setup is capable to acquire time resolved diffraction patterns, electron energy loss spectra (EELS) and images with total streaking times in the range between 100 ns and 10 μs.

IM2.LBP01
Local strain mapping of metallic networks via digital image correlation

N. Karpstein[1], N. Schrenker[1], P. Schweizer[1], T. Przybilla[1], M. Mačković[1], F. Niekiel[1], C. Ophus[2]
E. Spiecker[1]

[1]Friedrich-Alexander-Universität Erlangen-Nürnberg, Institute of Micro- and Nanostructure Research, Erlangen, Germany
[2]Lawrence Berkeley National Laboratory, National Center for Electron Microscopy, Berkeley, CA, United States of America

nicolas.karpstein@fau.de

Metallic networks have attracted a lot of attention due to prospective applications in various fields. For instance, networks of silver nanowires (Ag NWs) on a polymer film combine flexibility and transparency with electrical conductivity and can potentially replace brittle and expensive materials such as indium tin oxide, e.g. in printed electronics or organic solar cells [1]. Another example for metallic networks are nanoporous metals, which are of considerable interest for applications as catalysts, sensors or actuators. Nanoporous gold (npg), for instance, shows increasing mechanical strength with decreasing feature size. Stresses close to the theoretical strength have been reported [2,3] allowing for its use as a model material for the investigation of mechanical size effects.
Since mechanical failure in these networks can occur at sites of localized stresses, it is crucial to understand their local deformation behavior. To this end, local strain analysis via digital image correlation has been performed on series of SEM and TEM images of metallic networks acquired during *in situ* tensile and compression tests. In our algorithm, the displacement field is modeled using Bézier surfaces. This reduces the degrees of freedom to the position of their control points during fitting. With these control points the sample region is tracked as it is deformed. The resulting displacement field can then be translated into a strain distribution, revealing local strains and allowing for insights into the deformation mechanisms involved.
This local strain analysis has been performed on networks of Ag NWs on a flexible polymer substrate during *in situ* tensile tests in the TEM. Furthermore, npg samples compressed *in situ* in the SEM have also been analyzed to determine their local deformation behavior.
Analysis of the Ag NW network on PET (Fig. 1c) shows a mostly homogeneous strain distribution across the specimen under tensile load. The polymer is responsible for the brittle fracture of the sample, whereas the Ag NWs show necking, pointing to ductile behavior (not shown). In npg (Fig. 2), localized plastic deformation can already be seen at low stress levels. A decisive factor for the yield strength is the ligament diameter: At the same relative density, a finer structure exhibits a higher yield strength, revealing a distinct size effect.
In both cases, failure occurs at sites of localized stresses due to cross sections of lower strength. Digital image correlation provides crucial insights in the local deformation behavior and complements global stress-strain data. In order to achieve a comprehensive understanding of the behavior of these metallic networks under mechanical load, further tensile tests will be performed in an optical microscope, allowing for the determination of local strains on a larger scale.

References:
[1] F. Guo et al., Energy Environ. Sci. 8, pp. 1690-1697 (2015).
[2] C. A. Volkert et al., Appl. Phys. Lett. 89, 061920 (2006).
[3] J. Biener et al., Nano Lett. 6, pp 2379–2382 (2006).

Acknowledgement
The authors gratefully acknowledge the financial support of the German Research Foundation (DFG) within the research training group GRK 1896 In-situ Microscopy with Electrons, X-rays and Scanning Probes.

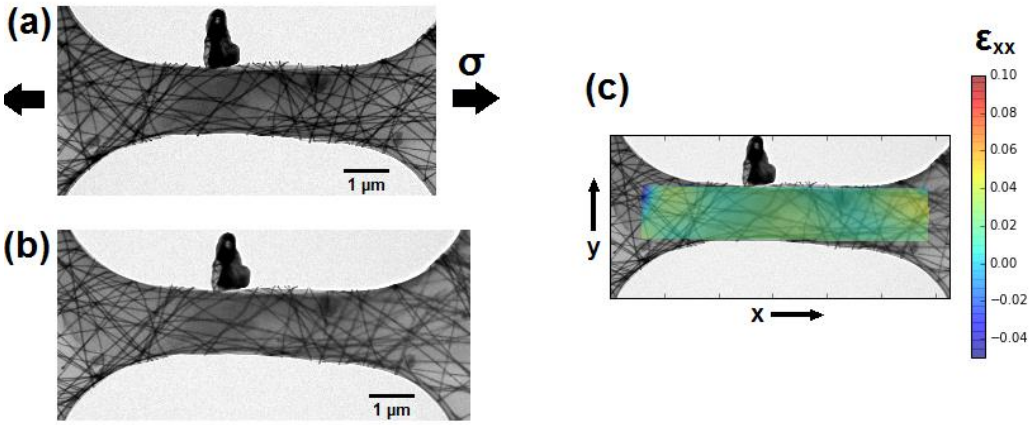

Figure 1. Ag NW on PET tensile sample (a) before and (b) during tensile loading. (c) shows local strains acquired by digital image correlation.

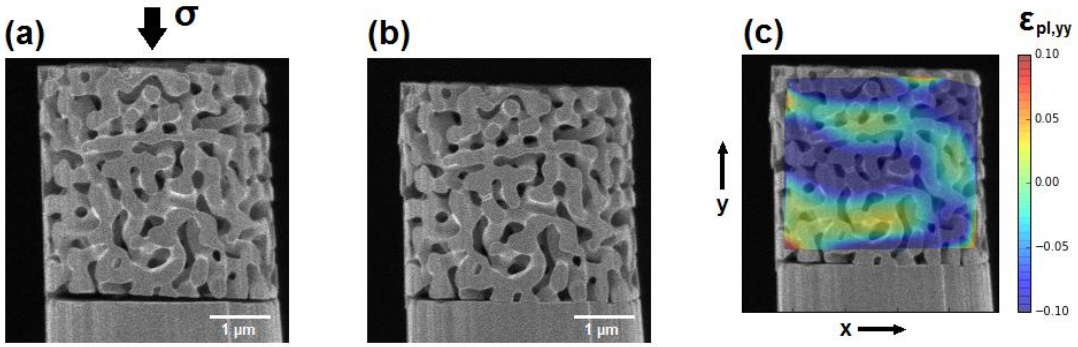

Figure 2. npg sample (a) before and (b) after compressive loading. (c) shows plastic strains remaining after unloading, acquired by digital image correlation.

IM 3: Image analysis and handling of big data sets

IM3.001 invited
Dealing with the challenges of large life science data sets from acquisition to archive

D. Flanders[1]

[1]Friedrich Miescher Institute for Biomedical Research, Basel, Switzerland

Use of technologies that generate large amounts of data is common in most research projects now. A lot of focus is placed onto the capacity or performance of a storage system, however, the entire data life cycle must be taken into consideration in order to truly facilitate a researchers work. At the FMI we have focused on improving the overall process of data acquisition, processing, analysis, and archiving. This is particularly challenging as the techniques used within and across research groups can be very heterogeneous. However, we have developed a general process that simplifies a workflow and can reduce tasks that take days to less one day by enabling a researcher to start processing and archiving of data during acquisition. This is important as it not only saves the researcher time, but also provides faster insight when designing the next set of experiments, and accelerates the overall research process.

IM3.002 invited
EnhanceR – solving data challenges for Swiss researchers

A. Upton[1]

[1]ETH Zürich, Zurich, Switzerland

Research presents unique challenges in IT. Supporting researchers in meeting these challenges has led to the creation of a network of specialist units at Swiss research organizations to provide Research IT support, allowing researchers to concentrate on their core tasks and accelerating time to results. EnhanceR is a national initiative to provide specialized research IT support to the entire Swiss research academic community, and achieves this goal by facilitating cooperation between academic Research IT groups in Switzerland. In this talk, an overview of the services that EnhanceR offers is given, as well as examples of previous support projects that have benefited researchers. In addition, the support process is presented, helping researchers identify whether their research could benefit from specialist EnhanceR support.

IM3.003
An open-source framework for scalable analysis of brain imaging data

H. Luetcke[1], R. Roškar[1], R. Murri[2], A. Gilad[3], F. Helmchen[3], T. Wuest[1], B. Rinn[1]

[1]ETH Zurich, Scientific IT Service, Zurich, Switzerland
[2]University of Zurich, S3IT, Zurich, Switzerland
[3]University of Zurich, Brain Research Institute, Zurich, Switzerland

hluetcke@ethz.ch

Over the last decade, advanced imaging techniques such as two-photon or light-sheet microscopy have become an important part of the neuroscience toolkit. However, the management and analysis of the huge amount of data produced by these techniques pose significant challenges for many labs. In particular, conventional approaches to data analysis (single workstation, custom-written scripts) scale poorly to datasets comprising hundreds of gigabytes or terabytes. These problems can be addressed by recently developed Big Data computing frameworks, notably Apache Spark [1], which promise easy-to-use, scalable data analysis on commercial cloud computing platforms. While these systems are powerful and their applicability to neuroscience has been demonstrated [2], the technical know-how required for implementing workflows based on Spark is still beyond what is available in most neuroscience labs. Moreover, the use of commercial cloud computing platforms may raise concerns regarding cost control and privacy. To address these issues, we have implemented a framework for scalable and easy-to-use analysis of brain imaging datasets, based on deploying Apache Spark in an open-source cloud computing environment (OpenStack). The workflow encompasses import of raw data (stored on OpenStack Swift), a customizable preprocessing pipeline, data visualization as well as higher-level analytics. User interaction is achieved simply with a web browser based on Jupyter notebooks. The whole setup is easily configurable and transferable between cluster instances. We apply our framework to the analysis of widefield calcium imaging data acquired in mice performing a texture-discrimination task. We found that preprocessing of full frame movies (512×512 pixels, 20 Hz frame rate) is considerably faster with our approach, compared to similar analysis on stand-alone machines, and scales well with the number of machines/cores in the cluster. More complex analyses, such as sliding-window correlation and regression, which are computationally too costly to run pixel-wise on a single machine, become possible with the distributed approach presented here. Our open-source framework is freely available to the community and is expected to become a useful tool for the analysis of similar datasets acquired in different laboratories.

References:

[1] H. Karau, W. Konwinski, P. Wendell, and M. Zaharia, *Learning Spark*. OReilly, 2015.
[2] J. Freeman, N. Vladimirov, T. Kawashima, Y. Mu, N. J. Sofroniew, D. V Bennett, J. Rosen, C.-T. Yang, L. L. Looger, and M. B. Ahrens, Mapping brain activity at scale with cluster computing, *Nat. Methods*, vol. 11, no. 9, pp. 941–950, 2014.

IM3.004
A live cell-tracking tool for non-motile 2D cell cultures with an integrated track quality evaluation algorithm

A. Cuny[1], A. Ponti[1], F. Rudolf[1]

[1]ETH Zürich, Department of Biosystems Science and Engineering, Basel, Switzerland

andreas.cuny@bsse.ethz.ch

The development of automated optical microscopy technologies combined with microfluidic cell culturing systems enables to study cellular processes in individual cells over a long time period. We are interested in the quantification of inheritance of physiological states in *S. cerevisiae* and *S. pombe* cells (Fig. 1). This requires an automated, almost error free tracking of individual cells and assignment of their physical relationships.
Tools enabling the tracking of cells within these (large) datasets are an important part of the analysis [1]. Commonly, tracks are assigned to individual cells based on the segmentation result. The simplest solutions assign cells solely based on their spatial location while more elaborate tools use advanced object tracking algorithms from other fields. A common problem for all solutions, are segmentation errors. Some tools circumvent this by executing a second segmentation based on the predicted position obtained from the initial tracking [2]. However, in all these cases manual validation and correction of the tracking result is required.
Here, we present a tool that automatically validates and corrects each track. The basic idea is that the quality of the initial tracks is assessed using the original images.
Initially, each cell gets assigned to a track by minimizing the sum of penalties between two subsequent frames [2]. Each track is validated using cut out squares of the raw images of two subsequent frames. In case the two images match, the track is seen as validated at that point, otherwise the assignment is removed.
How are the two small images compared? We devised a measure for cell identity in subsequent frames based on the Hamming distance when comparing the Fourier transformed image (Fig. 2A). Only the identical cell posses a measure close to 0 (red) while most other cells have a distance > 0.1 (blue). This is not specific to this small example, as an all against all comparison of images similar to the ones shown in Fig. 1 shows that the 1st percentile is located at ~ 0.1 (Fig. 2B, grey). For reasons of speed, we decided to compare the cell to only its neighbors in the subsequent frame (Fig. 2B red) and not to all cells in the respective frame (Fig. 2B blue). Next, we plotted the Hamming measure of a randomly selected cell over the 140 frames of the experiment (Fig. 2C, red). False positives (e.g. a segmentation of two cells as one) are easily detected as are false negative (e.g. no segmentation of a cell in the corresponding frame, where the position can be predicted from the previous frame) (Fig. 2C, red spikes). Additionally, as the cell center is obtained from the segmentation output, the control algorithm can label miss segmentation such that such untrustworthy quantification data are either deleted or marked for re-segmentation. Taken together, these results demonstrate that our measure is useful for distinguishing correctly assigned cells from miss-labeled ones.
The tool comes as a standalone *python* executable. The minimal input required is a segmentation output with the cell center and the cell dimension as well as the raw images. An option for the reconstruction of asymmetrically and symmetrically divining cells is included (this option additionally requires a fluorescence image marking the division event for asymmetrically dividing cells). Last, we implemented the tool in a frame by frame way such that tracking of cells can be performed while running a live experiment.

[1] Meijering, E., et al (2012). Methods for cell and particle tracking. *Methods in Enzymology*, *504*, 183–200.
[2] Ricicova, M. et al. (2013). Dissecting genealogy and cell cycle as sources of cell-to-cell variability in MAPK signaling using high-throughput lineage tracking. *PNAS*, *110*(28), 11403–8.

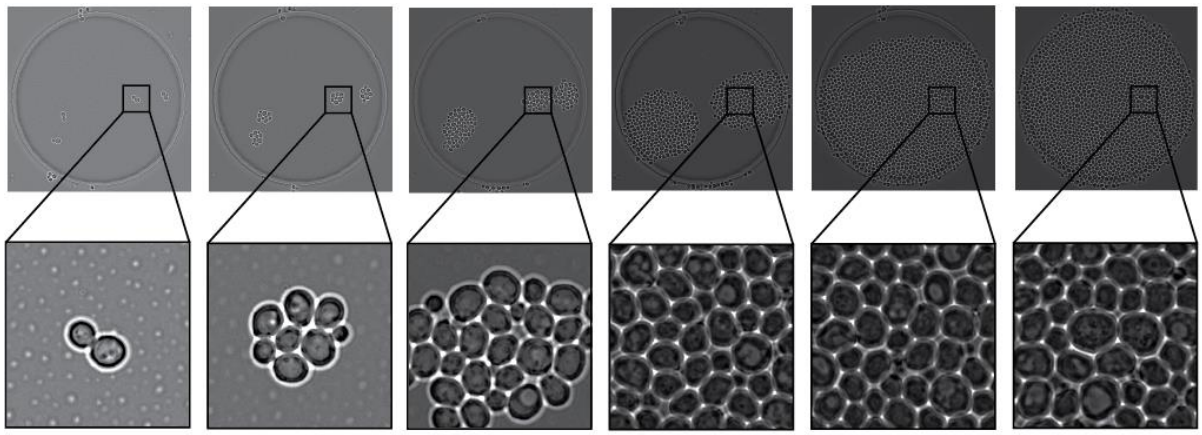

Figure 1. Representative images from a long-term time-lapse experiment using *S. cerevisiae.*

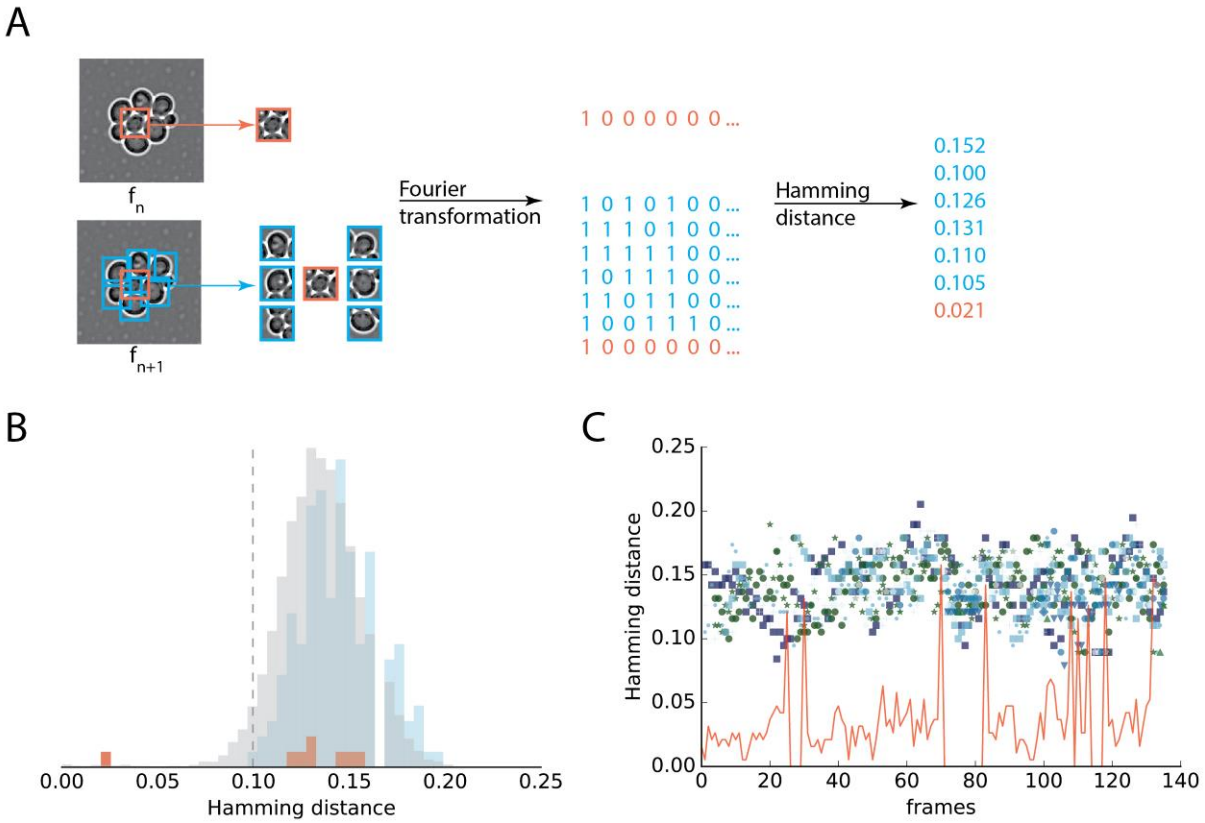

Figure 2. Quality control of each track A. Visualization of the control algorithm working principle. B Histogram of the Hamming distance derived from raw images for a cell for two consecutive frames as in A. C Hamming distance for one cell (red) and its neighbors (blue colored) plotted over time.

IM3.005
Analysis and simulation of STEM contrast and nano-beam diffraction of amorphous structures

M. Peterlechner[1], S. Hilke[1], M. Radek[1], J. G. Tenberge[2], G. Wilde[1]

[1]University of Münster, Institute of Materials Physics, Münster, Germany
[2]University Hospital Münster, Institute for Translational Neurology, Münster, Germany

martin.peterlechner@uni-muenster.de

Series of Nano-Beam Diffraction Pattern (NBDP) are a powerful tool to determine quantities as strain in crystals or medium ranged order (MRO) in amorphous phases [1]. This can be deduced by collecting hundreds of NBDPs and analyze them numerically. However, big data sets are easily achievable and can be analyzed quantitatively. The present work focuses the analysis and physical quantities which can be deduced from big series of experimental and simulated NBDPs.
As an experimental test system two differently processed amorphous phases of basically equiatomic NiTi were chosen, a sputter deposited (SD) and a deformation induced (DI) amorphous phase. The SD and DI samples show fundamentally different crystallization kinetics [2], giving rise to speculations on their MRO. Series of NBDPs of SD and DI amorphous NiTi were recorded, typically 400 micrographs. The data were evaluated by means of statistical intensity fluctuations in the diffraction patterns, reflecting the presence of coherently scattering domains according to the method of fluctuation electron microscopy (FEM) [1]. Additionally image simulations of structures generated by molecular-dynamic (MD) simulations were made, to test for the sensitivity and statistical reliability of the conclusions made by the FEM analysis. Analysis and simulation was accomplished using python programming and Digital micrograph™ scripting. Images of comparable large amorphous structures were simulated using a newly developed multi-GPU-based multislice algorithm. A software tool was developed by Manuel Radek and Jan-Gerd Tenberge based on the multislice algorithm by Kirkland [4] with several optimizations for GPU parallelization and a user interface based on python.
In Figure 1 a) a schematic drawing of the diffraction experiment is shown. A focused spot onto a selected atom with a size close to the interatomic distance reflects the symmetry of the surrounding atom positions. In Figure 1 b) it is shown that this can show crystal-like symmetry for selected NBDPs of DI amorphous NiTi, whereas this was not observed for SD NiTi. This ordering can be mapped using e.g. 400 NBDPs and a selection of the normalized intensity variance along a reciprocal k-value of 4-6 nm-1. At certain parameters, networks of MRO can be detected, as shown in Fig. 2 b).
Based on the simulation sensitivity check it is concluded, that coherently scattering domains (as MRO) can be unambiguously detected with a high sensitivity. Therefore the DI NiTi can be denoted as amorphous with networks of MRO, whereas the SD NiTi is fully amorphous. Experimental limitations of the given statistical approach are discussed and the simulation approach is critically reviewed.

[1] P.M. Voyles, D.A. Muller, "Fluctuation microscopy in the STEM", Ultramicroscopy 93 (2), (2002) 147-159.
[2] M. Peterlechner, J. Bokeloh, G. Wilde, T. Waitz, "Study of relaxation and crystallization kinetics of NiTi made amorphous by repeated cold rolling", Acta Mater. 58 (2010) 6637–6648.
[3] Kirkland, E. J. "Advanced Computing in Electron Microscopy" Springer (2010).

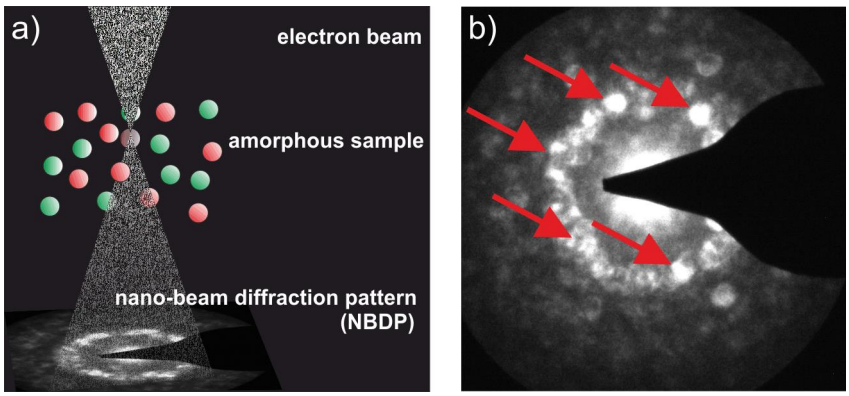

Figure 1. HAADF-STEM scan of an amorphous sample, acquiring NBDPs. In a) a schematic sketch of an acquisition is shown, illustrating the diffraction of a well-focused convergent beam with a disordered structure. b) Symmetries in the experimental NBDPs of NiTi are analyzed showing crystal-like structural MRO. The red arrows mark reflections (speckles) with a 6-folded rotational symmetry.

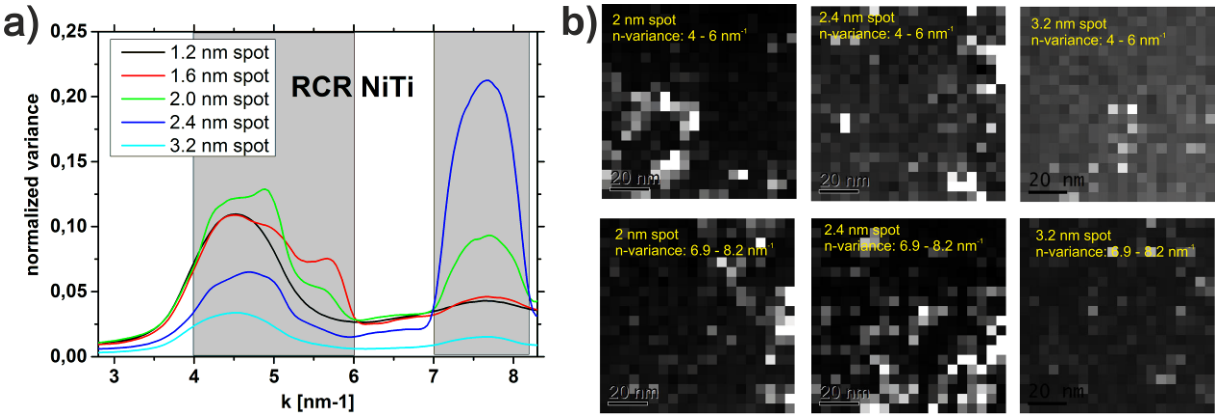

Figure 2. a) Normalized variance as function of k-values deduced from NBDPs. A variance selection was used to calculate the images in b), where networks of order can be detected with a spot size of 2 nm for correlations with 4-6 nm-1.

IM3.006
Imaging of solid oxide fuel/electrolysis cell material degradation by focused ion beam-scanning electron microscopy with 3-D elemental mapping capability

A. Nakajo[1], G. Rinaldi[1], M. Cantoni[2], Z. Wuillemin[3], J. Van Herle[1]

[1]EPFL, Mechanical Engineering, Sion, Switzerland
[2]EPFL, Interdisciplinary Centre for Electron Microscopy, Lausanne, Switzerland
[3]SOLIDpower-HTceramix, Yverdon-les-bains, Switzerland

arata.nakajo@epfl.ch

Solid Oxide Fuel Cells (SOFC) achieve nowadays >60% electric net *ac* efficiency for the conversion of natural gas in small scale systems (1-100kW). In reverse mode, solid oxide electrolysis cells (SOEC) are being developed intensely for storing growing excess renewable electricity into gas (H_2, CH_4), reaching close to 100% electrical-to-H_2 efficiency. The challenge remains to mitigate the performance degradation with time, which is now of a few % per year and becomes increasingly difficult to detect and quantify. The degradation stems from morphological, chemical and crystallographic changes, due to intrinsic material instabilities and (exo- and endogenous) impurities.

3-D imaging largely contributed to the current understanding of the relationships between the microstructure and performance of SOFC/SOEC materials. A significant body of literature based on focused ion beam-scanning electron microscopy (FIB-SEM) serial sectioning and/or synchrotron x-ray nanotomography (XNT) discusses the effects of aging on the metric, topological and effective properties of the heterogeneous electrodes. Analyses based on averaged (effective) properties have however limited sensitivity to local alterations that are believed to trigger and/or exacerbate degradation. Standard FIB-SEM and differential absorption contrast XNT imaging also provide limited possibilities for elemental mapping. 3-D FIB-SEM/energy dispersive x-ray spectroscopy (EDX) imaging enables overcoming largely these limitations.

The region comprising the yttria-stabilized zirconia (YSZ) electrolyte, the gadolinia-doped ceria (GDC) compatibility layer, the Ni-YSZ hydrogen electrode and the lanthanum strontium cobalt ferrite-based oxygen electrode has been imaged by FIB-SEM/EDX serial sectioning. The samples were extracted from a pristine cell and after 11000 h in SOEC (steam electrolysis, 710°C and 0.6 A cm^{-2}) and 16000 h in SOFC (dry H_2, 780°C and potentiostatic mode at 0.8 V). The SOFC test was performed in a special segmented-cell setup, allowing electrochemical impedance spectroscopy (EIS) measurements on individual segments to map the evolution of the spatial distribution of the degradation. FIB-SEM imaging was performed at an acceleration voltage of 1.8 kV. Before the acquisition, fiducial marks were milled to adjust the position of the FIB beam and guarantee isometric voxels of 10 nm, with a precision of 1 nm. Data from the secondary electron/secondary ion (SESI) and energy selective backscattered (EsB) was recorded simultaneously. Every 10 slices, the acceleration voltage was automatically switched from 1.8 kV to 10 kV for EDX. The reconstructed volumes was typically of 35x10x10 μm^3, which corresponds to the representative volume element for the effective properties of the heterogeneous electrode materials plus the electrolyte and compatibility layer thicknesses.

The combination of the 3-D SESI and EsB data with high spatial resolution and 3-D EDX elemental maps provides new insights into the microstructural alterations that occur during operation (a). Significant changes were observed in the 11000 h SOEC sample, such as the formation of a $SrZrO_3$ insulating secondary phase (b). Localized changes include intra-phase micro-cracks in the O_2 electrode and inter-phase cracks in the Ni-YSZ electrode (c), predominantly close to the YSZ electrolyte. Closed porosities form along the grain boundaries in the YSZ electrolyte, on the oxygen electrode side (d.). The weakening results in delamination over large area that impedes the transport of oxygen ions. Ni coarsening and depletion close to the electrolyte is also observed. The performance degradation simulated by 3-D polarization resistance measurements is in line with the EIS measurements. The reasons for the degradation is investigated further by computing the difference in the spatial distribution and local morphology of the electrocatalytic sites and their accessibility by the transport of ions and electrons.

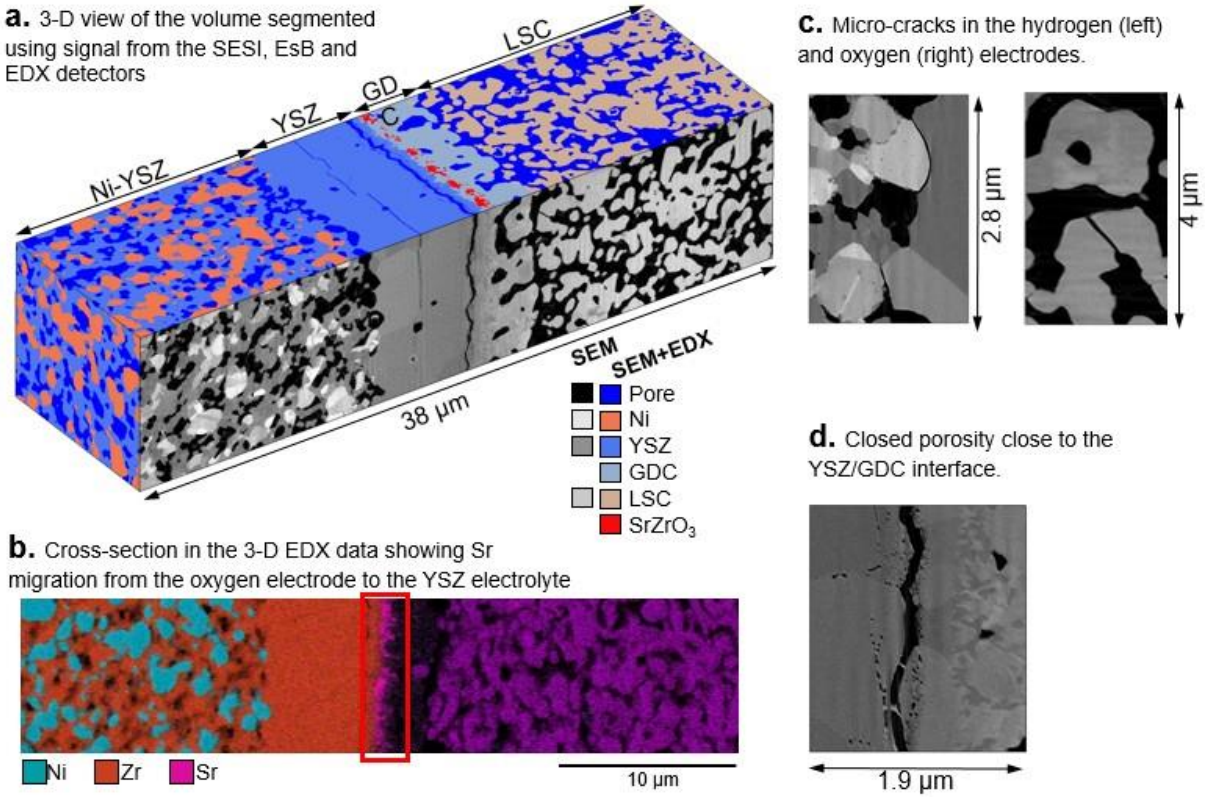

Figure 1. 3-D reconstruction of a sample operated in SOEC mode for 11000 h obtained by FIB-SEM/EDX.

IM3.P001
Resolution estimation of real sample images

R. Mizutani[1], R. Saiga[1], Y. Itoh[1], Y. Suzuki[2]

[1]Tokai University, Kanagawa, Japan
[2]University of Tokyo, Chiba, Japan

ryuta@tokai-u.jp

Image resolvability is the primary concern in microscopy. The spatial resolution of microscopic images depends not only on the microscope specifications, but also on many other factors including the ambient environment and the sample itself. We report here a method for estimating the resolution from real sample images [1].
In electron microscopy, Fourier ring/shell correlation has been used to estimate the sample image resolution [2]. Another method to estimate the resolution is to find a high-resolution limit in the frequency domain profile [3]. However, these methods rely on human-defined cutoffs, and hence involve arbitrariness in their nature.
The image resolvability is ascribable to the width of the point spread function (PSF) constituting the image. Therefore, the resolution can be determined from the PSF without defining any cutoffs. We have recently reported a method for extracting the PSF profile regardless of image types [1,4]. If we assume a Gaussian PSF, the logarithmic square norm of the Fourier transform $F(\mathbf{k})$ of the image is proportional to the square distance from the origin [1]:
$\ln|F(\mathbf{k})|^2 = -4\pi^2\sigma^2|\mathbf{k}|^2 + \text{constant}$, where $\mathbf{k}$ is the Fourier domain coordinate and σ is the standard deviation of the Gaussian PSF.
Figure 1a-c shows electron microscopic images of myelinated axons of a mouse brain. The original image was convolved with Gaussians having full width at half maximums (FWHM) of 2, 4, and 6 pixels. Bar patterns embedded in the images indicated that blurring corresponding to the Gaussian FWHM was introduced. The resolutions of these images were evaluated on logarithmic intensity plots [1,4] made using the RecView software (https://mizutanilab.github.io/). The obtained plots showed linear correlations proportional to squares of the FWHM (Figure 1d-f), indicating that the resolution can be determined with this method. A linear correlation was observed regardless of the image type, even using a cell phone picture [1] and a satellite image [4]. We suggest that this method can be an alternative measure of the spatial resolution that is independent of the imaging modality.

[1] R. Mizutani et al., J. Microsc. 261 (2016) 57
[2] W.O. Saxton & W. Baumeister, J. Microsc.127 (1982) 127
[3] C. Jacobsen et al., J. Opt. Soc. Am. A 7 (1990) 1847
[4] R. Mizutani et al., AIP Conf. Proc. (2017) in press

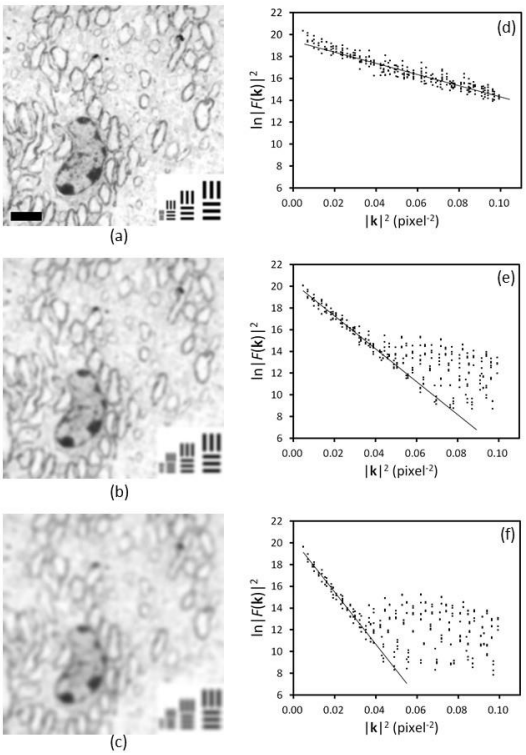

Figure 1. An electron microscopic image of myelinated axons of a mouse brain was convolved with Gaussians having FWHM of (a) 2 pixels, (b) 4 pixels, and (c) 6 pixels. Bar patterns with 2, 4, 6, and 8 pixel pitches indicated corresponding blurring was introduced. Scale bar: 2 μm. The resolutions of these images were evaluated on logarithmic intensity plots (d-f). The obtained plots showed linear correlations proportional to squares of the FWHM.

IM3.P002
STEM sensitivity for density change detection studied by image simulations

S. Hilke[1], M. Radek[1], J. G. Tenberge[2], V. Hieronymus-Schmidt[1], G. Wilde[1], M. Peterlechner[1]

[1]Institute of Materials Physics, Münster, Germany
[2]Institute for Translational Neurology, Münster, Germany

sven.hilke@uni-muenster.de

Amorphous solids and metallic glasses are in focus of research since decades. However, experimental structure analysis is not straight forward. Local diffraction experiments collecting nano-beam diffraction pattern (NBDP) are a powerful tool to analyze amorphous structures. Recently the methods of fluctuation electron microscopy (FEM) [1] as well as electron correlation microscopy (ECM) [2] were introduced in transmission electron microscopy (TEM). Diffraction is capable to study relaxation of amorphous samples and possibly volume diffusion in solid matter. In the present study, the sensitivity of TEM methods to measure single atomic jumps or missing atoms in solids is analyzed. High angle annular dark field (HAADF) scanning TEM (STEM) is sensitive enough to detect signals of single atoms. It is the aim of the present work to show that density changes can be quantitatively analyzed in crystalline silicon and amorphous copper zirconium () by STEM.
Image simulations of experimentally realistic sample dimensions are extremely time costly, thus a parallelized GPU-based multislice algorithm was developed at our institute [3]. For the image simulations a perfect crystalline Si box (e.g. 8000 atoms – 5.4x5.4x5.4 nm) in (100) direction as well as an amorphous CuZr box (e.g. 31292 atoms – 10x10x5 nm) is used. HAADF-STEM images of the MD structures were simulated using the multi-GPU-based multislice algorithm based on the multislice approach described by Kirkland [4]. Thermal vibrations were excluded. Typical slice thicknesses for the multislice simulations have been chosen to be 1.375 Å, motivated by the next neighbor distance in crystalline silicon. In Figure 1 the simulated HAADF-STEM images of crystalline Si and amorphous CuZr are presented. It should be noted, that parameter testing showed stable results. Quantitative simulation results of an extracted atom (in the scan area) are shown in Figure 2 a) and c). In Figure 2 b) and d) the actual contrast difference between the images with and without extracted atoms are shown.
The contrast in the HAADF-STEM images of crystalline samples reflects directly the atomic structure, whereas the speckle-like contrast of the amorphous structure shows smaller features sensitive to the very local structure. It turned out that single extracted atoms give rise to density changes of several percent, clearly detectable in HAADF-STEM images as well as in bright-field STEM images. The signal of the local density change can be quantitative analyzed by HAADF-STEM, whereas diffraction contributions lead to strong deviations in the bright-field images.
It is concluded, that density changes amounting to less than a single missing atom in solid amorphous and crystalline samples can be detected and quantified with good accuracy by HAADF-STEM images. Diffraction dominated contrast at low scattering angles (bright-field, high-resolution TEM) is not capable to quantify the density changes. However, bright-field/high-resolution TEM contrast can be used to qualitatively detect local changes (by e.g. diffusional jumps or structural relaxation) with high sensitivity in crystalline and particularly in amorphous structures.

[1] He, L., Zhang, P., Besser, M. F., Kramer, M. J., & Voyles, P. M. (2015). Electron correlation microscopy: a new technique for studying local atom dynamics applied to a supercooled liquid. Microscopy and Microanalysis, 21(04), 1026-1033.
[2] P.M. Voyles, D.A. Muller (2002). Fluctuation microscopy in the STEM, Ultramicroscopy, Volume 93, Issue 2, Pages 147-159.
[3] Radek, M., Tenberge, J.-G.; private communication.
[4] Kirkland, E. J. Advanced Computing in Electron Microscopy, Springer (2010).

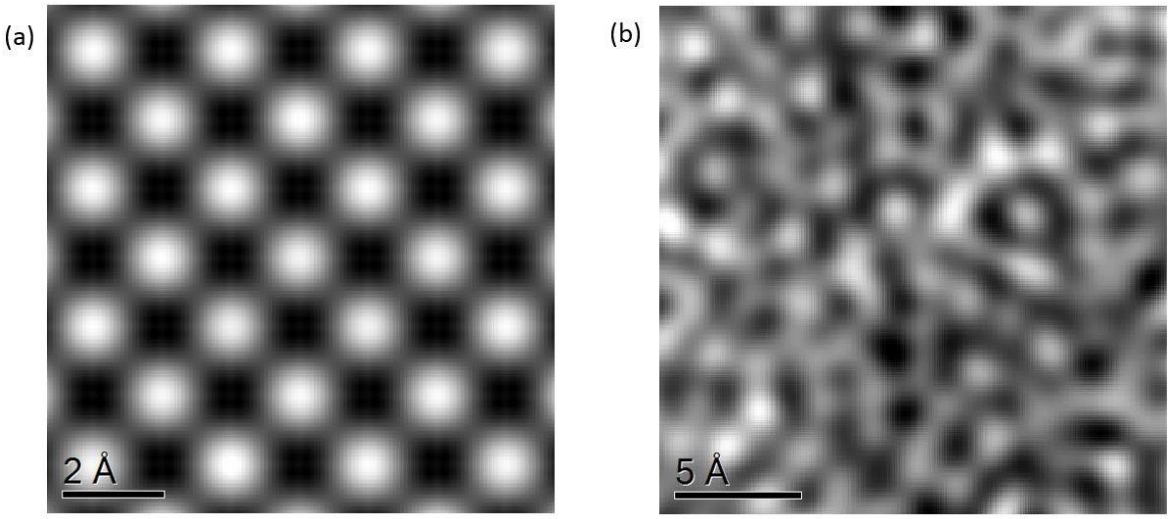

Figure 1. Simulated HAADF-STEM images of c-Si (a) and a-CuZr (b) are shown.

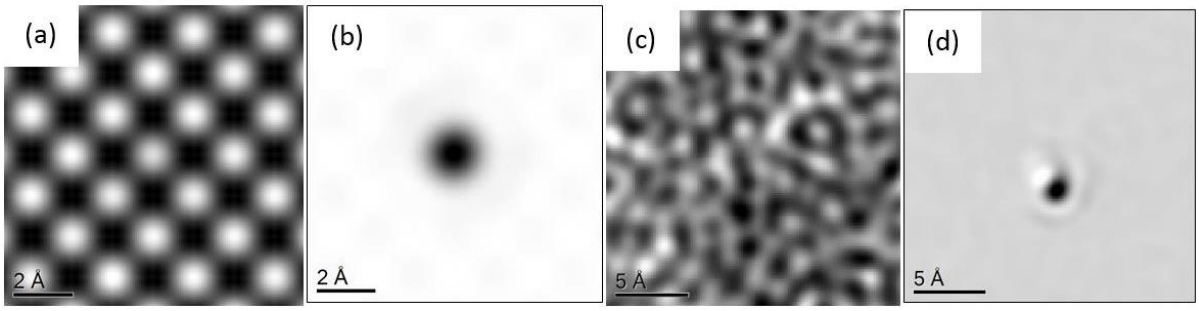

Figure 2. HAADF-STEM images after atom extraction. In (a) one Si atom at the center of the scan area has been extracted. The difference of Fig. 1 a) and Fig. 2 a) is shown in (b). The exemplary extraction of a Zr atom at the center of the scan area is shown in (c) and (d) illustrates the difference of Fig. 1 b) and Fig. 2 c).

IM3.P003
Automatic sample screening and particle analysis using MiniTEM

I. M. Sintorn[1,2], M. Ryner[1], G. Kylberg[1], P. Malm[1], M. Colomb-Delsuc[1]

[1]Vironova AB, Stockholm, Sweden
[2]Uppsala Unversity, Information Technology, Uppsala, Sweden

ida.sintorn@vironova.com

Introduction: The MiniTEM system is a transmission electron microscopy and analysis platform with a high degree of automation in the microscope operation, image acquisition and analysis process. The system is comprised of a low-voltage (25keV) transmission electron microscope and software combining microscopy operation and analysis. The result is an easy to use TEM analysis platform for manual, interactive and fully automated qualitative and quantitative characterization of biological as well as inorganic samples of e.g. nano-particles, nano-material, and thin tissue sections. The MiniTEM system thus allows for greatly reducing the time consuming tasks associated with manual imaging, particle marking, and particle measurements while at the same time reducing the user bias. The automation in addition allows for a far larger number of images and particles to be analyzed which make the results more consistent, statistically significant and reproducible.
Objectives: In this study we show how automatic image acquisition and image analysis can be combined in the MiniTEM system to 1) screen and analyze the integrity of Adenovirus particles in solution, and 2) search for retrovirus particles in thin tissue sections of cultured cells.
Materials and Methods: The Adenovirus samples were prepared using the sitting drop-procedure and stained with uranyl acetate. Cultured retrovirus infected cells were fixated and embedded in plastic resin, sectioned in 50nm sections and post-stained with uranyl acetate. Customized analysis scripts were created in the MiniTEM system. Scripts are created by dragging, dropping and connecting building blocks (imaging and analysis methods) in the system software. For the Adenovirus analysis the scripts contained and imaging module saying that a set of images should be acquired at five different locations on the grid, using auto-focus and auto-illumination. In each acquired image, particles were detected based on their circular shape and size. Each particle was next classified as intact or non-intact based on their internal staining pattern. For the cell section analysis, a template was interactively extracted from one manually acquired image. Virus particles were then detected while screening the sample using template matching.
Results: An illustration of the Adenovirus integrity analysis along with the final results comparing the proportion of intact versus non-intact particles in two samples are shown in Figure 1. In total 11 101 Adenovirus particles were detected and classified. Figure 2 illustrates using template matching to detect retro virus particles in an ultra thin cell section.
Conclusion: This work illustrates how utilizing the automation possibilities in the MiniTEM system greatly reduce the amount of manual labor and time required for imaging and characterizing the contents of samples of different types.

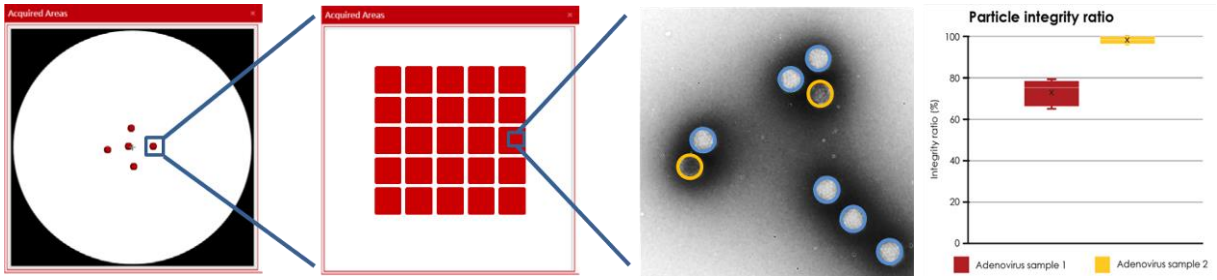

Figure 1. Illustration of automatic image acquisition and analysis of Adenovirus particle integrity. From left to right: Overview of the grid showing positions where images were acquired; At each position a set of images was acquired; Part of one image (field of view shown = 1µm) showing detected Adenovirus particles classified as intact (blue) or broken (yellow); Result plot comparing two different samples automatically analyzed by the same procedure.

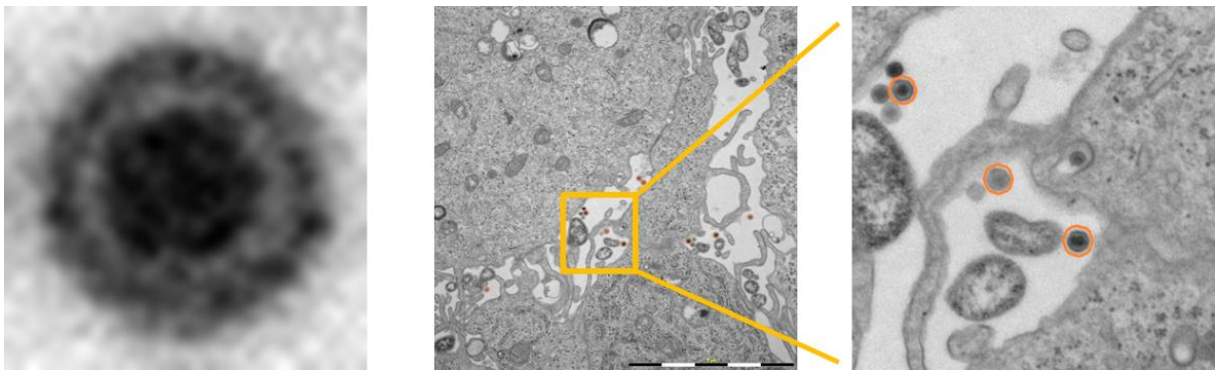

Figure 2. Illustration of retro-virus template matching in a thin section of cell culture. From left to right: Interactively extracted template (virus particle diameter= 145nm); Result of template matching in image with field of view 11 µm; Zoomed in part illustrating that only spherical particles resembling the template are detected.

IM3.P004
Palynomorphology of Iris humilis ssp. arenaria grown in Subotica sandS (Serbia)

M. Mačukanović-Jocić[1], S. Avramov[2], D. Smailagić[2], A. Kostić[3], M. Mladenović[4]

[1]Faculty of Agriculture University of Belgrade, Department of Botany, Belgrade, Serbia
[2]Faculty of Agriculture, University of Belgrade, Department of Agrobotany, Belgrade, Serbia
[3]Faculty of Agriculture, University of Belgrade, Department of Food Technology and Biochemistry, Belgrade, Serbia
[4]Faculty of Agriculture, University of Belgrade, Department of Pomology and Viticulture, Belgrade, Serbia

marmajo@agrif.bg.ac.rs

Introduction: Iris humilis ssp. arenaria (Waldst. & Kit.) A. Löve & D. Löve (Sandy iris; Iridaceae) is a Pontic-Pannonian endangered and protected species occurring in southeastern and southern part of Central Europe. This is a pioneer species of sandstone (Festucion vaginatae Soó 1929) and steppe (Festucion rupicolae Soó 1940) habitats, but in the spontaneous extinction. In Serbia, Sandy iris has only two naturally growing spots, in the Subotica Sands (landscape of outstanding features) and the Selevenj heath (special nature reserve). It blooms in April and May, flowering period is short and short-lived flowers last only one day each.
Objectives: The present study represents an integral part of the extensive palynological studies, aiming at possibly providing some new information, which would be helpful for assessing the taxonomic position of the species within the genus, as well as to contribute to the pollen atlas of Serbian apiflora.
Materials and Methods: Pollen material was collected in the field and fresh anthers were taken from the flowers at the beginning of anthesis. The pollen morphology was examined by scanning electron microscopy (SEM) using JEOL JSM-6390 LV electron microscope at an acceleration voltage of 20 kV. For SEM observation the samples were mounted directly on metallic stubs and coated with gold (in BAL-TEC SCD 005 Sputter Coater, 100 seconds in 30 mA) in a sputtering chamber. SEM micrographs were used mainly for studing the shape and size of grains, the length of polar (short) axis (P) and equatorial diameter (long axis - E), lumina diameter, muri thickness, as well as to get more detailed information on the ornametation (sculptural elements). The pollen grains were photographed in polar and equatorial views, and observations and measurements were done on a sample of 50 grains for each morphological character.
Results: The pollen grains of I. humilis ssp. arenaria are monosulcate, heteropolar and large in size. Aside from fertile and well-developed boat-shaped pollen grains with an infolded sulcus (Figs.1-3), there were also those that were irregular (abnormal). In addition, ***t*wo** different **size classes,** large and small grains, were observed. The long axis of large-sized grains averaged 88.28 ± 5.92 µm, and the short axis was in average 58.03 ± 2.62 µm. The shape of the pollen is oblate (P/E - 0.66 ± 0.05) with an elliptic equatorial outline. The smooth sulcus is normally as long as half of the circumference of the pollen grain. The exine ornamentation is reticulate with ornamented lumina polygonal or irregular in shape, up to 11.49 ± 3.01 µm in diameter. The surface of the lumina appeared granular, having sculptured elements such as granules 0.87 ± 0.18 µm in height. Occasionally, small perforations and irregular cracks 1-2.5 µm in diameter were observed along with more numerous granules, that were found to be distributed over the entire lumina surface (in average 15.36 ± 8.78 per lumen). Muri width averaged 1.13±0.19 µm.
Conclusion: The morphological features of pollen grains collected from the flowers of Iris humilis grown in Serbia were investigated using scanning electron microscopy. Pollen grains are monosulcate, heteropolar, elliptical in polar view, large in size. The exine surface pattern is reticulate with ornamented lumina, polygonal or irregular in shape, covered with numerous granules.

Acknowledgements
This study was supported by the Ministry for Education, Science and Technological Development of the Republic of Serbia, Project Nos. 46009, 173025 and TR 31069.

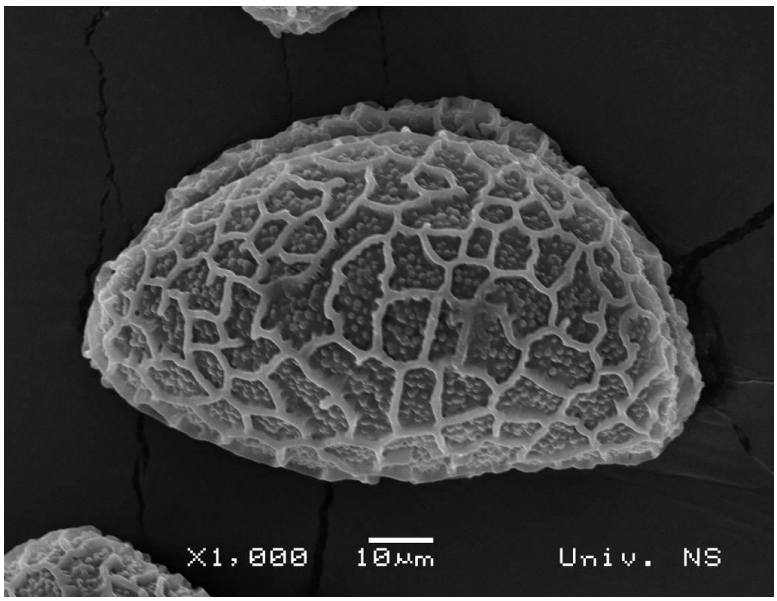

Figure 1. Monosulcate pollen grain of *Iris humilis* ssp. *arenaria.* General view (SEM).

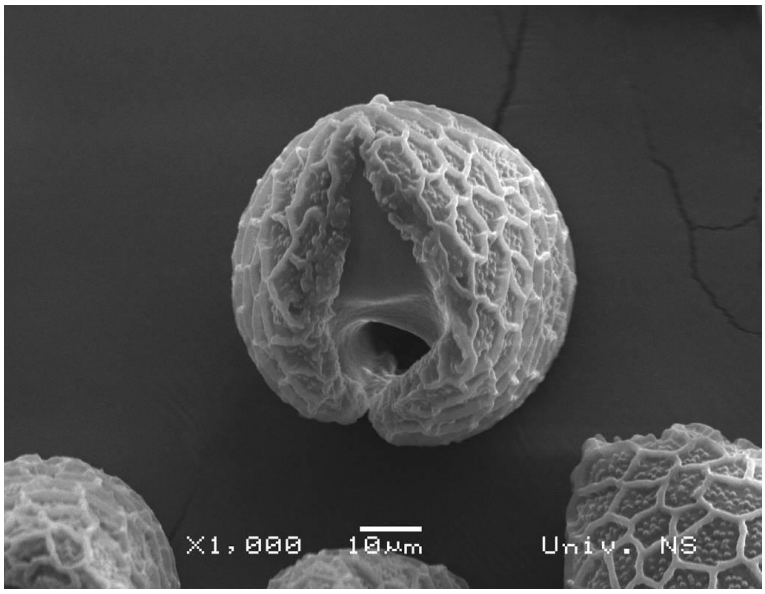

Figure 2. Pollen grain in equatorial view showing an infolded sulcus.

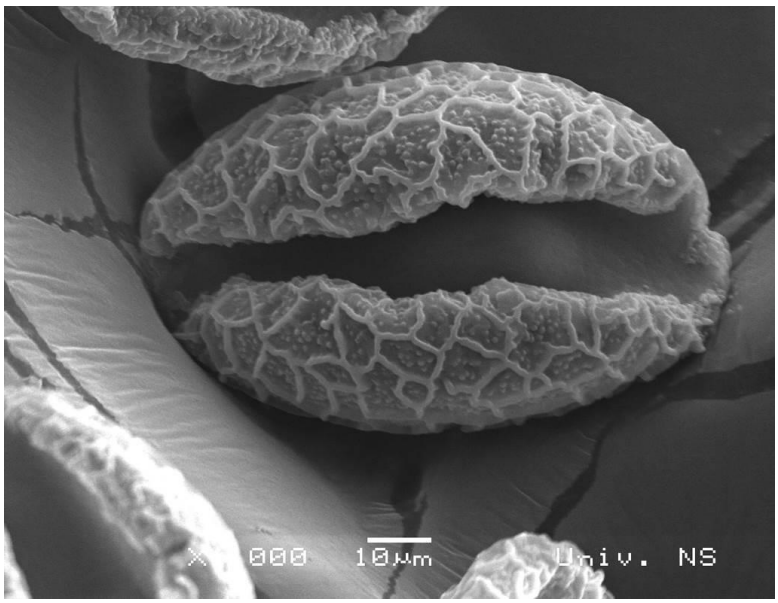

Figure 3. Boat-shaped pollen grain in distal polar view.

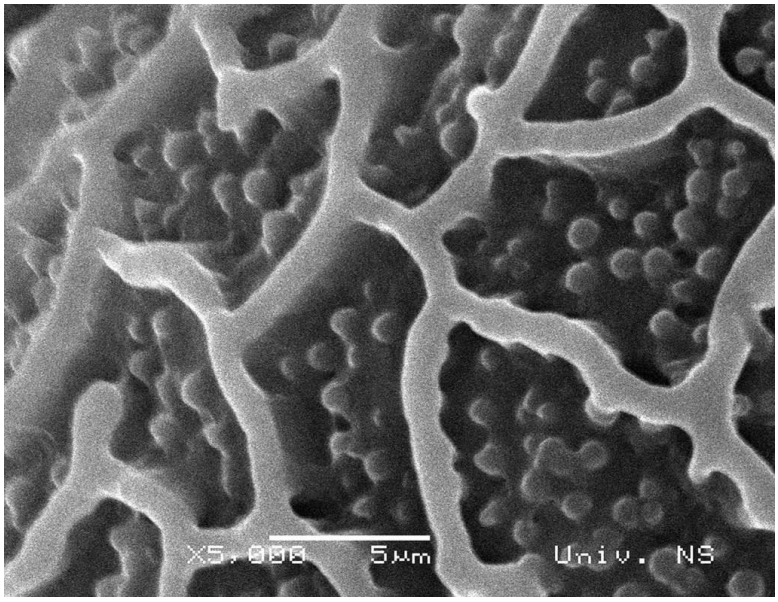

Figure 4. A detial of exine pattern showing reticuate ornamentation with granulate lumina.

IM 4: Quantification and modelling

IM4.001 invited
Delocalization of EMCD signal in spectrum images of samples tilted into three beam orientation

J. Rusz[1], J. Spiegelberg[1], S. Muto[2], T. Thersleff[3], M. Ohtsuka[2], K. Leifer[1], P. M. Oppeneer[1]

[1]Uppsala University, Uppsala, Sweden
[2]Nagoya University, Nagoya, Japan
[3]Stockholm University, Stockholm, Sweden

jan.rusz@physics.uu.se

Electron magnetic circular dichroism (EMCD) is an experimental technique utilising energy loss near edge structures (ELNES) to extract quantitative magnetic information about samples [1] using the EMCD sum rules [2]. Recently it was demonstrated that the EMCD signal can be detected with atomic size electron probes [3,4,5]. Approaching thus the atomic-column resolution or atomic-plane resolution in EMCD studies, it is important to know the physical limits of the spatial resolution achievable by this technique, caused by the well-known effect of delocalization of inelastic scattering [6].
We have approached this question for the recently employed experimental setups, where the sample is oriented in a three-beam orientation, as reported in [4,5]. We have performed simulations of the inelastic electron scattering cross-section [7], separating the total cross-section into a magnetic (EMCD) and non-magnetic component. Ref.[4] introduces a new atomic plane resolution approach (APR-EMCD), where only one spectrum image needs to be acquired for extraction of the EMCD signal. In Ref.[5] a classical setup requiring acquisition of four spectrum images (for four different detector orientations) is presented. The EMCD is then extracted using the double-difference method. We refer to this method as DD-EMCD. Localization properties for both DD-EMCD and APR-EMCD have been addressed on a same model system, a bcc iron crystal oriented in three-beam orientation with systematic row index G=(110).
Our simulations show the well-known oscillatory behavior of EMCD as a function of sample thickness. When avoiding the sample thicknesses with very low EMCD signal fraction, the EMCD signal is predicted to be strongly localized. For DD-EMCD this refers to a situation with an electron beam centered on the atomic plane. For APR-EMCD the signal is extracted from two sides of an atomic plane. In either case, the localization of the EMCD signal is stronger than the localization of the non-magnetic signal, where non-negligible contributions of about 10% from each of the two neighboring atomic planes are predicted. In addition, we observe strong double-channeling effects in DD-EMCD and somewhat higher sensitivity of APR-EMCD to sample thickness, as compared to DD-EMCD.
In conclusion, our study theoretically predicts that APR-EMCD and DD-EMCD experiments with atomic size electron probe will give access to atomic-plane-resolved magnetic properties of samples. This finding is important for the prospects of achieving high spatial resolution EMCD studies of surfaces and interfaces.

[1] P. Schattschneider, S. Rubino, C. Hebert, J. Rusz, J. Kunes}, P. Novak, E. Carlino, M. Fabrizioli, G. Panaccione and G. Rossi, Nature **441**, 486 (2006).
[2] J. Rusz, O. Eriksson, P. Novak, P. M. Oppeneer, Phys. Rev. B **76**, 060408(R) (2007).
[3] J. C. Idrobo, J. Rusz, J. Spiegelberg, M. A. McGuire, C. T. Symons, R. Raju Vatsavai, C. Cantoni, and A. R. Lupini, Adv. Chem. Struct. Imaging **2**, 5 (2016).
[4] J. Rusz, S. Muto, J. Spiegelberg, R. Adam, K. Tatsumi, D. E. Burgler, P. M. Oppeneer, C. M. Schneider, Nat. Comm. **7**, 12672 (2016).
[5] T. Thersleff, J. Rusz, B. Hjorvarsson, K. Leifer, Phys. Rev. B **94**, 134430 (2016).
[6] A.R. Lupini, S.J. Pennycook, Ultramicroscopy **96**, 313 (2003).
[7] J. Rusz, Ultramicroscopy **177**, 20 (2017).

IM4.002
Transmission electron microscopy as a tool for bottom-up chemical kinetics

E. Besley[1], S. Skowron[1], A. Chuvilin[2]

[1]University of Nottingham, School of Chemistry, Nottingham, United Kingdom
[2]NanoGUNE, San Sebastian, Spain

elena.besley@nottingham.ac.uk

Traditional chemical kinetics studies the rates of chemical reactions, in which atomic level information such as reaction mechanisms and activation energies are inferred from experiments concerning macroscopic, ensemble-averaged quantities. In contrast to this traditional *top-down* approach, the emergence of direct atomic-scale imaging with modern microscopy techniques such as transmission electron microscopy (TEM) provides an opportunity for a *bottom-up* approach, where a statistical treatment of multiple individually observed reactions can be used to measure kinetic parameters.
By using concepts informed by the field of chemical kinetics, we aim to transform TEM into a tool for providing quantitative information about the rates of dynamic processes occurring under the electron beam. This approach not only includes the rates and cross-sections of beam induced processes, but also encompasses the rates, rate constants and activation energies of equivalent thermally induced reactions. As the thermal processes also occur outside of the TEM, their wider relevance means that information about the barriers to these reactions is of general interest.
As a test case, we apply this methodology to transforamations of point defects in graphene. The cross-sections and threshold energies of irreversible (atom emission) and reversible (bond rotation) processes are measured. Observation of statistically significant number of events at variable experimental conditions allows us to decouple beam induced and thermal reaction pathways and obtain independent estimations of the cross-sections and activation energies for direct and back bond rotations. The back rotation is characterized by a very high value of the cross-section. Comparisons to theoretical estimations indicate that the assumed mechanism of direct knock-on damage cannot be the main cause of SW defect healing under electron beam.
In summary, the kinetics of bond rotations in pristine graphene were studied with the statistical treatment of a large number of individual atomic-scale observations in TEM. The reversibility of the process was taken into account, and the e-beam and background thermally activated contributions to the rates were decoupled, allowing the cross-sections and activation energies of the formation and healing of SW defects to be extracted from the TEM image series. The statistical atomic kinetics approach used here is widely applicable, and provides a promising route for the experimental determination of quantitative kinetics information of chemical reactions that can be imaged in TEM.

IM4.003
Determining oxygen relaxations at an interface – a comparative study between transmission electron microscopy techniques

N. Gauquelin[1], K. H. W. van den Bos[1], A. Béché[1], F. F. Krause[2], I. Lobato[1], S. Lazar[3], A. Rosenauer[2]
J. Verbeeck[1], S. van Aert[1]

[1]EMAT, University of Antwerp, Physics, Antwerp, Belgium
[2]University of Bremen, Institute of Solid State Physics, Bremen, Germany
[3]FEI Company, Eindhoven, Netherlands

nicolas.gauquelin@uantwerpen.be

Introduction: In order to go beyond silicon technology limitations, many researches are now focussing on the development of new electronic devices based on oxide materials [1]. In this field, interfaces between two perovskite ABO3 oxide materials are very promising as new exotic electronic properties can arise which are not present in the bulk material [2,3]. In order to understand the physical properties of such materials, it is mandatory to characterise the oxygen network across these interfaces.
Objectives: Nowadays, different transmission electron microscopy (TEM) techniques are capable of visualising light oxygen columns including low angle annular dark field (LAADF) STEM, annular bright field (ABF) STEM, integrated differential phase contrast (iDPC) STEM [4], negative spherical aberration imaging (NCSI) and imaging STEM (ISTEM) [5]. In order to help the microscope user select which technique is most suitable for his purpose, a quantitative comparison will be presented.
Materials and Methods: In electron microscopy, statistical parameter estimation theory provides an excellent tool to quantitatively extract structure parameters, such as column positions [6]. Here, an empirical model is fitted to an experimental image by optimising a criterion of goodness of fit. In this model, the shape of an atomic column is described by a Gaussian peak. In this work, the method is used to extract the column positions from experimental images of a NdGaO3-La0.67Sr0.33MnO3 (NGO-LSMO) interface (Fig. 1) and is compared to simulations. For ISTEM imaging two different focus values have been used as it was impossible to extract all column positions from a single recorded image.
Results: In this presentation, the accuracy (correctness of a measurement) of the extracted column positions along the interface for the different techniques is first evaluated (Fig. 2). Here, the evolution of the lattice parameters obtained by using the heavy Nd and La/Sr columns and the octahedral tilt of the oxygen columns [7] as a function of distance from the interface are examined. A high angle annular dark field (HAADF) STEM image served as a Reference: for the lattice parameter profiles. As results are all accurate on the NGO substrate, the precision (error on a measurement) is determined in the NGO bulk region (Fig. 3). In the presentation, the effect of sample drift correction will be discussed to enable a more fair comparison between scanning and imaging techniques. Furthermore, an outlook to the future will be given by determining the ultimate precision for the different techniques from Poisson distributed image simulations.
Conclusion: In conclusion, a quantitative comparison will be shown between different TEM techniques, which are capable of visualising light elements. Here, statistical parameter estimation theory is applied to experimental images of a NdGaO3-La0.67Sr0.33MnO3 interface to study both accuracy and precision.

[1] Lorenz *et al.,* J. Phys. D. Appl. Phys **49** (2016), 433001
[2] Mannhart and Schlom, Science **327** (2010), p. 1607
[3] Hwang *et al.*, Nat. Mater. **11** (2012), p. 103
[4] Lazić *et al.,* Ultramicroscopy **160** (2016), p. 265
[5] Rosenauer *et al.,* PRL **113** (2014), 096101
[6] De Backer, *et al.* Ultramicroscopy **171** (2016), p. 104
[7] Liao *et al.,* Nat. Mater. **15** (2016), p. 425

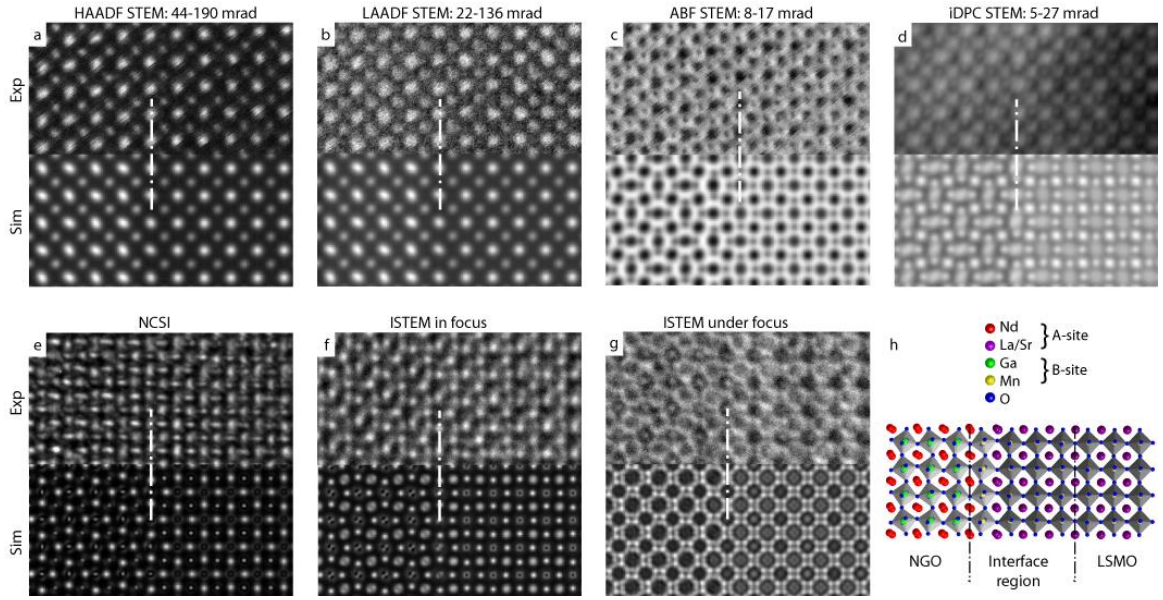

Figure 1. Experimental (top half of the panel) and simulated (bottom half of the panel) images for the different techniques investigated. The white dashed line is a guide to the eye of the location of the interface (h) Atomistic model of the NGO-LSMO interface used for the simulations.

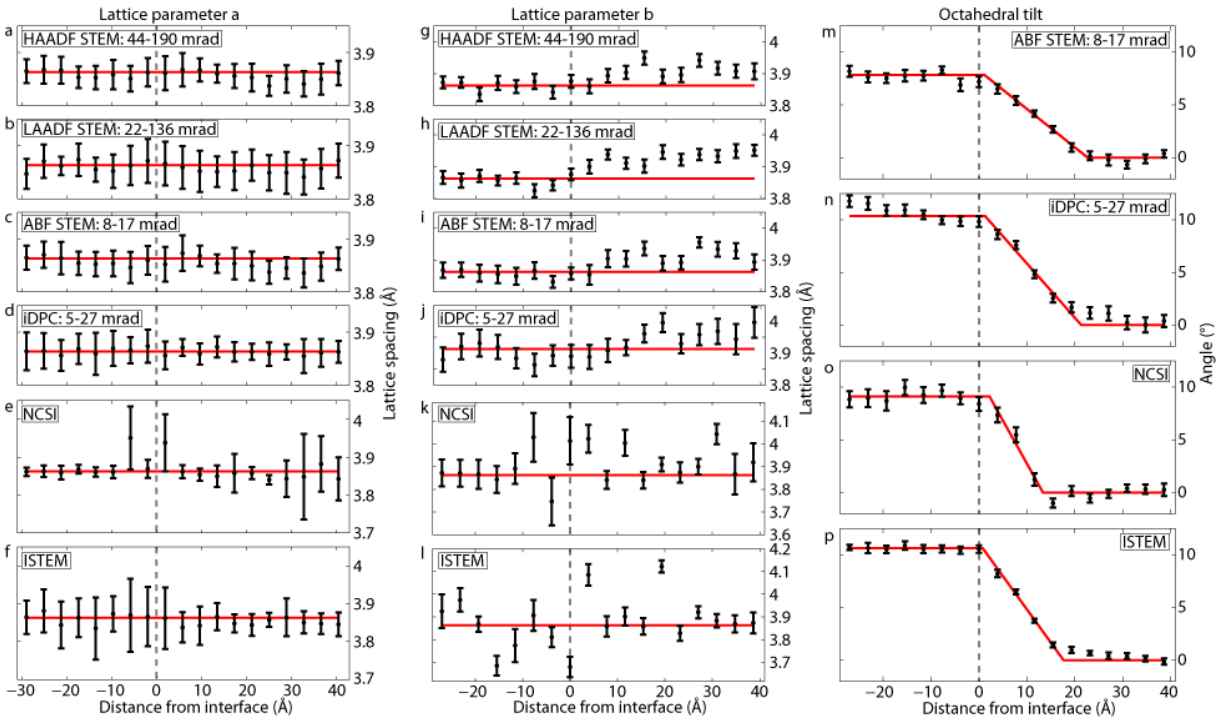

Figure 2. (a-f) The mean lattice parameter a, parallel to the interface, and (g-l) the mean lattice parameter b, perpendicular to the interface, as a function of distance from the interface. As expected, only an expansion of the lattice parameter b is seen as compared to the Reference: of 3.85Å, shown by the red line. (m-p) The mean octahedral tilt of the oxygen atomic columns around the B-site atoms as a function of distance from the interface. The change in octahedral tilt along the interface is characterised by fitting the results to a ramp function, shown by the red line.

Technique	Precision A-site (pm)	Precision B-site (pm)	Precision O columns (pm)
HAADF STEM	9.56 (*7.75 – 12.47*)	9.90 (*8.03 – 12.92*)	Not possible
LAADF STEM	12.15 (*9.85 – 15.84*)	12.65 (*10.26 – 16.50*)	Not possible
ABF STEM	9.85 (*7.99 – 12.85*)	10.88 (*8.82 – 14.19*)	14.21 (*12.10 – 17.21*)
iDPC STEM	12.83 (*10.41 – 16.74*)	10.87 (*8.82 – 14.18*)	18.88 (*16.08 – 22.86*)
NCSI	5.07 (*4.11 – 6.61*)	6.21 (*5.03 – 8.09*)	12.97 (*11.05 – 15.71*)
ISTEM in focus	Not possible	13.51 (*10.96 – 17.63*)	13.20 (*11.25 – 15.99*)
ISTEM underfocus	22.40 (*18.17 – 29.22*)	25.00 (*20.28 – 32.61*)	Not possible

Figure 3. Experimental precision with which the individual columns in the NGO bulk region can be located for the different techniques.

IM4.004
Structural and density functional theory investigation of stair-rod dislocations connected via v-shaped intrinsic stacking faults

N. Bologna[1,2], P. Agrawal[1,3], M. Campanini[1], M. Knödler[2], M. D. Rossell[1,2], R. Erni[1], D. Passerone[3]

[1]Empa, Electron Microscopy Center, Dübendorf, Switzerland
[2]IBM-Research, Rüschlikon, Switzerland
[3]Empa, Nanotech@surfaces, Dübendorf, Switzerland

nicolas.bologna@empa.ch

III-V semiconductor nanowires (NWs) are low dimensional compounds receiving an increasing interest from the research community thanks to their superior physical properties. Compared to silicon, their higher electron mobility combined with bandgap engineering results in perfectly suited materials for electronic devices. Furthermore, the nanowire geometry offers, besides novel architecture possibilities [1], a larger gap for critical dimensions below which misfit dislocations can be reduced, allowing a more optimal growth [2]. However, other types of defects can be present in the crystals, e.g. partial dislocations and stacking faults, acting as traps able to affect the performance of the device by inducing non-radiative recombination of the carriers [3]. For this reason, the structure and influence of such imperfections have been deeply studied in the last decade.
In the present work, we investigated, by means of aberration-corrected STEM, the atomic structure of {111}-oriented v-shaped intrinsic stacking faults merging together into two different stair-rod dislocations in gallium arsenide NWs (Fig. 1a,b,c). Atomic-scale elemental mapping obtained by energy dispersive x-ray spectroscopy (EDS) allowed us to determine the nature of the single gallium and arsenic columns at the dislocation cores (Fig. 1d,e), without relying only on the low Z-contrast intensity difference between Ga (Z=31) and As (Z=33) offered by the HAADF micrographs. A 3D atomic model was built using Rhodius [4] and its validity verified with Stem_Cell [5, 6] software by comparing the geometric phase analysis (GPA) of the experimental data. Concordantly, both simulated and experimental data show no strain in the direction parallel and perpendicular to the stacking faults but only a rotation of the atomic plane. The same model was then implemented in density functional theory (DFT) calculations to analyze the effect induced on the band gap and the density of states (DOS). A decrease in the gap from 1.15 eV (bulk) to 0.65 eV (defect) was observed. Furthermore, Figure 2 shows a shift in the DOS from the valence band of the gallium core to the conduction band of the arsenic dislocation core, along the intrinsic stacking fault. This confirms that the two connected dislocation cores act as carrier traps both for electron and holes affecting the efficiency of an ideal electronic device. [7]

[1] A. M. Ionescu and H. Riel, Nature, vol. 479, no. 7373, pp. 329–337, 2011.
[2] L. C. Chuang, M. Moewe, C. Chase, N. P. Kobayashi, C. Chang-Hasnain, and S. Crankshaw, Appl. Phys. Lett., vol. 90, no. 4, pp. 1–3, 2007.
[3] A. D. Schricker, F. M. Davidson, R. J. Wiacek, and B. a Korgel, Nanotechnology, vol. 17, no. 10, pp. 2681–2688, 2006.
[4] S. Bernal, F. J. Botana, J. J. Calvino, C. López-Cartes, J. a. Pérez-Omil, and J. M. Rodríguez-Izquierdo, Ultramicroscopy, vol. 72, no. 3–4, pp. 135–164, 1998.
[5] V. Grillo and E. Rotunno, Ultramicroscopy, vol. 125, pp. 97–111, 2013.
[6] V. Grillo and F. Rossi, Ultramicroscopy, vol. 125, pp. 112–129, 2013.
[7] This work was supported by the Swiss National Science Foundation (project no. 200021_156746 and 200021_147105).

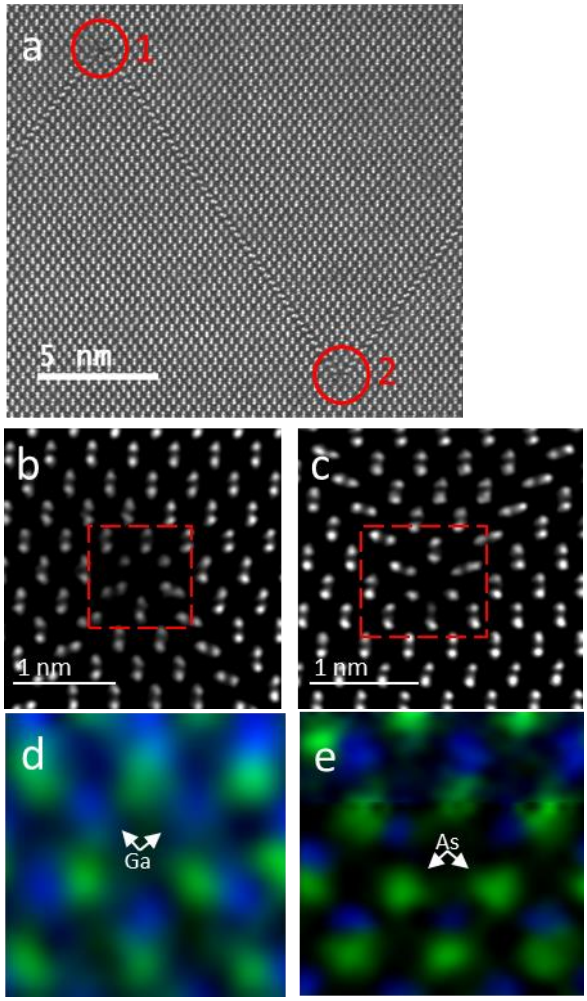

Figure 1. a) HAADF micrographs showing the two dislocation cores obtained by merging two intrinsic stacking faults lying on different {111} planes. b,c) Magnified images of the dislocations cores corresponding to the two red circles marked as 1 and 2 in panel a, respectively. Atomic-scale EDS chemical maps performed in the red dashed squares highlighting the presence of single d) gallium (blue) and e) arsenic (green) columns.

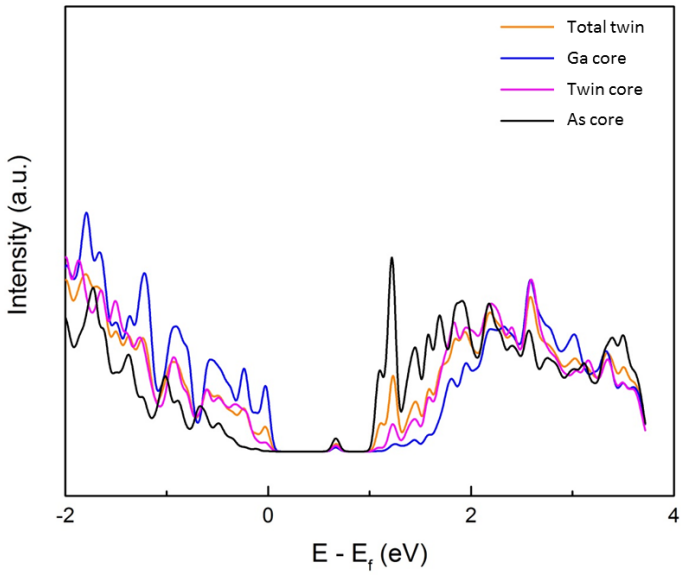

Figure 2. DOS distribution showing the gap states and the shift from the valence band states to the conduction band states in the gallium (blue) and arsenic (black) dislocation cores, respectively.

IM4.005
Using radial distribution function to quantify STEM diffraction for imaging complex glasses

X. Mu[1,2], D. Wang[1,3], A. Ahmadian[1], C. Kübel[1,2,3]

[1]Karlsruhe Institute of Technology (KIT), Institute of Nanotechnology, Eggenstein-Leopoldshafen, Germany
[2]Karlsruhe Institute of Technology (KIT), Helmholtz-Institute Ulm for Electrochemical Energy Storage (HIU), Ulm, Germany
[3]Karlsruhe Institute of Technology (KIT), Karlsruhe Nano Micro Facility (KNMF), Eggenstein-Leopoldshafen, Germany

xiaoke.mu@kit.edu

Scanning diffraction imaging (4D-STEM) techniques have seen an impressive development with automated crystal orientation mapping (ACOM) [1] opening the door to a variety of related approaches enabling a quantitative metallographic analysis [2], local strain measurements [3], or a description of the disordered structure in glasses [4] at the nanoscale. The combination of large area imaging with high spatial resolution and quantifiable information is providing unprecedented information to understand the structure and properties of materials. Furthermore, these techniques are suitable for *in situ* investigations to follow dynamic processes [2, 5].

In the present work, we are focusing on understanding the local structure in complex glasses. Only few experimental means offer a way to characterize these disordered structures. The atomic radial distribution function (RDF) is one of the important tools, which is was first developed for X-ray diffraction and afterwards extended to selected area electron diffraction for inorganic glasses [6]. The RDF describes the probability to find certain atomic pairs as a function of the pair separation and, consequently, provides short- and medium-range structural information. For a local analysis, RDF imaging, we use quasi parallel nano-beam electron diffraction in mpSTEM to acquire 4D-STEM dataset. The RDFs are calculated from all the diffraction patterns to construct a 3D data cube of RDFs. The data cube can be analyzed by hyperspectral techniques to obtain phase maps for the different amorphous materials (Fig. 1) [4]. Compared to fluctuation electron microscopy, RDF imaging has the advantage that the RDF of each phase can be analyzed in terms of bond distance, bond angle and coordination number to get direct structural information in addition to the phase distribution.

We have been applying RDF imaging to a variety of different materials and will illustrate the technique and the information that can be obtained by looking at multilayered metallic glasses, structure of shear bands as well as of nano glasses.

References:

[1] E.F. Rauch et al., Zeitschrift für Kristallographie, **2010**, *225*, p. 103.
[2] J. Lohmiller et al., *Acta Materialia*, **2014**, *65*, p. 295.
[3] C. Gammer et al, *Ultramicroscopy* **2015**, *155*, p. 1.
[4] X. Mu et al., *Ultramicroscopy*, **2016**, *168*, p. 1.
[5] A. Kobler et al., *Ultramicroscopy*, **2013**, *128*, p. 68.
[6] D.J.H Cockayne, D.R. Mckenzie, *Acta Crystallographica Section A*, **1988**, *44*, p. 870.

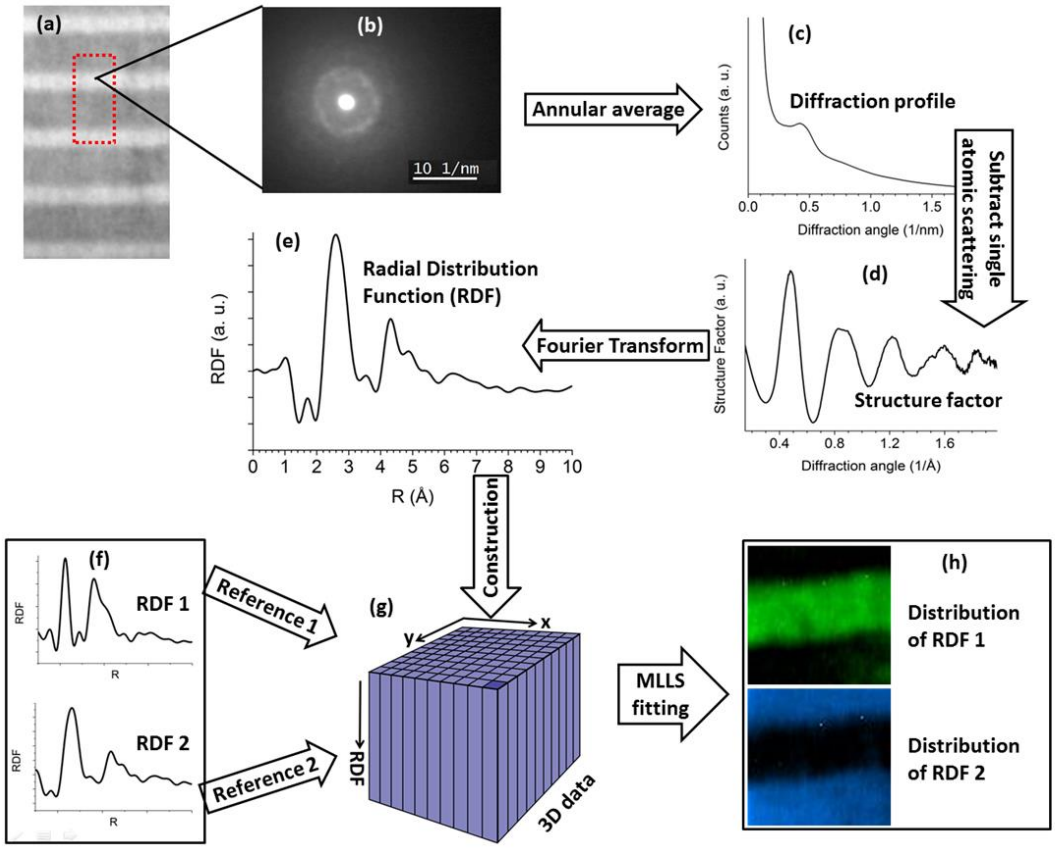

Figure 1. Sketch of procedures to calculate the RDF-cube from experimental STEM-diffraction data and MLLS analysis of the RDF-cube. (a) HAADF image. (b) A typical diffraction pattern in STEM-diffraction. (c) Annular averaged diffraction profile. (d) Structure factor. (e) RDF obtained by Fourier transform of structure factor. (f) Reference: RDFs. (g) Sketch of the constructed RDF data cube (RDF-Cube). (h) Imaging results: structural maps.

IM4.006
Influence of spatial and temporal coherences on atomic resolution high angle annular dark field imaging

A. Beyer[1], J. Belz[1], K. Jandieri[1], K. Volz[1]

[1]Philipps-Universität Marburg, Materials Science Center and Faculty of Physics, Marburg, Germany

andreas.beyer@physik.uni-marburg.de

Introduction: High resolution scanning transmission electron microscopy (STEM) has become a valuable method in the field of material sciences. Nevertheless, complementary simulations are needed if quantitative information should be extracted.
Objectives: In this contribution we investigate which experimental parameters have to be considered to achieve quantitative agreement between experimental and simulated high angle annular dark field (HAADF) images.
Materials and Methods**:** To this end we choose the binary semiconductor GaP with a defined stoichiometric composition. Moreover, the two constituents Ga and P exhibit a highly different scattering power resulting in high contrast in the experimental HAADF images. The measurements were performed in a double C_S-corrected JEOL JEM 2200FS operating at 200 kV. A representative experimental unit cell, which can be compared to simulations, was derived by averaging all unit cells present within the field of view of an image. Multi slice simulations were carried out in the frozen phonon approximation utilizing the STEMsim [1] and Stemsalabim [2] codes.
Results**:** The experimental GaP unit cell is shown in Figure 1 (a). The corresponding coherent simulation taking only the Geometric aberrations C_S and C_5 into account is depicted in (b). The simulation exhibits a significantly higher contrast as can be quantified from the difference plot (c). By consideration of the chromatic aberration, the simulated contrast is reduced (d) but still too high compared to the experimental one (e). The spatial coherence has been considered either via a Gaussian or a Lorentzian source distribution. Both source shapes resemble the strong scattering Ga columns well, whereas the Gaussian underestimates the weaker scattering of the P columns ((f) and (g)). The best match between simulation and experiment is achieved for a source size of 46 pm ((h) and (i)). In addition, the influence of amorphous layers introduced by the sample preparation will be discussed.
Conclusion: Taking into account all aforementioned experimental parameters in the simulations, quantitative agreement between experiment and simulation can be achieved. With the knowledge of the decisive parameters, the determination of the chemical composition of more complex, multinary materials becomes feasible.

References:
[1] A. Rosenauer, M. Schowalter, STEMSIM - A New Software Tool for Simulation of STEM, Microsc. Semicond. Mater. 2007. 120 (2008) 170–172. doi:10.1007/978-1-4020-8615-1_36.
[2] J.O. Oelerich, L. Duschek, J. Belz, A. Beyer, S.D. Baranovskii, K. Volz, STEMsalabim: A high-performance computing cluster friendly code for scanning transmission electron microscopy image simulations of thin specimen, Submitted to Ultramicroscopy. (2017).

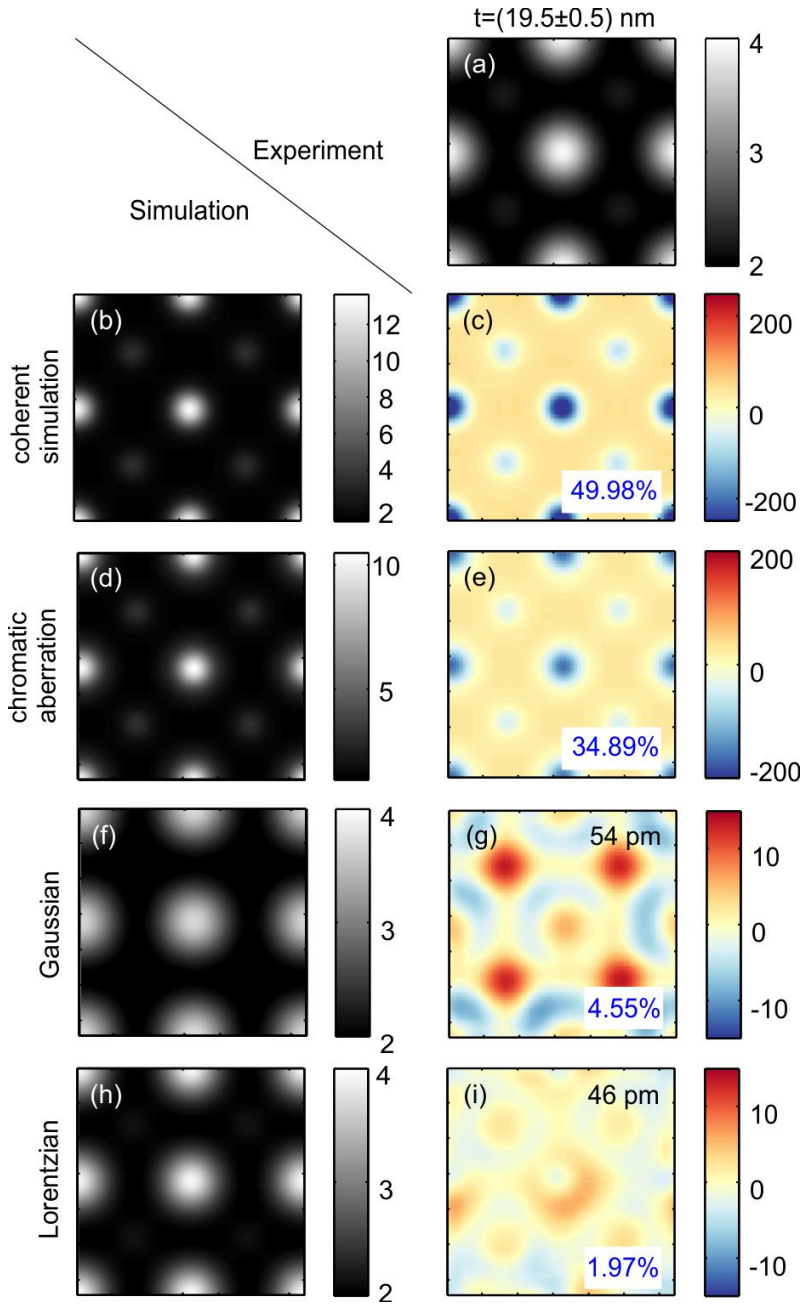

Figure 1. Comparison of simulation and experiment: The experimental unit cell for a GaP sample thickness of 19.5 nm is depicted in (a). The corresponding simulated unit cells are shown in the leftmost column. The individual images represent the simulation including geometric aberrations (b), additionally taking into account the chromatic aberration (d) and applying the source distribution as a Gaussian (f) and a Lorentzian (h). The grayscale is given in percent of the impinging beam. The corresponding differences between simulation and experiment normalized to the experimental intensity are shown color coded in (c), (g) and (i), respectively. The units of the intensity scale are given in percent deviation and are chosen symmetrically around zero. The blue numbers represent the relative error which is normalized to the intensity. The width of the source distribution yielding the best agreement between simulation and experiment is indicated in the individual plots.

IM4.007
Evaluating computational TEM specimen models for three-dimensional iterative algorithms using electron diffraction data

R. S. Pennington[1], C. T. Koch[1]

[1]Humboldt-Universitaet zu Berlin, Institut fuer Physik, Berlin, Germany

robert.pennington@physik.hu-berlin.de

Introduction: The accuracy and applicability of TEM specimen models directly affects TEM data interpretation, and improved models can both enable novel applications and enhance existing methods. For example, we have developed iterative, neural-network-optimization based algorithms that can retrieve strain states and ferroelectric polarization domains, and have comprehensively shown their effectiveness on simulated CBED data [1-4]. This multiscale structural optimizer already includes multiple scattering, but using experimental data requires an accurate specimen model suitable for iterative refinement.
Objectives: In this work, we compare and quantitatively evaluate computational TEM specimen models. We evaluate specimen models using both convergent-beam electron diffraction (CBED) intensities and iterative three-dimensional structural parameter retrieval.
Materials and Methods: Both elastic and inelastic scattering are considered for simulating structure factors, diffraction intensities, and three-dimensional structural parameters. For elastic scattering, isolated-atom scattering factors (IASF) [9] are compared with ground-state density functional theory (DFT) simulations using the GPAW code, previously applied to electron-holographic mean inner potentials [5-6], benchmarking against experimentally fitted structure factors [7]. Thermal diffuse scattering and absorption models are also evaluated. As criteria, our GPU-accelerated Bloch-wave simulations [8] are used with our three-dimensional iterative parameter retrieval algorithm; CBED intensity mismatch and retrieved parameter error are both considered.
Results: Figure 1 shows that DFT is more accurate than IASF models; structure-factor fitting can provide useful benchmarks. The diffraction intensities generated using DFT models are also qualitatively distinct. Figure 2 shows DFT is also fast enough to be used in iterative algorithms requiring thousands of DFT simulations, and model mismatch directly affects the accuracy of the retrieved parameters.
Conclusion: Density functional theory can provide useful ab initio modeling for TEM specimens, enabling improved accuracy in quantitative applications compared to isolated-atom models. TEM data can also be used as a constraint for a DFT-based structural optimizer.

Acknowledgements
We gratefully acknowledge financial support from DFG grant PE2500/1-1 (PolaRIS-3D).

References:
[1] RS Pennington, W Van den Broek, and CT Koch, Phys. Rev. B 89, 205409 (2014).
[2] RS Pennington and CT Koch, Ultramicroscopy 155, 42 (2015).
[3] RS Pennington and CT Koch, Ultramicroscopy 148, 105 (2015).
[4] RS Pennington and CT Koch, in preparation.
[5] JJ Mortensen, LB Hansen, and KW Jacobsen, Phys. Rev. B 71, 035109 (2005).
[6] RS Pennington, CB Boothroyd, and RE Dunin-Borkowski, Ultramicroscopy 159, 34 (2015).
[7] Y Ogata, K Tsuda, and M Tanaka, Acta Cryst. A 64, 587 (2008).
[8] RS Pennington, F Wang, and CT Koch, Ultramicroscopy 141, 32 (2014).
[9] I Lobato and D Van Dyck, Acta Cryst. A 70, 636 (2014).
[10] DM Bird and QA King, Acta Cryst. A 46, 202 (1990).

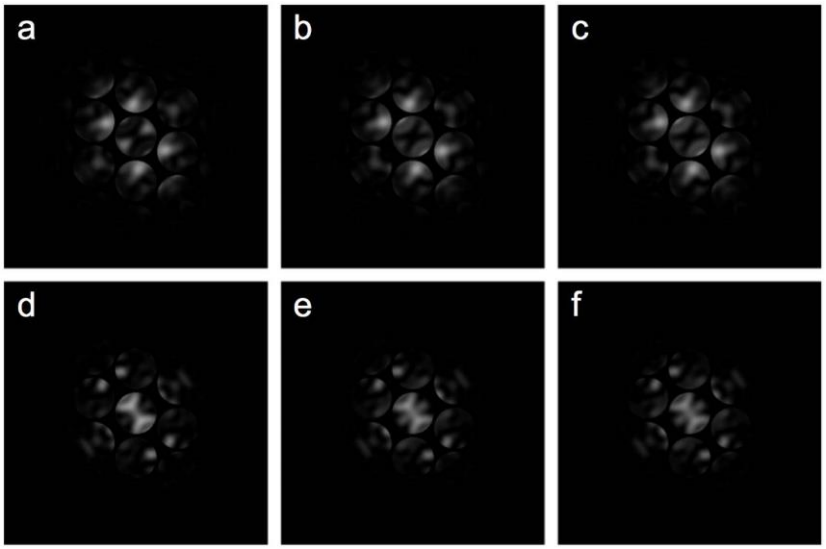

Figure 1. Simulated CBED patterns for 80nm bulk Si (n=173 beams) at 100kV. (a-c) only including elastic scattering: (a) Simulated using an isolated-atom model [9]. (b) Simulated using GPAW DFT (4^3 kpts, 24^3 gpts). (c) Simulated using experimental structure factors. (d-f) with inelastic scattering: (d-e) as (a-b) with Bird-King absorption and experimental Debye-Waller factor [7,10], (f) as (c), but with experimental structure factors at low angles [7] and Bird-King absorption at high angles.

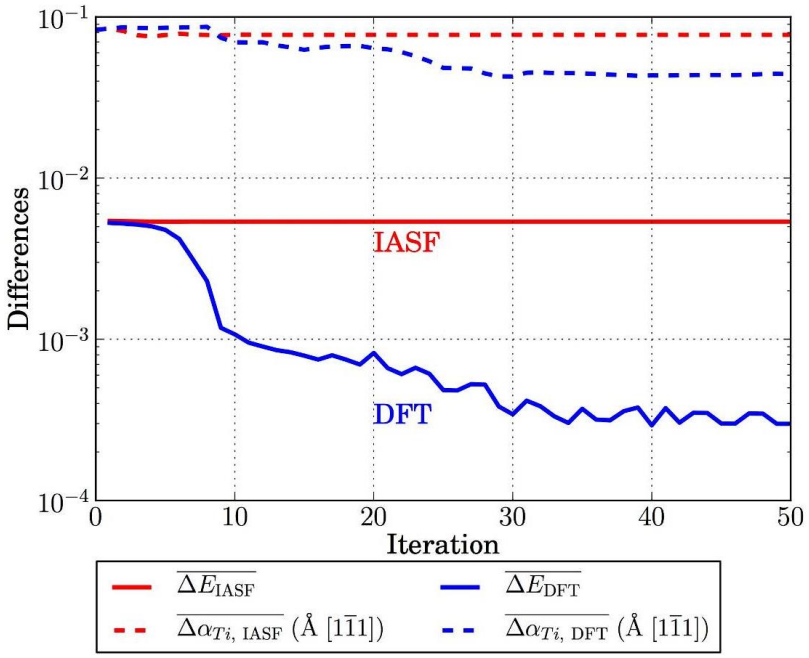

Figure 2. Three-dimensional parameter-retrieval results for ferroelectric polarization in 80nm BaTiO3 at 100kV, similar to [2, 4], showing that using a different model leads to convergence limitations. Solid lines are diffraction intensity mismatch, dotted lines are specimen parameter mismatch. Blue/Red: Simulated target data with the same/different model used for optimization, respectively.

IM4.P001
StatSTEM – an efficient approach for accurate and precise model-based quantification of atomic resolution electron microscopy images

A. De Backer[1], K. H. W. van den Bos[1], W. Van den Broek[2], J. Sijbers[3], S. van Aert[1]

[1]EMAT, University of Antwerp, Department of Physics, Antwerp, Belgium
[2]AG Strukturforschung/Elektronenmikroskopie, Institut für Physik, Humboldt-Universität zu Berlin, Berlin, Germany
[3]imec-Vision Lab, University of Antwerp, Department of Physics, Wilrijk, Belgium

annick.debacker@uantwerpen.be

Nowadays, the field of nanotechnology requires more and more quantitative characterisations of nanomaterials. This includes for example locating atomic column positions with picometer precision, counting atoms with single atom sensitivity and precise chemical composition determination. In order to facilitate these needs, we have developed a user-friendly software package called StatSTEM [2] in which advanced image quantifications are applied by using an efficient model-based fitting algorithm. This software package is freely available under the GNU public license and can be found at the website [1].
For atomic resolution (scanning) transmission electron microscopy ((S)TEM) images, statistical parameter estimation theory provides an excellent tool to quantitatively extract unknown structure parameters [3]. In these atomically resolved images, the intensity is peaked at the atomic column and can be modelled as a Gaussian function [4,5]. A direct implementation, where all parameters are simultaneously estimated, is computationally very intensive and can only be applied when dealing with a limited number of projected atomic columns. Therefore, we propose a new, efficient algorithm in which the image is divided into smaller segments containing individual columns without ignoring the overlap of image intensities between neighbouring columns.
In order to elucidate the benefits of this new method in a statistical manner, the accuracy and precision with which structure parameters can be measured are evaluated by using annular dark field STEM images. It is shown that even for low electron dose images structure parameters are accurately measured with the highest attainable precision (Fig. 1). Furthermore, the advantages of our model-based approach are illustrated as compared to the computationally less expensive approach where the overlap between neighbouring columns is neglected. This is first shown by estimating the spacing between two neighbouring atomic columns as a function of distance (Fig. 2a) when taking overlap into account and when neglecting it (Fig. 2b). Secondly, a comparison between the volumes under the fitted Gaussian functions and the integrated intensity from a Voronoi cell reveals that the volumes give more accurate results for predicting the total scattered intensity of an atomic column, the scattering cross-section (Fig. 2c). Therefore, this comparison further highlights the advantages of our model-based approach.
In conclusion, a new efficient algorithm is developed enabling a quantitative analysis of (S)TEM images having a large field of view. As this algorithm still accounts for the overlap of image intensities between neighbouring columns, it provides accurate measurements of structure parameters with the highest attainable precision. To provide end-users this powerful quantification method, a user-friendly software package is available [1].

[1] https://github.com/quantitativeTEM/StatSTEM
[2] De Backer et al., Ultramicroscopy **171** (2016) p 104
[3] Van Aert et al., Ultramicroscopy **109** (2009) p 1236
[4] Van Dyck, Adv. Imaging Electron Phys. **123** (2005) p 105
[5] Nellist, Science of Microscopy (2007), Springer, Vol 1, Chapter 2, p 65
[6] Funding from the Research Foundation Flanders (postdoc grant to ADB, PhD grant to KVDB, G.0374.13N, G.0368.15N, G.0369.15N, WO.010.16N) is acknowledged.

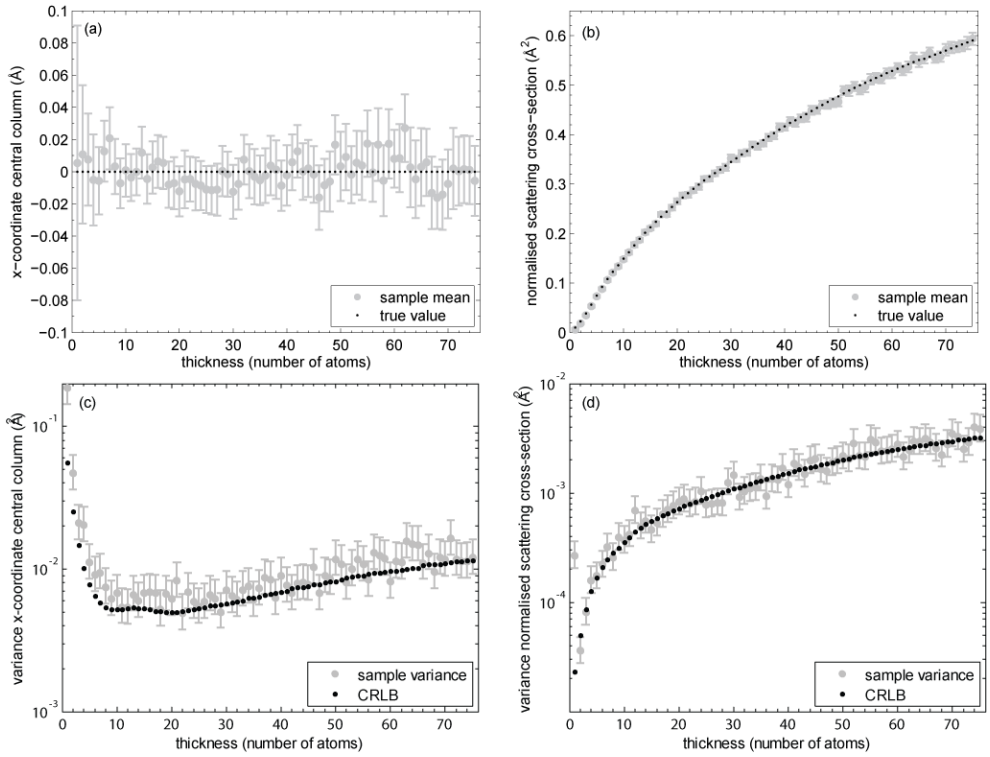

Figure 1. Accuracy and precision of the estimated position coordinate and scattering cross-section as a function of thickness in a Pt crystal for an incoming electron dose of $5 \cdot 10^2$ e·Å^{-2}. (a,b) True values and the sample mean together with the 95% confidence intervals. (c,d) The highest attainable precision, the Cramér-Rao lower bound (CRLB), and the sample variance together with the 95% confidence intervals.

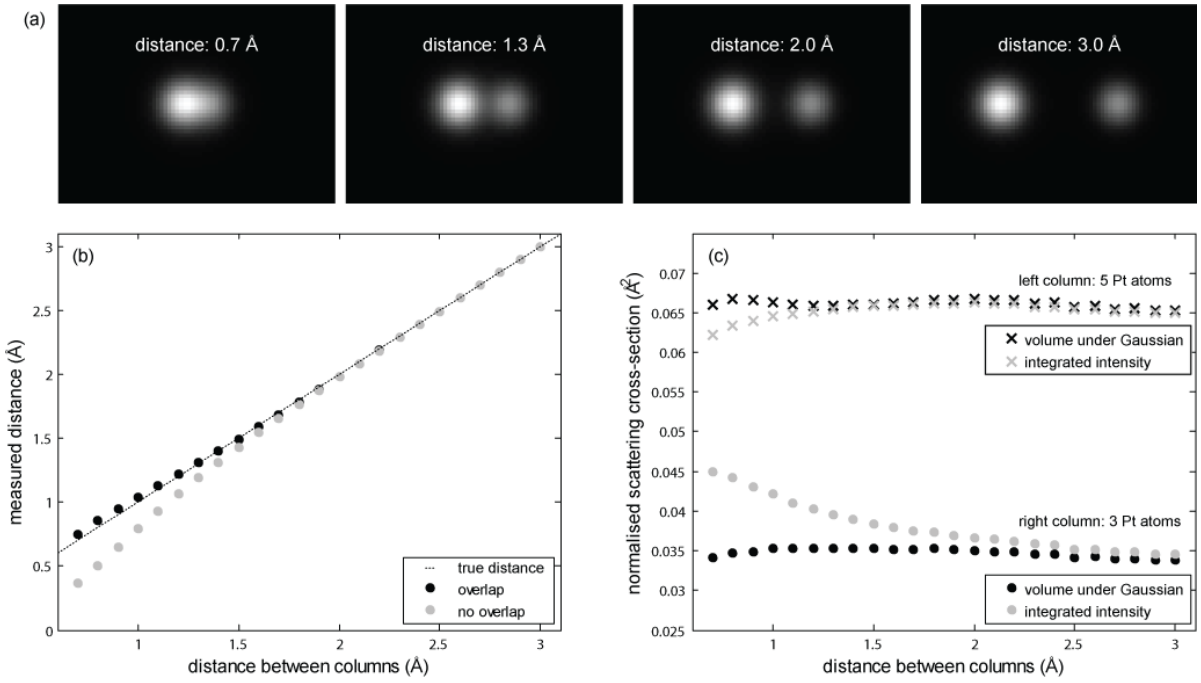

Figure 2. Influence of a neighbouring column on the estimated parameters. (a) Examples of simulated images of a 5 and 3 Pt thick column with a varying distance between the columns. (b) The estimated distance when taking the overlap of neighbouring columns into account and when neglecting it. (c) The estimated scattering cross-sections obtained by the volumes under the fitted Gaussian functions and by integrating intensities from Voronoi cells.

IM4.P002
Hybrid statistics-simulations based method for atom-counting using scanning transmission electron microscopy

A. De wael[1], A. De Backer[1], L. Jones[2], P. D. Nellist[2], S. van Aert[1]

[1]University of Antwerp, Department of Physics, Antwerp, Belgium
[2]University of Oxford, Department of Materials, Oxford, United Kingdom

annelies.dewael@uantwerpen.be

Annular dark field (ADF) scanning transmission electron microscopy (STEM) combined with atom-counting has become a powerful technique to recover the 3D atomic structure of nanoparticles. Images are then treated as datasets from which the number of atoms per column is determined by comparison with image simulations [1] or by using statistical parameter estimation theory [2-4]. First, the so-called scattering cross sections (SCSs), corresponding to the total scattered intensity of each atomic column in a nanoparticle, are quantified [2-6]. The image simulations-based method directly compares experimental and simulated SCSs. A potential drawback, however, is that small discrepancies between actual and measured parameters such as sample tilt or detector inner angle may remain undetected, yielding inaccurate atom counts [3,5]. The statistics-based method does provide accurate and precise atom counts, but has a limited reliability for small nanoparticles and low dose images [4,7]. The increasing relevance of radiation damage in the study of nanostructures [8] demands a quantitative method enabling the analysis of low dose images with a low signal-to-noise ratio. Therefore, a hybrid method for atom-counting is proposed, which overcomes the limitations of the existing methods. This method incorporates prior knowledge from image simulations into the statistical framework while taking possible inaccuracies in the experimental parameters into account.

The hybrid method is illustrated in fig 1, where the number of atoms of a Pt/Ir nanoparticle is determined from the estimated SCSs which are shown in the histogram. The distribution of these SCSs can be described by a so-called Gaussian mixture model of which the unknown parameters are determined using a maximum likelihood estimator. The number of atoms of each column is then determined by assigning each SCS to the component with the largest probability. The performance of the method depends on the average number of columns per component (N/G) and the relative width of the components (σ/δ). Small particles contain few atomic columns N with a limited maximum thickness G, resulting in a small N/G. Moreover, low electron doses cause a large σ/δ and thus a large overlap (yellow area in fig 1b). A combination of low N/G and large σ/δ impedes reliable atom-counting. The required N/G to reach a given percentage with the hybrid method at a constant σ/δ is lower than the required N/G with the statistics-based method, as shown in fig 2. In other words, the percentage of correctly counted atomic columns by the hybrid method far exceeds the percentage obtained by the statistics-based method. The greatest improvement is achieved for small nanoparticles and low dose images. This explains why the hybrid method could successfully retrieve the number of atoms in this example using an electron dose of $6.5 \cdot 10^4$ $e^-/Å^2$.

Electron beam-sensitive nanomaterials, however, require doses that are at least an order of magnitude lower. Therefore, an image corresponding to a dose of only 10^3 $e^-/Å^2$ was simulated taking Poisson noise into account (fig 3). The close match of the estimated and input atom counts clearly shows the benefits of the hybrid method. In conclusion, the hybrid method holds great promise for quantitative analyses of beam-sensitive nanostructures, owing to its ability to overcome challenges presented by low electron doses.

[1] J M LeBeau et al., Nano Lett. 10 (2010) p 4405
[2] S Van Aert et al., Nature 470 (2011) p 374
[3] S Van Aert et al., PRB 87 (2013) p 064107
[4] A De Backer et al., Ultramicroscopy 134 (2013) p 23
[5] L Jones, IOP Conf. Series: Mat. Science and Eng. 109 (2016) p 012008
[6] H E et al., Ultramicroscopy 133 (2013) p 109119
[7] A De Backer et al., Ultramicroscopy 151 (2015) p 56
[8] J Meyer et al., Ultramicroscopy 145 (2014) p 13

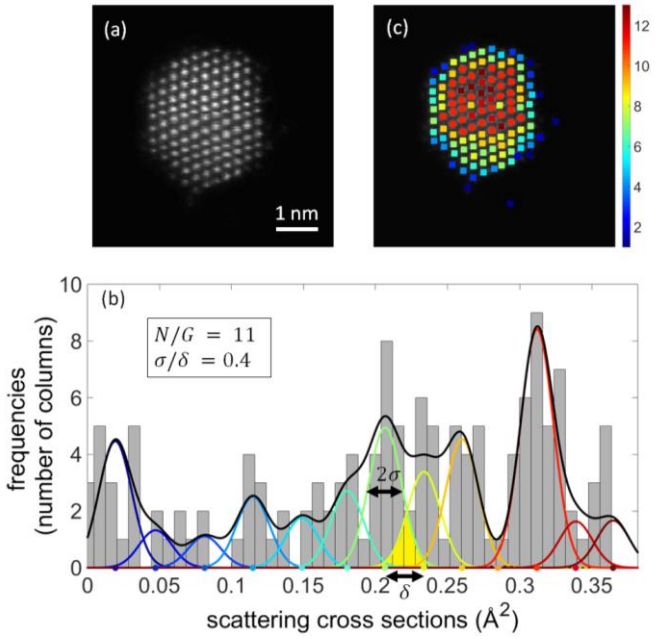

Figure 1. (a) *Experimental* ADF STEM image of a Pt/Ir nanoparticle acquired using an electron dose of $6.5 \cdot 10^4$ e$^-$/Å^2 [7]. (b) Estimated Gaussian mixture model describing the SCSs obtained from the experimental image. (c) Atom counts obtained with the hybrid method.

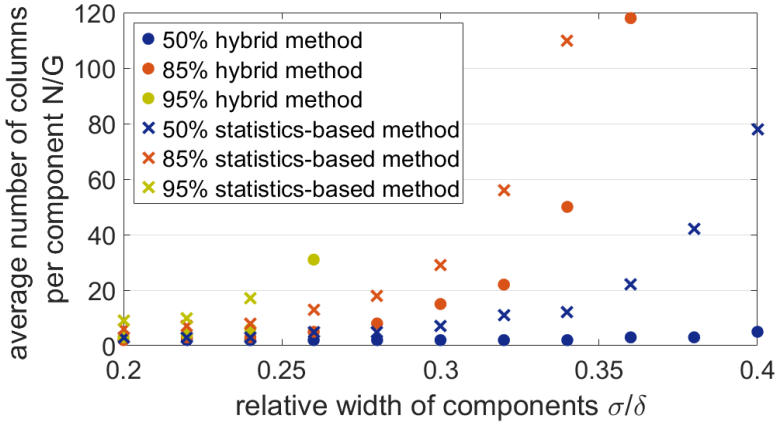

Figure 2. The average number of columns per component needed to obtain 50%, 85% or 95% correctly counted atomic columns with the hybrid or statistics-based method, for a certain relative width of the components.

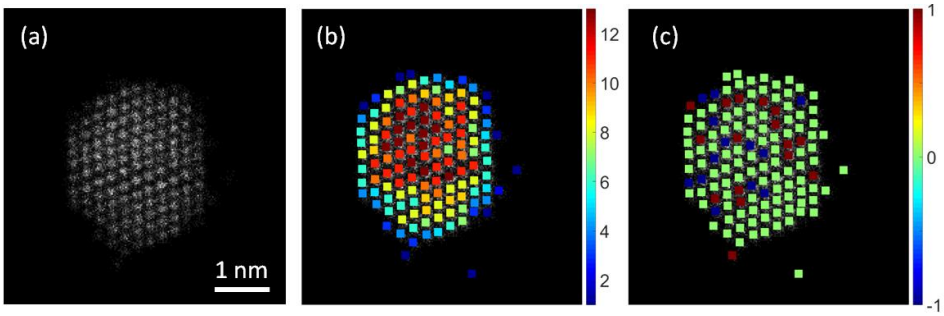

Figure 3. (a) *Hypothetical* ADF STEM image corresponding to a dose of 10^3 e$^-$/Å^2, based on the nanoparticle from fig 1. (b) Atom counts obtained with the hybrid method. (c) Difference between the input and estimated atom counts.

IM4.P003
Application of quantitative microstructural analysis for understanding the behavior of raw materials and their response to crushing loads.

A. Bravo[1], G. Heide[1], O. Popov[2]

[1]TU Bergakademie Freiberg, Institut für Mineralogie, Freiberg, Germany
[2]TU Bergakademie Freiberg, Institut für Aufbereitungsmaschinen, Freiberg, Germany

geoarturobravo@gmail.com

Introduction: Smaller particle size of the milling product causes a disproportional increase of energy costs. In addition, plenty of water is required for the sorting process. The demand and consumption of energy and water resources as well as land usage leads to environmental damage and affects worker health. These are some of the main ideas that motivated the InnoCrush group to find a solution to the project´s goal that consists of the reduction of energy and material costs by increasing the selectivity in extracting of strategic economic primary raw materials with a focus on small deposits. A multidisciplinary group is conducting studies from extraction, through processing and automation, to the economic and environmental review, flanked by mineralogy and modelling.
Objectives: A key stage for the processing of mineral raw materials corresponds to the process of comminution the rocks and understand the properties of these. Even though the current mineralogical-petrographic rock characterization allows the description of microstructures, a quantitative one delivers an assessment of the rock in terms of crushability and product particle shape. Considering a systematic analysis of the cracking propagation of rocks, with appropriate analytical techniques, delivers valuable information when understanding the behaviour of raw materials and their response to crushing loads.
Materials and Methods: To characterize such effects, a series of techniques have been considered, including: x-ray diffraction (XRD), Computer Tomography (CT), Electron Backscatter Diffraction (EBSD) and Conventional Optical Microscopy, considering the mathematical-statistical modelling exposed by Lieberwirth (2014), Quantitative Microstructural Analysis (QMA), for Gneiss Freiberger samples, obtained in Reiche Zeche exemplars.
Preliminary evaluation of the feasibility of this methodology (QMA) for gneiss samples are included in this work. Since minerals have mostly a complex three-dimensional texture, gneiss thin sections have been prepared in 3 orthogonal directions and oriented to obtain mathematical-petrographic results under optical microscopy using stereological methods. This has permitted to quantify correlations between properties of the rock (e.g. grain shape, grain size, mineral intergrowth, etc) and parameters of the beneficiation process (Figure 1)
Results and Conclusion: First results have demonstrated that the technique is useful for the evaluation of gneiss rocks even though, due to its textural oriented nature, some crystals are complex to individualize and measure. This is because the samples have been described with the least objective for a better evaluation. For this purpose, some minerals with similar mechanical properties, such as alkali feldspar and plagioclase, are grouped together.
The upcoming step, will be to relate the QMA measurements with the EBSD analysis of the 3 orthogonal thin sections since it provides a crystallographic preferred orientation (CPO), and allows the description of the follow up of the microstructures. With such information, it will be possible to evaluate product parameters (particle size and particle shape distribution) in more details.

Acknowledgement
This work is financially supported by the European Union (European Social Fund) and the Saxonian Government (Grant No. 100270113) and part of the Project *InnoCrush - Dynamic methods of mechanical excavation and comminution for high selective production chains in Critical Raw Materials in Saxony*

References:
[1] Lieberwirth, H., Popov, O. & Folgner, T., 2014. Quantitative characterization of rocks to predict the influence of the rock on relevant product properties and system parameters. AT MINERAL PROCESSING. 55, No 7-8, pp. 76-88

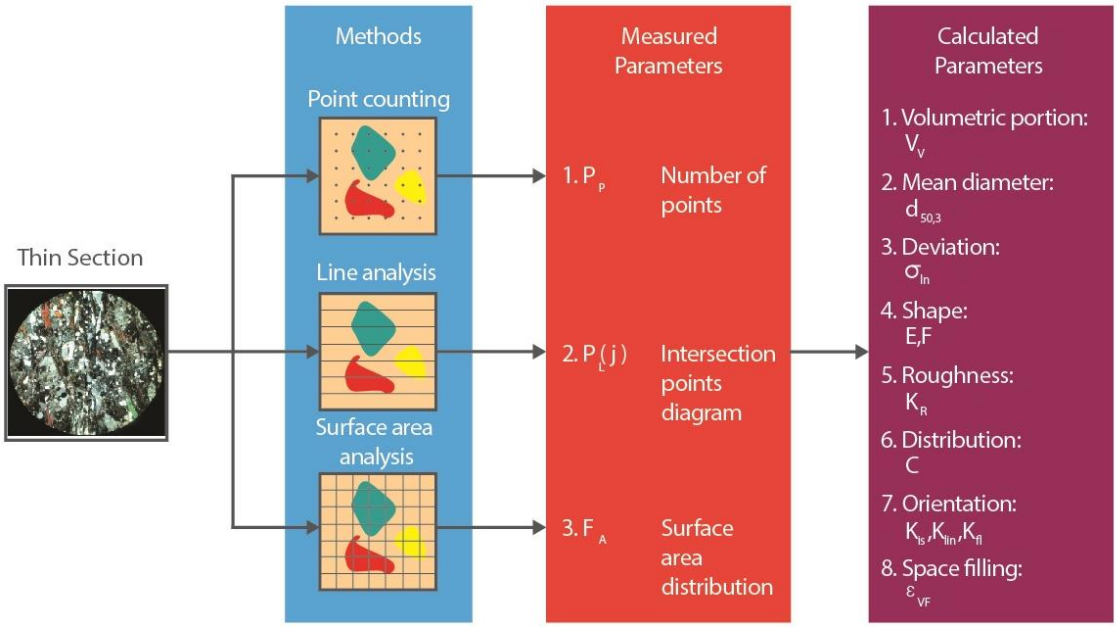

Figure 1. Thin section evaluation methods.

IM4.P004
Multislice simulations of elemental maps within a relativistic framework

S. Majert[1], H. Kohl[1]

[1]WWU Münster, Physikalisches Institut, Münster, Germany

stephan.majert@gmail.com

For acceleration voltages of 200 kV and beyond, routinely used in the Transmission Electron Microscope (TEM), the speed of the beam electrons exceeds 70% of the speed of light. Thus relativistic corrections have been shown to lead to an increased ionization cross section [1] and to strongly modify intensity distributions in elemental maps of thin specimens obtained by Energy-Filtered Transmission Electron Microscopy (EFTEM) [2].
To simulate EFTEM images of thick specimens within a relativistic framework, we use a multislice algorithm derived from the Dirac equation [3,4]. Atomic inner-shell ionizations are incorporated by use of projected matrix elements. Utilizing Darwin wave functions [5], we can obtain these matrix elements without explicitly calculating the Dirac spinors of the ejected atomic electrons, leading to a comparatively simple formalism. Integrating the relativistic algorithm into a program that can also perform conventional (i.e. based on the Schrödinger equation) multislice simulations, we can directly see the impact of relativistic corrections on the final EFTEM image.
Fig. 1a and 1b show a relativistic and a conventional multislice simulation of the background-subtracted EFTEM image of the Ti-$L_{2,3}$-edge in $SrTiO_3$. The parameters of the simulation have been chosen to resemble the ones used in [6]. Plotting the intensity profiles of fig.1a and 1b along the titanium columns and oxygen columns (fig. 1c) and along the columns containing strontium and oxygen (fig. 1d), one can clearly see differences between the intensity distributions of the relativistic and conventional image. These differences are even more pronounced for objective aperture angles smaller than the 38 mrad used within the simulation shown in fig. 1, because the influence of relativistic corrections on the cross section is usually greatest for small scattering angles [1].
In conclusion, the noticeable differences between elemental maps calculated with the conventional multislice algorithm or a multislice algorithm utilizing the Dirac equation indicate that relativistic effects have to be considered when simulating elemental maps of thick specimens obtained by EFTEM.

[1] R. Knippelmeyer et al., Ultramicroscopy 68 (1997) 25
[2] R. Knippelmeyer et al., J. Microsc. 194 (1999) 30
[3] A. Rother, Ultramicroscopy 109 (2009) 154
[4] A. Lubk, PhD thesis, TU Dresden (2010)
[5] C. G. Darwin, Proc. Roy. Soc. A 118 (1928) 654
[6] B. D. Forbes et al. Ultramicroscopy 147 (2014) 98

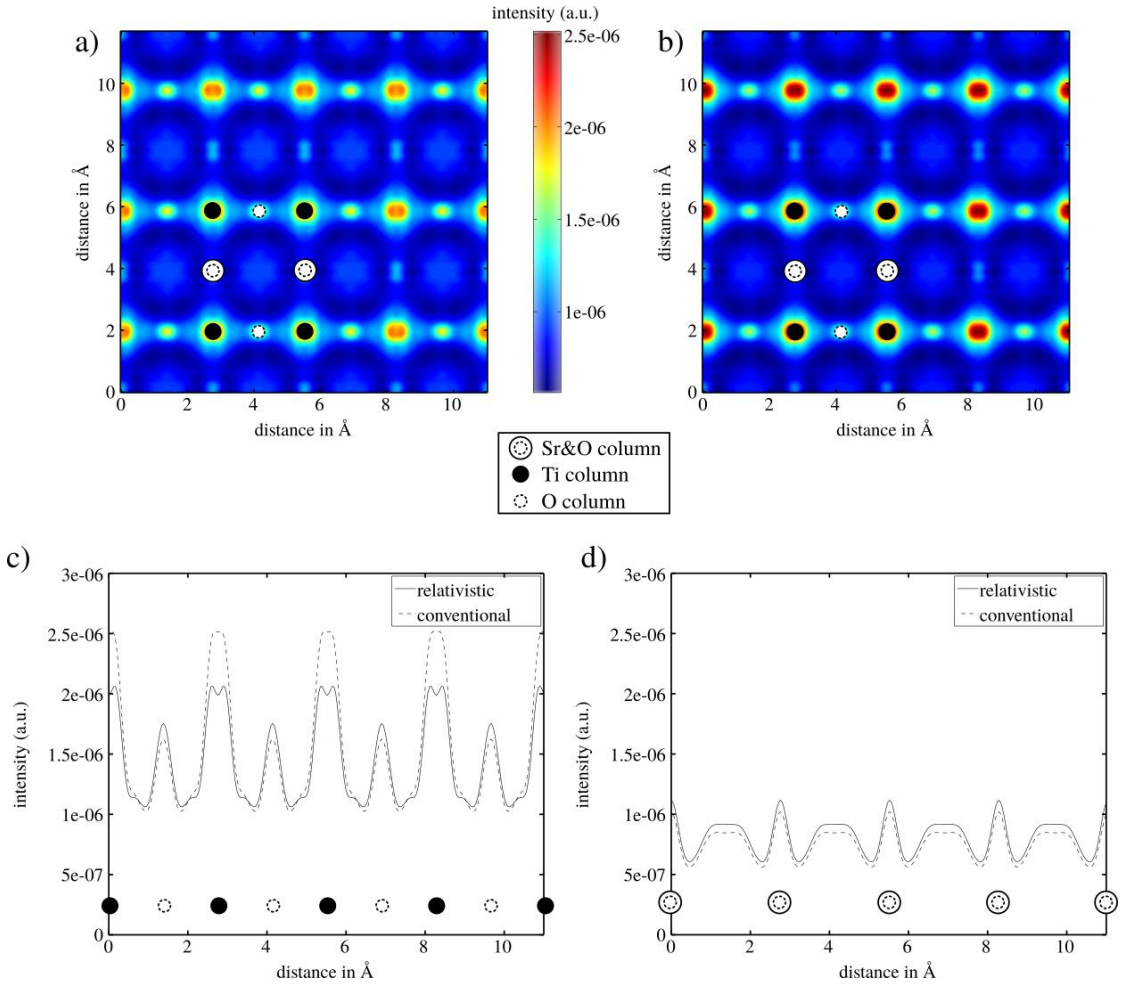

Figure 1. a,b) Simulated background-subtracted EFTEM images 10 eV above the Ti-$L_{2,3}$-edge in $SrTiO_3$ calculated with the relativistic and conventional multislice algorithm respectively. For both simulations, the $SrTiO_3$ specimen is oriented in [110]-direction and roughly 30 nm thick, the acceleration voltage is 200 kV, the angle of the objective aperture is 38 mrad and the spherical aberration coefficients are C_1 = 40 Å, C_3 = -6 µm and C_5 = 1.5 mm. Because the microscope used in [6] is chromatic-aberration-corrected, the chromatic aberration of the objective lens is neglected in the simulation. To model the inelastic scattering events, the projected matrix elements of all dipole allowed transitions were calculated within a 16 by 16 Angstrom box around each atom.
c,d) Intensity profiles of fig.1a,b along the titanium columns and oxygen columns (c) and along the columns containing strontium and oxygen (d).

IM4.P005
The effects of dose limitation and Poisson noise on compressed sensing in HAADF-STEM

W. Van den Broek[1], A. Parvizi[1], A. Béché[2], J. Verbeeck[2], C. T. Koch[1]

[1]Humboldt-Universität zu Berlin, Institut für Physik, Berlin, Germany
[2]University of Antwerp, EMAT, Antwerp, Belgium

vandenbroek@physik.hu-berlin.de

Introduction: In the field of compressed sensing (CS) superior results have been proven attainable by including prior knowledge in the solution of underdetermined systems [1]. This usually means enforcing sparsity in the pixel base or total variation minimization (TVM) [2].
Objectives: In this abstract we investigate the influence of the dose reduction and the resulting Poisson noise that comes with a decrease in number of measurements; an effect that is seldom discussed in CS literature as the measurements are often assumed noise-free.
Materials and Methods: A 128 x 128 Shepp-Logan phantom x, bandwidth limited to the Nyquist frequency, is used as the test case. The measurements y are produced by the so-called measurement matrix A: $y = Ax$, with x in long vector format.
In case of traditional sampling (TS) A is the identity matrix and y corresponds directly to x. With Random sampling (RS) A is all zeros except for one randomly chosen element per row. This records only a fraction of the pixels and we need to use the free software TVAL3 [3] to retrieve a TVM estimate of x.
The results of TS and RS are compared for (a) the noiseless case, (b) 2000 electrons and (c) 3 electrons per pixel of the *reconstruction*. For RS A was chosen to have five times fewer rows than columns and hence the electron dose per *recorded* pixel was increased five-fold to ensure an equal dose between TS and RS.
Results: For all cases the root mean squared error (RMSE) is calculated. Case (a): $RMSE_{TS}$ = 0.0%, $RMSE_{RS}$ = 9.0%. Case (b): $RMSE_{TS}$ = 0.8%, $RMSE_{RS}$ = 9.2%. Case (c): $RMSE_{TS}$ = 20.0%, $RMSE_{RS}$ = 10.5%. See Fig. 1.
Conclusions: Traditional sampling (TS) outperforms random sampling (RS) for doses common in materials science. For very low doses, however, the latter is preferable, and it seems largely unaffected by dose. [4]

References:
[1] R.G. Baraniuk, IEEE Signal Processing Magazine 4 (2007) 118-121.
[2] E.J. Candes et al. IEEE Transactions on Information Theory 52 (2006) 489-509.
[3] C. Li, PhD Thesis, Rice University, Houston, Texas (2011).
[4] W.V.d.B., C.T.K. acknowledge the DFG projects BR 5095/2-1 and KO 2911/7-1, respectively. A.B., J.V. acknowledge the FWO project G093417N ('Compressed sensing enabling low dose imaging in transmission electron microscopy')

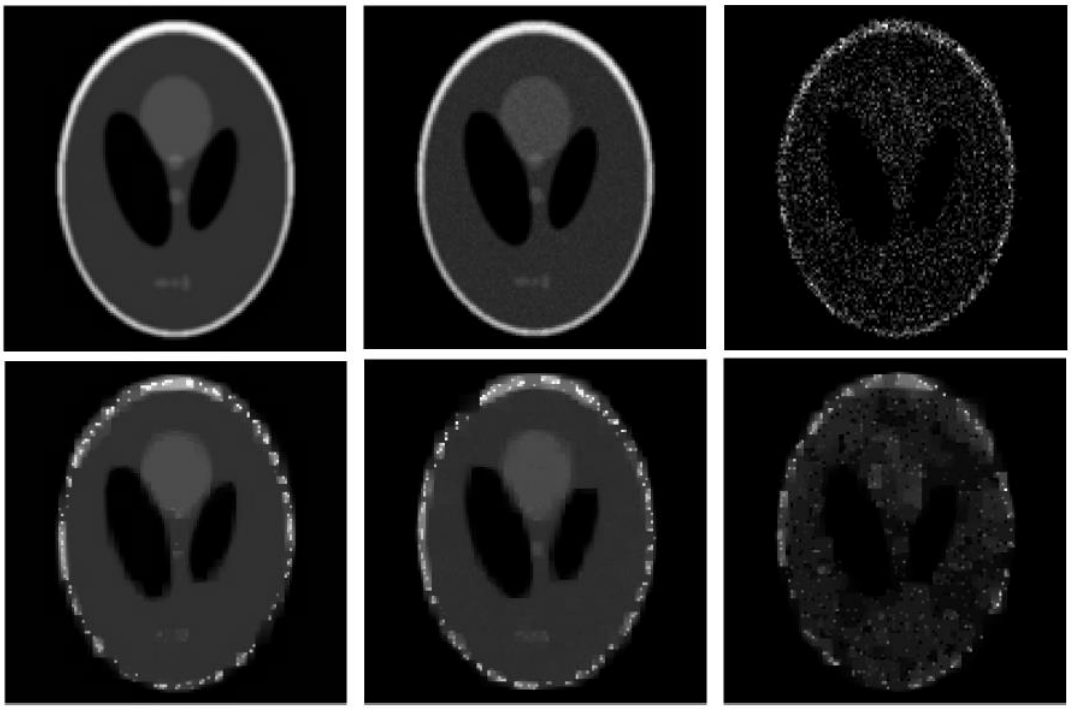

Figure 1. *Upper row*: Traditional sampling (TS). *Lower row*: Random sampling (RS). *Left*: Case (a): noise-free, $RMSE_{TS}$ = 0.0%, $RMSE_{RS}$ = 9.0%. *Middle*: Case (b): 2000 electrons per pixel, $RMSE_{TS}$ = 0.8%, $RMSE_{RS}$ = 9.2%. *Right*: Case (c): 3 electrons per pixel, $RMSE_{TS}$ = 20.0%, $RMSE_{RS}$ = 10.5%.

IM4.P006
Automatic lamella thinning featuring smart end-point detection and live thickness measurement

T. Volkenandt[1], F. Perez-Willard[1], M. Rauscher[1]

[1]Carl Zeiss Microscopy GmbH, Oberkochen, Germany

tobias.volkenandt@zeiss.com

Introduction: The preparation of electron transparent lamellae for analysis in (scanning) transmission electron microscopes ((S)TEM) is one of the most important applications of a focused ion beam scanning electron microscope (FIB-SEM). While the demands on the quality of these lamellae are growing, there is almost no technical solution available to measure their thickness during the preparation. The operators experience has a strong influence on the preparation result and reproducibility.
Objectives**:** Here, we present a solution that allows live measurement of the lamella during the preparation process. The solution is integrated into the microscope control software and enables also automatic end-point detection, meaning that the thinning process can be stopped automatically when a predefined target thickness is reached.
Materials and Methods**:** The thickness is derived from the backscattered electron (BSE) signal, which depends (among other parameters) on the maximum depth that electrons can still escape from. The BSE signal of a bulk sample with a thickness larger than this maximum backscatter depth (MBD) is stronger, than the signal of a thinner sample. This is because in the latter case more electrons traverse the sample and are not detected as BSE. By means of Monte Carlo simulation, a global normalized BSE transmission function (GNTF) was derived for all elements in the periodic table as measure for the MBD in dependence of the primary electron energy. [1]
Results: It was possible to integrate the GNTF data into the microscope control software. After a quick calibration of the minimum and maximum grey levels in the image, this allows the operator to determine the sample thickness in each pixel and display it as colour-coded thickness map overlay. Figure 1 shows such a thickness map on top of a BSE image of a silicon TEM lamella with several thinned windows.
Since the BSE signal is not affected by FIB induced secondary electrons, it is possible to observe the thickness map also live during the lamella polishing. In combination with a predefined target thickness for a Reference: area, this enables automatic end-point detection and lamella thinning. Figure 1 shows two examples of such an automatic thinning process. The targeted thicknesses for the windows in the color-coded area were 100 and 50 nm respectively, as indicated by the color scale. To evaluate the polishing result, the very same lamella was imaged edge on in top-view as shown in Figure 2. A direct measurement of the lamella thickness in this image yielded 99 and 54 nm respectively.
Conclusion: We showed first results of a solution that enables live thickness measurements of lamellae based on BSE contrast. The solution is connected to the microscope control software and capable of stopping the lamella thinning process automatically at a given target thickness. The result of the automatic thinning was evaluated by SE top-view imaging of the lamella. The accuracy is estimated to be better than 20%, which is comparable to other methods for lamella thickness determination in the TEM, e.g. based on EELS. In addition, the presented solution has the advantage that it can be used live during the FIB polishing process, providing direct feedback and facilitating reproducible results.

References:
[1] R Salzer et al, Microsc Micronal **15(Suppl 2)** (2009), p. 340.

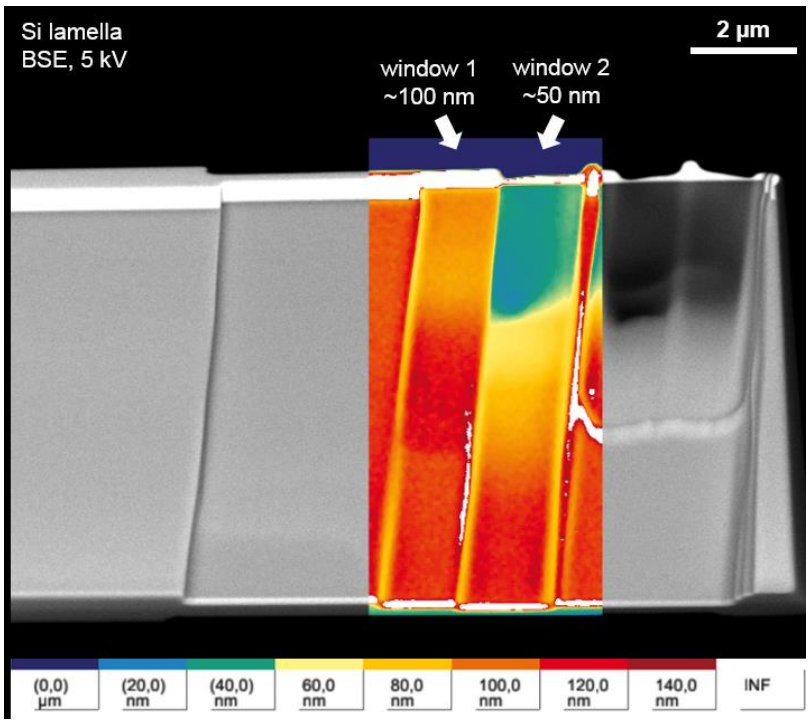

Figure 1. Side view image of a silicon lamella at 5 kV with color-coded thickness map overlay. Automatic end-point detection was used to polish two windows, with target thicknesses of 100 nm (left, orange) and 50 nm (right, blue/green).

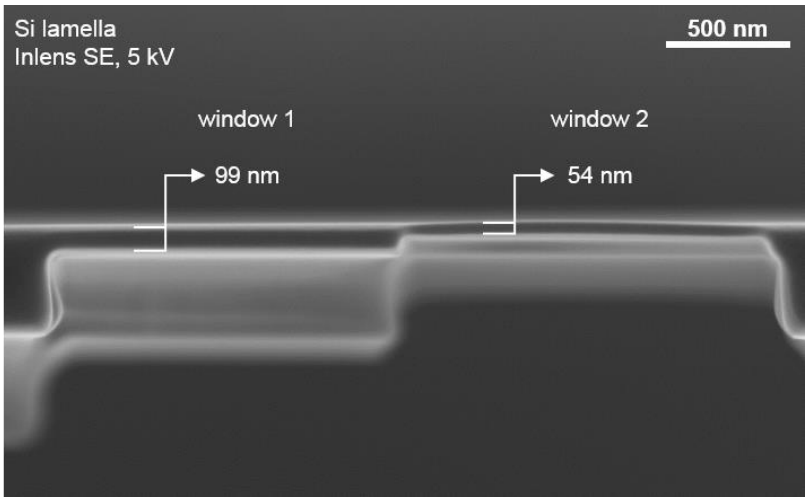

Figure 2. Top view image of the same silicon lamella as in Figure 1. The thicknesses of the polished windows could be measured as 99 and 54 nm, respectively.

IM4.P007
Electron-beam broadening in amorphous carbon films in low-energy scanning transmission electron microscopy

E. Müller[1], H. Drees[1], M. Dries[1], D. Gerthsen[1]

[1]Laboratory for Electron Microscopy, Karlsruhe Institute of Technology (KIT), Karlsruhe, Germany

erich.mueller@kit.edu

Scanning transmission electron microscopy (STEM) at low primary electron energies $E_0 \leq 30$ keV is performed in a scanning electron microscope. The technique is well suited to achieve high material contrast even for low atomic number materials. However, electron-beam broadening occurs within the sample and worsens the lateral resolution of the technique. Several approaches to calculate electron-beam broadening are summarized in [1]. These approaches were recently complemented by Gauvin and Rudinsky [2] who suggested a general description for beam broadening for a large range of specimen thicknesses.

We present a method to measure beam broadening that relies on STEM imaging with a multi-segmented STEM detector. An amorphous carbon (aC) film with 10 nm thickness is used as test object.

Fig. 1 shows a bright-field (BF) STEM image taken close to a crack in the aC-film. Multiple folding of the aC-film occurs which creates regions with a defined thickness according to the number of folds. Beam broadening b at the bottom of the sample with thickness t is measured by assuming $b = t \tan \varphi$ with the scattering angle φ (Fig. 2a) which is an established concept [1]. The detector contains six different segments with the scattering angles related to the outer segment diameters (cf. scheme Fig. 2b).

The same sample region was imaged sequentially with all detector segments giving intensity values which are normalized with respect to the intensity of the incident electrons. The accumulated intensities up to the indicated detector segment and corresponding scattering angles θ_0 are plotted in Fig. 3 for $E_0 = 30$ keV as a function of t. We refer to b as the beam diameter that contains 68 % of the total probe current, which is marked by the dotted grey line in Figure 3. The crossings of the dashed vertical lines with the grey line indicate the film thicknesses at which the intensity falls below 68 % for the different detector segments. At these thicknesses the beam is broadened up to θ_0 of the different detector segments. The same procedure was performed for different E_0 from 10 to 30 keV and the resulting beam diameters plotted in Figure 4. The colored lines show calculated beam widths $b \sim t^2 / E_0^{1.5}$ according to Eqs. (21) and (26) from [2] without any fit parameters. The calculated curves excellently agree with the experimental data for 25 and 30 keV with a trend to underestimate b at lower E_0 values and increasing aC-thickness. This latter effect can be assigned to the electron intensity at large scattering angles which may be enhanced by thermal diffuse scattering, that are not taken into account in the model.

The measured b values show that the beam diameter increases to a multiple of the diameter of the incident electron beam - even for small thicknesses and a low-density material like aC. In the future, analogous measurements are planned for crystalline materials to assess the effect of channeling along zone-axis orientations.

[1] R. Michael, D.B. Williams, J. Microsc. 147 (1987) 289–303.
[2] R. Gauvin, S. Rudinsky, Ultramicroscopy 167 (2016) 21–30.
[3] We acknowledge funding by the Deutsche Forschungsgemeinschaft (DFG).

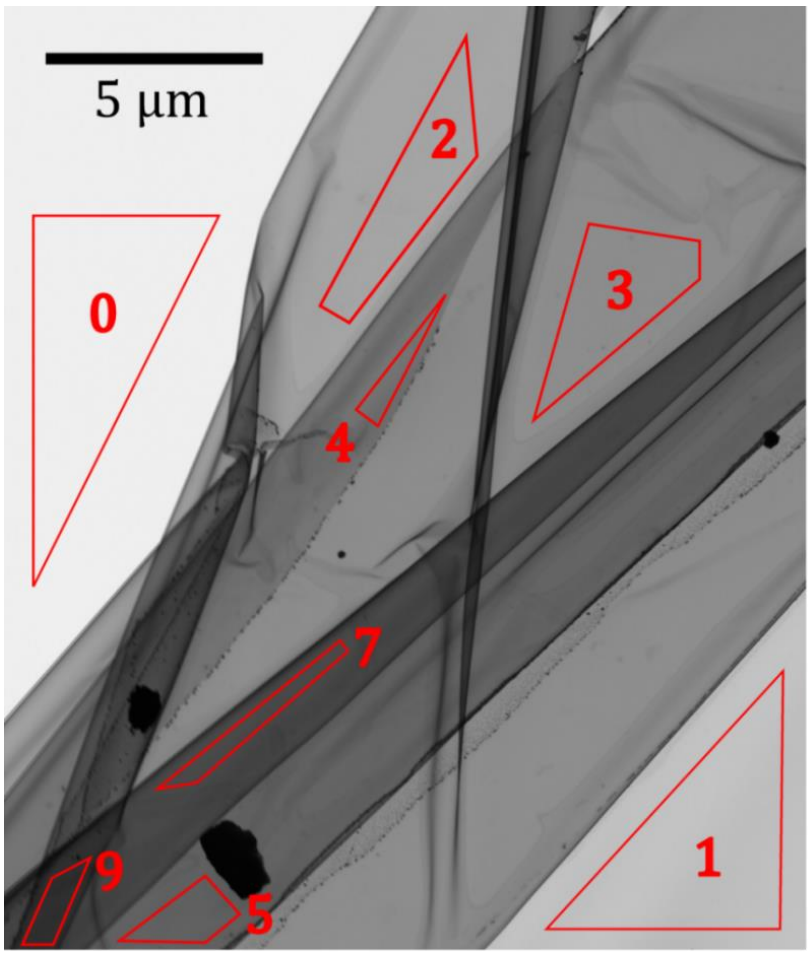

Figure 1. 20 keV BF-STEM image of a folded thin aC-film with the number of folds indicated.

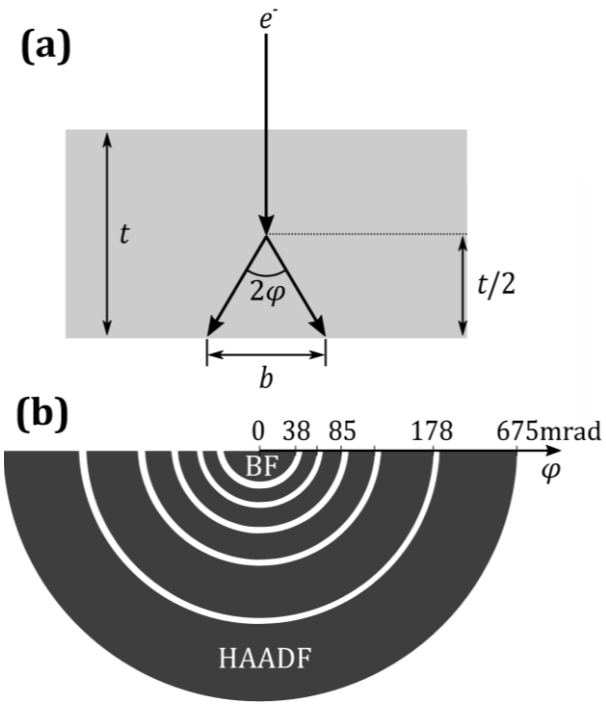

Figure 2. (a) Calculation of beam broadening b in sample with thickness t. (b) Scheme of the different STEM detector segments (not to scale) with corresponding outer detection angles.

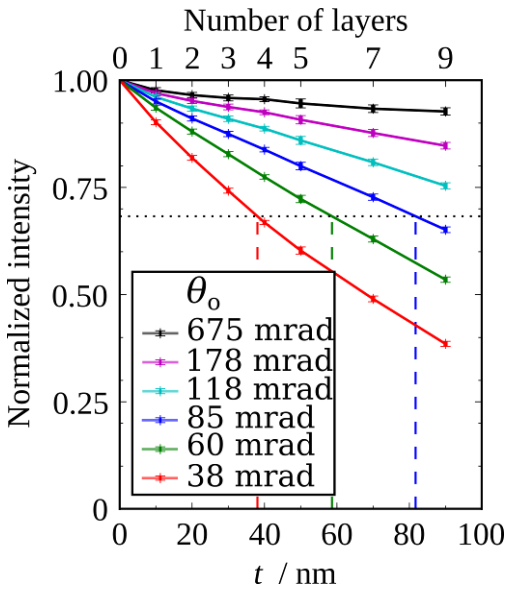

Figure 3. Accumulated intensities up to the detection angles θ_0 given in the legend as a function of the aC-thickness at $E_0 = 30$ keV. The angles θ_0 are defined by the outer diameters of the different STEM detector segments.

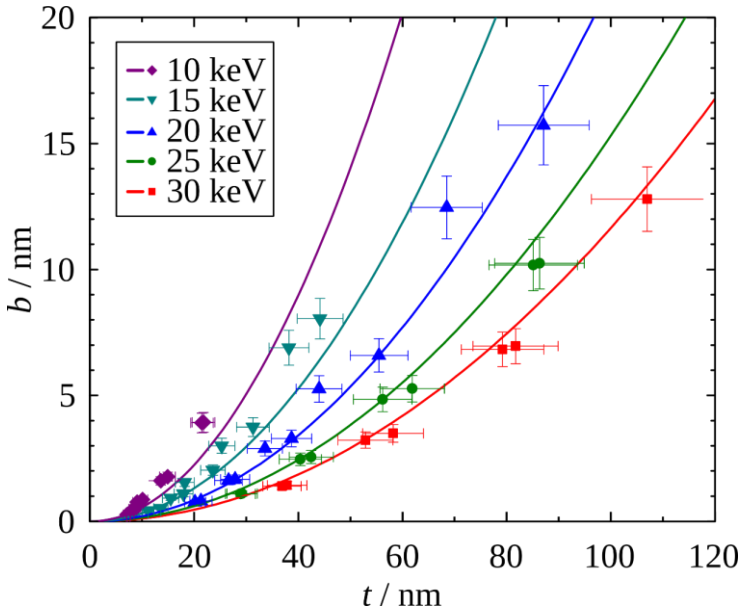

Figure 4. Beam width over thickness t for E_0 from 10 to 30 keV. Dots denote measured data while lines denote calculations $b \sim t^2 / E_0^{1.5}$.

IM4.P008
Characterizing amorphous specimens by the three particle structure factor

S. Vrana[1], H. Kohl[1]

[1]University of Münster, Münster, Germany

semir.vrana@uni-muenster.de

The structure of amorphous materials can be described by n-particle correlation functions $g_n(r_1,..., r_n)$ where $g_n(r_1, ..., r_n)\ d^3r_1 \cdots d^3r_n$ gives the probability of finding particle i in the volume d^3r_i and so on [1]. The pair correlation function $g_2\ (r_1, r_2)$ can be determined from scattering experiments. However, it describes only the distribution of atomic distances. Information about bond angles is lost. This would be accessible if the triple correlation function $g_3\ (r_1, r_2, r_3)$ could be measured.
The Fourier transforms of the correlation functions are the so-called structure factors. These can be directly obtained from experimental images [2]. Recently we were able to determine the three particle structure factor of an amorphous specimen [3] from the measurements of an amorphous silica layer on a graphene substrate in [4]. The relevance of three particle correlations can most easily be demonstrated using simulations.
In 1932 Zachariasen [5] proposed that amorphous matter was formed from a network of atoms where each atom is perfectly coordinated, i.e. each atom has the same number of bonds. These atoms form a uniform network without any long-range order. In 1985 Wooten, Winer and Weaire [6] proposed an algorithm to produce a particle configuration that fulfills Zachariasen"s requirements. Starting from an ideal crystal they introduced a dynamic into the system consisting of random bond switches and relaxations to deform it while preserving the coordination. In the first phase all such bond switches were accepted corresponding to an infinite temperature. The resulting system is then cooled down in a second phase using a simulated annealing mechanism [7] guided by a Keating-like potential [8] as shown in figure 1.
We used this to simulate a silica layer assuming rigid Si-Si-bonds (see fig. 2) and obtained the two and three particle structure factors as well. Since the experimental structure factor was obtained by Fourier transformation of experimental images from silica on a substrate, whereas the theoretical data were calculated as lattice sums over the particle positions, only the qualitative structure of the resulting functions can be compared. The results are shown figures 3 and 4 for different bond bending factors β.
The simulated two particle structure factor $S^{(2)}$ seems to agree qualitatively well for small spatial frequencies. Even though the simulated two particle structure factors are very similar, the three particle structure factors strongly depend on the bond bending parameter, particularly for small angles between the spatial frequencies.

References:
[1] J. Ziman, Models of disorder: the theoretical physics of homogeneously disordered systems (Cambridge University Press, 1979).
[2] M. Hammel and H. Kohl, in Inst. phys. conf. ser. 93 (1988), pp. 209–210.
[3] S. Vrana and H. Kohl, in European microscopy congress 2016: proceedings (Wiley Online Library, 2016).
[4] P. Y. Huang et. al., Nano Letters 12, 1081 (2012).
[5] W. H. Zachariasen, Journal of the American Chemical Society 54, 3841 (1932).
[6] F. Wooten, K. Winer, and D. Weaire, Physical review letters 54, 1392 (1985).
[7] F. Wooten and D. Weaire, in Adaption of simulated annealing to chemical optimization problems, Vol. 15, edited by J. H. Kalivas, Data Handling in Science and Technology (Elsevier, 1995), pp. 329–349.
[8] P. N. Keating, Phys. Rev. 145, 637 (1966).

$$E = \frac{3}{16}\frac{\alpha_0}{d^2}\sum_{\langle ab\rangle}\left(|\vec{r}^{ab}|^2 - d^2\right)^2 + \frac{3}{8}\frac{\beta_0}{d^2}\sum_{\langle abc\rangle}\left(\vec{r}^{ab}\cdot\vec{r}^{ac} + \frac{1}{2}d^2\right)^2$$

Figure 1. The Keating potential [8]. The default values are $\alpha_0 = 2.965\ eVÅ^{-2}$, $\beta_0 = 0.285\alpha_0$ and d = 3.2 Å [6].

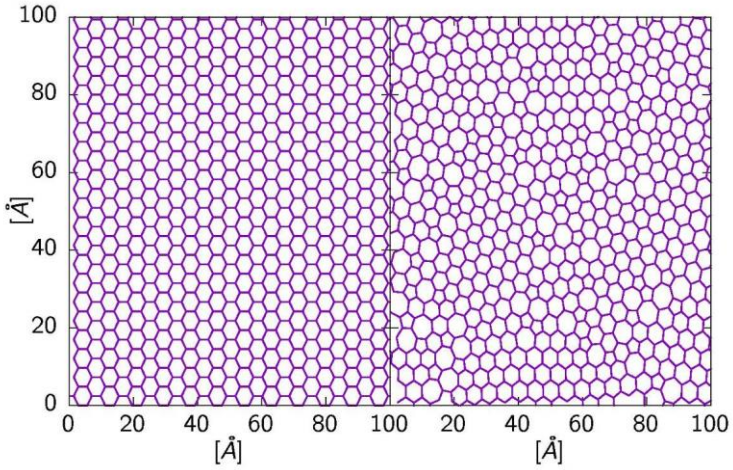

Figure 2. The simulated data. Left: The initial condition. Right: The resulting cluster.

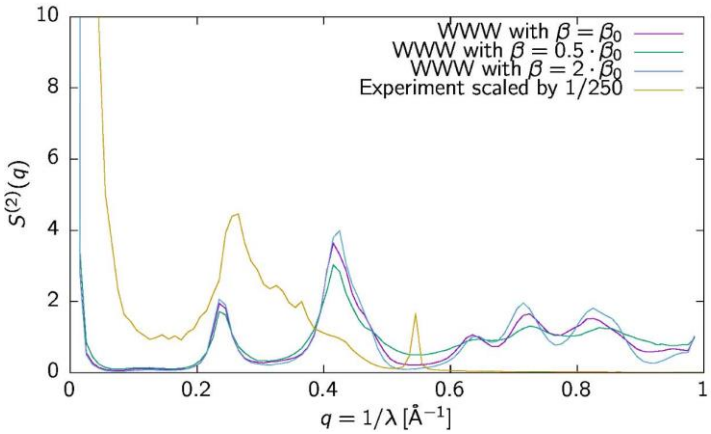

Figure 3. The two particle particle structure factor of amorphous silica from the WWW model with varying bond bending force compared to experimental data [4].

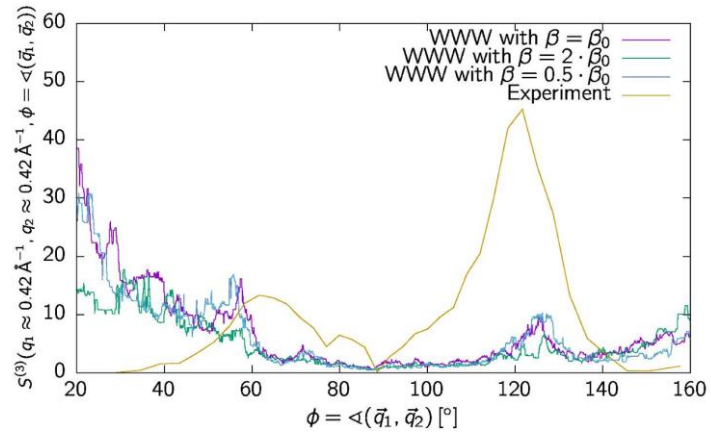

Figure 4. The three particle structure factor of amorphous silica from the WWW model with varying bond bending force compared to experimental data [4]. The simulated data was flattened using a median-filter.

IM4.P009
Atom in a harmonic potential – a model system for scattering due to lattice vibrations

T. Niermann[1]

[1]Technische Universität Berlin, Institut für Optik und Atomare Physik, Berlin, Germany

niermann@physik.tu-berlin.de

The literature about electron-phonon scattering and thermal diffuse scattering (TDS) can lead to confusions [1-3]. There are even diverging statements whether both effects are identical. There are several reasons for this: phonon scattering has only energy losses in the lower meV range, which are experimentally not resolvable by current energy loss spectrometers. The electron-phonon interaction is non-local and the number of phonon states involved is large, thus some approximations are required in theoretical modeling. Additionally, the thermal excitation of phonons can only described by statistical means. And eventually both terms (electron-phonon scattering and TDS) are used with different meanings within the literature.
Some of these restrictions can be strongly mitigated, when the vibrational system is simplified. We report on the theoretical scattering properties of a single atom placed in a harmonic potential. This resembles the situation found for a single atom in the potential of its surrounding atoms (Einstein model), and neglects collective motions of the atoms (Debye model). As we just want to study the scattering from atom vibrations, we further neglect interactions between the fast electron and the electronic system of the specimen as well as interactions between the specimen"s electrons and the motion of the nucleus (Born-Oppenheimer approximation). For such a system, the quantum mechanical treatment of the vibration dynamics is concise and the interaction region is rather small. Hence the interactions between the fast electron and the vibrating atom can be calculated by numerical propagation of the relativistically-corrected form Schrödinger equation in the high-energy approximation. No further approximation are made.
This model system allows studying the scattering-properties of the different effects separately. Fig. 1 shows the elastic scattering sub-channel of an incident plane wave (300kV) scattered by different vibrational eigenstates of an gold atoms (eigenfrequency 8 THz). Shown are the amplitude and phase of the scattered wave front backpropagated into the plane of the atom"s rest position. The states are identified by quantum state numbers in x, y, z directions. Here the scattering potential is mainly convoluted with the probability distribution of the atom. In Fig. 2 the backpropagated projections of the joint wave function of an plane wave impinging an atom initially in its ground state projected onto the atom"s eigenstates are shown. The different momentum transfer is nicely visible as phase shifts of different sign (+π/2 vs. -π/2). Obviously, the intensities in the inelastic sub-channels are non-zero, already showing for 0 K that TDS (i.e. the elastic channel of the ground state, see Fig. 1) and inelastic electron-phonon scattering are not the same.

[1] D. Van Dyck. Ultramicroscopy 109 (2009) 677
[2] A. Rother, T. Gemming, H. Lichte. Ultramicroscopy 109 (2009) 139
[3] B. D. Forbes, A. V. Martin, S. D. Findlay, A. J. D"Alfonso, L. J. Allen, Phys. Rev. B 82 (2010) 104103

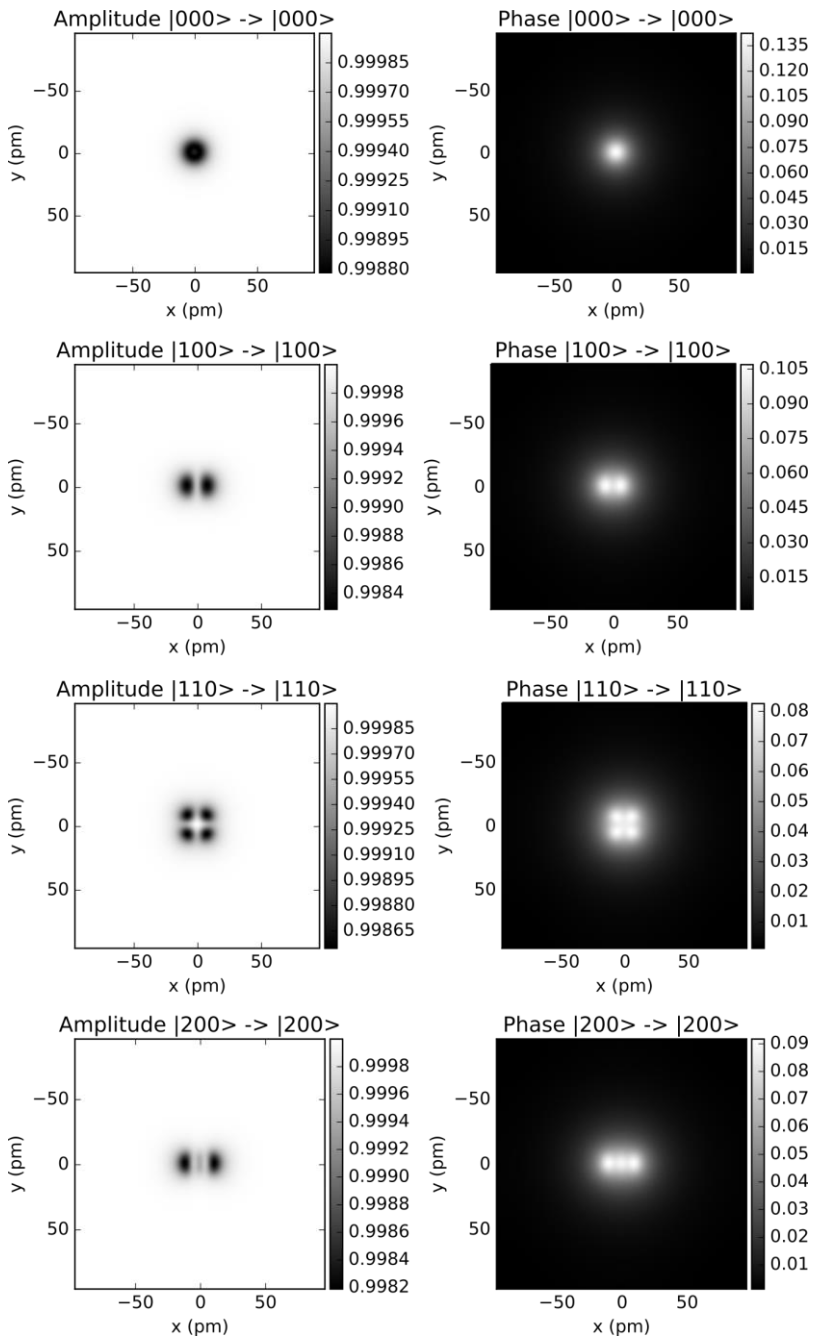

Figure 1. The elastic sub-channel for a plane wave scattered by different vibrational eigenstates of a gold atom.

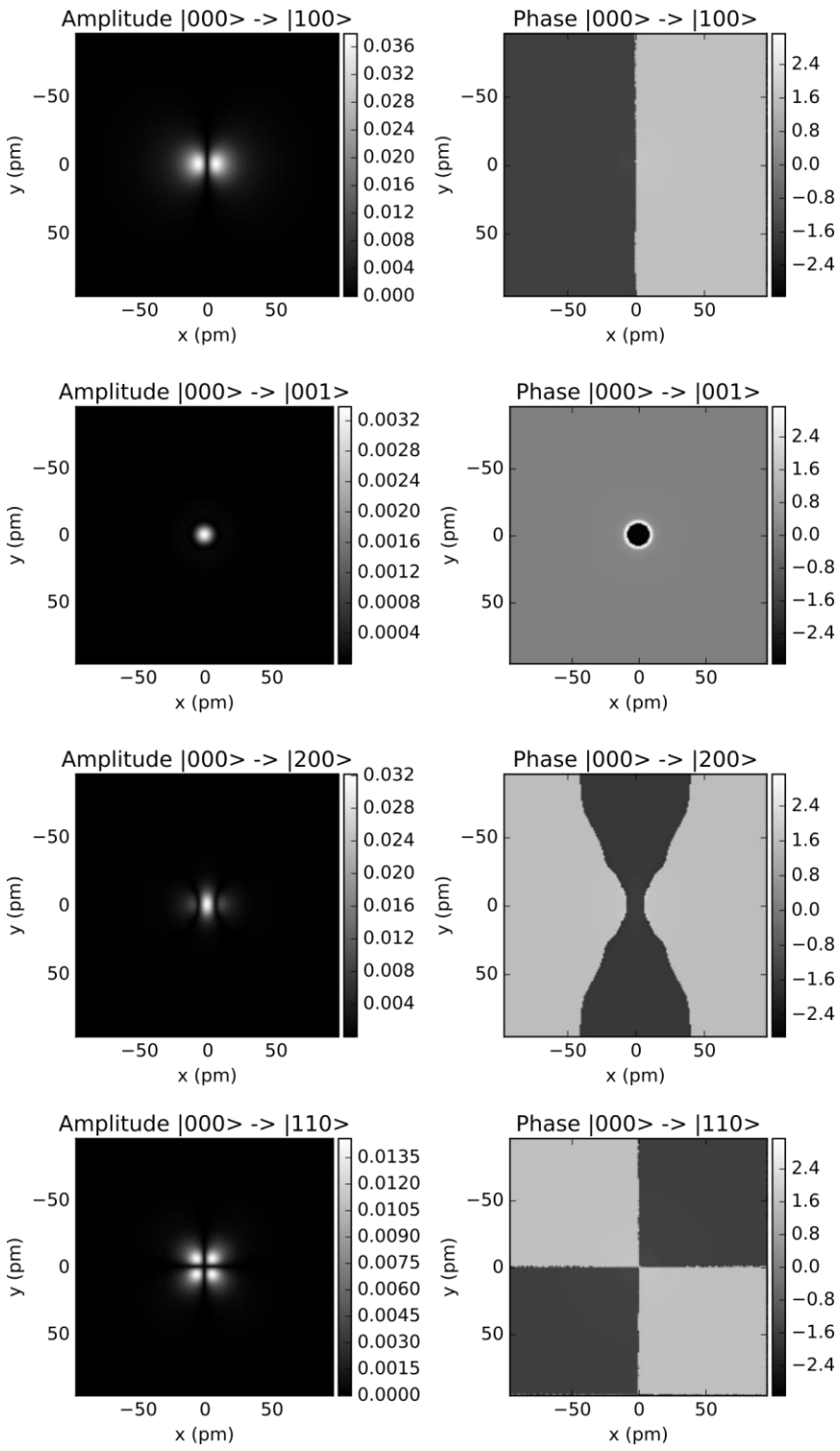

Figure 2. Projections of the outgoing wave onto the eigenstates of the atom after scattering at an atom in its ground state

IM4.P010
STEMsalabim – high-performance computing cluster friendly code for scanning transmission electron microscopy image simulations of thin specimens

J. O. Oelerich[1,2], L. Duschek[1,2], J. Belz[1,2], A. Beyer[1,2], S. D. Baranovskii[1], K. Volz[1,2]

[1]Philipps-Universität Marburg, Physics, Marburg, Germany
[2]Materials Science Center, Marburg, Germany

jan.oliver.oelerich@physik.uni-marburg.de

Since the early 1980s scanning transmission electron microscopy (STEM) has evolved into an indispensible tool for the structural analysis of thin crystalline specimens. Using high-angle annular dark field (HAADF) detectors, chemically sensitive scattering of the focused electron probe can reveal valuable information about the sample, such as chemical composition, strain fields, thicknesses, etc. In order to extract quantitative information from STEM images, however, it is still necessary to compare measured data to computer simulations of the interaction between incident electron beam and the specimen.
The most common method to model the interaction of the electron probe and the specimen is via the multislice method, which is widely applied today for the analysis of experimental (S)TEM images [1]. Although there are many existing implementations of the multislice algorithm for the simulation of STEM images, almost all of them are designed for desktop computers with a single or very few processors or do not comply with common parallelization standards and are therefore not suited for realistic large-scale simulations, parameter sweeps, or iterative optimization. Particularly surprising is the lack of a freely available code for massive parallelization on high-performance computing (HPC) clusters, even though the many necessary multislice simulations for a single STEM image are independent from each other and therefore perfectly suited for efficient parallelization.
In this contribution we present STEMsalabim [2], a new implementation of the multislice algorithm that is built specifically for concurrent calculations on many computing nodes. The package uses a combination of the message passing interface (MPI) and threads for efficient intra- and inter-machine parallelization while maintaining a small memory footprint, a feature that is not present in existing software packages but crucial for the simulation of large images.
In our contribution, we present the technicalities of STEMsalabim and briefly discuss some research results that became feasable using the program, such as composition determination of quaternary semiconductor alloys [3] or influences of surface relaxation of strained layers on ADF intensity [4]. Additionally, we show benchmarking data to display the scaling behaviour of STEMsalabim in parallelized calculations.
STEMsalabim is free and with our contribution we hope to spark some interest in the package and motivate other researchers to apply it to new research questions.

[1] S. J. Pennycook, D. E. Jesson, Ultramicroscopy 37, 1 (1991).
[2] J. O. Oelerich, L. Duschek, J. Belz, A. Beyer, S. D. Baranovskii, K. Volz, Ultramicroscopy (in press, 2017).
[3] L. Duschek, A. Beyer, J. O. Oelerich, K. Volz, submitted (2017).
[4] A. Beyer, L. Duschek, J. Belz, J. O. Oelerich, K. Jandieri, K. Volz, submitted (2017).

IM4.P011
Quantitative EDXS analysis on multi detector configuration and variable specimen tilt in transmission electron microscopy

T. Withaar[1], M. Borodachenkova[1], B. Freitag[1]

[1]Thermo Scientific, FEI, Eindhoven, Netherlands

thijs.withaar@fei.com

Introduction: When determining the chemical composition of a sample by using energy dispersive x-ray analysis (EDXS), absorption effects can be significantly alter the result. Traditionally, absorption literature in TEM focuses on side entry detectors with a relatively low solid angle and absorption correction on the sum-signal of multiple detectors like the Super-X or Dual-X detectors is often not covered. In this contribution we present a correction method including the effect of shadowing of double tilt holders, of solid angles beyond 1 sterradian and arbitrary detector configuration including the quantification of summed signals for multiple detector configurations. To calculate absorption correction, the basic principle for the absorption correction presented here is described in [1]. The most noticeable difference of our method is that the corrections are based on the real CAD design of the holder and work on the summed signals of multi detector EDXS systems. Figure 1 shows the CAD model used. The method is validated against both Super-X and Dual-X systems and the standard analytical double tilt holder, which have a quite distinctive geometry.
Materials and Methods: To determine that the accuracy of absorption correction holds, different samples were measured with multiple sample tilts using DualX and SuperX detectors. On each tilt, a spectrum is acquired which is then analyzed with the new method.
Results: The method presented above was tested on both a Super-X and a Dual-X system. Spectra were acquired for each detector independently. Those spectra were summed before analysis. Figure 1 shows the results for a Super-X and Dual-X system. Without absorption correction the EDS analysis of a 160nm Si3N4 sample [3] gives results which are clearly off the nominal 57at% nitrogen concentration. Using traditional absorption correction, modelling just the sample thickness, results in the green graph. This leads to a clearly better quantification result, but still a dependence on tilt is observed. Enabling the holder corrections (red graph) shows a nearly constant correct quantification result across the entire tilt range for Dual-X and Super-X detector systems.
Multiple performance tests with different acceleration voltage including a detailed analysis of the individual detectors (figure 2) is presented. Although analysis speed on a single spectrum is often satisfactory without effort, analyzing spectrum images can be challenging in the analysis time required. Measurements show that enabling absorption correction results in only a ~2x increase in analysis time. Since the geometry calculations can be done once for the whole spectrum image, the overhead of holder corrections is negligible.
Conclusion: The accuracy of quantitative EDXS analysis can be improved greatly, when taking absorption effects of holders into account. The correction algorithm presented is designed for multiple detector systems. In contrast to previously published methods [2], it works on the summed-signal of multiple detectors, as well as on single detector signals. We show that even for relatively thick samples, Si3N4 of ~160nm, absorption correction can result in an absolute quantification error less than 2 atomic percent. The more sophisticated quantification method increases the analysis time only by a factor of ~2, allowing an accurate and fast analysis of even EDXS maps not only single spectra. It is available under the Velox 1.4 and upwards software for Dual-X and Super-X configurations on Thermo Fisher Scientific TEMs.

Bibliography:
[1] Xu – A numerical model for multiple detector EDS in the TEM
[2] Kraxner – Quantitative EDXS: Influence of geometry on a four detector system
[3] Si3N4 sample: www.lionixbv.nl

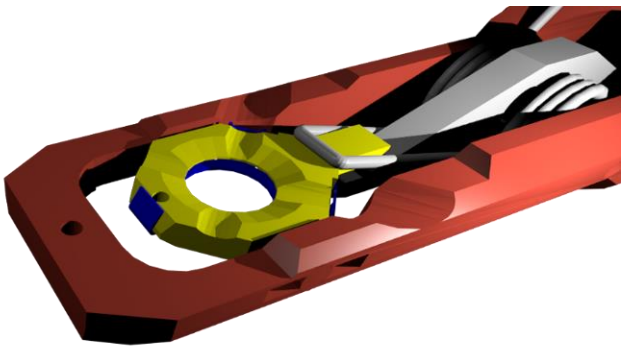

Figure 1. CAD model used for absorption correction.

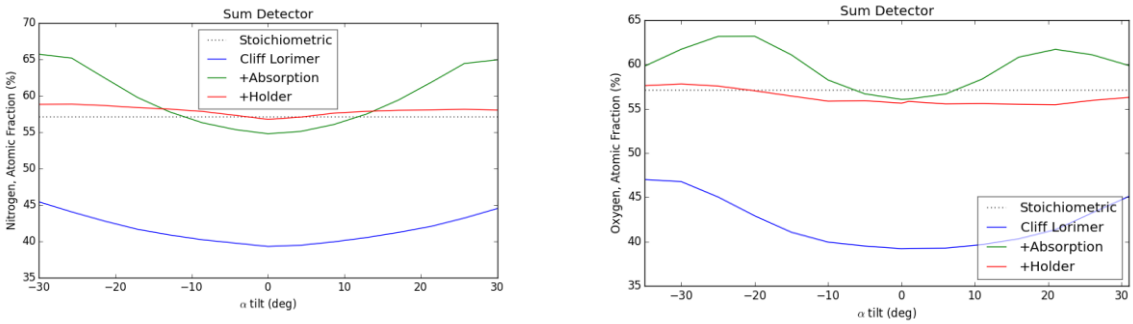

Figure 2. Absorption corrected EDXS analysis of Si3N4 on a Talos system using SuperX (left) and DualX (right). Both are measured at 200kV, in TEM 4300x magnification.

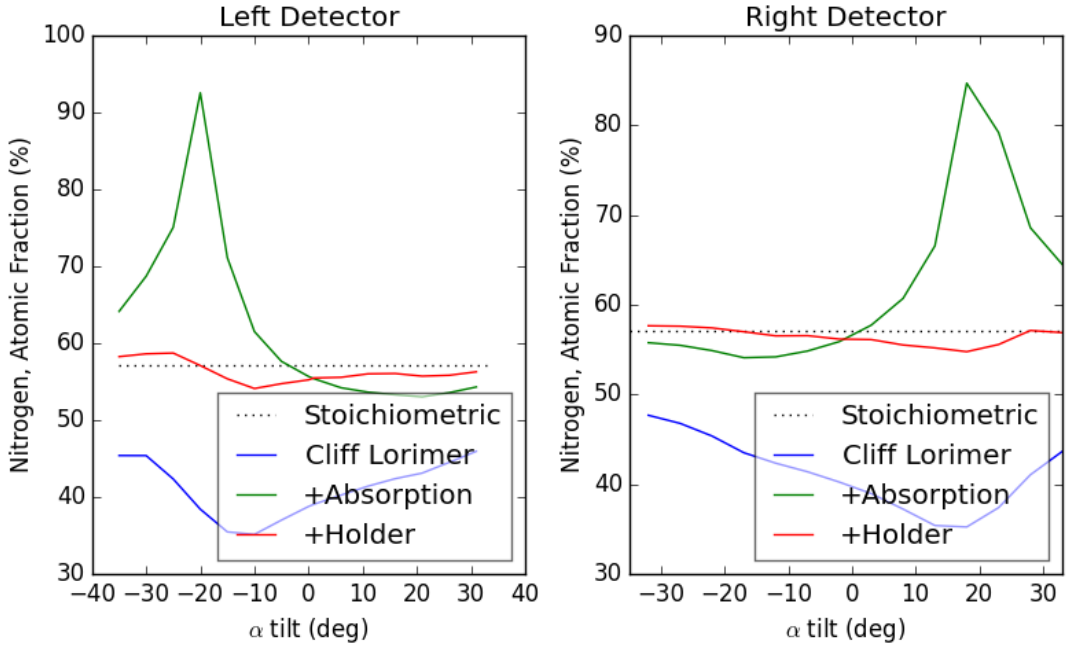

Figure 3. EDXS quantification results per detector on a Dual-X system, 200kV in TEM mode.

IM4.P012
On the ADF-STEM dislocation contrast

M. C. Spadaro[1], E. Oveisi[1,2], E. Rotunno[3], V. Grillo[3,4], C. Hébert[1,2]

[1]EPFL, Interdisciplinary Centre for Electron Microscopy (CIME), Lausanne, Switzerland
[2]EPFL, Electron Spectrometry and Microscopy Laboratory (LSME), Lausanne, Switzerland
[3]National Research Council, Institute of Materials for Electronics and Magnetism (IMEM-CNR), Parma, Italy
[4]National Research Council, Institute of Nanoscience (NANO-CNR), Modena, Italy

emad.oveisi@epfl.ch

Analysis of defects in crystal structures is pivotal in understanding their impact on the mechanical and opto-electronic properties of many materials across a broad range of applications[1,2]. Recently, annular dark-field imaging in scanning transmission electron microscopy (ADF-STEM) has been extended to defect analysis, in particular for studying dislocations in thick specimens and for obtaining images suitable for tomographic reconstructions[3-5].
Different scattered state wave vectors are integrated over the acceptance annulus of the ADF detector to form an image[6]. Therefore, depending on the detector geometry, there are several independent mechanisms contributing to defect contrast in the ADF-STEM images, making the interpretation of the contrast complex. Different mechanisms have been proposed for interpreting STEM defect contrast, including de-channelling, the reduction of the 1s contribution caused by inter-band transition between the 1s and non-1s Bloch states, as well as diffuse scattering, in particular the Huang scattering[6,7].
A systematic study of ADF contrast of dislocations in gallium nitride revealed a number of characteristic contrast features that are shown to depend on both angular detection range and the specific position of the dislocation in the sample[8]. For a dislocation close to entrant foil surface, the contrast in the low-angle ADF regime is composed of a narrow dark line surrounded by regions with higher intensities relative to the background. This contrast changes to a single sharp peak in the medium-angle ADF (MAADF) regime, and in the high-angle ADF (HAADF) regime it becomes complementary to that of LAADF regime. A bottom configuration dislocation however gradually looses its visibility from LAADF to HAADF regimes. This highlights the need for models that take into account all these effect to comprehend better the mechanisms underlying these contrast features.
In this contribution, we further refine the Grillo's equation model and apply an improved equation system to explore such depth-dependent ADF dislocation contrast[9,10]. With this new model, all the aforementioned conditions were simulated and resulting computational micrographs of dislocations show a good agreement with the experimental images. A rationale based on electron channeling and Bloch-wave theories is proposed to account for such complex contrast phenomena. These results provide new insights and a link to understand the ADF dislocation contrast.

References:
[1] Mott, N.F. Dislocations and the theory of solids. *Nature* **171**, 234-237 (1953).
[2] Hua, G.C. *et al.* Microstructure study of a degraded pseudomorphic separate confinement heterostructure blue-green laser diode. *Appl. Phys. Lett.* **65**, 1331-1333 (1994).
[3] Perovic, D.D., Rossouw, C.J. & Howie, A. Imaging elastic strains in high-angle annular dark field scanning transmission electron microscopy. *Ultramicroscopy* **52**, 353-359 (1993).
[4] Phillips, P.J., Mills, M.J. & De Graef, M. Systematic row and zone axis STEM defect image simulations. *Philos. Mag.* **91**, 2081-2101 (2011).
[5] Phillips, P.J., Brandes, M.C., Mills, M.J. & de Graef, M. Diffraction contrast STEM of dislocations: Imaging and simulations. *Ultramicroscopy* **111**, 1483-1487 (2011).
[6] Perovic, D.D., Howie, A. & Rossouw, C.J. On the image contrast from dislocations in high-angle annular dark-field scanning transmission electron microscopy. *Philos. Mag. Lett.* **67**, 261-272 (1993).
[7] Cowley, J.M. & Huang, Y. De-channelling contrast in annular dark-field STEM. *Ultramicroscopy* **40**, 171-180 (1992).
[8] Oveisi E. Three-dimensional STEM imaging of dislocations. PhD thesis, EPFL, Lausanne, 2014.
[9] Grillo, V. The effect of surface strain relaxation on HAADF imaging. *Ultramicroscopy* **109**, 1453-1464 (2009).
[10] Grillo, V. & Rotunno, E. STEM_CELL: A software tool for electron microscopy: Part I—simulations. *Ultramicroscopy* **125**, 97-111 (2013).

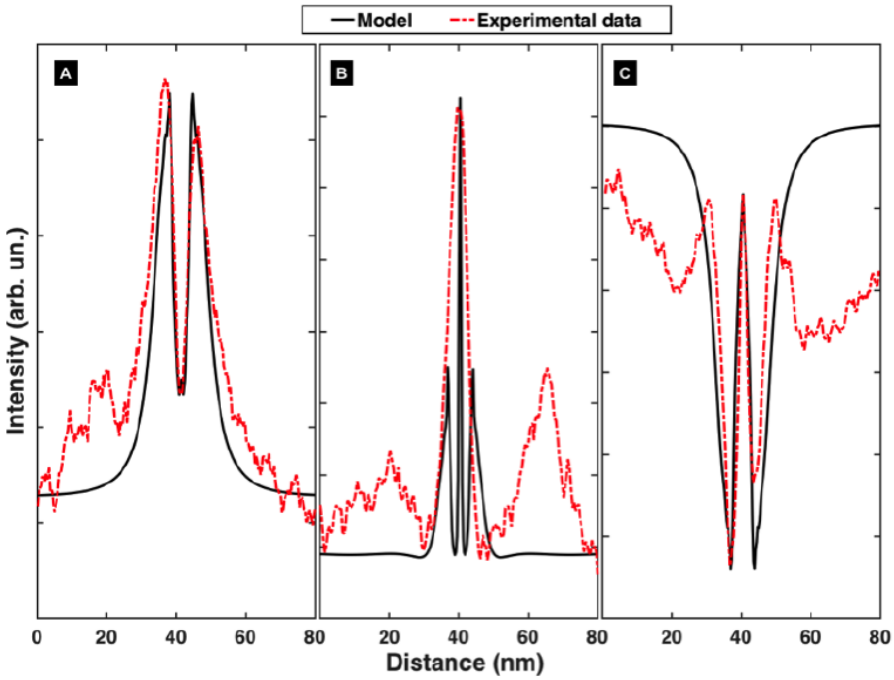

Figure 1. Comparison between experimental and simulated line scan of intensity profiles across a dislocation located close to the entrant foil surface in A) LAADF, B) MAADF, and C) HAADF regimes.

IM4.P014
The limiting effect of amorphous surface layers on quantitative HRTEM image analysis

T. Remmele[1], T. Schulz[1], M. Albrecht[1]

[1]Leibniz-Institut für Kristallzüchtung, Berlin, Germany

thilo.remmele@ikz-berlin.de

Introduction: With aberration corrected high-resolution transmission electron microscopy (HRTEM) the direct imaging of atomic columns is achievable without critical artefacts caused by delocalisation. For many investigations a precise measurement of the positions of atomic columns is mandatory, e.g. to estimate compositional fluctuations locally in InGaN quantum wells with a precision of 1 % a measuring precision in atomic column distances of 1 pm has to be achieved. Van Aert et al [1] discuss the image analysis in form of a statistical parameter estimation problem, which is limited by noise - provided that the model is sufficient accurate. The highest attainable measurement precision of atomic column distances is rated there by the rule of thumb $\sigma \approx \sqrt{2}\ \rho\ N^{-½}$, where ρ is the width of the atomic column and $N^{-½}$ represents the shot noise from the electron detection. From this perspective a measurement precision beyond 1 pm should be achievable. However, e. g. in c-lattice parameter analysis from HRTEM images of GaN structures standard deviations (STD) in the range of 3-5 pm are reported [2,3]. This essential higher STD in the measurement is found to originate from amorphous surface layers (Figure 1).
Objectives: We study the influence of amorphous surface layers on the measurement precision of atomic column positions in HRTEM images in detail based on the analysis of image series of thin GaN samples. Image simulations are used to identify the important characteristics of amorphous layers concerning their limiting effect on the measurement precision.
Material and Methods: The study is exemplarily carried out with the c-lattice parameter measurement of GaN imaged in the [1-100] projection. The peak positions representing the atomic columns are estimated with an iterative center of mass approach to sub-pixel accuracy. Simulations for comparison to experiment were performed with the multislice software of Kirkland [4]. Further image processing and evaluation were done with in-house software.
Results: Using, in HRTEM image simulations, a noise model derived from amorphous contrast of experimental images the STD in distance measurements found in experiment can not only be matched, but in addition the observation that the STD does not drop $\sim M^{-½}$ when averaging over M images in a series, as expected for a random measurement error, is also reproduced (Figure 2). Residual correlations in amorphous patterns could be excluded as cause for that observation since using uncorrelated amorphous patterns in simulations still produces the observed deviation. It is interesting that with a simple atomistic model for the amorphous surface layers, just by randomly placing atoms, the deviation from the $\sim M^{-½}$ drop is not achieved. But if next nearest neighbour distances are taken into account deviations from the $\sim M^{-½}$ drop occur.
Conclusions: Amorphous surface layers are found to be the limiting factor in quantitative HRTEM image analysis with respect to precision in position measurements. The next nearest neighbour distances in the amorphous network appear to cause a considerable reduction in precision gain when averaging over a image series. As the neighbour distances are in the range of crystal lattice distances filtering in the Fourier space domain is not suitable. Additionally modelling amorphous layers by randomly placing atoms may give too optimistic results in simulations.

References:
[1] Van Aert et al, IEEE Transaction on Instrumentation and Measurement 51, 611 (2002)
[2] T. P. Bartel and C. Kisielowski, Ultramicrocopy 108, 1420 (2008)
[3] T. Schulz et al, J. Appl. Phys. 112, 033106 (2012)
[4] Earl J. Kirkland, Advanced Computing in Electron Microscopy 2nd Edition, Springer 2010

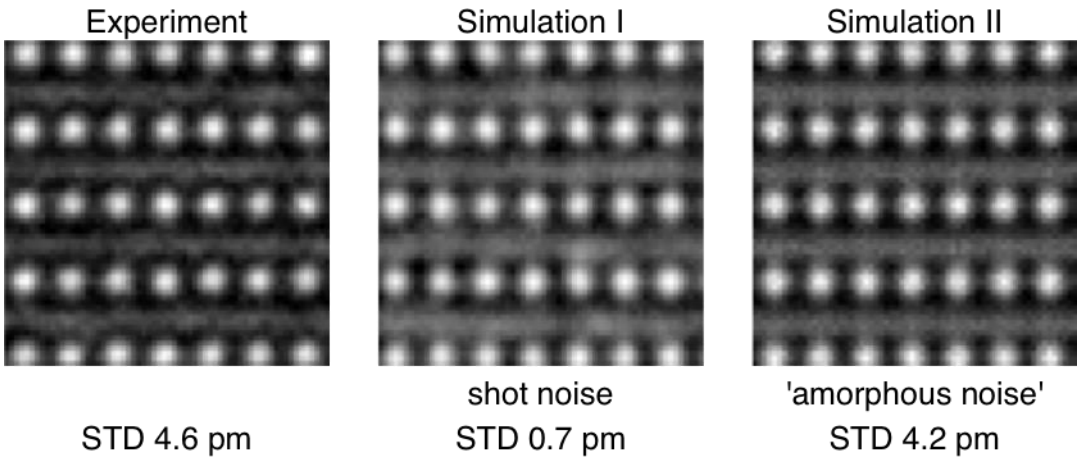

Figure 1. HRTEM of GaN in [1-100]-projection, experiment compared to simulations with shot noise and with amorphous noise model. The respective STD value of the c-lattice distance estimationare displayed.

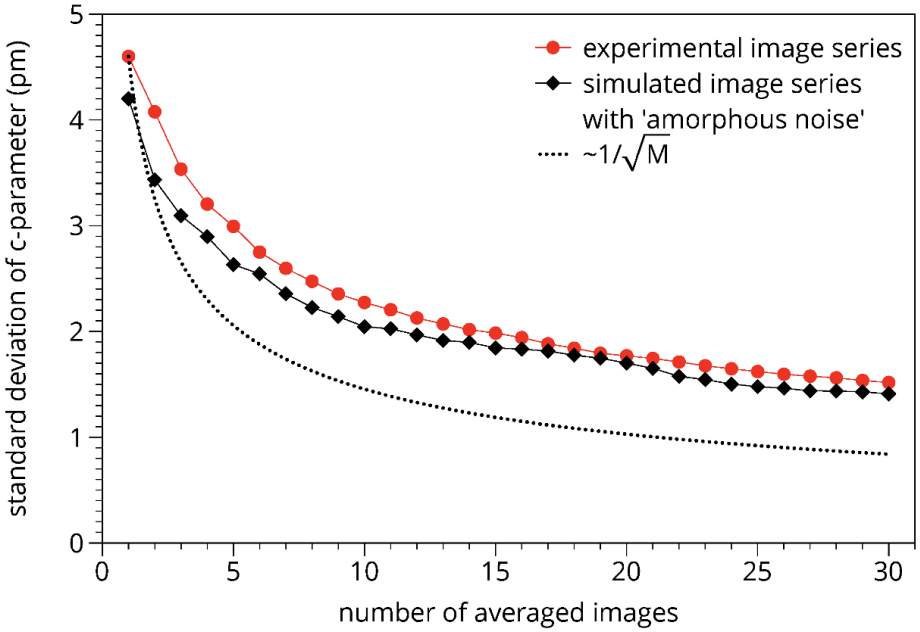

Figure 2. STD of c-lattice parameter measurement as a function of the number M of averaged images.

IM4.LBP01
Quantitative analysis of cell migration in the wound healing scratched assay by using active contour model and speeded up robust features

A. Jamshidzadeh[1], M. Farshad[1], S. Mardani Samani[1]

[1]Shiraz University of Medical Sciences, Pharmaceutical Sciences Research Center, Shiraz, Islamic Republic of Iran

ajamshid@sums.ac.ir

Introduction: Scratch wound healing assay has been widely adapted and modified by researchers to study the effects of a variety of experimental conditions, for instance, gene-knockdown or chemical compound treatment, on cell migration and proliferation. In this study, we propose an automatic method for segmenting the scratched areas for quantitative determination of fibroblast and other cells migration to and proliferation into the wounded monolayer. This is achieved by combining the Speeded-Up Robust Features (SURF) and Active Contour Model (ACM).
Methods: Cell migrating and growth towards the center of the gap was photographed and measured using digital image processing. The scratched area was segmented from the image and then some features like the mean, variance, RGB and HSV parameters are extracted. The work has been tested on different cell monolayer at first and 3 times after scratching.
Results: Comparing the segmentation results by use of Otsu thresholding method, ACM and SURF show the superiority of ACM method over the two others. The proposed method for scratched cell segmentation which is a combination of SURF and ACM gives the best results. To assess the practical robustness of our method, we have used it for segmentation of different types of cell migration.
Conclusion: Result of applying the proposed method on different cells shows the high performance, speed and accuracy of it. We believe that this work is applied the most powerful and newest methods of image processing to estimate the relative migration cells in wound healing in vitro test.

IM 5: Spectroscopy in microscopy

IM5.001 invited
High-resolution electron energy-loss spectroscopy – applications to Li-based cathode materials and plasmonic structures

G. Botton[1], E. Bellido[1], I. Bicket[1], V. Kapetanovic[1], H. Liu[1]

[1]McMaster University, Hamilton, Ontario, Canada

gbotton@mcmaster.ca

Electron energy-loss spectroscopy (EELS) is a very valuable technique to provide chemical composition information of materials at high spatial resolution. In the last decade, however, this technique has become a powerful tool to probe the electronic structure of materials with both high spatial resolution (down to the atomic level) and high energy resolution (even below 0.1eV).
In this communication, we highlight recent examples of applications of this technique in two areas of materials research. First, we will show how EELS Near-Edge Structures (ELNES) provide valuable information on the electronic structure and evolution of Li–based cathode battery materials. We show how the charge compensation process can be effectively probed with the study of transition metal $L_{2,3}$ edges and oxygen K edges. We also show how a range of cathode materials evolves following extensive charge and discharge cycles. We will discuss how the ELNES can provide valuable insight on the bonding and structural configuration of atoms in the solid before and after the degradation processes [1].
We will also provide examples of recent progress in the study of the plasmonic response of metallic nanostructures highlighting the insight on the hybridization behavior and enhanced spectral range achieved with this technique [2-4]. Finally, we will show how new instrumentation and data processing methods allow to extract more detailed information on the electronic excitations in materials [5].

References:
[1] Liu, H.; Bugnet, M.; Tessaro, M. Z.; Harris, K. J.; Dunham, M. J. R.; Jiang, M.; Goward, G. R.; Botton, G. A., Spatially resolved surface valence gradient and structural transformation of lithium transition metal oxides in lithium-ion batteries, Physical Chemistry Chemical Physics 18, 29064-29075. (2016).
[2] Bellido, E.P.; Manjavacas, A.; Zhang, Y.; Cao, Y.; Nordlander, P.; Botton, G. A., Electron Energy-Loss Spectroscopy of Multipolar Edge and Cavity Modes in Silver Nanosquares, ACS Photonics 3, 428-433. (2016)
[3] Bellido, E.P.; et al. Electron Energy-Loss Spectroscopy of Fractal Structures, in submission (2017).
[4] Barrow, S.J.; Collins, S. M.; Rossouw, D.; Funston, A. M.; Botton, G. A.; Midgley, P. A.; Mulvaney, P., Electron Energy Loss Spectroscopy Investigation into Symmetry in Gold Trimer and Tetramer Plasmonic Nanoparticle Structures, ACS Nano 10, 8552-8563. (2016)
[5] This research was supported by the Natural Sciences and Engineering Research Council (NSERC). This work was carried out at the Canadian Centre for Electron Microscopy, a facility supported by the Canada Foundation for Innovation under the Major Science Initiative program, NSERC and McMaster University.

IM5.002 invited
Reflection and phase matching in mesoscopic plasmonic tapers investigated by relativistic electrons

S. Guo[1], N. Talebi[1], W. Sigle[1], C. Lienau[2], A. Campos[3], M. Kociak[3], M. Esmann[2], S. F. Becker[2]
R. Vogelgesang[2], P. A. van Aken[1]

[1]Max Planck Institute for Solid State Research, Stuttgart Center for Electron Microscopy, Stuttgart, Germany
[2]Carl von Ossietzky University, Oldenburg, Germany
[3]Centre National de la Recherche Scientifique, Université Paris Sud, Orsay-Paris, France

p.vanaken@fkf.mpg.de

Introduction: Plasmonic metallic tapers with conical shapes show capabilities of nanofocusing and strong field enhancement [1]. Such tapers can serve either as waveguides or nanoantennas in near-field scanning optical microscopy and as ultrafast photoemission point sources in electron microscopy.
Objectives: The plasmonic response of mesoscopic tapers is studied in a wide energy range using electron energy-loss spectroscopy (EELS). However, the interpretation of EELS signatures is intricate by different resonance mechanisms, namely phase matching [2] and reflection [3] (Fig. 1a). Here we clarify the origin of the EELS resonances observed for conical gold tapers [4].
Materials and Methods**:** We systematically investigated the plasmonic modes of gold tapers with various opening angles from 5° to 47° both experimentally and theoretically by using both EELS and numerical finite-difference time-domain simulations. Single crystalline gold tapers were fabricated by electrochemical etching in HCl [4]. The tapers were mounted on a 3-mm copper ring for TEM analysis. EELS experiments were conducted at the Zeiss SESAM microscope operated at 200 kV. EELS data were acquired with an energy resolution of 90 meV and an acquisition time per spectrum between 0.2 and 0.8 s.
Results: Distinct resonances along the taper shaft are observed in tapers independent of opening angles (Fig. 2). Despite their similarity, the formation of these resonances is from a competition between two coexisting mechanisms (Fig. 1b). Phase matching between the field components of the fast electron and of higher-order angular momentum modes of the taper is the dominant contribution when the interaction length between the swift electron and the taper near-field becomes large enough, so that the higher-order angular momentum orders are excited. In contrast, reflection from the taper apex dominates when mostly the fundamental M=0 mode is excited. A gradual transition of these two mechanisms is observed.
In addition to EELS, cathodoluminescence (CL) has been applied to study the mere radiative behavior of the excited gold tapers plasmons, where plasmons at both the apex and the shaft (Fig. 3b) are couple to the far-field radiation (Fig. 3a).
Conclusions: In conclusion, we disentangle the link and distinct between the two different dynamic mechanisms, reflection and phase matching of surface plasmons excited by relativistic electrons in a three-dimensional single-crystalline gold taper.

References:
[1] M. Stockman, Phys. Rev. Lett. 93(2004) 137404
[2] N. Talebi *et al.*, ACS Nano **9** (2015) 7641
[3] B. Schroeder *et al.*, Phys. Rev. B **92** (2015) 085411
[4] S. Guo *et al.*, Nano Lett. **16** (2016) 6137

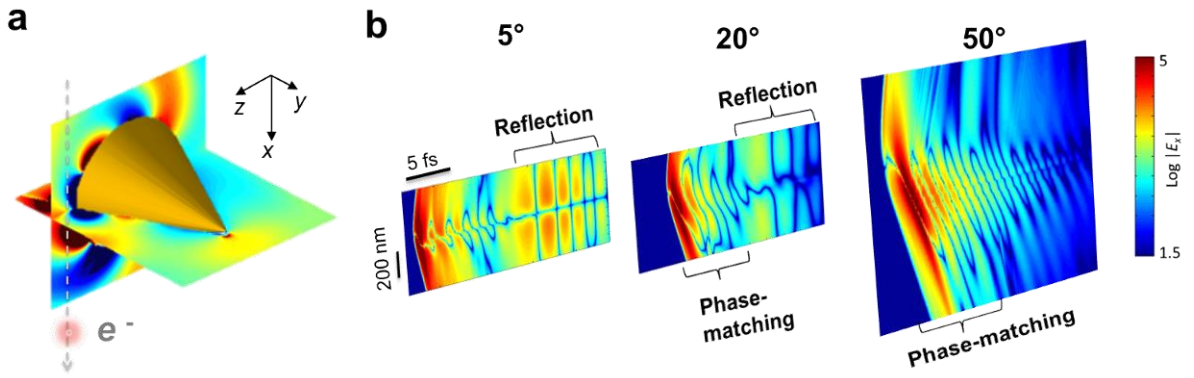

Figure 1. (a) Coexisting interaction mechanisms of phase matching and reflection when a relativistic electron is passing by a taper surface. (b) Transition from phase matching to reflection revealed by numerically calculating the total scattered electric field along the electron trajectory versus electron trajectory (nm) and time (fs) for tapers with different opening angles of 50°, 20° and 10° at a constant distance of L = 1460 nm from the apex.

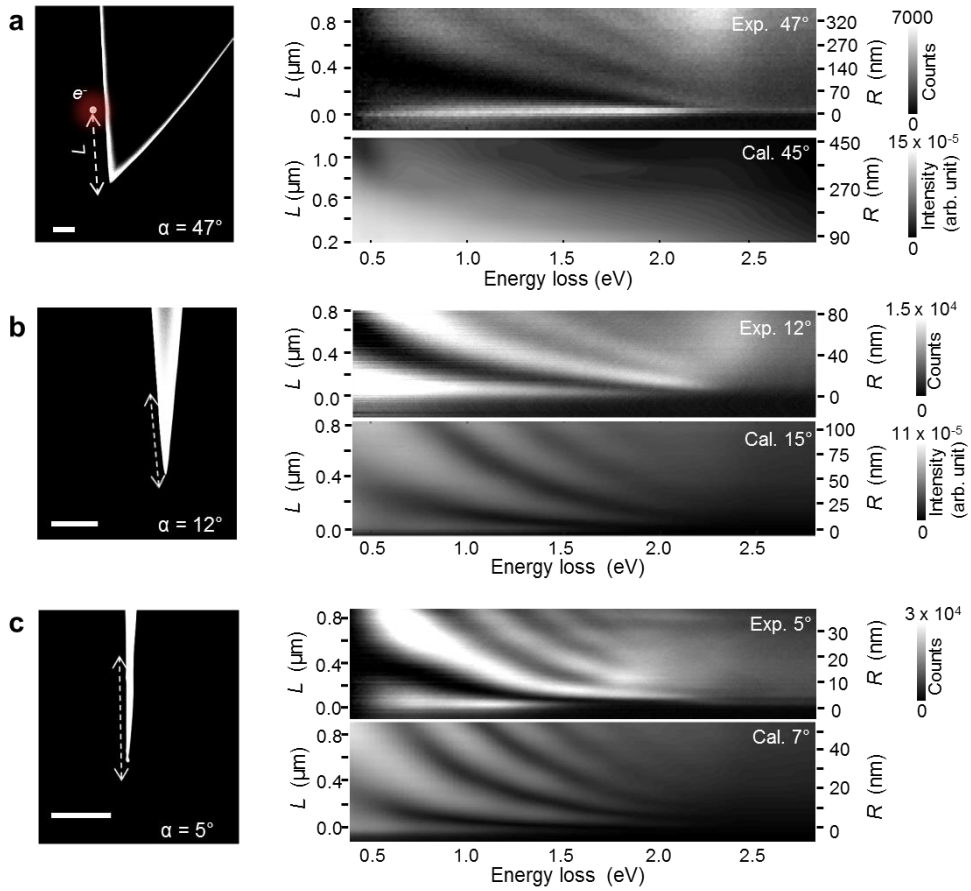

Figure 2. Dark-field imaging and spectroscopy of gold tapers with full opening angles of (a) 47°, (b) 12°, and (c) 5°, respectively. Both experimental and computed EELS are plotted as a function of impact location along the taper shaft and the corresponding local radius. Scale bar lengths are 500 nm. Adapted with kind permission from [4]. Copyright (2016) American Chemical Society.

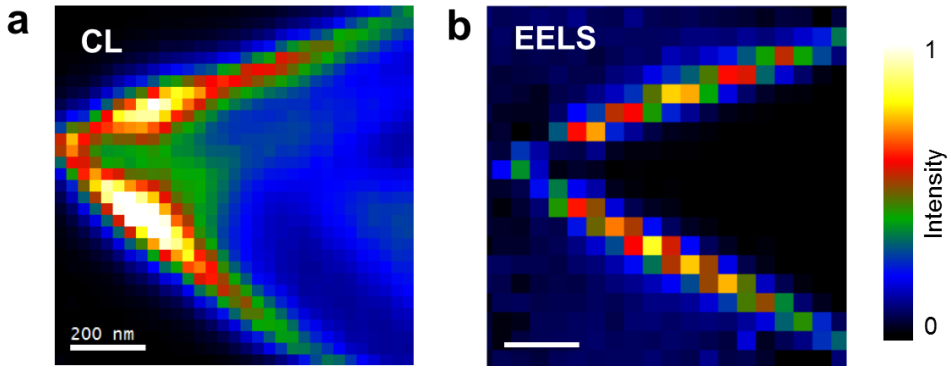

Figure 3. (a) CL and (b) EELS images of a taper with an opening angle of 47° at the same energy loss of 1.91 eV. Scale bar lengths are 200 nm.

IM5.003
Influences of the CMR effect on energy loss signal

W. Wallisch[1], M. Stöger-Pollach[1,2], S. Löffler[1,2], E. Navickas[3]

[1]Technische Universität Wien, University Service Centre for TEM, Wien, Austria
[2]Technische Universität Wien, Institute of Solid State Physics, Wien, Austria
[3]Technische Universität Wien, Institute of Chemical Technologies and Analytics, Wien, Austria

wolfgang.wallisch@tuwien.ac.at

Introduction: Double perovskite oxides are promising in a wide spectrum of applications due to their structural, physical and electronic properties. In particular, the colossal magnetoresistance (CMR) of La_2CoMnO_6 (LCM) is a consequence of a metal-insulator transition [1]. It describes the change of the resistance in the presence of a magnetic field. These days, transmission electron microscopes (TEMs) equipped with energy filters are powerful tools. Their main advantage for probing band gaps is the high spatial resolution, limited primarily by the inelastic delocalization and the excitation of Čerenkov light [2].
The optical properties and band gaps show up in the low energy part of the electron energy loss spectrometry (EELS) spectrum and the technique called valence EELS (VEELS). The opportunity to detect energy loss magnetic chiral dichroism (EMCD) with high spatial resolution [3, 4] and chemical sensitivity [5] is an additional advantage of EELS.
Objectives: In our study, we show that the physical consequences of the CMR effect also influence the EELS signal. We are able to detect the change of the band structure in the low losses caused by the CMR effect and observe the magnetic behaviour of the material with chemical sensitivity by using EMCD. Different LCM thin film layers are investigated to ensure the reproducibility of our evaluation. To confirm the experimental results, we use density functional theory (DFT) calculations.
Material and Methods: The LCM thin film samples are prepared by pulsed laser deposition. The LCM layers are epitaxially grown on different substrates, $SrTiO_3$ and $LaAlO_3$. For the TEM analysis the preparation of the cross section specimens is done by focused ion beam milling. Analytical TEM investigations are performed by using two TECNAI TEMs.
We varied the magnetic field and the temperature, in order to study the influence of the CMR effect on the EELS spectrum. The band gaps and optical properties are detected in the low energy range of the energy loss spectrum by VEELS. The beam energy is set in the range from 20 keV to 200 keV. The magnetisation of the material is measured by EMCD, which allows a characterisation in the nanometre range. The experiments are performed in the classical scheme to achieve a three-beam diffraction geometry. By considering the theoretical aspects the experimental results are supported by DFT calculations using the WIEN2k [6] code.
Results: The 40 keV and the 200 keV spectra are shown at a temperature of 85 K in Fig. 1. A difference in the energy loss range of 1.5 eV to 4 eV is observed. Concerning the comparison of the 40 keV VEELS spectra at different temperatures (Fig. 2), an intensity variation is caused by the CMR effect and not by the Čerenkov effect. The chemical sensitivity of EMCD is shown in Fig. 3 and Fig. 4. The EMCD effect can be observed at the Co L-edge (779 eV) in the 85 K experiment, whereas the same edge at room temperature exhibits no EMCD effect.
Conclusion: The influences of the CMR effect on the band gap are detected by observing the double perovskite LCM and the element specific magnetisation by means of EELS. Consequently, EELS can be employed at least qualitatively to investigate electronic properties of CMR materials.

Acknowledgements
The authors kindly acknowledge financial support by the Austrian Science Fund (FWF, F4501-N16 and F4509-N16).

References:
[1] Mahato, R. N., et. al. (2010) Journal of Applied Physics, 107, 09D714.
[2] Stöger-Pollach, M. (2010) Micron, 41, 577-584.
[3] Schattschneider, P., et. al. (2006) Nature, 441, 486-488.
[4] Schattschneider, P., et. al. (2008) Physical Review B, 78, 104413.
[5] Ennen, I., et. al. (2012) Journal of Magnetism and Magnetic Materials, 324, 2723-2726.
[6] Blaha, P., et. al. (2001) WIEN2k.

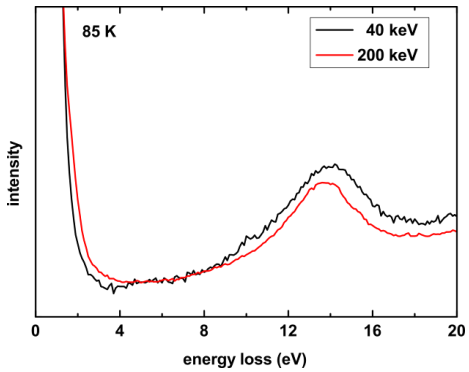

Figure 1. Unprocessed VEELS spectra recorded at 85 K using 40 keV and 200 keV.

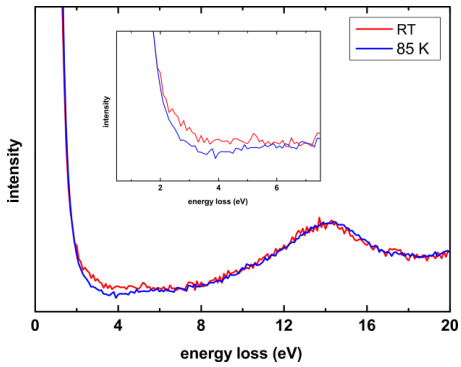

Figure 2. VEELS spectrum recorded at RT and 85 K using 40 keV. The insertion shows the difference between both spectra.

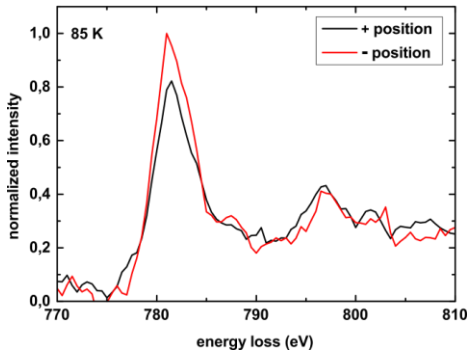

Figure 3. Normalised EELS spectra of the Co L-edge at 85 kV.

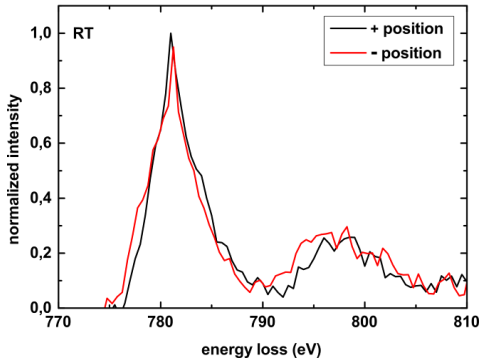

Figure 4. Normalised EELS spectra of the Co L-edge at RT.

IM5.004
Electronic structure properties of planar defects in oxygen deficient SrFeO3 thin films

P. Agrawal[1,2], M. D. Rossell[1], C. Hébert[3], D. Passerone[2], R. Erni[1]

[1]Empa, Swiss Federal Laboratories for Materials Science and Technology, Electron Microscopy, Dübendorf, Switzerland
[2]Empa, Swiss Federal Laboratories for Materials Science and Technology, Nanotech@surfaces laboratory, Dübendorf, Switzerland
[3]Ecole Polytechnique Fédérale de Lausanne, Interdisciplinary Centre for Electron Microscopy, Lausanne, Switzerland

piyush.agrawal@empa.ch

Perovskite-type ferrites with iron in a rather unusual high oxidation state 4+ reveal a variety of interesting electronic properties. SrFeO3 is one of them, showing high electrical conductivity, and could potentially be employed as electrodes in fuel cell1 systems containing other perovskite-like materials. SrFeO3 has been the subject of many investigations not only because it contains tetravalent iron but also due to the structural features displayed by its oxygen deficient phases2. These oxygen-deficient Fe-based perovskites exhibit a wide variety of structural and physical properties depending on their oxygen vacancy concentration.

In this study, planar defects in SrFeO3 thin films grown on SrTiO3 substrates1 are investigated using a combined experimental and theoretical strategy based on high-angle annular dark-field (HAADF) and annular bright-field scanning transmission electron microscopy (ABF- STEM), atomic-resolution electron energy loss spectroscopy (EELS) and atomistic simulations. Fig 1 shows a HAADF-STEM image of ordered planar defects in this material and a comparison of the oxygen *K* edge EEL spectra obtained from different regions, *i.e.* the planar defects and the bulk SrFeO3. Planar defects were modelled based on the STEM images and different oxygen vacancy concentrations were included for first-principles calculations. With focus on the oxygen *K*- and the iron *L*-edges an initial set of calculations were performed on these models using the WIEN2k code3. Comparison of the calculated EELS with experimentally recorded spectra was critical to validate the model with the corresponding vacancy concentration. The density of states and valence band structure were analyzed for both the bulk and the defect structure. This combined theoretical and experimental approach allows for developing an understanding about the site coordination of oxygen in these defects and their hybridization with the Fe atoms, which is crucial for the functional properties of these transition metal oxides.

The comparison of the experimental spectrum with the calculated EELS allows shedding atomistic insight into the EELS peak structure. In particular, it is possible to explain to which extent a particular defect in a bulk material locally affects its electronic properties, thus enhancing the power of electron energy-loss spectroscopy in the high-resolution description of complex materials. Also, a deeper understanding of these defects will offer new routes to regulate the materials properties and enhance their applications.

References:

[1] Solís, C.; Rossell, M. D.; Garcia, G.; Figueras, A.; Van Tendeloo, G.; Santiso, J. Microstructure and High Temperature Transport Properties of High Quality Epitaxial SrFeO3 − δ Films. *Solid State Ion.* **2008**, *179* (35–36), 1996–1999.

[2] Hirai, K.; Kan, D.; Ichikawa, N.; Mibu, K.; Yoda, Y.; Andreeva, M.; Shimakawa, Y. Strain-Induced Significant Increase in Metal-Insulator Transition Temperature in Oxygen-Deficient Fe Oxide Epitaxial Thin Films. *Sci. Rep.* **2015**, *5*, 7894.

[3] Blaha, P.; Schwarz, K.; Madsen, G. K. H.; Kvasnicka, D.; Luitz, J. *WIEN2K, An Augmented Plane Wave + Local Orbitals Program for Calculating Crystal Properties*; Karlheinz Schwarz, Techn. Universität Wien, Austria: Wien, Austria, **2001**.

Acknowledgments

This work was supported by the Swiss National Science Foundation (project no. 200021_147105)

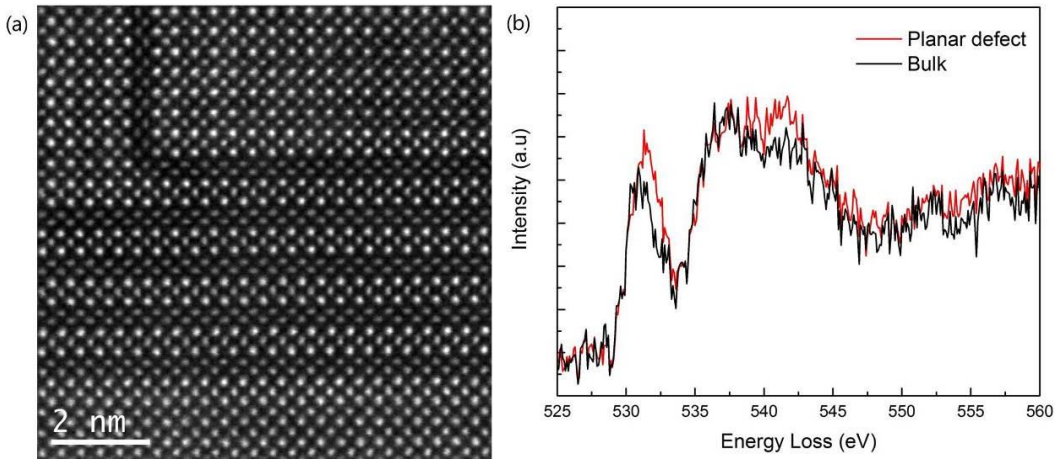

Figure 1. (a) HAADF+STEM image of planar defects within a SrFeO3 thin film grown on a SrTiO3 substrate. (b) Oxygen *K* edge EEL spectra for obtained at the planar defects and the SrFeO3 bulk (*i.e.* far from the defects).

IM5.005
Ultrahigh resolution of electron energy loss spectroscopy by a conventional monochromated TEM – towards challenging nanomaterials characterization

S. Lopatin[1], W. T. Liu[1,2], B. Cheng[1], M. L. Tsai[2], J. H. He[1], A. Chuvilin[3,4]

[1]KAUST, Core Lab, Thuwal, Saudi Arabia
[2]National Tsing Hua University, Hsinchu, Taiwan
[3]CIC nanoGUNE Consolider, San Sebastian, Spain
[4]IKERBASQUE, Bilbao, Spain

sergei.lopatin@kaust.edu.sa

Electron Energy Loss Spectroscopy (EELS) applied in TEM is a powerful analytical technique for the characterization of modern nano-materials. The majority of monochromated TEMs has the energy resolution in the range of 150-200meV. However, for a considerable number of scientific challenges the key characteristic features of EELS require the resolution better than 50meV. Among those are the vibrational spectroscopy for organic materials and the detection of hydrogen [1], measurement of phonons distribution or bandgap states with high spatial resolution [2], and study of Van der Waals (vdW) materials [3].

A recent progress in EELS-TEM systems performance is mainly associated with specialized systems (UHV STEM plus a monochromator), with a regular energy resolution of about 10meV [1]. At the same time, it has been predicted that the original design of FEI"s monochromator could deliver a comparable energy resolution (16meV) subject to the availability of an adequate energy detection system [4].

The successful attempt to extend the capabilities of FEI"s monochromator is described in [3]. Here we report a detailed description of the optimization routine providing the ultimate energy resolution of general purpose TEM-EELS systems based on a monochromator and Gatan imaging filter. The optimized setup is tested both for HR-TEM imaging and spectroscopy applications. In TEM mode at 80kV the energy resolution of 40meV can be achieved with unprecedented beam current of 600pA. While usefully for EELS in case high spatial resolution is not required, such a monochromated beam also significantly reduces the effects of the chromatic aberration for HR-TEM imaging with Cs correctors. In STEM mode (80kV) our optimization routine resulted in the energy resolution of 30meV with a probe current ~ 40pA.

Our approach for achieving the ultrahigh energy resolution we applied for the investigation of electrical properties of ultrathin two-dimensional transition-metal dichalcogenides. These materials started to attract a significant interest due to their remarkable chemical and mechanical stability [5] and new physical properties through various quantum confinement effects [6]. The in-plane atomically sharp interfaces between a monolayer WSe_2 and MoS_2 films was studied. The conduction band onsets (Fig.1a) of these 2D materials can be reliably traced across the WSe_2/MoS_2 interface, allowing us to plot the bandgap distribution in the composite film (Fig.1b). Having significant beam current in TEM mode we utilized the ultrahigh energy resolution for the momentum-transfer (q) resolved EEL spectroscopy. For a monolayer WSe_2 film the analysis of the conduction band onsets variation with the momentum-transfer (Fig.1c) should allow to verify the direct bandgap of that 2D material.

The measurement of surface plasmons distribution in various nanomaterials (order of magnitude smaller energy losses) is another application for ultrahigh energy resolution. The plasmons even with the energy ~ 100meV can be reliably detected and visualized (Fig.1d).

The estimated number of monochromated FEI"s TEMs currently available at different research facilities is considerably higher than 100 and up until now they not are exploited to the full power. Thus, we believe our results of EELS-TEM systems optimization might be useful for the scientific community.

[1] O Krivanek et al, Nature **514** (2014), p.209.
[2] W Bowman et al, Ultramicroscopy 167 (2016), p.5.
[3] A Govyadinov *et al*, Nature Comm, in press (2017)
[4] P Tiemeijer, Inst. Phys. Conf. Ser. Vol. 161. (1999) p.191
[5] J Coleman *et al.*, Science 331 (2011) p.568
[6] K Mak *et al.*,Phys. Rev.Lett. 105, 136805 (2010)

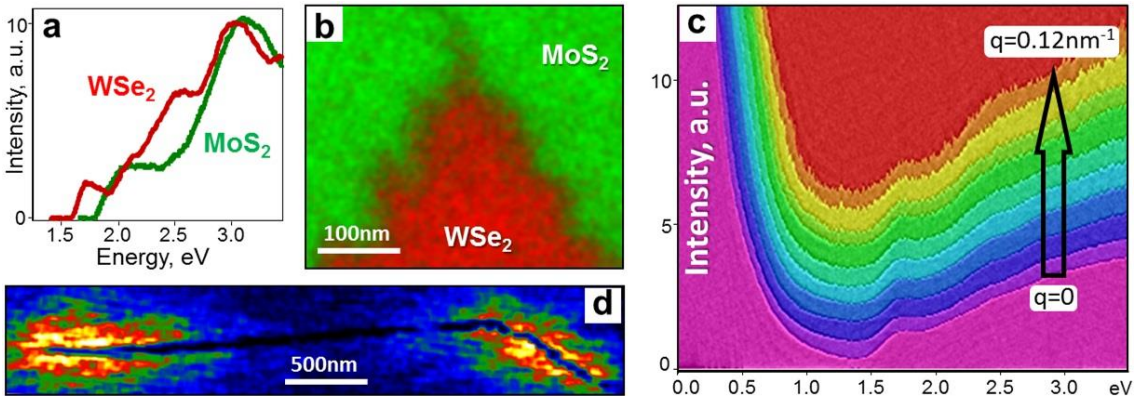

Figure 1. a Valence-loss spectra from a monolayer WSe_2 (red) and MoS_2 (green) after ZLP subtraction. b EELS mapping of WSe_2/MoS_2 interface based on EELS features in a**.** c Momentum-transfer resolved EELS of the conduction band onset in a monolayer WSe_2. d First harmonic (110meV) plasmon map of Ag nanowire.

IM5.006
Spectroscopic electron tomography analysis of 3D interfacial nanostructures appearing in annealed Si rich SiC films

L. Xie[1], K. Jarolimek[2], R. A. C. M. M. Van Swaaij[2], K. Leifer[1]

[1]Uppsala University, Engineering Department, Uppsala, Sweden
[2]Delft University of Technology, Photovoltaic Materials and Devices, Delft, Netherlands

ling.xie@angstrom.uu.se

Insulating or semiconducting films containing Si nanoparticles (NPs), fabricated by thermal annealing have emerged as a highly absorbing layers for third-generation solar cells.[1] The interfacial nanostructure between the precipitated NPs and surrounding matrix has not been studied in all three dimensions with the nanometer resolution. In this work, a complete 3D characterization of the percolated Si and SiC nanostructures embedded in the SRSC film has been performed by using transmission electron microscopy (TEM) and electron energy-loss spectroscopy (EELS) related techniques. The 3D spectroscopic nanoscale study shows that decomposition processes in the SRSC generates a complex materials system. In the reconstructed tomograms, we observed the formation of a Si network structure and could localize the a-SiC as a 1-3 nm thick interfacial layer between the 3C-SiC and the Si regions. Using 3D spectroscopic analysis in the TEM the different components of the complex 3D system can be disentangled. The spectroscopic dataset has also enabled us to extract EELS spectra voxel by voxel from 3D volumes. Thus, the analysis of such a spectroscopic dataset can contribute to understand the structural evolution of these complex materials systems.

References:

[1] G. Conibeer, M. Green, E.-C. Cho, D. Koenig, Y.-H. Cho, T. Fangsuwannarak, G. Scardera, E. Pink, Y. Huang, T. Puzzer, S. Huang, D. Song, C. Flynn, S. Park, X. Hao and D. Mansfield, *Thin Solid Films*, 2008, **516**, 6748–6756.

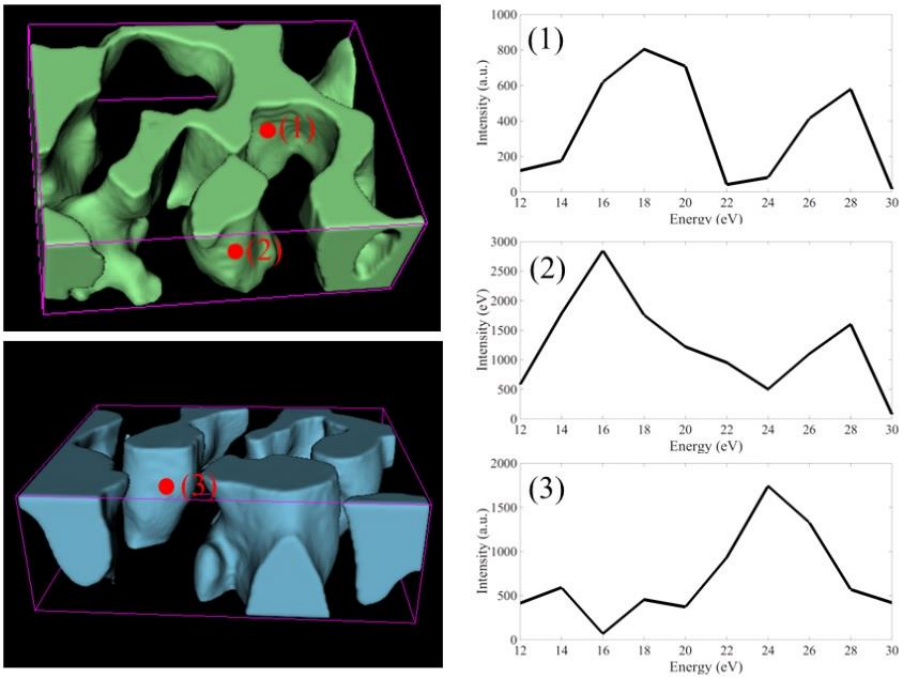

Figure 1

IM5.P001
Short-range ordering, electronic structure and morphological surface fetures of iron-based amorphous metal alloys

V. Artemyuk[1], V. Karbivskyy[1], L. Karbivska[1]

[1]NAS Ukraine, G.V. Kurdyumov Institute for Metal Physics , Kiev, Ukraine

artemyukviktor@ukr.net

Using scanning tunneling microscopy, atomic resolution, tunneling spectroscopy, XPS and EXAFS spectroscopy were studied the effect of processes occurring at different stages of crystallization on the morphological features of the surface and electronic structure of iron-based amorphous metal alloys (AMA).

In this work we represent results of morphological changes of the iron-based AMA surface during structural relaxation after annealing of amorphous tapes in the temperature range from 250 °*C* to 700 °*C*. Nonmonotonic dependence of surface subroughness over annealing temperature of AMA at range from RT to 700 °*C* was established. At 500 °*C* the formation of regular shape nanostructures with the form of rods was observed.

For initial samples the presence of significant oxidized surface layer with depth up to 150 *nm* was shown. During doping of amorphous Fe-B system by metalloid its surface segregation was observed. During process of thermalinduced structural relaxation, a higher redistribution of boron atoms in contrast with Fe and Si atoms was found. Carbon at the surface of the studied AMA mainly occurs at oxidized state, while in the volume it forms compounds with silicon.

The tunneling spectroscopy method revealed areas with low conductivity, which is typical for the formation of nanophase Fe-Si and Fe-B. There are substantial heterogeneities of the electronic density of states at the intercluster boundaries, indicating on their complex organization. The Fermi level of the alloys is located in a local minimum of the electronic density of states, which meets the criterion of Nagel-Tauc for formation of the amorphous state.

After complete crystallization at 700 °*C* the terraced structures were observed forming of substantially flat planes of more than 200 *nm* size. Increasing the content of Co atoms in the AMA Fe-Co-B system according EXAFS-studies, leads to decreasing in the radius of the first coordination sphere of a boron atom, reduction of the unit cell volume in the crystalline alloy (Co, Fe)3B, which indicates at amplification of bond of the transition metal with boron. The results obtained by the EXAFS-spectroscopy for amorphous Fe-Co-B and Fe-Cr-B systems are well interpreted in terms of the cluster microinhomogeneous model of AMA structure.

IM5.P002
STEM SI Warp – a digital micrograph script tool for warping the image distortions of atomically resolved spectrum image

Y. Wang[1], U. Salzberger[1], V. Srot[1], W. Sigle[1], P. A. van Aken[1]

[1]Max Planck Institute for Solid State Research, Stuttgart Center for Electron Microscopy, Stuttgart, Germany

y.wang@fkf.mpg.de

Besides conventional imaging techniques, an important capability of modern scanning transmission electron microscopy (STEM) is its integration with microanalysis techniques, such as electron energy loss spectroscopy (EELS) and energy dispersive X-ray spectroscopy (EDXS). In these methods, a focused electron probe raster across the sample and at each probe position imaging signal (s) (ADF or HAADF) and analytical signal(s) can be acquired simultaneously. The marked progress of the instrumentation hardware, i.e., aberration correctors, monochromators, better detectors /cameras, and more stable electron optics, sample holder and instrument environments, has made the chemical analysis at atomic resolution readily possible nowadays. Generally, STEM EELS and EDXS require much higher electron dose and longer dwell time (pixel exposure time) than STEM imaging. As a consequence, the scanning distortion becomes more serious in spectrum imaging. In case of lower-magnification spectrum mapping, these instabilities may be negligible, but at atomic resolution level, instabilities combined with long dwell times may create substantial image distortions, i.e. expansion, compression, and/or shearing of the lattice, that limit the interpretability of the spectrum image.
In this contribution, we report the development of a software tool, written in Digital Micrograph scripting language [1, 2], to post correct the image distortions of atomically resolved spectrum images. It can be used to correct two typical image distortions, i.e., linear (Fig. 1a) and nonlinear (Fig. 1b) distortions, as shown in Fig. 1. Two methods have been implemented to correct these distortions, pure pixel shift (i) without and (ii) with bilinear interpolation. Bilinear interpolation [3] considers the closest 2x2 neighborhood of known pixel values surrounding the unknown pixel. It then takes a weighted average of these 4 pixels to arrive at its final interpolated value. The weight on each of the 4 pixel values is based on the computed pixels distance from each of the known points. With the prior knowledge of the crystal structure, the diagnosis of the image distortions was performed on the simultaneously acquired ADF. Then, the correction of image distortions was applied to ADF, SI and/or elemental maps. Using two practical examples, i.e., 2-dimensional Ba doped La2CuO4 [4, 5] and SrTiO3 bulk material, we demonstrate that the script could correct the image distortions and warp the deformed SI, finally resulting in a refined color elemental map.
The plugin was composited by several scripts: scripts for linear and nonlinear warping, scripts for synchronizing the ROI between the images and for cropping the ROI as new image, and a script for filtering the final color map. This plugin is available by request to the authors [6].

References:
[1] B Schaffer in Transmission Electron Microscopy, Diffraction, Imaging, and Spectrometry ed. C.B. Carter and D.B.Williams, (Springer, Switzerland), Chapter 6, p.167.
[2] D R G Mitchell, B Schaffer, Ultramicroscopy **103** (2005), p.319.
[3] https://en.wikipedia.org/wiki/Bilinear_interpolation [Accessed 24January2017]
[4] Y Wang *et al*., ACS Appl.Mater.Interfaces **8** (2016), p.6763.
[5] F Baiutti *et al*., ACS Appl.Mater.Interfaces **8** (2016), p.27368.
[6] The research leading to these results has received funding from the European Union Seventh Framework Program under Grant Agreement 312483-ESTEEM2 (Integrated Infrastructure Initiative I3).

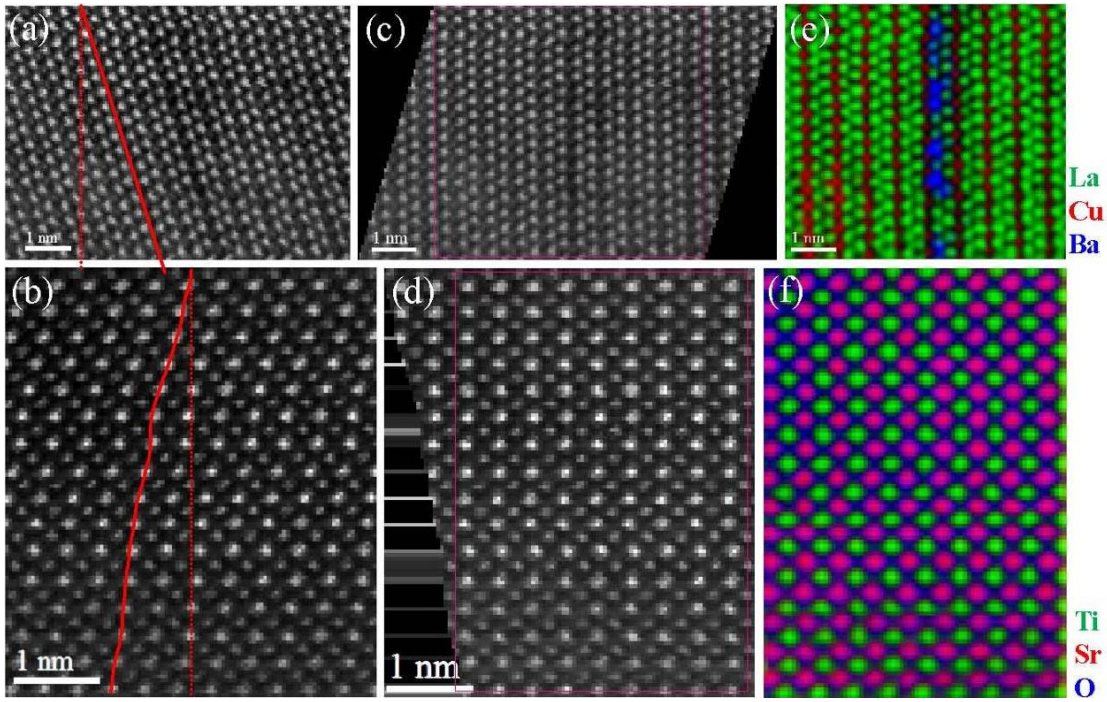

Figure 1. Typical image distortions in spectrum imaging: (a) linear and (b) nonlinear distortions. As can be seen the straight lattice (indicated by the dotted lines) has been distorted into an inclined or curved line. (c) Linear image distortion removed ADF image, the raw ADF image is shown in Fig. a. (d) Nonlinear image distortion removed image, the raw ADF image is shown in Fig. b. (e) Final warped and cropped RGB color figure of the Overlaid elemental maps, Cu-L2,3(Red), La-M4,5 (Green), and Ba-M4,5 (Blue). (f) Final warped and cropped RGB color figure of the overlaid elemental maps, Sr-L2,3 (Red), Ti-L2,3 (Green), and O-K (Blue). The STEM-EELS experiments were performed on a JEOL JEM-ARM 200CF microscope with Gatan GIF Quantum ERS electron energy-loss spectrometer operated at 200kV. A collection semi-angle of 111 mrad and 5 ms dwell time were used for the EELS acquisition. The SIs was de-noised by the multivariate weighted principal component analysis.

IM5.P003
Ni and Al elemental distribution in Ni-rich layered oxide Li-Ion cathodes by atomic resolution X-ray EDS analysis

P. Mukherjee[1], P. Lu[2], N. Faenza[3], N. Pereira[3], G. Amatucci[3], F. Cosandey[1]

[1]Rutgers University, Materials Science, Piscataway, NJ, United States of America
[2]Sandia National Laboratory, Albuquerque, NM, United States of America
[3]Rutgers University, Energy Storage Research Group, North Brunswick, NJ, United States of America

fred.cosandey@gmail.com

Ni-rich $LiNi_{0.8}Co_{0.15}Al_{0.05}O_2$, (NCA), is one of the highest capacity cathode materials currently being used commercially [1]. It has long been argued that Al plays a critical role in structural stability of NCA, but the exact manner in which Al stabilizes the structure is not known yet. The low concentration of Al in NCA makes quantitative analysis difficult. In this work, we are studying the distribution of Al by X-ray energy-dispersive spectroscopy (EDS) at both nanometer and atomic levels in a series of compounds starting with $LiAlO_2$ (LAO), $LiNi_{0.8}Al_{0.2}O_2$ (LNA), and $LiNi_{0.8}Co_{0.15}Al_{0.05}O_2$ (NCA). This study includes pristine condition as well as electrochemically stressed at a high voltage of 4.75V with LiPF6 and LiBF4 electrolytes.

Atomic resolution EDS measurements were performed in a FEI TitanTM G2 80-200 STEM with a Cs probe corrector at Sandia National Laboratories. Nanometer resolution X-ray EDS mapping and STEM imaging were performed at Brookhaven National Laboratory in a FEI Talos microscope. Both microscopes were fitted with four super EDS Bruker detectors.

The Al composition as a function of distance from the edge of the particle is shown in Figure 1 for (a) pristine NCA and for electrochemically stressed NCA at 4.75V and 60^{o}C for 10 hrs with (b) $LiPF_6$ and (c) $LiBF_4$ electrolytes. In all cases there is Al enrichment at the surface. For pristine NCA the Al enrichment decreases to an Al composition about 4.5% below the surface. However, at 4.75V, the Al composition decreases to 2.5 and 3 at% Al for $LiPF_6$ and $LiBF_4$ respectively. So, under chemically stressed conditions, some Al has dissolved from the electrode. This kind of preferential distribution of Al is also observed in pristine $LiNi_{0.8}Al_{0.2}O_2$ (Figure 1d). The Al is distributed preferentially at the corners and some facets of the particle. The core of the particle remains essentially Al deficient. The atomic resolution HAADF STEM image of one such particle is shown in Figure 2a. The layered LNA compound is electron beam sensitive and in order to obtain sufficient X-ray counts for obtaining atomic resolution EDS maps, a summation of all unit cell within the map has been performed as described previously [2]. The averaged HAADF STEM image is shown in Figure 2b with the corresponding atomic-scale EDS maps for (c) O-K, (d) Ni-K and (e) Al-K. It can be seen that Ni and Al occupy the same octahedral sites. The X-ray intensity profiles for Ni and Al are shown in Figure 2f. For Ni, the intensity profile is sharp while some broadening in the Al position is observed which could be due to smaller Al-O distance for some Al positions as compared to Ni-O distance. After the second EDS map from the same region, some Ni atoms have migrated (induced by the electron beam) to the Li layer position as revealed by the small peak between the Ni positions [3].

References:

[1] Sallis S.*et.al*. Applied Physics Letters 2016, 108, 263902.
[2] Lu, P. *et.al,* Nano Lett. 2016, 16, 2728−2733.
[3] The funding for this work is provided by NECCESS, an Energy Frontier Research Center funded by the U.S. Department of Energy, Office of Science, Office of Basic Energy Sciences under Award Number DE-SC0001294. This research used resources of the Center for Functional Nanomaterials, which is a U.S. DOE Office of Science Facility, at Brookhaven National Laboratory under Contract No. DE-SC0012704. Sandia National Laboratories is a multi-program laboratory managed and operated by Sandia Corporation, a wholly owned subsidiary of Lockheed Martin Corporation, for the US Department of Energys National Nuclear Security Administration under contract DE-AC04-94AL85000.

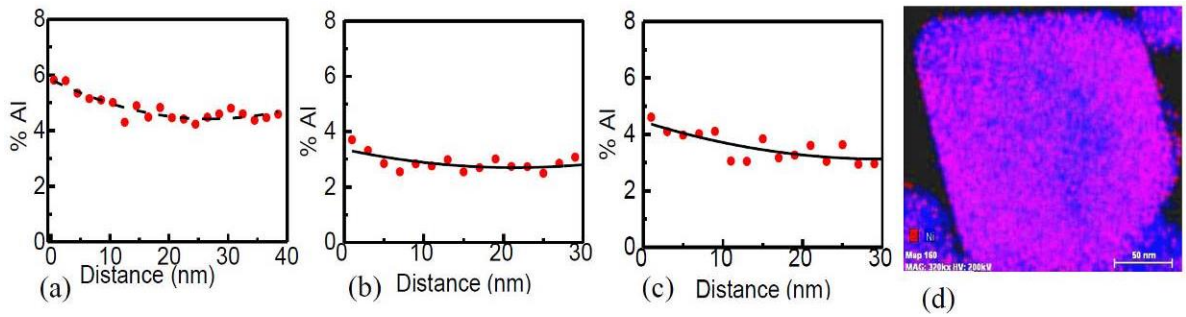

Figure 1. (a-c) Variation of Al content in NCA as a function of distance from the edge of (a) NCA pristine, (b) NCA held for 10 hrs at 4.75 V in LiPF6 electrolyte and (c) NCA held for 10 hrs at 4.75 V in LiBF4 electrolyte. (d) Quantitative X-ray EDS map in pristine LNA showing Al enrichment at the surface. (Red represents Al and blue represents Ni).

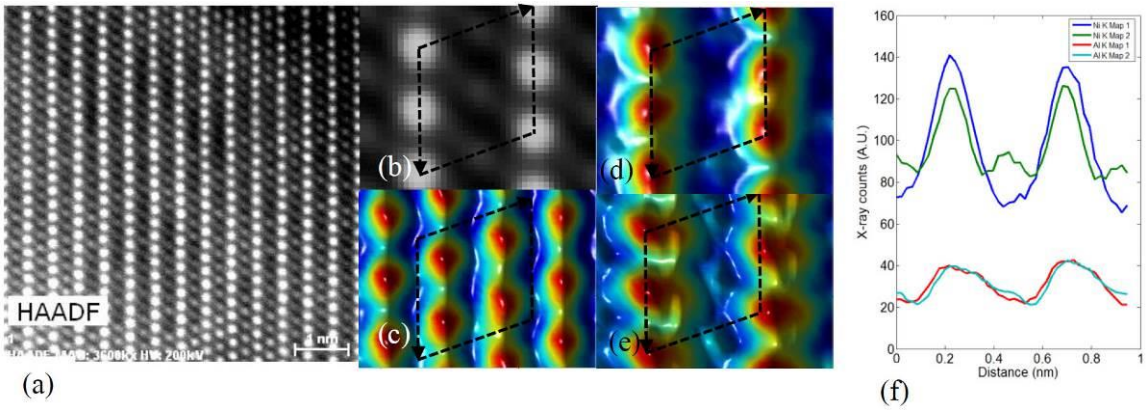

Figure 2. (a) HAADF-STEM image of LNA with (b) unit cell averaged STEM image and corresponding atomic resolution X-ray EDS maps of (c) O-K, (d) Ni-K and (e) Al-K and in (f) the intensity profile of Ni-K and Al-K after first and second scan map.

IM5.P004
Quantitative experimental determination of site-specific magnetic structures and magnetization curve by transmitted electrons

X. Zhong[1], Z. Wang[1], H. Jiang[1], D. Pohl[2], V. Neu[2], R. Yu[1], Q. Zhan[3], H. Piao[4], J. Zhu[1], B. Rellinghaus[2]

[1]Tsinghua University, Beijing, China
[2]IFW Dresden, Institute for Metallic Materials, Dresden, Germany
[3]University of Science and Technology Beijing, Department of Material Physics and Chemistry, Beijing, China
[4]China Three Gorges University, College of Science, Yichang, China

xyzhong@mail.tsinghua.edu.cn

Introduction: With the development of nanostructured magnetic materials and devices, the detection of magnetic information on the nanometer scale has increasingly become a major challenge. Electron Energy-loss Magnetic Chiral Dichroism (EMCD) technique is invented as a new route for detecting magnetic signals in a transmission electron microscope [1]. Compared with X-ray magnetic circular dichroism (XMCD), EMCD can easily achieve a higher spatial resolution down to the nanoscale [2,3].
Objectives: Using our newly-developed site-specific EMCD [3] method based on traditional EMCD, our goal is to achieve the measurement of magnetic structure and magnetization curve in magnetic materials at a nanometer scale.
Materials and Methods: We developed site-specific EMCD method, and first experimentally demonstrate that the use of transmitted electrons allows us to quantitatively determine atomic site-specific magnetic structure information on a nanometer scale. In this work, the sample on which we have applied our method is one NiFe2O4 nanograin in a hetero-epitaxial composite thin film formed by perovskite BiFeO3 and spinel NiFe2O4, which was grown on (001) SrTiO3 single-crystal substrate. From one NiFe2O4 nanograin in composite films, we extract its atomic site-specific magnetic circular dichroism spectra and achieve the quantitative magnetic structure information by constructively selecting the specific dynamical diffraction conditions in the experiments.
Results: We can reach a high spatial resolution, and get site-specific and element-specific magnetic information, as well as distinguish the orbital and spin magnetic moments. For example, we determined mL/mS ratios of Fe atoms in octahedral and tetrahedral sites. We have further measured the magnetization curve of both iron and nickel atoms. The magnetization data is shown to be in very good agreement with a simulated magnetization curve, which is calculated by micromagnetic simulation. The simulation took the structural details of the nanograin into account, thereby confirming the reliability of our method.
Conclusion: Our work of the determination of magnetic structures site-specifically opens a door to meet the challenge of exploring the magnetic structures of magnetic materials at the nanoscale using transmitted electrons. Besides, in the case of measuring magnetization curve, abundant information about microstructures, such as exchange bias effect, can be obtained and better understood based on our measurement. Our method thus has the potential to bridge the magnetization behavior and atomic structures of magnetic materials.

References:
[1] P. Schattschneider et al., Nature 441 (2006) 486.
[2] J. Salafranca et al., Nano Lett. 12 (2012) 2499.
[3] Z. Q. Wang et al., Nat. Commun. 4 (2013) 1395.

IM5.P005
Increasing throughput in EDX spectroscopy with the new compact Rococo2 preamplifier detector system

A. Liebel[1], A. Schöning[1], R. Lackner[1], A. Bechteler[1], A. Niculae[1], H. Soltau[1]

[1]PNDetector GmbH, Munich, Germany

andreas.liebel@pndetector.de

Introduction: New challenges for Energy Dispersive X-ray spectroscopy (EDX) detectors are frequently generated in electron microscopy. An increasing number of applications in life science or the semiconductor market work with low primary beam energies and currents for nondestructive analysis. Other applications require a huge amount of X-Ray signal for their analysis in order to increase throughput and lower the measurement time and accordingly costs.
Objectives: For such applications it is vital to collect as much of the available signal as possible and to detect it with shortest possible processing times. The annular "Rococo2" Silicon Drift Detector (SDD) is the ideal candidate to achieve this and is presented here in a new and compact design.
Materials and Methods: This new "Rococo2" preamplifier module was built in order to simplify the integration of the system into any kind of electron microscope or similar instruments. It features a four-channel preamplifier subsequent to the detector chip in order to reduce parasitic influences, guaranteeing stable operation and best possible energy resolution. A drawing of the new "Rococo2" Detector System is shown in Figure 1. It can be positioned right below the pole piece (Figure 2) while the electron beam is guided through the center hole. This arrangement enables a very close proximity to the sample resulting in huge solid angles. The same setup can be equipped with different generations of the "Rococo2" sensor. Every sensor consists of four SDD cells arranged evenly around a center hole, all combined on one monolithic chip. The standard version uses 15 mm² SDD cells and achieves solid angles up to 1.4 sr [1]. The next generation of the "Rococo 2" SDD pushes the boundaries even further. The chip has four 19 mm² cells which, due to the further optimized geometry, enable solid angles up to 2.4 sr. Despite the large area, this detector still has an optimum energy resolution of 124 eV FWHM @ Mn-Kα and -20 °C sensor temperature.
Results: Most EDX detectors currently available on the market use SDD sensors with active areas between 10 mm² and 30 mm². This translates to solid angles of typically 0.01 sr to 0.05 sr. Compared to these numbers the Rococo 2 sensor can deliver a hundred times higher signal intensity and therefore reduce the measurement time significantly. This is shown in Figure 3 where two EDX mappings of a duplex brass sample were recorded using a round 10 mm² SDD and the Rococo2 detector at the same conditions and acquisition time.
Conclusion: We will present further results with the compact Rococo2 detector system demonstrating the large solid angle and its advantages in electron microscopy. The new system with integrated preamplifier simplifies the integration into various electron microscopes and makes this sensor type now more easily assessable for a much broader community.

References:
[1] A Niculae et al, Microscopy & Microanalysis, vol. 18 S2 (2012) p. 1202-1203

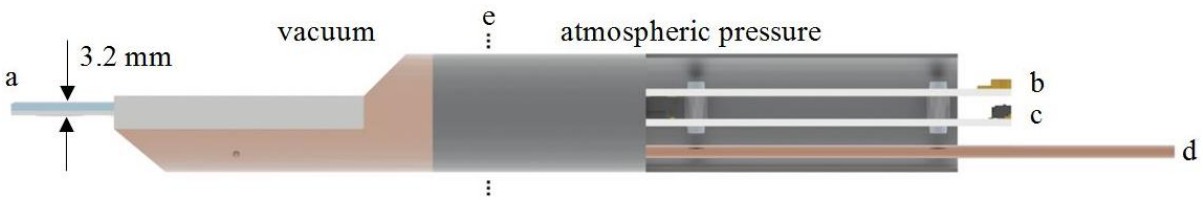

Figure 1. Schematic of the Rococo 2 Detector System, a) SDD on substrate, b) preamplifier signal output, c) supply voltages, d) water cooling connection, e) vacuum interface.

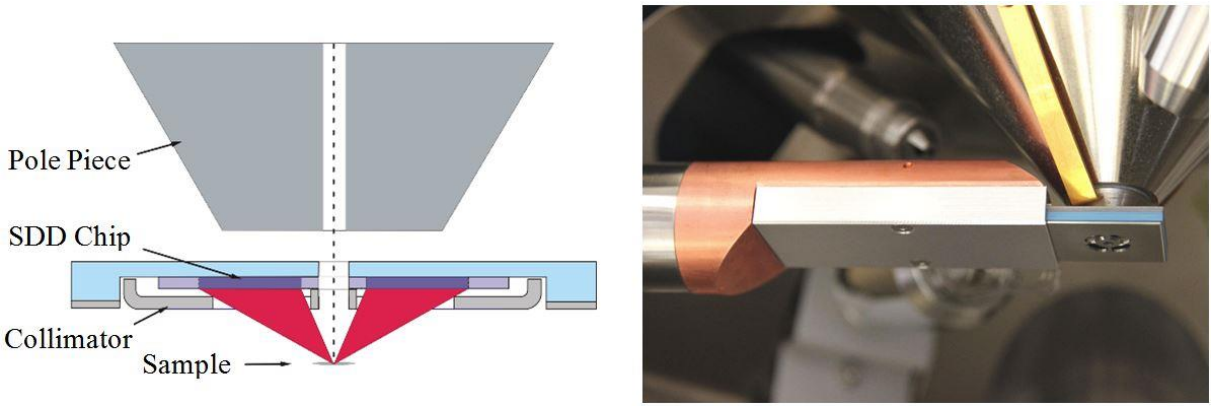

Figure 2. Schematic drawing of the Rococo EDX detector positioned below the pole pice (left). A picture of the detector system inside a SEM (right). Backscattered electrons are stopped within thin filter foils. By choosing the right filter materials light element performance with high energy resolution can be realized.

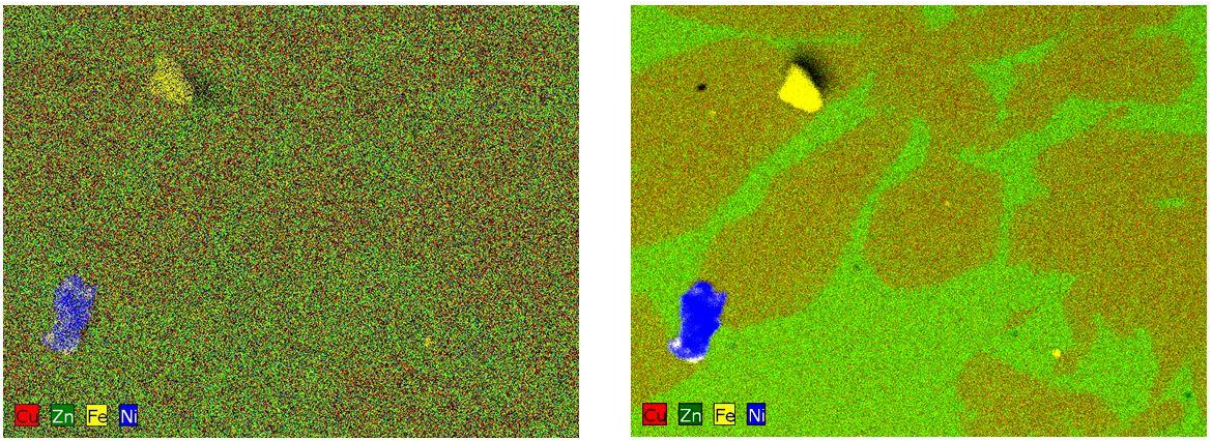

Figure 3. EDX Mapping of a duplex brass sample showing α and β phases with different concentrations of copper and zinc. The left image was obtained with a conventional 10 mm² SDD with approximately. 0.01 sr solid angle, the right one with the Rococo 2 detector with a solid angle of more than 1 sr at the same conditions and acquisition time. Images are shown without any post-editing.

IM5.P006
Detection and quantification capabilities of X-ray energy dispersive spectrometry data acquired using FEI G2 electronics processed in Velox 1.4

C. A. Wade[1,2], T. Withaar[2], M. Ovsyanko[2], B. Freitag[2], G. Burke[1]

[1]The University of Manchester, Materials Performance Centre, Manchester, United Kingdom
[2]Thermo Fisher Scientific, Materials & Structural Analysis, Eindhoven, Netherlands

austin.wade@manchester.ac.uk

The Talos F200A analytical scanning transmission electron microscope (STEM) with a high brightness X-FEG electron source and a SuperXTM X-ray energy dispersive spectrometry (XEDS) detection system at the University of Manchester has recently been equipped with the new Thermo Fisher G2 pulse processing electronics. Accompanying the hardware upgrade the Velox software for STEM image and XEDS data acquisition has been updated. This new Velox version incorporates a quantification engine for post processing of spectra and spectrum images along with the ability to record time resolved spectrum images to observe changes in composition that occurred during multi frame chemical mapping. Damage effects during mapping can be easily removed in post processing and more general dynamic behavior in chemistry can be studied using this capability. This study seeks to characterize the detection capabilities of the SuperX XEDS detection system in the FEI Talos F200A equipped with G2 electronics using the previously equipped G1 electronics and Bruker Esprit 1.9 software as a basis of comparison.

The detection capabilities of the SuperX with the G1 and G2 electronics were determined using spectra from a 52 nm thick NiOx thin film and the XUtils plug-in for DigitalMicrograph [1]. Figure 1 provides a comparison of energy resolution across alpha tilt values for the three available pulse processor settings of the G2 electronics with the best energy resolution acquisition setting of the G1 electronics. A marked improvement in energy resolution is achievable using the G2 electronics.

Quantification of the matrix and precipitates in additively manufactured (AM) Alloy 718 has been investigated using the two electronics and software configurations. These results are compared to previous STEM EDX experiments [2]. In Alloy 718 the nm-scale g² and g¢ precipitates, nominally Ni3Nb and Ni3Al, respectively, have complex compositions first revealed via atom probe field-ion microscopy analysis [2]. The presence of measurable Ti and Al in the g² precipitates, as well as the presence of Nb and Ti in the g¢ precipitates can now be directly measured in the analytical electron microscope (AEM) with SuperX XEDS configuration. Figure 2a shows a high-angle annular dark-field (HAADF) image of γ'' in the matrix, γ. The presence of γ'' is seen in the combined chemical map, Figure 2b, where the Al corresponds to γ'' forming on the sides of the γ''. The chemical distribution of major components of γ'' and γ'' are displayed in the elemental maps in Figure 3.

As each spectrum image (SI) is acquired in Velox 1.4 the data is tagged with the frame number, making each SI time resolved and allowing users to strip frames from the end of the dataset in post processing. Figure 4a and 4b show the quantification results as a function of frame number for select elements present in Alloy 718.

The Thermo Fisher G2 electronics significantly improve the achievable energy resolution of the SuperX XEDS detection system, reducing the minimum resolution from ~135 to 131 eV across all alpha tilt ranges. New functionalities introduced in Velox 1.4, namely XEDS quantification and time resolved SI allow for complete processing of XEDS data acquired via AEM, including the ability to remove beam damaged frames and assess compositional changes to samples that occur during SI acquisition. The new capabilities of chemical mapping are illustrated on Alloy 718.

References:

[1] M. Watanabe, *Microsc. Microanal.*, **16**, Suppl. 2, (2010), pp. 260-261
[2] M.G. Burke, and M. Miller, *Superalloys 718,* (1991), pp. 337-343.

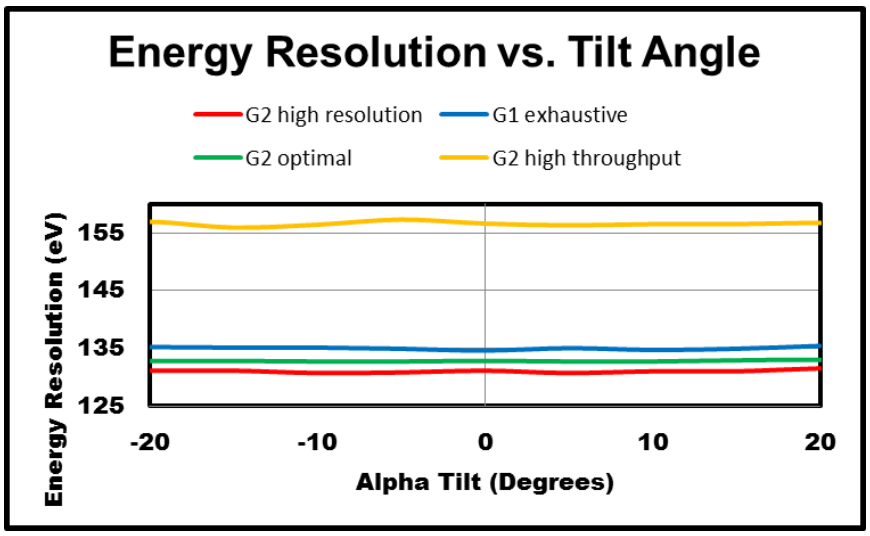

Figure 1. Energy resolution (FWHM of Mn Kα X-ray peak) calculated from a NiOx thin film as a function of alpha tilt for each G2 electronics pulse processor setting and the G1 electronics "exhaustive" setting.

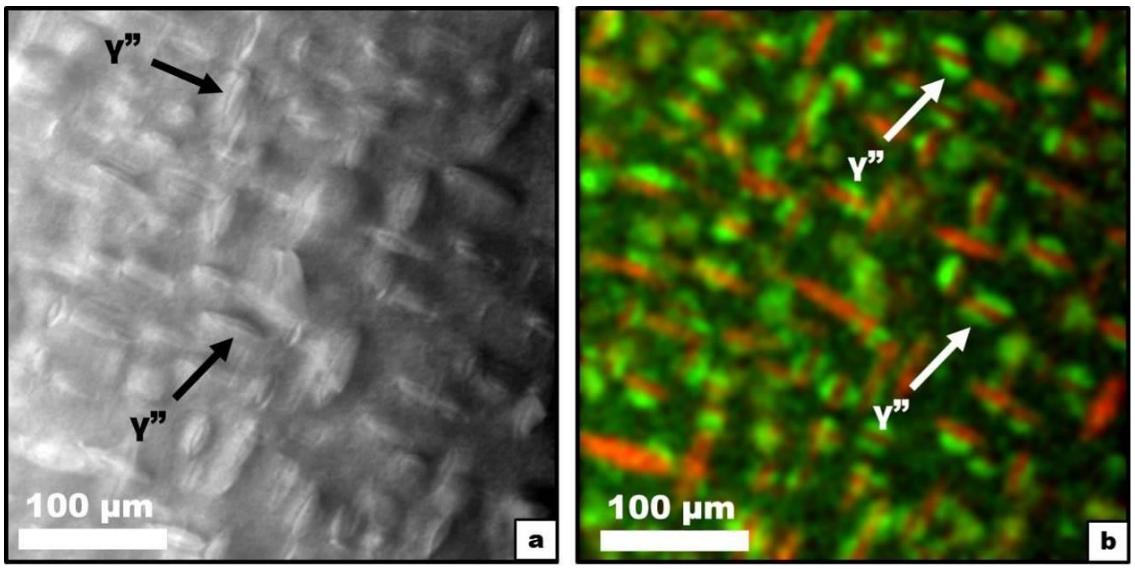

Figure 2. HAADF image of γ'' in γ (a) and a composite map of Al and Nb that marking the location of γ'' on γ'' (b).

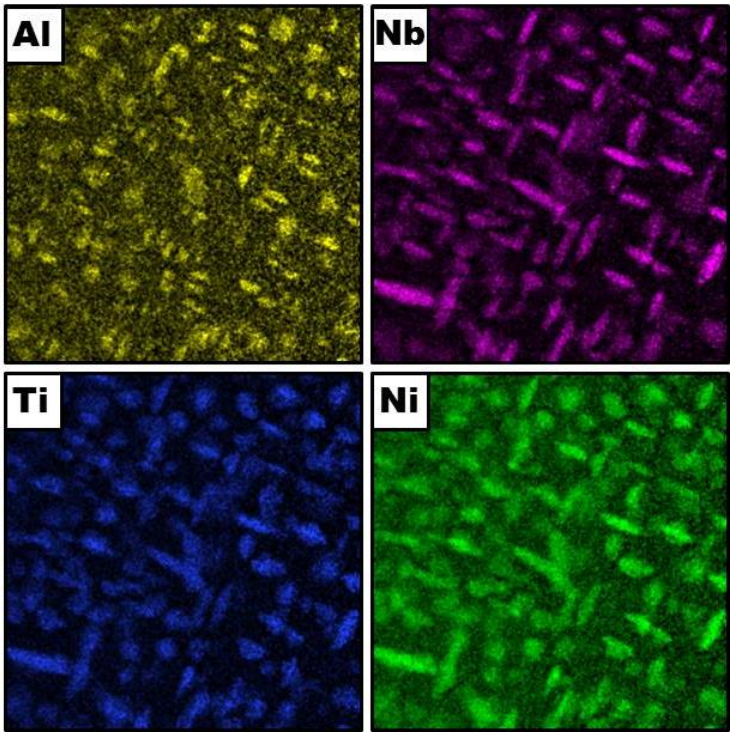

Figure 3. XEDS maps of the distribution of Al, Nb, Ti, and Ni in AM Alloy 718.

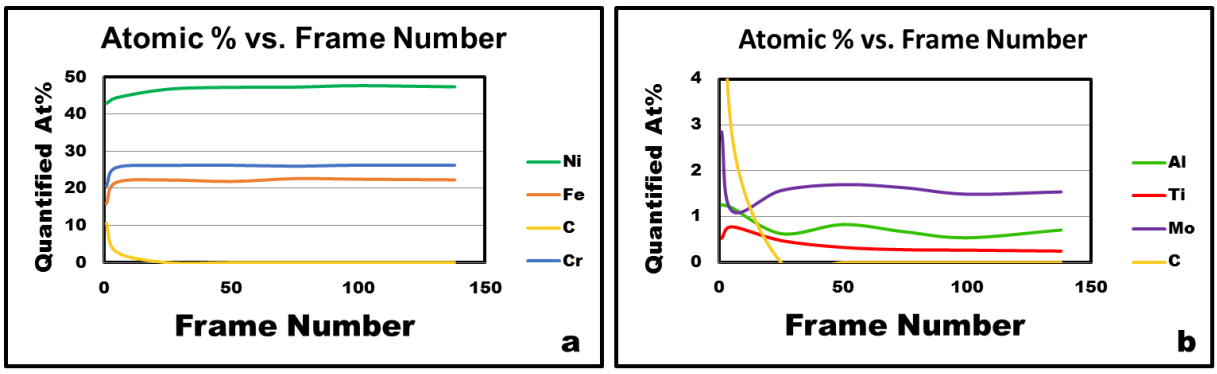

Figure 4. Quantified major (a) and minor (b) compositional components of the Alloy 718 matrix in Velox 1.4 at various stages throughout an SI acquisition by use of the frame removal too.

IM 6: Tomography

IM6.001 invited
Recent advances in limited data tomography

K. J. Batenburg[1], H. Kohr[1], Z. Zhong[1], X. Zhuge[1]

[1]Centrum Wiskunde & Informatica, Amsterdam, Netherlands

joost.batenburg@cwi.nl

Introduction: Over the past two decades, tomography has transformed from a technique that was mainly used in medical CT imaging into a broadly applicable tool. On the one hand, there has been a strong increase in the number of imaging modalities (various contrast generating mechanisms using X-rays, electrons, neutrons, etc.) that can be used to acquire tomographic projection images. On the other hand, the mathematical theory behind the computations that turn a series of 2D projections into a 3D image has advanced far beyond the original inverse Radon transform methods.
However, many of the novel imaging techniques and modalities result in datasets that are limited (e.g. limited number of projections, limited angular range, noisy data), resulting in strong challenges for the reconstruction algorithm.
Objectives: Here, we consider three different approaches for augmenting the collected data with additional information about the scanned object. The key objective is to improve the quality of the reconstructed images with respect to the actual object under investigation, and to do so in a reliable and robust way.
Materials and Methods: We consider the following approaches for integrating additional information into the tomographic reconstruction process:
Incorporation of prior knowledge on the discreteness of the sample. This is the domain of discrete tomography (DT). While algorithms for DT have been applied successfully in both electron tomography and X-ray tomography, the first generation of algorithms (e.g. the DART algorithm) was not very robust with respect to deviations from the perfect, linear imaging model. Recent advances, such as the TVR-DART algorithm, show strongly improved robustness and applicability.
Incorporation of additional measurements from a secondary modality In cases where it is difficult to define prior knowledge about the object itself, a second imaging modality can be used to improve the reconstruction quality of the primary modality. Here, we consider as an example a recent approach for combining HAADF-STEM and EDX imaging in electron microscopy.
Incorporation of adaptive prior knowledge, based on input of an application expert. Here, we consider the possibility of having an expert user indicate particular structures of interest (e.g. edges, interfaces), after which the reconstruction algorithm can incorporate such annotations.
Results: Results for each of the three approaches demonstrate that the incorporation of additional information about the object can indeed strongly improve the quality and fidelity of the reconstruction in different use cases.
Conclusion: The increasing number of strategies available for incorporating additional information about the object composes a toolbox for advanced imaging, where the goal is to utilize as much prior knowledge as possible, while at the same time ensuring that all assumed prior knowledge is justified, either based on additional measurements or on direct expert interpretation.

References:
[1] X. Zhuge, W.J. Palenstijn, K.J. Batenburg, TVR-DART: A More Robust Algorithm for Discrete Tomography from Limited Projection Data With Automate Gray Value Estimation, IEEE Trans. Image Processing, 25(1), 455-468, 2015
[2] X. Zhuge et al., Automated Discrete Electron Tomography: Towards routine high-fidelity reconstruction of nanomaterials
[3] Z. Zhong et al., A bimodal tomographic reconstruction technique combining EDS-STEM and HAADF-STEM, Ultramicroscopy, 174, 35-45, 2017
[4] H. Kohr, Total variation regularization with variable Lebesgue prior, arXiv:1702.08807 [math.NA]

IM6.002
Including atomicity as prior knowledge in atomic resolution HAADF-STEM tomography by means of compressed sensing

W. Van den Broek[1], A. Parvizi[1], C. T. Koch[1]

[1]Humboldt-Universität zu Berlin, Institut für Physik, Berlin, Germany

vandenbroek@physik.hu-berlin.de

Introduction: In the field of compressed sensing (CS) superior results have been proven attainable by including prior knowledge in the solution of underdetermined systems [1]. This usually means enforcing sparsity in a particular base, for instance the pixel, voxel or wavelet base.
Objectives: In this abstract we investigate the possible benefits of enforcing atomicity in atomic resolution HAADF-STEM tomography, i.e. if a voxel in the reconstuction is non-zero, it's neighborhood will be made more likely to consist of zeros.
Materials and Methods: The data set has been made available by Xu et al. [2] and consists of 62 projections of an etched W-tip taken over a 180° tilt range which have been aligned and their background removed. In [2] a reconstruction was made of such quality that 3767 atoms could be identified and their three-dimensional positions extracted. These were then used for strain analysis.
Here, the image formation is modeled as linear, i.e. the sought-after three-dimensional object x is written in long vector format and yields the projections y by multiplication with the projection matrix A. Following [3], the matrix A accounts for the atoms' spatial extent too, so that the solution x can be thought of as sparse in the voxel basis.
We developed an alternating directions augmented Lagrangian (ADAL) method [4] that solved the following minimization problem:
$\min \sum_k |z|_k \left([|z| \otimes B]_k \right)$ s.t. $z = x$ and $Ax \cong y$. (1)
Where $\otimes$ indicates a three-dimensional convolution. The first term in this expression minimizes atomicity in the sense that it enforces a pReference: for zeros in the environment B around z_k when z_k is non-zero.
This is contrasted to the more usual CS approach where the following system was solved with ADAL:
$\min \sum_k |z|_k$ s.t. $z = x$ and $Ax \cong y$. (2)
Results: In Fig. 1 the ADAL solution of Eq. (1) is shown on the right and that of Eq. (2) in the middle. In neither case noise seems to be a limiting factor. When atomicity is enforced atoms are clearly resolved all over the field of view. In the case of sparsity elongated artifacts are observed. For comparison, a multiplicative SIRT reconstruction is shown on the left.
Conclusions: The machinery of compressed sensing was used to enforce atomicity on the reconstruction of HAADF-STEM atomic resolution tomography. This gave rise to a solution with relatively little noise and with atoms more clearly resolved than in the more conventional case of enforced sparsity. [5]

References:
[1] R.G. Baraniuk, IEEE Signal Processing Magazine 4 (2007) 118-121.
[2] R. Xu et al., Nature Materials 14 (2015) 1099-1103.
[3] W. Van den Broek et al., Ultramicroscopy 109 (2009) 1485–1490.
[4] X. Jiang, et al., Opt. Express 24, 7006-7018 (2016).
[5] W.V.d.B. and C.T.K. acknowledge the DFG projects BR 5095/2-1 and KO 2911/7-1, respectively. The authors of [2] are acknowledged for the data set, and C.O. in particular for our discussions.

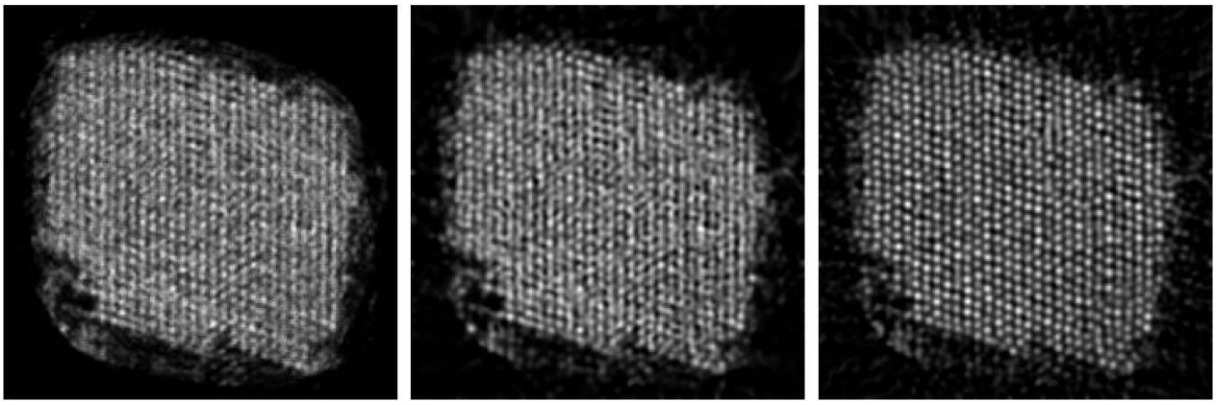

Figure 1. Slice of the reconstruction perpendicular to the tilt-axis; width: 10.1 nm. *Left*: SIRT, 512th iteration, 3x3 averaging is applied to suppres noise. *Middle*: Solution of Eq. (2) or enforced sparsity. *Right*: Solution of Eq. (1), enforced atomicity.

IM6.003
The Rytov approximation in electron holographic tomography – a computational proof-of-concept for atomically resolved electron tomography

J. Krehl[1], A. Lubk[1]

[1]IFW Dresden, Advanced Methods of Electron Microscopy, IFF, Dresden, Germany

j.krehl@ifw-dresden.de

Electron holography (EH) within the Transmission Electron Microscope (TEM) reconstructs an electron beam in amplitude and phase from suitable interference patterns. As a consequence of the electric and magnetic Aharonov-Bohm effect, the phase directly encodes information about the electric and magnetic potentials of the specimen . At high resolution studies the signal is chiefly produced by the phase shift due to the atoms' electric potential, which renders EH uniquely suited for quantitative investigations at high resolution.
The reconstructed wave function only offers a projected view of the three-dimensional specimen but with the depth-information gone. This information can be regained by tomographic techniques, where a series of recordings under different specimen orientations is used to uniquely invert the diffraction process to some extent. Commonly, the scattering process is modeled with the Phase Grating Approximation (PGA) which completely neglects the propagation of the scattered waves at the length scales of the specimen. This is a reasonable assumption for small scattering angles and facilitates a relatively straight-forward numerical implementation of the reconstruction algorithms.
At atomic resolution the significant scattering angles and the consequently relevant propagation effects, even at thin specimen, beget considerable artifacts in PGA based tomographic reconstructions [J. Krehl, A. Lubk, Ultramicroscopy 150, 2015]. Consequently, more elaborate scattering models are required in order to reconstruct atomic potentials in 3D. Here, we propose the use of the Rytov Approximation (RA), which basically assumes that the complex logarithm of the wave propagates similarly to a wave function, yielding an approximation that is linear in the scattering potential [J. Krehl, A. Lubk, submitted to PRB, 2017]. While the RA can be justified in a weak phase case the treatment of, inherently strong phase object, electron scattering is more complicated. From our work it seems, that the RA here reproduces propagation effects to a large extent without introducing meaningful artefacts. The circumstance that it yields a linear model is very advantageous since the inversion of linear models is quite well-understood in contrast to non-linear.
In order to test the fidelity of the tomographic reconstruction we simulated a full tilt series of a three-layered WS_2 nanotube (diameter: 10nm) with a custom wide-field-of-view multislice algorithm. The resulting waves were dampened by an envelope to a spatial resolution of about 1 Å at 200 keV and some Lenz model noise was added to provide a realistic reproduction of a tilt series, although issues of alignment have been omitted for now. This tilt series was reconstructed using the LSQR conjugate gradient algorithm to minimize the eucledian distance between the projected potential (with the projector implemented as a real-space convolution with a symmetry-reduced tensor) and the tilt series. In this example one Rytov-based iteration step takes about times as long as the standard PGA-based one.
The reconstructed potential shows a significantly improved quality, in that all atoms are clearly confined in separate peaks without any of the artefacts present in the PGA-based reconstruction, such as elongations and fusing of the peaks, streaks and inter-layer phantom peaks. In the amplitude, the behaviour of the PGA is more benign and closer to the RA, which may be owed to the much weaker signal but that also caues a much higher background noise for both methods.
In summary the Rytov approximation holdes surprisingly well for high-energy electron scattering and models propagation for the tested resolution of 1 Å and distances of some nanometers rather accurately. This allows a tomographic reconstruction of the electrostatic potential of ananotube at atomic resolution with much higher fidelity from wave functions reconstructed from a close-to-real hologram tilt series.

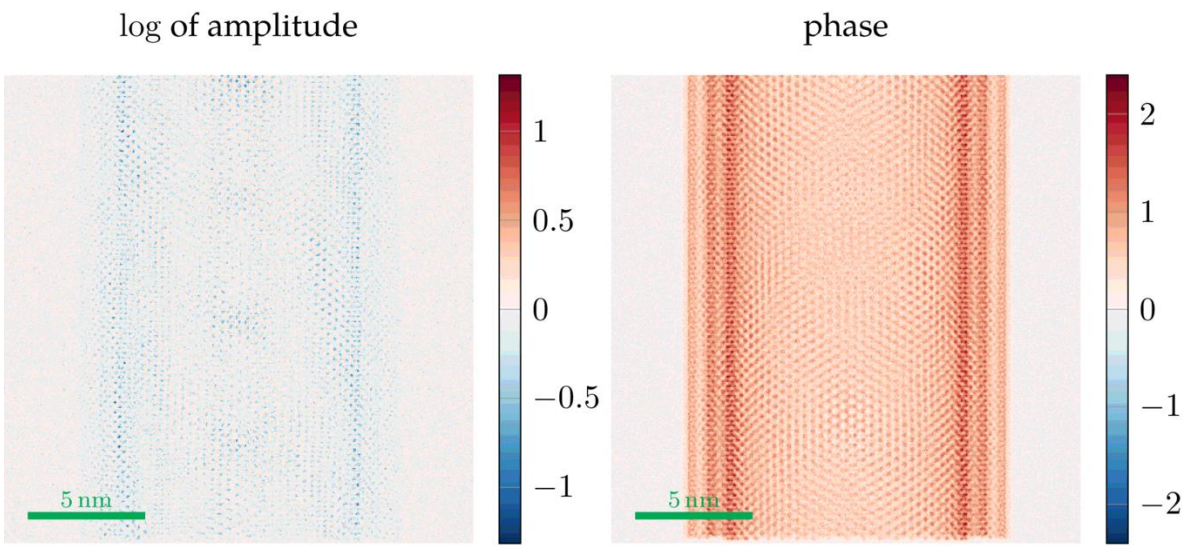

Figure 1. A simulated object-exit wave of the three-layer WS_2 nanotube using realistic envelopes and noise levels, refocussed into the center of the tube. The amplitude is shown on a logarithmic scale.

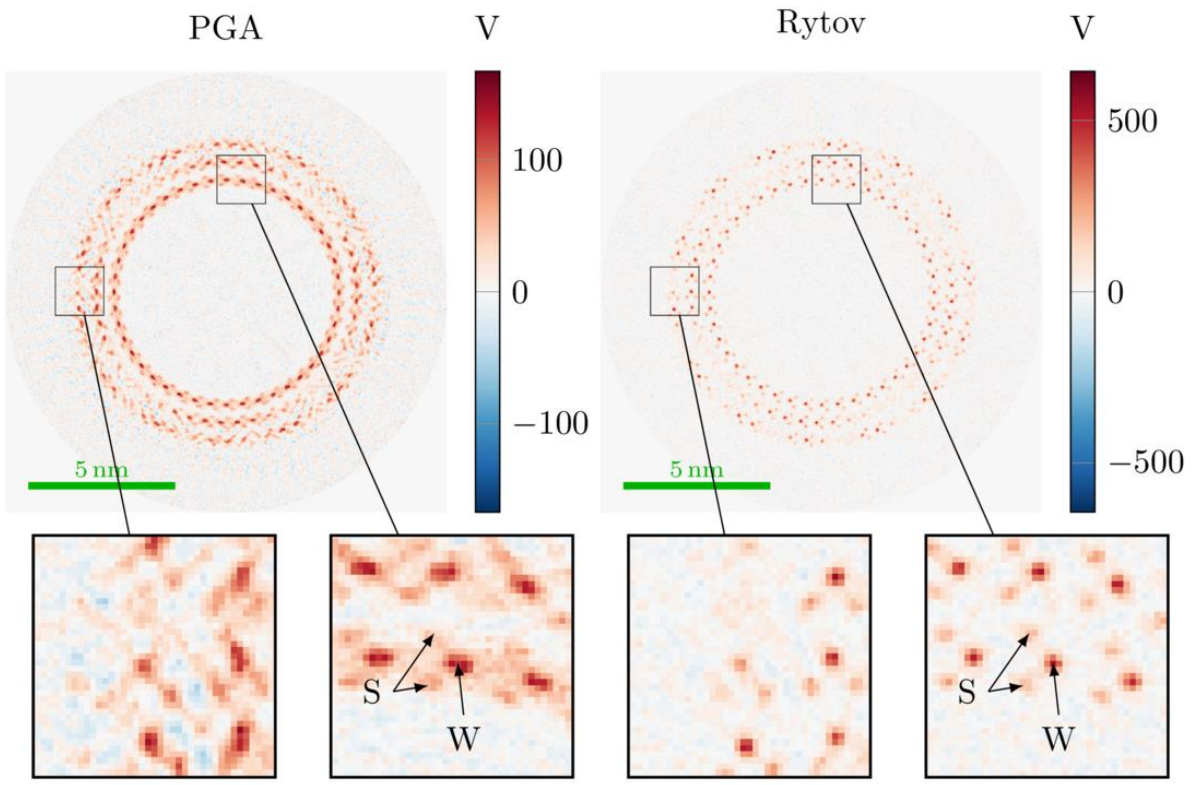

Figure 2. Comparison of the electric potential between reconstructions using the PGA and the RA of a noised tilt series simulated from a WS_2 nanotube. Due to the different chirality of the layers only the inner ring of tungsten atoms lie completely inside the depicted cross-section.

IM6.004
Quantitative 3D analysis of supported Pd/CMK-3 catalysts at the nanoscale

W. Wang[1,2], D. Wang[1,3], C. Kübel[1,3,4], A. Villa[5]

[1]Karlsruhe Institute of Technology, Insititute of Nanotechnology, Eggenstein-Leopoldshafen, Germany
[2]Technische Universität Darmstadt, Joint Research Laboratory Nanomaterials, Darmstadt, Germany
[3]Karlsruhe Institute of Technology, Karlsruhe Nano Micro Facility, Eggenstein-Leopoldshafen, Germany
[4]Karlsruhe Institute of Technology, Helmholtz-Institute Ulm for Electrochemical Energy Storage, Eggenstein-Leopoldshafen, Germany
[5]Università di Milano, Dipartimento di Chimica, Milano, Italy

wu.wang@partner.kit.edu

Introduction: Metal nanoparticles supported by porous carriers are widely used for catalysis due to their large surface area and the confining effect, which can be used to tailor the desired catalytic reactions [1]. In heterogeneous catalysis, particle size, shape, location, dispersion, and accessibility of the active sites within the porous support have significant impact on the catalytic properties. Electron tomography provides quantitative three-dimensional (3D) information at the nanoscale that is indispensable to understand the catalytic behaviors of supported nanoparticles [2].
Methods: Pd nanoparticles were loaded on ordered porous CMK-3 carbon support (pore diameter 3-4 nm) by three different methods: incipient wetness (Pd_{IW}/CMK-3), wet impregnation (Pd_{IMP}/CMK-3) and immobilization of preformed PVA stabilized nanoparticles (Pd_{PVA}/CMK-3). The three as-prepared Pd/CMK-3 catalysts were tested for hydrogenation of furfural. Several HAADF-STEM tomograms of the three Pd/CMK-3 catalysts before and after the catalytic reaction were reconstructed from tilt series with a tilt angle range of ±70° or higher. The size and location of the Pd nanoparticles are quantitatively measured after segmentation using Amira 6.1 and compared for the different types of loading.
Results: The conversion after 3 hours of reaction time with the Pd_{IW}/CMK-3, Pd_{IMP}/CMK-3 and Pd_{PVA}/CMK-3 catalysts are 51%, 76% and 68%. The Pd nanoparticle size of all three catalysts is similar, around 2.5 nm as measured from 2D HAADF-STEM images. The process for distinguishing Pd nanoparticles on the surface and inside the pores based on the reconstructed 3D data is illustrated in Fig.1. Fig.2a shows a representative 3D visualization of a segmented Pd_{IMP}/CMK-3 catalyst with surface particles marked in green and particles inside the support marked in red. The relative amount of particles on the surface of each Pd/CMK-3 catalyst is calculated from several tomograms for each sample after segmentation and identification and classification of the particles. The results are summarized in Fig.2b. The percentage of particles on the support surface is around 20%-30% in case of Pd_{IW}/CMK-3, almost independent of the size of the CMK-3 support, whereas all Pd nanoparticles are locate on the CMK-3 surface in case of Pd_{PVA}/CMK-3. In case of Pd_{IMP}/CMK-3, the amount of catalyst on the surface roughly scales with the surface area/volume ratio of the CMK-3 support, meaning that especially the smaller the CMK-3 exhibit a high Pd particle fraction on the surface. With the higher fraction of particle at the surface, Pd_{IMP}/CMK-3 shows a higher activity compared to Pd_{IW}/CMK-3, for which the accessibility of reactants to the catalyst inside particles is confined by the CMK-3 pore structure. The lower activity of Pd_{PVA}/CMK-3 is possibly due to residual PVA stabilizing agent on the Pd nanoparticles, which might block some active sites. Fig.2c shows the size of the Pd particles on the surface and inside the CMK-3 support before and after catalysis as measured by electron tomography. While the size of the Pd nanoparticles in Pd_{IW}/CMK-3 and Pd_{PVA}/CMK-3 are almost unchanged, the Pd nanoparticles within and on the surface of Pd_{IMP}/CMK-3 grew suggesting a poor stability of this catalyst despite the higher initial activity.
Conclusion: Pd nanoparticle locations and size are precisely determined by quantitative electron tomography for different Pd/CMK-3 catalysts. The Pd nanoparticle location is one of the key factors for the catalytic activity, which is related to the confinement effects of the pore structure for active particles. Further work, evaluating e.g. particle shape/faceting and blocking of active sites is currently performed in order to further understand the activity of the catalysts.

References:
[1] De Jong, K. P. (ed.) Synthesis of Solid Catalysts (Wiley), 2009.
[2] Prieto G, Zečević J, Friedrich H, et al. Nature materials, 2013, 12(1): 34-39.

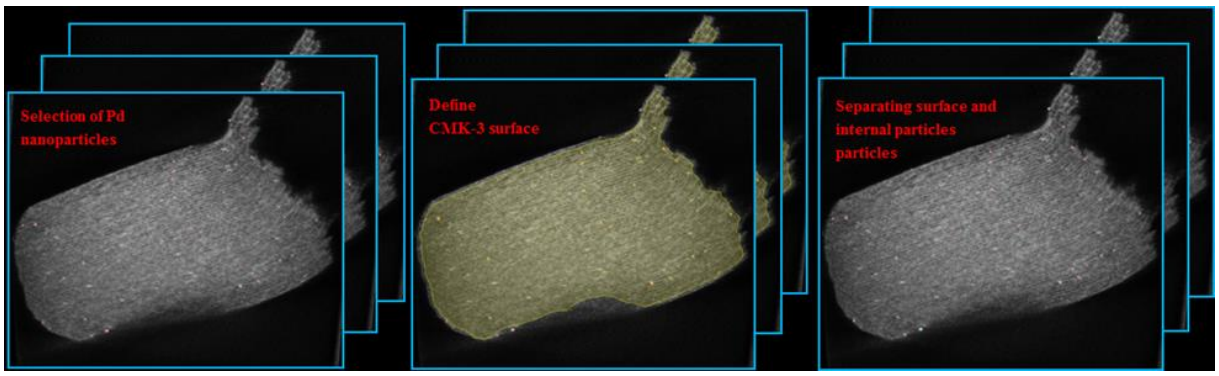

Figure 1. Particle segmentation and determination of particles on the surface and inside the CMK-3 support from the reconstruction 3D data.

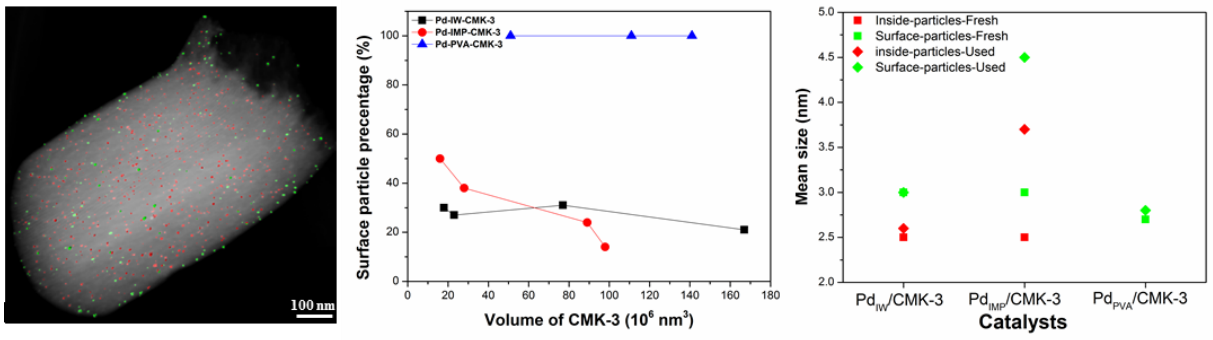

Figure 2. a) Representative 3D visualization of a Pd_{IMP}/CMK-3 catalyst, b) fraction of particles on the surface for the as-prepared Pd/CMK-3 catalysts and c) mean particle diameter of Pd/CMK-3 before and after catalytic reaction.

IM6.005
Enabling nanometer scaled tomography of dynamic materials with vacuum-cryo-transfer capabilities

S. Gerstl[1], S. Tacke[1], R. Wepf[2]

[1]ETH Zurich, ScopeM, Zurich, Switzerland
[2]University of Queensland, Centre for Microscopy and Microanalysis, Brisbane, Australia

gerstls@ethz.ch

Introduction: Atom probe tomography (APT) has become an increasingly integral part of the characterization toolbox due to its capability of measuring nanometer chemical details in 3-dimensions – of predominantly hard & dense materials. Developments at ETH Zurich [1] enables the transfer of cryogenically arrested materials into the analysis chamber, thereby facilitating the analysis of dynamic – rapidly diffusing, soft, or even liquid – materials to be investigated via local electrode atom probe (LEAP) tomography.
Objectives: In order to transport frozen samples, a high vacuum or inert gas environment with temperature control is necessary to prevent changes to the sample surface (Fig.1).[2] Both environments are realized to enable the cryo-transfer method: cryogenically frozen samples are stored in either (1) a cryo-vacuum chamber or (2) LN2. In case (1), samples are moved directly with Leicas Vacuum Cryo Transfer (VCT) shuttle to the analytical machine of choice. In case (2), samples are transferred into an inert gas glove box (such as dry N2), to manipulate them into a shuttle, used for transporting them to a post-processing unit to achieve high vacuum, followed by (as in case 1), VCT to either Cryo-FIB or Cryo-transfer-enabled LEAP.
Materials and Methods: Cryo-transfer-enabled LEAP is achieved with a VCT port on the Load-lock (Fig.2, inset), where the sample is transferred at < 3E-7 mbar through a cryogenically cooled anti-contamination tunnel into a cryo-carousel, which has been actively cooled to below -190°C from a Dewar mounted on the LL. Thermal measurements recorded during the cryo-transfer show the sample remains below recrystallization temperatures of ca. -140°C until it reaches the analysis chamber at < -200°C. Comparative electron microscopy images from multiple VCT movements between FIB to LEAP to FIB have confirmed the vacuum and low temperature fidelity, such as when transferring ½-grids with plunge frozen aqueous solutions on them, demonstrated in Fig. 3.
Results: By enabling the transport of specimens in vacuum and cryogenically arrested states, a variety of new materials classes can be analyzed via APT. These include, but are not limited to, dynamic materials such as: alloy surfaces prone to corrosion, materials with rapidly diffusing solutes, such as H or D in steels [3], polymers, and even liquids. An example of the rapid aggregation of Mg in an Al 6XXX alloy (first solution annealed, then air quenched), reveals the growth, Fig. 4, of nanometer sized chemical features resulting from just 20 min. aging at room temperature. For even more dynamic materials, early results [4] show APT measurements are possible of small volumes of aqueous solutions.
Conclusions: The capability to cryogenically transfer specimens into an atom probe enables the interrogation of dynamic materials details not accessed previously, thereby increasing the materials space APT can investigate.

References:
[1] Gerstl S.S.A.; Wepf R. Microsc. Microanal. 21, 517 (2015).
[2] Wepf R. et al. High Resolution Cryo SEM of Macromolecular Complexes in Biological Field Emission Scanning Electron Microscopy, edited by R. Fleck and B. Humble (Wiley, submitted)
[3] Chen Y-S.; Haley D.; Gerstl S.S.A.; London A.J.; Sweeney F.; Wepf R.; Rainforth W.M.; Bagot P.A.J.; Moody M.P., (Science, 17.Mar.2017, vol. 355 no. 6330 1196-1199).
[4] Moody M.P., Vella A., Gerstl S.S.A., Bagot P.A.J. (2016). MRS Bulletin, 41, pp 40-45.
[5] S.G. acknowledges funding from ScopeM (formerly EMEZ) R&D grants.

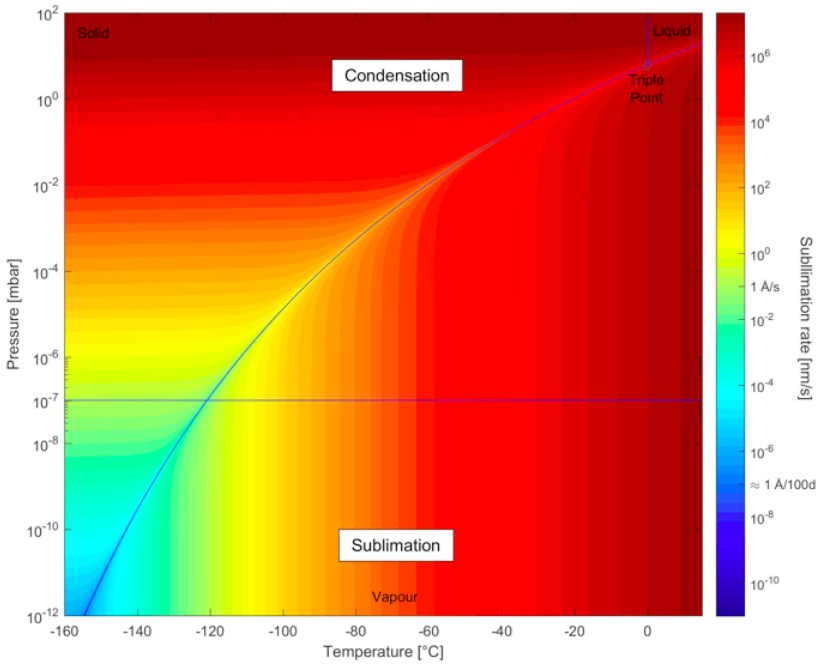

Figure 1. The portion of the water phase diagram showing critical relationships to regard while transferring cryogenically arrested materials between chambers.

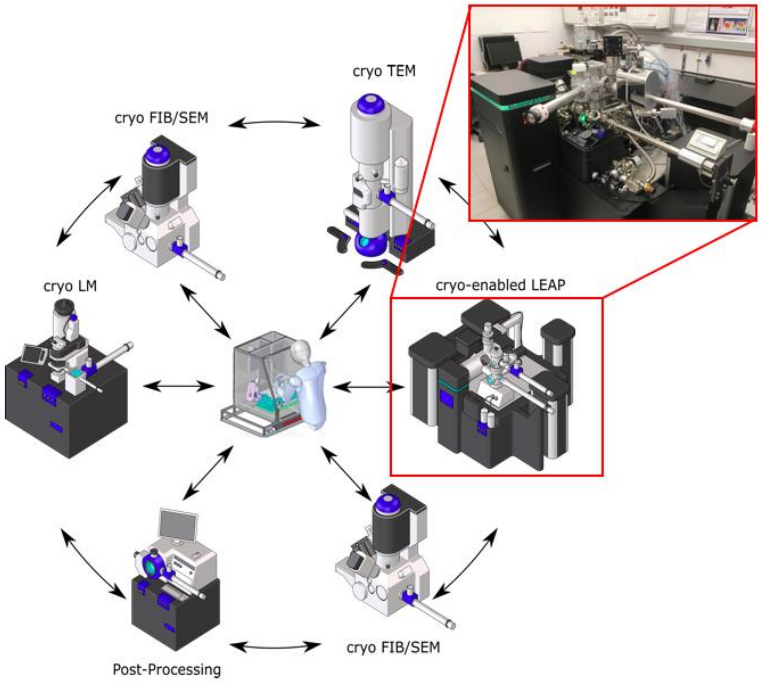

Figure 2. The typically dry N2 filled glove box (at center) is instrumental in transferring specimens without contamination between multiple stations & microscopes; inset image of Cryo-enabled LEAP tomograph.

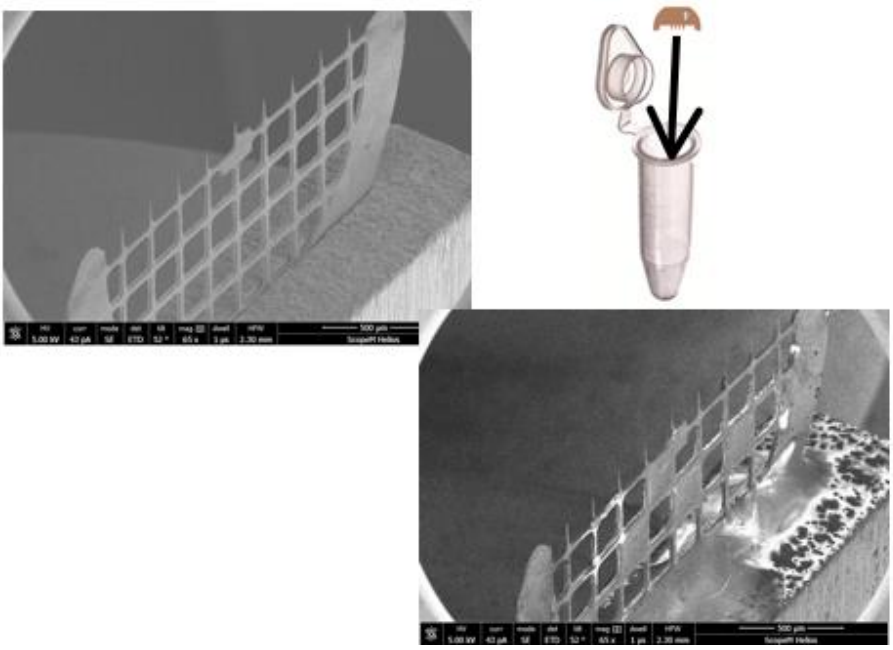

Figure 3. (Left) ½-grid field developed tips, dipped in a fluid ROI, then plunge frozen & cryo-transferred is a method applied to analyze aqueous solutions.

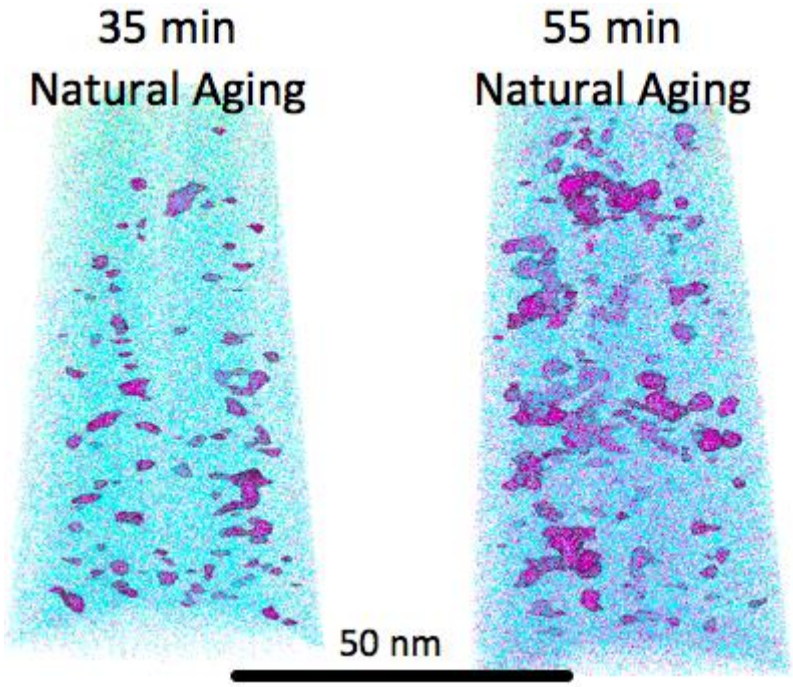

Figure 4. Two reconstructions from two analyses (on the same needle specimen) displaying the *same* Mg isosurface, after 35 or 55 min. aging following cryo-transfer from an as quenched state; aged in the buffer chamber at room temperature.

IM6.006 invited
Multi scale 3D microstructure analysis through correlation of X-ray computed tomography and focused ion beam serial sectioning

T. Burnett[1], P. Withers[1]

[1]The University of Manchester, School of Materials, Manchester, United Kingdom

timothy.burnett@manchester.ac.uk

There are a huge array of characterization techniques available today and increasingly powerful computing resources allowing for effective analysis and modelling of large datasets. However, a majority of these experimental and theoretical tools span only very limited time and length scales.
Correlative tomography can be thought of as the extension of correlative microscopy (e.g. the use of optical fluorescence microscopy to identify a region of interest followed by high resolution electron microscopy of the chosen region) into three dimensions. By establishing rigorous ways of connecting different techniques operating at different scales it is possible to cover a large range of scales not restricted by one particular technique.
In this talk I will focus on the linking of X-ray Computed Tomography (CT) to serial sectioning electron tomography using the focussed ion beam (FIB)-scanning electron microscope (SEM). I will show how correlative tomography has provided a new level of detail by delivering a multiscale 3D picture of a sample with detailed analysis focussed on regions of interest [1].
Specifically I will focus on the use of the Xe+ Plasma FIB [2] as an enabling tool for large volume high resolution serial sectioning of materials but also a tool for preparation of microscale test samples and samples for Nanoscale X-ray CT imaging. The examples I will use focus on the microstructure of metals during different failure mechanisms including ductile fracture of steel and corrosion of aluminium and magnesium alloys. I will discuss the results on the specific materials use cases as well as more general aspects regarding the experimental and analysis workflow.
Correlative tomography has already allowed for some significant insights into materials linking together information from different instruments across different scales. As we continue to refine this approach and feed the results into multiscale models we believe there will be increasing value to be derived from this approach both in materials science but also in other areas particularly where hierarchical structures are being investigated.

References:
[1] Burnett et al, Correlative Tomography, Scientific Reports 4, Article number: 4711 (2014)
[2] Burnett et al, Large volume serial section tomography by Xe Plasma FIB dual beam microscopy, Ultramicroscopy, Vol 161, Pp. 119-129 (2016)

IM6.P001
Multimode tomography to investigate the structure of Au nanoparticles

N. Winckelmans[1], T. Altantzis[1], M. Grzelczak[2], A. Sánchez Iglesias[2], L. M. Liz-Marzán[2], S. Bals[1]

[1]University of Antwerp/EMAT, physics, Antwerp, Belgium
[2]CIC biomaGUNE, San Sebastián, Spain

naomi.winckelmans@uantwerpen.be

Introduction: For Au nanoparticles (NPs), it is known that the properties can be tuned in a reproducible manner by controlling their morphology. Their synthesis is mature and the present understanding enables chemists to tune particle size and shape.[1] However, little is known about the exact roles that different experimental parameters have in directing anisotropic growth at the atomic scale. Many studies have focused on the characterization of NPs synthesized by the seed mediated approach. In such systems, the shape of the seed as well as the presence of twins can have a strong impact on the morphology of the final products.[2]
Objectives: Here, we investigate the growth of pentatwinned (PTW) Au NPs grown from a decahedral Pd coated Au seed.[3] The difference in atomic number between Au and Pd enables us to differentiate between the seed and the grown Au shell when using HAADF-STEM. Furthermore, we will combine HAADF-STEM and LAADF-STEM tomography to locate the modified Au/Pd seed inside the final Au structure with respect to the twins.
Materials and Methods: The seed-mediated growth approach was used to grow PTW NPs from Au/Pd seeds.[3] Tilt series were acquired simultaneously in HAADF-STEM and LAADF-STEM mode within a tilt range from -72° to +70° with a tilt increment of 2°. All images are acquired using an FEI-Titan electron microscope operated at 300 kV. For the reconstruction of both series the SIRT algorithm was used as implemented in the ASTRA toolbox.[4]
Results: One of the bottlenecks for the 3D visualization of defects is that the projection requirement for tomography needs to be fulfilled.[5] Therefore, tomography is often combined with HAADF-STEM (high collection angle). However, the diffraction contrast, yielding information on the presence of defects, is lost. In order to collect that signal, the so-called LAADF-STEM (low collection angle) technique should be used. In this study, the HAADF-STEM and LAADF-STEM signals are simultaneously collected by using two different annular detectors. In this manner, both the morphology of the NPs as well as the presence of defects can be investigated in 3D. Fig. 1b presents a LAADF-STEM image from which the twin boundaries in the PTW Au bipyramid are clear. An orthoslice through the corresponding HAADF-STEM reconstruction is shown in Fig. 1c, in which the Pd shell surrounding the Au seed appears darker. From the LAADF-STEM orthoslices (Fig. 1d), it is clear that the twins are present throughout the whole NP. After segmentation, both reconstructions were combined. In this manner, we were able to determine the shape of the NP, as well as the position of the seed with respect to the twin planes (Fig. 1e).
Conclusion**:** In this study a novel approach is proposed for the investigation of twin planes in a NP in 3D, through the simultaneous acquisition of HAADF-STEM and LAADF-STEM tilt series. After a stringent segmentation, both reconstructions are overlaid in order to reveal the position of the seed with respect to the twins. It is clear that both the seed as well as the grown Au shell are PTW and that the seed is located at the connection point of the twins.

References:
[1] Burda, C.; Chem Rev **2005**, 105 (4), 1025–1102
[2] Lu, X.; Annu Rev Phys Chem **2009**, 60, 167-92
[3] Sánchez-Iglesias, A., J Am Chem Soc **2017**, 139 (1), 107–110
[4] van Aarle, W.; Ultramicroscopy **2015**, 157, 35-47
[5] Hawkes, P. W.; Springer New York **2007**, 83-111

The authors acknowledge financial support from the Research Foundation Flanders (FWO, Belgium) through Project No. G038116N. S. Bals and N. Winckelmans acknowledge funding from the European Research Council (ERC Starting Grant 335078-COLOURATOMS)

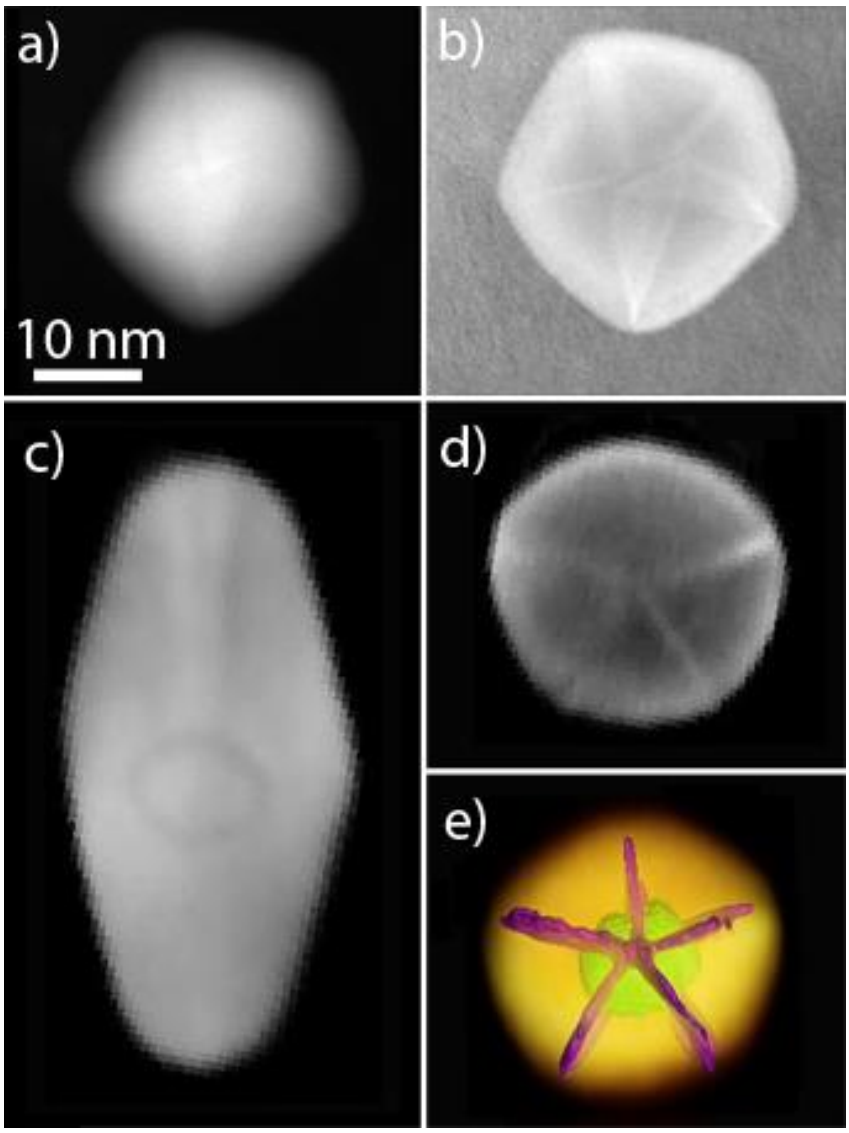

Figure 1. a) HAADF-STEM and b) LAADF-STEM image of a PTW bipyramid, acquired simultaneously using two different detectors. Orthoslice through the HAADF-STEM (c) and LAADF-STEM (d) reconstruction from which the seed and the twins can be segmented, respectively. e) The segmented seed and twins were overlapped with the HAADF-STEM reconstruction to visualize their location with respect to each other and to the correct morphology.

IM6.P002
Reconstructing three-dimensional atomic details of nanostructures from single Z-contrast electron microscopy images

A. De Backer[1], L. Jones[2], I. Lobato[1], T. Altantzis[1], P. D. Nellist[2], S. Bals[1], S. van Aert[1]

[1]EMAT, University of Antwerp, Department of Physics, Antwerp, Belgium
[2]Department of Materials, Oxford University, Oxford, United Kingdom

annick.debacker@uantwerpen.be

Modern experimental characterization techniques should be able to determine the structure of nanoparticles at the atomic scale, since the particle"s properties are directly related to the atomic structure. Scanning transmission electron microscopy (STEM) is established as a valuable method to investigate nanomaterials. However, two-dimensional (2D) projection images may result in an incomplete characterization of the material"s structure. Therefore, different techniques to retrieve the three-dimensional (3D) atomic structure have been suggested in the field of electron microscopy.
In recent years, the resolution of electron tomography has reached the atomic scale [1,2]. However, such tomography typically requires several images demanding substantial electron dose. A newly developed alternative [3,4] circumvents this by counting the number of atoms across a single projection image [5,6]. These atom counts can be used to create an atomic model, and next an energy minimization can be applied to obtain a relaxed 3D reconstruction.
In this work, we validate our new atom-counting/energy minimization approach against state-of-the-art compressive sensing electron tomography [2]. For this purpose, three projection ADF STEM images of a Au nanorod have been acquired along different major zone axes. In Fig. 1, a comparison is shown between the atom-counting/energy minimization method and electron tomography reconstruction. An excellent agreement was found.
As an example, the utility of this new approach is illustrated by the 3D characterization, at the atomic scale, of a Au nanodumbbell on an *in situ* heating holder. An atomic resolution STEM image has been acquired along a single viewing direction available from the *in situ* heating holder, before and after ramping up the temperature to 330°C. Fig. 2 shows the 3D atomic models before and after heating along different directions. The changes in facet-type and facet-area ratio can be clearly observed for the entire tip and a significant increase of low index facets is observed after heating. Part of the facets could be observed from the projection image; however, the 3D atomic models give us additional information about the height of the facets along the beam direction. We expect these measured properties to be of critical importance for the study of catalysis.
In conclusion, an impressive agreement was found between our new atom-counting/energy minimization approach and state-of-the-art compressive sensing electron tomography. This result opens up the possibility for the study of beam-sensitive materials, 2D self-assembled structures [7], or where *in situ* hardware makes tomography impossible. As an illustration, the surface facets of a Au nanodumbbell on an *in situ* heating holder were characterized.

References:
[1] Van Aert et al., Nature **470** (2011) p 374
[2] Goris et al., Nature Materials **11** (2012) p 930
[3] Bals et al., Nature Communications **3** (2012) p 897
[4] Jones et al., Nano Letters **14** (2014) p 6336
[5] Van Aert et al., Physical Review B **87** (2013) 064107
[6] De Backer et al., Ultramicroscopy **134** (2013) p 23
[7] Geuchies et al., Nature Materials **15** (2016) p 1248
[8] Funding from FWO Flanders (postdoc grants to ADB and TA, G.0374.13N, G.0369.15N, G.0368.15N, WO.010.16N) is acknowledged.

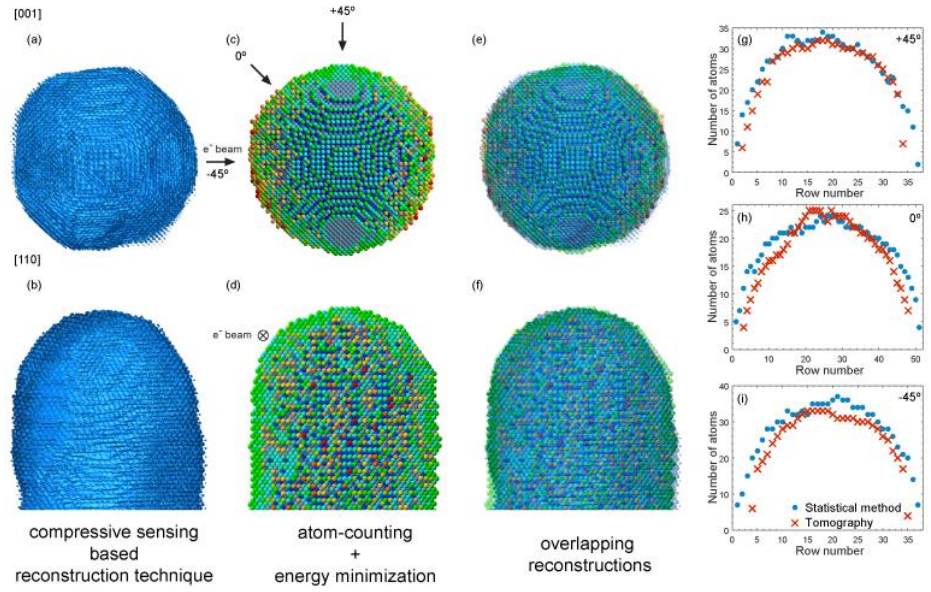

Figure 1. Comparison of the atom-counting/energy minimization and atomic resolution tomography reconstruction (a,b) Compressive sensing based reconstruction of a Au nanorod. (c,d) Reconstruction based on the atom-counting/energy minimization approach (the coloring of the Au atoms indicates the nearest neighbor coordination). (e,f) Overlap of reconstructions shown in (a,c) and (b,d). (g,h,i) Comparison of atom-counts along different orientations from an orthogonal slice from the compressive sensing based reconstruction (red crosses) and atom-counting results obtained from the three ADF STEM projection images (blue dots).

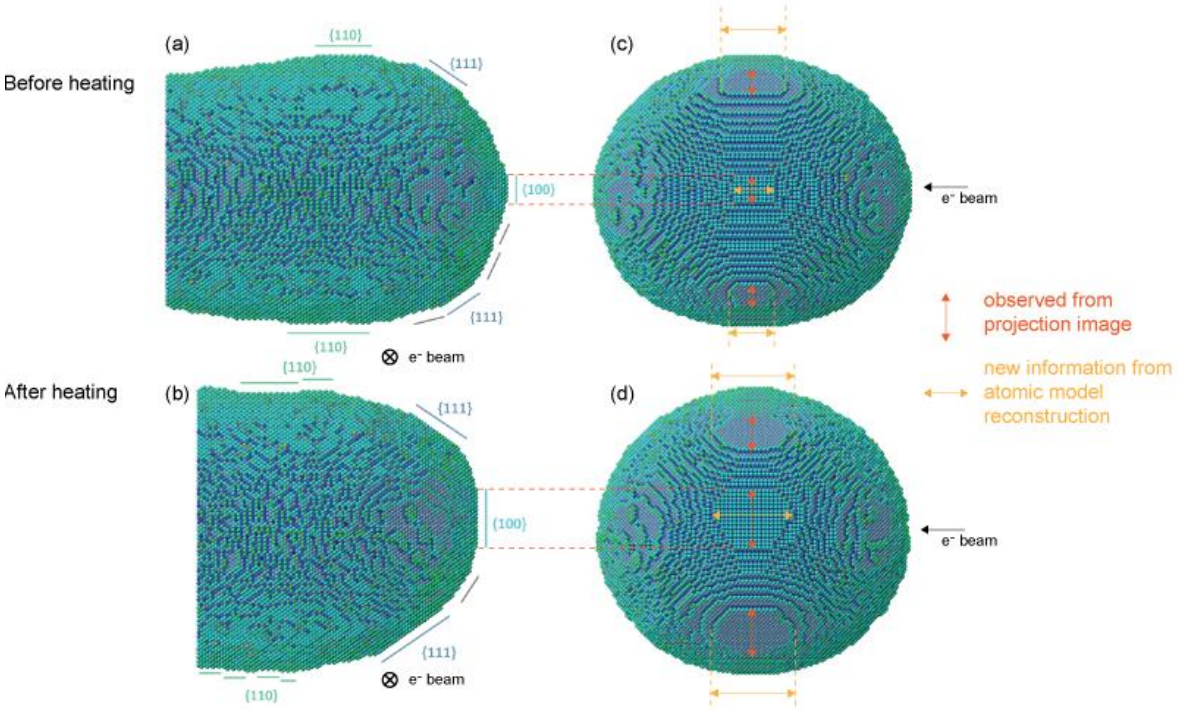

Figure 2. 3D atomic models before and after heating along different viewing directions. (a,c) Au dumbbell before heating, (b,d) Au rod after heating. The coloring of the Au atoms determines the nearest neighbor coordination.

IM6.P003
Quantitative structural characterization of porous Pt nanoparticles by advanced electron tomography

H. Vanrompay[1], K. Sentosun[1], B. Geboes[1], J. Ustarroz[2], T. Breugelmans[1], A. Hubbin[2], S. Bals[1]

[1]University of Antwerp, Antwerp, Belgium
[2]VUB, Brussel, Belgium

hans.vanrompay@uantwerpen.be

Introduction: The investigation of porous nanoparticles (NPs) is currently an area of intense scientific interest due to a wide variety of potential applications in separation, catalysis and energy storage. Owing to their intrinsic high surface-to-volume ratio (SVR), porous NPs have a high chemical reactivity as reactions occur at the surface of a material. Therefore, a quantitative reliable analysis of the SVR is of outmost importance in order to control and optimize the NPs applicability.
Objectives During the synthesis, several parameters can be tuned to alter the structure of the deposited Pt NPs. Changing the deposition potential, may for instance lead to NPs with a higher SVR. Since this ratio is a measure for the catalytic activity of the NPs, we will search for the deposition conditions that maximize this value using quantitative electron tomography.
Materials and Methods: The electron tomography experiments were performed using a FEI Tecnai G2 and Tecnai Osiris microscope operated at 200 kV. The tilt series were acquired over a tilt range of ±74° with a 3° tilt increment. For the reconstruction both the SIRT as TVM algorithm were used, as implemented in the ASTRA toolbox1. A tailor made quantification procedure, implemented in MATLAB, enabled us to generate accurate statistics on the porous structure of the investigated Pt NPs.
Result: By the use of electron tomography, both the 3D morphology as the internal structure of the Pt NPs is investigated. In order to retrieve the SVR, an objective and automatic 3D quantitative characterization procedure is proposed2 (Figure 1). The most important feature of the developed strategy, is the ability to differentiate between pores connected to the outer surface and non-connected cavities in a 3D manner (Figure 1(d)). This connectivity is of paramount importance for the employment of the porous materials in, for example, catalytic reactions.
In Figure 2, 3D visualizations of a Pt NP (a) before and (c) after electrocycling in an electrolyte are shown. The changes in porosity before and after electrocycling are quantified using the proposed characterization procedure (Figure 2(b)).
Conclusion: A characterization procedure was designed that enables one to obtain quantitative information from porous Pt nanoparticles at the nanoscale, as function of the synthesis conditions. An important feature of this strategy is that neither information averaged over a large amount of particles is provided nor any assumptions on the morphology of the investigated structure are involved. The outcome of such a procedure can be used to establish the connection between functionalities and structure. As nanoporous systems become smaller and structurally more complex, we foresee that quantitative tomography will turn out into their standard characterization technique.

References:
[1] Van Aarle W., Palenstijn W J., De Beenhouwer J., Altantzis T., Bals S., Batenburg K. J., Sijbers J., *Ultramicroscopy*, **2015,** 157, pp. 35–47
[2] Vanrompay H, Sentosun K., Geboes B., Ustarroz J., Breugelmans T., Hubin A., Bals S., *ACS Catal.*, **2016**, *6* (9), pp. 5856–5864

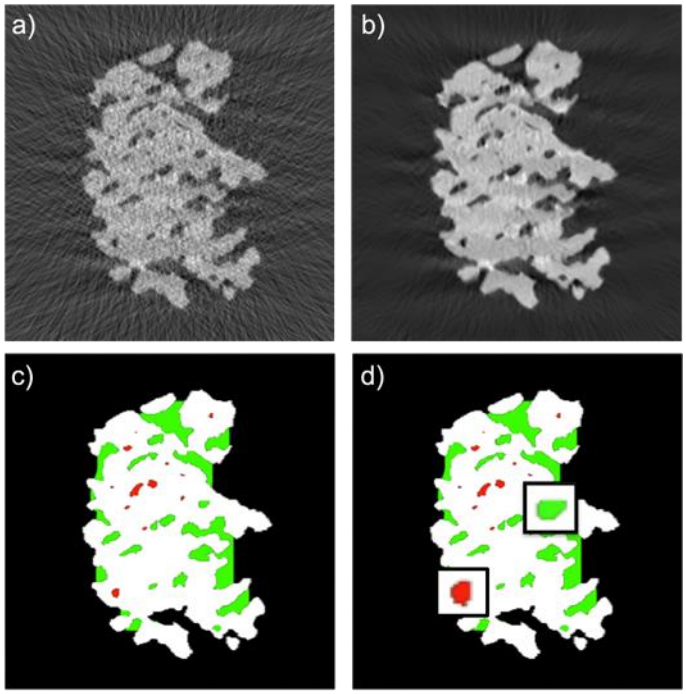

Figure 1. To quantify the 3D tomographic reconstruction (Fig 1a), a dedicated global filter is applied (Fig 1b). Afterwards the filtered reconstruction is automatically segmented based on Otsus thresholding method (Fig 1c). Next the segmented reconstruction is analyzed from different directions to determine which voxels belong to the object, the exterior, a cavity, or to a pore (Fig 1d).

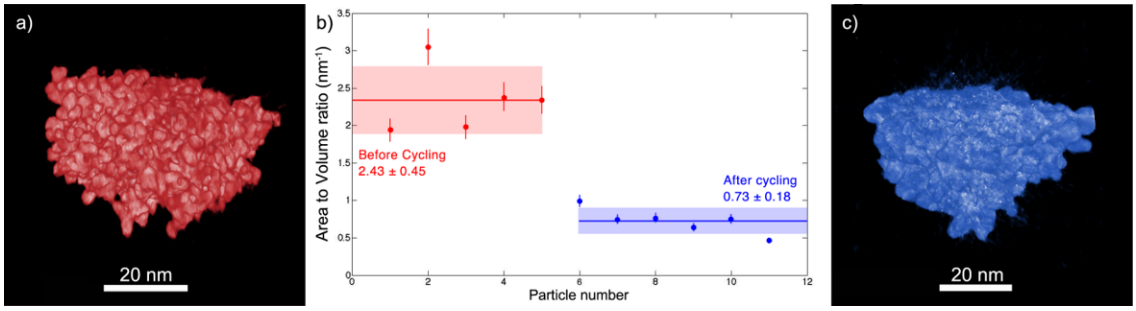

Figure 2. a) 3D visualization of a porous Pt nanoparticle before electrocycling. b) Quantitative analysis of the surface to volume ratio for Pt samples before and after cycling. c) 3D reconstruction of a Pt sample after electrocycling.

IM6.P004
Novel workflows for tomography sample preparation using ultra-short-pulsed lasers

M. Krause[1], G. Schusser[1], S. T. Kelly[2,3], T. Höche[1]

[1]Fraunhofer IMWS, Nanomaterials and Nanoanalytics, 06120, Germany
[2]Carl Zeiss Microscopy, LLC, Pleasanton, CA, United States of America
[3]Carl Zeiss Microscopy, LLC, Pleasanton, CA, United States of America

michael.krause@imws.fraunhofer.de

Knowledge on the three-dimensional microscopic structure as well as composition of materials is essential for understanding their properties and designing functional devices. While advances in instrumentation and software of certain measurement methods like x-ray microcopy (XRM) or atom-probe-tomography (APT) have led to unprecedented new possibilities of microstructure diagnostics, associated sample preparation workflows have not been improved to the same extent yet.
In this paper, the use of ultra-short-pulsed lasers for generating sophisticated, tomography-specific sample geometries will be presented. Special emphasis will be placed on the basic mechanism of material ablation as a function of pulse-lengths as well as novel concepts for preparing and safe handling of tiny samples produced by laser micromachining.
In order to estimate the extent of structural damage in certain materials, the laser-affected zone caused by different types of Laser-sources ranging from micro-second to femto-second pulse-length has been analyzed using scanning electron microscopy (SEM) and transmission electron microscopy (TEM). Sample preparation for subsequent high resolution x-ray microcopy (using a Carl Zeiss 810 Ultra) has been accomplished using a novel laser-micromachining tool for microstructure diagnostics (Gatan microPREP™) featurting a ps-laser source. Two different workflows which leave either a monolithic sample from a thin sheet of base-material or a tiny XRM-Chunk™ from an arbitrary sample surface, transferred to a supporting structure, have been used to obtain XRM-specimen from glass-ceramic material and oil shale. In each case, regions of interest have been thinned down by concentrically top-down-milling in order to end up with final sample dimensions which fit well to the absorptions length of the particular materials.
XRM results of the ps-laser prepared samples reveal no significant structural damage within the materials under investigation, at least within the spatial resolution of the technique/measurement settings. The according 3D datasets will be presented as well as the results of the microstructural investigations regarding the structural damage caused by different laser sources, which have been determined to be in the order of some micrometers (ns pulsed laser) to less than a few hundred nanometers (ps pulsed laser).
Since the overall preparation time required for the laser workflow (w/o additional mechanical pre-stages if required) is in general between 30-60 minutes, laser-based sample preparation for tomographic methods is a powerful alternative compared to common workflows. Beside its use for XRM-sample preparation, it also offers a significantly improved preparation routine for atom-probe tomography if the laser-thinning is followed by a focused ion beam final polishing of the cylinders/cones down to the required diameter (< 100 nm).

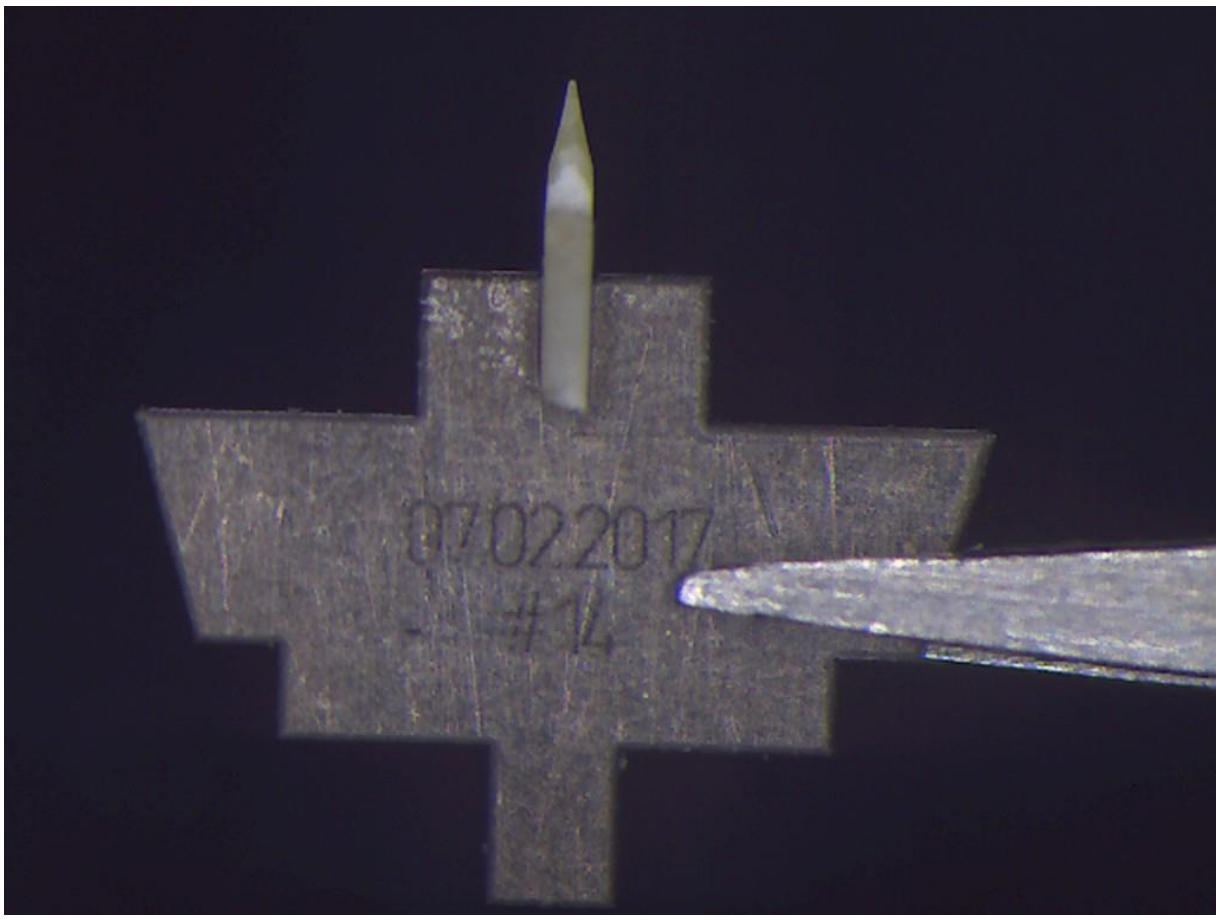

Figure 1. XRM-Chunk™ of an YAG-sample glued to a supporting structure made of Titanium and thinned down to 25 µm diameter.

IM6.P005
Investigating 3D pore structures in oxide layers of Co-base superalloys using FIB tomography

N. Buchinger[1], M. Lenz[1], Y. Eggeler[1], T. Przybilla[1], M. Weiser[2], E. Spiecker[1], S. Virtanen[2]

[1]Center for Nanoanalysis and Electron Microscopy (CENEM), Erlangen, Germany
[2]Chair for Surface Science and Corrosion, Erlangen, Germany

nadine.buchinger@fau.de

Keywords: cobalt-base superalloy, oxidation, FIB-tomography

Superalloys have to withstand corrosion and oxidation due to their exposure to ambient air at high temperatures in combustion chambers of turbine engines [1]. Apart from the well-established Ni-base superalloys Co-based ones have recently attracted a lot of interest because of the beneficial impact of the positive γ-γ lattice misfit on the creep properties [2]. However, research on the oxidation behaviour of Co-base superalloys is still in its infancy [3].
For the investigation of the pores and their properties mentioned above, a Co-base superalloy (Co-9Al-9W) was oxidized in synthetic air (20% O2, 80% N) at 900°C for 12 hours. SEM images of sample cross-sections clearly reveal the different oxidation layers that were formed (Figure 1). To visualize the structure of the oxidation layer including the porosity, a cuboid has been milled out of the bulk sample using a Helios NanoLab 660 Dual Beam FIB (Figure 2a). By applying the slice and view technique 700 slices were cut and imaged with different detectors starting at the pure superalloy moving towards the outer edge of the transition layer (Figure 2b). With these slice-images, a 3D-reconstruction of the respective volume was obtained, as displayed in Figure 3, showing the inner pore surface within the analyzed volume.
The pores are mostly closed but show a clear texture, which can be attributed to the propagation of the interface towards the pure superalloy upon high temperature oxidation. These closed individual pores do not facilitate the oxygen transport towards the base material. In order to gain insight into the volume fraction of the pores the reconstructed oxidized volume will be further evaluated and the results will be compared to complementary 3D studies by X-ray tomography.
Acknowledgement: The authors gratefully acknowledge financial support by the DFG via the collaborative research center SFB-TR 103 and the Cluster of Excellence EXC315.

References:
[1] R.C.Reed, Superalloys Cambridge University Press, (2006)
[2] A. Suzuki et al., L12-Strengthened Cobalt-Base Superalloys, Annu. Rev. Mater. Res. (2015), Vol. 43
[3] C.A. Stewart et al., Oxide scale formation in novel γ-γ Cobalt-based alloys, TMS (2016)
[4] M. Knop, Diploma Thesis, University of California Santa Barbara (2011)

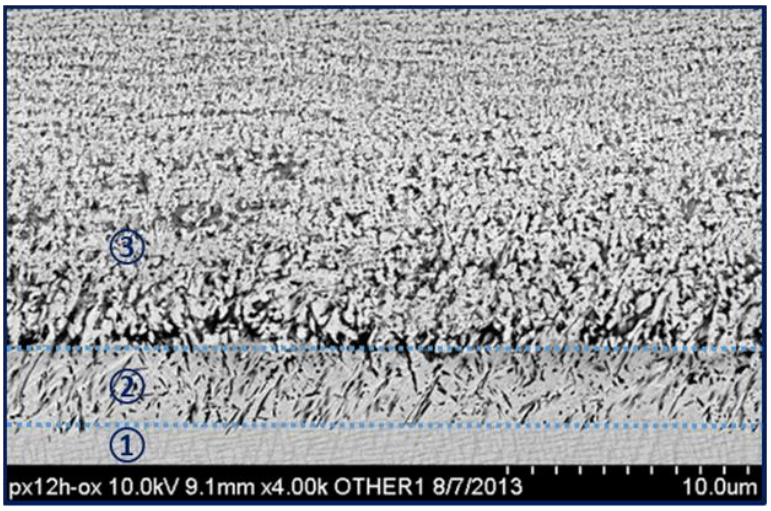

Figure 1. SEM image of the 12h oxidized Co-9Al-9W-superalloy: The superalloy (1), inner oxidation front (2), transition layer including pores (3).

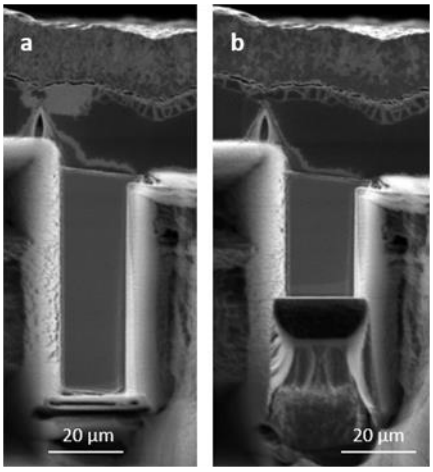

Figure 2. Cuboid a) before b) after slicing process.

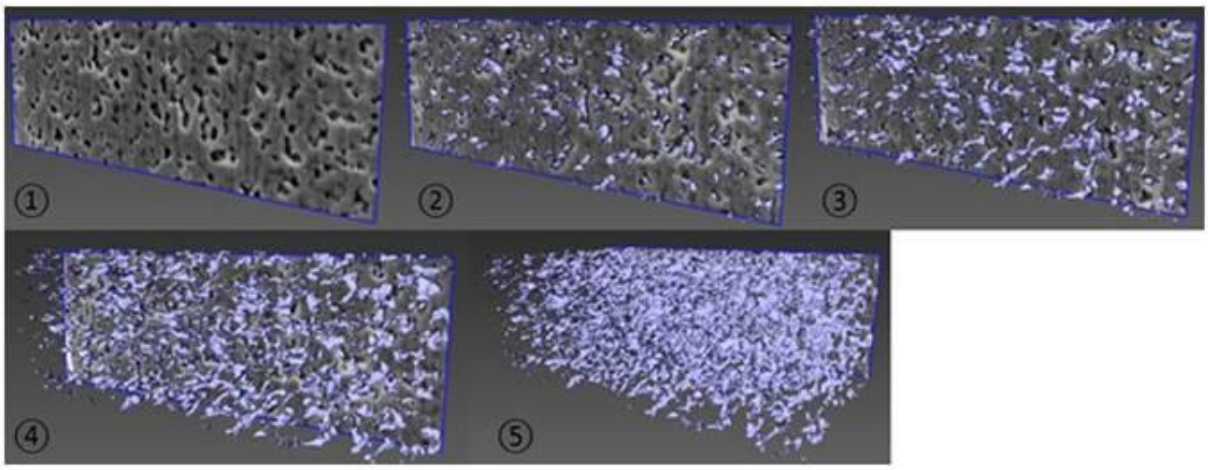

Figure 3. Reconstruction of pores through a selected area of the transition oxidation layer.

IM6.P006
Investigating human cytomegalovirus entry using STEM tomography

M. E. A. Abdellatif[1], P. Walther[1]

[1]Ulm University, The Central Facility for Electron Microscopy, Ulm, Germany

mohamed.abdellatif@uni-ulm.de

Introduction: Scanning transmission electron microscopy (STEM) tomography can be used for three-dimensional (3D) data analyses of biological samples(1). It does have advantages over transmission electron microscopy (TEM) tomography with respect to sample thickness and contrast(2). In order to understand biological processes, it is necessary to identify their morphological manifestations in addition to the biochemical characterization. This is witnessed in the processes involving viral entry into the host cell, whereby a rapid endogenous cellular response is manifested by membranous involvement along with other cellular intake mechanisms(3). The human cytomegalovirus (HCMV) mechanism of entry into various cell types is under debate (4-7). Although it has been investigated on the ultrastructural level utilizing electron microscopy(7,8), a comprehensive study in different cell types based on advanced electron microscopy techniques in a 3D context is still lacking.
Objectives: HCMV uptake shall be visualized with STEM tomography in 3D to understand the interactions of viral particles with the host cell membrane and with various endocytic mechanisms.
Materials and Methods: Viruses: highly- and poorly-endotheliotropic dual tagged HCMV strains (BACkl7-SE-UL100mCherry-UL32EGFP and BACkl7-SE-UL128+A332-UL100mCherry-UL32EGFP respectively). Cells: Human foreskin fibroblasts and HEC-LTT endothelial cells(9). Sample preparation: Cells grown on sapphire discs were cryofixed by high-pressure freezing then freeze substituted and embedded in Epon as described previously(10).STEM tomography: The STEM tilt series of 500 nm thick sections were acquired with a Jeol JEM-2100F Transmission Electron Microscope using the STEM mode and the bright field signal. The specimens were tilted from -72º to 72º with 1.5º increment. The tomographic reconstruction was done using IMOD(11)
Results:

1) Optimizing growth conditions for the enrichment of biologically active virions titers was achieved.
2) Improved resolution of membranous structures was achieved.
3) HCMV Entry related events are identified through various STEM tomography observed profiles as can be seen in the figures.

Conclusion: HCMV entry investigation using STEM tomography is a multi-step procedure. It requires the orchestration of various key players starting from cells in cultures and ending with tomographic reconstruction. The method allowed us to explore various HCMV entry mechanisms into host cells. Of note: No membrane fusion events were observed so far.

References:

[1] Höhn K, Sailer M, Wang L, Lorenz L, Schneider EM, Walther P. *Histochem Cell Biol***2011**. 135, 1-9..
[2] Rez, P.; Larsen, T.; Elbaum, M. *Journal of structural biology***2016**, *196*, 466.
[3] Marsh, M.; Helenius, A. *Cell***2006**, *124*, 729.
[4] Compton, T.; Nepomuceno, R. R.; Nowlin, D. M. *Virology***1992**, *191*, 387.
[5] Haspot, F.; Lavault, A.; Sinzger, C.; Laib Sampaio, K.; Stierhof, Y. D.; Pilet, P.; Bressolette-Bodin, C.; Halary, F. *PloS one***2012**, *7*, e34795.
[6] Sinzger, C. *J Clin Virol***2008**, *41*, 174.
[7] Hetzenecker, S.; Helenius, A.; Krzyzaniak, M. A. *Traffic***2015**.
[8] Bodaghi, B.; Slobbe-van Drunen, M. E. P.; Topilko, A.; Perret, E.; Vossen, R. C. R. M.; van Dam-Mieras, M. C. E.; Zipeto, D.; Virelizier, J. L.; LeHoang, P.; Bruggeman, C. A.; Michelson, S. *Invest Ophth Vis Sci***1999**, *40*, 2598.
[9] Lieber, D.; Hochdorfer, D.; Stoehr, D.; Schubert, A.; Lotfi, R.; May, T.; Wirth, D.; Sinzger, C. *Biotechniques***2015**, *59*, 127.
[10] Stegmann, C.; Abdellatif, M. E. A.; Laib Sampaio, K.; Walther, P.; Sinzger, C. *Journal of virology***2017**, *91*.
[11] Kremer, J. R.; Mastronarde, D. N.; McIntosh, J. R. *Journal of structural biology***1996**, *116*, 71.

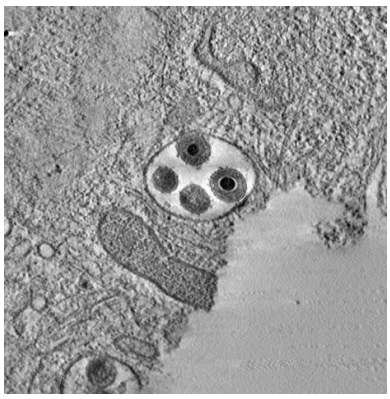

Figure 1. Virtual sections of STEM tomograms exhibiting enveloped virions within vesicles.

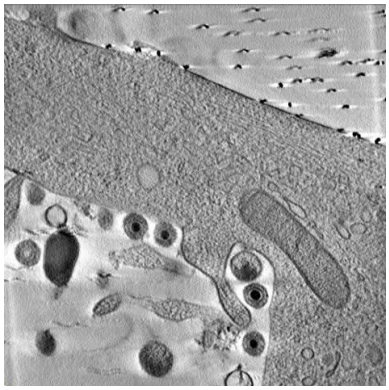

Figure 2. Virtual sections of STEM tomograms exhibiting a macropinocytic-like entry.

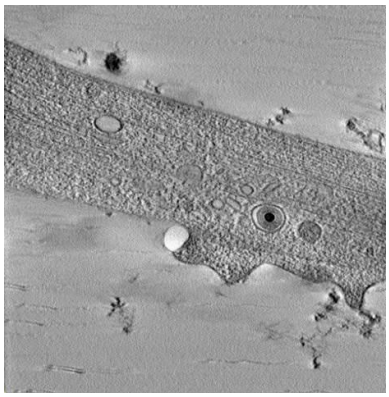

Figure 3. Virtual sections of STEM tomograms exhibiting a viral particle in a caveosome.

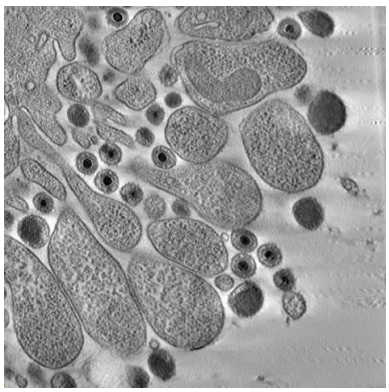

Figure 4. Virtual sections of STEM tomograms exhibiting membranous ruffling

IM6.P007
Comprehensive microstructural analysis of austenitic steels after neutron irradiation using APT, TEM and SEM

B. Gurovich[1], E. Kuleshova[1,2], A. Frolov[1], G. Zhuchkov[1], L. Kutuzov[1], D. Maltsev[1]

[1]NRC KI, Moscow, Russian Federation
[2]NRNU MEPhI, Moscow, Russian Federation

frolov.alex@list.ru

Fast neutron irradiation of austenitic steels leads to the evolution of its structural-phase state: formation of pores [1], dislocation loops, formation of secondary phases [2,3], and redistribution of chemical elements along the grain boundaries [4].
Complex phase analysis of these materials requires the use of various techniques (transmission electron microscopy, scanning electron microscopy and atom probe tomography), possessing different locality and allowing to carry out qualitative and quantitative research on different scales (from mm to angstrom).
In this work, comprehensive studies of the structural state of Cr-Ni-Ti based austenitic steels irradiated in BOR-60 and VVER-1000 reactors in the temperature range of 320-450°C up to damaging doses from 12 to 150 dpa were conducted.
The results of APT- and TEM-investigations of the phase components having a size in the range from 3 to 20 nm and a number density from $1 \cdot 10^{21} m^{-3}$ to $5 \cdot 10^{23} m^{-3}$ (for example, G-phase - globular precipitates based on Ni, Mn and Ti [5]) were shown to be in a good agreement with each other (see Figures 1 and 2).
TEM-observation of precipitates with quite a small average size (less than 2 nm) and the number density reaching $1.6 \cdot 10^{24} m^{-3}$ is quite a nontrivial problem, since the using of weak beam method (which is normally used for imaging of radiation-induced structural elements of reactor materials) is difficult due overlapping of particles and strain fields from them. In this case it is preferable to use atom probe tomography, because this method has no limitations on the maximum number density of investigated phases. This situation is typical for austenitic steel samples irradiated in the VVER-1000 reactor up to 12 dpa at 320°C (see Figure 3).
At the same time, this technique for analyzing precipitates (with number density less than $1 \cdot 10^{21} m^{-3}$) is applicable in the case of a large data set only due to the relatively small volume of standard APT-sample (needle shaped with a radius of curvature ~ 50 nm).
On the other hand, identification using APT of some structural component (such as the vacancy pores or dislocation loops) is difficult, therefore, it is necessary to combine APT and TEM for a comprehensive analysis of the microstructural evolution of the austenitic steels after neutron irradiation. Furthermore TEM allows to determine the type of the crystal lattice of the phase components which sizes are over 20 nm (see Figure 4).

References:
[1] Garner F.A. et al. Void Swelling of Austenitic Steels Irradiated with Neutrons at Low Temperatures and Very Low Dpa Rates // 12th International Conference on Environmental Degradation of Materials in Nuclear Power System - Water Reactors, August 14-18, 2005, Snowbird Resort Salt Lake City, Utah, USA , 439-448.
[2] Maziasz P.J. Formation and stability of radiation-induced phases in neutron-irradiated austenitic and ferritic steels // J. Nucl. Mater. 1989. Vol. 169. P. 95–115.
[3] Maziasz P.J. Overview of microstructural evolution in neutron-irradiated austenitic stainless steels // J. Nucl. Mater. 1993. Vol. 205. P. 118–145.
[4] Renault A.-E. et al. Microstructure and Grain Boundary Chemistry Evolution in Austenitic Stainless Steels Irradiated in the BOR-60 Reactor up to 120 Dpa // 14th, Int. Conf. Environ. Degrad. Mater. Nucl. power Syst. water React. Virginia Beach, VA, August 23-27. 2009. P. 1324–1334.
[5] Gurovich B.A. et al. Investigation of high temperature annealing effectiveness for recovery of radiation-induced structural changes and properties of 18Cr–10Ni–Ti austenitic stainless steels // J. Nucl. Mater. 2015. Vol. 465. P. 565–581.

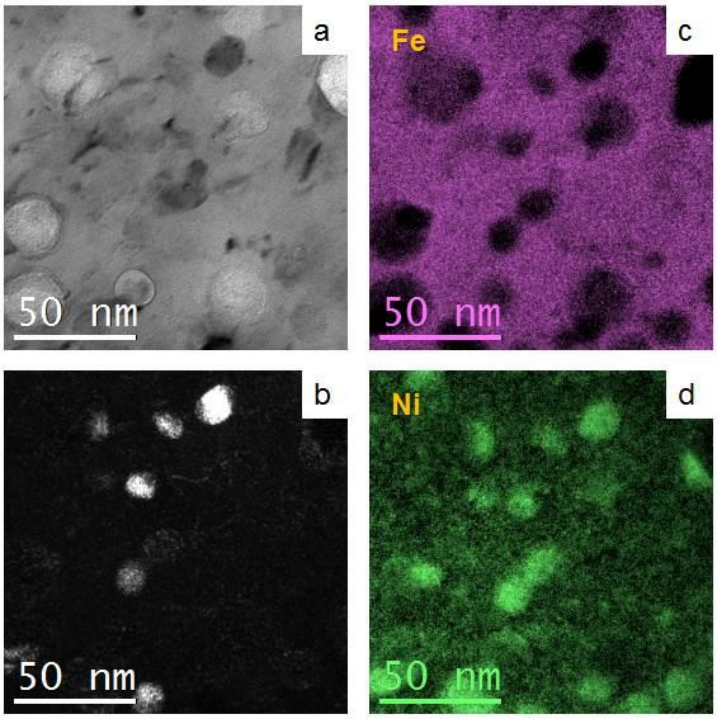

Figure 1. Bright field (a) and darkfield (b) TEM -images of austenitic steel sample, irradiated in the BOR-60 reactor up to ~ 100 dpa in the temperature range of 330-400°C, EELS-map of iron (c) and nickel (d) distribution [5].

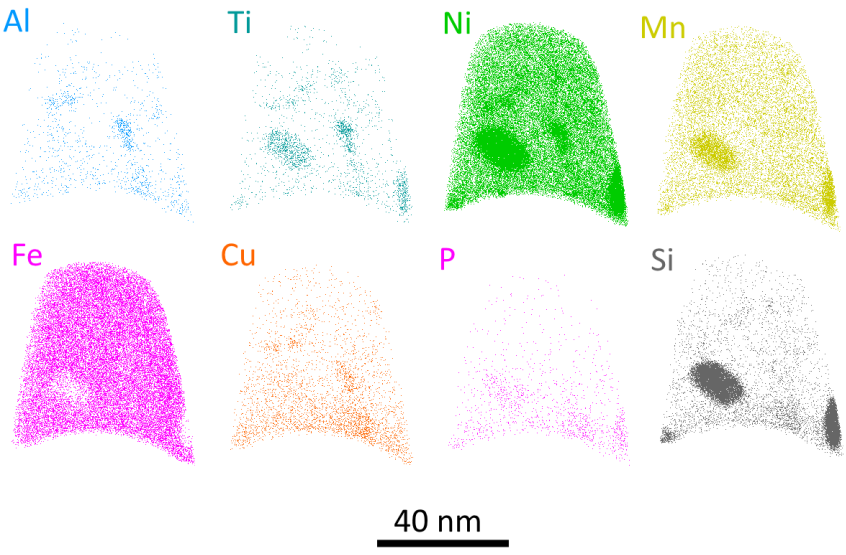

Figure 2. Typical 3D-atom maps in austenitic steel, irradiated in the BOR-60 reactor up to 100 dpa in the temperature range of 330-400°C.

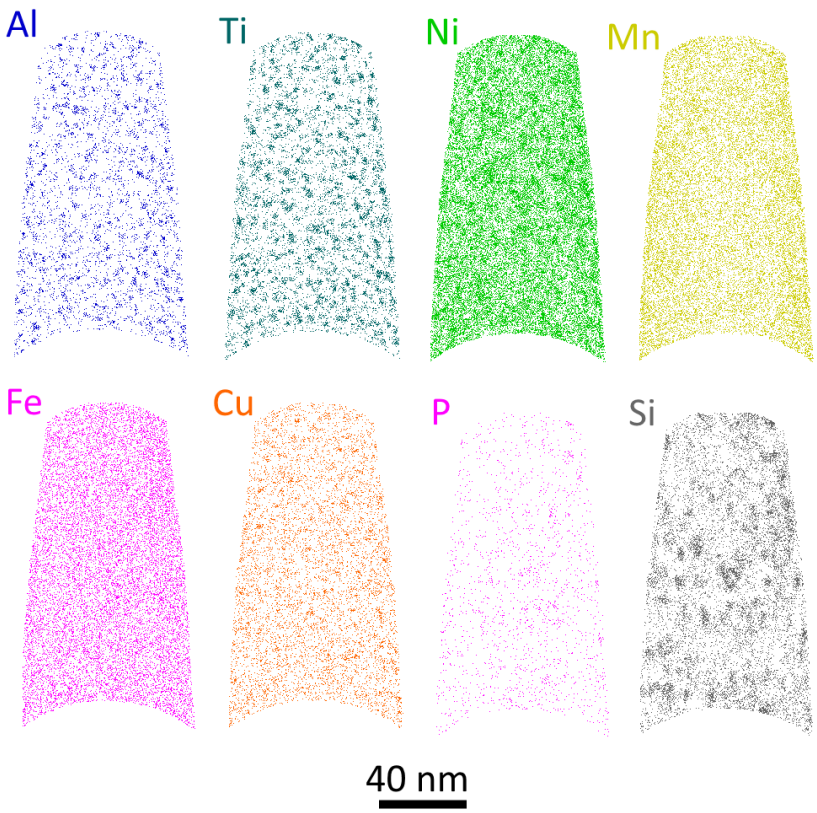

Figure 3. Typical 3D-atom maps in austenitic steel, irradiated in the VVER-1000 reactor up to 12 dpa at the temperature of 330-400°C.

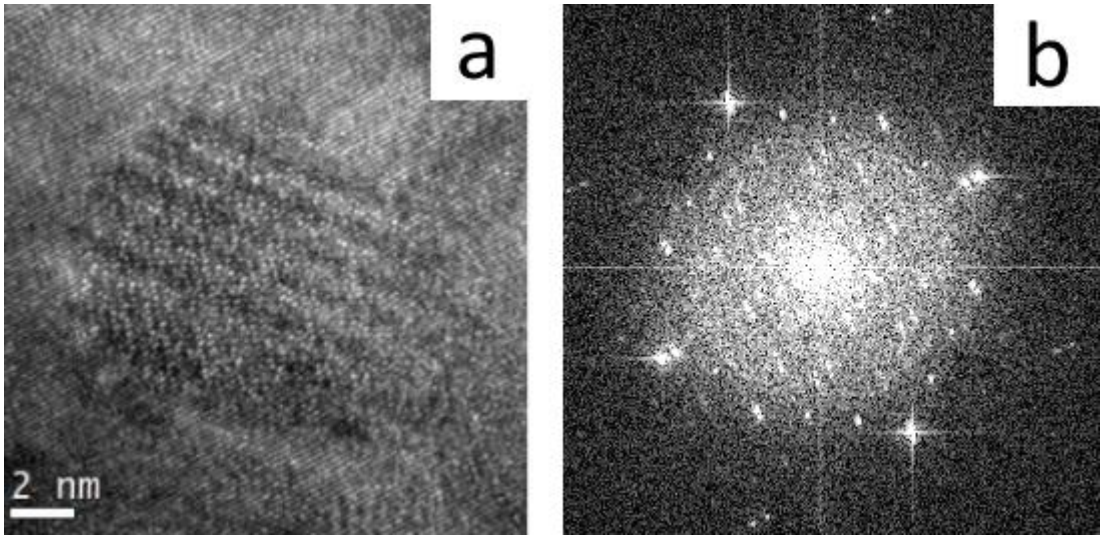

Figure 4. HRTEM-image of G-phase (a) in the austenitic steel sample irradiated in the BOR-60 reactor up to 100 dpa in the temperature range of 330-400°C, corresponding Fourier-transform (b), used to determine the crystal lattice parameters.

IM6.P008
Detection of 3D pigment arrangement in organic coatings using X-ray microscopy

L. Berthold[1], C. Patzig[1], S. T. Kelly[2], T. Höche[1]

[1]Fraunhofer Institute for Microstructure of Materials and Systems IMWS, Halle, Germany
[2]Carl Zeiss Microscopy, LLC, Pleasanton, CA, United States of America

lutz.berthold@imws.fraunhofer.de

Introduction: Plate-like effect pigments (possessing diameters of 5 to 50 µm and thicknesses below 1 µm) are key constituents of coatings deposited on cars, printed media, plastic goods, and architectural objects to just name a few. Besides color impression (caused by interference layers deposited onto core substrates) an important characteristics of pigments in organic coatings is their concentration and the way they are arranged in 3D in the polymer film (Fig. 1). In particular, the orientation distribution and the uniformity of the latter is responsible for what is called sparkle when exposed to intense light. The orientation distribution to be adjusted depends on the application area of the coating. While for metallic appearance, an alignment parallel to the coated object is desired, sparkle is forced by intentionally adding desorienters to the polymeric coating.
Objectives: So far, pigment distributions could only be determined by serial cuts of 2D sections using light or scanning electron microscopy (Fig. 2). Attempts to use X-ray computer tomography proved only successful for comparatively large and thick pigments, embedded in coatings due to the limited spatial resolution of the method (typically a few microns). With the advent of X-ray microscopy (XRM), a lab-based tomographic method becomes available that is characterized by a much better spatial resolution of up to 50 nm. We demonstrate the capabilities of cutting-edge X-ray microscopy for the imaging and determination of 3D orientation distributions of effect pigments in organic coatings.
Materials and Methods: The x-ray microscope used, a Carl Zeiss Xradia 810 Ultra, uses Cr K radiation to image samples in two different fields of view (64^3 µm³ or 16^3 µm³) and two imaging modes (absorption and phase contrast). For polymers, the absorption length is typically large enough so that (ideally cylindrical) samples of a few 100 µm in diameter can be penetrated, also when strongly absorbing pigments are embedded. Utilizing two model coatings (with different orientation distributions of effect pigments), the emerging new capabilities of XRM for the characterization of 3D effect pigment distributions in organic coatings are demonstrated.
Results: Details of sample preparation (mechanical and/or using laser micromachining) will be discussed as well as 3D data assessable via XRM. Besides a 3D representation of the orientation distribution, a quantitative description of the orientation distribution is derived and discussed.
Conclusion: Exemplified by model coatings containing effect pigments, the novel capabilities of XRM in terms of unprecedented spatial resolution of relatively large volumes will be demonstrated. In general, the results can serve as a blueprint for the study of particle orientations in systemic applications. In the future, stitching approaches will make larger 3D volumes accessible.

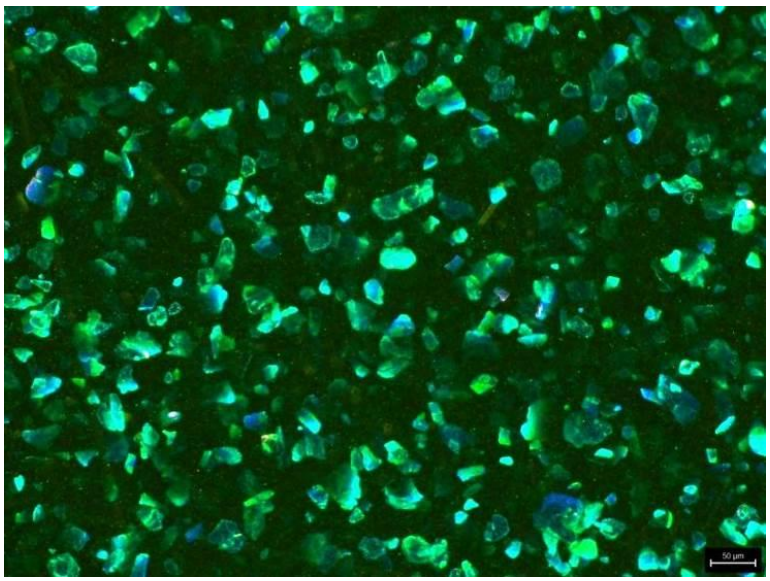

Figure 1. Light microscopy image of pigments in coating.

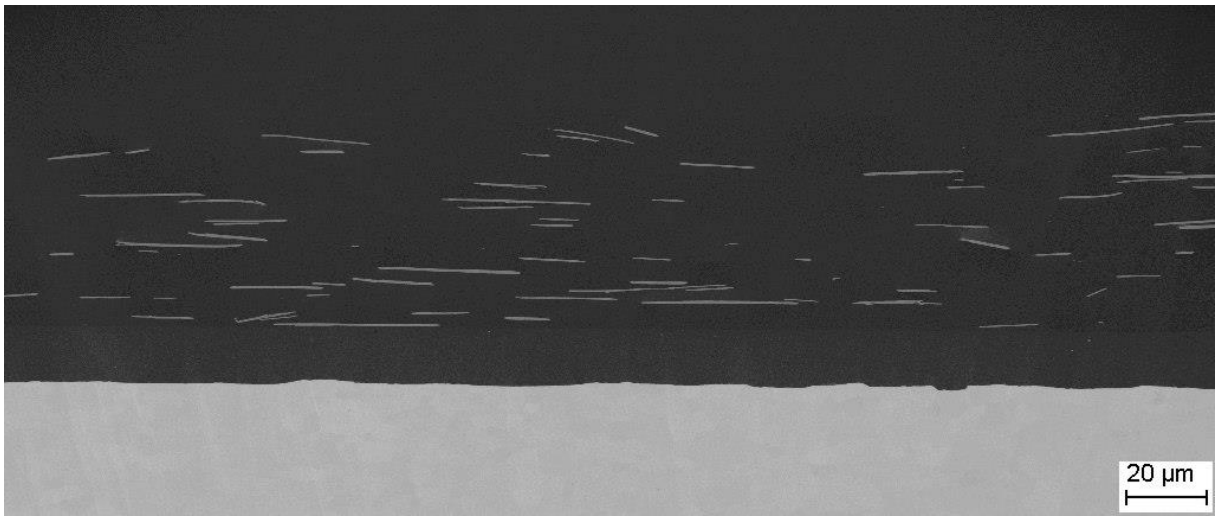

Figure 2. Scanning electron microscopy cross section image of coating with pigments.

IM6.P009
Investigation of the effect of oxide and metal microstructure on the corrosion and hydrogen-uptake behavior using 3D FIB tomography – case of 3 and 9 cycle zircaloy-2 claddings

A. Baris[1], S. Abolhassani[1], Y. L. Chiu[2], H. E. Evans[2]

[1]Paul Scherrer Institut, Villigen, Switzerland
[2]University of Birmingham, Birmingham, United Kingdom

adrienn.baris@psi.ch

The first barrier used in Light Water Reactors is a cladding composed of zirconium based alloys. These alloys are resistant to the reactor"s severe environment. However after a long residence time, they degrade and the fuel rod is extracted from the reactor. This limits the fuel burn-up level and creates waste.
This study concentrates on the oxidation and hydrogen uptake which are among the important factors responsible for degradation [1]. In the case of Zr oxidation, the reaction takes place at the metal surface and hydrogen enters the metal during this process. Once the solubility limit of hydrogen in Zr is reached it precipitates as brittle hydrides. Although these processes have been intensively studied [2-4], certain mechanisms still need to be further understood. The aim here is to characterize the material and correlate the microstructure to its properties. FIB Tomography is one of the recent methods used to study the microstructural changes occurring in the oxide. It is used not only to explore the oxide and its cracks as a function of the number of cycles (i.e. years), but to examine the metal and explore the role of cracks on the H-uptake and oxidation. Automatic slice-and-view by NVision40 FIB-SEM has been applied followed by the computational reconstruction using ImageJ 1.50 software.
The results obtained from claddings with 3 and 9 annual cycles in a Boiling Water Reactor are presented here. Figure 1A represents the surface of the 9 cycle cladding segment. Figure 1B and 1C show an example of the cross sectional SEM images obtained from different sites of the cladding and used for the reconstruction. FIB Tomography results on the 9 cycle sample show that the oxide layer formed in the first three cycles is dense with very few cracks (Fig. 2A). The comparison of this region with the oxide of the 3 cycle material (Fig. 3) shows that an already formed oxide preserves its microstructure with further service and it serves as a "fossil" to study the evolution the oxide microstructure in time. In the 9 cycle material the oxide at the metal-oxide interface, i.e. the oxide formed at the last cycle (Fig 2B) revealed a large number of cracks. It is concluded that the oxide microstructure changes significantly with the number of cycles and must have an influence on the oxidation and H-uptake. The visualization of the hydrides in the metal revealed that in the case of the 9 cycle material hydrides are large phases (Fig. 2C). At some sites at the metal-oxide interface groups of cracks can be found extending from the hydrides (circled area of Fig. 2C). In conclusion, the oxidation of the hydrides may contribute to the crack formation and conversely cracks could be one of the causes of the H-uptake.

References:
[1] B. Cox et al., *Waterside corrosion of zirconium alloys in nuclear power plants*, IAEA TECDOC 996, Vienna 1998.
[2] S. Abolhassani et al., *Zirconium in the Nuclear Industry: 17th Volume*, ASTM International, 2015.
[3] A. Couet et al., *Journal of Nuclear Materials*, 451.1 (2014): 1-13.
[4] B. Cox, *Journal of nuclear materials*, 264.3 (1999): 283-294.

Acknowledgements: swissnuclear and KKL are acknowledged for support of the project.

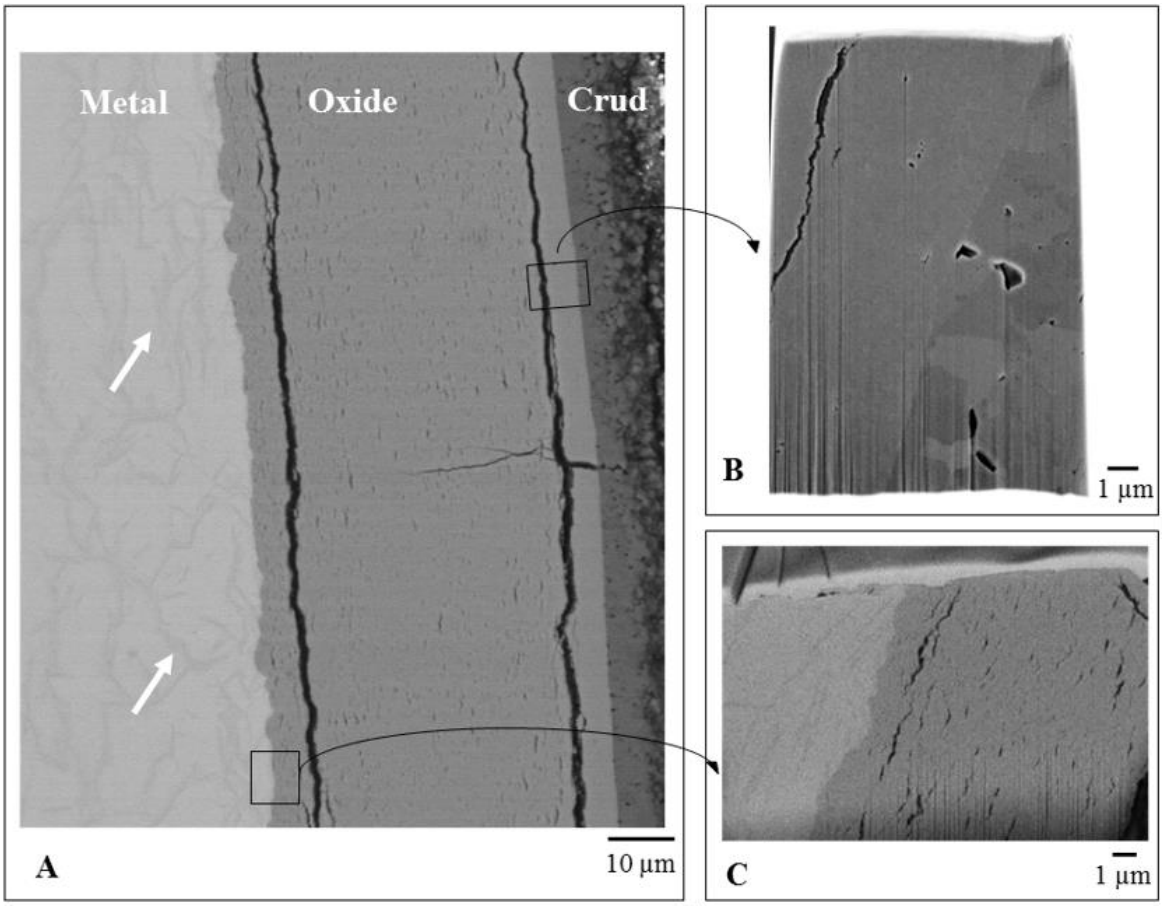

Figure 1. (A) BSE image of the outer part of the 9 cycle cladding (white arrows indicate hydrides). Example images used for the 3D reconstruction of the oxide formed (B) in the first 3 cycles and (C) in the last cycle (i.e. metal-oxide interface).

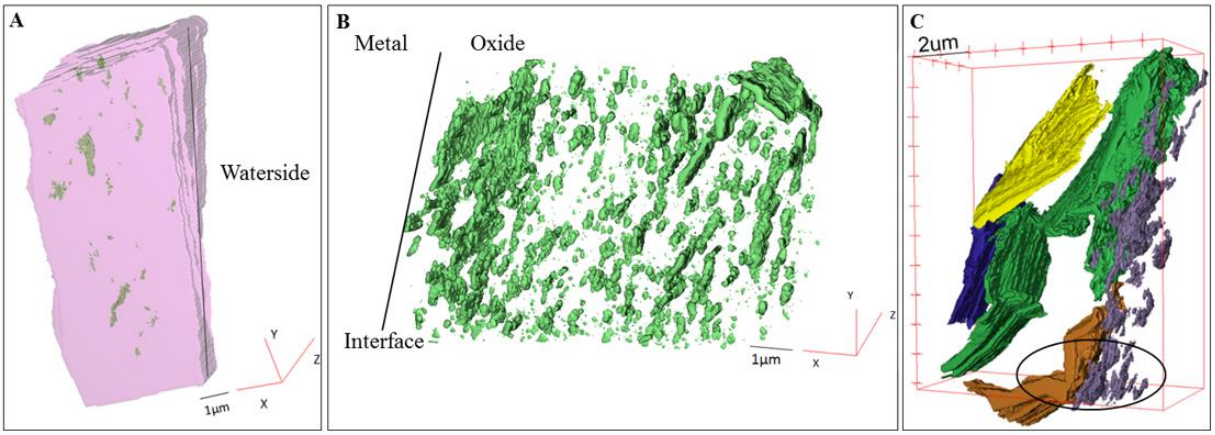

Figure 2. 3D reconstruction of the different parts of the 9 cycle cladding. (A) Waterside oxide as in Fig. 1B (green: cracks, pink: bulk oxide). (B) Cracks in the oxide at the metal-oxide interface as in Fig 1C. (C) Microstructure of the metal-oxide interface. Hydrides are shown in yellow, blue, green, and orange, cracks in the oxide are in purple. Groups of cracks can be found extending from the hydrides (circled area).

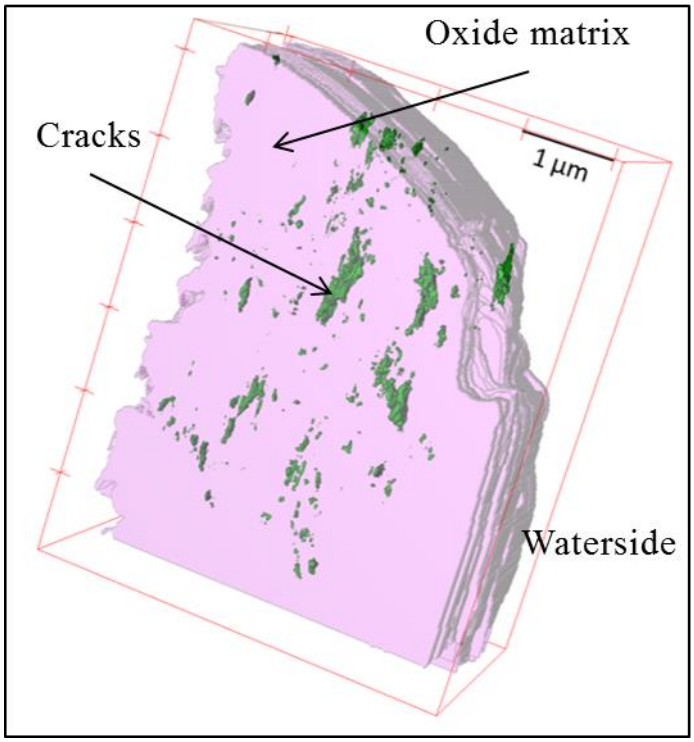

Figure 3. 3D reconstruction of the oxide layer of the 3 cycle cladding segment.

IM6.P010
3D Investigations at structural analysis of high temperature materials

U. Jäntsch[1], M. Klimenkov[1], M. Rieth[1]

[1]Karlsruher Institut für Technologie KIT, Institut für Angewandte Materialien IAM-AWP, Eggenstein-Leopoldshafen, Germany

ute.jaentsch@kit.edu

The development of new high temperature and reduced-activation materials for applications in future fusion-power reactors is an important part of international research activities. Current standard of investigations (state-of-art) on these highly-developed materials include tensile tests as well as metallographic and microstructural investigations using electron microscopy by SEM and TEM, which are completed by analytical methods EDS/EBSD.
In this connection, the Workstation (FIB/SEM) AURIGA 40 with 3D (EDS/EBSD) System, a new tool for research micro and nanostructure on advanced materials plays an important role. Discovering the real existing shapes and location of particles, phases or precipitates in a matrix is an important supplementary information during experimental test series. 3D investigations at the Workstation (FIB/SEM) were running over a long time (18 hours and more) by performing 120 slices in maximum with a voxel size between 50nm and 30nm.
One example is the investigation of two-phase tungsten alloys. The obvious reason of differences in mechanical tests of two alloys with comparable chemical composition could only be discovered by analyzing the different particle shapes in 3D. [1]
Nanostructured tungsten foils that could be used as structural laminate material in future fusion-power reactors, can be successfully investigated only by high-resolution measurements as provided by the Workstation (FIB/SEM). This presentation discusses the results of a 3D measurement of such a nanostructured tungsten foil with a thickness of 100µm.
Another example highlights an additional positional benefit of 3D investigations using EDS and EBSD within one measurement process. In this case, 3D investigations on intermetallic NiAl-Cr (a potential high-temperature turbine material), which shows two phases of equal crystallographic structure, enable a clear allocation of these phases. The result of the investigation was the exact reconstruction of shape and dimension of chromium particles, which strengthened the intermetallic phase NiAl.
As a conclusion, results of 3D investigations are valuable additions to standard investigations (including mechanical testing and SEM/TEM microstructural analyses) and they are important elements for further research and developmental work.

[1] M. Rieth, A. Hoffmann, Influence of microstructure and notch fabrication on impact bending properties of tungsten materials, International Journal of Refractory Metals & Hard Materials, 28 (2010) 679-686.

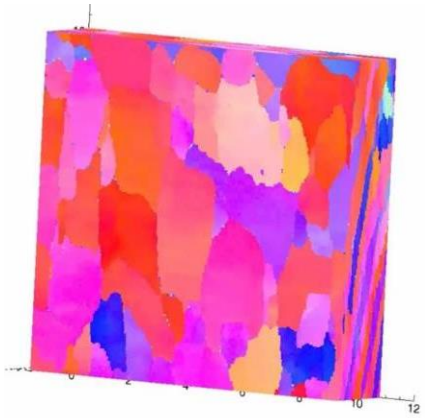

Figure 1

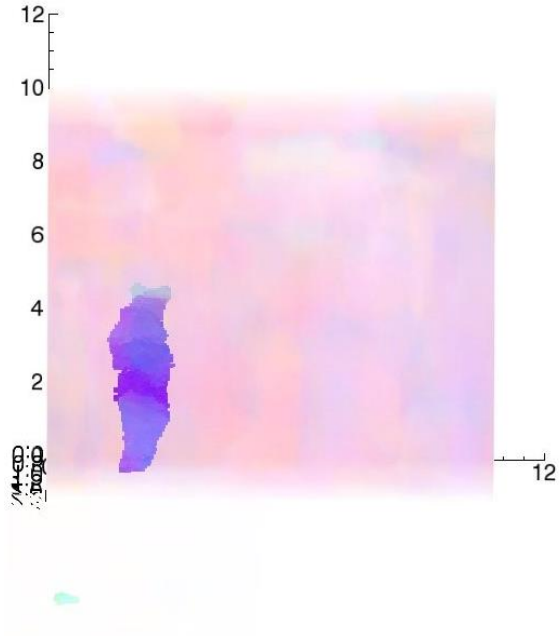

Figure 2

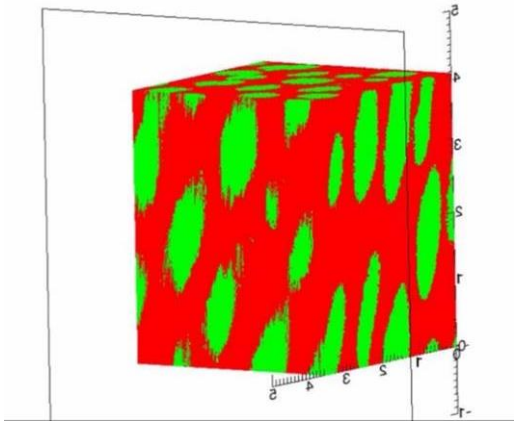

Figure 3

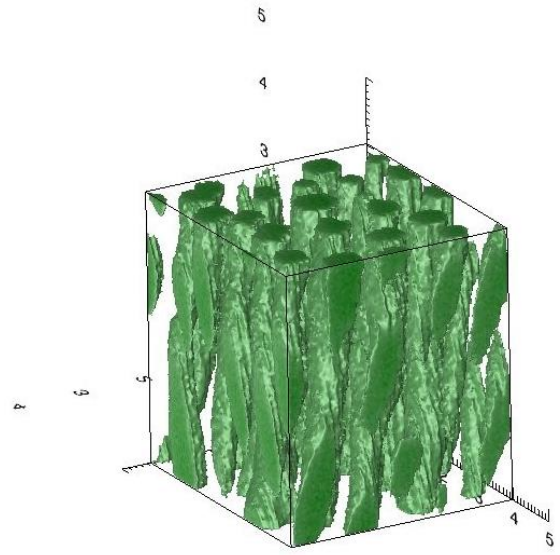

Figure 4

IM6.P011
Electron tomography analysis of islet amyloid polypeptide aggregates in drosophila melanogaster

L. Xie[1,2], K. Okamoto[2], X. Gu[2], G. T. Westermark[2], K. Leifer[1]

[1]Uppsala University, Engineering Department, Uppsala, Sweden
[2]Uppsala University, Uppsala, Sweden

ling.xie@angstrom.uu.se

The aggregation process of the amyloid polypeptides has a great impact on human health and intense research is ongoing to understand their nature[1]. Though, to our knowledge, a detailed analysis of the 3-dimensional structure of amyloid aggregates is still lacking to date. In this work, we have taken a model system to study the structure of such aggregates, the human islet amyloid polypeptide (hIAPP) aggregates that are present in the fat body tissue surrounding the brain of *Drosophila melanogaster*. Electron tomography technique showed clear crystalline structures of the aggregates in 3D. For the first time, we could find the presence of a 5-fold twinned structure in biology that otherwise is only present in crystalline nanoparticles. An intriguing finding is the filament like interconnection of hIAPP protein granules observed predominantly along the nearest neighbor directions. The observation from single particle counting algorithms of the filaments connecting the hIAPP protein granules suggests the existence of the directional binding forces between two nearest protein granules in addition to dipole-dipole interactions taking so far to model the protein granule binding forces. This observation thus shades new light on the aggregation mechanisms of amyloid polypeptides.

References:
[1] Sipe JD, et al., Amyloid, 2012,19:167

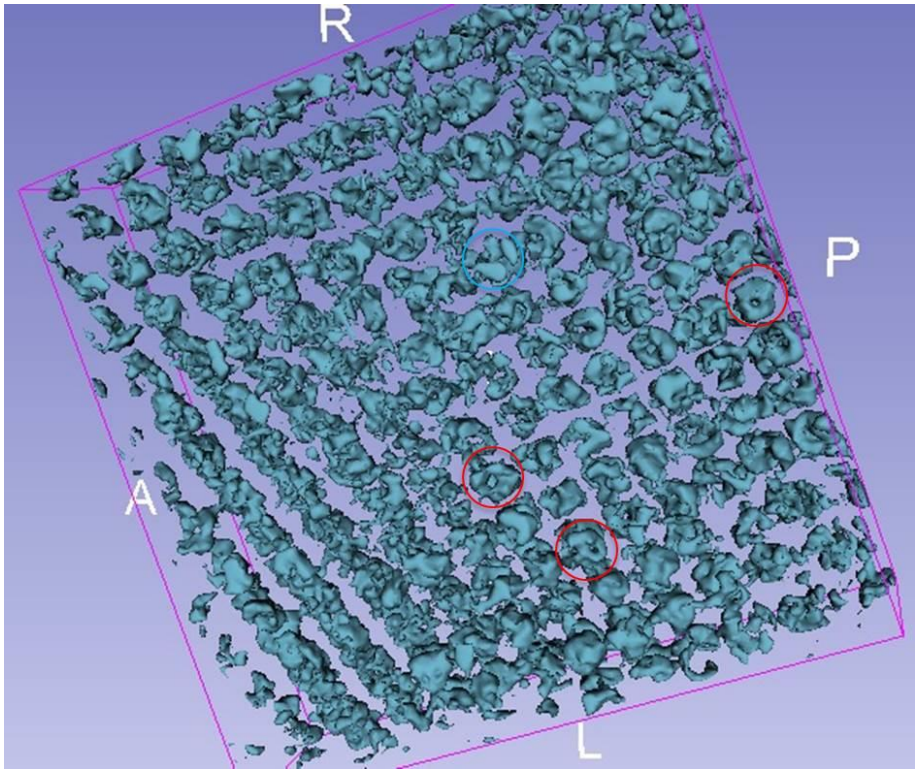

Figure 1

IM6.P012
Insights into the 3D electric potential structure of III-V semiconductor core-multishell nanowires through combined STEM and holographic tomography

D. Wolf[1,2], R. Hübner[1], S. Sturm[2], A. Lubk[2]

[1]Helmholtz-Zentrum Dresden-Rossendorf, Institute of Ion Beam Physics and Materials Research, Dresden, Germany
[2]Leibniz Institute for Solid State and Materials Research, Dresden, Germany

d.wolf@hzdr.de

Off-axis electron holographic tomography (EHT) has been successfully applied to reveal the 3D structure of III-V semiconductor core-shell nanowires (NWs) [1,2]. The technique probes the phase shift of an electron wave transmitted through such a NW that is proportional to the NWs projected electrostatic potential. Thus, a tilt series of phase images (projected potentials) can be used as input to compute a 3D tomogram of the electrostatic potential by tomographic reconstruction algorithms. Typically, the recovered 3D potential is dominated by the mean inner potential (MIP), which is related to the materials composition. Consequently, space charge potentials determining for example the electric properties, *e.g.*, at interfaces or pn-junctions in semiconductors [2] may be superimposed by MIP variations caused by compositional changes within the heterostructures.
Here, we show on the example of a GaAs/AlGaAs core-multishell NW, how the space charge potentials can be uncovered from materials contrast (MIP) by determining the latter independently: To this end, high-angle annular dark-field (HAADF) STEM tomography was applied in addition to EHT on the same NW. STEM tomograms provide solely materials contrast that depends exponentially on the atomic number. Fig. 1 compares both methods in terms of the relation between reconstructed signal and projected property, exemplary for three different tomogram regions identified as pure Au, GaAs and AlGaAs: In case of EHT between the reconstructed potential and the MIP, and in case of STEM tomography between the reconstructed intensity and the atomic number. The latter relation enables converting the STEM tomogram in units of (mean) atomic numbers.
Tilt series were acquired from -70° to +71° with 3° tilt steps in holography mode, and from -68° to +68° with 2° tilt steps in STEM mode. Since phase images of axially scattered electrons are used for EHT, it suffers much more from diffraction contrast than STEM tomography (high-angle scattering). Consequently, only 39 projections could be used for tomographic reconstruction in the case of EHT compared to 68 in the case of STEM tomography. For this reason, resolution and contrast in the 3D potential are slightly lower than in the STEM tomogram, which can be seen on the cross-section of the NW in Fig. 2. Nevertheless, the core-shell structure, the ca. (5-10) nm thick GaAs shell acting as quantum well tube (QWT), and unintended Al segregations are clearly resolved in both cases. Last but not least, longitudinal slices (Fig.3) exhibit clear differences of both tomograms that strongly suggest additional local space-charge related potentials to be investigated in greater detail in a next step.

References:
[1] A Lubk, D Wolf, P Prete, N Lovergine, T Niermann, S Sturm and H Lichte, Phys. Rev. B **90** (2014) p. 125404.
[2] D Wolf, A Lubk, P Prete, N Lovergine and H Lichte, J. Phys. D: Appl. Phys. **49** (2016) p. 364004
[3] We thank N Lovergine of University of Salento, Lecce for provision of the samples.
[4] We thank the group of Michael Lehmann at TU Berlin for access to the TEM FEI Titan 80-300 Berlin Holography Special.
[5] DW acknowledges financial support within the European Union"s Horizon 2020 research and innovation program under Grant Agreement No 688072 (Project IONS4SET). AL has received funding from the European Research Council (ERC) under the European Union"s Horizon 2020 research and innovation programme (grant agreement No 715620).

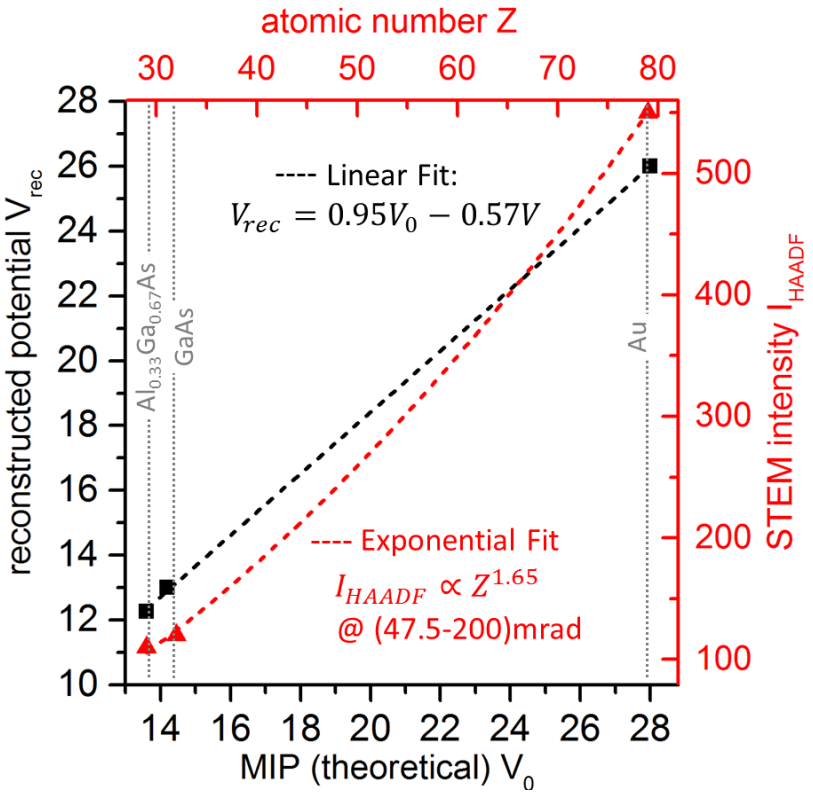

Figure 1. Signals in STEM and EH tomograms of an AlGaAs/GaAs core-multishell NW. Three representative tomogram regions for the three materials AlGaAs, GaAs, and gold present in the NW are used to plot their reconstructed potential vs. mean inner potentials (black) and their reconstructed STEM intensity vs. atomic number (red).

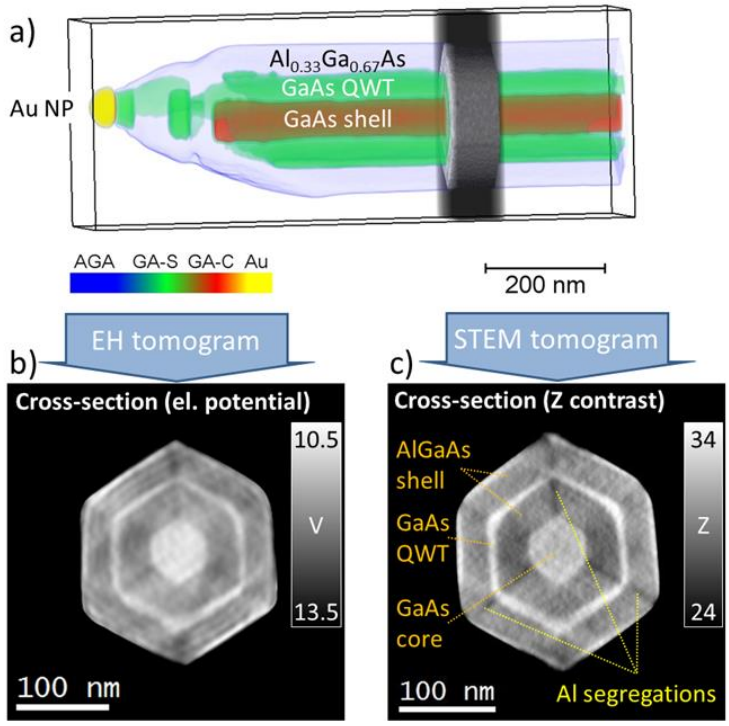

Figure 2. 3D reconstructions of a GaAs/AlGaAs core-multishell NW. (a) Segmented 3D volume rendering. (b,c) Cross-sections at position as indicated in (a) ave-raged over 100 nm thickness for the 3D potential (b) and the Z-contrast tomogram (c) show clearly the core-shell structure but also Al segregations (black lines).

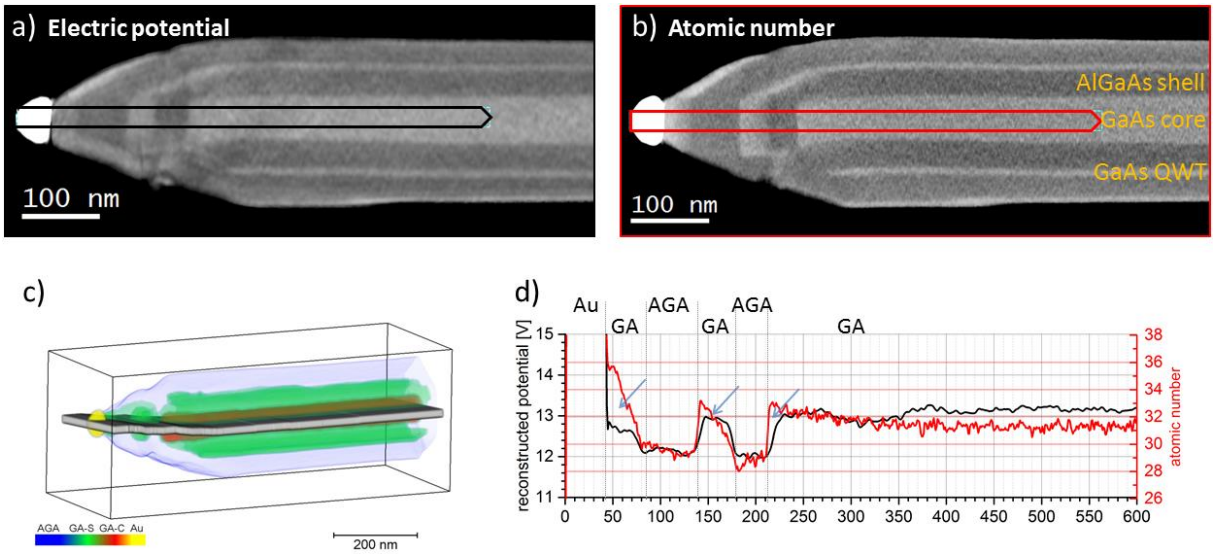

Figure 3. Longitudinal slices (a,b) through the tomograms following the NW center as indicated in the segmented volume rendering (c). (d) Line profiles along the arrows marked in (a,b) show clear differences (blue arrows) in the alternating GaAs AlGaAs segments suggesting additional space-charge related potentials.

IM6.P013
CryoEM to reveal mechanism of broad-spectrum virucidal nanoparticles

M. Müller[1], F. Stellacci[1]

[1]EPFL, STI IMX, Lausanne, Switzerland

marie.mueller@epfl.ch

Viral infections affect millions of people every year. Whilst vaccination successfully prevents certain viral infections and some antiviral substances do exist they are all virus specific and hence limited to a small group of viruses. An efficient equivalent to a broad-spectrum antibiotic is still lacking.
To develop a broad-spectrum antiviral, we choose to mimic a highly-conserved ligand that various viruses utilize to attach onto cells: herparan sulfate proteo glycans (HSPG)1. Previous research has established that sulfonate -functionalized gold-nanoparticles (NPs)2 resemble HSPG such as to be able to bind to viruses and exert an antiviral effect. One of the main obstacles though is that the published antiviral effect is merely virustatic, meaning that upon dilution the nanoparticle detaches from the viruses and releases an unaltered virus. An ideal broad-spectrum antiviral should not only be virustatic, but virucidal – the virus should actually be altered in such a way that it is permanently unable to infect. We therefore developed NPs with longer, more flexible ligands that are able to associate to the viruses in a substantially stronger manner leading to an actual virucidal effect.3
To elucidate the mechanism of this virucidal effect we resorted to electron microscopy (EM). After treatment with virucidal NPs altered viruses could be observed in negatively stained TEM. Although some NPs could be observed near virus capsids or envelopes artefacts caused by adsorption and drying4 of the sample hamper further clear deductions. Consequently, we moved further to CryoEM that permitted us to study the interaction of NPs and viruses in their native solvated state avoiding such artefacts.
Viruses treated with virucidal NPs could be shown to become fully NP-covered and distorted in contrast those treated with virustatic NPs that only marginally attach to the viruses. The three-dimensional distribution of the NPs on the virus was further studied by Cryo-electron tomography. Virucidal NPs both attach faster and to a greater extent to the viruses than virustatic NPs do. The degree of coverage is in agreement with the timeline of the virucidal effect.
To summarize we designed and synthesized virucidal nanoparticles that strongly attach to viruses and used CryoEM to depict the NP-binding and induced virus structure alteration.

References:
[1] Spillmann, D. Heparan sulfate: Anchor for viral intruders? Biochimie 83, 811-817, doi:10.1016/s0300-9084(01)01290-1 (2001).
[2] Baram-Pinto, D., Shukla, S., Gedanken, A. & Sarid, R. Inhibition of HSV-1 attachment, entry, and cell-to-cell spread by functionalized multivalent gold nanoparticles. Small (Weinheim an Der Bergstrasse, Germany) 6, 1044--1050, doi:10.1002/smll.200902384 (2010).
[3] Cagno, V., Andreozzi, P., DAlicarnasso, M., Silva, PJ., Mueller, M., Jones, ST., Vallino, M., Hodek, J., Weber, J., Sen, S., Janeček, ER., Bekdemir, A., Sanavio, B., Martinelli, C., Donalisio, M., Han, Y., Kaiser, L., Vukovic, L., Tapparel, C., Král, P., Krol, S., Lembo, D., Stellacci, F. (paper submitted)
[4] Adrian, M., Dubochet, J., Lepault, J., & McDowall, A. W. (1984). Cryo-electron microscopy of viruses. Nature. http://doi.org/10.1038/308032a0

IM 7: Phase-related techniques

IM7.001 invited
Mapping of atomic electric fields and charge densities by momentum-resolved STEM

K. Müller-Caspary[1], M. Duchamp[2], F. F. Krause[3], A. Béché[1], F. Winkler[2], S. Löffler[4], H. Soltau[5]
J. Zweck[6], J. Verbeeck[1], S. van Aert[1], R. Dunin-Borkowski[2], A. Rosenauer[3]

[1]Universiteit Antwerpen, EMAT, Antwerp, Belgium
[2]FZ Jülich, Jülich, Germany
[3]University of Bremen, IFP, Bremen, Germany
[4]TU Wien, USTEM, Wien, Austria
[5]PN Detector GmbH, Munich, Germany
[6]University of Regensburg, Regensburg, Germany

knut.muller-caspary@uantwerpen.be

Aberration-corrected STEM currently achieves a *spatial* resolution down to 50 pm. In contrast, recording STEM diffraction patterns with established circular, annular or segmented detectors provides no or very coarse *momentum* resolution due to the integration of diffracted intensities over large angular domains. Attaining both high spatial and momentum resolution is now feasible by employing ultrafast cameras in STEM. By recording 2D diffraction patterns on a 2D scan raster, a 4D data set is obtained as the central quantity in momentum-resolved STEM. Here we show in simulations and experiments how this can be used to measure atomic electric fields and charge densities directly.

In quantum mechanics, the first moment of a diffraction pattern is related to the expectation value of the momentum transfer and quantitatively yields the angular deflection of the STEM probe [1]. This overcomes ambiguities in conventional differential phase contrast STEM where segmented detectors record portions of the diffraction pattern [2]. Our concept is explained in Fig. (a), showing a focused STEM probe at (1) a nearly field-free region and (2) close to an atom. Whereas the propagation direction is preserved in case (1), the interaction with the electric field for case (2) causes both a distorted wave front and a deflection to the right. For a Ga column in a GaN crystal with 1.3 nm thickness, we simulated the Ronchigrams on the right and determined the first moments as indicated. In this way, the complexity of the Ronchigram condenses to a single vector with fundamental physical meaning: the average deflection of the STEM probe.

Due to Ehrenfests theorem, is proportional to the expectation value of the electric field. For sufficiently thin specimens, is also proportional to the projected electric field , convolved with the STEM probe intensity. Furthermore, its divergence directly yields the projected charge density, convolved with the probe intensity [1,3]. An early 4D STEM experiment for $SrTiO_3$ is shown in Fig. (b), where a slow-scan CCD camera was employed to raster a unit cell with 20^2 STEM pixels. The redistributing Ronchigram intensity in the vicinity of the atomic columns is clearly seen (left). From the first moments, the atomically resolved electric field is obtained (right). As expected from the screened nuclear charge, atoms are sources of the electric field, their magnitude being determined by the atomic number.

We then present 4D-STEM results on 2D sheets of MoS_2 employing the ultrafast pnCCD camera [4] with 4 kHz frame rate. Fig. (c) depicts the projected charge density measured at a mono-/bilayer (ML/BL) edge (left) with respective unit cell averages (right). By comparison with DFT and 4D STEM simulations we show that the data agrees with theory quantitatively. Additionally, a comprehensive analysis of partial coherence effects is given. Finally, we find an AA stacking of the BL and a Mo-terminated ML/BL edge.

With its ability to map electric fields directly without structural input, momentum-resolved STEM can shed light on the electrical configuration of vacancies, dopant atoms or polarisation fields in future, which we exemplarily discuss using simulations [3].

References:
[1] Nat. Commun. **5**, 5653, 1-8 (2014).
[2] Nat. Phys. **8**, 611-615 (2012).
[3] Ultramicroscopy **178**, 62-80 (2017).
[4] Appl. Phys Lett.**101**, 212110 (2012).

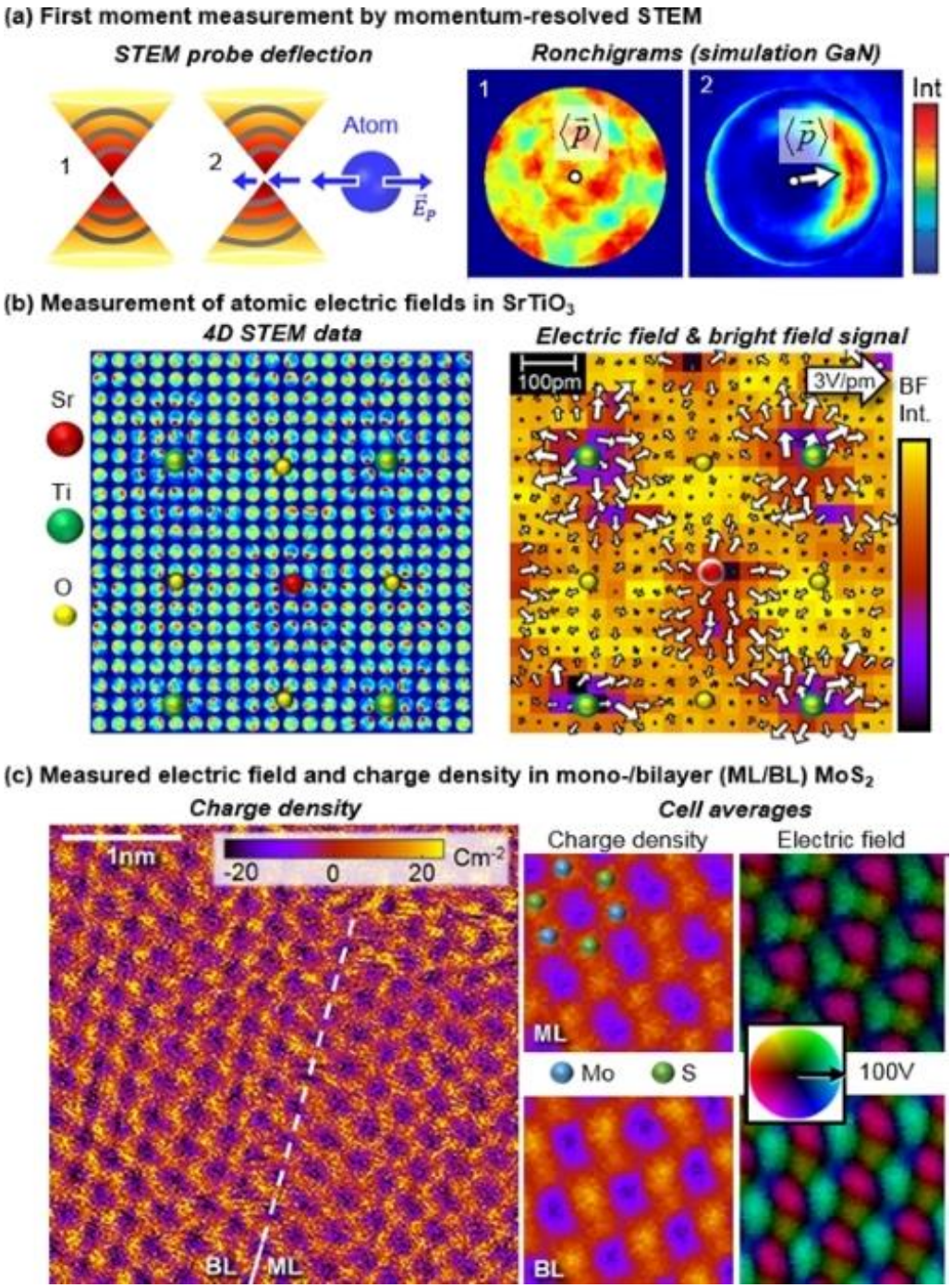

Figure 1. Demonstrating the principle and applications of momentum-resolved STEM: (a) The first moment (centre of mass) is an exact measure of the average angular deflection of the beam. (b) Using a slow-scan CCD, the Ronchigrams of $SrTiO_3$ (left) were acquired on a 20^2 STEM raster. The electric field (right) was calculated from the first moments employing Ehrenfests theorem. (c) Application to 2D-MoS_2 using the ultrafast pnCCD camera at 4kHz frame rate. The STEM raster was 256^2 pixels. Average monolayer (ML) and bilayer (BL) charge densities and electric fields are shown on the right.

IM7.002
Time-resolved electron holography by interference gating

T. Wagner[1], T. Niermann[1], M. Lehmann[1]

[1]TU Berlin, IOAP, Berlin, Germany

tolga.wagner@physik.tu-berlin.de

Electron holography (EH), with its advantage of providing amplitude and phase information of an object-exit wave, directly measures the associated static electric potentials and magnetic fields [1]. The extension to dynamic processes is challenging, as the time-resolution of EH is limited by the long exposure times, which are needed to obtain data well above noise. For reversible processes this hurdle usually is overcome by pump-probe techniques which are technically very demanding and require dedicated TEM hardware to be realized [2,3].
A simple, yet promising approach for a temporal gating is presented by exploiting the high sensitivity of interference setups like electron holography to controlled instrumental instabilities. An elegant way for introducing small instabilities as a gating in off-axis EH is the synchronized modulation of the biprism voltage and hence the angle between the interfered beams.
To prove the possibility of time-resolved electron holography by interference gating, the electrical field of a capacitor as a simple exemplary object was used in the FEI Titan 80-300 Berlin Holography Special TEM (left part of Fig. 1). The electrical wiring of the capacitor and biprism is shown in the right part of the schematic in Fig. 1. The voltages $U_c(t)$ applied to the capacitor and the additional biprism voltage $u_f(t)$ were generated utilizing the D/A converter of a PC sound card (Realtek ALC883 chip) operated at 48 kHz with 16 Bit PCM samples. The biprism was additionally biased by U_{bat} = 47 V using five serially connected 9V batteries.
A visualization of the gating mechanism is shown in Fig. 2. A a square wave signal $U_c(t)$ between -0.81 V and 0.85 V with a frequency of 1 kHz was applied to the capacitor. The gating was realized by adding a white noise signal ($u_f(t)$ of ± 1.92 V) to U_{bat} outside the gating interval, hence destroying the interference pattern. Inside the gating interval $u_f(t)$ vanishes allowing the hologram to be observed. The chosen gating intervals #2 and #4 are centered on the two edges of the square wave, while gatings #1 and #3 sample its constant levels. For the latter a constant slope in between the plates of the capacitor is expected, where gating intervals #2 and #4 should produce a signal similar to double exposure electron holography [4].
The reconstructed phases of the temporally gated holograms in Fig. 2 show the expected behavior in the region between the plates. With this setup, time-resolved electron holography was demonstrated allowing the measurement of periodically changing potential variations of the sample on microsecond time scales with nanometer spatial resolution currently limited by the simple hardware of the D/A converter.

References:
[1] H. Lichte & M. Lehmann: *Rep. Prog. Phys.* 71 (2008) 016102
[2] O. Bostanjoglo et al.: Ultramicroscopy 81 (2000) 141
[3] A. Feist et al.: Ultramicroscopy, (in press) 2016.
[4] C. Gatel et al.: Journal of Physics D, 49 (2016) 324001.
[5] We gratefully thank Dr. Martin Linck and Dr. Heiko Müller (CEOS Corrected Electron Optical Systems GmbH) for help with the special setup of the image Cs-corrector and Dirk Berger (ZELMI) and Udo Hömpler for help with the FIB preparation of the capacitor.

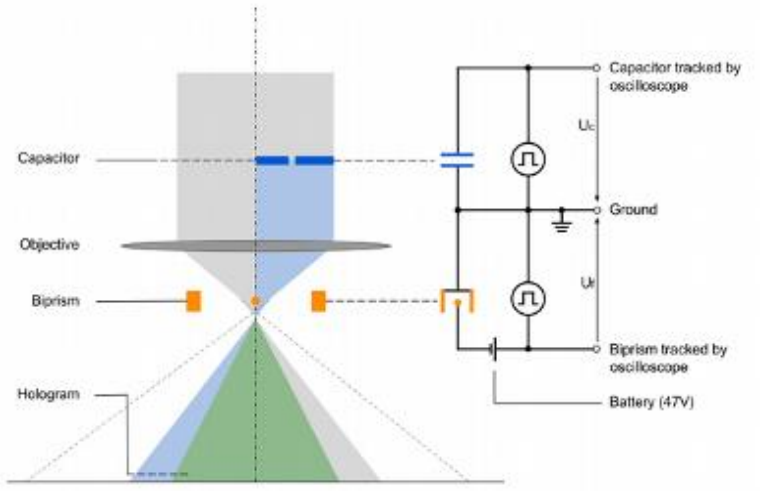

Figure 1. Schematic experimental setup. Left, simplified ray path inside the TEM. Right, electrical wiring of the capacitor and biprism.

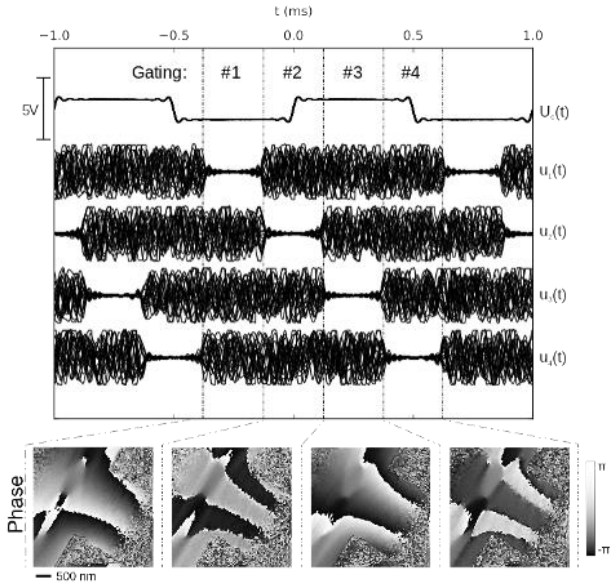

Figure 2. Top, signal $U_c(t)$ applied to the capacitor and the additional voltages $u_f(t)$ applied to the biprism filament for the four different gatings (#1 to #4). For each voltage 20 periods are plotted over each other. Bottom, the reconstructed phases obtained for the individual gating intervals of the square wave: (#1) at negative level (-0.81 V), (#2) edge from negative to positive voltage, (#3) at positive level (+0.85 V),(#4) edge from positive to negative voltage.

IM7.003
Thin-film phase plates for transmission electron microscopy fabricated from metallic glass alloys

M. Dries[1], M. Obermair[1], S. Hettler[1], P. Hermann[1], K. Seemann[2], F. Seifried[2], S. Ulrich[2], D. Gerthsen[1]

[1]Karlsruhe Institute of Technology (KIT), Laboratory for Electron Microscopy (LEM), Karlsruhe, Germany
[2]Karlsruhe Institute of Technology (KIT), Institute for Applied Materials (IAM), Karlsruhe, Germany

manuel.dries@kit.edu

In the past few years, physical phase plates (PP) emerged as an interesting tool to enhance the contrast of weak-phase objects in transmission electron microscopy (TEM). Research has focused on thin-film PPs, which are typically fabricated from thin amorphous carbon (aC) films. Impressive results have been achieved by the application of aC film PPs in the imaging of cells, organelles and proteins [1]. However, the illumination with the electron beam initiates an irreversible degeneration of the aC film, which causes electrostatic charging and affects the phase-shifting properties. Hence, recent investigations have concentrated on the search for alternative PP materials with an improved material stability [2].
This work presents thin-film PPs fabricated from metallic glass alloys, which are characterized by an amorphous structure and a high electrical conductivity. In particular, the zirconium-based alloy $Zr_{65.0}Al_{7.5}Cu_{27.5}$ (ZAC) was identified as a promising PP material with a range of beneficial characteristics, such as a low probability for inelastic plasmon scattering [3]. The only unfavorable effect is surface oxidation of the ZAC alloy at ambient air. The oxide layer reduces the electrical conductivity and leads to electrostatic charging under electron-beam illumination [4]. To avoid surface oxidation, the ZAC alloy was enclosed between two aC layers. For use as a Zernike PP, an aC/ZAC/aC layer system of 7 nm aC, 8 nm ZAC and 9 nm aC was sputter-deposited on freshly cleaved mica substrates. During deposition, the recipient was kept under permanent vacuum, to prevent oxidation of the ZAC alloy. The aC/ZAC/aC film was floated off the mica substrates and placed on gold grids. Using a focused ion beam system, circular holes with different radii were structured into the aC/ZAC/aC film to obtain Zernike PPs with different cut-on frequencies. The Zernike PPs were mounted in the back focal plane of a Philips CM 200 FEG/ST operated at 200 kV. The aC/ZAC/aC film induces a phase shift of 0.75π, which deviates from the ideal value of 0.5π, but is still sufficient to significantly increase phase contrast.
The Zernike PP was applied to image a sample of carbon nanotubes (CNT) on a holey carbon film. The CNTs are arranged in bundles with the individual nanotubes running parallel to each other. Fig. 1a depicts a conventional TEM image taken without the Zernike PP of a CNT bundle positioned across a vacuum region in the holey carbon film. The image was acquired close to focus as can be deduced from the absence of Thon rings in the power spectrum given in the upper right inset. In Fig. 1a, the CNT bundle shows a homogeneous contrast with the individual nanotubes being invisible. Fig. 1b depicts a phase-contrast TEM image taken with the Zernike PP of the same sample region. The hole of the Zernike PP appears as a white circle in the power spectrum, whose radius corresponds to the cut-on frequency of 2.5 nm (0.4 nm^{-1}). In contrast to Fig. 1a, the individual nanotubes are well resolved in Fig. 1b. The CNT bundle shows a fine structure of equidistant fringes corresponding to the individual nanotubes. The periodicity of the fringes is given by 1.4 nm (0.7 nm^{-1}), which is well reproduced in the linescans shown in Fig. 1c.
Zernike PPs fabricated from aC/ZAC/aC films exhibit outstanding charging characteristics. The charging is so weak, that the Thon rings are not distorted, when the PP is inserted in the electron beam. Apart from fringing effects, which are inherent to Zernike PPs due to the abrupt phase onset along the edge of the PP hole, imaging of weak-phase objects is enabled with a high contrast and free of charging artifacts [5].

References:
[1] R. Danev and K. Nagayama, J. Struct. Biol. 161 (2008), p. 211.
[2] M. Marko et al., J. Struct. Biol. 184 (2013), p. 237.
[3] M. Dries et al., Microsc. Microanal. 22 (2016), p. 955.
[4] S. Hettler et al., Micron (2017), accepted.
[5] Financial support by the Deutsche Forschungsgemeinschaft (DFG).

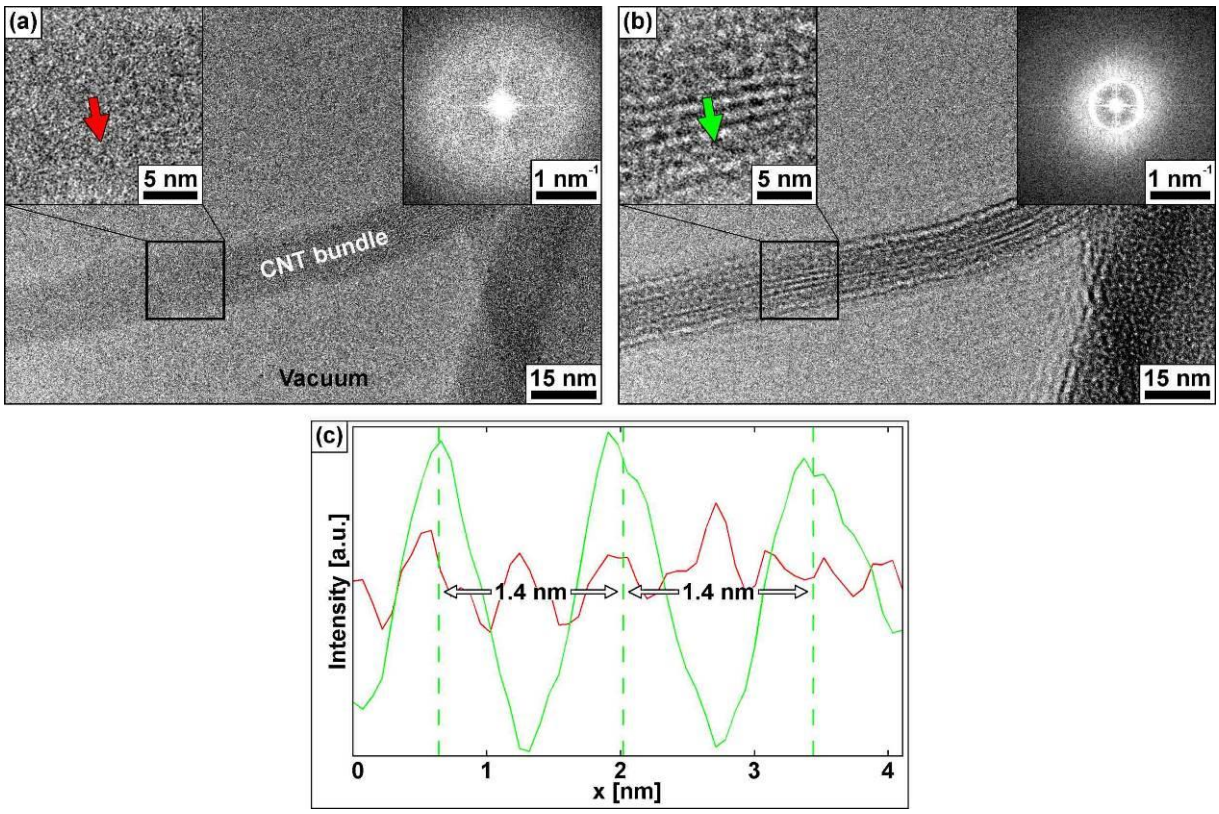

Figure 1. TEM images of CNTs. (a) Conventional image taken without Zernike PP. (b) Phase-contrast image taken with Zernike PP. (c) Linescans along the red and green arrows in Fig. 1a,b.

IM7.004 invited
Electron vortices in solids – from crystalline to amorphous materials

S. Löffler[1,2], S. Sack[2], T. Schachinger[1,2]

[1]TU Wien, USTEM, Wien, Austria
[2]TU Wien, Institute of Solid State Physics, Wien, Austria

stefan.loeffler@tuwien.ac.at

Introduction: Since their discovery [1,2], the interest in electron vortex beams (EVBs) has increased dramatically. As their potential ranges from the detection of magnetic moments on the atomic scale [3] to the manipulation of nanoparticles [4], they hold great promise for advances in many fields, particularly physics and materials science. Most, if not all, future applications will use the interaction of EVBs with samples. Therefore, it is vital to understand how such vortices are affected by materials.
Objectives: In this work, we are mostly concerned with the elastic scattering of EVBs in solids as the inelastic interaction can readily be described using the mixed dynamic form factor (MDFF) approach commonly used, e.g., in energy-loss magnetic chiral dichroism (EMCD). The elastic scattering has already been studied to some extent for crystalline materials [5,6], where a transfer of orbital angular momentum (OAM) and a significant deviation from OAM eigenstates was found. Here, we extend this investigation to amorphous materials which are of huge practical importance. For example, due to the lack of periodicity, classical EMCD is not possible with amorphous materials – but EVB-EMCD is, provided that elastic scattering does not alter the probe electrons wave function substantially.
Materials and Methods: To investigate the propagation of the probe electron, we use the multislice approach. On the one hand, we develop a general and unified theoretical framework based on the multislice equation in cylindrical coordinates to derive conditions under which OAM is exchanged with the sample, thus turning an L_z eigenstate into a coherent superposition of components with different OAM. On the other hand, we use numerical simulations for common materials such as Si to elucidate the underlying physics and support the theoretical calculations.
Results: As shown in Fig. 1, the expectation value of the L_z operator does not deviate much from the nominal value of 1 ħ for reasonably thin amorphous specimens in stark contrast to the crystalline case [5]. At the same time, the contribution of the m=1 eigenstate steadily decreases while other orders emerge. Due to the very similar contributions of m=1+Δm and m=1-Δm, the overall expectation value remains nearly unchanged. These other OAM components can, however, influence the performance of EMCD, nanoparticle manipulation, and similar techniques. For reasonably thin Si and atom-sized vortex beams (Fig. 1), the decrease in m=1 intensity is not too dramatic, but for heaver elements and/or different densities, stronger deviations are found. In addition, the convergence/divergence angle plays a crucial role as differently-sized EVBs scatter differently.
Conclusion: In this work, we have investigated the elastic scattering behavior of electron vortex beams in solids. Going from crystalline to amorphous materials, we have developed a general, unified theory based on the multislice approach and performed numerical simulations. This gives new insights into the behavior of EVBs and paves the way for their efficient use in novel, emerging techniques such as EVB-EMCD or nanoparticle manipulation. [7]

References:
[1] M. Uchida & A. Tonomura, Nature 464 (2010) 737[2] J. Verbeeck et al., Nature 467 (2010) 301
[3] J.-C. Idrobo et al., Adv Struct Chem Imag 2 (2016) 5
[4] J. Verbeeck et al., Adv Mat 25 (2013) 1114
[5] S. Löffler & P. Schattschneider, Acta Cryst A 68 (2012) 443
[6] A. Lubk et al., PRA 87 (2013) 033834
[7] The authors acknowledge financial support by the FWF (J3732-N27, I543-N20)

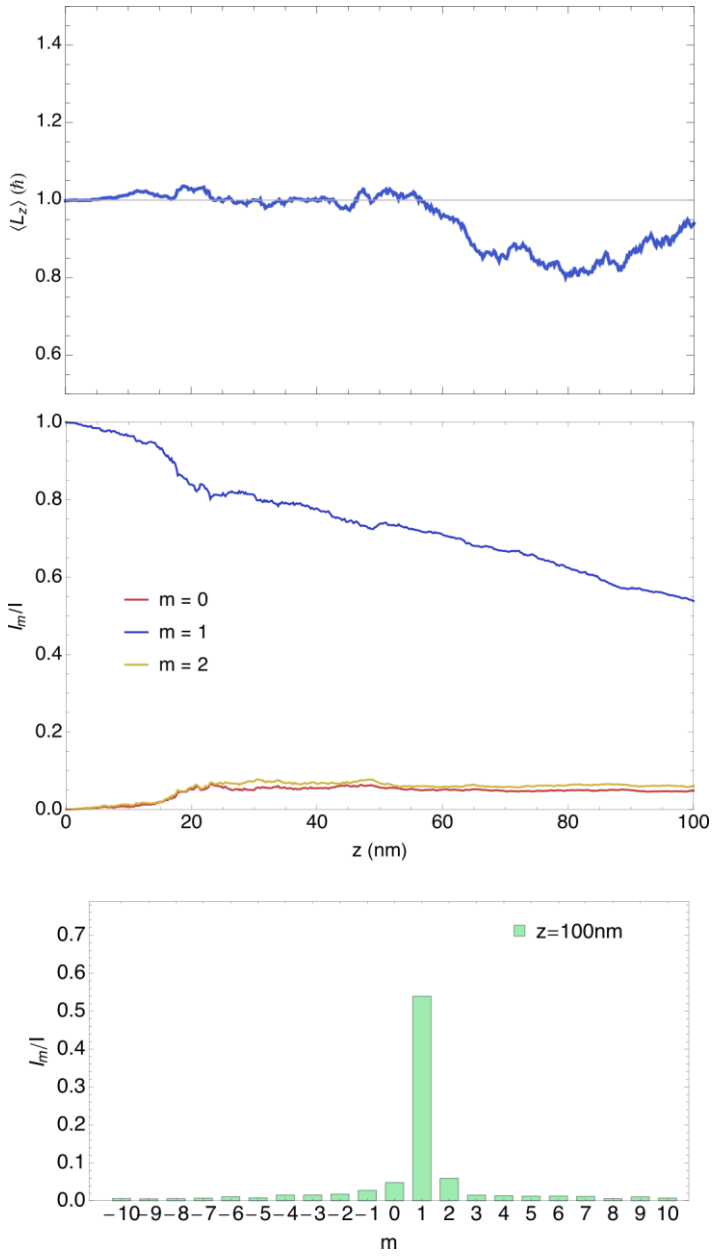

Figure 1. Thickness dependence of the expectation value of L_z (top) and the intensities of different components with OAM=*m* ħ (middle), together with the intensity histogram at 100 nm (bottom) as simulated for amorphous Si with an incident *m*=1 EVB with 20 mrad convergence semi-angle.

IM7.005
Phase imaging – compressive sensing approach

S. Schneider[1,2], A. Stevens[3,4], N. D. Browning[3,5], D. Pohl[1], K. Nielsch[1,2], B. Rellinghaus[1]

[1]IFW Dresden, Dresden, Germany
[2]TU Dresden, Dresden, Germany
[3]Pacific Northwest National Laboratory, Richland, WA, United States of America
[4]Duke University, Durham, NC, United States of America
[5]University of Washington, Seattle, WA, United States of America

sebastian.schneider@ifw-dresden.de

Introduction: Since Wolfgang Pauli posed the question in 1933, whether the probability densities $|\Psi(\mathbf{r})|^2$ (real-space image) and $|\Psi(\mathbf{q})|^2$ (reciprocal space image) uniquely determine the wave function $\Psi(\mathbf{r})$ [1], the so called Pauli Problem sparked numerous methods in all fields of microscopy [2, 3]. Reconstructing the complete wave function $\Psi(\mathbf{r}) = a(\mathbf{r})e^{-i\varphi}(\mathbf{r})$ with the amplitude $a(\mathbf{r})$ and the phase $\varphi(\mathbf{r})$ from the recorded intensity, enables the possibility to directly study the electric and magnetic properties of the sample through the phase.
Objectives: In transmission electron microscopy (TEM), electron holography is by far the most established method for phase reconstruction [4]. Requiring a high stability of the microscope, next to the installation of a biprism in the TEM, holography cannot be applied to any microscope straightforwardly. Recently, a phase retrieval approach was proposed using conventional TEM electron diffractive imaging (EDI). Using the SAD aperture as reciprocal-space constraint, a localized sample structure can be reconstructed from its diffraction pattern and a real-space image using a hybrid input-output algorithm [5].
Materials and Methods: We present an alternative approach using compressive phase-retrieval [6], which does not require a real-space image. The compressive sensing problem has the following formulation. First, we note that the complex-valued reciprocal-space wave-function is in approximation the Fourier transform of the (also complex-valued) real-space wave-function, $\Psi(\mathbf{q}) = FT[\Psi(\mathbf{r})]$, and subsequently the diffraction pattern image is given by $|\Psi(\mathbf{q})|^2 = |FT[\Psi(\mathbf{r})]|^2$. We want to find $\Psi(\mathbf{r})$ given a few differently coded diffraction pattern measurements $y_n = |FT[H_n\Psi(\mathbf{r})]|^2$, where the matrices Hn encode the mask structure of the aperture. This is a nonlinear inverse problem, but has been shown to be solvable even in the underdetermined case [6]. Since each diffraction pattern yn contains diffraction information from selected regions of the same sample, the differences in each pattern contain local phase information, which can be combined to form a full estimate of the real-space wave-function.
Results: To differently code the diffraction patterns, random complimentary pairs of checkerboard masks are cut into a 1.7 µm Pt foil covering a conventional TEM aperture (cf. Figure 1). Used as SAD aperture, subsequently diffraction patterns are recorded from the same sample area (cf. Figure 1). Hereby every mask blocks different parts of gold particles on a carbon support (cf. Figure 1 (Right)). First results of phase reconstruction of this novel approach are presented [7].

References:
[1] W. Pauli in Die allgemeinen Prinzipien der Wellenmechanik, ed. H Geiger and W Scheel, (Julius Springer, Berlin).
[2] A. Tonomura, Rev. Mod. Phys. **59** (1987), p. 639.
[3] J. Miao *et al*, Nature **400** (1999), p. 342.
[4] H. Lichte *et al*, Annu. Rev. Mater. Res. **37** (2007), p. 539.
[5] J. Yamasaki *et al*, Appl. Phys. Lett. **101** (2012), 234105. [6] P. Schniter and S. Rangan, IEEE Trans. on. Signal Proc. **63 (4)** (2015), p. 1043. [7] Supported by the Chemical Imaging, Signature Discovery, and Analytics in Motion initiatives at PNNL. PNNL is operated by Battelle Memorial Inst. for the US DOE; contract DE-AC05-76RL01830.

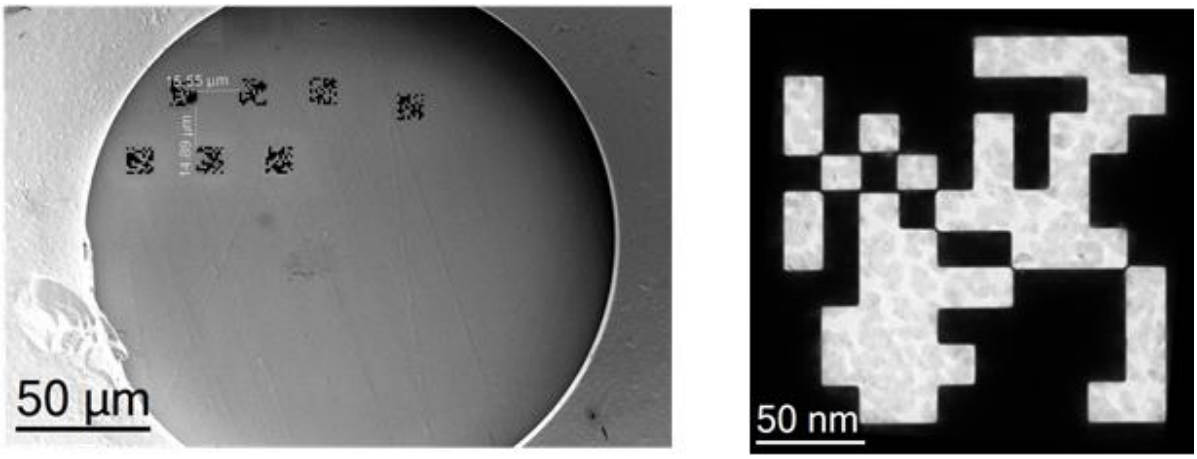

Figure 1. (Left) Conventional TEM aperture covered with 1.7 µm nm Pt foil. Random checkerboard masks are cut into the film using FIB. The masks have a size of 10 µm by 10 µm. (Right) Random mask in the SAD aperture holder blocking the image of gold nanoparticles on a carbon support. The diffraction pattern of this sample area is used for the phase reconstruction.

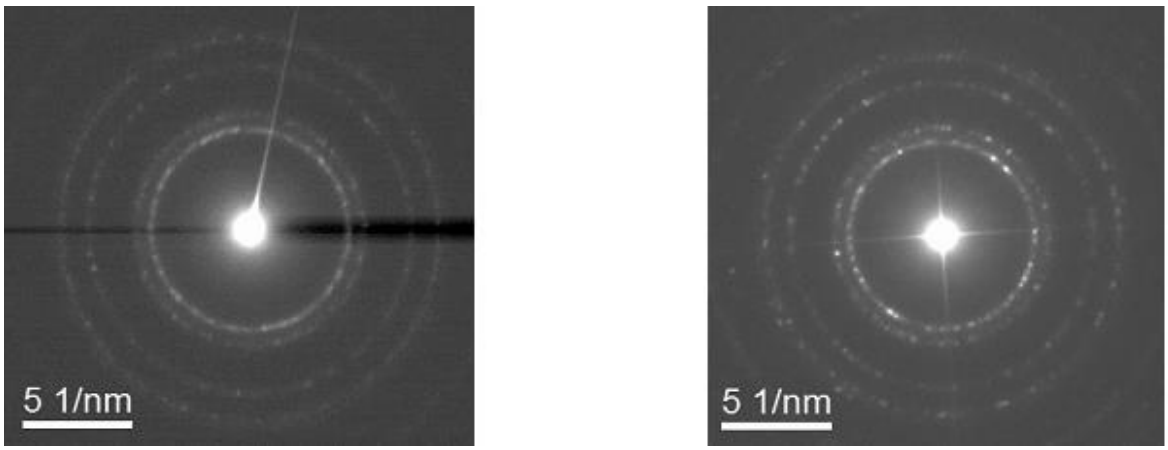

Figure 2. (Left) Diffraction pattern of gold nanoparticles acquired with no SAD aperture inserted. (Right) An example of a coded diffraction pattern using the SAD aperture in Figure 1.

IM7.006
High dose efficiency atomic resolution phase contrast imaging via ptychography

T. J. Pennycook[1], G. T. Martinez[2], L. Jones[2], H. Yang[3], P. D. Nellist[2], J. Meyer[1]

[1]University of Vienna, Vienna, Austria
[2]University of Oxford, Oxford, United Kingdom
[3]Molecular Foundry, Lawrence Berkeley National Laboratory, Berkeley, CA, United States of America

timothy.pennycook@univie.ac.at

Radiation damage places a fundamental limitation on the ability of microscopy to resolve the structure of many types of materials at high resolution. Phase contrast imaging with electrons is recognised as one of the most efficient means of performing low dose imaging at high resolution [1]. In single particle analysis, many identical particles are imaged at very low doses, and these low dose images are then combined to build a model of the object. Thanks to advances in the quantum efficiency of pixelated detectors, single particle analysis in high resolution transmission electron microscopy (HRTEM) has become an increasingly powerful and popular method for determining the structure of delicate beam sensitive materials at the Ångstrom scale [2]. The method does not require that the objects be grouped together into a lattice, allowing many molecules that resist crystallization to be imaged.

However phase contrast imaging in the conventional HRTEM has its drawbacks. Aberrations are intentionally injected to obtain useful levels of image contrast, by forming a virtual phase plate. Such virtual phase plates are far from ideal, with frequency responses that hinder interpretation and offer poor low frequency contrast. In materials science, scanning transmission electron microscopy (STEM) has become an increasingly popular alternative to the HRTEM, due to its ability to collect scattering information as a function of probe position. However, phase contrast in STEM has until recently been relatively inefficient, with the conventional bright-field detector making use of only a very small fraction of the bright field disk. Recent developments in fast pixelated detectors have made electron ptychography practical, and methods to perform efficient ptychography in STEM at atomic resolution have been developed [3, 4]. The method has been shown to be the most efficient imaging mode in STEM. Efficiency is achieved by determining for each spatial frequency where transfer occurs in probe reciprocal space, collecting phase information from these entire regions, and rejecting other areas which contain only noise.

Here we compare the dose efficiency of ptychographic STEM phase contrast to the conventional HRTEM. Image simulations of simple graphene and an adenosine triphosphate (ATP) macromolecule are used to compare the efficiencies of the two methods and tease out the origin of their differences. The results show the ptychographic method to be considerably more resilient to temporal incoherence, resulting in greater contrast at a given dose than in conventional HRTEM. The reason for this resilience is the presence of achromatic lines in the double disk overlap regions of the ptychgraphic data. In addition to the simulations we will show experimental dose series of graphene collected with STEM ptychography and HRTEM. These findings suggest that with the ever increasing capabilities of pixelated detectors, STEM ptychography may become a method of choice for low dose imaging.

References:
[1] R. Henderson, *Q. Rev. Biophys*. **28**, 171 (1995).
[2] E. Callaway, *Nature* **525,** 172 (2015).
[3] T. J. Pennycook et al., *Ultramicrosopy* **151,** 160 (2015).
[4] H. Yang et al, *Nat. Comms.*, **7**, 12532 (2016).
[5] This research was funded by the EU Marie Skłodowska-Curie grant No. 655760 – DIGIPHASE (TJP).

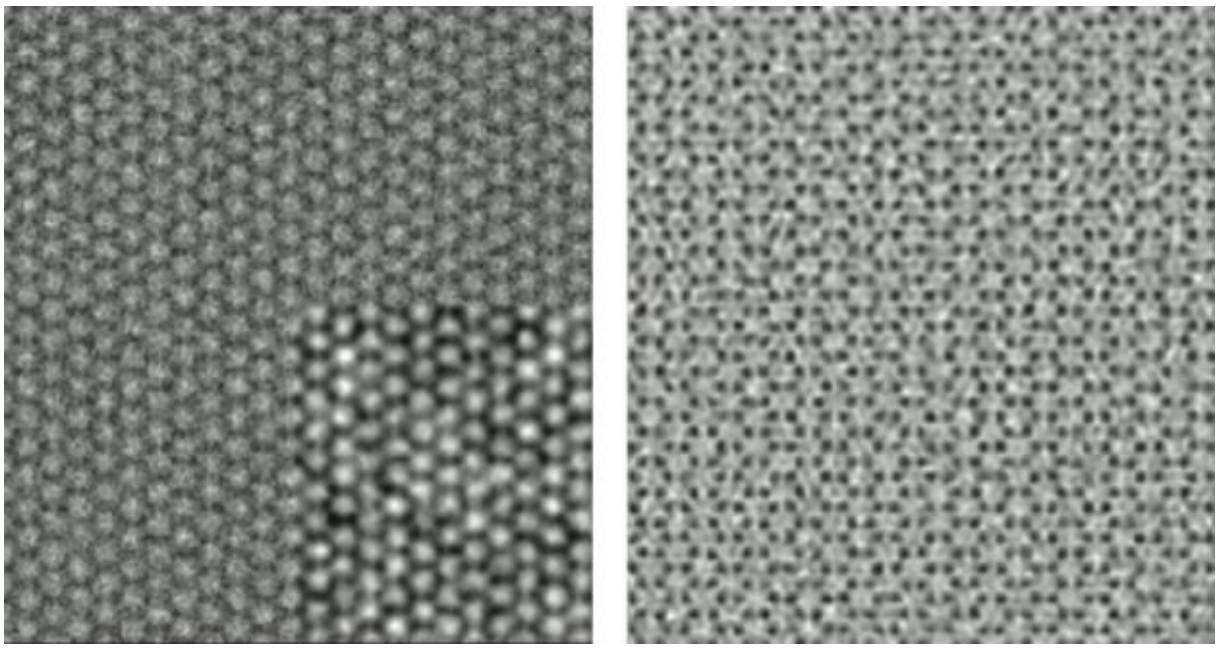

Figure 1. Phase contrast images of graphene simulated with the same dose of 20,000 e-/Å2 and defocus spread of 3.2 nm for both STEM ptychography (left) and HRTEM (right). Scherzer conditions were used for HRTEM, while ptychography was performed on aberration free data. A Butterworth low pass filter is applied in the bottom right of the HRTEM image to illustrate that the ptychography is not just acting as a low pass filter.

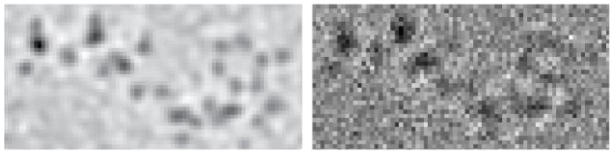

Figure 2. Phase contrast imaging of an ATP molecule, simulated with the same dose of 20,000 e-/Å2 and defocus spread of 3.2 nm for both STEM ptychography (left) and HRTEM (right). A defocus of 2 nm was found to optimize the contrast for the HRTEM image, and again the ptychography was performed on aberration free data.

IM7.P001
Characterization of doping distribution in GaAs nanowires by off-axis electron holography

E. M. Fiordaliso[1]

[1]Center for Electron Nanoscopy, DTU, Lyngby, Denmark

e.fiordaliso@cen.dtu.dk

The development of III−V nanowires on Si, with the aim of reducing production costs while achieving high conversion efficiency, has been a continuing area of photovoltaic research in the last decades[1]. Significant improvements in the understanding of semiconductor device performance are expected if doping and electrostatic potential distributions can be measured quantitatively and reliably with sufficient sensitivity and spatial resolution. The doping in semiconductor nanowires has been assessed by a variety of techniques[2]. Off-axis electron holography in a transmission electron microscope is one of the most powerful methods for dopant assessment, since it enables to measure a spatially-resolved phase contrast from a specimen due to its electrostatic potential[3].Here use electron holography to assess the p-type Be doping of Ga-assisted GaAs NW arrays grown by gas source molecular beam epitaxy (GS-MBE). A cross-sectional specimen for off-axis electron holography was prepared perpendicular to the growth direction of the NWs using focused ion beam milling. A phase map and its corresponding build-in potential map are shown in Figure 1. We find that the Be dopant incorporation is limited by diffusion from three-fold symmetric facets of the NWs, resulting in a remarkable radial and azimuthal distribution of active dopants.

References:
[1] Y.B. Bolkhovityanov and O.P. Pchelyakov, *Physics-Uspekhi* 51 (2008), 437.
[2] J. Wallentin and M.T. Borgström, *J. Mater. Res.* 26 (2011), 2142.
[3] S. Yazdi et al, *Small* 11 (2015) 2687.

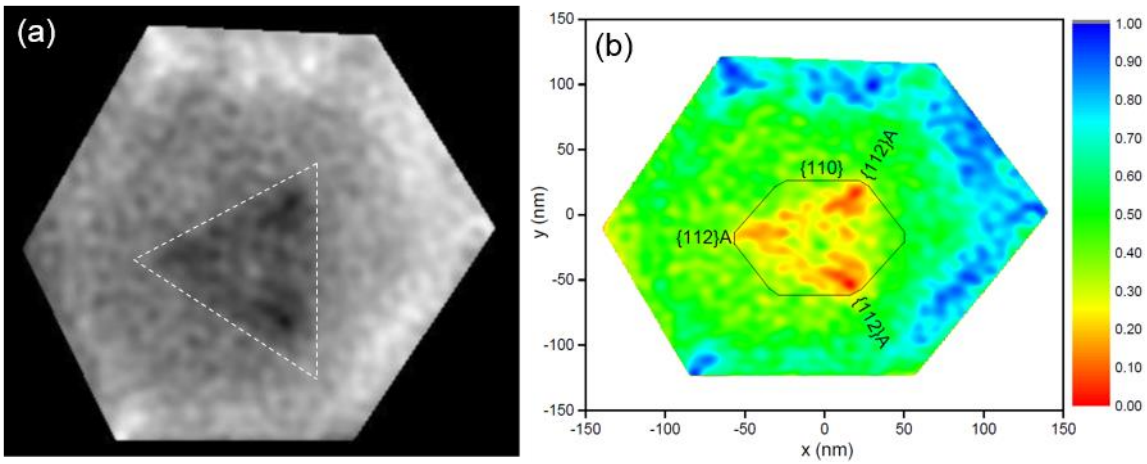

Figure 1. (*a)* Phase map along a NW cross-section. Dashed lines forming a triangle indicate a region of dark phase contrast in the p-core of the GaAs NWs. (b) Corresponding built-in potential *map.*

IM7.P002

Single-shot Quantitative Phase Imaging by using Trifocal Transport of Intensity Equation (T-TIE)

K. Khakurel[1]

[1]Hokkaido University, Sapporo, Japan

krishna.khakurel@gmail.com

Specimens such as cells are transparent to the visible light. As a consequence, the conventional bright field microscopes cannot provide the contrast of the specimen at the focal image plane. Method such as Zernike phase contrast and Differential interference contrast has been developed to overcome the limitation of the conventional bright field microscopes. However, they provide only qualitative phase images and precludes the quantitative phase imaging. A wide variety of interferometric techniques has been introduced for quantitative phase imaging. These methods are instrumentally sophisticated and are prone to loss in sensitivity due to the temporal fluctuation in the interfering beams. Transport of Intensity is a non-interferometric quantitative phase imaging technique which makes use of multiple intensity measurements about the focus [1]. This precludes the method to be useful for the measurement of faster phenomenon in cells such as cell membrane mechanics and nuclear membrane mechanics. Here, we propose a new form of transport of intensity equation method where we measure all the three intensity measurement at a single plane using a trifocal imaging setup. The schematic of the experiment for the proposed method is shown in the Figure 1. To this end, we present the numerical study of the proposed method. Our numerical study proves the feasibility of the single-shot quantitative phase imaging by using trifocal transport of intensity equations.

References:

[1] N. Streibl, Phase retrieval by the transport equation of intensity, Optics Communications 49(1), 6-10 (1984).

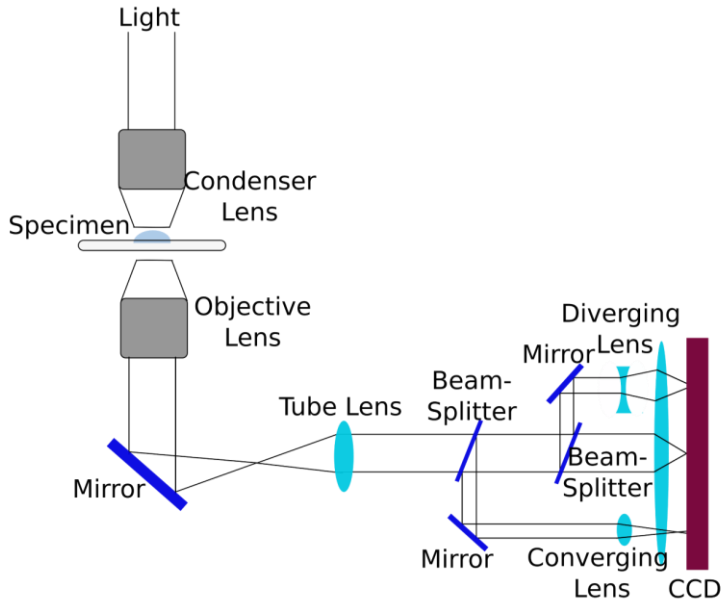

Figure 1

IM7.P003
Contamination and charging of amorphous thin films in a transmission electron microscope

S. Hettler[1], M. Dries[1], P. Hermann[1], M. Obermair[1], D. Gerthsen[1], M. Malac[2]

[1]KIT, Laboratory for Electron Microscopy, Karlsruhe, Germany
[2]National Institute for Nanotechnology, Edmonton, Canada

simon.hettler@kit.edu

Contamination and charging of the specimen is a limiting factor in electron microscopy [1,2]. It can lead to artifacts in transmission electron microscopy (TEM) and especially in scanning (S)TEM, where the electron beam is focused on the sample. On the other hand it is exploited, e.g., in hole-free phase plate (HFPP) TEM [3]. However, the physical reason for charging and thus for the functionality of HFPPs is not yet fully understood. This motivates the study of charging and contamination on amorphous thin films under focused electron-beam illumination using electron-energy loss spectroscopy (EELS) and HFPP imaging. The experiments also provide insight in the behavior of contamination buildup and its prevention which are general issues in EM.

Using the customized electron-optics of a Hitachi HF-3300 allowed us to acquire series of either EEL spectra or HFPP images in dependence of the electron dose with a thin film implemented in the standard sample plane. In a subsequent analysis, the evolution of the relative thickness increase (t/λ) and the phase shift (PS) generated by a beam-induced charge or contamination was obtained [4]. We present results on amorphous carbon (aC) thin films fabricated by electron-beam evaporation (E-Beam aC) and Thread evaporation (Thread aC) as well as on thin films consisting of the metallic glass alloy $Pd_{77.5}Cu_6Si_{16.5}$ (PCS) and SiO_2. The studies were carried out under different experimental conditions and pre-treatments to prevent contamination.

Experiments on untreated thin films shortly after transfer to the microscope show a strong increase in t/λ upon electron-beam illumination (Figure 1). The increase can be attributed to the electron-beam induced deposition of a carbonaceous contamination layer originating from adsorbed hydrocarbon molecules. The PCS sample was pumped overnight in the microscope leading to a decrease in contamination thickness due to desorption of hydrocarbon molecules (Figure 1). Further analysis and C-K edge EELS reveals, that the contamination layer is mainly graphitic carbon [4]. The additional material on the thin film causes a PS which can be estimated if values for its inelastic mean free path and mean inner potential are assumed. The expected PS caused by the thickness increase corresponds well with the measured PS indicating that the deposited graphitic contamination layer does not carry strong charges [4]. Different measures such as UV cleaning, heating or beam showering can inhibit the formation of contamination layers [4].

Clean thin films that do not show contamination may still charge [3]. Figure 2 and 3 show the analysis of the PCS (dashed red line) and the SiO_2 (blue line) thin films. Both thin films were UV cleaned prior to transfer in the microscope and show a minor decrease in thickness upon electron-beam illumination (Figure 2). Corresponding measurements of the induced PS reveal the buildup of a negative PS caused by a negative charging of the illuminated area which is more pronounced for the SiO_2 thin film (Figure 3). The decreasing thickness suggests that desorption processes are involved in the charging of thin films. Electron-stimulated desorption of surface layers can lead to a local work-function change which results in electrostatic fields emerging in the adjacent vacuum causing the detected PS.

The systematic study of contamination and charging of amorphous thin films in TEM shows that both effects can be separated and that contamination deposits created at high current densities are not prone to charging. Thin films not showing contamination may still charge negatively [5].

References:
[1] J. J. Hren, *Ultramicroscopy* **3** (1979), 91-95.
[2] J. Brink et al., *Ultramicroscopy* **72** (1998), 41-52.
[3] M. Malac et al., *Ultramicroscopy* **118** (2012), 77-89.
[4] Hettler et al., *Micron* (2017), 10.1016/j.micron.2017.02.002.
[5] Funding from DFG, KHYS and NRC is acknowledged.

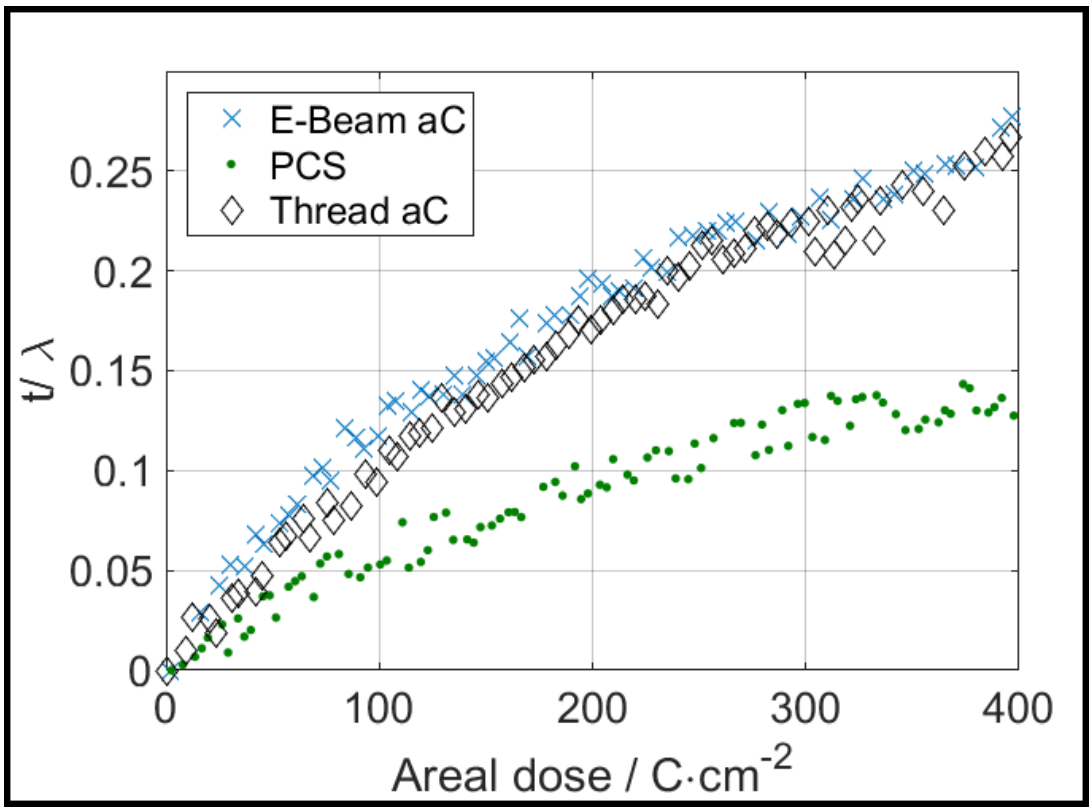

Figure 1. Exemplary evolution of t/λ for three different thin films showing contamination.

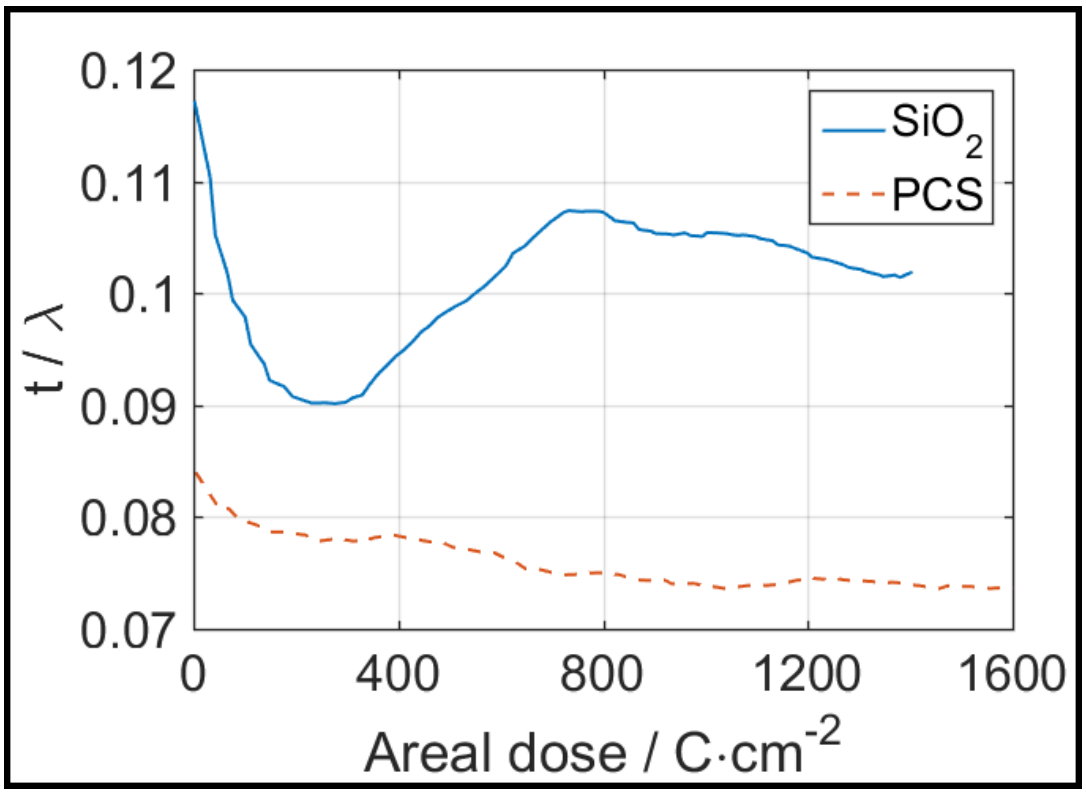

Figure 2. Evolution of t/λ for UV cleaned PCS and SiO_2 thin films.

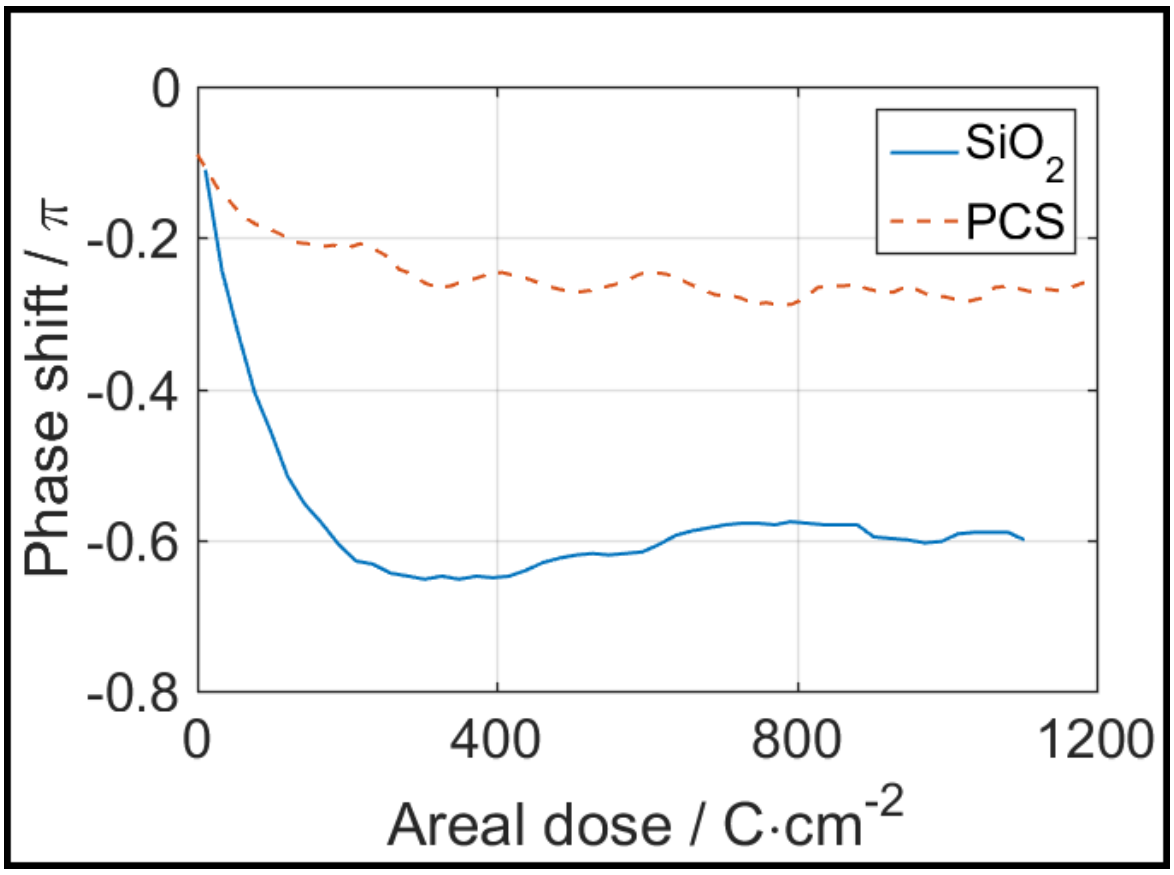

Figure 3. Phase shift evolution of contamination-free PCS and SiO_2 thin films.

IM7.P004
Non-diffractive electron Bessel beams for electron microscopy using direct phase masks

S. Hettler[1], M. Dries[1]

[1]KIT, Laboratory for Electron Microscopy, Karlsruhe, Germany

simon.hettler@kit.edu

Shaping the electron beam for novel applications has gained interest since the generation of an electron vortex beam has been successfully demonstrated [1,2]. Structured thin films or apertures influencing the amplitude and/or phase of an illuminating electron wave allow the production of different types of electron beams. In this research project we focus on fabrication and application of non-diffractive electron beams [3,4] using direct phase masks (PMs) to create single beams with high intensity. The shape of a non-diffractive electron beam is constant upon propagation possibly allowing focused imaging of thick samples in scanning modes in electron microscopy (EM) [5]. Additionally, non-diffractive beams theoretically have the smallest beam diameter.

Fabrication of the PMs is performed by electron-beam evaporation of a Pt protective layer on a Si_3N_4-membrane and subsequent structuring using a FEI Dual-beam Strata 400S focused ion beam system. To ensure reasonable conductivity under electron-beam illumination, the backside of the PM is coated with a thin layer of amorphous carbon. SEM, TEM and atomic force microscopy (AFM) techniques are used to characterize the PMs. The evolution of the propagating electron wave after transmission through the PM is analysed in the low-magnification mode of a FEI Titan³ 80-300.

SEM and AFM analysis of a PM producing a single non-diffractive beam is displayed in Figure 1. The SEM image of the tilted PM shows the protective Pt coating with a round aperture and the structured thickness profile within the Si_3N_4-membrane which consists of rings with a depth of approximately 25 nm as revealed by the AFM image. The Pt protection ensures that illuminating electrons can only propagate through the PM leading to the contrast observed in a focused TEM image of the PM (Figure 2a). Shortly after transmission through the PM, the electron wave evolves in a Bessel function with a central maximum of high intensity and surrounding concentric rings (Figure 2b). This shape is conserved upon further propagation revealing the non-diffractive property of the electron beam (Figure 2a-d).

A decreasing size of the entire electron beam can be observed in the TEM images in Figure 2a-d indicating the presence of a focusing lens. Depending on the electron wavelength λ, the periodicity of structured rings k_0 and the diameter of the aperture D, the non-diffractive property is maintained in field-free space up to a specific propagation length, which is $L = D/(2\lambda k_0) = 1$ m for the used PM. The intensity of the central maximum (ICM) is increasing upon propagation and reaches its maximum at L [3,4]. Figure 3 shows the evolution of ICM determined from the series of TEM images in dependence of the propagation length. In the presence of the focusing lens, ICM is increasing up to a distance of only 135 mm before rapidly decreasing again. The final strong increase is caused by the focusing lens when the beam reaches the back focal plane.

An implementation of a PM in the condenser lens system of an electron microscope allows the generation of non-diffractive electron beams which can be used for imaging. Control over the beam shape is not only given by the geometry of the mask but also by excitation of the condenser lenses [6].

References:
[1] J. Verbeeck et al, Nature **464** (2010), 737-739.
[2] J. Verbeeck et al, C R Phys **15** (2014), 190-199.
[3] J. Durnin et al, Phys Rev Lett **58** (1987), 1499-1501.
[4] V. Grillo et al, Ultramicroscopy **166** (2016), 48-60.
[5] J.K. Hyun et al, Ultramicroscopy **109** (2009), 1-7.
[6] S. Hettler acknowledges funding from the Carl-Zeiss Stiftung.

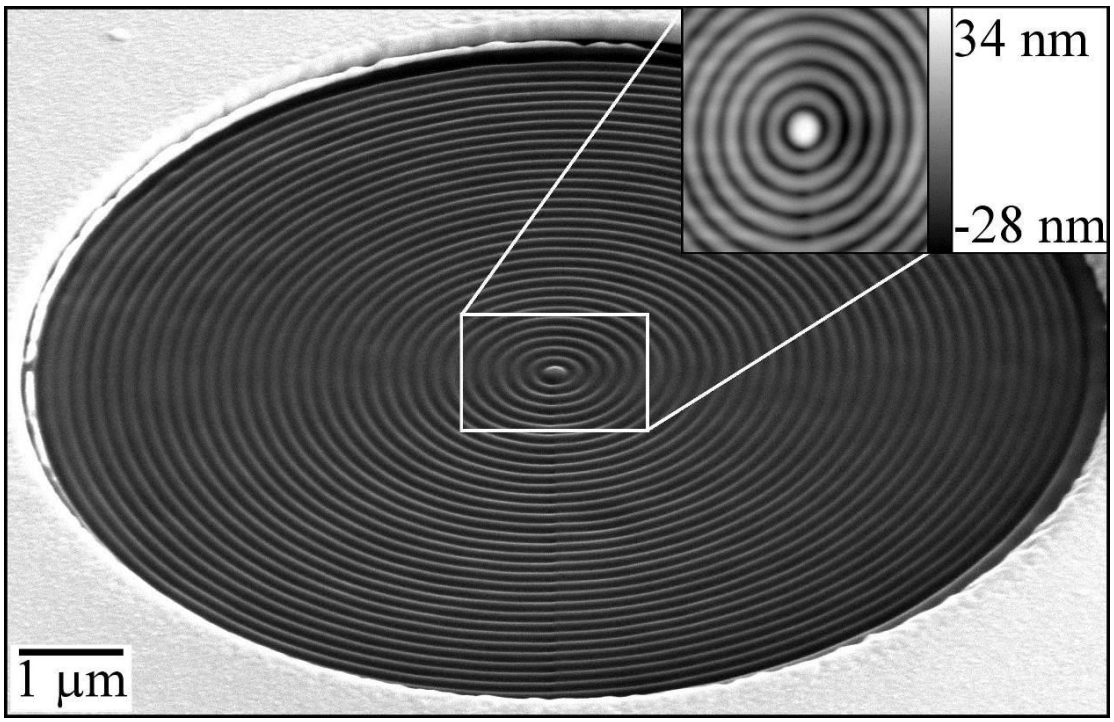

Figure 1. SEM and AFM analysis of a PM for production of a single non-diffractive electron beam with high intensity. The SEM image shows the surrounding Pt protective layer (bright) and the thickness profile within the Si_3N_4 membrane which is revealed in the AFM image (inset).

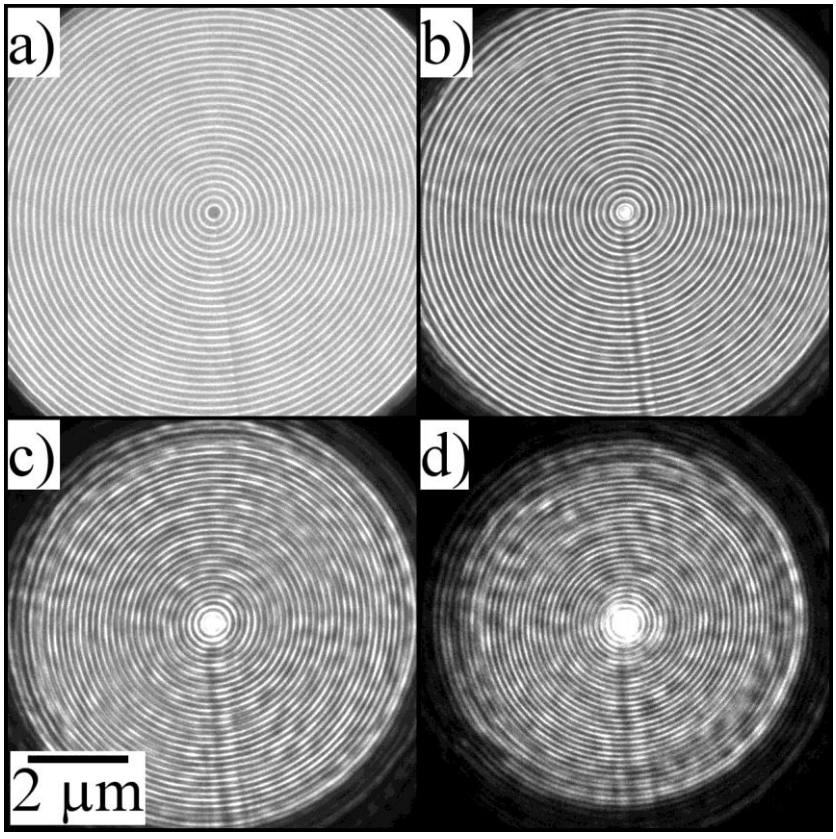

Figure 2. TEM images of the electron wave after transmission through the PM and a following propagation of (a) 0 mm, (b) 21 mm, (c) 42 mm and (d) 64 mm.

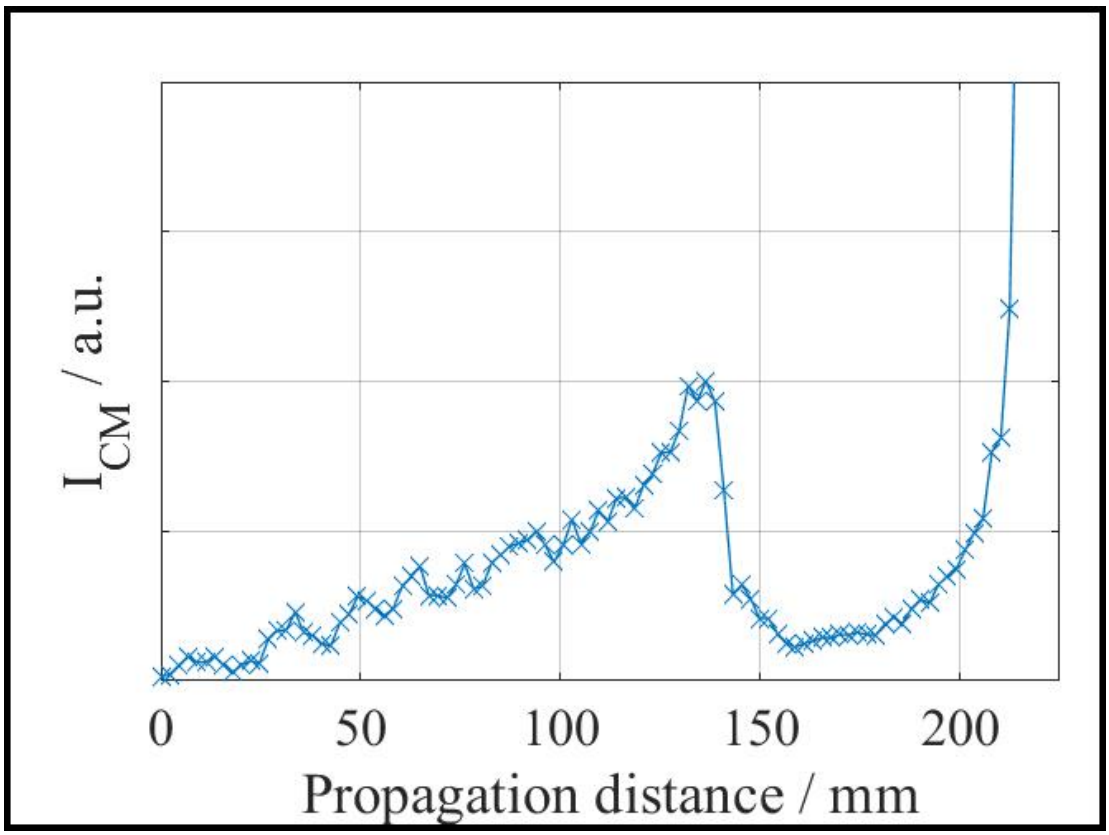

Figure 3. Evolution of ICM in dependence of the propagation distance determined from experimental images.

IM7.P005
Vortex filter-EMCD – challenges and prospects of an alternative EMCD technique

T. Schachinger[1,2], S. Löffler[1,2], A. Steiger-Thirsfeld[1], M. Stöger-Pollach[1,2], S. Schneider[3], D. Pohl[3]
B. Rellinghaus[3], P. Schattschneider[2]

[1]TU Wien, Universitary Service Centre for Transmission Electron Microscopy (USTEM), Vienna, Austria
[2]TU Wien, Institute of Solid State Physics, Vienna, Austria
[3]IFW Dresden, Institute for Metallic Materials, Dresden, Germany

thomas.schachinger@tuwien.ac.at

Introduction: The holographic technique, applied to matter waves, introduced the possibility to produce arbitrarily formed electron wavefronts. A prominent example are electron vortex beams (EVBs). They carry quantized orbital angular momentum $m\hbar$ (OAM) as well as a quantized magnetic moment and can be produced by placing a holographic vortex mask (HVM) in a TEM [1]. Due to their intrinsic chirality, they have become a promising candidate for energy-loss magnetic chiral dichroism (EMCD) measurements using EVBs incident on the sample. However, it soon became clear that atom-sized EVBs are needed to achieve this goal [2,3].
Objectives: In magnetic materials, atom-sized EVBs are naturally produced in inelastic electron scattering events. This study aims at exploring the limitations and possibilities of detecting spin polarized transitions by detecting the OAM content of the outgoing wave field using a post-specimen HVM as a vorticity filter, see Fig. 1 (a). This approach does not rely on the standard EMCD geometry and the specimen's role as a beam splitter, thus it does not require the precise alignment of the crystal – or, in fact, any crystallinity at all. The experiment is intended to be done in TEM mode, but in principle this is a STEM geometry, allowing EMCD measurements down to sub-nm resolution, see Figure 1 (b).
Materials and Methods: To estimate the EMCD signal strength at the $L_{2,3}$-edge of ferromagnetic Cobalt, a single atom scattering approach was used. This approach was justified by multislice simulations (MS), which confirmed that OAM is mostly conserved in amorphous materials over an extended range of sample thickness, see Figure 1 (c). Different artefact sources like spot size, mask tilt, defocus differences between opposing vortex orders (see Fig. 1 (d)) and astigmatism have been identified as crucial parameters for the detection of an EMCD signal [4]. Additionally, inelastic MS were performed confirming the visibility of an EMCD signal in the proposed setup but also pointing out a more complex defocus dependent nature of the EMCD effect.
Results: Preliminary experiments show the feasibility of the proposed setup, see Fig. 2 (a), and are in good agreement with the simulation, see Fig. 2 (b). Curiously, the experimental radial profiles show stronger differences in the central region than is expected from the simulation. Including defocus variations between $m = \pm 1$ EVBs can partially explain the central intensity deviations. However, the achievable signal-to-noise ratio (SNR) poses experimental challenges.
Conclusion: Upon improvement of the SNR and rigorous control of artefacts, this setup can be applied to study magnetic properties of amorphous and nano-crystalline materials on a sub-nm scale to tackle challenging and technologically interesting questions like interface and surface magnetism, as well as magnetic properties close to defects. [5]

References:
[1] J. Verbeeck et al., Nature **467**, 301-304 (2010).
[2] J. Rusz, S. Bhowmick, Phys. Rev. Lett. **111**, 105504 (2013).
[3] P. Schattschneider et al., Ultramicroscopy **136**, 81–85 (2014).
[4] T. Schachinger et al., Ultramicroscopy, submitted
[5] Financial support by the FWF (I543-N20, J3732-N27) is acknowledged.

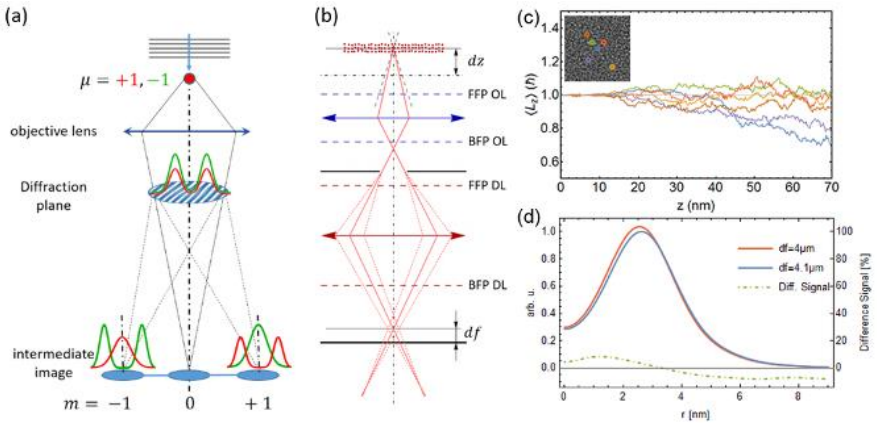

Figures 1. (a) Vortex filter EMCD principle; the EMCD effect leads to an intensity asymmetry in the centre of two opposing vortex orders m = ±1, which are produced by a post-specimen HVM. (b) Detailed vortex filter setup, which basically resembles an adopted STEM geometry. (c) MS of an amorphous Fe-based alloy for different beam positions (see 5 x 5 nm² inset), show negligible OAM exchange of an atomic-sized vortex with the sample, thus justifying the single atom scattering approach. (d) A possible artefact source: the simulation shows the influence of defocus variations between opposing vortex orders on the difference signal.

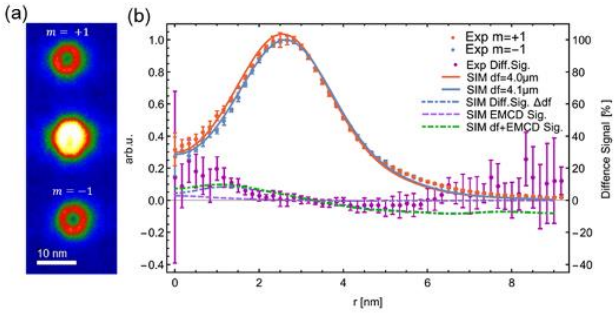

Figures 2. (a) Energy-filtered vortices produced by a SAD HVM at the Co-L_3-edge. Azimuthally averaged radial intensity profiles of m = ±1 EVB in (a) compared to the simulation. Including a defocus variation of 0.1 µm improves the agreement between the simulation and the experiment.

IM7.P007
Determination of parasitic phase shifts of thin-film phase plates

R. Janzen[1], J. Schundelmeier[1], M. Dries[1], D. Gerthsen[1]

[1]Laboratory for Electron Microscopy, Karlsruhe, Germany

roland.janzen@kit.edu

In the past few years, physical phase plates (PP) have become a viable tool to enhance the contrast of weak-phase objects in transmission electron microscopy. Here, we focus on thin-film PPs where the mean inner potential is exploited to impose a phase shift on electrons propagating through the PP [1]. The application of thin-film PPs is hampered by deviations of the phase shift from its desired value which occur due to contamination effects and possibly beam-induced structural changes of the film. It is therefore highly desirable to know the de-facto phase mask installed in the back focal plane (BFP) of the objective lens (OL).

In this work we use an object-wave reconstruction technique, namely the Gerchberg Saxton (GS) algorithm [2], to determine the phase mask from a diffraction pattern and images of two defocus series of an amorphous object.

The GS algorithm [2] is an efficient tool to calculate the phases of a wave in two different planes based on the knowledge of the intensities in these planes. We applied it to the intensities in the BFP of the OL and the image plane of a transmission electron microscope (TEM) equipped with a PP. Doing this twice, namely once with the PP installed and once without it, allows to get information about the phase mask that is introduced by the PP. Unfortunately the phase contrast transfer function (PCTF) which governs the transfer of phase information into image contrast is ambiguous. It has the form $PCTF=sin(\chi)$, where χ is a polynomial in the spatial frequency, the coordinate in the BFP. Thus the reconstruction of the phase is undefined wherever the PCTF is zero. Furthermore, the validity of $sin(+-\pi/2+x)=sin(+-\pi/2-x)$ means that the phase reconstruction in every pixel of the BFP has two possible solutions: $\phi_{GS1}=\phi_{BFP}+\chi$ and $\phi_{GS2}=\phi_{BFP}+-\pi-\chi$, where $-\pi$ holds for negative χ and $\phi_{BFP}=\phi_{Obj}+\phi_{PP}$ is the sum of the object phase ϕ_{Obj} and ϕ_{PP} which is the contribution of the PP, if installed.

If ϕ_{BFP} is known, e. g. in a computer simulation, the phase reconstruction in the BFP yields to branches for the PCTF that are mirrored at π/2 for positive values of χ and -π/2 otherwise. The pixels in the BFP turn out to be randomly assigned to the branches, but the assignment of a pixel changes within a defocus series. Thus it is theoretically possible to reconstruct an unknown ϕ_{BFP} (plus defocus independent terms of χ) in any pixel of the BFP by linear regression with respect to the N results of an N-fold defocus series. The difference between the phase reconstruction with and without PP yields the phase mask ϕ_{PP}.

Before feeding our algorithm with experimental data, we had to test it by computer simulations. We assumed a virtual TEM with an amorphous test object. An image simulation procedure was used to calculate a diffraction pattern and a defocus series comprising 40 images at defocus values varying from $-5|\Delta f_{Sch}|$ to $-2|\Delta f_{Sch}|$ (with Δf_{Sch} denoting the Scherzer defocus). A charged Hilbert PP in the BFP of our virtual TEM was then assumed and the calculation of the defocus series was repeated. The algorithm was applied to calculate ϕ_{PP} which was compared with the input. Figure 1 shows the good agreement between input and calculated phase distributions.

A GS-based algorithm was used to reconstruct a phase mask introduced by a virtual Hilbert PP from a simulated diffraction pattern and two simulated defocus series with a signal-to-noise ratio of 10:1. Thus its application to experimental data is promising. [3]

References:

[1] R. Danev and K. Nagayama, J. Phys. Soc. Jpn. 73 (2004), p. 2718.
[2] R. W. Gerchberg and W. O. Saxton, Optik 35 (1972), p. 237
[3] Financial support by the Deutsche Forschungsgemeinschaft (DFG).

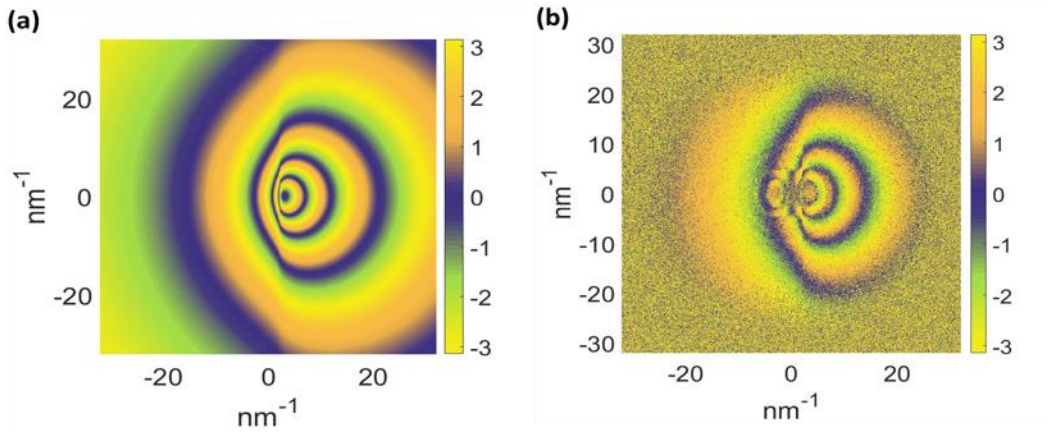

Figure 1. (a) Cyclic false color representation of the assumed phase mask of a charged virtual Hilbert PP and (b) its reconstruction calculated by the GS algorithm from a simulated diffraction pattern and 80 images (spiked with 10% noise) of two simulated defocus series.

IM7.P008
Efficient holographic imaging by focus- and astigmatism-series

A. Eljarrat[1], J. Müller[1], F. Wang[1], C. T. Koch[1]

[1]Humboldt Universität zu Berlin, Physik, Berlin, Germany

aeljarrat@physik.hu-berlin.de

Introduction: Inline holography methods are able to reveal quantitative phase information from images obtained in simple set-ups. Nevertheless the somehow complex data processing involved has established a barrier for its broader application. Hence general-purpose phase imaging is commonly achieved in laboratories using interference methods. In turn, these methods need relatively complex set-ups and in many cases obtain only qualitative phase information. Our approach to exit-wave reconstruction involves the design of an optical microscopy analysis suite offering the exciting possibility of efficient phase inline holographic (PIH) imaging. In this presentation, the theoretical elements behind this approach are reviewed.
Objectives: Our methodology is either based on focal-series analysis, involving the acquisition of through-focus images, an option available in most modern microscopes, or on an astigmatic imaging set-up. Finally, thanks to modern graphical processing unit (GPU) computing the implementation of these methods in a user oriented and scriptable software is also very efficient in terms of speed and cost.
Materials and Methods: In conventional imaging systems phase information is seemingly lost in any direct measurement process. The introduction of optical aberrations, e.g. defocus and astigmatism, gives a chance to access the phase information if we analyze the images in an appropriated framework. For instance, the transport of intensity equation (TIE) establishes a deterministic relationship between the through-focus variation of the measured intensity and the intensity and phase of the exit-wave [CT Koch, Ultramicroscopy 108 (2008) 141]. The TIE provides the foundation for deterministic PIH with a straightforward data processing pipeline.
The direct application of a naïve TIE inversion is prevented by several pitfalls, one of them being the difficulty of obtaining an estimate of the axial intensity derivative, since the information content contained in a single defocus plane is bandwidth limited. This problem is generally circumvented by performing a multi-focus (MFTIE) inversion combining the information of many defocus planes. Another problem that will generally affect phase reconstruction is the impact of spatial incoherence present in conventional illumination systems. Finally, any focal-series based algorithm faces a fundamental insufficiency of the defocus derivative alone to establish the boundary conditions for the TIE inversion and is only indicated for use in weak phase objects.
Results: Following these considerations, we have developed a novel homogeneous-noise-distribution sampling scheme that automates MFTIE and includes a convergence envelope that accounts for partial spatial coherence. This deterministic algorithm is able to recover low spatial-frequencies in noise-limited scenarios. Furthermore, it provides a stable solution that can be further refined using iterative algorithms. We have performed benchmarks using simulated and experimental data, and assessed the performance of this algorithm against other state-of-the-art MFTIE solutions.
In order to extend the applicability of the deterministic TIE method we propose to use an astigmatic imaging set-up. It can be shown that such set-up solves the problem of undetermined boundary conditions and thus facilitates a robust TIE inversion. This approach has already been tested using simulated datasets and experimental prototypes. Currently, our work focuses on the development of a compact prototype that will enable PIH using astigmatism, as an extension to a conventional microscopy set-up. This extension accompanied by a PC equipped with a high-end GPU will provide affordable live phase imaging [Patent pending].
Conclusions: Our multi-focus TIE algorithm allows recovering a wider range of high and low spatial-frequencies than other state-of-the-art algorithms. Meanwhile, our astigmatic TIE prototype can extend the applicability of this method to conventional imaging systems. The proposed methodologies combine robust PIH with speed- and cost-efficient data acquisition strategies.

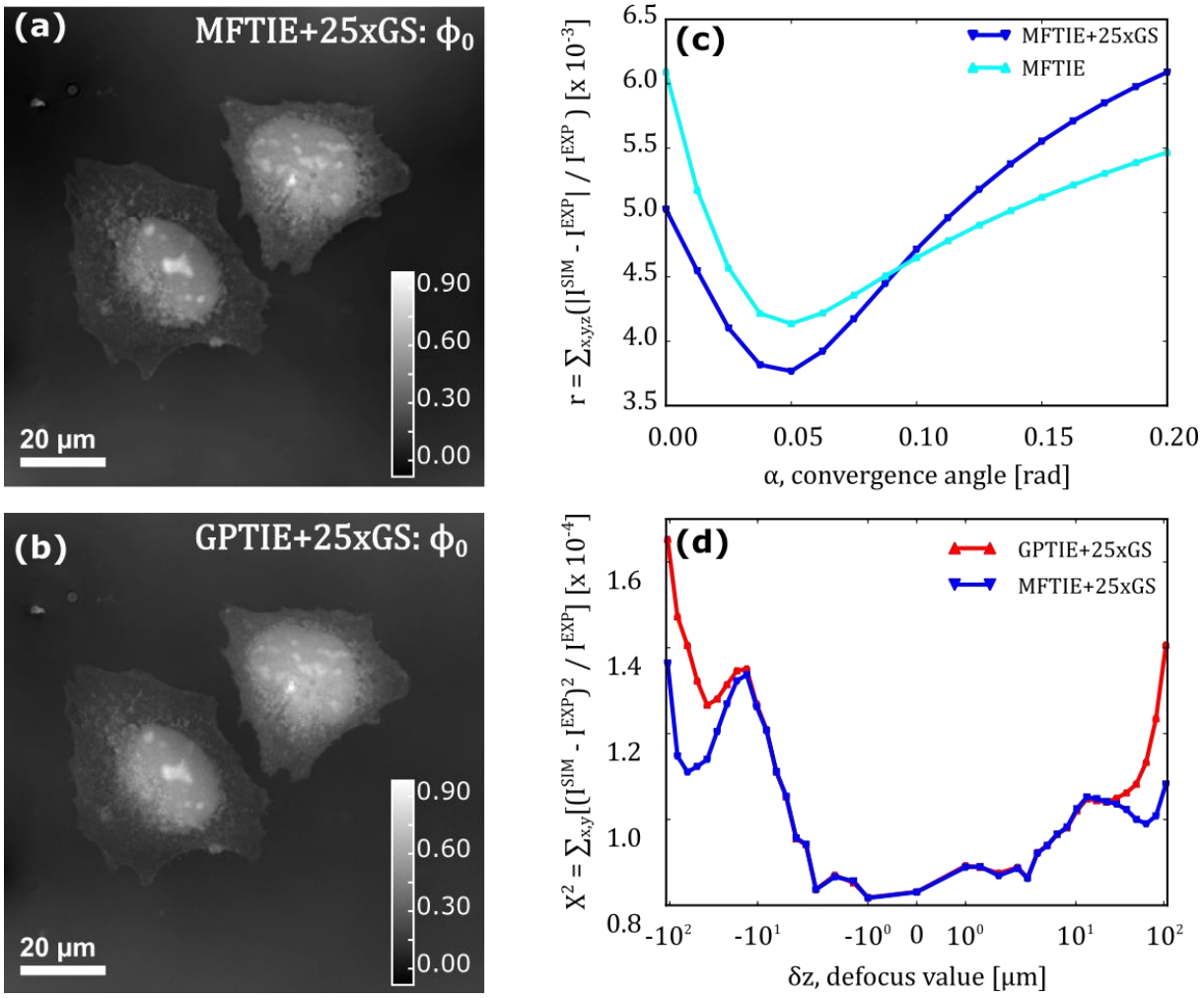

Figure 1. (a-b); MFTIE-phase vs. Gaussian process TIE [Z Jingshan et al., Optics Express 22 (2014) 10661]. LED illuminated He-La cell sample. (c); improvement after applying the convergence envelope. (d); the MFTIE solution is in better agreement with highly defocused images, indicating that low spatial-frequencies are better recovered.

IM7.P009
Correlative micro-diffraction and differential phase contrast study of mean inner potential and subtle beam-specimen interaction

M. Wu[1], E. Spiecker[1]

[1]Institute of Micro- and Nanostructure Research, Materials Science, FAU Erlagnen-Nuremberg, Erlangen, Germany

mingjian.wu@fau.de

Differential phase contrast (DPC) using electrons in the scanning transmission electron microscopy (STEM) has recently seen an increasing interest with application in this area [1,2]. Due to the highly dynamical scattering of electrons, the direct interpretation of DPC signal received by quadrant segmented detector as simple beam deflection is not necessarily justified [3]. In order to reliably interprete DPC-STEM signals, the evaluation of the transmitted beam disk (i.e., micro-diffraction direct beam pattern) is indispensable. When nanoscale electrostatic potentials in materials are to be measured the mean inner potential (MIP) has to be determined in the first place as it typically is the dominant contribution to DPC. MIP of a crystalline material characterized by repeated unit cells is a well-defined quantity and has been extensively studied both experimentally and theoretically for many materials. Therefore, the measurement of MIP of a well-known material by DPC or micro-diffraction can be regarded not only as an additional independent measure of MIP of this particular material, but also as an approach to validate/calibrate the methods themselves for their further application in extracting electrostatic potentials and electric fields in samples quantitatively.
In this contribution, we present a correlative micro-diffraction and DPC study on the determination of MIP (cf. the setup in Fig. 1a and b) and explain the origin of subtle beam-specimen interactions at the edge of wedge-shaped crystals using both experiment and simulation. Our measurement of MIP of Si and GaAs resulted in 12.48±0.22 V and 14.15±0.22 V, respectively, from directly evaluating beam refraction in micro-diffraction mode. DPC-STEM measurements gave very similar values (Fig. 2). Fresnel fringes within the diffraction disk resulting from interaction of the highly coherent electron beam with the aperture are observed and a numerical simulation scheme is implemented to reproduce the effect of the specimen on the fringe pattern. Perfect agreement between experiment and simulation has been achieved in terms of subtle displacements of the fringes upon approaching the sample edge with the electron probe (Fig. 3). The existence of the fringes has minor effect on the DPC-STEM signal, which is well below the noise level of our setup at practically reasonable acquisition times. We suggest the possibility to perform pseudo-contactless probing of weak potential differences in beam sensitive samples by evaluating the subtle displacements of Fresnel fringes quantitatively.

The authors gratefully acknowledge financial support by the German Research Foundation through the Research Training Group GRK1896 In situ microscopy with electrons, X-rays and scanning probes and the Cluster of Excellence EXC315 Engineering of Advanced Materials.

References:
[1] M. Lohr, R. Schregle, M. Jetter, et. al. Ultramicroscopy, **117**, 7–14, 2012.
[2] N. Shibata, S. Findlay, H. Sasaki, et. al. Sci. Rep., **5**, 10040 2015
[3] I. MacLaren, L. Wang, D. McGrouther, et. al. Ultramicroscopy, 154, 57–63. 2015
[4] M. Wu and E. Spiecker. Ultramicroscopy, **177** 1-13, 2017.

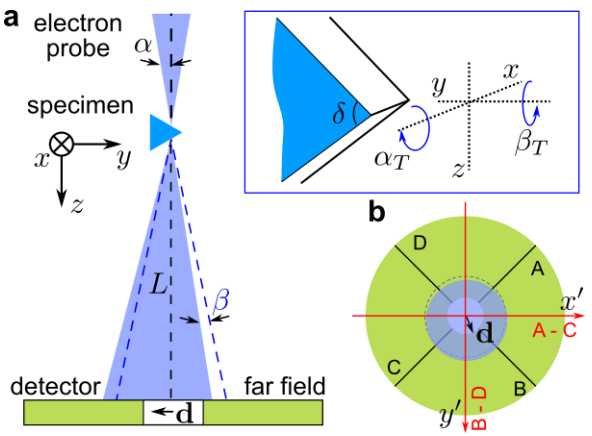

Figure 1. (a) DPC-STEM and micro-diffraction setup for the determination of MIP with cleavage 90o crystal wedge. (b) Schematic view of the quadrant segmented DPC detector.

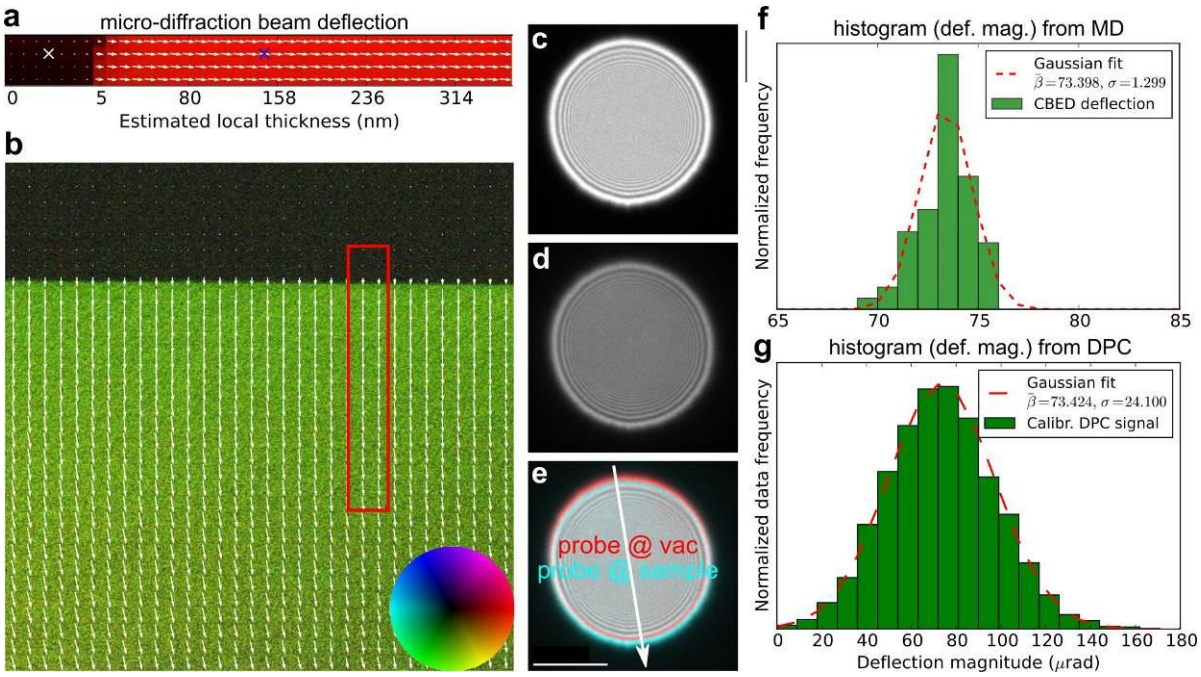

Figure 2. Micro-diffraction and DPC measurements from Si wedge sample. Derived beam disk deflection from (a) micro-diffraction raster array and (b) DPC-STEM mapping. The micro-diffraction direct beam disk marked by crosses in (a) are shown in (c) when the electron probe located at vacuum position and (d) when the probe is located at a local thickness of about 150 nm. The beam deflection is highlighted by the false color mix of (c) and (d), as shown in (e). The statistics of the magnitude of deflection measured from (a) and (b) is presented in (f) and (g). Field of view in (b) and (f) is 400 nm.

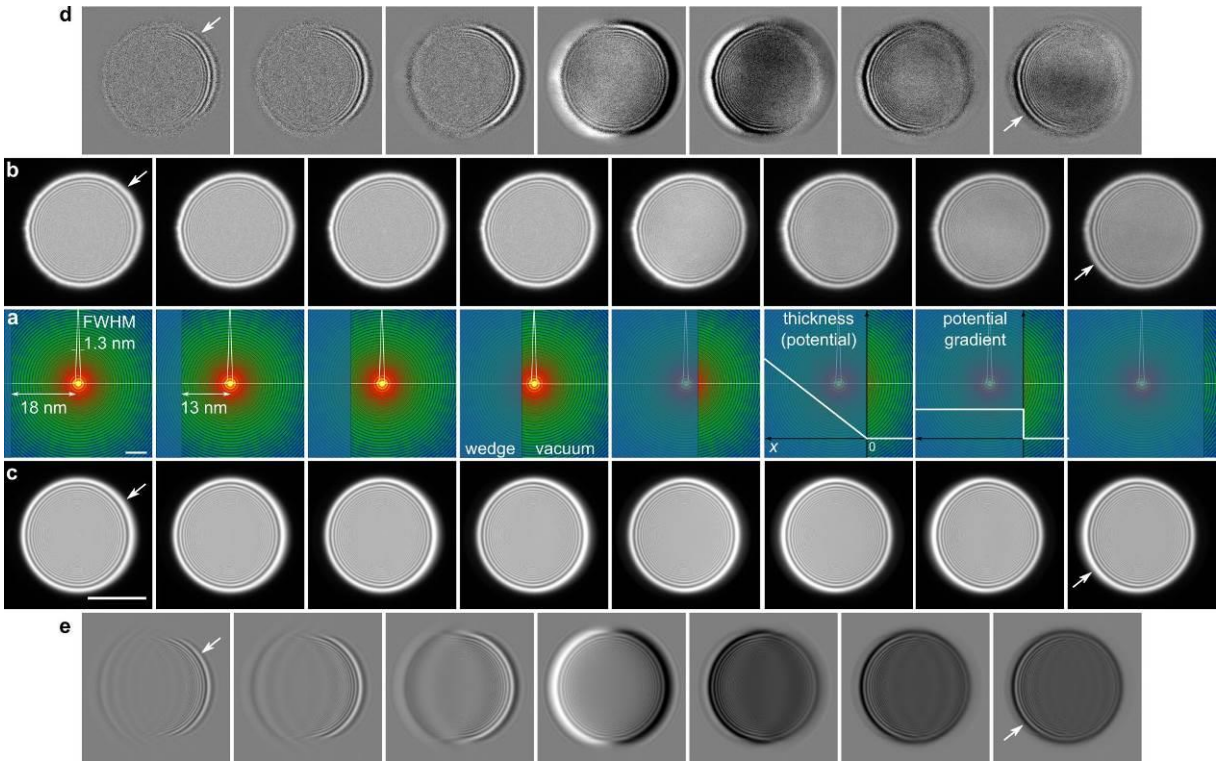

Figure 3. Experimental and simulated micro-diffraction patterns with the electron probe at the vicinity of the edge of crystal wedge.

IM7.P010
Strain analysis of InGaAs/GaAs quantum dots

L. Meissner[1], D. Eckert[1], D. Berger[2], T. Niermann[1], M. Lehmann[1]

[1]Technische Universität Berlin, Institut für Optik und Atomare Physik, Berlin, Germany
[2]Technische Universität Berlin, ZE Elektronenmikroskopie ZELMI, Sekr. KWT2, Berlin, Germany

laura.meissner@physik.tu-berlin.de

Measuring the strain field of quantum dots is a real challenge. In principle, it is possible to gain detailed information on the displacement field using dark field electron holography (DFEH) [1] and Geometric Phase Analysis (GPA) [2]. Both methods, DFEH and GPA, provide comparable information about strain fields. The interpretation of the resulting geometric phases, however, is not trivial. The aim of this paper is to achieve a clearer understanding of the influence of dynamical diffraction on the geometric phase.
The sample under investigation consists of InGaAs quantum dots (QDs) grown in Stranski-Krastanow regime in a GaAs matrix. DFEH was carried out in strong beam conditions with excited {220} reflection on one single QD and its surrounding. The DFEH contains the geometric phase, which provides information about the displacement field. Out of this, the strain can be calculated in this particular direction. GPA in strong beam condition is another applied method to measure the strain field of QDs. The phase of the GPA, opposed to DFEH, which directly gives the complex amplitude of the reflection, is given by the product of the complex amplitudes of {220} reflection and the zero-beam. Figure 1 shows the reconstructed phases from DFEH (left) and GPA (right) for the very same QD also using {220} reflections. Because of the dynamical diffraction of the three dimensional object the interpretation of the results is complicated: The relation between the geometric phase and the displacement field depends on the depth of the QD within the QD-Layer [3]. Moreover, in GPA and DFEH (fig. 1), the geometric phase differs in comparison of the area of the QD to its surroundings. As shown in figure 1 (right), the strain fields are asymmetric. However, this is expected, because of the asymmetrical shape of the QDs themselves.
Therefore the expected outcome for QDs located in different depths within a sample of 100 nm thickness is simulated (fig. 2). The calculation contains the geometry, which is here assumed spherical for the sake of simplicity, the QD-layer and displacement field of the QD together with the choice of the reflection used in dark field arrangement and position of the QD within the specimen, calculated by propagation of the Darwin-Howie-Whelan equations. Simulations illustrate the depth dependence of the geometric phase of a QD. For further investigations, it is of interest to create conditions which allow the determination of the depth of a QD. Considering this, a TEM-lamella with a 45° inclined QD-layer is prepared by focused ion beam (FEI Helios Nanolab 600 FIB) (fig. 3) [4]. Therefrom, the depth of a single QD is determinable by the distance of the QD to the edge of the QD-layer.
In conclusion, DFEH and GPA are applicable to investigate strain fields of QDs. For reproducible results, it is all-important to be aware of the depth, in which the investigated QD is embedded within the lamella.

References:
[1] Hÿtch, M.; Houdellier, F.; Hüe, F. & Snoeck, E. Nanoscale holographic interferometry for strain measurements in electronic devices, *Nature,* 2008, 453, 1086.
[2] Hÿtch, M.; Snoeck, E. & Kilaas, R., Quantitative measurement of displacement and strain fields from HREM micrographs, *Ultramicroscopy,* 1998, 74, 131-146.
[3] A.Lubk et al., Dynamical scattering theory for dark-field electron holography of 3D strain fields, Ultramicroscopy, 2014, 136, 42.
[4] D. Berger et al., Advanced TEM-Lamella Preparation with FIB/SEM, these proceedings.
[5] We kindly acknowledge the support of Professor Pohl and his workgroup by providing the wafer with InGaAs/GaAs quantum dots, Axel Lubk for discussions providing the idea for this paper and the SFB787 for financial support.

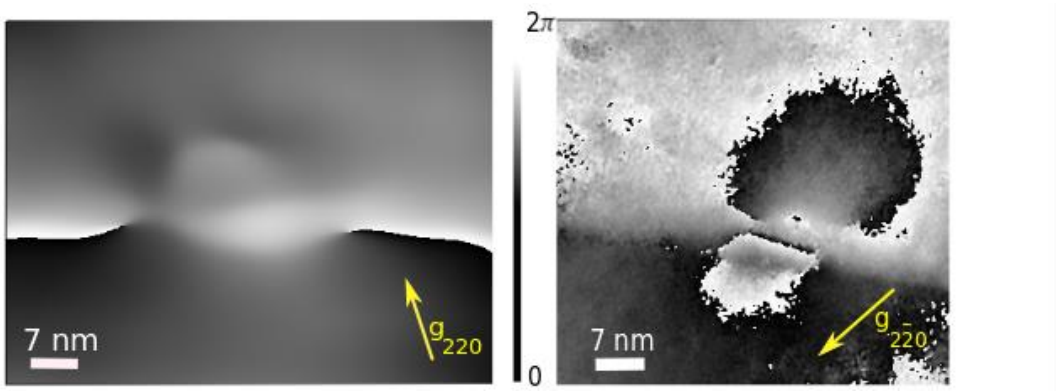

Figure 1. Phase of DFEH (left) and GPA (right) of the very same InGaAs QD showing asymmetric strain fields.

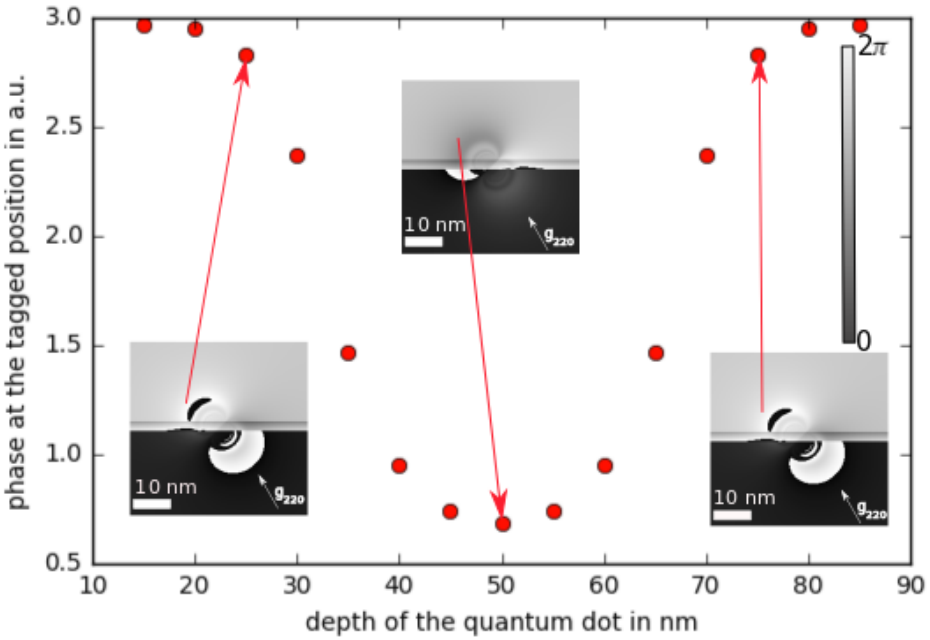

Figure 2. Simulation of the phase of beam g = 220 of InGaAs/GaAs QDs in different depths within the QD-layer. Phase evaluated at the same position for different dephts.

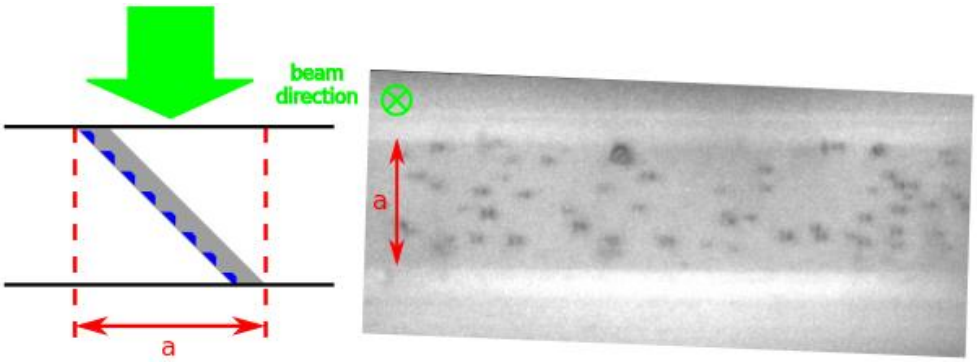

Figure 3. Schematics of the TEM-lamella with a 45° inclined QD-layer (left). Dark field depiction using strong beam condition for {200} reflection.

IM7.P011
On the measurement of polarization fields in GaN heterostructures with electron holography

M. Narodovitch[1], T. Niermann[1], J. Enslin[2], T. Wernicke[2], M. Kneissl[2], M. Lehmann[1]

[1]TU-Berlin, Institut für Optik und Atomare Physik, Berlin, Germany
[2]TU-Berlin, Institut für Festkörperphysik, Berlin, Germany

michaeln@physik.tu-berlin.de

The phase of an electron wave transmitted through a sample can be measured with the transmission electron microscope (TEM) using electron holography. This phase information is used to determine the electrostatic potential within a semiconductor structure. However, the direct evaluation of the phase information can give results that significantly deviate from other measurements or theoretical expectations. For instance, in case of a GaN p-n diode the holographically measured built-in potential of <1 V in a sample prepared by focused ion beam is significantly lower then the ~3 V, known from electrical IV-measurements. The reason for this systematic deviations is a matter of active research. It was shown that beam induced currents, sample damage, and preparation-related surface contributions significantly influence the holographic phase signal [1].
In the GaN material system, the polarization induced potential contribution has also to be considered. They occur typically in layers of an $Al_yIn_xGa_{1-x-y}N$ alloy, embedded in a matrix material, i.e. GaN. Especially for thin layers < 10 nm, as used for photonic devices, measurement and interpretation of the polarization induced phase signal is much more challenging. Reasons are the small structures, the TEM diffraction conditions and the material related signal contributions. Considerable effort was made to the measurement and quantitative interpretation of the corresponding phase signal [2]. However, there are no studies of the TEM related systematic deviations, as known from p-n junctions.
In order to study the polarization related phase signal a sample structure was grown. The structure consists of a collection of $Al_{0.3}Ga_{0.7}N$ layers, embedded in an n-doped GaN matrix (Fig. 1a). The sample preparation was performed with a focused ion beam (FIB). A lamella structure was cut out of the wafer and mounted to a TEM-grid. Afterwards, trenches were cut into the lamella in order to transmit the Reference: wave. For the holograms, the biprism was placed along the trenches and a voltage was applied to the biprism. The interference pattern of the object wave with the Reference: wave was recorded and the phase of the object wave was reconstructed. Hologram averaging was performed in order to increase the S/N ratio.
Figure 1b shows a reconstructed phase image at four different specimen positions. The highly homogeneous and reproducible phase signal reflects that the excellent measurement accuracy. The error due to spatial averaging and choosing a specific position for the measurement can be kept very small. Figure 2a shows the phase profiles calculated by averaging perpendicular to the 30 nm thick $Al_{0.3}Ga_{0.7}N$ layer. In the error limit of **±**0.003 rad/nm, no phase gradient was measured.
Without free carriers a polarization induced field of 3 MV/cm can be expected [3]. Additionally, the screening of the free carriers has to be taken into account. As the dopant concentration is increased, additional free carriers are introduced to the system. which increasingly screen the polarization induced field (Fig. 2b). With the actual doping of $4*10^{17}$ cm^{-3} and the 30 nm thick layer the expected field reduces to 1.1 MV/cm.
For our sample thickness of 200 nm this would result in a phase gradient of 0.08 rad/nm, which deviates significantly from the measured phase gradient of 0**±**0.003 rad/nm. To explain the deviation between the measurement and the theory we propose that the additional free carriers generated by the electron beam screen the polarization induced field in our specimen.

References:
[1] J. Park, T. Niermann et.al., Appl. Phys. Lett. 105, 094102 (2014)
[2] M.R. McCartney and D.J. Smith, Ann. Rev. Mater. Res. 37 (2007) 729
[3] O. Ambacher, J Majewski, J. Phys: Condens. Matter 14 3399-3434 (2002)
[4] We kindly acknowledge support of the DFG within the Collaborative Research Center 787

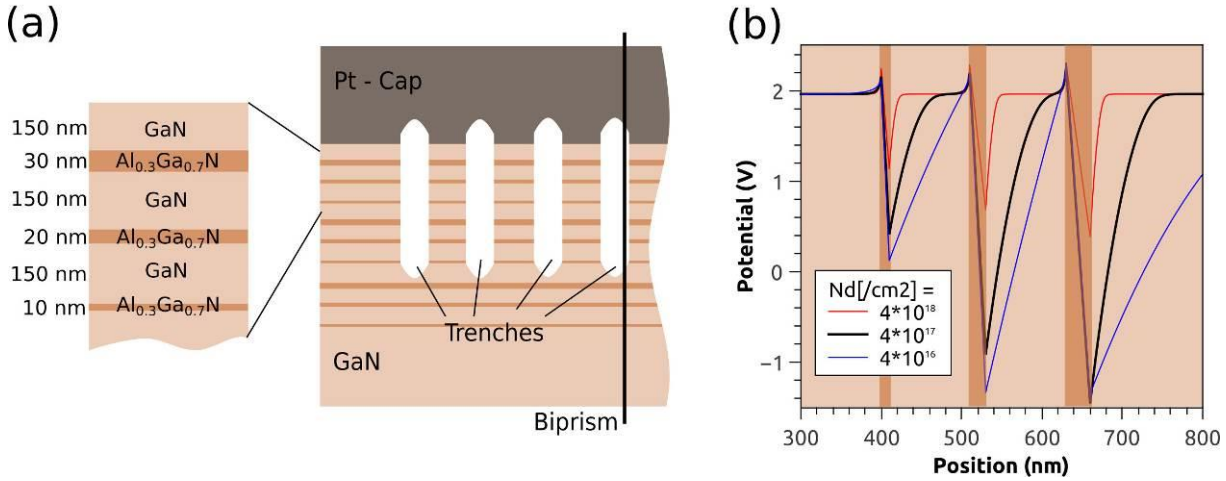

Figure 1. a) The sample structure, used for the present study. b) Phase images of a 30 nm thick $Al_{0.3}Ga_{0.7}N$ layer, recorded at different sample positions. The phase signal is homogeneous and well reproducible.

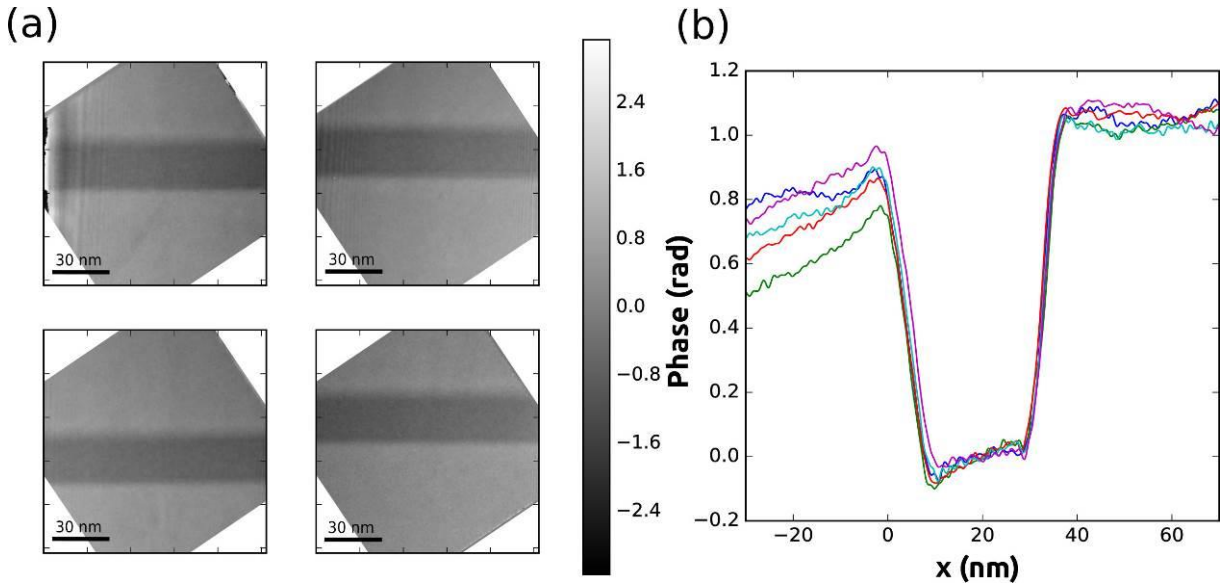

Figure 2. a) Phase profiles at different sample positions. No significant gradient is visible. b) Simulations of the electrostatic potential for the present structure.

IM7.P012
Approaching atomic resolution in magnetic measurements using electron vortex beams on Sr^2FeMoO_6

D. Pohl[1], J. Rusz[2], J. Spiegelberg[2], P. Zeiger[2], S. Schneider[1,3], X. Zhong[4], P. Tiemeijer[5], S. Lazar[5]
K. Nielsch[1], B. Rellinghaus[1]

[1]IFW Dresden, Dresden, Germany
[2]Uppsala University, Department of Physics and Astronomy, Uppsala, Sweden
[3]TU Dresden, Institute for Solid State Physics, Dresden, Germany
[4]Tsinghua University, NCEM Beijing, Beijing, China
[5]FEI Company, Eindhoven, Netherlands

d.pohl@ifw-dresden.de

Introduction: X-ray magnetic circular dichroism is a well-established method to study element specific magnetic properties of a material, while electron energy-loss magnetic chiral dichroism (EMCD), which is the electron wave analogue to XMCD, is still scarcely used today. Recently discovered electron vortex beams (EVBs), which carry quantized orbital angular momenta (OAM) L, promise to also reveal magnetic signals [1]. Since electron beams can be easily focused down to sub-nanometer diameters, this novel technique provides for the possibility to quantitatively determine local magnetic properties with unrivalled lateral resolution. In order to generate the spiralling wave front of an EVB, specifically designed apertures are needed. Dichroic signals on the L_3 and L_2 edges related to the orbital and spin magnetic moments are expected to be of the order of 5% of the electron energy loss intensity [2,3].
Objectives: For the measurement of magnetic properties down to the atomic scale using electron vortex beams, three prerequisites can be formulated: (i) single EVBs must be prepared with a well defined OAM to avoid a concurrent superposition of OAM [4], (ii) the EVBs need be to be of atomic size [2,3] and (iii) electron energy loss spectra need to be measured from individual magnetic atomic columns [2,3]. Hence, it will be shown as a proof of principle that for atomically resolved EMCD, pure EVBs carrying a single and user-selecteble OAM can be used to perform EEL spectroscopy on individual (magnetic) atom columns.
Materials and Methods: The generation of EVBs in a double aberration-corrected FEI Titan^3 80-300 transmission electron microscope (TEM) is achieved by the implementation of a 50 µm dislocation-type apertures into the condenser lens system. A special setup allows for scanning TEM investigations (STEM) with vortex beams, whose OAM is selected by means of an additional discriminator aperture in the C3 aperture plane. This approach allows to generate atom-sized EVBs with Angstrom-sized probes and a well-defined OAM, which are shown to provide for atomic resolution HR-STEM images. Although this selection of OAM and thus the limitation in total beam current results in a decrease of the signal-to-noise ratio, this novel technique still allows for atomic resolution EELS measurements [5].
For the present proof-of-principle investigations, a sample has been chosen that provides for a comparabley large spatial separation of those atomic columns, which carry the magnetic moments. We have chosen Sr_2FeMoO_6, which is a ferrimagnet with a strong EMCD signal on the Fe-L edge [6] and large lattice spacing. Fig. 1a shows the HAADF image of the Sr_2FeMoO_6 in [100] zone axis, where the nearest Fe-Fe distance is 4.8Å. At such decently large spacing, the Fe-L edge can be easily mapped from individual Fe columns using a state of the art aberration corrected microscope.
Results: Spectrum images have been acquired with electron vortex probes carrying OMA of L = ±1 ħ. Then EEL spectra are extracted only from the positions of the Fe columns. To overcome the low signal, 1200 spectra are summed and principal-component analysis is used to reduce the noise. Fig. 1b shows the resulting Fe-L edge spectra and the corresponding EMCD signal. An intensity difference of the two spectra (L=±1) can be seen on the Fe-L_3 and the Fe-L_2 which is indicative of the EMCD signal.
Conclusion: The quality of the HR-STEM images and EELS-based elemental maps, which both provide atomic resolution, promise to open the door for future quantitative measurements of magnetic properties with ultimate spatial resolution and their local correlation with structural features at the very same position within the identical sample.

References:
[1] J. Verbeeck et al., Nature 467 (2010), p. 301-304.
[2] P. Schattschneider et al., Ultramicroscopy 136 (2014), p. 81-85.
[3] J. Rusz and S. Bhowmick, Phys. Rev. Lett. 111 (2013), 105504.
[4] D. Pohl et al., Ultramicroscopy 150 (2015), 16-22.
[5] D. Pohl et al. (2017).
[6] Z.C. Wang et al., Ultramicroscopy (2017)

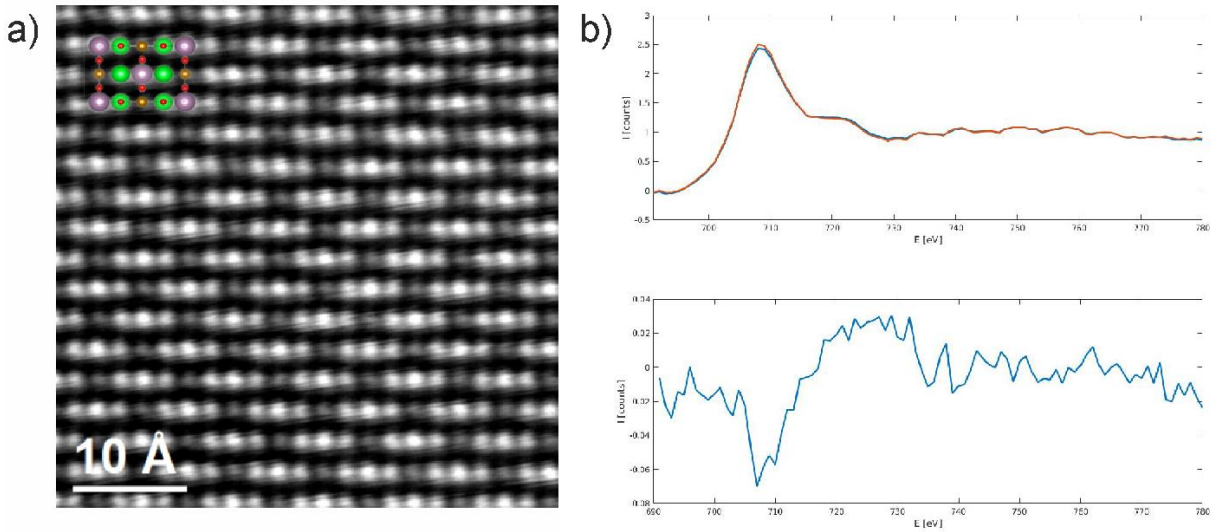

Figure 1. Vortex HR-STEM EMCD measurements. **a**, HAADF image of Sr_2FeMoO_6 (inset: atomic model) **b**, Summed Fe-L edge spectra acquired with L=±1 electron vortex beams (top) extracted only from Fe atom position and corresponding EMCD signal (bottom).

IM7.P013
Exploring the use of electron ptychography to map charge transfer in monolayer hexagonal boron nitride using a fast pixelated detector in the scanning transmission electron microscope

G. T. Martinez[1], T. J. Pennycook[2], T. C. Naginey[1], L. Jones[1], H. Yang[3], J. Meyer[2], T. Susi[2], J. R. Yates[1] R. J. Nicholls[1], M. Huth[4], M. Simson[4], H. Soltau[5], L. Strüder[5], R. Sagawa[6], Y. Kondo[6], P. D. Nellist[1]

[1]University of Oxford, Materials, Oxford, United Kingdom
[2]University of Vienna, Faculty of Physics, Vienna, Austria
[3]Lawrence Berkeley National Laboratory, Berkeley, CA, United States of America
[4]PNDetector GmbH, Munich, Germany
[5]PNSensor GmbH, Munich, Germany
[6]JEOL Ltd, Tokyo, Japan

gerardo.martinez@materials.ox.ac.uk

Introduction: Recent developments of fast pixelated detectors, such as the pnCCD (S)TEM camera developed by PNDetector, have enabled the acquisition of 4D-datasets that contain the convergent beam electron diffraction pattern for each probe position in the scanning transmission electron microscope [1]. These type of datasets can be used for electron ptychography, which has been shown to allow phase imaging of a wide range of materials [2]. When using methods such as the Wigner Distribution Deconvolution (WDD) algorithm [3], aberration free phase imaging of light element materials can be achieved [2]. Electron phase imaging techniques can provide information on the atomic potential and the electronic charge density distribution [4], opening the possibility to acquire information about chemical bonds and ionization of atoms.
Objective: To profit from aberration free phase imaging using WDD electron ptychography to explore mapping of charge transfer in monolayer hexagonal boron nitride (hBN).
Materials and Methods: We acquired a 4D dataset of monolayer hBN using a double corrected JEOL ARM200CF instrument fitted with a pnCCD (S)TEM camera. The acceleration voltage was 60 kV and the datasets were acquired at 1000 frames per second. Multislice image simulations considering the so-called independent atom model (IAM) with the experimental dose settings were calculated using the MULTEM software [6]. The source size broadening was estimated to match the maximum experimental phase difference. 2D Gaussian functions were fitted to each N and B atom positions in the reconstructed phase images for both experiment and simulations. The heights of the fitted 2D Gaussian functions were used as measure of the phase difference caused by the atoms.
Results: When phase imaging hBN, it is expected that the contrast of N sites will be reduced due to the screening of the nuclear potential caused by the accumulation of charge transferred from the B site [4, 5]. Therefore, the contrast of N and B atoms is predicted be very similar. Figure 1 a) shows the aberration corrected experimental phase difference obtained from a WDD ptychographic reconstruction. Figure 1 b) shows the reconstruction of the simulation assuming a source size broadening effect of FWHM 1.05 Angstrom. Figure 1 c), and d), show the histograms of the 2D Gaussian function heights, to which a Gaussian function was fitted to determine the mean difference between the phase difference distributions. The experimental mean difference between phase differences at N and B sites is only 0.6 mrad. For the simulated dataset a mean difference of 5.5 mrad phase difference is obtained and the distributions are separated enough that the phase difference caused either by N or B can be identified.
Conclusions: The experimental measurements indicate mapping of charge transfer, since the mean difference between N and B sites is smaller than the one expected from IAM simulations, which do not consider the bonding effects between atoms. Further study using DFT calculations in the simulations to consider charge transfer for confirmation is work in progress [7].

References:
[1] H. Ryll et al, Journal of Instrumentation **11** (2016) p. P04006
[2] H. Yang *et al,* Nature Communications **7** (2016) p. 12532
[3] J. M. Rodenburg and R. H. Bates, Phil. Trans. R. Soc. Lond. A. **339** (1992) p. 521
[4] J.C. Meyer *et al,* Nature Materials **10** (2011) p. 209
[5] L. Pauling, Proc. Natl. Acad. Sci. USA **56** (1966) p. 1646
[6] I. Lobato and D. Van Dyck, Ultramicroscopy **156** (2015) p. 9
[7] The research leading to these results has received funding from the EPSRC (EP/M010708/1) and EU Marie Skłodowska-Curie grant No. 655760 – DIGIPHASE (TJP)

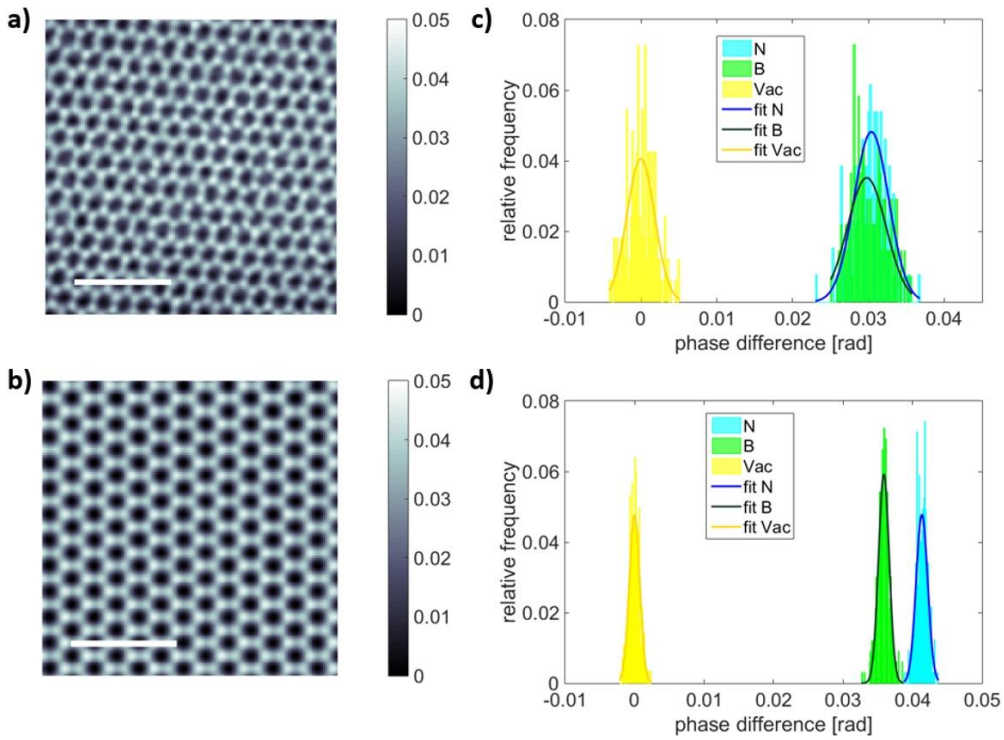

Figure 1. Aberration free phase image of monolayer hexagonal boron nitride using WDD electron ptychography a) experimental, b) simulated. Simulation assumed a source size broadening FWHM of 1.05 Angstrom. Scale bar corresponds to 1 nm. Histograms of phase differences for N and B sites and vacuum region as Reference: with overlay of corresponding Gaussian fits for c) experimental and d) simulation.

IM7.P014
Tunable electron vortex beam generator

A. H. Tavabi[1,2], P. Lu[1,2], M. Duchamp[3], R. Dunin-Borkowski[1,2], G. Pozzi[4,1]

[1]Forschungzentrum Jülich, Ernst Ruska-Centre for Microscopy and Spectroscopy with Electrons, Jülich, Germany
[2]Forschungszentrum Jülich GmbH, Peter Grünberg Institute, Jülich, Germany
[3]Nanyang Technological University, School of Materials Science and Engineering, Singapore, Singapore
[4]University of Bologna, Department of Physics and Astronomy, Bologna, Italy

a.tavabi@fz-juelich.de

An electron vortex beam (EVB) possesses one or more phase singularities at the center of its helical wavefront and is an eigenstate of the component of orbital angular momentum (OAM) along its propagation direction with eigenvalue $\ell\hbar$, making it an ideal probe for measuring the electronic and magnetic properties of materials. The ability to form EVBs in a transmission electron microscope (TEM) has been demonstrated using a helical phase plate [1], computer generated holograms [2, 3] and a magnetic monopole [4]. By taking advantage of their magnetic moment and angular momentum, EVBs have been applied to magnetic and shape dichroism measurements, chiral crystal structure characterization and nanoparticle manipulation. However, all of the methods that have been proposed to generate EVBs are limited by a constant value of OAM, which restrict their applications.
Here, we present a new concept for a helical phase plate for creating EVBs that is based on the electrostatic counterpart of the Aharonov-Bohm effect. We show both theoretically and experimentally that the phase plate is able to generate EVBs with any desirable value of OAM as a tunable and rapidly switchable device.
The proposed device creates an electrostatic monopole field, which can be realized using two narrow metallic parallel wires, to which an external voltage source is used to apply a potential difference. The device has been fabricated using a combined procedure involving electron beam lithography and focused ion beam milling. Details of its fabrication, performance in the TEM and possible applications will be discussed.

References:
[1] M. Uchida, A. Tonomura, Nature 464, 737 (2010).
[2] J. Verbeeck, H. Tian, P. Schattschneider, Nature 467, 301 (2010).
[3] B. J. McMorran, A. Agrawal, I. M. Anderson, A. A. Herzing, H. J. Lezec, J. J. McClelland, J. Unguris, Science 331, 192 (2011).
[4] A. Béché, R. Van Boxem, G. Van Tendeloo, J. Verbeeck, Nature Physics 10, 26 (2014).

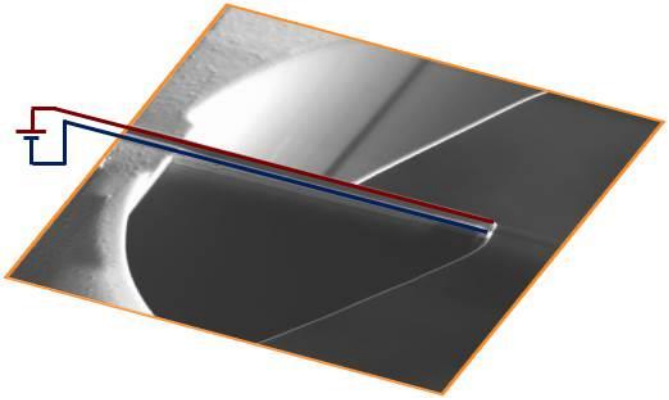

Figure 1. Secondary electron image of the tunable EVB generator. Two metallic nanorods that have a voltage applied between them are indicated by red and blue lines. The nanorods were patterned lithographically on a silicon-silicon nitride MEMS chip, in order to create an electrostatic monopole at their ends. The entire device is grounded to the microscope, while the wires are connected to an external voltage source. The use of a silicon nitride substrate prevents a short circuit between the metal lines.

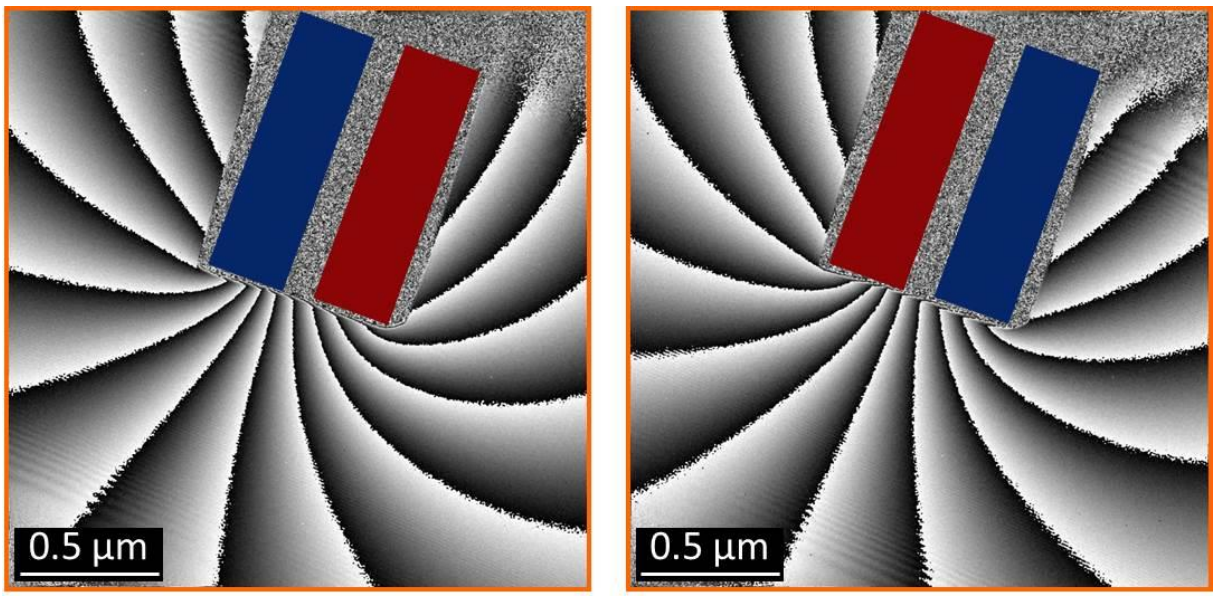

Figure 2. Reconstructed phase images (1× amplification) of the vacuum region around the end of the phase plate recorded using off-axis electron holography for voltages of -5 V (left) and +5 V (right) applied to the device.

IM7.P015
Realization of the Ehrenberg-Siday thought experiment –interaction-less electron microscopy

A. H. Tavabi[1,2], C. B. Boothroyd[3], E. Yücelen[4], R. Dunin-Borkowski[1,2], S. Frabboni[5,6], G. C. Gazzadi[5] G. Pozzi[7,1]

[1]Forschungzentrum Jülich, Ernst Ruska-Centre for Microscopy and Spectroscopy with Electrons, Jülich, Germany
[2]Forschungszentrum Jülich GmbH, Peter Grünberg Institute, Jülich, Germany
[3]Nanyang Technological University, School of Materials Science and Engineering, Singapore, Singapore
[4]FEI Company, Eindhoven, Netherlands
[5]University of Modena and Reggio Emilia, Department FIM, Modena, Italy
[6]CNR-Institute of Nanoscience-S3, Modena, Italy
[7]University of Bologna, Department of Physics and Astronomy, Bologna, Italy

a.tavabi@fz-juelich.de

In 1949, Ehrenberg and Siday observed that the expression for the electron-optical refractive index contains the vector potential and not the magnetic field strength, concluding that one might expect wave-optical phenomena to arise which are due to the presence of a magnetic field but not due to the magnetic field itself, i.e., which arise whilst the rays are in field-free regions only [1]. Here, we realize an experiment, whereby a magnetic flux that should result in a detectable phase shift is placed in the geometrical shadow between two interfering electron beams in a two-slit experiment. The magnetic flux is generated by a uniformly-magnetized Co nanorod of constant cross-section deposited between the slits. The Co nanorod has a negligible magnetic stray field, arising only from the closure field associated with its finite length (Fig. 1).

The presence of a magnetic flux between the slits is difficult to identify in a recorded interference pattern unless its magnitude or direction changes and differences between images are compared. In a first series of experiments, the specimen containing the slits and the Co nanorod was tilted about a horizontal axis, which was in the specimen plane and perpendicular to the lengths of the slits and the nanorod. The conventional electron microscope objective lens was used to apply a vertical magnetic field to the specimen while it was being tilted, in order to change the direction in which the Co nanorod was magnetized while observing the interference pattern. Figure 2 shows the result of this experiment. Although there are small shifts in the position of the pattern, the images shown in Figs 2(b) and 2(c) are clearly in registry, as are those in Figs 2(d) and 2(e). A phase shift of approximately , which can be seen between the patterns in (c) and (d), results from a reversal in the magnetization direction of the Co nanorod at a specimen tilt angle of approximately -5°. Intensity profiles generated from the Fraunhofer patterns in (c) and (d) are overlaid onto each other in Fig. 2(f) for specimen tilt angles of -4° (blue) and -6° (red).

The recorded phase shift can be used to study changes in the magnetic flux of the Co nanorod when its magnetic state is switched, despite the fact that the electron passes only through a field-free region: an example of interaction-less electron microscopy.

References:

[1] W. Ehrenberg and R. E. Siday, The refractive index in electron optics and the principles of dynamics Proc. Phys. Soc., Sec. B 62: 8–21, 1949.
[2] G. Pozzi, C. B. Boothroyd, A. H. Tavabi, E. Yücelen, R. E. Dunin-Borkowski, S. Frabboni and G. C. Gazzadi, Experimental realization of the Ehrenberg-Siday thought experiment Appl. Phys. Lett. 108: 083108, 2016.

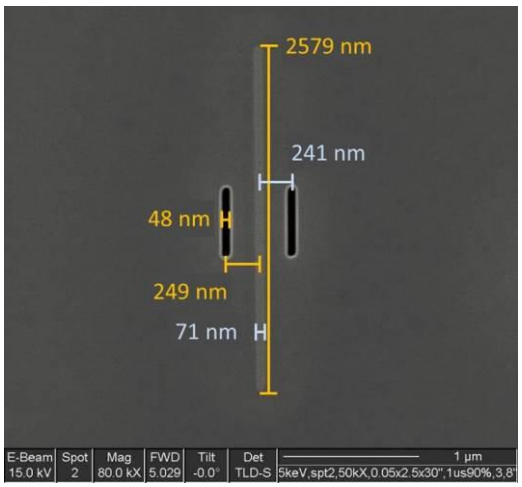

Figure 1. Secondary electron image of the two slits and the Co nanorod. The slits are the dark features on either side of the Co nanorod.

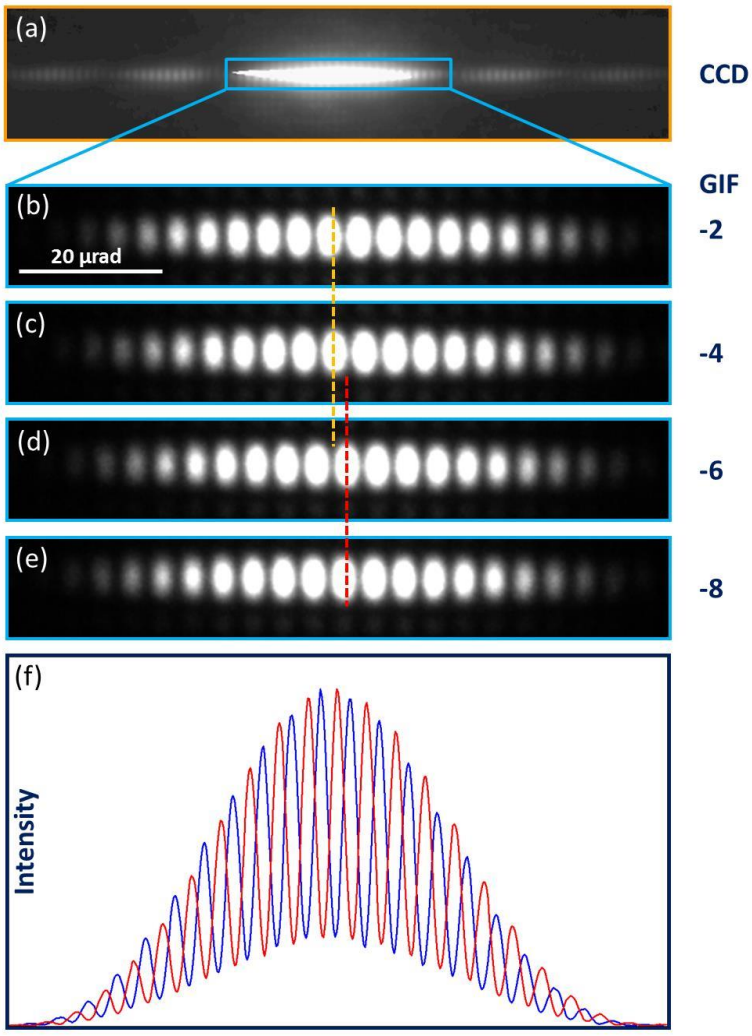

Figure 2. (a) Low-angle electron diffraction image recorded using a conventional charge-coupled device (CCD) camera located before the Gatan imaging filter (GIF). (b)–(e) Low-angle electron diffraction images recorded using the GIF CCD camera after tilting the sample between -2° and -8° in steps of -2°. (f) Line scans of (c) in blue and (d) in red.

IM7.P016
A new perspective for a tunable phase plate based on Ampere's law

A. H. Tavabi[1,2], M. Beleggia[3], V. Migunov[1,4], A. Savenko[5], O. Öktem[6], R. Dunin-Borkowski[1,2]
G. Pozzi[7,1]

[1]Forschungzentrum Jülich, Ernst Ruska-Centre for Microscopy and Spectroscopy with Electrons, Jülich, Germany
[2]Forschungszentrum Jülich GmbH, Peter Grünberg Institute, Jülich, Germany
[3]Technical University of Denmark, Center for Electron Nanoscopy, Lyngby, Denmark
[4]RWTH Aachen University, Central Facility for Electron Microscopy (GFE), Aachen, Germany
[5]FEI Company, Eindhoven, Netherlands
[6]KTH - Royal Institute of Technology, Centre for Industrial and Applied Mathematics, Department of Mathematics, Stockholm, Sweden
[7]University of Bologna, Department of Physics and Astronomy, Bologna, Italy

a.tavabi@fz-juelich.de

In-focus phase contrast devices that are analogues of the optical phase plate (PP) introduced by Zernike [1] have been investigated for decades and have emerged from a wide range of possible phase-sensitive imaging techniques as promising and viable methods for enhancing the contrast of biological specimens in the transmission electron microscope (TEM). However, most PPs for electrons that have been proposed so far suffer from deficiencies that include insufficient contrast enhancement, additional aberrations, short lifetime, difficult alignment and/ or electrostatic charging by the electron beam (even when self-charging is responsible for producing phase contrast) [2, 3]. Charging, in particular, is very difficult to measure and control, deteriorates device performance and limits widespread applications.
Here, we introduce a new substrate-free PP concept for TEM that is based on Amperes law and addresses all of these problems. We refer to the device as a "tunable Ampere phase plate" (TAPP). It is designed to provide almost-ideal phase contrast, while providing a spatial resolution of up to 1-4 Å, as well as both tunability and ease of application.
The operating principle of the TAPP is based on a magnetic field circulating around a vertical segment of current-carrying wire, which introduces a position-dependent phase shift to a passing electron wave. When the TAPP is positioned in the back focal plane of the imaging lens, it acts as an additional transfer function that enhances phase contrast arising from an object.
We have used focused ion beam (FIB) milling to fabricate a prototype TAPP from etched Au wires in the form of three orthogonal segments, thereby making a hook-shaped device, as shown in Fig. 1. The middle segment of the hook could then be positioned parallel and the other two segments perpendicular to the incident electron beam direction.
We have established the validity of the concept using both experimental electron holographic measurements of phase shifts around the device (Fig. 2) and a theoretical model based on Amperes law. We have also used computer simulations to predict the contrast enhancement expected for studies of biological cells and macromolecules.
The authors are grateful to Dr. Sara Sandin for valuable discussions.

References:
[1] Zernike, F. Phase contrast, a new method for the microscopic observation of transparent objects. Physica 9, 686-698 (1942).
[2] Danev, R. & Baumeister, W. Cryo-EM single particle analysis with the Volta phase plate. eLife. 5, e13046 (2016).
[3] Glaeser, R. M. Methods for imaging weak-phase objects in electron microscopy. Rev. Sci. Instrum. 84, 111101 (2013).

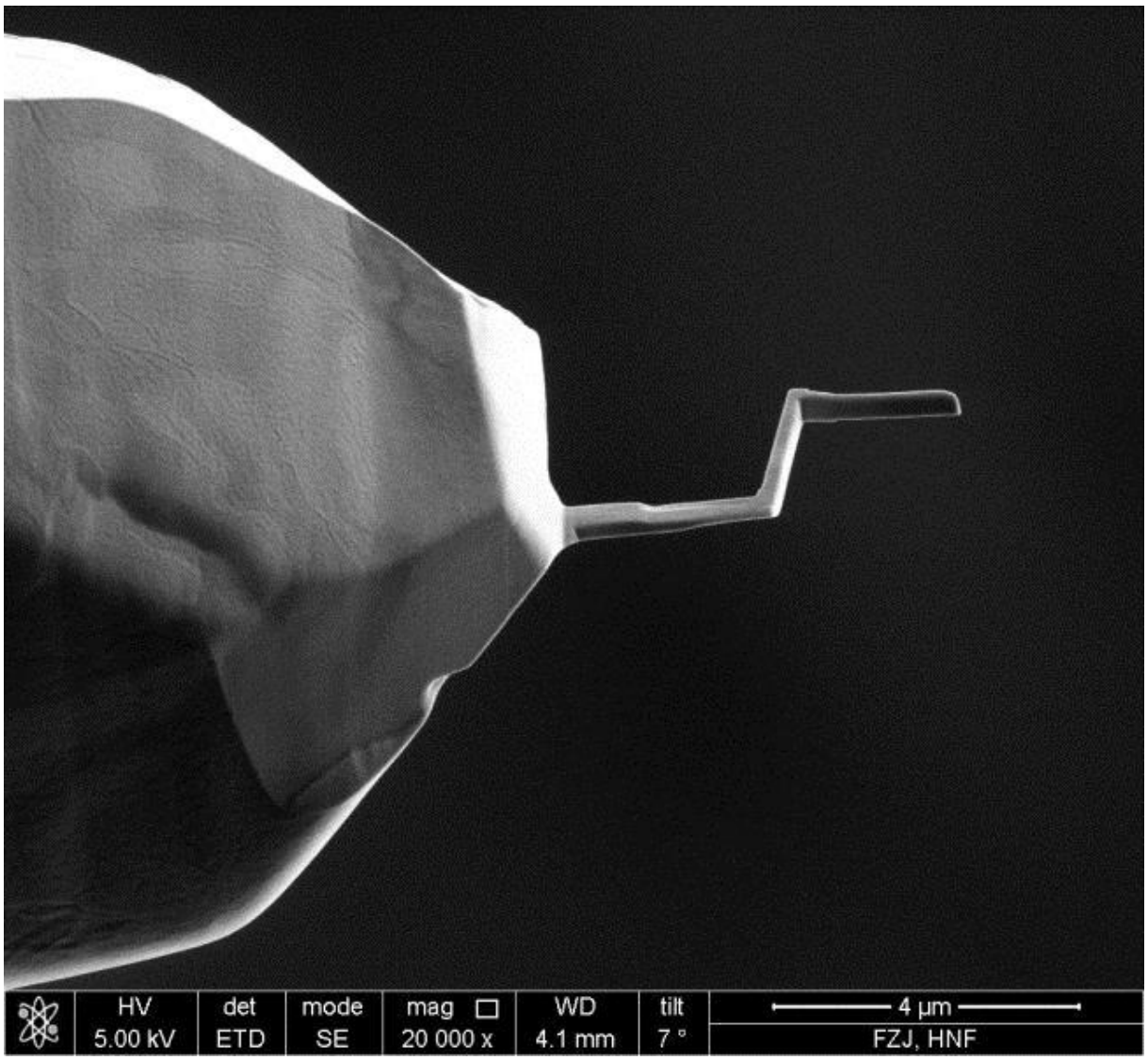

Figure 1. Secondary electron image of one side of the TAPP.

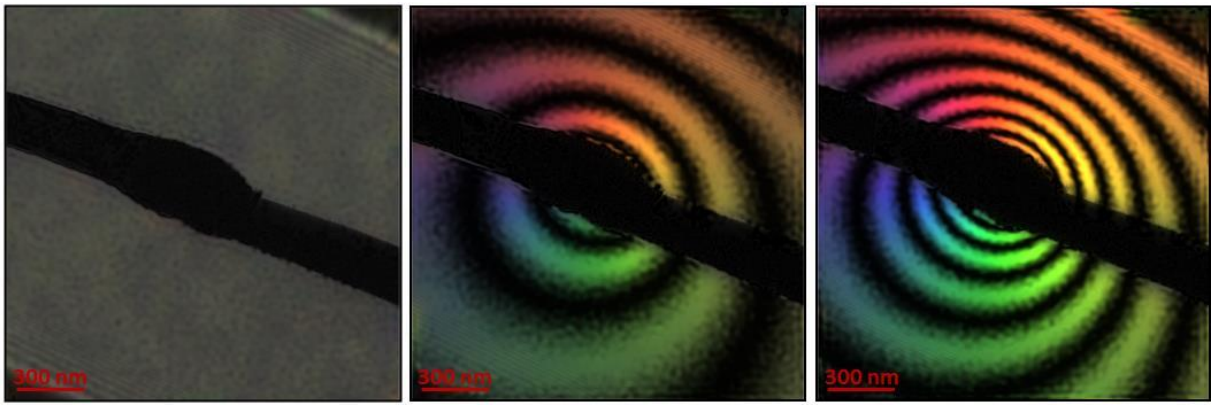

Figure 2. 8x amplified phase images of the vacuum region around the contacted TAPP recorded using off-axis electron holography for currents of 0 (left), 2 mA (middle) and 4 mA (right).

IM7.P017
Realization of the Feynman-Young thought experiment – controlled electron interference in Fraunhofer and image space

A. H. Tavabi[1,2], C. B. Boothroyd[3], E. Yücelen[4], S. Frabboni[5,6], G. C. Gazzadi[5], R. Dunin-Borkowski[1,2] G. Pozzi[7,1]

[1]Forschungzentrum Jülich, Ernst Ruska-Centre for Microscopy and Spectroscopy with Electrons, Jülich, Germany
[2]Forschungszentrum Jülich GmbH, Peter Grünberg Institute, Jülich, Germany
[3]Nanyang Technological University, School of Materials Science and Engineering, Singapore, Singapore
[4]FEI Company, Eindhoven, Netherlands
[5]University of Modena and Reggio Emilia, Department FIM, Modena, Italy
[6]CNR-Institute of Nanoscience-S3, Modena, Italy
[7]University of Bologna, Department of Physics and Astronomy, Bologna, Italy

a.tavabi@fz-juelich.de

Some of the key features of quantum mechanics are illustrated by the Feynman-Young double-slit thought experiment, whose second part discusses the electron distribution that is recorded when one of two illuminated slits is partially or totally closed by an aperture and whose analysis leads to the idea of the probability amplitude. Although this experiment has been attempted previously [1,2], the presence of diffraction phenomena in the Fresnel regime meant that these studies were only approximations to an ideal experiment. Here, we show how such shortcomings can be overcome in a modern microscope. We achieve an ideal Feynman-Young experiment, both in diffraction (Fraunhofer) space and in image space, by precisely tuning the microscope lenses to make use of conjugate plane(s) to the double slit plane.
Figure 1 shows the realisation of the controlled double slit experiment. The slits are in the object plane of an electron microscope, while a beam blocker (here, a Mollenstedt biprism) is placed exactly in a conjugate plane of the slits. The biprism is located in the image plane of an extra lens, which is just above the diffraction lens of the microscope. When the biprism covers one of the slits completely, the interference phenomena in the double slit regime transform into the diffraction envelope of a single slit. This experiment was carried out at 60 kV, in order to ensure that no electron could pass through the covered part of the slits or the beam blocker.
Figure 2 shows a controlled electron interference experiment performed in image space using two electron biprisms, with the lower biprism located close to the image plane of the diffraction lens. The upper biprism is tilted with respect to the slits, but is still in a conjugate plane. The lower biprism is slightly above the second conjugate plane and can be used to interfere the beams by applying a voltage to it. Changes in the spacing and direction of the interference fringes, which were observed when voltages were applied to one or both biprisms, will be discussed.

References:
[1] G. Matteucci and G. Pozzi. Two further experiments on electron interference. Am. J. Phys., 46(6):619{623, 1978.
[2] R. Bach, D. Pope, S.-H. Liou and H. Batelaan. Controlled double-slit electron diffraction. New J. Phys., 15(3):033018, 2013.

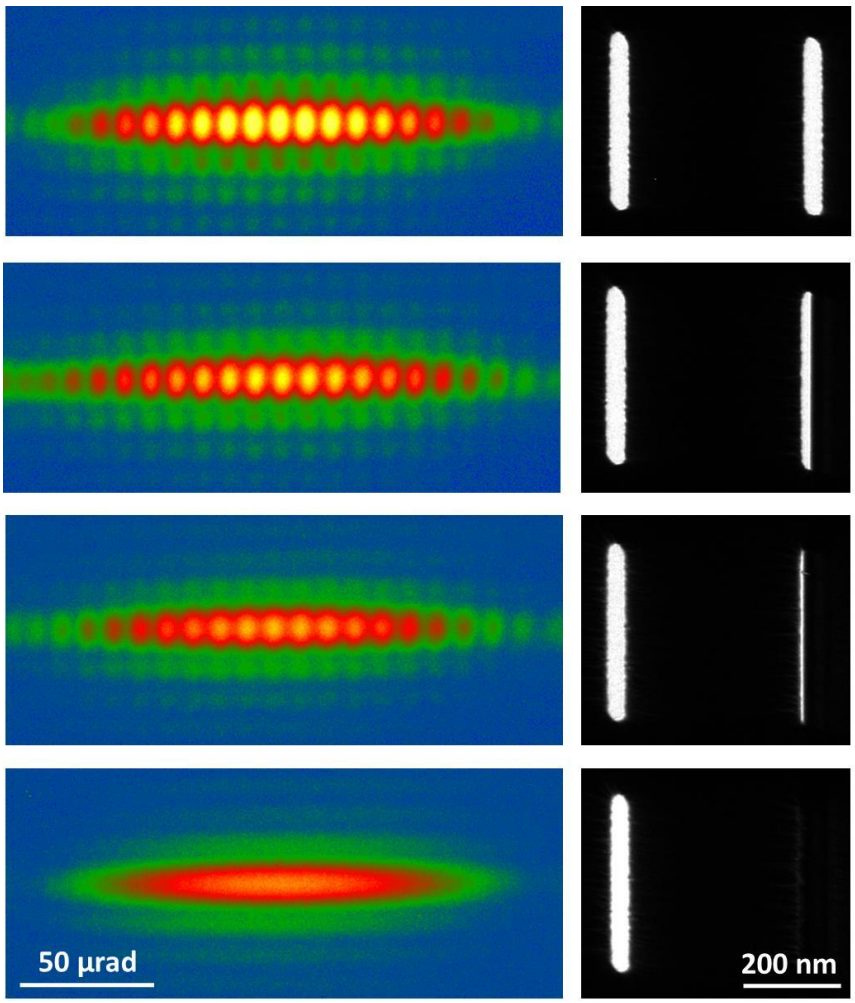

Figure 1. Double slit controlled electron beam experiment with a mask in a conjugate plane of the slits (right) and its effect on the corresponding Fraunhofer diffraction image (left).

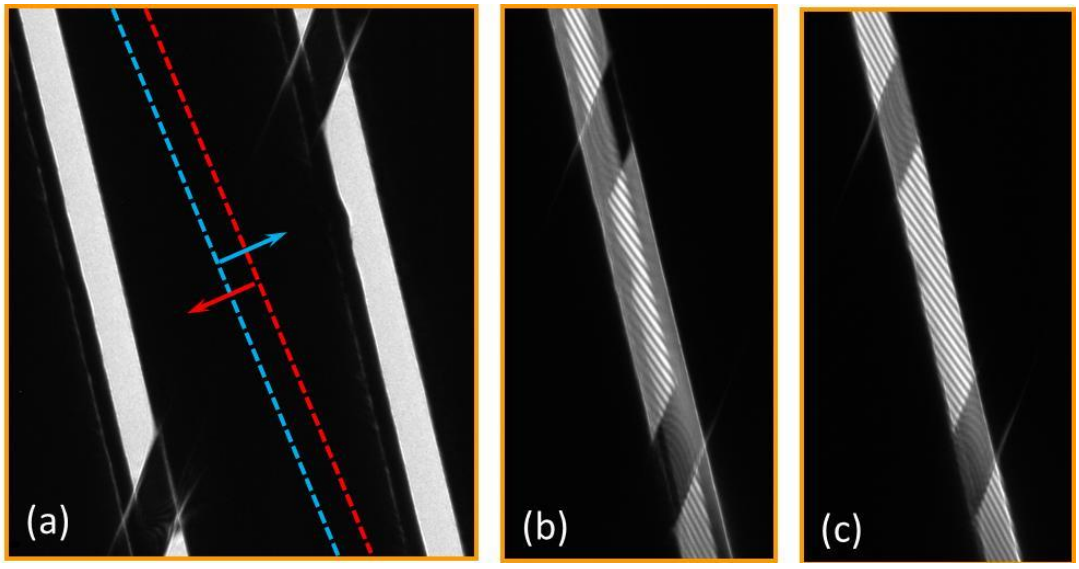

Figure 2. (a) Controlled electron interference experiments in image space performed using two electron biprisms. The lower biprism is located in the dark region between the two slits (and is positioned some distance above a conjugate image plane). Its edges are marked by dashed lines. The upper biprism is visible crossing the slits at an angle and is in a conjugate image plane. (b) Partial and (c) total overlap of the two slits was achieved when the bias applied to the lower biprism was increased, resulting in the formation of two-beam interference fringes.

IM7.P018
A comparison of phase-retrieval algorithms for focused-probe electron ptychography

G. T. Martinez[1], M. J. Humphry[2], P. D. Nellist[1]

[1]University of Oxford, Materials, Oxford, United Kingdom
[2]Phasefocus, Sheffield, United Kingdom

gerardo.martinez@materials.ox.ac.uk

Introduction: Historically, the scanning transmission electron microscope (STEM) has not been widely used for phase contrast imaging because the small bright-field detector, that by the principle of reciprocity would give images equivalent to phase contrast in the conventional transmission electron microscope (CTEM), detects only a small fraction of the incident electrons. Furthermore, the requirement for lens aberrations to generate phase contrast is not optimal for the incoherent imaging modes such as annular dark-field (ADF) or spectrum imaging. Recent developments in fast pixelated detectors have enabled the full 2D detector plane intensity in STEM to be recorded as a function of probe position during a 2D scan, thereby providing a 4D dataset. It has been shown that such data allows phase imaging simultaneously with focused ADF imaging, aberration correction and the retrieval of 3D information [1]. Electron ptychography in the STEM was first demonstrated more than 20 years ago in the context of improving image resolution [2] and was based on simplified versions the Wigner Distribution Deconvolution (WDD) approach [3]. More recent work has focused on the use of lower convergence angles and large defocus to provide a broader illuminating probe that required fewer probe positions [4]. For this setup, the ePIE algorithm is used, which is an iterative approach for phase imaging. Therefore, an understanding of the performance of these methods is important to optimise the processing of these datasets.
Objective: To compare the retrieved phase images formed using different ptychographical reconstruction algorithms such as WDD and ePIE. We discuss the transfer of information to the final retrieved phase image and the degree to which the phase images can be interpreted quantitatively.
Materials and Methods: Using the MULTEM software [6], a 4D dataset of hexagonal boron nitride (hBN) with a boron vacancy was simulated considering the so-called independent atom model under the multislice approach. An acceleration voltage of 60 kV and a convergence angle of 28 mrad was used. This dataset was processed using the WDD and ePIE algorithms to retrieve a phase image. A plane-wave simulation of the same model was performed to be used as a Reference: for comparison.
Results: Figure 1 compares WDD and ePIE reconstructions from the simulated data. It can be seen that the WDD approach gives an artefact of higher phase for the N atoms neighbouring the vacancy, which does not occur for the ePIE reconstruction. We will show how the sharper Fourier truncation of transfer in the WDD approach leads to this artefact. We also note that the ePIE reconstruction reflects more closely the ratio between the B and N phase shifts that would be seen for plane-wave illumination. Note that this is a neutral atom simulation, and that it is known that charge transfer affects this ratio. In the ePIE approach there are a number of possible ambiguities, including an arbitrary phase ramp in the reconstruction that can be fitted and removed.
Conclusion: The increasingly routine availability of 4D focused-probe data suitable for ptychographical reconstruction raises the question of how the data is most optimally processed, and we are likely to see further developments and optimisation of methods to most precisely and accurately retrieve phase information [6].

References:
[1] H. Yang et al., Nature Communications **7** (2016) 12532.
[2] P.D. Nellist et al., Nature, **374** (1995) 630.
[3] J.M. Rodenburg, R.H.T. Bates, Phil. Trans. R. Soc. London A, **339** (1992) 521.
[4] M.J. Humphry, et al., Nat Commun, **3** (2012) 730.
[5] I. Lobato and D. Van Dyck, Ultramicroscopy **156** (2015) 9.
[6] PDN and GTM acknowledge support from the EPSRC (grant numbers EP/M010708/1 and EP/K040375/1) and technical collaboration with JEOL Ltd and PNDetector GmbH.

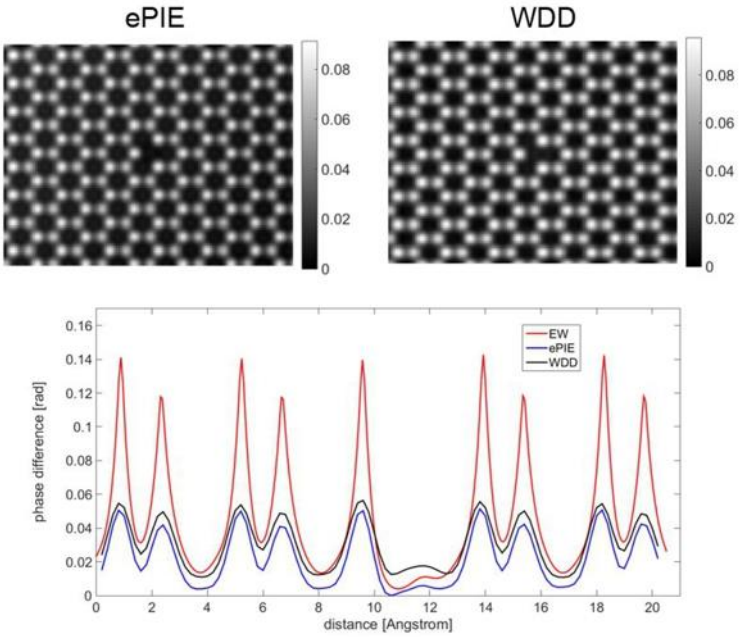

Figure 1. Ptychographic phase images reconstructed using the WDD and ePIE approaches from simulated data of a B vacancy in hBN. A line profile of phase taken horizontally across the image through the defect is shown for WDD (black), ePIE (blue) and the exit wave (red) of plane-wave illumination.

IM7.P019
Sorting the orbital angular momentum of a wavefront in a spectrum – towards quantum electron microscopy

A. H. Tavabi[1,2], V. Grillo[3,4], F. Venturi[5,3], H. Larocque[6], R. Balboni[7], G. C. Gazzadi[5], S. Frabboni[5,3]
P. Lu[1,2], E. Mafakheri[5], F. Bouchard[5], R. Dunin-Borkowski[1,2], R. Boyd[2,6,8], M. P. J. Lavery[9]
M. J. Padgett[9], E. Karimi[6,10]

[1]Forschungzentrum Jülich, Ernst Ruska-Centre for Microscopy and Spectroscopy with Electrons, Jülich, Germany
[2]Forschungszentrum Jülich GmbH, Peter Grünberg Institute, Jülich, Germany
[3]CNR-Institute of Nanoscience-S3, Modena, Italy
[4]CNR-IMEM Parco Area delle Scienze 37/A, Parma, Italy
[5]University of Modena and Reggio Emilia, Department FIM, Modena, Italy
[6]University of Ottawa, The Max Planck Centre for Extreme and Quantum Photonics, Department of Physics, Ottawa, Canada
[7]CNR-IMM Bologna, Bologna, Italy
[8]University of Rochester, Institute of Optics, Rochester, New York, NY, United States of America
[9]Glasgow University, School of Physics and Astronomy, Glasgow, United Kingdom
[10]Institute for Advanced Studies in Basic Sciences, Department of Physics, Zanjan, Islamic Republic of Iran

a.tavabi@fz-juelich.de

Quantum complementarity states that particles exhibit wave-like properties such as diffraction and interference upon propagation. Electron waves that are defined by helical wavefronts are referred to as twisted electrons and have additional mechanical and magnetic properties that are associated with spin-to-orbit coupling.
Here, we introduce an electron-optical setup that can be used to measure the OAM content of an electron by using a transformation of an OAM-carrying azimuthal phase variation into transverse phase gradients that can be spatially resolved and separated using a lensing element, thereby creating an OAM spectrometer.
We will present different experimental ray paths in an electron microscope, which can be used to measure OAM components that are introduced to the wave function of an incident electron as it passes through an object (Fig. 1).
We will show experimental results illustrating the acquisition of OAM spectra (Fig. 2) in an electron microscope using holographic apertures (Fig. 1). We will also discuss the use of structured electrostatic fields to shape electron waves.
Our design is, in principle, able to transform the phase information carried by a single transmitted electron into intensity information in an OAM spectrum. We will discuss possible applications of this approach to the study of magnetic and electronic properties in materials. We will also consider the properties of more complex beams, which can be obtained by the superposition of vortex beams of different order.
Finally, we will assess the need for more unconventional electron-optical configurations, in the context of maximizing the information that can be recorded by single electron.

References:
[1] V. Grillo et al., arXiv:1609.09129 [quant-ph] (2016).

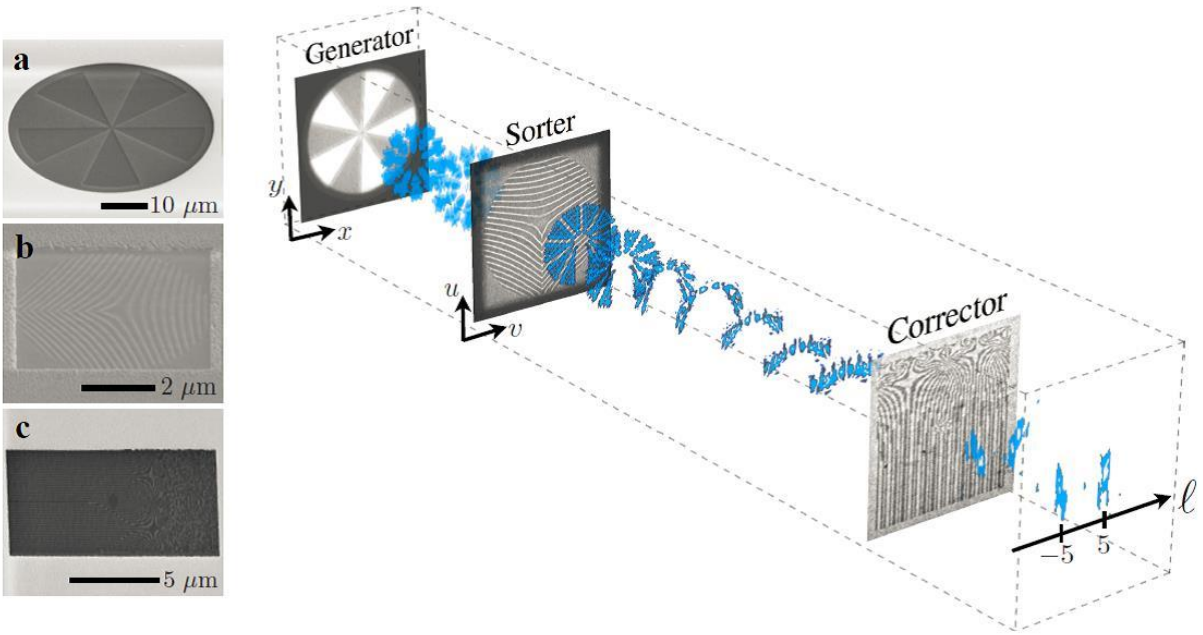

Figure 1. TEM images and schematic diagram of phase holograms and an electron beams transverse intensity profile recorded at different planes in the sorting apparatus.

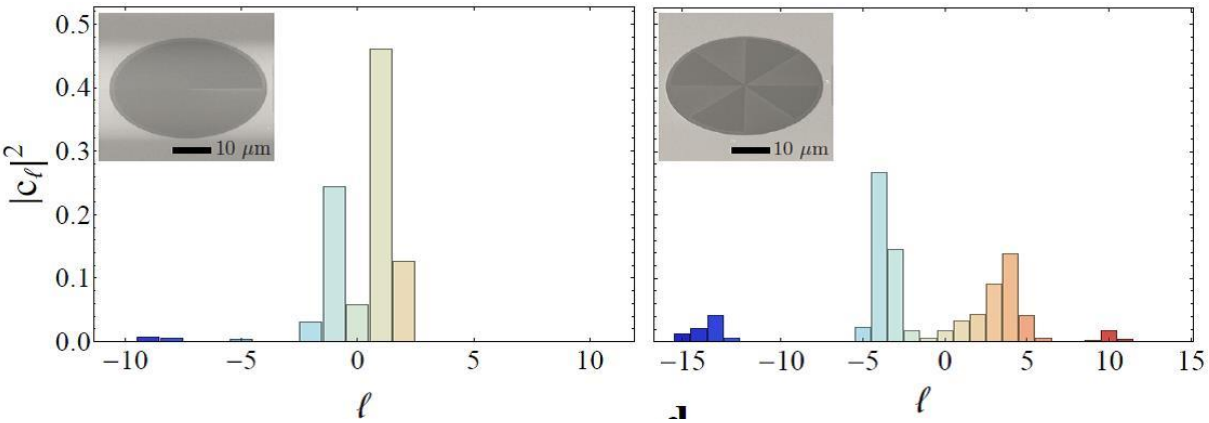

Figure 2. Experimentally recorded OAM spectra of different electron beams obtained from the sorters output for beams consisting of electrons defined by OAM values of +1,-1 produced using a spiral phase plate (left) and using a superposition of ±4 OAM states , produced using a phase mask (right).

IM7.P020
Using Wigner distribution deconvolution ptychography in strong dynamical objects

G. T. Martinez[1], H. Yang[2], P. D. Nellist[1]

[1]University of Oxford, Materials, Oxford, United Kingdom
[2]Lawrence Berkeley National Laboratory, Berkeley, CA, United States of America

gerardo.martinez@materials.ox.ac.uk

Introduction: The use of a fast pixelated detectors allow the recording of the full convergent beam electron diffraction pattern for each probe position when performing a scanning transmission electron microscope experiment [1]. This results in a 4D-dataset, from which electron ptychography can be performed [2]. Electron ptychography provides phase images that contain structural information of materials at the atomic level [3]. Using the Wigner Distribution Deconvolution (WDD) method [4], simultaneous phase imaging of light elements combined with incoherent high angle scattering imaging of heavy elements provide important information of radiation sensitive materials [3]. Moreover, probe aberrations can be estimated from these datasets and corrected, leading to aberration-free phase imaging [3]. An assumption on the reconstruction algorithm is that the sample should satisfy the multiplicative object approximation, which usually becomes invalid for strong scattering systems.
Objective: To analyze the reconstructed phase difference of strong dynamical objects in order to investigate the structural information that electron ptychography can retrieve for these type of materials.
Materials and Methods: Multislice simulations of a Pt system in [110] zone axis using a 200 kV acceleration voltage have been performed using the MULTEM software [5]. Simulations considered a plane wave (PW) and a convergent beam (CBED) with 28 mrad convergence angle for a crystalline structure and for an isolated atomic column 30 atoms thick. Simulations of convergent probe were processed using the WDD ptychography method to retrieve the modulus and phase at each thickness.
Results: Figure 1 shows the electron wave modulus and Figure 2 the phase difference across the atomic column for the simulations. These images indicate how the wave propagates inside the sample. Although CBED simulations consider an aberration free probe, we have found that an apparent defocus can be estimated as an aberration as the crystal thickness increases. This has been corrected for and it is displayed in Figures c). For the PW in a crystal case (a), the broadening and contribution of neighboring columns due to propagation can be observed in combination with channelling effects. In the case of the WDD reconstructions (b,c), the channeling effects can be appreciated, but the detailed features related to neighboring column interactions are lost. For the PW simulation of a single atomic column (d) only the channelling effects are observable. When comparing b), c) and d), it can be seen that WDD reconstructions appear to be sensitive to the channeling of the wave but neglect the contributions of neighboring columns.
Conclusion: WDD phase reconstructions appear to be somewhat insensitive to the environment of an atomic column. A discussion on the possible causes for this and how the ptychography method treats this information in the form of probe aberrations will be presented [6].

References:
[1] H. Ryll *et al*, Journal of Instrumentation **11** (2016) P04006
[2] P.D. Nellist *et al*, Nature **374** (1995) 630
[3] H. Yang *et al,* Nature Communications **7** (2016) 12532
[4] J. M. Rodenburg and R. H. Bates, Phil. Trans. R. Soc. Lond. A. **339** (1992) 521
[5] I. Lobato and D. Van Dyck, Ultramicroscopy **156** (2015) 9
[6] The research leading to these results has received funding from the EPSRC (EP/M010708/1).

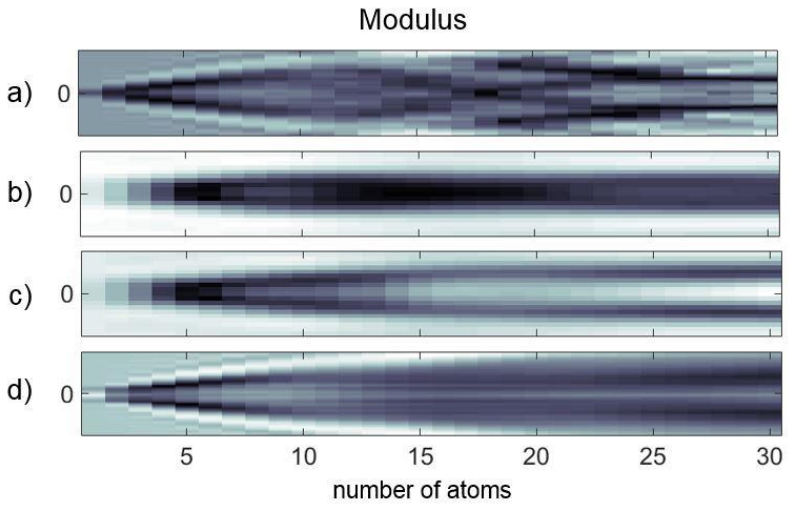

Figure 1. Modulus of electron wave for a) PW inside a crystal, b) WDD reconstruction of a crystal, c) WDD reconstruction of a crystal using aberration correction and d) PW inside an isolated atomic column. Vertical axis corresponds to the number or atoms in the column and horizontal axis is 2 Angstrom distance, in which the atoms are located at the middle (0 marker). Intensity ranges from black = 0 to white = 1.

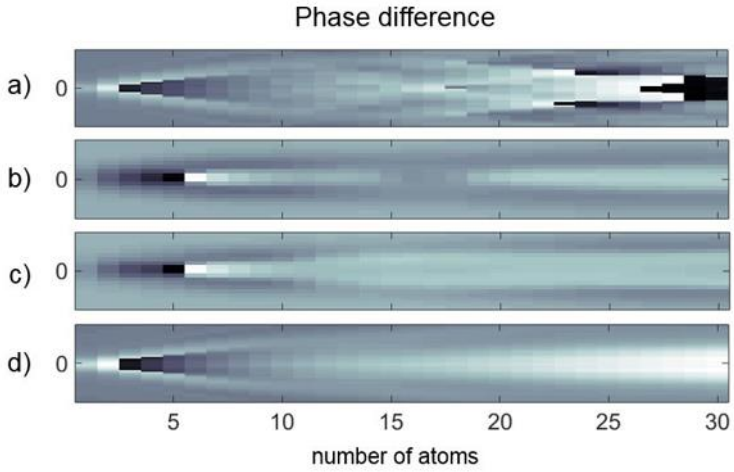

Figure 2. Phase difference of electron wave for a) PW inside a crystal, b) WDD reconstruction of a crystal, c) WDD reconstruction of a crystal using aberration correction and d) PW inside an isolated atomic column. Vertical and horizontal axes correspond to the same as in Figure 1. Intensity ranges from black = -π to white = π.

LS 1: Single particle EM, microscopy of membrane assemblies

LS1.001
Cryo-electron tomography – method development and application on the nuclear exploration

A. Frangakis[1]

[1]Goethe University Frankfurt, Institute of Biophysics, Frankfurt am Main, Germany

achilleas.frangakis@biophysik.org

My talk will focus on the understanding of the macromolecular supra-organisation in the nucleus. Within cryo-electron tomograms we could visualize the complete ribosome biogenesis in a frozen hydrated state, from which the structure of the elongating RNA Polymerase I was solved at 25 Å resolution. Subsequent cryo-EM single particle analysis of the isolated RNA Polymerase I led to a structure at 3.8 Å resolution that unravelled how the RNA Polymerase I is allosterically controlled. Ultimately my talk should highlight our efforts towards visualizing interactions of macromolecular machineries within the unperturbed cellular context.

LS1.002
The complete structure of the chloroplast 70S ribosome in complex with translation factor pY

P. Bieri[1], M. Leibundgut[1], M. Saurer[1], D. Boehringer[1], N. Ban[1]

[1]ETH Zurich, Zurich, Switzerland

boehringer@mol.biol.ethz.ch

Chloroplasts are cellular organelles of plants and algae that are responsible for energy conversion and carbon fixation by the photosynthetic reaction. As a consequence of their endosymbiotic origin, they still contain their own genome and the machinery for protein biosynthesis. Here, we present the atomic structure of the chloroplast 70S ribosome prepared from spinach leaves and resolved by cryo-EM at 3.4 Å resolution. The complete structure reveals the features of the 4.5S rRNA, which probably evolved by the fragmentation of the 23S rRNA, and all five plastid-specific ribosomal proteins (PSRPs). These proteins, required for proper assembly and function of the chloroplast translation machinery, bind and stabilize rRNA including regions that only exist in the chloroplast ribosome. Furthermore, the structure reveals plastid-specific extensions of ribosomal proteins that extensively remodel the mRNA entry and exit site on the small subunit as well as the polypeptide tunnel exit and the putative binding site of the signal recognition particle on the large subunit. The translation factor pY, involved in light and temperature dependent control of protein synthesis, is bound to the mRNA channel of the small subunit and interacts with 16S rRNA nucleotides at the A- and P-site, where it protects the decoding center and inhibits translation by preventing tRNA binding. The small subunit is locked by pY in a non-rotated state, in which the intersubunit bridges to the large subunit are stabilized.

LS1.003
Graphene liquid-enclosure facilitates single-cell analysis with high resolution electron microscopy

I. N. Dahmke[1], A. Verch[1], R. Weatherup[2], S. Hofmann[2], N. de Jonge[1]

[1]INM - Leibniz Institute for New Materials, Innovative Electron Microscopy, Saarbrücken, Germany
[2]University of Cambridge, Department of Engineering, Cambridge, United Kingdom

indra.dahmke@leibniz-inm.de

Introduction: The heterogeneity of cells in human tissues represents a major hurdle for the development of effective treatments for non-communicable diseases, such as cancer [1]. Genomic and proteomic analysis of single cells explores their individual structure, as well as response to treatments [2]. Yet, analysis of proteins on the single-molecule level in relation to the underlying cellular structure remains challenging. Electron microscopy (EM) would provide the necessary spatial resolution, but in the course of conventional sample preparation, information about the related cellular structures is usually lost [3].
Objective: We used a graphene liquid-enclosure to enable high-resolution EM of single cells for the analysis of certain cytoskeletal and membrane proteins. As a proof of principle, we examined the assembly of the growth factor receptor ErbB2 and actin fibres in human SKBR3 breast cancer cells.
Materials and Methods: SKBR3 cells were grown on silicon microchips. The cells were either stained with FITC-phalloidin to label actin fibers or with quantum dot (QD) nanoparticles bound to specific anti-ErbB2 Affibodies to label ErbB2 molecules, respectively. Then, the samples were covered with graphene and subjected to imaging with correlative light microscopy and EM (Fig. 1a). Cellular regions expressing high levels of ErbB2 emitted a red fluorescence (655 nm, Fig. 1b), whereas actin fibers appeared in green (520 nm, Fig. 1g). The integrity of the graphene was inspected with scanning EM (SEM, Fig. 1c, h). Subsequently, we performed high resolution imaging either with scanning transmission EM (STEM, 200 kV; Fig. 1e) or transmission EM (TEM, 200 kV, energy filter: 17eV; Fig. 1d, f, i).
Results: With STEM, we achieved a resolution better than 3 nm that allowed for the identification of single, paired and clustered QDs (Fig. 1e). Next, we performed pair correlation analysis to compare the number of functionally active homodimers in different cellular regions [4] (data not shown). Furthermore, using TEM, we visualized unstained cellular structures of low contrast, such as actin fibres (Fig. 1f).
Conclusion: In summary, a graphene enclosure enabled correlative light- and electron microscopy of intact, hydrated cells. It provided a versatile technique for studying distribution patterns of membrane proteins in single cells in relation to underlying cellular structures. Our approach can be used to investigate the immediate interaction of cancer therapeutics with their targets at the single-molecule level and to study potential causes of chemoresistance in heterogeneous cancer cell populations [4].

References:
[1] JR Heath, A Ribas, PS Mischel PS. Nat Rev Drug Discov. 2016;15(3):204-16.
[2] X Chen et al. Nat. Biotechnol. 34, 1111-1118 (2016).
[3] I N Dahmke *et al.*, Microsc. Microanal. **22** S5 (2016) p. 74.
[4] D Peckys, U Korf and N de Jonge, Sci Adv **1** (2015), p. e1500165.
[5] We thank J Hermannsdörfer, U Korf, and D Peckys for discussions and E Arzt for his support through INM. Research was supported by the Leibniz Competition 2014. R.S.W. received a Research Fellowship from St. Johns College, Cambridge & a Marie Skłodowska-Curie Fellowship (Grant ARTIST no. 656870).

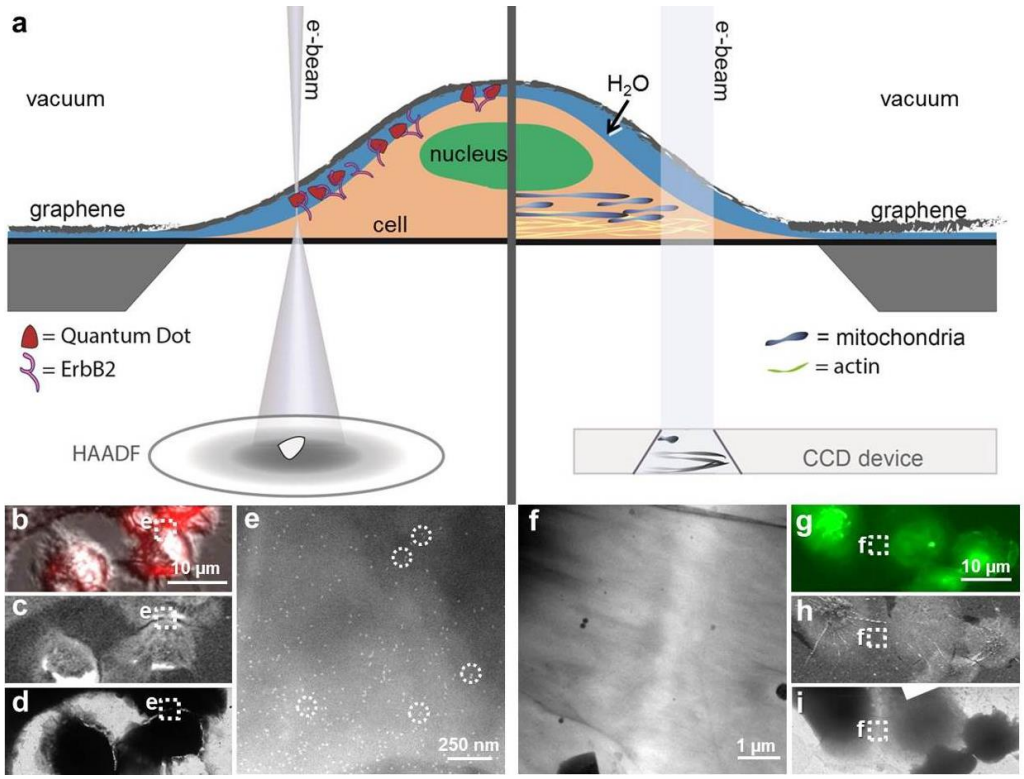

Figure 1. Correlative light- and electron microscopy of membrane proteins in intact, hydrated SKBR3 cells. a) Schematic of experimental approach. b) Differential interference contrast and fluorescence overlay of graphene covered cells on a microchip, labeled with QDs (red). c), h) SEM images of graphene layer. White regions indicate electric charging, due to cracks (black). d), h) Overviews in low magnification TEM. e) High-resolution dark-field STEM image. QDs appear as white dots, assembled into clusters, monomers and pairs (white, dotted circles). f) High resolution TEM of actin fibers in two adjacent cells. g) Fluorescence image of SKBR3 cells stained FITC-phalloidin (green).

LS1.004
Structure of Aβ(1-42) and light chain-derived amyloid fibrils visualized with cryo-EM

M. Schmidt[1], A. Schmidt[1], K. Annamalai[1], K. Lasker[2], N. Grigorieff[3], M. Fändrich[1]

[1]University Ulm , Institute of Protein Biochemistry , Ulm, Germany
[2]Stanford University, Stanford, CA, United Statesof America
[3]Howard Hughes Medical Institute, Janelia Research Campus, Ashburn, VA, United States of America

matthias.schmidt@uni-ulm.de

Amyloid fibrils are hallmarks in severe diseases like Alzheimer"s and Parkinson's in which misfolded proteins aggregate into filamentous structures and deposit within a variety of organs and tissues. Alzheimer"s disease (AD) is a fatal neurodegenerative disorder in humans and the main cause of dementia in aging societies. The disease is characterized by the aberrant formation of β-amyloid (Aβ) peptide oligomers and fibrils. Although the connection between Alzheimer"s disease and Aβ fibrillation is extensively documented, much is still unknown about the formation of these Aβ aggregates and their structures at the molecular level. In systemic AL amyloidosis, fibrils are formed by full light immunoglobulin light chains which leads to depositions in organs like heart, kidney and liver. The combined electron cryo-microscopy, three-dimensional reconstruction, and integrative structural modeling methods determined the molecular architecture of a fibril formed by Aβ(1-42), a particularly pathogenic variant of Aβ peptide and amyloid fibrils from light chain-derived 12 amino acid long peptide. We present a three-dimensional structure of a full-length Aβ(1-42) amyloid fibril that enabled us to build an atomic model of the filament core revealing the fold and packing of the polypeptide chains in the well-ordered parts of the structure.[1] And for the light chain derived fibrils we obtained different morphologies that display striking similarities in their lattice like structural organization. All fibrils peptide dimers are arranged in a face-to-face packed manner, adopting a steric zipper structure[2]. Modeling the atomic structure based on calculated density reveals intermolecular interaction stabilizing the protofilaments and the packing of multiple protofilaments into polymorphic fibrils.

References:
[1] Schmidt, M. et al. PNAS 112: 11858-11863 (2015).
[2] Nelson R, et al. Nature 435(7043):773–778 (2005).

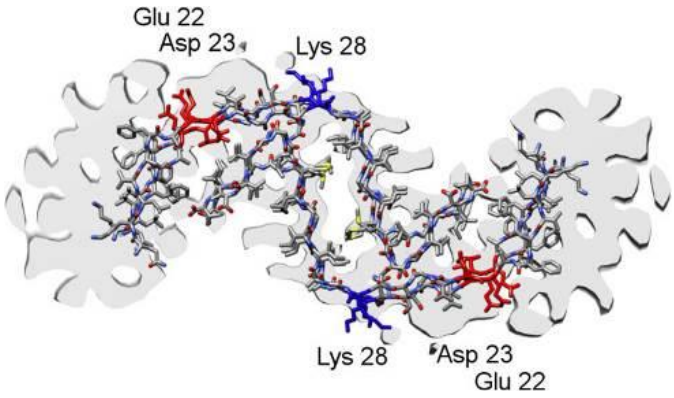

Figure 1. Density superimposed with the family of Aβ(17-42) peptide models producing the best fit to the data.

LS1.005
Freeze fracture analysis of astrocytomas graded WHO II, III and IV reveals a correlation of orthogonal arrays of particles and the grade of malignancy

P. Fallier-Becker[1], M. Nieser[1], U. Wenzel[1], R. Ritz[1,2], S. Noell[1,2,3]

[1]Institute of Pathology and Neuropathology, University Hospital of Tuebingen, Tuebingen, Germany
[2]Schwarzwald-Baar Klinik, Neurosurgery, Villingen-Schwenningen, Germany
[3]University Hospital of Tuebingen, Neurosurgery, Tuebingen, Germany

petra.fallier-becker@med.uni-tuebingen.de

Introduction: Aquaporin 4 (AQP4) is the main water channel in the brain and consists of at least two isoforms: AQP4-M23 and the 22 amino acids longer isoform AQP4-M1. AQP4 forms tetramers and higher order structures called orthogonal arrays of particles (OAPs). They are found in great quantities in astrocytic endfoot membranes at the blood-brain barrier. Formation of OAPs depends on the composition of the extracellular matrix. We know from our earlier studies that in glioblastomas, the most malignant glial tumor graded WHO IV, no typical OAPs are formed. due to changes in the composition of the extracellular matrix (e.g. loss of agrin, a heparansulfat proteoglycan) [1].
Objectives*:* Beyond that we wanted to know whether or not there is a correlation of the number of OAPs and the grade of malignancy in astrocytomas graded WHO II, III and IV.
Materials and Methods: Resected tissues from 22 patients with astrocytomas graded WHO II, III and IV were analyzed using the freeze fracture technique. In addition quantitative real-time PCR was performed in order to determine the ratio of the two different AQP4-isoforms M1 and M23 and to find out if there is a correlation to the grade of malignancy.
Results: Counting OAPs in freeze fracture replicas of resected tumor tissue we found a negative correlation with the grade of malignancy and the number of typical OAPs. The results are shown in Fig. 1 indicating that astrocytomas WHO grade II yielded significantly more OAPs than glioblastomas (WHO grad IV). Comparing the AQP4 M23/M1 ratio in healthy brains (>3) with the one in astrocytomas there was a clear decrease (1.14 – 1.94) but without any correlation to the grade of malignancy [2].
Conclusion: We conclude from these results that the changes of the microenvironment in astrocytomas proceeds stepwise with increasing grade of malignancy and formation of OAPs may serve as indicator for these processes.
Acknowledgments: We thank Mrs. Gabriele Frommer-Kaestle and Mrs. Eva-Maria Knittel for excellent technical work.

[1] Noell S, Wolburg-Buchholz K, Mack AF, Ritz R, Tatagiba M, et al. (2012) Dynamics of expression patterns of AQP4, dystroglycan, agrin and matrix metalloproteinases in human glioblastoma. Cell and Tissue Research 347: 429-441.
[2] Fallier-Becker P, Nieser M, Wenzel U, Ritz R, Noell S (2016) Is Upregulation of Aquaporin 4-M1 Isoform Responsible for the Loss of Typical Orthogonal Arrays of Particles in Astrocytomas? International Journal of Molecular Sciences 17.

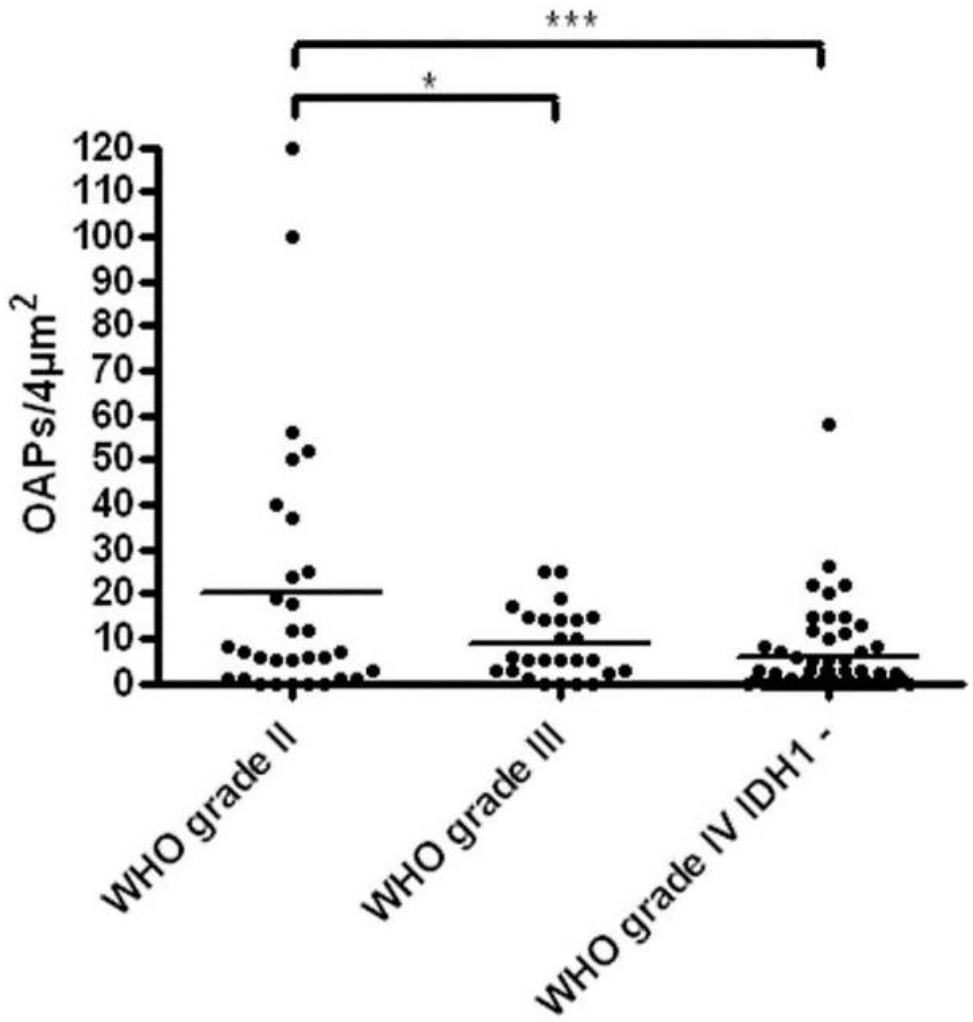

Figure 1. Number of OAPs counted per 4µm2 in astrocytoma WHO grade II, III and IV.

LS1.006
The role of grana margin components in the formation of the helical connections of grana-stroma thylakoids

Ů Kowalewska[1], K. Bednarska[2], D. Jakubauskas[3], M. Pribil[4], M. Garstka[2], A. Mostowska[1]

[1]University of Warsaw, Faculty of Biology, Department of Plant Anatomy and Cytology, Warsaw, Poland
[2]University of Warsaw, Faculty of Biology, Department of Metabolic Regulation, Warsaw, Poland
[3]University of Copenhagen, Niels Bohr Institute, Copenhagen, Denmark
[4]University of Copenhagen, Copenhagen Plant Science Centre, Department of Plant and Environmental Sciences, Copenhagen, Denmark

lucja.rudo@gmail.com

Complex spatial structure of grana together with molecular mechanisms of the chlorophyll-protein (CP) complexes reorganization are the main factors responsible for maintaining the maximal efficiency of photosynthetic apparatus. Grana exhibits helical arrangement of grana thylakoids (GTs) connected with stroma thylakoids (STs) by staggered membrane protrusions. The role of such complex structure in CP complexes reorganization is still not clear. Despite the fact that the lateral heterogeneity of thylakoid membranes and the stacking process are extensively studied, the mechanism of formation and maintaining of helical GT-ST connections is not known.
The objective of this study was to reveal the probable role of the main lipid (monogalactosyldiacylglycerol – MGDG) and protein (THYLAKOID CURVATURE1 – CURT1) components of the grana margin region in the formation of helical connections between GTs and STs. MGDG is the major thylakoid lipid forming the hexagonal phase instead of the lipid bilayer while CURT1 protein is capable of inducing the curvature of the grana membrane. Additionally, samples of isolated thylakoids were analyzed to point out the influence of isolation procedure on the grana spatial structure arrangement since isolated thylakoids are typically used for biochemical studies of grana dynamics.
Experiments were performed with the use of fully developed leaves and isolated thylakoids of *mgd1* mutants and *oeCURT1A-cmyc curt1a-2* plants of *A.* thaliana with a lowered level of MGDG and an increased level of CURT1A protein respectively. Samples were analyzed by electron tomography. Tilt series were reconstructed using the SIRT or SART algorithms, hand segmented and modeled with the use of 3Dmod software.
Substantial changes in grana spatial structure were observed. In *oeCURT1A-cmyc curt1a-2* plants no helical character of GT-ST connections was visible in the range of the modeled region. Only specific membrane turn-arounds connected neighboring thylakoids inside a grana stack. Image of spatial grana arrangement of *mgd1* mutants exhibited differences compared to the grana picture of *wt* plants however the general pattern of helical connections was still visible. 3D arrangement of isolated thylakoid membranes and grana within mesophyll cells were similar but differences between stacking repeat distance of neighboring membranes were observed.
Concluding, CURT1 protein seems to play the primary role in establishing helical connections between grana and stroma thylakoids.

Presented work was supported by the National Science Centre, grant 2014/13/B/NZ3/00413.
Tomography of *mgd1* samples was performed in the Laboratory of Electron Microscopy, Nencki Institute of Experimental Biology on TEM JEM 1400 (JEOL Co., Japan) equipped with tomographic holder and 11 Mpx TEM Camera MORADA G2 (EMSIS GmbH, Germany)

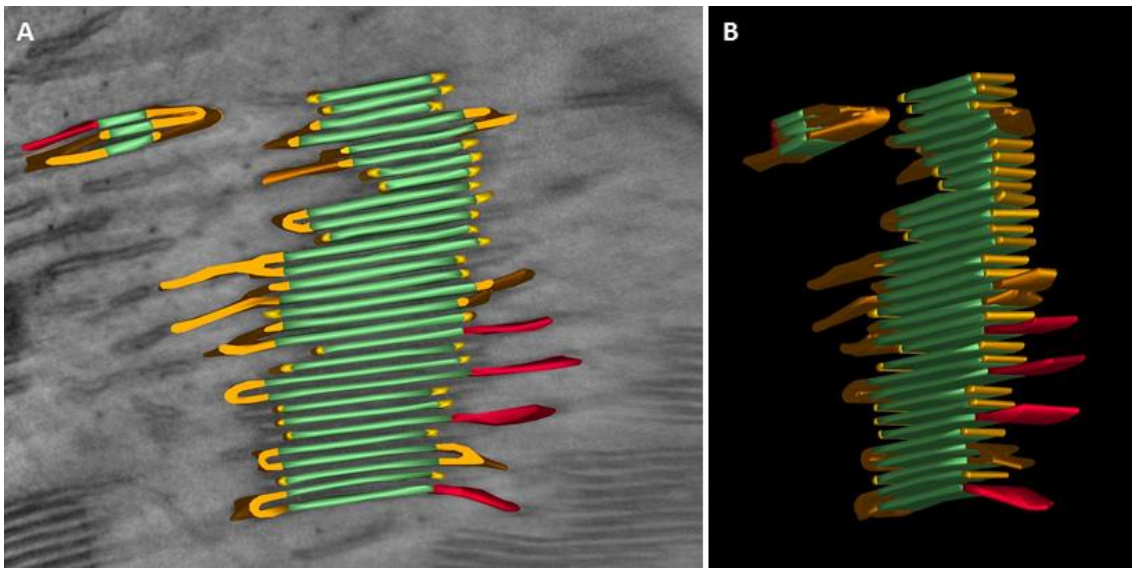

Figure 1. 3D model of granum of *oeCURT1A-cmyc curt1a-2 A. thaliana* plants (leaf sample). A – surface model embedded in the selected TEM layer, B – surface visualization (60°).

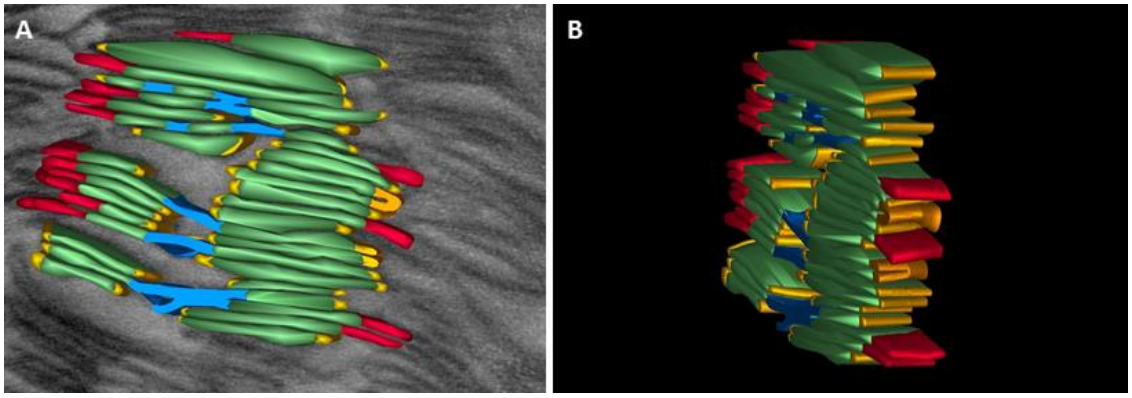

Figure 2. 3D model of granum of *oeCURT1A-cmyc curt1a-2 A. thaliana* plants (isolated membranes). A – surface model embedded in the selected TEM layer, B – surface visualization (60°).

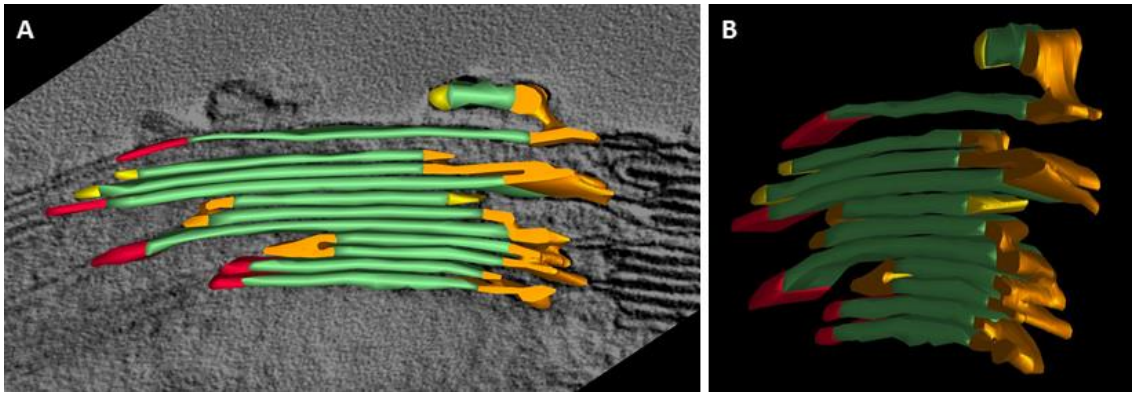

Figure 3. 3D model of granum of *mgd1 A. thaliana* mutant (leaf sample). A – surface model embedded in the selected TEM layer, B – surface visualization (60°).

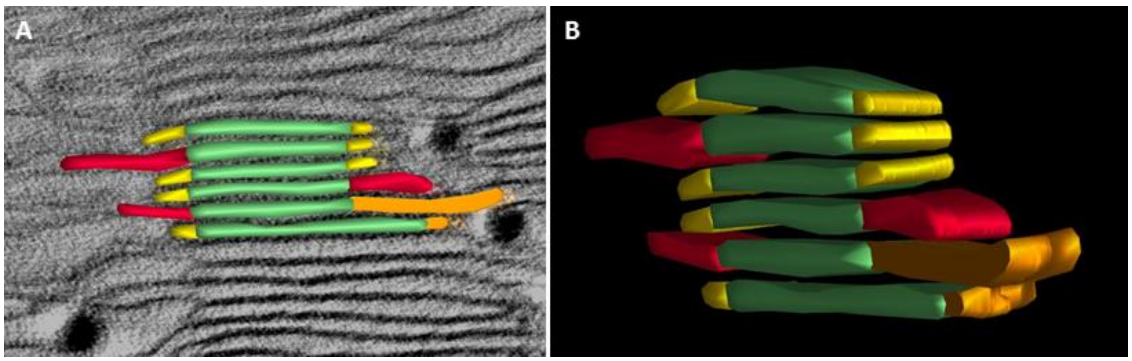

Figure 4. 3D model of granum of *mgd1 A. thaliana* mutant (isolated membranes). A – surface model embedded in the selected TEM layer, B – surface visualization (60°).

LS1.007
Structure of motor and flagellum of the archaeum Pyrococcus furiosus at molecular / atomic resolution

B. Daum[1], A. Bellack[2], R. Reichelt[2], P. Chaudhury[3], S. Albers[3], V. Gold[1], R. Rachel[4]

[1]University of Exeter, Living Systems Institute, Exeter, United Kingdom
[2]University of Regensburg, Archaea Centre, Regensburg, Germany
[3]University of Freiburg, Molecular Biology of Archaea, Freiburg, Germany
[4]University of Regensburg, Centre for EM, Regensburg, Germany

bertram.daum@biophys.mpg.de

Introduction: Archaea are prokaryotic cells inhabiting diverse habitats on this planet, ranging from extreme (in terms of acidity, salinity, temperature) to ambient environments, including the human body, e.g. skin and digestive tract. Fundamental to their prolific diversification and ability to invade new habitats is their capability to adhere to surfaces, and to be motile, i.e. to swim. In the course of evolution, archaea have developed their own propulsion and adherence machineries, also called 'archaellum', which is distinct from bacterial flagella with respect to their biogenesis, assembly, and architecture (1). Here, we present the structure of the motility apparatus of one of the fastest swimming cells known, the euryarchaeum *Pyrococcus furiosus* (2,3).
Objectives: To understand the mechanism of the archaeal way to swim, we have investigated the architecture of the archaellar motor and flagellum, the 'archaellum', using cutting-edge cryoEM.
Methods: We employed electron cryo-tomography to investigate the *in situ* structure and organization of the motor complexes in the intact cell, as well as single particle cryoEM to analyze the archaellum at atomic resolution. This was complemented with structural studies using STEM tomography of high-pressure frozen, plastic embedded samples in 500 to 800 nm thick sections.
Results: Most cells assemble a bundle of up to 50 archaella, which are held at one cell pole by a cytoplasmic protein sheet that resides ~40 nm below the plasma membrane. At the cell surface, the S-layer of *P. furiosus* forms gaps of ~18 nm in diameter to accommodate each extruding filament. Sub-tomogram averaging enabled us to elucidate the structure of the macromolecular motor and assembly complex at the base of each archaellum. The complex consists of a ring-shaped assembly surrounding a central barrel-shaped unit that spans the cytoplasm between plasma membrane and cytoplasmic sheet. Using cryoEM and helical reconstruction of isolated filaments, we have solved the structure of the *Pyrococcus* archaellum at 4.2 Å resolution. The structure revealed that the archaellum is a heavily glycosylated type-4 pilus consisting of a highly conserved alpha-helical backbone and a species-specific beta-strand-rich outer sheath.
Using a combination of electron cryo-tomography of natural mutants and targeted gene knockouts (5), single particle electron microscopy of heterologously expressed subunits, biochemical data and bioinformatics, we aim to identify the positions of individual protein components (4) within the map of the motor complex in order to build a pseudo-atomic structural model of the entire machinery.
Conclusion: Our work will provide invaluable and unprecedented insights into the structure and mechanism of the archaellum and will pave the way towards a complete understanding this fascinating molecular device.

References:
[1] Albers SV and Jarrell KF 2015 Front. Microbiol. 6: 23
[2] Naether DJ et al 2006 J. Bacteriol. 188: 6915-6923
[3] Herzog B and Wirth R 2012 Appl Environm Microbiol. 78: 1670-1674
[4] Chaudhury P et al 2016 Mol Microbiol 99: 674-685
[5] Waege I et al 2010 Appl. Environm. Microbiol. 76: 3308-3313

Figure 1. 3D model based on cryo-tomography data of a cell of *P. furiosus,* showing the cell envelope (petrol), the cytoplasmic protein sheet (green), and many archaella (lilac).

LS1.LBP01
Effects of synchronized and non- synchronized administration of hMG on ovarian tissues in nandrolon decanoate treated adult female rats – a histological, histochemical and ultrastructural study

F. Dehghani[1,2], F. Mesbah[2], H. Bordbar[1,2], T. Talaei[2], H. Mirkhani[3]

[1]Shiraz University of Medical Sciences, Histomorphometry & stereology research center, Shiraz, Islamic Republic of Iran
[2]Shiraz University of Medical Sciences, Anatomy, Shiraz, Islamic Republic of Iran
[3]Shiraz University of Medical Sciences, Pharmacology, shiraz, Islamic Republic of Iran

dehghanf@sums.ac.ir

Background: The follicular development and oocyte maturation may be affected by external factors such as drugs. Nandrolone decanoate (ND) as an anabolic androgenic steroid (AAS) has great popularity and acceptability and is abused by athletes and non-athletes of both sexes. Misuse of ND can damage the ovary and because of its crucial role in reproduction, may leads to reproductive failure. We aimed to evaluate the preventive effects of hMG on ovarian tissues in ND-treated female rats.
Methods: Forty female Sprague Dawley rats were divided into eight groups. The five experimental groups received 3 and/or 10 mg/kg of ND synchronized and non-synchronized with 10 IU of hMG and hMG alone. The three sham and control groups received solvents of ND and hMG. The animals' weight and serum levels of FSH, LH, progesterone and estrogen, as well as the weight, volume and dimensions of the ovaries were measured. The ovaries were prepared for histological, histochemical and ultra-structural studies.
Results: The rats weight had a normal trend in all the study groups and showed no significant difference. Ovarian weight and dimensions were not changed, but the ovarian volume and sex hormones in the experimental groups was decreased. The rate of apoptosis was increased in the experimental groups. Follicular and stromal cells were damaged in the experimental groups except the hMG group.
Conclusion: The ovarian tissue is irreversibly and irreparably damaged by ND and hMG cannot prevents the destruction of the follicles. This can be a serious warning to women who abuse ND.

Keywords: Apoptosis; Follicle; hMG; Nandrolon Decanoate; Ovary

LS 2: From cells to tissues: Cellular electron tomography and imaging of large volumes

LS2.001 invited
Deconstruction and reconstruction of neuronal computations in olfaction

A. A. Wanner[1], C. Genoud[1], R. W. Friedrich[1]

[1]Friedrich Miescher Institute for Biomedical Research, Basel, Switzerland

adrian.wanner@fmi.ch

In the olfactory bulb (OB) of zebrafish, odors evoke distributed patterns of activity across glomeruli that are reorganized by networks of interneurons (INs). This reorganization results in multiple computations including a decorrelation of activity patterns across the output neurons, the mitral cells (MCs). To understand the mechanistic basis of these computations it is essential to analyze the relationship between function and structure of the underlying circuit. We combined in vivo multiphoton calcium imaging with dense circuit reconstruction from serial block-face electron microscopy (SBEM) stacks of the larval zebrafish OB (figure 1). To address bottlenecks in the workflow of this emerging methodology we developed a procedure for conductive sample embedding, a pipeline for high-throughput image annotation and a workflow to correlate SBEM stacks with light microscopy data of the same specimen (Wanner et al. 2016a). We reconstructed all neurons (n > 1,000) in the olfactory bulb of a zebrafish larva with high accuracy (Wanner et al. 2016b) and annotated more than 400,000 synapses of different neuron types. We identified new, rare cell types and found that the IN network organization is governed by glomerular identity. For > 80% of the reconstructed neurons we were able to map neuronal activity that was measured in the same specimen prior to electron microscopy (EM). Decorrelation of activity patterns elicited by similar natural odors was present already before the emergence of granule cells, but is mediated by specific inter-glomerular IN projections. These results provide strong evidence that the topology of IN networks in the OB determines circuit function, and that the network is optimized, presumably by evolution, to process representations of natural odors.

References:

[1] Wanner A. A., Genoud C., Masudi T., Siksou L. & Friedrich R. W. (2016). Dense EM-based reconstruction of the interglomerular projectome in the zebrafish olfactory bulb. Nat. Neurosci. 19, 816–825

[2] Wanner, A. A., C. Genoud and R. W. Friedrich (2016). 3-dimensional electron microscopic imaging of the zebrafish olfactory bulb and dense reconstruction of neurons. Scientific Data 3.

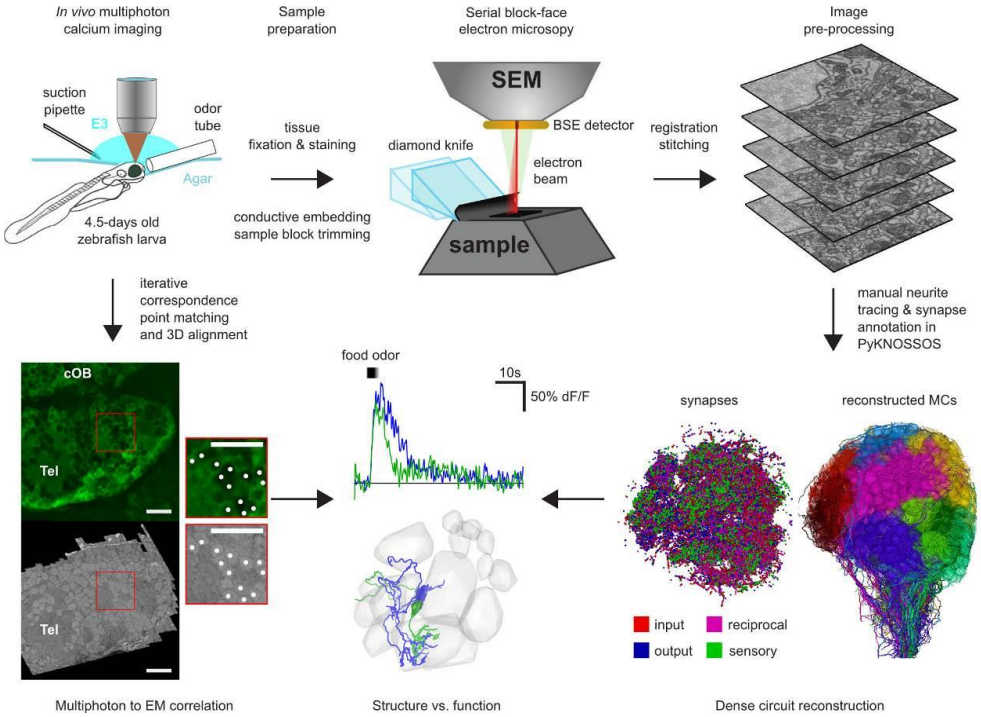

Figure 1. Workflow for correlative SBEM and high throughput neuronal circuit reconstruction.

LS2.002
In situ cryo-electron tomography of frozen hydrated specimens prepared by cryo-focused ion beam milling

M. Schaffer[1], B. D. Engel[1], S. Pfeffer[1], S. Kleindiek[2], S. Albert[1], T. Laugks[1], J. M. Plitzko[1]
W. Baumeister[1]

[1]Max Planck Institute of Biochemistry, Dept. of Molecular Structural Biology, Martinsried, Germany
[2]Kleindiek Nanotechnik GmbH, Reutlingen, Germany

schaffer@biochem.mpg.de

Recently, cryo-electron tomography (CET) has become a driving technique in structural biology. Due to technological advances in detector efficiency, contrast enhancement, and specimen preparation, it is now possible to visualize small macromolecules, such as membrane-bound complexes, within the native cellular environment [1-4]. These *in situ* studies of biological systems often reveal the molecular structures of specific conformational or assembly states, which are then mapped back into the cellular volume to gain new insights into biological processes (Fig.1.).
An essential step for *in situ* CET investigations is the preparation of vitreous frozen specimens by cryo-focused ion beam (cryo-FIB) milling. The thinning of plunge-frozen cells to produce lamellas directly on TEM grids has been developed into a standard technique with highly reproducible results [5]. However, thicker specimens, such as large eukaryotic cells or tissue samples, can only be vitrified by high-pressure freezing and thus cannot be prepared by this standard technique. To overcome this limitation, we recently developed a cryo-FIB lift-out routine utilizing a newly developed cryo-gripper tool. There is no strict sample size limitation with this approach because the volume of interest is completely extracted from the frozen bulk material and transferred to a separate TEM grid for final thinning.
In this presentation, we will describe the key aspects of the different cryo-FIB sample preparation methods for CET and showcase recent *in situ* studies of membrane-bound macromolecules, such as photosynthetic complexes and ribosomes.

References:
[1] B Engel et al, PNAS 112 (36) (2015), p.11264.
[2] S Pfeffer et al, Nature Communications 8 (2017), 14516.
[3] M Schaffer et al, J Struct Biol. 197(2) (2017), p.73.
[4] J Mahamid et al, Science 351(6276) (2016), 969-972.
[5] M Schaffer et al, Bio-protocol 5(17) (2015), e1575.

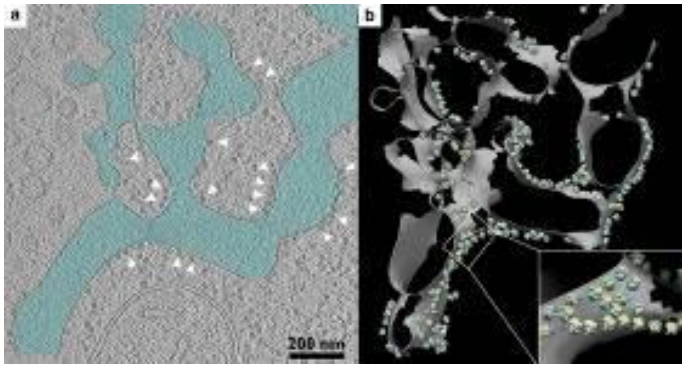

Figure 1. *In situ* CET investigation of plunge-frozen *Chlamydomonas reinhardtii* cellular volumes. (a) Slice through a reconstructed tomogram showing the endoplasmic reticulum (ER) in blue and ER-associated ribosomes (indicated by white triangles); (b) Subtomogram average of the ER-associated ribosomes, including the large (blue) and small (yellow) ribosomal subunits mapped onto a segmentation of the reconstructed membrane. Image adapted from S. Pfeffer et al, Nature Communications [2].

LS2.003
Cryo-FIB SEM observations of ultrastructural framework underlying intracellular mineral formation in alga Emiliania huxleyi

S. Sviben[1]

[1]Max Planck Institute of Colloids and Interfaces, Biomaterials, Potsdam, Germany

sanja.sviben@mpikg.mpg.de

Introduction: Cryo-focused ion beam (cryo-FIB) scanning electron microscopy (SEM) is an emerging technique for revealing the structural organization of cells in 3D at nanometric resolution (Schertel et al., 2013). Such information can provide new insights on the shape and morphology of organelles, and enable the accurate determination of the surface areas and volumes of cellular compartments.
We used cryo-FIB SEM to investigate ultrastructural features of coccolithophores. Coccolithophores are unicellular marine algae that produce mineralized scales composed of complex-shaped calcite crystals known as coccoliths. The coccolith formation takes place in a specialized compartment termed the coccolith vesicle. Upon completion the coccolith is extruded to the cell surface (Paasche, 2001). The coccolithogenesis process is of immense importance for the global cycle of carbonate as coccolithophore calcification sequesters massive deposits of CaCO3 into seafloor sediments (Ziveri et al., 2007).
Objectives: We investigated the ultrastructure of the most abundant coccolithophore *Emiliania huxleyi*. The morphological changes of the endomembrane system associated with the coccolith biogenesis remain largely unknown. Our aim was to acquire 3D information about the ultrastructural framework underlying mineral formation and to report its structural reorganizations during coccolith biogenesis.
Materials and Methods: The cells were cultured in an artificial seawater, high pressure frozen, and transferred to a Zeiss Cross Beam 540 FIB SEM microscope. In an automated process a thin slice of material was removed by FIB milling followed by SEM imaging of the freshly exposed block face. After each milling step (thickness 15 nm) secondary electron and back-scattered electron images were acquired simultaneously. The final voxel size was 5nm x 5nm x 15nm.
Results: All imaged cells contained an intracellular coccolith. For early-stage coccoliths a membranous structure termed reticular body was observed adjacent to the coccolith vesicle (Fig. 1). The reticular body was not visible in more advanced stages of coccolith formation. Instead, large vesicles exhibiting white contrast were observed close to the surface of the growing coccolith. We noticed several membrane systems on the distal side of the late-stage coccolith (Fig 2a). 3D visualization revealed them to belong to the same membrane system which showed no resemblance to the reticular body and covered most of the central area of the coccolith (Fig 2b). Due to the inherent limits of classical 2D imaging, this membrane system has never been described before.
Conclusion: Besides providing the first three-dimensional overview of the ultrastructure of *E. huxleyi* in a close-to-native state, we also present new insights into the changes in cellular ultrastructure that take place during coccolith biogenesis. In addition, acquired dataset enabled the most accurate determination of the surface area of the coccolith vesicle so far and provided information about surface areas of other organelles. This is critical for modelling transport routes that supply the biomineralization process inside the coccolith vesicle with substrates.

References:
[1] Schertel A *et al.* (2013) J Struct Biol 184, 355-360.
[2] Paasche E. (2001) Phycologia 40, 503-529.
[3] Ziveri P *et al.* (2007) Deep Sea Res PT II 54, 659-675.

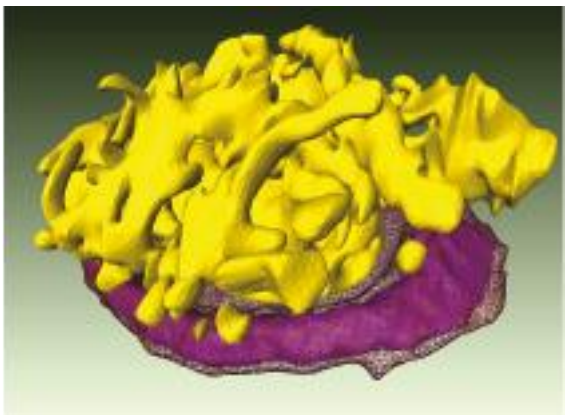

Figure 1. 3D reconstruction of an early-stage coccolith (violet) surrounded by a coccolith vesicle (magenta mesh) and in association with the reticular body (yellow).

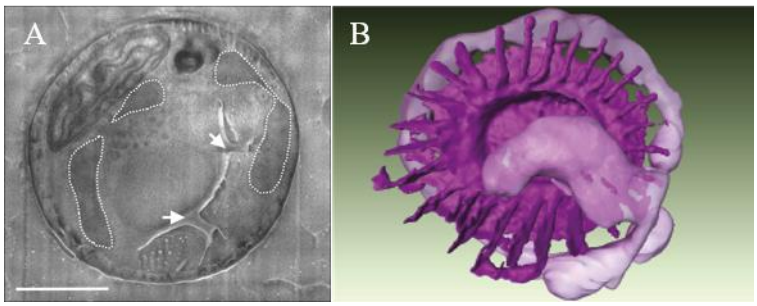

Figure 2. (A) FIB slice of an *E. huxleyi* cell reveals elliptical membrane structures (white dashed line) close to the surface of a late-stage coccolith (white arrows). Scale bar is 1 µm. (B) The 3D reconstruction of the membrane structures reveals a tubular system (light violet) surrounding the coccolith (violet).

LS2.004
Large volume imaging in ultrastructural pathology – 3D morphology and distribution of pathological deposits

I. Wacker[1], C. Dittmayer[2], J. Schroeder[3], R. Schröder[1,4]

[1]Universität Heidelberg, Cryo EM, Centre for Advanced Materials, Heidelberg, Germany
[2]Charité-Universitätsmedizin, Department of Neuropathology, Berlin, Germany
[3]Uniklinikum Regensburg, Central EM-Lab, Pathology Department, Regensburg, Germany
[4]Universitätsklinikum Heidelberg, Cryo EM, BioQuant, Heidelberg, Germany

irene.wacker@bioquant.uni-heidelberg.de

Introduction: In several diseases pathological deposits and inclusions need to be evidenced ultrastructurally [1] to provide a reliable diagnosis. Conventionally, 3D information is not necessary for such EM-diagnosis - for pathognomonic deposits few representative sections of the lesion are sufficient to detect the hallmarks of disease. However, in the inheritable CADASIL condition (Cerebral Autosomal Dominant Arteriopathy with Subcortical Infarcts and Leukoencephalopathy), a disease associated with migraine, dementia and stroke, the characteristic GOM-deposits (Granular Osmiophilic Material, consisting of mutated Notch3 proteins) may be focally distributed under the basement membrane of arteriolar smooth muscle cells with the potential of false negative diagnosis [2,3].
As counterpart to these extracellular deposits intracellular inclusions of unknown origin are found in some congenital myopathies with *DNM2* or *MTM1* mutations [4].
Objectives: We aim at reconstructing considerable 3D volumes from standard pathology samples, often containing only Osmium as a contrasting agent. This is in contrast to most 3D methods where a high degree of metallization has to be introduced during sample preparation, potentially creating problems in routine biopsy handling.
Materials and Methods: Skin biopsies of a CADASIL affected patient were immersed in Karnovsky-fixative, postfixed for 2h in 2% OsO4, dehydrated in graded ethanol, and embedded in Embed812 epoxy resin using an automated LYNX (Leica) tissue processor.
Muscle biopsies from a patient with a novel congenital myopathy were fixed with buffered 2,5% glutaraldehyde, postfixed with 1% OsO4 overnight, block stained for 1h with 0,5% uranyl acetate and 1% phosphotungstic acid in 70% acetone, dehydrated in graded acetone and embedded in renlam. Serial sections (100 nm) were placed on silicon wafers, poststained with uranyl acetate and lead citrate and imaged with ATLAS 5 AT (array tomography) in a SEM (Ultra 55, Zeiss). For 3D reconstructions with finer resolution in z, the block was sputter-coated with Au/Pd and imaged in a Crossbeam 540 using ATLAS 3D nanotomography (Zeiss).
Results: 3D reconstructions from 26 sections of vascular smooth muscle cells contained several complete GOMS with different morphologies (Fig. 1A, B). Steps in the reconstructed volume result from anisotropic voxels created by discrete sampling – as only the surface of the section is imaged in a SEM. 3D reconstructions from nanotomography data (Fig. 2 A, B) recorded with 5nm isotropic pixels are more adequate for resolving small structures such as GOMs.
For the muscle biopsy the question is whether the numerous inclusions inside the cells (Fig. 3 A, B) exist as single entities or are forming an interconnected network. We reconstructed 90 slices and are currently segmenting the inclusions.
Conclusion: We show that routine samples from the pathology lab may indeed be used for 3D analysis of large volumes. For AT the option to poststain section arrays imparts very good image contrast while nanotomography raw data are rather noisy - additional staining is not possible. Applying filters to the nanotomography image stacks helps to obtain un-interrupted membrane profiles allowing segmentation.

[1] Schroeder JA. Chapter 14 in: Lloreta-Trull J. ed., Essentials of Diagnostic Electron Microscopy in Pathology, Springer, 2017, in press
[2] Schultz A, et al. Ultrastruc Pathol, 1999, 23; 241-7
[3] Ishiko A, et al. Acta Neuropathol, 2006, 112; 333-9
[4] Bevilacqua JA, et al. Acta Neuropathol, 2009, 117; 283-291
[5] We thank L. Veith and M. van Ark for technical support and the BMBF for MorphiQuant grant FKZ 13GW0044.

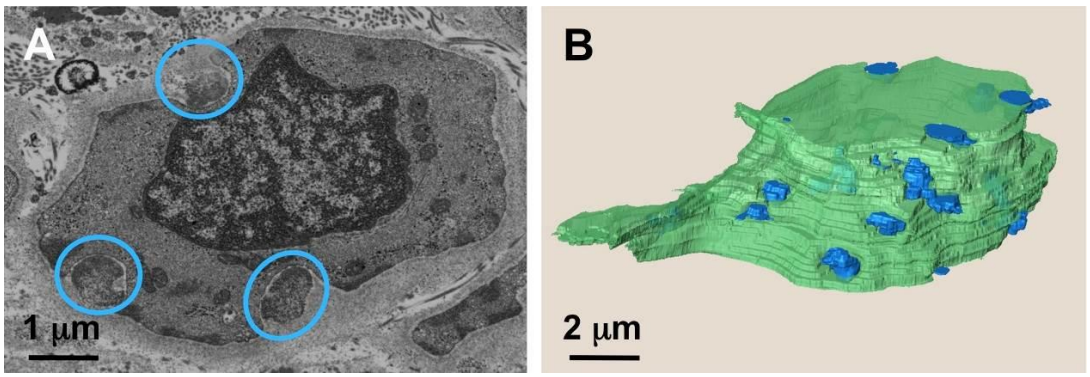

Figure 1. CADASIL, array tomography: Typical raw image (A) and 3D segmentation (B), plasmamembrane shown in green, GOMs in blue.

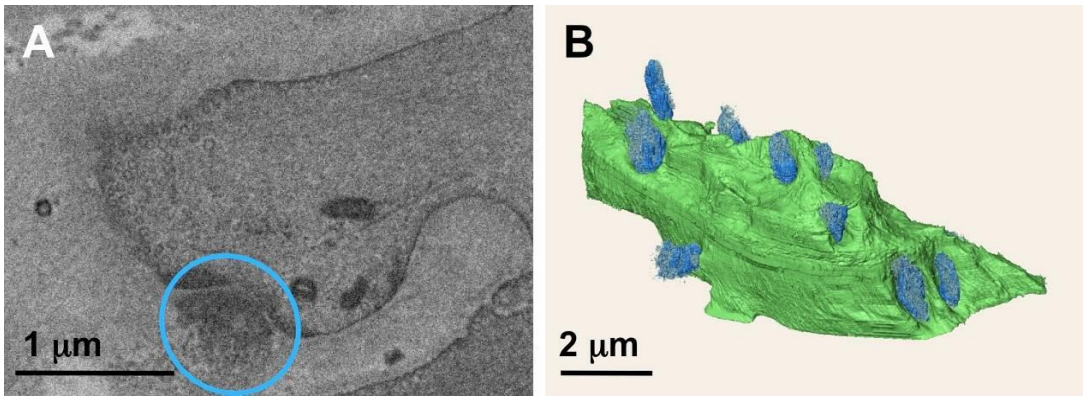

Figure 2. CADASIL, FIBSEM nanotomography: Typical raw image (A) and 3D segmentation (B), colours as above.

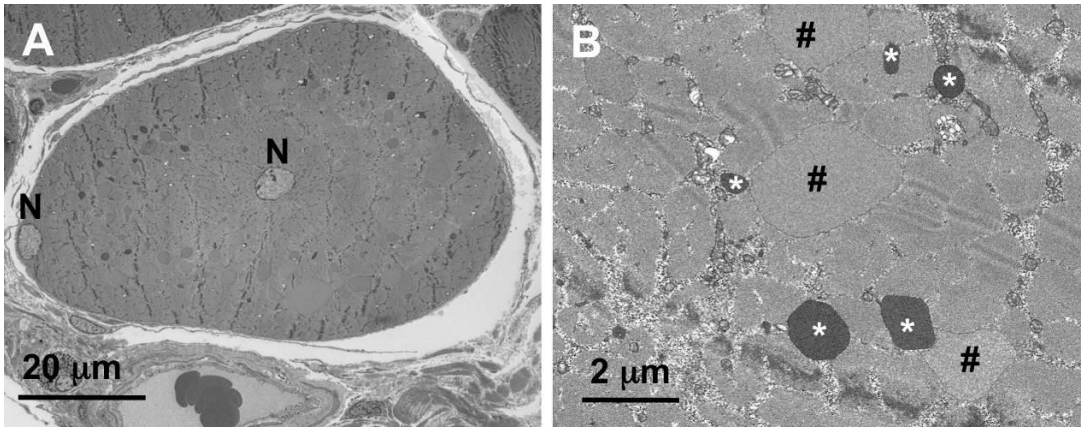

Figure 3. Congenital myopathy with inclusions: Cross section of whole muscle fibre (A), 10nm image pixels, N nucleus; detail (B) with dark (*) and bright (#) inclusions, 3nm image pixels.

LS2.005
Electron microscopy for the small model organisms research – correlative light and electron microscopy and 3D volume acquisitions

I. Kolotuev[1], C. Kizilyaprak[1], B. Humbel[1]

[1]Université De Lausanne, Lausanne, Switzerland

irina.kolotueva@unil.ch

Electron microscopy is an important tool to complement and expand information gained by light microscopy. Though the resolution of light microscopy has increased dramatically beyond the Raleigh criterion, it is restricted to a fluorescent probe. Electron microscopy, however, visualizes the complete fine structure of a cell and a label can be identified within the context. On the other hand, electron microscopy cannot follow processes in a living cell, and the field of view is very restricted making the search for a particular event lengthy and tedious.
A major challenge for electron microscopy is the identification of rare cellular events or the localization of specific cells of interest in processed samples of *Caenorhabditis elegans* and *Drosophila melanogaster* model organisms. The analysis of the multicellular samples is complicated because the overall body anatomy is unique and a certain area can only be analyzed in a limited manner in one organism, asking for repetition in many organisms. Acquiring the total information in several of such samples is time-consuming and tedious. Developing strategies that facilitate such analysis is required to make the electron microscopy on model organism more efficient and thus better accessible to a wider group of researchers. Further, the interpretation of the EM images is more demanding than those acquired by fluorescence microscopy. 3D volumes, allowing any viewing angle, will help to facilitate the analysis.
To this aim, we are developing a 'blind sectioning and screening' strategy. This approach combines retention of fluorescence in the EM sample and the acquisition of a high number on a silicon wafer. In the light microscope with the help of the fluorescence marker the sections that contain the area of interest can be identified in a fast manner. Then the fluorescence images can be combined with the high-resolution data obtained by electron microscopy of the very same section.
Our primary goal is developing novel EM approaches and the adaptation of the existing ones to facilitate the analysis multiple developmental stages and organ systems in *C. elegans* and *Drosophila*. We are combining several EM techniques such as correlative light and electron microscopy, array tomography and focused ion beam - scanning electron tomography to define analysis methods for a model organism that allow fast screening and identification of the cells, cell systems, of interest. With this approach direct targeting of the area of interest will become not only possible but fast, which is indispensable to characterize wild-type and mutant organism in a scientifically reliable number.
To illustrate our developments of correlative light and electron microscopy and array tomography methods for targeted 3D-volume acquisitions, we give examples from studies done both on embryos and different larval stages of *C. elegans* and *Drosophila*.

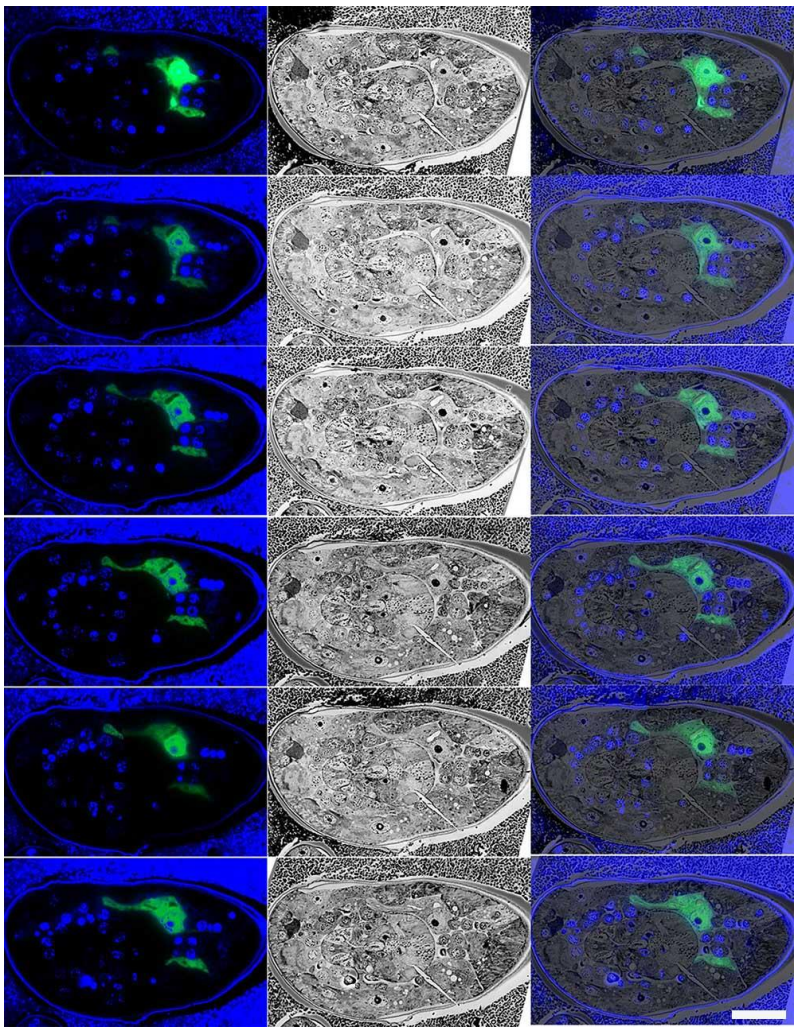

Figure 1. Six sections through the head region of the adult C. elegans larva. Excretory canal (GFP) and nuclei (DAPI) are superimposed over a SEM image. Scale bar 10 µm.

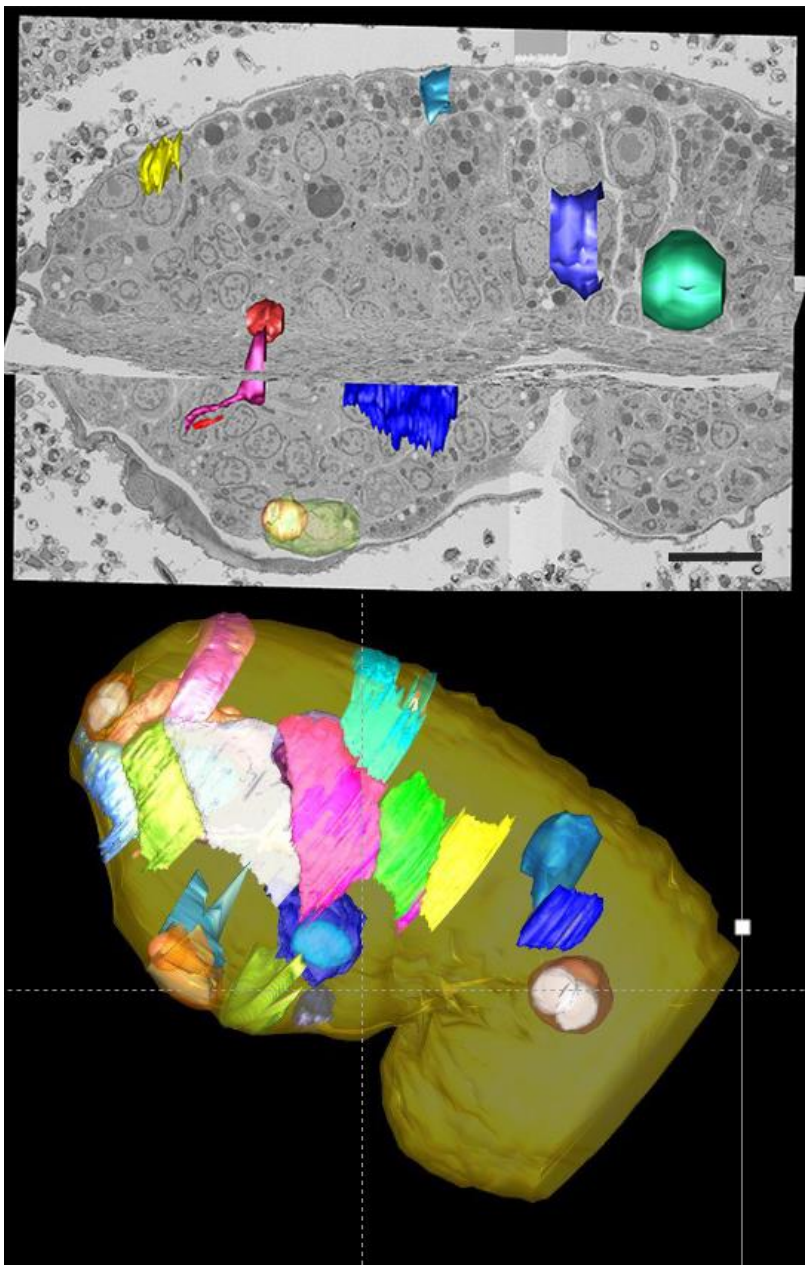

Figure 2. A reconstruction of a FIB acquisition of 1670 sections 25 nm thick through the C. elegans embryo. Scale bar 10 µm.

LS2.006
Clarifying lewy pathology through multimodal imaging and biophysical approaches

C. Genoud[1], A. Graff-Meyer[1], J. Hench[2], T. Moors[3], G. Schweighauser[2], J. Wang[4]
K. Goldie[4], R. Sütterlin[4], D. Castaño-Díez[4], P. Pérez-Navarro[4], E. Huisman[3], S. Ipsen[2], A. Ingrassia[3]
Y. de Gier[3], A. Rozemuller[5], A. De Paepe[6], J. Erny[7], A. Staempfli[7], J. Hoernschemeyer[7]
F. Großerüschkamp[8], D. Niedieker[8], S. El-Mashtoly[8], M. Quadri[9], W. van IJcken[10], V. Bonifati[9]
K. Gerwert[8], B. Bohrmann[11], S. Frank[2], M. Britschgi[11], H. Stahlberg[4], W. van de Berg[3], M. Lauer[6]

[1]Friedrich Miescher Institute for Biomedical Research, Basel, Switzerland
[2]University Hospital Basel, Division of Neuropathology, Institute of Pathology, Basel, Switzerland
[3]VU University Medical Center, Department of Anatomy and Neurosciences, section Clinical Neuroanatomy, Amsterdam, Netherlands
[4]University of Basel, Center for Cellular Imaging and NanoAnalytics (C-CINA), Biozentrum, Basel, Switzerland
[5]VU University Medical Center, Department of Pathology, Amsterdam Neuroscience, Amsterdam, Netherlands
[6]Roche Innovation Center Basel, Roche Pharma Research and Early Development, Chemical Biology, Basel, Switzerland
[7]Roche Innovation Center Basel, Roche Pharma Research and Early Development, Preclinical CMC, Basel, Switzerland
[8]Ruhr University Bochum, Department of Biophysics, Bochum, Germany
[9]Erasmus Medical Center, Department of Clinical Genetics, Rotterdam, Netherlands
[10]Erasmus Medical Center, Center for Biomics, Rotterdam, Netherlands
[11]Roche Innovation Center Basel, Roche Pharma Research and Early Development, NORD DTA/Neuroscience Discovery, Basel, Switzerland

sarah.shahmoradian@psi.ch

Introduction: Parkinson's disease is a progressive neurodegenerative disease with unclear etiology. A major hallmark is the appearance of intracellular aggregates, known as Lewy bodies and Lewy neurites, which are defined by the presence of the protein α-synuclein. The prominent concept of fibrils constituting the majority of Lewy bodies is originally based on research that used paired helical filament (PHF) extraction optimized from a protocol for Alzheimer's diseased brains, separate from dated electron microscopy studies that showed the appearance of putative fibrillar features in structures then identified as Lewy bodies. Combined with the fact that it is difficult for researchers to identify Lewy bodies in human brains using amyloid-based (i.e., beta-sheet) tracers, such observations warrant further investigation into the ultrastructure of clearly defined Lewy pathology in situ (non-extracted) within human brain samples.
Objectives: Understanding the ultrastructure of Lewy pathology is thought to be important for clarifying the formation of such aggregates and hence the pathophysiology of Parkinson''s disease. With such motivation, we aimed to investigate the structure and composition of Lewy pathology at the nanometer scale, and to rigorously validate our findings using a variety of biophysical approaches for establishing a solid foundation for further research on the mechanisms of Parkinson's disease pathogenesis.
Materials and Methods: We applied correlative light and electron microscopy, 3D transmission electron tomography and sub-tomogram averaging, and serial block-face scanning electron microscopy on postmortem brain tissues of Parkinson's patients. We isolated Lewy bodies by laser-capture microdissection and performed mass spectrometry followed by omics analysis to validate and complement our findings. We used chemical mapping on label-free tissue sections taken in parallel, followed by confocal imaging, to further validate our findings. We also used multi-labeling stimulated emission depletion microscopy to investigate specific sub-cellular motifs within the Lewy bodies.
Results: We identified abundant membrane fragments, vesicular structures, and mitochondria together with unorganized, non-fibrillar α-synuclein within the Lewy pathology in postmortem human brain tissues. We found specific motifs of organelles in the Lewy bodies at a level that had previously not been reported. We identified specific lipids in the Lewy bodies that were precisely collected by laser-capture microdissection and analyzed after liquid chromatography mass spectrometry.
Conclusion: While lipids have been implicated in Parkinson's disease, it was never shown clearly shown how they are involved in Lewy body organization and formation, especially considering that fibrils had such a prominent spotlight in Lewy pathology as opposed to lipids. While we do not exclude the possibility of fibrils existing in any Lewy bodies, our data importantly highlight the existence of lipid-rich Lewy bodies that are strongly immunopositive for alpha-synuclein yet lack visible fibrils. Such information would serve as a key foundation for designing effective tracers for identifying and monitoring Lewy bodies in living human patients, and for better understanding how such features may arise through destruction and aggregation of organelles in the cell via alpha-synuclein.

LS2.007
Using 3D electron microscopy to investigate developmental changes of hair cell ribbon synapses

S. Michanski[1,2], R. Chakrabarti[1,2], T. Henneck[3], C. Fischer[4], C. Wichmann[1,2]

[1]Institute for Auditory Neuroscience and InnerEarLab, Göttingen, Germany
[2]Institute for Biostructural Imaging of Neurodegeneration, Göttingen, Germany
[3]University of Veterinary Medicine Hannover, Foundation, Animal Biology and Biomedical Sciences, Hannover, Germany
[4]Johann-Friedrich-Blumenbach Institute for Zoology and Anthropology, Department of Morphology, Systematic, Biology of Evolution, Göttingen, Germany

susann.michanski@med.uni-goettingen.de

The mammalian inner ear carries sensory organs for two senses, hearing and balance. Both senses rely on hair cells (HCs), which are specialized for converting mechanical stimuli into electrical signals. The synapses of the HCs exhibit a presynaptic electron dense projection called the synaptic ribbon, which tethers synaptic vesicles (SVs) and transmits sensory information by Ca2+-dependent exocytosis at presynaptic active zones (AZs) (Nouvian et al., 2006; Matthews & Fuchs, 2010; Eatock and Songer, 2011; Wichmann & Moser, 2015). The cochlea is the receptor organ of the inner ear and transduces sound by the inner hair cells (IHCs), whereas the utricle converts rotational movements by type I and type II HCs. Morphological differences between type I and II cells (Wersall, 1956; Highstein et al., 2004; Eatock and Songer, 2011) led to the assumption that they might serve different functions in the utricle. Additionally, the morphological differences between cochlear and utricular HCs propose potential differences in the structural organization and formation of the HC ribbon synapse in the hearing and balance organs.
To address these questions, I examine HC ribbon synapses of the organs for hearing (cochlea) and balance (utricle) in different developmental stages of immature and mature wild-type mice. Using mainly electron-tomography in combination with the analysis of random sections, I determine the size and number of SVs, ribbons and the postsynaptic density (PSD) for all age groups in detail. Furthermore, I utilize serial block face scanning electron microscopy (SBF-SEM) for 3D reconstructions of whole HCs in order to study a potential morphological heterogeneity of HC ribbon synapses.
Based on my ultrastructural investigations the results indicate changes in ribbon and SV number and size as well as PSD arrangement upon maturation. Interestingly, I detected varieties in the morphology and development of ribbon synapses between cochlear and utricle HCs, which might explain functional differences like in the exocytosis rate of HCs (Dulon, 2009), the K+ conductance (Rüsch et al., 1998; Eatock & Rüsch, 1996) or in the firing pattern (Eatock and Songer, 2011).
This study demonstrates a successful application of 3D ultrastructural approaches to perform an in depth morphological analysis in order to investigate ribbon synapses within the HCs and identify possible differences between type I/II utricular HCs and cochlear IHCs.

LS2.P001
Microscopic examination of the pre-hatching development of the chicken ovary

M. Alsafy[1], S. El-Gendy[1], A. Karkoura[1], D. Shokry[1]

[1]Faculty of Veterinary Medicine, Alexandria University, Department of Anatomy and Embryology, Behera, Egypt

safy73@yahoo.com

The purpose of the current study was to investigate the development of the chicken ovary. One hundred fertilized egg of Alexandria breed of chicken used. The whole embryo has undergone the light microscopic examination at HH20 (E.3), HH21 (E.3.5), HH23 (E.4), HH29 (E.6) and HH34 (E.8). The ovary has undergone the light microscopic examination at HH38 (E.12) and HH42 (E.16), SEM at HH26 (E.5), HH29 (E.6), HH36 (E.10), HH38 (E.12), HH39 (E.13) and HH42 (E.16), TEM at HH38 (E.12) and HH42 (E.16). The genital ridge appeared by a thickening of the coelomic epithelium medio-ventral surface of the developing mesonephroi at HH20 (E.3). The boundaries of the undifferentiating gonads defined clearly separated from the mesonephroi. The undifferentiated gonads bulged as a distinct organ in the coelomic cavity at HH23 (E.4). At the initial stages of the gonadogenesis, the germinal epithelium was stratified squamous epithelium. The PGCs appeared at the genital ridge at HH21 (E.3.5). The PGCs observed at the dorsal mesentery with few microvilli and showed positive PAS reaction due to the glycogen content in their cytoplasm. The left-right gonadal asymmetry firstly detected by the number of PGCs migrating toward the left gonadal ridge more than the right at HH20 (E.3) and the macroscopic examination of gonadal asymmetry began at HH34 (E.8). The left ovary appeared a smooth rod-shape, its stroma showed lipid droplets and its parenchyma showed an extensive arrangement of interstitial cords at HH42 (E.16).

Keywords: Ovary, Alexandria Chicken, Light microscopy, SEM, TEM

LS2.P002
Ultrastructure of the visual system of the golden grey mullet *(*Chelon aurata)

M. Abumandour[1]

[1]Faculty of Veterinary Medicine, Alexandria University, Anatomy and Embryology, Rashid, Edfina, Egypt

m.abumandour@yahoo.com

Introduction: The visual system of the teleost fish gives indication about the ecological diversity and the vital activities of the fish life (De Busserolles *et al.*, 2013; Akat and Arikan, 2013)**.** The high degree of variations between the eye morphology reported in many articles (Locket, 1975; Pankhurst, 1989)**.** There are fish lives in the deepest darkest water whereas other fish adapted to lighting aquatic area and there are fish lives in area between them (Ali and Hanyu, 1963; Myrberg Jr and Fuiman, 2002)**.** The retina is most important structure in the eye and adapted to have a good vision in all aquatic media (Heb, 2009).
Objectives: To described the morphology of the eye of the golden grey mullet.
Materials and Methods: An examined fish collected after catching from Mediterranean Sea at Damiett coasts, Egypt. Then, it prepared to carry out the light and scanning electron microscopic examinations.
Results: The eyeball consists of three layers. The cornea consisted of three layers. By SEM examination, the cornea consisted of pentagonal and quadrigonal cells carrying microridges and microtubercles on their external surface (Fig. 1).
The retina is consists of ten. The photosensitive retinal layer organized into two areas; nervous and non-nervous area. The non-nervous area formed only by the thick pigmented epithelium layer which composed from a columnar epithelial cells containing melanin, which absorb the light passing through the photoreceptor layer (Fig. 2).
The photoreceptor layer consists of two types of cells; rods and cones which located below the thick pigmented epithelium layer. The cone cells were differentiated into two types; single and double cone cells. By SEM of the retinae, the rod cells appear as thin long uniform rod-like while the cone cells take the shape of the rod with ovoid base (Fig. 3).
Conclusion: The cornea consists of pentagonal and quadrigonal cells. The retina consists of ten layers. The photoreceptor layer consists of two types of cells; rods and cones. The cone cells differentiated into two types; single and double cells.

References:
[1] Akat E., Arikan H. A histological study of the eye in Hyla orientalis (Bedriaga, 1890) (Anura, Hylidae). *Biharean biologist 7*:61-63, 2013.
[2] Ali M. A., Hanyu L. A comparative study of retinal structure in some fish from moderately deep waters of the Western North Atlantic. *Canadian Journal of Zoology 41*:225–241, 1963.
[3] De Busserolles F., Fitzpatrick J. L., Paxton J. R., Marshall N. J., Collin S. P. Eye-Size Variability in Deep-Sea Lanternfishes (Myctophidae): .2013; 8(3): . *An Ecological and Phylogenetic Study 8*, 2013.
[4] Heb M. Triple cones in the retina of three anchovy species: Engraulis encrasicolus, Cetengraulis mysticeus and Anchovia macrolepidota (Engraulidae, Teleostei). *Vision Research 49*:1569–1582, 2009.
[5] Locket N. A. 1975. Some problems of deep-sea fish eyes. In: Ali, M. A. (Ed.): Vision in Fishes, pp. 645–656,,Plenum, Oxford.
[6] Myrberg Jr A., Fuiman L. The sensory world of reef fishes. *Coral reef fishes Dynamics and diversity in a complex ecosystem*:123-160, 2002.
[7] Pankhurst N. W. The relationship of ocular morphology to feeding modes and activity periods in shallow marine teleosts. *Environmental Biology of Fishes 26*:201 - 211, 1989.

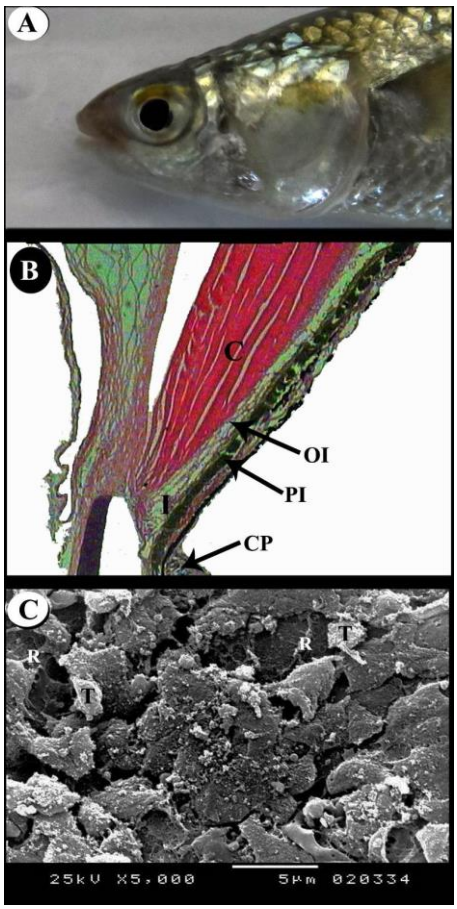

Figure 1. View A: the lateral view of the golden grey mullet, View B represent the Light photomicrograph of the cornea (C) and iris (I) showing; OI- Ossicles of iris; PI- pigment of iris, View C: represent the SEM of the cornea showing; undetermined shaped cells with microridges (R), microtubercles (T).

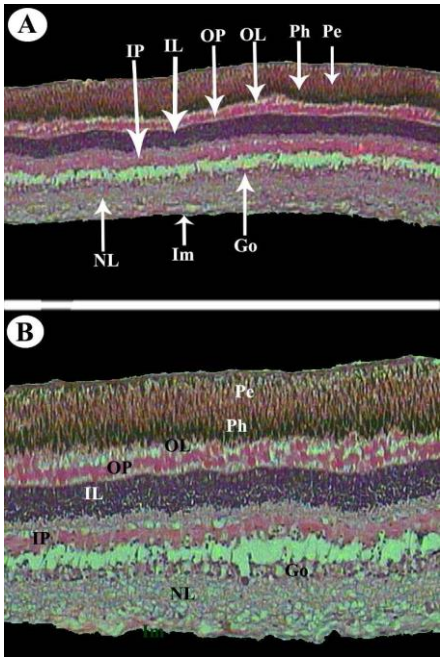

Figure 2. Light photomicrographs of a transverse section of the retina layer showing: im- inner limiting membrane; Ip- inner plexiform layer; IL- inner nuclear layer; OP- outer pexiform layer; OL- outer nuclear layer; Ph- photoreceptor cell; Pe: pigment epithelium; Go- ganglionic layer; NL- Nerve fiber layer.

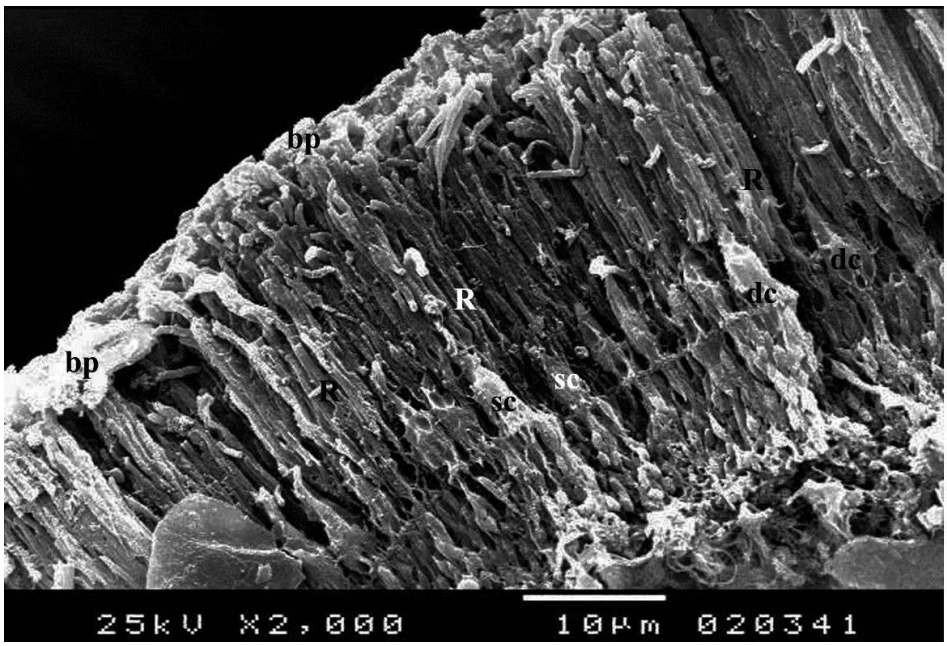

Figure 3. SEM of the rods and cones of the photosensitive layer showing; rods (R), single cones (sc) and double cones (dc), base of pigmented cell (bp).

LS2.P003
Comparative histological and ultrastructural study of the pecten oculi in black stork (Ciconia nigra, Ciconiiformes) and Sunda wrinkled hornbill (Aceros corrugatus, Bucerotiformes)

J. Klećkowska-Nawrot[1], K. Goździewska-Harłajczuk[1], K. Barszcz[2], K. Marycz[3], T. Nawara[3], D. Łupicki[4] W. Paszta[5], K. Zagórski[5], M. Janeczek[1]

[1]Wroclaw University of Environmental and Life Sciences, Department of Biostructure and Animal Physiology, Wroclaw, Poland
[2]Warsaw University of Life Sciences, Department of Morphological Sciences, Warsaw, Poland
[3]Wroclaw University of Environmental and Life Sciences, Electron Microscopy Laboratory, Wroclaw, Poland
[4]Wroclaw University of Environmental and Life Sciences, Museum of Natural History of the Faculty of Biology and Animal Science, Wroclaw, Poland
[5]Wroclaw Zoological Garden, Wroclaw, Poland

lestat_v@poczta.onet.pl

Introduction: The pecten of eye (*pecten oculi*) in birds is pigmented, highly vascular structure arises from the retina, at the ovoid exit point of the optic nerve and protrudes into the vitreous body (König et al., 2016). There are three types of the pecten oculi in birds: pleated (*pecten plicatus oculi*), vaned (*pecten vanellus oculi*) and conical (*pecten conicus oculi*). In spite of a lot of study, still the function of the pecten remains unclear. Based on different hypotheses the role of pecten is connected with protection of certain regions from glare, reduction of scattered light, immunocompetence, participation in motion perception and sensing of magnetic fields for the purpose of orientation. The pecten also has a nutritional function, supplying the vitreous body and avascular retina, and it contributes to intraocular pressure and temperature regulation (Braekevelt, 1991; Kiama et al., 2006; König et al., 2016).
Objectives: The aim of this study was the anatomical description of the pecten in black stork and Sunda wrinkled hornbill with using of two microscopic techniques.
Materials and Methods: The pectens were directly fixed in 4% buffered formaldehyde for 72 hours and washed in running water for 24 hours. The study samples were dehydrated using the ethanol procedure. Then they was then processed in a vacuum tissue processor – ETP (RVG3, INTELSINT, Italy), embedded in paraffin and cut using a Slide 2003 (PfmA.g., Germany) sliding microtome into 3-4 µm sections. The samples were then stained with haematoksylin & eosin and Masson-Goldner trichrome. For SEM study tissues were fixed in 4% glutaraldehyde in PBS and stored for one day at room temperature. After fixation, in order to dehydratation the samples were transferred to 50% ethanol and stored at room temperature for 2h. The process was repeated with 60% - 100% ethanol. Dehydrated tissues allowed to air-dry overnight. Samples were coated with gold using ScanCoat6 (Edwards) and observed using a SE1 detector, at 10kV filament tension (SEM, Zeiss Evo LS 15). Results: The pecten oculi in black stork and Sunda wrinkled hornbill was a pleated type. The pecten were located similar to other avian species over the optic nerve head (postero-inferior wall of the eyeball) and projects out into the vitreous chamber. In black stork the pecten measures about 6.39 mm in height, was 10.59 mm wide at the base and about 6.64 mm at the bridge. On the other hand in Sunda wrinkled hornbill the pecten was about 6.1 mm height, 8.7mm wide at the base and about 6.22 mm at the bridge. In black stork the pecten was formed by 16-18 thin and rectilinear pleats (folds), while in Sunda wrinkled hornbill is formed by12-14 pleats. The pecten oculi was composed of many capillaries and of two parallel vessels - arteriole and venule, whose caliber ranges in black stork between 10-60 µm (venule) and 100-160 µm (arteriole) and in Sunda wrinkled hornbill between 15- 50 µm (venule) and 110-130 µm (arteriole). Both avian species had numerous clusters of melanocytes which were located in the bridge of the pecten.
Conclusions: Microscopic techniques as light microscopy and scanning electron microscopy simplify to recognized the microstructure of the pecten oculi in different avian species, what enlarge the anatomical knowledge about the eye functioning especially in wild birds.

References:
[1] Braekevelt CR. 1991 Electron microscopic observations on the pecten of the great blue heron (*Ardea Herodias*). Histol Histopath. 6:345-351
[2] Kiama SG, Maina JN, Bhattacharajee J, Mwangi DK, Macharia RG, Weyrauch KD. 2006 The morphology of the pectin oculi of the ostrich *Struthio camelus*. Ann Anat. 188:519-528
[3] König HE, Korbel R, Liebich HG. 2016 Avian Anatomy. Textbook and Colour Atlas. 2nd edition. 5m Publishing Ltd. UK.

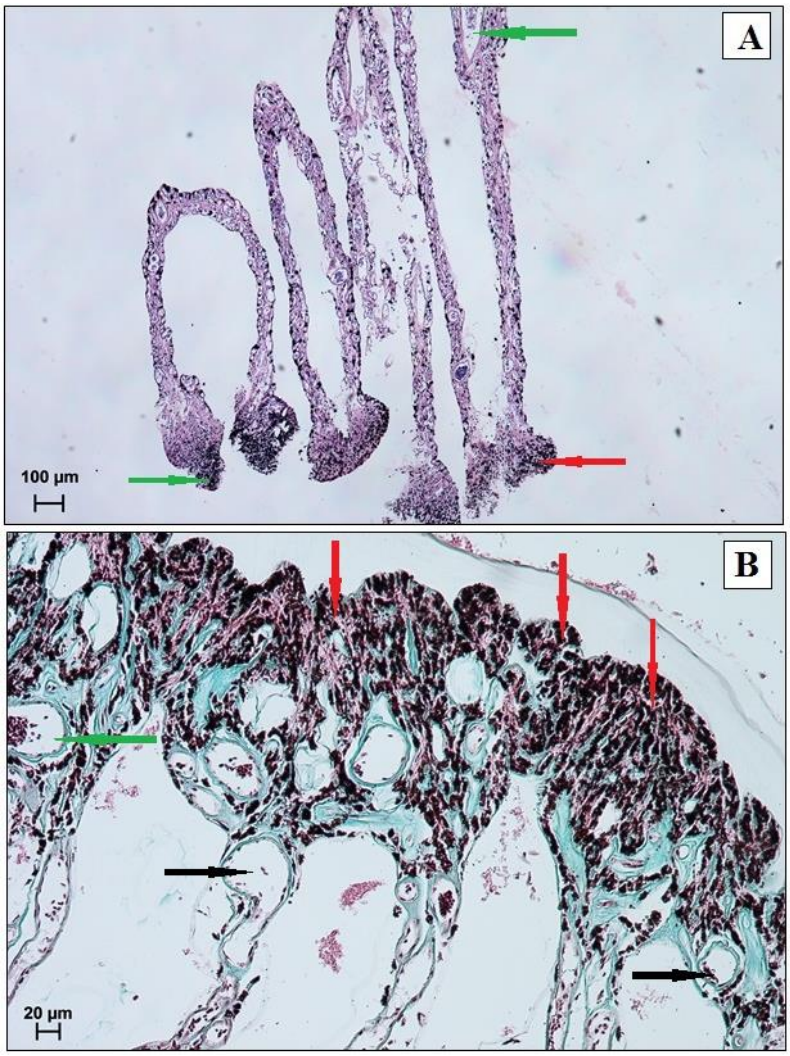

Figure 1. The pecten oculi of the black stork (A) (H&E stain, 100 µm) and Sunda wrinkled hornbill (B); Masson-Goldner trichrome stain, 20 µm. black arrows – venule, green arrows – arteriole, red arrows – melanocytes.

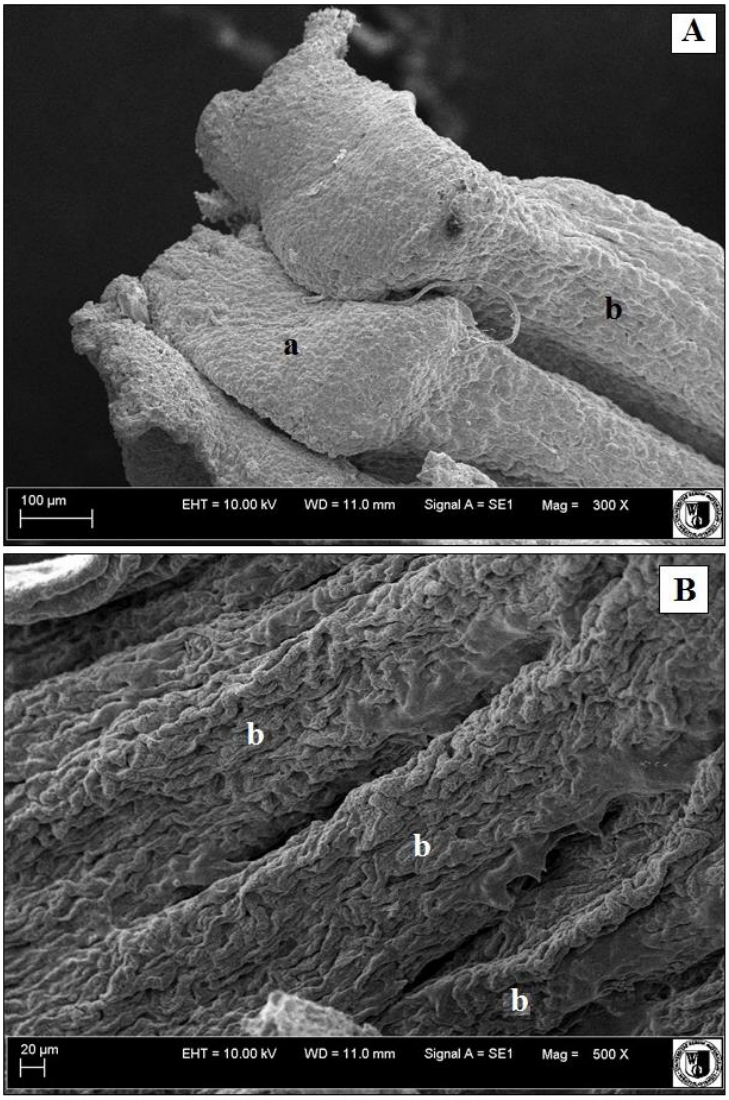

Figure 2. Scanning electron micrograph of the pecten oculi black stork (A) and Sunda wrinkled hornbill (B). a – bridge of pecten oculi, b - pleats (folds) of pecten oculi.

LS2.P004
Applications of scanning electron microscopy (SEM) in description of the forestomachs microstructure in two species of ruminants (atriodactyla)

K. Goździewska-Harłajczuk[1], J. Klećkowska-Nawrot[1], K. Barszcz[2], K. Marycz[3], T. Nawara[3], K. Olbrych[2] T. Szara[2], D. Łupicki[4]

[1]Wroclaw University of Environmental and Life Sciences, Department of Biostructure and Animal Physiology, Wroclaw, Poland
[2]Warsaw University of Life Sciences, Department of Morphological Sciences, Warsaw, Poland
[3]Wroclaw University of Environmental and Life Sciences, Electron Microscopy Laboratory, Wroclaw, Poland
[4]Wroclaw University of Environmental and Life Sciences, Museum of Natural History of the Faculty of Biology and Animal Science, Wroclaw, Poland

k.gozdziewska.wroc@gmail.com

Introduction: Forestomachs have an important role in stores and processes of the plant materials in poligastric mammals. Based on digestive strategies of ruminant species these animals are divided into two groups: with "cattle-type" digestive system and with "moose-type" digestive system (2, 3). Numerous investigations of gastrointestinal tract anatomy and physiology were performed in different domestic and wild ruminants (1-3), however there were a few study with application of scanning electron microscopy (*SEM*).
Objectives: The aim of this study was the comparative analysis of the forestomach microstructure (rumen, reticulum, omasum) in two different endangered species of ruminants: European bison (*Bison bonasus*) from Bialowieza National Park and one of the smallest ungulates Philippine mouse-deer (*Tragulus nigricans*) from Wroclaw Zoological Garden.
Materials and Methods: The samples of the forestomachs were collected from adult female of European bison (rumen, reticulum and omasum) and from adult female of Philippine mouse-deer (rumen, reticulum). The research material were fixed in 2.0 % glutaraldehyde dissolved in 0.1 M phosphate buffer at pH 7.4 for scanning electron microscopic study. Then the research material was rinsed in a phosphate buffer. After fixation, dehydratation of samples were performed up to 50 % ethanol and then materials were stored at room temperature for 2 hours. The process was repeated with 60%, up to 100 % ethanol. Dehydrated tissue allowed to dry. Samples were coated with gold using ScanCoat (Edwards) and was evaluate with using of SE1, at 10 kV filament tension (SEM, Zeiss Evo LS 15). The study was performed in the Microscopic Laboratory of the Wroclaw University of Environmental and Life Sciences.
Results: The surface of rumen in European bison had numerous elongate papillae around 0.5-1.4 cm heigh, while in Philippine mouse-deer were about 0.1-2 mm heigh, respectively (Fig. 1). Surface of each papillae was covered with epithelial cells with numerous cells undergoing desquamation in both animal`s species (Fig.1). Rumen papillae of mouse-deer had many pseudopapillae. The reticulum had a honey-combed appearance in European bison as well as in mouse-deer. There were conical papillae with pointed apex (Fig. 2). The height of papillae was approximately 0.2- 1.3 mm in European bison, while around 0.1-1 mm in mouse-deer. The surface of reticulum had similar surface as in rumen, there were numerous epithelial cells which undergoing desquamation (Fig. 2). The omasum was absent in Philippine mouse-deer, while surface of omasum in European bison was covered with small conical papillae and big conical papillae with well-rounded apex and irregular lateral surface (Fig. 3).
Conclusion**:** *SEM* study showed the differences in microstructure of the forestomachs in two different herbivores mammals, what is connect with feeding behavior and distinct of environmental conditions.

References:
[1] Agungpriyono S, Yamamoto Y, Kitamura N, Yamada J, Sigit K, Yamashita T. 1992 Morphological study on the stomach of the Lesser mouse deer (*Tragulus javanicus*) with special Reference: to the internal surface. Journal Vet. Med. Sci. 54: 1063-1069
[2] Clauss M, Hofmann RR, Fickel J, Streich WJ, Hummel J. 2009 The intraruminal papillation gradient in wild ruminants of different feeding types: implications for rumen physiology. J Morpho. 270: 929-942
[3] Clauss M, Hume ID, Hummel J. 2010 Evolutionary adaptations of ruminants and their potential relevance for modern production system. Animal 4: 979-992

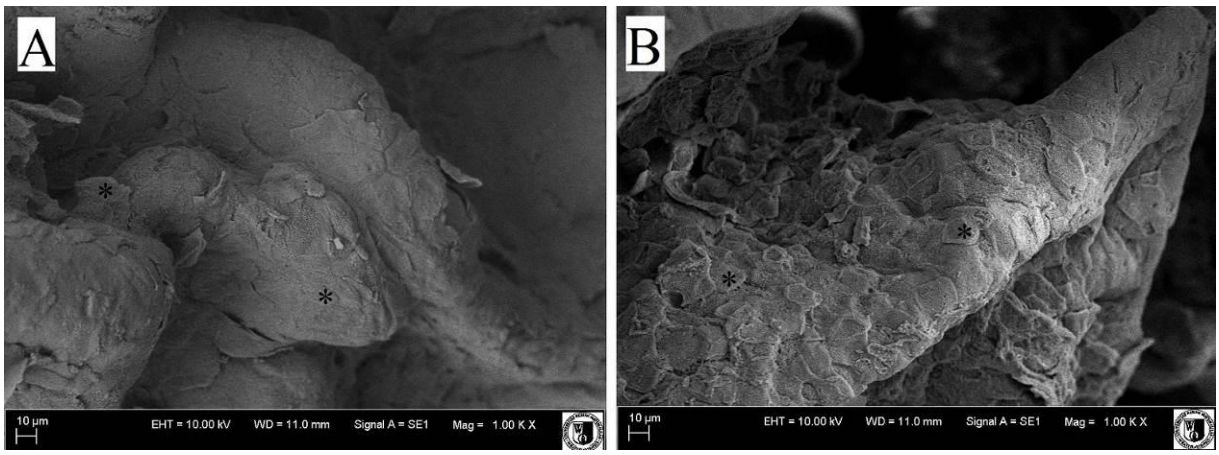

Figure 1. Microstructure of the European bison - A and Philippine mouse-deer - B rumen.
* - epithelial cells with numerous cells undergoing desquamation.

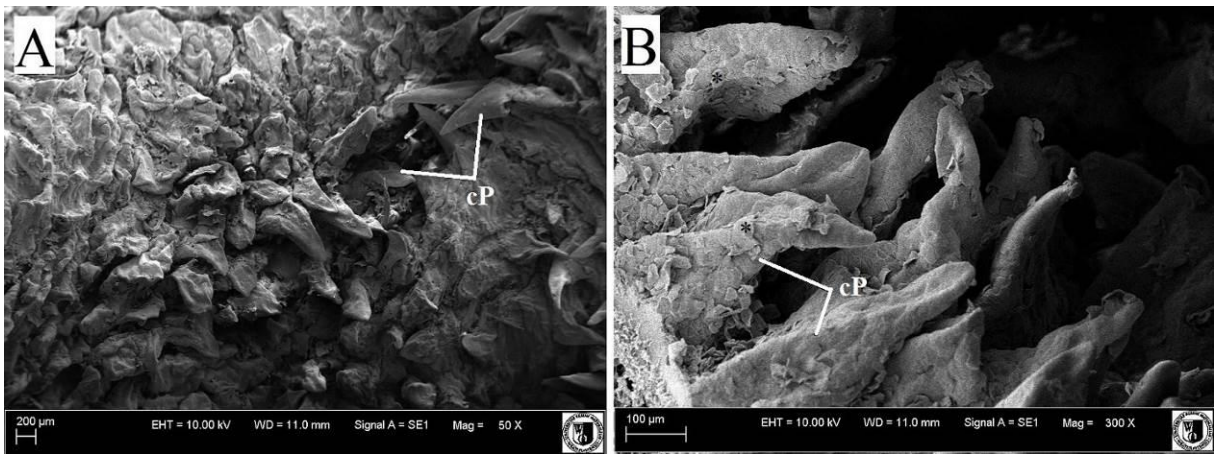

Figure 2. Microstructure of the European bison - A) and Philippine mouse-deer - B reticulum.
* - epithelial cells; cP - conical papillae with pointed apex.

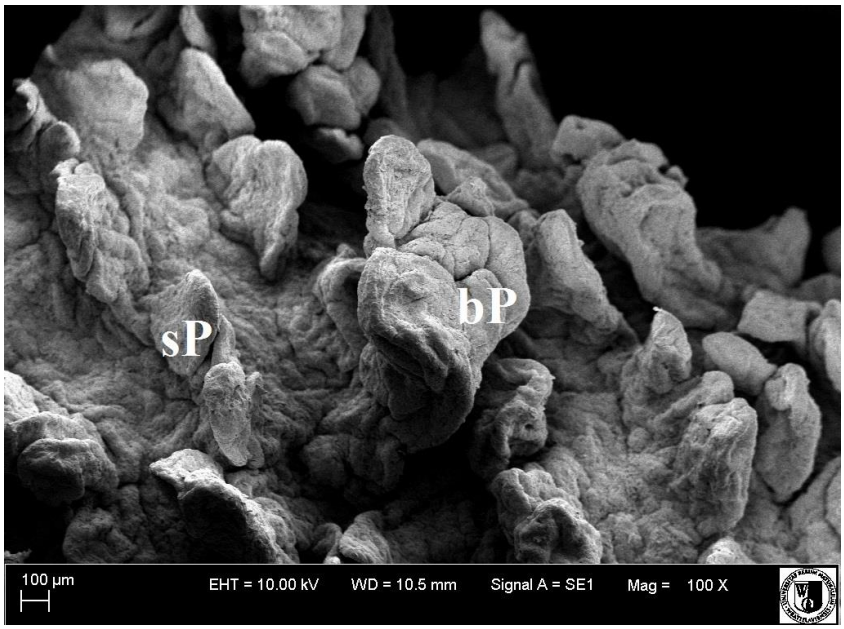

Figure 3. Microstructure of the European bison omasum. sP- small conical papillae with well-rounded apex; bP- big conical papillae with well-rounded apex.

LS2.P005
STEM tomography unveils lysosomal tubular networks in macrophages.

A. Bauer[1], G. Frascaroli[2], P. Walther[1]

[1]Ulm University, Central Facility for Electron Microscopy, Ulm, Germany
[2]University Medical Center Ulm, Institute of Virology, Ulm, Germany

andrea.bauer@uni-ulm.de

Questions: According to Mercer and Helenius[1] (2012) "the classification of endocytic mechanisms is still far from being complete." Novel three dimensional electron microscopic approaches enable us to reevaluate intracellular trafficking routes. Using these methods we recently described an endocytotic pathway in macrophages that we called megapinocytosis[2].
In addition, with the help of fluorescent light microscopy[3,4] and freeze-etch electron microscopy[5] tubular structures had been described in the literature that were classified as belonging to the lysosomal trafficking routes of the macrophages. In this work we searched and analyzed these structures using STEM (scanning transmission electron microscopic) tomography.
Methods: Human monocyte-derived M2 Macrophages were high pressure frozen with a Wohlwend Compact 01, freeze substituted as described[6] and embedded in Epon. 600 nm thick sections were cut, mounted on copper grids, labeled with 25 nm gold colloids as fiducial markers and coated with 5 nm of carbon from both sides to reduce the effects of beam damage[7]. Tomograms were obtained with a 200 kV Jeol 2100 F using the STEM mode and the bright field signal. The tilt series were recorded from -72° to +72° with 1.5° increment and reconstructed with the Imod software[8]. Virtual sections of such a tomogram are shown in the figure.
Results: We confirmed the presence of an extended tubular network in the macrophages" cytoplasm (see figure). The bright tubule (labeled with dark arrows) extended over several microns. Most of the tubules have a dense dark content (one of it is labeled with white arrows in the figure). They are surrounded by one bilayer only and, thereby, can be unambiguously discerned from mitochondria.
Conclusions**:** We have found an extended tubular network system that resembles the structures described earlier as tubular lysosomal network[3,4,5]. It looks very different from the spherical organelles commonly described as lysosomes in text books[9]. We consider STEM tomography as the method of choice to track this network, because thick sections (up to 600 nm in this study) can be analyzed, bearing the chance that a substantial portion of the network is within a section and the resolution is still good enough to resolve the two layers of the lipid bilayer membrane[10].

References:
[1] Mercer J, Helenius A. Nat Cell Biol (2009) 11, 510–520.
[2] Bauer A, Subramanian N, Villinger C, Frascaroli G, Mertens T, Walther P. Histochem Cell Biol. (2016) 145, 617-627.
[3] Knapp PE, Swanson JA. J. Cell Science. (1990) 95, 433-439.
[4] Saric A, Hipolito VE, Kay JG, Canton J, Antonescu CN, Botelho R. J. Mol Biol Cell. (2016) 27, 321-33.
[5] Haberland ME, Mottino G, Le M, Frank JS. J Lipid Res. (2001) 42, 605-619.
[6] Walther P, Ziegler A. J Microsc (2002) 208, 3–10.
[7] Walther P, Wehrli E, Hermann R, Müller M. J Microsc. (1995) 179, 229-237.
[8] Kremer JR, Mastronarde DN, McIntosh JR. J Struct Biol. (1996) 116, 71-76.
[9] Alberts B, Johnson A, Lewis J, Morgan D, Raff M, Roberts K, Walter P (2014) Molecular biology of the cell, 6th edn. Garland Publishing, New York.
[10] Höhn K, Sailer M, Wang L, Lorenz L, Schneider EM, Walther P. Histochem Cell Biol. (2011) 135, 1-9.

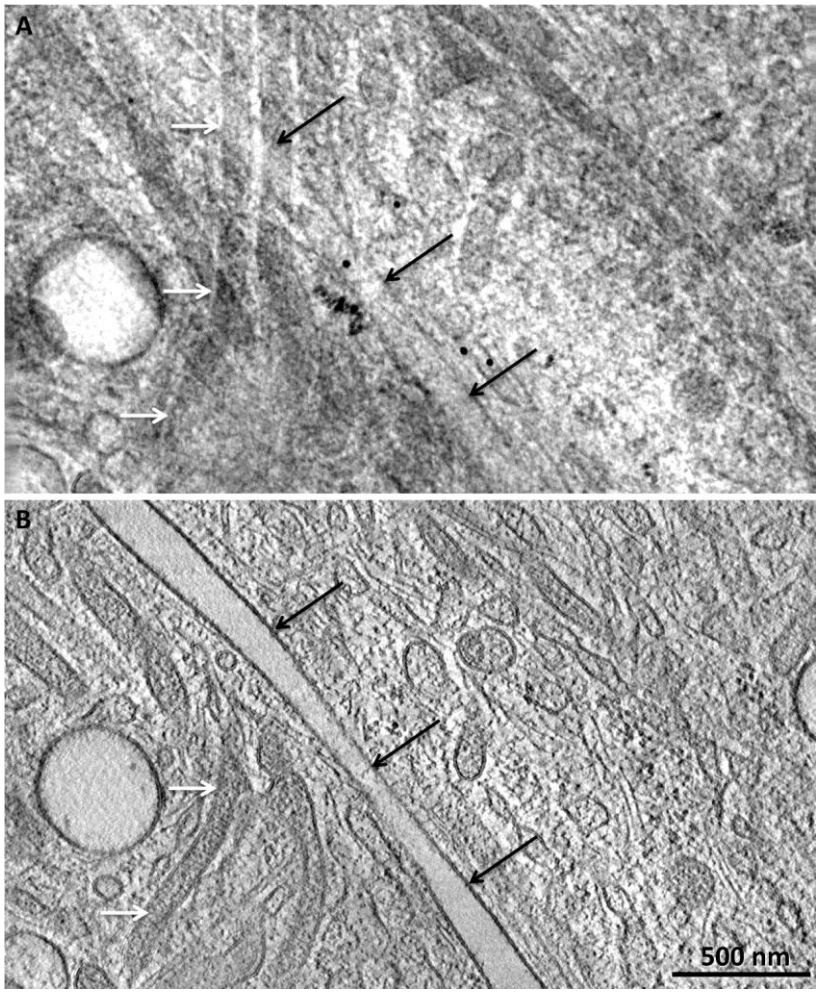

Figure 1. STEM tomogram of a portion of a macrophage, exhibiting an extended lysosomal tubular network. Fig. A is a thick virtual section (thickness 360 nm) from the tomogram. It shows many tubules with a dark content (white arrows) and one with no content (dark arrows). Fig. B is a thin virtual section of the same area with a thickness of 3 nm only. The membranes become well visible. Only the tubules" portions in the section plane can be seen.

LS2.P006
Preparation and characterization of a covalently immobilized biological surface coating using azide-functionalized clickECM

S. Keller[1], B. Endreß[1], P. Kluger[2,3], M. Bach[2]

[1]University of Stuttgart, Institute of Interfacial Process Engineering and Plasma Technology (IGVP), Stuttgart, Germany
[2]Fraunhofer Institute for Interfacial Engineering and Biotechnology (IGB), Institute of Interfacial Process Engineering and Cell and Tissue Engineering, Stuttgart, Germany
[3]Reutlingen University, School of Applied Chemistry, Reutlingen, Germany

silke.keller@igb.fraunhofer.de

Introduction: The extracellular matrix (ECM) is a complex network of biomolecules which surrounds the cells in a human tissue. Primary cells are capable of producing an ECM in vitro which can be isolated after several days of culture[1, 2]. Because of its diverse functions and due to the high biological activity, the isolated ECM is a promising biomaterial for use in tissue engineering and regenerative medicine. The ECM is able to promote cell adhesion, proliferation, and differentiation in a tissue specific manner[3, 4]. However, the use of ECM is limited, e. g. due to the lack of specific addressable functional groups, which are often required for their use as coatings or scaffolds[3].
Objectives: To overcome this limitation our approach was to covalently immobilize the human ECM on artificial surfaces. Therefore, we performed Metabolic Glyco Engineering (MGE) to introduce azide groups into the glycan structures of the ECM to create a variously deployable »*click*ECM« which can be used as a complex bioactive coating material.
Materials and Methods: Substrates were functionalized with activated alkynes to covalently immobilize the azide-modified *click*ECM on material surfaces via copper-free click reaction. Subsequently, laser scanning microscopy and multiphoton microscopy were used to characterize the biological composition of the *click*ECM and to evaluate the bioactive properties of the generated coatings. To further increase the density of *click*ECM-coating, we concentrated the *click*ECM coating suspension by using centrifugal filters. Moreover, we cross-linked the azide-modified biomolecules of the *click*ECM with a bi-functional alkyne crosslinking agent in order to further increase the coating thickness, denseness, and stability.
Results: By using laser scanning microscopy and multiphoton microscopy we could for the first time show that MGE can be used to introduce azide groups into the ECM of human dermal fibroblasts (Fig. 1). Just like the human skin and the unmodified ECM, this *click*ECM consists of glycans, collagens, and non-collagenous proteins. The *click*ECM could be covalently immobilized on alkyne-modified surfaces resulting in a significant increase in coating stability compared to a conventional ECM coating via physisorption. Cell proliferation was significantly enhanced on the *click*ECM-coated surfaces compared to uncoated glass substrates, which proved its exceptional biological activity (Fig. 2). Through the concentration of the coating suspension and the additional crosslinking of the azide-functional *click*ECM with alkyne-modified crosslinking agents, we were able to increase the density and the thickness of our *click*ECM-coating (Fig. 3).
Conclusion: These results demonstrate that our *click*ECM is a promising biomaterial, e. g. for the generation of bioactive surface coatings with an increased stability and a high biological complexity. The covalent immobilization mediates an increased stability while preserving the high biological activity of the human dermal ECM.
We propose that the additional incorporation of selected alkyne-functional (bio)molecules into the *click*ECM-coatings could enable the preparation of stable, tissue-specific, and bioactive scaffolds for tissue engineering and regenerative medicine.

Reference:
[1] L. E. Fitzpatrick and T. C. McDevitt, *Biomater. Sci.*, 2015, **3**, 12-24.
[2] S. Hinderer, S. L. Layland and K. Schenke-Layland, *Advanced drug delivery reviews*, 2016, **97**, 260-269.
[3] S. M. Ruff, S. Keller, D. E. Wieland, V. Wittmann, E. M. T. G, M. Bach and P. J. Kluger, *Acta Biomater*, 2016
[4] T. Rozario and D. W. DeSimone, *Developmental Biology*, 2010, **341**, 126-140.

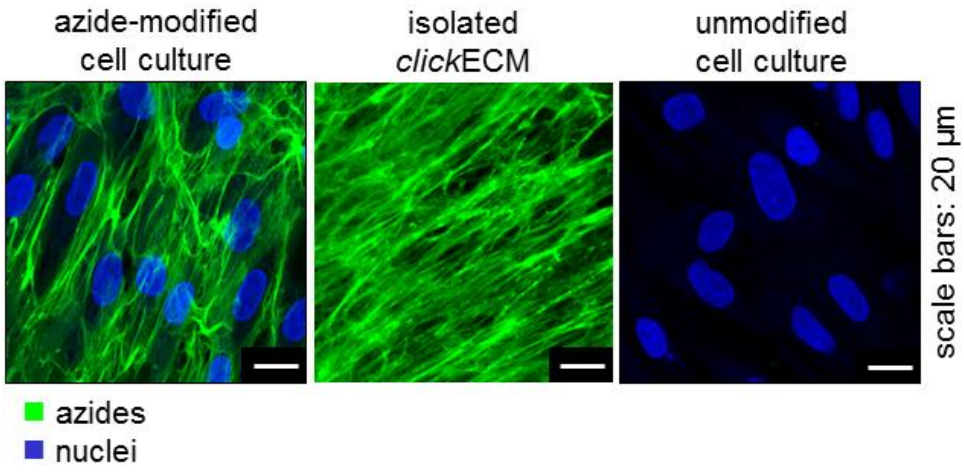

Figure 1. MGE is a useful tool to incorporate click groups into the glycans of cell-derived ECM.

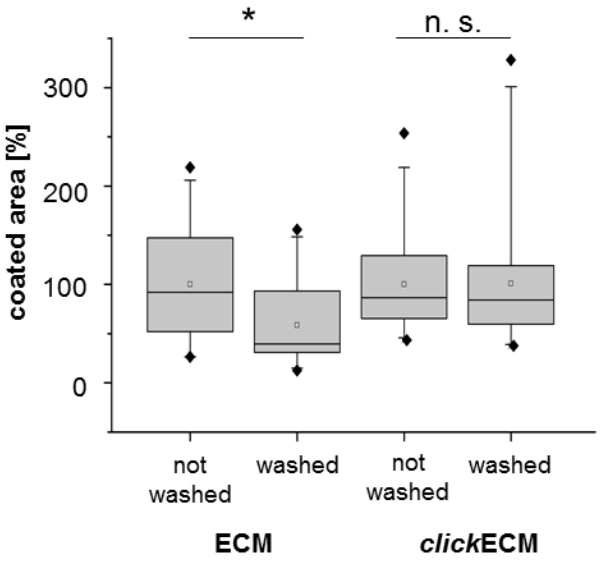

Figure 2. The covalent ***click***ECM coating was significantly more stable compared to a conventional ECM coating based on physisorption.

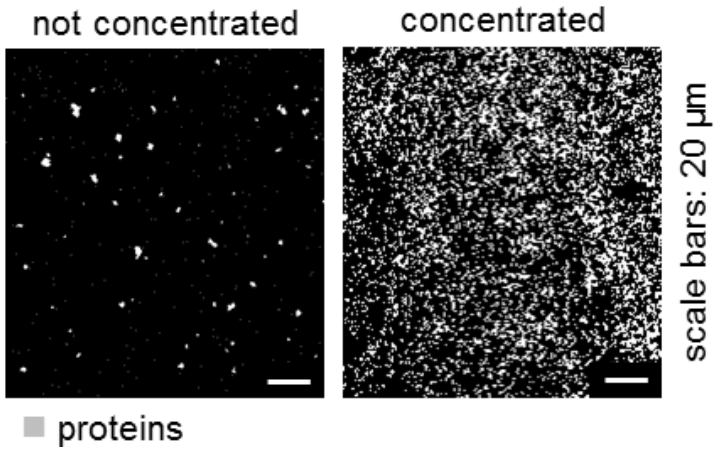

Figure 3. Concentrating the ***click***ECM prior to the coating step increases the coating denseness and thickness.

LS2.P007
Drug delivery to human leukemia cancer cells using magneto-fluorescent iron oxide nanoparticles

R. Ali[1], K. El Boubbou[1,2]

[1]King Abdulah International Medical Research Center (KAIMRC), Core Imaging Lab, Riyadh, Saudi Arabia
[2]King Abdulah International Medical Research Center (KAIMRC), Riyadh, Saudi Arabia

rizwanali79@gmail.com

Question: Development of a controlled drug delivery system using drug-loaded nanoparticles.
Background: Controlled drug delivery systems using drug-loaded nanoparticles are gaining lot of attention these days. Of the many available systems, magneto-fluorescent nanoparticles are considered promising drug-carriers due to their large surface areas, ease of synthesis, different functionalities, imagability, low toxicity and high biocompatibility. However, synthesizing such uniform, colloidal, biocompatible, and water-dispersible particles that simultaneously exhibit large magnetization, high drug content and maximized fluorescence has been challenging. Herein, we have developed a simple approach to create a novel chemotherapeutic formulation made of fluorescently-labeled PVPylated magnetic metal (iron) oxide nanoparticles (PMONPs) loaded with the anticancer drug Doxorubicin (Dox). Previously we have tested it in breast cancer cell lines with success. In this work we have studied the delivery of these particles to two different types of Leukemia cell lines, human promyelocytic leukemia cells (HL60) and human monocytic cell line derived from an acute monocytic leukemia patient (THP-1) along with normal human peripheral blood mononuclear cells (PBMCs).
Methods: We have used live cell confocal laser scanning microscopy and electron microscopy techniques to monitor and visualize the uptake of PMONPs in the living Leukemia cells as well as normal PBMCs.
Results: We show that the PMONPs are not toxic to the tested cell lines even up to 100 µg/mL, whereas the two cell lines tested are sensitive to Dox-loaded PVP-MONPs effectively killing the cells in comparison to normal PBMCs which showed almost no effect. We then used confocal laser scanning microscopy (cLSM) and scanning electron microscopy (SEM) techniques to visualize the uptake and internalization of the Dox-loaded fluorescently-labeled PMONPs (Dox@Fl-PMONPs). Our results show that the nanoparticles were successfully endocytosed and packaged into vesicles (endosomes/lysosomes) inside the cytoplasm, releasing the drug and causing rounding of cells within 2 h of Dox@Fl-PMONPs exposure and cell death within 6 h of exposure (**Fig. 1**). Calcein AM staining of viable cells was used to validate these results. Moreover, live cell imaging at different time points showed that Dox was delivered to the nucleus causing apoptotic cell death in relatively short period of time (12h). We anticipate that the observed cytotoxic effect from the Dox@Fl-PMONPs is dependent upon both free drug released once encountering the cell membrane, and uptake of the nanoparticles by cells, both enhancing the effectiveness of Dox released intracellularly.
Conclusions: We are now characterizing the cellular/molecular mechanisms underlying the promising activity of these particles. Moreover, we are testing the effects of these nanoparticles in patient tumor biopsies. Importantly, the Dox@Fl-PMONPs can potentially open new avenues for *in vivo* cancer therapeutic imaging and hyperthermia where they can serve as multi-photon and magnetic resonance dual-modal imaging probes.

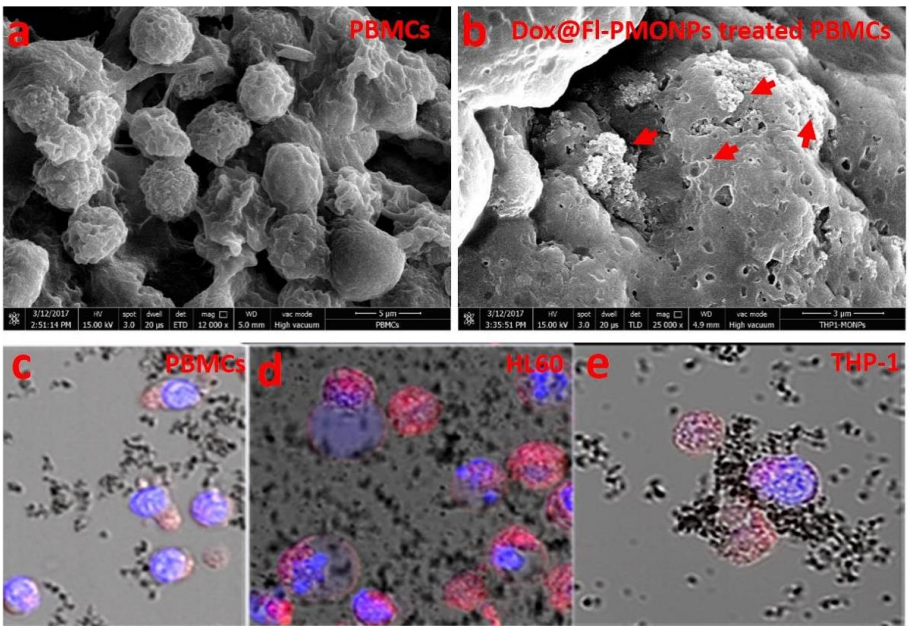

Figure 1. SEM and cLSM images of Leukemia cells treated with Dox@Fl-PMONPs (10 µg/mL PMONPs; 1.25 µg/mL Dox; 2.3 µM Dox)**.** (a) SEM Image of untreated PBMCs; (b) SEM Image of PBMCs treated with Dox@Fl-PMONPs. Red arrowheads show aggregates of Dox@Fl-PMONPs attached to the cells. (c-e) cLSM images of PBMCs (c), HL60 cells (d) and THP-1 cells (e) treated with Dox@Fl-PMONPs (Red) for 6 hours. Nucleus is stained in blue and surrounding the cells are Dox@Fl-PMONPs (Black aggregates).

LS2.P008
Three-dimensional organization of minerals in calcifying turkey leg tendon revealed by FIB-SEM imaging

Z. Zou[1], L. Bertinetti[1], P. Fratzl[1]

[1]Max Planck Institute of Colloids and Interfaces, Potsdam, Germany

zhaoyong.zou@mpikg.mpg.de

Introduction: The deposition of minerals in the early stage of bone formation is important to understand the mineralization process. Turkey leg tendon (TLT) is often used as a model system for studying the relationship between the mechanical properties and hierarchical structure of mineralized collagen fibres. TLT is composed of uniaxial oriented collagen fibre array and become mineralized as the animal ages.1-2 The structure of turkey leg tendon has been characterized by various multiscale methods from nano- to microscale, including transmission electron microscopy, small-angle X-ray scattering and atomic force microscopy, scanning electron microscopy, light microscopy, confocal Raman microscopy, and micro-computed tomography, etc. It has been demonstrated that in addition to the minerals associated with collagen fibres, it contains mineral-containing vesicles, which might contribute to/be responsible of the mineralization process. However, the three-dimensional distribution of the mineral and vesicles as well as the spatial relationship between these minerals and cells are not well characterized. With the development of focused ion beam scanning electron microscopy (FIB/SEM) technique, it is now possible to investigate the microstructure of bone at both high resolution (tens of nanometer) and large volume (hundreds of micrometer).
Objectives: The aim of the study is to describe the initial stage of mineral deposition in calcifying turkey leg tendon by investigating the three-dimensional organization of the minerals and the spatial relationship between these minerals and cells using the FIB/SEM imaging.
Materials and Methods: Specimens (tibialis cranialis tendons) originated from turkeys sacrificed after 20−25 weeks and were sectioned with a cryomicrotome into slices with a thickness of about 150 µm in thickness along the longitudinal direction. The slices were then freeze-dried overnight and coated with carbon or Au before measuring. FIB-SEM imaging was performed with a Zeiss Crossbeam 540, Gemini 2 ((Carl Zeiss, Konstanz, Germany)).
Results: A typical backscattered SEM image of the cross section of the turkey leg tendon after milling with the focused ion beam clearly showed bundles of mineralized collagen fibres and separate mineral vesicles (Figure 1). In addition, several cell like structures with a size of 4 – 6 µm were situated in between the collagen fibres. From the image analysis of 3D stacks of volumes up to about 50 µm, with a minimum voxel size of 24 * 24 * 24 nm3, we observed that the interface between the collagen fibre bundles were all connected with the cell-likes structures. The mineral vesicles are not randomly distributed in the tissue; instead, they seem to follow the pattern of the bundle interface at the mineralization front. The preliminary results suggest that the deposition of the mineral vesicles is strongly related to the position of the cells.
Conclusion: FIB-SEM imaging is a promising technique to investigate the distribution of minerals in the calcifying tissue and understand the mineralization process of bone. Further experiments will focus on analysing the fresh sample directly after high pressure freezing under cryo-conditions, which is expected to provide more information on the early stage of mineralization.

Reference:
[1] Landis, W. J., A STUDY OF CALCIFICATION IN THE LEG TENDONS FROM THE DOMESTIC TURKEY. *Journal of Ultrastructure and Molecular Structure Research* **1986,** *94* (3), 217-238.
[2] Spiesz, E. M.; Zysset, P. K., Structure-mechanics relationships in mineralized tendons. *Journal of the Mechanical Behavior of Biomedical Materials* **2015,** *52*, 72-84.

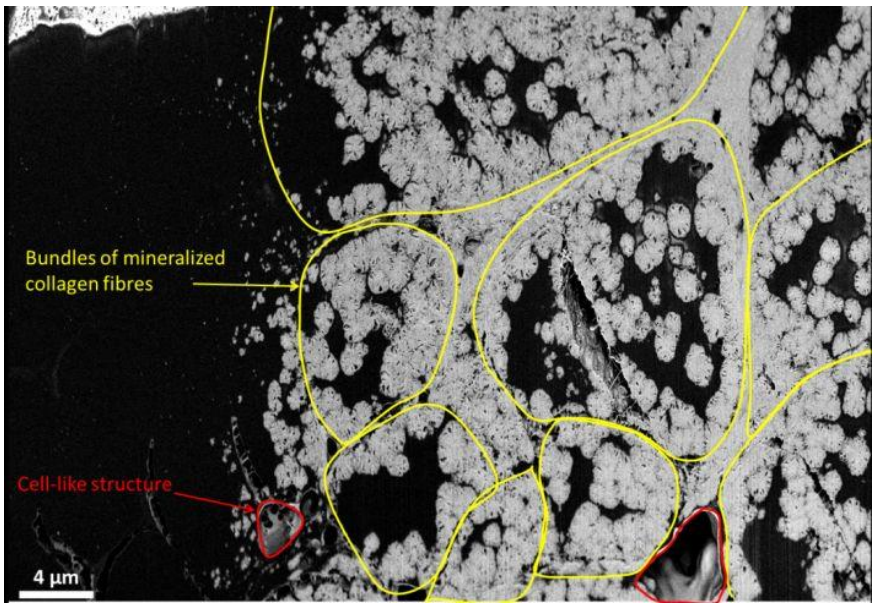

Figure 1. A backscattered SEM image of the cross section of the turkey leg tendon.

LS 3: Microorganisms, pathogens and EM in diagnostics

LS3.001 invited
High-speed atomic force microscopy – the dawn of dynamic structural biochemistry

S. Scheuring[1]

[1]Weill Cornell Medicine, Bio-AFM Lab, New York, NY, United States of America

sis2019@med.cornell.edu

The advent of high-speed atomic force microscopy (HS-AFM[1]) has opened a novel research field for the dynamic analysis of single bio-molecules: Molecular motor dynamics[2,3] membrane protein diffusion[4],assembly[5] and conformational changes[6] could be directly visualized. Further developments for buffer exchange[7] and temperature control[8] during HS-AFM operation provide breakthroughs towards the performance of dynamic structural biochemistry using HS-AFM.

[1] Ando et al, Chem Rev 2014, 114(6):3120-88
[2] Kodera et al, Nature 2010, 468(7320):72-6
[3] Uchihashi et al, Science 2011, 333(6043):755-8
[4] Casuso et al, Nat Nanotechnol 2012, 7(8):525-9
[5] Chiaruttini et al, Cell 2015, 163(4):866-79.
[6] Ruan et al, PNAS 2017, doi: 10.1073/pnas.1616413114
[7] Miyagi et al, Nat Nanotechnol 2016, 11(9):783-90
[8] Takahashi et al, Small 2016, 12(44):6106-6113

LS3.002 invited
Large volume CLEM deciphers the intracellular niche formation of the human pathogens Shigella and Salmonella

J. Enninga[1]

[1]Institut Pasteur, Paris, France

jostenn@pasteur.fr

Intracellular pathogens reside either in membrane-enclosed vacuoles/phagolysosomes or they escape from this compartment to live within the host cytoplasm by rupturing the surrounding endomembranes. We have developed highly sensitive fluorescent approaches that measure the translocation of intracellular pathogens from an endomembrane-bound compartment to the cytoplasm. Our assays have high spatiotemporal resolution and work in single cells. Furthermore, they can be scaled up to be used in conjunction with chemical or genetic screens. This allows the identification of physiological conditions that favour pathogen localizations either within the cytoplasm or within a membrane-enclosed vacuole. I will discuss the design of our fluorescent reporters for the measurement of the precise intracellular localization using *Shigella*, and *Salmonella* as model pathogens. Secondly, I will describe how our methods can be combined with large volume ultrastructure pipelines mainly through focused ion beam scanning electron microscopy (FIB-SEM). The fluorescent reporters provide the molecular specificity of the studied events, and the ultrastructure provide the overall cellular morphology. Such correlative light electron microscopy workflows have provided unprecedented information on the endomembrane subversion by the bacterial pathogens. Our work also shows how methods developed for the study of intracellular pathogen localization can be exploited to decipher other cellular processes.

LS3.003
Tailored liposomes against bacterial toxins

E. B. Babiychuk [1], A. Draeger[1]

[1]University of Bern, Institute of Anatomy , Bern, Switzerland

draeger@ana.unibe.ch

Gram-positive bacterial pathogens that secrete cytotoxic pore-forming toxins, such as *Staphylococcus aureus* and *Streptococcus pneumoniae*, cause a substantial burden of disease. Using a combination of life imaging and cryo-electron microscopy we show that pneumolysin, released by cultured bacteria, is capable of permeabilizing the plasmalemma of host cells. However, such permeabilization does not lead to cell lysis since pneumolysin is actively removed by the host cells. The process of pore elimination starts with the formation of pore-bearing plasmalemmal nanotubes and proceeds by the shedding of pores that are embedded in the membrane of released microvesicles. Pneumolysin prepores are likewise removed. Inspired by the principles that govern natural toxin-host interactions, we have engineered artificial liposomes that are tailored to effectively compete with host cells for toxin binding. Liposome-bound toxins are unable to lyse mammalian cells in vitro. We use these artificial liposomes as decoy targets to sequester bacterial toxins that are produced during active infection in vivo. Liposomes protect mice against death by pneumococcal septicaemia or pneumonia. Composed exclusively of naturally occurring lipids, tailored liposomes are not bactericidal and could be used therapeutically either alone or in conjunction with antibiotics to combat bacterial infections

LS3.004
Structural and functional compartmentalization in a hyperthermophilic prokaryote

J. Flechsler[1], T. Heimerl[2], R. Rachel[3]

[1]LMU Munich, Planegg-Martinsried, Germany
[2]Philipps Universität, Marburg, Germany
[3]Universität Regensburg, Regensburg, Germany

jennifer.flechsler@biologie.uni-muenchen.de

Introduction**:** The hyperthermophilic prokaryote *Ignicoccus hospitalis* exhibits a compartmentalized ultrastructure, comprising a cytoplasm that is separated from an outer cellular membrane (OCM) by an inter membrane compartment (IMC) [1]. The IMC contains membrane-surrounded tubes and vesicles, derived from the cytoplasm. Altogether, the ultrastructure is reminding of the eukaryotic endogenous membrane system [2]. Besides the spatial compartmentalization, also a functional compartmentalization was shown for cells of *I. hospitalis*: DNA replication and protein biosynthesis take place in the cytoplasm, separated from the energy conserving reactions in the IMC [3].
Objectives**:** The unique location of the ATP synthase and H2:sulfur oxidoreductase in the outer cellular membrane inevitably leads to the presence of a tremendous amount of ATP in the IMC. This raises questions about the subcellular distribution of other metabolic pathways, which depend on the availability of ATP, e.g. different steps of the carbon fixation pathway [4].
Materials and Methods: To address these questions, we cryo-immobilized and freeze substituted cells of *I. hospitalis*. This was followed by a variety of methods for 3D electron microscopy in combination with immunogold labelling (serial sectioning, electron tomography, immunogold labeling of Epon-embedded cells and of cryo-sections).
Results and Discussion: Immuno-electron microscopy revealed that the Acetyl-CoA synthetase, an enzyme providing the primary acceptor molecule for the CO2 fixation pathway, is located in the IMC, tightly associated with the outer cellular membrane [5]. Additionally, we were able to detect further enzymes involved in the carbon fixation pathway in the IMC of *Ignicoccus,* not in the cytoplasm (e.g. the Crotonyl-CoA hydratase and the PEP carboxylase).
Conclusion: From our results we conclude that the whole carbon fixation pathway takes place in the IMC of *I. hospitalis*. Furthermore, our investigations show a unique example of functional compartmentalization in an unusual prokaryotic cell.

References:
[1] Huber et al., Antonie van Leeuwenhoek 102 (2012) p 203-219.
[2] Heimerl, 2012, EMC 2012 proceedings (2012).
[3] Küper *et al.*, PNAS 107 (2010), p. 3152.
[4] Jahn *et al.,* J Bacteriol 189 (2007), p. 4108.
[5] Mayer *et al.,* J Bacteriol 194 (2012), p. 1572-81.
[6] This research was supported by grants from the DFG (Germany).

LS3.005
Variability in calcium content in the spores of Clostridium species by STEM EDX

B. Bartova[1], J. Jamroskovic[1,2], Z. Chromiková[2], C. List[1], I. Barák[2], R. Bernier-Latmani[1]

[1]EPFL, EML, Lausanne, Switzerland
[2]Slovak Academy of Sciences, SAS, Institute of Molecular Biology, Bratislava, Switzerland

barbora.bartova@epfl.ch

Introduction: Spores of a number of clostridial species, and their resistance to thermal treatment is a major concern for the food industry. Spore resistance to wet heat is related to the level of spore hydration, which is inversely correlated with the content of calcium and dipicolinic acid (DPA) in the spore core. It is widely believed that the accumulation of DPA and calcium in the spore core is a fundamental component of the sporulation process for all endospore forming species.
Objectives**:** In the present work, we focus on several *Clostridium* species belonging to Cluster I of genus *Clostridium* (*sensu stricto*). This cluster is morphologically and physiologically the best described group of the genus *Clostridium*, which contains over 160 species divided into multiple sub-groups according to results of 16S rRNA analysis (Gupta and Gao, 2009).
Here, we examine the group of industrially important species belonging to this cluster, specifically *C. acetobutylicum* DSM1731 and DSM792, *C. beijerinckii* strains DSM791 and NCIMB 8052 and *C. collagenovorans* 3089, for their level of resistance to wet heat as well as for their DPA/Ca content. The goal of the study is to evaluate the link between heat resistance and DPA/Ca content, as well as to compare DPA/Ca levels among *Clostridium* species.
Materials and Methods: Scanning transmission electron microscopy (STEM) with energy dispersive spectroscopy (EDS) was used to obtain elemental composition maps and to perform comparative characterization of elemental content in studied *Clostridium* species with focus on Ca. In this study, an X-ray EDS system (Esprit/Quantax Bruker) in STEM mode in a FEI Tecnai Osiris microscope (200 kV X-FEG field emission gun, X-ray detector (Super-X) with 4 × 30 mm2 windowless SDD diodes and 0.9sr collection angle was applied. In each spore population, at least 10 spore were analyzed (except of C. beijerinckii DSM 791 where only 4 spore were found) in order to obtain statistically relevant overview of Ca presence. The details on the strains used in the study as well as bacterial growth and spore preparation are described in (Jamroskovic et al., 2016).
Results: High Angle Angular Dark Field STEM microscopy (HAADF-STEM) image shows the morphology of representative spore. The spore core, which is denser, and the cortex are clearly distinguishable Figure 1.
STEM-EDS analysis of the spores of *C. acetobutylicum* DSM 1731 and *C. collagenovorans* DSM 3089 revealed uniformly high levels of calcium in the spore core (8.02 and 8.58%, respectively) (Figure 2). The same was found in two control strains *D. reducens* MI-1 and *B. subtilis* PY79 (7.96 and 7.29%, respectively). In contrast, *C. beijerinckii* DSM 791 was found to have very low calcium content. Two stains (*C. acetobutylicum* DSM 792 and *C. beijerinckii* NCIMB 8052) exhibit great variability in calcium content.
Conclusion: Overall, this study shows that there is great variability in the calcium, DPA concentrations in *Clostridium* Cluster I spores and that those concentrations correlate well with spore heat resistance.

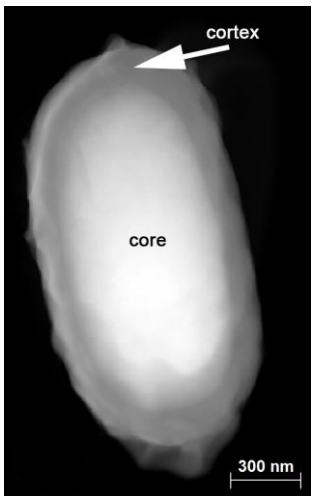

Figure 1. HAADF image presents typical morphology of the spore, which is formed by several layers. Here we see the core and the cortex of *C. beijerinckii* NCIMB 8052.

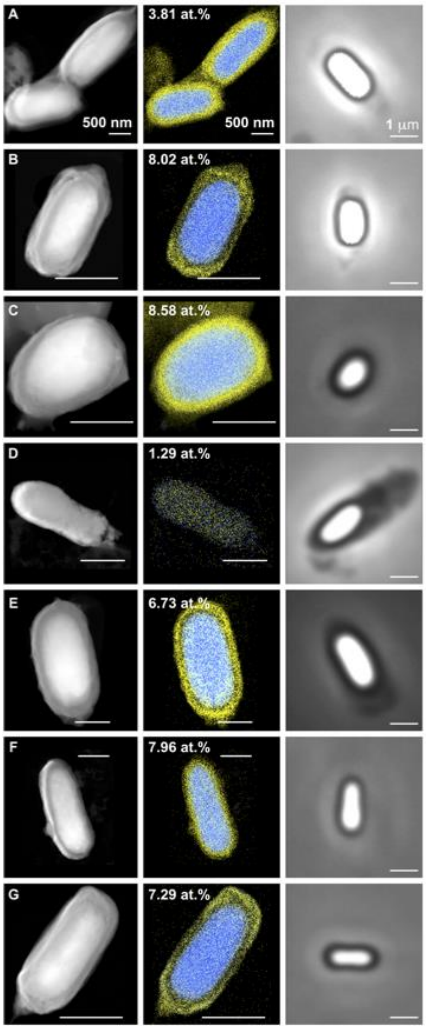

Figure 2. STEM-EDS and bright field images of clostridial spores: (A) *C. acetobutylicum* DSM 792 (spore width 0.9 mm) , (B) *C. acetobutylicum* DSM 1731 (spore width 0.5 mm), (C) *C. collagenovorans* DSM 3089 (spore width 0.8 mm), (D) *C. beijerinckii* DSM 791 (spore width 0.5 mm), (E) *C. beijerinckii* NCIMB 8052 (spore width 1 mm), (F) *D. reducens* MI-I (spore width 0.75 mm), (G) *B. subtilis* PY79 (spore width 0.5 mm). Calcium is false colored in blue and chlorine in yellow in EDS images. Number in EDS images represents atomic percentage of calcium.

LS3.006
FIB-SEM tomography and serial sectioning TEM reveal rate-determining steps of herpesvirus egress

C. Villinger[1], G. Neusser[2], P. Walther[3], T. Mertens[1], J. von Einem[1]

[1]Institute of Virology, University Medical Center Ulm, Ulm, Germany
[2]Institute of Analytical and Bioanalytical Chemistry, Ulm University, Ulm, Germany
[3]Central Facility for Electron Microscopy, Ulm University, Ulm, Germany

clarissa.villinger@uni-ulm.de

Electron microscopy (EM) of high-pressure frozen and freeze-substituted samples allows unambiguous identification and detailed analysis of the various stages during human cytomegalovirus (HCMV) maturation. However, EM *per se* cannot provide dynamic information. Nevertheless, quantitative structural imaging can provide some insight into HCMV egress dynamics since EM captures slow and/or frequent events with a higher chance than quick and/or rare events. Additionally, application of 3D EM techniques enables quantifications with higher accuracy.
By application of the two 3D EM techniques focused ion beam-scanning electron microscopy (FIB-SEM)[1] and serial sectioning transmission electron microscopy (TEM)[2] and reassessment of 2D micrographs from over 40 TEM experiments we evaluated the number of HCMV capsids present at different stages of egress: (I) within the nucleoplasm, (II) budding (primary envelopment) into the perinuclear space (PNS), (III) within the PNS, (IV) leaving the PNS and (V) in the viral assembly complex (vAC), which is the site of secondary envelopment and therefore final virus maturation. The capsids in the vAC were also quantified regarding their stage of secondary envelopment (*free*, *budding* and *enveloped*). The numbers were then summarized in a snapshot model which was analyzed by including dynamic data from life cell imaging studies[3,4]. Since results of different experiments are combined, the snapshot model is based on estimates and not on exact numbers.
First, analysis of the snapshot model suggested nuclear egress and release of virions at the plasmamembrane as bottlenecks for the production and release of infectious virions. This knowledge could be useful to identify promising targets for future development of new antiviral drugs. Second, much more capsids were either in the process of secondary envelopment or enveloped at the vAC compared to primary envelopment of nuclear capsids and primary enveloped capsids in the PNS, although both envelopment processes might occur with similar velocities. This demonstrates the importance of the vAC to facilitate secondary envelopment at host cell membranes by concentrating these membrane systems at a distinct site in the cytoplasm.

[1] Villinger et al. 2015. Viruses 7:5686–5704.
[2] Schauflinger et al. 2013. Cell Microbiol 15:305–314.
[3] Sampaio et al. 2005. J Virol 79:2754–2767.
[4] Bosse et al. 2014. mBio 5:e01909-14.

LS3.007
New giant virus in free-living amoeba

B. Hauröder[1], C. Wylezich[2], J. Eisenkolb[1,3], R. Michel[1]

[1]Central Institute of the Deutsche Bundeswehr Medical Service, I/EM, Koblenz, Germany
[2]Friedrich-Loeffler-Institut, Greifswald-Insel Riems, Germany
[3]University Koblenz-Landau, Institute for Integrated Natural Sciences, Koblenz, Germany

b-hauroeder@t-online.de

Introduction: A Mimivirus-like endoparasite (KSL-5) of a Saccamoeba sp. (SL-5) was isolated from the bark a sycamore tree (Michel and Hauröder, 2015). Since this is the first mimivirus-like organism that was isolated from a Saccamoeba we suggest the name "Platanovirus saccamoebae". In order to study the developmental stages of this new giant virus (KSL-5) from free-living amoeba (FLA) a continuous culture of the endoparasite in its original host (SL-5) was investigated. We attempted to see if observations made by various authors (Susan Monti et al. 2013; Raoult et al 2007, La Scola et al. 2008; Claverie and Abergel, 2009) could be compared our findings in a natural host-parasite system. We also investigated if FLA other than saccamoebae were susceptible to an infection with the new isolate KSL-5.
Objectives: Saccamoeba sp., Mimivirus-like, Megavirales, satellite virus
Material and Methods: Small pieces of loose fitting bark of a sycamore tree were transferred onto NN-agar plates preseeded with Enterobacter cloacae as food bacteria. After liberation from various concomitant organisms mass culture for ultrastructural investigations were initiated. Plates with infected saccamoebae were incubated at 20C harvested at various time intervals. To study the infection cycle cured, virus free SL-5 cells were reinfected with KSL-5 suspensions and samples were taken from 0 to 96 hours post infection. Various other amoebas were infected with equal aliquots of KSL-5. TEM preparation was preceded as described before (Michel and Hauröder, 2015).
Results: KSL-5 is a polyhedral virus. The average size of the capsids is 290 nm. The average length of the fibrils is 140 nm, resulting in an average virion size of 430-450 nm. Replication of the virus has a long lag phase of at least 12h. First viruses and a developing virus factory were detected after 18h with a peak at 30h. There were still viable host cells after 96 h post infection. After 24 h a small icosahedral virus of 50-60 nm became visible within the virus factory. It seemed to interfere with the replication of KSL-5. All attempts to transfer KLS-5 to 12 other amoeba species failed. Preliminary results of a sequence analysis show the highest similarity of KSL-5 to Megavirus chilensis (~75%).
Conclusions: This is the first giant virus reported in Saccamoeba. The average size of the virus capsid is is smaller than other Megavirales but their fibrils are longer. Ultrastructure and the association with a satellite virus suggest it to be a Mimivirus-like virus whereas a preliminary sequence analysis shows high similarities to *Megavirus chilensis* (Mimiviridae linage C). 12 other amoebas were not susceptible to an infection with KLS-5. We therefore consider it to be a new giant virus within the Mimiviridae and suggest the name "Platanovirus saccamoebae".

References:
[1] Claverie JM, Abergel C, 2009. Annu. Rev. Genet. 43:49–66.
[2] La Scola B, et al. 2008. Nature 455:100–104.
[3] Michel R, Hauröder B.2015.. Endocyto Cell Res. 26:63-66 Raoult D, et al. 2007. Clin Infect Dis. 45:95-102.
[4] Suzan-Monti M et al. 2007.PLoS One. 2:e328.

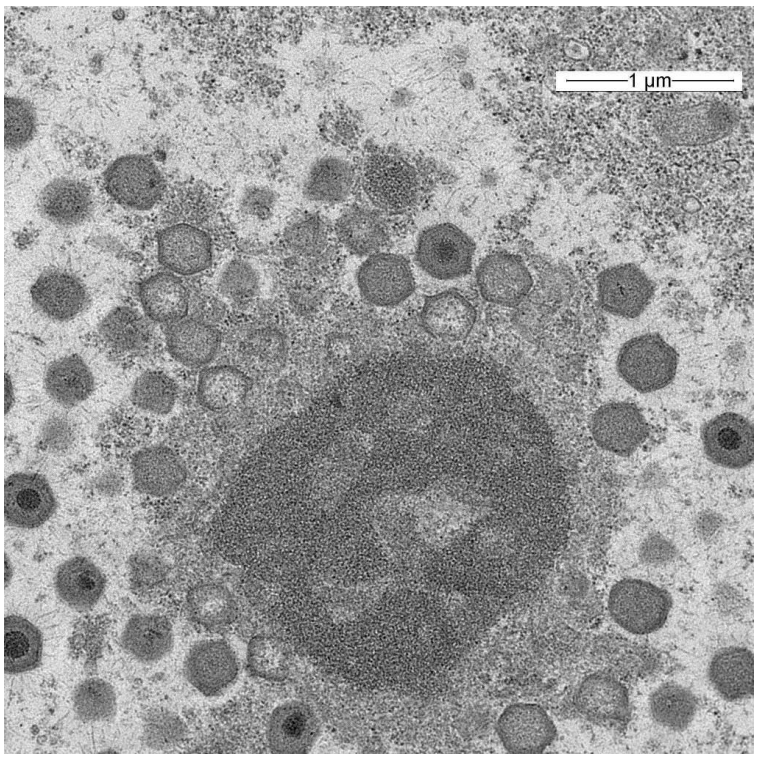

Figure 1. Saccamoeba spec. with giant virus 18 h post infection.

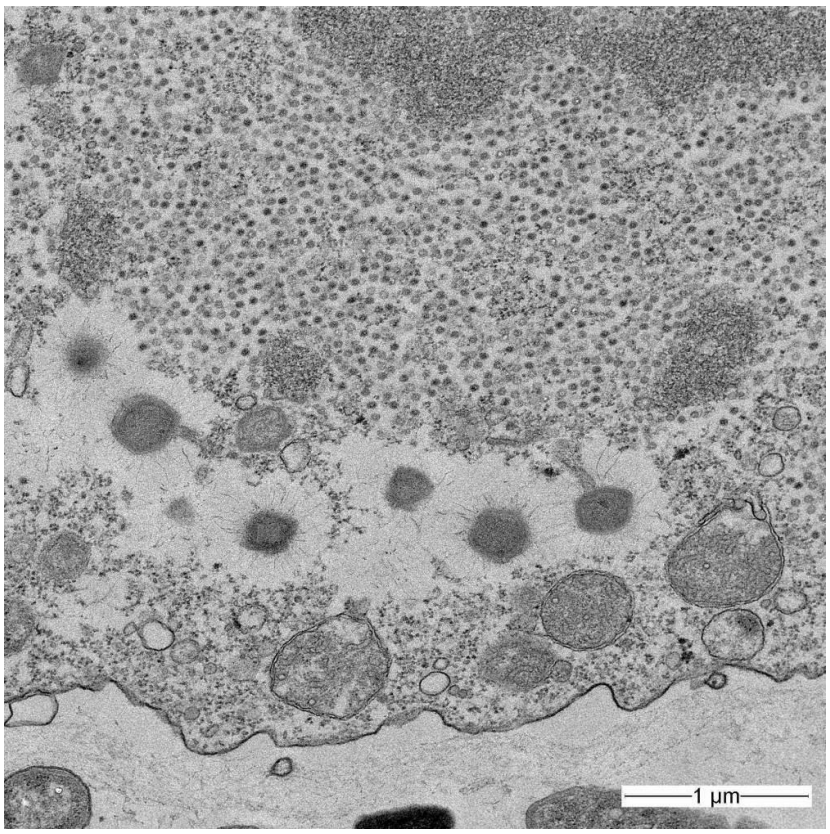

Figure 2. Saccamoeba spec. with giant virus and satellite virus 24 h post infection.

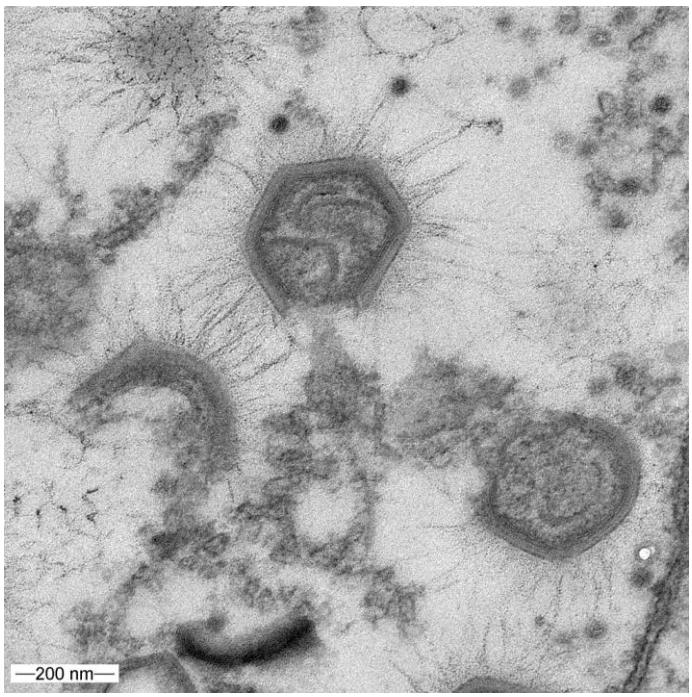

Figure 3. Assembly of giant virus capsids.

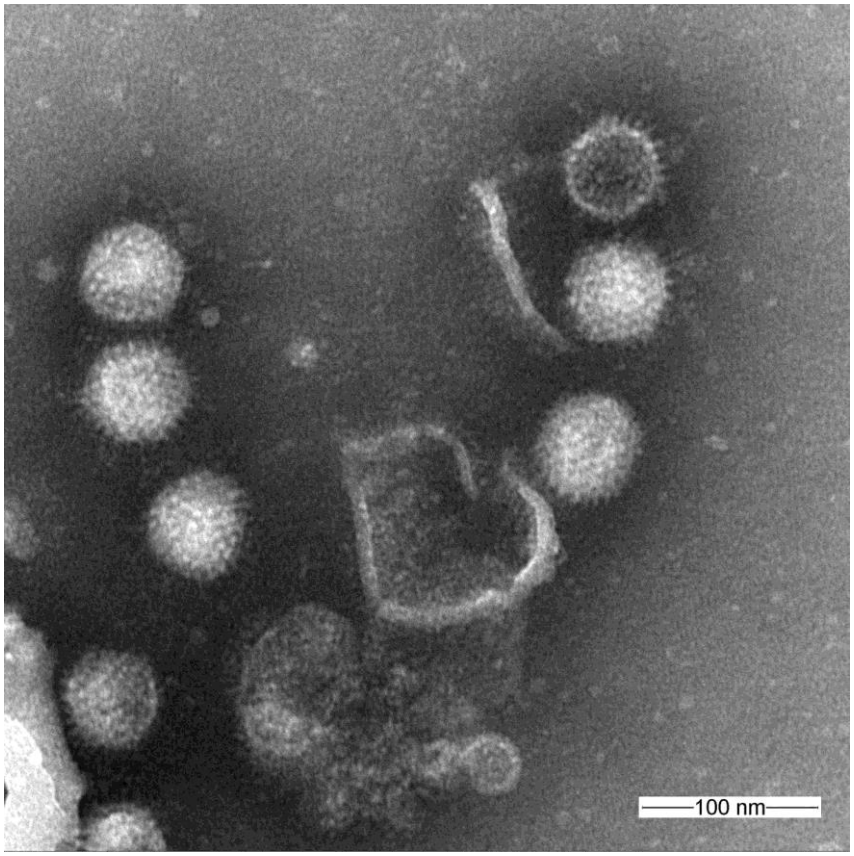

Figure 4. Satellite virus, negative staining.

LS3.P001
Electron microscope makes the difference in the development of systematics, life cycles and pathological effect of the phylum Myxozoa

F. Abdel-Ghaffar[1], A. R. Bashtar[1], R. Abdel-Gaber[1], S. Al Quraishy[1]

[1]Faculty of Science, Cairo University, Cairo, Egypt

fathyghaffar@yahoo.com

Since the first discovery of light microscopy by Leeuwenhoak in 1673 until the middle of 19th century, microscopists had accepted that it was simply not possible to resolve structures of less than half a micrometer development of electron microscopy and the improvement of preparation methods of biological materials and the study of microorganisms is greatly improved. In the present study, forty-three out of 120 (35.8 %) African catfish *Clarias gariepinus* were collected from different sites of the River Nile in Egypt and examined for the prevalence of myxozoan parasites infection. The infection appeared as clusters of ovoid to ellipsoidal plasmodia being embedded within the hyaline cartilage of the suprabranchial organ of the fish. Histological studies indicate tissue distortion at the sites of infection. The continuous growth of the plasmodium led to deformation of the filament structure as well as disorganization and displacement of the gill lamellae. Also, a severe atrophy occurred in the hyaline cartilage of the gills and the gill lamellae. Based on the structure and measurements of fresh spores by light microscopy, this parasite was identified as *Henneguya suprabranchiae*. Spores are oval in shape, and they measured 13 (11–14) × 3 (2–5) µm length by width. It has two polar capsules inside, each measured 3 (2.5–5) × 1 (1.5–4) µm length by width. Each polar capsule has a spirally coiled (7–9 turns) polar filament. The ultrastructural analysis showed that the plasmodia were surrounded by single-unit membrane which invaginates into pinocytotic canals. The generative cells and the early developmental stages were arranged at the periphery of the plasmodia, while immature and mature spores were centrally arranged. The developmental stages characterizing sporogenesis, capsulogenisis, and valvogenesis of the present parasite were ultrastructurally studied. The first recognizable stage of sporogenesis is represented by generative cells. The earliest pansporoblast stage was represented by the enclosure of a generative cell by an envelope cell followed by cellular division resulted in pansporoblast with sporont progony cells. The early stage of capsulogenesis is the capsular primordium followed by the appearance of the external tubule inside the cytoplasm of the capsulogenic cells forming several loops. As a sequence of polar capsule development, these tubules fuse with the capsular primordium and become shortened and eventually disappeared forming the filamentous materials inside the primordium. The capsular maturation of all stages usually occurs asynchronously. During sporoplasm maturation, several bounded electron-dense bodies (the sporoplasmosomes) are appeared. Valvogenesis is initiated when valvogenic cells start to surround the capsulogenic and sporoplasmic cells and rapidly adhere from their ridges through the desmosome-like junctions. The posterior end of the valves protrudes, forming the primordia of the posterior process. In immature and mature spores, the valves appear uniformly smooth with slightly thickened ridges joined in a suture line, and later they will protrude posteriorly into two posterior processes. Host-parasite relationship and the pathological effect of the parasite is also recorded and discussed.

LS3.P002
Stripe-like S-layer proteins with p2-Symmetry in Acidithiobacillus – a focus on the thermo-tolerant strain HV2/2

M. Ostermeier[1], H. Huber[2], A. Klingl[1]

[1]LMU Munich, Plant Development, Planegg-Martinsried, Germany
[2]University of Regensburg, Institute for Microbiology, Regensburg, Germany

a.klingl@lmu.de

Introduction**:** The biological oxidation of iron and sulfur plays an important role in acidic environments. In such natural habitats like the drainage water in mines or solfataric regions, bacteria generally perform iron and sulfur oxidation reactions. In most cases, these bacteria belong to the genera *Acidithiobacillus* and *Leptospirillum*. The bacteria usually exhibit cell surface structure for attachment like pili, fimbriae, flagella, proteinaceous surface layers (S-layers), as well as extracellular polymeric substances (EPS). Some of these extracellular structures might also be involved in the decomposition of iron and sulfur compounds [3].
Objectives**:** The main focus of this work was to characterize the *Acidithiobacillus* isolates SP5/1 and HV2/2 ultrastructure and physiology [1] and to find out if they were covered by special extracellular structures like a regularly arranged S-layer with a distinct symmetry.
Materials and Methods**:** The major focus of this electron microscopic survey of iron oxidizing acidophilic bacteria proteins was on a rod-shaped proteobacterium strain HV2/2 (DSM 24413), originating from Hveravellier (Iceland). In a minor and comparative side project, we also investigated the *Acidithiobacillus* strain SP5/1 (DSM 24419), sampled in the Solfatara region (Pisciarelli, Italy) [1]. The determination of growth temperature ranges [1,2] and substrate spectra as well as the preparation of the strains, isolation of DNA, phylogeny, preparation of the S-layer proteins, sequencing, preparation of cells for electron microscopy like high-pressure freezing and freeze-etching and the characterization of the S-layer protein itself was performed as described previously [1,2,3,4].
Results and Discussion**:** Whereas genetic analysis could show, that that strain SP5/1 is closely related to the type strain *Acidithiobacillus ferrooxidans* DSM 14882T and as well as strain ATCC 33020, our second strain HV2/2 revealed a genetic proximity to *Acidithiobacillus caldus* (DSM 8584T). Especially the latter finding was very interesting as *A. caldus* is described to be unable to grow in Fe2+ as sole energy source. In contrast to this, strain HV2/2 is able to grow on pyrite (FeS2) as well as FeSO4.
Within the electron microscopic studies, both strains depict cell wall architectures typical for Gram-negative bacteria: a cytoplasm surrounded by a cytoplasmic membrane, the periplasm with a thin peptidoglycan layer and an outer membrane. As an unexpected result, the outer membrane itself was also covered by another structure: an electron dense Surface layer (S-layer) with p2-symmetry [3]. This S-layer not only seems to be involved in iron complexation or oxidation and could therefore play a role in pyrite degradation via the "contact" mechanism [5] but it might also depict a genus specific feature as it could also be shown on the surface of the type strains *A. ferrooxidans* DSM 14882T and *A. thiooxidans* DSM 14887T.
Conclusion**:** Within our current studies, we are investigating the ability of the thermo-tolerant strain HV2/2 to oxidize Fe2+ in more detail. The fact that the reaction takes place at 45°C instead of 28°C like in strain SP5/1 could be very interesting for industrial applications as this could lead to higher turnover rates due to faster reaction kinetics.

References:
[1] G. Huber, H. Huber and K.O. Stetter, Biotechnol Bioeng Symp **16** (1986), 239.
[2] H. Huber, PhD thesis, University of Regensburg (1987)
[3] A. Klingl, C. Moissl-Eichinger, G. Wanner, J. Zweck, H. Huber, M. Thomm and R. Rachel, Arch Microbiol **193** (2011), 867.
[4] A. Klingl, Struktur und Funktion von S-layern acidophiler Bakterien und Archaeen, ihre Rolle bei der Pyrit-Oxidation sowie die Adhäsion an Oberflächen, PhD thesis, University of Regensburg, 2011.
[5] W. Sand and T. Gehrke, Res Microbiol **157** (2006), 49.

LS3.P003
Insight into the morphology of the ammonia-oxidizing archaeon Nitrososphaera viennensis sp. nov.

I. Görens[1], R. Rachel[2], M. Stieglmeier[1], A. Klingl[1]

[1]LMU Munich, Plant Development, Planegg-Martinsried, Germany
[2]University of Regensburg, Institute for Microbiology, Regensburg, Germany

a.klingl@lmu.de

Introduction**:** The high abundance of ammonia-oxidizing archaea already hints to their significant impact on the global nitrogen cycle. Although we are still lacking cultivated or enriched strains for the majority of these organisms, *Nitrososphaera viennensis* represents an exception in this regard because it can be grown in pure laboratory cultures. It is therefore amenable to detailed investigations concerning ultrastructure and surface layer (S-layer) as well as 3-dimensional structure.
Objectives**:** Herein, we tried to obtain further information on this first type strain of the novel class Nitrososphaeria within the novel phylum Thaumarchaeota of the domain Archaea on an ultrastructural level [1].
Materials and Methods**:** The visualization of *N. viennensi*s cell ultrastructure and 3-dimensional arrangement using a conventional transmission electron microscope (TEM) as well as a scanning transmission electron microscope (STEM) was carried out with ultrathin/semithin sections of chemically fixed and high pressure frozen cells. The characterization of the S-layer was carried out using negatively stained purified protein sheets or whole freeze-fracture and freeze-etched cells. In the latter case, image processing via correlation averaging delivered information about the S-layer symmetry and lattice constants.
Results and Discussion: *N. viennensis* cells are irregular shaped motile cocci and possess appendages like flagella and pili. The relatively small cells exhibit a diameter of about 0.78 ± 0.13 µm. Small inclusions with high and low electron density and a clearly discernable, larger area within the cytoplasm became apparent in ultrathin sections. This discernable "subcompartment" might represent a storage area for polyhydroxyalkanoate produced by *N. viennensis* cells. The irregular coccoid shape common to *N. viennensis* and Sulfolobales cells might result from the p3-symmetry of the S-layer.
Conclusion: The detailed characterization of *N. viennensis* not only extends our knowledge about the morphology of Thaumarchaeota, it also reveals interesting intracellular features, which might play important roles in cell stability or metabolism.

References:
[1] Stieglmeier M. et al. (2014). *IJSEM* **64**(8): 2738-52.

LS3.P004
Inorganic particle analysis in lung tissue of patients with occupational lung diseases.

B. K. Kuhn[1]

[1]Staublungenlabor der silag, c/o Institut für Geochemie & Petrologie, Zürich, Switzerland

barbara.kuhn@erdw.ethz.ch

Introduction: Occupational lung diseases, also known as pneumoconiosis, represent a group of interstitial lung diseases triggered by inhalation of inorganic particles or fibers. The overlap in clinical-radiological-pathological presentation and long latency period in the majority of cases frequently hampers a correct diagnosis of pneumoconioses. To improve diagnostics accuracy subtyping of inhaled fibers and particles is important.
Objectives: We combine histological investigations with inorganic fiber and particle analyses of the same peripheral lung tissue samples to improve the identification of the type and origin of occupational lung diseases.
Materials and Methods: Lung tissue samples of patients with suspected pneumoconiosis are ashed at low temperature in an O2-plasma to separate the inorganic particles from the organic matter. The particles are then suspended in water and filtrated on Nuclepore filters at known concentrations. These filters are carbon coated, punched and transferred to Cu grids for analysis by TEM-EDX to identify the particles by their chemical composition. In the case of asbestos related diseases, the fibers are also counted and the amount of asbestos fibers per gram dry lung tissue calculated to estimate the degree of exposure.
Results: In cases with suspicion of asbestos exposure, the analysis focus is on fiber count and identification. The amphibole asbestos fibers are easily recognized by their EDX spectra. To distinguish magnesium-silicate fibers chrysotile, anthophyllite (both asbestos fibers) and talc (non-asbestos) selected area electron diffraction (SAED) and fiber morphology in addition to their chemical composition is used. Other fibers frequently encountered during the analysis of dust extracted from lung tissue are micas, rutile, feldspar, Al-silicates and clay minerals.
In cases with a working history compatible with silicosis, mixed dust pneumoconiosis, hard metal lung or lung disease of unknown cause at least 100 particles are analysed and identified. The relative amount of particle groups is a strong indicator for the type of disease and prior exposure. For example, if more than half of the particles are quartz, it is most likely that the corresponding pathology is silicosis. A combination of feldspars, mica, and other silicates with little quartz is indicative for mixed dust pneumoconiosis. In hard metal disease the abundance of tungsten carbide (WC) particles together with chromium, nickel, titanium and sometimes tantalum and niobium are typical. In cases of arc welder's lung abundant iron, chromium and nickel oxides are indicative for the exposure to welding fumes.
Conclusions: Analysis of inorganic fibers and particles combined with histopathological investigations of peripheral lung tissue enhances the diagnostic accuracy of subtyping dust-induced lung diseases. Mineral analyses also provide additional information to working histories gained through questionnaires concerning work place conditions as they also indicate forgotten or unknown exposures. Therefore, dust analysis is a useful additional tool for insurance companies (e.g. SUVA) to assess their liability in cases of suspected occupational lung disease.

LS3.P005
Tuberculosis lymphadenitis in northwest Ethiopia – implications for public health

F. B. Degeneh[1], B. Anagaw[1]

[1]Bahir Dar University, Department of Medical Microbiology, Bahir Dar, Ethiopia

fantahun.degeneh@gmail.com

Objective: In Ethiopia where there are limited diagnostic facilities, the actual burden of tuberculosis (TB) lymphadenitis is not well known. Therefore, we conducted this study to determine the proportion of TB lymphadenitis (TBL) in childhood and adults in Northwest Ethiopia.
Materials and Methods**:** A prospective cross sectional study was con- ducted from April to May 2012. Fine needle aspiration cytology (FNAC) for cytological diagnosis of TBL was used. The diagnosis of TBL was established when cytological features from lymph node aspirates are strongly suggestive of TB. Descriptive and multivariate analysis was done using SPSS version 16.
Results: Out of 1070 patients attending the cytological diagnosis in the study sites 437 (41%) were positive for TBL. Of the 437 registered TBL, 59 (13.5%) were pediatric patients and 378 (86.5%) were adults. There were more females than males with a male to female ratio of 0.8:1. The cervical region had the most common group of TBL with 321 (73.2%) patients. Most of all these patients 314 (75.3%), were matted with a majority of (250/314) being in the cervical region. Individuals who had contact history with TB patients (P = 0.046) were more likely to have TBL.
Conclusions**:** In the studied region high prevalence of TBL was documented. Screening of TBL particularly for those who had contact with TB patients is recommended. Most patients in our study presented with matted lymph nodes, indicating that late arrival of patients to health institutions. Thus continuous and intensified public health strategies on health education and early referral system have to be done in order to link them to health institutions earlier than at present.

LS3.P006
Model for cryoelectronmicroscopic study virus, bacteria and protozoa

K. Hovnanyan [1]

[1]Institute Molecular biology of NAS RA, Electron Microscopy, Yerevan, Armenia

hovkarl@mail.ru

Electronomicroscopiccryoultramicrotomy its most important advantage is that this method allows biological samples to study cells ultrastructural natural conditions. Our studies of viruses, bacteria conditions, and their interaction is important cryoultramicrotomyentamoeba weather advantage. In this paper presents data on electron microscopy studypolyxenic culture of Ent.histolytica, using cryoultramicrotomy. We used a strain of Ent.histolytica(strain SH, previously studied by the classical method. It was received ultrastructural characterization of associated bacterial culture, entamoeba cytoplasmic structures, including virus symbiont. Cryofixation, impregnation cryoprotectants conducted by the method of Bernhard W., LeducW. (1967). Cryosectionsobtained on ultramicrotome with a prefix Krio-Kit. The sample temperature of sample was -l200C, and glass cutting knife -900C.Cutting speed was equal to 5 mm/sek.Receivedcryosections contrasted with 2% uranyl acetate or 1% solution of phosphotungsticacid. Electron microscopy research and microphotography was performed in electron microscopeJEM-100B. Electron microscopic study of the culture Ent.histolyticacryosections showed that of associated bacteria are generally Gram negative bacteria. External membrane of the bacteria cell wall shows a single-outer membrane paraplasmatic space and cytoplasmic membrane adjacent to the granular cytoplasm (Figure 1a). Ultrastructural analysistrophozoitesof entamoebashowed that the cells are surrounded by single-cytoplasmic membrane, the cytoplasm forming microvesicles Viewed small microvesicles surrounded by single-membrane. In cytoplasmic component presented with bundle ofmicrofibrils (fig.1b), granular component varying measures. Incryosections cytoplasm of entamoeba able to detect longitudinal and cross sections of virus-like symbionts (Fig.1c,d) Dimensions longitudinal sections symbionts equal to 200nm,diameter 70nm.A comparative study of entamoebaelectronmicroscopy using cryoultramicrotomy and classic method yielded comparable results ultrastructuralorganization entamoeba. At the same time cryoultramicrotomy expanded and helped visualize the cytoplasmic structures in more detail and particularly studied microfilaments.

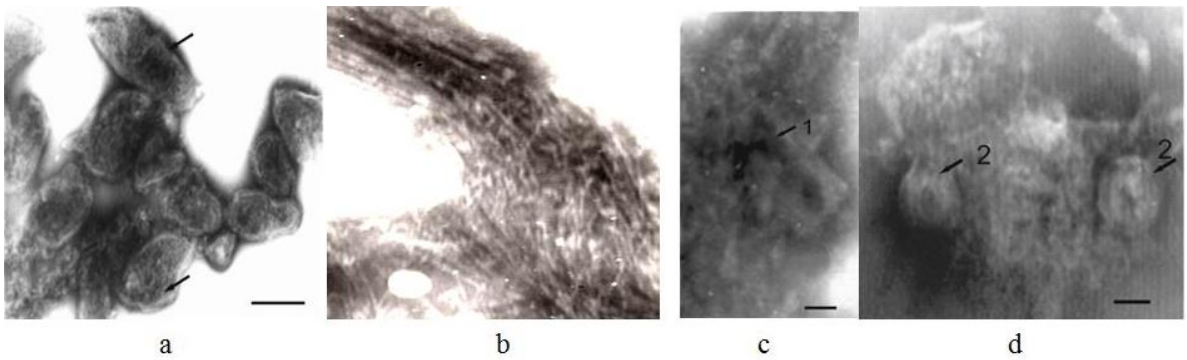

Figure 1. TEM. (a) Cryoultrathin section gramnegativ bacterial association of polymixenic culture of Ent. histolytica (strain SH)- accompanying gram-negative cels (→) of bacteria;(b) Bundle of citoplasmaticmicrofibrils(→).(c,d) viruslikesymbionts(→1,2);Scale bars:100nm.

LS3.P007
Morphological and ultrastructural characteristics of Myxobolus ridibundae n. sp. (Myxosporea: Bivalvulida) infecting the testicular tissue of the marsh frog Rana ridibunda (Amphibia: Ranidae) in Egypt

R. Abdel-Gaber[1], F. Abdel-Ghaffar[1], H. El-Fayoumi[1]

[1]Faculty of Science, Cairo University, Cairo, Egypt, Cairo, Egypt

rewaida@sci.cu.edu.eg

Myxozoans are one of the most economically important groups of protozoan parasites causing many serious diseases of their hosts. In the present study, a total of 60 live adult male specimens of the marsh frog Rana ridibunda have been randomly captured during the period of January–December 2015 in different areas at Kafr El-Sheikh Governorate, Egypt and were examined for infection by myxosporidian parasites. A total of 48 (80.0 %) out of 60 frog specimens were found to be infected with Myxobolus species. Parasitic infection was restricted to the testicular tissue of the examined frogs. Macroscopic cysts (plasmodia) which heavily infested different parts of the testes were recovered. Morphological and ultrastructural characteristics of these myxosporidian species were carried out using light and transmission electron microscopy. Plasmodia measured 0.16–0.53 (0.34 ± 0.01) mm in diameter. Mature spores appeared oval in frontal view, measuring 8.9–11.5 (9.6 ± 0.1) µm in length and 7.5–9.1 (8.4 ± 0.1) µm in width containing 5–6 turns of polar filaments. Morphometric characterization revealed that the very small size of the present Myxobolus species was the most distinctive feature that separates them from all previously described Myxobolus species. Ultrastructural analysis showed that the plasmodia are surrounded by a plasma membrane with numerous pinocytotic protrusions extending toward the host cell. The generative cells and the different developmental stages are arranged at the periphery of the plasmodia, while immature and mature spores are centrally located. Sporogenesis, capsulogenesis, valvogenesis, and spore maturation of the present parasite are also described. The present species is described as Myxobolus ridibundae and represents a new species.

LS3.P008
Electronmicroscopy analysis inhibition effects pruduction of Lactobacillus acidophilus on the Staphylococcus aureus

K. Hovnanyan [1], S. A. Barkhudaryan[2], M. K. Hovnanyan[1], A. D. Hambartsumyan[2]

[1]Institute Molecular biology of NAS RA, Electron Microscopy, Yerevan, Armenia
[2]Yerevan State Medical University, Yerevan, Armenia

hovkarl@mail.ru

Antibacterial probiotics, lactic including acid bacteria the advantage of being safe for human and animal body. Accompanied by a variety of treatment and prevention of interhospital infections mikrobprotective expediency, the purpose is ultrastructural changes to find out the specifics production of metabolism of lactic acid bacteria on the Staphylococcus aureus[1]. Cultivation of *Staphylococcus aureus(strain 906)* in the presence or absence of *Lactobacillus acidophilus. fermentum Narine F*supernatant at a subinhibitory dose (50 % of MIC). electron microscopy(TEM): the suspension of the biosamples was applied drop-wise, in the liquid was removed and the specimens were negatively stained with phosphorous tungsten solution and uranyl acetat[3].Electron microscopic preparations ultrathin sections were prepared using methods common to TEM standart methods.Their transmission electron microscopy (TEM) images were registered in the JEM-100B,Tesla-500, operating at accelerating voltage of 80 kv, provided with the image recording digital system.Scanning electron microscopy(SEM): the samples were placed in aluminum pieces, metallized with a vacuum evaporator JEOL, and viewed under a scanning electron microscope Vega Tescan.Study with the help of negative contrast lactobacilli allowed to identify villi -pili evenly distributed over the entire surface of the cell wall (fig.1a). By the diameter of the saws varies from 40 to 100A. Electronmicroscopic analysis of control cultures of lactobacillus and staphylococcus showed that bacterial cells have an ultrastructural organization typical of Gram-positive bacteria [2](fig.1b,1c). An ultrastructural analysis of the effect of lactobacillus products on the culture of staphylococci has shown that structural changes in products in the cell wall occur in the form of a dense wall of the cell wall from the cytoplasmic membrane and a breach of integrity(2a).As well as the formation of osmiophobic zones in the cytoplasm of staphylococcus(fig.2b).Ultrastructural changes under the influence of products of Lactobacillus acidophilus on the Staphylococcus aureus basis for concluding that electronmicroscopic weather is an important means of comparative studies and identify bacteriostatic and bactericidal features of probiotic.

[1] A.Dz. Hambartsumyan Lactic acid bacteria aplicable in the case prophilacty interhospital infections.Yerevan,Vahan, 2012, 246p.
[2] A. A. Avakyan, L.N..Kats, I.B. Pavlovva Atlas of anatomy of pathogen for man and animals bacteria, M.,Medicina, 1972, 182p.
[3] N. A. Pereverzev, P.S.Marinova-Petrova Molecular organization of villi "Pilli" from E. coli K-12. Proceediings of Symposium 'Supramolecular organization of viruses, bacteria and protozoa' M., Y., 1968, p.119-121.

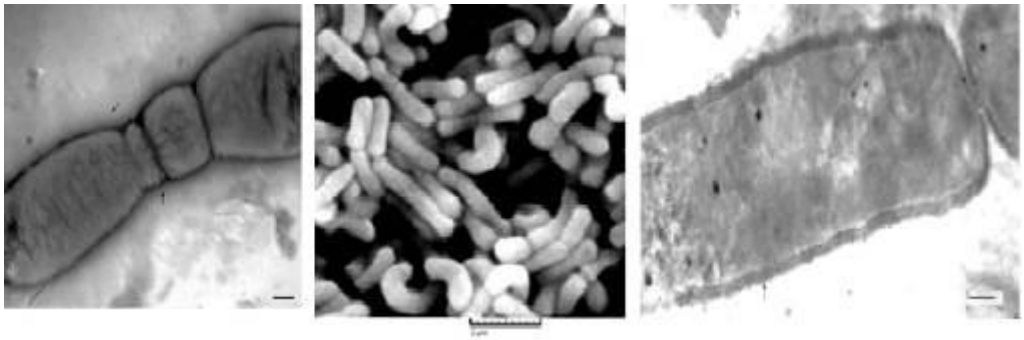

Figure 1. a) TEM. Negativ contrasting. *Lactobacillus acidophilus(strain F)*. .Pili of cell. Scale bare: 0,5µm, b) SEM. *Lactobacillus acidophilus (strainF)..Scale bare:2µm.*, c) TEM.Ultrathin section of Lactobacillus acidophilus(strainF).Wall and division of cell(showed). Scall bare:0,5µ.

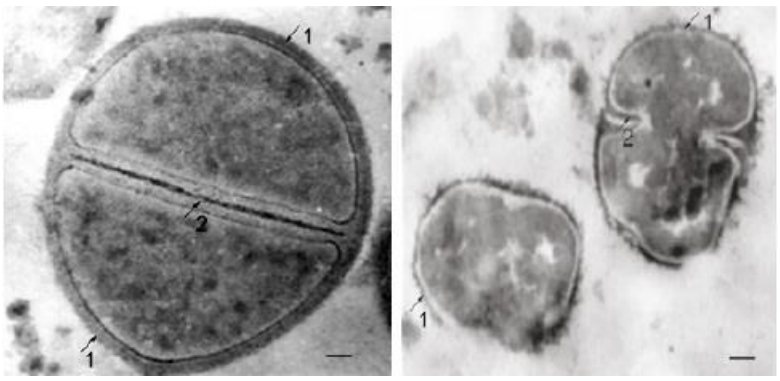

Figure 2. a) TEM.Ultrathin section of Staphylococcus aureus (stain906).Wall and division of cell(showed). Scall bare:0.5µ., b) TEM.Ultrathin section of Staphylococcus aureus (stain 906). Wall and decision of cell. the cell wall occur in the form of the cell wall from the cytoplasmic membrane and a breach of integrity Scall bare:0.5µ.

LS3.P011
Light microscopy and scanning electron microscopy studies of the scolex of cestode Passerilepis parina (Fuhrmann 1908)

S. Mohtasebi[1], G. Mowlavi[1], I. Mobedi[1], H. Abbasian[1], S. Elikaee[1]

[1]Tehran University of Medical Sciences, Medical Parasitology And Mycology, Tehran, Islamic Republic of Iran

The scolex morphology of cestode *Passerilepis parina* (family: hymenolepididae) has been studied by light microscopy. Scanning electron microscopy three dimensional pictures will be prepared and compared with the light microscopy.
This cestode is parasite of passeriformes birds and insects act as intermediate hosts. This parasite was isolated for the first time in Iran from great tit *Parus major*.
Like other hymenolepididae cestodes, this cestode is minute with the length of 13 mm and contains about 100 segments with rudimentary male genital organs and unilateral genital pores. This cestode has a scolex with 4 suckers and a retractable rostellum with a single row of 10 hooklets.
Scolex with the width of 0.36-0.40 mm diameter and suckers 0.135-0.175x0.115-0.130 mm and hooklets with 0.06 mm length.
The size of parasite was measured by light microscopy techniques and pictures were drowned by camera lucida but for further comparisons the scanning electron microscopy pictures will be prepared for confirming the size and species identification.

LS3.P012
Evaluation of p27 gene knockout mutant of Leishmania major (MRHO/IR/75/ER) with light and electron microscopy

S. Elikaee[1], M. Mohebali[1,2], H. Keshavarz[1,2], B. Akhoundi[1], S. Mohtasebi[1], H. Eslami[3]

[1]Tehran University of Medical Sciences, School of Public Health, Medical Parasitology and Mycology, Tehran, Islamic Republic of Iran
[2] Center for Research of Endemic Parasites of Iran (CREPI), Tehran University of Medical Sciences, Tehran, Islamic Republic of Iran
[3] Tehran University of Medical Sciences, School of Advanced Technologies in Medicine, Department of Medical Biotechnology, Tehran, Islamic Republic of Iran

elikaees@gmail.com

Leishmaniasis as a parasitic disease with manifestations ranging from cutaneous to fatal visceral infection is caused by several *Leishmania* species. These protozoan parasites in the gut of a sandfly vector or in culture media replicate as extracellular, flagellated promastigotes and inside the parasitophorous vacuole of vertebrate host macrophages as amastigotes. In Iran Zoonotic Cutaneous Leishmaniasis (ZCL) caused by *Leishmania major* (*L. major*). *L. major* p27 is an important gene encoding cytochrome c oxidase (COX) component and is a mitochondrial membrane protein. It expresses a 27 kDa protein that has potential role in ATP synthesis. This study aimed to evaluate morphology of *L. major* mutant (deficient in the p27 gene) with light and Scanning electron microscopy (SEM) imaging methods and its pathogenicity in BALB/c mice.
Evaluation of *L. major* mutant promastigotes with invert light microscope (400X) showed that proliferation and differentiation is slower than virulent ones but in term of morphology with light microscope (1000X) and Gimsa staining, we didn't see any difference in nucleus, kinetoplast, body and flagella between them. Results of Scanning electron microscopy also demonstrated no difference between body and flagellum although the parasites have a highly resolution in cell shape and form. Also in BALB/c mice the mutant didn't cause any lesion and in 75% of them we didn't see any amastigote in their smears (1000X). In conclusion, there is no difference between Knockout and Virulent *L. major* with light microscopic and SEM methods. It seems Transmission electron microscopy (TEM) is more useful in analysis of morphology and differentiation of produced p27 gene knockout mutant.

LS3.P013
FIB/SEM in microbiology – bacterial biofilms, hyperthermophilic archaea and unicellular algae

T. Heimerl[1], J. Flechsler[2], G. Wanner[2], R. Rachel[3], D. Geist[1], G. Bange[1], A. Klingl[2], K. Gries[4], U. Maier[1]

[1]Philipps University of Marburg, LOEWE Center for Synthetic Microbiology (SYNMIKRO), Marburg, Germany
[2]LMU Munich, Plant Development and Electron Microscopy, Planegg-Martinsried, Germany
[3]University of Regensburg, Center for Electron Microscopy, Regensburg, Germany
[4]Philipps University of Marburg, Struktur- & Technologieforschungslabor, Marburg, Germany

thomas.heimerl@synmikro.uni-marburg.de

FIB/SEM is an increasingly popular method for obtaining insight into 3D arrangements of cellular structures. The power of the technique is to cover rather large volumes like eukaryotic cells or tissue (e.g. [1]). On the basis of three examples from Bacteria, Archaea and unicellular Eukaryotes we show the value of FIB/SEM analysis for smaller organisms. For best possible preservation all samples were cryo-immobilized by high pressure freezing, freeze substituted using different "cocktails" and embedded in Epon 812 substitute resin. After embedding, the top of the blocks was cut with a saw and mounted on SEM stubs with conductive silver. Image acquisition was done on a Zeiss Auriga and a JEOL JIB 4610F, respectively. However, preceding concentration/preparation steps of cells were different depending on the sample: Cell suspensions of the diatom *Phaeodactylum tricornutum* were centrifuged for concentrating the cells. Due to damaging of cells because of its unusual ultrastructure, centrifugation was not possible for the hyperthermophilic archaeon *Ignicoccus hospitalis*; these cells exhibit an outer cellular membrane as an outmost structure [2]. Therefore, *Ignicoccus hospitalis* cells had to be gently filtered through a polycarbonate or PVDF membrane to obtain good cell densities in the samples. *Bacillus subtilis* biofilms were transferred to the high pressure freezing platelets using a biopsy punch with a diameter of 2 mm. Applying FIB/SEM to our samples we could visualize asymmetrical cells and a complex endomembrane system in *Ignicoccus hospitalis* with cytoplasmic protrusions reaching out to the outer cellular membrane. Against assumptions based on single ultrathin sections, the unicellular diatom *Phaeodactylum tricornutum* exhibits only one large branched single mitochondrium per cell that winds along the (complex) plastid. Furthermore, our data showed that *Bacillus subtilis* biofilms are heterogeneous consisting of living and dead rod shaped cells, spores and also living and dead odd shaped cells. In addition 3D data clearly showed that the cells are oriented in the same direction. Thus, our examples show that spatial information is essential for reasonable structural studies and FIB/SEM is a powerful tool not only for large volumes like tissues, but also for smaller microorganisms dealt with in Microbiology.

[1] Knott G et al., (2008), J Neurosci, 28(12):2959-2964
[2] Huber H et al., 2012, A van Leeuw, 102:203-219

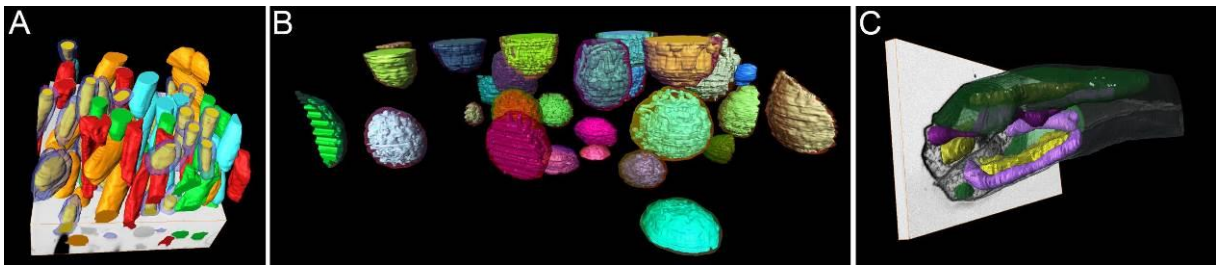

Figure 1. (A) *Bacillus* biofilm; (B) *Ignicoccus hospitalis*; (C) *Phaeodactylum tricornutum*.

LS3.P014
A microscopic approach for in vitro analysis of nanomaterial cytotoxicity applying fluorescence based assays

A. Pflieger[1], S. Eisenhuth[1], K. H. Feller[1]

[1]Ernst-Abbe-University of Applied Sciences Jena, Medical Engineering/ Biotechnology, Jena, Germany

astrid.pflieger@eah-jena.de

Introduction: Due to the rapid development of novel nanomaterial based commercially available products that include direct exposure to the human body in biomedical applications like drug-delivery systems, efficient and sensitive systems to test possible cytotoxic side effects are required. Many toxicological standard assays are unspecific for nanomaterials. Because of their unique characteristics arising from their size, interaction effects and compatibility problems with the assay chemistry have been demonstrated especially for engineered nanoparticles [1]. This requires new techniques and concepts in the field of nanotoxicology to interpret their interaction within the human body [2].
Objectives: The aim was to develop a microscopic detection system utilizing the fluorescence characteristics of two common cytotoxicity assay substances to overcome the shortcomings of their colorimetric detection in nanomaterial application. The scope was to establish optical assays with differing underlying mechanism to detect cytotoxicity to provide a versatile portfolio of independent assays. Idea of the microscopic detection system was a parallel microscopic control of cell morphology to identify interferences of the tested nanomaterials with the assay substances and provide a suitable method for nanotoxicological studies.
Materials and Methods: Resazurin (measurement of metabolic activity) and Sulforhodamine B (determination of absolute protein content) assays were used to perform cytotoxicity testing with silicon dioxide nanoparticles (Ø 20 nm), zinc oxide nanoparticles (Ø 25 nm) as test substances and cadmium chloride as Reference: on A549 cells (human lung adenocarcinoma). Absorbance measurements were carried out on TECAN plate reader. Fluorescence measurements were performed on upright microscope Axio Imager or inverted microscope Axio Observer with CCD camera AxioCam HRc and EMCCD camera Rolera em-c² using different filter sets (F14, F62 HE). Additionally LSM measurements were done using LSM 710.
Results: Interference studies with the assay dyes showed dependencies on the nanoparticle concentration for absorbance measurements (figure 1) caused by light scattering. These effects were not apparent in fluorescence measurement.
The transfer of the fluorescence detection on a microscopic system was carried out on an upright and inverted microscope, showing results independent of the used system. However an effect of the used filter sets and cameras could be observed. The best linear correlation was reached when using an EMCCD camera (figure 2). These results could be further improved by applying laser scanning techniques.
Conclusion: A microscopic detection system could be established which provides besides accurate dose-responsive cytotoxicity measurements parallel phase contrast images of the cells as internal control of the assay used (figure 3). The designed system allows for nanotoxicological application of interference susceptible assays.

References:
[1] Lewinski, N., Colvin, V. and Drezek, R.: Cytotoxicity of nanoparticles. *small* 4.1 (2008), pp. 26-49.
[2] Maynard, A. D.: Nanotoxicology: Laying a firm foundation for sustainable nanotechnologies. *Nanotoxicology—Characterization, Dosing and Health Effects. Informa Healthcare USA* (2007), pp. 1-6.

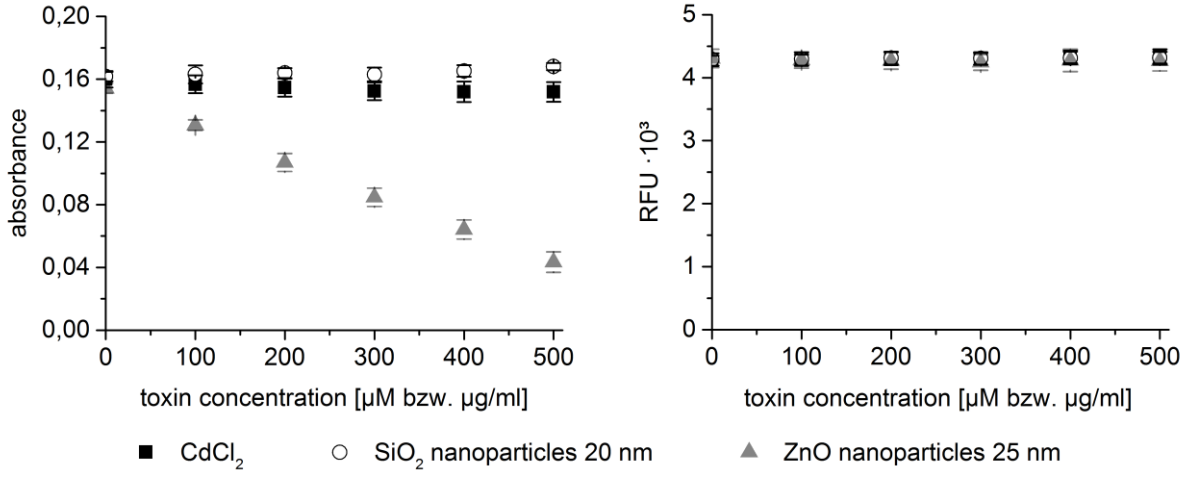

Figure 1. Influence of toxin concentration on the detection signal measuring absorbance (left) or fluorescence (right). Mean ± SD, n = 3.

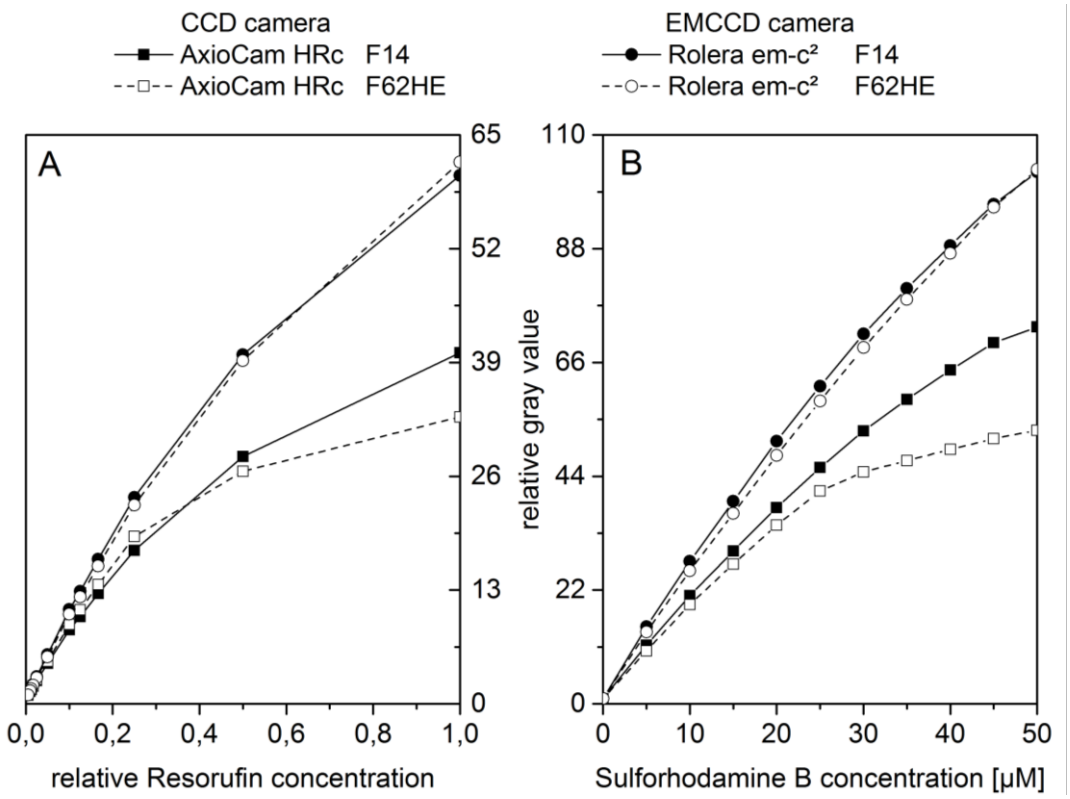

Figure 2. Comparison of different cameras and filter sets for microscopic detection of the assay dyes resorufin (A) and sulforhodamine B (B).

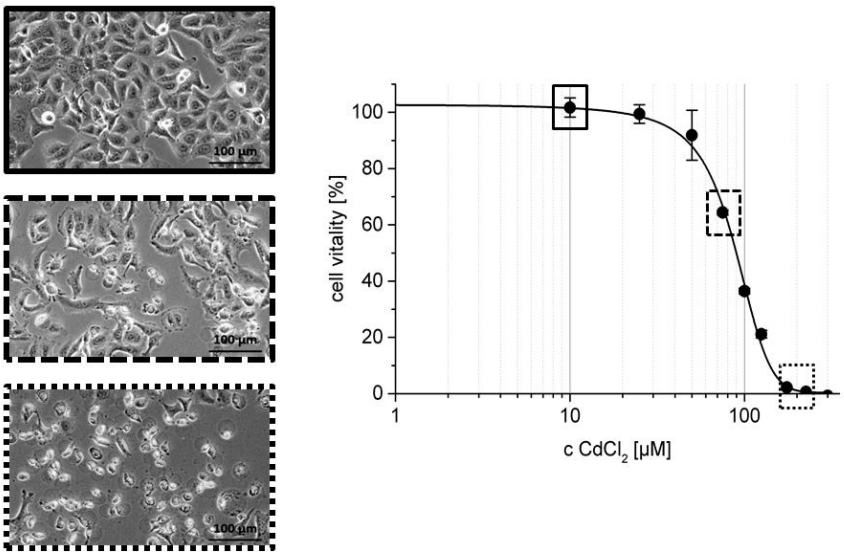

Figure 3. Dose-response-curve of cadmium chloride (Resazurin assay). The boxes show the corresponding phase contrast images of cell morphology for the indicated toxin concentrations to validate assay results. Mean ± SD, n = 5.

LS 4: Subcellular processes in plants and animal cells

LS4.001 invited
The power of cryo-electron tomography

W. Baumeister[1]

[1]Max Planck Institute of Biochemistry, Martinsried, Germany

baumeist@biochem.mpg.de

Traditionally, structural biologists have approached cellular complexity in a reductionist manner by characterizing isolated and purified molecular components. This 'divide and conquer' approach has been highly successful, as evidenced by the impressive number of entries in the PDB. However, awareness has grown in recent years that only rarely can biological functions be attributed to an individual macromolecule. Most cellular functions arise from their acting in concert. Hence there is a need for methods developments enabling studies performed *in situ*, i.e. in unperturbed cellular environments. Sensu stricto the term 'structural biology *in situ'* should apply only to a scenario in which the cellular environment is preserved in its entirety. Cryo electrontomography has unique potential to study the supramolecular architecture or 'molecular sociology' of cells. It combines the power of three-dimensional imaging with the best structural preservation that is physically possible. Key methods developments, such as correlative LM/EM, Focussed Ion Beam Milling (cryo FIB) or phase plate imaging, will be discussed as well as applications highlighting the potential of this post-reductionist approach to structural biology.

LS4.002
Filaments formed by the translation initiation factor eIF2B – high-resolution insights into a survival strategy.

G. Marini[1], E. Nueske[1], S. Alberti[1], G. Pigino[1]

[1]MPI-CBG, Dresden, Germany

marini@mpi-cbg.de

Introduction: An increasing number of soluble metabolic enzymes has been found to form ordered filamentous assemblies in yeast cells under stress conditions (Narayanaswamy et al., 2009). These assemblies show morphological properties of mesoscale structures, ranging from foci to bundles of filaments. The self-assembly process has two main features: 1) it silences the enzymatic activity, slowing down the metabolic rate of cells; 2) it is reversible, with rapid depolymerization upon replenishment of energy, allowing yeast cells to quickly re-enter into the cell cycle. Thus, filament formation may be an energy-saving strategy of yeast to endure extreme conditions of starvation (Petrowska et al., 2013).
Aims: At present, not much is known about the structural basis of the stress-induced self-assembly. Many questions need to be answered, starting from what ultrastructural arrangement and cellular distribution is adopted by the filaments and bundles, to how polymerization leads to enzymatic inactivation.
To answer these questions, we focused on one of the major *S. cerevisiae* filament-forming enzymes, the eukaryotic translation initiation factor eIF2B. This hetero-pentameric enzyme is a guanine nucleotide exchange factor (GEF) and a major target for translational control in both yeast and mammalian cells.
Materials and Methods: By using high-pressure freezing, correlative light and electron microscopy (CLEM) and electron tomography coupled to high-resolution 3D-reconstruction techniques, we investigate the ultrastructure of the stressed yeast cytoplasm and the 3D organization of eIF2B self-assemblies.
Results: Our structural comparison of control and energy depleted yeast cells reveals a massive rearrangement of cytoplasmic structures, in addition to the enzyme compartmentalization. We speculate that water loss, cell volume reduction and increased crowding are major changes that contribute to drive the assembly of eIF2B into filaments.
Correlation of light and electron microscopy of cells overexpressing eIF2B-GFP allowed us to firstly locate fluorescent signals in the cytoplasm of energy-depleted yeast cells and then observe the mesoscale structures at higher magnification in the TEM. Tomographic reconstructions showed that the condensed fluorescence corresponds to bundles of self-assembled eIF2B (fig. 1). As proof that eIF2B self-assembly happens intrinsically, filaments have also been found in wild-type energy depleted yeast cells, expressing untagged eIF2B at endogenous level.
Subtomogram averaging reveals an ordered stacking of the hetero-pentameric eIF2B dimers in the filaments, with a ~13 nm longitudinal periodicity. The reconstructed 3D-model shows also frequent lateral connections between neighboring filaments in the bundle, which might contribute in keeping their regular pattern and spacing.
Conclusions: Our structural analysis provides insights into a survival strategy that is used by yeast to cope with extreme environmental conditions and stress. With our work, we demonstrate that cells that become dormant present extensive re-organization of their cytoplasm. Vesicle fragmentation and invagination of the plasma membrane in yeast cells go along with a reduction of the cell volume, coupled to crowding and increased ribosome density.
We have shown that eIF2B complexes redistribute into bundles of filaments in stressed yeast, supporting our model that proteins involved in metabolic activities can be shut down during dormancy by being sequestered into these mesoscale self-organizing structures.

Bibliography:
[1] Narayanaswamy R, Levy M et al. (2009) Widespread reorganization of metabolic enzymes into reversible assemblies upon nutrient starvation. *Proc NatlAcadSciUSA*. Jun23;106(25):10147-52.
[2] Petrovska I, Nüske E et al. (2014) Filament formation by metabolic enzymes is a specific adaptation to the energy-depleted cellular state. *eLife,* 3:e02409.

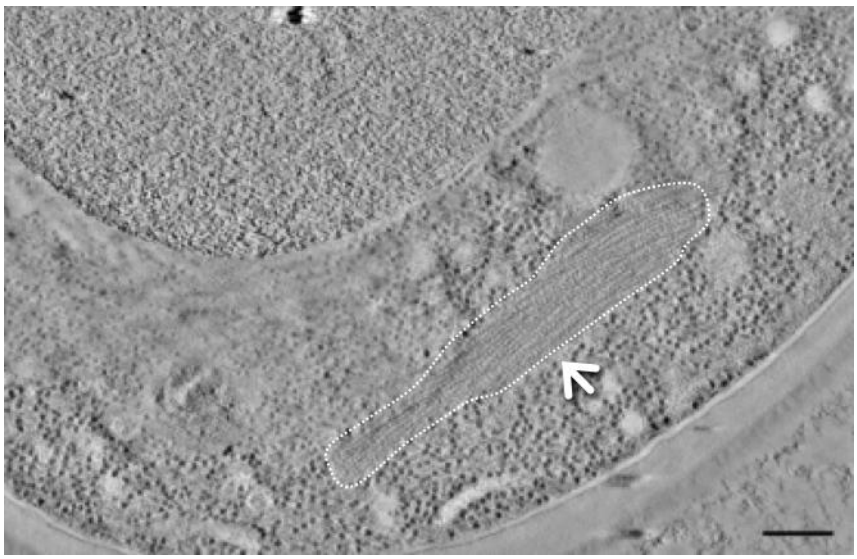

Figure 1. Central slice of the tomogram showing a big bundle of self-assembled eIF2B enzymes in the cytoplasm of an energy depleted yeast cell. Scale bar=200 nm.

LS4.003
Dynamics of the Golgi apparatus in response to endocytic flow and cellular stress – a morpho-functional 3D-analysis

C. Ranftler[1], B. Santler[1], M. Vetterlein[1], A. Ellinger[1], J. Neumüller[1], M. Pavelka[1]

[1]Medical University of Vienna, Center for Anatomy and Cell Biology, Vienna, Austria

margit.pavelka@meduniwien.ac.at

It is well known that the ability of the Golgi apparatus to rapidly reorganize its membranes and subcompartments is crucial for its function as a central crossroads in the secretory and endocytic traffic, both in physiology and pathology (for review 1). Previous studies in our laboratory have shown that endocytic retrograde transport of internalized wheat germ agglutinin (WGA) in cultured cells is accompanied by extensive Golgi membrane dynamics (2) and treatment with the ATP-lowering and cellular stress-inducing glucose analogue 2-deoxy-D-glucose (2DG) causes rapid and reversible Golgi reorganizations leading to a loss of the classic Golgi stacks, which are replaced by tubulo-glomerular Golgi bodies (3). The present work is focused on the 2DG-induced reorganizations of the endocytic Golgi elements with the goal to answer whether these become separated from the other compartments of the reorganizing Golgi apparatus or remain parts of it. We studied the changing Golgi architectures by 3D-electron tomography and traced the endocytic elements throughout all phases of the 2DG-induced Golgi dis- and reorganizations.

Cultured human epithelial HepG2 hepatoblastoma cells were treated with peroxidase-labeled WGA (WGA-HRP; 33µg/100 µl) for various periods before administration of 50 mM 2DG for 5, 10, 30, 45, 60 or 90 min and various post-incubation periods in medium after removal of 2DG. After fixation in 1% glutaraldehyde in 0.1M cacodylate buffer, visualization of the internalized WGA-HRP was done by means of oxidation of diaminobenzidine. After post-fixation in 1% veronal-acetate-buffered OsO_4, the specimens were dehydrated and embedded in epoxy resin. Electron tomography was performed in a 200kV transmission electron microscope (Tecnai20, FEI company); for reconstruction of the volume of the 200-300 nm thick sections into virtual slices, the Inspect 3D software (FEI company) or the IMOD software (Boulder Laboratory, University of Colorado, USA) were used; 3D-models were drawn with the aid of the Amira 5.3 software (Mercury Computer Systems, Merignac, Cedex, France).

Our results clearly show that the endocytic Golgi compartments are not separated during the 2DG-induced Golgi stack reorganizations but remain parts of the changing Golgi architectures. Endocytic Golgi elements could be followed during all stages of Golgi stack changes. They were visible within the early occurring intra-stack networks, appeared in the 2DG-induced tubulo-glomerular Golgi bodies and were integrated into the re-forming Golgi stacks following removal of 2DG. At all stages of the 2DG-induced Golgi reorganizations, endocytic and non-endocytic compartments were found to be continuous. The findings visualize possible endocytic transport routes in the reorganizing Golgi structures and indicate that the Golgi apparatus under the influence of 2DG is still able to subcompartmentalize certain functions, although the classic stack architecture is lost.

References:

[1] F. Perez and D.J. Stephens Eds. *Methods in Cell Biology Vol 118, Methods for analysis of Golgi complex function.* Elsevier Academic Press Inc. San Diego (2013)
[2] M.Pavelka et al. Histochem. Cell Biol. 129: 277 (2008)
[3] C.Ranftler et al. Histochem. Cell Biol. In press (2017) DOI 10.1007/s00418-016-1515-7

LS4.004 invited
Plants on chips – microfluidic devices for live imaging of organ development and root-environment interactions

C. E. Stanley[1,2], J. Shrivastava[3], R. Brugman[3], D. van Swaay[1], G. Grossmann[3,4]

[1]ETH Zürich, Institute for Chemical and Bioengineering, Zürich, Switzerland
[2]Agroscope, Institut für Nachhaltigkeitswissenschaften INH, Zürich, Switzerland
[3]Universität Heidelberg, Centre for Organismal Studies (COS), Heidelberg, Germany
[4]Universität Heidelberg, CellNetworks-Cluster of Excellence, Heidelberg, Germany

guido.grossmann@cos.uni-heidelberg.de

Plant roots grow in highly heterogeneous environments where they need to locally adapt their architecture to optimally absorb nutrients and water, interact with pathogenic and symbiotic microbes, and cope with diverse abiotic stress conditions. My lab is interested in plastic adaptation of root development and intercellular communication in response to changing environmental conditions. To enable microscopic studies of root-environment interactions, we are developing RootChips, integrated microfluidic perfusion and imaging platforms that combine on-chip root cultivation, microscopic access and precise control over the root microenvironment. Here I will present our recent findings using an organ-on-a-chip approach to investigate how roots perceive and respond to local stimuli and develop in asymmetric environments, where one side of the root is exposed to beneficial and the other side to adverse conditions. The dual-flow-RootChip (dfRootChip) employs a micropillar array for guided root growth and utilizes laminar flow to treat both sides of a root separately. I will present applications for the dfRootChip that range from monitoring of physiology and development under asymmetric conditions, tracing molecular uptake and selective drug treatments, to local inoculation with microbes. We measured calcium responses in roots treated with biotic and abiotic elicitors and observed elicitor-specific signal propagation across the root from treated to untreated cells. We further demonstrate cell-autonomous regulation of root hair growth under local availability of phosphate, a nutrient that often exhibits patchy distribution in soil. Our approach sheds light on cell autonomy and lateral coordination of morphological adaptation and facilitates studies on root physiology, signaling and development in heterogeneous environments at the organ level.

LS4.005
Biomineralization in dinoflagellates

A. Jantschke[1], L. Addadi[1], S. Weiner[1]

[1]Weizmann Institute of Science, Structural Biology, Rehovot, Israel

anne.jantschke@weizmann.ac.il

Introduction: Biomineralization, the formation of complex inorganic materials by biological processes, is a widespread phenomenon. Beautiful examples of biomaterials occur in unicellular, eukaryotic microalgae. Among them dinoflagellates constitute one of the largest groups. Dinoflagellates are the second most abundant calcareous phytoplankton group and contribute substantially to the oceanic carbonate flux. Many species are associated with harmful algal blooms. For this reason there is a strong ecological interest in learning more about their complex life cycle. Surprisingly, dinoflagellates - one of the major constituents of phytoplankton - have remained largely unexplored.
Many dinoflagellate species produce (mineralized) resting stages (cysts) as a dormant, zygotic stage of their life cycle.[1] These cysts exhibit organic walls or calcareous and sometimes siliceous walls. Recently, fossilized calcite-cysts were shown to have extremely interesting, interwoven fibre-like structures.[2] These structures so far observed only in fossil cysts raise questions concerning biomineral formation in living dinoflagellate cysts.
Objectives: The focus of previous studies has been the structural characterization of cysts and the en-/excystment process. At the moment, neither the detailed structure/function relations, nor the formation and stabilization mechanism of the mineral phase are known. For this reason, the primary goal is to obtain a detailed understanding of the biomineralization processes present in dinoflagellates during their complex life cycle.
Materials and Methods: Using the analytical methods Cryo-SEM/EDS, Cryo-FIB-SEM, (Cryo-)fluorescence, FT-IR, (Cryo-)micro-Raman spectroscopy and flow cytometry the biomineral formation process in several dinoflagellate species was studied to understand the cellular mechanisms, particularly for calcium carbonate in the cyst stage and organic crystals in the vegetative state.
Results:
Calcification in *Leonella granifera*
Cryo-SEM images of freeze-fractured cysts of *L. granifera* (Fig. 1a) show vacuoles of different sizes on the cell periphery. These vacuoles are rich in potassium and phosphate (Cryo-EDS) and include small particles of unknown composition. After Decalcification with EDTA the cells start to recalcify and these vacuoles start to form a ring surrounding the cell. To analyse if these vacuoles are part of the biomineralization process the cells were stained with Calcein-AM, a dye sensitive to calcium ions. Staining with Calcein-AM revealed enrichment in intracellular compartments and could be used to follow the shell formation process.
Guanine crystals in *Calciodinellum operosum aff.*
Cryo-SEM sections of vegetative cells of *C. operosum aff.* revealed vesicles filled with crystalline material in close association with the chloroplasts of the cell (Fig.1b). The crystals exhibit no significant backscattering signal and are nitrogen-rich (Cryo-EDS). Crystalline anhydrous guanine could be identified from the FT-IR spectra of whole cells.
Conclusion: In *L. granifera* strong evidence for a calcification mechanism proposed by Inouye and Pienaar [3] was found. Golgi-derived vesicles filled with particles are supposed to be part of the biomineralization process. Correlative approaches (Cryo-SEM, -fluorescence and -Raman) are planned for a more detailed understanding of the shell formation process.
Guanine crystals could be identified in the dinoflagellate species *C. operosum aff.* Because of the proximity of the crystal-filled vesicles and the chloroplasts we propose that in this non-bioluminescent dinoflagellate these vesicles might act as light-scattering organelle enhancing photosynthesis efficiency.

[1] a) F. J. R. Taylor, The Biology of dinoflagellates. Blackwell, Oxford, 1987; b) D. L. Spector, Dinoflagellates, Academic Press 1984.
[2] J. E. Wendler, P. Bown, Nat. Commun. 2013, 4.
[3] I. Inouye, R. N. Pienaar, S. African. J. Bot. **1983**, *2*, 63–75.

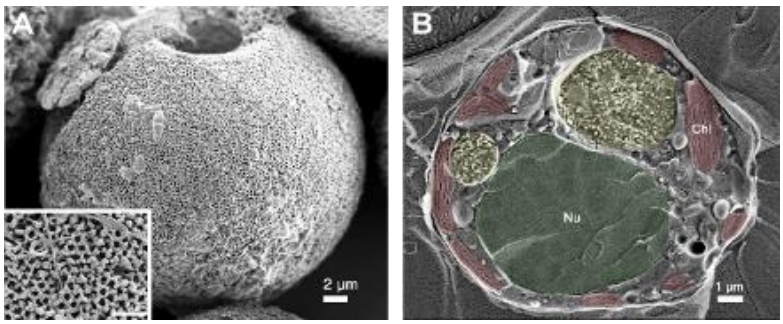

Figure 1. a) SEM image of calcarous cyst of *L. granifera* b) Cryo-SEM section of a single cell of *C. operosum aff.*

LS4.P001
Degradation of pS261-AQP2 is regulated by Atg7-dependent canonical autophagy

W. Y. Kim[1], S. A. Nam[1], A. Choi[1], M. Y. Lee[1], Y. W. Moon[2], H. L. Kim[3], T. R. Riew[1], K. H. Han[4]
M. S. Lee[5], Y. K. Kim[6], J. Kim[1]

[1]The Catholic University of Korea, Anatomy and Cell Death Disease Research Center, Seoul, South Korea
[2]The Catholic University of Korea, Biology, Seoul, South Korea
[3]The Catholic University of Korea, Integrative Research Support Center, Seoul, South Korea
[4]Ewha Womans University, Anatomy, Seoul, South Korea
[5]Yonsei University, Severance Biomedical Science Institute, Seoul, South Korea
[6]The Catholic University of Korea, Internal Medicine, Seoul, South Korea

wanyoung@catholic.ac.kr

Question: Prolonged hypokalemia induces a decrease of urinary concentrating ability via down-regulation of aquaporin 2 (AQP2) expression; however, the precise mechanisms remain unknown.
Methods: To investigate the role of autophagy in the degradation of AQP2, we generated a mouse model with principal cell-specific Atg7 deletion.
Results: In hypokalemic wild-type mice induced by K^+-depleted diet for 2 weeks, huge irregular shaped LC3-positive autophagic vacuoles accumulated mainly in inner medullary collecting duct (IMCD) cells. Total- and pS261-AQP2 were redistributed from apical and subapical domains into these vacuoles, which were not co-localized with LAMP1, LAMP2, and Rab9, but were surrounded by a double membrane and therefore represent canonical autophagosomes. This suggests that autophagic AQP2 degradation is stimulated by hypokalemia but that autophagic flux is diminished by a reduction of fusion between autophagosomes and lysosomes, resulting in canonical AQP2-containing autophagosome accumulation in IMCD cells. However, in the IMCD cells of Atg7 knockout mice with hypokalemia, these canonical autophagosomes were markedly reduced, whereas numerous small regular shaped LC3-negative, LAMP1-, LAMP2- and Rab9-positive non-canonical autolysosomes surrounded by single membranes were observed along with diffusely distributed total- and pS261-AQP2. Thus, total- and pS261-AQP2 degradation is primarily regulated by canonical autophagy. No pS256-AQP2 was observed in either canonical or non-canonical autophagic vacuoles.
Conclusions: These findings suggest that AQP2 down regulation in hypokalemia might in part be caused by reduced total- and pS261-AQP2 degradation in IMCD cells via an LC3/Atg7-dependent canonical autophagy pathway and define a novel role for autophagy in IMCD cells of the mouse kidney

LS4.P002
Autophagic vacuoles in the hepatocytes of house sparrow (Passer domesticus) from Tehran

E. Keyhani[1]

[1]Laboratory for Life Sciences, Laboratory for Life Sciences, Tehran, Islamic Republic of Iran

keyhanius2002@yahoo.com

Introduction: Life and proliferation of house sparrows is intimately associated with human activity. Intensive building and ensuing destruction of trees and bushes have contributed, along with environmental pollution and infectious diseases, to a constant reduction in the number of sparrows in Tehran, as well as in other cities worldwide. Liver is the principal organ of metabolism and detoxification, and thus key for survival in a hostile environment.
Objectives: The purpose of our research was to study the fine structure of liver hepatocytes in house sparrow (*Passer domesticus*) from Tehran.
Materials and Methods: Four male and female house sparrows (1-1.5 years old), of healthy aspect, purchased from a local dealer in Tehran, were killed by rapid cervical dislocation. Livers were removed after abdominal incision; portions were diced with razor, doubly fixed for two hours in 2.5% glutaraldehyde, 0.1 M phosphate buffer, pH 7.4, post-fixed for two hours in 1% OsO4 in 0.1 M phosphate buffer, pH 7.4, dehydrated in graded concentrations of ethanol, washed three times in propylene oxide, and embedded in Epon. Sections, done with a Porter-Blum ultramicrotome equipped with diamond knife, were mounted on grids (mesh 400), doubly stained by uranyl acetate and lead citrate, and examined in a Phillips EM 300 electron microscope (60 KV accelerating voltage, 25 µm objective aperture).
Results: An interesting observation in all four house sparrows" hepatocytes was the presence of numerous autophagic vacuoles without any sign of apoptosis or necrosis of the cells. Figure 1 shows, at low magnification, the general aspect of four hepatocytes. Nuclei (N) were either circular or of irregular shape. Salient features of the cytoplasm were the presence of numerous autophagic vacuoles (AV) and the presence of mitochondria that were in majority spheric (90%), but occasionally elongated (9%) or irregular (1%). The general aspect and organization of autophagic vacuoles in different cells is illustrated in Figures 2 and 3. Among the five autophagic vacuoles (AV) displayed in Figure 2A, four presented a digested content and the fifth one (arrow) revealed mitochondria in the process of digestion. Figure 2B showed an autophagic vacuole with membrane fragments inside a mitochondrion, and a digested membrane fragment outside the mitochondrion. In Figure 2C, a mitochondrion, with well visible cristae, was surrounded by an autophagic membrane, and a small vacuole (arrow) had engulfed a number of polysomes and ribosomes. Figure 3 showed two large autophagic vacuoles (of diameter, respectively, 1.53 and 2.00 µm) that displayed mitochondria and granular endoplasmic reticulum at various stages of digestion.
Conclusion: The most important conclusion from this paper and the accompanying one on street pigeon is that, in cities, air pollution and environmental pollution due to domestic and industrial waste are likely to change the fine structure of hepatocytes and probably other tissues. In early studies, autophagic vacuoles were considered a food supply to be used by starving cells [1 and References: therein]. Now they are also believed to play a role in apoptosis, a cell death program activated by intrinsic [2, 3 and References: therein] or extrinsic [4 and References: therein] pathways. While the function of autophagic vacuoles needs more clarification, caution must be considered in the consumption of house sparrows.

References:
[1] Keyhani E (1970) C. R. Acad. Sci. Paris 271:530-533. [2] Breckenridge DG et al. (2003) Oncogene 22:8608-8618. [3] Keyhani E, Keyhani J (2004) Ann. N. Y. Acad. Sci. 1030:369-376. [4] Keyhani E et al. (2009) Ann. N. Y. Acad. Sci. 1171:284-291.

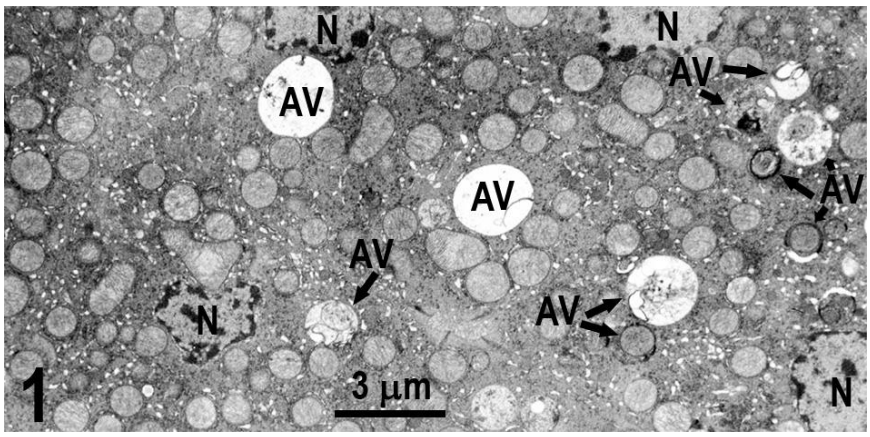

Figure 1. Four hepatocytes at low magnification. Note abundant autophagic vacuoles (AV); 90% of mitochondria are spheric; (N): nucleus.

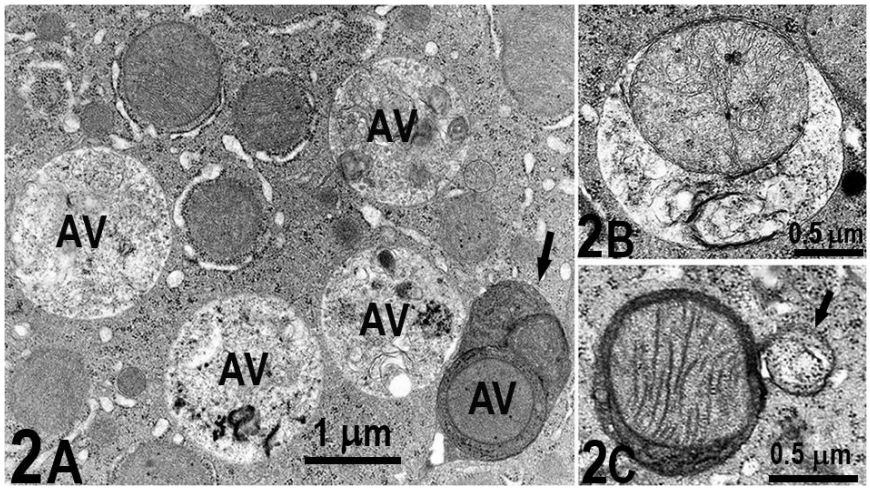

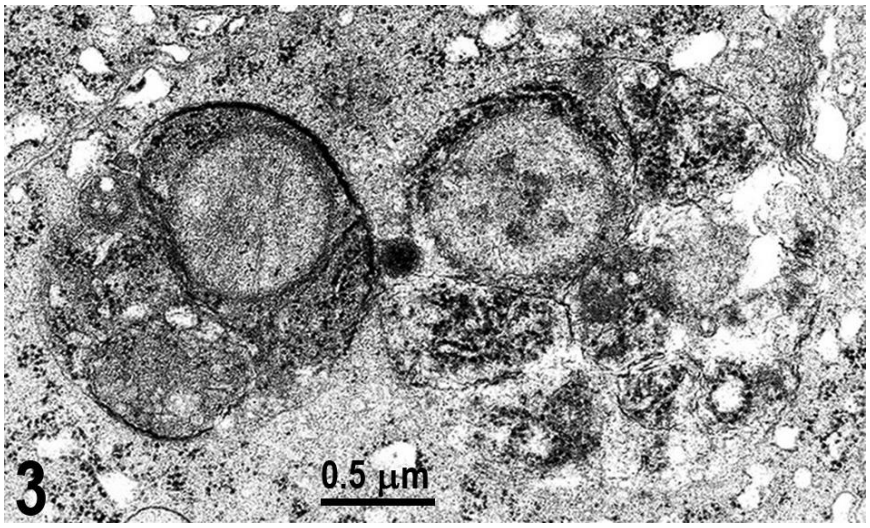

Figures 2 and 3. Various aspects of autophagic vacuoles (see text for details).

LS4.P003
Ultrastructural characterization of hepatocytes in feral pigeon (Columba livia domestica) from Tehran

E. Keyhani[1]

[1]Laboratory for Life Sciences, Laboratory for Life Sciences, Tehran, Islamic Republic of Iran

keyhanius2002@yahoo.com

Introduction: Common inhabitants of city parks and forests, pigeons have long been valued as message carriers while being also appreciated for recreation as well as for gastronomy. However, they actively participate in the spreading of a broad spectrum of infectious diseases, and pigeon droppings have been identified as the main source of pathogenic yeasts all over the world [1 and References: therein]. Pigeons are understudied, especially in terms of their organs ultrastructure. Liver, a key organ in biosynthesis and detoxification, actively participates in blood sugar regulation, blood clotting proteins synthesis, proteins and fat metabolism, and in the detoxification of chemical and metabolized drugs.
Objectives: The purpose of our research was to study the fine structure of liver hepatocytes in feral pigeon (street pigeon) from Tehran.
Materials and Methods: Three male and female adult healthy street pigeons (~ 1.5 – 2.5 years old), purchased from local dealers in Tehran, were killed by rapid cervical dislocation. After plucking of the abdominal region, livers were rapidly removed by ventral access. A small portion was chopped by razor, doubly fixed in 2.5% glutaraldehyde, 0.1 M phosphate buffer, pH 7.4, for two hours, postfixed in 1% OsO4 in 0.1 M phosphate buffer, pH 7.4 for two hours, dehydrated in graded concentrations of ethanol, washed three times in propylene oxide, and embedded in Epon. Sections, done with a Porter-Blum ultramicrotome equipped with diamond knife, were mounted on grids (mesh 400), doubly stained by uranyl acetate and lead citrate, and examined in a Phillips EM 300 electron microscope, at accelerating voltage 60 KV with 25 µm objective aperture.
Results: Figure 1 shows, at low magnification, the general aspect of pigeon hepatocytes. Nuclei were round and had a well visible nucleolus. In the cytoplasm, mitochondria were numerous and, although for the most part filamentous, their size and shape varied in different parts of the cells, going from round, to oval, and to elongated; branched (Fig. 2A) and other forms of mitochondria (Fig. 2B) were also seen. Granular endoplasmic reticulum was dispersed in the cytoplasm between mitochondria. Smooth endoplamic reticulum, also dispersed in the cytoplasm, did not form clusters. Golgi was seen in different parts of cells. Lysosomes were round, exhibiting a light density content, and were of diameters ranging from 0.28 to 0.31 µm and from 0.37 to 0.42 µm. The most important aspect of these cells was the presence of glycogen particles. Some cells contained only a few particles, others exhibited a moderate amount of them, and a third category of cells contained a large number of α glycogen particles with intense electron dense aspect (Fig. 3A). In some cells, glycogen particles exhibited an unusual reticular aspect (Fig. 3B). Peroxisomes, round (~ 0.35 µm in diameter) and oval (0.4 x 0.3 µm), contained a rhomboid crystalloid (Fig. 3C,D).
Conclusion: Hepatocytes in these pigeons exhibited different characteristics with respect to distribution and density (low, intermediary, high) of glycogen, probably corresponding to different activity states of the cells. Glycogen"s unusual organization seen in some cells possibly indicated alterations in its metabolism. Some mitochondria also showed large-scale changes in their morphology. Hence, consumption of feral pigeon should be considered with caution.

References:
[1] Keyhani E (2012) In: Microbes in applied research. (Méndez-Vilas A, ed.) World Scientific, Singapore, pp 593-597.

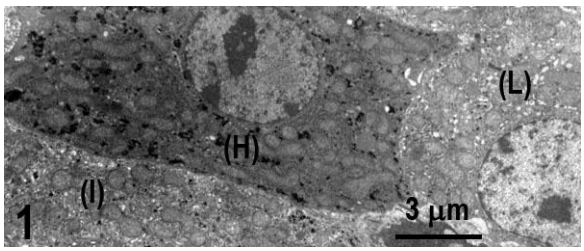

Figure 1. Low magnification of pigeon hepatocytes. Note abundant mitochondria and distribution of glycogen particles in high (H), intermediate (I), low (L) density.

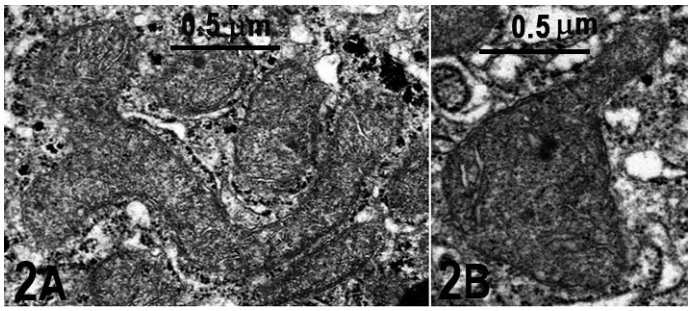

Figure 2. A) Branched mitochondrion; B) Triangular mitochondrion.

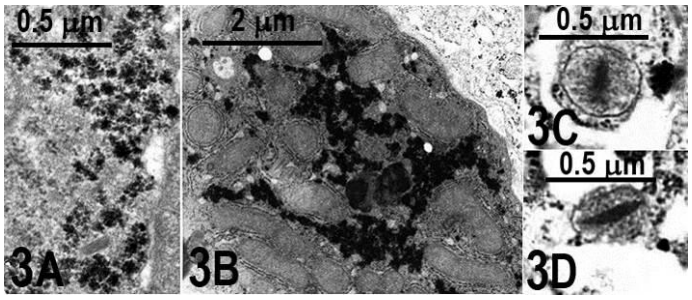

Figure 3. A) α glycogen particles. B) Abundant glycogen forming an unusual reticular shape. C) and D) Peroxisomes with central crystalloid.

LS4.P004
Induction of nestin and platelet-derived growth factor receptor-β in vessel-associated cells in the striatum of rats subjected to 3-nitropropionic acid

T. R. Riew[1], J. H. Choi[1], H. L. Kim[2], X. Jin[1], Y. W. Moon[3], J. Kim[1], W. Y. Kim[1], M. Y. Lee[1]

[1]College of Medicine, The Catholic University of Korea, Anatomy, Seoul, South Korea
[2]College of Medicine, The Catholic University of Korea, Integrative Research Support Center, Laboratory of Electron Microscope, Seoul, South Korea
[3]College of Medicine, The Catholic University of Korea, Medical Lifescience, Seoul, South Korea

taeryong.riew@gmail.com

Introduction: Nestin is a type VI intermediate filament protein and has been reported to be induced in the vasculature-associated cells that undergo dynamic structural changes in the ischemic core in a rat model of ischemic stroke.
Objectives: The current study was designed to investigate the potential role of vessel-associated nestin-positive cells in the fibrotic scar formation, which is characterized by excess deposition of fibrous extracellular matrix, in the striatum of rats treated with the mitochondrial toxin 3-nitropropionic acid (3-NP).
Materials and Methods: Adult male Sprague Dawley rats were injected with 3-NP and sacrificed at 3, 7, 14, 28 days after the final injection. Double or triple immunofluorescence immunohistochemistry was performed with antibodies to nestin, laminin, glial-fibrillary acidic protein (GFAP), platelet-derived growth factor-β (PDGFR-β), type IV collagen, fibronectin, Ki-67, and Iba1. Ultrastructural characteristic of nestin expressing cells are analyzed with immuno-electron microscopy.
Results: Nestin expression was exclusively induced within the vasculature in the lesion core, where the blood-brain barrier is broken and astrocytes are virtually absent, while nestin-positive cells in the peri-lesional area were indeed GFAP-positive reactive astrocytes. Vasculature-associated nestin was induced by 3 days post-lesion, and persisted until 28 days, and was largely co-labeled with PDGFR-β. At 14 days after the injury, nestin and PDGFR-β double-positive cells had long interwined processes and started to form a network within the lesion core. Also, these cells were in close contact with type IV collagen and fibronectin, both of which are markers for fibrotic extracellular matrix, implying their role in formation of fibrotic scar. Immunoelectron microscopic findings demonstrated that nestin-positive cells in early time points had euchromatic nuclei with a prominent nucleolus, and long processes. They were closely apposed to vessel walls but clearly distinguishable from endothelial cells, pericytes, smooth muscle cells, or perivascular microglia/macrophages. During the chronic phase (> 14 days post-injury), nestin was observed not only in cells forming the multilayered sheath that was apposed to vessels, but also in cells extending extremely long, tenuous processes in the lesion parenchyma but not being associated with blood vessels, These cells were juxtaposed to collagen fibril bundles. PDGFR-β-positive cells showed similar ultrastructural finding as nestin-positive cells, and correlative light-electron microscopic study confirmed such finding.
Conclusions: Thus, our data revealed that the correlated localization of nestin and PDGFR-β was first observed in vascular adventitial cells, but was also observed in fibroblast-like cells without any association with blood vessels at later time points, during which the fibrotic scar formation occurs, suggesting an active role for nestin in cellular structural remodeling of vascular adventitial cells that contribute to the fibrotic scar formation in response to brain insults.

This research was supported by the Basic Science Research Program through the National Research Foundation of Korea (NRF) funded by the Ministry of Science, ICT and future Planning (NRF-2014R1A2A1A11050246).

LS4.P005
Progressive accumulation of autofluorescent granules in macrophages in rat striatum after systemic 3-nitropropionic acid – a correlative light- and electron-microscopic study

H. L. Kim[1], T. R. Riew[2], J. H. Choi[2], X. Jin[2], Y. W. Moon[3], J. Kim[3], M. Y. Lee[3]

[1]College of Medicine, The Catholic University of Korea, 2Integrative Research Support Center, Laboratory of Electron Microscope, Seoul, South Korea
[2]College of Medicine, The Catholic University of Korea, Anatomy, Seoul, South Korea
[3]College of Medicine, The Catholic University of Korea, Department of Natural Sciences, Seoul, South Korea

wgwkim@catholic.ac.kr

Introduction: A variety of tissue biomolecules and intracellular structures are known to be autofluorescent. However, autofluorescent signals in brain tissues often confound the analysis of fluorescent markers used for immunohistochemistry.
Objectives: While investigating tissue and cellular pathologies induced by 3-nitropropionic acid (3-NP), a mitochondrial toxin selective for striatal neurons, we encountered many autofluorescent signals confined to the lesion core. The purpose of the present study is to define the structural details of the autofluorescent signals induced by 3-NP injection.
Materials and Methods: Adult male Sprague Dawley rats were injected with 3-NP and sacrificed at 3, 7, 14, 28 days after the final injection. To visualize the autofluorescent materials in the 3-NP–injected rat brain, coronal cryostat sections were labeled with 4′,6-diamidino-2′-phenyindole, or with antibody to glial fibrillary acidic protein, ionized calcium-binding adaptor molecule 1 (Iba1), ED1, or lysosomal-associated membrane protein 1 (Lamp1). Antibody staining was visualized with Alexa Fluor 647-tagged goat anti-rabbit antibodies or with goat anti-mouse antibodies (1:300; Molecular Probes, Inc., Eugene, OR, USA). We also applied a method that allows the researcher to correlate the light microscopic signals with the respective subcellular structures as visualized by electron microscopy. This correlative approach offers an informative and efficient way to identify specific targets for further examination at the ultrastructural level.
Results: Confocal microscopic findings from sections immunolabeled with Iba1 revealed these autofluorescent cells to be activated microglia/macrophages. These structures were excited by blue (wavelength = 488 nm) and yellow-orange (555 nm), but not by red (639 nm) or violet (405 nm) lasers, indicating that this autofluorescence overlaps with the emission spectra of commonly used fluorophores. Almost all of the autofluorescence was localized in activated microglia/macrophages, while reactive astrocytes emitted no detectable autofluorescence. Amoeboid brain macrophages filled with autofluorescent granules revealed very weak expression of the microglial marker, Iba1, while activated microglia with evident processes and intense Iba1 immunoreactivity contained scant autofluorescent granules. In addition, immunolabeling with two lysosomal markers, ED1 and Lamp1, showed a pattern complementary with autofluorescent signals in activated microglia/macrophages, implying that the autofluorescent structures reside within the cytoplasm free of intact lysosomes. Thus, these data indicate that autofluorescent granules usually accumulated within the lysosome-free cytoplasm of activated microglia/macrophages. By means of a correlative approach using light and electron microscopy (an excellent tool for the detailed ultrastructural study of specific targets), we confirmed that these light-microscopic, autofluorescent granules corresponded to clusters of lipofuscin granules with various morphologies.
Conclusions: Thus, the present study demonstrates that autofluorescence tends to increase within the striatal lesion over time after 3-NP injection, which is attributable to an accumulation of lipofuscin granules within activated microglia/macrophages. Thus, our data indicate that special care should be taken when verifying unknown fluorescent signals likely to be especially correlated with activated microglia/macrophages after brain insults.

This research was supported by the Basic Science Research Program through the National Research Foundation of Korea (NRF) funded by the Ministry of Science, ICT and future Planning (NRF-2014R1A2A1A11050246).

LS4.P006
The influence of the Satureja montana L. leaves methanol extract on the rat erythrocytes membrane

M. Marin[1], M. Novakovic[2], A. Korac[1]

[1]University of Belgrade, Faculty of Biology, Belgrade, Serbia
[2]University of Belgrade, Institute of Chemistry, Technology and Metallurgy, Belgrade, Serbia

majamarin@bio.bg.ac.rs

Introduction: In the recent years many investigations have showed that medicinal plant extracts cause alterations of the shape and physiology of erythrocytes (Chikezie, 2006). Changes in shape and size of erythrocytes can contribute to their elimination by phagocytes from circulation, and subsequently, can lead to anemia development (Stasiuc et al., 2009). *Satureja montana* L. (Lamiaceae), is an aromatic species with proved very strong pharmacological activities and antioxidative properties due to the presence of phenolic compounds. The present study investigated possible influence of the *Satureja montana* L. leaves methanol extract on the rat erythrocytes membrane.
Objectives: The aim of this study was to determine the effect of the various concetrations of the *Satureja montana* L. leaves methanol extracts on the rat erythrocytes morphology *ex vivo*.
Materials and Methods: The red blood cells (RBC) of male rats of Wistar strain were *ex vivo* treated with *S. montana* leaves methanol extract. We used following concentration: 100µg/ml (I), 150µg/ml (II) and 300µg/ml (III) and incubated with RBC at 37°C for 1h (Bors et al., 2012). The erythrocytes incubated with phosphate buffered saline – PBS (P) and PBS + dimethyl sulfoxide – DMSO (D), (PD) were used as controls. The percentage of erythrocytes with different shape morphology (e.g. echinocytes, stomatocytes) were calculate.
Results: In contrast to the biconcave disc shape of control red blood cells, the RBC incubated with the different concentration of methanol extracts underwent shape changes typical for echinocyte and stomatocyte formation. We found that within creasing concentration of methanol leaves extracts (I-100µg/ml, II-150 µg/ml and III-300 µg/ml), gradually raised the percentage of different erythrocytes shape forms in comparison to both controls. The most significant changes were observed at concentration of 300µg/ml, with the highest percentage of echinocytes and stomatocytes forms. It is possible that phenolic compounds, predominantly present in *S. montana* leaves methanol extracts, could interacted with or incorporated into either erythrocyte membrane outer monolayer promoting echinocytosis or erythrocyte membrane inner monolayer prompting stomatocytosis.
Conclusion: The methanol extract of *S. montana* leaves in dose-dependent manner stimulates phospholipid scrambling of the rat erythrocyte cell membrane, an effect probably in part dependent on entry of secondary constituents. Its beneficial effect via protecting the cell membrane against oxidation *in vivo* could be suggested.

Ackowledgement
This study was supported by Ministry of Education, Science and Technological Development of the Republic of Serbia, Projects No. 173055.

References:
[1] Bors M., Sicinska P., Michalowicz, J., Wieteska, P., Gulewicz, K., Bukowska, B.2012. Evaluation of the effect of *Uncariatomentosa* extracts on the size and shape of human erythrocytes (in vitro). Environ. Toxicol. Pharmacol. 33:127-34.
[2] Chikezie, P.C.2006. Studies on the anti-sickling effects of*Azadirachtaindica* and Vernonia *amygdalina* on HbSS erythrocytes.Inter. J. Nat. Appl. Sci.2:24-28. Stasiuk, M., Kijanka, G., Kozubek, A. 2009. Changes in the shape of erythrocytes and factors causing them. Adv. Biochem. 55:425-433.

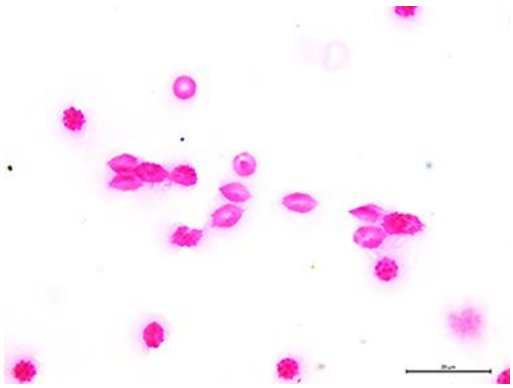

Figure 1. Morphological changes of the erythrocytes induced by methanol extract concentration. 300µg/ml. Magnification x100.

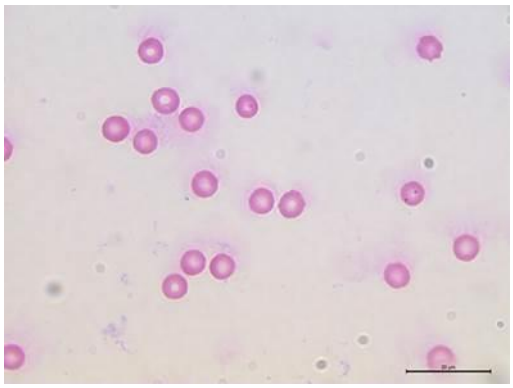

Figure 2. Control erythrocytes incubated with PBS + DMSO. Magnification x100.

LS4.P007
Systemic administration of lipopolysaccharide induces early changes in cytokine/chemokine production within the mouse spleen

I. Lalić[1], R. Bichele[2], A. Repar[1], S. Despotović[1], S. Petričević[3], M. Laan[2], P. Peterson[2], J. Westermann[4] Z. Milićević[1], N. Milićević[1]

[1]University of Belgrade, Faculty of Medicine, Institute of Histology and Embryology, Belgrade, Serbia
[2]University of Tartu, Institute of Biomedicine and Translational Medicine, Molecular Pathology, Tartu, Estonia
[3]Galenika a.d., Belgrade, Serbia
[4]University of Lübeck, Institute of Anatomy, Center for Structural and Cell Biology in Medicine, Lübeck, Germany

ivanalalic5@gmail.com

Introduction: Lipopolysaccharide (LPS) is a major structural component of the outer membrane of almost all Gram negative bacteria [1]. Recognition of LPS initiates intracellular signaling pathways and production of proinflammatory mediators by myeloid and/or non-myeloid cells [1, 2]. Previously, we have detected significantly reduced numbers of B lymphocytes within the splenic red pulp 24 hours after systemic administration of LPS. At the same time, we found increased percentage of B cell zone and white pulp in relation to the total area of the mouse spleen. However, it remained unclear which cytokines/chemokines could be responsible for these changes.
Objectives: The aim of our study was to investigate the effect of LPS on the production of a palette of homeostatic and proinfammatory cytokines, that might be involved in LPS-induced relocation of B lymphocytes from the splenic red pulp.
Materials and Methods: Eight week-old C57BL/6 mice of both sexes were separated into three groups: the untreated mice (n=6), experimental mice sacrificed 1 hour after injection of LPS (n=6) and experimental mice sacrificed 2 hours after injection of LPS (n=6). The experimental mice were injected into the lateral tail vein with 50 μg of LPS diluted in 200 μl of pyrogen-free physiological saline. The expression of homeostatic and proinfammatory cytokines in splenic tissue was analyzed by quantitative real-time PCR (qRT-PCR). Additionally, 8 week-old C57BL/6 mice were injected intravenously with 50 μg of LPS (n=3) or phosphate buffered saline (PBS) (n=3) and sacrificed 2 hours after the treatment. The expression of CCL20 was determined by qRT-PCR in different splenic compartments (white pulp, red pulp and marginal zone), obtained by laser microdissection. Immunofluorescence was performed on splenic tissue collected 2 hours after LPS treatment. Splenic cryostat sections were stained for T lymphocytes and CCL20. Images were captured with a Zeiss LSM 710 inverted confocal microscope.
Results: One and two hours after intravenous injection of LPS, we detected increased mRNA levels for 13 homeostatic and proinflammatory cytokines (XCL1, CXCL9, CXCL10, CCL3, CCL4, CCL5, CCL17, CCL20, CCL22, TNFα, IL-1β, IL-6 and LTα) within the mouse spleen. However, mRNA levels for "homeostatic" chemokines such as CXCL13 and CXCL21 remained unchanged after the treatment. In addition, LTβ and "homeostatic" chemokines CXCL12 and CCL19 exhibited reduced mRNA expression two hours postinjection. Very notably, after treatment with LPS, an extreme increase in mRNA levels for CCL20 was detected. Two hours after LPS injection, CCL20 was produced in the white pulp of the mouse spleen, whereas it was not detected in red pulp and marginal zone (Figure 1). At the same time point, CCL20-producing cells were located at the outer parts of periarteriolar lymphoid sheath (PALS) (Figure 2).
Conclusion: LPS induces early changes in cytokine/chemokine production within the mouse spleen. LPS-induced production of CCL20 in the splenic white pulp may be involved in chemoattraction of B lymphocytes from the splenic red pulp.

References:
[1] Rhee SH. Lipopolysaccharide: basic biochemistry, intracellular signaling, and physiological impacts in the gut. Intest Res. 2014; 12: 90-5.
[2] Heumann D and Roger T. Initial responses to endotoxins and Gram-negative bacteria. Clin Chim Acta. 2002; 323: 59–72.

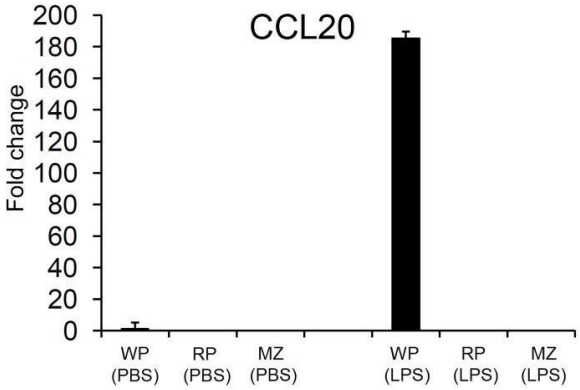

Figure 1. Systemic administration of LPS induces production of CCL20 within the white pulp of the mouse spleen, 2 hours after treatment. Different compartments of mouse spleen (WP, RP and MZ) were obtained by laser microdissection. The relative fold change of CCL20 was measured by qRT-PCR. WP = white pulp; RP = red pulp; MZ = marginal zone; PBS = phosphate buffered saline; LPS = lipopolysaccharide.

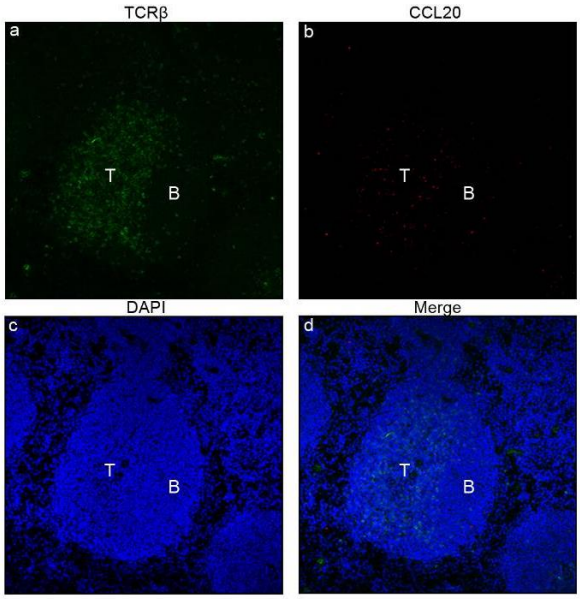

Figure 2. CCL20-producing cells are distributed in the outer parts of periarteriolar lymphoid sheath (PALS). (a-d) Immunofluorescence performed on splenic frozen section, 2 hours after treatment with LPS. green (T lymphocytes); red (CCL20); blue (DAPI). The original magnification was x200.

LS4.P008
Mechanical response of the kinetochore revealed by laser microsurgery in live cells.

J. Gregan[1], G. Cojoc[2], E. Roscioli[2,3], D. Cimini[3], I. Tolic[2]

[1]Comenius University, Department of Genetics, Bratislava, Slovakia
[2]Max Planck Institute of Molecular Cell Biology and Genetics, Dresden, Germany
[3]Virginia Polytechnic Institute and State University, Blacksburg, VA, United States of America

juraj.gregan@univie.ac.at

Introduction: Accurate chromosome segregation depends on proper kinetochore–microtubule attachment. Upon microtubule interaction, kinetochores are subjected to forces generated by the microtubules. The function of many biological systems is known to depend on the mechanical properties of the system components, however, we know very little about mechanical properties of the kinetochore.
Objectives: Our aim was to characterize mechanical response of the kinetochore using laser microsurgery combined with live-cell microscopy.
Materials and Methods: In this work, we used laser ablation to sever microtubules attached to a merotelic kinetochore, which is laterally stretched by opposing pulling forces exerted by microtubules, and inferred the mechanical response of the kinetochore from its length change. The mechanical properties of the kinetochore were then interpreted by using two simple theoretical models that took into account the kinetics of kinetochore length changes. We performed experiments in both the fission yeast *S. pombe* and mammalian PtK1 cells.
Results: In both mammalian PtK1 cells and in the fission yeast, kinetochores shortened after microtubule severing. Interestingly, the inner kinetochore–centromere relaxed faster than the outer kinetochore. Whereas in fission yeast all kinetochores relaxed to a similar length, in PtK1 cells the more stretched kinetochores remained more stretched.
Conclusion: Our study establishes merotelic kinetochores as an experimental model for studying the mechanical response of the kinetochore in live cells and reveals a viscoelastic behavior of the kinetochore that is conserved in yeast and mammalian cells.

LS4.P009
The simultaneous effect of methimazole and sucrose on granules of β-cells

M. Ukropina[1], R. Glisic[2], T. Vukov[3], M. Cakic-Milosevic[1]

[1]University of Belgrade, Faculty of Biology, Institute of Zoology, Belgrade, Serbia
[2]University of Kragujevac, Faculty of Natural Sciences and Mathematics, Institute of Biology and Ecology, Kragujevac, Serbia
[3]University of Belgrade, Institute for Biological Research "Siniša Stanković", Belgrade, Serbia

mirela@bio.bg.ac.rs

Introduction: Thyroid hormones are necessary for normal function of almost all organs; their importance in carbohydrate metabolism has been known for decades. Primary stimulus for insulin secretion and for insulin gene transcription and translation is rise in blood glucose concentration [1]. Transcription factors which stimulate insulin gene expression are at the same time positively regulated by T3 [2]. Continuous intake of carbohydrates represents a form of stress in which pancreas intensively produces insulin. In long term this can lead to pathophysiological processes at the level of intracellular organelles, and eventually to loss of β-cells, i.e. to type 2 diabetes.
Objectives: The aim of this work was to gain insight into the ultrastructural characteristics of β-cells under the influence of sucrose rich diet, in terms of systemic hypothyroidism induced by methimazole.
Materials and Methods: Male Wistar rats used in this study were divided into groups according on fluid intake. C group (control) had free access to tap water, M group to 0.02% methimazole water solution, S group to 10% sucrose water solution, while MS group was offered to drink combined solution of methimazole and sucrose of the same concentrations as in M and S groups. After three weeks of treatment pancreas was routinely prepared for electron microscopy and photographed. Morphometric analysis on β-cells was performed using Image J. Mature and immature granules were distinguished by the presence of polygonal and round protein core, respectively. Numerical data were expressed as mean±SEM; statistical analysis of the results was performed by two-way ANOVA and Bonferroni post hoc test.
Results: In control animals granules of β-cells were of usual appearance, containing protein core encircled by halo (Figure 1). In M group accumulation of smaller granules in β-cells indicate a delay in the insulin synthesis/secretion. In S group insulin granules appeared larger and were characterized by great halo around protein core, while in MS group granules were similar to those in control. Immature and total granules per unit area of cytoplasm of β-cells were more numerous in M group, comparing to all other groups; mature granules were more abundant in S group, in respect to all other groups, while the number of mature granules in M group is decreased comparing to control. Ratio of mature and immature granules was significantly increased in S group. Profile area of protein dense core was significantly enlarged in S group comparing to all other groups, and in MS group in comparison to M group (Table 1).
Conclusion: Sucrose intake in hypothyroid rats distinguishes β-cells fine structure away from those treated only with methimazole and from euthyroid sucrose fed animals, and approaches them to the control in respect of granule's ultrastructural and stereological features.

[1] Goodison S, Kenna S and Ashcroft SJ. (1992) Control of insulin gene expression by glucose. Biochem J 285: 563-568.
[2] Lin Y and Sun Z. (2011) Thyroid hormone potentiates insulin signaling and attenuates hyperglycemia and insulin resistance in a mouse model of type 2 diabetes. Br J Pharmacol 162: 597-610.

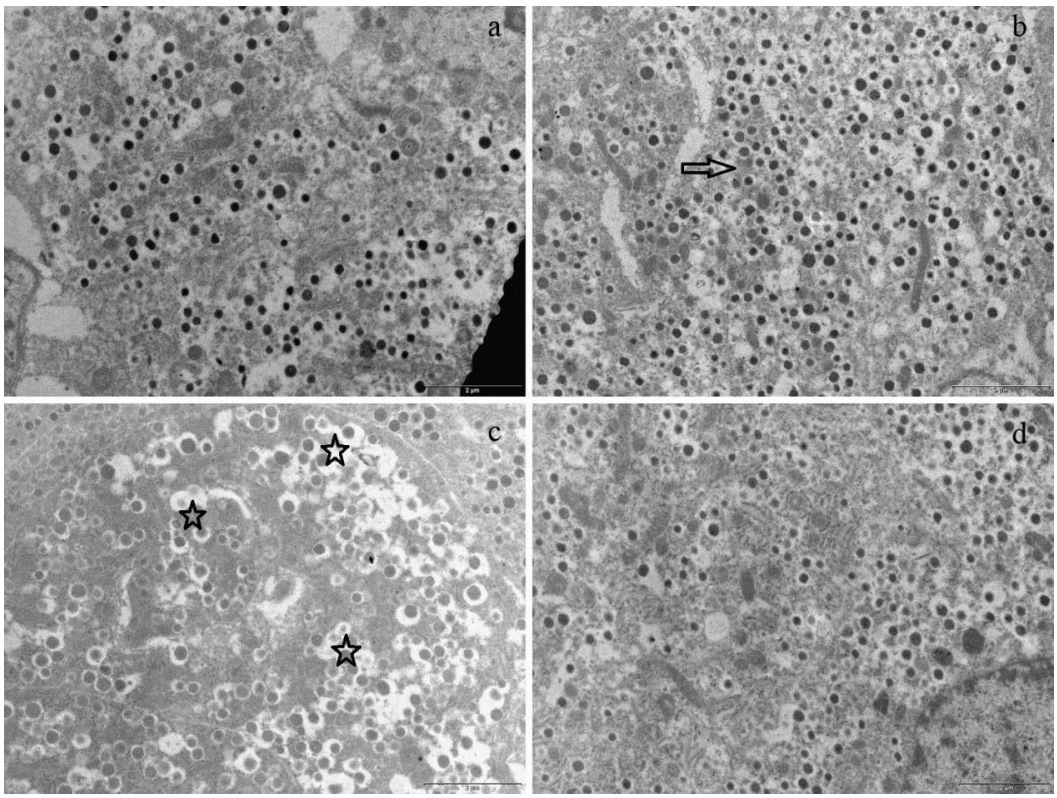

Figure 1. The appearance, size and abundance of granules of Langerhans islet β-cells vary according to experimental treatment: granules are densely packed in M group (b, arrow), they collide/blend together in S group (c, stars), and resemble to control (a) in MS group (d) (x8800)

	C	M	S	MS
Immature granules (number/100 μm^2)	150.21±11.49	312.01±41.37*	100.14±7.23	141.90±9.15
Mature granules (number/100 μm^2)	44.31±4.67	19.35±5.19c	76.23±5.58*	30.31±2.66
Mature/Immature	0.08±0.15	0.04±0.02	0.53±0.30*	0.09±0.12
Total (number/100 μm^2)	194.52±14.90	331.36±44.55*	176.37±8.28	172.20±9.95
Granule profile area (μm^2)	0.029±0.001	0.028±0.001	0.045±0.002*	0.035±0.002m

$p < 0.05$ was considered significant; to all other groups *, to control c, to M group m.

Table 1. Morphometric analysis of β-cell granules.

LS4.P010
Studies on microscopic features and histomorphometry of foetal and adult ovaries and uteri in white fulani cattle (bos indicus)

I. Nwaogu[1], K. Okorie[1], C. Egejuru[1], C. Abiaezute[2]

[1]University of Nigeria, Nsukka, Veterinary Anatomy, Nsukka, Nigeria
[2]University of Nigeria, Nsukka, Veterinary Anatomy, Nsukka, Nigeria

innocent.nwaogu@unn.edu.ng

In this work we studied the microscopic features of 45 foetal and 15 adult ovaries and uteri obtained from slaughtered white Fulani cows in Nsukka abattoir, Enugu State, Nigeria. The age of the adult were determined by dentition and that of fetuses by crown rump length methods. The foetal and adult ovaries and uteri were divided into four (4) groups using specific age intervals as gestation day (GD) 90-152, 153-215, 216-278 and adults. For microscopic studies the ovaries and uteri were fixed in Bouins fluid, processed and routinely stained with Hematoxylin and Eosin. The ovarian follicles were classified into five types according to granulosar cell layers surrounding the oocytes. The endometrial and myometrial thickness were also determined. The ovary of GD 90-152 had no distinct cortex and medulla. Types 1 and 1A primordial follicles were present. By GD 153-215, the ovaries contained types 1, 1A, 2, 3 and 4 follicles, and GD 216-278 had type5 follicles in addition. The adult ovaries contained types 2, 3, 4 &5 follicles as well as corpus albicans while very few type1 follicles were observed. Precursors of uterine glands in form of shallow invaginations of luminal epithelium into the endometrium were observed by GD 90-152. These invaginations deepened further by GD 153-215 and became clusters of cells by GD 216-278. The adult uterus exhibited the mocroscopic features characteristic of ruminants. The endometrial and myometrial wall thickness of the adults were significantly ($p<0.05$) larger than those of the foetuses. These results provide baseline information on ovarian development and uterine adenogenesis in the white Fulani cattle.
Keywords: Adults, Cattle, Foetuses, Microscopy, Ovary, Uterus.

LS4.P011
Possible role of brown adipose tissue in thyroid thermogenesis

M. Cakic-Milosevic[1], R. Glisic[2], M. Ukropina[1]

[1]University of Belgrade, Faculty of Biology, Institute of Zoology, Belgrade, Serbia
[2]University of Kragujevac, Faculty of Natural Sciences and Mathematics, Institute of Biology and Ecology, Kragujevac, Serbia

maja@bio.bg.ac.rs

Introduction: Brown adipose tissue (BAT) is engaged in cold-induced thermogenesis. Uncoupling protein 1 (UCP1) of the brown adipocyte (BA) mitochondria acts as decoupler of oxidative phosphorilation and enables heat dissipation instead of ATP production. Mitochondrial UCP1 content is considered to be the best measure of BAT thermogenic capacity [1]. BAT function is dominantly regulated by noradrenaline, but it can be modulated by many other hormones [2]. Among them, thyroid hormones (THs) are of particular interest due to their involvement in regulation of temperature homeostasis and body energetics. THs defficiency negatively affects BAT thermogenis and UCP1 synthesis, but the exact influence of THs in excess is not yet fully understood. For a long time it has been accepted that in systemic hyperthyroidism, thyroid thermogenesis (TT) reduces the need for BAT thermogenesis. However, several years ago it has been demonstrated that THs may stimulate sympathetic activity in BAT, through centrally mediated mechanisms, suggesting that BAT is the effector of TT [3]. Later reports were not conclusive to finally confirm or reject the idea that systemic hyperthyroidism increases functional capacity and/or activity of BAT.
Objectives: The aim of this study was to evaluate the effects of experimentally induced systemic hyperthyroidism on morphological characteristics of BA, and their thermogenic capacity.
Materials and Methods: Male Wistar rats (n=18), kept under standard laboratory conditions were randomly alocated into 3 equal groups and injected i.p. during 5 days as follows: (a) 200 μg/kg of triiodothyronine in 9 mM NaOH (T3); (b) 300 μg/kg of thyroxine in 9 mM NaOH (T4); (c) 1 ml/kg of 9 mM NaOH (control). Analyses were performed on semifine sections of plastic embedded interscapular BAT. UCP1 was immunohistochemically detected by LSAB method, using anti-UCP1 polyclonal antibody (ab 10983, Abcam, 1/1000). Signal was semiquantified by ImageJ software.
Results: In control group, BAT showed typical morphology (Fig. 1A). After treatment with T4, BA lipid content was apparently increased, with quite well preserved multilocularity. Representative BA was characterized by large, euchromatic nucleus with prominent nucleolus (Fig. 1B). In T3 treated rats lipid content was also apparently increased, lipid droplets were very large and often coalesced with each other (Fig. 1C). Immunohistochemically labeled mitochondria were seen as dark-brown granules in the BA cytoplasm. In control and T3 group, they were located mainly around the lipid droplets (Fig. 2A,C), while in T4 group they occupied a large part of lipid-free cytoplasm as well (Fig. 2B). Semiquantitative evaluation of UCP1 immunopositivity showed that signal (expressed as % of lipid-free cytoplasm with UCP1 positivity) was significantly increased in T4 group (C: 43.9±2.61; T4: 53.0±0.92, $p<0.001$; T3: 49.3±1.39, n.s.).
Conclusion: T4 treatment increases BAT thermogenic capacity and possibly stimulates its thermogenic activity as demonstrated by increase in mitochondrial UCP1 content together with well preserved multilocularity.

[1] Cannon B, Nedergaard J. (2004) Phys Rev 84, 277.
[2] Reddy NI, Tan BK, Barber TM, Randeva HS. (2014) BMC Obesity 1,13.
[3] López M, Varela L, Vázquez MJ, Rodríguez-Cuenca S, González CR, Velagapudi V, et al. (2010) Nat Med 16, 1001.

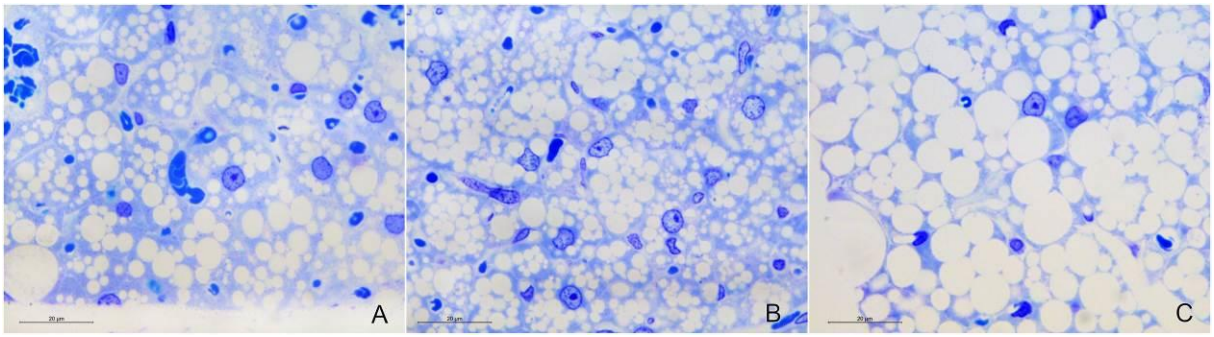

Figure 1. Semifine sections of BAT from C (A), T4 (B) and T3 (C) group of rats (toluidine blue, bar=20 μm).

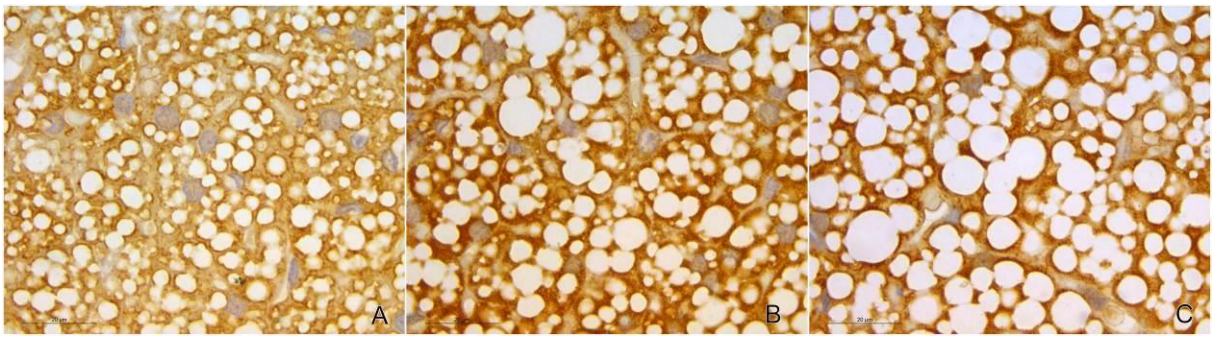

Figure 2. Immunohistochemical detection of UCP1 in BAT from C (A), T4 (B) and T3 (C) group (immunohistochemistry, LSAB method, bar=20 μm).

LS4.LBP01
Effects of inhibiting the Angiotensin converting enzyme and Angiotensin II receptor blocker on heart tissue of male rats with renal hypertension

T. Esmaeilpour[1], A. A. Nekoeian[2], A. R. Pour[1], F. Dehghani[1,3], E. M. A. Zekr[2]

[1]Shiraz University of Medical Sciences, Department of Anatomy, Shiraz, Islamic Republic of Iran
[2]Shiraz University of Medical Sciences, Department of Pharmacology, Shiraz, Islamic Republic of Iran
[3]Shiraz University of Medical Sciences, Histomorphometry and Stereology Research Center, Shiraz, Islamic Republic of Iran

esmaeilpor@yahoo.com

Introduction: hypertension disease has adverse effects on heart and blood vessels. Studies have shown that Anti hypertensive drugs such as captopril (CAP) and losartan (LOS) can lead to useful changes in cardiovascular structure by interference in rennin-angiotensin system, and then, reduce the mortality caused by blood pressure disease.
Objective(s): The aim of this study was to investigate the cardiac structural changes in renal-induced hypertension rat model and effect of inhibiting the Angiotensin converting enzyme and Angiotensin II receptor blocker by stereological methods.
Materials and Methods: 48 male Sprague-Dawley rats were randomly divided into 6 groups (n=8): All animals except the sham group underwent surgical procedure, two-kidney one-clip renovascular-induced hypertension, by renal artery constriction were fitted with a plexiglass clip. In the sham operated rats the abdominal wall was opened, closed without clipping the renal artery. Both sham and vehicle animals were received distilled water p.o./4 weeks. The experimental groups 3 and 4 have received CAP (100 and 50 mg /kg p.o./4 weeks) and experimental groups 5 and 6 received LOS (50 and 25 mg /kg p.o. /4 weeks). Systolic blood pressure was monitored by means of tail-cuff plethysmography at the end of each week. After 4 weeks treatment the animals were dissected and the heart removed, fixed, sectioned and stained by H&E and PAS. Stereological methods were used for estimation of the total volume of heart, volume density of Myocardium, endocardium, matrix and vessels, number of myocytes and purkinje fibers.
Results: our results showed that both doses of CAP and LOS significantly reduce the blood pressure compared to the Vehicle**.** All experimental animals showed significant reduction of cardiac weight compared to vehicle group and CAP100 has significantly reduced in comparison to LOS 50 and LOS25. Comparison between body weight at the end of treatment showed that only CAP 50 rats group had a significant increment compared with LOS 50 rats group ($P<0.03$) and there was no significant statistical difference between the other groups. CAP 50 could significantly reduce the heart volume compared with the Sham and CAP 100 groups ($P<0.001$) and There was no significant difference between other groups**.** The comparison of volume density of Myocardium showed that taking the CAP 100 could significantly reduce the volume density of Myocardium compared to LOS 50, LOS 25, and Vehicle groups ($P<0.001$). The mean number of myocytes in different groups showed that the CAP 100 group has a significant increase compared to Vehicle, CAP 50, LOS 50, and LOS 25 ($P<0.03$).
Conclusions: Renovascular hypertension has destructive effects on different parameters of the heart. Both CAP and LOS have protective effects on cardiac structures against hypertension. It seems that between two doses of CAP and LOS, CAP 100 has most protective effects on the cardiac structures.

Keywords: Heart, Renal hypertension, CAP, LOS, two-kidney one-clip, Stereology.

LS4.LBP02
Effect of Platelet-Rich plasma (PRP) on rat ovaries in Cyclophosphamide-induced infertility

F. Dehghani [1,2], H. Aboutalebi [1,2], T. Esmaeilpour[2], M. R. Panjehshahin [3], H. Bordbar [1,2]

[1]Shiraz University of Medical Sciences, Histomorphometry and Stereology Research Center, Shiraz, Islamic Republic of Iran
[2]Shiraz University of Medical Sciences, Department of Anatomy, Shiraz, Islamic Republic of Iran
[3]Shiraz University of Medical Sciences, Department of Pharmacology, Shiraz, Islamic Republic of Iran

dehghanf@sums.ac.ir

Introduction: Ovarian failure is diagnosed by atrophy of ovary and follicles reduction. Growth factors can stimulate growth and development of follicles. Platelet rich plasma (PRP) contains several growth factors that induce tissue repair and may be stimulate folliculogenesis.
Objective(s): The aim of this study was to evaluate the effect of PRP on ovarian structures in Cyclophosphamide (Cy)-induced ovarian failure in female rat by stereological method.
Materials and Methods: Thirty–two female Sprague–dawley rats were divided into 4 groups (Control, Cy, Cy+ PRP and PRP Groups). Female infertility was induced by Cy (75 mg/kg, single dose, Intraperitoneal injection. Animal were treated by PRP (200 ul, single dose, intraperitoneally). At the end of experiment, blood samples were collected for preparation of PRP and measurement of estradiol and progesterone. The animals were dissected and the ovaries were removed, fixed, sectioned and stained by H&E. Stereological methods were used for estimation the volume of cortex and medulla, number and diameter of different ovarian follicles by light Microscopy.
Results: Cyclophosphamide reduced the volume of ovary especially on cortex and decreases the number and diameter of antral follicle. The levels of estradiol and progesterone were significantly decreased in comparison with the control group. PRP had the most positive effect on number and diameter of antral follicle and increased the level of estradiol in infertile animals ($P<0.001$).
Conclusion: It seems that PRP has a protective role on infertile female rat model.

Keywords: ovary, follicle, PRP, Cyclophosphamide, Stereology.

LS4.LBP03
Structural ensemble of regreening plastid of nicotiana change under bright light

A. Zavaleta-Mancera[1], I. Scott[2], H. Thomas[2]

[1]Colegio de Postgraduados en Ciencias Agricolas, Botany, Texcoco, Mexico
[2]University of Wales, Biological, Environmental & Rural Sciences (IBERS), Aberystwyth, United Kingdom

arazavaleta@colpos.mx

Introduction: Senescent leaves of *Nicotiana* can be induced to regreen in the presence of 1-6 benzylamino-purine (BAP) under dim light (12 µmol m^2 s^{-1}) recovering over 98% of their former chlorophyll [1]. Chloroplast proteins are expressed: chlorophyll biosynthesis enzyme NADPH-protochlorophyllide oxidoreductase (POR) responsible for the morphogenesis of new thylakoids in young leaves, the light harvesting chlorophyll a/b binding protein LHCP-2, and the small and large subunit of Rubisco (LSR, SSR) [1]. Recovery of gerontoplasts structure during regreening is limited by light intensity, because brighter light inhibits the process [1]. Structural changes promoted for bright light after regreening are poorly understood.
Objectives: The present study monitored the structural changes in regreening plastids of *Nicotiana rustica* promoted by exposure to bright light.
Materials and Methods: Natural senescent leaves of *N. rustica* were treated with 10^{-4} M benzylaminopurine (BAP) for 7 d under dim light (12 µmol m^2 s^{-1}) for 20 d. Then they were exposed to brighter light (100 µmol m^2 s^{-1}) for 43 d more. Samples were taken at 0, 13, 20, and 63 d. Photosynthetic pigments were measured according to Lichtenthaler and Wellburn [3]. Leaf tissue was fixed (2h) in 5% (w/v) glutaraldehyde and 2% paraformaldehyde in 67 mM sodium cacodylate buffer pH 7.4 and post fixed in 1% OsO_4 (2 h). LR White resin sections were stained and observed in a Jeol 2010 at 80 Kev
Results: Yellow senescent leaves (0.069 mg Chl g FW^{-1}) treated 7 d with BAP regreened (0.674 mg Chl g FW^{-1}) after 20 d. Plastids of yellow leaves (gerontoplasts) were rounder and smaller (1-2 µm) than green chloroplasts (3-6 µm); characterized by disorganized grana thylakoids, few polyribosomes, large plastoglobuli bodies and broken thylakoid (Fig. 1A). After 13 d, gerontoplast differentiate few thylakoids (Fig. 1B). Later (20 d) grana and inter-granal membranes are organized (Fig. 1C). The morphology was observed as previously described [1]. In contrast, regreening plastids exposed to 100 µmol m^2 s^{-1} for 43 d, showed irregular shapes, large starch grains and less plastoglobuli. Golgi apparatus and endoplasmic reticulum were conspicuous (Fig 1D).
Conclusions: Regreening plastids under dim light changed in structure when they were transferred to brighter light, starch and thylakoid synthesis were promoted.

References:
[1] Zavaleta H.A., Franklin K.A., Ougham H.J., Thomas H., Scott I.M. "Reappearance of NADPH-protochlorophyllide oxidoreductase and light-harvesting chlorophyll a/b-binding protein" (1999a) J. Exp. Bot. Vol. 50: 1677-1682.
[2] Zavaleta H.A., Thomas H., Scott I.M. "Redifferentiation of plastids" (1999b) J. Exp. Bot. Vol. 50: 1683-1689
[3] Lichtenthaler H.K., Wellburn A.R." Determinations of total carotenoids and chlorophyll a and b in leaf extracts in different solvent" (1983). Biochem. Soc. Trans. 11: 591-592.

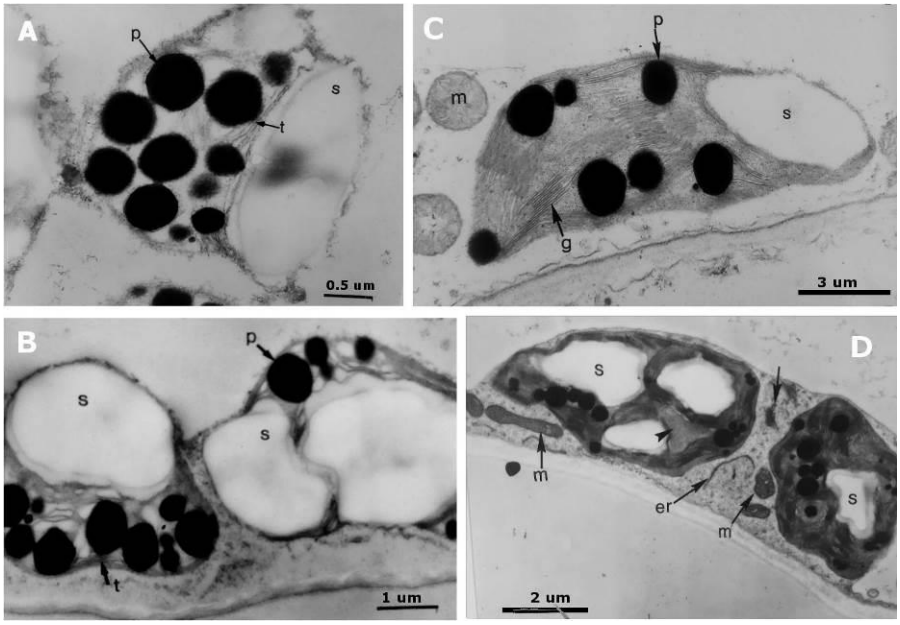

Figure 1. Regreening chloroplasts under dim and bright light. (A) Senescent, (B) 13 days and (C) 20 days at 12 µmol m^2 s^{-1}) (D) 20 dim light + 45 days at 100 µmol m^2 s^{-1}). m, mitochondria; p, plastoglobuli; s, starch; t, thylakoid; g, grana.

LS 5: Cytoskeleton, cellular traffic and membrane dynamics

LS5.001 invited
Microtubule organization in a Xenopus laevis meiotic spindle resolved with electron tomography

E. M. Tranfield[1,2], I. Peristere[2], L. Maillant[2], A. Barros[1], F. Nédélec[2], C. Antony[2,3]

[1]Instituto Gulbenkian de Ciência, Oeiras, Portugal
[2]European Molecular Biology Laboratory, Heidelberg, Germany
[3]L'Institut de Génétique et de Biologie Moléculaire et Cellulaire, Illkirch, France

etranfield@igc.gulbenkian.pt

Measuring the packing density, length, spacing, and polarity of the microtubules (MTs) in the vertebrate spindle is important to understand the chromosome segregation machinery. Light microscopy studies in the well-established Xenopus laevis egg extract system suggest a dynamic tiled array of MTs that are cross-linked and focused during bipolar spindle assembly. However, the three-dimensional (3D) organization of the vertebrate spindle at the resolution of single microtubules remains still largely unresolved. Recent approaches have tried to elucidate the vertebrate spindle structure with 3D scanning electron microscopy techniques. However, electron tomography (ET) can offer detailed high-resolution 3D imaging which is why it has been successfully used to investigate the organization of full and partial cell volumes in other biological model systems. We developed a protocol to image the Xenopus laevis meiotic spindle with ET. A partial spindle volume of approximately 11.4 x 30 x 12.9 µm was acquired on a FEI Tecnai F30 transmission electron microscope. Within this volume microtubules were imaged from one pole to the midzone of the spindle, with a 2 nm pixel size. MTs and chromosome masses were identified by automatic image analysis and refined manually using the Filament Editor tool in Amira, yielding a model with more than 22,000 microtubules. Analysis has been done on MT spacing, length, packing and distribution in the modeled volume.

LS5.002 invited
Exploring the molecular landscape of Chlamydomonas with in situ cryo-electron tomography

B. D. Engel[1], M. Schaffer[1], S. Albert[1], S. Pfeffer[1], A. Martinez-Sanchez[1], L. K. Cuellar[1]
S. Mosalaganti[2], M. Beck[2], Y. S. Bykov[3], J. A. G. Briggs[3], J. M. Plitzko[1], W. Baumeister[1]

[1]Max Planck Institute of Biochemistry, Department of Molecular Structural Biology, Martinsried, Germany
[2]European Molecular Biology Laboratory, Structural and Computational Biology Unit, Heidelberg, Germany
[3]MRC Laboratory of Molecular Biology, Structural Studies Division, Cambridge, United Kingdom

engelben@biochem.mpg.de

We are leveraging new advances in cryo-electron tomography (cryo-ET) to investigate macromolecular complexes within the native cellular environment. Thin slices of vitrified Chlamydomonas reinhardtii cells are prepared by cryo-focused ion beam (cryo-FIB) milling and then imaged by state-of-the-art cryo-ET. The resulting 3D views of cellular volumes have provided new insights into the molecular organization of organelles. Within the chloroplast, we identified fine membrane tubules that likely serve as conduits for the directed diffusion of metabolites between the pyrenoid and the chloroplast stroma. We were also able to directly visualize photosynthetic complexes within native thylakoid membranes, as well as the organization of RuBisCO complexes in the pyrenoid. In the Golgi, we identified protein arrays that establish the narrow membrane spacing of the trans-Golgi cisternae, and also solved the in situ structure of the COPI coat complex. Subtomogram analysis of ER-bound ribosomes enabled us to dissect the molecular architecture of the TRAP translocon component. Current efforts include the structural characterization of proteasomes that encircle nuclear pore complexes on the inside of the nuclear envelope. In addition to the in situ characterization of individual macromolecular complexes, in the future we will aim for a visual proteomics approach to identify and classify every macromolecule within the cellular volumes.

References:
[1] Pfeffer S, Dudek J, Schaffer M, Ng BG, Albert S, Plitzko JM, Baumeister W, Zimmermann R, Freeze HH, Engel BD, Förster F. (2017). Dissecting the molecular organization of the translocon-associated protein complex. Nature Communications 8: 14516.
[2] Schaffer M, Mahamid J, Engel BD, Laugks T, Baumeister W, Plitzko J (2017). Optimized cryo-focused ion beam sample preparation aimed at in situ structural studies of membrane proteins. Journal of Structural Biology 197: 73-82.
[3] Asano S, Engel BD, Baumeister W (2016). In situ cryo-electron tomography: a post-reductionist approach to structural biology. Journal of Molecular Biology 428: 332–343.
[4] Engel BD, Schaffer M, Albert S, Asano S, Plitzko JM, Baumeister W (2015). In situ structural analysis of Golgi intracisternal protein arrays. Proceedings of the National Academy of Sciences USA 112: 11264-11269.
[5] Engel BD, Schaffer M, Cuellar LK, Villa E, Plitzko JM, Baumeister W (2015). Native architecture of the Chlamydomonas chloroplast revealed by in situ cryo-electron tomography. eLife 4: e04889.

LS5.003
Increased membrane LC-3 lipidation but impaired autophagic flux in Vacquinol-treated glioblastoma linked to methuosis

M. Schneider[1], H. Mostafa[1], P. Sander[1], A. Soboh[1], P. Walther[2]

[1]Univeristy Hospital Ulm, Division of Experimental Anesthesiology, Ulm, Germany
[2]Ulm University, Central Facility for Electron Microscopy, Ulm, Germany

marion.schneider@uni-ulm.de

Background: Glioblastoma multiforme derived cell lines (GBM) are sensitive to methuosis induced by a small molecule derivative named Vacquinol (Kitambi et al. 2014; Sander et al. 2017). Methuosis is a unique type of cell death occurring by Rac-1 linked hyperstimulation of vacuole formation (Li et al. 2010; Nara et al. 2012), but impaired vesicle trafficking and lysosome-guided degradation. Vacquinol also stimulates autophagy. Autophagy is a catabolic pathway in which normal or dysfunctional cellular components that accumulate during growth and differentiation are degraded via the lysosome; during starvation it is a survival mechanism that reallocates nutrients from unnecessary processes to more vital processes in the cell. In autophagy, cytoplasmic LC3 protein is processed and recruited to the autophagosomal membranes. The autophagosome then fuses with the lysosome to cause the breakdown of the autophagosome vesicle and its contents. Methods. Establishment and immune phenotypical characterization of glioblastoma (GBM) cell lines from primary tumor material. Analysis of cell death by Vacquinol was accomplished by long-term video microcopy and fluorescence imaging using IncuCyteZOOM® (EssenBiosciences.com). Ultra-structural analysis was performed by cryo-electron microscopy; specimens were examined a JEOL 1400, at 120 keV. Western Blots were done using LC-3B, p62 (SQSTM1) and ERK-1,2 and specific antibodies. Lysosome and mitochondrial staining was recorded by lysotracker and mitotracker based fluorescence microscopy. Caspase3/7 activation was monitored by a chemiluminescence-based enzyme-activity assay (Glomax, Promega.com) Results. Individual GBM cell lines differed regarding their sensitivity to treatment with Vacquinol. #12537-GBM was very sensitive to Vacquinol (Sander et al. 2017) in that almost 100% cell death was obtained after 12h of incubation with 7µM Vacquinol. Cell death was accompanied by massive vacuolization and increased caspase 3/7 activation but nuclear fragmentation was absent. Ultrastructural investigations demonstrated a shift from upregulated mitophagy under steady state culture conditions to a homogenous enrichment of amphisomes (lacking the inner lipid bilayer) via autophagosomes (with an inner lipid bilayer) following 1.5h of Vacquinol treatment. Lysosome and mitochondrial stainings imply impaired vesicular trafficking which appears to constitute the primary action of Vacquinol-inducible cell death in GBM. Western blots proved the significant upregulation of LC-3B lipidation by Vacquinol but inhibition of autophagic flux as indicated by accumulation of p62 (Pugsley et al. 2008). Summary and Conclusion. Cryoelectron microscopy in Vacquinol treated cells deminstrated the impressive amplification of more mature autophagolysosomes presenting by cytoplasmic vacuolization occurring before cell death. Vacuoles were composed of vesicles derived from macropinosomes as well as autophagosomes. These vesicles eventually fuse with lysosomes to generate amphisomes. Impaired trafficking of such large vacuoles caused by rupture of the plasmamembrane, a characteristic of methuosis.

References:
[1] Sander, S et al. Vacquinol-1 inducible cell death in glioblastoma multiforme is counter regulated by TRPM7 activity induced by exogenous ATP. ONCOTARGET, 2017 in press Kitambi SS et al. Vulnerability of glioblastoma cells to catastrophic vacuolization and death induced by a small molecule. Cell. 2014; 157: 313–28.
[2] Li, C. et al. Nerve growth factor activation of the TrkA receptor induces cell death, by macropinocytosis, in medulloblastoma Daoy cells. *Journal of Neurochemistry*. 2010; 112:882-899.
[3] Nara, A et al. Hyperstimulation of macropinocytosis leads to lysosomal dysfunction during exposure to methamphetamine in SH-SY5Y cells. *Brain Research*. 2012; 1466:1-14.
[4] Pugsley, H et al. Measuring autophagic flux by assessing LC3, p62 and LAMP1 co-localization using imaging flow cytometry (TECH2P.908). 2015; Vol. 194. 206.18-206.18.

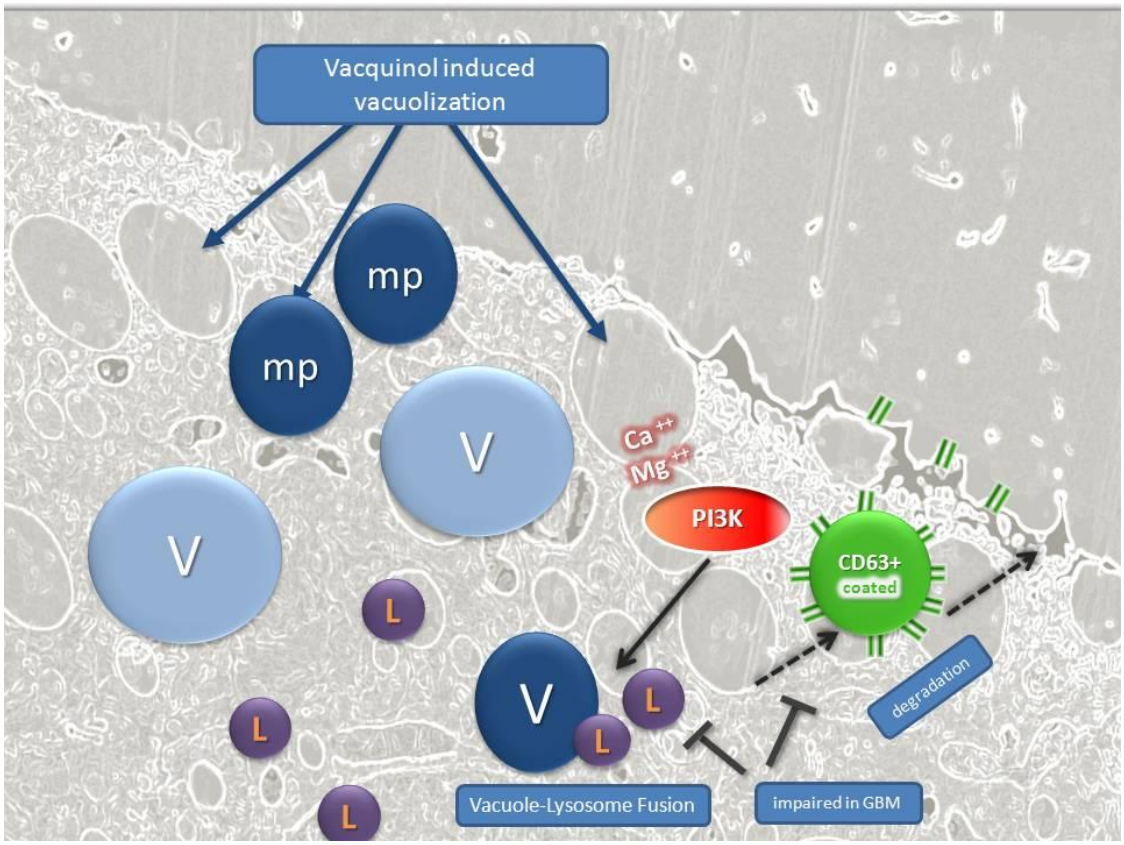

Figure 1. Hypothetical action of Vacquinol in glioblastoma. Fluorescence-based light microscopy and trans electron-microscopical imaging showed that Vac leads to massive vacuolization (V) related to macropinocytosis (mp) and autophagy upregulation, followed by cell death via cell rupture. The process implies PI3 kinase activation and impaired trafficking and extrusion of CD63 positive autophagolysosomes.

LS5.004
3D CLEM to map multiple protein and RNA localizations to the full ultrastructural context of cells and tissues in a near-native state

C. Stigloher[1]

[1]University of Würzburg, Biocenter, Theodor-Boveri-Institute, Würzburg, Germany

christian.stigloher@uni-wuerzburg.de

Array Tomography (AT) is an easy-to-use and yet very powerful technical approach to map multiple molecular identities to the full ultrastructural context of cells and even entire tissues. By advancing AT with high-pressure freezing / freeze substitution for superior structural preservation and super-resolution light microscopy, subcellular structures can now be systematically mapped in 3D in a near-native state. We established protocols for the application of super-resolution AT for a multitude of biological samples – from model organisms to some quite exotic samples. Recently, we also devised an adaptation of the super-resolution AT protocol to reveal RNA localizations. I will showcase the versatility of our protocols and give several examples for biological questions that can be answered with these techniques.

LS5.005
Architecture of mammalian slit diaphragm and liver desmosomes using electron tomography

C. Wigge[1], F. Grahammer[1], Z. Yu[1], M. Kunz[1], T. Huber[1], A. Frangakis[1]

[1]Buchmann Institute for Molecular Life Sciences and Institute for Biophysics, Goethe University Frankfurt, Frankfurt, Germany

wigge.christoph@gmail.com

Modern 3DEM methods are allowing us to study the organization of cellular adhesion molecules in different contexts. In mammalian kidney neph1 and nephrin are forming a specialized cell-cell contact between the podocyte foot processes which is defined as the slit diaphragm (SD). We isolated wild type glomeruli out of mouse kidney after a mild perfusion fixation. By using a combined approach of cryo electron tomography (CET) and sub tomogram averaging as well as classical electron tomography we were able to demonstrate the dynamic multilayered architecture of the SD. While the molecules are periodically spaced 7 nm apart the neph1 forms the lower part of the SD with a width of ca. 23 nm whereas nephrin forms the upper part of the junction with a width of ca. 45 nm. Both proteins show an Ig domain rich structure which indicates the SD to be a highly dynamic and flexible cell-cell contact within the renal filtration apparatus. In contrast to the SD desmosomes resemble another class of cell-cell contact proteins which are part of the adhesion apparatus and therefore keep tissue integrity. These junctions are formed by desmocolin and desmoglein and are anchoring to intracellular intermediate filaments in order to maintain a tissue. In mouse liver desmosomes are prominently formed along bile canaliculi. We isolated these structures from wild type mice liver and used CET and sub tomogram averaging to analyze the architecture of native desmosomes. These molecules also show an intermolecular periodic spacing of ca. 7 nm and form a distance of ca. 30 nm between two neighbouring cells. Although the proteins are consisting of Ig domains which gives them a potential flexibility we could not observe a bimodal cell-cell junction similar to the case of the slit diaphra.

LS5.P001
Fairy tales and facts in herpes virus envelopment

E. M. Schraner[1], A. Kaech[2], M. Ackermann[3], P. Wild[1]

[1]Institutes of Vet. Anatomy and Virology, EM Lab, Zürich, Switzerland
[2]University of Zurich, ZMB, Zürich, Switzerland
[3]Insitute of Virology, Zürich, Switzerland

elisabeth.schraner@uzh.ch

Introduction: Herpes viruses consist of the DNA-containing capsid, the tegument protein layer surrounding the capsid, and an envelope with embedded glycoproteins, visible as spikes in good electron micrographs. Capsids are assembled in the nucleus, filled with DNA and released into the cytoplasm. Tegument and envelope derive by budding at cell membranes.
Objectives and Methods: Electron microscopy has led more to confusion than elucidation of herpes virus morphogenesis and intracellular transport during the last 5 decades. Here, we summarize data obtained by electron microscopy (TEM and Cryo-FESEM) of cells infected with herpes simplex virus 1 (HSV-1) or bovine herpes virus-1 (BoHV-1) prepared for improved spatial and temporal resolution. Critical consideration of published data turned out that many of them are fairy tales rather than facts.
Results: Fairy Tale I: Capsids are enveloped by budding at the inner nuclear membrane (INM), de-enveloped by fusion of the viral envelope with the outer nuclear membrane (ONM), and re-enveloped by wrapping at the trans Golgi network (TGN) [1].
Facts: i) The process at the ONM is identical to the one at the INM showing positive and negative curvatures and formation of a dense coat. Fusion pores and fusion necks have never been shown. ii) Capsids of mutants lacking the fusion proteins gB/gH interact with the ONM leading to accumulation of virions in the perinuclear space (PNS). This is the ultimate prove that capsids bud at the ONM and do not fuse. [2]. Therefore, capsids gain access to the cytoplasmic matrix via another way. TEM and Cryo-FESEM revealed dilation of nuclear pores through which capsids are released. Pore dilation is the initial step in breakdown of the nuclear envelope as in mitosis.
Fairy Tale II: De-envelopment and re-envelopment are essential for production of infectious progeny virus.
Facts: The protein Us3 is not essential for production of infectious progeny virus. Virions of Us3 deletion mutants derived by budding at the INM cannot be released out of the PNS. Nevertheless, Us3 deletion mutants are infective [3] implying that de-re-envelopment is not needed at all for production of infectious virus. Virions produced after disintegration of the Golgi complex are also infective provided Golgi function is not disturbed for a minimum of 5 hours post inoculation.
Fairy Tale III: Secondary envelope takes place at the TGN by wrapping [1].
Facts: i) Lateral Golgi cisternae contain dozens of virions. ii) Capsids bud into Golgi cisternae [4, 5]. iii) Virions are transported form the PNS into the endoplasmic reticulum (ER) and probably farther via ER-Golgi transitions into Golgi cisternae. iv) Wrapping describes a process whereby capsids bud at Golgi membranes simultaneously forming envelope and vacuole. Wrapping takes place at any site of the Golgi complex.
Conclusion: Nucleus to cytoplasm capsid translocation follows 2 diverse pathways: One via budding at the INM followed by intraluminal transportation probably directly into Golgi cisternae, the other via impaired nuclear envelope followed by budding at or wrapping by Golgi membranes.

References:
[1] Mettenleiter, T.C., et al., Cell Microbiol, 2013. **15**(2) 170-178.
[2] Farnsworth, A., et al., Proc Natl Acad Sci U S A, 2007. **104**(24): 10187-92.
[3] Reynolds, A.E., et al., J. Virol. 2002. **76**(17): 8939-52.
[4] Leuzinger, H., et al., J. Virol. 2005. **79**(20): 13047-59.
[5] Homman-Loudiyi, M., et al., J. Virol. 2003. **77**(5): 3191-203.

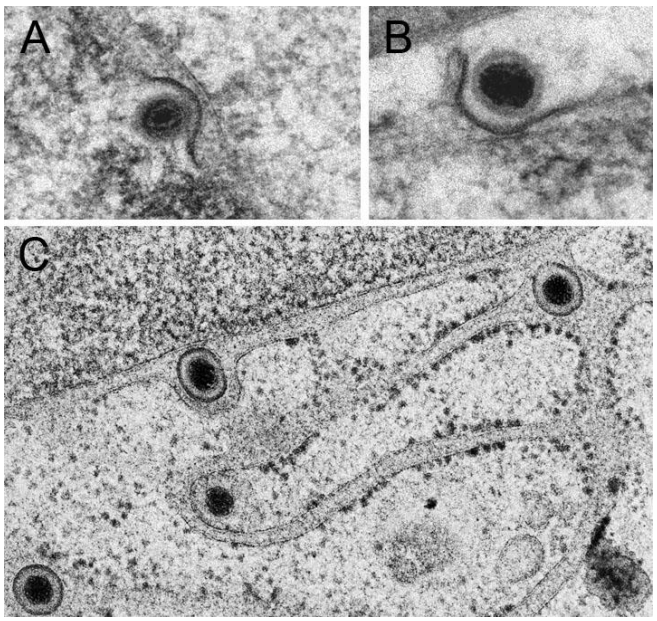

Figure 1. Budding of capsids at the INM (A) and ONM (B) results in virions in the PNS (C).

Figure 2. Virion transport from the PNS into the ER (C) and probably into Golgi cisternae (D).

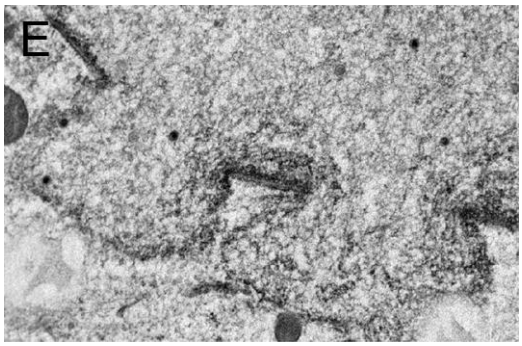

Figure 3. Capsids release via impaired nuclear envelope (E).

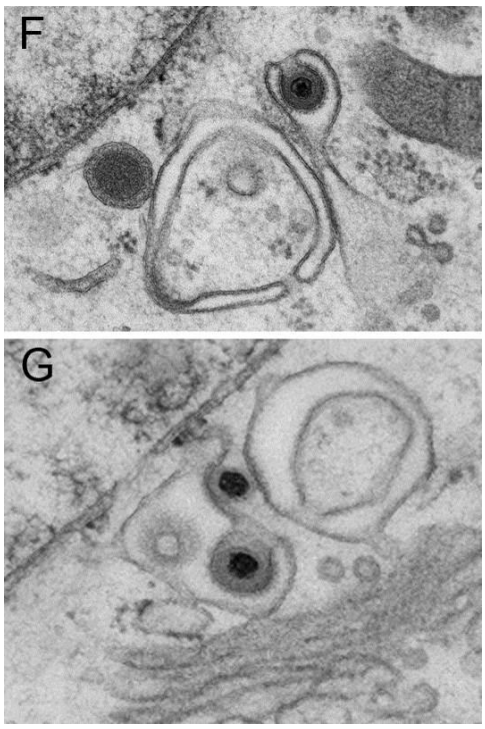

Figure 4. Budding at or wrapping by Golgi membranes (F,G).

LS5.P002
Identification of cytoskeleton and cellular traffic and membrane dynamics of Iranian Leishmania infantum by LC-mass spectrometry

H. Hajjaran[1], R. Burchmore[2], M. Mohebali[1], E. Kazemi-Rad[1], M. Mohammadi Bazargani[3]

[1]Tehran University of Medical Sciences, Tehran, Islamic Republic of Iran
[2]University of Glasgow, Glasgow, United Kingdom
[3]Agriculture institute, Iranian Research organization for Science and Technology, Tehran, Islamic Republic of Iran

hajaranh@tums.ac.ir

Introduction: Leishmania parasites cause a broad spectrum of clinical disease. The outcome of infection is influenced of both host immune situation and the parasite species. The mechanisms of species differences and virulence are under the influence of gene expression regulation at post transcriptional stages. Proteomic studies by using the 2 dimentional electrophoresis (2-DE) and mass-spectrometry increase our understanding of the mechanism of the physiological or pathological process.
Objectives: Here in, we report the dynamic roles of Cytoskeleton and cellular traffic in *L. infantum* through the 2-DE and liquid mass spectrometry (LC-MS).
Materials and Methods: As a preliminary study, we compared the proteome mapping of the Iranian isolate of *Leishmania infantum* through the (2-DE), and identified the prominent proteins by Liquid Chromatography (LC) mass spectrometry.
Results: We reproducibly detected about 700 protein spots in *L. infantum* by using the Melanie software. Of the 135 proteins that were detected on the analytical gels, 61 proteins were detected reliably on CBB-stained preparative gels which were analyzed using LC/MS/MS after excitation from CBB stained gels. These proteins according to their functions and biological processes were classified in twelve categories: carbohydrate metabolism process, protein synthesis and assembly, cell signaling and vesicular trafficking, intracellular survival/proteolysis, antioxidant defense, stress related proteins/protein folding, cell motility and cytoskeleton, nucleoside, nucleotide and nucleic acid metabolism.
Conclusion: One of the cell signaling proteins was calmodulin-like protein. Calmodulin is a kind of calcium binding protein which expresses in all eukaryotic cells including members of the genus *Leishmania*; it participates in calcium signaling pathways that regulate multiple critical processes such as growth and proliferation. Moreover, it plays a vital role in virulence of *Leishmania* during invasion of macrophage. On the other hand vacuolar sorting-like protein as a vesicular trafficking protein involved in sorting and delivering of vacuolar proteins to each intracellular compartment. Also this protein as a member of endosome sorting and authophagy pathways is essential for differentiation and virulence of *Leishmania*.

LS5.LBP01
Tracig non-canonical sphingolipids by electron microscopy using novel click-chemistry detection

C. Lamberz[1], M. Hesse[2], A. Al-Amoudi[1], G. Kirfel[2], D. Fürst[2], L. Kuerschner[2]

[1]DZNE, Bonn, Germany
[2]Uni Bonn, Bonn, Germany

christian.lamberz@gmail.com

During the last few decades lipid associated diseases (e.g. diabetes, lysosomal storage diseases, obesity and arteriosclerosis) were brought into the focus of life sciences. This is also illustrated by the continuous discovery of new lipid species, metabolic pathways and lipophilic signaling molecules. In general ultra-structural localization studies and tracing of lipids in biological systems is still a challenge. A recent approach employs alkyne lipids as tracers, which can be detected upon click-reaction [1, 2].
Here we present a novel method to localize alkyne lipids in virtually any biological system on nano-scale. We termed that approach the "Golden-Click-Method" (GCM). GCM is based on functionalized gold-nanoparticles as reporters. These electron dense reporters contain azide-groups. They are covalently conjugated to alkyne lipids during GCM labeling, involving a copper catalyzed click-reaction [3]. Alkyne lipids are lipid tracers which act virtually native in biological systems. A broad library of different alkyne lipids has become available for applications in animal models and culture systems [4, 5, 6]. They allow for parallel tracing of lipid metabolism over time using complementary quantitative methods. For metabolite identification, complex lipid mixtures, extracted from biological systems after incubation with the tracers, are first click-reacted with fluorescent reporters and then separated by thin layer chromatography (TLC). In parallel, the GCM approach benefiting from the high spatial resolution of TEM-tomography enables for a correlative analysis of lipid localization at the sub-organelle level. This tandem of methods can be further complemented by light microscopy analysis visualizing alkyne-lipid distribution in a broader perspective [7].
In the present study we applied the GCM to study the cellular fate of non-canonical sphingolipids, a lipid class relevant for type 2 diabetes or HSAN1 (hereditary sensory and autonomic neuropathy type 1) [8]. Cells were incubated with alkyne-deoxysphinganine, a tracable analogue of 1-deoxysphinganine (DOXSA). Elevated levels of DOXSA are reported in blood plasma of the affected patients ultimately suffering from neuronal degeneration. Cellular DOXSA accumulation is associated with mitochondrial dysfunction and neurons with their high demand for energy overly suffer from a damage of these cell organelles [9]. Here, we report on an electron microscopy localization study of the intracellular distribution of alkyne-DOXSA using the new method GCM developed in our lab.

References:
[1] Sharpless et al., Click Chemistry: Diverse Chemical Function from a Few Good Reactions (2001)
[2] Jao et al., Salic Metabolic labeling and direct imaging of choline phospholipids in vivo.
[3] Sivakumar et al., A Fluoragenic 1,3-Dipolar Cycloaddition Reaction of 3-Azidocoumarins and Acetylenes. (2004)
[4] Thiele et al., Tracing Fatty Acid Metabolism by Click-Chemistry (2012)
[5] Hoffmann et al., A novel alkyne cholesterol to trace cellular cholesterol metabolism and localization (2013)
[6] Kuerschner and Thiele, Multiple bonds for the lipid interest (2014)
[7] Hoffmann et al. , A novel alkyne cholesterol to trace cellular cholesterol metabolism and localization (2014)
[8] Penno et al. , Hereditary sensory neuropathy type 1 is caused by the accumulation of two neurotoxic sphingolipids (2010)
[9] Alecu et al. , Localization of 1-deoxysphingolipids to mitochondria induces mitochondrial dysfunction (2017)

LS 6: Imaging techniques: X-ray microscopy, live/in vivo imaging and correlative approaches

LS6.001 invited
Catch me if you CLEM – multimodal correlative microscopy of tumor cells at the blood-brain barrier

M. Karreman[1,2], N. Schieber[1], G. Solecki[2], M. Feinauer[2], A. Berghoff[2], L. Mercier[3,4,5,6], J. Goetz[3,4,5,6]
F. Winkler[2], Y. Schwab[1]

[1]EMBL Heidelberg, Cell Biology and Biophysics, Heidelberg, Germany
[2]DKFZ Heidelberg, Clinical Cooperation Unit Neurooncology, Heidelberg, Germany
[3]Inserm U1109, MN3T, Strasbourg, France
[4]Université de Strasbourg, Strasbourg, France
[5]Université de Strasbourg, LabEx Medalis, Strasbourg, France
[6]Université de Strasbourg, Fédération de Médecine Translationnelle de Strasbourg (FMTS), Strasbourg, France

m.a.karreman@gmail.com

Metastasis is the main cause of cancer-related mortality, but how tumor cells spread through the tissue *in vivo* is still largely unknown. Intravital microscopy (IVM) enables studying crucial steps of the metastatic process [1], but it is limited in resolution and it fails to reveal the structural context. Combining IVM to 3D Electron Microscopy (3DEM) enables to correlate functional and dynamic in vivo imaging to high-resolution of the tumor cells and their microenvironment. However, keeping track of single tumor cells when moving from IVM to EM imaging is highly challenging in complex tissue samples [2].
We have developed a method that exploits x-ray microscopic computer tomography (microCT) [3] to correlate IVM to EM [4]. First, fluorescent tumor cells are xenotransplanted to living mice, and monitored by IVM. 3D datasets of the tumor cells and the surrounding fluorescently stained vasculature are obtained. Next, the region of interest is processed for EM and embedded in resin. The sample is then scanned with microCT, revealing the outlines of the resin block, the biopsy and the vasculature within. Using 3D imaging software, the IVM and microCT volumes are registered, enabling to map the position of the tumor cell within the resin-embedded specimen. Finally, targeted trimming enables to quickly approach the tumor cell inside the resin block and expose it for 3D imaging with FIB-SEM or electron tomography.
The method will be demonstrated on capturing arrested tumor cells in the vasculature of mouse brain samples [4,5]. Enabling to predict the position of the tumor cell within the resin block with an accuracy of >5 µm significantly speeds up the process of correlating IVM to EM; from several months to ~2 weeks. The correlative approach uniquely enables multiple high-resolution observations of rare metastatic events in tissue, allowing obtaining statistically relevant conclusions on the crucial steps in the dissemination of tumor cells [4].

References:
[1] CLGJ Scheele, C Maynard and J Van Rheenen, Trends in Cancer **2** (2016), p 205-216.
[2] MA Karreman *et al*. PLoS One **9** (2014), e114448.
[3] S Handschuh *et al*. Front Zoology **10** (2013), p 1-16.
[4] MA Karreman *et al*. Journal of Cell Science **129** (2016), p. 444-456
[5] Y Kienast, L von Baumgarten, M Fuhrmann, WE Klinkert, R Goldbrunner, J Herms, F Winkler. Nature Medicine 16 (2010), p 116-122.

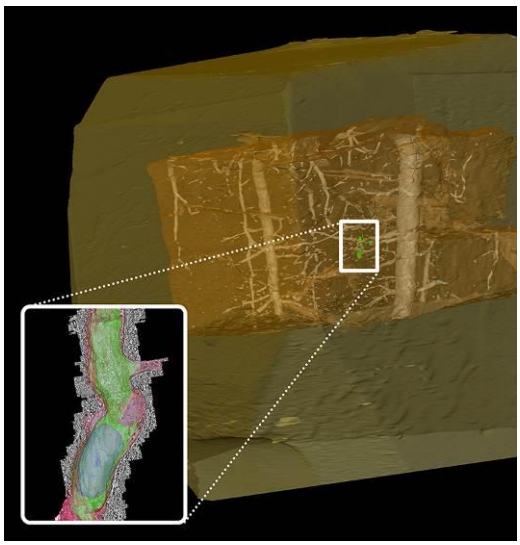

Figure 1. Multimodal Correlative Microscopy enables to predict the position of single tumor cells inside brain biopsies that processed for EM and embedded in resin. In this way, it is possible to quickly retrieve the tumor cell inside the sample and image it with Focussed Ion Beam Scanning Electron Microscopy [4].

LS6.002 invited
Time-resolved correlative light and 3D electron microscopy for fast intracellular processes

L. Stepanek[1], G. Pigino[1]

[1]MPI-CBG, Dresden, Germany

stepanek@mpi-cbg.de

Intraflagellar transport (IFT) is an example of highly dynamic cellular trafficking process. Anterograde and retrograde IFT trains constantly shuttle cargo proteins between ciliary base and tip with velocities exceeding 4 microns per second.
Many gaps in our knowledge of IFT were filled since its discovery in 1993, but some fundamental question persisted until recently due to the lack of appropriate imaging technology: (i) the differences in the structure of anterograde and retrograde IFT trains and (ii) the mechanism that prevents collisions upon encounter of oppositely directed trains in the confined space of the cilium. Techniques combining high spatial and temporal resolution are crucial to understand structure and dynamics of such fast processes. Electron microscopy (EM) itself can provide adequate spatial resolution, but no information on the transport dynamics. In fact, it is impossible to decide whether and anterograde or retrograde IFT train is being observed by using EM alone.
To compensate for this limitation, we present the methodology required to combine live cell imaging at millisecond frame rates with electron tomography. Using this approach, we were able to correlate the direction of movement of every IFT train in a cilium with its morphology and microtubule track. This enabled us to show the different structure of anterograde and retrograde IFT trains unambiguously for the first time. An unexpected third structural type of IFT train was observed, which corresponds to the non-moving fluorescence signal in light microscopy. Moreover, the correlative microscopy combined with single particle tracking of live cell time-lapse series showed that the anterograde IFT trains use B-tubules of the ciliary microtubule doublets, while the retrograde trains use A-tubules, thus avoiding collisions.
As we have successfully established our time-resolved correlative methodology as a tool for study of the IFT machinery, it is ready to be further adapted for other cellular transport systems, or even *in vitro* single molecule assays.

LS6.003
NIR-II Mult NIR-II multi-harmonic imaging of nanoparticle-labeled stem cells as monitoring tool in tissue depth

L. Dubreil[1], V. Kilin[2], J. Riporto[2], K. Rouger[1], L. Bonacina[2]

[1]INRA UMR703 PAnTher, Nantes, France
[2]University of Geneva, Applied Physics, Geneva, Switzerland

luigi.bonacina@unige.ch

Introduction: In order to assess the therapeutic potential of cell-based strategies, it is of paramount importance to elaborate and validate new tools for monitoring the behavior of injected cells in terms of tissue dissemination and engraftment properties. Here, we apply Bismuth Ferrite harmonic nanoparticles (BFO HNPs) to *in vivo* expanded human skeletal muscle-derived stem cells (hMuStem cells), an attractive therapeutic avenue for patients suffering from Duchenne Muscular Dystrophy. 1
Objectives: We first demonstrate the possibility of identifying isolated HNPs in depth of muscle tissue at more than 1 mm from the surface, taking full advantage of the extended imaging penetration depth allowed by multiphoton microscopy in the second near infrared window (NIR-II).2 We also show that the simultaneous acquisition of Second and Third Harmonic Generation (SHG and THG) from BFO HNPs help separating their response from tissue background, with a net increase in imaging selectivity,3 which could be particularly important in pathologic context defined by a highly remodeling tissue. Successively, we succeed in detecting individual HNPs-labeled hMuStem cells in skeletal muscle tissue after their intramuscular injection.
Methods: Multiphoton imaging in NIR I and NIR II
A Nikon microscope A1RMP coupled with an Insight Deepsee laser (Spectra Physics), tunable in the 680-1300 nm range, <120 fs pulse.
Results: On the left side of Fig.1, we present a three-dimensional image-stack of muscle tissue obtained at 1300 nm. The vertical dimension extends for more than 1.3 mm from the sample surface on the top. In the image, one can recognize the intense emission by HNPs as individual or aggregated elements in blue and green over the predominant yellowish autofluorescence by the tissue. Very notably, HNPs can be detected also in the lowest region of the volume at depths exceeding > 1 mm. The plots on the right are a split channel representation of the SHG and THG of a region of interest embedded in the tissue volume at approximately 1 mm depth. The HNPs pattern appears very similar in both detection channels at first sight.
To assess the possibility of using HNPs-based labeling to track cells of interest in tissue, BFO-PEG hMuStem cells were injected in mice muscle. As reported in Fig.2, twenty-four hours later, injected tissue was removed and the presence of hMuStem cells identified by multiphoton microscopy in a 25 mm thick slice by specific human lamin A/C immunolabeling and by HNPs SHG (in yellow and blue , respectively). hMuStem cells and HNPs are mainly localized in the central region of the image. By inspecting the close-up frame, one can see how the HNPs appear as isolated blue spots in close vicinity of yellow labeled cells. The blue region extending vertically on the left side of the figure corresponds to the intense SHG emission by a bundle of collagen fibers.
Conclusions: BFO HNPs in association with NIR-II multiphoton microscopy represent an innovative research platform for assessing cell therapies at high spatial resolution. Here we demonstrate this procedure by labeling hMuStem cells, a human skeletal muscle-derived stem cell population with promising therapeutic potential for muscular dystrophies. We show the possibility to retrieve hMuStem cells in mice muscles up to 24 hours post-injection. BFO-PEG are able to generate intense SHG and THG simultaneously. Such a multi-harmonic emission deems essential to distinguish particles from the SHG generated by collagen and THG by lipids in muscles.

References:
[3] K. Rouger *et al.*, The American journal of pathology 179, 2501–2518 (2011).
[2] L. A. Sordillo *et al.*, Journal of biomedical optics 19, 056004–056004 (2014).
[3] A. Rogov *et al.*, ACS Photonics 2, 1416–1422 (2015) ; C. Schmidt *et al.*, Scientific reports 6 (2016).

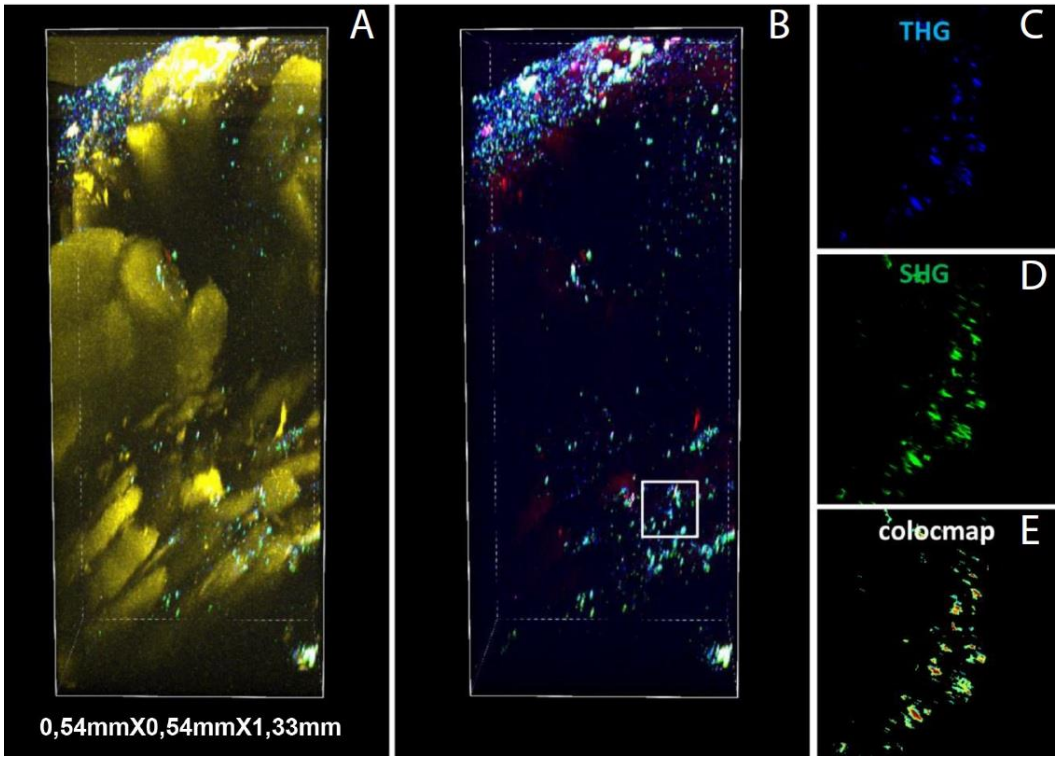

Figure 1

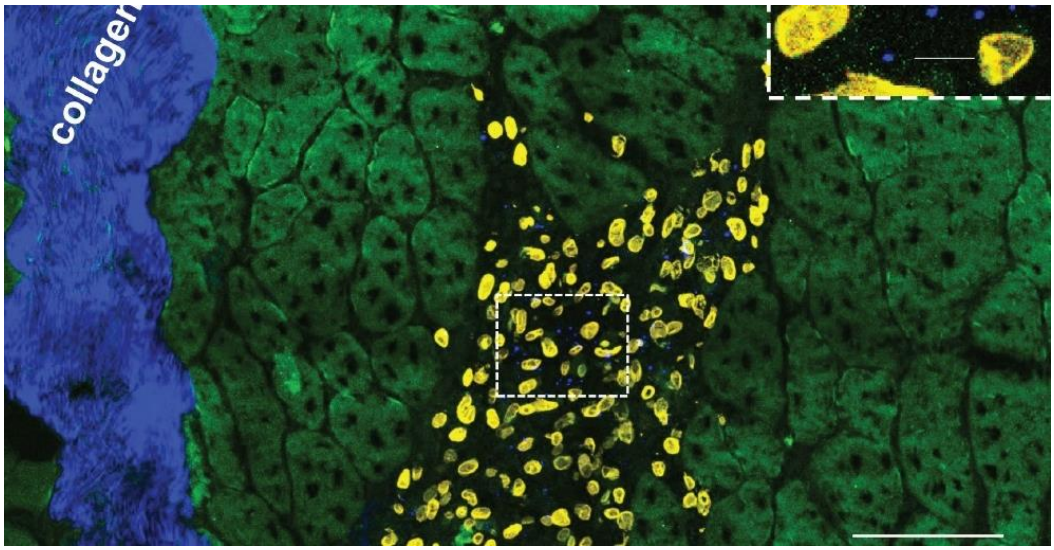

Figure 2

LS6.004
Correlative super resolution microscopy and cryo-solf X-ray tomography

T. Dadosh[1], N. Varsano[1], S. Kapishnikov[2], E. Pereiro[3], E. Shimoni[1], J. Xueting [4], H. Kruth[4]
L. Leiserowitz[1], L. Addadi[1]

[1]Weizmann Institute of Science, Chemistry, Rehovot, Israel
[2]Helmholtz-Zentrum, Soft Matter and Functional Materials, Berlin, Germany
[3]ALBA Synchrotron Light Source, Barcelona, Spain
[4]National Institutes of Health, Bethesda, MD, United States of America

tali.dadosh@weizmann.ac.il

One of the most versatile imaging techniques in biology, fluorescence microscopy, allows noninvasive imaging with molecular specificity. However, the resolution of a conventional wide-field fluorescence microscope is limited by the diffraction of light (~200-300 nm). Recent advances in far-field optical nanoscopy provide spatial resolution of 20-50 nanometers that is well below the diffraction limit. Combining super resolution fluorescence microscopy with additional high resolution imaging technique is highly attractive. Correlation of two imaging approaches allows specific cellular characterization together with a highly complete view of the cell ultrastructure. We therefore were inspired to develop a high resolution correlative method involving cryo-soft X-ray tomography (cryo-SXT) and stochastic optical reconstruction microscopy (STORM), which provides information in three dimensions on large cellular volumes at 70 nm resolution. Cryo-SXT morphologically identifies and localizes aggregations of carbon-rich materials. STORM identifies specific markers on the desired epitopes, enabling colocalization between the identified objects, in this case cholesterol crystals, and the cellular environment. The samples were studied under ambient and cryogenic conditions without dehydration or heavy metal staining. The early events of cholesterol crystal development were investigated in relation to atherosclerosis, using as model macrophage cell cultures enriched with LDL particles. Atherosclerotic plaques build up in arteries in a slow process involving cholesterol crystal accumulation. Cholesterol crystal deposition is a crucial stage in the pathological cascade. Our results show that cholesterol crystals can be identified and imaged at a very early stage on the cell plasma membrane and in intracellular locations. This technique can in principle be applied to other biological samples where specific molecular identification is required in conjunction with high resolution 3D-imaging.

References:
[1] Neta Varsano, et al., J. Am. Chem. Soc., 2016, 138 (45), 14931–14940

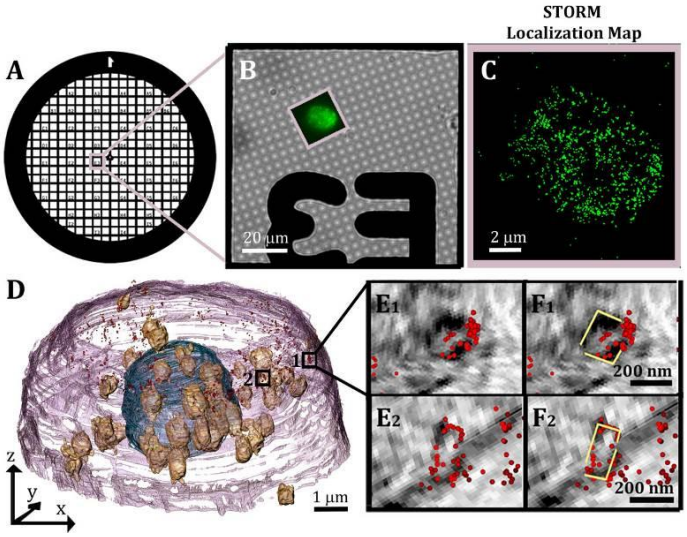

Figure 1
.

LS6.005
Preservation of fluorescence associated with self-labeling protein tags in epoxy resin for correlative light and electron microscopy at high resolution

A. Müller[1,2,3], M. Neukam[1,2,3], A. Ivanova[1,2,3], A. Sönmez[1,2,3], C. Münster[1,2,3], S. Kretschmar[4,5]
Y. Kalaidzidis[6,7], T. Kurth[4,5], J. M. Verbavatz[6,8], M. Solimena[1,2,3,6]

[1]Paul Langerhans Institute Dresden of the Helmholtz Zentrum München at TU Dresden, Molecular Diabetology, Dresden, Germany
[2]University Hospital and Faculty of Medicine Carl Gustav Carus, TU Dresden, Dresden, Germany
[3]German Center for Diabetes Research (DZD e.V.), Neuherberg, Germany
[4]Center for Regenerative Therapies Dresden (CRTD), Dresden, Germany
[5]Biotechnology Center of the TU Dresden (BIOTEC), Dresden, Germany
[6]Max Planck Institute of Molecular Cell Biology and Genetics (MPI-CBG), Dresden, Germany
[7]Moscow State University, Moscow, Russian Federation
[8]Université Paris Diderot, Paris, France

andreas.mueller8@mailbox.tu-dresden.de

Introduction: Correlative light and electron microscopy (CLEM) approaches can be divided in pre-embedding and post-embedding CLEM depending on the time-point when fluorescence light imaging (FLM) is performed. The goal of post-embedding CLEM is the preservation of fluorescence in the section, which can then be used for both FLM and electron microscopy (EM). This allows for greater precision of correlation and higher-throughput compared to pre-embedding analysis. In the field of EM it is commonly assumed that the initial fluorescence of the sample (mostly based on self-fluorescent protein tags) cannot be preserved in epoxy resins, which have been the most widely used embedding media for EM. Recently developed protein tags such as SNAP and CLIP are not self-fluorescent but bind specific fluorescent substrates based on organic fluorophores.
Objectives: Our goal was to test the preservation of fluorescence directly associated with protein tags (SNAP or CLIP) in epoxy resins for CLEM combining super resolution microscopy and EM. If so, this approach could then be used to investigate the life-cycle insulin secretory granules (SGs) and their intracellular degradation.
Materials and Methods: We labeled insulin SGs of different age in beta cells of isolated pancreatic islets from SOFIA (Study of insulin aging) mice, in which an insulin2-SNAP allele had been knocked-in in the Ins2 locus. After labeling the islets were fixed by high pressure freezing (HPF), followed by freeze substitution (FS) and Epon embedding. Combining structured illumination microscopy and transmission electron microscopy (TEM) for correlative light and electron microscopy (CLEM) we precisely tracked age-distinct insulin SGs in Epon sections of SOFIA mouse pancreatic islet beta cells. We furthermore performed electron tomography to investigate the interaction of age-defined insulin SGs with microtubules. This protocol was also applied to insulinoma cells transfected with different proteins fused with SNAP- or CLIP tags and also combined with initial chemical fixation.
Results: We could show for the first time the preservation of fluorescence directly associated with protein tags in epoxy resin. This allowed for CLEM of age-distinct insulin SGs in SOFIA mouse islets fixed by (HPF) and embedded in Epon epoxy resin, providing optimal ultrastructural preservation and contrast1. With this novel approach we could formally demonstrate that the characteristic translucent halo surrounding the insulin SG core is an artifact of chemical fixation leading to overestimation of the SG size. Morphometric analysis further revealed a significantly smaller diameter of 2-day-old insulin SGs compared with the whole SG population. By using the CLIP tag fused to the autophagosomal marker LC3 together with hIns-SNAP we could perform dual color CLEM to image intracellular degradation of SGs by autophagy. To demonstrate the robustness of our method we successfully performed CLEM with cytosolic, nuclear, membrane- and cytoskeleton-associated proteins tagged with SNAP or CLIP, even after chemical fixation and Epon embedding.
Conclusion: Further exploitation of this approach for morphometric analysis of labeled and unlabeled SGs will provide quantitative information about the life cycle of insulin SGs in different metabolic conditions. CLEM in Epon sections after HPF will allow for investigating the interaction of insulin SGs with the cytoskeleton at nanometer-resolution. Preservation of fluorescence in epoxy resin after HPF or after chemical fixation is a major simplification of post-embedding CLEM due to the simple embedding procedure, superior sectioning properties and lesser toxicity compared to acrylic resins.

References:
[1] Müller, A. *et al.* A Global Approach for Quantitative Super Resolution and Electron Microscopy on Cryo and Epoxy Sections Using Self-labeling Protein Tags. *Sci. Rep.* **7,** 23 (2017).

LS6.006
Correlative live-cell-3D electron microscopy of single endo-lysosomal compartments

J. Fermie[1,2], N. Liv[1], E. van Donselaar[1,3], W. Müller[3], N. Schieber[4], Y. Schwab[4], H. Gerritsen[2]
J. Klumperman[1]

[1]University Medical Center Utrecht, Cell Biology, Utrecht, Netherlands
[2]Utrecht University, Soft Condensed Matter and Biophysics, Utrecht, Netherlands
[3]Utrecht University, Biomolecular Sciences, Utrecht, Netherlands
[4]EMBL Heidelberg, Electron Microscopy Core Facility, Heidelberg, Germany

j.fermie@umcutrecht.nl

Introduction: Correlative live-cell imaging - electron microscopy (live cell-CLEM) methods integrate information on the dynamic behavior of fluorescently labelled molecules with their ultrastructural context at nanometer resolution. A major challenge in live-cell CLEM is to retrace individual organelles in 3 dimensions (3D), especially for small objects.
Objective: In order to increase the resolution of live cell CLEM in 3D we introduce focused ion beam scanning electron microscopy (FIB-SEM) to a live-cell CLEM pipeline and use this set up for the first time to integrate the dynamics and ultrastructure of individual endo-lysosomal compartments.
Materials and Methods: Hela cells were transfected with the endo-lysosomal marker LAMP-1-GFP for live-cell imaging over several minutes. We then fixed the cells directly in the microscope chamber to prevent a time gap between live-cell imaging and made a confocal z-stack for 3D information. Then we stained the cells with heavy metals and embedded them in resin, after which we performed automated serial imaging of the region of interest (ROI) using FIB-SEM.
Results: Using the contours of the cell revealed by the fluorescent z-stack we could reliably retrace the cell and ROI by FIB-SEM (fig. 1, 2). This allowed us to study fusion, fission and trafficking dynamics of individual organelles and link this to their ultrastructure and cellular context. FIB-SEM has sufficient resolution to identify fine morphological features like intraluminal vesicles (ILVs, fig. 3). Our data show that LAMP-1-GFP positive spots greatly vary in nature and by FIB-SEM could be identified as early endosome, late endosome, lysosome or autolysosome, respectively. This highlights how information on membrane organization is required to establish compartment identity (fig. 4). Another important feature of the FIB-SEM data was that non-fluorescent cellular context of the fluorescent compartments, like endoplasmic reticulum (fig. 3) or mitochondria in close proximity of the correlated spots, was visualized. Thus, our method is highly suited to study membrane contact sites in 3D.
Conclusion: We have successfully developed a live cell 3D CLEM pipeline with the resolution to study individual subcellular compartments. We refer to our method as Single Organelle Microscopy (SOM), since it integrates essential dynamic and ultrastructural information on a single organelle basis. We are currently applying SOM to identify general parameters of dynamic behavior of distinct endo-lysosomal intermediates. We will use this as basis for further studies in which we interfere with endo-lysosomal transport by depletion of specific transport machinery proteins or mimicking disease conditions with impaired endo-lysosomal trafficking. SOM is not restricted to the endo-lysosomal system, but can be applied to other organelles or be combined with functional imaging probes.

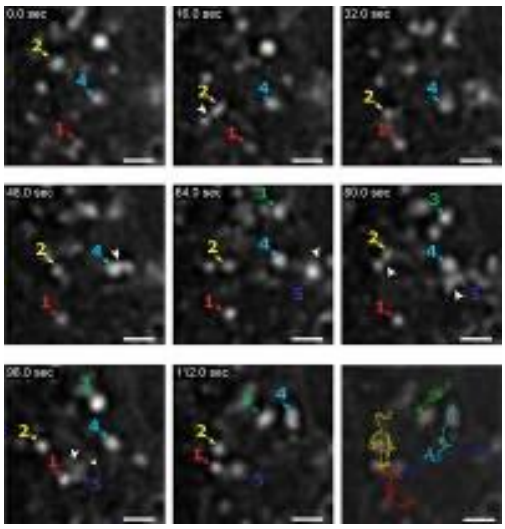

Figure 1. Correlative live cell – FIB-SEM links live-cell dynamics of compartments to their ultrastructural context: Stills from a ROI from a live-cell movie of LAMP-1 positive compartments. Tracked compartments are numbered and color-coded. The bottom right panel shows the tracks of the compartments over the duration of imaging.

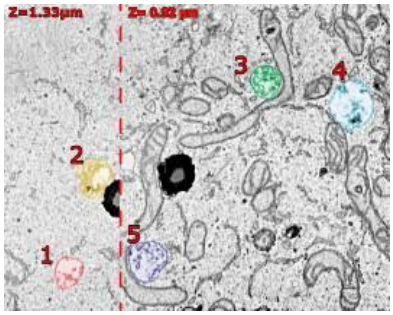

Figure 2. Correlative live cell – FIB-SEM links live-cell dynamics of compartments to their ultrastructural context: FIB-SEM reconstruction of the same ROI as figure 1. Organelles 1 through 5 were all retraced from live cell to FIB-SEM data. Compartments are numbered and color coded as in figure 1.

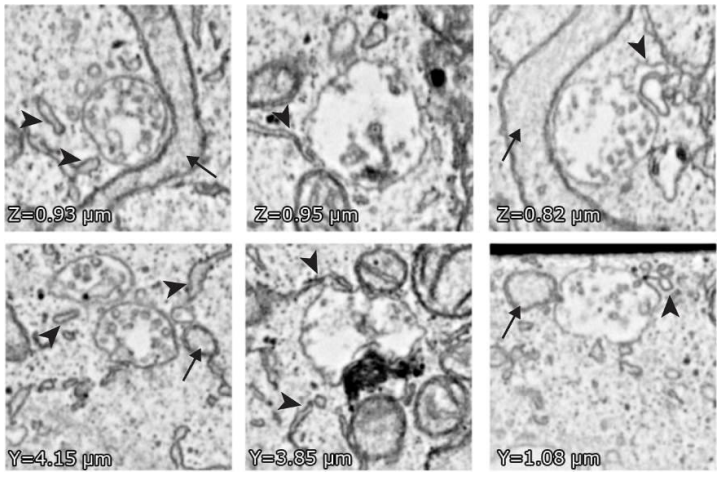

Figure 3. Correlative live cell – FIB-SEM links live-cell dynamics of compartments to their ultrastructural context: Individual slices from the FIB-SEM dataset visualized in figure 2 showing the ultrastructural context of endo-lysosomal compartments. Arrows indicate mitochondria in close contact with an endo-lysosomal compartment. Arrowheads indicate ER cisternae in close contact with an endo-lysosomal compartment. Top row shows XY plane, bottom row shows XZ plane of same organelles.

	Avg. Speed (µm/s)	Peak speed (µm/s)	Displacement (µm)	Dynamics of LAMP-1-GFP	Dextran	Size (by FIB-SEM)	Morphology	Approximate # of ILVs	Organelle type	ER contact	Mitochondrial contact
Spot 1	0,185	1,334	3,34	Diffusive movement† . No streak formation. In close contact with spot 5 for less than a second at 100.8s	+/-	0,55 µm wide, 0,41 µm high, 0,54 µm deep	Electron-lucent lumen, endocytic vesicles are seen near the endosome.	25	Early endosome	1	No mitochondria nearby
Spot 2	0,251	2,034	2,098	Stop-and-go movement‡. Fuses with LAMP-1-GFP spot at 87 secs.	+/-	0,55 µm wide, 0,41 µm high, 0,54 µm deep	Small electron-lucent area surrounded by ILVs. Small vesicles surround the limiting membrane.	50	Late endosome	0	No mitochondria nearby
Spot 3	0,197	0,69	*1,977*	Diffusive movement. Becomes undiscernable from second GFP+ spot at 92.8 seconds with a local increase in brightness.	+	0,49 µm wide, 0,5 µm high, 0,60 µm deep	Two separate compartments without fusion profile.	70	Late endosomes	2	Mitochondrial membrane within 30nm of the lysosomal membrane.
Spot 4	0,159	1,172	3,323	Stop-and-go movement. Transient interaction with GFP+ spots.	+	0,83 µm wide, 0,76 µm high, 0,90 µm deep	Large compartment, lument contains electron-lucent cargo and electron-dense membrane whirls. Endocytic compartment near limiting membrane.	60	Lysosome	4	Mitochondrial membrane within 30nm of the lysosomal membrane.
Spot 5	0,204	0,904	*5,692*	Stop-and-go movement. Multiple streaks forming towards surrounding GFP+ spots.	+	0,71 µm wide, 0,61 µm high, 0,74 µm deep	Electron-lucent lumen, majority of volume is filled with ILVs.	100	Maturing early endosome	5	Mitochondrial membrane within 30nm around the organelle for >500nm.

† Random, non-directional movement

‡ Alternating periods of fast, directional movement and slow, non-directional movement

* Membranes within 30 nm of each other

Figure 4. Correlative live cell – FIB-SEM links live-cell dynamics of compartments to their ultrastructural context :Summary of both the dynamic and the ultrastructural information of compartments visualized in figures 1-3.

LS6.007
A novel cryo correlative SEM-EDS-fluorescence technique used to study biomineralization pathways in foraminifera

G. Mor Khalifa[1], D. Kirchenbuechler[2], N. Koifman[3], O. Kleinerman[3], Y. Talmon[3], M. Elbaum[2], J. Erez[4] L. Addadi[1], S. Weiner[1]

[1]Weizmann Institute of Science, Structural Biology, Rehovot, Israel
[2]Weizmann Institute of Science, Materials and Interfaces, Rehovot, Israel
[3]Technion-Israel Institute of Technology, Chemical Engineering and the Russell Berrie Nanotechnology Institute (RBNI), Haifa, Israel
[4]The Hebrew University of Jerusalem, Institute of Earth Sciences, Jerusalem, Israel

gal.mor@weizmann.ac.il

We have developed a novel cryo correlatvie technique that combines optical cryo-fluorescence imaging with high resolution morphological (cryo-SEM), spectroscopic (cryo-EDS) and electron density (BSE) characterization in the scanning electron microscope. We use the cryo correlative approach to study the intracellular biomineralization pathways in foraminifera. Foraminifera are highly abondant marine protozoans. Their external mineralized shells constitute a major part of global calcium carbonte production and their chemistry and isotopes are the main paleoceanographic archive. This makes the understanding of their shell formation processes important and interesting. However, this is challenging as most parts of the cell that produce these shells are inaccessible for optical imaging.

We use in vivo labeling with the cell impermeable fluorescent dye, calcein, to target locations of interest in the biomeralization pathway. Using high pressure freezing we cryo fix the live samples and freeze fracture them to expose the interior part of the shell and observe the cells as close as possible to physiological conditions, ie, fully hydrated and with no EM labeling for contrast. Each foraminifer is first imaged in cryo-SEM at low magnification to obtain an overview image of the fracture surface, and then systematically scanned in SE and BSE modes at medium magnification. The images are stitched together to provide a detailed view of the cytoplasm contents. Specific areas of interest are further imaged at higher magnification and analyzed for their cryo EDS spectrum. The vitrified specimen is then transferred in a cryo-Correlative Light Electron Microscopy (cryo-CLEM) stage to the laser scanning confocal microscope. Cryo- fluorescence images are taken and aligned with the detailed SEM images. Adjustments to the alignment are made using the shell outline and the intracellular symbionts as anchors in the SE mode collage and the fluorescence image (Fig. 1). The sample is then transferred back to the electron microscope where we further collect EDS spectra at locations of interest chosen based on their fluorescent signal in correlative aligned cryo SEM fluorescence image. We than produce a correlated data set coming from four different techniques all taken in cryo mode for each and every location on the sample. Using this correlative approach, we studied the foraminifer cell cytoplasm and analyzed the elemental compositions of different phases within its cellular context.

We observed intracellular Mg2+ rich dense mineral particles. We suggest these may be related to the mechanism of removal of excess Mg2+ from sea water during the mineralization process. We also confirmed the presence of endocytosed sea water vesicles which take part in the mineralization process.

The new cryo correlative approach provides a high resolution view of the cytoplasm, symbionts, and transport vesicles where ions may be concentrated or removed. Ion-sensitive fluorescent dyes and cryo EDS mapping are used to identify the ions. This technique may well have widespread applications to many other shelled single-cell organisms in addition to foraminifera, such as coccolithophorids, diatoms, radiolaria, ciliates and acantharia, as well as for documenting aspects of mineral transport pathways in multicellular organisms.

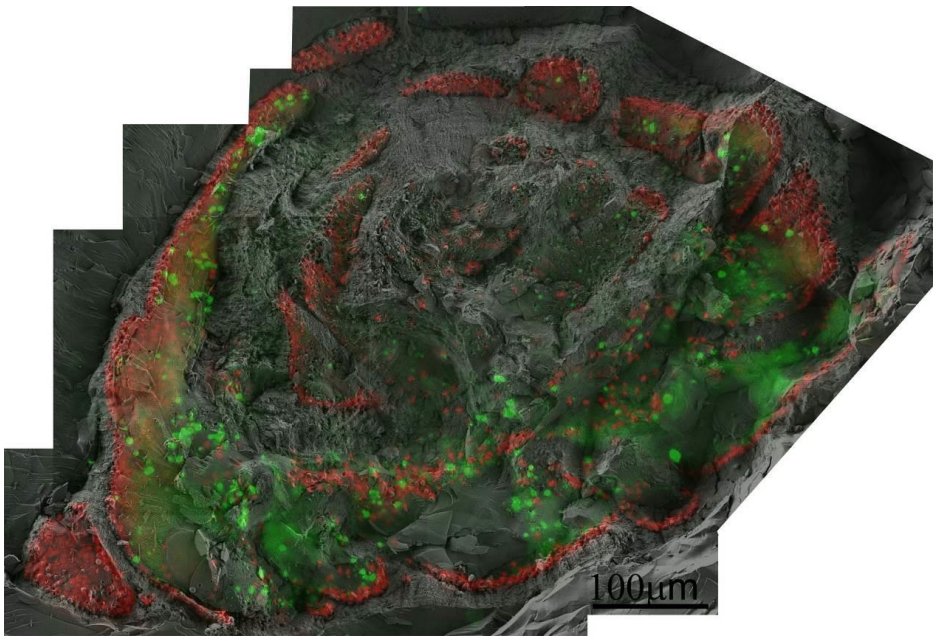

Figure 1. Overlaid Cryo- SEM (secondary electron)/ fluorescence micrograph of a foraminifer (*Amphistegina lobifera*) freeze fracture surface overview. Red fluorescence is of intracellular algal symbionts. Green fluorescence is calcein labelling.

LS6.008
Exploring cryo X-ray microscopy for the visualization of biological tissue in three dimensions

A. Diaz[1], S. Shahmoradian[1], E. H. R. Tsai[1], M. Guizar-Sicairos[1], V. Panneels[1], F. R. Shaik[1]
A. Menzel[1], T. Ishikawa[1], G. Schertler[1], M. Holler[1]

[1]Paul Scherrer Institut, Villigen PSI, Switzerland

ana.diaz@psi.ch

Introduction: X-ray microscopy provides a label-free, non-destructive alternative for imaging biological specimens. Conventional X-ray microscopy operates in the so-called water window, i.e. at photon energies between the absorption edges of carbon and oxygen, at which there is a large natural contrast between organic matter and water [1]. This allows the visualization in 3D of entire cells of a few microns in size at a resolution of approximately 50 nm, or even higher resolution for smaller volumes. However, for visualization of thicker biological specimens, one needs to work at higher photon energies, at which the contrast is very low.
Objectives: We develop X-ray ptychographic tomography at photon energies in the multi-keV regime [2]. This synchrotron-based microscopy technique offers resolutions not limited by lenses, and contrast that is based on the phase shift experienced by the X-rays upon propagation through the specimen, which is much larger than absorption contrast at such energies. A unique instrument for ptychographic tomography, OMNY, has been recently built at the Swiss Light Source, featuring a sample cryo stage in vacuum with nanometer positioning accuracy, based on a successful prototype in air and room temperature that has been previously tested [3]. Key objectives are the development and application of cryogenic preparation protocols of biological cells and tissues that are compatible with subsequent ptychographic tomography measurements, and the development of acquisition strategies allowing these samples to be successfully measured. We aim to establish ptychographic tomography as a viable option to image large 3D volumes of tissue for subsequent higher-resolution characterization with electron microscopy.
Materials and Methods: We first tested ptychographic tomography using unicellular organisms *Chlamydomonas* in plastic-embedded, plunge-frozen, and high-pressure frozen states as test samples [4]. The thickness of the different samples ranged from 18 to 50 microns, using a photon energy of 6.2 keV. More recently, we have uniquely applied and demonstrated this imaging modality to create 3D tomograms of thick biological tissue samples, including plastic-embedded and cryogenically prepared mouse brain and mouse retinal samples.
Results: We show that ptychographic tomography can be successfully used to image the ultrastructure of biological specimens with large volumes of approximately 80x80x40 cubic microns at a resolution of approximately 100 nm in 3D. Despite the tissues being completely unstained, the image quality still allows for the visualization of cells and sub-cellular compartments, as shown in Fig. 1, further providing additional quantitative mass density contrast with a certainty of up to 94%.
Conclusion: Ptychographic tomography shows great potential to become a non-destructive microscopy technique for biological applications, e.g. for locating regions in large volumes for subsequent high-resolution electron microscopy. The volumes and resolutions that we have achieved thus far do not represent a strict cutoff limit, and we continue to improve these numbers through a combination of testing even newer sample preparation strategies and algorithm/software development.

References:
[1] G. McDermott, et al., Ann. Rev. Phys. Chem. 63 (2012) 225-239.
[2] M. Dierolf et al., Nature 467 (2010) 436-439.
[3] M. Holler et al., Sci. Rep. 4 (2014) 3857.
[4] A. Diaz et al., J. Struct. Biol. 192 (2015) 461-469.

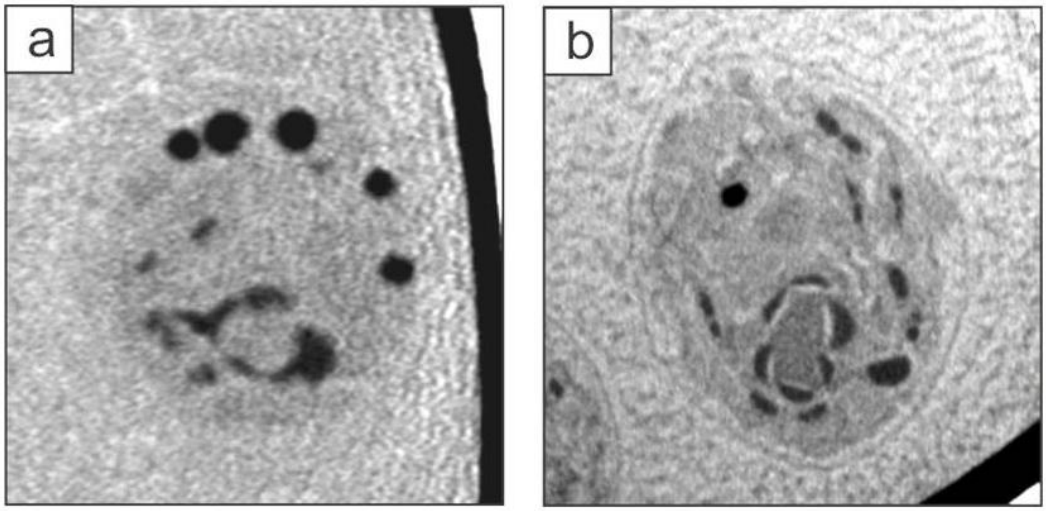

Figure 1. Single slices of approximately 40 nm thickness from 3D tomograms of frozen-hydrated *Chlamydomonas* cells acquired by X-ray ptychographic tomography. (a) Measurement with setup in air using a cryo-jet and (b) measurement with high-accuracy cryo stage in vacuum.

LS6.P001
Reconstruction of brain network with micro/nano tomography

R. Saiga[1], R. Mizutani[1], S. Takekoshi[1], M. Osawa[1], M. Arai[2], A. Takeuchi[3], K. Uesugi[3], Y. Suzuki[3]
V. De Andrade[4], F. De Carlo[4]

[1]Tokai University, Kanagawa, Japan
[2]Tokyo Metropolitan Institute of Medical Science, Tokyo, Japan
[3]JASRI/SPring-8, Hyogo, Japan
[4]Argonne National Laboratory, Lemont, IL, United States of America

tuml_rs19@yahoo.co.jp

The brain consists of a huge number of neurons that form a 3D network. This neuronal network exerts brain functions including memory, consciousness, and verbal ability. We visualized neuronal networks of human [1], mouse [2], and fruit fly [3] brains by using synchrotron radiation micro/nano tomography. The obtained 3D distributions of x-ray attenuation coefficients or phase shift values were traced to build skeletonized models of brain networks [4]. The 3D images themselves were so complicated that they were difficult to comprehend, whereas skeletonized models described in 3D Cartesian coordinates were rather intelligible and better suited for exploring the network configuration. The reconstructed models revealed that the fly brain (Figure 1) exhibits well-organized structures, of which each wiring should be dedicated for a certain information path [5]. In contrast, the network of the human cerebral tissue of nearly the same size (Figure 2) showed randomness and redundancy, which should be relevant to the versatility of our brains.

References:
[1] R. Mizutani et al., Cerebral Cortex 20 (2010) 1739
[2] R. Mizutani, R. Saiga et al., Scientific Reports 6 (2016) 35061
[3] R. Mizutani, R. Saiga et al., J. Struct. Biol. 184 (2013) 271
[4] R. Saiga et al., Microsc. Microanal. 21(S3) (2015) 919
[5] R. Mizutani, R. Saiga et al., Microscopy Today 23 (2015) 12

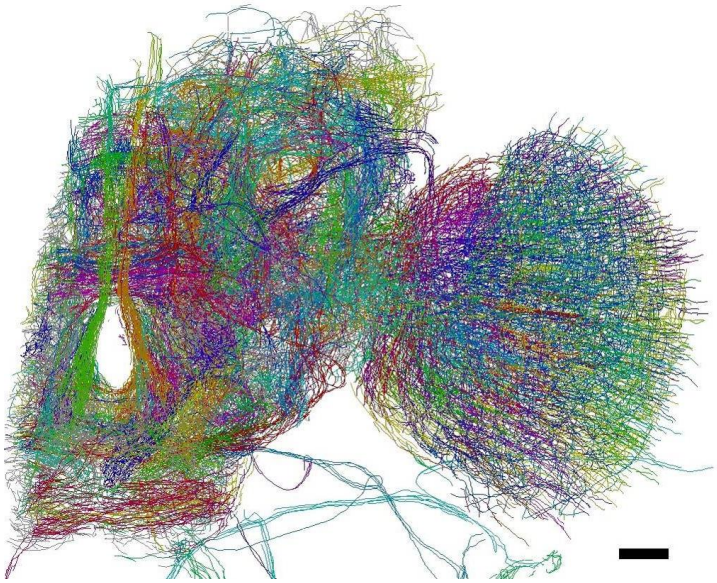

Figure 1. Neuronal network of the left brain hemisphere of a fruit fly *Drosophila melanogaster*. Structural groups are color-coded. Anterior view. Scale bar: 20 μm.

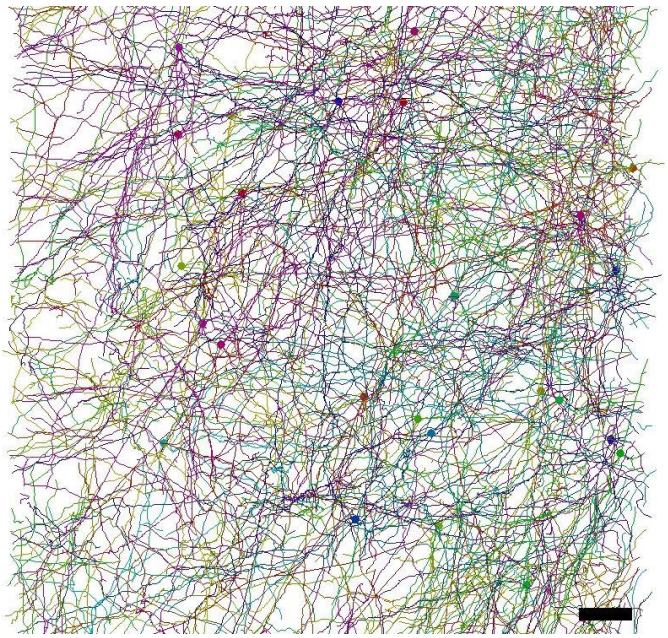

Figure 2. Neuronal network of the internal pyramidal layer of the human cerebral cortex. Neurons are color-coded and their somas are indicated with solid circles. Brain surface is toward the top. Scale bar: 20 μm.

LS6.P003
Development of in situ transmission infrared microspectroscopy system and its application to observation of living cell

T. Ishiguro[1], T. Ube[1], Y. Yoneyama[1]

[1]Tokyo University of Science, Materials Science and Technology, Tokyo, Japan

t.ube@rs.tus.ac.jp

The objective of this study is to develop the method for transmission infrared (IR) spectroscopy of the singe living cell in culture medium solution using conventional IR spectroscopic microscope.
We developed an optical device which designed to perform the processes used in typical cell culture experiments with continuous perfusion of culture medium. Two CaF2 windows exhibiting high IR transmittance were used in the optical cell, which was sealed by Viton O-ring. The interstice between two windows was set to be 12 or 20 micrometer using PET spacer. The medium previously solution exposed to the ambience of a mixture of air and 5vol%-CO2 was supplied using high-performance liquid chromatography (HPLC) pump. The temperature of the specimen was maintained at 307K. A Fourier transform IR spectrometer (FT/IR-6200FV, JASCO Inc.) equipped with an infrared microscope system (IRT-5000, JASCO Inc.) was employed for measurements.
Here we report the use of this IR spectroscopic technique to investigate time-dependent changes in IR spectral features from identical living cells (normal cell of NIH/3T3 and B16 melanona cancer cell). Their initial spectra did not inform the difference of its state of health (i.e. normal or cancerous). However, a time-lapse measurement highlighted the difference of metabolic mechanism. We noticed an absorption peak due to the lactic acid, which was a byproduct of anaerobic glycolysis, and found the characteristic absorption peak of CH3 out-plane bending vibration at 1050 cm-1. Most cancer cells rely on the aerobic glycolysis, a phenomenon to generate adenosine triphosphate (ATP) as the energy source, i.e., the Warburg effect. Therefore the amount of lactic acid can be used as one of the common indexes of the cancerous cells. Our present non-invasive IR spectroscopy technique can be applied to distinguish the state of the health of bio-tissue at the cellular level. Furthermore we observed change of the amount of protein and/or phosphate compounds during the cell division.
As a conclusion, it can be said that present IR micro-spectroscopic method applies to detect the change of the amount of biomolecules at living cellular level.

LS6.P004
Characterizing mineral-bearing vesicles in sea urchin embryos

K. Kahil[1], N. Varsano[1], E. Shimoni[2], I. Kaplan-Ashiri[2], E. Pereiro[3], L. Addadi[1], S. Weiner[1]

[1]Weizmann Institute of Science, Structural Biology, Rehovot, Israel
[2]Weizmann Institute of Science, Chemical Research Support, Rehovot, Israel
[3]ALBA Synchrotron Light Source, MISTRAL Beamline−Experiments Division, Barcelona, Spain

keren.kahil@weizmann.ac.il

Sea urchin embryos have endoskeletons comprised of two calcitic spicules. Spicule growth takes place by the initial deposition of amorphous calcium carbonate (ACC)1 in vesicles inside the spicule-forming cells2(PMCs). The calcium in the mineral-bearing vesicles was recently reported to originate from body fluid internalization and in part from calcium channels3.
Our questions are: what is the Ca concentration in the vesicles? Is there a difference in Ca concentrations in the vesicles ranging from sea water to mineralized CaCO3? What is the mineral phase of CaCO3 in the vesicles? Answering these questions will allow us to better understand the processes and events leading to the initial precipitation of mineral in the PMCs.
Methods: cryo-scanning electron microscopy (SEM), cryo-SEM - energy dispersive spectroscopy (EDS) and cryo-soft X-ray tomography (SXT).
Results: Using cryo-SEM to image high pressure frozen and cryo-sectioned samples of embryos, we were able to detect several types of vesicles inside the PMCs. Some vesicles have granulated texture, some appear smooth, some have backscattered electrons signal, and some contain lipids or proteins (Fig. 1). Performing EDS measurements under cryogenic conditions revealed that some of these vesicles are rich in sodium, which indicates sea water internalization. Other vesicles give signals for potassium and calcium and are still under investigation.
In order to perform quantitative Ca mapping of the cell content in 3D we apply cryo-soft X-ray tomography (SXT). Performing cryo-SXT using energies in the Ca near-edge region will allow us to determine the Ca concentrations in intra-cellular vesicles in PMCs. Preliminary results obtained by this method provided a proof of concept of the feasibility of the technique. Figure 2 shows a slice through a 3D reconstruction of a tilt series obtained by cryo-SXT. In this image the many vesicles around the nucleus have different grey levels, indicating different levels of carbon and perhaps even different levels of calcium.
We conclude that the compositional landscape of the vesicles in the PMCs, some of which fulfil a fundamental role in the mineralization of the spicules, is complex

References:
[1] E. Beniash, J. Aizenberg, L. Addadi, S. Weiner, Amorphous calcium carbonate transforms into calcite during sea urchin larval spicule growth. P. Roy. Soc. B-Biol. Sci., 264 (1380), 461-465, (1997).
[2] N. Vidavsky, S. Addadi, J. Mahamid, E. Shimoni, D. Ben-Ezra, M. Shpigel, S. Weiner, L. Addadi, Initial stages of calcium uptake and mineral deposition in sea urchin embryos. Proc. Natl. Acad. Sci. U.S.A, 111 (1), 39-44, 2014.
[3] N. Vidavsky, S. Addadi, A. Schertel, D. Ben-Ezra, M. Shpigel, L. Addadi, S. Weiner, Calcium transport into the cells of the sea urchin larva in relation to spicule formation. Proc. Natl. Acad. Sci. U.S.A, 113(45), 12637-12642,2016.

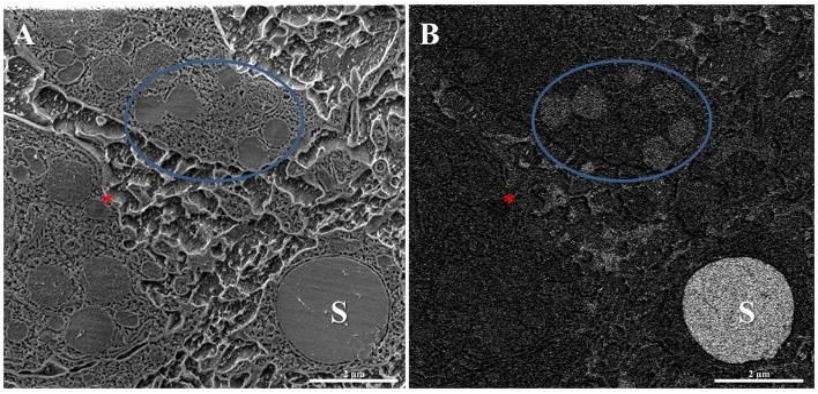

Figure 1. Cryo-SEM images of a high pressure frozen and cryo-sectioned sample showing a spicule (S) with two adjacent PMCs. (A) SE image, (B) BSE image. Six vesicles (in the circle) with different textures have BSE signals, which indicate electron dense contents. The vesicle marked by an asterisk appears darker than the surrounding, indicating carbon rich content such as in lipids or proteins.

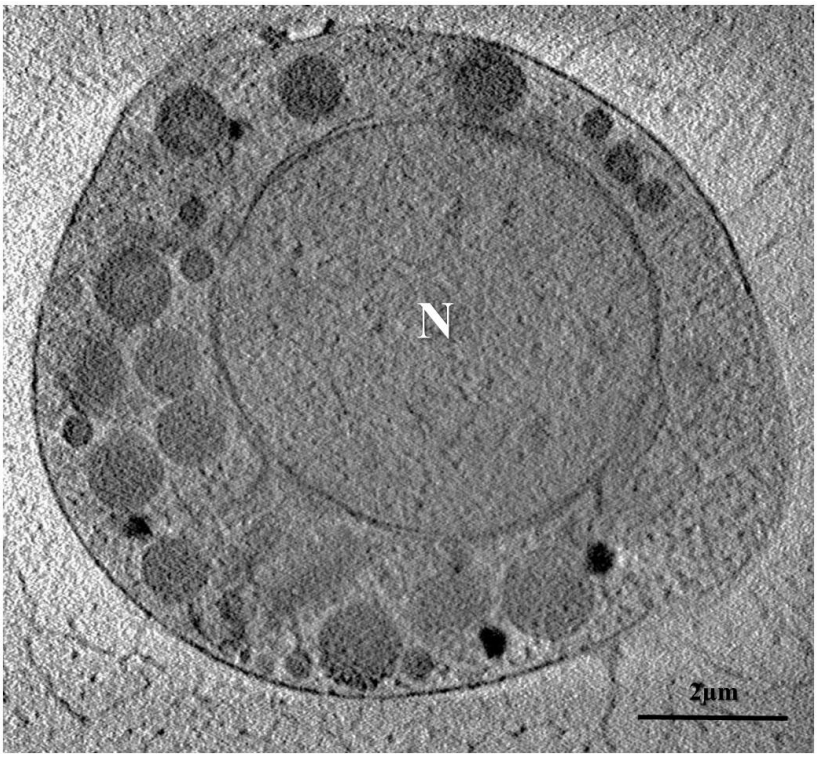

Figure 2. A slice through a 3D reconstruction of soft X-ray tomogram of a cell disaggregated from a sea urchin embryo. The different levels of grey in the vesicles around the nucleus (N) are indicative of variations in carbon and calcium content.

LS6.P005
Raman microspectroscopy and multiphoton microscopy for label-free monitoring of cardiac tissue remodeling

J. Marzi[1,2], E. Brauchle[1,2], A. Biermann[3], K. Brockbank[4], U. A. Stock[3], K. Schenke-Layland[1,2,5]

[1]Universitätsklinikum Tübingen, Forschungsinstitut für Frauengesundheit, Tübingen, Germany
[2]Fraunhofer Institute for Interfacial Engineering and Biotechnology (IGB), Department of Cell and Tissue Engineering, Stuttgart, Germany
[3]University Hospital Frankfurt, Department of Thoracic-, Cardiac and Thoracic Vascular Surgery, Frankfurt, Germany
[4]Tissue Testing Technologies LLC, Clemson University, Medical University of South Carolina, Charleston, SC, United States of America
[5]David Geffen School of Medicine at UCLA, Department of Medicine/ Cardiology, Cardiovascular Research Laboratories, Los Angeles, CA, United States of America

julia.marzi@igb-extern.fraunhofer.de

Introduction: For the clinical application of natural and engineered tissues there is a need to improve methods for long-term storage that can preserve extracellular matrix (ECM) tissue structures. Transplanted heart valve leaflets require intact ECM structures to retain physiological and biomechanical function, which extends lifetime post-transplantation. Preservation methods, such as conventional cryopreservation (CFC), have been shown to result in ice formation and tissue damage, limiting the leaflet"s lifetime. An alternative is vitrification (IFC), which avoids ice formation.
Objectives: The aim is to analyze ECM remodeling in IFC and CFC treated leaflets in an ovine animal model 12 months post-transplantation. Current monitoring techniques such as echocardiography or immunological assays only allow for analysis of physiological function or inflammatory processes. Raman microspectroscopy and multiphoton (MP) microscopy were applied as new tools for the label-free monitoring of remodeling in the leaflets ECM.
Materials and Methods: Raman spectra from ovine untreated, CFC and IFC cryopreserved leaflet tissues were obtained to define the influence of cryopreservation and transplantation on the heart valve"s ECM. The collagen-rich fibrosa layer of CFC and IFC heart valves was analyzed after 12 months in vivo. Untreated heart valves served as a control. All samples were explanted, placed on glass-bottom dishes with PBS and measured within 48 h. A custom-built near-infrared Raman microspectroscope was used for all measurements. 30 spots in each tissue were targeted to define the ROI of spectral data acquisition. Spectra of collagen structures in the fibrosa were collected (10x10s each spectrum) and multivariate data analysis (MVA) techniques were applied to compare the resulting biological fingerprint and to identify tissue alterations on a molecular level.
MP/Second-Harmonic-Generation (SHG) excitation was applied for label-free imaging of collagen and elastic fibers. Images were taken with a MP/SHG laser system at the excitation wavelength of 760 nm inducing ECM structure-dependent autofluorescence (Collagen) and SHG (Elastin).
Results: Raman microspectroscopy and MVA of the ECM specific Raman fingerprint region were able to define differences in ECM remodeling of CFC- and IFC-treated leaflets. Long-term results of explanted leaflets could show that after one year of implantation the ECM of IFC treated leaflets resembled the native tissue, whereas the ECM of CFC treated leaflets lack integrity after cryopreservation treatment and transplantation. Similar results were obtained in MP/SHG images, visualizing collagen and elastin structures. Collagen structures are more sensitive to the freezing procedure than elastic fibers. CFC treated leaflets did not show differences in their overall SHG signal intensities. In comparison to IFC-treated leaflets, which obtain the same collagen alignment and structure as fresh tissues, CFC-treated tissues show alterations in their structural ECM arrangement (Fig.1). Those results indicate tissue remodeling but no degradation in CFC treated tissues. This work demonstrates that the IFC method allows for preservation of matrix structures, potentially enabling a longer lifetime within the patient.
Conclusion: Raman microspectroscopy and MP imaging are powerful tools, able to evaluate the current state of ECM integrity before and after cryopreservation on a molecular and structural level. Combined with MVA the sensitivity of these technologies is appropriate for the contact-free identification of structural damages on tissues.

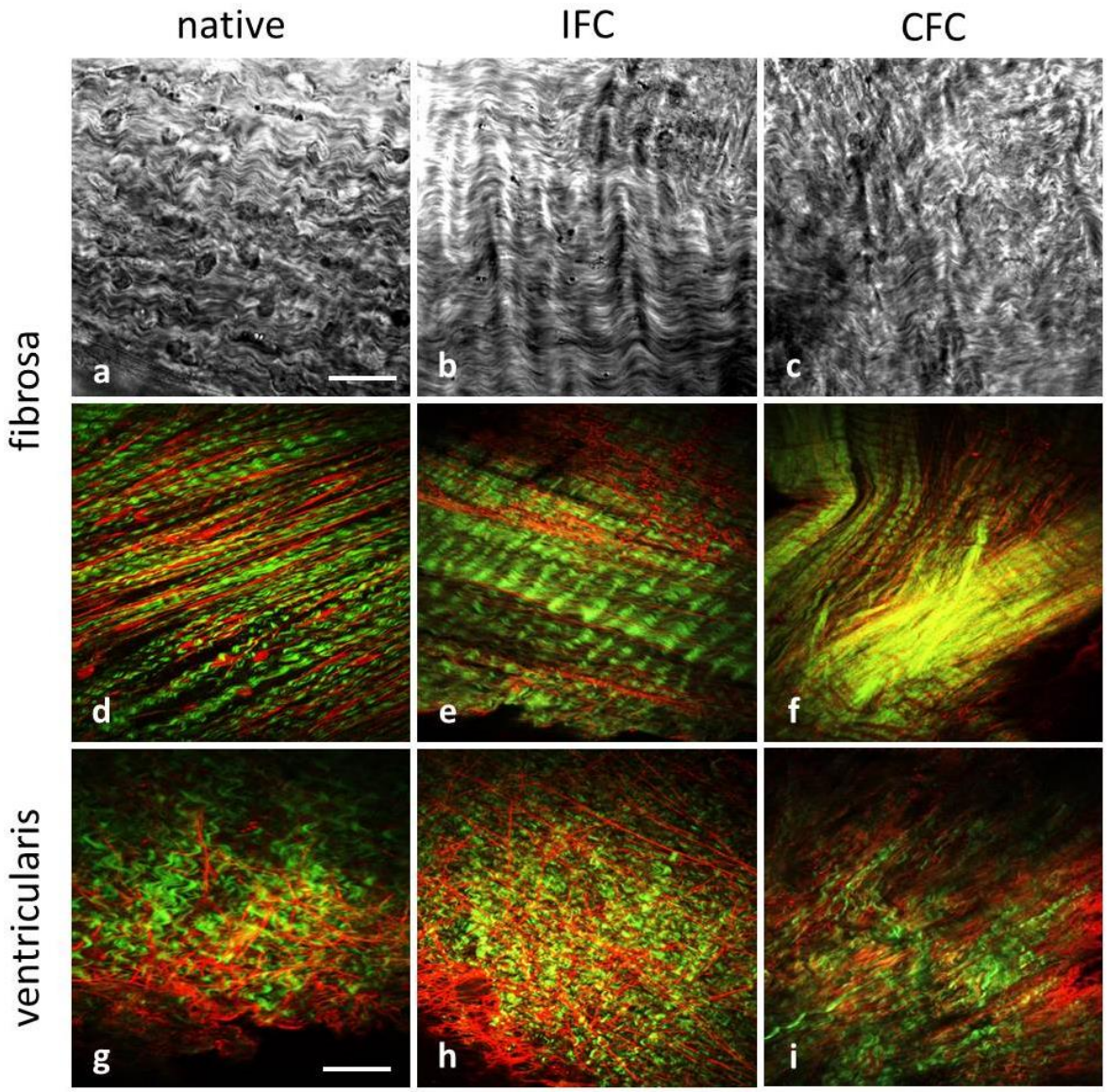

Figure 1. Brightfield (**A-C**) and MP/SHG (**D-I**) images of fibrosa (**A-F**) and ventricularis (**G-I**) of fresh and treated leaflets after 12 months in vivo. CFC leaflets (**C, F, I**) show broken collagen structures. IFC leaflets (**B, E, H**) resemble the native ECM (**A, D, G**). green: collagen, red: elastic fibers; scalebar brightfield = 20µm, MP = 60µm.

LS6.P006
Real-time monitoring the endothelial reaction induced by R-deprenyl using holographic microscopy and impedance-based method.

E. Lajkó[1], K. Magyar[2], L. Kőhidai[1]

[1]Semmelweis University, Department of Genetics, Cell- and Immunobiology, Budapest, Hungary
[2]Semmelweis University, Department of Pharmacodynamics, Budapest, Hungary

lajesz@gmail.com

Introduction: There is an increasing interest in therapies, which can promote the endothelial repair or prevent the endothelial cell damage in various diseases attributed to the endothelial injury (e.g. atherosclerosis, neurodegeneration). The *R*-deprenyl (RD) was shown to exert positive effects in the aforementioned diseases [1] and its effects were suggested to be partly mediated by modulating the re-endothelization. The impedimetry [2] and holomicroscopy [3] allowing real-time and quantitative monitoring of cellular functions (adhesion, migration, and viability) could represent useful tools for the high content analyses of drug effects.
Objectives: In this work, our aim was to analyze the effect of RD and its derivatives on endothelial (i) cell adhesion, (ii) migration and (iii) viability as well as (iv) to evaluate if the metabolites could contribute to the actions of RD.
Materials and Methods: The effects of *R*- and *S*-deprenyl (SD) as referent molecules and the metabolites of RD (*R*-amphetamine (RA), *R*-methamphetamine (RMA), *N*-desmethyl-*R*-deprenyl (DMD) and *R*-deprenyl-*N*-oxide (DNO)) were examined on HMEC-1 microvascular endothelial cell line. The adhesion modulator and cytoprotective effects of the tested ligands were detected by the impedance-based xCELLigence SP System. The holographic microscope, HoloMonitor M4, was used for the morphometry and migration studies. The expression of adhesion molecules and apoptosis marker were measured by FACSCalibur flow cytometer.
Results: The RD (10^{-10} - 10^{-8} M) had slight, but significant adhesion inducer effect, which was proved to be stereoselective. The observed changes in the morphometry parameter (area and optical thickness) corresponded well with the adhesion modulator effects of the enantiomers. Among the metabolites DNO also increased the cell adhesion, which effect was more pronounced and expressed in a wider concentration range (10^{-12} - 10^{-7} M) than in case of RD. Based on the impedance curves and morphological indices (e.g. irregularity) as viability markers the deprenyls did not have toxic effect; the cells showed typical flat and elongated shape during time interval. The deprenyl derivatives elicited no significant effect on the expression of β1-, β3-, α2-integrin molecules as compared to the control. *R*-deprenyl (10^{-9} M) provoked the straight movement of HMEC-1 cells by increasing the migration (distance) and decreasing the motility (actual path). In contrast, the SD (10^{-8} M) decreased all migratory indices (migration, motility and motility speed). The impedimetric measurements showed that both RD (10^{-12} - 10^{-9} M) and DNO (10^{-6} M) could prevent/moderate the cytotoxic effect of L-homocysteine known as an inductor of endothelial damage.
Conclusion: Our results indicate that the endothelial cell adhesion and locomotion could be a new therapeutic target of RD. *R*-deprenyl could have a potential role in rescuing endothelium, facilitating endothelial repair and its metabolites (e.g. DNO) could contribute to these effects. The applicability of impedimetry and holographic phase imaging for characterizing pharmacological effects of drugs on endothelial repair mechanisms was also clearly suggested.

References:
[1] Magyar K. et al. (2010) Neurochem Res, 35:1922-32.
[2] Lajkó E. et al. (2012) Neural Transm, 119:545-56.
[3] Tóth, A. E. et al. (2014) PLoS One 9: e100152

LS6.P008
Spatial structure of female seminal receptacle sperm-storage site in Drosophila by 3-D correlative microscopy

K. Rechav[1], V. Brumfeld[1], E. Zelinger[2], Y. Heifetz[2]

[1]Weizmann Institute of Sciense, Chemical Recearch Support, Rehovot, Israel
[2]The Hebrew University of Jerusalem, Entomology, Rehovot, Israel

emrechav@weizmann.ac.il

Drosophila females have two types of internal sperm storage organs. A pair of spermathecae (long term sperm storage) and single seminal receptacle (short term storage). The seminal receptacle is an elongated closed end tubular structure. The sperm cells keep motility during storage in it for several weeks with no docking period as in mammalians or further activation. The seminal receptacle provides a microenvironment that maintains the active, motile sperm. Thus, it is possible that motile sperm interact with molecules secreted by the epithelium and that this sperm-female interaction plays a role in maintaining and/or regulating sperm functionality. There is relatively little known and much to be learned about the factors that govern sperm storage in the female reproductive tract.
Herein we present a triple volumetric correlative approach combining confocal laser fluorescent light microscopy, micro-CT X ray tomography and focused ion beam - scanning electron microscopy (FIB-SEM) to study morphological aspects of the seminal receptacle to gain an insight into the cellular features of mated females and examine possible interactions between sperm and epithelium. We have developed a modular approach with modified preparation protocols, allowing sequential visualization at the different instruments.
Using this triple correlative approach we show spatial distribution of fluorescent markers in localized areas of the seminal receptacle, make visible the cellular differences between vesicle formation in the seminal receptacle before and after mating. We also examined the lumen lining of the distal seminal receptacle before and after mating and noted a close interaction between sperm and the cellular secretary layer lining the lumen suggesting a possible interaction. Correlative methods refer to any application of two or more distinct microscopy techniques to the same region of a sample, generating complementary morphological, structural and chemical information that exceeds what is possible with any single technique.

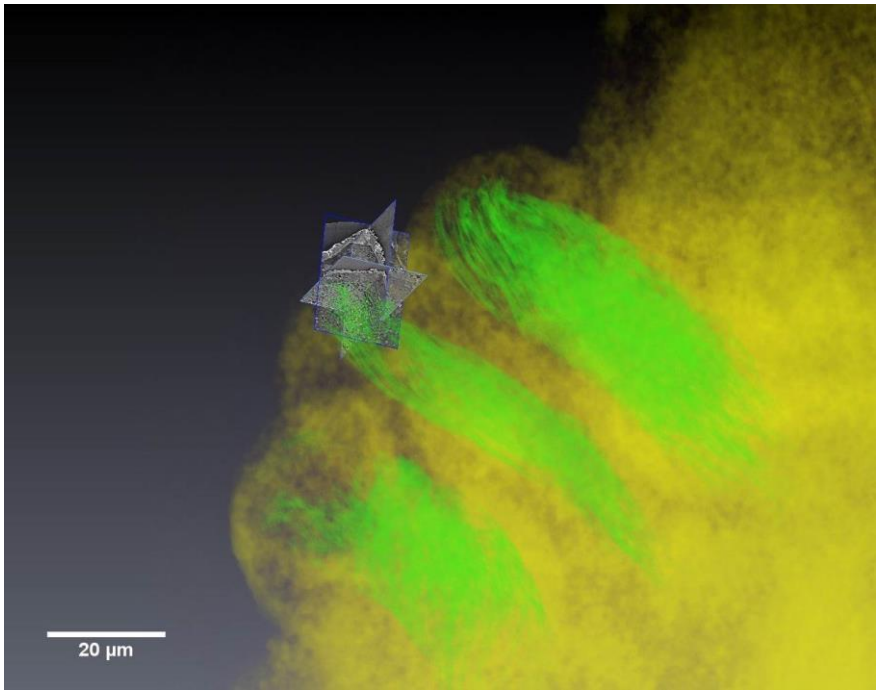

Figure 1. Triple correlative volume imaging. The seminal receptacle whole organ (CT) with localised bundles of sperm cells (FM) and FIB-SEM imaging of a particular site of seminal receptacle tube.

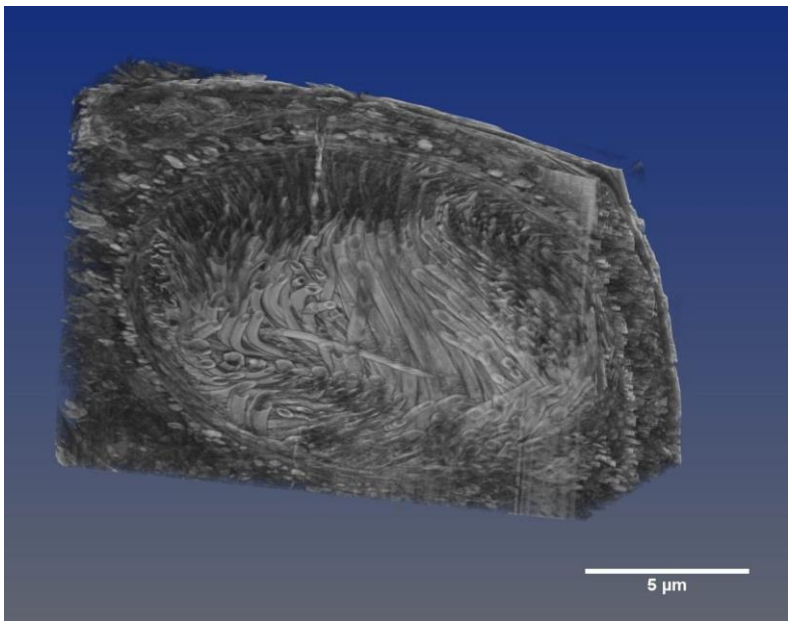

Figure 2. FIB-SEM 3D model. Zoom-in on the internal organization of seminal receptacle channel and spatial distribution of the sperm cells.

LS6.P009
Early effects of ionizing radiation on the extracellular matrix of bladder and recturm visualized by atomic force microscopy

S. Kotova[1,2], P. Timashev[3], G. Belkova[1], M. Kochueva[4], K. Babak[5], A. Maslennikova[4], A. Solovieva[1]

[1]N.N.Semenov Institute of Chemical Physics, Polymers and Composites, Moscow, Russian Federation
[2]Federal Research Clinical Center of the Federal Medico-Biological Agency of Russia, Moscow, Russian Federation
[3]Institute of Photonic Technologies, Research center "Crystallography and Photonics", Troitsk, Moscow, Russian Federation
[4]Nizhny Novgorod State Medical Academy, Nizhny Novgorod, Russian Federation
[5]N.I.Lobachevsky Nizhny Novgorod State University, Nizhny Novgorod, Russian Federation

slkotova@mail.ru

Introduction: The adverse effects of radiation therapy of pelvic area on the normal tissues still present an important problem of the modern clinical oncology. Only scarce information is available on the processes of damage and subsequent remodeling of the extracellular matrix (ECM) occurring early after the action of ionizing radiation.
Atomic force microscopy (AFM), extensively used in the studies of the ECM complex architecture, may provide a new insight into this problem.
Objectives: To apply AFM for tracking the early damaging effect of ionizing radiation on the collagen structures in the submucosal region of the experimental animals" bladder and rectum.
Materials and Methods: The studies were performed on white outbred rats. The pelvic area was irradiated with a 60Co γ-irradiation source (beam energy 1.25 MeV), the total doses were 2, 8, 10, 12 and 22 Gy. The intact (non-irradiated) rats were used as a control group.
AFM images of the fixed tissue slices on glass slides were acquired with a Solver P47 AFM instrument, in the semi-contact mode. For the quantitative assessment, we applied a flicker-noise spectroscopy (FNS) parameterization technique.
A standard van Gieson"s staining protocol was applied for the histological study.
Results: Our AFM study suggests that collagen fibers and fibrils in the submucosa of intact rat bladder are packed in densely interlaced bundles forming a wavy pattern. The microstructure of the collagen backbone of the rectal submucosa is formed by a 3D meshwork of fibers, which consists of a smaller-scale finely interlaced network of thin collagen fibrils.
The low-dose (2Gy) radiation treatment had no immediate (1 day post-treatment) effect on the hierarchical collagen structures in the bladder and rectum. 1 week post-treatment, the first changes at the level of fibrils were detected: in the bladder, a visible decrease in the fraction of naked collagen fibrils (Figure 1), as well as appearance of regions entirely covered with a thick layer of unstructured material; in the rectum, appearance of regions with essentially thicker and denser fibrils. We assign these changes to the initial matrix protein destruction processes taking place early in the course of radiation damage development.
Drastic alterations of the ECM structure were observed 1 month after the low-dose (2 Gy) irradiation. AFM imaging visualized thick bundles of collagen fibers with a pronounced unidirectional orientation. The fibrils inside the fibers were tightly packed in a quasi-parallel manner. These findings may indicate the onset of post-radiation fibrotic changes.
With the dose increase, the negative effects of irradiation on the ECM became more evident. The higher doses caused a visible radiation damage in the bladder and rectum ECM, ranging from relatively minor changes at the 8 Gy dose up to severe destructive effects at the dose of 22 Gy. The signs of the ECM destruction included: loosening of the collagen network, release of non-fibrous ECM material, thickening and disordering of collagen fibrils. At the highest dose of 22 Gy, the entire collagen hierarchical structure underwent major changes with collagen fibers forming thick oriented bundles continuously covered with the non-fibrous matrix elements. The observed visual changes in the ECM morphology correlated well with the findings of the FNS analysis.
Unlike the AFM study, the parallel histological study did not reveal any significant ECM alterations indicative of the radiation damage.
Conclusion: The AFM study appears superior to the optical microscopy-based studies in its sensitivity to early radiation damage of tissues, providing valuable additional information on the onset and development of the ECM destruction and remodeling.
Acknowledgement: This study was financially supported by the RFBR grant 15-02-04505 and by the RSF grant 16-15-10432.

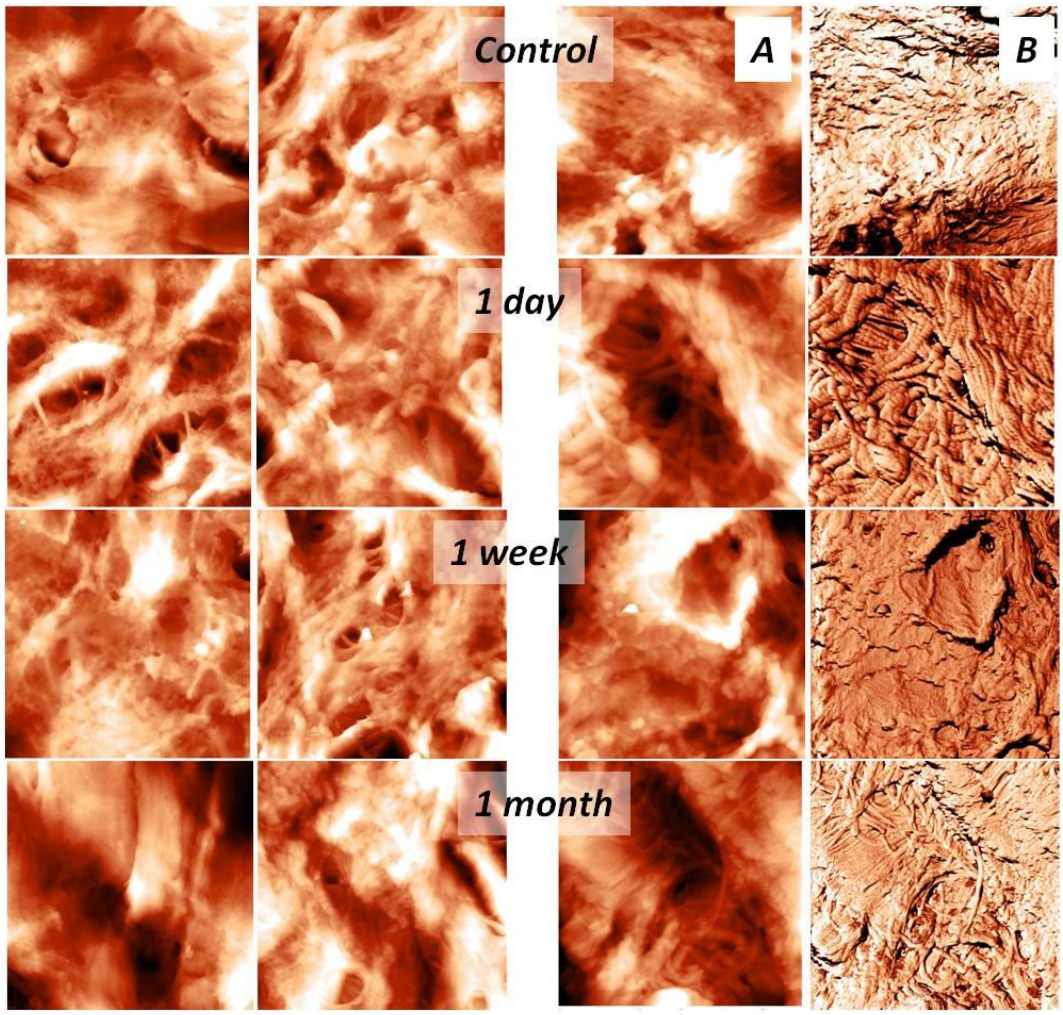

Figure 1. The bladder ECM changes with the time elapsed from the low-dosage (2 Gy) treatment. Left panel – topography images (14x14 µm), Right panel – topography (A) and corresponding phase (B) images (6x6 µm).

LS6.P010
CLEM and SEM in inflammatory responses

R. Oosterveld[1], M. Baumgarten[2], H. Herwald[2], G. Mulder[1], J. Zahn[1]

[1]Phenom World, Eindhoven, Netherlands
[2]University of Lund, Department of Clinical Sciences, Lund, Sweden

ria.oosterveld@phenom-world.com

Introduction: Correlative microscopy refers to the combination of light and electron microscopy. The Delphi is an all-in-one solution for correlative light and electron microscopy (CLEM). It is an integrated desktop scanning electron microscope (SEM) including an inverted widefield fluorescence microscope. This integration enables scientists to perform correlative microscopy without the challenges typically associated with CLEM:

- The Region of Interest (ROI) does not need to be retrieved, as working with the Delphi offers staying in the same ROI switching from LM to EM and vice versa;
- The sample does not need to be transferred from one microscope to the other, saving sample quality as well as time;
- Correlation accuracy is fully automated, highly accurate and user-independent.

The Delphi is the world's first fully integrated CLEM solution that enables fast correlative microscopy with unique overlay precision. It is suitable for a wide range of applications in life science research, as up to four fluorescent colors can be observed and put into context with electron microscopy images. Furthermore, several sample types including whole cells, thin cells or tissue sections can be imaged. Here we examine the modulation of inflammatory responses to bacterial infections.

Severe infectious diseases, including sepsis, remain a serious medical challenge worldwide. Clinical symptoms of patients suffering from sepsis are a culmination of complex interactions between the infecting microorganism and host immune responses, such as massive vascular leakage, induction of overwhelming inflammatory reactions, systemic activation of the coagulation system, and impaired fibrinolysis.

Neutrophils (figure 1) play an important role in these processes as their systemic activation can lead to such overreactions. Once activated neutrophils change their morphology and release their content including antimicrobial substances, reactive oxygen species, and vasodilating substances. Consequently, blood constituents can leak into the surrounding tissue and evoke additional damage in organs such as lungs (figure 2). In order to counteract these lesions the host is equipped with an arsenal of antimicrobial agents. Many of these substances such as collagen VI have endogenous antibacterial activity and are able to kill the invading pathogen (figure 3).

A better understanding of the molecular mechanisms that regulate these host responses is needed to develop novel antimicrobial therapies. Notably, our previous work has shown that microscopes are an important tool to monitor bacteria-induced tissue damage and counteracting host responses. Objectives: This study aims to identify and characterize molecular mechanisms that lead to these kind of complications. To accomplish these tasks various models will be employed to examine the inflammatory responses.

Materials and Methods: Various tissue and cell cultures will be studied with SEM and CLEM using the Delphi system in order to visualise the different aspects of the inflammatory responses. The initial SEM experiments focus on the structural changes. Furthermore, details on functional and molecular changes will be explored using the additional information from fluorescent labelling imaged with CLEM.

Results: Preliminary results (figure 1-3) confirm that the Delphi is able to visualise the relevant structures in various samples that need evaluation to further explore the mechanisms that play a role in inflammatory responses.

Conclusion: The SEM images of healthy tissues as well as of bacterial killing provide a good visualisation of different aspects in the inflammatory responses. CLEM will provide even better results as the fluorescence targeted proteins will show the exact locations of the structures of interest.

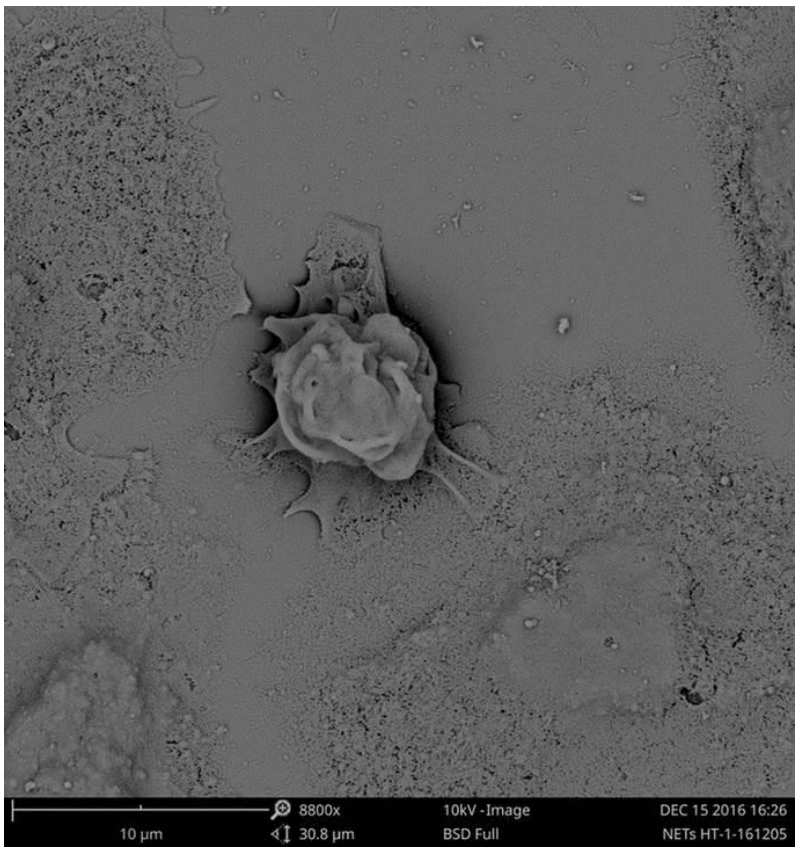

Figure 1. SEM image of inactive neutrophils. Magnification 8,800x.

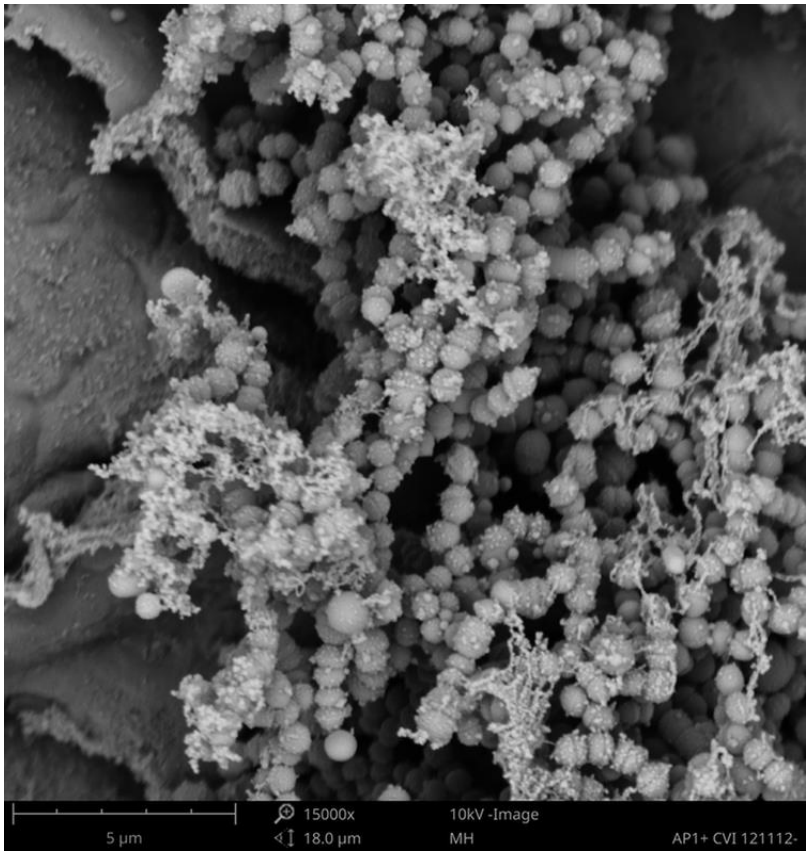

Figure 2. SEM image of healthy lung tissue. Magnification 800x.

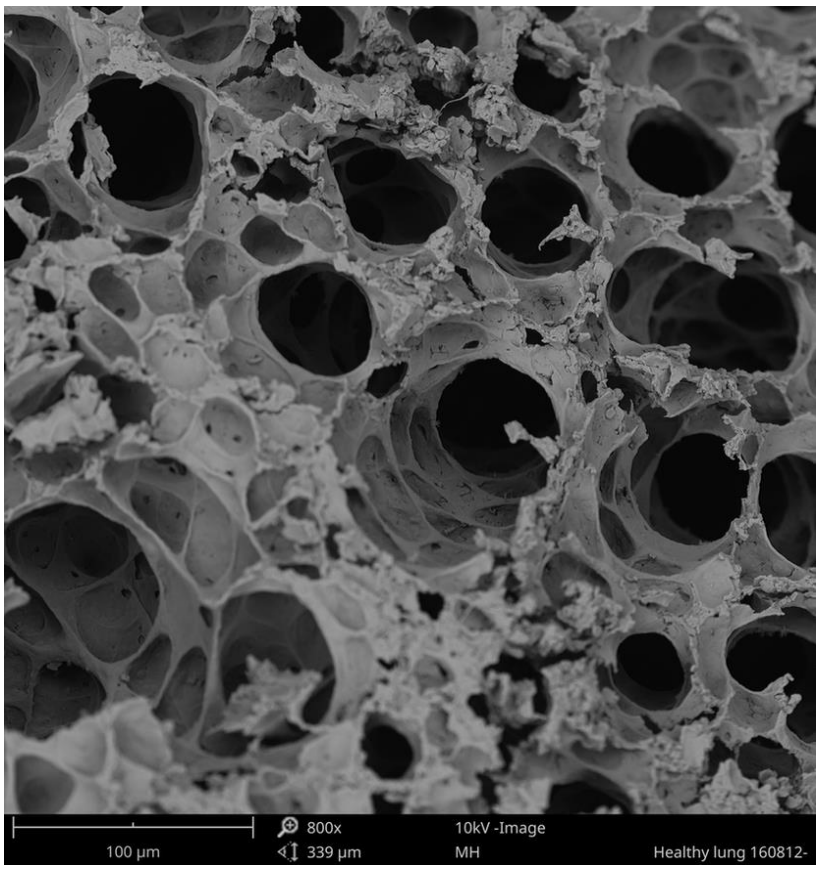

Figure 3. SEM image of pathogen Streptococcus, killed by antimicrobial agent Collagen VI. Magnification 15,000x.

LS6.P011
Optical quantitative phase imaging by focal series reconstruction with a module attachable to microscope camera ports and with a microscope with computer-controlled z-stage

J. Müller[1], A. Eljarrat[1], F. Wang[1], K. Blessing[2], C. T. Koch[1]

[1]Humboldt-Universität zu Berlin, Department of Physics, Berlin, Germany
[2]Friedrich-Alexander-Universität Erlangen-Nürnberg, Interdisciplinary Center for Clinical Research, Erlangen, Germany

johannes.mueller@physik.hu-berlin.de

Introduction: Live cells are almost transparent and must therefore be imaged either by staining to increase their amplitude contrast or by imaging the induced phase shift of light that passes through them. Unlike standard phase imaging methods (e.g. Zernike phase contrast microscopy), quantitative phase imaging (QPI) can measure this phase shift precisely and determine cell characteristics without time consuming and often poisonous staining leading to only qualitative image contrast. Many QPI methods require special equipment, are expensive or introduce significant artefacts. We focus with our approach of QPI by focal series reconstruction (QPIFSR), on a low cost method that only requires standard optical microscopes. We will present two approaches to QPIFSR, our multi focus transport of intensity equation (MFTIE) algorithm that requires an automated sample stage for defocusing and our phase inline astigmatic holography (PIAH) method based on a camera module (patent pending) attached to a standard camera port that avoids having to change the objective lens focus and facilitates an even more quantitative phase reconstruction.
Objectives: Our goal is to offer low cost and quantitative methods for live phase imaging (~2 fps) of live cells that can be used with existing microscopes and their equipment, while preserving the full resolution and field of view. We will introduce MFTIE and PIAH and present their applications in life sciences (e.g. cell morphology, cell monitoring), highlighting their advantages over other cell imaging methods.
Materials and Methods: The data acquisition for MFTIE consists in the acquisition of a special focal series and requires a microscope with a computer-controlled z-stage. The PIAH module, on the other hand, consists of a rotating cylindrical lens plus a camera and can be attached to a standard camera port. Both methods work with halogen illumination with a colour filter or LED illumination. They work with a normal optical microscope and are thus compatible with other imaging techniques, like fluorescence imaging. Both hybrid phase reconstruction algorithms combine variants of the transport of intensity equation (TIE) with an iterative Gerchberg–Saxton-type algorithm (GS) and consider the partial coherence of the light source. PIAH, however, promises a better phase reconstruction over all spatial frequencies by mathematically overdetermining the boundary conditions. Both algorithms run with graphics processing unit (GPU) support.
Results: Figure 1 shows the in-focus image of a HeLa cell without staining from a focal series acquired with a Zeiss Axiovert 200M optical microscope with a 40x objective lens (1.35 NA), a pco.edge 5.5 sCMOS camera and LED illumination with an average wavelength of 525 nm (figure 2). Figure 3 shows the reconstructed phase shift by MFTIE of the HeLa cell, all the spatial frequencies are nicely recovered. Figure 4 is a render of our new PIAH module which can be attached to standard camera ports of optical microscopes.
Conclusion: Our QPIFSR approaches can be used with existing optical microscopes with standard illumination and a PC equipped with a GPU to run the reconstruction. No staining and no special equipment, like gratings or dedicated microscopes are needed. The PIAH camera module can also be used for other imaging applications, like fluorescence imaging. Our approaches have the potential of being simple, fast, low-cost and versatile methods for quantitative phase imaging. We will present our MFTIE algorithm, our PIAH method and compare them with other dedicated methods and discuss their viability.

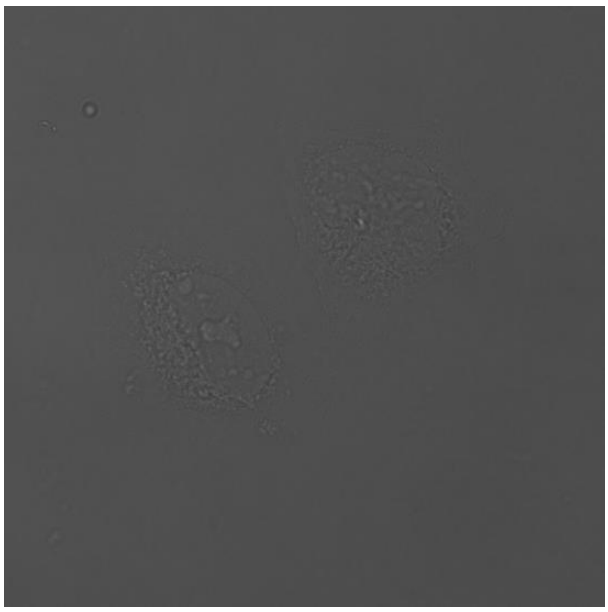

Figure 1. Shows the in-focus image of a HeLa cell without staining from a focal series acquired with a Zeiss Axiovert 200M optical microscope.

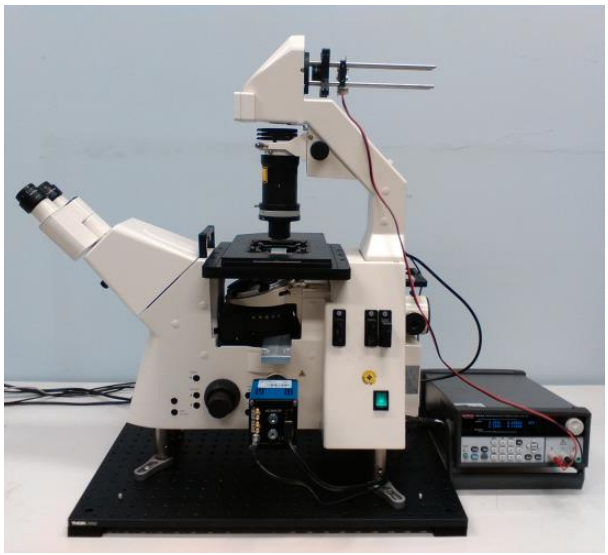

Figure 2. A Zeiss Axiovert 200M optical microscope with a 40x objective lens (1.35 NA), a pco.edge 5.5 sCMOS camera and LED illumination with an average wavelength of 525 nm.

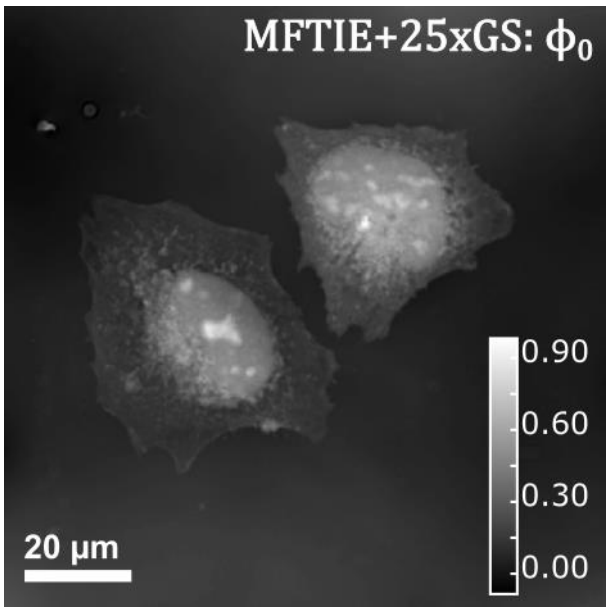

Figure 3. Shows the reconstructed phase shift by MFTIE of the HeLa cell, all the spatial frequencies are nicely recovered.

Figure 4. Is a render of our new PIAH module which can be attached to standard camera ports of optical microscopes.

LS6.P012
Imaging soft tissues in micro-CT using new ethanol method

M. Patzelt[1], J. Mrzilkova[2], P. Zach[2], J. Dudak[3,4], J. Zemlicka[3], F. Krejci[3], J. Karch[3,4], V. Musil[5]
A. Sukop[1], Z. Wurst[2]

[1]Royal Vinohrady Teaching Hospital, Clinic of Plastic Surgery, Prague, Czech Republic
[2]Third Faculty of Medicine, Charles University, Department of Anatomy, Prague, Czech Republic
[3]Czech Technical University in Prague, Institute of Experimental and Applied Physics, Prague, Czech Republic
[4]Czech Technical University in Prague, Faculty of Biomedical Engineering, Kladno, Czech Republic
[5]Third Faculty of Medicine, Charles University, Centre of Scientific Information, Prague, Czech Republic

matej.patzelt@centrum.cz

Introduction: Micro computed tomography (micro-CT) uses X-Rays to create a 3D voxel-based model of the examined object using a set of 2D radiographic projections acquired under different angles. X-Ray imaging of native soft tissues is very problematic due to their low intrinsic contrast. In the past years, several techniques for enhancing the attenuation contrast of soft tissues were developed. It is possible to use either intravascular contrast agents or fixative agents. Most of these techniques are, however, quite expensive, very difficult to use or even toxic. The goal of our study was to create a simple fixation method for ex-vivo soft tissue imaging in micro-CT.
Methodology: In this study, hearts and lungs from 30 mice were used. After meticulous preparation, organs from 27 mice were fixated in ethanol and organs from 3 mice were examined as native specimens. Different concentrations of ethanol and different periods of time of fixation were used. Organs were fixated either in 97%, 50% ethanol solution or in a row of ascending ethanol concentrations (25%, 50%, 75%, 97% each for 12 hours). These organs were scanned after 72 hours, 168 hours and 336 hours of fixation and afterwards compared to native hearts and lungs which were embedded in phosphate-buffered saline (PBS solution) and scanned after 2 hours. All specimens were scanned in custom-built micro-CT systems equipped by photon counting detectors Timepix.
Results: The ethanol method provided contrast enhancement in both studied organs in all used types of ethanol fixation. Fixation in 97% ethanol provided very fast fixation and the contrast among the tissues was visible already after 72 hours of fixation. Fixation for periods of 168 and 336 hours gave better details, especially in lung tissue, where alveolar sacs were visualized. Conversely, this type of fixation caused hardening of the organs. Fixation in 50% ethanol provided best results after 336 hours of fixation, details were not visualized as well as in 97% ethanol, however, samples were not as stiff as in fixation in 97% ethanol. Best results were obtained in fixation in a row of ascending ethanol concentrations; in this type of fixation, all organs were visualized in great details without being damaged.
Conclusion: Our ethanol method is a great option for soft tissue fixation as well as for enhancing contrast among tissues in organs. After the scanning, tissues are available for further staining, for example in phosphotungstic acid and they are still usable for other methods, such as histochemical procedures, or classical histology. The best results were obtained with fixation of the organs in a row of ascending ethanol concentrations.

Keywords: Micro-CT, X-ray microtomography, heart, lungs, morphology, ethanol

LS6.P013
FIB/SEM for site-specific 3D-studies on micropatterned substrates

A. G. Bittermann[1], N. Goedecke[2], U. Keller[3], J. Trahe[3], J. Klingauf[3]

[1]ETH Zürich, ScopeM, Zürich, Switzerland
[2]MicroDuits GmbH, Zürich, Switzerland
[3]WWU Münster, Institut für Medizinische Physik und Biophysik, Münster, Germany

annegreet.bittermann@scopem.ethz.ch

The interaction of cells with their substrate is of particular interest in biomaterial research. Cells react directly on local differences in surface properties. They respond to the topography as well as to the chemical composition of their substrate.
Thin layer plastification (TLP) allows cells to remain on their original substrate while being processed for electron microscopy. Focused Ion Beam-Scanning Electron Microscopy (FIB/SEM) is a technique with which materials of different hardness can be cross sectioned in situ, keeping the interface intact. The milling is highly site specific. Different regions within a micropattern can be accessed individually.
Structuring the substrate surface allows to provoke specific cellular responses. We present some examples of 3D-imaging the ultrastructure of cells at defined spots within a micropattern array: *a)* 2D micropattern as a chemical surface modification: Neurons were cultivated on a glass substrate stamped with a synaptic cell adhesion molecule. Functional xenapses were formed. *b)* 3D micropattern as a topographic surface modification: HuO9 cells were cultivated on an array of PDMS-microposts with a spring constant of 0.8nN/mm. The cells pull on these flexible pillars.
The interaction zone cell-to-substrate is our target of investigation, therefore it was of uttermost importance to keep that zone intact. Cells have been fixed, stained, dehydrated and resin penetrate. After removing the excess of resin (TLP) only a thin layer of resin covered the sample, which was then polymerized, sputter coated and mounted onto SEM-stubs.
Regions-of-interest (ROI) were selected via correlation with light microscopy data (CLEM). For fine localization also topography, high voltage backscatter electron imaging and FIB-manufactured landmarks were used. Cross sections were performed and FIB/SEM slice&view tomograms were acquired.
FIB/SEM in combination with TLP is an excellent tool for in-situ interface studies on an ultrastructural level. As multiple sites can be accessed with high precision, functionally different areas within a patterned array can be discriminated and specific cellular responses can be visualized.

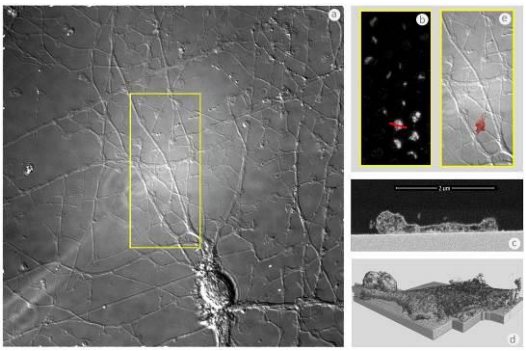

Figure 1. a) DIC-image of a neuron grown on micropatterned glass coverslip. b) Fluorescent image of the boxed area in (a). Red line indicates, where FIB cross sections were performed. c) Example of one FIB/SEM cross section, taken from the indicated area in (b). d) 3D-representation of the reconstructed xenapse. e) Overlay of 3D-reconstruction on LM-image.

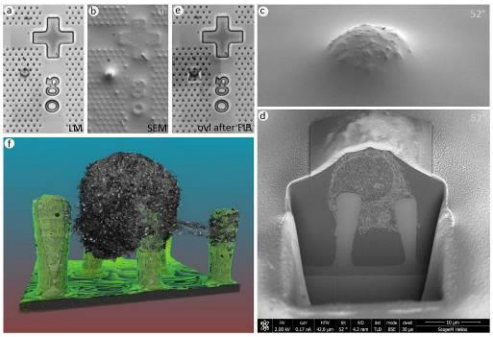

Figure 2. a) Bright field LM image of a micropost array sub-area. b) secondary electron SEM image of the same region as in (a) after thin layer plastification. c) SEM image (SE-mode) of ROI at 52° stage tilt. d) SEM-image (BSE-mode) of ROI in cross section ROI at 52° stage tilt. e) SEM image from ROI (SE-mode) after FIB/SEM tomography at 0° stage tilt overlayed with LM image from (a). f) 3D-visualization of tomogram.

LS6.P014
Schottky BIO FE-SEM for life science applications

T. Schmidt[1]

[1]Hitachi High Technolgies Europe, Electron Microscopy Business, Krefeld, Germany

thomas.schmidt@hht-eu.com

Introduction: The innovative analytical Schottky FE-SEM SU5000 from Hitachi allows a simple transition between high vacuum and variable pressure mode without need to change any differential aperture. With a pressure range up to 300Pa and going from evacuation to observation in 3 minutes or less, the FE-SEM is suitable for most of the samples in life science.
With the Automatic axis adjustment technology (auto-calibration) the user can restore the microscope to its "best condition" on demand providing excellent beam settings / quality even for long term runs, for example during Serial Sectioning or EBSD measurements on bio minerals. The state-of-the-art Back Scatter Detector (BSE) acquires high depth pictures under any conditions.
The robust "draw-out" specimen chamber accommodates large specimens and allows simple tilting and sample rotation; the image stays centered and in focus with the 3D MultiFinder tool. In addition the chamber door can be completely and easily replaced by specialized door systems like Gatan 3View In-Situ Microtome System or the Delmic SECOM In-Situ CLEM system.
Objectives: In the following we would like to show some examples imaged on this system in the various configurations. This also includes samples prepared by the Hitachi Ionic Liquid IL1000 as well as Reconstructed Sections and CLEM Overlays.
Material and Methods: A: Sample had been incubated in IL1000:H2O solution for 30 minutes briefly washed by distilled water and quickly dried on air. Afterwards the sample had been attached to a microscope stub and observed under various conditions to show the IL1000 performance together with SU5000.
B: Sample had been stained by Gatan receipt book method (OTO) and cut to fit in the provided holder. The Serial Sectioning was executed fully automated overnight under variable pressure mode to avoid charging.
Results **–** *please see attached pictures*.
Conclusion: As hopefully shown that Hitachi High Technologies can provide a wide range of products to solve the problem researchers in life science and related fields face every day when handling biological samples in electron microscopes.

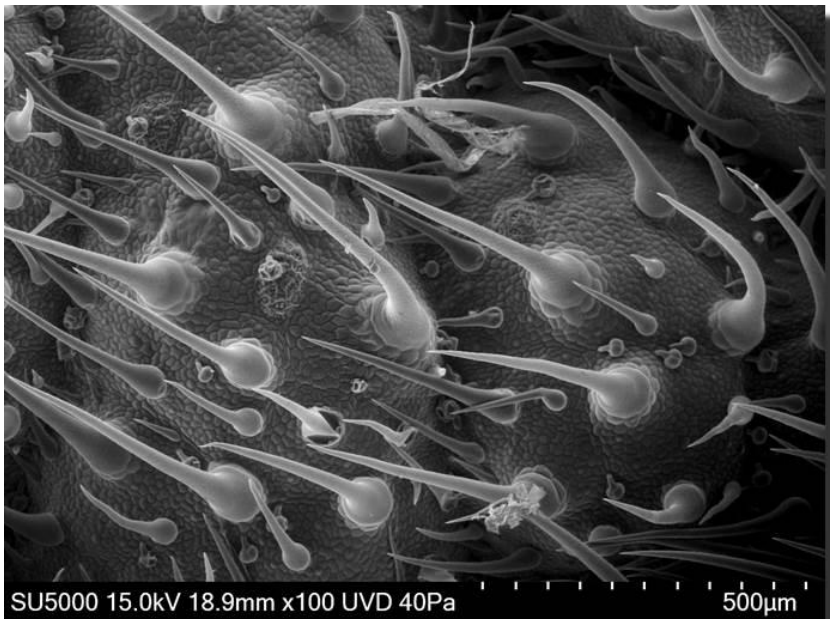

Figure 1. Nettle leave from outside Hitachi High Technologies European Headquarter, uncoated and without any further preparation, observed under 40Pa and 15kV in FE-SEM SU5000.

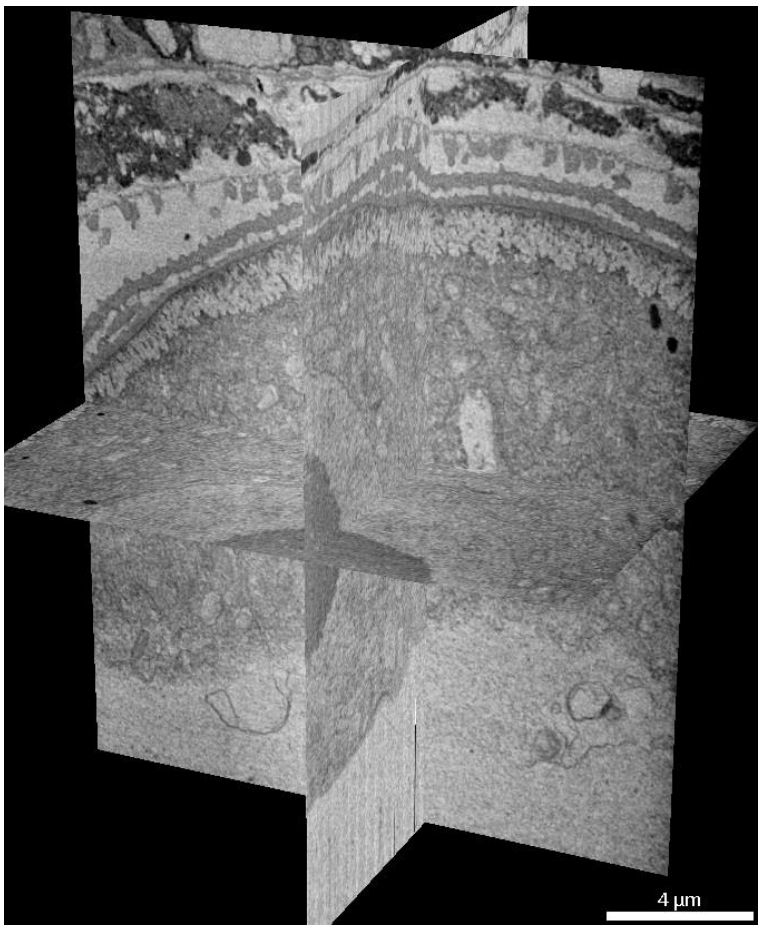

Figure 2. A. thaliana tissue cuts, variable pressure mode (25 Pa), 300 cuts by Gatan 3View 2XP & Hitachi SU5000.

LS6.P015
Quantum dot immunolabeling for exact correlative light and electronmicroscopy– ultrastructural visualization of the targets selected by fluorescent microscopy

T. Uchihara[1], M. Uematsu[1,2], S. Tatsumi[1,2,3], R. Takahashi[2], M. Yoshida[3], E. Adachi[1]

[1]Tokyo Metropolitan Institute of Medical Science, Structural Neuropathology, Tokyo, Japan
[2]Kyoto University, Clinical Neurology, Kyoto, Japan
[3]Aichi Medical University, Neuropathology, Nagakute, Aichi, Japan

uchihara-ts@igakuken.or.jp

Introduction: Quantum dots (QDs) are nanocrystals composed of cadmium (Cd) and selen (Se), which exhibit dual (fluorescent and electron-dense) physical properties.
Objective: Application of QD immunolabeling on human brain containing pathological tau-positive lesions to compare fluorescent image and its counterpart.
Materials and Methods: Human autopsied samples (Pick body disease, Alzheimer disease, corticobasal degeneration) containing tau-positive lesions were routinely fixed with formalin, sliced into 30mm thick floating sections and immunolabeled with an anti-tau monoclonal antibody (AT8)/Quantum dot.
Results: Fluorescence microscopy detected tau-positive lesions (Fig 1 A B). Among them, some target lesions were selected, trimmed and embedded in epon for electron microscopic examination (Fig 1C). Immunofluorescent image of the target lesion and ist immunomicroscopic counterpart were successfully compared with this approach. Ultrastructural details (Fig 1D and C) demonstrates fibers labelled by QD (arrows). Identity of QD was confirmed on the electron microscopic field by the presence of Cd/Se detected though energy-dispersive X-ray spectra (Fig 2, a&b on QD, c&d on back ground). Mapping these Cd/Se-positive pixels highlighted QD (Fig2B) contrasted against the background (Fig2C). It is now possible to compare ultrastructural details of Pick bodies (Am J Med 2012;180:1349-1397) and various neurofibrillary tangles (Acta Neuropathol Comm 2014;2:161) with its light microscopic counterpart.
Conclusion: Correlative light and electron microscopy was successfully achieved with QD immunolabeling on routine autopsy human brain samples. Because tau-positive lesions are quite heterogeneous even in a microscopic field, light microscopic identification of a target prior to immunoelectron microscopy for exact comparison is the prime advantage of this approach, which has not been achieved so far.

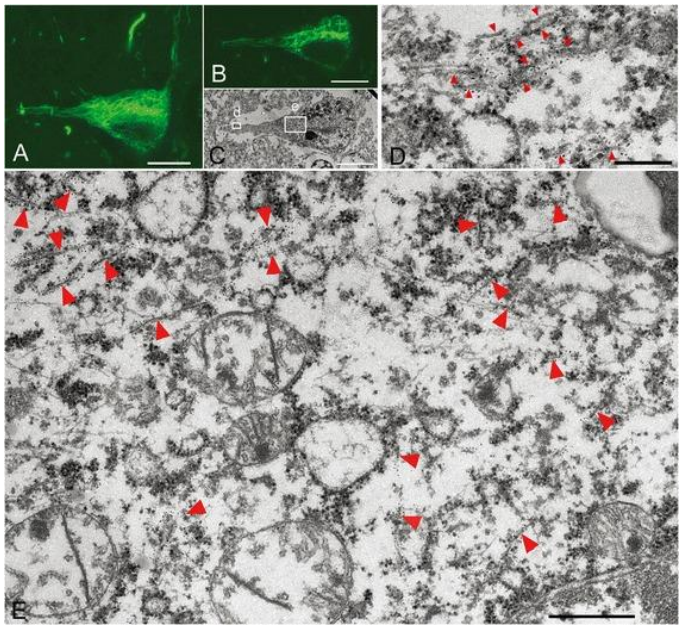

Figure 1

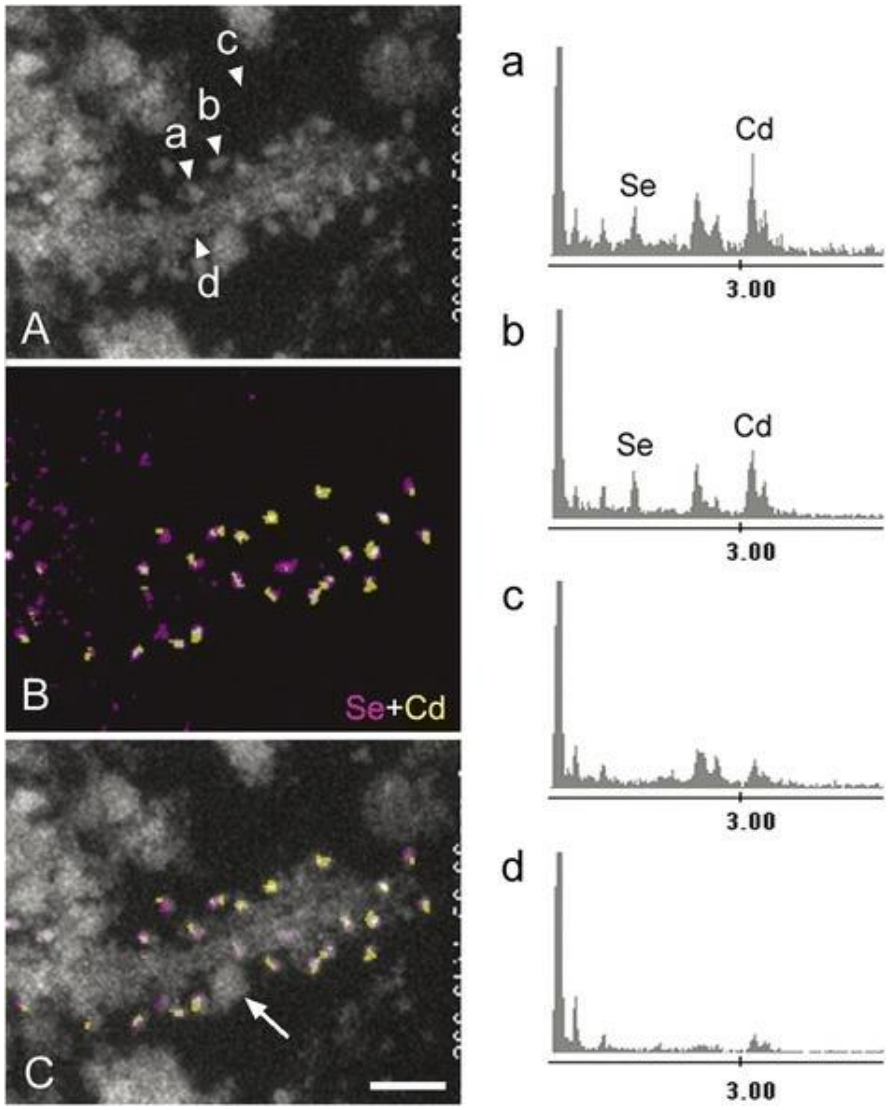

Figure 2

LS6.P016
Correlative imaging by time-lapse holographic microscopy and 3D FIB-SEM tomography – a unique look at cancer cell behavior

J. Balvan[1,2], K. Rosikova[1], J. Javurek[1], M. Masarik[2], A. Hampl[3], V. Kostal[1]

[1]TESCAN, Brno, Czech Republic
[2]Masaryk University, Faculty of Medicine, Department of Physiology, Brno, Czech Republic
[3]Masaryk University, Faculty of Medicine, Department of Histology and Embryology, Brno, Czech Republic

vratislav.kostal@tescan.com

Introduction: Cancer cells have been known to use a number of cellular mechanisms, which allow them to survive chemotherapy treatment or avoid triggering the immune system response. Some of these hallmarks are linked to rare dynamic events, such as to changes in cellular morphology, reorganization of cellular mass and intercellular interactions (e.g. with immune cells). Therefore, time-lapse microscopy is an essential technique for their detection because they can be easily left undetected by flow cytometry. Moreover, occurrence of those events can be affected by fluorescence labeling or long observations, so the ultimate goal is to use label-free microscopy. Multimodal holographic microscopy (MHM) has become a unique method for label-free assessment of cellular dynamics. High contrast, minimal phototoxicity, and extreme sensitivity for the smallest changes in cellular mass are the key advantages over the classical bright field microscopy. On the other hand, the connection between the morphological data recorded by MHM and the cellular ultrastructure is still limited. Therefore, correlation of MHM data with focused ion beam scanning electron microscopy (FIB-SEM) is essential for detailed interpretation of the observed behavior. As the serial FIB-SEM tomography has been routinely used for providing 3D reconstructions of analyzed cells, it makes it an ideal technique for justifying the cellular mass data obtained by MHM.
Objectives: The goal of this work is to use MHM for the label-free visualization of unique proliferative properties of cancer cells and their changes in time. Using the time-lapse microscopy we are able to identify the cell-cell interactions of co-cultivated T-cells with prostate cancer cells, and to use correlative approach to subsequently analyze their ultrastructure by FIB-SEM tomography.
Materials and Methods: The human prostate cancer cells (22Rv1) were cultivated directly in gridded flow microchambers (Ibidi, Germany). The MHM imaging was done on a multimodal holographic microscope (TESCAN Q-PHASE, Czech Republic). After recording the MHM data, the cells were fixed with glutaraldehyde and tannic acid in cacodylate buffer, postfixed in OsO4 and potassium ferrocyanide, uranyl acetate and finally resin-embedded. After the polymerization, the blocks were removed from the chambers, carbon coated and processed with a FIB-SEM system (TESCAN GAIA3, Czech Republic). A cross-section was milled with 20 nA ion beam current, polished at 800 pA. and serial sectioned with 400 pA, while the images were collected using a back-scattered electron detector (BSE).
Results: Cells in gridded chamber were periodically monitored in MHM over the 12hrs interval (Fig. 1), which was possible due to minimum photo-toxicity induced by the MHM. The insert shows a single snapshot of a cancer cell #11 during its interaction with a T-cell just right before the fixation. Resin-embedded cells were overlaid with a MHM image using the CORAL software module (TESCAN, Czech Republic) to easily find the cell of interest in the FIB-SEM (Fig. 2). After the successful recognition of the target region, the cancer cell was milled with a FIB. The internal structures of the cancer cell were clearly visualized with a BSE detector (Fig. 3).
Conclusion: We successfully combined label-free imaging using a multimodal holographic microscope and the FIB-SEM ultrastructural analysis. Using the MHM we were able to identify rare changes in cancer cell behavior in large populations. Subsequently, we matched the dynamic data with a high resolution FIB-SEM ultrastructure analysis using a correlative workflow. Using the proposed MHM-FIB-SEM we were able to look deep into proliferative properties and morphology of cancer cells and their interactions with the external environment.

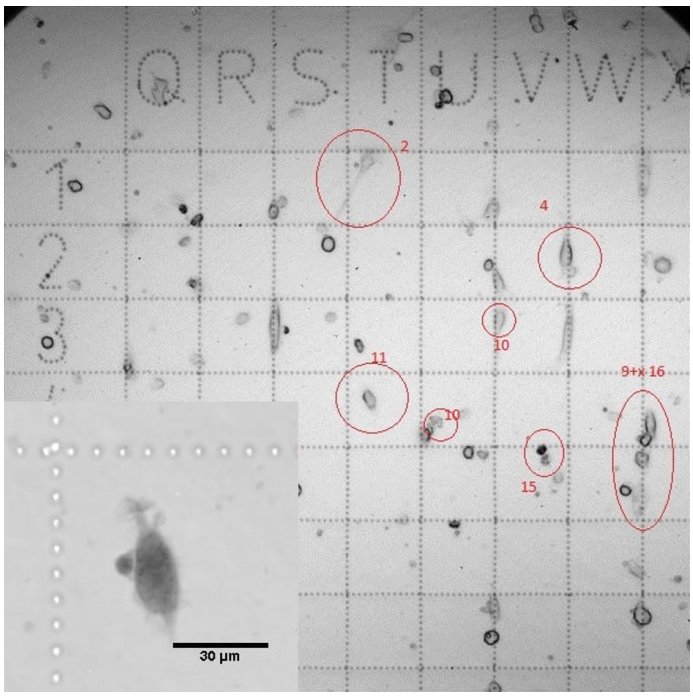

Figure 1. Gridded chamber for MHM imaging. The insert shows a particular cell of interest interacting with a T-cell.

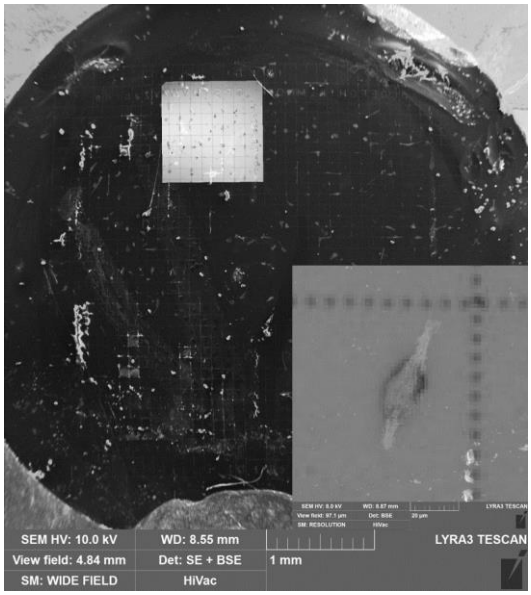

Figure 2. Overview image of an embedded gridded chamber for MHM imaging. The insert shows a detail on an overlaid cell of interest.

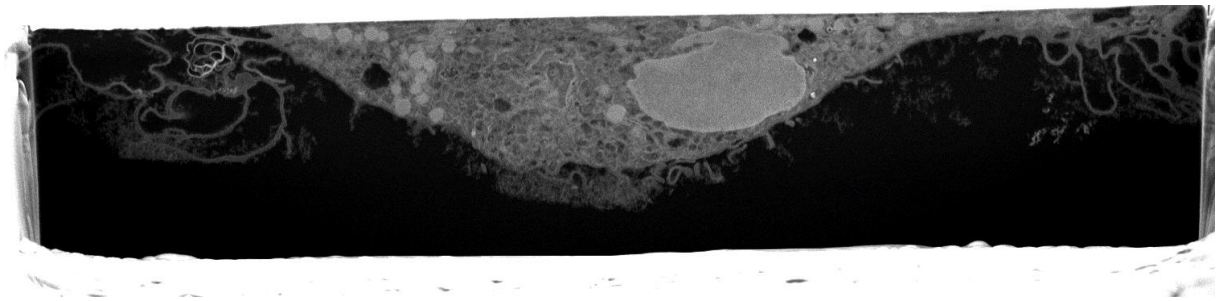

Figure 3. A FIB-SEM cross-section of a selected cell.

LS6.LBP01
8K pixels, 60 frames/sec, real-3D, and VR-guided imaging in living mice

S. Nishimura[1]

[1]Jichi Med Univ, Tochigi, Japan

snishi-tky@umin.ac.jp

To grasp whole-mice information in real-time manner, we developed high-through put CMOS imaging in living mice. We utilized 4/8K CMOS sensor, which enabled broader imaging field, longer observation time, and deeper imaging, also with conventional spatial and time resolutions in living mice. We integrated three technologies into one system; Optics, Mechanics and Electronics. To visualize rapid dynamic cell behaviors, which is one of the vital components of cardiovascular and immune diseases in broad space- and time scales, mice are hold in customized chamber during observation, and controlled by mechanical (stepping motor and piezoelectronic) devices in synchronization with CMOS shutters and scanning to trace single cell with feed back systems. Pixel numbers for in vivo imaging of mice are increased to 8K, to transmit high amount of information per limited time. Interactive imaging was guided by VR (virtual reality), and real-time 3D imaging was performed by two optical path for left and right images, and sequential shutter. Low-power-magnification, high-NA objective lens, broader path, multi-color 8K CMOS sensors, and spinning confocal disk systems were integrated into new imaging setup, for high-resolution imaging in broad imaging area.

Application 1: Visualization of thrombus formation by intravital vessel imaging

One of our application is visualization of dynamism of cardiovascular events. We revealed individual platelet kinetics in thrombus at micro level, and also tissue responses at macro. The in vivo imaging for living mice also revealed that neutrophils were accumulated after endothelial damages with platelet aggregations. To repair leakage of blood fluids into lymphatic stromal space, immune cells including inflammatory macrophages were transmigrated. In this sytem platelet activation and morphological changes in millisecond order, and inflammatory reactions in hours are simultaneously evaluated by single imaging modality.

Application 2: Lymphatic vessels and lymphocyte dynamics

Another application is lymphatic systems, which is difficult to be visualized by conventional imaging modalities. We elucidated antigen imaging processes in lymph-node of intestine in living mice, with lymph cells dynamics from differentiation into cell death. Lymphatic vesse flows were also analyzed.

In sum, high-through-put, real-time, and VR guided in vivo imaging can transmit detailed information of single cells and whole-structure at same time, which covered micro to macro scale in space and time dimensions.

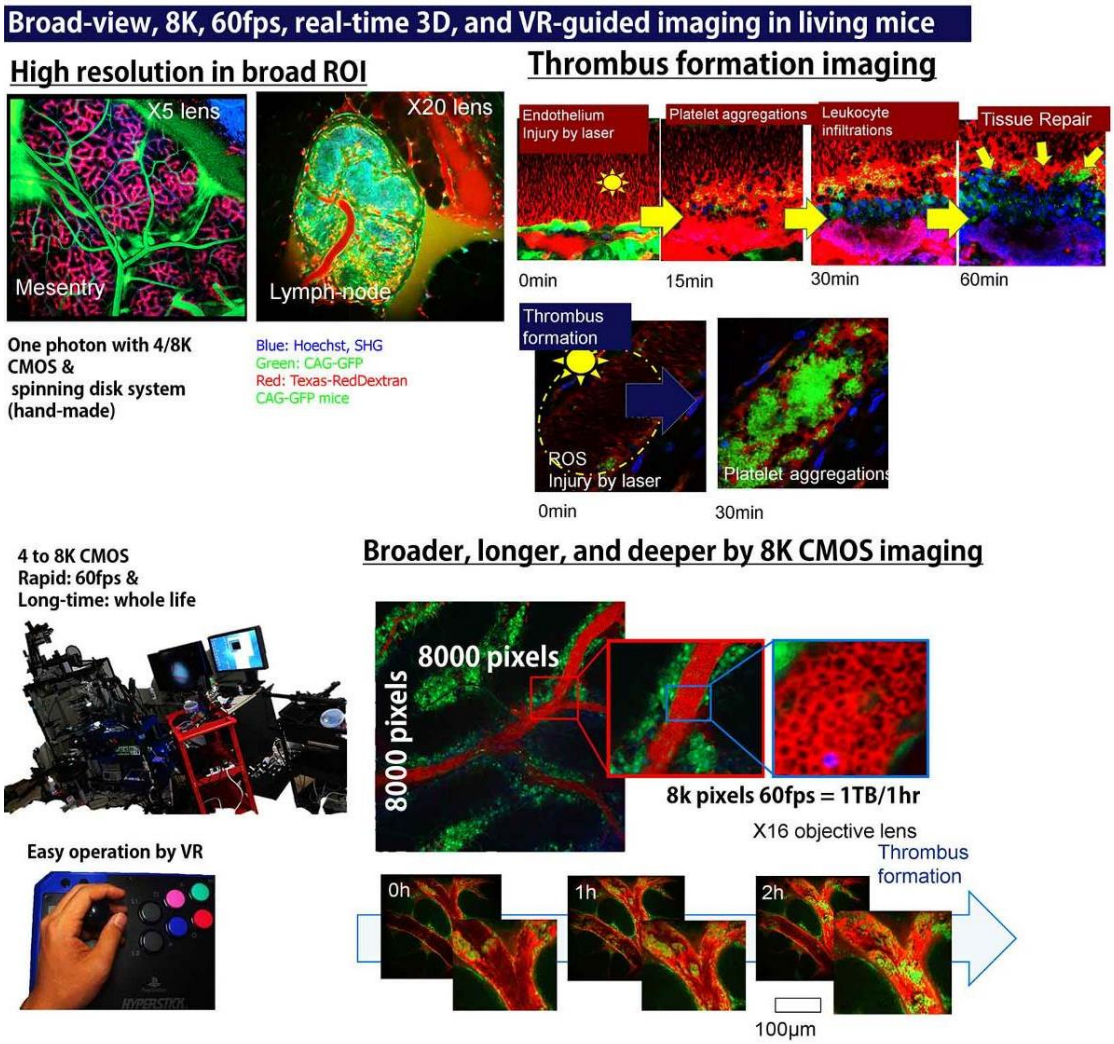
Broad-view, 8K, 60fps, real-time 3D, and VR-guided imaging in living mice
High resolution in broad ROI
X5 lens
Mesentry
X20 lens
Lymph-node
One photon with 4/8K CMOS & spinning disk system (hand-made)
Blue: Hoechst, SHG
Green: CAG-GFP
Red: Texas-RedDextran
CAG-GFP mice
Thrombus formation imaging
Endothelium Injury by laser
Platelet aggregations
Leukocyte infiltrations
Tissue Repair
0min
15min
30min
60min
Thrombus formation
ROS Injury by laser
Platelet aggregations
0min
30min
4 to 8K CMOS
Rapid: 60fps &
Long-time: whole life
Broader, longer, and deeper by 8K CMOS imaging
8000 pixels
8000 pixels
8k pixels 60fps = 1TB/1hr
Easy operation by VR
X16 objective lens
Thrombus formation
0h
1h
2h
100μm

Figure 1

LS6.LBP02
Inducing fluorescence of uranyl acetate as a dual-purpose contrast agent for correlative light-electron microscopy with nanometre precision

M. Tuijtel[1]

[1]Leiden University Medical Center (LUMC), Department Molecular Cell Biology, Leiden, Netherlands

m.w.tuijtel@lumc.nl

Correlative light-electron microscopy (CLEM) combines the high spatial resolution of transmission electron microscopy (TEM) with the capability of fluorescence light microscopy (FLM) to locate rare or transient cellular events within a large field of view. CLEM is therefore a powerful technique to study cellular processes. Especially the in-resin fluorescence sample protocol (IRF), which consists of the high-pressure freezing of cells, and subsequent freeze-substitution, embedding in lowicryl, using 0.1% uranyl acetate. This enables the retention of fluorescence from endogenously expressed fluorescent proteins in samples simultaneously stained for TEM.
Here, we describe how uranyl acetate, a commonly-used contrast agent for TEM, can be induced to fluoresce brightly at cryogenic temperatures (-195°C) and imaged by cryoFLM using standard filter sets (see **Fig. 1A**). This dual-purpose contrast agent can be used as a general tool for CLEM, whereby the staining allows for direct inspection of the cellular outline in FLM mode and easy and intuitive sample navigation between FLM and TEM modalities (see **Fig. 1B** & **C**). Furthermore, the uranyl acetate stain can be exploited to precisely align FLM to corresponding TEM images, facilitating high accuracy and locally adjusted correlations.
We demonstrate the potential of this approach by performing multi-colour CLEM of cells infected with equine arteritis virus mutated to include red fluorescent protein, and achieve high-precision localization of virus-induced intracellular membrane modifications (see **Fig. 2**). Using uranyl acetate as a dual-purpose contrast agent, we achieve an image alignment precision of ~30 nm, twice as accurate as when using fiducial beads, which will be essential for combining TEM with the evolving field of super-resolution light microscopy.

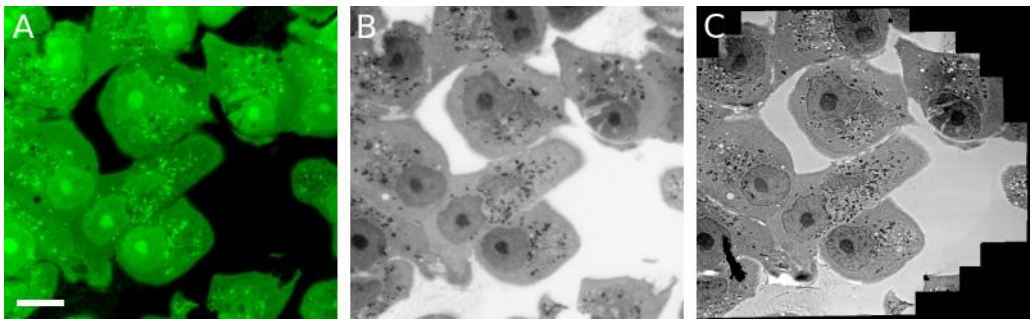

Figure 1. Uranyl acetate as a dual-purpose fluorescent and electron dense stain for correlative light electron microscopy. (A) Fluorescence microscopy image at -195°C of Vero E6 cell sections prepared for IRF. (B) Inverted grey-scale fluorescence microscopy image of A**.** (C) TEM image of the same region as panels A and B. Scale bar represents 10 µm and applies to all panels.

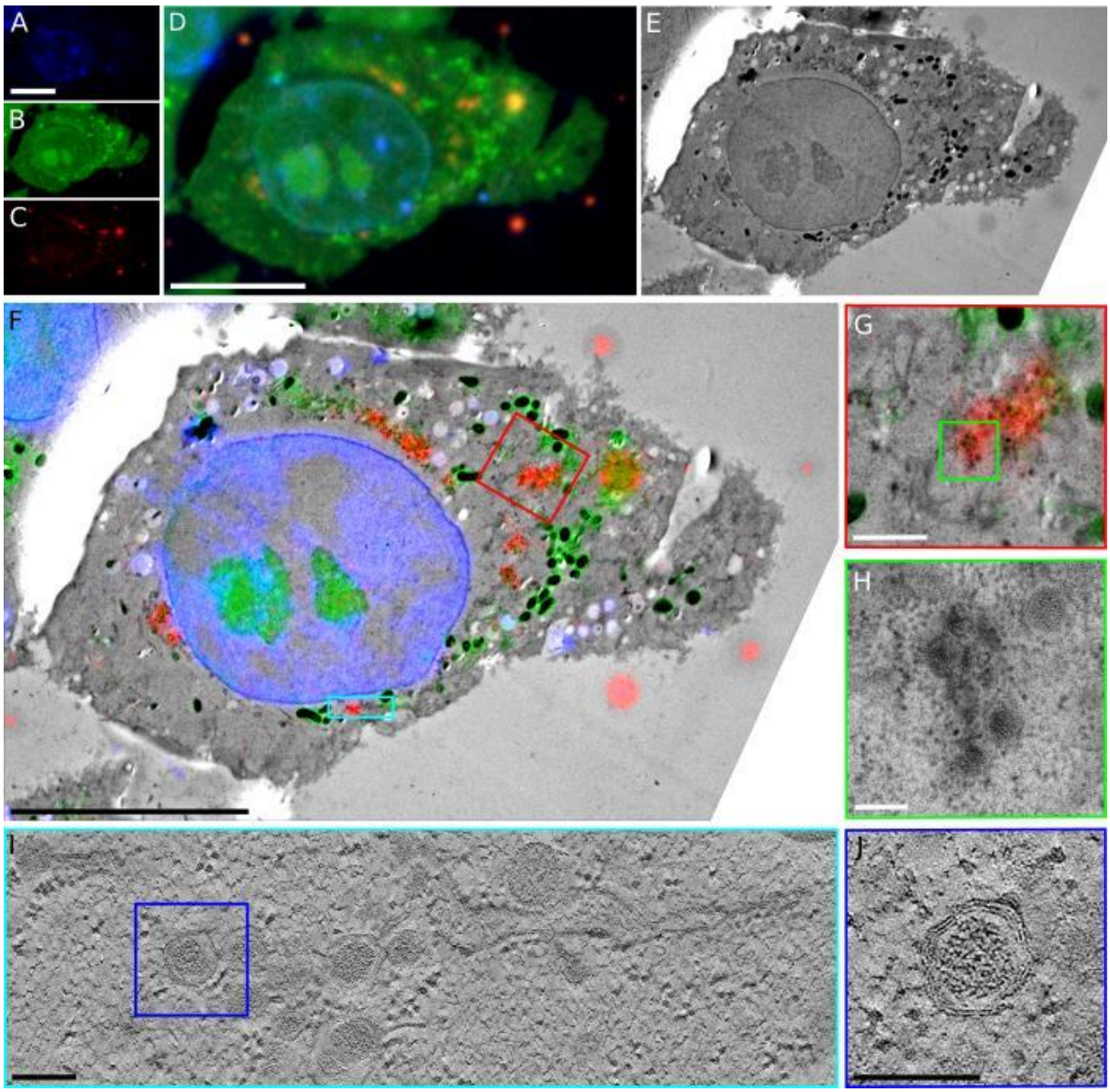

Figure 2. Three-colour CLEM using uranyl acetate to localise virus-induced membrane rearrangements. (A-D) Three colour images of sections of E6 Vero cells infected with EAV-RFP2, showing DAPI stain (blue, A), uranyl acetate (green, B), RFP (red, **C**), and the merged channels (D). **(E**) TEM image of the same cell shown in (A**-**D). **(F) ** Overlay of the three-colour cryoFLM images with the TEM image. **(**G**)** A higher magnification image of the red-boxed region in F**. (**H**)** A higher magnification image of green-boxed region in G, showing the typical morphology of a region with virus-induced double-membrane vesicles. **(I**) A 10 nm-thick slice through a tomographic volume acquired at the cyan-boxed region in F. **(**J**)** Higher magnification view of the blue-boxed region in **I** showing the typical morphology of a double-membrane vesicle. Scale bars: 10 µm in A-F, 1 µm in G and 150 nm in H, I and J.

LS 7: Advances in sample preparation and analysis

LS7.001 invited
Cryo-scanning transmission electron tomography for deep views into vitrified intact cells

S. Wolf[1]

[1]Weizmann Institute of Science, Chemical Research Support Dept, Rehovot, Israel

sharon.wolf@weizmann.ac.il

Cryo-transmission electron tomography (CET) of vitrified biological cells provides rich detail on the organization of macromolecules and organelles. The recent implementation of hole-free phase plate technology and direct electron detectors, coupled with developments in sub-tomogram averaging methods, have recently provided for unprecedented detail on macromolecular structure in-situ[1-2]. However, sample thickness is limited to around 300 nm (close to the mean free path for inelastic scattering) for CET, due to the dependence on phase contrast from elastically scattered electrons. Using energy filters, inelastically scattered electrons can be blocked off, but this reduces signal at higher tilts while still depositing damaging energy into the sample. Thus, imaging is limited to the thin areas of cells, or the cells must be thinned by either cryo-microtomy (CEMOVIS) or focused ion beam milling.
An alternative imaging mode is provided by scanning transmission electron microscopy (STEM), where the signal is acquired incoherently; simply counting electrons scattered to a certain angle for every position in the field of view. Contrast is provided by variations in mass thickness along the path of the electron, and is also dependent on atomic number. The natural limit for sample thickness is extended to the realm of the mean free path for elastic scattering, which is roughly three times that for inelastic scattering for vitrified biological specimens consisting of light elements[3]. In addition, the STEM data acquisition naturally allows for dynamic focusing, providing fully focused images even at high tilts.
We recently developed cryoSTEM tomography (CSTET) to provide highly detailed 3D information on areas of vitrified intact prokaryotic and eukaryotic cells up to one micron in thickness[3-6]. We have identified widely distributed amorphous deposits of calcium phosphate granules within the mitochondrial matrices of mammalian cells. Their chemical composition was identified by on-the-spot EDX spectroscopy.
These so-called "dense granules" have been studied in isolated mitochondria[7] but solid-phase ion storage in mitochondria within intact cells has not been well characterized. In the context of bone formation, mitochondria have been proposed to transport calcium phosphate to the cell surface[8]. We show that phosphate and calcium storage in mitochondria is a widespread phenomenon and may occur for purposes other than export for mineralization.

References:
[1] BM Beck and W Baumeister, *Trends in Cell Biology* **2(11)** 825-837 (2016).
[2] I Orlov *et al*, *Biology of the Cell* **109**: 81–93. doi:10.1111/boc.201600042 (2017).
[3] P Rez, T Larsen and M Elbaum, *J. Struct.Biol.* **196(3)** 466-478 (2016).
[4] SG Wolf, L Houben and M Elbaum, *Nature Methods* **11(4)**, 423-428 (2014).
[5] SG Wolf, P Rez and M Elbaum, *J. Microsc*. **260(2)**, 227-233 (2015).
[6] M Elbaum, SG Wolf and L Houben, *MRS Bulletin* 41(7), 542-548 (2016).
[7] AL Lehninger, *Biochem. J.* **119** 129-138 (1970).
[8] S Boonrungsiman et al, *PNAS* **109** 14170-14175 (2012).

LS7.002 invited
In situ structural studies of macro molecular complexes by cryo-electron tomography with Volta phase plate

Y. Fukuda[1], R. Danev[1], F. Beck[1], W. Baumeister[1]

[1]Max Planck Institute of Biochemistry, Department of Molecular Structural Biology, Martinsried, Germany

fukuda@biochem.mpg.de

Introduction: Single particle analysis of purified protein complexes with cryo-transmission electron microscopy (cryo-TEM) has been contributing for understanding protein function by visualizing the details of the structure. For further understanding of the protein function in cells, however, it seems to be important to study the macro molecular assemblies in cellular environment.
Objectives: For the in situ structural studies of macro molecular assemblies, it requires to visualize macro molecular complexes in cells. However, because of the low signal-to-noise ratio in cryo-TEM, it is difficult to visualize macro molecules in situ. In this study, we applied a Volta phase plate (VPP) to cryo-electron tomography (CET) of frozen-hydrated primary cultured neurons to visualize macro molecular complexes in situ.
Materials and Methods: Neuronal cell culture. Neurons were isolated from the hippocampi of 2-d postnatal rats. Neurons were cultivated for 18 d. Neurons cultivated on grids were plunge-frozen with fiducial marker in a liquid ethane/propane mixture at close to liquid nitrogen temperature using a Vitrobot (FEI).
Cryo-electron tomography. Tilt-series images with a tilt range of ±60° were collected on a Titan Krios operated at an acceleration voltage of 300 kV with the Volta phase plate. The pixel size at specimen level was 4.21 Å. The tomograms were reconstructed by MATLAB using the AV3 and TOM-toolbox.
Image Processing. A 26S proteasome (EMD-2165), a human tripeptidyl peptidase II homo-36-mer (EMD-2036) and homo-32-mer (EMD-2037) were used as templates after rescaling. Template matching, subtomogram averaging, and 3D auto-focus classification were carried out by PyTom.
Results: Due to the improvement of visibility provided by VPP, 26S proteasome particles could be detected in tomograms of primary cultured neurons by visual inspection. For the in situ structural studies, we attempted template matching using a 3D model of 26S proteasome and subtomogram averaging of matched particles. Two of major conformational states ground state and substrate-processing state are obtained by classification.
As well as 26S proteasome, a tripeptidyl peptidase II (TPPII) could be detected in the tomograms by visual inspection. We also attempted template matching using 3D models of TPPII 36-mer and 32-mer. The particles matched with 36-mer and 32-mer were merged and removed duplicated particles. The subtomogram averaging of matched particles showed spindle shape. The averaged particles could be classified into two different assembly states such as homo 36-mers and 32-mers.
The TPPII is believed to act downstream of the 26S proteasome. In tomograms, 26S proteasome particles were occasionally found in close proximity to the TPPII complexes. The distance analysis between TPPII and 26S proteasome comparing measured and simulation indicates that the TPPII and 26S proteasome have a spatial association in the distance closer than ~110 nm.
Conclusion: An improved visibility of cellular features provided by VPP enables to detect macro molecular complexes such as 26S proteasome and TPPII in cellular environment without any labeling. Detecting protein complexes in situ provides opportunities for investigating not only conformations of the complexes in situ but also spatial association between these complexes. We expect that the in situ structural studies will open new horizons in 3D cryo-TEM of cellular specimens.

LS7.003
Ultrastructure, composition and calcite orientation in the transparent cornea cuticle of the compound eyes of marine and supralittoral isopods

A. Ziegler[1], F. Alagboso[1], E. Griesshaber[2], C. Reisecker[3], S. Hild[3]

[1]University of Ulm, Central Facility for Electron Microscopy, Ulm, Germany
[2]Ludwig Maximilian University, Department of Earth and Environmental Sciences, München, Germany
[3]Johannes Keppler University, Institute of Polymer Science, Linz, Austria

andreas.ziegler@uni-ulm.de

The crustacean cuticle is a hierarchically organised composite material consisting of organic fibrils and a mineral phase. Its physical properties are evolutionary adapted to the function of specific skeletal elements by variations in its structure and composition. In the complex eyes of isopoda the cuticle forms the cornea consisting of arrays of transparent micro-lenses. This makes the cornea cuticle to an interesting biological material that has to compromise between mechanical strength and optical properties. We have therefore, analyzed the ultrastructure of the organic matrix, composition, mineral phase distribution, and the crystallographic properties of calcite within the ommatidia of a marine and supralittoral isopod species.

We polished internal faces of the cornea cuticle and head capsule with an ultramicrotome and a diamond knife resulting in plane and smooth surfaces well suited for EPMA, Raman spectroscopic imaging, and EBSD analysis. For SEM we etched mineral from the polished surface and simultaneously fixed the organic matrix prior to critical point drying. Ultrathin sections were obtained from decalcified resin embedded cornea samples and from native non-decalcified material.

We found that the structure of cornea cuticle has significant structural differences from the cuticle of the surrounding head capsule or tergites. Pore canals which vertically oriented fibres play an important role for the mechanical properties of the cuticle are restricted to regions between the ommatidia (Fig. 1). In all three isopod species, local thinning of endocuticle forms the lens shape of the cornea (Fig. 2). The distal layer of calcite is much thinner than in the surrounding head capsule. In *Ligia oceanica* an unusual differential mineral distribution within the endocuticle leads to lens doublets (Fig. 2). The calcite crystal orientation changes from a polycrystalline to highly ordered mesocrystalline distribution. In *Tylos europaeus* calcite forms graded mesocrystalls with a horizontal c-axis orientation preference (Fig. 3). In the cornea of *Sphearoma serratum* and *T. europaeus* we observe larger calcite crystals in comparison to the general cuticle.

The results show that in the isopod cornea the structure of organic fibres and the crystallographic properties minimize light scattering. The horizontal c-axis orientation, the mesocrystalline and graded microstructure of calcite may improve mechanical properties, compensating for the loss of vertical pore canal fibres.

Supported by the DFG SPP 1420 (Zi 368/8-2)

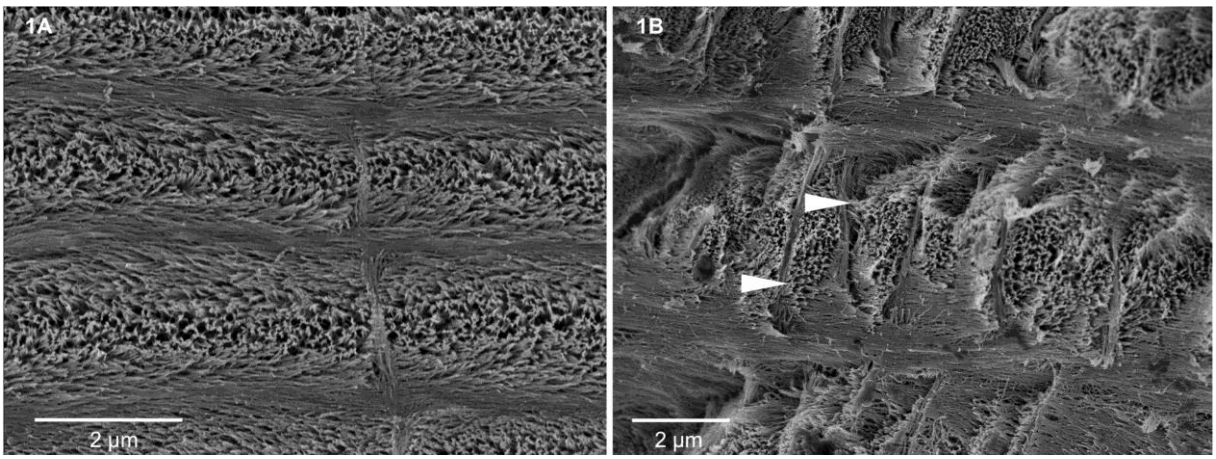

Figure 1. Organic matrix of cornea (1A) and adjacent head capsule cuticle in *Sphaeroma serratum*. The samples were polished, and edged and simultaneously fixed using a solution of 50 mM EDTA, 250 mM HEPES buffer, and 2.5% glutaraldehyde. Pore canals (arrow heads in 1B) that would led to light scattering are lacking in the cornea cuticle.

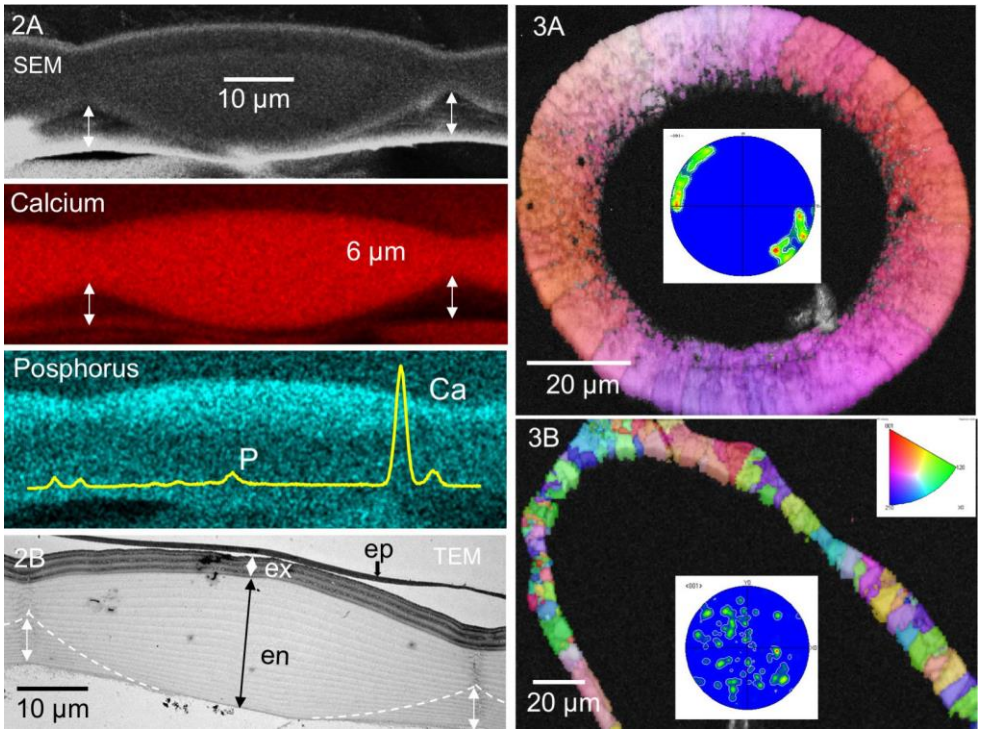

Figure 2. EDX analysis (2A) and TEM micrograph (2B) of the cornea of *Ligia oceanica.* The calcium map shows that interommatidial regions (double arrows) are not mineralised, resulting in lens shaped interface between mineralised and unmineralised cuticle. Phosphorus is concentrated apically. The dashed line in 2B indicates the inner border oft mineral. Stacks formed by the twisted plywood of fibres are only partly mineralised; en, endocuticle; ep, epicuticle; ex, exocuticle.

Figure 3. Colour coded EBSD maps and pole figures of crystallographic c-axis distributions in *Tylos europaeus* cuticle. Calcite is mesocrystalline organised and graded in the cornea cuticle (3A). In the head capsule calcite has a polycrystalline organisation (3B).

LS7.004
Selective double-labeling of cell-free synthesized proteins for more accurate smFRET studies

M. Sadoine[1], M. Cerminara[1], N. Kempf[1], J. Fitter[1], A. Katranidis[1]

[1]Forschungszentrum Juelich, Institute of Complex Systems ICS-5, Juelich, Germany

m.sadoine@fz-juelich.de

Single molecule FRET (smFRET) is a powerful tool for looking at protein folding and conformational dynamics (1). The conventional method to double-label the protein is via cysteine residues (2). Even though the double-labeling is site-specific at the two cysteine positions, it lacks selectivity due to the same functionality of the two residues, thus giving rise to heterogeneously labeled populations and leading to an inaccurate picture of the studied population (3). Selective labeling can be achieved by incorporation of unnatural amino acids carrying an orthogonal chemistry, a method mainly performed *in vivo* (4, 5).
Our aim was to develop a new approach for site-specific and selective labeling of cell-free synthesized proteins, in order to expand the application of smFRET studies for difficult-to-express or toxic proteins, very often associated with pathologies.
The human calmodulin (CaM) expressed in a cell-free protein synthesis (CFPS) system was used as a model protein and smFRET studies were carried out with fluorescence confocal microscopy.
Our approach allowed us to double-label the cell-free synthesized CaM selectively. By performing binding experiments in the presence of ligands and partners, we demonstrate that the structure and subsequently the functionality of the labeled CaM were not affected. We also show that the selective double-labeling achieved with our approach, allows obtaining of sharper smFRET histograms compared to the conventional double cysteine labeling method, which can significantly improve the precision in estimating molecular distances.
To conclude, we have developed a simple and fast method that enables more accurate smFRET studies of cell-free synthesized proteins. Our approach expands the range of smFRET studies to proteins that are difficult to express *in vivo*, like toxic or membrane proteins.

References:
[1] Tan, Y. W., J. A. Hanson, J. W. Chu, and H. Yang. 2014. Confocal single-molecule FRET for protein conformational dynamics. Methods Mol. Biol. 1084:51-62.
[2] Kim, Y., S. O. Ho, N. R. Gassman, Y. Korlann, E. V. Landorf, F. R. Collart, and S. Weiss. 2008. Efficient site-specific labeling of proteins via cysteines. Bioconjug. Chem. 19:786-791.
[3] Joo, C., and T. Ha. 2012. Labeling proteins for single-molecule FRET. Cold Spring Harb. Protoc. 2012:1009-1012.
[4] Kim, J., M. H. Seo, S. Lee, K. Cho, A. Yang, K. Woo, H. S. Kim, and H. S. Park. 2013. Simple and efficient strategy for site-specific dual labeling of proteins for single-molecule fluorescence resonance energy transfer analysis. Anal. Chem. 85:1468-1474.
[5] Seo, M. H., T. S. Lee, E. Kim, Y. L. Cho, H. S. Park, T. Y. Yoon, and H. S. Kim. 2011. Efficient single-molecule fluorescence resonance energy transfer analysis by site-specific dual-labeling of protein using an unnatural amino acid. Anal. Chem. 83:8849-8854.

LS7.005
Cellfi-flash – a first step towards spatio-temporal control of chemical fixation

C. Schmid[1], K. Schelkle[2], K. Yserentant[3], I. Wacker[1], M. Bender[2], M. Petzold[2], M. Hamburger[2]
D. P. Herten[3], R. Wombacher[4], U. Bunz[2], R. Schröder[5,1]

[1]Centre for Advanced Materials, Cryo Electron Microscopy, Heidelberg, Germany
[2]University Heidelberg, Institute of Organic Chemistry, Heidelberg, Germany
[3]University Heidelberg, Institute for Physical Chemistry, Heidelberg, Germany
[4]University Heidelberg, Institute of Pharmacy and Molecular Biotechnology , Heidelberg, Germany
[5]Universitätsklinikum Heidelberg, Cryo Electron Microscopy, Heidelberg, Germany

rasmus.schroeder@bioquant.uni-heidelberg.de

Introduction: To analyse dynamic events or short-lived states imaged with a light microscope in living cells at ultrastructural resolution it would be desirable to have the means of a controlled, selective and immediate stopping of all dynamics at once when the desired event occurs. Chemical fixation with glutaraldehyde is not instantaneous [1], even with cryofixation [2] a short delay is unavoidable, caused by the necessity to remove the sample from the microscope stage and insert it into the high pressure freezer for fixation. Using such a workflow only one event per sample can be fixed and analysed, it is not possible to collect many events on the same slide.
Objectives: Our aim was to generate a compound that 1- can enter cells and accumulate inside, 2- is non-cytotoxic, 3- can be activated by illumination, ideally flash photolysis [3], and 4- acts as a fixative after photocleavage, stopping events instantaneously.
Materials and Methods: Caged glutaraldehyde (caged-GA, Fig. 1) was synthesized as described [4]. Stock solutions were prepared with dioxane or DMSO. For toxicity tests HeLa cells were incubated for 1h at 37°C with different concentrations of caged-GA in HEPES-buffered Krebs-Ringer (HKR) solution before live-dead staining with propidium iodide and Calcein. To demonstrate the fixation capability of caged-GA HeLa cells grown in Labtek chamber slides were incubated with the compound over night, washed twice with HKR buffer, and labelled with Mitotracker for 1 h Moving mitochondria were imaged for 2 min then the cells were illuminated for 1 min with UV light (l= 300nm) in a home-built chamber, and imaged again. Movement of mitochondria was tracked in Fiji using the kymograph plugin.
Results: Caged-GA (Fig.1) is not cytotoxic as shown in Fig. 2 – the proportion of dead cells (red nuclei) is comparable for controls (A, B) and samples treated with inactive caged-GA (Fig. 2C). Representative kymographs from cells before (Fig. 3A) and after (Fig. 3B) illumination with UV light demonstrate that no movement of mitochondria was observed after photocleavage. This could be achieved by caged-GA concentrations as low as 65mM – after addition of that concentration of conventional GA to the chamber slide it takes 20 minutes till mitochondrial movement stops.
Conclusion: As a proof of principle we synthesized a compound representing a caged glutaraldehyde which can accumulate within cells and act as fixative upon uncaging by illumination with UV light.
Using patterned illumination or sequential flashing of multiple events many cells on a coverslip may be treated allowing spatial as well as temporal control. Such a coverslip could then either be post-fixed and conventionally embedded or cryofixed and freeze substituted. We are planning to change the compound in such a way that longer wavelength light will suffice to release the active moiety. We are also planning to build a setup for flash photolysis directly on the microscope stage.

References:
[1] Hopwood, D. *Histochem. J.* (1972) *4*: 267-303 [2] Brown, E. et al. *Methods in Cell Biology* (2012) 111: 175-201
[3] Ellis-Davies, G.C.R. *Nat. Methods* (2007) 4: 619 - 628
[4] Schelkle, K. et al. *Angew. Chem. Int. Ed.* (2017), in press
[5] We thank C. Bartels for technical support and the BMBF for MorphiQuant-3D grant FKZ 13GW0044.

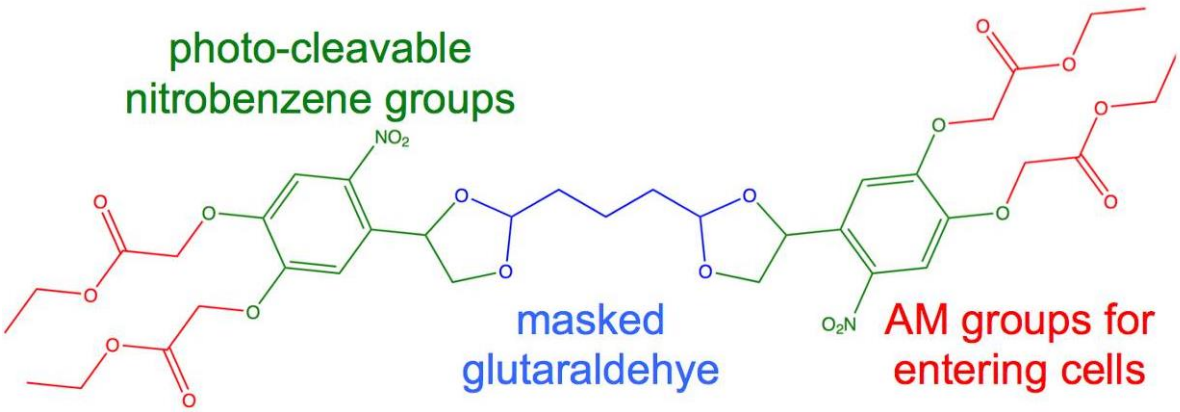

Figure 1. Chemical structure and functional groups of caged-GA (AM = acetmethoxy).

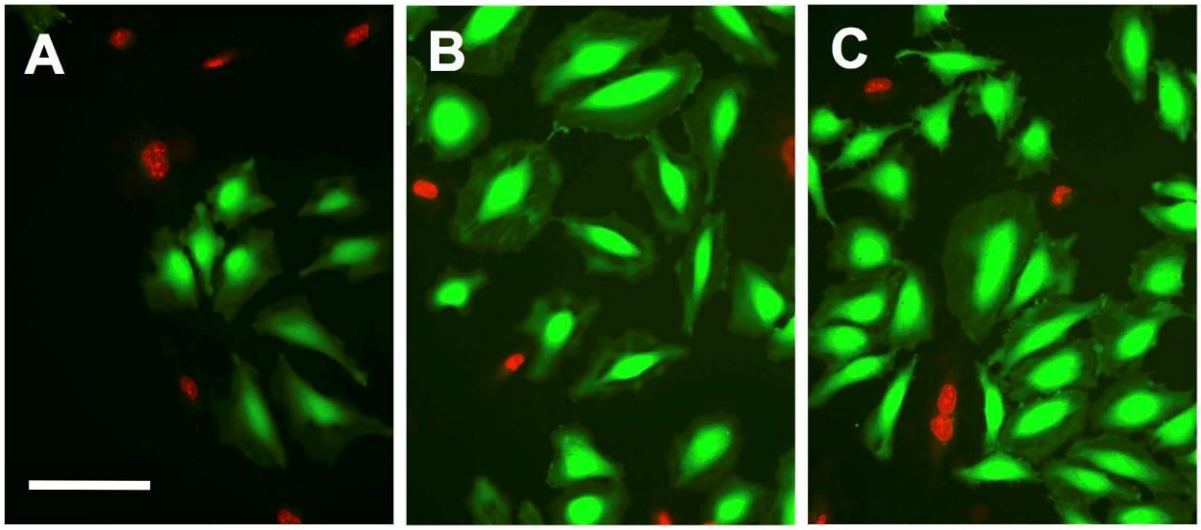

Figure 2. HeLa cells incubated for 1h at 37°C in HKR (A), 0.6% dioxane/HKR (B), or 300mM caged-GA in 0.6% dioxane/HKR (C) and stained with 1mM CalceinAM /7.5mM propidium iodide in HKR buffer. Scale bar 100mm.

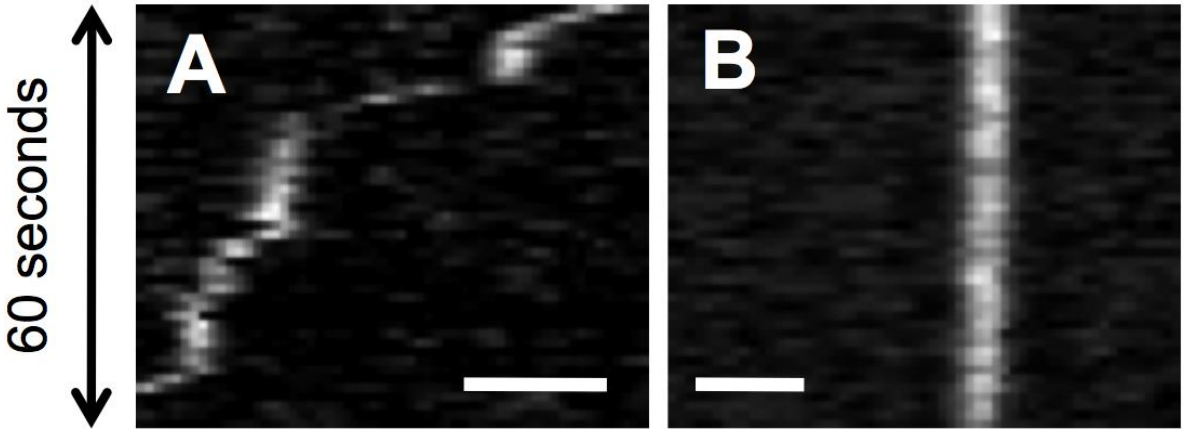

Figure 3. Representative kymographs of mitochondrial movement in the presence of caged-GA before (A) and after (B) 2 UV illumination (l = 300nm). Scale bar 2mm.

LS7.P001
The morphology and ultra-structure of a new 2-methoxyethanol utilizing pseudomonas sp.

F. O. Ekhaise[1]

[1]University of Benin, Faculty of Life Sciences, Microbiology, Benin, Nigeria

frederick.ekhaise@uniben.edu

A new strain of *Pseudomonas* designated as *Pseudomonas* sp. strain VB degrading 2 – Methoxyethanol was isolated from anaerobic sewage sludge. The cells are rod-shaped, motile with polar lophotrichous flagella numbering between 7 and 9. Electron microscopy revealed cells aggregating to form a network connected by interconnecting filaments. A thin section of the filaments showed an outer sheath surrounding a core area and an inner electron dense area.. A trhin section of the cell showed the typical Gram – negative bacterial cell structure.

Keywords: Pseudomonas *s*p. strain VB, electron microscopy, morphology and ultrastructure.

LS7.P003
FIB-SEM approach to study membrane trafficking events with the lamprey giant reticulospinal synapse model

E. Majorovits[1], E. Sopova[2], O. Shupliakov[3]

[1]Carl Zeiss Microscopy GmbH, Oberkochen, Germany
[2]St. Petersburg University, Institute of Translational Biomedicine, St. Petersburg, Russian Federation
[3]Karolinska Institutet, Department of Neuroscience, Stockholm, Sweden

endre.majorovits@zeiss.com

Giant reticulospinal synapse in lamprey is a well-established model system to study the vesicle cycle in interneuronal synapses. Unique anatomical organization of this synapse allows microinjections of selective active compounds that perturb protein-protein and protein-lipid interactions with subsequent analysis of utrastructural changes at defined synaptic compartments using electron microcopy. For a number of years, conventional transmission electron microscopy (EM) and primarily serial ultrathin section analysis have been utilized in these studies. One of the problems with the reconstruction of large branched cellular membrane compartments from serial section analysis is in deformation of individual ultrathin sections placed on a Formvar support film under electron beam. Thus 3D-reconstructions become complicated and unreliable. Recently, focused ion beam scanning EM (FIB-SEM) tomography, which allows collecting serial sections with subsequent reconstruction of the volume without displacement has been introduced to study cellular structures.
The main goal of our experiments was to develop a technology to perform detailed reconstructions of lamprey giant synapses in 3D using FIB-SEM technique.
Lamprey spinal cords were chemically fixed and embedded in Durcupan using a published protocol (www.emc.missouri.edu/pdf/Ellisman's_SBFSEM_sampleprep_protocol.pdf). Blocks were trimmed in an ultratome to expose the frontal sections of the giant axons and coated with thin layer of platinum to reduce the surface charge. Image data were acquired using a Zeiss FIB-SEM Crossbeam 540. Regions of interest were located with a 2 keV electron beam using the SE detector. Cross-sections were milled and polished with a Ga ion beam. 3D data sets were collected by simultaneously milling the cross-section and imaging with a 2 kV; 2 nA electron beam using the energy selective backscatter (EsB) detector. The FIB-SEM imaging software Atlas (Fibics Inc., Ottawa, Canada) allowed the automated acquisition of up to 7x9x24 µm3 data cubes with a lateral pixel size of 3 nm and a slice thickness of 6 nm. The data were processed and movies were generated using the visualization software ORS Visual (ORS Inc., Montreal, Canada).
Reticulospinal axons were fixed under resting condition (n=3) and after 30 min stimulation at 5 Hz (n=3) were milled with 6nm steps. Giant synapses (Fig. 1A) were identified on their surface, imaged with the SEM and reconstructed in 3D. Our experiments show that this approach allows detailed reconstruction of continuous membrane structures such as endoplasmic material, endosomal compartments, vesicles, and endocytic intermediates. These structures can be followed in different planes at synapses as shown in Fig. 1 A-D for the case of an endosome.
Our studies show that FIB-SEM technology provides unique possibilities for investigation of membrane trafficking events and molecular signaling mechanisms controlling biogenesis of continuous membrane structures and organelles around synaptic active zones that has been difficult to accomplish using conventional TEM techniques thus opening new avenues for research using the lamprey giant synapse model.

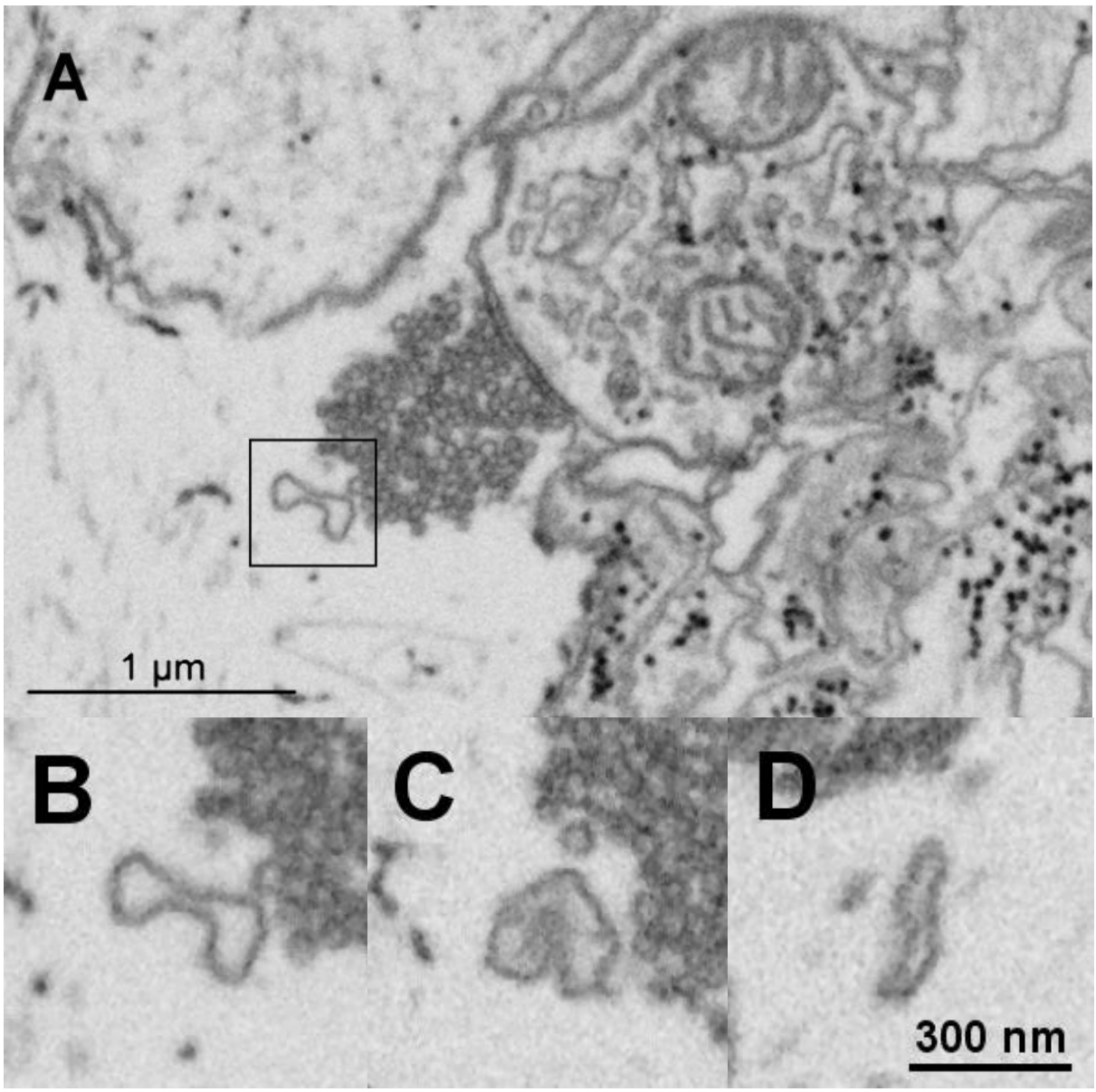

Figure 1. Digital section of a lamprey giant synapse (A) and the endosomal synaptic structure boxed in (A) in XY, XZ and YZ planes respectively (B-D). Experiments were funded by the Swedish Research Council and the Russian Science Foundation grant № 16-15-10273 and Carl Zeiss Microscopy GmbH.

LS7.P004
Calcium phosphate biominerals in plants – more than exotic curios

H. J. Ensikat[1], A. Mustafa[1], M. Weigend[1]

[1]Nees-Institut für Biodiversität der Pflanzen, Bonn, Germany

ensikat@uni-bonn.de

Introduction: The biomineral calcium phosphate or hydroxyapatite [$Ca_5(PO_4)_3(OH)$] is the main inorganic component of the skeletons and teeth of vertebrate animals, but it had never been recognized in higher plants. Generally, it was believed that plant biominerals are strictly limited to silica, calcium carbonate, and calcium oxalate. A study of the south-American plant family of Loasaceae (rock nettle family), densely covered with stinging hairs and complex scabrid-glochidiate trichomes, using SEM and EDX element analyses, revealed deposits of calcium phosphate, replacing the more common silica in stinging hair and trichome tips (Ensikat et al., 2016, 2017). In some Loasaceae, three biominerals (calcium phosphate, silica, and calcium carbonate) co-occurred side-by-side in the wall of single trichome cells in a well-defined arrangement.
Objectives: The examination of several other plant families, carrying stinging hairs or ordinary trichomes, should reveal whether or not calcium phosphate biominerals occur in native and common plants.
Materials and Methods: Various plant species from the Botanical Gardens, Bonn, were examined by scanning electron microscopy with EDX element analysis. Preparation methods included Cryo-SEM, Freeze-substitution, Critical-point-drying, Block-face imaging of embedded samples.
Results: Calcium phosphate was found in several species of different plant families. We documented its presence in some species of *Urtica* (stinging nettle) together with silica, and in such common plants like *Phacelia* (a cultivated honey plant) or *Aubrieta* (false rockcress), a popular garden plant, and several others, where it replaces silica in the trichome tips.
Conclusions: Our survey of a limited selection of common plants showed that the occurrence of calcium phosphate in plant trichomes is not at all a rare curiosity. It seems surprising that a widespread plant biomineral has remained unrecognized to the present day, although it can be detected easily with standard SEM / EDX equipment.
References: Ensikat, H. J. et al., 2016. A first report of hydroxylated apatite as structural biomineral in Loasaceae – plants teeth against herbivores. Sci. Rep. 6, 26073; doi: 10.1038/srep26073 (2016). Ensikat, H. J. et al., 2017. Complex patterns of multiple biomineralization in single-celled plant trichomes of the Loasaceae. American Journal of Botany 104(2): 195-206.

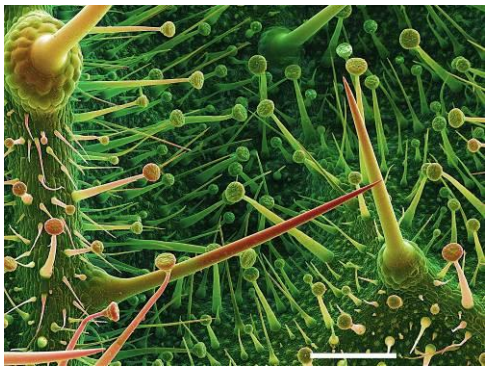

Figure 1

LS7.P005
Cryo-electron microscopy at full warp

D. Tegunov[1]

[1]MPI for Biophysical Chemistry, Göttingen, Germany

dteguno@mpibpc.mpg.de

Recent advances in electron detector technology have enabled a dramatic increase in the resolution of structures obtained through cryo–electron microscopy. Thanks to the higher signal-to-noise ratio, sample movement and local warping can be tracked and corrected *in silico*.
Our software tool, Warp, takes over and improves several steps in the processing pipeline. As a pre-processor, it performs on-the-fly frame alignment and defocus estimation while the micrographs are acquired, using an arbitrarily complex model for the sample geometry. After classification and refinement in other packages, Warp refines the sample deformation model and the maps further through Reference:-based alignments. Model regularization is ensured through parametrization as a coarse grid of spatial and temporal anchor points. In tomography mode, Warp performs the optimization for the entire tilt series, and offers CTF-aware sub-tomogram reconstruction and automated particle picking. The high computational complexity of the algorithms is mitigated through GPU acceleration in every step. Data storage costs can be reduced dramatically with integrated compression.
Using Warp, we improved some of the highest-resolution single particle maps published to this date: 2.4 vs. 2.2 Å for the 20S proteasome; 2.2 vs. 2.1 Å for the β-galactosidase. Applied to *in vitro* sub-tomogram averaging, the resolution increased from 10.6 to 8 Å for the 80S ribosome (1400 sub-tomograms). The biggest improvement was achieved for *in situ* tomograms of eukaryotic cells prepared through focused ion beam milling: We were able to resolve the 80S ribosome in its native environment at 8 Å, as opposed to the previously best resolution of 17 Å. In addition, the number of sub-tomograms needed for sub-20 Å averages was reduced dramatically, allowing for a very fine analysis of the translocation states in polysome chains.
With these improvements, we envision Warp playing an important role in making cryo–electron tomography – applied to *in situ* data, in particular – a tool for high-resolution structure determination.

LS7.P006
High-pressure freezing of microorganisms using polyester filter membranes as substrat

C. Schaudinn[1], M. Laue[1], C. Dittmann[1], J. Piesker[1]

[1]Robert Koch Institute, Berlin, Germany

lauem@rki.de

Introduction: Microorganisms are highly diverse in their morphology and adaptation to their environment. As a consequence their cultivation also needs particular conditions. Many microorganisms can be propagated in suspension or on solid agar, others need host cells for propagation while another group requires solid substrates and special environmental factors to form 3D structures such as biofilm. To conserve their delicate ultrastructure by high-pressure freezing, microorganisms must be transferred into special sample containers. During our work with various microorganisms we experienced that thin polyester filter membranes provided a suitable and above all universal sample substrate for high-pressure freezing. Similar filters, made of polyethylene, have been used before for high-pressure freezing of adherent eukaryotic cells [1], but were rarely used ever since.
Objectives: The main goal was to establish a universal sample substrate for high-pressure freezing of various pro- and eukaryotic microorganisms.
Material and Methods: Polyester filter membranes (pore size = 0.2 µm; thickness = 10 µm) were purchased from different vendors (e.g. Pieper Filter GmbH). For direct cultivation of cells on the filter membranes, discs of the membrane were punched out using a tissue biopsy punch (3 mm in diameter) and autoclaved before usage. Concentration of cells grown in suspension was performed in filter units taken from spin columns after replacing the original filter (RotiSpin Mini-100, Carl Roth) with the polyester membrane filter. Suspensions were either centrifuged or pressed through the filter by using a pistil from a syringe. High-pressure freezing was done with a Wohlwend HPF01 compact and freeze-substitution in a Leica AFS2 with 0.2% osmium tetroxide (0.05% uranyl acetate) and 5% water in acetone.
Results: Microorganisms grown in suspension or cultivated directly on the filter membrane could be high-pressure frozen at a satisfying quality and with a high reproducibility (see Figure for an example). The filter membrane material was compatible with epoxy and acrylate resin (LR and Lowicryl resin) and could be easily sectioned. The rapid concentration of in suspension grown cells on the filter membrane was particularly suitable for time course experiments such as the germination of bacterial spores.
Conclusion: Our presentation shows multiple applications of the polyester filter membranes as substrate for high-pressure freezing of microorganisms and thereby expanding the portfolio of suitable sample supports for high-pressure freezing [2].

References:
[1] Morphew, M.K.; McIntosh, J.R. (2003): The use of filter membranes for high-pressure freezing of cell monolayers. Journal of Microscopy 212: 21-25.
[2] McDonald, K.; Schwarz, H.; Müller-Reichert, T.; Webb, R.; Buser, C.; Morphew, M. (2010): "Tips and Tricks" for High-Pressure Freezing of Model Systems. In: Electron Microscopy of model systems. Hrsg.: T. Müller-Reichert. Amsterdam, Boston, Heidelberg: Elsevier. Page 671-693. (Methods in Cell Biology 96).

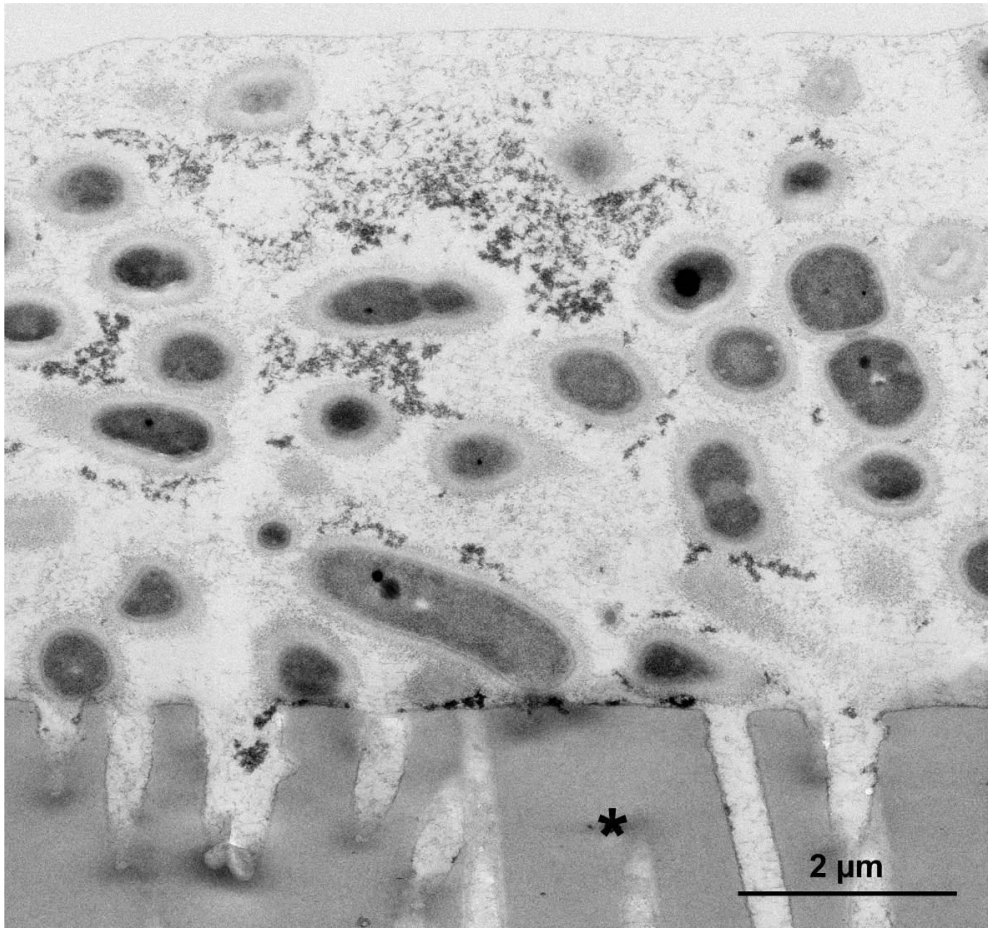

Figure 1. High- pressure frozen and freeze-substituted *Acinetobacter baumannii* biofilm grown on porous polyester filter membrane (*) in a so-called drip-flow reactor. Epon embedding.

LS7.P007
Effects of different preparation techniques on the microstructural features of potato tissue for scanning electron microscopy

S. Youneji[1], E. Ahmadi[1], M. Khaninour[1], S. Azami[1], J. Karcz[2]

[1]Bu-Ali Sina University, Hamedan, Islamic Republic of Iran
[2]Silesia university, Katowice, Poland

s.yoneji@basu.ac.ir

Introduction: The microstructure of potato tissue is made up of liquid-filled and thin-walled cells (Gibson, 2012). Scanning electron microscopy (SEM) is a high-resolution technique for investigating plant surfaces. The tissue specimens need to the chemical fixation (Fix) and drying without significant distortion (Pathan *et al*., 2010; Karcz *et al*., 2012; Uwins *et al*., 1993). Talbot and White (2013) and applied many techniques of SEM preparation techniques for plant tissues. The standard preparation of biological material for SEM analysis includes 3% glutaraldehyde (Gl) Fix and ethanol (Eth) dehydration (dehyd) (Karcz *et al*., 2009). The various methods of drying including air-drying, freeze-drying (Blaszczak *et al*., 2005) and hexamethyldisilazane (HMDS) drying (Karcz *et al*., 2012; Pathan *et al*., 2010; Berger *et al*., 2016) were applied in many studies. Monitoring of microstructural features (Mf), such as cell area (A), cell perimeter (P) and cell shape is done by microscopy methods (Konstankiewicz *et al*., 2001).
Objectives: The objective of this research is to identify a protocol that would preserve the Mf better than standard chemical fixatives and dehyd regimes. This paper compares different preparation techniques of potato tissue to study of A, P and cell roundness (R) by image analysis.
Materials and methods: From each potato cultivar of Marfona a surface sample 1 × 10 × 10 mm was sliced by using a razor blade. The Fix and Dehyd steps were done as the different methods outlined below:

1. 100% methanol (Meth) Fix, 100% Meth Dehyd and air dry
2. 100% Meth Fix, 100% Eth Dehyd and air dry
3. 100% Eth Fix, 100% Eth Dehyd and air dry
4. Formaldehyde-acetic acid-alcohol (FAA) fixation, Eth series Dehyd and air dry
5. 2.5% Gl Fix (5 min, 1 h and 2 h), Eth series Dehyd and air dry
6. 2.5% Gl Fix (2 h), Eth series Dehyd and freeze-drying
7. 2.5% Gl Fix (2 h), Eth series Dehyd and HMDS drying (5 min, 15 min and overnight)
8. 2.5% Gl Fix (2 h), Eth series Dehyd and 100% Eth -100% HMDS drying (3:1, 1:1 and 1:3, 15 min each)

The SEM images were analyzed using Microstructural Image Processing (MIP) software to determine A, P and R of potato tissue.
Results**:** The quantitative SEM image analysis was carried out to determine the Mf of potato tissue. The analysis of SEM images was carried out according to the approach worked out by Konstankiewicz *et al*. (2001). The A (as cell projected area) and P were computed by MIP software and R was estimated as $(4\times\pi\times A) / (P2)$. Statistical results indicated that there was significant different between the Mf of the eight techniques ($P < 0.05$). Strong differences in the preservation of cell structure between the processed potatoes are clearly shown by SEM images in Fig. 1-4. Results show that the Meth of 100% Eth Fix and 100% Eth Dehyd was the best for preservation rather than 100% Meth and FAA protocol (Fig. 1). As shown in Fig. 2, air drying altered the cellular dimensions significantly higher than the freeze drying. However, A, P and R of HMDS drying (5 min) samples showed the significant difference to the Eth-HMDS drying (Fig. 3). Fig. 4 indicated that high remarkable preservation of potato microstructure without distortion was obtained by 2.5% Gl Fix (2 h) and Fix Eth series followed by HMDS alcohol (overnight) as a valuable result in this study, which had significantly the highest A, P and R.
Conclusion: We found that 2.5% Gl was superior fixative rather than FAA for SEM processing of potato tissue. 100% Meth Fix and Dehyd followed by further 100% Eth or 100% Meth Dehyd also, air drying and freeze-drying methods resulted in undesirable shrinkage of potato microstructure. The most remarkable preservation of tissue dimensions was related to 2.5% Gl Fix (2 h) and Dehyd Eth series followed by HMDS alcohol (overnight).

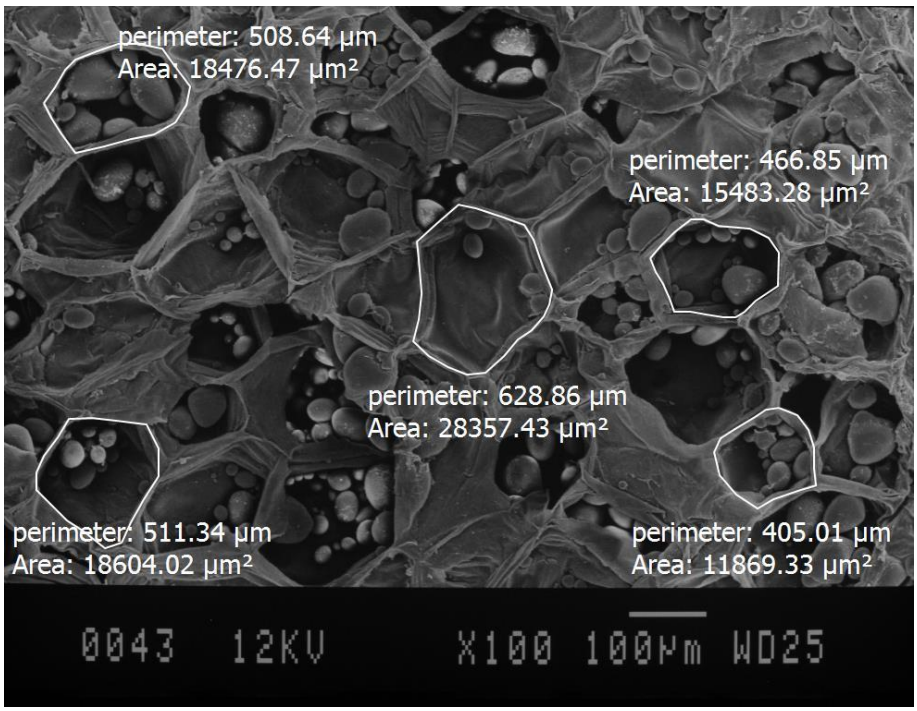

Figure 1. SEM image for method of 100% Eth Fix, 100% Eth Dehyd and air drying.

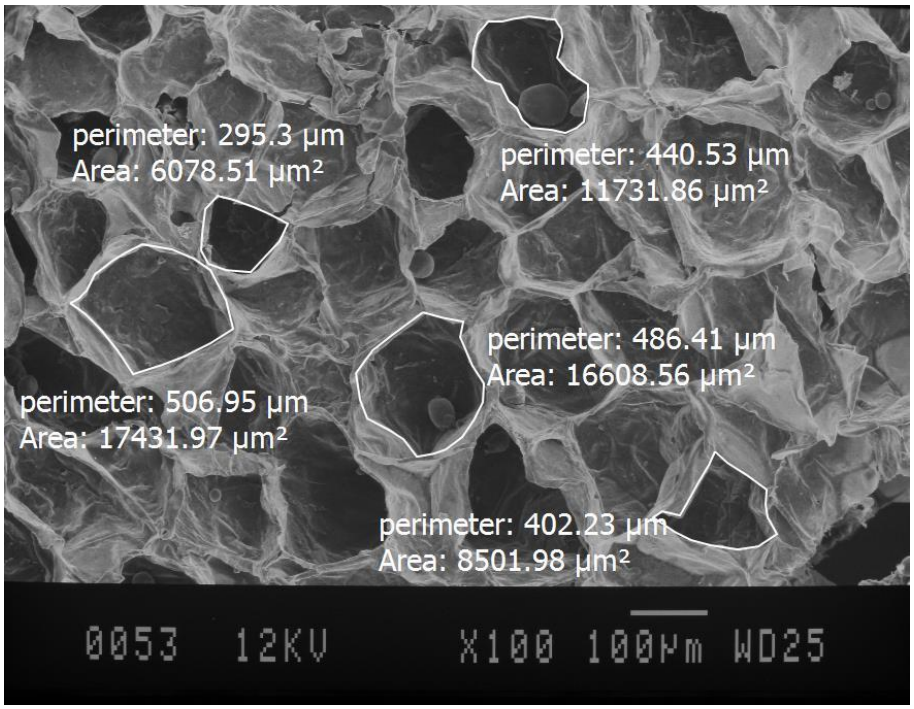

Figure 2. SEM image for method of 2.5% Gl Fix, Eth series Dehyd and freeze-drying.

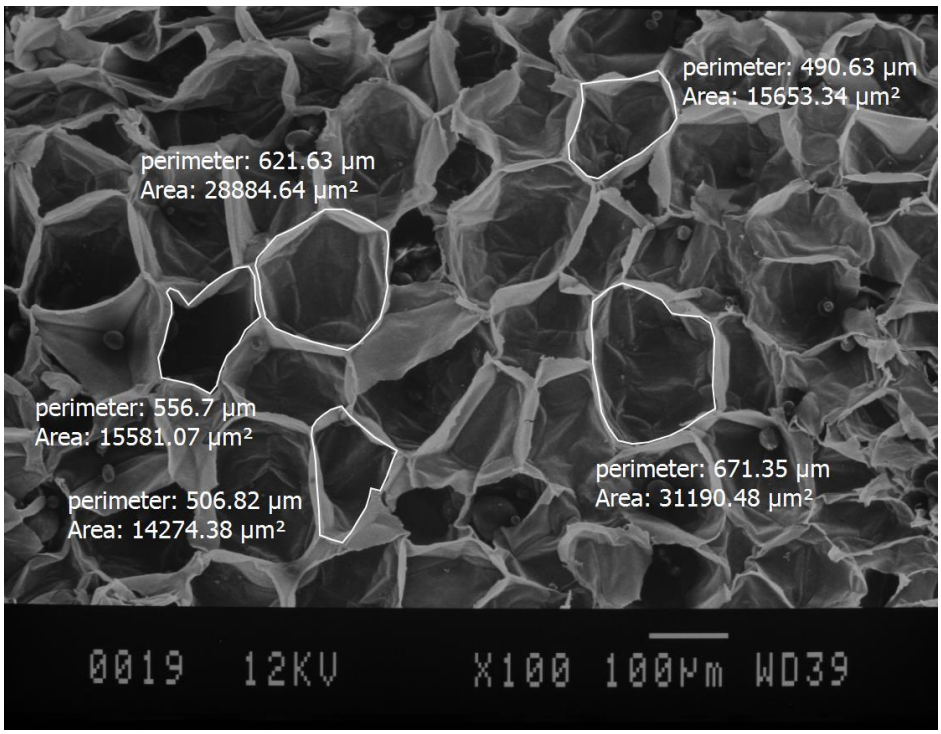

Figure 3. SEM image for method of 2.5% Gl Fix, Eth series Dehyd and HMDS drying (5 min).

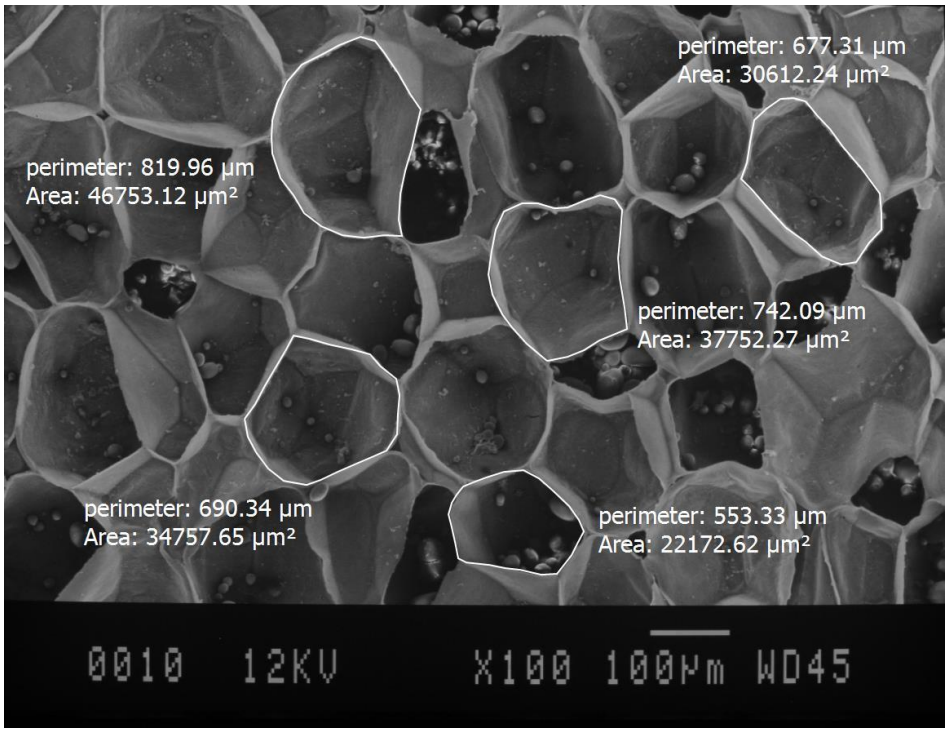

Figure 4. SEM image for method of 2.5% Gl Fix, Eth series Dehyd and HMDS drying (overnight).

LS7.P008
High-resolution microscopy of waxes and self-healing after wax removal on leaves of Eucalyptus gunnii

M. A. Huth[1], A. Hinnemann[1], K. Koch[1]

[1]Hochschule Rhein-Waal, Life Sciences, Kleve, Germany

miriam-anna.huth@hochschule-rhein-waal.de

Introduction: The outermost interface of plants is built by the cuticle and its waxes. Plant waxes form varying three dimensional micro and nano structures. The main role of this multifunctional interface is the limitation of water loss and many other lifesaving features such as the reflection of harmful radiation. To maintain this vital functionality some plants are able to heal voids in their waxes after wax removal.
Objectives: Here the morphology and allocation of wax on *Eucalyptus gunnii* leaves in different developmental stages were investigated by field emission scanning electron microscope (FE-SEM). The wax regeneration ability after partial wax removal was characterized over a time period of 7 days.
Materials and Methods: Wax structures were investigated on adaxial sides of young, medium aged and mature leaves of *E. gunnii*. Investigations were performed with FE-SEM (Gemini Supra 40VP, Zeiss, Oberkochen, Germany). Leaves were prepared by glycerol-liquid-substitution and sputter coated with gold (108auto SE, Cressington, Watford, UK). To quantify the allocation of wax SEM micrographs were transformed into binary images by ImageJ (Wayne Rasband, version 1.46). The level of wax allocation was calculated by measuring the ratio of white to black pixels (fig. 1). The regeneration of waxes on *E. gunnii* leaves was investigated 1, 3, 5 and 7 days after mechanical dewaxing with glue.
Results: Morphology of waxes on *E. gunnii* leaves
Three different types of wax structures were found on every investigated leaf age: smooth tubules (ß-diketone type, fig. 2a), a transitional form of tubules (fig. 2b) and helically wound ribbons (fig. 2c). The tubules had a hollow structure with openings at their ends, an inner diameter of 0.04 µm ± 0.01 µm and an outer diameter of 0.14 µm ± 0.02 µm (n=20). Tubules were 1.5 µm to 4 µm long, bended or straight and often branched in acute angles. Transitional tubule forms and helically wound ribbons were both bended and coiled. Transitional tubule forms were tightly coiled, forming an almost hollow cylindrical tubular like structure. In top view their endings were ring or kidney shaped. The coiling of helically wound ribbons had a less narrow winding than the transitional form without a ring closure at the tip of the tubule like structure. The wax allocation differed between leaves of different ages. Mature leaves showed the highest wax allocation (53.37 % ± 4.29 %) compared to medium aged leaves (46.03 % ± 6.96 %) and young leaves (42.47 % ± 12.04 %).
Self-healing after wax removal on leaves of *E. gunnii*
Leaves of all different ages showed regeneration of similar wax structures on dewaxed areas. The regenerated waxes showed the same morphologies as the native waxes. One day after wax removal tubular waxes were visible. The number of regenerated tubular waxes increased until day 5 after dewaxing on leaves of all investigated ages. On day 7 the number of regenerated tubules remained constant.
Conclusion: In this study typical ß-diketone tubules, helically wound ribbons and a transitional form of both were detected on *E. gunnii* leaves. Leaves in different developmental stages showed the same wax morphologies but differed in the amount of wax allocation. The combination of recording with In-lens detector and processing micrographs into binary images might be a useful tool for future wax allocation analysis by FE-SEM. *E. gunnii* is able to regenerate its waxes. Regeneration occurs on young as well as on mature leaves. There were no differences in the number of regenerated wax tubules on leaves in different developmental stages.

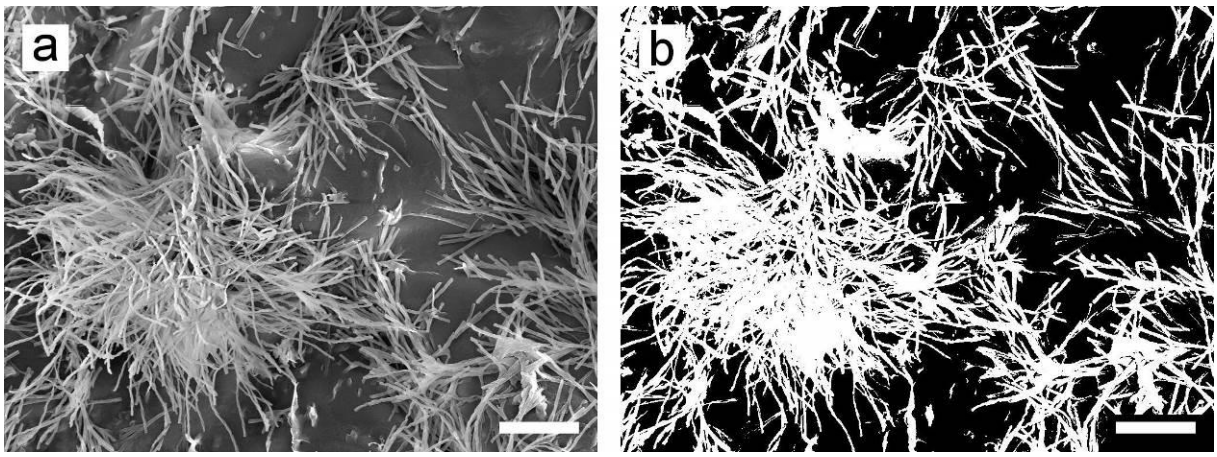

Figure 1. Determination of wax allocation - a: In-lens SEM micrograph; b: same micrograph after processing into binary image - scale bars: 5 µm.

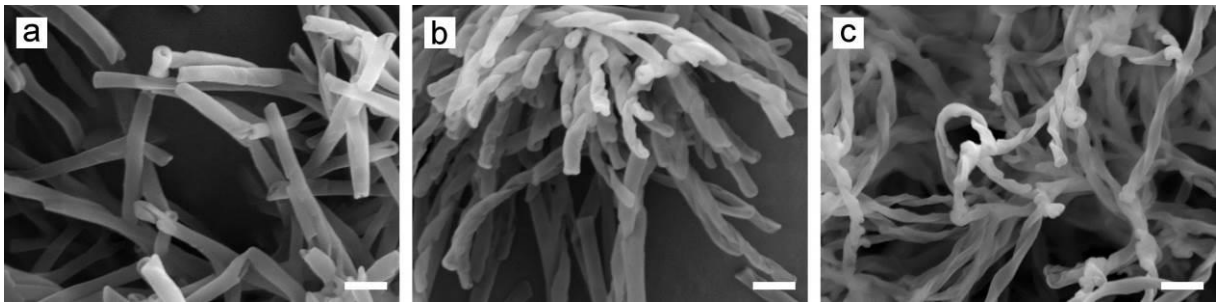

Figure 2. SEM micrographs of wax tubules - a: smooth tubule; b: transitional form; c: helically wound ribbon - scale bars: 400 nm.

LS7.P009
EBL Patterns for localization and observation of embryonal cells

M. Hrabovský[1,2], J. Pospíšil[3,4], R. Váňa[1], J. Jaroš[3,4]

[1]Tescan Brno s. r. o., Brno, Czech Republic
[2]Brno University of technology, Faculty of Electrical Engineering and Communication, Department of Microelectronics, Brno, Czech Republic
[3]Masaryk University, Faculty of Medicine, Department of Histology, Brno, Czech Republic
[4]St. Anne`s Hospital, International Clinical Research Centre (ICRC), , Brno, Czech Republic

milos.hrabovsky@tescan.cz

Introduction: Natural clusters of cells are composed of extracellular matrix and cell-cell interactions [1]. These components play crucial roles in biological processes including proliferation, adhesion and differentiation. For a better understanding of cell-cell contact at the level of single receptor-ligand interactions it is necessary to use a sophisticated system with nanometre-scale distributions of bioactive molecules [2].
Objectives: The goal of this study is to demonstrate the preparation of biological samples for localization of specific cell-types and to show that embryonal cells only stick to the predefined pattern, so they can be later observed and studied for a variety of biological applications. We also show that there is a difference between applying PEG polymer to help the passivation of the surface so that the linker-protein sticks only to the Pt pads.
Materials and Methods: The substrate used in this work was a circular glass slide with a diameter of 12 mm with a 20 nm layer of ITO deposited on top. The sample was spin coated with the adhesion promoter AR 300-80 and with CSAR 62 to a thickness of 200 nm. The sample was then patterned using electron beam lithography with a current of 325 pA, a working distance of 9 mm, a write-field of 100 µm and a step size of 20 nm. After exposure development using amyl acetate for 1 minute, 20 nm of Pt were deposited on top of it and NEP was used to lift-off the final design (Fig. 1) [3]. After the cleaning the surface in deionized water, PEG polymer was applied followed by application of the immobilization protein (Fig. 2).
Results: The Pt pads on the ITO surface had very good adhesion to the linker-protein and thus to the embryonal cells themselves, but the linker-protein also showed a detectably large adhesion to the ITO surface itself. This creates localization centres outside of the desired patterns and this was resolved by additional functionalization of the surface using PEG polymer. It selectively blocks the bond between ITO and the linker-protein but does not affect the Pt – linker-protein bond. Figure 3 shows a patterned surface after all the treatments, with one localized embryonal cell on the Pt pads and the rest of the cells in a state of decay or already dead.
Conclusion: The addition of PEG polymer functionalized the patterned surface, ensuring that the linker-protein only bonds to the Pt pads, thus the embryonal cells are only present in the predefined areas of interest.

References:
[1] F. Gattazo, A. Urciuolo, P. Bonalrdo, Biochim Biophys Acta 1840(8). 2506 (2014)
[2] A. Curtis, Ch. Wilkinson, Topographical control of cells, Biomaterials 18 (24), 1573 (1997)
[3] J. Pospíšil, R. Váňa, M. Hrabovský, et. al., DACH-FIB Workshop 11 (2016)[Poster]
[4] J. Pospíšíl, M. Hrabovský, J. Jaroš, EBL patterned surface preparation (2017)[unpublished work]
[5] This work was supported by the Technology Agency of the Czech Republic project No. TE01020233

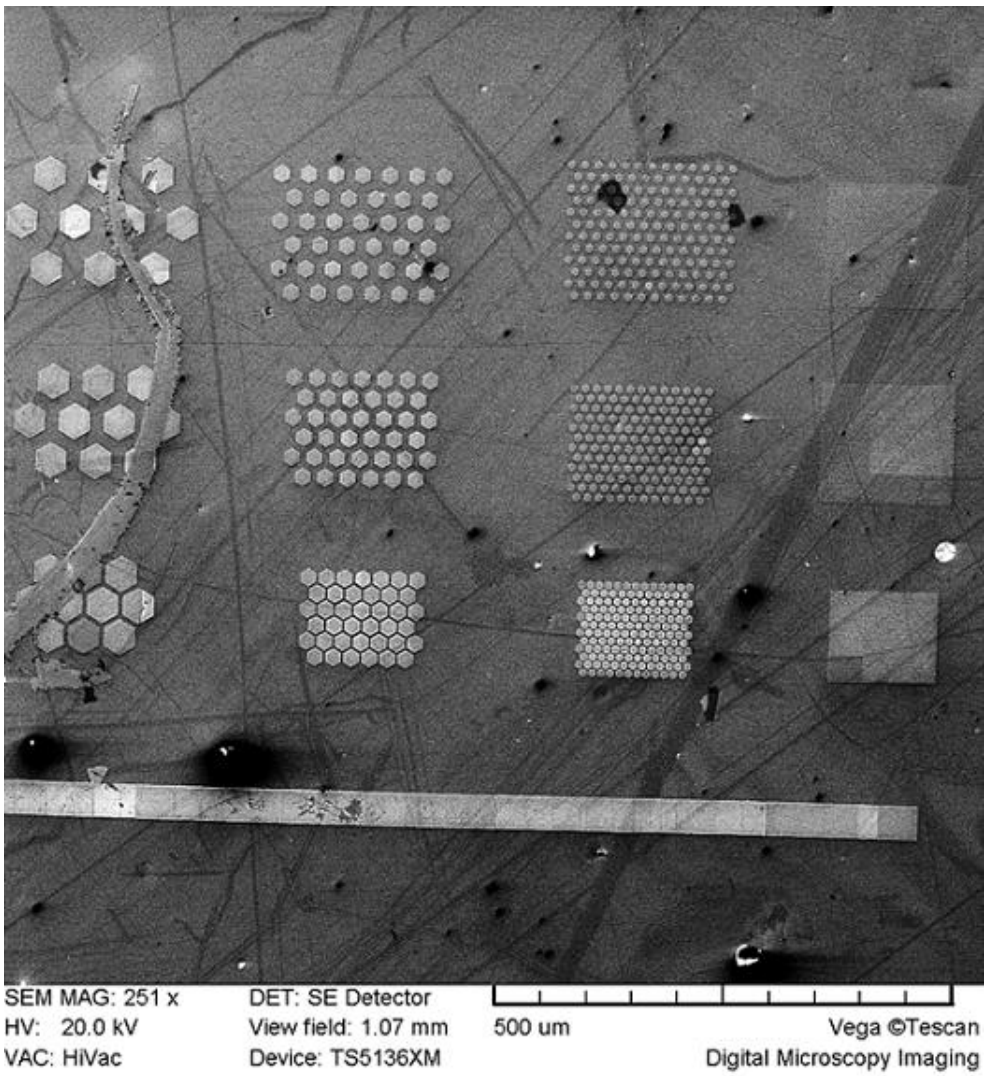

Figure 1. Patterned surface after the deposition of Pt and lift-off in NEP. The distance between the pads increases from the bottom to the top and the actual size of the pad decreases from left to right [4].

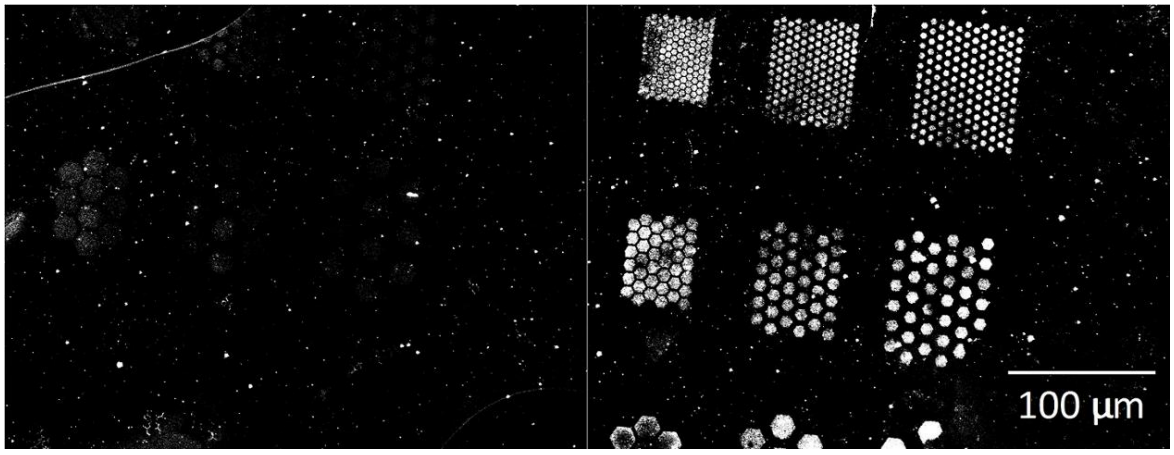

Figure 2. Fluorescence microscopy images of the surface before (left) and after (right) PEG polymer and linker-protein treatment [4].

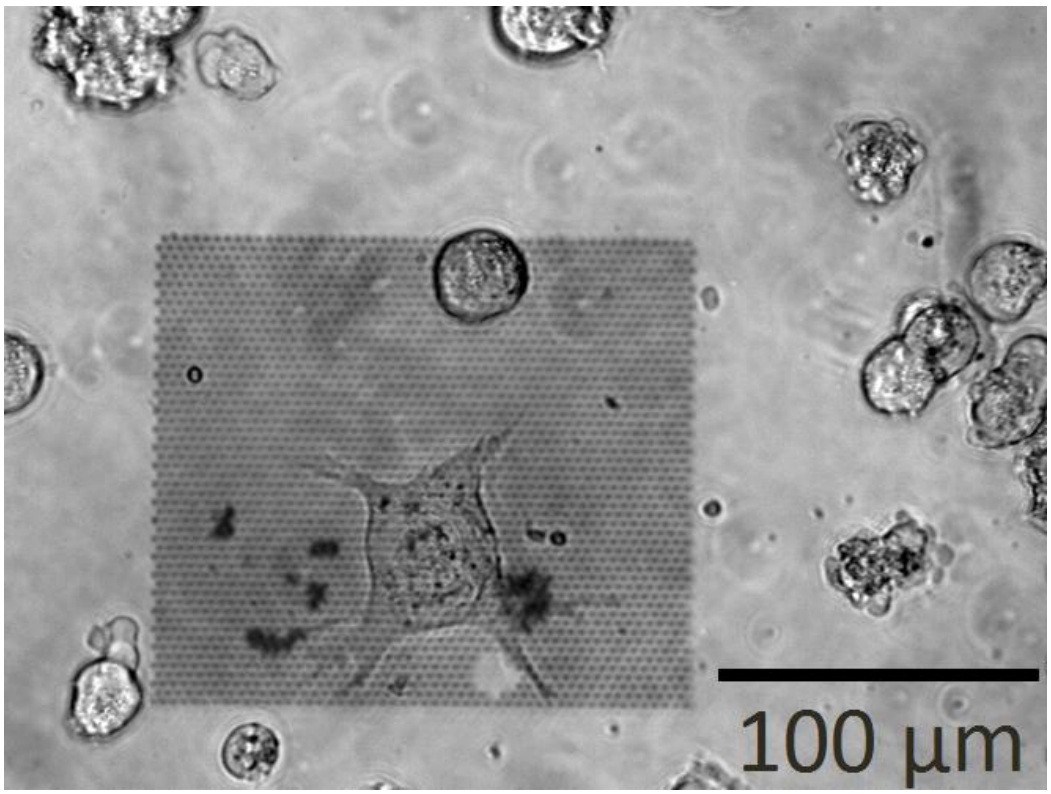

Figure 3. Embryonal cell localized on the surface of the micropattern [4].

LS7.P010
Water soluble gold nanoparticles – a new tool in amyloid research

U. Cendrowska[1], P. J. Silva[1], S. Vieweg[1], A. Chiki[1], H. Lashuel[1], F. Stellacci[1]

[1]EPFL, Lausanne, Switzerland

urszula.cendrowska@epfl.ch

Introduction: Amyloid fibrils are highly ordered, insoluble filamentous protein aggregates which originate from soluble proteins and peptides. All of amyloid fibrils posses common feature with cross β-sheet structure, meaning that β-strand segments run perpendicular to the fibril axis. This motif is shared for all amyloids regardless of their constituent polypeptide. These aggregates are linked with several neurodegenerative disorders, e.g., Parkinson"s disease, Huntington"s disease and Alzheimer"s disease. Various techniques have been applied to characterize and study properties of amyloids; however, this task still remains complex. We believe, that nanoparticles are potential tool in amyloid studies where they can be applied as a probing tool and contrast agent for Electron Transmission Microscopy (TEM). We have found that amphiphilic gold nanoparticles protected by sulfonated (11-mercapto-1-undecanesulfonate) and hydrophobic (1-octanethiol) ligands can discriminatively adsorb onto surface of amyloid fibrils made of two proteins: exon 1 huntingtin and α-synuclein.
Objectives: Use of specific interactions between nanoparticles and surface of amyloid fibrils in order to develop new contrast agent for TEM. Another objective is to verify our nanomaterial as a probing tool for molecular studies of amyloid fibril structure.
Materials and Methods: We synthetized gold nanoparticles with diameter size ranging from 1 to 6 nanometers. Gold core of these nanoparticles was protected by ligand shell consisted of 11-mercapto-1-undecylosulfonate (MUS) and 1-octanethiol (OT) in different ratios. We incubated our nanomaterial with different types of amyloids. In this studies we used mature amyloid fibers made from exon 1 huntingtin, alpha synuclein and their truncated versions. Images of fibrils and nanoparticles were taken with use of cryogenic electron microscopy.
Results: Our group established how different types of water soluble gold nanoparticles interact with different types of amyloid fibrils. We show that our engineered nanomaterial interacts with biological structure without the use of antibodies. This system can be used as a useful marker for electron microscopy imaging of proteins in the amyloid state.
Conclusion: Nanoparticles synthetized in our group can be considered as a new class of material that can be used in amyloid research not only for imaging techniques but also for molecular structure determination.

References:
[1] Knowles TPJ, Vendruscolo M, Dobson CM. The amyloid state and its association with protein misfolding diseases. Nat Rev Mol Cell Biol 2014;15:384-396.
[1] Uzun O, Hu Y, Verma A, Chen S, Centrone A, Stellacci F. Water soluble amphiphilic gold nanoparticles with structured ligand shells. Chem Commun 2008;196-198.

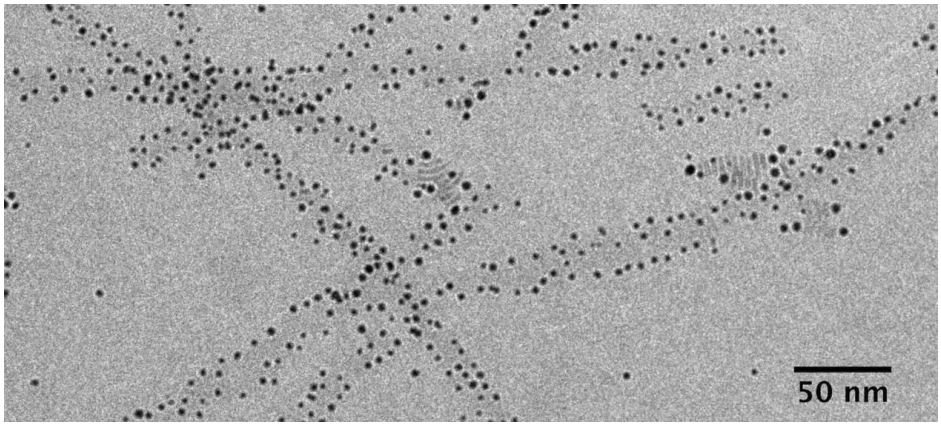

Figure 1. Cryo TEM image of full length exon 1 huntingtin 42Q amyloid aggregate decorated by allMUS gold nanoparticles.

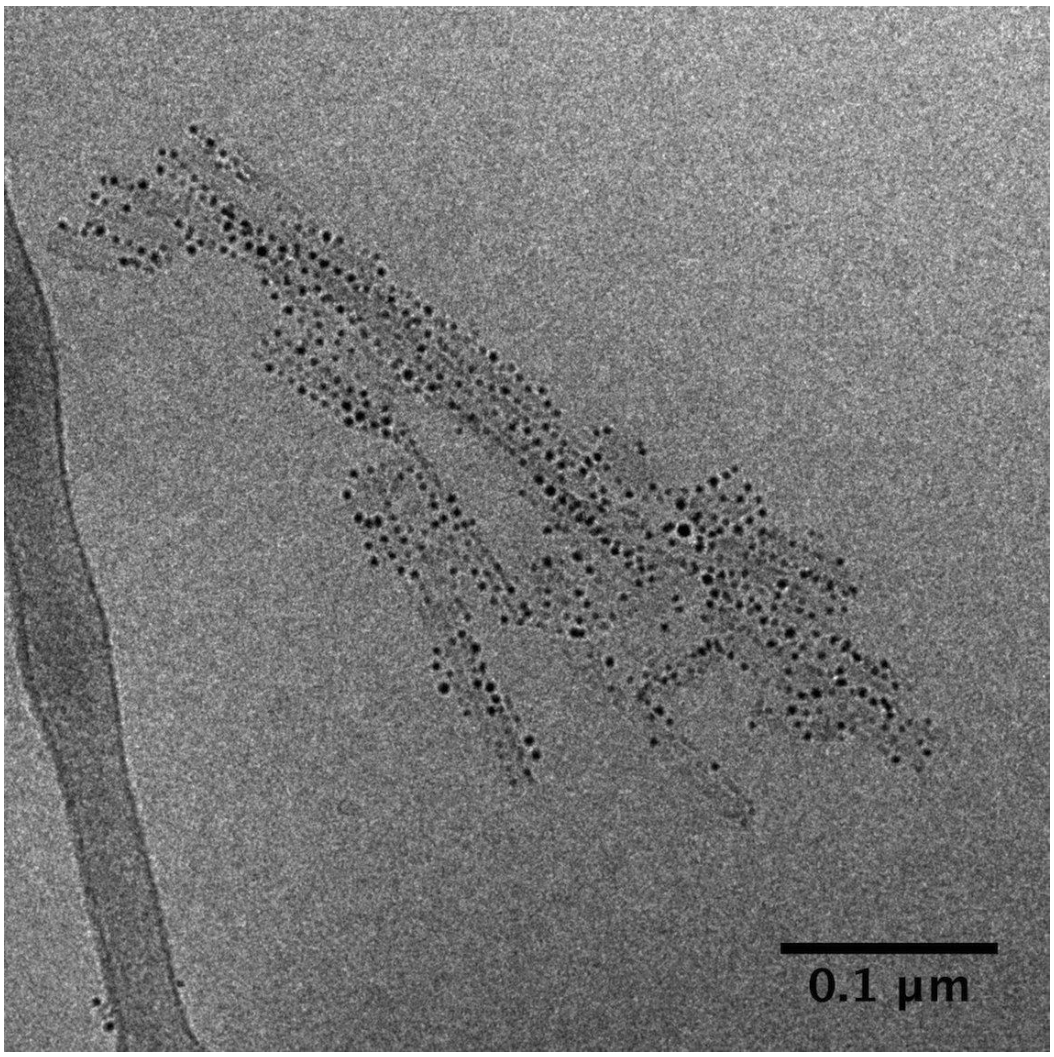

Figure 2. Cryo TEM image of C-terminus truncated α-synuclein amyloid aggregate decorated by 7:3 MUS:OT ratio gold nanoparticles.

LS7.P011
Pre-embedding immunogold EM localizes Major Basic Protein-1 (MBP-1) in subcellular compartments from eosinophils during the experimental acute Schistosoma mansoni infection

F. Ferraz Dias[1,2], K. Karoline Malta[2], K. Batista Amaral[2], P. Fahey Weller[3], R. Correa Netto de Melo[2,3]

[1]UFMG, Center of Microscopy, Belo Horizonte, Brazil
[2]UFJF, Biology, Juiz de Fora, Brazil
[3]Harvard Medical School, Medicine, Boston, MA, United States of America

ffdias@gmail.com

Introduction: Schistosomiasis mansoni is a well known parasitic disease caused by the trematoda species *Schistosoma mansoni* which triggers exsudative granuloma formations [1]. Eosinophis, cells of the innate immune system, play effector functions against parasite eggs through the release of secretory granule-derived products. These granules exhibit a unique and distinct ultrastructure, and store a plethora of preformed cytokines and cationic proteins mainly Major Basic Protein-1 (MBP-1) [2]. Release of MBP-1 by eosinophils is a key event in the pathogenesis of helminthic infections [3], but little is known about the secretory processes of MBP-1 from eosinophils in response to these infections.
Objectives: Here, we used a pre-embedding immunonanogold technique for superior detection of MBP-1 at subcellular compartments of eosinophils in a mouse model of *S. mansoni* infection. Materials and Methods: Female Swiss mice (n=4) were infected with 100 cercarie of *S. mansoni* percutaneously. Animals were euthanized after 55 days post-infection (acute phase) and liver fragments were processed for histological analyses and both conventional transmission electron microscopy (TEM) and immunogold EM (*immunonanogold*) [4].
Results: A well-characterized granulomatous inflammatory response with a high number of infiltrating eosinophils surrounding the *S. mansoni* eggs was observed in the hepatic granulomas of infected mice. TEM revealed piecemeal degranulation (PMD) as the major eosinophil degranulation processes in the *S. mansoni*-infected livers (Fig. 1A, B). PMD was identified by morphological changes of specific granules (enlargement, reduced electron-density, core disarrangement and coarse granule matrix) and presence of a high number of cytoplasmic vesicles, indicative of a vesicle-mediated transport of granule-stored products. Immunogold EM showed a consistent labeling for MBP associated with secretory granules in process of PMD (Fig. 1C, D, E, F). Moreover, extragranular sites of MBP were identified. MBP was present within vesicles distributed in the cytoplasm and attached to or surrounding the surface of emptying granules. Extracellular MBP deposition was also observed (Fig. 1A).
Conclusion: Our study demonstrates, for the first time, a vesicular trafficking of MBP-1 within eosinophils elicited by the helminthic infection. These extragranular sites may be relevant for the rapid release of small concentrations of MBP under cell activation. However, the impact of the selective secretion of MBP-1 on the direct defense against the parasite or regulation of other immune responses awaits further investigation.

References:
[1] Gryssels (2012). *Infect Dis Clin N Am*, 26(2): 383–397
[2] Spencer *et al.* (2014). *Frontiers in Immunology*, 5(496): 1–9
[3] Melo *et al.* (2009). *Laboratory Investigation*, 89:769–781
[4] Melo *et al.* (2014). *Nature Protocols*, 9(10): 2382–2394

Supported by CAPES, CNPq, and FAPEMIG (Brazil) and NIH (USA)

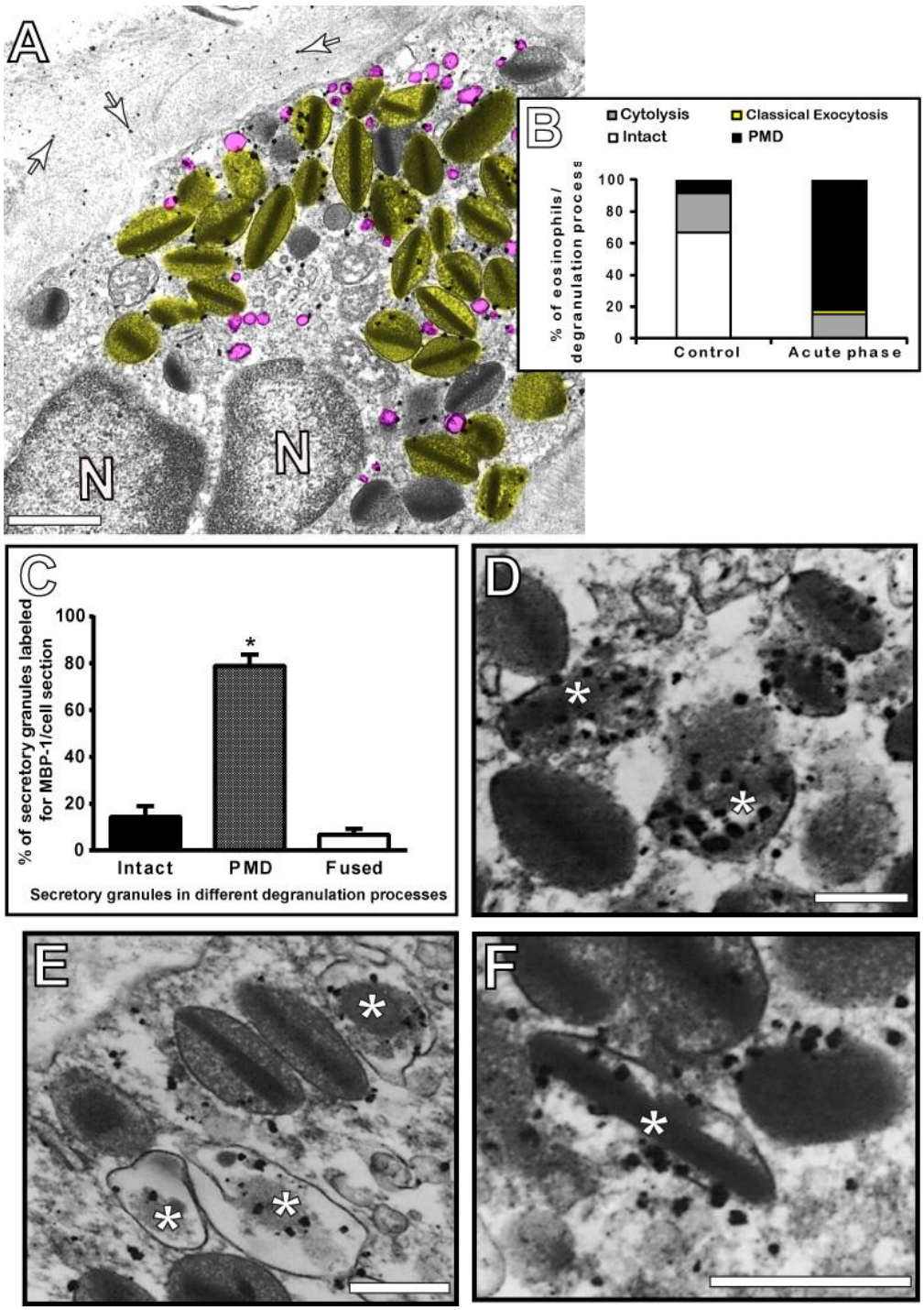

Figure 1. (A) Electron micrograph of an eosinophil in process of piecemeal degranulation (PMD) showing ultrastructural changes indicative of granule-content emptying process. Major Basic protein (MBP-1) is labeled within secretory granules (highlighted in yellow), on granule-associated vesicles (highlighted in pink) and in the extracellular matrix (arrows). (B) Quantification of eosinophil degranulation processes by conventional TEM and (C) after immunolabeling for MBP-1. (D, E, F) Eosinophil secretory granules immunolabeled for MBP-1 (*) show different degrees of protein emptying. *: Differences *($p \leq 0,05$)* between granules in different degranulation processes. Liver fragments from *S. mansoni*-infected mice were processed for conventional TEM and pre-embedding immunonanogold EM. N: nucleus. Bar (A): 0.7µm; (D, E, F): 0.4µm.